Crack Coalescence in Molded Gypsum and Carrara Marble

by

Ngai Yuen Wong

BSc., Earth Sciences (1999)
The University of Hong Kong

Submitted to the Department of Civil and Environmental Engineering

in Partial Fulfillment of the Requirements for the Degree of

Doctor of Philosophy in the field of Geotechnical and Geoenvironmental Engineering

at the

Massachusetts Institute of Technology

February 2008

Signature of Author ……..
Department of Civil and Environmental Engineering
October 9, 2007

Certified by …….…….....
Herbert H. Einstein
Professor of Civil and Environmental Engineering
Thesis Supervisor

Accepted by……...
Daniele Veneziano
Professor of Civil and Environmental Engineering
Chairman, Departmental Committee for Graduate Students

Crack Coalescence in Molded Gypsum and Carrara Marble

by

Ngai Yuen Wong

Submitted to the Department of Civil and Environmental Engineering
on October 9, 2007 in Partial Fulfillment of the
Requirements for the degree of Doctor of Philosophy in
the field of Geotechnical and Geoenvironmental Engineering

ABSTRACT

This thesis investigates the fracturing and coalescence behavior in prismatic laboratory-molded gypsum and Carrara marble specimens, which consist of either one or two pre-existing open flaws, under uniaxial compression. In previous experimental studies, the determination of crack types (shear/tensile) was mainly based on the identification of fractographical features on the crack surfaces. In the present study, a high speed video system was used, which allowed one to precisely observe the cracking mechanisms.

Seven crack types, which were characterized by different nature (shear/tensile) and orientations were identified to initiate from the pre-existing flaws in gypsum and marble in the present experimental study. Nine crack coalescence categories with different crack types and trajectories were also identified. The flaw inclination angle (β), the ligament length (L), i.e. intact rock length between the flaws, and the bridging angle (α), i.e. the inclination of a line linking up the inner flaw tips, between two flaws, have all shown to have different effects on the coalescence patterns. Comparing the fracturing and coalescence behaviors in the two tested materials, tensile fracturing generally occurs more often in marble than in gypsum for the same flaw pair geometries.

One of the pronounced differences observed between marble and gypsum during the compression loading test was the development of macroscopic white patches prior to the initiation of macroscopic cracks in marble, but not in gypsum. With the use of the scanning electron microprobe (SEM) and the environmental scanning electron microprobe (ESEM) techniques, the development of white patches and their evolution into macroscopic tensile cracks in marble, and the initiation of hair-line tensile cracks and their evolution into macroscopic cracks in gypsum were studied and compared. The SEM study identified that the white patches in marble were associated with microcracking zones (process zones). The parallel ESEM study on gypsum showed that

the extent of process zone development associated with macroscopic tensile cracking was less. The different extents of process zone development, related to the inherent material strength and textural properties, are hypothesized to be the key factors in leading to different macroscopic fracturing behavior in gypsum and marble.

Thesis Supervisor: Herbert Einstein
Title: Professor of Civil and Environmental Engineering

ACKNOWLEDGMENTS

I would like to thank my advisor, Herbert Einstein, for giving me the opportunity to work on this challenging project, and also for all of his unswerving encouragement and support during my time at MIT. I would also like to thank him for being a great role model for me in pursuing a scientific career and for his enthusiasm in the pursuit of knowledge.

Lallit Anand, Brian Evans and John Germaine are very generous to be in my PhD thesis committee to provide constructive comments and insightful project discussions over the years. Antonio Bobet of the Purdue University offered assistance on the use of FROCK. He also demonstrated to me on how to execute and communicate high quality scientific research. UROP students Margot Spiller, Christopher D'Annunzio and particularly master student James Miller for their assistance with laboratory work. The following people are also especially thanked for their technical assistance in using different pieces of equipment – James Bales, Patrick Boisvert, Nilanjan Chatterjee, Stephen Rudolph and Ken Stone.

Jason Ali, Lung Chan, Raymond Chan, Yun-Cheung Chan, Hugh Choy, Philip Chung, Jimmy Jiao, Aesop Ng, Andrew Malone, John Maplas, Sam Ng, T.K. Tam, H.N. Wong, Robina Wong, Sidney Wong and Peter Yung have all served as excellent my mentors in my geosciences education and early stage of career in Hong Kong. They are thanked for instilling in me an ethic of work and perseverance that was indispensable in completing my PhD study. Cheo K. Lee of the Handong Global University, South Korea, is thanked for offering me an opportunity to work with him and his students for two weeks in Korea.

I am very grateful to the Croucher Foundation and the Sir Edward Youde Memorial Fund for financing my study.

Last but not least, I would also like to thank my family members, fellow group mates and friends, in particular Ivy Lee for her unfailing support over the past years.

Table of Contents

CHAPTER 1 – Introduction

1.1 Problem Statement

The principal objective of this thesis is to understand the crack coalescence processes in rocks and the underlying fracturing mechanisms. The specific issue to address is how and to what extent the material properties and flaw geometries influence the crack coalescence processes.

The study of crack coalescence not only assists structural geologists to better understand how the continental crust deforms and evolves through a better understanding of how cracks evolve and interact, but is also of practical engineering significance. A better understanding of the crack initiation, propagation, interaction and eventual coalescence processes in rock can lead to a more satisfactory characterization and assessment of the overall rock mass behavior and performance. This in turn can benefit geotechnical engineering design and implementation such as rock slope stability assessment, tunnel support design, fluid flow prediction in rock masses, etc.

1.2 Approach

Experimental approaches and theoretical approaches, which have long been relied on to tackle the above problem in the past decades, form the basis of the present research. The research tasks involve mainly experimental and a few numerical studies on pre-cracked prismatic specimens loaded under uniaxial compression.

Different research groups have studied similar problems experimentally with different specimen sizes and flaw dimensions in a wide range of materials types (man-made materials and natural rocks). These preceding studies were however associated with different limitations in experiments and no thorough comparison of all the preceding

results has been comprehensively made. The research approach of the present study is aimed at increasing the understanding of the fracturing and coalescence processes in rock materials. Specifically, the research involves the following key tasks:

- To conduct experimental tests on molded gypsum specimens and Carrara Marble with the same specimen and flaw dimensions, and also under the same experimental set-up.

- To observe the fracturing processes in detail with the use of the high speed camera, particularly to determine the nature (shear/tensile) of the new cracks and the crack development sequence.

- To conduct SEM (scanning electron microscope) and ESEM (environmental scanning electron microscope) imaging studies on marble and gypsum, respectively, to study the cracking and deformation processes on a microscopic scale, and to correlate these observations with the macroscopic observations.

- To generalize the influence of various flaw parameters on the overall coalescence processes and patterns.

- To use the in-house computer code FROCK for some numerical modeling studies.

1.3 Organization of the dissertation

The issues mentioned in the previous section are addressed in the following chapters within this thesis:

- Chapter 2 provides further background of the past studies.

- Chapter 3 reviews the high speed video recordings obtained by Martinez (1999) on fracturing and coalescence processes in Vermont White Marble.

- Chapter 4 describes the specimen preparation procedures and the experimental details of the uniaxial compression tests to be conducted for the present thesis.

- Chapters 5 and 6 summarize the results of the experimental studies obtained from the uniaxial compression tests on specimens containing single flaws and double flaws respectively.

- Chapter 7 describes SEM and ESEM work conducted on marble and gypsum respectively. The objective is to study the cracking and deformation processes on a microscopic scale, and to correlate these observations with the macroscopic observations described in previous chapters.

- Chapter 8 summarizes the numerical work investigating the sensitivity of the cracking processes to input parameters by using the computer code FROCK.

- Chapter 9 discusses the crack coalescence problem as a whole. It tries to establish a correlation between the macroscopic observations made from video recordings (chapters 5 & 6) and the microscopic observations made from the SEM and ESEM studies (chapter 7). The different macroscopic cracking and deformation behaviors regarding process zone development, tensile crack initiation and shear crack initiation due to the material influence are attempted to be explained by the differences in inherent material properties and texture. The crack type classification scheme and the crack coalescence classification scheme proposed in this thesis are also discussed, with an emphasis placed on the material and geometrical influences on cracking and coalescence patterns.

- Chapter 10 offers a summary and conclusions of the present investigation. A section of recommendation for future research is also provided.

CHAPTER 2 – Background

2.1 Introduction

This chapter provides the background of the past research in fracture mechanics, and specifically in crack coalescence. In the first part, the development in theoretical fracture mechanics is briefly described. The second part focuses on the three major approaches (analytical, numerical and laboratory experimental) for crack coalescence study. In the final part, relevant research on the field occurrence of tensile wing cracks, anticracks and crack coalescence are described. These parts not only highlight crack coalescence is a quite common phenomenon in nature, but also indicate the relevant challenges involved in different approaches in tackling with this problem.

2.2 Background

Fracture is a problem that society has faced for as long as there have been man-made structures (Anderson, 2005). In the analysis of an elliptical hole (2*a* long, 2*b* wide) embedded in an infinitely large flat plate subjected to an applied stress perpendicular to the major axis of the ellipse (figure 2.1a) provided by Inglis (1913), the stress at the tip of the major axis at point A is given by

$$\sigma_A = \sigma\left(1+\frac{2a}{b}\right) \tag{2.1}$$

The above expression implies that σ_A depends on the ratio, instead of the absolute size, of the elliptical opening. Equation (2.1) is more conveniently expressed as

$$\sigma_A = \sigma\left(1+2\sqrt{\frac{a}{\rho}}\right) \tag{2.2}$$

where ρ is the radius of curvature and is equal to b^2/a. Further approximation to equation (2.2) can be made for a sharp flaw in which the flaw major axis is much longer than its minor axis, i.e. $a >> b$,

$$\sigma_A = 2\sigma\sqrt{\frac{a}{\rho}} \tag{2.3}$$

The above expression suggests that at **sharp** flaw tip, stress concentration is more significant for longer flaw length (large value of a).

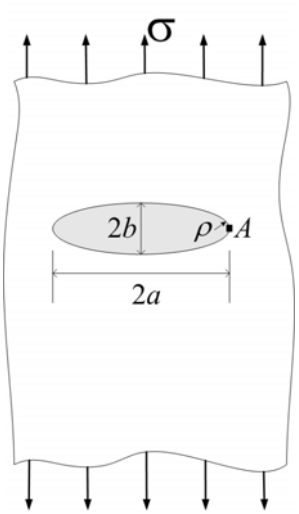

Figure 2.1a – An elliptical flaw of length 2*a*, width 2*b* embedded in an infinitely wide plate subjected to a far-field tensile stress σ.

Based on the first law of thermodynamics, an energy balance fracture theory was proposed by Griffith (1920) to account for the relationship between the strength and the flaw size in glass specimens. Consider a pre-existing flaw of length *2a* embedded in a sufficiently large plate, which is subjected to a constant tension stress σ (figure 2.1b). Sufficient potential energy must be available to overcome the surface energy of the material in order for the flaw to increase in length. The above statement is formulated for an incremental increase in the flaw area *d*A as:

$$\frac{dE}{dA} = \frac{d\Pi}{dA} + \frac{dW_s}{dA} = 0 \tag{2.4}$$

$$-\frac{d\Pi}{dA}=\frac{dW_s}{dA} \tag{2.5}$$

where

E = total energy

Π = potential energy supplied by the internal strain energy and external forces

W_s = work required to create new surfaces

where

$$W_s = 4aB\gamma_s \tag{2.6}$$

γ_s = surface energy of the material

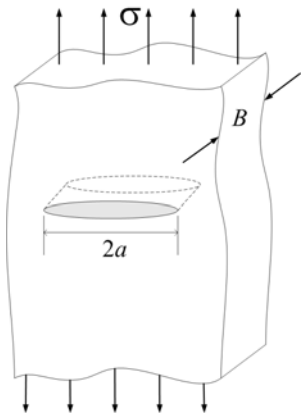

Figure 2.1b – An elliptical flaw of length 2*a* embedded in an infinitely wide plate subjected to a far-field tensile stress σ.

The potential energy Π is given by the following relationship

$$\Pi = \Pi_o - \frac{\pi\sigma^2 a^2 B}{E} \tag{2.7}$$

where Π_o is the potential energy of the uncracked plate and B is the plate thickness.

Differentiating equations (2.6) and (2.7) and using equation (2.4), the stress required for crack propagation (σ_f) is given by

$$\sigma_f = \sqrt{\frac{2E\gamma_s}{\pi a}} \tag{2.8}$$

Note that the Griffith energy balance relationship (2.8) predicts that fracture strength is inversely proportional to the square root of the flaw length for an infinitely sharp crack.

The Griffith energy balance concept was extended by Irwin (1956) to formulate the energy release rate concept. Irwin (1957) later showed that the stresses and displacements around a flaw tip can be expressed in terms of a stress-intensity factor K, which can be related to the energy released when the crack grows infinitesimally. Since that time, a number of crack initiation criteria have also been proposed to predict the **initiation angle** of a new crack initiating from a pre-existing flaw and the corresponding required **load** under a mixed mode I-II loading condition (figure 2.2), instead of the simple tension loading situation as illustrated in figures 2.1a and b. These criteria can be generally classified into three main types based on the physical quantities being considered – **energy-based, stress-based** and **strain-based** (table 2.1).

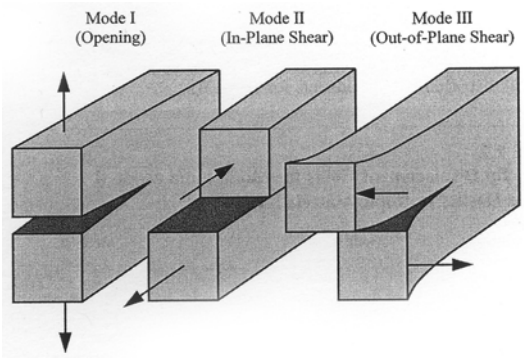

Figure 2.2 – Three loading modes applied to a crack (Anderson, 2005).

The idea of **energy-based criteria** is similar to the Griffith's energy balance theory that a new crack will initiate or continue to propagate if the amount of released potential energy for an incremental increase in the crack area *d*A is greater than the total amount of work requited to create the crack area *d*A. The idea of the **stress-based criteria** is that a new crack will initiate in the most vulnerably oriented (critical) flaws in a population of

randomly oriented flaw if a large enough local stress is available to overcome the local material strength. The idea of **strain-based criteria** is similar to that of the stress-based criteria as the stress tensor and the strain tensor can be conveniently related to each other constitutively. In the literature, the three most commonly used criteria are the maximum tangential stress criterion (Erdogan & Sih, 1963), the maximum energy release rate criterion (Hussain et al., 1974) and the minimum strain energy density criterion (Sih, 1973, 1974).

Due to the presence of a stress singularity and hence the inability of linear elastic fracture mechanics to define the stress state at the and in the immediate vicinity of the sharp flaw tips, a core region is often assumed to be present at the flaw tip. The boundary of the core region separates the inside material which is believed to be a plastic zone from the outside material which is assumed to behave elastically. As also shown in table 2.1, some crack initiation criteria are listed as CR, indicating that they use a constant core radius, while some criteria are listed as VR use a variable core radius. As reported by Khan and Khraisheh (2004), if the core region is assumed to have constant core radius, the crack initiation angle is then independent of the radius '*r*' when a singular elastic stress field (see equation (1) of appendix Q) is used and the higher-order non-singular terms are ignored at the flaw tip. The authors continued to state that "*if non-singular terms (independent of r in the denominator) are added to the elastic solution in conjunction with the singular elastic field, then the value of 'r' affects the crack initiation angle.*" For those criteria which use a variable core radius (VR), the elastic-plastic boundary is often defined along a contour of constant distortional strain energy (maximum dilatational strain energy criterion, maximum stress invariant function, modified max tangential stress criterion). Since the core radius varies around the flaw tip, the value of '*r*' certainly affects the crack initiation angle.

As further shown mathematically by Khan and Khraisheh (2004), the actual size of the core region is dependent on two parameters – the initial flaw length and the applied load. As the flaw propagates to lengthen, the size of the core region also increases. For a fixed

flaw length, the size of the core region grows with the square of the ratio (σ_{app}/σ_{YS}), where σ_{app} is the applied stress and σ_{YS} is the tensile yield strength.

Except for the two criteria proposed previously by the MIT rock mechanics group, which will be discussed separately in chapter 8, refer to appendix Q for the underlying principles and the mathematical details of other crack initiation criteria as shown in table 2.1. See also Qian and Fatemi (1996), Khan and Khraisheh (2000, 2004) for reviews of some of these criteria. As observed by the above authors, there is no single criterion which can give satisfactory predictions under all loading conditions (modes I, II, III). Experimental results which do not agree with the predictions can often be found.

Energy-based	**Stress-based**	**Strain-based**
CR – max energy release rate (G)	CR – max tangential stress (MTS)	max tensile principal strain (MTPSN) [(2)]
CR – min strain energy density (S)	VR – modified max tangential stress (modified MTS)	
VR – max dilatational strain energy (T_v)	CR – zero shear stress ($\tau_{r\theta}$)	
VR – max stress invariant function (I_p)	CR – max stress triaxiality (M)	
J contour integral (J)	CR – critical tensile strength & critical shear strength [(1)]	

Note : [(1)] criterion proposed by MIT rock mechanics group (Bobet, 1997, Bobet & Einstein, 1998b)
[(2)] criterion proposed by MIT rock mechanics group (Reyes, 1991, Reyes & Einstein, 1991)
CR – core region is a circle with a constant radius
VR – core region with a variable radius

Table 2.1 – Summary of crack initiation criteria (for details see appendix Q).

Later research focus shifted from linear elastic fracture mechanics to crack-tip plasticity, especially to account for the yielding at the flaw tip (e.g. Irwin, 1961, Dugdale, 1960, Barenblatt, 1962, Wells, 1961). One of the most notable developments was the work on the characterization of the nonlinear material behavior ahead of a flaw by Rice (1968), who expressed the nonlinear energy release rate as a path-independent line integral. This integral has then been known as *J* integral. See appendix Q for the formulation of the *J* integral. The recent development in fracture mechanics has focused on the application of fracture mechanics to time-dependent nonlinear material behavior such as viscoplasticity and viscoelasticity (Anderson, 2005).

The present thesis focuses on the fracturing and coalescence behavior of man-made rocks and natural rocks. Although liner elastic fracture mechanics had often been considered applicable in characterizing the fracturing behavior of rocks due to its more pronounced *brittle* nature as compared to metal, they are actually *quasi-brittle* materials. Inelastic material deformation in metals occurs as *plasticity*, but it is due to microcracks in rocks and concrete (Anderson, 2005). There has been considerable recent effort in identifying the presence of fracture-process zones (inelastic material deformation) in front of flaw tips (Friedman et al., 1972, Segall & Pollard, 1983). As stated by Maji and Wang (1992),

> *The fracture-process zone may consist of microcracking ahead of the propagating crack and traction forces behind the crack tip, due to crack bridging. These traction forces transmitted across the crack influence the stress concentrations in the vicinity of the crack tip.*

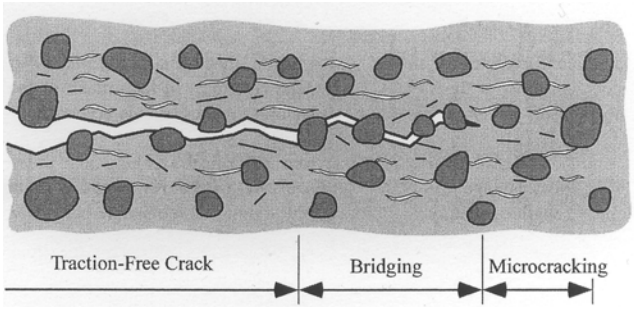

Figure 2.3 – Schematic illustration of a fracture-process zone ahead of a crack in concrete (Anderson, 2005).

The length of the process zone induced ahead of a propagating fracture is assumed to have a maximum length equal to 10% of the length of the pre-existing flaws (An & Sammis, 1996). The formation of a fracture-process zone, which is schematically illustrated in figure 2.3 ahead of a flaw tip, can be accounted for by using the cohesive zone model (Dugdale, 1960, Barenblatt, 1962), e.g. Hillerborg (1976, 1991) in concrete and Reyes (1987) in rock. As it will be shown in chapter 8, the presence of the fracture-process zone has also been considered in the MIT in-house computer code FROCK (Bobet & Einstein, 1998b). A core region of process zone with a constant radius is assumed to exist around the flaw tip. Stresses are computed along the boundary of this region, which are then compared against the crack initiation criteria. See further details in chapter 8.

To experimentally investigate the deformation and fracturing behavior of open flaws embedded in natural rocks, through-specimen artificial flaws are usually first created by means of drilling and sawing. The dimensions and quality of the flaws hence obtained vary among different research groups[1]. Nonetheless, it is always difficult (or impossible) to create and test the classic mathematical sharp flaws in natural rocks. The tested flaws were usually of a finite flaw aperture size and of a blunt/rounded flaw tip. A very obvious mechanical consequence is that stresses at flaw tips become finite, i.e. the stress singularity is removed, which is conventionally considered to be present in the classical linear elastic stress analysis of sharp flaws.

As will be discussed in chapter 8, the numerical code FROCK, which is used in the present study for modeling fracturing and crack coalescence processes in rock, a plastic zone of a finite radius is incorporated in the code to take into account of the inelastic material deformation ahead of the flaw tips. Since the code is formulated based on the Dispalcement Discontinuity Method (DDM), flaws are modeled as linear features and flaw tips are hence considered to be sharp. However, it would be of a great scientific interest if the code could be modified in a way as to take into account of blunt/rounded flaw tips. Although this research task is out of the scope of the present thesis, a brief

[1] Refer to section 2.7 for the various laboratory procedures adopted in previous researches.

literature review was carried out to identify some of the existing approaches that may serve as foundation for future work. See below.

2.3 Stress distribution around a rounded flaw tip

In most of the conventional treatments in the fracture mechanics literature, the pre-existing flaws are assumed to have the major axis much longer than the minor axis ($a >> b$) and the flaw tip is infinitely sharp, i.e. $\rho \rightarrow 0$ as illustrated in figure 2.1. In the present experimental study, two flaw aperture sizes of 0.05" and 0.004" were tested, which correspond to a/b ratios of 10 and 125 respectively (flaw length was 0.5"). Besides, the tips of the tested open flaws had rounded tips. These experimental dimensions appear to be incompatible with the sharp flaw tip assumption. To provide a better understanding of the mathematical treatment of rounded flaw tips and the associated fracturing behavior, a brief literature review on this subject was conducted (appendix R). Two different approaches are found to be commonly used to characterize the engineering behavior of flaws with rounded tips.

In the first approach, which is based on the pioneering work of Inglis (1913) and Griffith (1924), stresses are computed around open flaws which are modeled as elliptical flaws under compression (Hoek, 1968, Jaeger & Cook, 1969, Lajtai, 1970). When the major flaw axis is significantly longer than its minor axis, the engineering behavior of the flaw is then often characterized by the flaw length and the radius of curvature of the flaw tip. However, when the major and minor axes have a similar order of magnitude, the above approximation cannot be made and the roundness/sharpness of a flaw tip is simply characterized by the ratio of the minor to the major axis of the flaw. In other words, it is the ratio between the flaw aperture size and the flaw length which determines the stress distribution along the perimeter of the flaw and hence the overall behavior of the flaws.

In the second approach, the sharpness of the flaw tip is characterized by the root radius ρ of the flaw tip. The stress field ahead of flaw tips and the associated notch stress intensity factors (N-SIFs) (Creager & Paris, 1967, Atzori et al., 1999) are then computed based on

ρ. It has to be emphasized that in both approaches, the major axis of the pre-existing flaw is no longer assumed to be much longer than the minor axis of the pre-existing flaw. Refer to appendix R for further discussion of these two approaches.

2.4 Crack propagation and coalescence in rock

Crack propagation and coalescence in rock have been observed and systematically recorded in the field (e.g. Gamond, 1983) and experimental studies (e.g. Reyes & Einstein, 1991) in different length scales for over decades. Tensile wing cracks were observed and regarded to be the most common form of cracks to initiate from a single pre-existing flaw (discontinuity) in a variety of materials from the early field (e.g. Chinnery, 1966, Roering, 1968, Freud, 1974) and experimental studies (e.g. Bombolakis, 1963). Later research explored the validity of the initiation and propagation of shear cracks from a pre-existing flaw (e.g. Petit & Barquins, 1988). The view on this is still diverging. Some believe that the development of shear cracks/faults in brittle rocks is due to the interaction and coalescence of the previously-initiated tensile microcracks (e.g. Blakey, 1952, Peng & Johnson, 1972, Reches & Lockner, 1994, Healy et al., 2006), while recent experimental studies with the use of the high speed camera were able to observe the initiation of shear cracks in granite and marble (Martinez, 1999, Wong & Einstein, 2006, 2007).

The investigation of crack development is not limited to rock, but also includes many other brittle materials such as glass, sulphur mortar, concrete, masonry and ice, which also contain a distribution of fine cracks and voids. Wang and Shrive (1995) reported that similar cracking patterns were observed in the above materials in similar uniaxial compression tests. The presence of pre-existing flaws, voids, or heterogeneities serve as stress concentrators which raise the local tensile stress, even under a general compressive stress field. At localities where the material tensile strength (cohesive strength of the material) is exceeded, cracks initiate. In concrete, apart from the voids and cracks present within the hardened cement past and aggregates, the interface between aggregates and cement-paste, which is known as the Interfacial Transition Zone (ITZ), also serves as

a favorable site for crack nucleation (Maso, 1994, Elkadi, 2005). The ITZ, which has a typical thickness of 20 to 60 μm, is characterized by a clearly open structure with large porosity gradient, being higher close to the aggregate contacts. In rocks, in addition to the microcraks, heterogeneity is also due to the various proportions of the different constituent minerals with varying mechanical properties.

The **sliding wing crack model** is one of the most widely employed models used to explain the tensile crack growth of brittle material under compression and macroscopic specimen deformation and failure (e.g. Gramberg, 1965, Moss & Gupta, 1982, Germanovich & Dyskin, 2000). According to this model, when a specimen containing an inclined pre-existing flaw (either closed or open) is subjected to uniaxial compression, curvilinear tensile (extensile) cracks displaying wing appearance initiate from the flaw tips and propagate along the loading direction (figure 2.4). Since the initiation of the tensile wing cracks is usually accompanied by a relative sliding movement between the upper face and the lower face of the flaw, hence the name **sliding wing crack model**. Successful applications of this model include the modeling of borehole breakout (e.g. Lee & Haimson, 1993), surface spalling and breakage associated with tunnel instability (Germanovich & Dyskin, 2000, Cai et al., 2004, Mitaim & Detournay, 2004). Recent research interest has extended to 3-dimenaional (3D) cracks (Dyskin et al., 1994, 2003) and quasi 3-dimenaional (3D) cracks (Wong et al., 2007) experimentally and numerically (Healy et al., 2006).

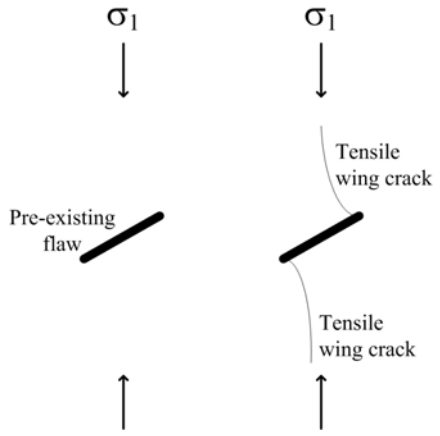

Figure 2.4 – Schematic illustration (two-dimensional) of the development of a pair of tensile wing cracks initiating from a pre-existing flaw under uniaxial compression.

Although the tensile wing crack model has been successful in explaining the initiation of tensile cracks, it is not versatile in accounting for all the mechanisms of compressive brittle fracture which are still not completely understood (Hallam & Ashby, 1990, Wang & Shrive, 1995). The most challenging issue is when pre-existing flaws are close to each other, how the interaction and coalescence of pre-existing flaws and growing cracks influence the overall specimen behavior. It has now been established that when pre-existing flaws are subjected to a deviatoric stress[2], different types and numbers of new cracks can develop from the pre-existing flaws (e.g. Bobet & Einstein, 1998a). The way in which these cracks propagate and coalesce depends on the geometrical relationship between the pre-existing flaws. Some of these new newly-developed cracks can propagate towards and coalesce with the neighboring flaws, or other new cracks initiating from the neighboring flaws. Some of them, however, may never take part in coalescence over their whole courses of crack propagation.

Various approaches have been developed to enhance the understanding of the crack development and coalescence behavior in rocks, namely analytical approaches, numerical approaches and laboratory experimental approaches.

2.5 Analytical approach

Analytical studies of the interaction among neighboring cracks help predict the compression strength of a brittle specimen. In most of these analytical models, there is a common assumption that all the new cracks initiated from the pre-existing flaws are all tensile wing cracks, and propagate along the loading axis. Crack interaction and

[2] Apart from the deviatoric compression stress, the stresses can also be applied in a **uniform** manner. Uniform compression is considered exert very little effect on crack nucleation. However, since uniform compression likely decreases the magnitude of stress concentrations near flaw tips and increases the frictional resistance between contacting crack faces, the crack growth and interaction activities are likely to be inhibited (Kranz, 1983).

coalescence are due to the mutual influence of the propagating tensile wing cracks. Three of such analytical models are described below.

(1) Costin (1985) – Similar to the sliding wing crack model mentioned earlier, all new cracks are assumed to grow in a direction normal to the applied compressive stress (figure 2.5). As they grow, the average spacing between them decreases and some interaction occurs. The presence of neighboring flaws has the effect of creating local tensile stresses that drive crack growth even when all the applied principal stresses are compressive. The degree to which the above effect operates is governed by the ratio of *a/d* as shown in figure 2.5(a), where *a* is the half-flaw length and *d* is a parameter which measures of the size of the local tensile field. The solution of this complex problem which involves multiple cracks, is broken down into a number of subproblems. Each subproblem involves solving the problem of an infinite homogeneous solid containing one single crack under applied far field stresses. For each subproblem, there are unknown quantities called "pseudotractions", which are the tractions exerted by other cracks on the specific crack considered in the subproblem. The requirement that the sum of the subproblems must be equivalent to the original problem leads to consistency conditions from which crack tip stress intensity factor K_I can be numerically calculated.

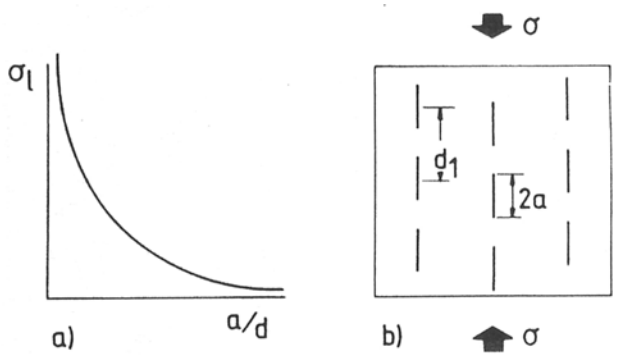

Figure 2.5 – Schematic illustration of Costin's (1985) model. (a) Crack-tip stress (σ_I) relieves when the length of crack (a) increases: d is a measure of the size of the local tensile field. (b) Crack interactions model: cracks are parallel to the applied compressive stress σ. d_1 is the initial flaw spacing (Gueguen et al., 1990).

(2) Ashby & Hallam (1986), Hallam & Ashby (1990) – Based on the sliding wing crack model, tensile wing cracks are assumed to initiate from pre-exiting flaws in response to applied loading (figure 2.6). The stress intensity factor K_I at the wing-crack tip is the superposition of a term due to the stress field of the pre-existing flaw and a term due to the opening force caused by the sliding displacement of the flaw. The angle ψ is calculated so as to maximize K_I. In a solid which consists of multiple pre-existing flaws, from which tensile wing cracks initiate and lengthen, these new cracks will interpenetrate. They thus divide the solid into beams, which lengthen as the cracks propagate. In response to the remote compressive stress, bending deflections will occur in these beams. This bending thus leads to an additional term in the expression for K_I.

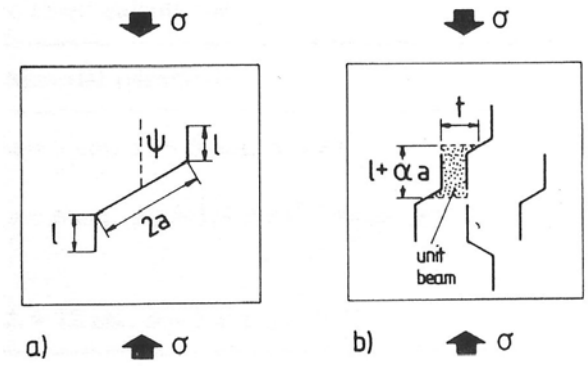

Figure 2.6 – Schematic illustration of wing-crack model (after Ashby & Hallam, 1986, and Hallam & Ashby, 1990). (a) Wing cracks initiate from an inclined pre-existing flaw under uniaxial compression σ. (b) Crack interactions model: The solid is divided into beams (one is shaded). As beams become longer, bending takes place simulating crack interactions. t is the smallest distance between wing cracks (Gueguen et al., 1990).

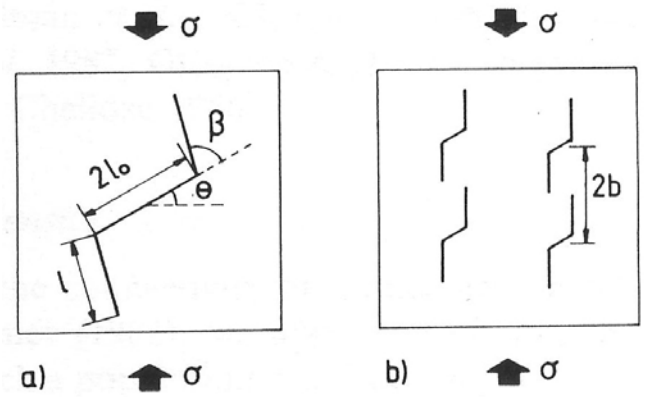

Figure 2.7 – Schematic illustration of wing-crack model (after Kemeny & Cook, 1987). under uniaxial compression σ. (a) Wing cracks initiate from the pre-existing flaw by an angle β. The wing cracks become aligned with σ as they propagate. (b) Crack interactions model: axially aligned columns of sliding cracks are used. Crack interactions take place either within a single column (axial failure) or shear failure between columns (Gueguen et al., 1990).

(3) Kemeny & Cook (1987) – Their model is similar to that proposed by Ashby & Hallam (1986) above, but with some modifications. Tensile wing cracks initiate from the pre-existing flaws at an angle β which takes into account of the curving shape of the initial segments of the tensile wing cracks (figure 2.7). The angle β is calculated so as to maximize K_I. As the wing cracks propagate, they will become aligned with the applied compressive stress. Interactions are considered by extending the K_I calculation to the case of an axially aligned column of sliding cracks (two such columns are shown in figure 2.7b). Crack interactions occur either within a single column (axial failure) or between columns (shear failure).

The three analytical models above individually predict a crack tip stress intensity factor K_I which is then used for computing the axial failure stress. See the review by Gueguen et al. (1990) for further details.

2.6 Numerical approach

With the rapid advance of computing power, there has been a huge volume of literature on the numerical studies of simulating crack growth and interaction. These developments have been concisely summarized by Ingraffea and Wawrzynek (2001). They observed that *"many of the numerical approaches were born of computational or modeling necessity, rather than from better understanding of the fundamental physics of crack growth"*. According to the authors, the common modeling techniques can be broadly classified into two major approaches – geometrical approach and non-geometrical approach (figure 2.8).

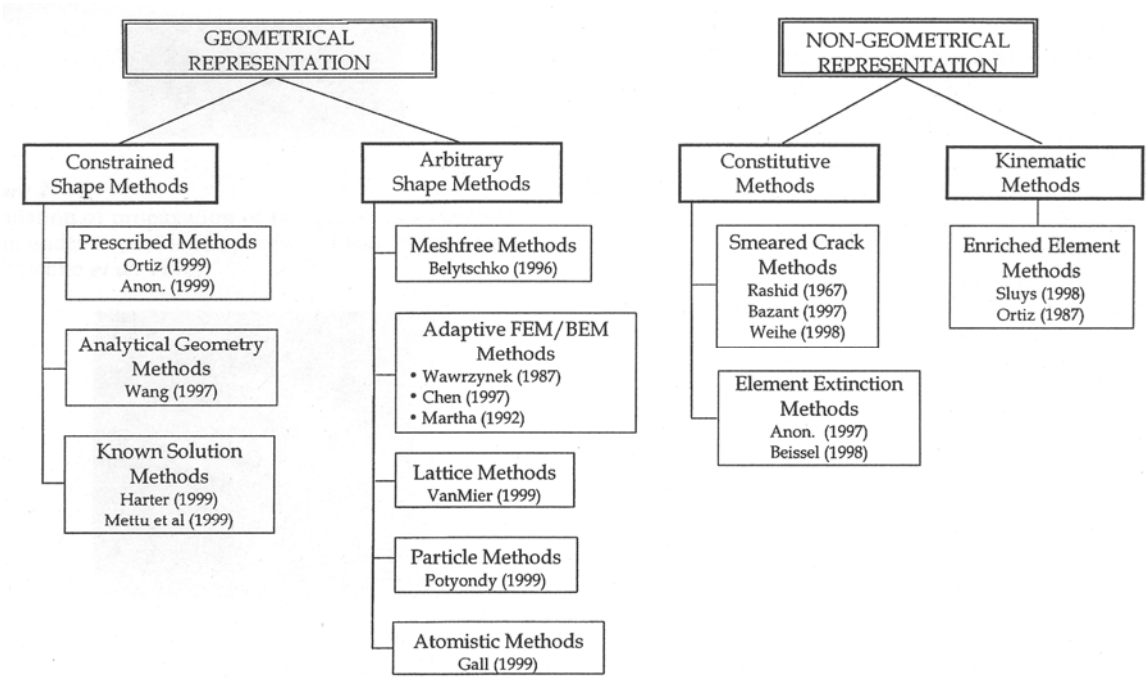

Figure 2.8 – A taxonomy of approaches to the numerical simulation of crack propagation and interaction (Ingraffea & Wawrzynek, 2001).

The authors explained that :

> *"In the first approach the crack is a geometrical entity; the geometry and discretization, if needed, are updated with crack growth. In the second approach the*

underlying geometry model does not contain the crack, and neither it nor the discretization, if needed, changes during crack growth."

Under the **geometrical** representation category, the crack growth can be modeled as either constrained or arbitrary. "*If growth is restricted by the discretization method, or restricted to certain analytical shapes such as flat and/or elliptical, growth is said to be* ***constrained***." On the other hand, if "*the crack takes the shape predicted by the physics and mechanics of growth, restricted only by the assumptions therein*," the growth is said to be **arbitrary**. There are two different methods belonging to the **non-geometrical** representation category – **constitutive** and **kinematic**. In the constitutive method, "*the material stiffness is approximately degraded to mimic the displacement discontinuity created by a crack, while the underlying geometry and mesh models are left unchanged.*" In the kinematic method, "*the effect of a crack on the surrounding strain and/or displacement fields is embedded in the local approximant.*" Refer to the review article by Ingraffea and Wawrzynek (2001) for details.

The analytical and theoretical treatment of crack coalescence problem by the MIT rock mechanics group can be dated back to the work by Chan et al (1990). Based on the LEFM (Linear Elastic Fracture Mechanics) principles, stress intensity factors (SIFs) were used in the hybridized indirect boundary element code FROCK, which was a class of the Displacement Discontinuity Method (DDM). The crack initiation and subsequent initial crack propagation could be satisfactorily modeled, but the modeling of crack coalescence events was less satisfactory. In later work, the cohesive zone model (strip-yield model) proposed by Dugdale (1960) and Barenblatt (1962) was extended and incorporated in the hybrid boundary element method by Reyes (1987). The stresses are finite in the strip-yield zone at the tip regions and the stress singularity at the flaw tip is absent. Based on that, she was able to satisfactorily model the tensile crack propagation, but there is limitation regarding the mixed-mode processes. By later combining a smeared crack/damage mechanics approach with a strain based failure criterion, Reyes (Reyes, 1991, Reyes & Einstein, 1991) was able to predict the location of coalescence cracks accurately. Bobet (1997) however recognized that the above model, which was solely

based on a continuum approach, was unable to reproduce the crack initiation and propagation process in detail. He then extensively modified the code FROCK with the objective of better predicting the tensile crack and shear crack initiation, propagation and hence coalescence behavior (Bobet, 1997, Bobet & Einstein, 1998b). The newly proposed crack initiation criterion, which was stress-based, stated that crack initiation depends on the local stress state relative to the strength of the material. Specifically, it is assumed that tensile crack initiation stress and direction can be related to the maximum tensile tangential stress around the flaw tip, and that shear crack initiation stress and direction can be related to the maximum absolute shear stress around the flaw tip. More theoretical background about the strain-based damage model formulated by Reyes and the FROCK extended by Bobet will be provided in chapter 8.

2.7 Laboratory experimental approach

Since Bombolakis (1963) reported the propagation of tensile wing cracks from a pre-existing straight flaw under uniaxial compression, fracturing processes and crack coalescence patterns in pre-cracked samples under compression have been extensively studied experimentally on different materials (table 2.2):

Rock-like brittle/semi-brittle materials

- **Columbia Resin 39** (Bombolakis, 1963, Brace & Bombolakis, 1963, Nemat-Nasser & Horii, 1982, Horii & Nemat-Nasser, 1985),
- **Glass** (Hoek & Bieniawski, 1965, Bieniawski, 1967),
- **Plaster of Paris** (Lajtai, 1970, Nevetova & Lajtai, 1973),
- **PMMA** (Petit & Barquins, 1988, Chaker & Barquins, 1996),
- **Molded gypsum** (Reyes, 1991, Reyes & Einstein, 1991, Shen et al., 1995, Bobet, 1997, Bobet & Einstein, 1998, Sagong, 2001, Sagong & Bobet, 2002),
- **Sandstone-like molded barite** (Wong, 1997, Wong & Chau, 1997, 1998, Wong et al., 2001),
- **Sandstone-like concrete mix** (Mughieda & Alzo'ubi, 2004).

Natural rocks

- **Sandstone** (Petit & Barquins, 1988),
- **Granodiorite** (Ingraffea & Heuze, 1980),
- **Limestone** (Ingraffea & Heuze, 1980),
- **Granite** (Martinez, 1999),
- **Marble** (Huang, 1990, Chen el al., 1992, Martinez, 1999, Li et al., 2005),
- **Ice** (Schulson et al., 1999).

Differences occurred among the above tests not only with respect to the materials tested, but also the dimensions of tested prismatic specimens and flaws. The specimens ranged from a small size of 50mm x 32mm x 5mm (Petit & Barquins, 1988) to a large size of 635 mm x 279 mm x 203 mm (Mughieda & Alzo'ubi, 2004). The flaw length tested by different research groups also varied between 10mm and 50mm; and the flaw aperture of open flaws varied between 0.1 mm and 3 mm. Note that in some cases, closed flaws were also studied (e.g. Hoek & Bieniawski, 1965, Bieniawski, 1967, Nemat-Nasser & Horii, 1982, Horii & Nemat-Nasser, 1985, Petit & Barquins, 1988, Shen et al., 1995, Bobet & Einstein, 1998a, Wong, 1997). From now on, the term "flaw" will be used to describe an artificially created, pre-existing crack or fracture, which can be either open or closed.

Authors	Material & method to make flaws (if mentioned)	Dimension of Specimens	Nature of pre-existing flaws	Loading Mode
Bombolakis (1963) ^ #, Brace & Bombolakis (1963) ^ #	Plexiglass, Columbia Resin 39	4.5"x 4.5"x 0.25"	Dumbbell-shaped hole, slot or ellipse (all open); 0.5" long flaw with radius of curvature of 1/16" or 1/32"	Uniaxial
Hoek & Bieniawski (1965)^	Glass; flaw ultrasonically machined	6"x 6"x 1/4"	Open and closed crack, 1/2" long, axis ratio of 25:1	Biaxial
Bieniawski (1967)^	Glass; hair-like flaws made by a hardened roller-type glass tool	6"x 6"x 1/8"	Closed	Biaxial
Lajtai (1970)^	Plaster of Paris; flaws made by displacement method	6"x 6"x 3" (uniaxial) 6"x 3"x 3" (biaxial)	All open: length (2.0", 1.5", 1.0", 0.5"), aspect ratio (0.01, 0.015, 0.02, 0.04), width (0.02")	Uniaxial and biaxial
Nesetova & Lajtai (1973)^	Plaster of Paris; flaws made by displacement method	6"x 6"x 3"; 10"x 10"x 3"	Open flaws of three types - circular, ellipse (1.5" long), straight flaws (1/16" wide, ¼" – $3^1/_2$" long)	Uniaxial
Ingraffea & Heuze (1980)^*	Granodiorite, limestone	4"x 4"x 3/4"	0.4" long, 0.008" wide open flaws	Uniaxial
Nemat-Nasser & Horii (1982)^ #	Columbia Resin 39; central hole drilled first, then followed by sawing	100mm x 100mm x 6mm	0.4 mm wide, 25 mm long flaws inserted with 2 thin brass sheets (each of 0.2 mm thick)	Uniaxial
Horii & Nemat-Nasser (1985)^ #	Columbia Resin 39; central hole drilled first, then followed by sawing	not mentioned	Flaws of two lengths were made : Long flaws – 0.4 mm wide, 25 mm long, inserted with two 0.2 mm thick brass sheets; The dimensions of the short flaws were not mentioned.	Uniaxial
Petit & Barquins (1988)^	PMMA	50 mm x 32 mm x 5 mm	0.15 mm diameter hole drilled in center and sawed to either side for an 8mm long & 0.3mm wide slot	Uniaxial and biaxial
	Sandstone - High Atlas (Morocco) red sandstone with 4% porosity - Brive (France) pink sandstone with 18% porosity	50 mm x 50 mm x 5 mm	0.15 mm wide, inserted with 0.15mm thick steel shim	Uniaxial
Huang et al. (1990)^	Fangshan Marble	104 mm x 80 mm x 6 mm	20mm long, <1mm wide open flaws ; some with mortar-infilled slots	Uniaxial

Key : ^ single flaw, * double flaws, # multiple flaws

Table 2.2 – Research on fracturing processes and crack propagation in pre-cracked specimens.

Authors	Material	Dimension of Specimens	Nature of pre-existing flaws	Loading Mode
Reyes (1991)*, Reyes & Einstein (1991)*	mixture of hydrocal B-11 (gypsum), celite, and water at mass ratios of 700:8:280; flaws made by displacement method	6” x 3” x 1.25”	12.7 mm (0.5”) long, ~0.25 mm wide open flaws	Uniaxial
Chen et al. (1995) ^#	Marble (type not mentioned); central hole first ultrasonically drilled, then sawing by a diamond impregnated wire	110mm x 80mm x 10 mm	0.1mm wide open flaws with hemi-cylindrical tips, length varies (8, 10, 12, 15, 16, 20mm)	Uniaxial and biaxial
Shen et al. (1995)*	Same as Reyes (1991)	6” x 3” x 1”	12.7 mm (0.5”) long open and closed flaws	Uniaxial
Chaker & Barquins (1996)^	Polymethyl methacrylate (PMMA)	50 mm x 32 mm x 5 mm	0.3mm wide, 10mm long flaws inserted with very thin steel plates	Uniaxial
Bobet (1997) *, Bobet & Einstein (1998a)*	Same as Reyes (1991)	6” x 3” x 1.25”	12.7 mm (0.5”) long, 0.1 mm wide open and closed flaws	Uniaxial and biaxial
Wong (1997)* , Wong & Chau (1997, 1998)*, Wong et al. (2001)#	Sandstone-like molded barite; flaws made by displacement method	60 mm x 120 mm x 25 mm	12 mm long closed flaws of varying friction coefficient (μ = 0.6, 0.7, 0.9) created by inserting 0.3 mm thick steel sheets into the molded specimens.	Uniaxial
Martinez (1999) *	Barre Granite and Vermont White marble	6” x 3” x 1.25”	12.7 mm (0.5”) long, 2 mm wide open flaws with cylindrical tip shape	Uniaxial
Sagong & Bobet (2002)#	Same as Reyes (1991)	203.2 mm x 101.6 mm x 30 mm	12.7 mm long, 0.1 mm wide open flaws	Uniaxial
Ko (2005), Ko, et al. (2006)	Same as Reyes (1991)	6” x 3” x 1.25”	12.7 mm (0.5”) long, 0.1 mm wide open flaws	Uniaxial cyclic
Mughieda & Alzo'ubi (2004) *	mixture of 72% silica sand, 16% cement, 12% water by weight; flaws made by displacement method	635 mm x 279 mm x 203 mm	3mm wide open flaws. Flaw length was not mentioned.	Uniaxial
Li et al (2005) *	Huangshi marble; central hole drilled first, then followed by sawing	110 mm x 62 mm x 25 mm	0.5 - 1mm wide flaw with a 6 mm diameter center hole (flaw length not mentioned)	Uniaxial

Key : ^ single flaw, * double flaws, # multiple flaws

Table 2.2 – Research on fracturing processes and crack propagation in pre-cracked specimens (continued).

Despite the abundant information about crack coalescence gathered from the experimental work on different materials, experimental studies with equivalent flaw parameters were rarely attempted in natural rock and artificial rock in a parallel manner by any research group (except at the MIT rock mechanics group with equivalent tests on molded gypsum, granite and marble). This wide range of materials types, specimen types and flaw dimensions tested among different previous experimental studies thus poses challenges in directly comparing the fracturing processes and crack coalescence patterns. The question of whether the same coalescence patterns can be observed in artificial material and natural rock with the same flaw geometries and loading conditions is still not fully answered. Although there have been many studies trying to study the relationship between material nature, particularly the constituent grain size on the overall macroscopic specimen strength (e.g. Fredrich et al., 1990, Olsson, 1990, Wong et al., 1996, Costamagna et al., 2007), there have been few attempts directly addressing the relationship between the material properties and the crack initiation and coalescence behavior. Nevertheless, the work by Eberhardt et al. (1999) offered some insights on this issue. Based on strain gauge and acoustic emission techniques, the authors concluded from their experimental study on a variety of granitic rocks[3] that the crack initiation stress threshold was more dependent on the strength of the constituent minerals than the grain size. Note that "intact" cylindrical rock cores free of observable cracks were tested[4]. The determination of the onset of crack initiation was not based on direct observation on the rock cores, but inferred from the corresponding stress-strain plot (figure 2.9). However, after the cracks had initiated, larger grains provided longer paths of weakness for growing cracks to propagate along, hence increased the chance for different cracks to coalesce and interact, i.e. lower the crack coalescence and crack damage thresholds (figure 2.9). Therefore, rock strength was found to decrease with increasing grain size.

[3] The average grain sizes of the three tested rocks are 1mm for granodiorite, 3mm for granite, and 20mm (between 10 and 40 mm) for pegmatite.

[4] This is different from the tests listed in table 2.2 in which a pre-existing flaw is artificially created in the specimens before the loading tests are conducted.

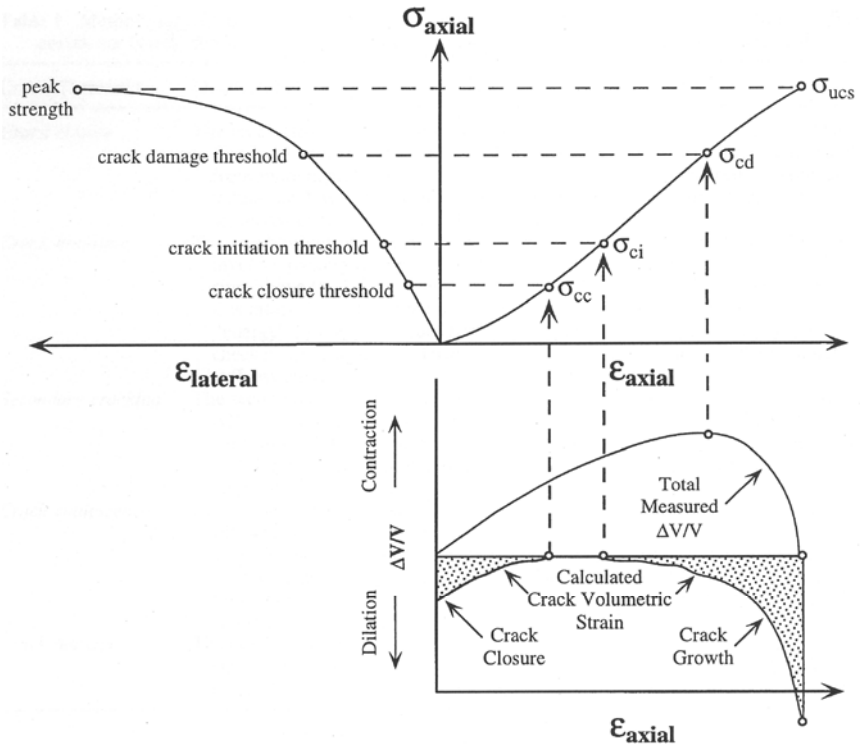

Figure 2.9 – Stress-strain diagram showing the various stages of crack development. Only the axial and lateral strains are measured; the volumetric and crack volume strains are calculated. Crack initiation threshold (σ_{ci}) is where the lateral and volumetric strain curves depart from linearity. Crack coalescence / crack damage threshold (σ_{cd}) is where there is a reversal in the volumetric strain curve (Eberhardt et al., 1999).

Past work of the MIT and the Purdue University rock mechanics groups on initiation, propagation and coalescence of rock fractures began in the late 1960's with model rock experiments (Einstein et al., 1969, Einstein and Hirschfeld, 1973), mostly of phenomenological character. Systematic investigations of the interaction of two pre-existing flaws have been undertaken in the past 15 years to study the influence of a number of various parameters and loading conditions (table 2.3) on the coalescence behavior experimentally (Reyes & Einstein, 1991, Shen et al., 1995, Bobet & Einstein, 1998a, Sagong & Bobet, 2002, Ko et al., 2006, Wong & Einstein, 2006, 2007). These recent experimental works identified that tensile wing cracks are not the only cracks that can lead to crack coalescence (e.g. Bobet and Einstein, 1998a). Shear cracks, or combinations of shear and tensile cracks can also lead to coalescence. The variation has been confirmed to depend on the pre-existing flaw geometries. Since then, there is a

continuation of efforts on studying the effect on coalescence due to different flaw geometries. Further comments will be made in section 2.7.2.

Specimen Parameters	• rock type (molded gypsum, Barre Granite, Vermont White Marble, Carrara Marble) • number of flaws (single *vs* double) • flaw nature (closed *vs* open) • flaw aperture (0.1 mm, 0.2mm, 1.3mm) • flaw inclination angle (β)* • bridging angle (α)* • ligament length (L)*	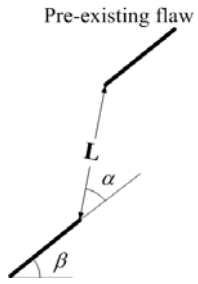 * schematic representation of flaw pair
Loading Conditions	• uniaxial compression • biaxial compression • uniaxial cyclic loading	

Table 2.3 – Various specimen parameters and loading conditions tested by MIT rock mechanics group.

In the rock mechanics literature, since the **tensile wing cracks** were usually found to be the first cracks to appear, they were also called the **primary cracks**. Cracks initiated later than the tensile wing cracks were usually referred to as **secondary cracks**, without specifying the crack origin (tensile/shear). For example, in the study by Chen et al., (1995), after the initiation of the tensile wing cracks at the flaw tips, additional new cracks were observed to initiate and propagate towards the loading direction (figure 2.14). Being uncertain whether these additional cracks were tensile or shear in origin, the authors named these cracks **secondary cracks** and called those previously initiated tensile cracks **primary cracks**.

Later studies suggested that secondary cracks are usually **shear** in origin. As time went by, researchers began using "**secondary cracks**" and "**shear cracks**" interchangeably. However, in certain cases when the authors were uncertain about the nature of the crack

(tensile/shear?), they continued the old practice of using the term **secondary** with the intention of indicating the temporal relationship without implying the crack nature. Confusion was thus often created for later readers.

It will be later shown in the present study (chapters 3, 4, 5, 6) that in some flaw geometries, **shear cracks** are however not the only crack types that can initiate from the pre-existing flaws **after** the conventional tensile wing cracks have initiated. Other types of tensile cracks have also been identified to develop. In addition, **shear cracks** can also initiate in some flaw geometries as the **first** cracks. To avoid confusion, throughout the discussion within this thesis, all the newly initiated cracks that form in response to the applied loading will be simply named as either **tensile or shear,** and the terms **primary** and **secondary** will also not be used wherever possible. Qualifying terms will be included where necessary to describe the shape and/or trajectory of the cracks.

The following sections review some of the past key experimental studies – first on crack initiation and propagation from single flaws, second on crack interaction and coalescence.

2.7.1 Experimental study of specimens with single flaws

Various crack types were observed to develop in specimens containing single flaws under uniaxial loading tests by different authors. As noted in previous sections regarding the confusing use of terminologies, caution has been exercised to comprehend the crack types identified by different authors. This section simply describes the observation made by previous researchers. The information presented in this section will be reviewed again and compared against the experimental results obtained from the present study later in chapter 9.

In the work reported by Lajtai (1974), the crack development sequence in Plaster of Paris specimens containing single open flaws which were loaded uniaxially as shown in figure 2.10 was observed. He claimed that this figure was representative for a wide range of flaw inclination angles tested (also refer to table 2.2 for the different flaw lengths and aperture sizes tested). The cracking sequence (with the original terminologies) is (a) tensile fractures, (b) normal shear fractures, (c) normal shear fractures, (d) inclined shear fractures. Lajtai (1974) noticed that the development of shear zones around the flaw tips after the initiation of the first normal shear fractures was due to subsequent formation of additional normal shear fractures and perhaps tensile fractures.

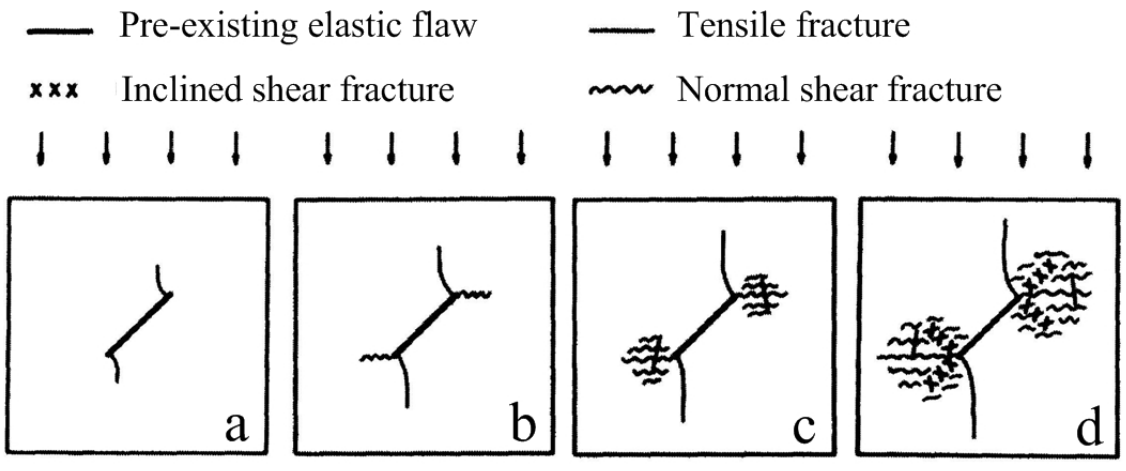

Figure 2.10 – The evolution of fracture from a single open flaw (Lajtai, 1974).

In a literature review, Ingraffea and Heuze (1980) identified the influence of material on fracturing behavior under uniaxial compression. They observed that in specimens with a single open flaw inclined to the compression axis, **primary cracks**, which were originated from points of initially highest tension stress, were observed in previous tests on glass, polymethylmethacrilate (PMMA), CR39 and also rocks. **Secondary cracks**, which were originated from points of initially compressive stress concentration, were however absent in glass and plastic, but were only observed in rocks. Notice that Ingraffea and Heuze (1980) appeared to have used the term **primary cracks** interchangeably with **tensile wing cracks** and the term **secondary cracks** interchangeably with **shear cracks.**

Ingraffea and Heuze (1980) conducted their own experimental study to observe the crack initiation and propagation from a single pre-existing flaw (0.4" long, 0.008" wide) in limestone (table 2.2, figure 2.11). The authors again used the terms **primary cracks** to describe the wing cracks; and the term **secondary cracks** to describe the longer curvilinear cracks. They noticed that the secondary cracks did not initiate from the flaw tips, but at regions indicated by circles (figure 2.11) at a distance away from the flaw tips. After their initiation, individual secondary cracks propagated towards the flaw tips and towards the top and bottom edges of the specimen (directions indicated by arrows).

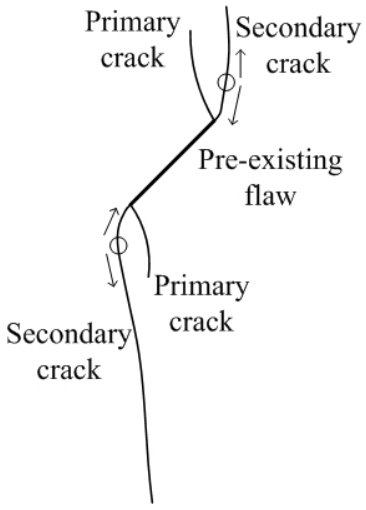

Figure 2.11 – Primary and secondary cracks initiated from a pre-existing flaw (0.4", 10 mm long) in limestone under uniaxial compression. (after Ingraffea and Heuze, 1980).

Petit and Barquins (1988) tested low porosity and high porosity sandstone specimens (50 mm x 50 mm x 5 mm) both containing 20 mm long single flaws (< 1 mm flaw aperture). The flaws were created by first drilling a 0.15 mm diameter hole in the center and then sawed to either side for an 8 mm long slot with 0.3 mm flaw aperture size. In addition, to the initiation of branch fractures[5], shear zones were observed to extensively develop in the specimens (figure 2.12). Notice that some of the shear zones were almost coplanar with the pre-existing flaws, while some of them were almost orthogonal to the pre-existing flaw (indicated by the arrow pair with asterisks *).

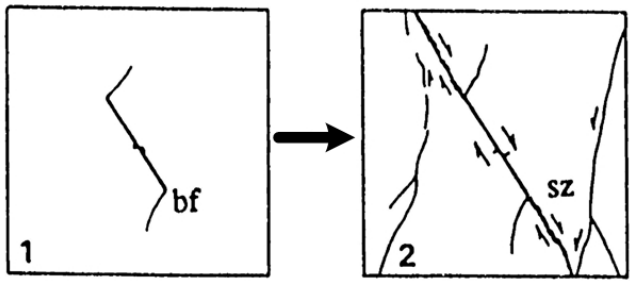

High porosity sandstone

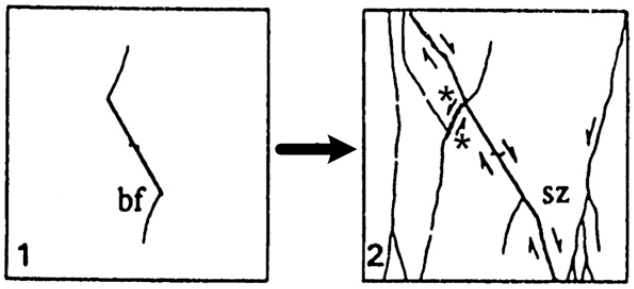

Low porosity sandstone

Figure 2.12 – Crack growth (bf = branch fracture; sz = shear zone) from a single flaw in low and high porosity sandstone specimens. Sketches labeled "1" on the left show branch fracture formation before maximum stress and sketches labeled "2" on the right show shear zone formation and secondary fractures at or after maximum stress (after Petit and Barquins, 1988).

[5] The authors used the term "branch fractures" instead of "tensile wing cracks" in their discussion.

In the uniaxial compression loading tests on Fangshan Marble specimens (104 mm x 8 mm x 6mm) containing single flaws conducted by Huang et al. (1990), the following crack development stages were observed and generalized (figure 2.13). The flaws were 20 mm long with a flaw aperture size less than 1 mm. Notice that the original terminologies used by the authors are reproduced below. The terms **primary** and **secondary** were clearly used by the authors for indicating temporal relationship among different cracks.

(1) Initiation and propagation of **primary forward tensile cracks** (PFTCs).

(2) Initiation and propagation of **secondary forward tensile cracks** (SFTCs).

(3) Initiation and intensification of **shear belts** (backward shear belts, BSBs & forward shear belts, FSBs).

(4) Initiation and propagation of **backward tensile cracks** (BTCs).

(5) Specimen failure.

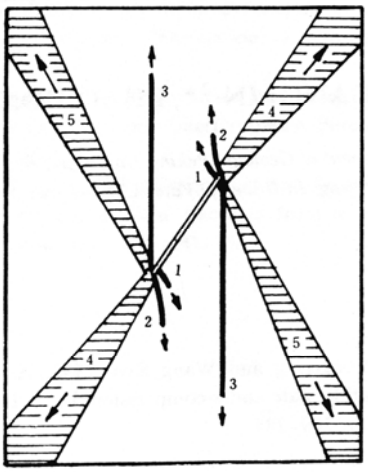

Figure 2.13 – A schematic diagram showing various cracking features in marble containing a single open flaw. 1-PFTCs; 2-SFTCs; 3-BTCs; 4-FSBs; 5-BSBs (Huang et al., 1990).

Uniaxial compression loading tests were conducted on marble specimens (110 mm x 80 mm x 10 mm) containing 0.1 mm wide single flaws (figure 2.14 a) by Chen et al. (1995). A central hole was first ultrasonically drilled in the specimen, which was followed by sawing by a diamond impregnated wire on both sides. Three stages of crack growth were identified :

(1) **Primary cracks** propagated perpendicularly to the direction of the flaw (figure 2.14 b).

(2) **Secondary cracks** propagated in the direction of major principal stress. Secondary cracks developed faster and were longer than the primary cracks. Both primary and secondary cracks were stable and had finite lengths (figure 2.14 c).

(3) Final failure of the specimen occurred by the development of an **"X" shaped black band**. Although the authors stated that it was a band of microcracks, they did not provide further experimental evidence (e.g. microscopic study) to confirm its identity (figure 2.14 d).

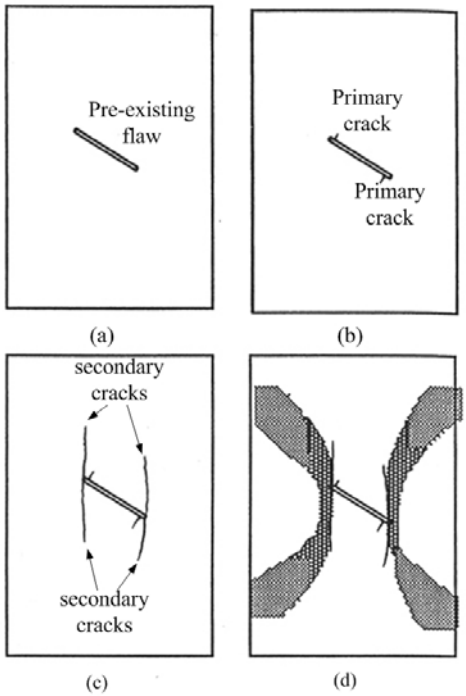

Figure 2.14 – Schematic representation of the various stages of initiation and propagation of new cracks from a pre-existing flaw under uniaxial compression (vertical) in marble (Chen et al., 1995). The flaws were 0.1 mm wide and had various lengths (8, 10, 12, 15, 16 mm) were tested.

Chen et al. (1995) described the cracks as either **primary** or **secondary** throughout their paper. Although they correlated the **primary cracks** with the tensile cracks, they did not indicate whether the **secondary cracks** were tensile or shear in nature. They only postulated that the ends of the flaws from which the secondary cracks appeared were the "**compressive stress areas**". The authors also correlated the observed secondary cracks with those observed and analyzed by Ingraffea and Heuze (1980). However, the secondary cracks reported by Ingraffea and Heuze (1980) had a curvilinear shape (figure 2.11), while those observed by Chen et al. (1995) were relatively straight (figure 2.14 c). In addition, Ingraffea and Heuze (1980) observed that the secondary cracks did not initiate from the flaw tips, but in the intact material which was located at a distance away from the flaw tips, and then propagated both towards the flaw tips and the upper and lower edges of the specimen. This type of crack initiation and propagation was not reported by Chen et al. (1995). A correlation of the secondary cracks observed by Chen et al. (1995) with those observed by Ingraffea and Heuze (1980) thus appears unjustified.

In uniaxial compression loading tests on Huangshi Marble specimens (110 mm x 62 mm x 25 mm) which contained single flaws (0.5 – 1 mm wide with a 6 mm diameter center hole; the measurement of the flaw length was not given) oriented at two different inclination angles conducted by Li et al., (2005), the following crack growth phenomena were reported (table 2.2, figure 2.15):

a) Single flaw (35^o flaw angle) – "wing cracks" initiated from the end tips.

b) Single flaw (45^o flaw angle) – "wing cracks" and "secondary quasi-coplanar cracks" initiated from the end tips. The latter led to specimen failure.

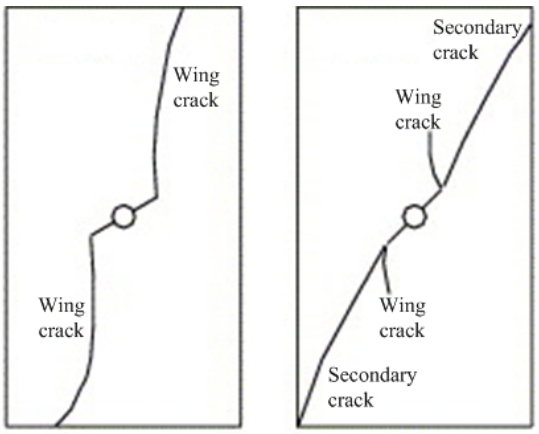

(a) (b)

Figure 2.15 – (a) Wing cracks (tensile cracks) initiated from a flaw with inclination angle 35°. (b) Wing cracks (tensile cracks) and secondary cracks (shear cracks) initiated from a flaw with inclination angle 45°.

Once again, the authors did not use the terms **tensile** and **shear** to describe the identity of the newly-initiated cracks, but "**wing cracks**" and "**secondary quasi-coplanar cracks**" instead. From the description within their paper and the trajectories of the cracks, it is reasonable to assume that the authors used the term "wing cracks" to indicate "tensile wing cracks", and the term "secondary cracks" to indicate "shear cracks".

They also reported that preferentially stressed white patches appeared on the specimen surfaces before actual cracking occurred:

> "*The newly initiated cracks behaved as a narrow white belt at the beginning, which indicated deviation and failure of crystalline grains in marble. The white area expanded continuously and its color became deeper*."

Li et al. (2005) regarded that the origin of white patches was due to the *deviation and failure of crystalline grains* in response to loading. However, this statement was based on speculation and they did not provide further experimental evidence (e.g. microscopic study) to confirm their identity.

A recent experimental study conducted by Wong and her collaborators (Wong et al., 2006, 2007, Guo et al., 2006) on prismatic natural rock specimens (gabbro, marble,

sandstone & granite) containing single 3-dimensional (3D) surface flaws (figure 2.16) led to the formation of "anti-wing cracks". The dimensions of a 3D surface flaw are defined by the flaw length ***2c***, and the depth ***d*** embedded into the prismatic specimen. The latter has dimensions *L* x *W* x *t*.

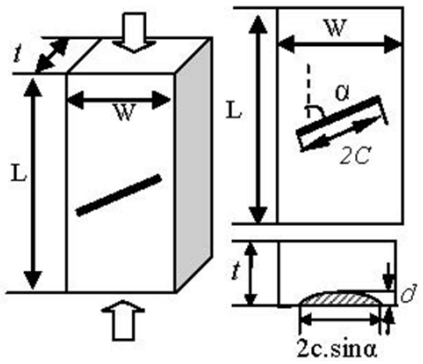

Figure 2.16 – Layout of a specimen containing a 3-D surface crack (Wong et al., 2006).

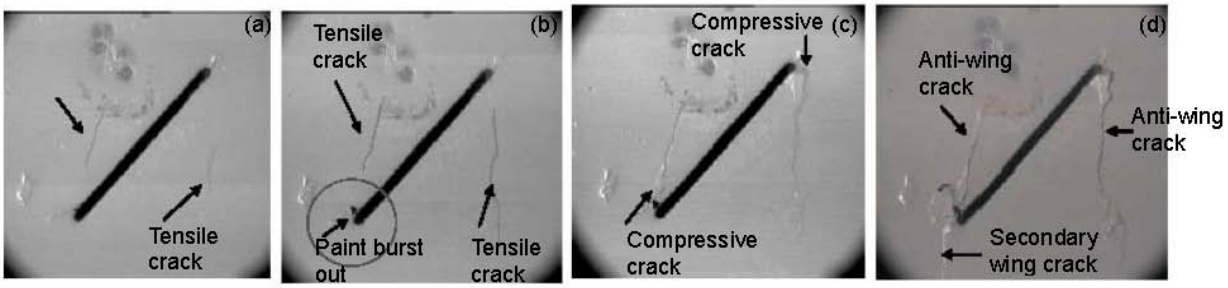

Figure 2.17 – Growth of anti-wing cracks from a 3-D flaw in a gabbro specimen (Wong et al., 2006).

Although the authors claimed that this crack type had not been reported by others before, this crack type had already been extensively reported in previous experimental studies (figures 2.13 & 2.14) and field studies (see section 2.8.4 for the relevant literature review). The various stages of anti-wing crack development were described by the authors as:

a) A tensile crack initiated close to but not at the flaw tip. The trajectory of this tensile crack was different from that of a conventional wing crack. More specifically, it was located on the other side of the flaw (figure 2.17 a).

b) The circled region in figure 2.17 b indicated a region of local surface spalling.
c) The above-mentioned anti-wing tensile crack grows in two different directions – one towards the nearest flaw tip and the other one towards the edge of the specimen. The authors observed that *"compressive cracks initiated at each flaw tips and coalesced with the growing cracks."* (figure 2.17 c)
d) Additional cracks, such as "*secondary wing cracks*" as shown in figure 2.17 d initiated from the flaw tips at a later stage.

To summarize this review section on the fracturing behavior of single flaws, the following key points are noted. In all the tested specimens, **tensile wing cracks** (which were commonly called **primary cracks**) were always found to be the first cracks to initiate, while shear cracks were never observed to be the first cracks. Additional applied loading led to the initiation of **secondary cracks**. In most cases, the authors called the shear cracks they observed as secondary cracks, e.g. Li et al. (2005). In cases when the authors were unable to determine the nature of the new cracks which developed after the initiation of the tensile wing cracks, they simply described them as **secondary cracks** without implying the mode of crack initiation, e.g. Chen el al. (1995). In addition to the shear cracks, tensile cracks initiating sometime after the first crack (primary crack) were also identified (Huang et al., 1990). In this case, the authors used the term **secondary forward tensile cracks** to describe this crack type, and "secondary" here simply implies a temporal relationship.

Preferentially stressed zones which appeared as regions of color change were identified by Chen et al. (1995) and Li et al. (2005) in their tested marble specimens. They were suspected to be due to the presence of induced microcracks (Chen et al., 1995) or deviation and failure of crystalline grains (Li et al., 2005). However, there were no experimental attempts (e.g. microscopic imaging) by these authors to confirm their identity.

Another common observation was the preferential development of shear zones (Lajtai, 1974, Petit & Barquins, 1988) or shear belts (Huang et al., 1990) right before the specimen maximum stress was reached. These shear zones/belts, which propagated towards the edges of the specimens, were observed to cause (be associated with) specimen failure.

2.7.2 Experimental study of specimens with multiple flaws

One of the earliest reported experimental studies was due to Brace and Bombolakis (1963) who performed uniaxial compression tests on plexiglass containing echelon flaws (figure 2.18). Tensile cracks initiated from the flaw tips and propagated along the vertical loading direction. However, neither secondary cracks nor coalescence cracks were observed.

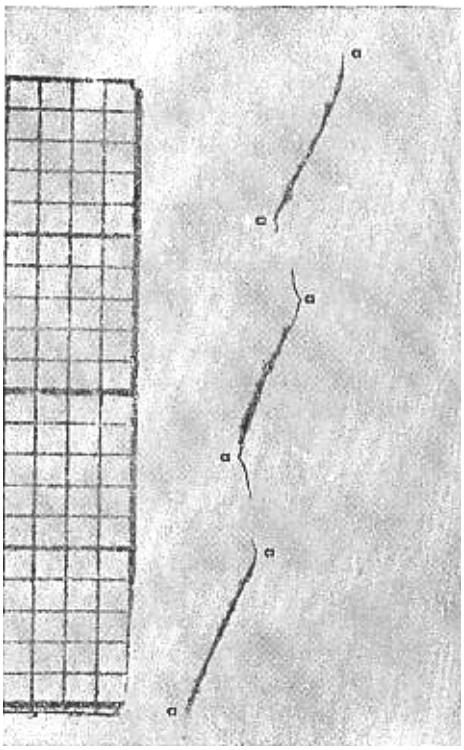

Figure 2.18 – Development of tensile cracks from pre-existing flaw tips '**a**' in plexiglass under uniaxial compression. The length of one small square grid is 1mm (Brace & Bombolakis, 1963).

Since Brace and Bombolakis (1963) published their results, there has then been a growing interest in the experimental study of crack growth in various materials (discussed previously in table 2.2). Systematic studies were conducted to study the influence of various flaw parameters on the fracturing and coalescence patterns. Given the complexity of the problem, researchers usually reduced the problem to some simple and well-defined geometries, e.g. parallel straight flaw arrays. In the literature, the geometry of a flaw pair is usually defined by one of the two methods, either **ligament length – flaw inclination angle – bridging angle** or **flaw inclination angle – spacing – continuity**. See figure 2.19 for illustration.

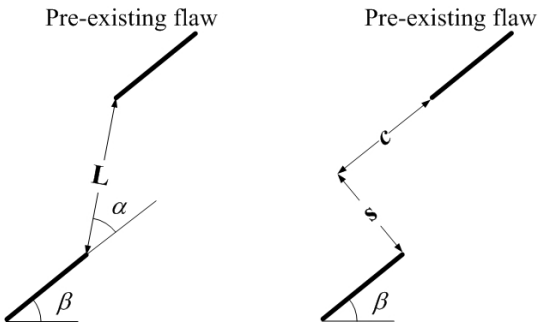

Figure 2.19 – Flaw pair geometry defined by (a) flaw inclination angle β, bridging angle α and ligament length L, or (b) flaw inclination angle β, spacing s and continuity c.

Horii and Nemat-Nasser (1985) carried out loading tests on Columbia Resin CR 39. The tested specimens contained two general different flaw geometries. (1) specimens containing a row of short flaws and several long flaws (figures 2.20, 2.21) and (2) specimens containing multiple rows of short flaws and several long flaws (figure 2.22). Five flaw pairs (A to E) with well-defined coalescence patterns were identified from these figures. Their configuration details and the type of coalescence cracks involved are summarized in table 2.3. Note that the crack types are determined in the present review, which is based on the crack trajectories shown in the original images and information provided in the original paper.

All the coalescence patterns reported in table 2.4 were all achieved by connecting the inner flaw tips (figures 2.20, 2.21, 2.22). In flaw pairs A and D, from the trajectories of the coalescence cracks, it is very likely that the coalescence events in these cases were achieved by two coalescence cracks. However, in flaw pairs B, C and E, an equivalent statement cannot be made. Based on the much more continuous and less undulating trajectory of the coalescence cracks, either one or two cracks may be possible to have involved in the coalescence.

Flaw pair number	**Geometry parameters** [(1)]					**Type of coalescence cracks** [(2)]
	β (°)	**s**	**c**	**α (°)**	**L**	
A (fig 2.14)	45	a	a	45	1.4a	T + S
B (fig 2.14)	45	3a	a	72	3.2a	T
C (fig 2.15)	45	a	0.5a	63	1.2a	T
D (fig 2.16)	45	3a	a	72	3.2a	T + T
E (fig 2.16)	45	0.7a	0	0	0.7a	T

Remarks:

(1) Refer to figure 2.18 for definition of different geometry parameters. 'a' = half flaw length and was 12.5mm long.

(2) T = tensile crack, S = shear crack.

Table 2.4 – Summary of coalescence crack types identified from the figures given by Horii and Nemat-Nasser (1985). The crack types are interpreted by N.Y. Wong (this thesis) based on information in original paper.

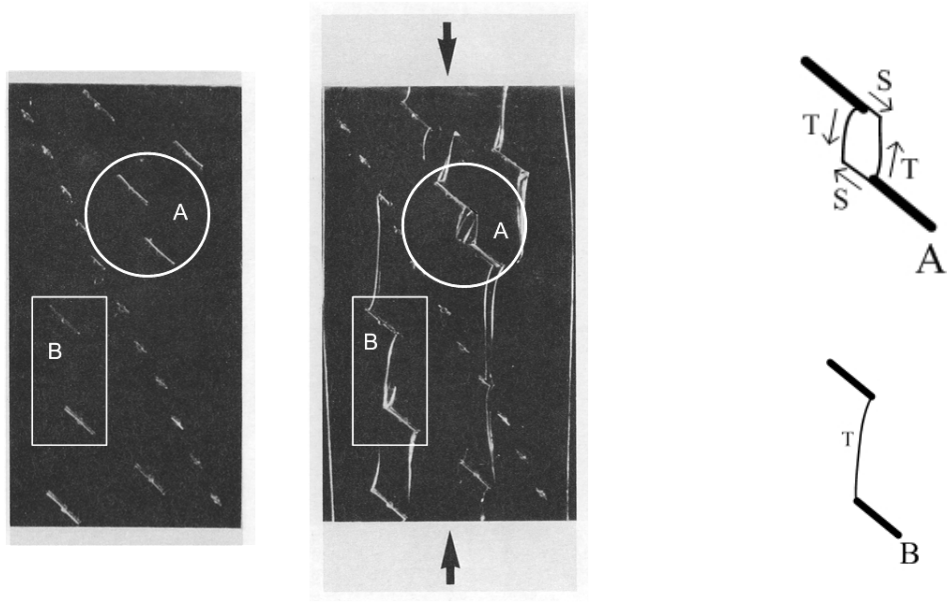

(a) (b) (c)

Figure 2.20 – (a) specimen containing a row of short flaws and several long flaws, (b) coalescence occurred for flaw pairs A and B, (c) sketches of the coalescence cracks involved.

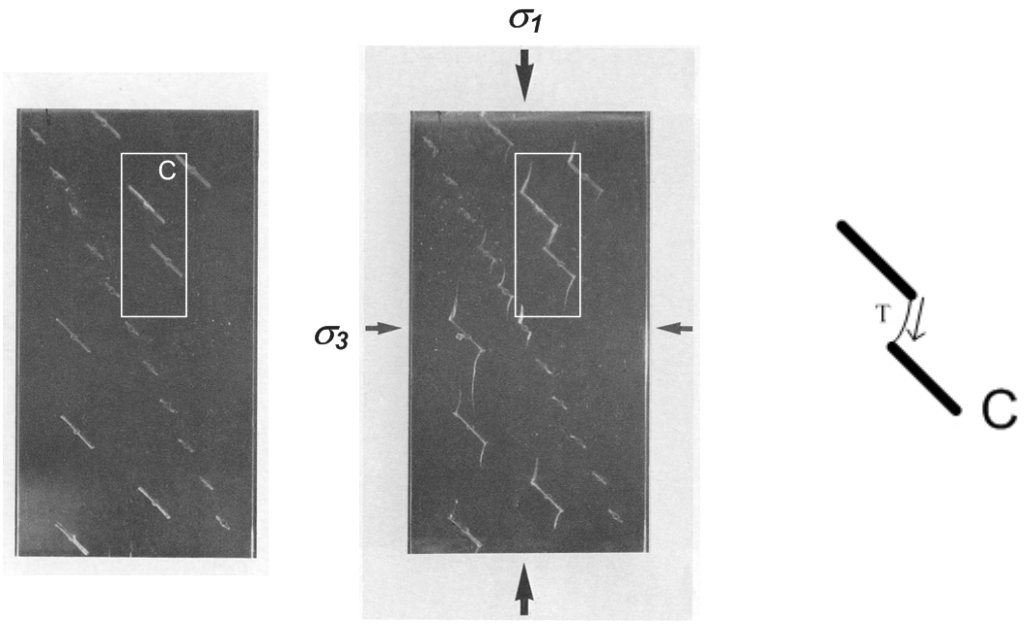

(a) (b) (c)

Figure 2.21 – (a) specimen containing a row of short flaws and several long flaws, (b) coalescence occurred for flaw pair C, (c) sketches of the coalescence cracks involved.

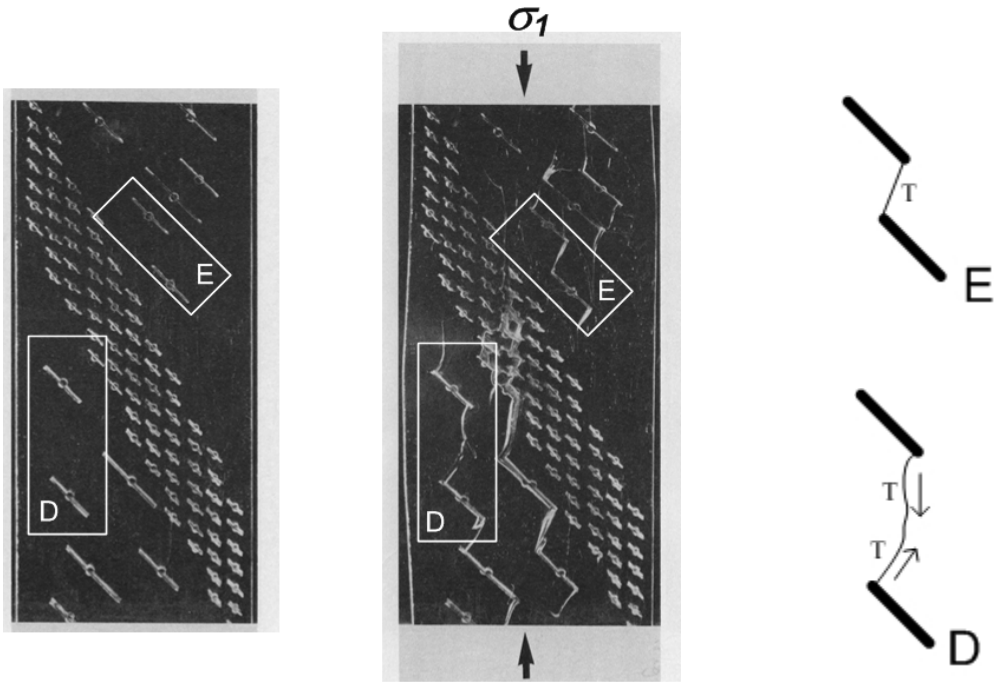

(a) (b) (c)

Figure 2.22 – (a) specimen containing multiple rows of short flaws and several long flaws, (b) coalescence occurred for flaw pairs D and E, (c) sketches of the coalescence cracks involved.

Chen et al. (1995) carried out loading tests on marble to observe coalescence patterns for multiple flaws with different arrangement patterns (table 2.2). Also refer to the previous section for his similar tests on specimens containing **single flaws** of the same material. Sketches of the observed coalescence patterns were provided by Chen et al. (1995) as shown in figure 2.23 A to C. Notice that the length of the multiple flaws was not specified by the authors.

Flaw group number	**Geometry parameters** [1]					**Number of coalescence cracks** [4]
	β (°)	**s**	**c** [2]	**α (°)**	**L** [3]	
a (fig 2.22A)	30	0	0.3a	0	0.3a	2 secondary cracks
b (fig 2.22A)	30	0.8a	0.5a	58	0.9a	1 secondary crack
c (fig 2.22B)	30	0.8a	-0.6a	127	a	1 primary crack
d (fig 2.22B)	30	0.8a	-1.1a	144	1.4a	1 primary crack
e (fig 2.22C)	30	0.8a	-0.6a	127	a	1 primary crack
f (fig 2.22C)	30	0.8a	-0.6a	-127	a	1 secondary crack
g (fig 2.22C)	30	0.8a	0.5a	-58	0.9a	1 secondary crack

Remarks:

[1] Refer to figure 2.19 for definition of different geometry parameters.

[2] Overlapping flaws have negative continuity (**c**) values.

[3] 'a' = half flaw length and its measurement was not provided by the authors.

[4] The authors did not specify the nature (shear/tensile) of the secondary cracks, where all cracks which initiated later than the primary cracks were referred to as secondary cracks.

Table 2.5 – Summary of flaw pair geometries and the types of coalescence cracks tested by Chen et al. (1995).

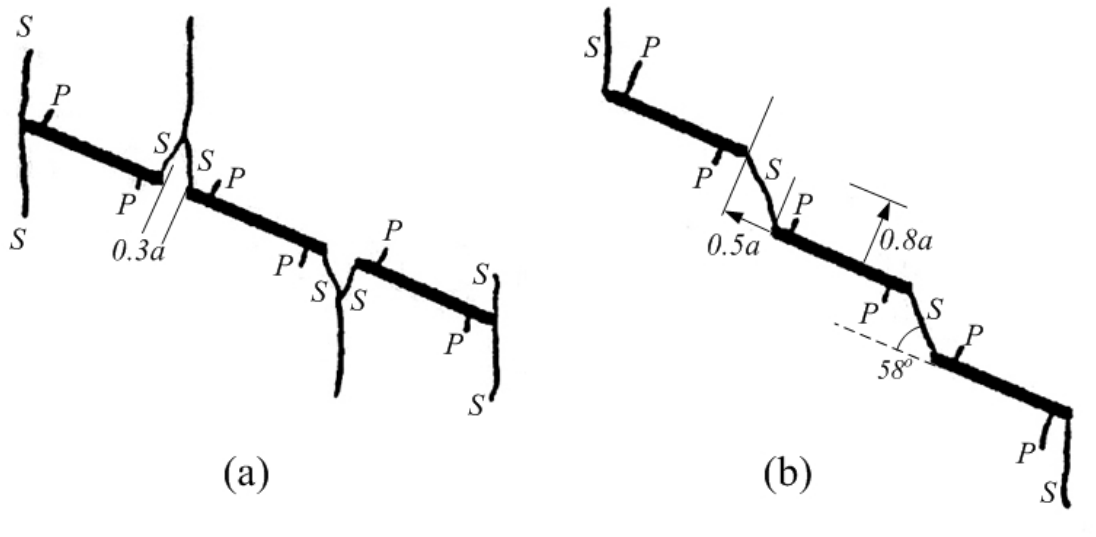

Figure 2.23A – Crack coalescence by secondary cracks in (a) and (b) under uniaxial compression, where P = primary crack, S = secondary crack with nature (shear/tensile) undetermined. The spacing and continuity measurements in terms of half flaw length '*a*' are also given (Chen et al., 1995).

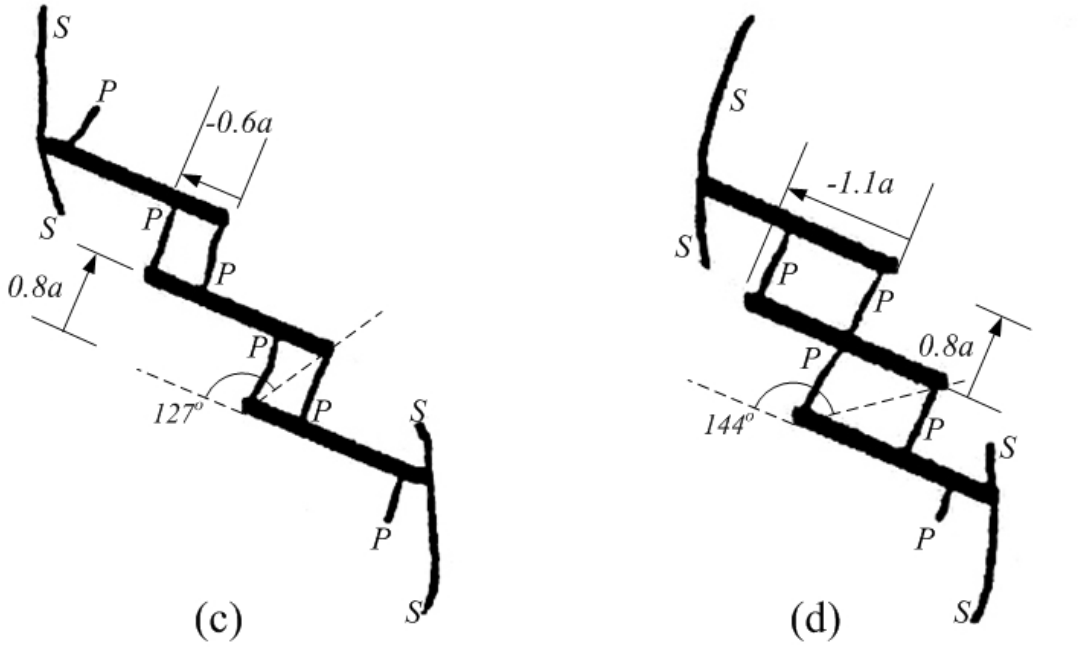

Figure 2.23B – Crack coalescence by tensile cracks in (c) and (d) under uniaxial compression, where P = primary crack, S = secondary crack with nature (shear/tensile) undetermined. The spacing and continuity measurements in terms of half flaw length '*a*' are also given (Chen et al., 1995).

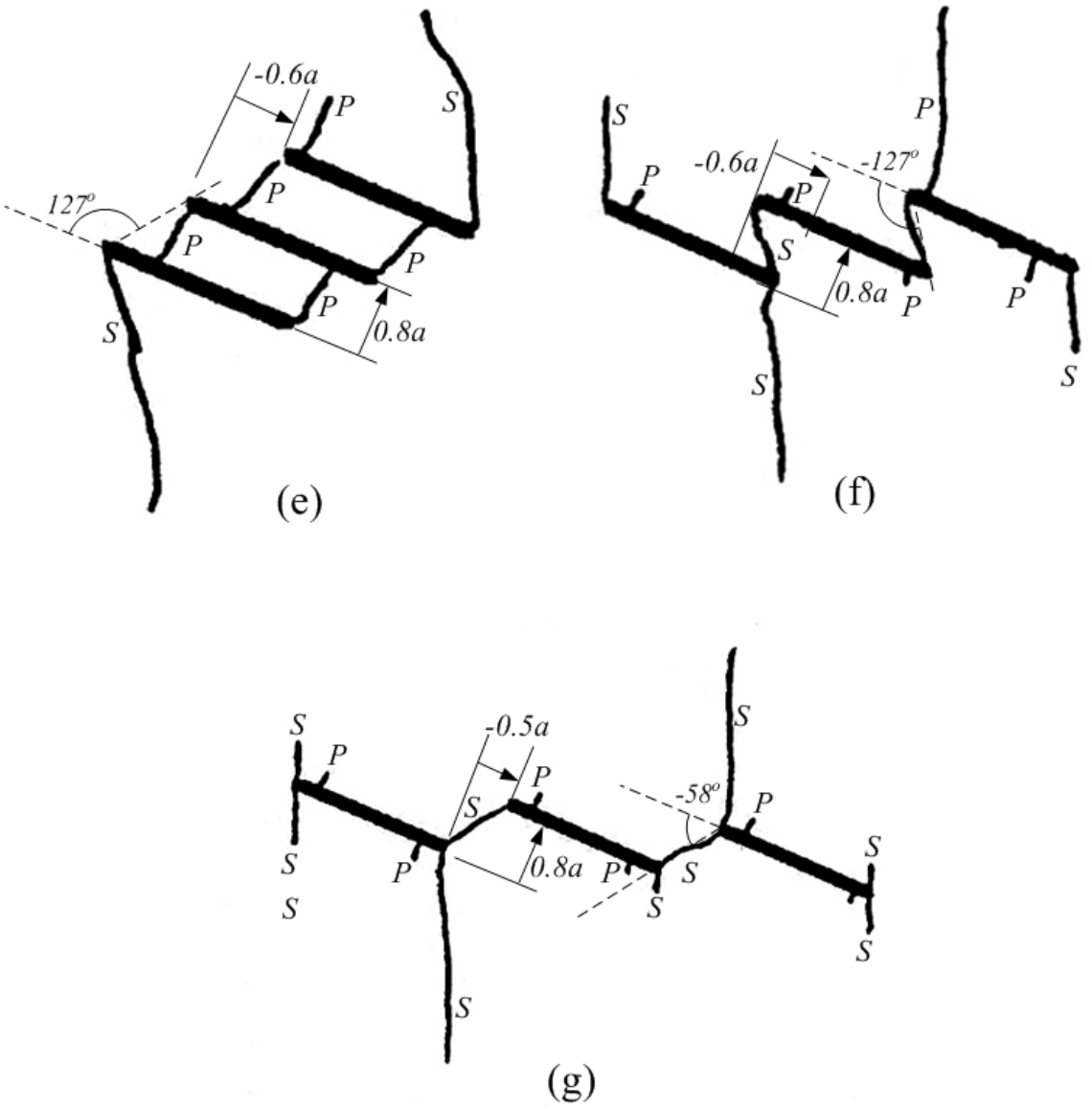

Figure 2.23C – Crack coalescence patterns (e) to (g) under uniaxial compression, where P = primary crack, S = secondary crack with nature (shear/tensile) undetermined. The spacing and continuity measurements in terms of half flaw length '*a*' are also given (Chen et al., 1995).

Similar to their discussion on fracturing behavior of single flaws (previous section), the authors used the terms "primary cracks" and "secondary cracks" throughout their discussion on multiple flaws. From the initiation position and trajectories of the primary cracks, it is very likely that they were tensile wing cracks. For the secondary cracks, the authors did not specify the nature (tensile/shear) of them.

Chen et al (1995) summarized the crack coalescence processes in marble as consisting of the following two stages:

a) **Crack initiation stage** – primary cracks first appeared near but not at the flaw tips in a direction normal to the flaw face. Secondary cracks, which appeared later, initiated from the flaw tips and propagated as the load increased.

b) **Coalescence stage** – The flaws were either linked up by the primary cracks (cases c, d, e) or secondary cracks (a, b, f, g). Note that under uniaxial compression of specimens consisting of only one single inclined flaw (also Chen et al., 1995), the direction of the secondary cracks was always concordant with σ_1 (see figure 2.14). For multiple parallel flaws, although most of the secondary cracks were also concordant with σ_1, depending on the geometrical relationship between the neighboring flaws, some trajectories of secondary cracks deviated from the direction of σ_1. For example, the coalescence secondary cracks in cases (b), (f) and (g) propagated towards the tip of the nearest flaw at an inclination with the vertical. In case (a), although the upper segment of the coalescence secondary crack was vertical, its initial segment adjacent to flaw tips was curvilinear. The flaw geometries also affected where the initiation of secondary cracks was more favored or suppressed. In certain flaw geometries (b), (c), (d) and (e), the secondary cracks developed more preferentially from the left tip of the leftmost flaw and the right tip of the rightmost flaw than the rest of the flaw tips.

c) **Specimen failure** – Close to the moment of specimen failure, similar to the single flaw cases, an "X" shaped band often developed from the tips of the outermost flaws, and propagated towards the specimen edges.

In her PhD thesis, Reyes conducted uniaxial compression tests on prismatic molded gypsum specimens (6" x 3" x 1.25") containing a pair of open pre-existing flaws (each 0.5", 12.7 mm long; refer to table 2.2). The ligament length was fixed and equal to the flaw length. The bridging angle was varied in 15^o increments. Three series ($\beta = 30^o, 45^o, 60^o$) were tested (Reyes, 1991, Reyes & Einstein, 1991).

β (^{o})	α (^{o})	L
30	0	2a
30	15	2a
30	30	2a
30	45	2a
30	60	2a
30	90	2a
30	105	2a
45	0	2a
45	15	2a
45	30	2a
45	45	2a
45	90	2a
60	-15	2a
60	0	2a
60	15	2a
60	30	2a
60	45	2a
60	75	2a
60	90	2a

Table 2.6 – Flaw geometries tested by Reyes (1991). 'a' = half flaw length and was 6.4mm long.

Reyes concluded from her tests that if the pre-existing flaws overlap, they coalesced by the initiation and propagation of tensile wing cracks. If the pre-existing flaws did not overlap, coalescence occurred through secondary cracks, which appeared in addition to and after the wing cracks. Sketches of some of the coalescence patterns provided by Reyes (1991) are reproduced in figure 2.24.

Note that Reyes used the term **secondary cracks** to describe all the cracks that appeared after the initiation of the first cracks.

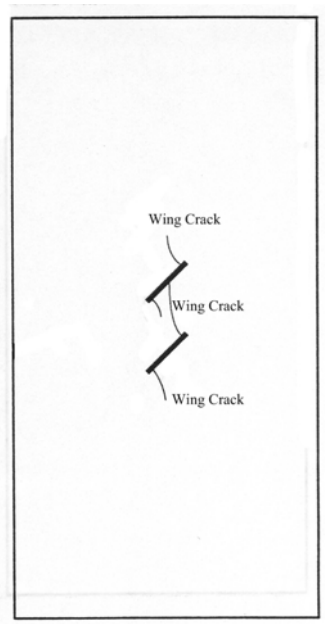

(a) $\beta = 45^o$, $\alpha = 90^o$

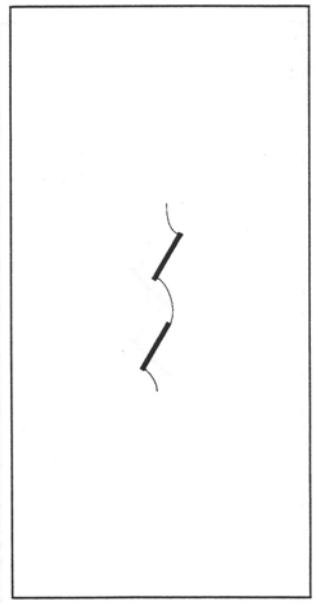

(a) $\beta = 60^o$, $\alpha = 45^o$

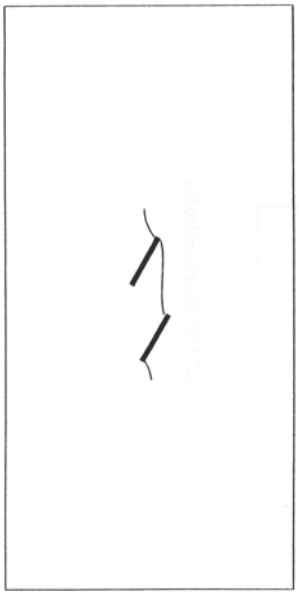

(c) $\beta = 60^o$, $\alpha = 75^o$

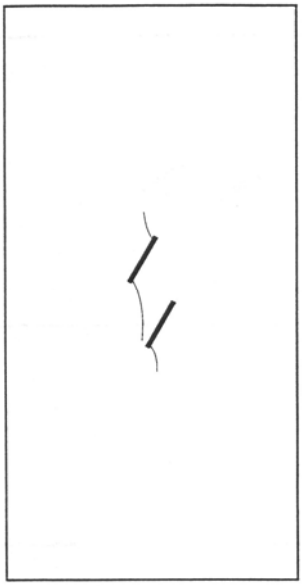

(d) $\beta = 60^o$, $\alpha = 90^o$

Figure 2.24 – Coalescence patterns achieved by wing cracks for certain overlapping flaw geometries observed by Reyes (1991).

In the experiments conducted by Shen et al. (1995), the coalescence patterns of two flaws (closed or open) arranged either in a coplanar manner or a stepped manner were studied (table 2.2). The tested material was molded gypsum, which was the same as that previously tested by Reyes (1991). The coalescence patterns are shown in figure 2.25 and summarized in table 2.7. Two crack types were identified by Shen et al. – **wing cracks** and **secondary cracks**.

Identification Number	**Configuration** [1]			**Type of coalescence cracks** [3]	
	β (°)	α (°)	L [2]	Closed	Open
1	30	15	2a	No coalescence	S + S
2	45	0	2a	S + S	S + S
3	45	15	2a	S + S	S + S
4	45	30	2a	S + W + S	S + T + S
5	45	45	2a	W + S or S + S	S + S
6	45	60	2a	W + S	W
7	45	75	2a	W	W + W
8	60	-15	2a	S + S	S + S
9	60	0	2a	S + S	S + S
10	60	15	2a	S	W + S
11	60	30	2a	W	W + S
12	60	45	2a	W	W
13	60	60	2a	S + S	S + S

Remarks:

[1] Refer to figure 2.19 for definition of different geometry parameters.

[2] 'a' = half flaw length and was 6.4 mm long.

[3] S = secondary crack, W = wing crack

Table 2.7 – Summary of coalescence crack types identified by Shen et al. (1995).

Number	Specimen	Critical Load at Coalescence, MPa	Schematic Path of Coalescence (a) frictional (b) nonfrictional	Description of Coalescence	Mode of Coalescence
1	30°/15° (2 specimens with friction fractures + 1 specimen with nonfrictional fractures)	No coalescence (frictional fractures) 17.2 MPa (nonfrictional fractures)	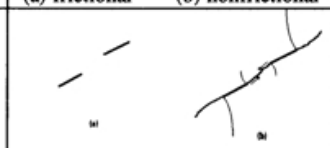	Type of coalescing fracture: secondary fracture. Initiation position: preexisting fracture tips. Surface characterization: rough, with many small kink steps; containing crushed gypsum.	Shearing
2	45°/0° (2 + 2)	21.9, 22.2 MPa (frictional fractures) 19.4, 17.9 MPa (nonfrictional fractures)	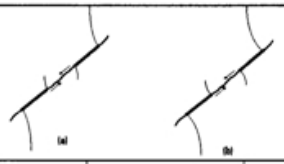	Type of coalescing fracture: secondary fracture. Initiation position: preexisting fracture tips. Surface characterization: rough, with many small kink steps; containing crushed gypsum.	Shearing
3	45°/15° (1 + 1)§	17.8 MPa (frictional fractures) 14.1 MPa (nonfrictional fractures)	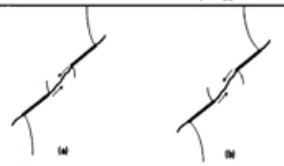	Type of coalescing fracture: secondary fracture. Initiation position: preexisting fracture tips. Surface characterization: rough, with several large kink steps. Noticeable crushed gypsum presented.	Shearing
4	45°/30° (1 + 1)§	19.2 MPa (frictional fractures) 14.1 MPa (nonfrictional fractures)	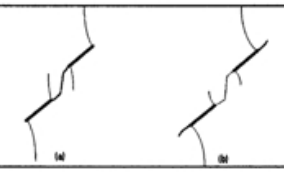	Type of coalescing fracture: secondary fracture. Initiation position: unclear. Surface characterization: rough, with two big kink steps. No noticeable crushed gypsum.	Shearing +tension
5	45°/45° (2 + 1)	(a) 17.8, MPa (a') 16.8* MPa (frictional fractures) (b) 16.4 MPa (nonfrictional fractures)	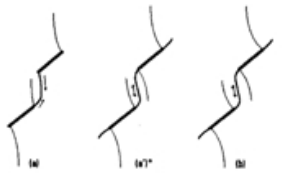	Type of coalescing fracture: (a) wing fracture + secondary fracture; (a') and (b) secondary fracture. Initiation position: (a) preexisting fracture tips; (a') and (b) intact material. Surface characterization: some parts are clean and smooth while other parts are rough with crushed gypsum.	Shearing +tension
6	45°/60° (2 + 1)	17.8, 16.8 MPa (frictional fractures) 16.4 MPa (nonfrictional fractures)		Type of coalescing fracture: wing fracture. Initiation position: preexisting fracture tips. Surface characterization: smooth and clean. Note: additional secondary fractures occur from the outer tips in case (b).	Tension
7	45°/75° (2 + 1)	(a) 21.0 MPa (a') 23.1 MPa (frictional fractures) (b) 17.6 MPa (nonfrictional fractures)	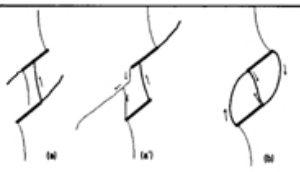	Type of coalescing fracture: wing fracture. Initiation position: preexisting fracture tips. Surface characterization: smooth and clean. Note additional coalescence by secondary fractures occurs in case (b).	Tension

Figure 2.25 – Crack coalescence patterns observed by Shen et al. (1995).

Number	Specimen	Critical Load at Coalescence MPa	Schematic Path of Coalescence (a) frictional (b) nonfrictional	Description of Coalescence	Mode of Coalescence
8	60°/-15° (2 + 1)	22.4, 21.4 MPa (frictional fractures) 17.8 MPa (nonfrictional fractures)	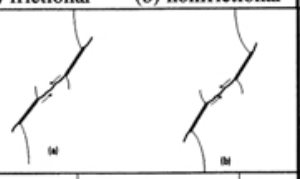	Type of coalescing fracture: secondary fracture. Initiation position: preexisting fracture tips. Surface characterization: rough, with many small kink steps; containing crushed gypsum.	Shearing
9	60°/0° (4+ 1)	20.5, 17.8, 20.3, 20.9 MPa (frictional fractures) 15.2 MPa (nonfrictional fractures)	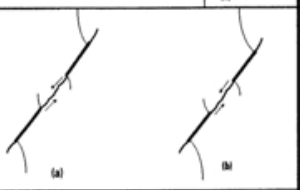	Type of coalescing fracture: secondary fracture. Initiation position: preexisting fracture tips. Surface characterization: rough, with several large kink steps. Noticeable crushed gypsum presented.	Shearing
10	60°/15° (1 + 1)§	18.5 MPa (frictional fractures) 13.7 MPa (nonfrictional fractures)		Type of coalescing fracture: (a) secondary fracture ; (b) secondary fracture + wing fracture. Initiation position: pre-existing fracture tips. Surface characterization: rough, with a few kink steps. No noticeable crushed gypsum.	Shearing +tension
11	60°/30° (1 + 1)§	19.2 MPa (frictional fractures) 14.2 MPa (nonfrictional fractures)		Type of coalescing fracture: (a) wing fracture ; (b) wing fracture + secondary fracture. Initiation position: preexisting fracture tips; Surface characterization: most parts are clean and smooth.	Tension +shearing
12	60°/45° (2 + 1)	19.9, 22.2 MPa (frictional fractures) 18.0 MPa (nonfrictional fractures)	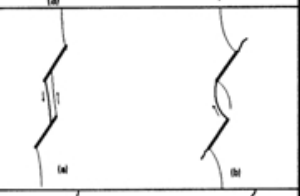	Type of coalescing fracture: wing fracture. Initiation position: preexisting fracture tips. Surface characterization: smooth and clean.	Tension
13	60°/60° (1 + 1)§	23.5 MPa (frictional fractures) 21.0 MPa (nonfrictional fractures)	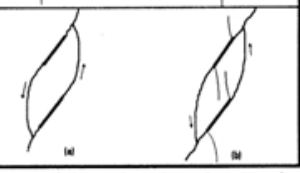	Type of coalescing fracture: secondary fracture. Initiation position: preexisting fracture tips. Surface characterization: very rough, coated with a lot of crushed gypsum.	Shearing

§ Only two of the three specimens produced useful results, the other specimen failed due to mismanipulation of the loading machine.

* The frictional fractures in this specimen have weaker contact than other frictional fractures. The polyethylene sheets were left longer (45 min) by mistake before they were pulled out. As a result, the created fractures did not close firmly.

Figure 2.25 – Crack coalescence patterns observed by Shen et al. (1995) (continued).

Shen et al. (1995) concluded from his experimental study that by varying the bridging angle of the pre-existing flaw pairs, while keeping the ligament length constant, there was a general trend of variation of coalescence patterns:

Small positive bridging angle and negative bridging angle

The coalescence was mainly achieved by **shear cracks** linking up the inner flaw tips.

Intermediate bridging angle

The coalescence was mainly achieved by **shear cracks** and **tensile cracks**.

Large bridging angle

The coalescence was mainly achieved by **tensile cracks**.

It is interesting to note that coalescence event induced mainly by shear cracks always initiated from **flaw tips** and then propagated towards the center of the bridging region (figure 2.26 a), while the coalescence event induced by combined tension and shearing often started from the **center of the bridging region** and propagated towards the flaw tips (figure 2.26 b).

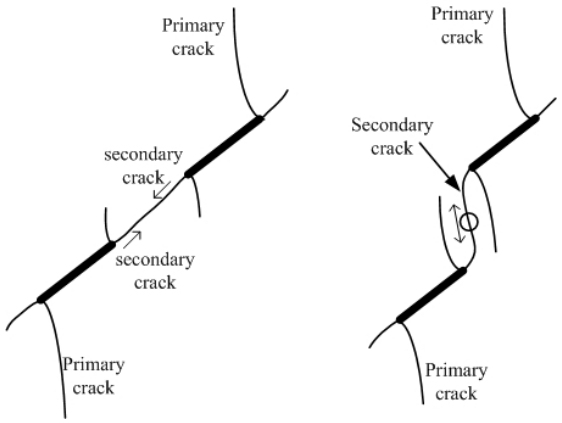

(a) (b)

Figure 2.26 – (a) Initiation of secondary cracks from flaw tips in open flaw pair of number 1 in figure 2.25. (b) Initiation of secondary cracks in the center of bridging region in open flaw pair of number 5 in figure 2.25. As described in figure 2.25, some parts of the secondary cracks in figure (b) were clean and smooth, while other parts were rough with crushed gypsum. However, the authors did not specify on the sketch where the tensile crack was and where the shear crack was.

A better understanding of the nature of the secondary cracks has also been gained from the work of Shen et al. (1995). From the descriptions given by the authors in figure 2.25, it appears that the authors regarded all of the secondary cracks as shear cracks. Secondary cracks displaying three different trajectories were identified (figure 2.27). The first type is more or less coplanar with the pre-existing flaw (figure 2.27 a). The second type displayed a curvilinear shape adjacent to the flaw tips, which became oriented along the uniaxial compression direction along its subsequent propagating path (figure 2.27 b). The third type also displayed a curvilinear trajectory, but it propagated in an opposite direction to the nearest wing crack (figure 2.27 c).

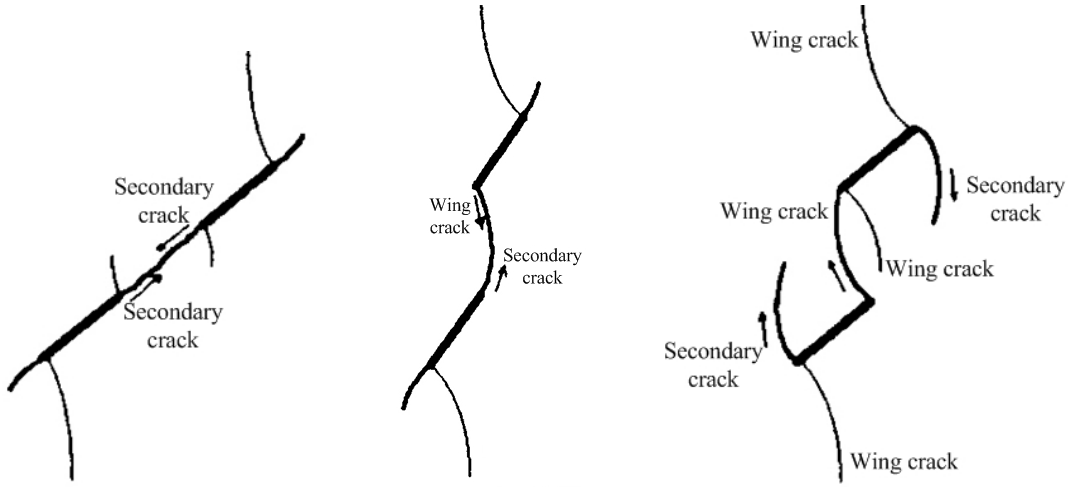

(a) (b) (c)

Figure 2.27 – (a) two coplanar secondary cracks initiated independently from the inner flaw tips, (b) a curvilinear secondary crack initiated from the right tip of the bottom flaw, (c) curvilinear secondary cracks initiated from the outer tips of the two pre-existing flaws (after Shen el at., 1995).

Another key finding in their work was related to those coalescence patterns, which involved two new cracks. Most of the coalescence events observed in the literature involving two new cracks were associated with the linkage of the **tips** of them (e.g. figure 2.28 a). In the study by Shen et al. (1995), linkage of the **tip** of one new crack with the **face** of another new crack was observed. In figure 2.28 b, the **tip** of a curvilinear secondary crack linked up to the **face** of a coplanar secondary crack, while in figure 2.28 c, the **tip** of a coplanar secondary crack linked up to the **face** of a wing crack.

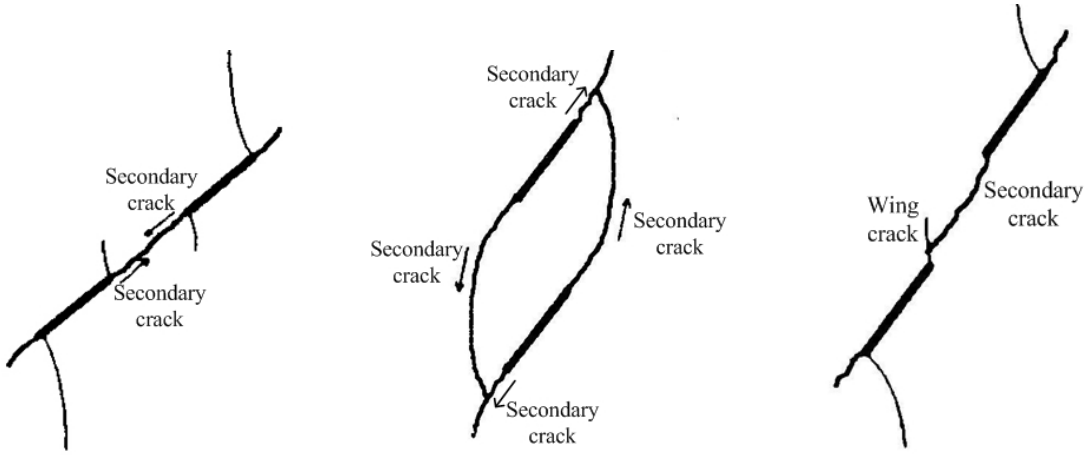

(a) (b) (c)

Figure 2.28 – (a) coalescence due to two coplanar secondary cracks initiated independently from the inner flaw tips. (b) a curvilinear secondary crack initiated from the right tip of the bottom flaw coalesced with the face of a coplanar secondary crack. (c) the tip of a coplanar secondary crack linked up to the face of a wing crack (after Shen el at., 1995).

In his PhD thesis, Bobet investigated crack coalescence in prismatic molded gypsum specimens (dimensions and composition equivalent to that tested by Reyes, 1991) under uniaxial and biaxial compression (Bobet 1997, Bobet & Einstein, 1998a). The aperture of the tested flaw pairs embedded in the specimens was either closed or open (table 2.2). They observed that tensile wing cracks, which initiated from the flaw tips, were the first cracks to appear in the specimens under loading. Secondary cracks appeared later and in most cases initiated in a direction coplanar to the pre-existing flaws. Based on the observed spalling events during the loading tests and the presence of crushed material (gypsum powder) left on the crack faces, they concluded that secondary cracks were shear cracks. They thus called all **shear cracks** as **secondary cracks.** In addition, they called all **tensile cracks** as **wing cracks**.

Flaw Geometry					MIT-Purdue Coalescence Type (fig 2.23)	
β (°)	s	c	α(°)	L	Open flaws	Closed flaws
30	0	2a	0	2a	I	NC
30	0	3a	0	3a	NC	I
30	0	4a	0	4a	-	-
30	a	a	45	1.4a	II	II
30	a	2a	27	2.2a	II	II
30	a	3a	18	3.2a	I	I
30	a	4a	14	4.1a	-	-
30	2a	2a	45	2.8a	II	II
30	2a	3a	34	3.6a	II	II
30	2a	4a	27	4.5a	-	-
30	3a	2a	57	3.6a	II	II
30	3a	3a	45	4.2a	II	II
30	3a	4a	37	5a	II	II
30	4a	3a	43	5a	II	NC
30	4a	4a	45	5.7a	NC	NC
45	0	2a	0	2a	I	I
45	0	3a	0	3a	I	I
45	0	4a	0	4a	I	I
45	a	a	45	1.4a	II	II
45	a	2a	27	2.2a	II	II
45	a	3a	18	3.2a	I	I
45	a	4a	14	4.1a	I	I
45	2a	2a	45	2.8a	II	III
45	2a	3a	34	3.6a	II	II
45	2a	4a	27	4.5a	II	II
45	3a	3a	45	4.2a	II	III
45	3a	4a	37	5a	II	III
45	4a	4a	45	5.7a	III	III
60	0	2a	0	2a	I	I
60	0	3a	0	3a	I	I
60	0	4a	0	4a	I	I
60	a	2a	27	2.2a	II	III
60	a	3a	18	3.2a	II	II
60	a	4a	14	4.1a	III	II
60	2a	4a	27	4.5a	III	III

Table 2.8 – Crack coalescence patterns observed by Bobet and Einstein (1998a). ‘a’ = half flaw length and was 12.7mm long.

Type	Schematic path of Coalescence	Description of Coalescence	Mode of Coalescence
I	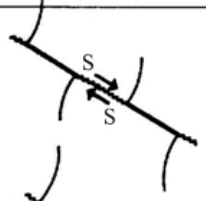	Type of coalescing fracture: secondary shear crack. Initiation position: preexisting flaw tips. Crack surface characterization: rough, with many small kink steps; contains crushed gypsum	Shearing
II	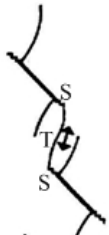	Type of coalescing fracture: secondary shear and tensile cracks. Initiation position: preexisting flaw tips. Crack surface characterization: some parts are clean and smooth while other parts are rough with crushed gypsum	Shearing + tension
III	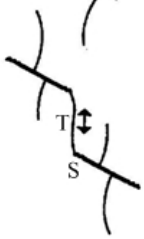	Type of coalescing fracture: secondary shear crack and wing crack. Initiation position: preexisting flaw tips. Crack surface characterization: some parts are clean and smooth while other parts are rough with crushed gypsum	Shearing + tension
IV	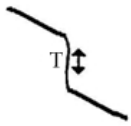	Type of coalescing fracture: wing crack. Initiation position: preexisting flaw tips. Crack surface characterization: smooth and clean.	Tension
V	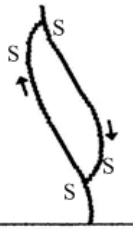	Type of coalescing fracture: secondary crack. Initiation position: preexisting flaw tips. Crack surface characterization: very rough, coated with a lot of crushed gypsum	Shearing?

Figure 2.29 – Crack coalescence modes in molded gypsum specimens observed by Bobet & Einstein (1998a). T = tensile crack. S = shear crack.

Table 2.8 and figure 2.29 summarize the coalescence types observed by the authors under uniaxial loading. **Type I coalescence** occurred between the inner flaw tips of two coplanar/almost coplanar flaws and it was achieved by secondary cracks (shear cracks). In **type II coalescence**, which involved three coalescence cracks, favorably occurred in flaw pairs with spacing to continuity ratio grater than 1/3. It was achieved by the linkage of the two secondary cracks (shear cracks) initiated independently from the inner flaws by another tensile crack. **Type III coalescence** involved two coalescence cracks and it

was achieved by the linkage of a secondary crack (shear crack) initiated from one flaw tip and a wing crack (tensile crack) initiated from another flaw tip. **Type IV coalescence** involved one coalescence crack which was a wing crack (tensile crack) initiated from the tip of one flaw and propagated towards the tip of the other flaw. **Type V coalescence** involved one coalescence crack which was a curvilinear secondary crack (shear crack) linking up the tips of the same side of the two pre-existing flaws.

Note that table 2.8 focuses solely on the coalescence patterns but not specifically on crack initiation sequence. Most of the coalescence for open flaws and closed flaws were the same, except for a few geometries (highlighted in table 2.8). It is also interesting to note that a new crack always initiated from a pre-existing flaw **tip** (but not at a distance away from the flaw tip), and it either terminated at the other pre-existing flaw **tip** or the **tip** of another new crack independently (but not on the face of the other pre-existing flaw or the face of the other newly initiated crack).

Martinez (1999) extended the work of Bobet (1997) to study the fracturing and coalescence behavior in natural rocks of the same dimensions (Vermont White Marble and Barre Granite) under uniaxial compression loading (table 2.2). The artificial pre-existing flaws were created by using a water abrasive jet. In his experimental study, a high speed imaging system up to 250 frames/second was used to record the details of fracturing processes. Similar coalescence patterns observed previously by Bobet in molded gypsum were observed in the natural rocks (figure 2.30). With the use of the high speed camera, it became possible to identify a new coalescence type IVB which involved the initiation and propagation of tensile cracks independently from both inner flaw tips. His work will be reviewed separately in detail in chapter 3.

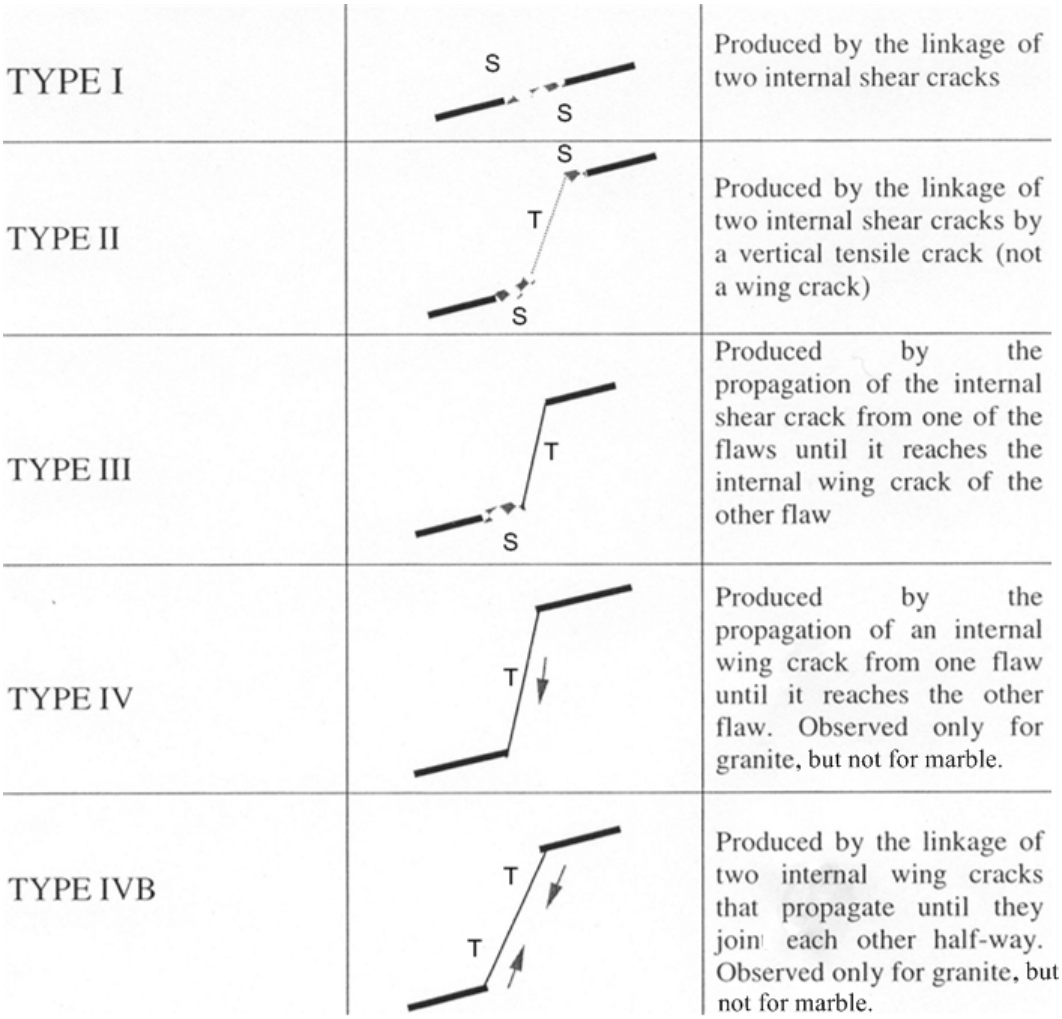

Figure 2.30 – Coalescence patterns observed and summarized by Martinez (1999). S = shear crack. T = tensile crack.

Sagong and Bobet (2002) carried out tests on the molded gypsum specimens with the same composition and dimensions as that used previously by the MIT rock mechanics group (table 2.2). Specimens containing three and 16 parallel flaws were studied. Crack coalescence patterns observed previously in specimens containing double flaws were again observed by the authors (figure 2.31). Additional (new) crack coalescence types were also identified in the flaw geometries, which were not tested before (Types VI, VII, VIII, IX). The authors also generalized that secondary cracks (shear cracks) of two different trajectories were present: (1) coplanar or quasi-coplanar with the pre-existing

flaws, which took part in coalescence types I, II, III, V and IX, and (2) oblique to the pre-existing flaws, which took part in coalescence types VI, VII, VIII and IX.

Type	Left Stepping	Type	Right Stepping	Coalescence cracks
I	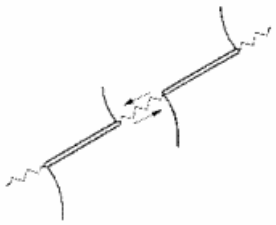	VI	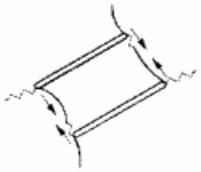	Type I: Quasi-coplanar secondary cracks. Type VI: Oblique secondary cracks and wing crack.
II	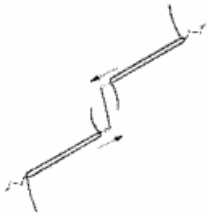	VII		Type II: Quasi-coplanar secondary cracks and out of plane tensile secondary crack. Type VII: Oblique secondary cracks and out of plane tensile secondary crack.
III	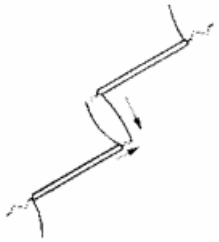	VIII		Type III: Quasi-coplanar secondary crack and wing crack. Type VIII: Oblique secondary cracks.
IV	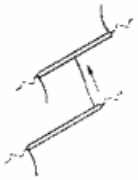	IX	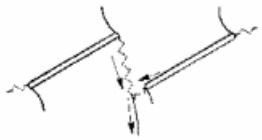	Type IV: Wing crack Type IX: Oblique secondary crack and quasi-coplanar secondary crack.
V	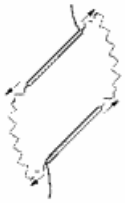			Type V: Quasi-coplanar secondary crack and out of plane secondary shear crack.

Figure 2.31 – Various crack coalescence types observed in molded gypsum specimens containing three flaws (Sagong & Bobet, 2002).

Ko extended the experimental work on prismatic molded gypsum specimens by Bobet (1997) to include uniaxial cyclic loading tests (Ko, 2005, Ko et al., 2006). **Wing cracks** and **secondary cracks** were observed in both monotonic and cyclic tests (table 2.2). They also confirmed that wing cracks were tensile cracks, which initiated at (or near) the tips of the pre-existing flaws and propagated parallel to the compressive loading axis. The term **shear cracks** was used interchangeably with **secondary cracks** by the authors in their discussion. The **shear cracks,** which led to final failure, always appeared after the initiation of the wing cracks. They initiated at the flaw tips and propagated in a direction coplanar with the pre-existing flaw or in a horizontal direction (orthogonal to the vertical loading direction).

Six types of coalescence patterns were reported by the authors (figure 2.27). Note that the classification scheme adopted by Ko was slightly different from those proposed previously by Bobet (figure 2.24), Martinez (figure 2.25) and Sagong and Bobet (figure 2.26). The original type I and type II coalescence types were retained by Ko. However, he divided type III into III-A and III-B, and type IV into IV-A, IV-B and IV-C. The original type III coalescence involved one quasi-coplanar shear crack and one tensile crack, while the original type IV coalescence involved one tensile crack. Ko's type III describes coalescence which was achieved by one coalescence crack consisting of either one (type III-A) or two (type III-B) crack segments, while Ko's type IV describes coalescence which was achieved by two independent but symmetrical coalescence cracks. Each of the coalescence again consisted of either one (type IV-A, IV-B) or two (type IV-C) crack segments. Ko's type IV-C, however, also corresponds to the old type VI (coalescence by one tensile crack and one oblique crack). Note also that the old type V was not included in Ko's classification scheme. On the other hand, Ko's type V and VI were not observed in previous classification schemes.

For coplanar geometry specimens, coalescence occurred between inner flaw tips by shear cracks. For non-coplanar geometry specimens, coalescence occurred through combinations of shear cracks, tensile wing cracks and/or other tensile cracks not displaying wing appearance. In contrast to the monotonic tests, cyclic tests produced

fatigue cracks. The fatigue cracks either initiated in a direction coplanar with the pre-existing flaws or orthogonal to the vertical loading direction (not shown in figure 2.32).

Type	Coalescence Pattern [1]	Characteristic [2]
I	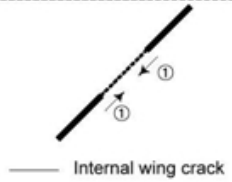	Type of crack: shear crack. Coalescence crack surface: rough with crushed gypsum.
II	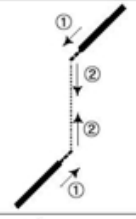	Type of crack: internal shear and tension crack. Coalescence crack surface: 1)
III-A	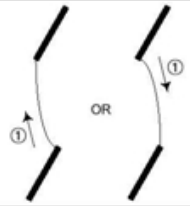	Type of crack: internal wing crack. Coalescence crack surface: 2)
III-B	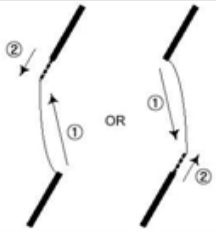	Type of crack: internal wing crack and internal shear crack. Coalescence crack surface: 1)
IV-A	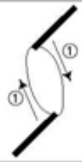	Type of crack: internal wing crack. Coalescence crack surface: 2)
IV-B	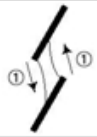	Type of crack: internal wing crack. Coalescence crack surface: 2)
IV-C	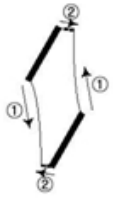	Type of crack: internal wing crack and internal shear crack. Coalescence crack surface: 1)
V	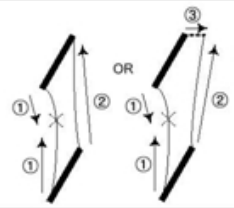	Type of crack: internal wing crack and internal shear crack. Coalescence crack surface: 1)
VI	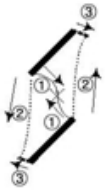	Type of crack: internal wing crack, internal shear crack and tension crack. Coalescence crack surface: 1)

Remarks :

[1] In the central column showing the coalescence patterns, the numbers indicate the crack development sequence.

[2] In the rightmost column describing crack characteristics, (1) indicates that the crack surfaces were rough with crushed gypsum near the flaw tips, and clean and smooth in other parts. (2) indicates that the crack surfaces were clean and smooth.

Figure 2.32 – Coalescence patterns summarized by Ko et al. (2006) in molded gypsum under monotonic and cyclic uniaxial compression tests.

Wong and Chau (1998) conducted uniaxial compression tests on sandstone-like specimens (60 mm x 120 mm x 25 mm, see table 2.2). They observed three main modes of crack coalescence between two parallel flaws each of length 12mm (table 2.9): (1) shear (S) mode - shear cracks occurred between the two flaws; (2) the mixed shear/tensile (M) mode - both wing and shear cracks propagated between the two flaws; (3) wing tensile (W) mode - wing cracks coalesced the two flaws. Figure 2.34 shows the detailed crack patterns in this experiment.

Identification number	**Coalescence classification**	**Description of coalescence cracks by Wong and Chau (1998)**
a	S	**Two shear cracks** independently initiated from the inner flaw tips and coalesced in the bridging area.
b	M I	**Two wing cracks** independently initiated from the inner flaw tips were later linked up by a **shear crack**. (The authors were unsure if the **shear crack** initiated from the center of the bridging area or from **the wing cracks**.)
c	M II	A **shear crack** initiated from one inner flaw tip coalesced with a **wing crack** initiated from the other flaw tip. (The authors were unsure if the **shear crack** initiated from the inner tip of upper crack or from the end of the **wing crack**)
d	W I	**Two wing cracks** initiated independently from inner flaw tips and coalesced.
e	W II	A **wing crack** initiated from the inner tip of one flaw coalesced with the face of the other flaw.
f	W III	A **wing crack** linked up the tips of the same side of the two pre-existing flaws.
g	W I/II	Combination of coalescence types **W I** and **W II**.
h	W I/III	Combination of coalescence types **W I** and **W III**.
i	W II/III	Combination of coalescence types **W II** and **W III**.

Note : S (shear mode), W (Wing tensile mode), M (Mixed shear/tensile mode)

Table 2.9 – Coalescence types observed in sandstone-like molded barite by Wong and Chau (1998).

Various crack pair configurations have been tested by Wong and Chau (1998) by varying the flaw inclination angle (β) and the bridging angle between inner flaw tips (α') as shown in figure 2.33. Note that the definition of α' by Wong and Chau (1998) was different from that of α shown in figure 2.19 ($\alpha = \alpha' - \beta$).

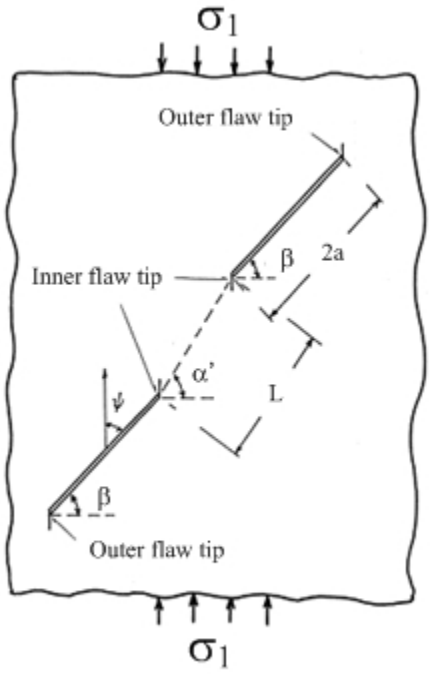

Figure 2.33 – Definition of flaw inclination angle (β) and bridging angle between inner crack tips (α') for a pair of parallel flaws in the specimens tested by Wong and Chau (1998).

Although nine different patterns (a to i) are shown in figure 2.34, the last three (g, h, i) are simply combinations of the previous coalescence patters, i.e. W I/II, W I/III and W II/III. It means that two coalescence wing cracks of different types were observed to link up the two pre-existing flaws. However, due to the limited time-resolution of the camera, they were unable to determine which coalescence crack was earlier. Thus the types of both coalescence cracks were reported. Due to the same limitation of their camera, the propagation directions of a number of the coalescence cracks were unknown.

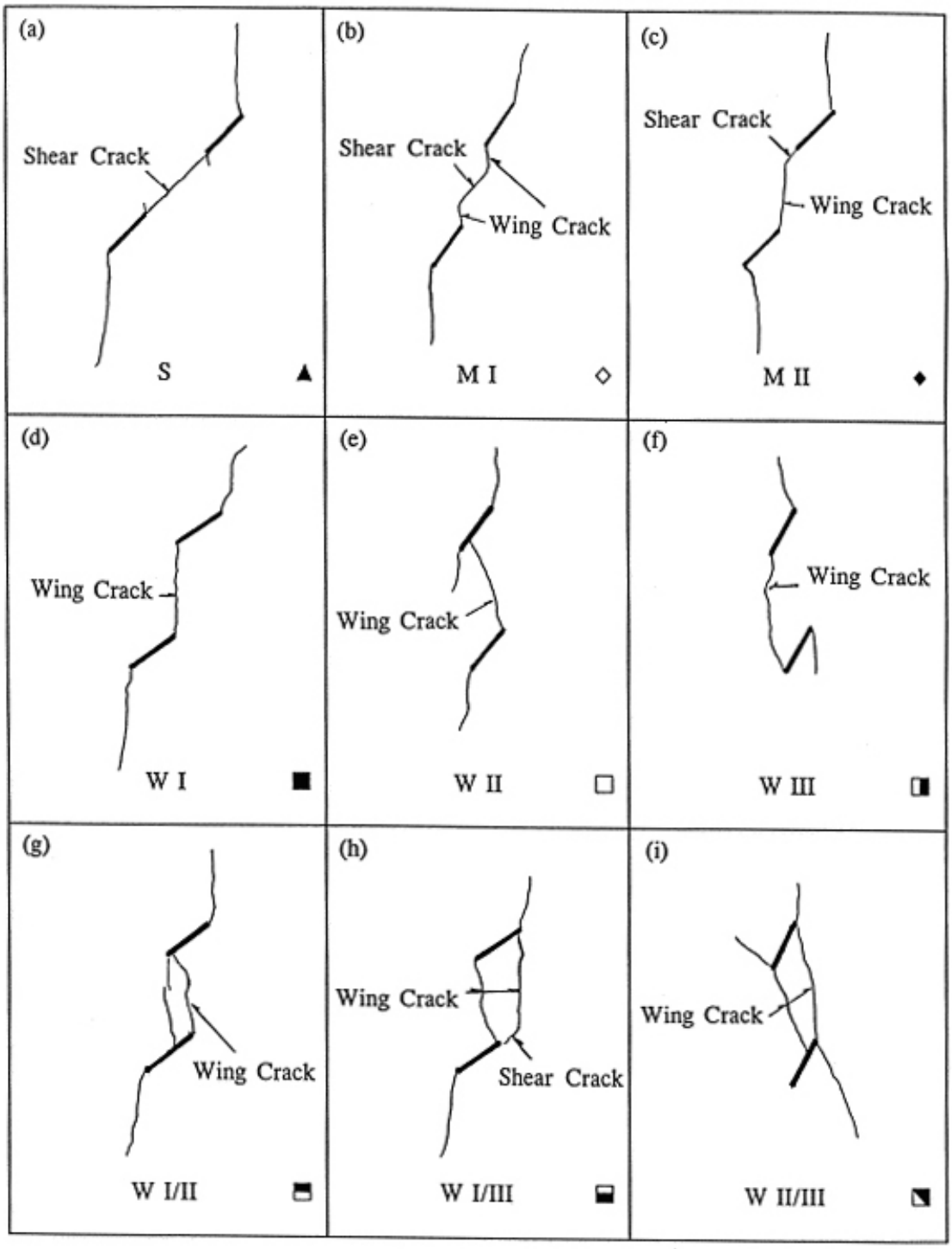

Figure 2.34 – Coalescence patterns observed by Wong and Chau (1998) in sandstone-like molded barite. The letters S, M and W indicate shear, mixed shear/tensile and wing tensile modes respectively. The triangular, rhombic and square symbols are used in figures 2.35 – 2.37 for regime classification.

All their tested flaws were closed flaws with varying friction coefficients (μ). The effect of friction on the mode of crack coalescence is illustrated in the plots of α'- β regimes for different crack calescence modes (S-regime, M-regime and W-regime) for μ = 0.6, 0.7 and 0.9 (figures 2.35 – 2.37). When μ increased from 0.6 to 0.7, the S-regime shrank with a corresponding expansion of the M-regime. It means that those crack configurations preferentially coalesced by shear cracks for μ = 0.6 tended to coalesce by mixed shear and tensile cracks when μ = 0.7. The extent of the W-regime, however, remained the same for various values of μ.

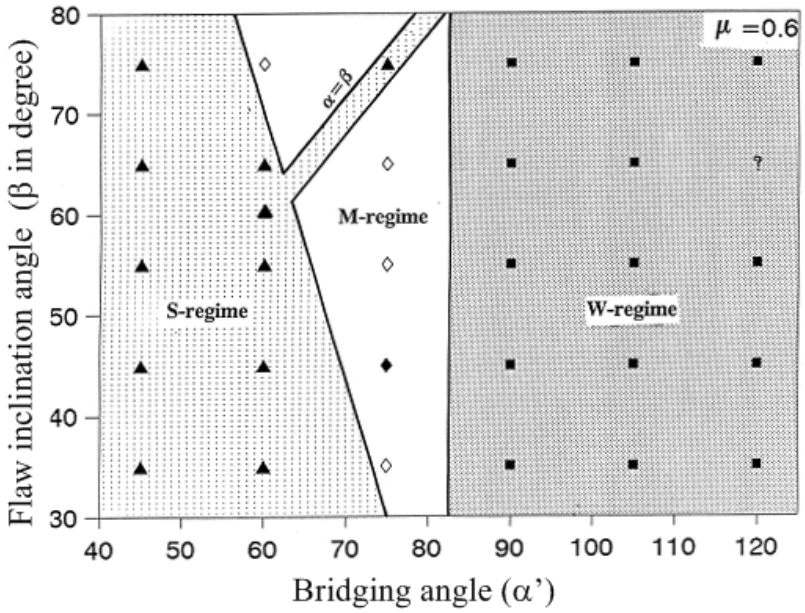

Figure 2.35 – The regime classification in the $\alpha'-\beta$ space for μ=0.6. The dotted S-regime with a strip parallel to $\alpha'-\beta$ on the left is for the shear mode coalescence, the M-regime in the centre is for the mixed mode coalescence, and the dotted W-regime on the right is for the wing tensile mode coalescence. The symbol of '?' is for sample failure without crack coalescence (Wong and Chau, 1998).

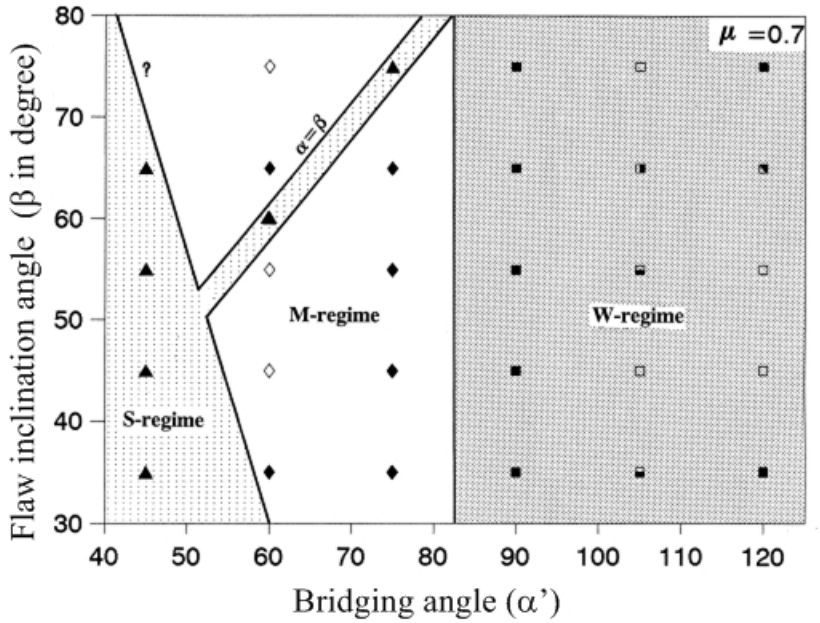

Figure 2.36 – The regime classification in the $\alpha' - \beta$ space for μ =0.7. Other captions are the same as those for figure 2.35 (Wong & Chau, 1998).

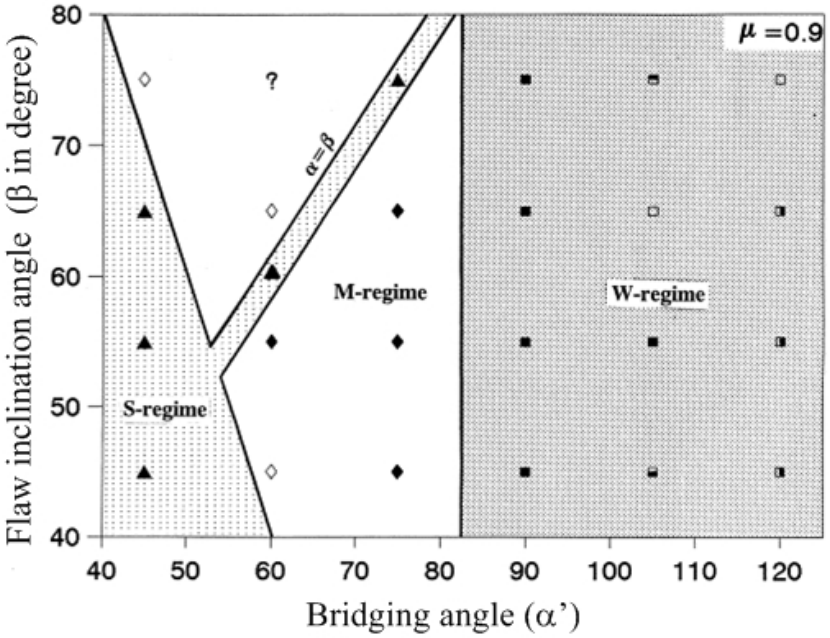

Figure 2.37 – The regime classification in the $\alpha' - \beta$ space for μ =0.9. Other captions are the same as those for figure 2.35 (Wong & Chau, 1998).

Wong and Chau (1998) again used the terms **secondary cracks** and **shear cracks** interchangeably, and **wing cracks** and **tensile cracks** interchangeably. More specifically, they called all tensile cracks as wing cracks, despite their actual trajectories. One typical example was the tensile coalescence crack which was involved in coalescence type M II. Although its general trajectory (reproduced in figure 2.38 a) was different from that of a conventional tensile wing crack (figure 2.38 b), it was still designated as a wing crack by the authors.

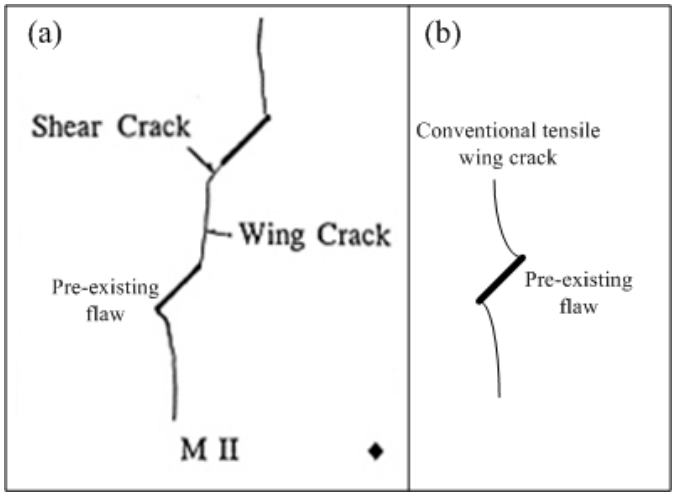

Figure 2.38 – (a) A tensile crack not displaying a typical wing appearance was labeled by Wong and Chau (1998) as a wing crack. (b) Trajectories of two typical tensile wing cracks.

Li et al., (2005) conducted uniaxial compression loading tests on Huangshi marble specimens which contained double flaws (0.5 – 1 mm wide with a 6 mm diameter center hole; the measurement of the flaw length was not given) oriented at different orientations. The following coalescence patterns were reported (figure 2.39):

Specimen (d) with double flaws (30^o flaw inclination angle, 10 mm ligament length, 60^o bridging angle) – Wing cracks initiated from the outer crack tips. A coalescence tensile crack developed between the inner flaw tips (figure 2.39 a).

Specimen (e) with double flaws (45^o flaw inclination angle, 7 mm ligament length, 90^o bridging angle) – The initiation of wing cracks was followed by the initiation of secondary cracks which were coplanar with the wing cracks but in opposite direction. No new cracks initiated from the inner flaw tips. The nature of the two curvilinear cracks (with **?** marked beside the crack traces in figure 2.39 b) initiated from the outer flaw tips was undetermined.

Specimen (f) with double flaws (45^o flaw inclination angle, 10 mm ligament length, 45^o bridging angle) – Wing cracks and secondary cracks initiated at outer flaw tips. Secondary cracks bifurcated at the right tip of the top flaw. One such secondary crack propagated towards the loading direction. The authors stated that the coalescence crack between the two inner flaw tips was of **tension-shear-mixed mode,** which was unclear in their original sketch (figure 2.39 c).

As mentioned already in the previous section, the authors did not use the terms **tensile** and **shear** to describe the identity of the newly-initiated cracks throughout their whole discussion, but the terms **wing cracks** and **secondary cracks** instead.

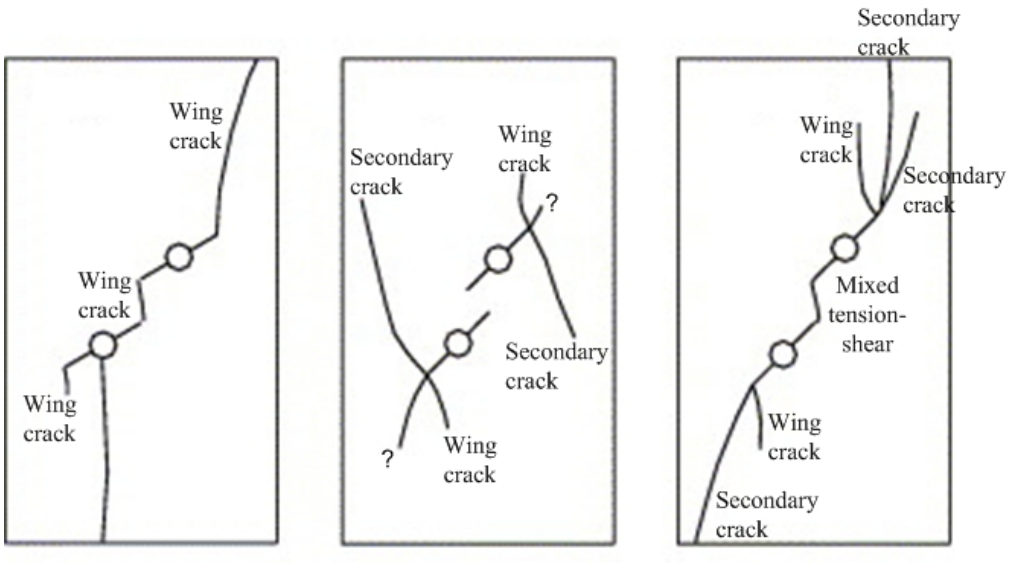

(a) specimen d (b) specimen e (c) specimen f

Figure 2.39 – (a) Coalescence achieved by a wing crack between inner flaw tips. (b) No coalescence. (c) Mixed tension-shear coalescence mode (Li et al., 2005).

Mughieda and Alzo'ubi (2004) conducted uniaxial compression tests on prismatic specimens of man-made sandstone which was made from a mixture of 72% silica sand, 16% cement and 12% water by weight (table 2.2). The flaw inclination angle (β) was maintained at 45^o for all specimens, while varying the bridging angle (α) from 0^o to 120^o with an increment of 15^o. The flaw aperture was 3 mm, while the flaw length was not mentioned by the authors. The coalescence patterns are summarized in figure 2.40. Notice that the authors used the terms **primary** and **secondary** strictly to indicate the temporal relationship of the newly initiated cracks. From the morphology of the crack surfaces, the authors attempted to determine the nature of the coalescence crack segments. They determined that **tensile cracks** were always the **primary cracks.** In addition, they also determined that some secondary cracks were **tensile cracks** and some secondary cracks were **shear cracks**.

As shown in figure 2.40, **small bridging angle** ($\alpha = 0^o$) favored coalescence between the inner flaw tips, which was achieved by coplanar **shear cracks**. **Intermediate bridging angles** ($\alpha = 30^o, 45^o$) favored coalescence which was achieved by **tensile and shear crack segments**. **Large bridging angle**s ($\alpha = 60^o, 75^o, 105^o, 120^o$) favored coalescence which was solely achieved by **tensile cracks**. It is of great interest to note that for $\alpha =$ **60^o**, instead of initiating from the tips of the pre-existing flaw, the coalescence crack first initiated as a vertical tensile crack segment in the middle of the bridging region.

Bridging angle (^{o})	Fracturing and coalescence patterns	Coalescence cracks observed by authors
0	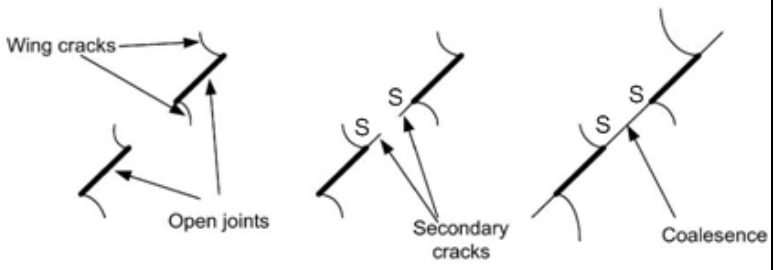	Coplanar secondary shear cracks initiated from the inner flaw tips
30	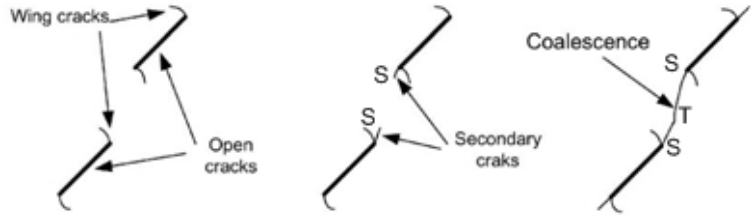	Oblique secondary shear cracks initiated from the inner flaw tips; tensile crack along the central segment
45	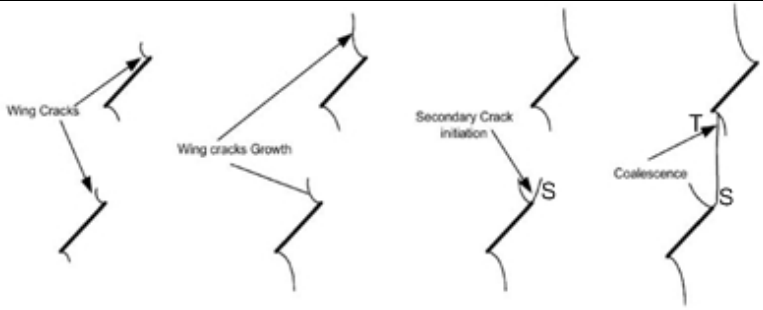	An oblique secondary shear crack initiated from one inner flaw tip linked up to the other flaw by a tensile crack
60	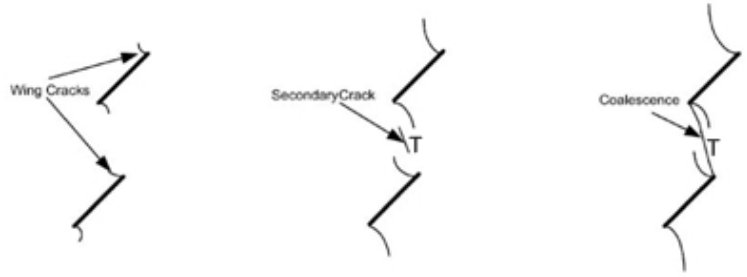	A short tensile crack segment initiated in the middle of the bridging region, which extended to reach the inner flaw tips

Figure 2.40 – Fracturing and coalescence patterns in man-made sandstone specimens observed by Mughieda and Alzo'ubi (2004). S = shear crack. T = tensile crack.

Bridging angle (^{o})	Fracturing and coalescence patterns	Coalescence cracks
75	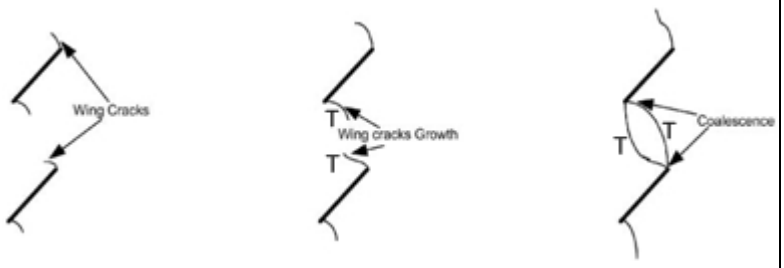	Tensile wing cracks initiated from the inner flaw tips
105	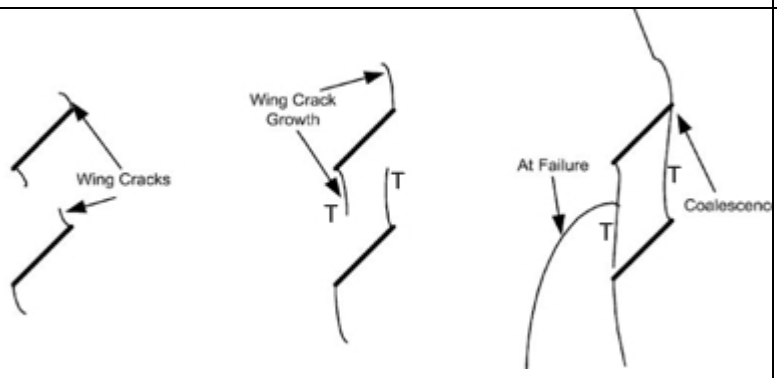	Tensile wing cracks initiated from the flaw tips
120	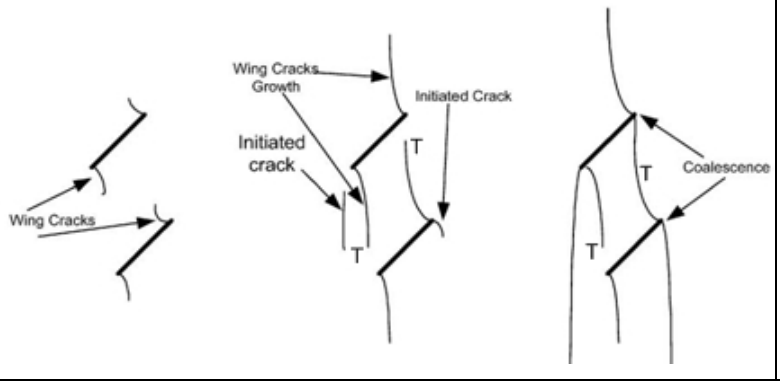	Tensile wing cracks initiated from the flaw tips

Figure 2.40 – Fracturing and coalescence patterns in man-made sandstone specimens observed by Mughieda and Alzo'ubi (2004). S = shear crack. T = tensile crack. (continued).

To summarize this section on the literature review of the past experimental studies on crack coalescence in man-made materials and natural rocks, the following key points are noted.

Since **tensile wing cracks** were always the first cracks to initiate in the specimens containing multiple flaws, the terms **tensile cracks**, **wing cracks** and **primary cracks** were used interchangeably by most authors. However, using these terms in an interchangeable manner sometimes led to confusion. For example, all the tensile cracks observed by Wong and Chau (1998) were all labeled as wing cracks. However, there were obvious cases in which some tensile cracks did not display a conventional wing appearance.

A similar issue also occurs for the terms **secondary cracks** and **shear cracks**. Since in most cases, signs of shearing were found on the surfaces of the secondary cracks, there was a strong tendency for the authors to use the terms **secondary cracks** and **shear cracks** interchangeably. Confusion thus arose when the shear nature of the secondary cracks was actually uncertain or difficult to determine. For example, Chen el al., (1995) simply refereed to all cracks appearing after the first cracks as **secondary cracks** without identifying the mode of crack initiation. Another possible confusion occurred as subsequent research found that **secondary cracks** were not limited to **shear cracks**, but also included **tensile cracks**. As shown in figure 2.40 for $\alpha = \mathbf{60^o}$, after the initiation of the tensile wing cracks, another tensile crack initiated in the middle of the bridging region at a later stage. Mughieda and Alzo'ubi (2004) thus described this crack as **secondary tensile crack** and the term **secondary** here was restricted to temporal meaning, indicating that it initiated later than the first (primary) cracks.

More than one type of shear cracks (different crack trajectories) were recognized by different authors (Shen et al., 1995, Martinez, 1999, Sagong & Bobet, 2002, Mughieda & Alzo'ubi, 2004, Ko et al., 2006). They were different from each other with respect to the shape and direction of the propagating crack trajectories – (1) shear crack coplanar or quasi-coplanar with the pre-existing flaw (figure 2.40 a), (2) curvilinear shear crack

initiated from the flaw tip which propagated in a general direction similar to the nearby tensile wing crack, i.e. either both upward or downward (figure 2.40 b). (3) oblique shear crack initiated from the flaw tip which propagated in a direction opposite to that of the nearby tensile wing crack, i.e. one crack upward and the other crack downward (figure 2.40 c).

Crack type	**Examples**		
(a) Coplanar shear crack (secondary crack)	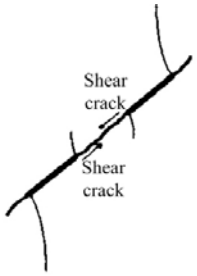 Shen et al. (1995)	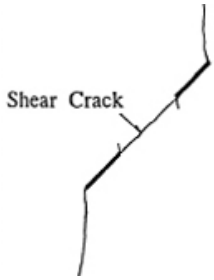 Wong & Chau (1998)	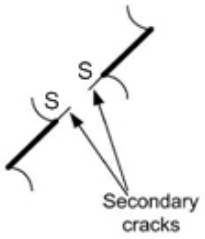 Mughieda and Alzo'ubi (2004)
(b) Curvilinear shear crack (secondary crack)	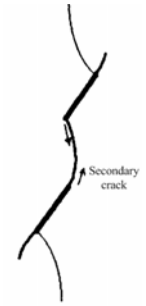 Shen et al. (1995)	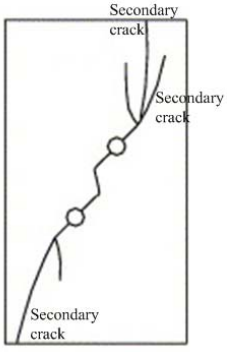 Li et al. (2005)	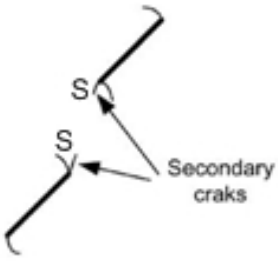 Mughieda and Alzo'ubi (2004)
(c) Oblique shear crack (secondary crack)	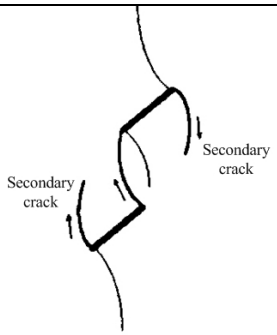 Shen et al. (1995)	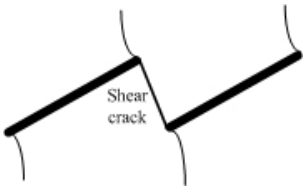 Sagong & Bobet (2002)	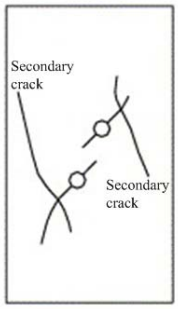 (Li et al., 2005)

Figure 2.40 – Summary of three different shear crack types observed by previous researchers.

The location of the new crack initiation was found not to be restricted to tips of the pre-existing flaws, but can be in the intact material at a distance away from the flaw tip. Examples were provided by Ingraffea and Heuze (1980), Shen et al. (1995) and Mughieda and Alzo'ubi (2004). See figure 2.41 below.

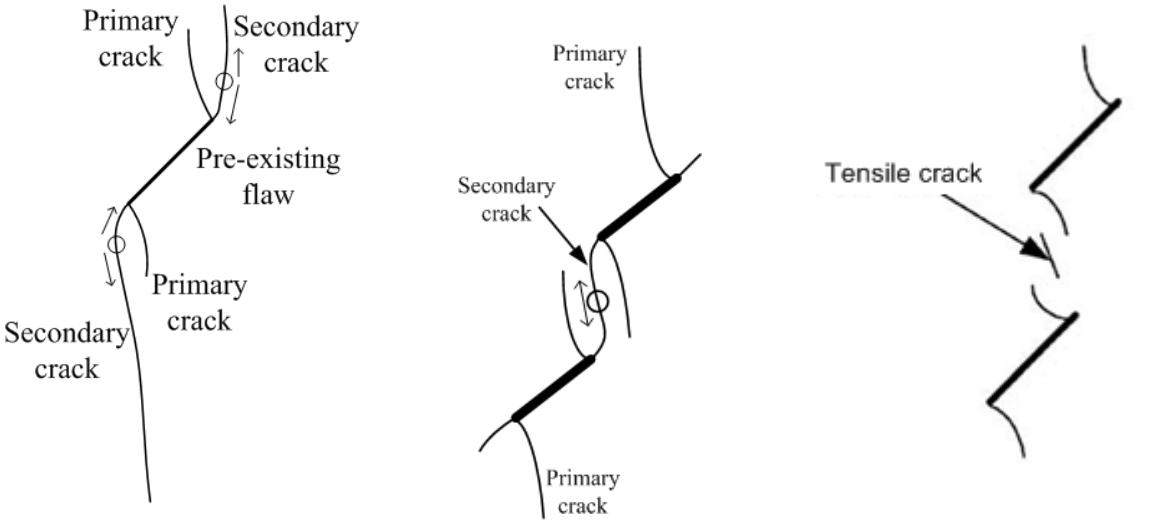

(a) Ingraffea and Heuze (1980) (b) Shen et al. (1995) (c) Mughieda and Alzo'ubi (2004)

Figure 2.41 – Initiation of secondary cracks in intact material at a distance away from flaw tips. The circles shown in (a) and (b) indicate the crack initiation location.

Regarding the crack coalescence issue, in general, overlapping flaws coalesce through tensile crack coalescence. Non-overlapping flaws coalesce differently, which depend on the specific flaw pair geometry. It can be achieved only by shear cracks, or by a combination of shear and tensile cracks initiating from the flaw tips. It has also been widely observed that the tensile crack propagation is stable, while the shear crack propagation is unstable. As noted above, although crack types could be generally classified as tensile or shear cracks, crack coalescence complexities arise due to the various types of tensile cracks and shear cracks initiating at different times during the specimen loading processes.

2.8 Crack development and coalescence in nature

2.8.1 Introduction

As noted in section 2.4, the sliding wing crack model has been successful in modeling the behavior of fractured rock for engineering applications. Research in the past decades by structural geologists also recognized that discontinuities displaying wing shapes in outcrops are also often due to tensile cracking (**tensile wing cracks, TWCs**). Since the trajectories of the TWCs preferentially align with the major compression axis, a proper recognition of their trajectories in the field can assist geoscientists to reconstruct the palaeostress fields (e.g. Rispoli, 1981, Rawnsley et al., 1992, Peakcock, 2001). In addition, understanding of the interaction and **coalescence** between flaws also helps geologists comprehend fault evolution mechanisms (e.g. Barlett et al., 1981, Willemse et al., 1997, Martel & Boger, 1998, Vermilye & Scholz, 1999, Kim el al., 2003, Grant & Kattenhorn, 2004) and predict the influence of the corresponding fault system on fluid flow through reservoirs and aquifers (Cooke, 1997). However, it has to be emphasized that the jointing and faulting features (collectively known as discontinuities) in nature are usually more complex than the laboratory observations. The continuing research interest in both the structural geologist and rock engineer communities is aimed at gaining a better understanding of how cracks evolve and coalesce in different length scales.

As observed in recent publications such as those contained in the *Journal of Structural Geology*, field mapping, laboratory experiment and numerical modeling are the three major approaches commonly adopted by structural geologists to study the deformation events in rocks. Based on the quantitative geological field data gathered from the field, being aided by computer modeling based upon continuum and fracture mechanics, and/or experimental studies on molded material/natural rocks with a reduced (laboratory) scale, a variety of fundamental questions of faulting, fracturing, and rock deformation can then be comprehensively addressed.

Different research groups around the world employed the above research techniques on different geological settings. One of the established research groups notable in this field, which successfully integrate the above techniques, is the structural geology and geomechanics group led by Aydin and Pollard at the Stanford University (see review papers by Pollard & Segall, 1987, Pollard & Aydin, 1988, Aydin, 2000).

One example involving integrated field, laboratory experimental and theoretical studies is the investigation of the nature and development echelon cracks in rocks (Pollard et al., 1982, Du & Aydin, 1991, Olson & Pollard, 1991, Thomas & Pollard, 1993, Cooke & Pollard, 1996, Crider & Pollard, 1998). Based on the observation of the occurrence of echelon cracks, the mechanics of their development was studied using linear elastic fracture mechanics. The theoretical predictions were then verified against laboratory studies on loading a model material. An idealized block diagram illustrating the geometry of multiple echelon cracks initiating from a single parent crack is shown in figure 2.42. In natural rocks, the echelon cracks are oriented as twisted surfaces that systematically diverge from the orientation of the parent crack. A narrow break-down zone, which marks the periphery of the parent crack can always be traced. See figure 2.43 for the relationships of these features in a hand specimen.

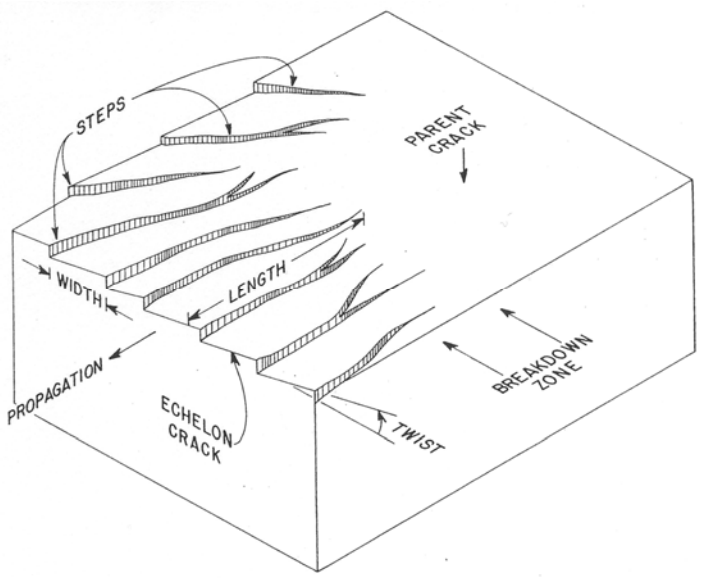

Figure 2.42 – Schematic illustration of multiple echelon cracks initiating from a parent crack. The breakdown zone is located between the echelon cracks and the parent crack (Pollard et al., 1982).

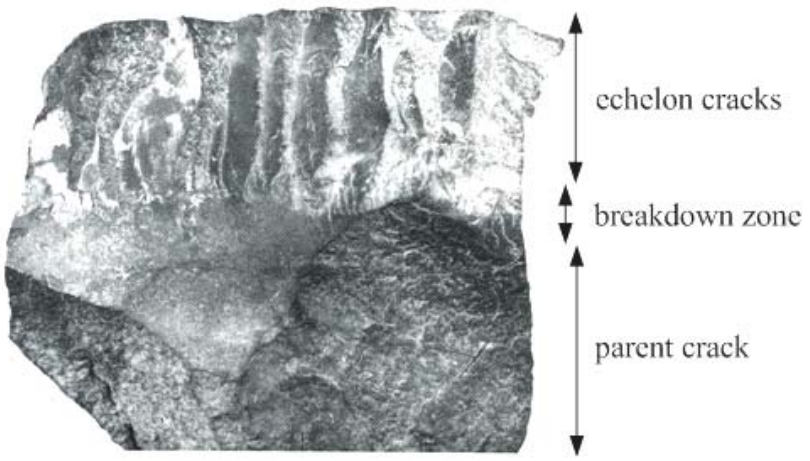

(a)

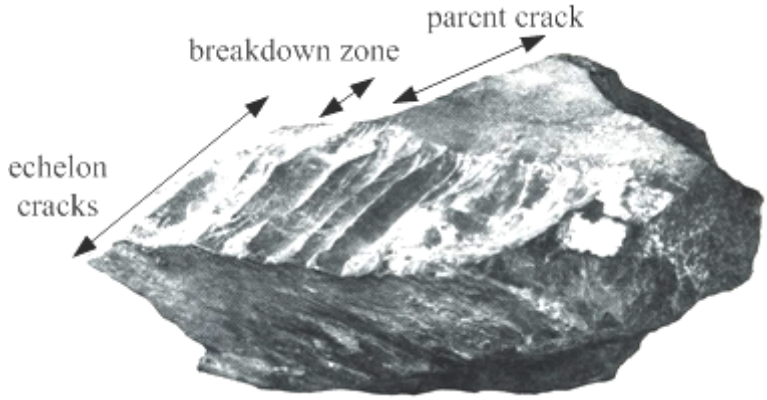

(b)

Figure 2.43 – A hand specimen of shale with well-developed surfaces of echelon cracks initiating from a parent crack. (a) photograph taken normal to the parent crack, (b) photograph taken oblique to the parent crack for the same specimen. Length scale was not given in the original paper (Pollard et al., 1982).

The development of echelon crack arrays is believed to be caused by a spatial or temporal rotation of the remote principal stresses about an axis parallel to the crack propagation direction. In other words, it is due to the introduction of a component of mode II or III loading to a pre-existing mode I fracture which then leads to a mixed-mode loading condition. From the energy point of view, such a cracking phenomenon is more favorable than the continual propagation of the parent crack as a single crack because less work is required in creating the *arrays*

of helicoidal echelon cracks, which sweeps out less surface area than one *single* parent crack twisting through the same angle (Pollard et al., 1982).

The fracture propagation paths were also observed experimentally under a mixed mode I + III loading condition within rectangular transparent blocks of polymethyl methacrytale (Cooke & Pollard, 1996). From their analysis, the observed angle of twist (β in figure 2.44) of echelon cracks from the parent crack plane increases with the ratio of stress intensity factors corresponding to mode III and mode I loading (K_{III}/K_I) as predicted qualitatively by Pollard et al. (1982):

$$\beta = \frac{1}{2}\tan^{-1}\left[\frac{K_{III}}{K_I\left(1/2 - \nu\right)}\right] \qquad (2.9)$$

where ν is the Poisson's ratio.

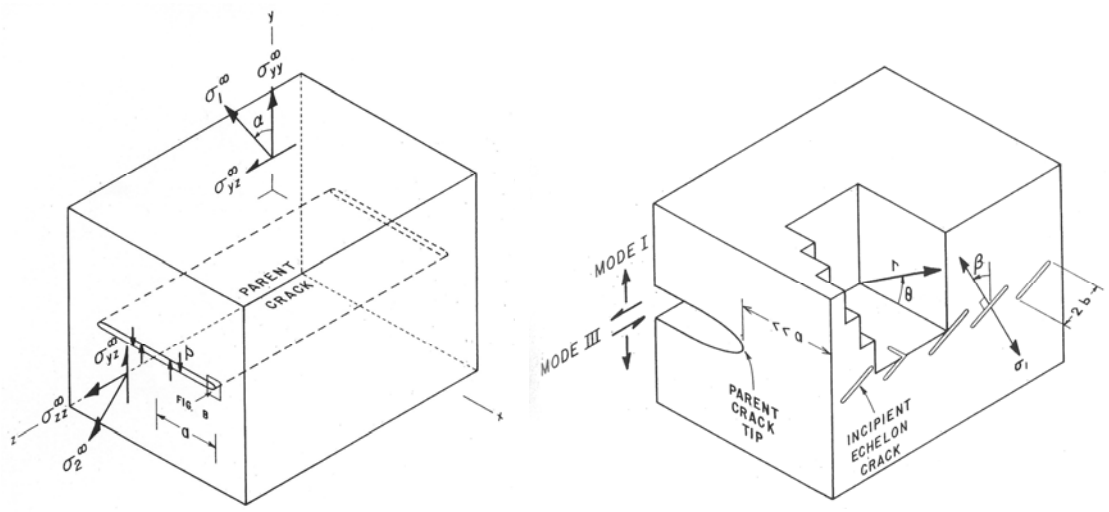

(A) (B)

Figure 2.44 – Idealized block diagram illustrating relations among applied stresses and cracks. A: Parent crack of length 2a and infinite width in *z* is loaded by pressure p and remote principal stresses σ_1^∞ , σ_2^∞ . Rotation α of principal stresses about *x* introduces stresses σ_{yy}^∞ and σ_{yz}^∞ acting on the crack plane. B: Magnified view of a small element at the parent-crack tip with incipient echelon cracks of width 2*b* at angle β to parent-crack plane loaded by maximum local tension σ_1. Polar coordinates centered at parent-crack tip are *r*, θ. Heavy arrows indicate relative motion of parent-crack walls when subject to mode I and mode III deformation (Pollard et al., 1982).

As shown in equation (2.9), when $K_{III} = 0$, β then becomes 0, which indicates that the incipient cracks grow in the parent-crack plane and no 'twisting' occurs. For $K_{III} \neq 0$, incipient cracks then grow at an angle β to the parent-crack plane. However, the experimentally observed β was found to fall below the theoretical predictions. Cooke and Pollard (1996) accounted for the discrepancy hypothesizing that apart from the ratio K_{III}/K_I, the eventual echelon crack geometry also depends on sample geometry, loading configuration, and interaction among growing fractures.

Numerical experiments were also conducted to study the interaction among multiple echelon cracks (Du & Aydin, 1991, Olson & Pollard, 1991, Thomas & Pollard, 1993). In these studies, echelon cracks are modeled as two-dimensional features and their propagation is modeled numerically by Boundary Element Method, which is based on linear elastic theory. The maximum tangential stress criterion was used to compute the crack initiation stress and the crack propagation direction. Numerically-predicted fracture paths that are similar to those from the laboratory experiments in PMMA are obtained for a variety of length scales (Thomas & Pollard, 1993).

The purpose of the subsequent sections is to review the literature on the general crack formation mechanisms and the typical occurrence of crack coalescence in nature, but with no particular reference to specific locations or geologic settings. Apart from describing the field occurrence of tensile wing cracks, the field characteristics of **anticracks** will also be described. In contrast to the tensile wing cracks which develop in the tensile quadrant, anticracks develop from the pre-existing discontinuities in the compressive quadrant. A section is also dedicated to the development of **shear cracks** and their recognition in the field. Although the pool of evidence indicating the occurrence of shearing along the pre-existing discontinuities has been well established, there are still diverging views on whether natural faults can propagate under *mode II*

condition[6] (Petit & Barquins, 1988). To follow the consistency of the terminology throughout this thesis, the pre-existing discontinuities observed in the field, including faults and joints (secondary features) from which new cracks initiated, are all collectively called pre-existing flaws or simply flaws in the present literature review. The terms **primary** and **secondary** will be used where necessary to indicate temporal relationship, without any implication of the nature (shear/tensile) of the flaws.

2.8.2 Terminology

As shown in the literature review in the past sections on the laboratory study of fracturing and crack coalescence processes, there has been a specific set of terminologies commonly used by the researchers. The literature review of natural fractures suggests that the geologist community has its own set terminologies for the same research subject. A comparison is provided in the schematic sketches shown in figures 2.45 to 2.47.

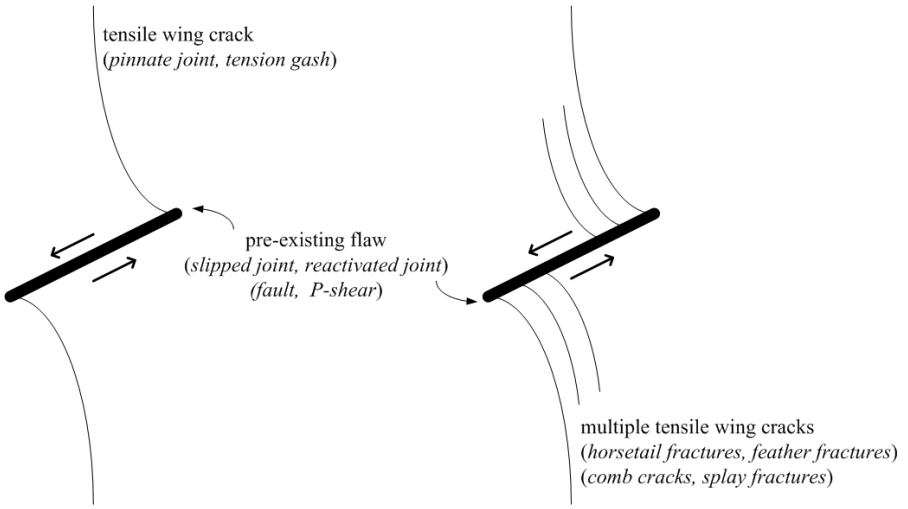

Figure 2.45 – Schematic representation of the development of single and multiple tensile wing cracks from a pre-existing flaw. The *italic* terms in parentheses are the terms commonly used by structural geologists in the literature. Arrows on the pre-existing flaws indicate possible shearing direction, which can sometimes be observed. Refer to the relevant sections in the text for literature references.

[6] The statement means that whether the pre-existing flaw can lengthen itself by the initiation and propagation of a shear crack from its flaw tips, in a direction coplanar with the pre-existing flaw.

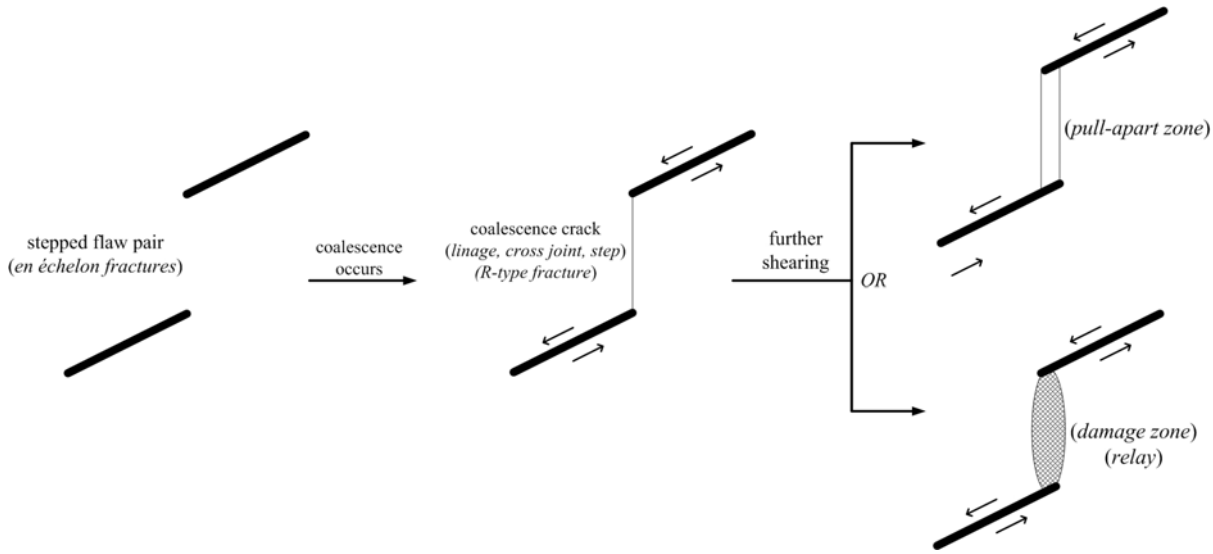

Figure 2.46 – Schematic representation of the development of a *pull-apart zone* (empty void) and a *damage zone* (intense fracturing) from a pair of parallel non-coplanar pre-existing flaws. Refer also to the caption of figure 2.45.

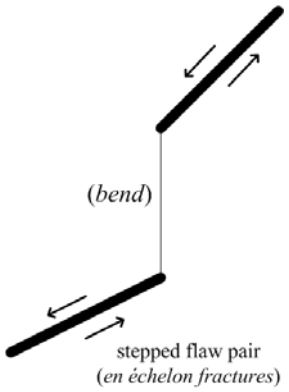

Figure 2.47 – The coalescence feature is called a bend when the pre-existing flaws are differently oriented. Refer also to the caption of figure 2.45.

2.8.3 Tensile wing cracks

Tensile wing cracks, also known as **pinnate joints** (Hancock, 1985), **tension gashes** (Rispoli, 1981) or **tail cracks**, are opening-mode fractures, which may either appear as a single out-of-plane crack initiated from or around flaw tips (figures 2.45 & 2.48) or

appearing as multiple subparallel fractures (figures 2.50 & 2.51) with tapered tips branching out from the ends of flaws along the slipping flaw interfaces (Cook, 1997, Kattenhorn & Marshall, 2006). Their occurrence is agreed to be related to the sliding along pre-existing flaws (faults) (Granier, 1985).

Groups of multiple tensile wing cracks developed from the same side of the pre-existing flaw are also known as **feather features** (Roering, 1968, Hancock, 1985) **horsetail fractures** (Granier, 1985, Cruikshank et al., 1991), **splay fractures** (Chinnery, 1966, Freud, 1974, Martel, 1990, Cooke, 1997, Myers & Aydin, 2004) or **comb cracks** (Renshaw & Schulson, 2001). They are commonly spaced a few centimeters apart and are also inclined at an angle with the pre-existing flaw/joint (Cruikshank et al. 1991). However, long single tensile wing cracks and horsetails extending up to several kilometers have also been reported (Martel, 1990, Kattenhorn & Marshall, 2006) as shown in figure 2.49. The development of horsetail fractures is favored by the variations in frictional strength along pre-existing flaws, which produces a slip gradient. Fault slip is the difference between displacements above and below the fault (pre-existing flaw) and slip gradient is the rate of change of fault slip per unit fault length. Since slip gradients may produce uneven distribution of local tensile stresses along the fault, at locations where they are large enough to initiate opening-mode fractures, multiple splay fractures then initiate not necessary at the flaw tip (Rawnsley et al., 1992, Cooke, 1997).

Some authors have used the terms **wing cracks** and **horsetail cracks** in a different way to imply the shape of crack trajectories (e.g. McGrath & Davison, 1995), which is different from that discussed in the previous paragraph. According to McGrath and Davison (1995), wing cracks are those tip cracks curving inwards from the flaw tips towards the maximum principal stress direction (σ_1), while **horsetail cracks** are those tip cracks curving outwards from the flaw tips towards σ_1 (figure 2.52). A literature review of the field occurrence of tip cracks however reveals that in addition to these two curving trajectories (figure 2.52), straight tensile tip cracks are also very common (figures 2.48 & 2.50). In the field study conducted by Risploli (1981), both straight and curving types initiated from the same flaw were identified (figure 2.51). Regarding the inconsistent use

of terminology in the literature, in the discussion below from now on, the terms **"wing cracks"** and **"horsetail cracks"** will not be used to describe the shape of crack trajectories to avoid confusion. A **"wing crack**" will only be used to describe a **single crack** which initiates from a pre-existing flaw and displays a conventional wing appearance; while the term **"horsetail cracks"** refers to a **group** of **"wing cracks"**. (figure 2.45).

Mineral infills, e.g. calcite, quartz, epidote, chlorite, muscovite, prehite, which could have come from the dissolution of neighboring zones of closing (stylolite), are often found along the tensile wing cracks (Raynaud & Delair, 1978, Rispoli, 1981, Gamond, 1983, Martel, 1990). Please refer again to figure 2.51 and see the next section on **anticracks**.

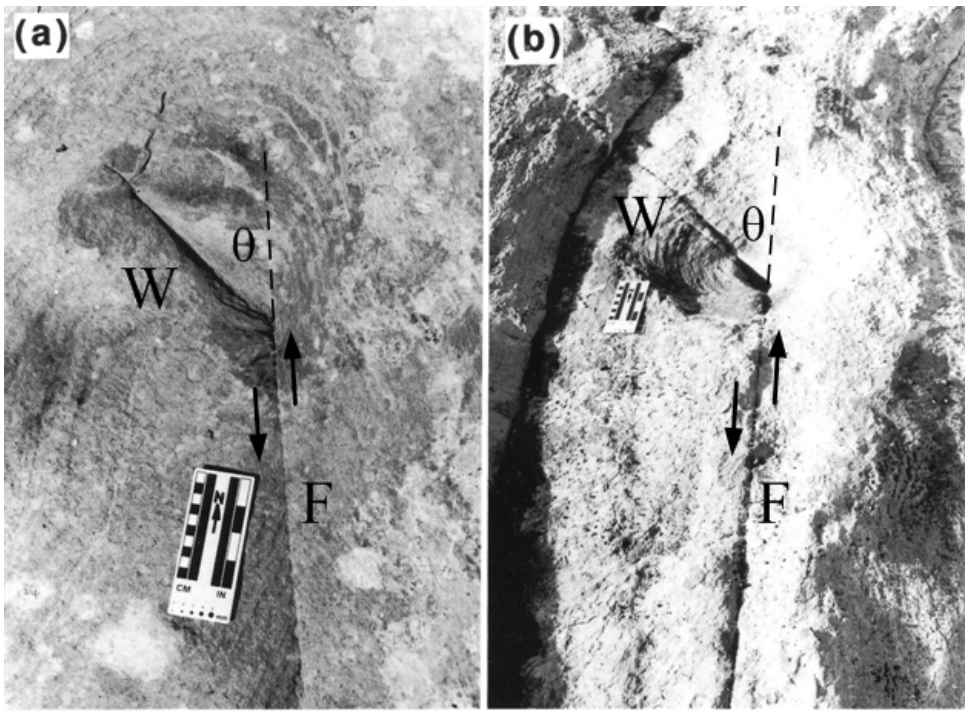

Figure 2.48 – Kinked wing cracks (W) initiated from pre-existing flaws (F). (a) The wing crack was about 1.5 dm long and the kink angle (θ) is about 43°. (b) The wing crack consisted of three segments and the kink angle is 50°. The sense of left-lateral shearing is indicated by the arrow pairs (Cruikshank et al., 1991).

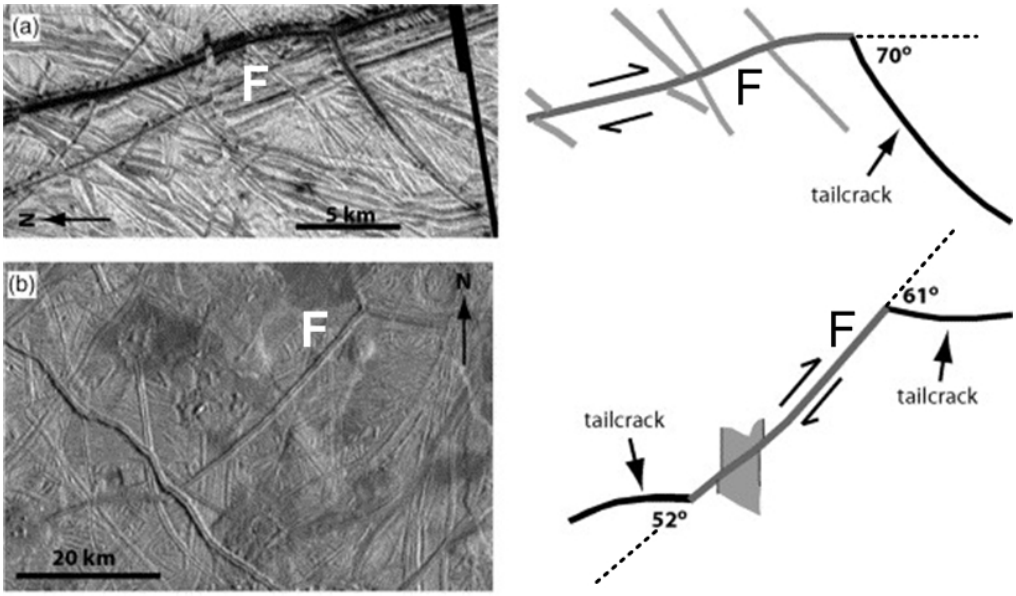

Figure 2.49 – Examples of long (measured in km) tensile wing cracks (structures) developed from right-lateral fault (F). The angles indicated in the sketches are the kink angles (after Kattenhorn & Marshall, 2006).

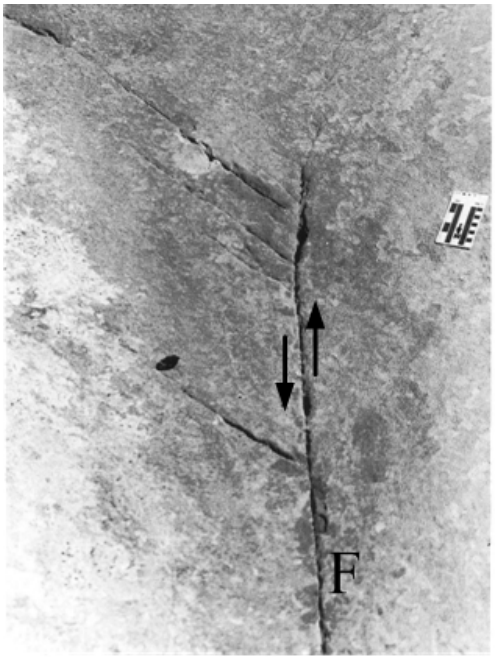

Figure 2.50 – Horsetail fractures at the end of a faulted joint (F). The term "horsetail" here is used to describe the occurrence of multiple tip cracks, instead of implying the shape of crack trajectories. The sense of left-lateral shearing is indicated by the arrow pair (Cruikshank et al., 1991). Note the ruler on the right for scale reference.

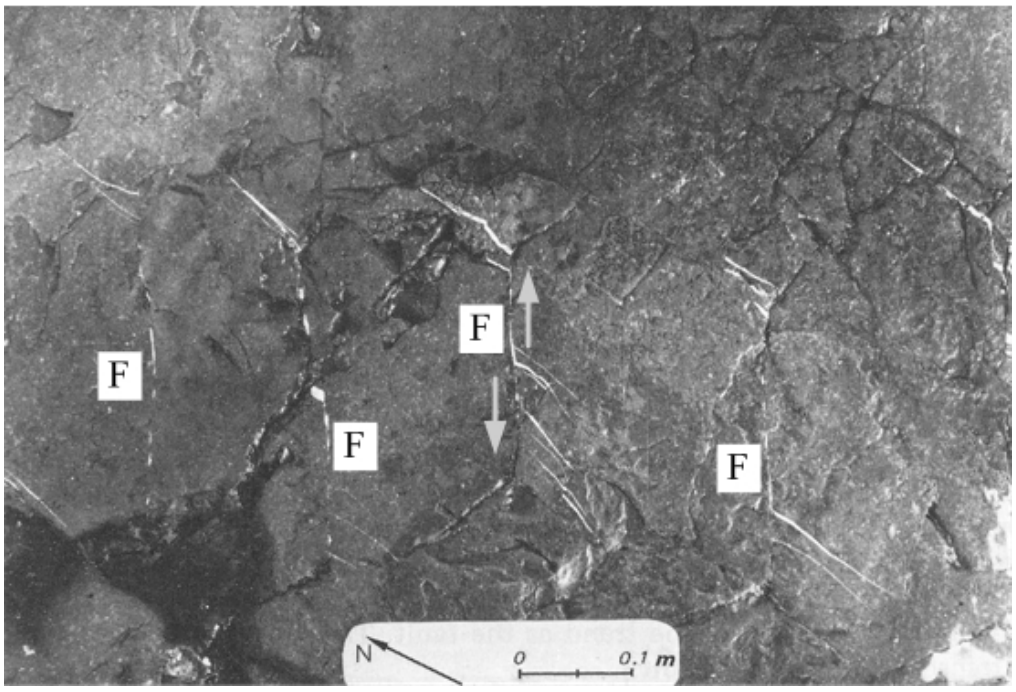

Figure 2.51 – Multiple horsetail fractures with vein infills developed from en echelon pre-existing flaws which trend N60^{o}. The sense of left-lateral shearing is indicated by an arrow pair (after Rispoli, 1981).

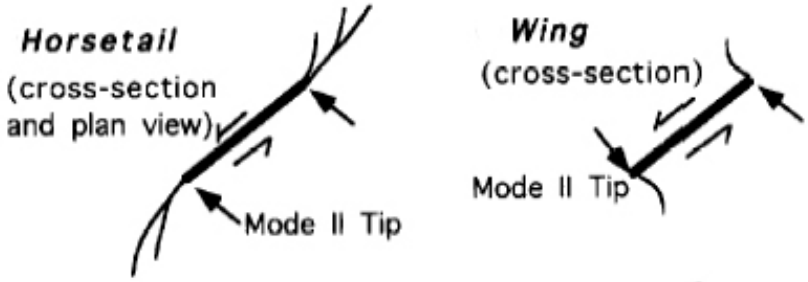

Figure 2.52 – Classification of tip cracks according to the shape of crack trajectories. Horsetail fractures and wing cracks curving in a different manner away from the flaw tips (McGrath & Davison, 1995).

2.8.4 Anticracks

In addition to the tensile wing cracks, which develop from the extensional quadrant of the pre-existing sliding flaws (figure 2.53), anticracks are also another common feature initiated from the pre-existing flaws, but in the compressional quadrant (Fletcher &

Pollard, 1981, Rispoli, 1981, Willemse et al., 1997, Kattenhorn & Marshall, 2006). The anticracks originate at stress concentrations and propagate through rock as cracks (figure 2.54), and occasionally appear as discrete solution surfaces (stylolites). Some field exposures of anticracks, along with the tensile wing cracks, are shown in figures 2.55 and 2.56.

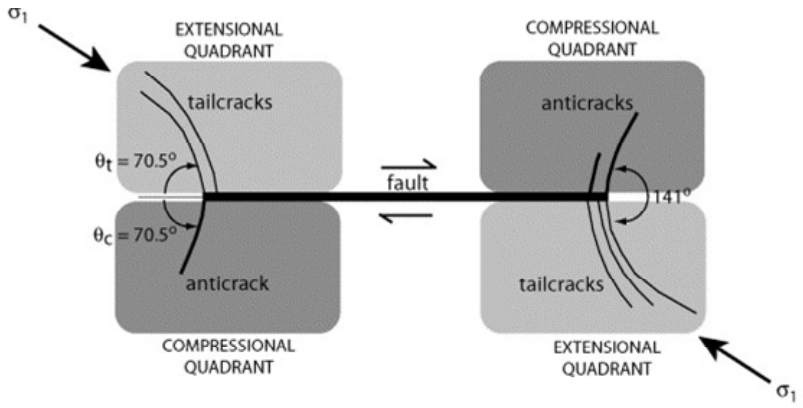

Figure 2.53 – Development of tailcracks (tensile wing cracks) in the extensional quadrants and anticracks in the compressional quadrants. The right-lateral sense of shearing is indicated by the central arrow pair (Kattenhorn & Marshall, 2006).

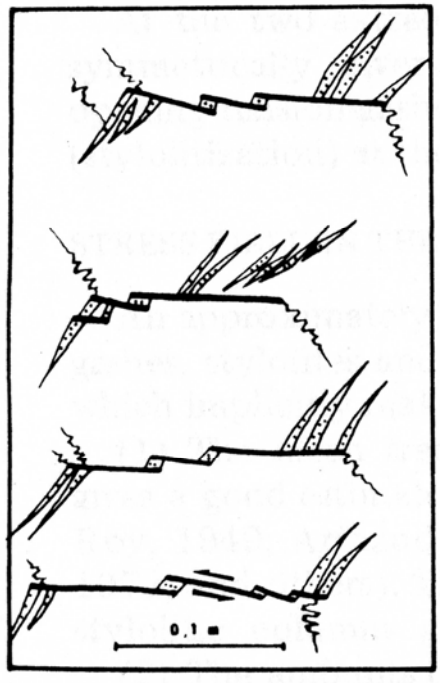

Figure 2.54 – Examples of anticracks (zig-zag lines) developed from pre-existing flaws (dark thick line) along with the horsetail veins (dotted tapered teeth). The sense of shearing is left-lateral (Rispoli, 1981).

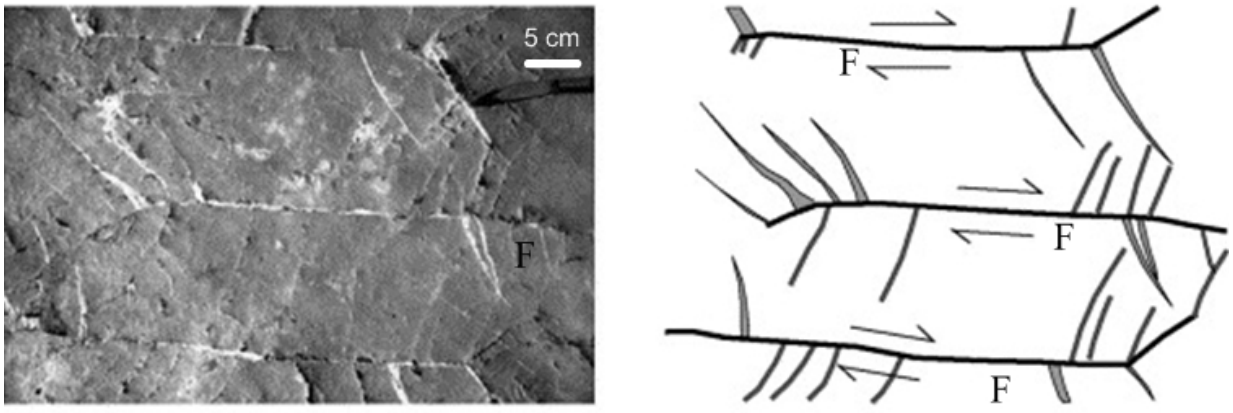

Figure 2.55 – Horsetail fractures with white infills (left picture) developed from pre-existing flaws (F) which have been subject to right-lateral shearing as indicated by the arrow pairs (right picture) in limestone. A knife blade on the top right corner below the scale mark serves as scale. The other group of dark thin short crack traces was anticracks (after Kattenhorn & Marshall, 2006).

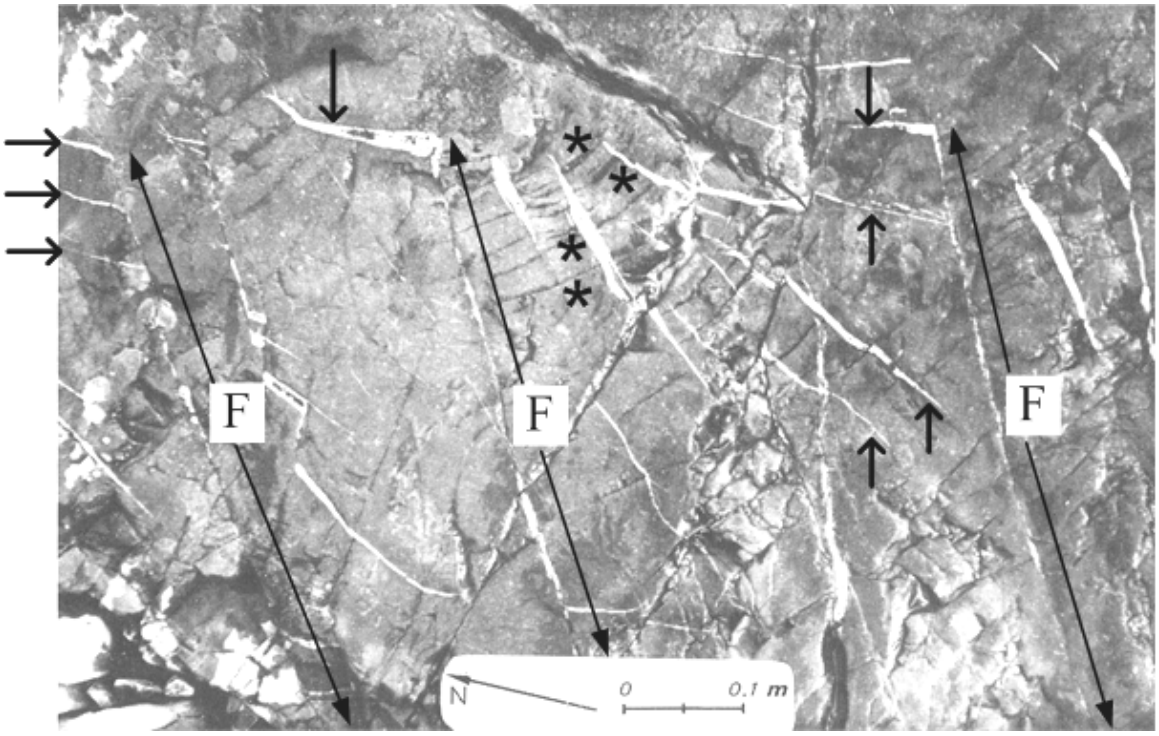

Figure 2.56 – Development of tensile wing cracks with calcite infills (indicated by short arrows) from pre-existing flaws (F). Most of the tension gashes are straight and some are curvilinear. Thin lines (some of them are indicated by *) which appeared on the other side of the pre-existing flaws are pressure solution on stylolites (Rispoli, 1981).

2.8.5 Flaw coalescence

Interaction and coalescence (also known as **linkage**, e.g. Crider & Pollard, 1998, Peacock et al., 2000, Mansfield & Cartwright, 2001, Kim et al., 2003) between pre-existing flaws by later cross-joints (figure 2.46) allows the slipping flaws (reactivated joints or faults) to increase in length and to facilitate shear across those cracks, eventually leading to a fault zone (Peacock, 2001). An incipient development of such coalescence (no coalescence at this stage) is illustrated in figure 2.57. In the literature, when two parallel non-coplanar flaws coalesce, a **step** (figure 2.46) is formed; and when two non-parallel flaws coalesce, a **bend** (figure 2.47) is formed (Martel, 1990, Childs et al., 1996).

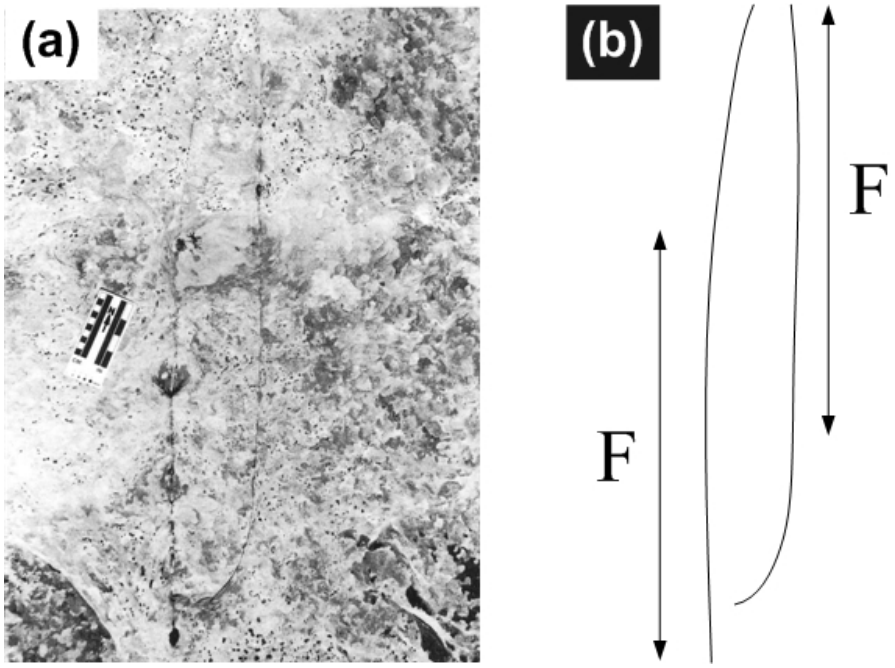

Figure 2.57 – (a) Curvilinear crack segments grown from two pre-existing overlapping flaws F. (b) sketch of the main features shown in the photograph (Cruikshank et al., 1991).

Further shearing occurring along the pre-existing flaws usually leads to the development of a **pull-apart zone** (e.g. Gamond, 1983, Peacock & Sanderson, 1995, Willemse et al., 1997, Kim et al., 2003) in the bridge region between the flaw tips (figures 2.46, 2.58-2.61, 2.63 a & b). If the shearing is very intense, a highly fractured rhombohedral area called

relay (Granier, 1985, Peacock et al., 2000) or **damage zone** (e.g. Mollema & Antonellini, 1999, van der Zee & Urai, 2005) would form (figure 2.62).

As the intensity of shearing further increases and the development of coalescence cracks is extensive, new geological structures form. Based on a field study, Martel (1990) identified the formation of **simple fault zones** due to the coalescence of multiple non-coplanar faults (slipped flaws) by multiple splay fractures in a side-to-side and end-to-end manner (figure 2.63 c). Compound fault zones develop as **additional** splay fractures linking up small faults and simple fault zones, which developed earlier (figure 2.63 d).

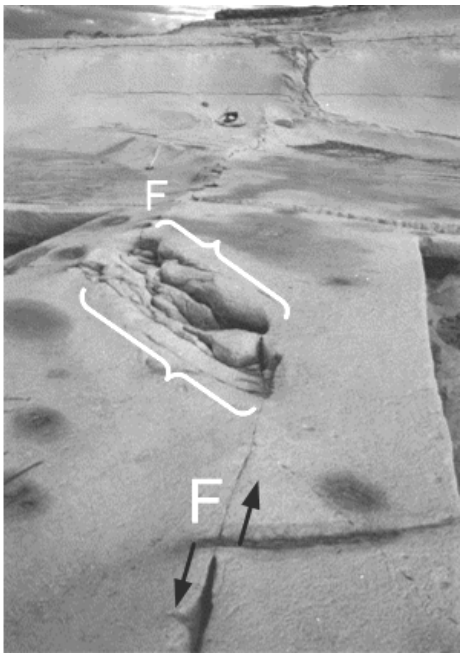

Figure 2.58 – Pull-apart zone (bracketed region) consisting of a number of coalescence cracks developed between two pre-existing flaws (F) in limestone. The sense of left-lateral shearing is indicated by an arrow pair (after Kim et al. 2003). A scale is not provided in this figure, but a map of this structure is shown in figure 2.60 (exact location not specified however).

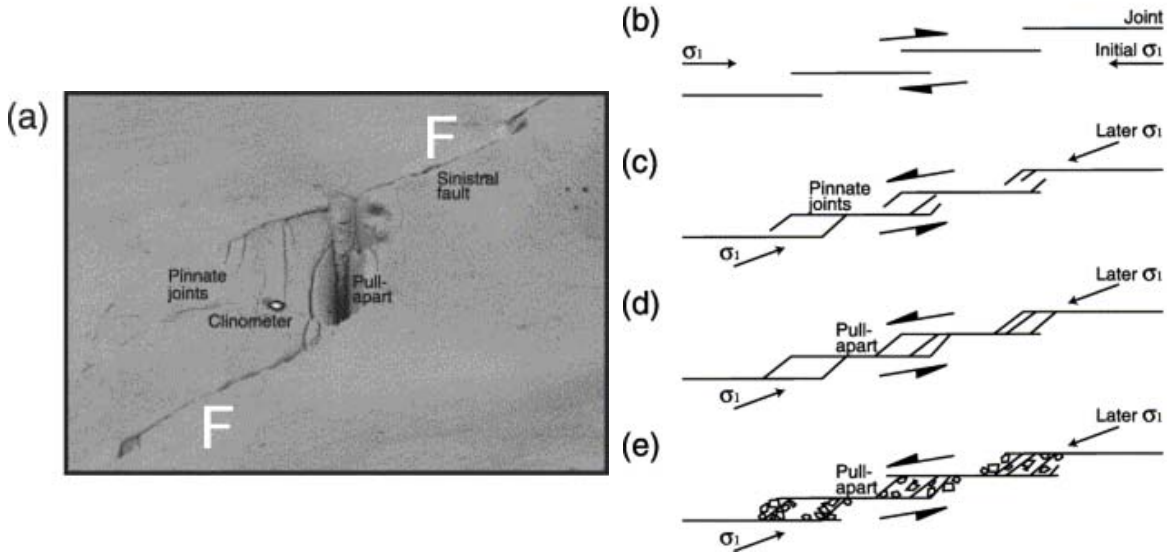

Figure 2.59 – (a) Oblique view of a horizontal surface on which a sinistral strike-slip fault zone that initiated as stepping joints (F) in limestone. Coalescence wing cracks developed from the ends of those faults **F** and further shearing along them leads to the formation of central unfilled pull-apart zone up to hundreds of millimeters wide. Note the clinometer to the left of the pull-apart zone for scale. (b) Schematic sketch showing the development multiple pull-apart zones (after Peacock, 2001, Crider & Peacock, 2004).

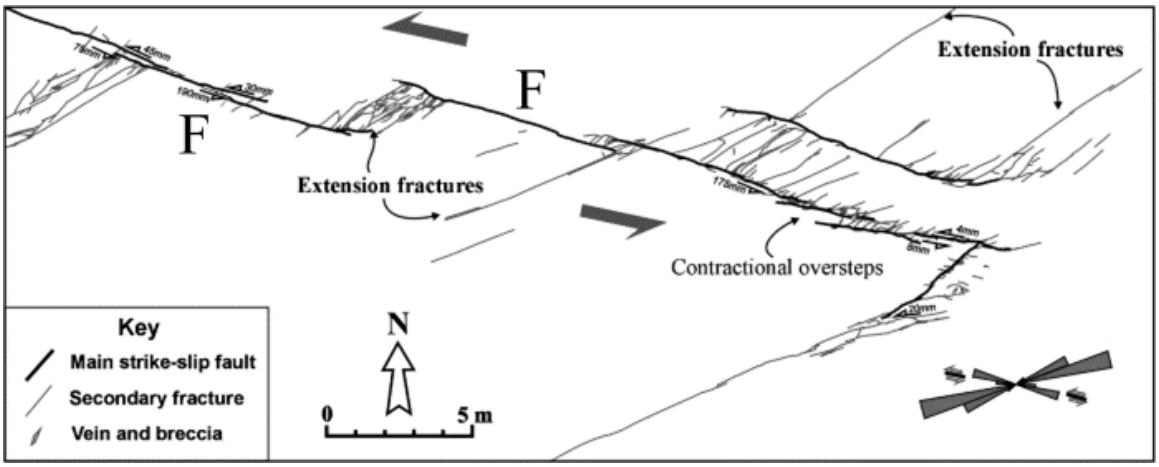

Figure 2.60 – Coalescence achieved by multiple secondary fractures at the tip regions between two main overlapping strike-slip faults (marked with letter F) in limestone. The sense of shearing is left-lateral (after Kim et al., 2003).

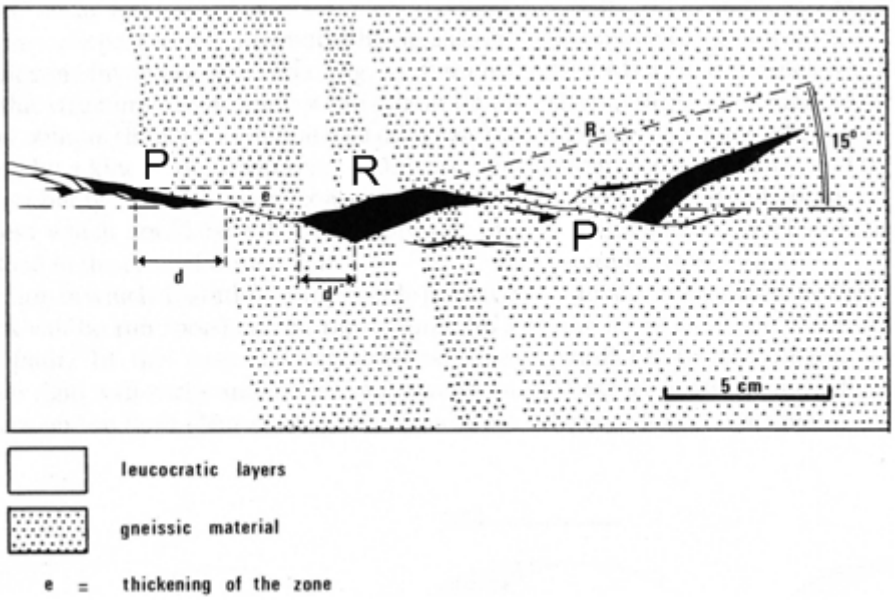

Figure 2.61 – Coalescence crack (R fracture) link up the pre-existing flaws (P fractures) in gneiss. The sense of shearing is left-lateral. Pull-apart zones (shaded black) also develop (Gamond, 1983).

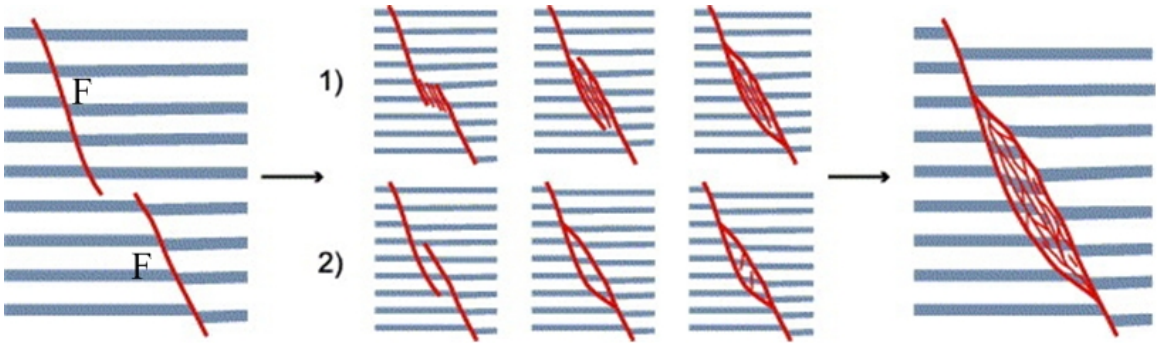

Figure 2.62 – Schematic sketches (no scale provided in the original paper) of two scenarios for the development of fault-bounded lens-shaped bodies by coalescence of two pre-existing stepped faults (F) associated with left lateral shearing. In scenario 1, the interior of the future lens is deformed before actual coalescence of the faults through the initiation of new cracks from flaw tips. In scenario 2, new cracks propagate from the flaw tips before major deformation of the region in the lens region (after van der Zee & Urai, 2005).

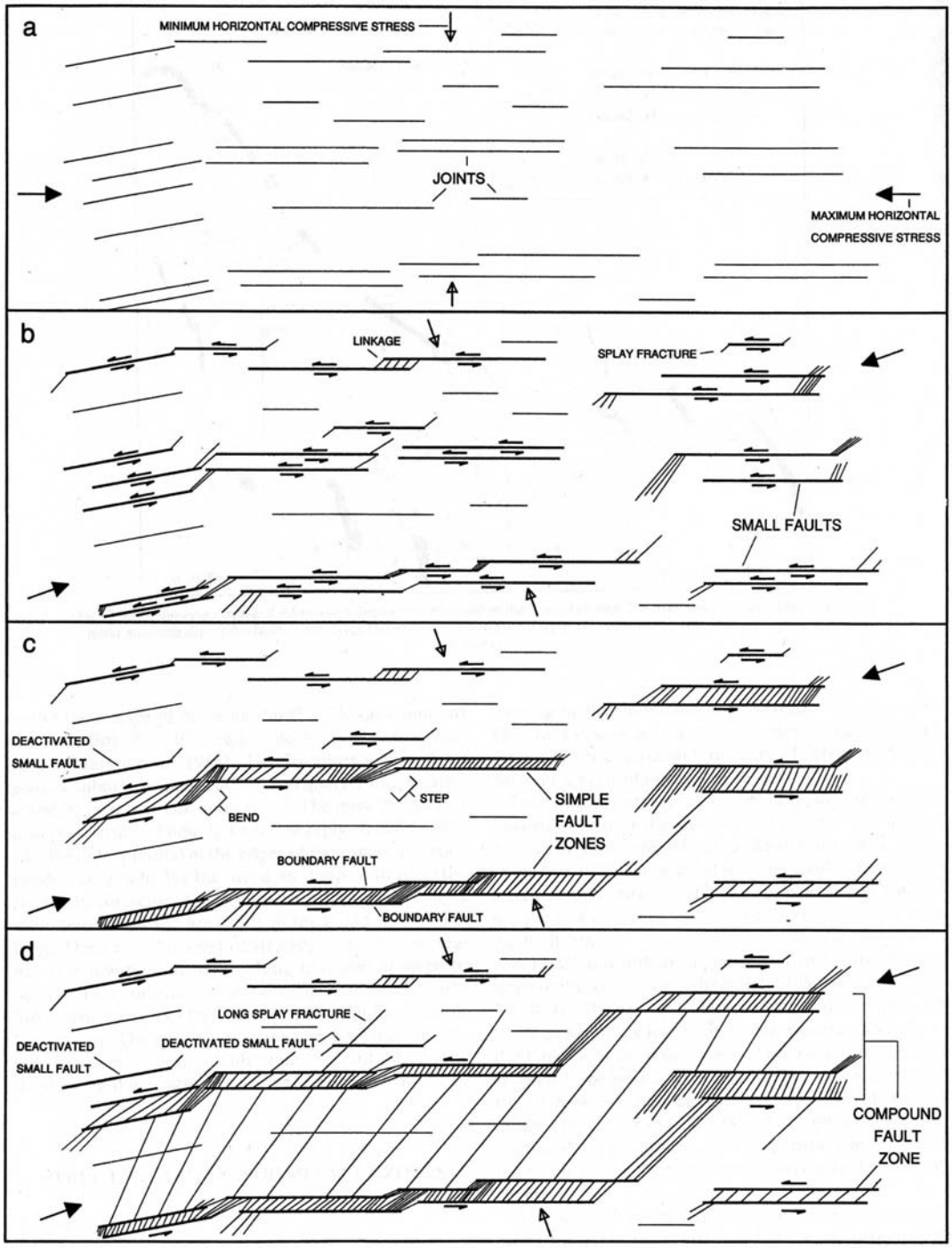

Figure 2.63 – Four stages of fault development in the Bear Creek area underlain by intrusive igneous rocks. (a) Opening of joints (flaws). (b) Left-lateral shearing occurred along the flaws associated with the development of coalescence horsetail cracks. (c) Development of simple fault zones. (d) Formation of compound fault zones by coalescence of earlier developed small faults in (b) and simple fault zones in (c) (Martel, 1990).

2.8.6 Shear cracks

In nature, faulting processes involve sliding / shearing of pre-existing adjacent rock faces past each other. The sense of movement, amount and intensity of shearing can be determined from various relict deformation and structural features left in the geological bodies. In addition to the above shearing processes, there is always an interest in how shear cracks propagate from the tips of pre-existing discontinuities. Specifically, *can natural faults propagate under mode II conditions* ? (Petit & Barquins, 1988)

In contrast to crack growth under mode I loading condition, crack growth under mode II loading condition has been investigated to a lesser extent (Petit and Barquins, 1988, Isaksson & Ståhle, 2002). Nevertheless, recent experimental (e.g. Reyes & Einstein, 1991, Shen et al., 1995, Bobet & Einstein, 1998a, Martinez, 1999) and theoretical studies (Melin, 1986, 1987, Shen & Stephansson, 1993, Bobet, 2000, Isaksson & Ståhle, 2002) illustrate that the initiation of shear cracks from a pre-existing flaw is plausible, especially if a high confining pressure is present.

Compared to the laboratory experimental and theoretical studies, the field identification of mode II crack initiation and propagation is more limited and difficult. As observed by Petit and Barquins (1988), since the field observations "*are often based on traces of structures on more or less planar surfaces, it is difficult to localize both the preexisting fracture front geometry and/or the direction and sense of slip on the fracture.*" The direct observation of a definite trace of shear crack propagating from the tips of pre-existing discontinuities is rarely reported (Crider & Peacock, 2004). On the other hand, the development of shear cracks in the field is usually found to be due to the formation of individual dominantly tensile microcracks along the plane of future shear fracture, which then propagate and coalesce (Engelder, 1987). One of such examples is shown in figure 2.64 (Petit & Barquins, 1988). Based on their field observation on incipient normal faults in Languedoc limestone and the field observation by Vita-Finzi ad King (1985), the authors illustrated the evolution of a normal fault which propagated in multilayered horizontal sedimentary rocks. The strata shown in figure 2.64 initially consist of bottom

layers with a pre-existing fault and top layers which are initially unfaulted. Shearing along the normal fault leads to the formation of a high density of open joints in the upper layers. Brecciation is first due to the formation of blocks (limited by stress-induced tension fractures and pre-existing bedding joints) which are then subject to rotation and further fragmentation by local stress concentrations (figure 2.64 a). Further shearing along the pre-existing normal fault leads to the formation of a through-going slip surface (figure 2.64 b).

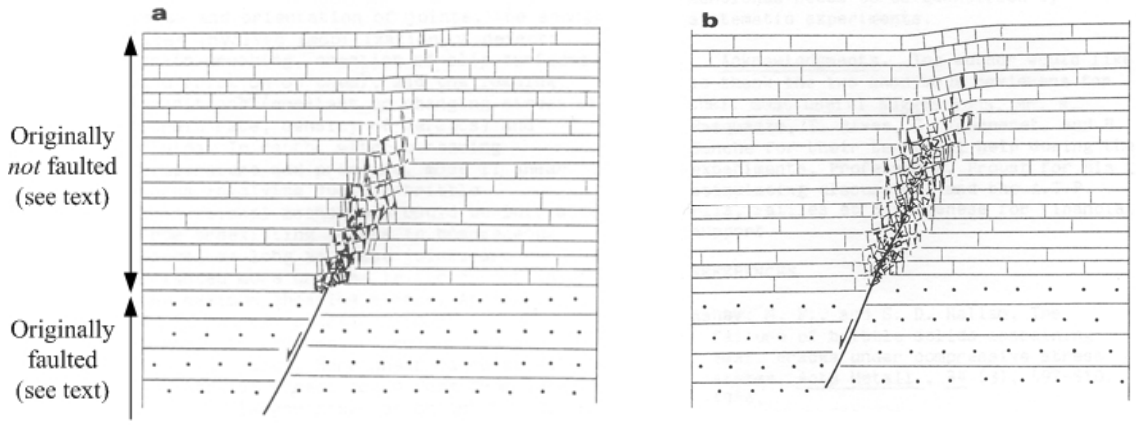

Figure 2.64 – Schematic illustration of the propagation of a normal fault (a) development of a high density open joints which leads to localized brecciation (b) formation of an eventual through-going slip surface (Petit & Barquins, 1988).

In another study, the microcrack density beside fault traces (within a ~5 m wide zone measured from the fault trace) was mapped systematically by Vermilye and Scholz (1998). It revealed that the microcrack density (the extent of the damage zone) decreased exponentially with distance from the fault. As stated by Scholz et al (1993), if the damage zone is interpreted as the wake of a process zone (figure 2.65), i.e. the zone of inelastic deformation formed in the stress concentration of the propagating tip, this is the expected form of the falloff with distance from the fault.

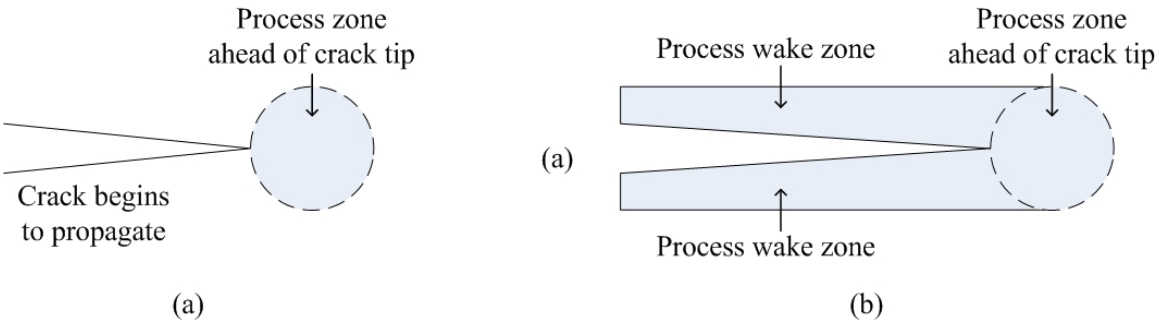

Figure 2.65 – (a) Idealized shape of a process zone present ahead of a crack tip. (b) As the crack propagates to the right, process wake zones flanking the two sides of the crack faces.

2.9 Summary and conclusions

The field occurrence of **tensile wing cracks, anticracks, shear cracks** and **coalescence events** have been briefly reviewed in this section. The review suggests that despite the different terminologies being used by the community of geologists and the community of rock engineers, crack coalescence has long been a challenging topic that draws a common research interest. Although the present research is based mainly on laboratory studies, it is also worthwhile to note that scaling might be possible.

The review suggests that crack coalescence is a quite common phenomenon in nature and is conventionally studied by three major approaches, namely numerical study, experimental study and field study. Since heterogeneities, voids and cracks are abundantly present in rock, the research focus in most **numerical studies** on rock is thus to model how these features interact and lead to eventual failure. Computational power required for rigorous modeling and simulation work is no longer the largest challenge to the research community. One of the most challenging issues still remains is how well the modeling results represent the real conditions since there are a countless number of rock types on earth, with each being characterized by a unique inherent texture and strength.

To address the above issues, different research groups have conducted **laboratory experiments** to study the fracturing and coalescence behavior in different molded rocks

and natural rocks. To reduce the experimental complexity and to enable researchers pinpointing the specific parameters that may potentially influence the fracturing behavior, a specific number of artificial flaws with specific dimensions are often created in the specimens for subsequent loading tests. Although these tests clearly demonstrated that fracturing and coalescence behavior vary among the rock types, the influence of different experimental set-ups, specimen and flaw dimensions, and means of crack observation (e.g. whether high speed camera imaging was used or not) have not been fully assessed. There is a wide acceptance that the generation of fracture-process zones, which are associated with microcracks induced ahead of flaw tips, can lead to a *quasi-brittle* behavior in rocks. There are however still no conclusive results to tell how different rock types influence the nature of these fracture process-zones.

It should also be noted that most of the experimental studies mentioned above were conducted on limited rock specimen sizes at a relatively high strain rate as compared to most of the natural processes operated in the **field** scale. Although some mechanisms, such as tensile wing crack initiation and their subsequent coalescence, which were well documented in the laboratory studies, have been successfully used to account for certain brittle deformations of geological bodies, the scaling effect still remains as a puzzle for the rock mechanics and structural geology research communities. Further observations collected from field studies would definitely offer key directions for future experimental studies. On the other hand, laboratory studies conducted under well-controlled experimental conditions can help providing plausible explanations to account for the complex geological processes that have operated in the geological past.

CHAPTER 3 – Review of Martinez's Work

3.1 Introduction

Martinez (1999) extended the work of Bobet (1997) to study the fracturing and coalescence behavior in natural rocks (Vermont White Marble and Barre Granite, which will simply be called marble and granite respectively within this chapter). In his experimental study, a high speed imaging system was used to record the details of fracturing processes which thus allowed the adoption of a continuous loading scheme during the uniaxial compression test, in contrast to an incremental loading scheme (Bobet, 1997). Another innovation offered by Martinez was the use of water abrasive jet to create pre-existing open flaws in rocks. Using that technique, he was able to cut through-specimen straight flaws precisely of specified geometries. The water abrasive jet technique which is again used in the present study will be described in detail in Chapter 4.

In Martinez's research, it is not only possible to generalize the crack coalescence patterns for different pre-existing flaw geometries in rocks similar to what Bobet (1997) did on gypsum, but also possible to determine with high level of confidence on the mode of crack initiation (shear/tensile) with the help of high speed video imaging system. During the loading test, the front face of the specimen was monitored and continuously videotaped onto VHS tapes by a high speed camera since the application of loading.

In the present study, the Martinez's VHS tapes recording the marble fracturing processes were digitized and reviewed. The review serves the following purposes:

1) To familiarize the author with the fracturing and coalescence behavior in natural rocks.
2) To identify other fracturing features which are phenomenal in natural rocks besides crack coalescence.
3) To provide direction on for future experimental work to be conducted.

Section 3.2 first describes the background of the experimental study conducted by Martinez (1999). Section 3.3 describes the fracturing and coalescence behavior observed for each specimen. Section 3.4 generalizes the different types of cracks observed. Sections 3.5 studies the influences of different flaw parameters on crack coalescence patterns. This chapter is then concluded in section 2.6.

3.2 Background of Martinez's Study

In the Martinez's study, uniaxial compression tests were conducted on Vermont White Marble and Barre Granite prismatic specimens of dimensions 6" x 3" x 1.25" (152 mm x 76 mm x 32 mm). In his study, each specimen consisted of a pair of pre-existing flaws (aperture = 0.08", 2mm, flaw length = 0.5", 13mm) which were arranged in different configurations. The term "flaw" will be used to describe an artificially created, pre-existing crack or fracture. The geometries are represented by three basic parameters: flaw inclination angle β, spacing s and continuity c (figure 2.1). For example, *45-a-2a* corresponds to a pair of flaws with a common flaw inclination angle of 45^o, spacing of "*a*" (half flaw length) and continuity of "*2a*" (flaw length).

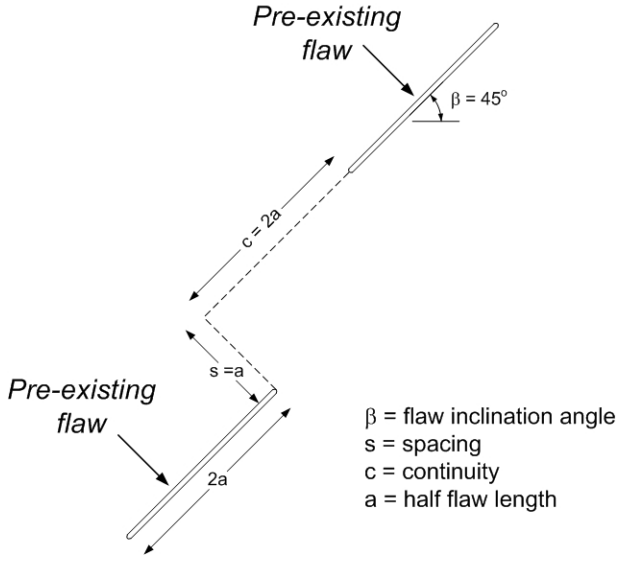

Figure 3.1 – Configuration of a pair of pre-existing flaws of geometry of 45-a-2a.

During the loading test, the specimen front face was monitored and recorded by a high speed recording system, which was set at a frame rate of 250 frames/second. The captured videos were transferred to a VHS recorder and recorded onto VHS tapes.

3.3 Review of videos

In the present study, the VHS tapes containing the high speed videos for both marble and granite were digitized and reviewed on a computer. Generally, the image quality of granite videos was much worse than that of marble videos. The poor image quality makes the observation of most fine cracks in granite difficult. This chapter will thus focus solely on the review of marble and the fracturing behavior of granite will not be discussed. The flaw geometries and specimen numbers corresponding to those 42 uniaxial compression tests on marble, which have been reviewed, are summarized as follow:

Flaw Inclination Angle (^{o})	Flaw Geometry	Specimen Labels	Number
30	30-0-a	MA04, MA05, MA35, MA36	4
	30-0-2a	MA06, MA07, MA37, MA38	4
	30-a-2a	MA12, MA13, MA41	3
	30-a-a	MA10, MA11, MA40	3
	30-2a-2a	MA08, MA09, MA30, MA31	4
45	45-0-a	MA14, MA15, MA45	3
	45-0-2a	MA16, MA17, MA44	3
	45-a-2a	MA20, MA21, MA46	3
	45-a-a	MA22, MA23, MA42, MA43	4
	45-2a-2a	MA18, MA19, MA47	3
60	60-0-a	MA24, MA25, MA33, MA34	4
	60-0-2a	MA26, MA27	2
	60-a-2a	MA28, MA29	2
			42 (total)

Before discussing the fracturing and coalescence behavior, it is necessary to highlight the following two points. First, the field of view on those recordings was limited to an area around the pair of flaws instead of the whole specimen. The fracturing events occurring close to the top and bottom edges of the specimen could thus not be observed. Second, the present review will not include any relevant stress analysis, but will solely focus on the fracturing events observed in the video images.

The specific objectives of the present review not only include the determination of crack coalescence patterns for each specimen, but also the development sequence of other cracks initiating from the pre-existing flaws. Different types of deformation of the pre-existing flaws, e.g. aperture reduction of the pre-existing flaws, relative displacement between the upper face and lower face of the pre-existing flaws are also noted.

The tables shown on the following pages (figure 3.2) for specimen MA12 illustrate a typical analysis of fracturing and coalescence processes. Newly developed cracks are identified by reference letters, e.g. **B**, **C** etc. These letters are only for identification purposes and they do not imply any crack initiation sequence. Each letter is then followed by a letter **T** or **S** in parentheses, which refers to the tensile mode or shear mode of crack initiation, respectively. The sequence of crack initiation is indicated by numbers shown beside the cracks. The first crack to initiate is designated as 1, the second crack as 2, etc. The same number will be assigned to multiple cracks which are observed to initiate simultaneously.

Digitized videos of the other marble specimens were also reviewed following the same system as shown for MA12. Sketches illustrating the key cracks initiating from the pre-existing flaws and the coalescence cracks (if any) of all the 42 specimens are summarized in figures 3.3 to 3.14.

Specimen : MA12 (30-a-2a)

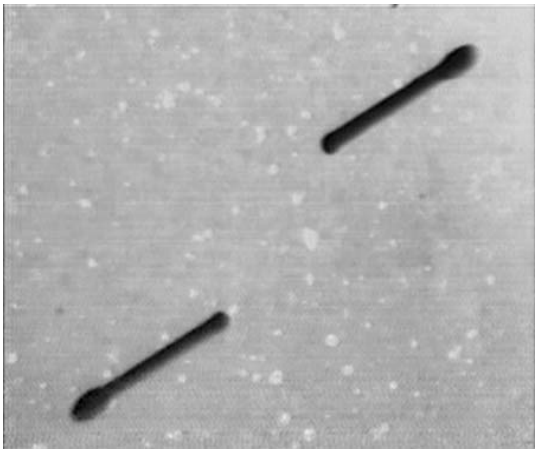	Initial flaw geometry.
 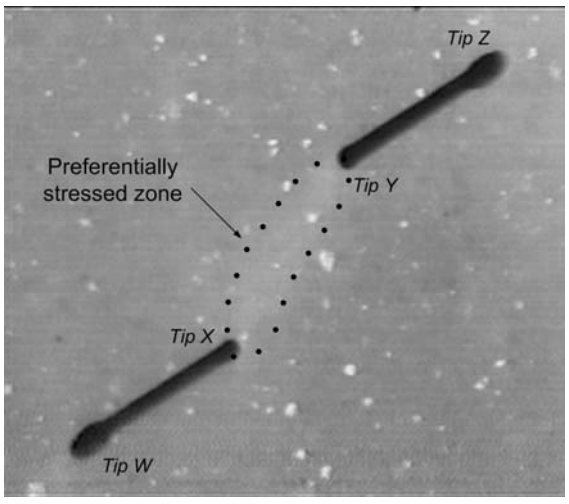	Time : 1m33s A gradual whitening color change (became more light reflective) appeared along an elongated strip in the bridging region between the two inner flaw tips (X & Y).

Figure 3.2 – Images captured from high speed video of specimen MA12

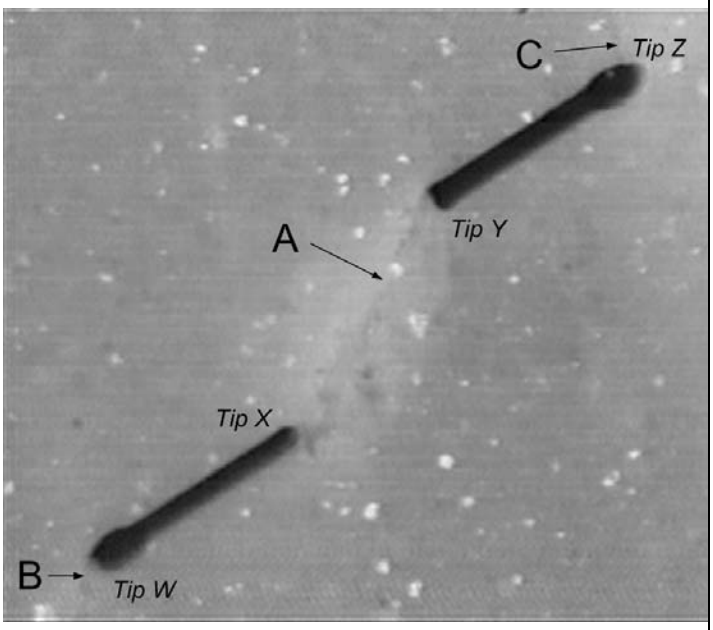	Time : 1m34s (Image -223) Coalescence shear crack A developed between tips X and Y. Tensile crack B initiated from tip W of the lower flaw. Tensile crack C initiated from tip Z of the upper flaw. The deformed shape of tips W and Y indicated the occurrence of a relative displacement between the upper faces and lower faces the pre-existing flaws.
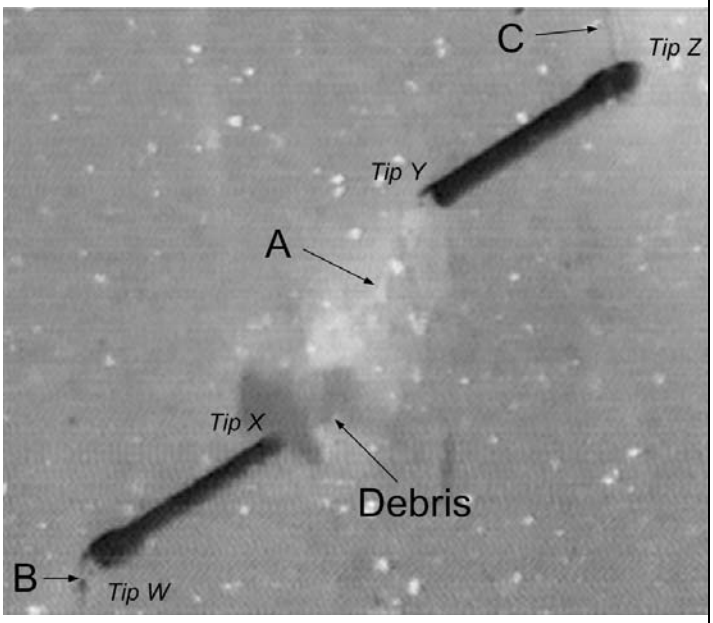	Time : 1m34s (Image -168) Shearing continued on the coalescence shear crack A and shear fragments continued to fall off from the specimen front face. Further deformation (aperture reduction of flaw and relative displacement between the upper faces and lower faces the pre-existing flaws) on the pre-existing flaws occurred. Note the tooth-shaped tips (W & Y) resulted and the further tensile opening of crack B.

Figure 3.2 – Images captured from high speed video of specimen MA12 (continued)

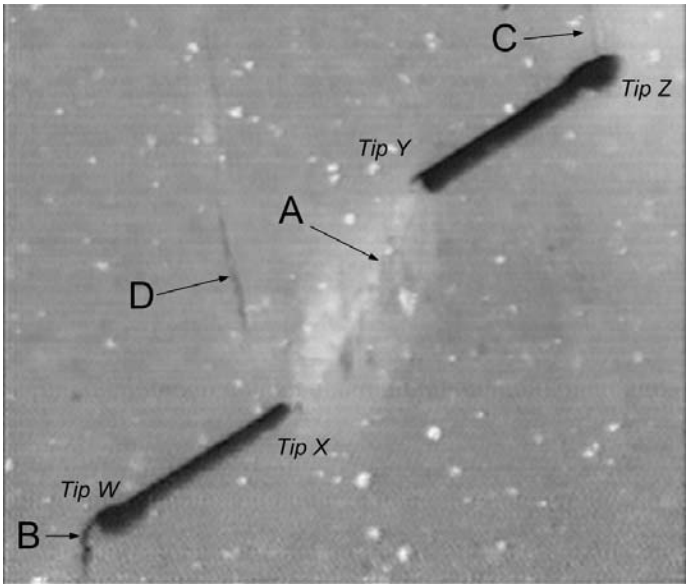

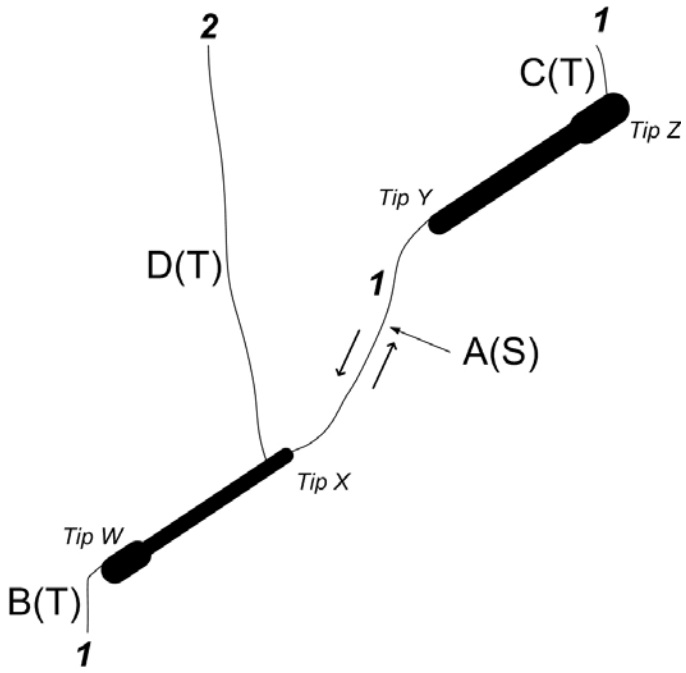

(sketch)

Time : 1m34s (Image -135)

A new tensile crack D developed from the upper face of the lower flaw near flaw tip X.

Figure 3.2 – Images captured from high speed video of specimen MA12 (continued)

30-0-a

MA04

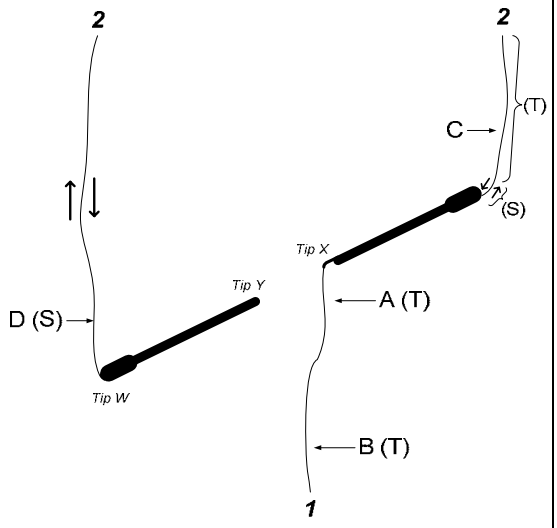

MA05

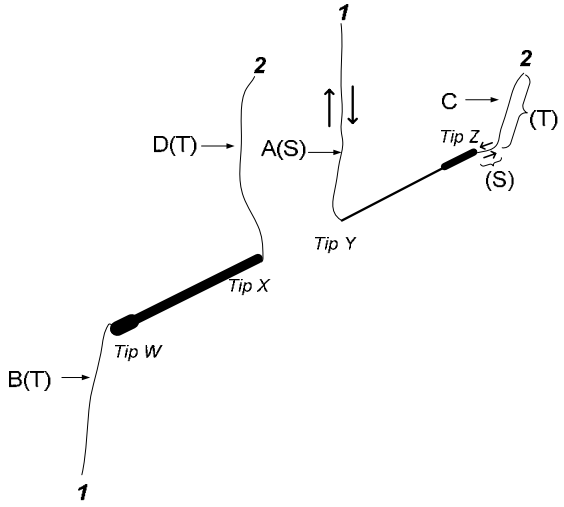

MA35

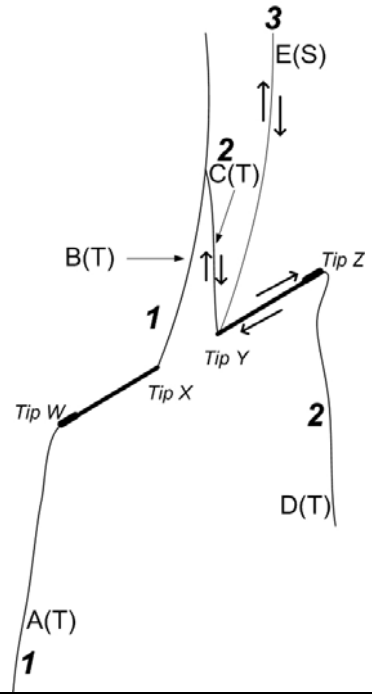

MA36

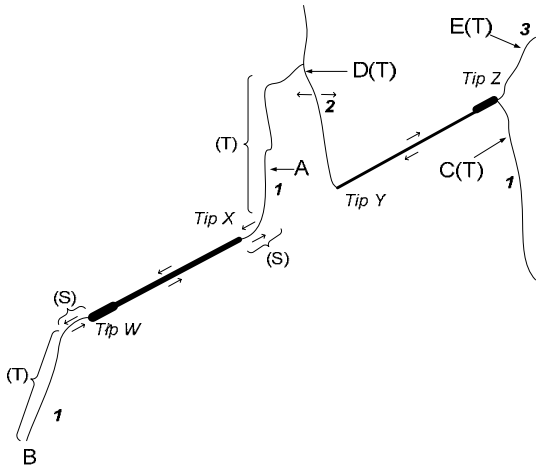

Notes:

- In 2/4 cases (MA04 & MA05), there was no coalescence. In 2/4 cases (MA35 & MA36), coalescence was achieved by steeply inclined ***tensile*** cracks initiating from inner flaw tips.

Figure 3.3a – Fracturing and coalescence patterns in marble specimens with flaw geometry of 30-0-a.

30-0-a

Notes (continued):

- Compression of the flaws leading to their aperture reduction, which was concurrent with the ***crushing*** of material at the flaw tips, was associated with the almost simultaneous formation of the steeply-inclined shear cracks initiating from flaw tips, e.g. crack D in MA04, crack A in MA05 and crack E in MA35.

- The opening up of a tensile crack would sometimes ***facilitate*** the sliding and compression of the neighboring flaw. In MA35, the tensile crack opening of crack C was concurrent with the dextral sense of relative sliding between the upper face and lower face of the right flaw. The shearing occurred along crack C and a subsequent crack E was also associated with substantial aperture reduction of the right flaw (refer to high speed images # -108, -94, -86 in figure 2.3b). The shearing motions along the above mentioned cracks suggested a rotation about a center north-east to the right flaw. The location of the center of rotation is not exact and for illustrative purposes only.

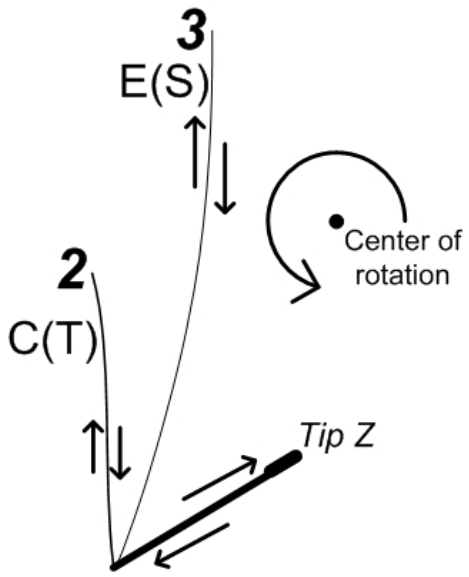

- Most of the cracks initiated from the outer tips of the pre-existing flaws were ***tensile*** and more or less aligned with the loading direction. ***Shearing*** sometimes occurred along their initial short segments adjacent to flaw tips.

Figure 3.3a (continued)

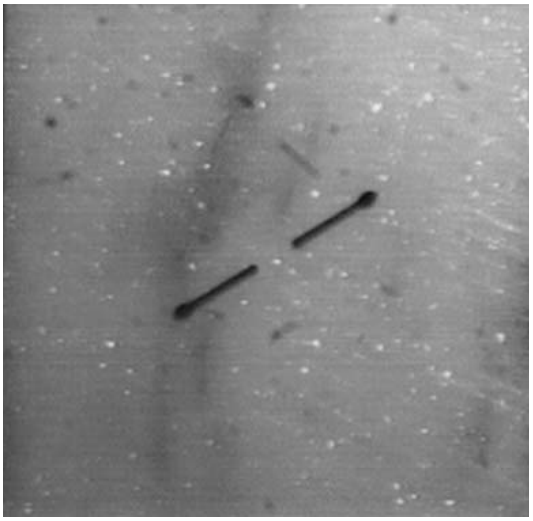	Initial flaw configuration.
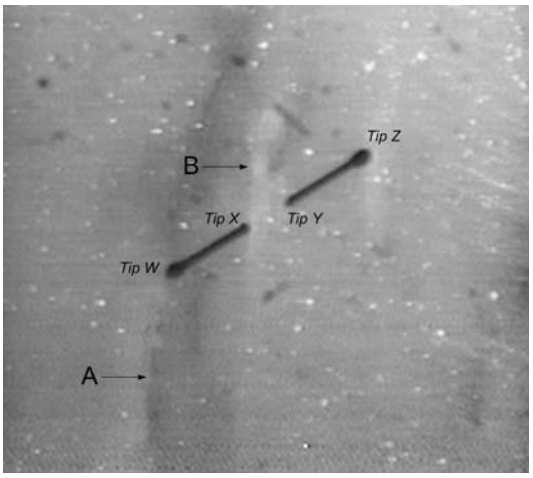 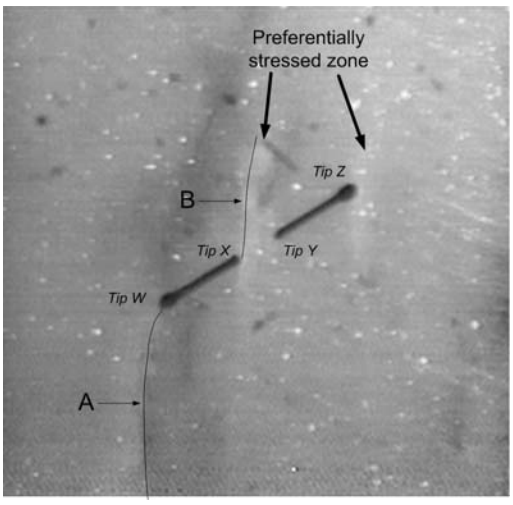	High Speed Image # - 146 A sudden whitening color change (became more light reflective) appeared along an elongated strip between the two inner flaw tips and around the outer flaw tips. There was also an incipient development of tensile crack A at tip W and tensile crack B at tip X of the left flaw, but their aperture was still tight.

Figure 3.3b – Detailed analysis of high speed images of marble specimen MA35.

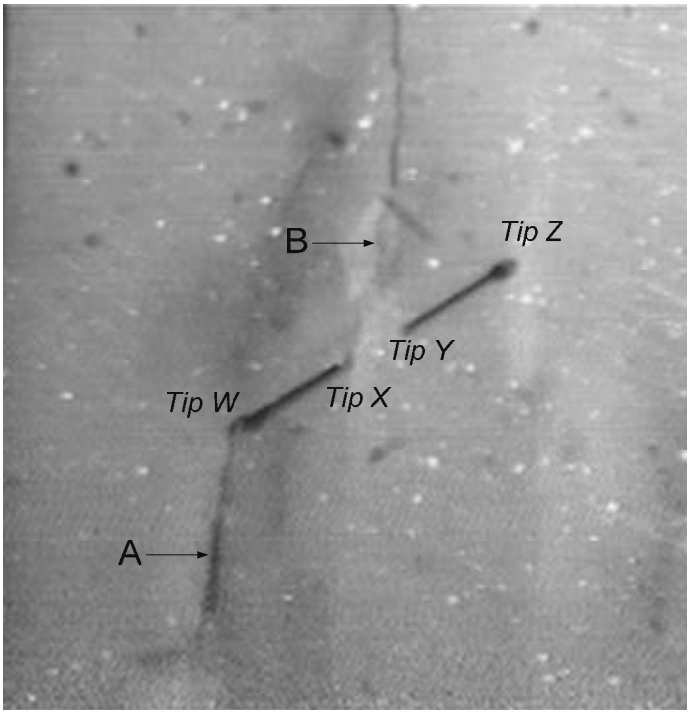

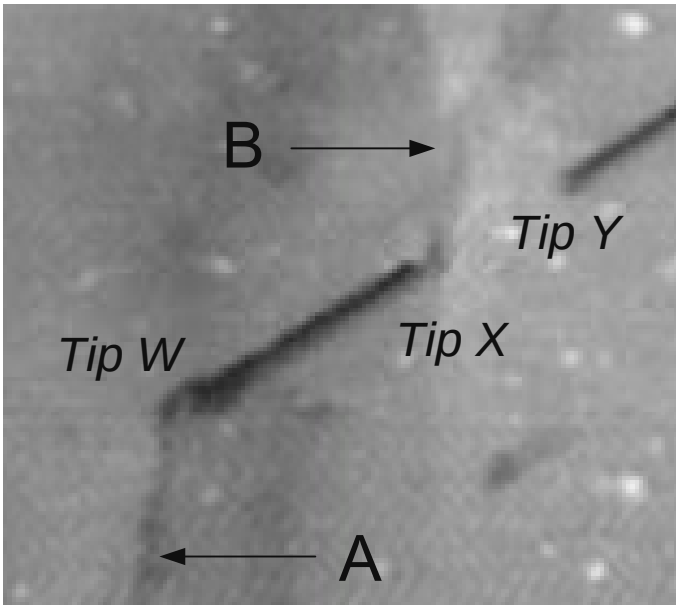

(close-up of the left flaw)

High Speed Image # - 127

The aperture of tensile cracks A and B increased.

Figure 3.3b (continued)

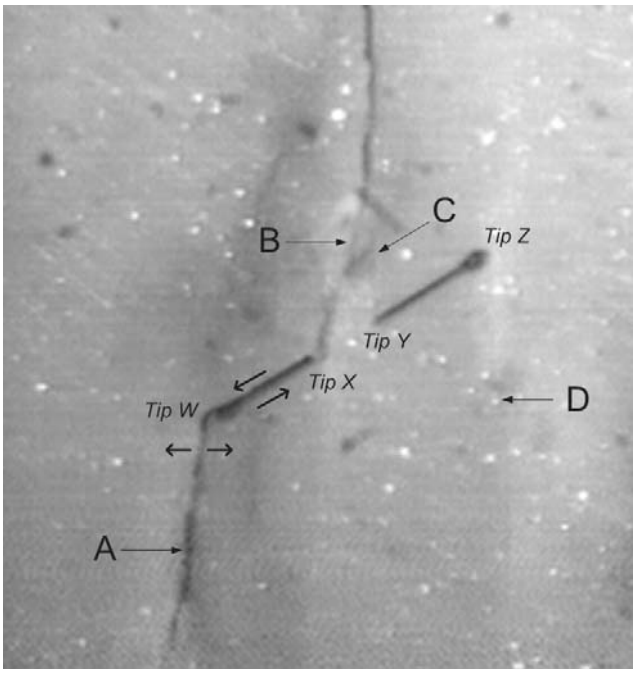	High Speed Image # - 124 (Coalescence) A new vertical tensile crack C initiated from tip Y of the right flaw which coalesced with crack B. A new tensile crack D initiated from the outer tip Z of the right flaw and propagated downwards.
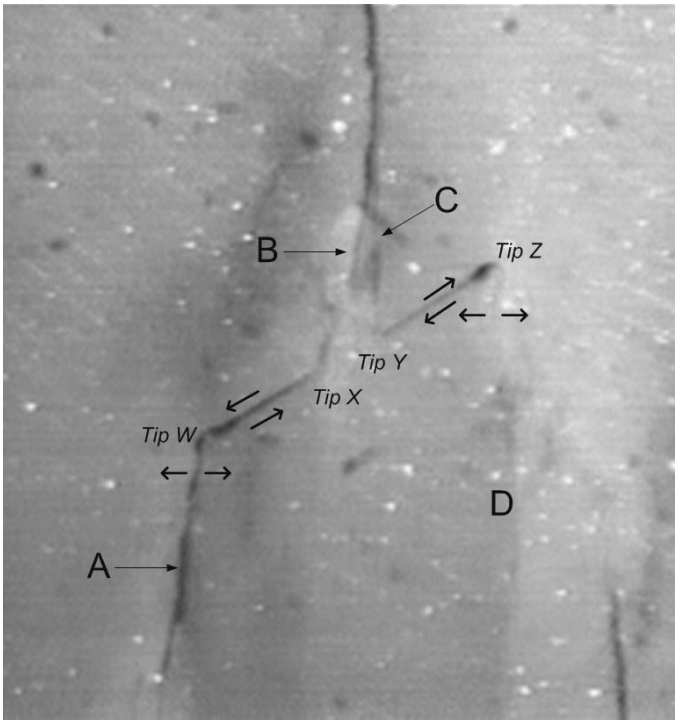	High Speed Image # - 108 The aperture of steep tensile cracks B and C increased and shearing occurred along these two cracks. It was concurrent with an observable aperture decrease of both pre-existing flaws. There was also a relative displacement between the upper face and the lower face of the pre-existing flaws as revealed from the aperture increase of cracks A and D. The sense of movement was **sinistral** for the left flaw and **dextral** for the right flaw.

Figure 3.3b (continued)

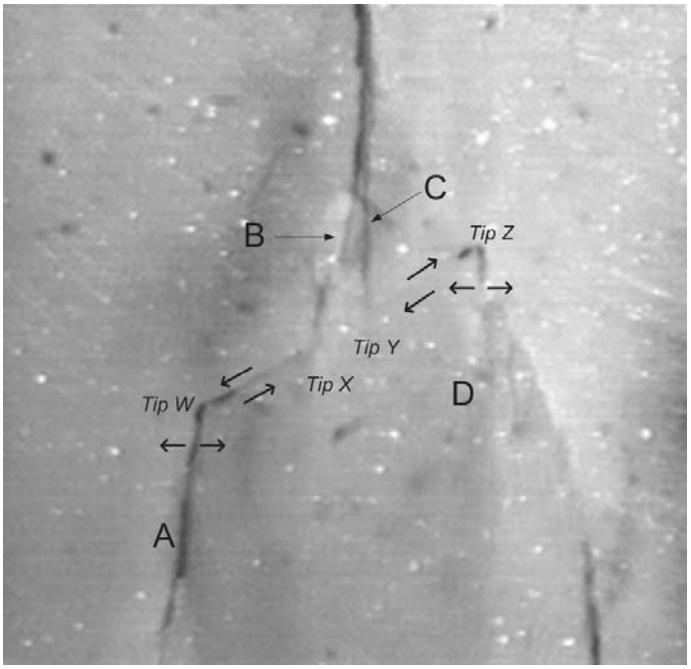	High Speed Image # - 94 A continual aperture increase of crack C led to a further dextral displacement along the right flaw as revealed from the further aperture increase of crack D. Further shearing occurred along crack C also led to further aperture reduction of the right flaw.
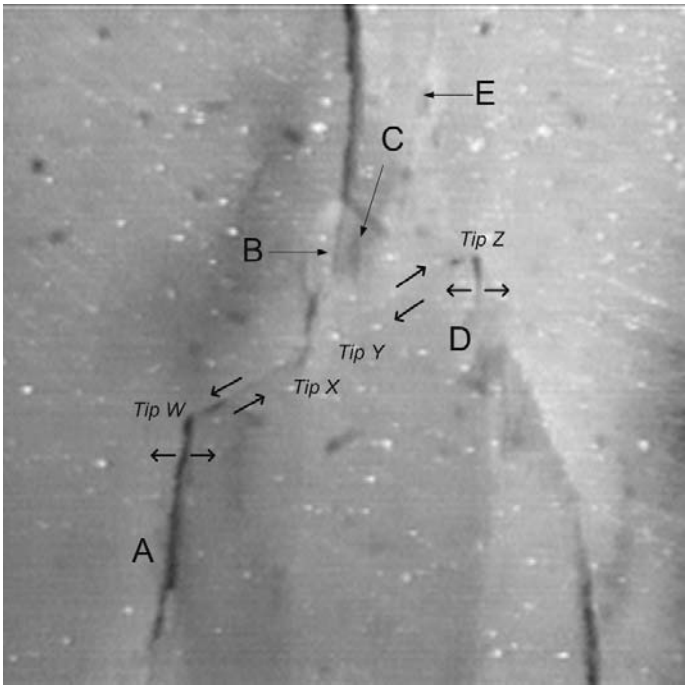	High Speed Image # - 86 A new shear crack E initiated from tip Y of the right flaw. Note that both flaws were almost completely closed.

Figure 3.3b (continued)

30-0-2a

MA06

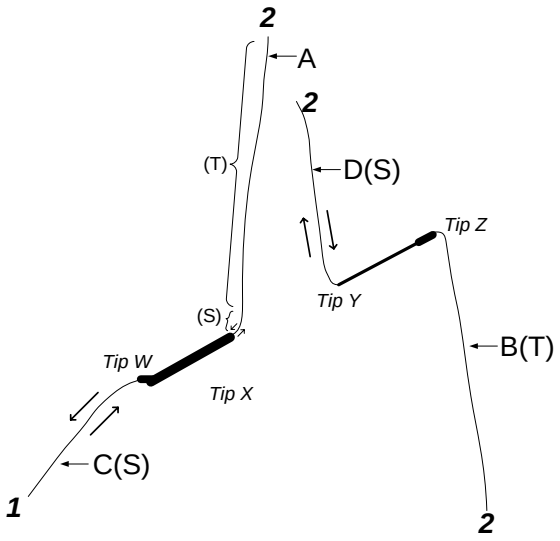

MA07

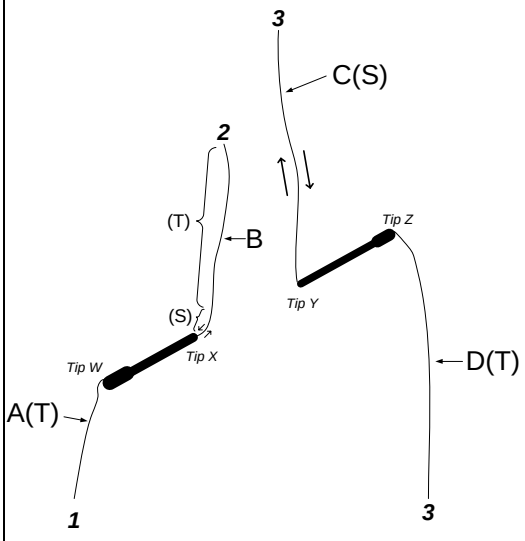

MA37

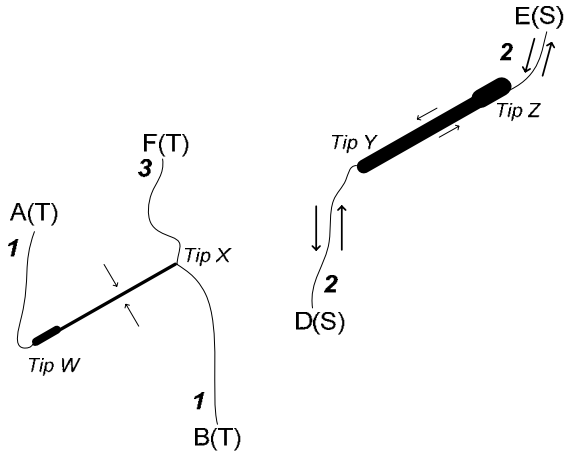

MA38

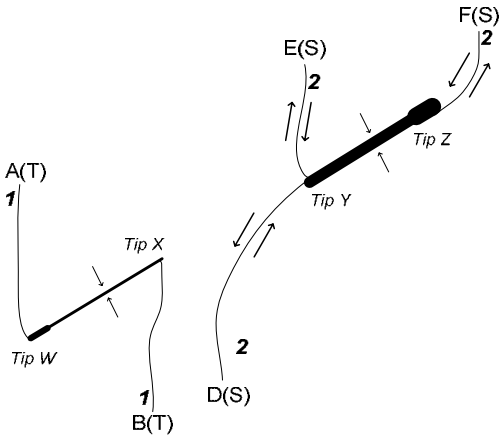

Notes:

- In all cases, ***no coalescence*** occurred.
- The new cracks initiated from the flaw tips were vertical or steeply-inclined cracks of tensile or shear origin.
- The initiation of those inclined shear cracks from flaw tips was always associated with the ***compression (aperture reduction)*** of the flaws and ***crushing*** of material at the flaw tip regions.

Figure 3.4 – Fracturing and coalescence patterns in marble specimens with flaw geometry of 30-0-2a.

30-a-2a

MA12

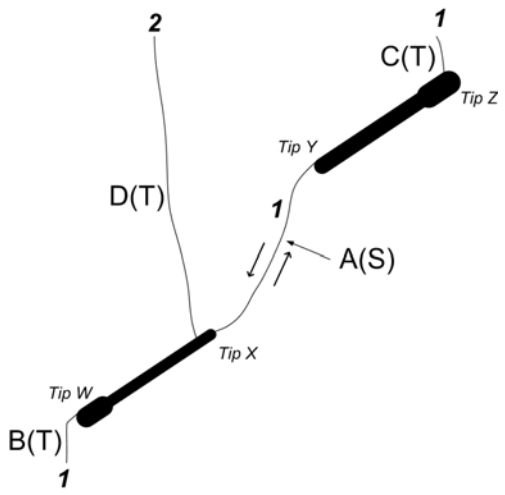

MA13

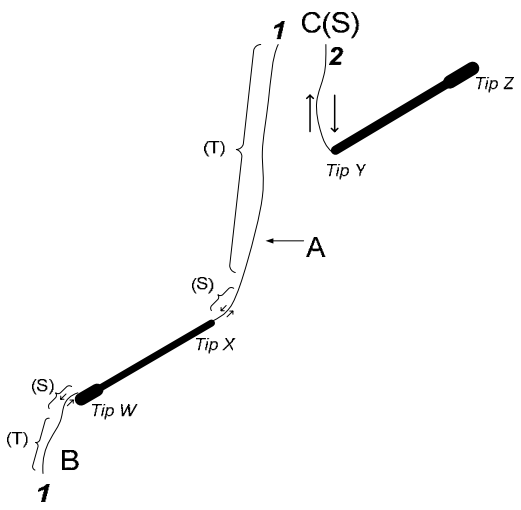

MA41

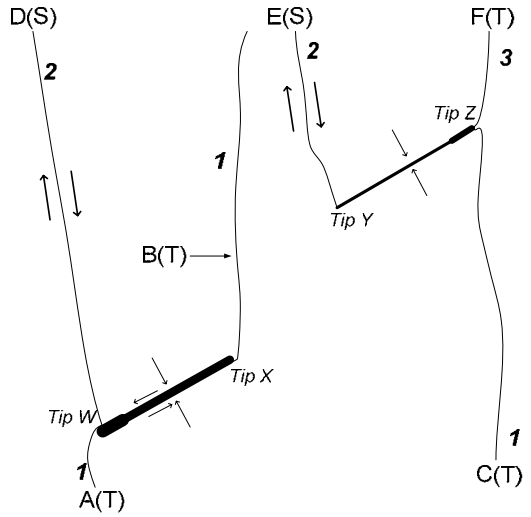

Notes:

- In 1/3 cases (MA12), coalescence occurred by a ***shear crack*** which linked up the inner flaw tips. In 2/3 cases (MA13, MA41), ***no coalescence*** was observed.
- In MA 12 where coalescence occurred, the amount of ***compression (aperture reduction)*** of the flaws was ***small***. In MA13 and MA41, where ***no coalescence*** occurred, ***substantial compression*** of the flaws was observed. In these two specimens, a steeply-inclined tensile crack initiated from one inner flaw tip and an ***oblique shear crack*** initiated from the other inner flaw tip.
- The new cracks initiated from the outer tips of the flaws were either ***tensile or shear*** in origin.

Figure 3.4 – Fracturing and coalescence patterns in marble specimens with flaw geometry of 30-a-2a.

30-a-a

MA10

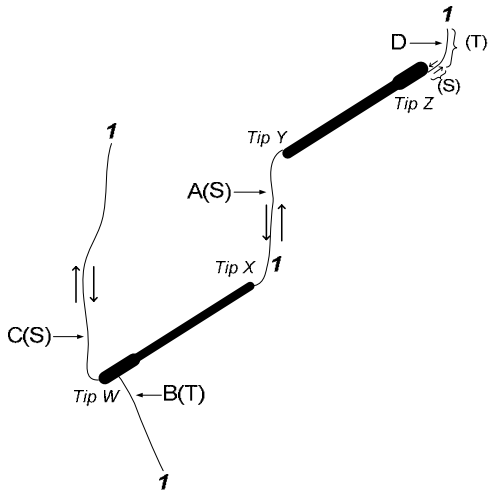

MA11

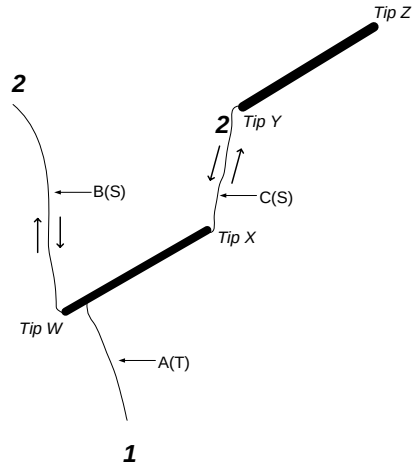

MA40

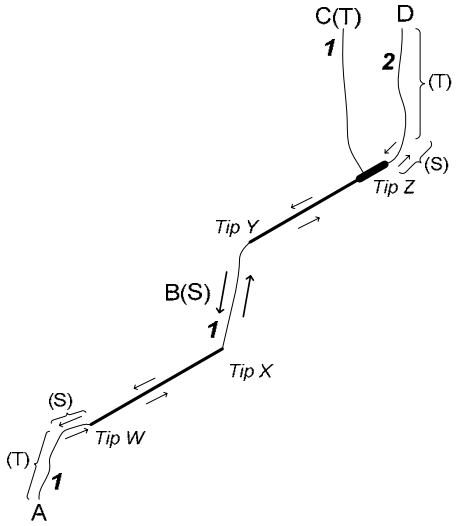

Notes:

- In all cases, ***coalescence*** occurred by a ***shear crack*** linking up the two inner crack tips. The shearing motion along the coalescence shear cracks occurred simultaneously with the ***compression*** (aperture reduction) of the two flaws and the ***crushing*** of material at the flaw tip regions.

- In 2/3 cases (MA10, MA11) the ***compression*** of the flaws and the ***crushing*** of the material at the flaw tips was associated with the initiation of an ***oblique shear crack*** at the outer tips (crack C in MA10 and crack B in MA11).

- Most of the cracks initiated from the outer tips were ***tensile*** with ***some shearing*** along their initial short segments adjacent to flaw tips (crack D in MA10, cracks A & D in MA40).

Figure 3.5 – Fracturing and coalescence patterns in marble specimens with flaw geometry of 30-a-a.

30-2a-2a

MA08

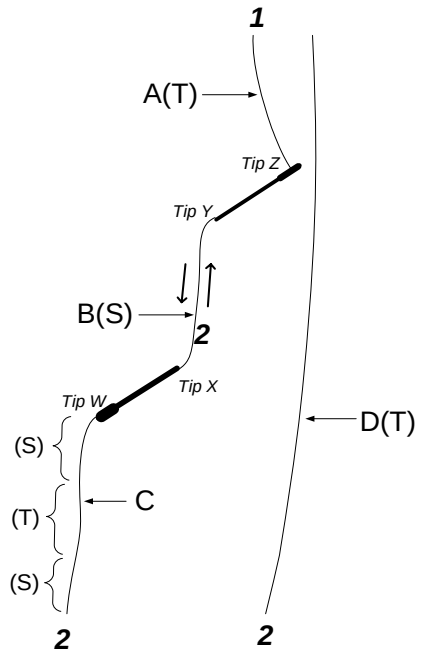

MA09

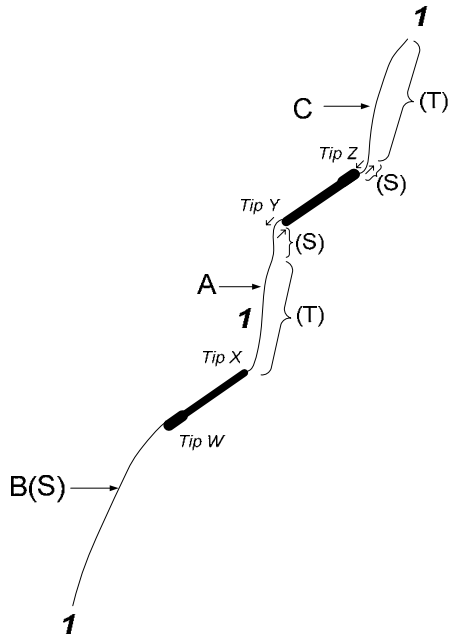

MA30

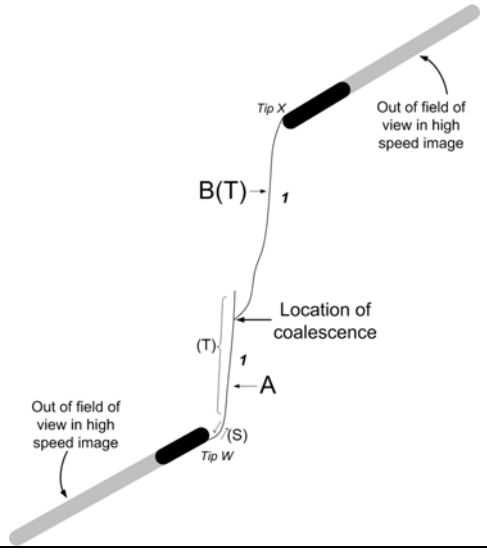

MA31

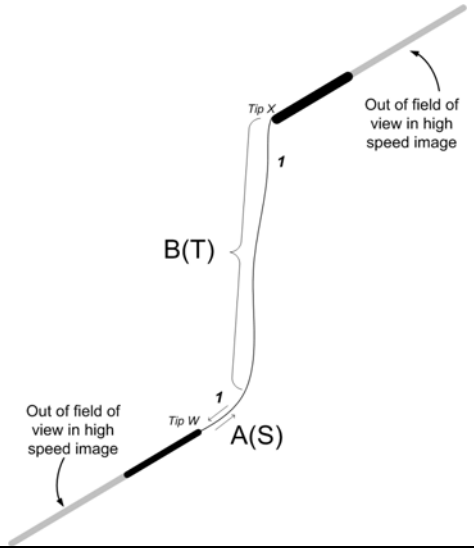

Notes:

- In MA08, coalescence was achieved by a single ***shear crack***. In MA 09, coalescence was achieved by a single ***tensile crack***. In MA 30 and MA 31, coalescence was achieved by initiation and propagation of two cracks independently from the inner flaw tips. In MA30, two tensile cracks were involved. In MA31, one tensile crack and one shear crack were involved.

Figure 3.6 – Fracturing and coalescence patterns in marble specimens with flaw geometry of 30-a-a.

30-2a-2a

Notes (continued):

- In MA08, the development of the ***coalescence shear crack*** was associated with the ***aperture reduction*** of the flaws and the ***crushing*** of material at the flaw tip regions. In MA09, MA30, MA31, the opening of ***coalescence tensile crack(s)*** was associated with the relative ***displacement*** between the upper face and the lower face of the flaws.

- In MA08 and MA09 where the field of view was wide enough, cracks of both ***tensile origin and shear origin*** were observed to have initiated from the outer flaw tips.

Figure 3.6 (continued)

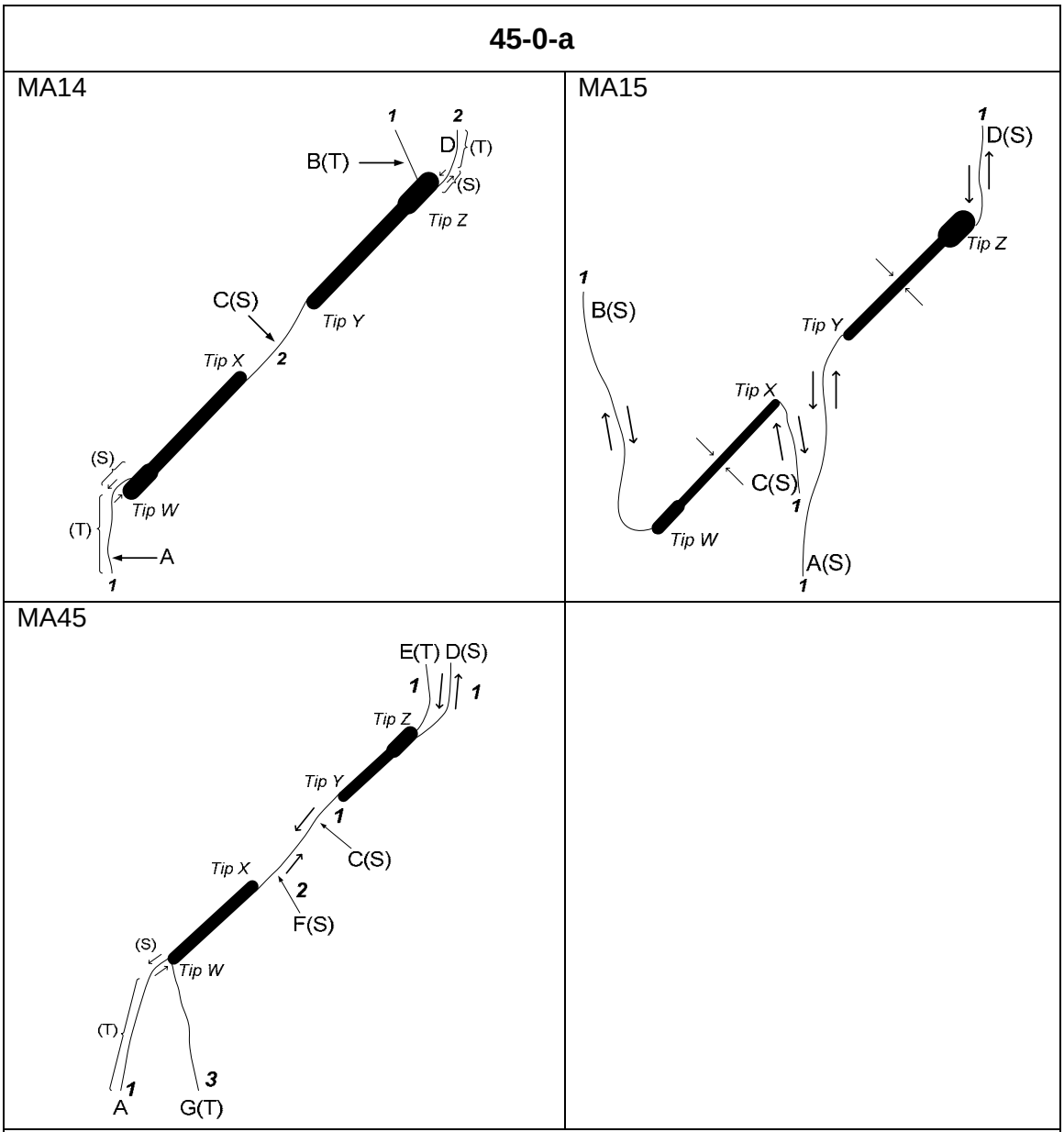

Notes:

- In 1/3 cases (MA15), ***no coalescence*** occurred. In 2/3 cases, coalescence was achieved by a single ***shear crack*** (MA14) or two shear cracks independently initiating from the inner flaw tips.

- When there was a substantial ***compression*** (aperture reduction) of the two flaws and ***crushing*** of material at the flaw tip regions, ***oblique shear cracks*** instead of coplanar shear cracks would favorably develop from the inner flaw tips (MA15).

- In cases where coalescence was achieved by ***coplanar shear crack(s)*** in the bridging region, most of the cracks initiated at the outer tips were then ***tensile cracks*** with ***some shearing*** along their initial short segments adjacent to flaw tips (cracks A & D in MA14, crack A in MA45).

Figure 3.7 – Fracturing and coalescence patterns in marble specimens with flaw geometry of 45-0-a.

45-0-2a

MA16

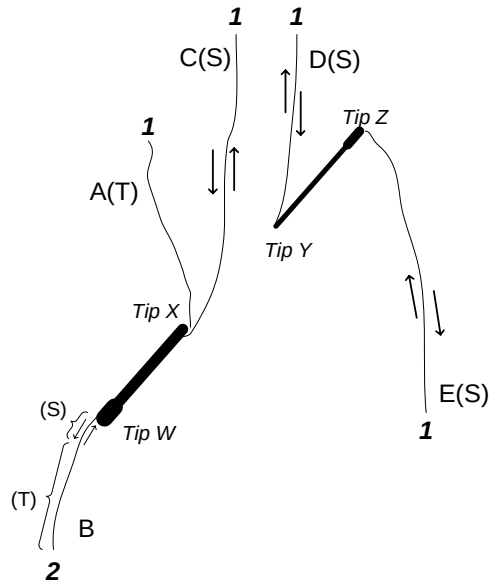

MA17

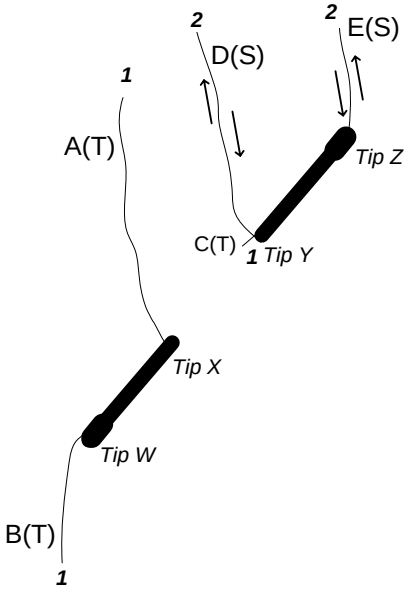

MA44

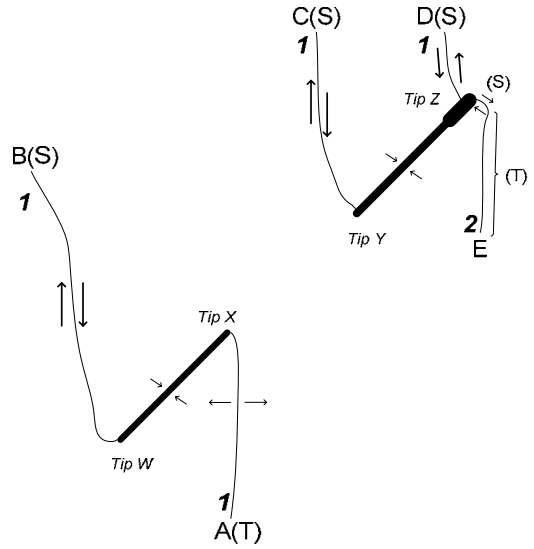

Notes:

- No coalescence occurred in all three cases.
- When there was a substantial ***compression*** (aperture reduction) of the two flaws and ***crushing*** of material at the flaw tip regions, ***oblique shear cracks*** instead of coplanar shear cracks would favorably develop from the inner flaw tips (MA15).

Figure 3.8 – Fracturing and coalescence patterns in marble specimens with flaw geometry of 45-0-2a.

45-a-2a

MA20

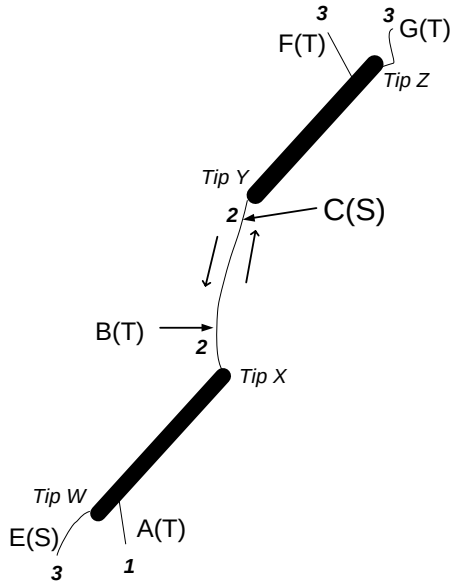

MA21

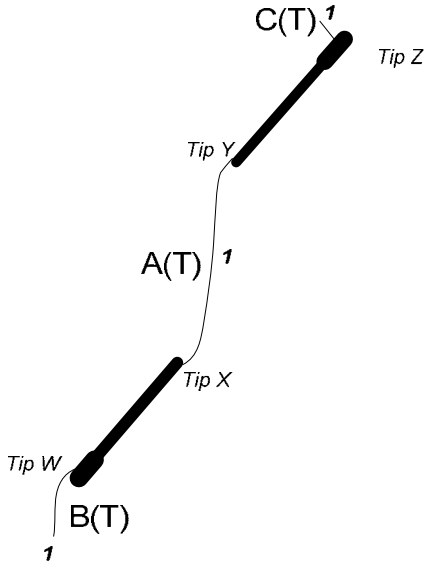

MA46

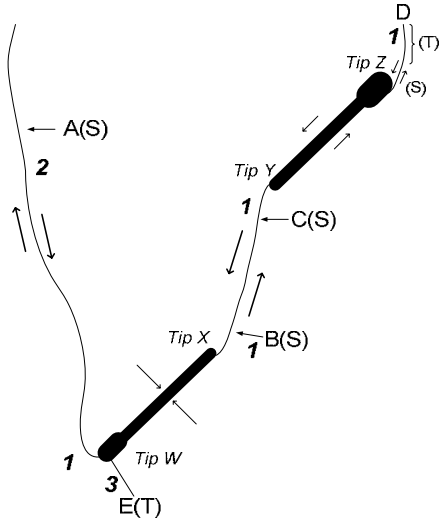

Notes:

- Coalescence occurred in all three specimens, but the nature and number of cracks involved was different among them.
- In MA 20, a ***tensile crack*** from tip X coalesced with a ***shear crack*** from tip Y.
- In MA 21, a single ***tensile crack*** linked up the inner flaw tips X & Y.
- In MA 46, a shear crack propagated upwards from tip X coalesced with another shear crack propagated downwards from tip Y.

Figure 3.9 – Fracturing and coalescence patterns in marble specimens with flaw geometry of 45-a-2a.

45-a-a

MA22

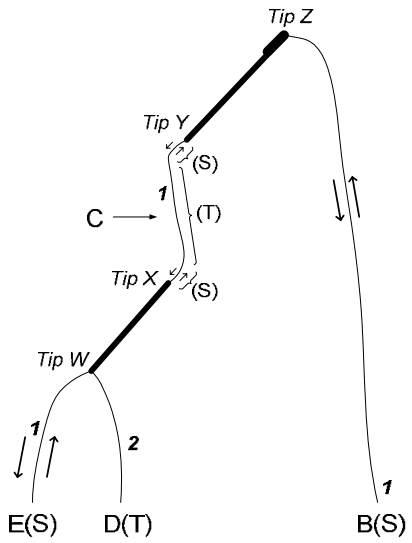

MA23

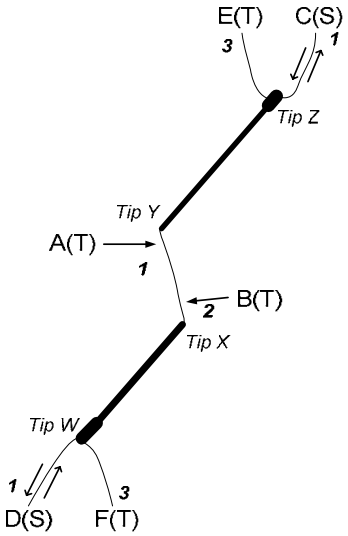

MA42

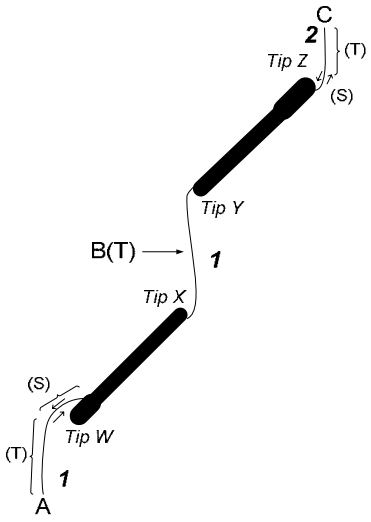

MA43

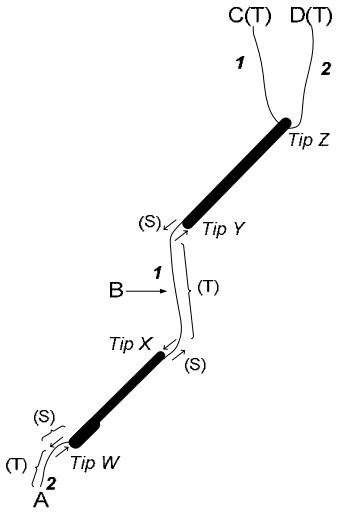

Notes:

- ***Coalescence*** in all four cases was achieved by ***tensile crack(s)*** – single coalescence cracks in MA22, 42 and 43, while two tensile cracks propagated and coalesced in MA23. The initiation of those tensile cracks was concurrent with the occurrence of a ***relative displacement*** between the upper face and lower face of the two flaws.

- In cases where substantial observable ***compression (aperture reduction)*** of the flaws and ***crushing*** of material at the flaw tip regions occurred, ***shear cracks*** favorably developed from the outer flaw tips. Otherwise, ***tensile cracks*** favorably developed from the outer flaw tips.

Figure 3.10 – Fracturing and coalescence patterns in marble specimens with flaw geometry of 45-a-a.

45-2a-2a

MA18

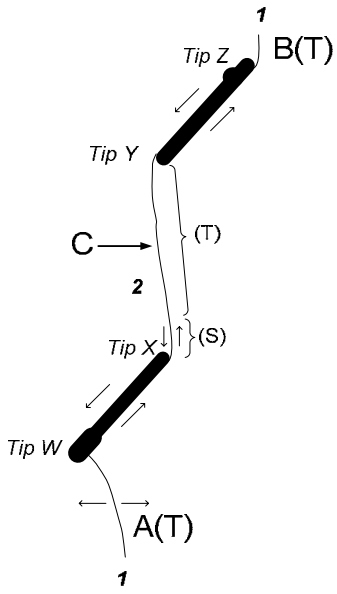

MA19

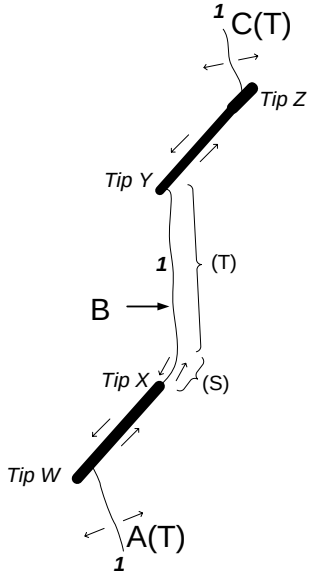

MA47

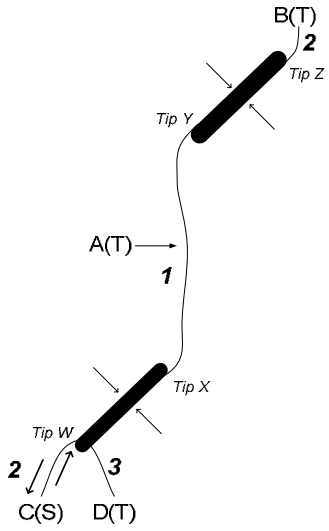

Notes:

- ***Coalescence*** in all three cases was achieved by a single ***tensile crack***, which was accompanied by some observable shearing movement adjacent to internal flaw tips.
- The occurrence of coalescence was concurrent with ***the occurrence of relative displacement*** between the upper face and lower face of the flaws.
- ***Both tensile and shear cracks*** were observed to have developed from the outer flaw tips.

Figure 3.11 – Fracturing and coalescence patterns in marble specimens with flaw geometry of 45-a-a.

60-0-a

MA24

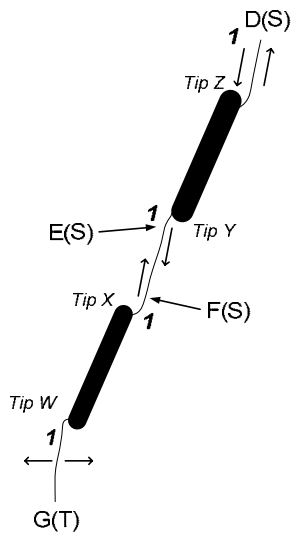

MA25

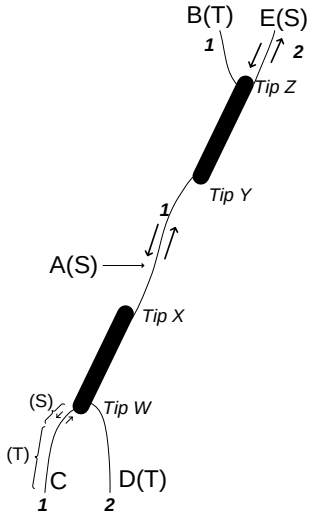

MA33

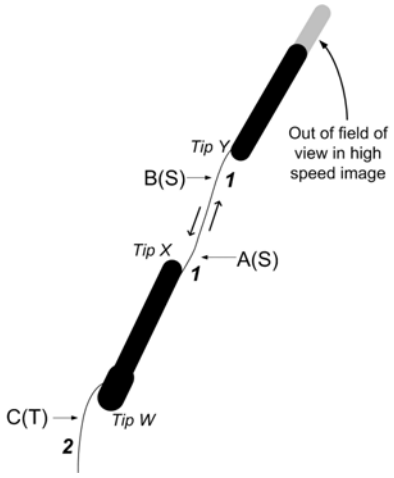

MA34

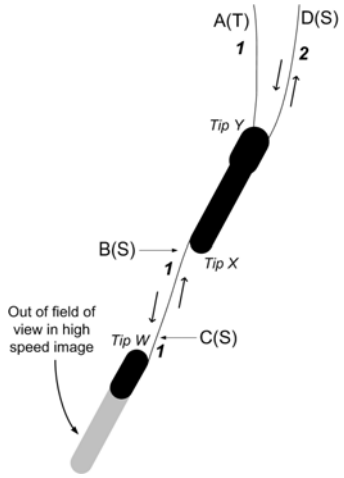

Notes:

- ***Coalescence*** in 3/4 cases (MA22, MA33, MA34) was achieved by propagation of ***two coplanar shear cracks*** initiated independently from the inner flaw tips. In the remaining case (MA25), coalescence between inner flaw tips was achieved by a single ***coalescence shear crack***.

- The coalescence cracks always linked up a locality close to the ***bottom face*** of the left flaw and a locality close to the ***top face*** of the right flaw.

- ***No substantial compression*** of the flaws occurred as compared with those flaws oriented at a smaller inclination angle (30^o, 45^o). The deformation of the flaws was solely due to the ***relative displacement between*** the upper face and lower face of the flaws. About ***half*** of the new cracks initiated from the outer tips are ***tensile*** and the other ***half*** are ***shear***.

Figure 3.12 – Fracturing and coalescence patterns in marble specimens with flaw geometry of 60-0-a.

60-0-2a

MA26

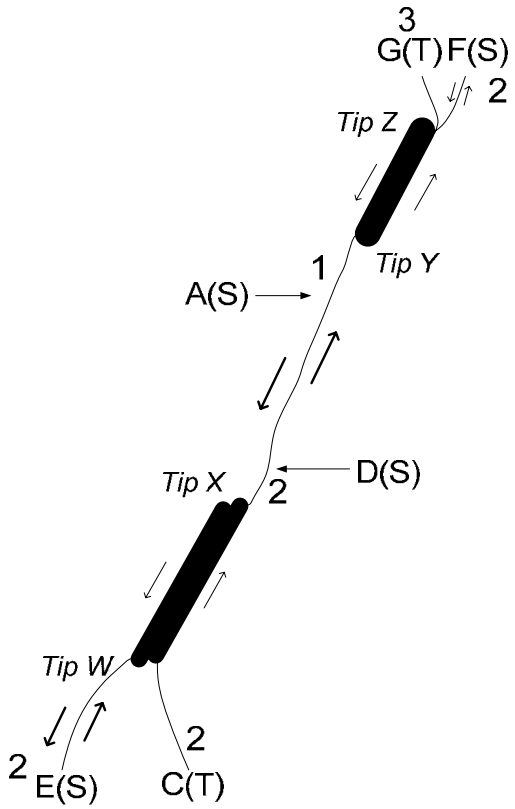

MA27

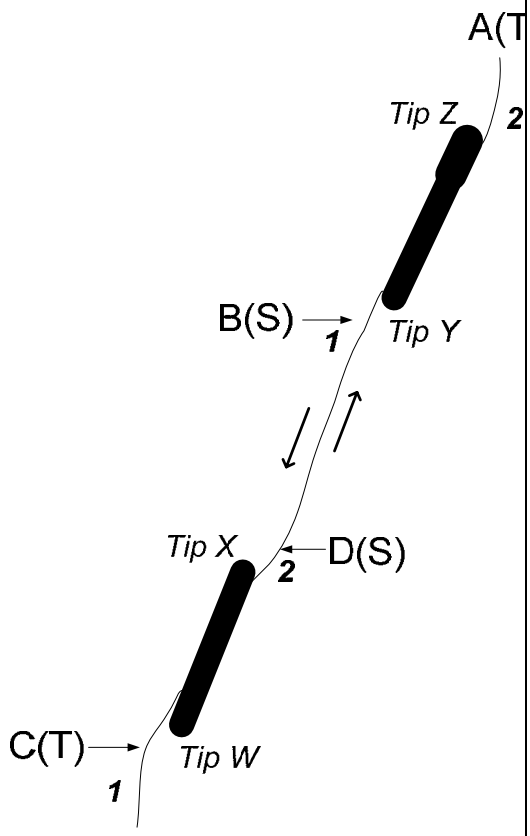

Notes:

- ***Coalescence*** in both cases was achieved by the propagation of ***two coplanar shear cracks*** initiated individually from the inner flaw tips. In MA26, crack D from tip X coalesced with crack A from tip Y; in MA27, crack D from tip X coalesced with crack B from tip Y.

- The coalescence cracks always linked up a locality close to the ***bottom face*** of the left flaw and a locality close to the ***top face*** of the right flaw.

- In MA 26, new cracks E and F propagated from the outer flaw tips in such a way that they were ***inclined at an angle*** (~30^{o}) with the loading direction. Once they had initiated, subsequent shearing occurred along them as external loading was continuously applied.

- In MA 27, new cracks A and C initiated and propagated from the outer flaw tips in such a way that they were almost ***coaxial*** with the loading direction.

Figure 3.13 – Fracturing and coalescence patterns in marble specimens with flaw geometry of 60-0-2a.

60-a-2a

MA28

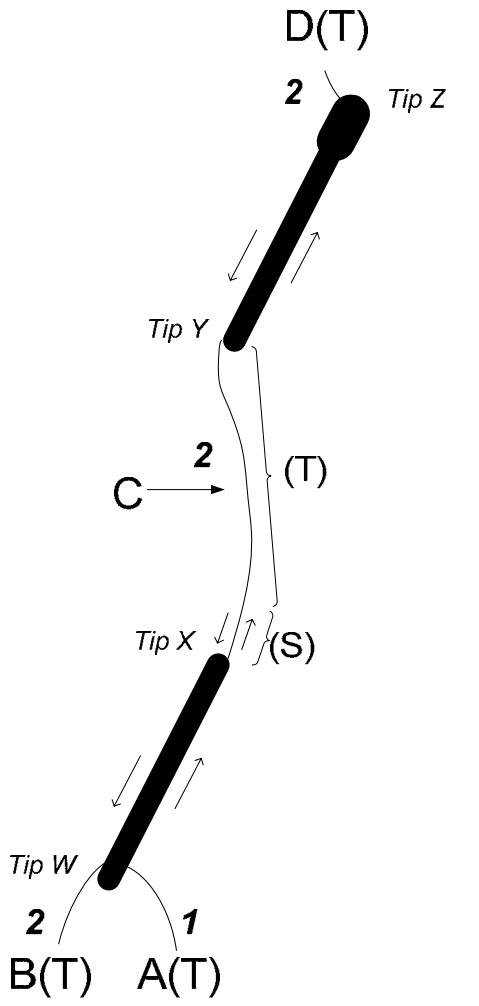

MA29

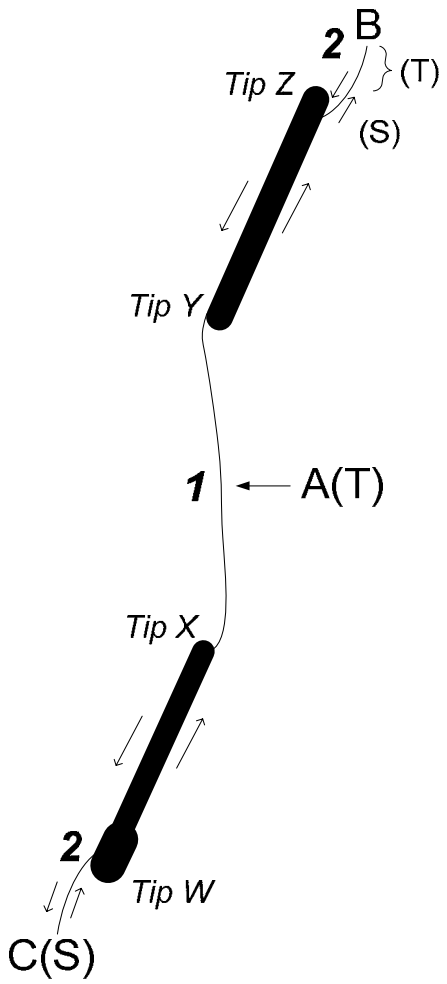

Notes:

- ***Coalescence*** in both cases was achieved by a single ***tensile crack*** linking up the inner flaw tips. In MA28, subsequent shearing occurred along the lower segment of the coalescence crack adjacent to the flaw tip.
- The initiation and opening of the ***coalescence tensile cracks*** was concurrent with a relative displacement between the upper face and the lower face of the two flaws.

Figure 3.14 – Fracturing and coalescence patterns in marble specimens with flaw geometry of 60-a-2a.

3.4 Types of cracks observed in Vermont White Marble

As illustrated in section 3.3, different types of cracks can develop in response to external loading. Generally speaking, cracks observed in the marble specimens can be classified as tensile (mode 1 crack) or shear (mode 2 crack). However, depending on the crack geometries and propagating behavior, the cracks could further be classified into one of the following six types as shown in figure 3.15. The characteristics of each crack type are discussed in this section.

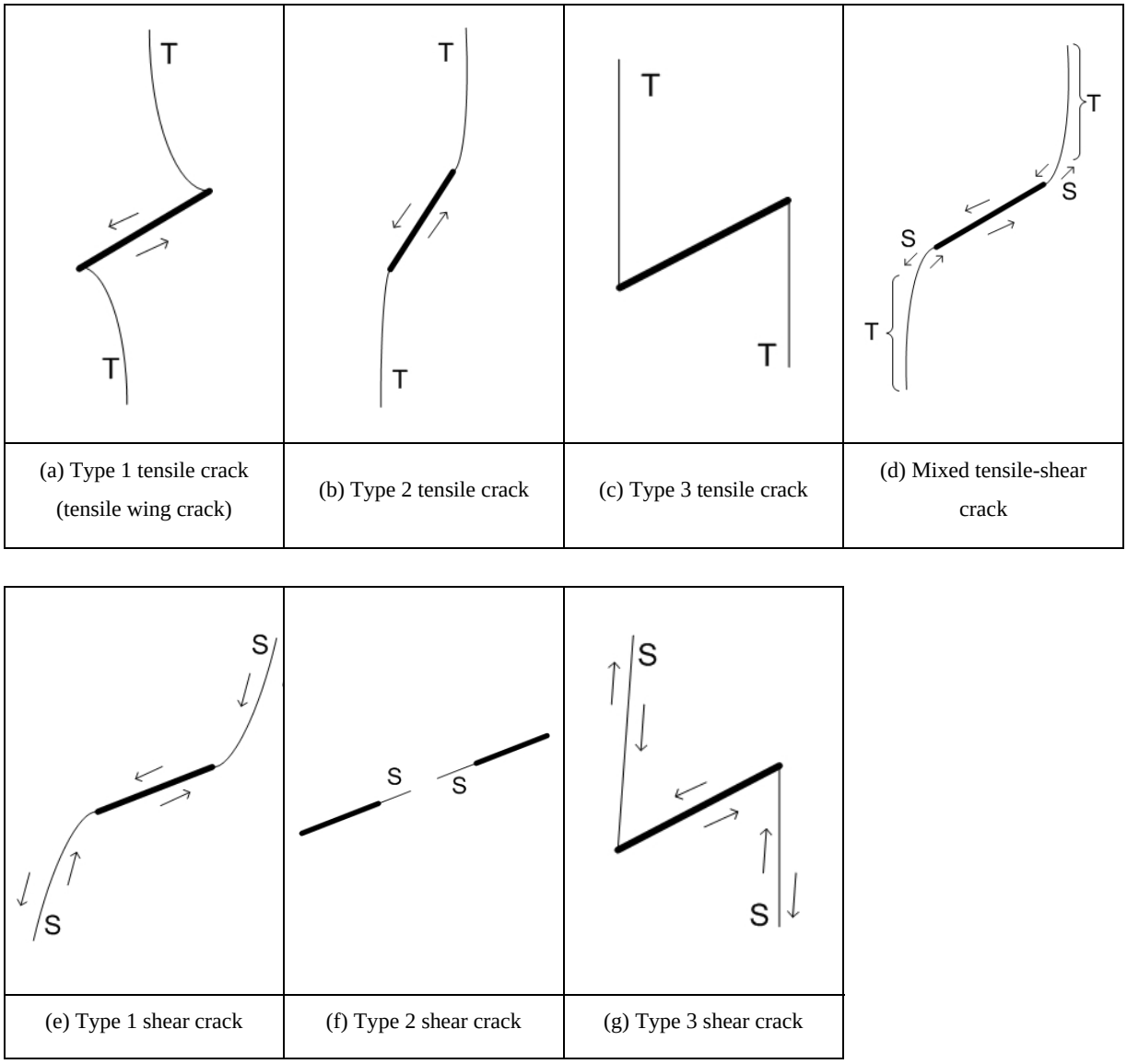

(a) Type 1 tensile crack (tensile wing crack) | (b) Type 2 tensile crack | (c) Type 3 tensile crack | (d) Mixed tensile-shear crack

(e) Type 1 shear crack | (f) Type 2 shear crack | (g) Type 3 shear crack

Figure 3.15 – Types of cracks observed in White Vermont Marble.

Type 1 tensile crack (Type 1 T)

This type of crack is also known as ***tensile wing cracks*** in the literature which displays a distinctive curvilinear shape (figure 3.15a). It usually initiates at or close to the flaw tips as a short hair-like feature, which subsequently propagates towards the loading direction usually with a simultaneous increase of crack aperture (figure 3.16).

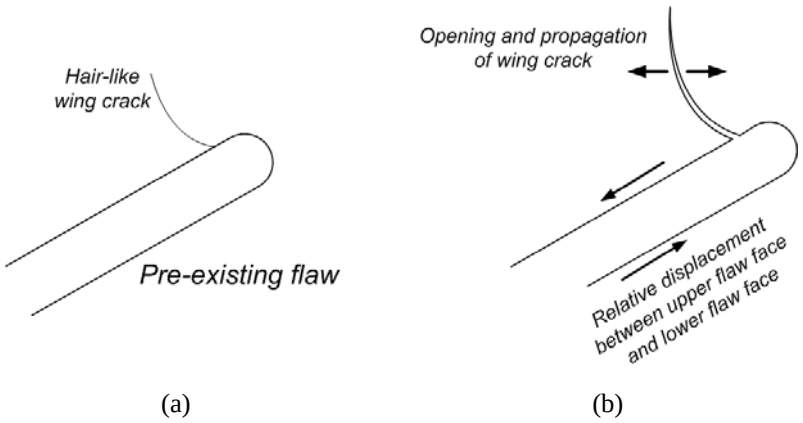

(a) (b)

Figure 3.16 – (a) hair-like tensile wing crack initiates from the tip region of the pre-existing flaw. (b) tensile wing crack propagates upwards with an increase of aperture.

Type 2 tensile crack (Type 2 T)

Similar to type 1 tensile crack, type 2 tensile crack also initiates at or close to the flaw tips as a short hair-like feature (figure 3.15b). However, the curving direction of type 2 crack is different from (opposite to) that of type 1 tensile crack (figure 3.15a). The initiation of type 2 crack is usually associated with a simultaneous relative displacement between the upper face and the lower face of the flaws (figure 3.15b). Continuation of such a relative displacement helps "tear apart" the subsequent propagating path of type 2 tensile crack in an orientation which is coaxial with the loading direction. The step-by-step initiation of such type 2 tensile cracks as observed on the high speed videos is generalized and illustrated in figure 3.17.

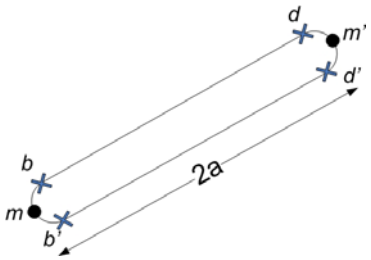	(a) undeformed pre-existing flaw
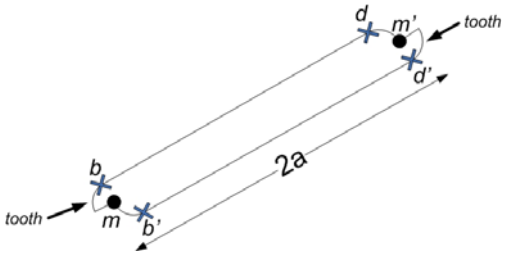	(b) fracturing at flaw tips
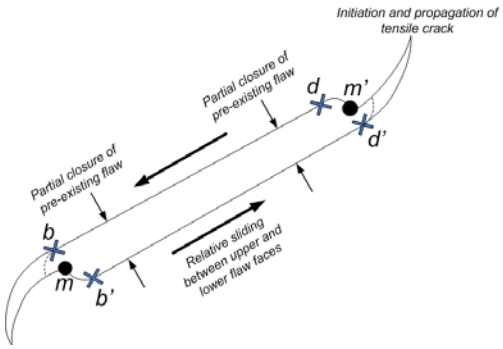	(c) initiation of tensile cracks from flaw tips
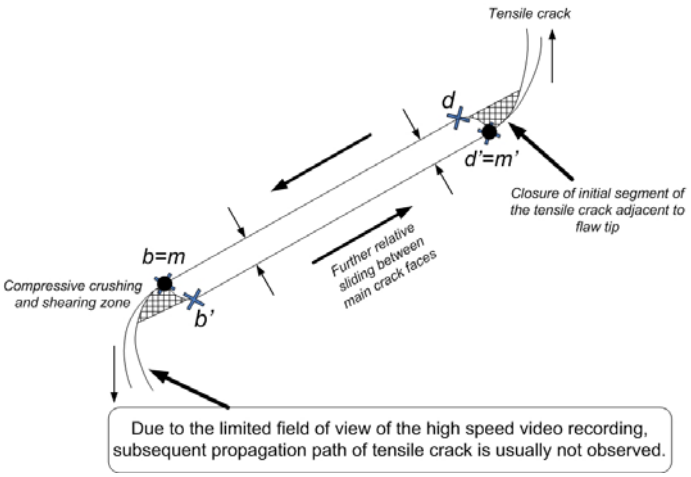	(d) crushing and shearing at the flaw tip regions. Note the progressive sliding and closure of the two faces of the flaw.

Figure 3.17 – Initiation of Type 2 wing cracks

Figure 3.17a shows an undeformed pre-existing flaw whose tips are marked ***m*** and ***m'***. The uniaxial loading direction is vertical. Two pairs of reference points are also marked as displacement indicators – b is opposite to b' and d is opposite to d'. When the specimen is loaded up to a particular stress level, fracturing occurs at the flaw tips (figure 3.17b) and a relative displacement between the upper flaw face and the lower flaw face continues. See the relative displacement of the displacement indicator pairs ***b-b'*** and ***d-d'*** which lead to the formation of two teeth at flaw tips. Associated with the displacement along the flaw, tensile cracks propagate from the two ***"teeth"*** which protrude from the flaw tips towards the loading direction. This is the incipient development of type 2 tensile cracks. The propagation of the two tensile cracks is accompanied by a progressive closure (aperture reduction) of the flaw and a continual relative sliding between the two faces of the flaw (figure 3.17c). Eventually, the two ends of the flaw make contact (point ***m'*** approaches point ***d'*** and point ***b*** approaches point ***m***). Such closure and sliding lead to respective compressive crushing and shearing of the triangular regions below ***m*** and above ***m'*** (figure 3.17d). Examples of type two tensile crack generation include MA42 & MA43 (45-a-a), MA45 (45-0-a), MA46 & 47 (45-2a-2a). Refer to Appendix A for some of their high speed video images.

To summarize, the formation of 'teeth' at flaw tips is very typical for type 2 tensile crack initiation. However, as will be discussed below, teeth are also produced prior to the initiation of type 1 shear cracks and mixed tensile-shear cracks which are also closely associated with a relative displacement between the upper face and lower face of the pre-existing flaw.

<u>Type 3 tensile crack – anti-wing crack (Type 3 T)</u>

This type of crack always initiates from the tip of the pre-existing flaw and its trajectory is opposite to the closest tensile wing crack initiated from the opposite flaw face (compare figure 3.15c and 3.15a). Its overall trajectory is very similar to that of type 3 shear crack (see description below). However, with the use of the high speed camera, it is possible to differentiate these two types regarding the mode of crack initiation (shear/tensile).

Type 1 shear crack (Type 1 S)

Similar to type 2 tensile cracks, type 1 shear crack is closely associated with a simultaneous relative displacement between the upper face and the lower face of the flaws (figure 3.15e). This type of crack first initiates as an out-of-plane or coplanar short hair-like feature from the flaw tips. Since its subsequent propagating crack path remains *inclined* with the loading axis at an angle as schematically illustrated in figure 3.15d, further shear continues to take place on it.

Mixed tensile-shear crack (Mixed T-S)

This is a transitional crack type between type 2 tensile crack and type 1 shear crack. Similar to type 1 shear crack, the crack also first initiates as an out-of-plane or coplanar short hair-like feature from the flaw tips. However, the subsequent propagating crack path becomes more parallel with the uniaxial loading direction and propagates as a tensile crack (figure 3.15d).

As will be discussed in the next section, geometries with small flaw inclination angle (large angle with the loading direction) favor compression (aperture reduction) of the pre-existing flaws, crushing of material at the flaw tip regions and hence initiation of type 1 shear cracks (figure 3.15e). On the other hand, the degree of flaw compression and tip crushing are less in geometries of large flaw inclination angle. The initiation of type 2 tensile cracks (figure 3.15b) is favored instead. The mixed tensile-shear crack is a transition between the above two crack types. Therefore, there appears to be a dependency of crack type (type 2 tensile, type 1 shear, mixed tensile-shear) on the inclination angle of the pre-existing flaws.

Type 2 shear cracks – coplanar shear crack (Type 2 S)

This crack type refers to the shear crack which is coplanar with the pre-existing flaw (figure 3.15f). The initiation and subsequent propagation of this type of crack is usually associated with an observable relative displacement between the upper face and the lower face of the pre-existing flaw. When two neighboring coplanar flaws are close enough to

each other, coalescence is usually achieved by the initiation and propagation of type 2 shear crack(s).

Type 3 shear cracks – oblique shear cracks (Type 3 S)

This type of crack always initiates from the tips of the pre-existing flaws and its initiation and subsequent propagation are always associated with a substantial compression (aperture reduction) of the pre-existing flaws and crushing of material at the flaw tip regions (figure 3.15g). The general propagating direction of this crack type is vertical and parallel to the loading direction.

3.5 Influence of flaw geometries on coalescence patterns

As illustrated in figures 3.3 to 3.14, the coalescence patterns in marble are observed to be influenced by the geometries of the pre-existing flaw pairs. In the following sections, the influence on the coalescence patterns due to individual changes of the flaw geometry parameters will be systematically discussed.

3.5.1 Influence of flaw inclination angle and ligament length for coplanar flaws

The coalescence behavior observed in marble specimens containing coplanar flaw pairs is summarized in table 3.1. The cracks involved in coalescence will be classified according to the scheme shown in figure 3.15. As shown in earlier sections, the development of type 3 shear cracks is always associated with substantial flaw compression (aperture reduction). In other words, the presence of type 3 shear cracks is an indicator that flaw aperture reduction occurred. This piece of information is also contained in the last column of table 3.1.

Geometries	Coalescence?	Type of coalescence cracks (figure 3.15)	Development of type 3 shear cracks?
30-0-a	2 out of 4	1 out of 2 : Type 2 T & Type 2 T 1 out of 2 : Type 2 T & Mixed TS	3 out of 4
30-0-2a	0 out of 4	Not applicable	4 out of 4
45-0-a	2 out of 3	1 out of 2 : Type 2 S & Type 2 S 1 out of 2 : Single Type 2 S	1 out of 3
45-0-2a	0 out of 3	Not applicable	3 out of 3
60-0-a	4 out of 4	3 out of 4 : Type 2 S & Type 2 S 1 out of 4 : Single Type 2 S	0 out of 4
60-0-2a	2 out of 2	Type 2 S – Type 2 S	0 out of 2

Table 3.1 – summary of crack coalescence behavior in coplanar flaw pairs

In geometries with small flaw inclination angle (30^o), coalescence if it occurred was solely accomplished by steeply inclined cracks initiated from the inner flaw tips. In one specimen, both of them were tensile cracks, while in another specimen, one was a tensile crack and the other was a mixed tensile-shear crack. For larger angles, coalescence was mainly accomplished by coplanar cracks initiated from the internal flaw tips. In most specimens, the propagation of two coplanar shear cracks initiated independently from the inner flaw tips led to coalescence. In one specimen of geometry 60-0-a, however, coalescence between the inner flaw tips was achieved by a single shear crack instead.

Throughout the loading process, in geometries with small flaw inclination angle (30^o), compression (aperture reduction) of the pre-existing flaws and crushing of the material at the flaw tip regions were generally more common than the initiation and propagation of coplanar shear cracks that occurred for large flaw inclination angles (45^o and 60^o). These phenomena have a physical implication on the type of the new crack formed. If coplanar shear cracks could form, part of the applied loading can be accommodated by the shearing movement along the coplanar cracks (typical in flaw geometries 45-0-a and 60-

0-a). In 30-0-a and 30-0-2a, however, the formation of coplanar shear cracks was not favored. The formation of oblique shear cracks (type 3 shear cracks as shown in figure 3.15) was instead more favored to accommodate the flaw compression and tip crushing events.

The distance between the two coplanar pre-existing flaws has a strong influence on the coalescence pattern. Coalescence did not occur when the pre-existing flaws were far apart for those geometries with small inclination angle (30-0-2a and 45-0-2a). In the specimens, development of coplanar shear cracks from the inner flaw tips was absent, and the steeply-inclined/vertical cracks initiated from the inner flaw tips did not coalesce. In the case for 60^o inclination angle, the development of oblique shear cracks (type 3 shear cracks) was not favored. Coalescence between neighboring flaws was achieved by coplanar shear crack(s) no mater how close the flaws were together (60-0-a) or far apart (60-0-2a).

To conclude, there was a competition between the formation of steeply inclined inner tip cracks (type 3 shear cracks and/or type 2 tensile cracks) and coplanar shear cracks (type 2 shear cracks) from the inner flaw tips during the loading process. Small flaw inclination angle favored the former and large flaw inclination angle favored the latter. Therefore, if coalescence occurred in flaw pairs of 30^o inclination angle, it would be achieved by linage of steep inner tip cracks. If coalescence occurred in flaw pairs of 45^o and 60^o inclination angles, it is achieved by coplanar cracks.

3.5.2 Influence of bridging angle and ligament length for stepped flaws

In this section, the influence of bridging angle and ligament length on the fracturing behavior and coalescence patterns in stepped flaw geometries is discussed. It will be divided into three sections according to the flaw inclination angles – 30^o, 45^o and 60^o.

Recall that the geometry of the pre-existing flaw pair is defined by three parameters (figure 3.1) – flaw inclination angle β, spacing s and continuity c. The other way to

represent the geometry is by flaw inclination angle β, bridging angle α and ligament length L (figure 3.18). Since both systems are found in the literature, the corresponding values of bridging angle and ligament length are also included for each geometry in tables 3.2 to 3.4 to facilitate discussion.

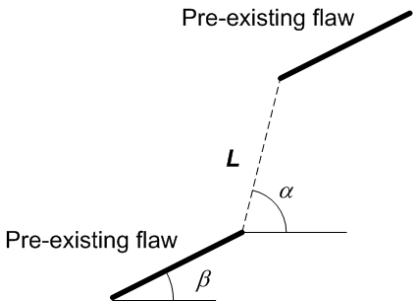

Figure 3.18 – Pre-existing flaw geometry defined by flaw inclination angle β, bridging angle α and ligament length L.

Flaw inclination angle = 30^o :

Geometries	Bridging angle (^{o})	Ligament length	Coalescence?	Type of coalescence cracks (Figure 3.15)	Development of type 3 shear cracks?
30-0-a	0	a	2 out of 4	1 out of 2 : Type 2 T & Type 2 T 1 out of 2 : Type 2 T & Mixed TS	3 out of 4
30-0-2a	0	2a	0 out of 4	Not applicable	4 out of 4
30-a-2a	26.5	2.24a	1 out of 3	Single Type 2 S	2 out of 3
30-a-a	45	1.41a	3 out of 3	Single Type 2 S	2 out of 3
30-2a-2a	45	2.83a	4 out of 4	1 out of 4 : Type 1 S 1 out of 4 : Mixed TS 1 out of 4 : Type 2 T & Mixed TS 1 out of 4 : Type 2 T & Type 2 S	0 of 4

* a = half flaw length

Table 3.2 – summary of crack coalescence behavior in flaw pairs of 30^o flaw inclination angle.

In geometries with small bridging angle (30-0-a, 30-0-2a), compression of the pre-existing flaws and crushing of the material at the flaw tip regions were common. The occurrence of flaw compression and tip crushing were also concurrent with the initiation and propagation of type 3 shear cracks and/or type 2 tensile cracks from the inner flaw tips. When the inner flaw tips were far apart as for geometry 30-0-2a, the newly initiated tip cracks would also be far apart and would not coalesce as they propagated. When the inner flaw tips were close enough, coalescence could sometimes occur, provided that the newly initiated tip cracks propagated in an inclined direction which allowed them to interact.

When the bridging angle increased to 45^o (30-a-a), the inner flaw tips tended to coalesce by steep shear cracks (Type 1 shear cracks). This coalescence behavior was consistent among the three specimens. The shearing motion along these newly initiated shear cracks throughout the course of loading was always concurrent with the flaw compression and tip crushing events.

In another geometry (30-2a-2a) which also had 45^o bridging angle, but its internal flaw tips were farther apart (2.83a), the coalescence behavior was less consistent among the four specimens. Coalescence was mainly due to the initiation, propagation and interaction of steeply-inclined cracks (type 2 tensile cracks, type 1 shear cracks, mixed tensile shear cracks) from inner flaw tips. Coalescence due to type 1 shear cracks as that observed in 30-a-a specimens was only observed in one 30-2a-2a specimen. Flaw *compression* and tip crushing events also occurred.

In 30-a-2a which has an intermediate bridging angle (26.5^o), the coalescence behavior seemed to the between those of small bridging angle (0^o) and large bridging angle (45^o). Coalescence occurred in one specimen similar to that observed in 30-a-a, i.e. coalescence by a single type 1 shear crack. In two other specimens, however, similar tip cracks as those observed in 30-0-2a developed, and no coalescence resulted.

To conclude, bridging angle appears to have a strong influence on the coalescence behavior in flaw pairs inclined at 30^o. **Small bridging angle** (0^o) favored formation of steep cracks (shear and/or tensile) from inner flaw tips. When the flaws were close, the inner tip cracks may coalesce; when the flaws were far apart, the inner tip cracks would not coalesce. **Large bridging angle** (45^o) favored coalescence which linked up the inner flaw tips in the bridging region by steep tip cracks. Coalescence could be achieved by a single type 1 shear crack (all specimens in 30-a-a and 2 out 4 specimens in 30-2a-2a), or by two tensile and/or shear cracks (2 other specimens of 30-2a-2a). In the case of stepped flaws with **intermediate bridging angle** (26.5^o), coalescence was far less consistent and appeared to be transitional between small bridging angle (0^o) and large bridging angle (45^o). Besides, compression of the pre-existing flaws and crushing of the material at the flaw tip regions were common for all flaw pairs inclined at 30^o disregarding the bridging angle of ligament length.

Flaw inclination angle = 45^o :

Geometries	Bridging angle (^{o})	Ligament length	Coalescence?	Type of coalescence cracks (figure 3.15)	Development of type 3 shear cracks?
45-0-a	0	a	2 out of 3	1 out of 2 : Type 2 S & Type 2 S 1 out of 2 : Single Type 2 S	1 out of 3
45-0-2a	0	2a	0 out of 3	Not applicable	3 out of 3
45-a-2a	26.5	2.24a	3 out of 3	1 out of 3 : Type 1 T & Type 1 S 1 out of 3 : Type 1 S & Type 1 S 1 out of 3 : Single Type 2 T	1 out of 3
45-a-a	45	1.41a	4 out of 4	2 out of 4 : Mixed TS 1 out of 4 : Single Type 2 T 1 out of 4 : Type 2 T – Type 2 T	1 out of 4
45-2a-2a	45	2.83a	3 out of 3	2 out of 3 : Mixed TS 1 out of 3 : Single Type 2 T	1 out of 3

* a = half flaw length

Table 3.3 – summary of crack coalescence behavior in flaw pairs of 45^o flaw inclination angle.

In geometries of coplanar flaws with **zero bridging angle** (45-0-a) where the inner flaw tips were close together, coalescence occurred favorably by the initiation and propagation of internal coplanar shear cracks. In one specimen, two coplanar cracks initiated independently from the inner flaw tips, while in another specimen, a single coplanar crack was observed to initiate and link up the inner flaw tips. In cases where compression of the flaws and crushing of the material at the flaw tip regions occurred, the development of new coplanar cracks and hence coalescence from the inner flaw tips was suppressed (in one of three specimens of geometry 45-0-a). Such a suppression of coalescence was also observed in the geometries of zero bridging angle where the inner flaw tips were far apart (45-0-2a) in which flaw compression and flaw tip crushing were dominant.

At the other end of the spectrum where the **bridging angle is large** (45^o), coalescence was mainly accomplished by steeply inclined tensile cracks (type 2 tensile cracks) or mixed tensile-shear crack initiated earlier from the inner flaw tips. The initiation of these cracks was observed to be closely associated with the relative displacement between the upper face and lower face of the pre-existing flaws. Substantial flaw compression and flaw tip crushing were not common.

For the **intermediate bridging angle** of 26.5^o corresponding to a stepped flaw geometry of 45-a-2a, the coalescence patterns became more varied. The observed fracturing processes and patterns however suggested that generally when there were compression of the flaws and crushing of the materials at the flaw tip regions, the generation of oblique type 1 shear cracks (MA46) from internal flaw tips and hence coalescence were favored. Otherwise, the generation of type 2 tensile tip cracks was favored (MA21). MA20 was transitional between the two specimens mentioned above in which the coalescence was due to the linkage of one tensile wing crack (type 1 tensile) and one oblique shear crack (type 1 shear).

Flaw inclination angle = 60^o :

Geometries	Bridging angle (^{o})	Ligament length	Coalescence?	Type of coalescence cracks (figure 3.15)	Development of type 3 shear cracks?
60-0-a	0	a	4 out of 4	3 out of 4 : Type 2 S & Type 2 S 1 out of 4 : Single Type 2 S	0 out of 4
60-0-2a	0	2a	2 out of 2	Type 2 S – Type 2 S	0 out of 2
60-a-2a	26.5	2.24a	2 out of 2	1 out of 2 : Single Type 2 T 1 out of 2 : Single Mixed TS	0 out of 2

* a = half flaw length

Table 3.4 – summary of crack coalescence behavior in flaw pairs of 60^o flaw inclination angle.

In geometries with flaw inclination angle equal to 60^o, **large bridging angle** (26.5^o in 60-a-2a) favored coalescence being accomplished by tensile cracks, while **small bridging angle** (0^o in 60-0-a & 60-0-2a) favored coalescence being accomplished by coplanar shear cracks. In all cases, the initiation of coalescence cracks was always associated with a relative displacement between the upper face and lower face of the pre-existing flaws. In contrast to those geometries with small flaw inclination angles (30^o, 45^o), compression (aperture reduction) of the pre-existing flaws and crushing of the material at the flaw tip regions throughout the loading process were absent in the geometries with flaw inclination angle equal to 60^o.

3.6 Summary and Conclusions

Forty-two high speed videos which recorded the fracturing and coalescence behavior in White Vermont Marble (Martinez, 1999) were digitized and reviewed in the present study. Playing back the video in a frame-by-frame manner, it was usually possible to observe and determine the nature (shear/tensile) of those new cracks initiated from the pre-existing flaws. The key findings concerning the fracturing and coalescence behavior, in particular its dependency on flaw inclination angle, bridging angle and ligament length of the flaw pairs in White Vermont Marble based on the present review are summarized below.

The present review shows that for coplanar flaw pairs, there was a competition between the formation of steeply inclined inner tip cracks (type 3 shear cracks and/or type 2 tensile cracks) and coplanar shear cracks (type 2 shear cracks) from the inner flaw tips during the loading process. **Small flaw inclination angle** favored the former and **large flaw inclination angle** favored the latter. Therefore, if coalescence occurred in flaw pairs of 30^o inclination angle, it would be achieved by linkage of steep inner tip cracks. If coalescence occurred in flaw pairs of 45^o and 60^o inclination angles, it would be achieved by coplanar cracks.

Within each group of specimens having the same inclination angle (30^o, 45^o & 60^o), the influences of **bridging angle** on the fracturing behavior and subsequent coalescence are summarized as follow[1]:

1) 30^o flaw inclination angle: **Small bridging angle** (0^o) favored formation of steep cracks (shear and/or tensile) from inner flaw tips. When the flaws were close, the inner tip cracks may coalesce; when the flaws were far apart, the inner tip cracks would not coalesce. **Large bridging angle** (45^o) favored coalescence which linked up the inner flaw tips in the bridging region by steep tip cracks. The coalescence for **intermediate bridging angle** (26.5^o) was far less consistent and appeared to be transitional between small bridging angle (0^o) and large bridging angle (45^o).

2) 45^o flaw inclination angle: **Small bridging angle** (0^o) favored coalescence (if occurred) which was achieved by coplanar shear cracks initiated from the inner flaw tips. **Large bridging angle** (45^o) favored coalescence which was accomplished by steeply inclined tip cracks. The coalescence for **intermediate bridging angle (**26.5^o) was far less consistent and appeared to be transitional between small bridging angle (0^o) and large bridging angle (45^o).

3) 60^o flaw inclination angle: Coalescence for **small bridging angle** (0^o) was accomplished by coplanar shear cracks, while that for **intermediate bridging angle** (26.5^o) was accomplished mainly by tensile cracks.

The present review also reveals that no coalescence occurred in certain flaw geometries when the pre-existing flaws were far apart enough – for example, coalescence occurred in flaw pairs of **ligament length L = 'a'** (30-0-a and 45-0-a), but not in flaw pairs of **ligament length L = '2a'** (30-0-2a and 45-0-2a). It is thus reasonable to postulate that when the pre-existing flaws are far apart enough, they will exert negligible influence on

151

[1] Notice that a change of bridging angle is usually accompanied by a change of ligament length, except in coplanar flaw pairs.

the neighboring cracks. However, in stepped geometries of **L = '2.24a'** (30-a-2a, 45-a-2a) and **L='2.83a'** (30-2a-2a, 45-2a-2a), coalescence could occur even when the flaws were far apart (>**2a**).

The above observations suggest that ligament length is not the only factor controlling the coalescence patterns. Apart from those coplanar flaws in which the coalescence behavior solely due to a change of ligament length can be studied, all the other flaw pair geometries involve a simultaneous change of **ligament length** and **bridging angle**. A more rigorous way in tackling the problem is to conduct a **parametric study** on the double flaw geometries with respect to the following three geometrical parameters – **flaw inclination angle**, **bridging angle** and **ligament length**. This system is followed in the present study (chapters 5 & 6).

Compression (aperture reduction) of the pre-existing flaws and **crushing** of the material at the flaw tip regions was absent in geometries with flaw inclination equal to 60^o, but it was common in geometries of flaw inclination equal to 30^o. As summarized earlier in this section, the coalescence behavior was very different between those specimens (both coplanar and stepped) of 30^o inclination angle and those of 60^o inclination angle. This suggests that the occurrence of these two events could have an influence on the type of new cracks being initiated from the pre-existing flaws, which in turn could have an influence on the eventual coalescence patterns.

Apart from the initiation of various types of cracks in marble specimens during uniaxial loading, there was also an observation of development of white patches around the flaw tips and in the bridging region. As shown in figure 2.2 for MA12, before the development of a coalescence shear crack which linked up the two inner flaw tips, the central bridging region had experienced a gradual whitening color change. Similar phenomenon was also observed in other specimens. Whether the presence of the white patches is related to any underlying microstrucural changes is unknown at the present review stage. Further investigation of their nature will be carried out in the present study.

The pre-existing flaws contained in the pre-cracked marble specimens studied by Martinez had a considerable aperture size (0.08 inch, 2mm) and significant bulging at the outer flaw tip regions (figure 3.2). Both of them were likely due to the inherent limitation of the water abrasive jet. In the previous studies in gypsum however, the aperture size of the pre-existing open flaws was only 0.004" (0.1 mm). In order to make a reasonably meaningful comparison between the crack coalescence patterns in marble studied by Martinez and those in gypsum studied by previous researchers at MIT (Reyes & Einstein, 1991, Bobet & Einstein, 1998a), further research is thus warranted to justify if flaw aperture has a significant influence on the fracturing behavior and coalescence patterns. Besides, additional work and study are required in order to achieve better cutting quality with the water abrasive jet. These issues will be addressed in subsequent chapters.

CHAPTER 4 – Specimen Preparation and Experimental Details of Uniaxial Compression Tests

4.1 Introduction

Fracturing and coalescence behavior in prismatic specimens of molded gypsum and Carrara Marble under uniaxial compression loading were investigated in the present study. During the loading process, the specimen front face was continuously monitored and recorded by a camcorder. In addition, a high speed video system was used to record crack initiation and propagation events during the occurrence of crack coalescence. Stress values associated with the onset of coalescence event and other cracking events were also obtained by correlating the videos with the load-displacement data.

The purpose of this chapter is to describe the experimental procedures involved in the present study. It begins by summarizing the properties of gypsum and Carrara Marble and the specimen preparation procedures. The subsequent sections focus on experimental procedures of the uniaxial compression test and the post-test image and data analysis.

4.2 Material properties

Molded gypsum has been used as a model rock at the rock mechanics research group at MIT in the past 40 years (Nelson, 1968, Einstein et al., 1969, Motoyama & Hirschfeld, 1971, Einstein & Hirschdeld, 1973, Reyes & Einstein, 1991, Shen et al., 1995, Bobet & Einstein, 1998, Ko et.al., 2006). The molded gypsum ($CaSO_4 \cdot 2H_2O$) is obtained by mixing commercially available (e.g. Hydrocal) gypsum powder with water. This gypsum powder is actually a hemihydrate ($CaSO_4 \cdot \frac{1}{2}H_2O$). As noted in the literature by Nelson (1968), hemihydrate is obtained by purifying and heating natural hydrated gypsum :

$$CaSO_4 \cdot 2H_2O \rightarrow CaSO_4 \cdot \tfrac{1}{2}H_2O + 1\tfrac{1}{2}\ H_2O$$

When the hemihydrate is mixed with water in the laboratory, hydrated gypsum is reformed ($CaSO_4 \cdot \frac{1}{2}H_2O + 1\frac{1}{2}\ H_2O \rightarrow CaSO_4 \cdot 2H_2O$). The gypsum specimens are then

stored in a 40^{o} oven to remove any excessive water after fabrication, but the water of crystallization ($2H_2O$) associated with $CaSO_4$ is still retained.

Environmental scanning electro microprobe (ESEM) images reveal that the average gypsum crystals are of a plate to needle shape 5 μm long and 2 μm wide. In-between the plates, small inter-connected pores with approximately 1 to 5 μm size are present (figure 4.1).

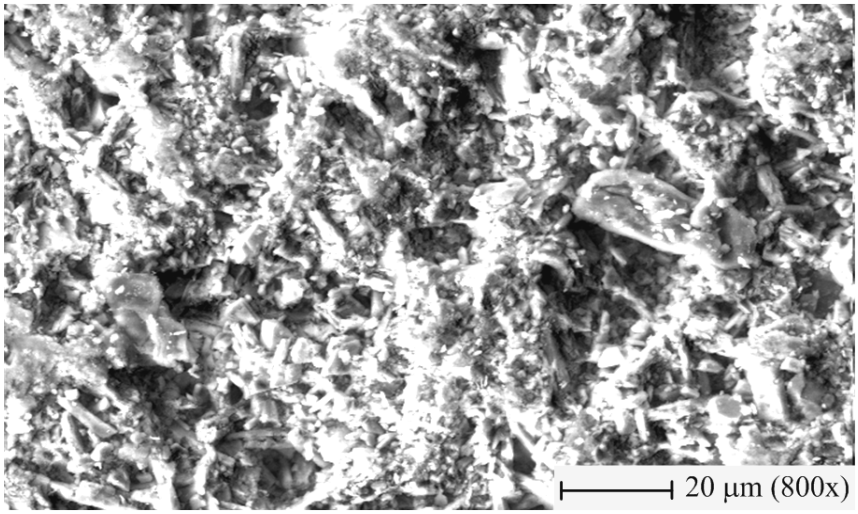

(a)

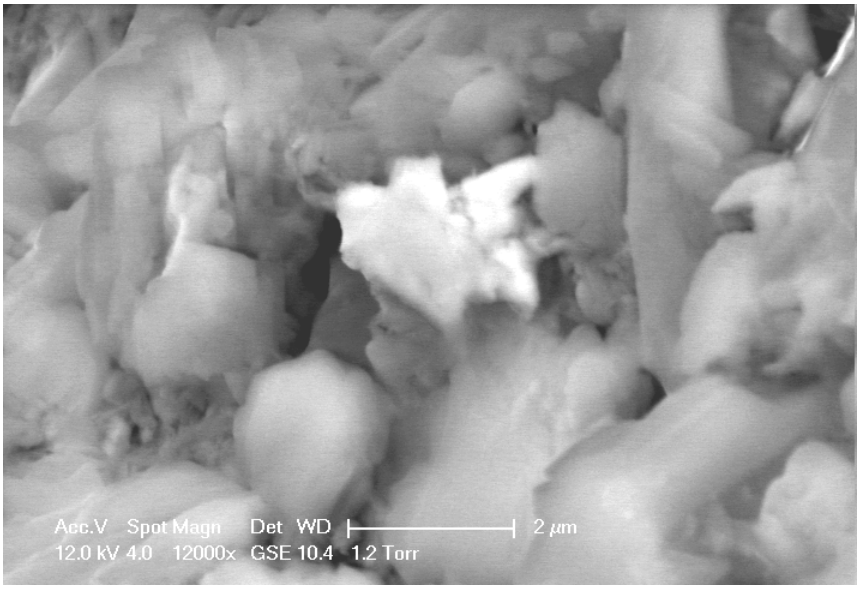

(b)

Figure 4.1 – ESEM micrograph of molded gypsum (a) magnification of 800x, (b) magnification of 12,000x.

Some of the mechanical properties of the molded gypsum used in the present study are summarized in table 4.1.

[1] Density, ρ	1.54 g/cm^3
[2] Young's modulus E	5960 MPa
[1] Uniaxial compressive strength, σ_c	33.85 MPa
[2] Uniaxial tensile strength, σ_c	3.2 MPa
[2] Poisson's ratio, ν	0.15

[1] Determined in the present study

[2] Determined by Bobet (1997)

Table 4.1 – Some mechanical properties of molded gypsum used in the present study.

Carrara Marble consists of 99% calcite crystals ($CaCO_3$) and 1% organic impurities. Its physical and chemical properties have been extensively studied due to its popularity of being quarried as building stones (Cardani & Meda, 1999, Siegesmund et.al., 2000, Rapp, 2002). It is also ideal in rock mechanics research due to its low intrinsic crack density and low porosity (Alber & Hauptfleisch, 1999).

A SEM image of the Carrara Marble used in the present study is shown in figure 7.5a, which is also reproduced below. It illustrates a crystalloblastic fabric (Best, 2001), which is characterized by a mutually interfering growth pattern in which the constituent polygonal equigranular calcite grains meet at approximately 120^o triple junctions. The grains display a well-fused interlocking texture. The grain size is within a general range of 50 to 200 μm. Careful inspection reveals that most of the grains are crack-free. Intragranular micro-cracks are only present in a small population of marble grains, and intergranular cracking along grain boundaries is less than 20%. Some physical properties of Carrara Marble are summarized in table 4.2.

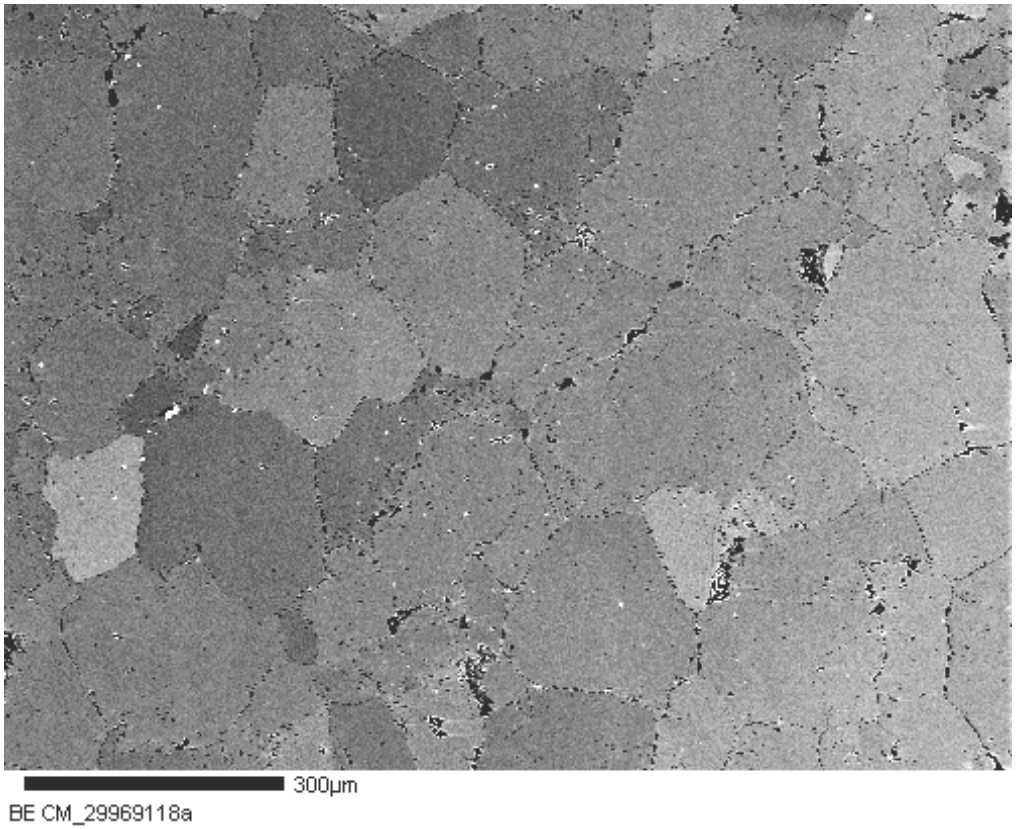

Figure 7.5a – A SEM image of intact marble specimen (magnification power = 100 X)

Dynamic properties	
Compressional wave velocity, V_p	6010 m/s
Shear wave velocity, V_s	3267 m/s
Poisson's ratio (dyn.), ν_d	0.29
Young's modulus (dyn.) E_d	73 GPa
Elastic and other properties	
Poisson's ratio, ν	0.19
Young's modulus (dyn.) E	49 GPa
Dry density, ρ	2.7 g/cm^3
Porosity, *n*	0.40%

Table 4.2 – Some properties of Carrara Marble (Alber & Hauptfleisch, 1999).

4.3 Specimen preparation

4.3.1 Introduction

In this section, the procedures concerning the preparation of gypsum specimens and marble specimens for uniaxial loading test are described. All the tests on gypsum and marble were conducted on prismatic specimens of dimensions 6" (height) x 3" (breadth) x 1.25" (thickness) (~152mm x ~76mm x ~32 mm). Straight flaws (0.5"; 12.5mm long) were created in the specimens parallel to the specimen thickness. Refer to figure 4.2. Gypsum specimens were obtained by pouring a mixture of gypsum powder and water into a mold. Open flaws were created by inserting metal shims into the fresh gypsum paste, which were later pulled out from the hardened specimen. Individual pieces of marble specimens were cut from a big block and flaws were cut by an abrasive jet. Further details are contained in the following sections.

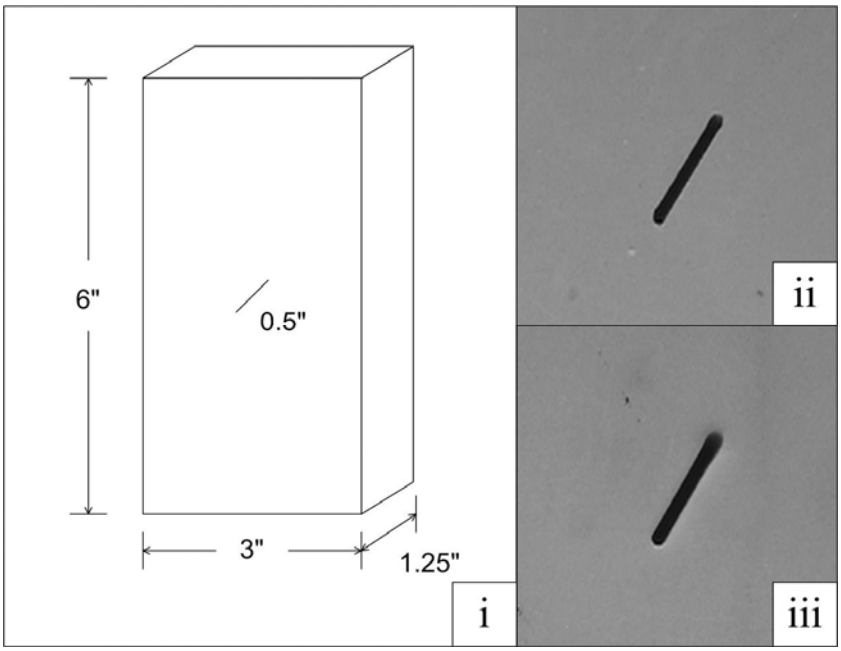

Figure 4.2 – (i) Dimensions of a prismatic specimen containing a central straight flaw. Open flaws with rounded tips of aperture size 0.05" (~1.3mm) in (ii) gypsum and (iii) marble. Note that flaws of aperture size 0.004" (0.1mm) were also tested in gypsum, but are not shown here. Specimens containing double flaws were also tested and not shown here.

4.3.2 Preparation of gypsum specimens

The pre-cracked gypsum specimens were artificially molded according to the same procedures as in previous studies conducted at MIT (Reyes & Einstein, 1991, Shen, et al., 1995, Bobet & Einstein, 1998a, Ko, et al., 2006). The gypsum specimens were cast from a mixture of Hydrocal B-11 powder, celite powder and water at mass ratios of 700:8:280. The addition of celite powder reduced the amount of bleeding (migration of water to the top of the fluid mix). After being thoroughly blended, the mixture was poured into a steel mold containing no (intact specimen), one (single flaw) or two (flaw pair) metal shim(s) depending on the flaw geometries required (figure 4.3a). The specific geometries tested in the present study are described in detail in chapters 5 and 6.

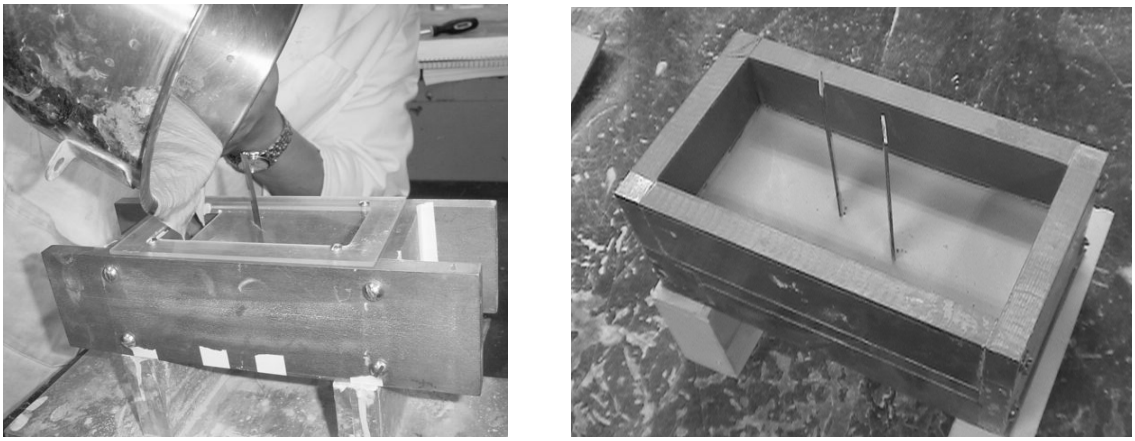

(a) (b)

Figure 4.3 – (a) Pouring freshly-mixed gypsum paste into a steel mold, (b) A hardened gypsum specimen which is going to be removed from the steel mold.

Open flaws were created by pulling out metal shims out of the hardened gypsum blocks (figure 4.3b). By varying the thickness of the metal shims, different flaw aperture sizes were obtained (0.004" & 0.05"). The scope of the present study is limited to open flaws only, and experiments on closed flaws as those studied by Bobet and Einstein (1998a) were not carried out. Hardened specimens were then removed from the mold and stored in an oven at 40^{o}C temperature before being tested. Before the compression tests, the

surfaces of the specimens were also polished with coarse (grit # 60) and then fine (grit # 200) sandpaper. The dimensions of the polished specimens were then measured to 2 decimal places in millimeters. The step-by-step procedure of the fabrication of gypsum specimens is presented in figure 4.4.

Procedures of Gypsum Specimen Fabrication

1. Measure **6.4 g** of celtie powder and **560 g** Hydrocal B-11 (gypsum) powder.
2. Measure **224 ml** of water.
3. Pour the celite powder into the mixing bowl.
4. Pour the water into the mixing bowl.
5. Put the bowl back in the mixer and switch on the mixer.
6. Switch off the mixer after **20 seconds**.
7. Remove the bowl from the mixer.
8. **Gently** pour the gypsum powder into the bowl.
9. Put the bowl back to the mixer and switch on the mixer.
10. Switch off the mixer after **four minutes**.
11. Remove the bowl from the mixer.
12. Pour the paste from the bowl into a prepared mold with the help of a rubber spatula.
13. Vibrate the mold for **two minutes**.
14. Record the time when the vibration is completed.
15. Put the mold on top of a horizontal bench.
16. After **one hour**, remove the specimen from the mold and measure the mass of the specimen along with the shims (if there are any).
17. Label the specimen on its edge.
18. Place the specimen into the oven set at 40^{o}C.
19. Measure the mass of the specimen periodically until the mass reaches a constant value.
20. Remove the metal shims from the specimen after it has been stored in oven for one day.
21. Polish all the faces of each specimen first with coarse (grit # 60) and then fine (grit # 200) sandpaper.
22. Measure the dimensions of the polished specimen to 2 decimal places in millimeters.

Figure 4.4 - Step-by-step procedure of fabrication of gypsum specimens

In the previous studies conducted at MIT by Bobet (1997) and Ko (2005), the uniaxial compression tests on gypsum specimens were conducted four days after their fabrication. As mentioned earlier, a high speed video system was used in the experimental tests. They were either on loan from the Edgerton Center of MIT or rented from an external source (see more details in Appendix D) for a very short period every time (usually two to three days). To facilitate the use of the high speed camera, a large number of gypsum specimens were usually tested within each reservation/rental period. In this case, most of the tested gypsum specimens would then have been stored in the 40^{o}C oven for more than four days (varying from days to weeks) before undergoing the uniaxial compression tests.

To address the issue of whether the strength of the gypsum specimen is sensitive to oven storage time, a series of uniaxial compression tests were conducted on gypsum specimens which had been stored at the 40^{o}C oven for different lengths of time (from four days up to 76 days) since fabrication. The study found out that the mass of the specimens became constant about four days after being fabricated. In addition, the length of oven storage time (four days or longer) appeared not to have a significant influence on the specimen uniaxial compressive strength values. Refer to Appendix B for the experimental background and results.

4.3.3 Preparation of marble specimens

Slabs of Carrara Marble of the appropriate thickness (1.25", ~32 mm) were first cut from a big block (multiple marble blocks were made available by Prof. Brian Evans, MIT) by a 24 inch-diameter saw (figures 4.5 & 4.6a). All the blocks were of different lengths, but roughly the same cross-sectional area (6" x 10 ½"). The 1.25" thick slabs were further cut into smaller pieces by the OMAX abrasive jet (figure 3.6b), which was also used later for cutting 0.5" (13 mm) long straight open flaws in the marble specimens. The OMAX abrasive jet derives its extremely high erosive cutting power from a pressurized stream of garnet abrasive-laden water which is ejected at a speed of about 100 feet per second. Details of the operation of the OMAX abrasive jet are summarized in Appendix C.

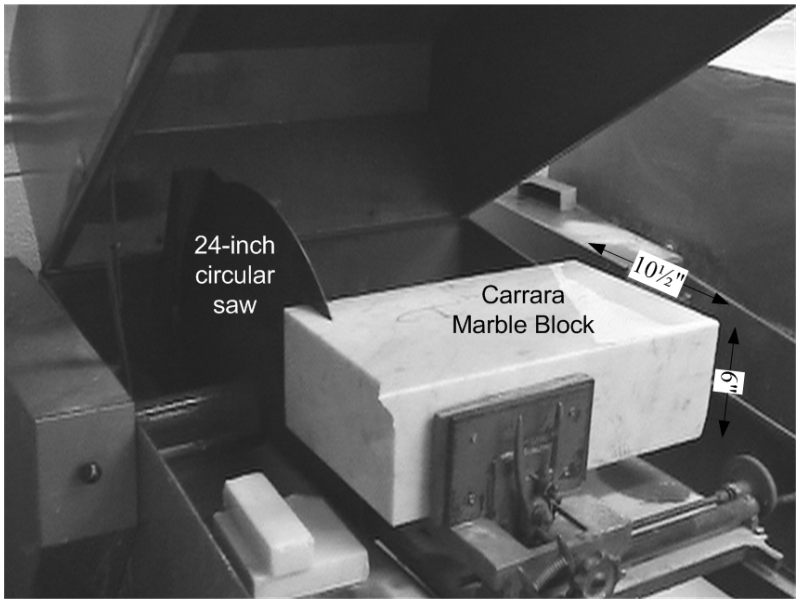

Figure 4.5 – A 24-inch circular saw used to cut 1.25” slabs from a Carrara Marble block.

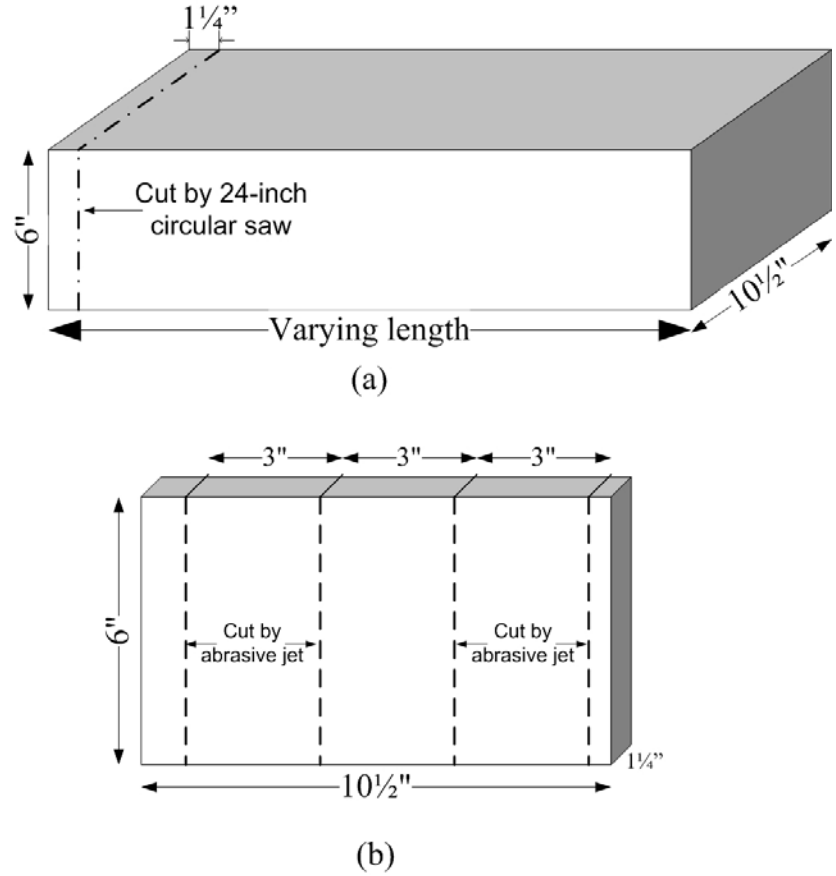

Figure 4.6 – (a) Individual slabs are cut from a marble block by a 24-inch circular saw, (b) Specimens of the right dimensions (6” x 3” x 1¼ ”) are then cut from the 1¼ ” thick slabs by the abrasive jet.

4.4 Uniaxial compression test

Prepared gypsum and marble specimens were loaded uniaxially in a Baldwin 200 Kips Loading Machine, which was controlled by a computer program called MTESTW*indows*^{TM} (figures 4.7 & 4.8). Load and displacement data were automatically logged at a rate of 2000 samples/minute. Refer to Bobet (1997) and Ko (2005) for further details of the Loading Machine.

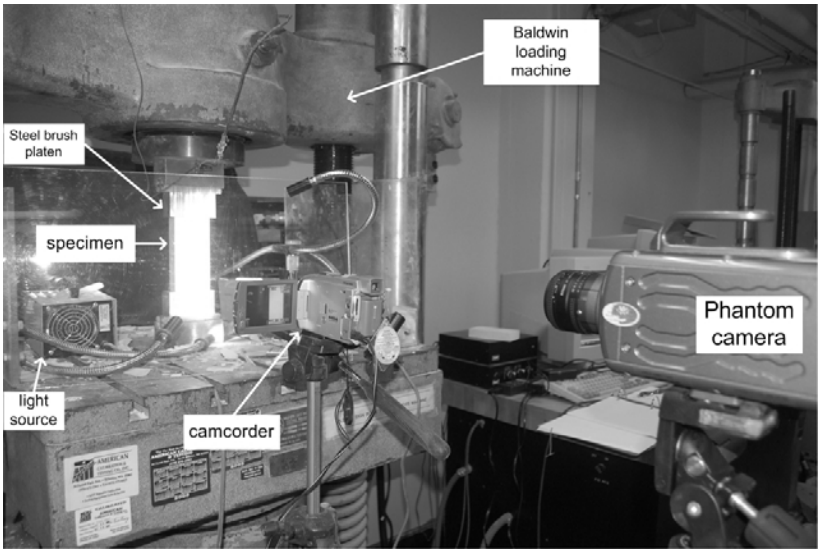

Figure 4.7 – Experimental setup for uniaxial compression test.

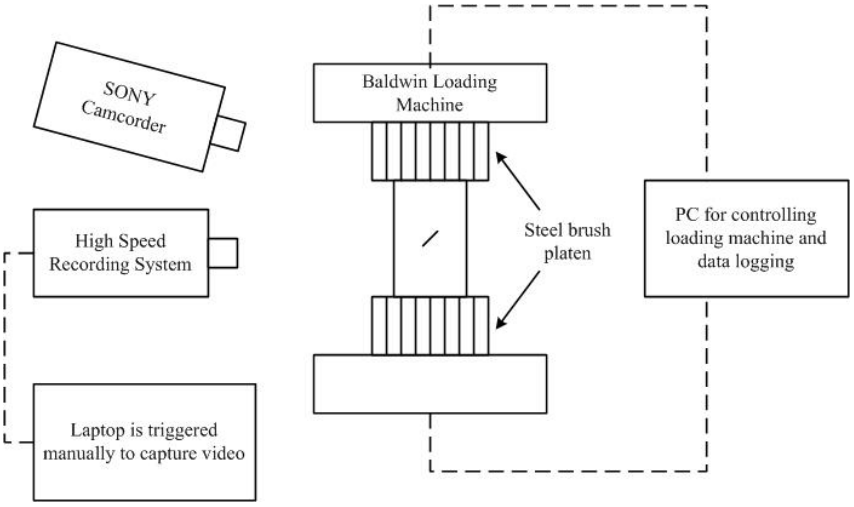

Figure 4.8 – Schematic representation of experimental setup.

In earlier research at MIT, two different loading schemes have been used. (1) The specimen was loaded in an incremental manner with multiple interim pauses for crack inspection (Bobet & Einstein, 1998a), (2) The specimen was continuously loaded and the front face of the specimen was continuously monitored and recorded (Martinez, 1999, Ko et al., 2006). In the present research, a scheme similar to the second one was adopted and loading was continuously applied till specimen failure occurred. For both gypsum and marble specimens, three loading stages of different ranges were used (table 4.3).

	Loading Rate	Gypsum	Marble
Stage 1	0.1 in/min	0 – 1000 lb	0 – 4000 lb
Stage 2	0.015 in/min	1000 – 5000 lb	4000 – 10000 lb
Stage 3	2300 lb/min	5000 lb – failure	10000 lb – failure

Table 4.3 – Loading schemes for gypsum and marble specimens.

Some of the merits of using a continuous loading scheme are:

(1) Specimens can be loaded to failure without interruption.
(2) Cracking events observed with the camcorder and the high speed camera can be synchronized with the stress-strain data with a higher accuracy.
(3) The occurrence of occasional violent spalling and localized failure of the specimen makes close inspection of specimen faces dangerous. Continuous loading with video recording can avoid this problem.

During the loading test, the specimen front face was continuously video-taped by a SONY digital camcorder (DCR-HC65) (figures 4.7 & 4.8). The specimen was also simultaneously monitored by the Phantom high speed recording system (figure 4.9). Due to the limited internal memory size of the high speed recording system, only images spanning over several to tens of seconds can be captured and stored. A continuous recording from the start to the end of the loading test which lasted for more than several

minutes was thus impossible. Details of the high speed recording system, its inherent limitations and methodology to capture images are described in detail in Appendix D.

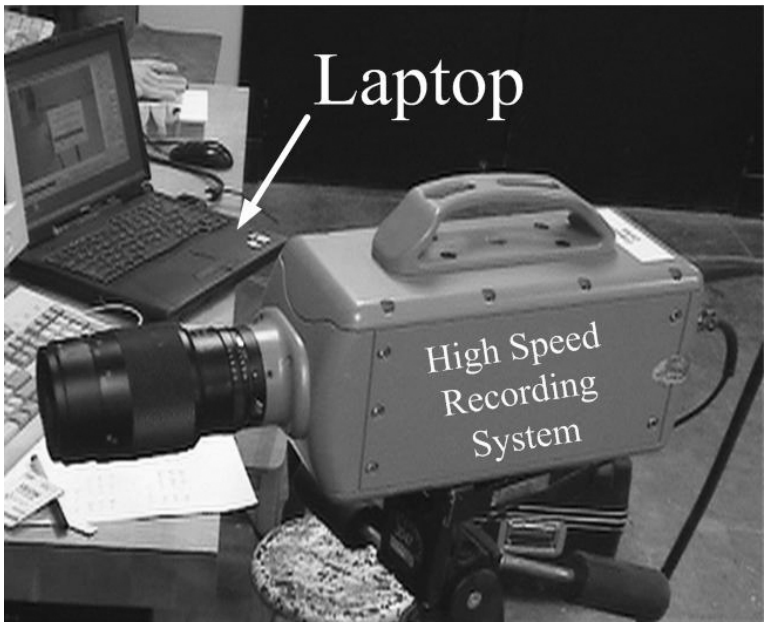

Figure 4.9 – View of the PHANTOM V5.0 high speed recording system and the controlling laptop.

4.5 Data analysis

The purpose of this section is to describe what types of data were collected from the each uniaxial compression test and how the data were analyzed. Examples of selected specimens will be shown for illustrative purposes. However, complete sets of experimental results and relevant analyses will not be covered in this chapter but will be systematically described in later chapters.

From each uniaxial compression test, qualitative and quantitative data as listed in table 4.4 were collected. These data were further analyzed to characterize the fracturing and

coalescence processes (in specimens containing double flaws, but not in intact specimens and those specimens containing single flaws) occurring in each specimen.

Category	Data	Data properties
Quantitative	Specimen dimensions	Height, width and thickness of each specimen were measured to two decimal places in millimeters before loading test (figure 3.2).
	Load-displacement data	Load-displacement data pairs were automatically logged at a rate of 2000 data pair/second, which were then corrected by specimen cross-sectional area and height to obtain stress-strain data.
Qualitative	Digital photos	Digital photos of the specimen before and after failure were taken.
	Camcorder videos	The specimen front face was monitored and recorded continuously in digital format at a rate of 15 frames per second since the start of the compression till specimen failure. Individual images can later be captured from the videos.
	High speed videos	High speed videos were recorded digitally at a high frame rate (usual range used is 2,000 – 24,000 frames per second) for a short period of time (several seconds) showing fine details of crack initiation and propagation processes, and also crack coalescence events. Frame rate and image resolution settings varied among specimens and camera models. Individual images can later be captured from the videos.

Table 4.4 – Data collected from the experimental study

By studying the photos taken before and after the uniaxial compression test, it is easy to identify the dependency of coalescence patterns on the pre-existing flaw geometries.

Figure 4.9 shows a Carrara marble specimen before and after the uniaxial compression test. In addition to the coalescence cracks developed between the inner flaw tips (indicated by arrows), other new cracks also developed, preferentially from the outer flaw tips.

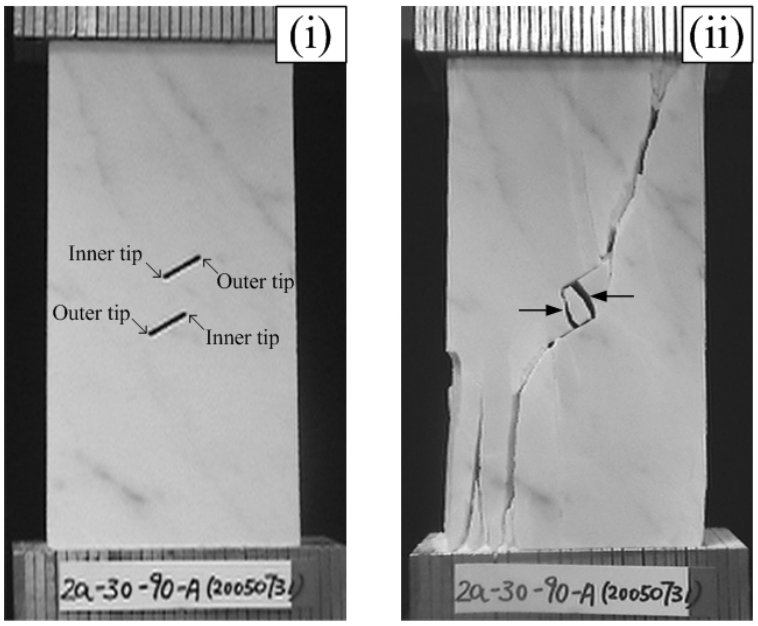

Figure 4.10 – A marble specimen (number 2a-30-90-A) of flaw inclination angle $\beta = 30^o$ and bridging angle $\alpha = 90^o$ (i) before and (ii) after uniaxial compression. The two coalescence cracks are marked by a pair of horizontal arrows.

However, the above preliminary analysis did not offer any information about the cracking **processes** involved. Further details were retrieved from the two corresponding video recordings – a normal speed video from the camcorder and a high speed video from the high speed camera (table 4.4). These two videos of each specimen were played back individually to observe and identify the occurrence of any significant cracking events. Due to the relatively low time-resolution of the camcorder recording, details concerning crack propagation could never be observed from it. In high speed videos, however, the initiation and propagation of cracks could usually be observed. See the example in figure 4.11 which illustrates a detailed analysis of the cracking processes a marble specimen.

The left column of figure 4.11 contains individual high speed images. The right column of figure 4.11 contains the corresponding descriptions of cracking processes and/or other deformations observed in the specimen. Each description is preceded by two numbers at the top, for example, the numbers corresponding to the first image are:

(54.78 MPa)
HS Image # -6147

The first number indicates the stress value of the image. This was obtained by correlating the videos and the stress-strain data in a way to be described later in this section. The second number refers to the image number of the high speed (HS) video. By noting the recording frame rate, which is 6600 frames per second in the example shown in figure 4.11, the time difference between any two images can be calculated. For example, the image number of the second image shown in figure 4.11 is 4273. The time difference is given by the difference of 6147 and 4273, which is then divided by 6600, i.e. 0.283 seconds.

On each high speed image on the left column, every crack (thin solid line) and/or other features (see below) related to the cracking process are identified by reference letters, e.g. **B**, **C,** etc. These letters are only for identification purposes and they do not imply any crack initiation sequence. Each letter is then followed by a letter **T** or **S** in parentheses, which refers to the tensile mode or shear mode of crack initiation, respectively. The sequence of crack initiation is indicated by numbers shown as subscripts at the end. The first crack to initiate is designated as 1, the second crack as 2, etc. The same number will be assigned to multiple cracks which initiate simultaneously. Take $F'(T)_3$ as an example. It was identified to initiate in a tensile mode from right tip of the top flaw after the initiation of other cracks with numbers 1 and 2. A pair of arrows over its trace indicates that shearing occurred along it after its initiation as a tensile crack. Note however that feature E, for instance, which is represented by a thick grey line in the sketch at the end of figure 4.11, is not a crack in this specimen. It is a white patch, which is speculated to

be the process zone. Other white patches are also labeled in the pictures. For further discussion of the white patches, see sections 5.3.2, 6.6 and chapter 7.

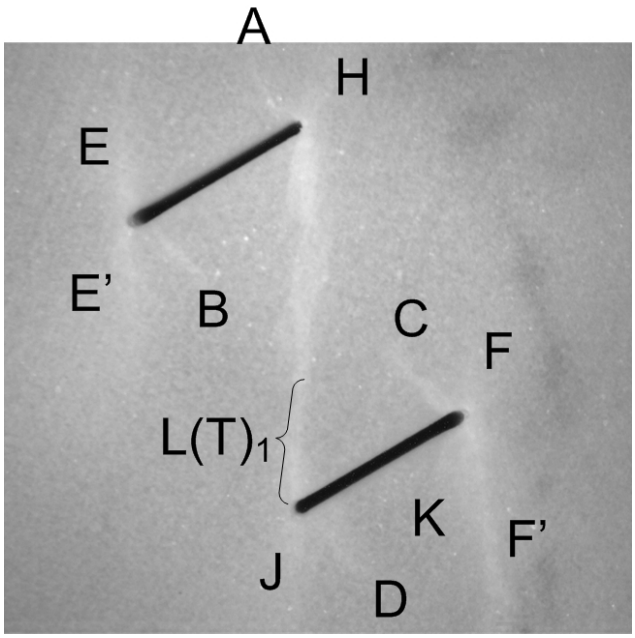

(54.78 MPa)
HS Image # - 6147

Tensile crack opening occurred along white patch L adjacent to the left tip of the bottom flaw.

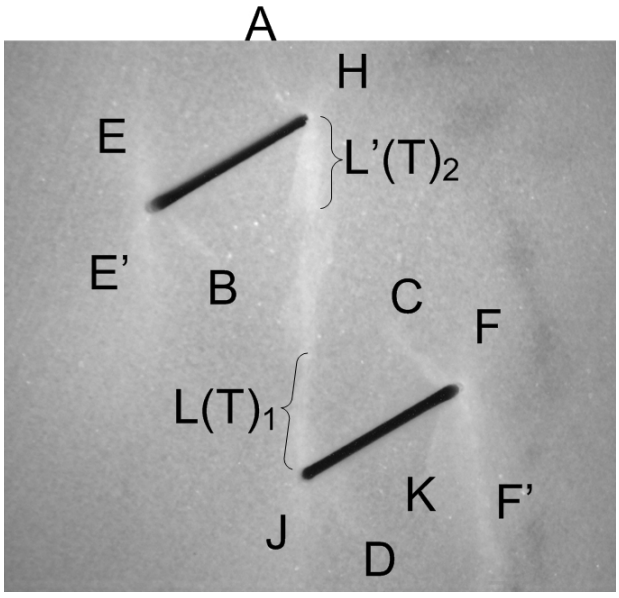

(54.67 MPa)
HS Image # - 4273

Tensile crack opening occurred along the upper portion (as crack L') of the central coalescing white patch.

Figure 4.11 – Cracking processes recorded at a frame rate of 6600 frames per second in marble specimen CM 4a-30-120-C.

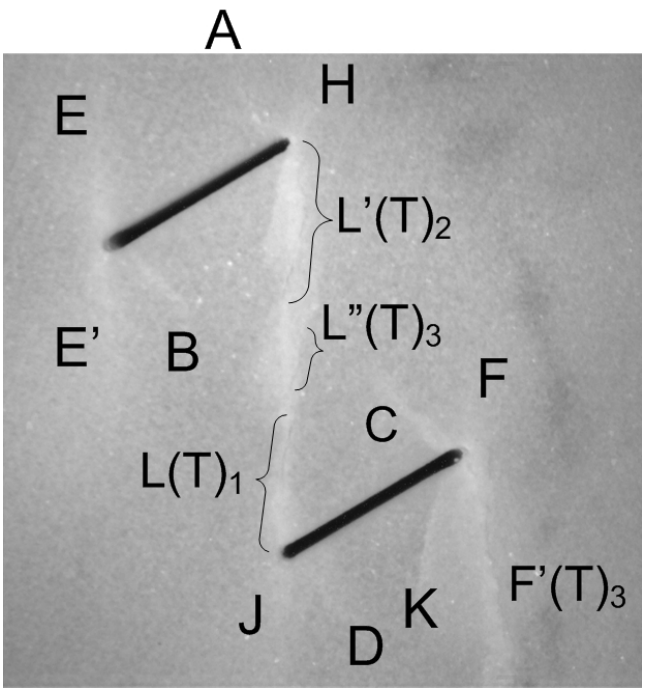	(54.64 MPa) HS Image # - 3007 Another new short tensile crack (L") opened up in the middle portion of the central coalescing white patch. Tensile crack L' also lengthened. Tensile crack opening also occurred along white patch F'.
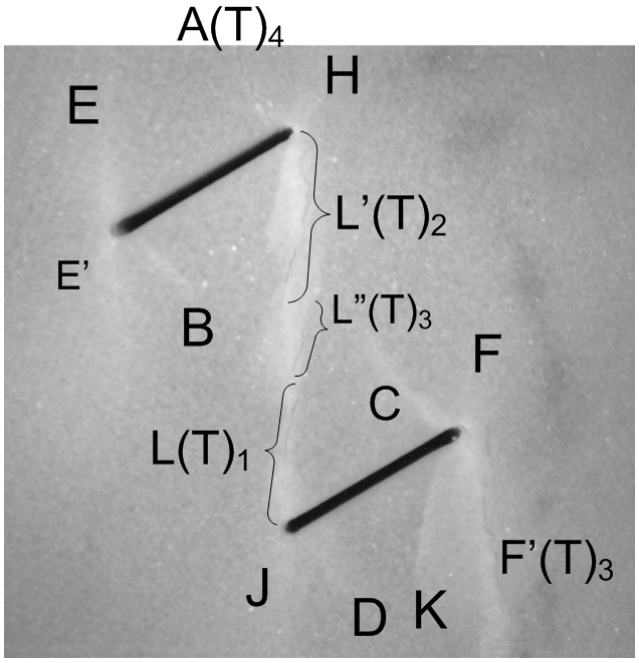	(54.64 MPa) HS Image # - 3006 Tensile crack opening occurred along white patch A. The aperture and length of cracks L, L' and L" increased.

Figure 4.11 (continued)

<table>
<tr>
<td> 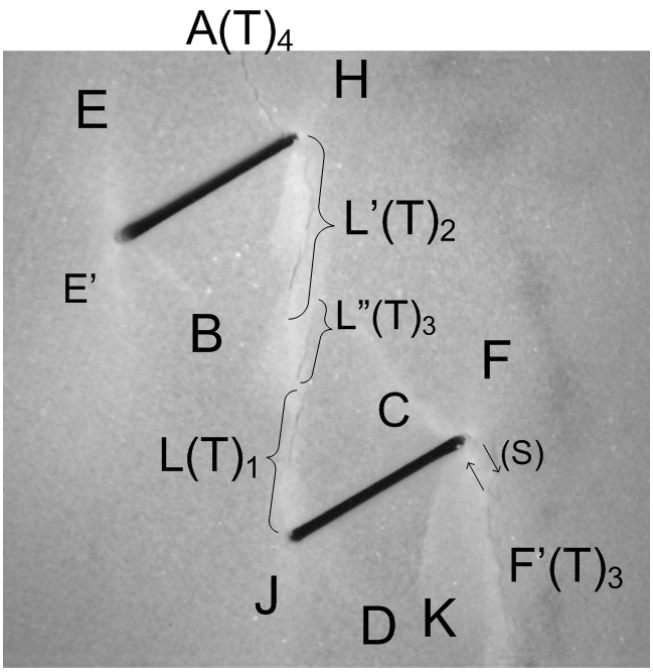
</td>
<td>(54.64 MPa)
HS Image # - 3005

The aperture of cracks L, L' and L" increased further.

Shearing occurred at the top segment of crack F' adjacent to the right tip of the bottom flaw. White patch C propagated upwards.</td>
</tr>
<tr>
<td> 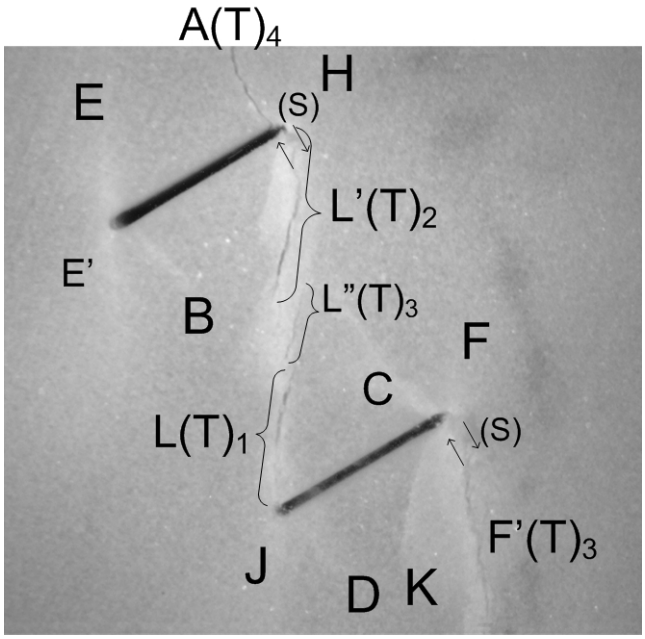
</td>
<td>(54.64 MPa)
HS Image # - 3000

Shearing occurred at the top segment of crack L' adjacent to the right tip of the top flaw.

 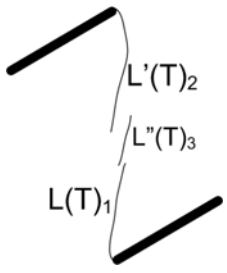

(sketch)</td>
</tr>
</table>

Figure 4.11 (continued)

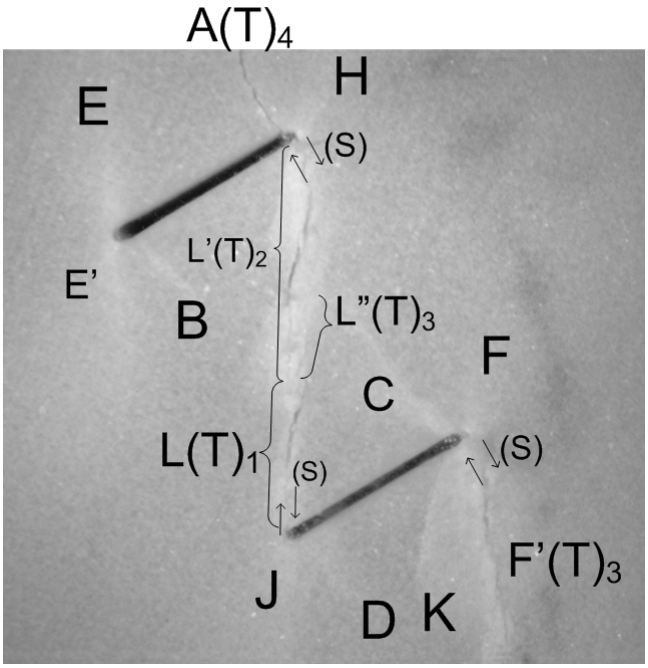

(54.64 MPa – coalescence)
HS Image # - 2990

The aperture of cracks L, L' and L" increased further. Crack L' propagated downwards to coalesce with crack L.

Shearing occurred at the bottom segment of crack L adjacent to the left tip of the bottom flaw.

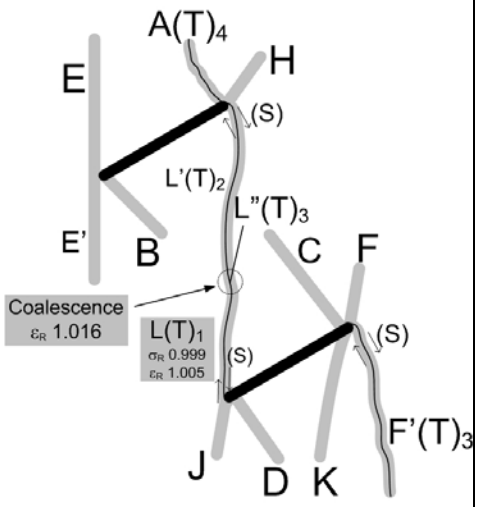

(sketch)

Figure 4.11 (continued)

The stress-strain (σ-ε) curve corresponding to each uniaxial compression test was also obtained (figure 4.12), and the maximum stress (uniaxial compressive strength) of the specimen, crack initiation stress and coalescence stress were identified.

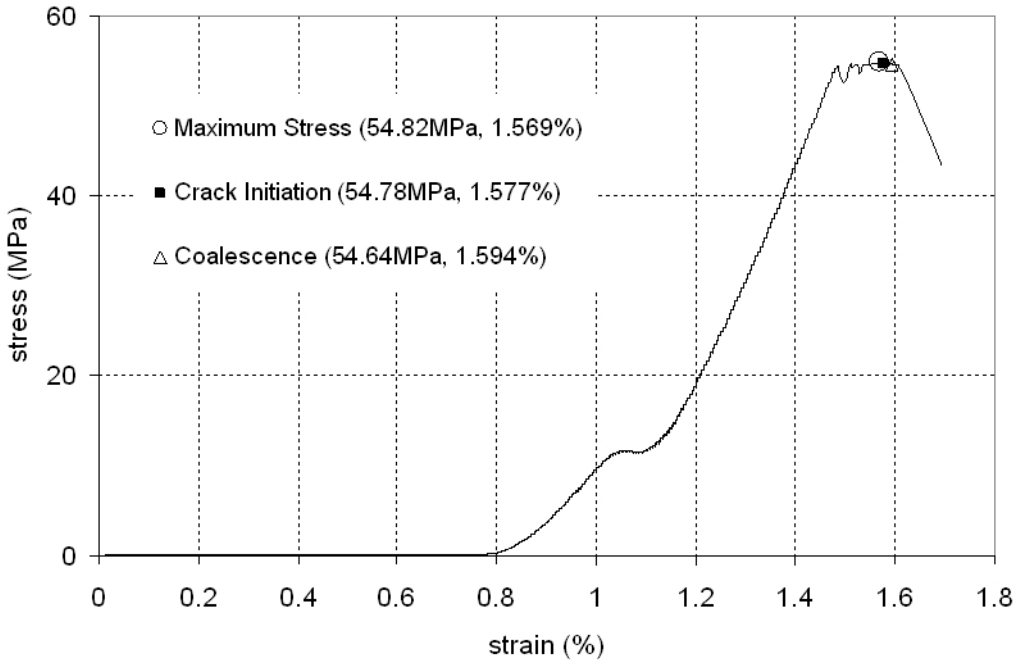

Figure 4.12 – Stress-strain curve of the marble specimen (4a-30-120-C). The numbers in parentheses are stress and strain values.

Notice that the camcorder video recording, high speed video recording and the logging of the load-displacement data were all operated independently during the experiment, i.e. they were not automatically synchronized. One key step in the analysis was thus to correlate the stress-strain data with the two video recordings. The following phenomena recorded during the tests and subsequent analyses usually served this purpose.

- A distinct cracking sound (recorded by the camcorder[1]) due to the initiation of a new crack often corresponded to an abrupt change of gradient on the σ-ε curve.

[1] No sound was recoded by the high speed camera.

- Images corresponding to the onset of several relatively large and abrupt deformation cracking-related events close to specimen failure were first identified from the high speed video. Since these events (e.g. initiation of a new shear crack, reduction of flaw aperture size, surface spalling around flaw tips) were usually associated with multiple identifiable stress drops on the σ-ε curve, the high speed video recording could then be synchronized with the σ-ε curve.

- Substantial aperture reduction of the pre-existing flaws and/or abrupt occurrence of shearing along certain cracks was very often associated with a sharp and sudden drop on the σ-ε curve.

In some specimens, all of the above indicators were observed and could be used for the correlation task. In some specimens, however, only two or even one of them were clearly identified.

As noted in the sketch of figure 4.11, which is reproduced below, apart from the above identifiers, two more parameters are defined and marked beside some cracks.

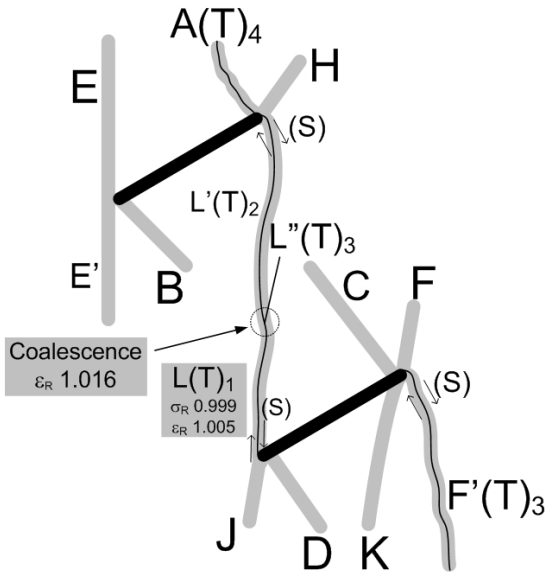

A sketch of cracks initiated from a stepped flaw pair in marble (extracted from figure 4.11)

The crack initiation stress ratio $\boldsymbol{\sigma_R}$ is defined as

$$\sigma_R = \frac{\text{first crack initiation stress}}{\text{specimen maximum stress}} \tag{4.1}$$

A $\boldsymbol{\sigma_R}$ value equal to one indicates that the initiation of the first cracks is concurrent with the specimen maximum stress. In the same sketch of figure 4.11, $\boldsymbol{\sigma_R}$ corresponding to the initiation of crack L is 0.999. However, this ratio is not adequate to indicate whether this event occurs before or after the maximum stress. Another parameter called uniaxial strain ratio $\boldsymbol{\varepsilon_R}$ is thus defined:

$$\varepsilon_R = \frac{\text{strain corresponding to a specific event}}{\text{strain corresponding to specimen maximum stress}} \tag{4.2}$$

Also in the same sketch, the $\boldsymbol{\varepsilon_R}$ corresponding to the initiation of first crack is 1.005 and that corresponding to the coalescence event achieved by the linkage of cracks L and L" is 1.016, i.e. first crack initiation occurred just slightly after the maximum stress and coalescence occurred at a later stage.

CHAPTER 5 – Results on Uniaxial Compression in Specimens Containing Single Flaws

5.1 Introduction

The use of a high speed video system allows one to precisely observe the cracking mechanisms, in particular if shear or tensile fracturing is taking place. The present experimental study on gypsum and marble specimens containing single flaws confirms that tensile cracks are in most cases the first cracks to appear in fracture propagation from existing flaws independent of aperture and material. The study, in addition, has shown that complex additional cracking occurs which depends on orientation of the existing flaws and material type. Also important is the formation of a process zone which could be visually observed in some marble experiments, but not in gypsum experiments.

This chapter first describes the single flaw geometries that are tested in gypsum and marble. In subsequent sections, after the experimental results (fracturing behavior) for gypsum and marble specimens are summarized, the influence of flaw aperture (narrow *vs* wide) and material (gypsum *vs* marble) on fracturing behavior are discussed.

5.2 Experimental Details

Three series of uniaxial compression tests are conducted on gypsum specimens and Carrara Marble specimens which are prepared according to the procedures described in chapter 4. The three series are:

- molded gypsum containing narrow flaws of 0.004” (0.1mm) aperture (figure 5.1a),
- molded gypsum containing wide flaws of 0.05” (~1.3mm) aperture (figure 5.1b),
- Carrara marble containing wide flaws of 0.05” (~1.3mm) aperture (figure 5.1c).

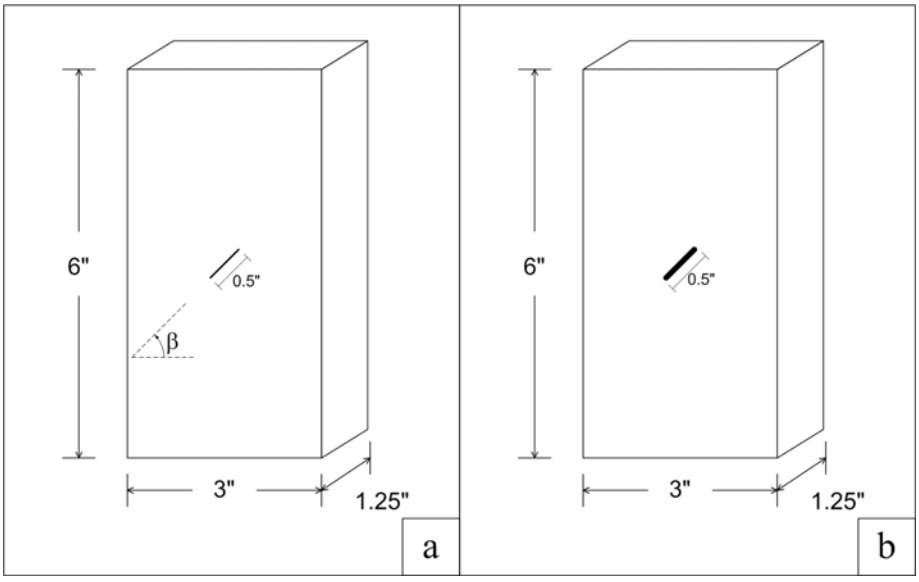

Figure 5.1 – (a) Narrow and (b) wide flaws (0.5", 13mm long) contained in prismatic specimens. β is the flaw inclination angle measured from the horizontal.

In each series of tests, various flaw inclination angles (β) (figure 5.2 & table 5.1) are tested and generally three or more tests are conducted for a specific flaw inclination in order to observe consistent fracturing behavior. In the discussion below, flaws of 0.004" and 0.05" aperture will be respectively referred to as *narrow* flaws and *wide* flaws.

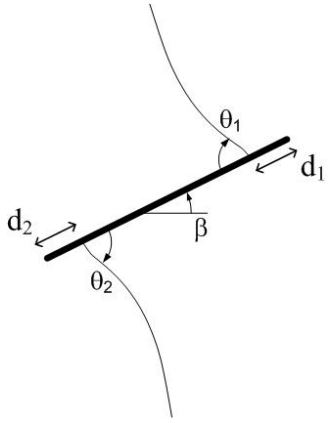

Figure 5.2 – A pair of tensile wing cracks (TWCs) initiated from a pre-existing flaw of inclination angle β. θ_1 and θ_2 are the crack initiation angles. d_1 and d_2 are the distances between the point of TWC initiation and flaw tip.

Series	Material	Flaw Aperture	Flaw Inclination β (^{o})
1	Gypsum	0.004”	0, 15, 30, 35, 40, 45, 50, 55, 60, 70, 75
2	Gypsum	0.05”	0, 30, 45, 60, 75
3	Marble	0.05”	0, 30, 45, 60, 75

Table 5.1 – Flaw geometries tested in gypsum and marble speimens

5.3 Results

5.3.1 Fracturing behavior in gypsum

Eleven and five flaw inclination angles ranging from 0^o to 75^o are tested in gypsum specimens containing narrow and wide flaws, respectively. It is found that the fracturing behavior of gypsum specimens containing narrow flaws (table 5.2) and wide flaws (table 5.3) is similar (figure 5.3). Notice that figure 5.3 contains fracture images for both gypsum and marble specimens, and will be used for discussion throughout this chapter. For the discussion of fracturing behavior in gypsum in this section, only the left and the central columns are relevant. In tables 5.2, 5.3 and figure 5.3, T indicates tensile, S indicates shear, T-S describes a crack consisting of both tensile and shear segments and TWC indicates tensile wing crack. Also refer to figure 3.15 (reproduced below after figure 5.3) for the crack type classification.

Detailed analyses of the fracturing behavior for gypsum specimens containing narrow flaws and wide flaws are summarized in Appendix E and Appendix F respectively.

Flaw Inclination Angle, β (^{o})	First cracks Appeared	Failure cracks
0	TWCs (type 1 T cracks)	Other type 2 T cracks from tips and/or T cracks in middle of pre-existing flaws
15		Other mixed T-S cracks from tips and/or T cracks in middle of pre-existing flaws
30		
35		
40		
45		Other mixed T-S cracks and type 2 T cracks from tips
50		
55		
60		
70		Same TWCs (type 1 T cracks)
75		

Table 5.2 – Cracks initiated in gypsum containing 0.004" pre-existing flaws (T indicates tensile, S indicates shear, mixed T-S describes a crack consisting of both tensile and shear segments, TWC indicates tensile wing cracks). Refer to figure 3.15 for crack type classification.

Flaw Inclination Angle, β (^{o})	First cracks Appeared	Failure cracks
0	TWCs (type 1 T cracks)	Other mixed T-S cracks from tips
30		
45		Other mixed T-S cracks and Type 2 T cracks from tips
60		Same TWCs (type 1 T cracks)
75		

Table 5.3 – Cracks initiated in gypsum containing 0.05" pre-existing flaws (T indicates tensile, S indicates shear, mixed T-S describes a crack consisting of both tensile and shear segments, TWC indicates tensile wing cracks). Refer to figure 3.15 for crack type classification.

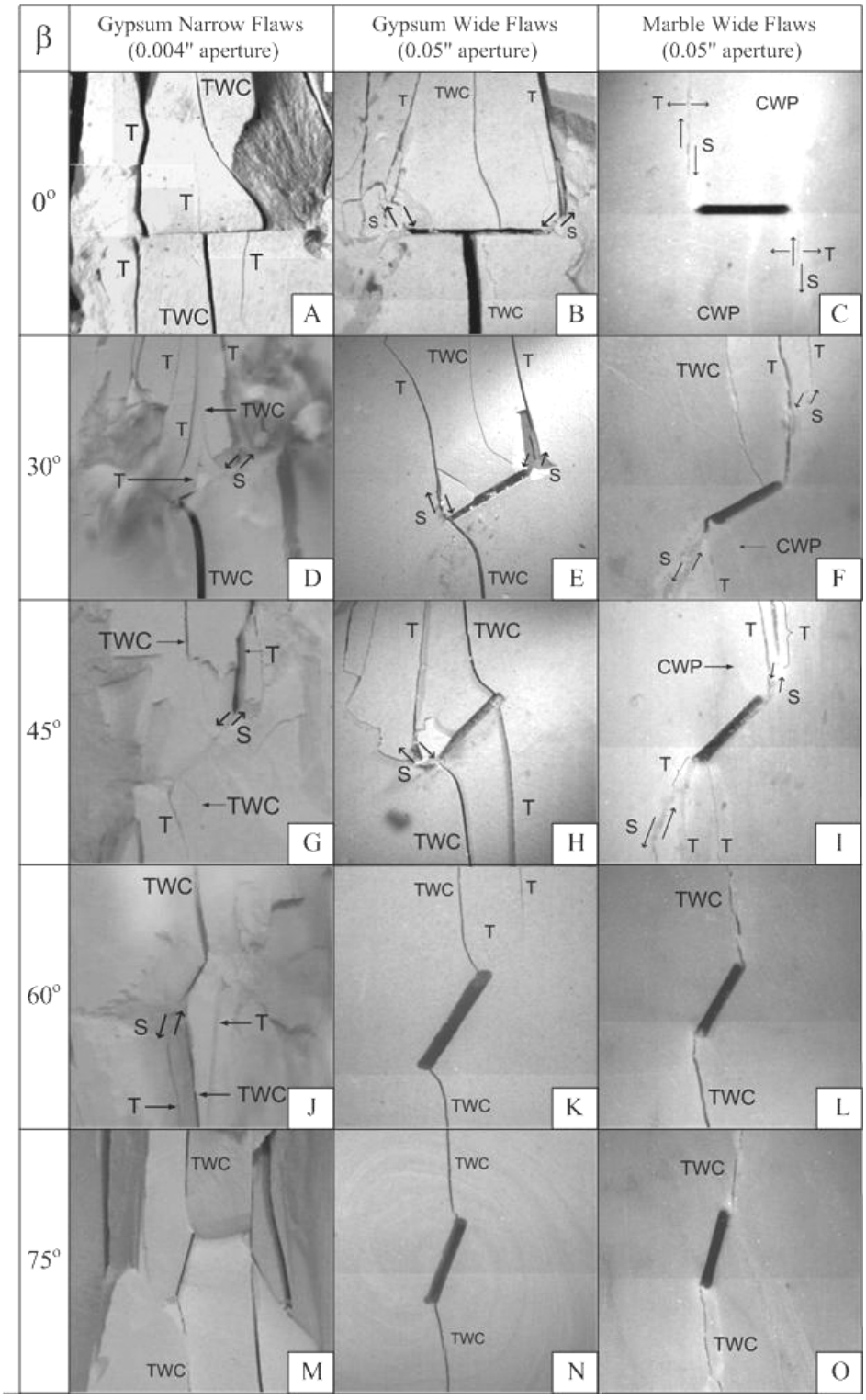

Figure 5.3 – Fracturing behavior in gypsum and marble specimens containing flaws at different inclination angles (β). Length of the pre-existing flaws is 0.5". (TWC – tensile wing crack, CWP – curvilinear white patch, T – tensile crack, S – shear crack).

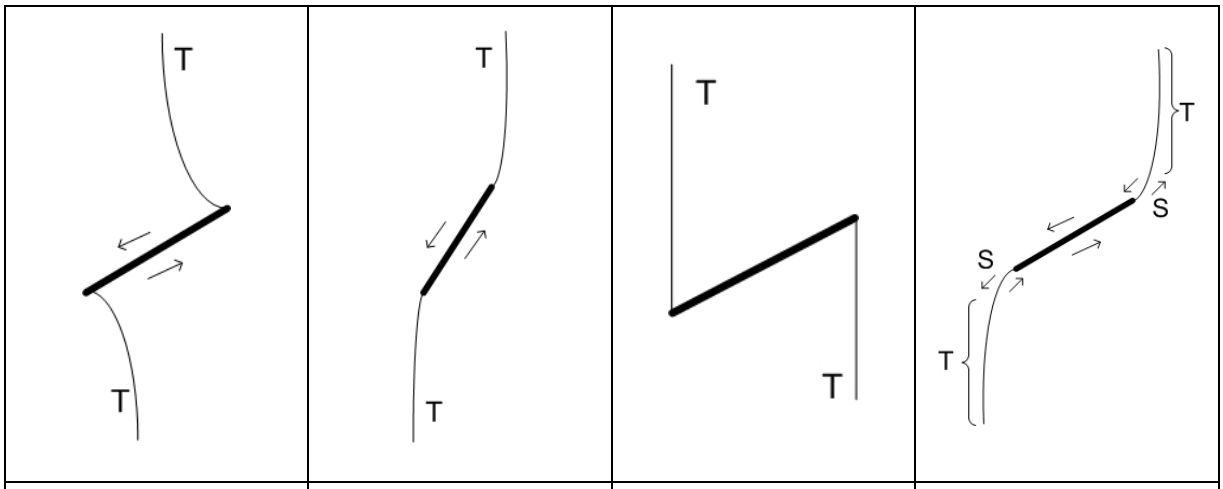

(a) Type 1 tensile crack (tensile wing crack)	(b) Type 2 tensile crack	(c) Type 3 tensile crack	(d) Mixed tensile-shear crack

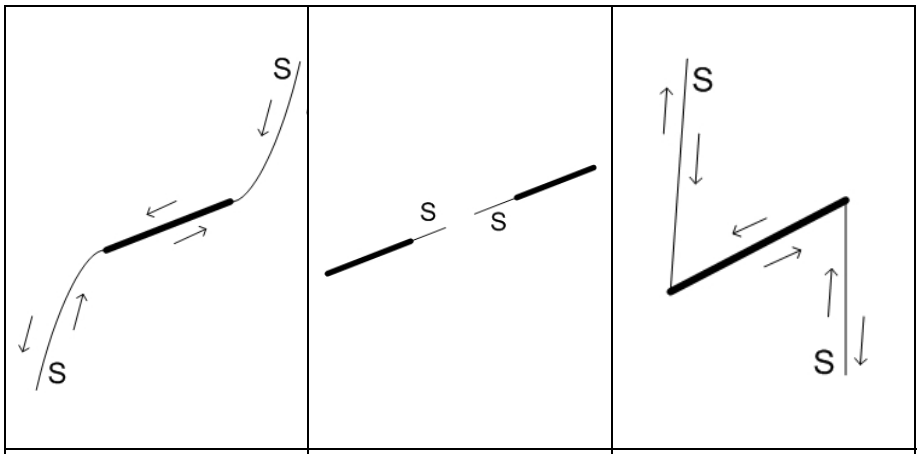

(e) Type 1 shear crack	(f) Type 2 shear crack	(g) Type 3 shear crack

Figure 3.15 – Types of cracks observed in White Vermont Marble.

Two main types of cracks – tensile (T) and shear (S), are identified from the unaxial compression tests on prismatic specimens. The surface of tensile cracks is characterized by a plumose structure with hackle marks, which are also relatively clean and free of any crushed gypsum powder (Reyes & Einstein, 1991, Bobet & Einstein, 1998a). In contrast, the surface of shear cracks is covered by a veneer of pulverized gypsum powder and the surfaces are rougher and more undulating (Reyes & Einstein, 1991, Bobet & Einstein, 1998a). Concern was raised by Reyes and Einstein (1991) that the presence of a pulverized product does not necessarily imply that the crack is initiated by shearing due to the possibility that the crack can be initiated in tension and is subject to subsequent shearing. In the present study with the use of the high speed video system, the initiation modes of the new cracks can be precisely determined and, for instance, tensile cracks subject to subsequent shearing have been successfully identified.

As shown in tables 5.2 and 5.3, cracks classified as T-S were also observed. These cracks refer to those consisting of segments initiated in different modes, e.g. tensile opening on one segment and shearing on the other segment.

Tensile wing cracks (TWCs) are always the first cracks to initiate, and in specimens containing flaws inclined at a high flaw inclination angle, the initiation of TWCs is concurrent with specimen failure. This is illustrated in figure 5.4, which shows the stress-strain curves for a gypsum specimen containing a wide flaw inclined at flaw inclination angle $\beta = 75^o$ and for a wide flaw inclined at $\beta = 0^o$. For $\beta = 75^o$, TWC initiated at the same stress level as the specimen failure. In these cases, the TWCs can thus also be regarded as the failure cracks, i.e. cracks whose initiation and propagation lead to an abrupt loss of specimen strength.

In specimens containing flaws inclined at lower angles (0^o to 60^o for narrow flaws and 0^o to 45^o for wide flaws), the initiation of TWCs usually does not lead to immediate specimen failure. After the initiation of TWCs, uniaxial loading stress has to be continuously applied to attain specimen failure. This is well illustrated in the other loading curve in figure 5.4 for $\beta = 0^o$. In these cases, failure is usually associated with

the initiation and propagation of additional cracks from the tips of the pre-existing flaws (figure 5.3). Most of these failure tip cracks are tensile, while some of them also have experienced shearing at segments adjacent to the flaw tips.

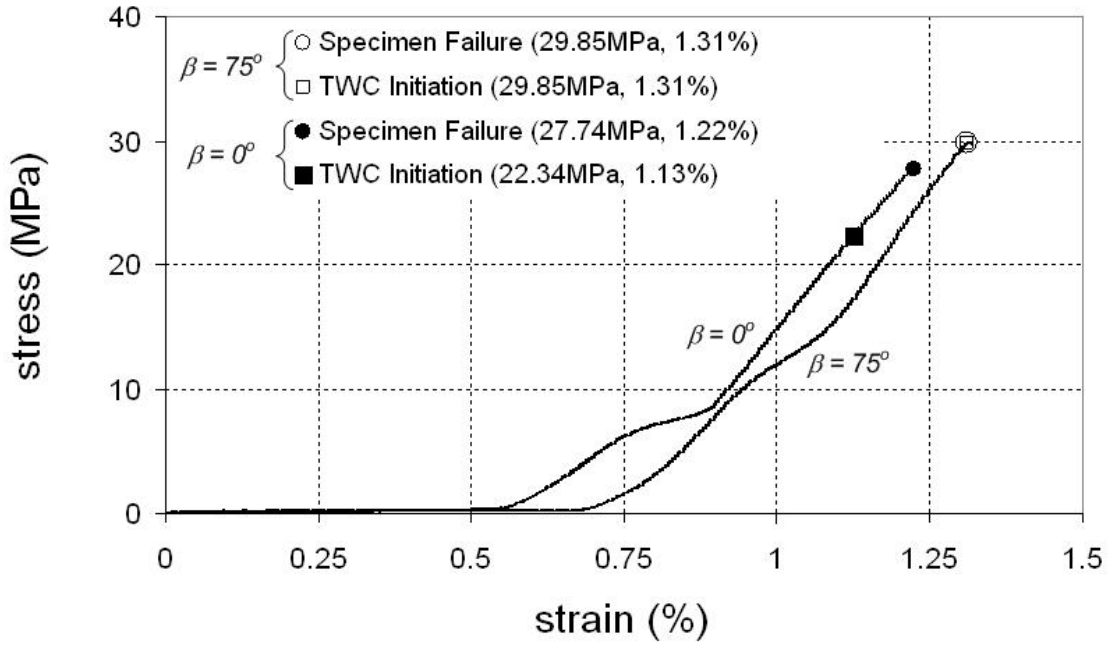

Figure 5.4 – Loading curves corresponding to two tests on gypsum specimens containing wide flaws at different flaw inclination angle (β).

Another interesting and so far not observed or not reported characteristic at crack initiation is the location of the crack relative to the flaw tip. In the present study, the position of the TWC initiation, which is quantified by the distances $\mathbf{d_1}$ and $\mathbf{d_2}$ denoted in figure 5.2, is determined. It is observed that as β decreases, the position where TWCs initiate shifts from a position close to/at the flaw tips towards the flaw centers (figure 5.5a). The degree of scatter of the measured data also increases as β decreases (figure 5.5b). These trends are clearly displayed for both narrow flaws and wide flaws.

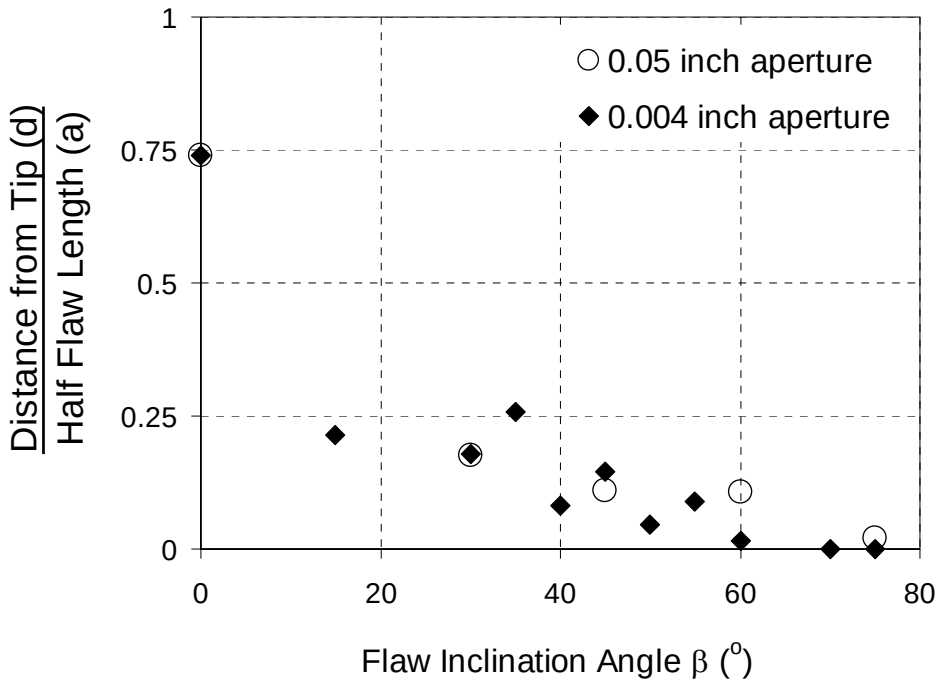

Figure 5.5a – Change of the distance [d] (mean values) between the point of TWC initiation and flaw tip, which is normalized by the half flaw length [a].

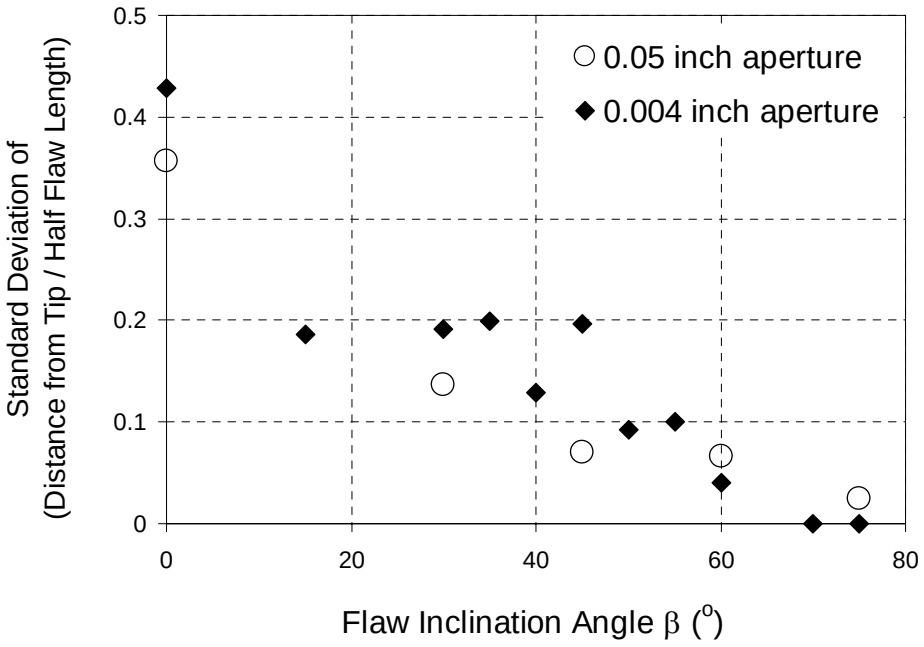

Figure 5.5b – Standard deviation of the corresponding data shown in figure 5.5a.

The above observations agree with the predictions offered by Lajtai (1970). As shown in figure 5.6, the region on the flaw perimeter where the maximum tensile hoop stress (most negative) occurs shifts away from the flaw tip ($\beta = 90^o$) towards the flaw center ($\beta = 0^o$) as β decreases. Secondly, the stress gradient on the flaw perimeter where the maximum hoop stress occurs is greater for steeply-inclined flaws, which explains the more closely clustered measured data and vice versa for flatly-inclined flaws, leading to higher degree of scatter of data.

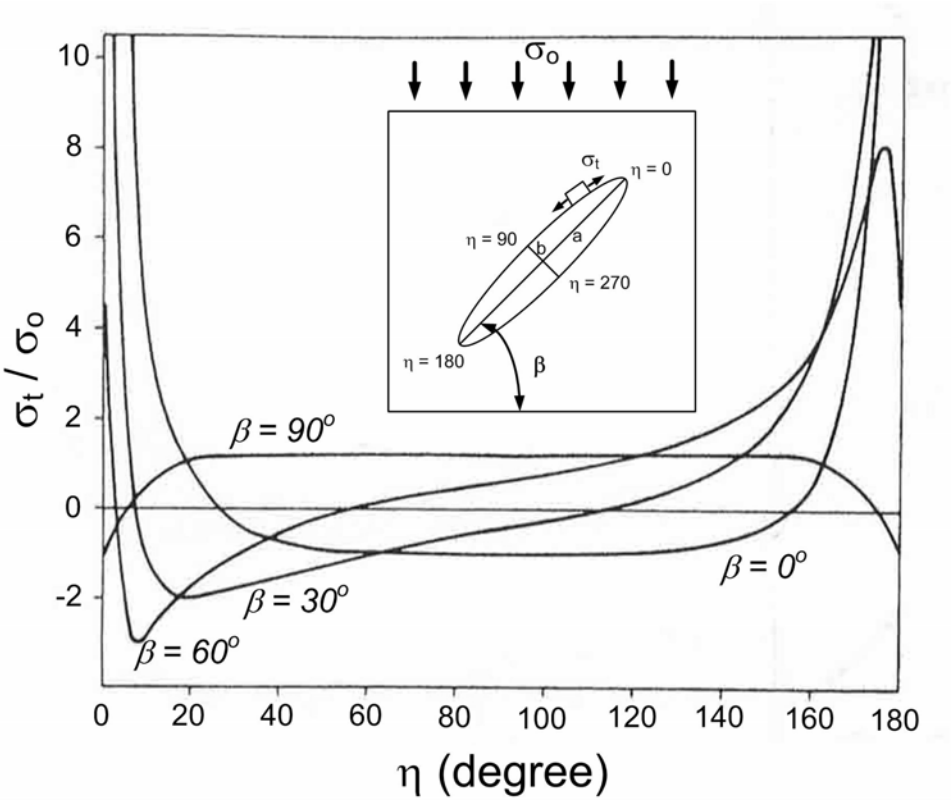

Figure 5.6 – Stress concentrations along an isolated flaw periphery. The flaw aspect ratio is b/a=0.1. Negative stress ratio indicates tension (Lajtai, 1970).

Another parameter to characterize the TWC trajectory is the crack initiation angle, which is defined as θ_1 (& θ_2) for the pair of TWCs as shown in figure 5.2. These angles are measured from the recorded images and the mean values are plotted in figure 5.7.

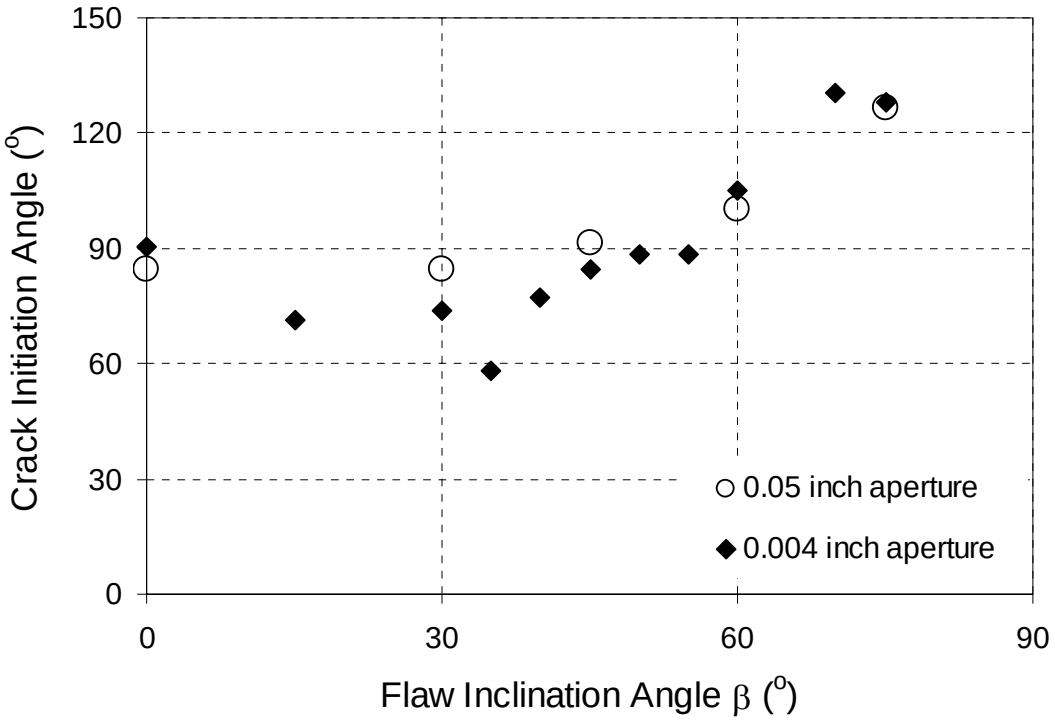

Figure 5.7 – Change of tensile wing crack (TWC) initiation angle (mean values) with flaw inclination angle in gypsum specimens.

For horizontal ($\beta = 0^o$) narrow and wide flaws, the crack initiation angle is very close to 90^o, i.e. the initial segment of TWC is almost orthogonal to the flaw faces. For steeply inclined flaws ($\beta = 75^o$), the crack initiation angle approaches a maximum value of about $125^o - 130^o$.

The stresses at which TWCs first initiated are also measured and the mean values are plotted in figure 5.8. The stress required to initiate TWCs generally increases with β. For flaws of the same inclination, the TWC initiation stress of wide flaws is generally lower than that of narrow flaws, with the exception of horizontal flaws. Observe also that the TWC initiation stress continually increases with β in the case of wide flaws. However, in the case of narrow flaws, as β reaches 60^o or above, the TWC initiation stress appears to approach a plateau value of around 40 MPa.

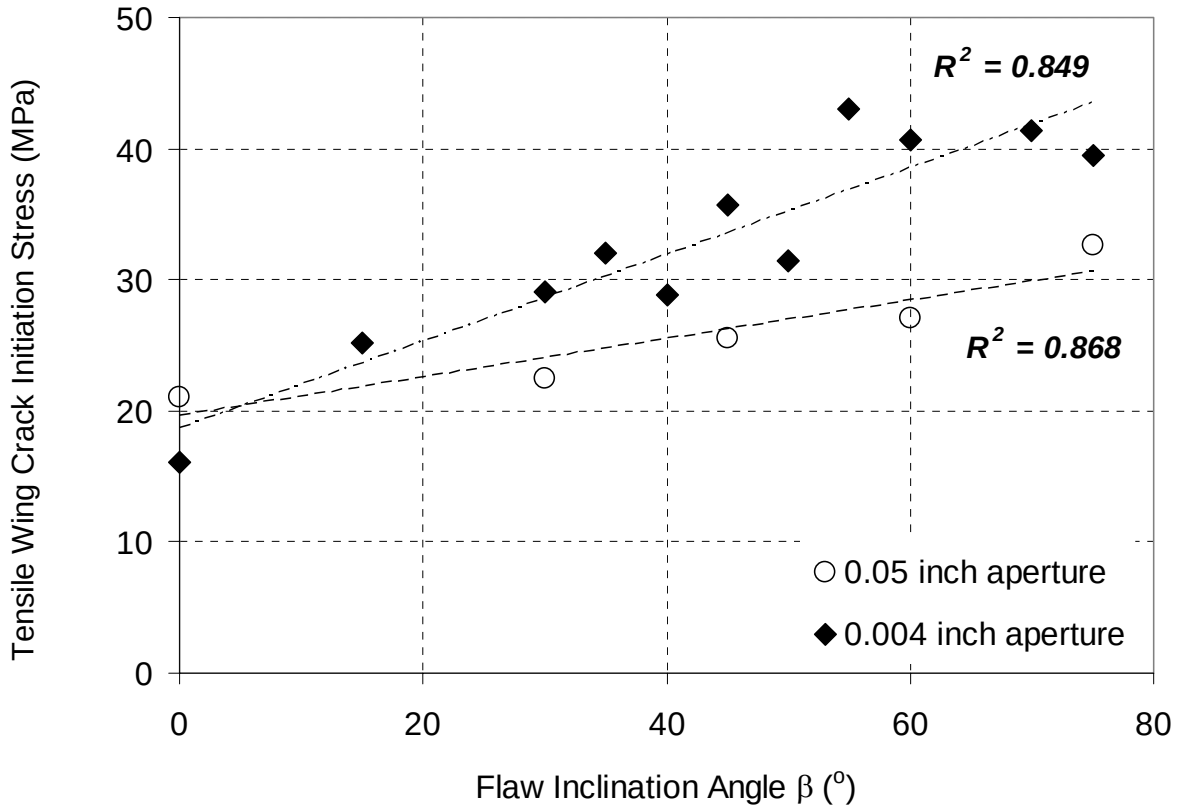

Figure 5.8 – Change of tensile wing crack initiation stress (mean values) with flaw inclination angle in gypsum specimens.

Figure 5.9 is a plot similar to the one shown in figure 5.8, but stress ratio instead of the TWC initiation stress is shown on the vertical axis. The stress ratio, which is defined as the TWC initiation stress divided by the specimen failure stress, offers quantitative information of how close the occurrence of crack initiation is to specimen failure. Figure 5.9 confirms that at high flaw inclination angles, TWC initiation is concurrent with specimen failure, with a stress ratio close to one.

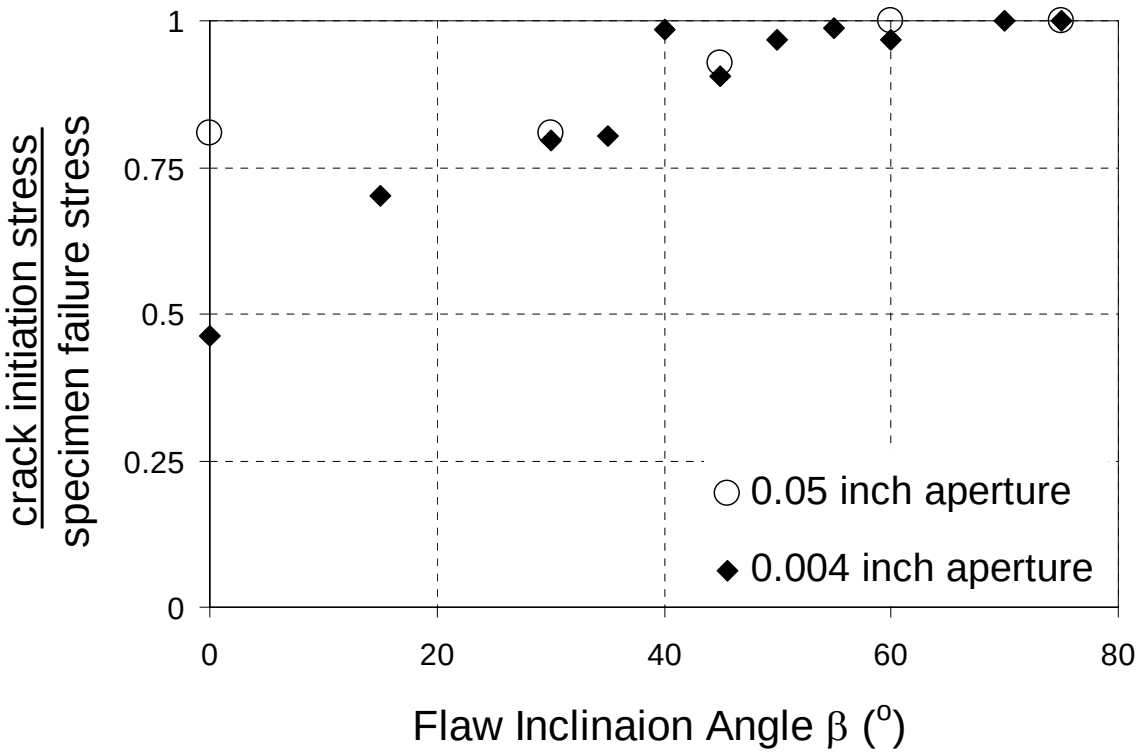

Figure 5.9 – Plot of mean stress ratios (crack initiation stress/specimen failure stress) against the flaw inclination angle.

5.3.2 Fracturing behavior in marble

The fracturing behavior of marble specimens containing flaws oriented at different inclinations is shown in the right column of figure 5.3 and is summarized in table 5.4. A major difference of fracturing behavior between marble and gypsum is that prior to the occurrence of the actual cracks in marble, the zone in which they eventually appear would always have already become distinctively white, indicating a process zone (see figure 5.10(i)).

Detailed analyses of the fracturing behavior for marble specimens containing single flaws are given in Appendix G.

Flaw Inclination Angle, β (°)	First cracks appeared	Failure cracks
0	Vertical T-S cracks	Type 1 S cracks
30	Type 1 T cracks (Tensile wing cracks)	
45		
60	Type 2 T cracks	Same type 2 T cracks
75		

Table 5.4 – Cracks initiated in marble containing 0.05" pre-existing flaws (T indicates tensile, S indicates shear, T-S describes a crack consisting of both tensile and shear segments).

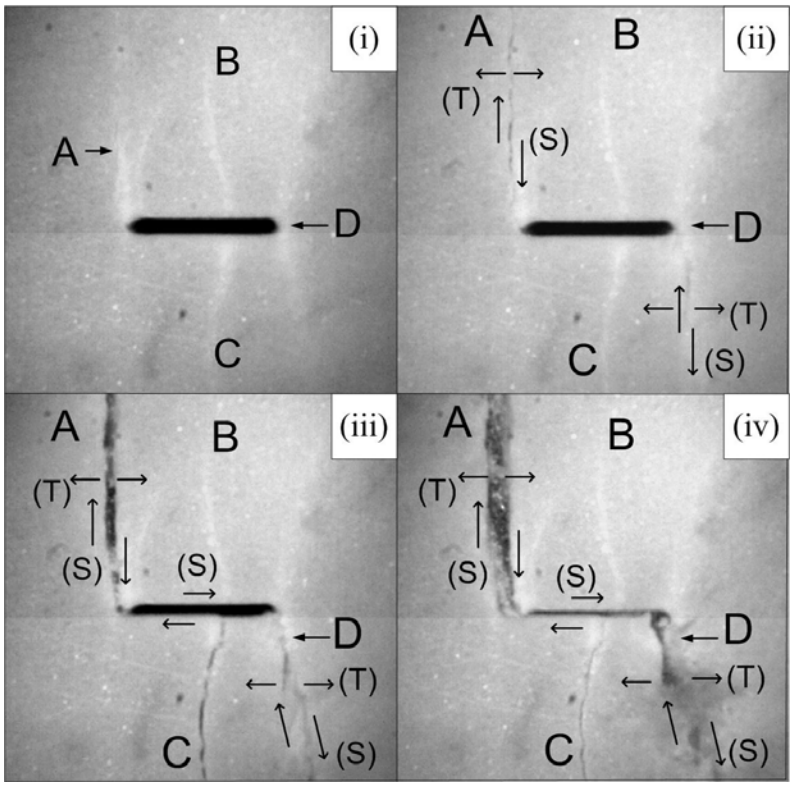

Figure 5.10 – Development of white process zones and cracks in marble upon loading. Length of the pre-existing flaw is 0.5". (i) White patches A, B, C and D develop prior to the initiation of any observable cracks. (ii) New cracks develop along white patches A and D, in a mixed tensile (Mode I) and shear (Mode II) manner. (iii) Shearing (S) and tensile (T) opening continue for cracks A and D. A TWC initiates along the curvilinear white patch (CWP) C. Note also the lateral shearing on the pre-existing flaw and a reduction of aperture size. (iv) Further shearing and tensile opening occur for cracks A and D. Note also that the CWP B remains intact and unopened throughout the course of loading.

In marble with small flaw inclination angles (30^o & 45^o), the trajectories of TWCs, if they develop, are generally similar to those observed in gypsum. However, as also shown in images F and I in figure 5.3, some curvilinear white patches (CWP) displaying wing appearance remain intact and observable cracking is not observed along the. Instead, tensile cracks curving in a different manner initiate from the neighboring flaw tip in images F and I, which are type 2 tensile cracks as observed in the Vermont White Marble (see the crack type classification scheme shown in figure 3.15). In geometries with large flaw inclination angles (60^o, 75^o), type 1 tensile cracks (TWCs) are not observed. The first cracks initiated from the flaw tip regions are all type 2 tensile cracks (images L and O in figure 5.3). Apart from the general shape of the trajectory, the exact points of crack initiation are also different from the gypsum specimens with the same large flaw inclination angles. As shown in pictures K, L, N, O in figure 5.3 (sketches of K and L are shown in figure 5.11), type 1 tensile cracks (TWCs) initiate from the inner side of the rounded flaw tips in gypsum (indicated by *), while type 2 tensile cracks initiate from the outer side of the flaw tips in marble (indicated by #).

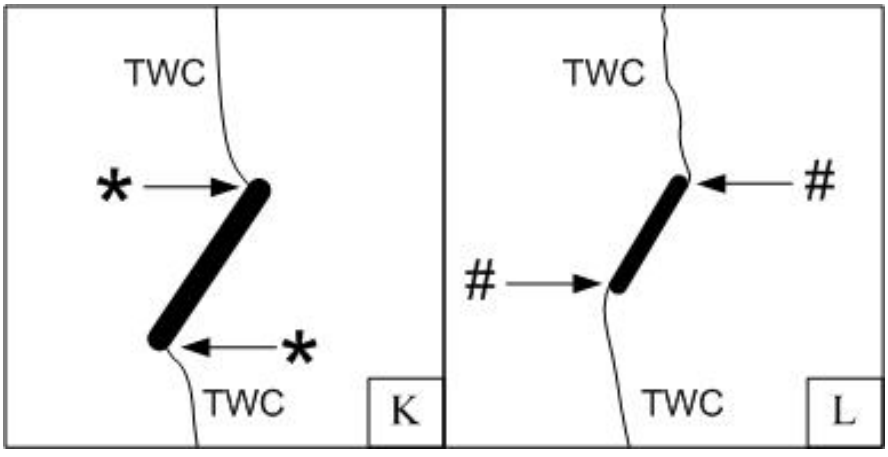

Figure 5.11 – Sketches of type 1 tensile cracks (TWCs) initiated from inner side of flaw tips in gypsum (K) and type 2 tensile cracks from the outer side of flaw tips in marble (L). Refer to figure 4.3 for the original pictures.

As discussed above, for β larger than or equal to 30°, the first cracks to initiate in marble are either type 1 tensile cracks or type 2 tensile cracks, which develop along the "white patches" (table 5.4). For horizontal flaws, however, the first cracks to initiate are not the TWCs, but tip cracks displaying a mixed mode I and mode II character, trending almost parallel with the loading direction (picture C in figure 5.3). Please refer to figure 5.10 for a detailed description of the fracturing processes around a horizontal flaw in marble. Figure 5.10 also reveals that prior development of white process zones is not limited to the initiation of TWCs. They also precede the initiation of other major cracks originating from the flaw perimeter (e.g. cracks A and D in figure 5.10).

Regarding the position of initiation, as β increases, the TWCs (or type 2 tensile cracks for large flaw inclination angles of 60° and 75°, or curvilinear white patches if actual cracks did not develop) will initiate at a position closer to the flaw tips (figure 5.12a). The degree of scatter of the measured data also decreases with the flaw inclination angle (figure 5.12b). In these plots, data corresponding to wide flaws in gypsum are also shown, which suggest a similar trend of variation for both gypsum and marble.

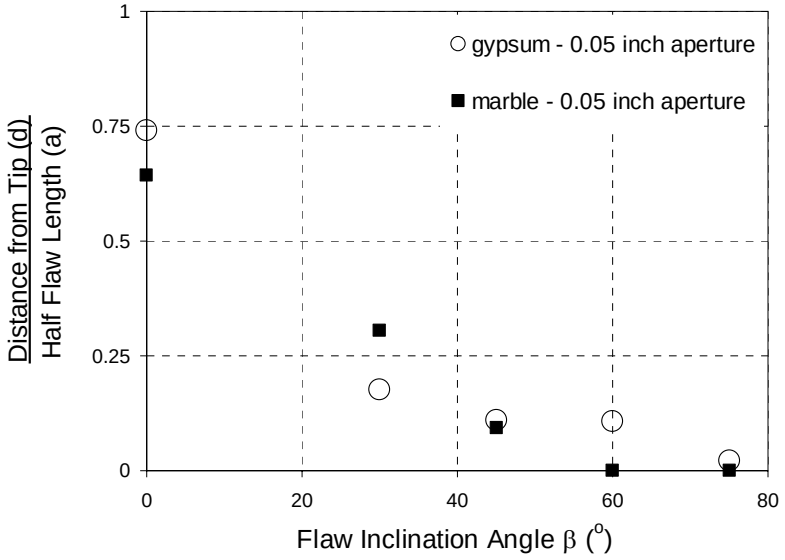

Figure 5.12a – Change of the distance [d] (mean values) between the point of TWC (or curvilinear white patches if actual cracks did not develop) initiation and the flaw tip, which is normalized by the half flaw length [a].

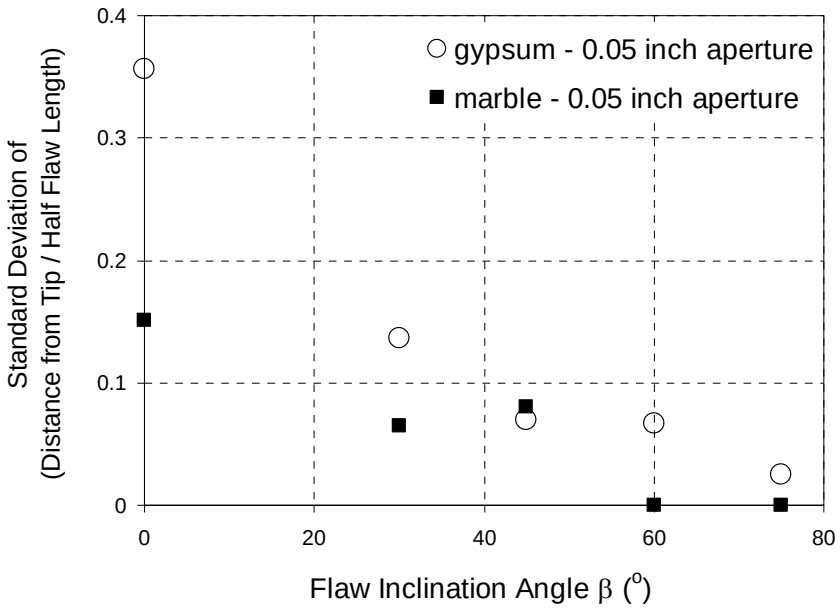

Figure 5.12b – Standard deviation of the corresponding data shown in figure 5.12a.

In specimens containing flaws inclined at high angles ($\beta = 60^o, 75^o$), specimen failure is concurrent with the initiation of the type 2 tensile cracks. In specimens containing flaws inclined at lower angles ($\beta = 0^o, 30^o, 45^o$), specimen failure does not occur when the tensile cracks first develop (type 1 tensile cracks for $\beta = 0^o$, types 1 and 2 tensile cracks for $\beta = 30^o, 45^o$), but is associated with cracks developed at a higher stress (third column in table 5.4). Most of these late cracks are *shear* cracks initiating from the flaw tips (figure 5.13) or *shear* cracks branching from the new tensile cracks developed earlier during the loading process (figure 5.14).

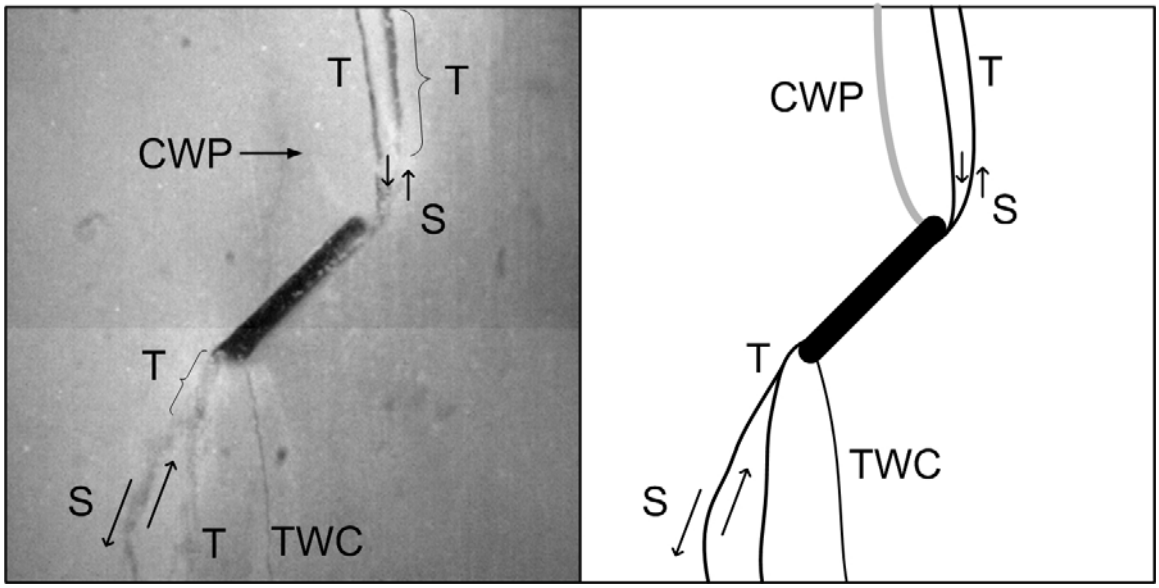

Figure 5.13 – Details of fractures shown in picture I of figure 5.3. CWP represents the curvilinear white patch which remains unopened. TWC (tensile wing crack) is the first crack initiated in the specimen. Note the subsequent development of shear cracks originated from flaw tips (S – shear crack, T – tensile crack).

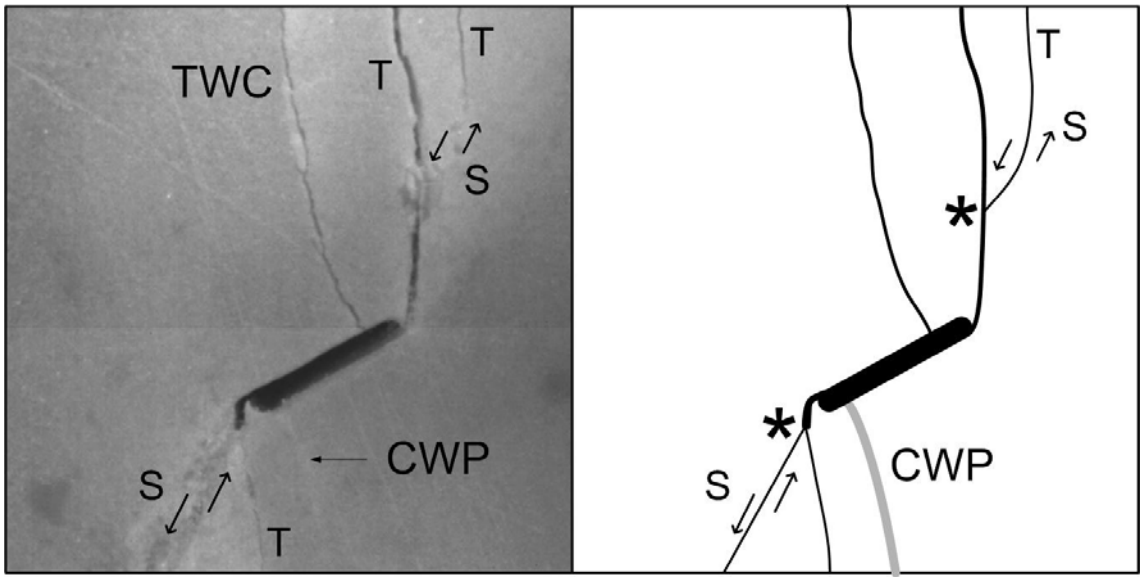

Figure 5.14 – Details of fractures shown in picture F of figure 5.3. The location on the tensile cracks where subsequent new shear cracks develop is marked by '*'. CWP represents the curvilinear white patch which remains unopened (S – shear crack, T – tensile crack).

5.4 Discussion

5.4.1 Influence of flaw aperture on fracturing behavior

As described in section 5.3.1, the fracturing behavior and the types of new cracks produced in gypsum specimens containing narrow and wide flaws are very similar. Similarity is also observed with respect to the location where TWCs initiate (figures 5.5a & 5.5b).

Close examination of the recorded images however reveals a distinct difference of the fracture pattern between narrow and wide flaws in gypsum. For specimens containing narrow flaws, additional tensile cracks usually initiate in the middle portions of the flaws, especially of those which are shallowly inclined (figure 5.15). These cracks usually develop later than the TCWs, i.e. at a higher stress, but their occurrence is rare in specimens containing wide flaws. The initiation of these late tensile cracks may be associated with the partial closure of the flaws which is more easily achieved in narrow flaws than in wide flaws.

Figure 5.16 shows schematically an inclined narrow flaw under uniaxial compression. The flaw faces are shown to consist of a number of small irregularities (asperities). Note that the figure is not drawn to scale and the roughness is exaggerated. Tensile wing cracks **A** and **B** initiate early from the tip regions in response to the uniaxial compressive load (figure 5.16a). As the prismatic specimen is further loaded, a reduction of flaw aperture occurs, i.e. the upper face and lower face of the flaw move towards each other. This type of flaw deformation is often observed in the experiments. The aperture reduction sometimes leads to the formation of contacts between asperities along the two flaw faces. The original flaw then appears to consist of individual segments which are either open or in intimate contact (figure 5.16b). The region between two neighboring contacts thus behaves as an open flaw (see the dotted-lined rectangle shown in figure 5.16b). A new tensile wing crack A' develops from the right tip region of this **"newly formed"** flaw segment. The above postulation, which needs further experimental justification to identify closure and contact of flaw faces during compression, may offer a

sensible explanation why the development of additional tensile cracks is more common in shallowly-inclined narrow flaws than in wide flaws (figure 5.15).

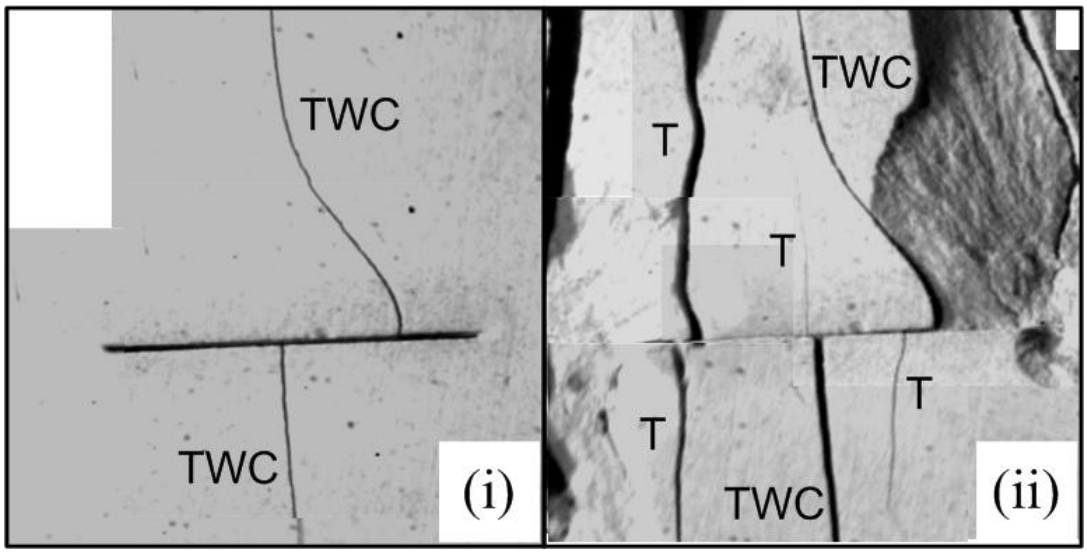

Figure 5.15 – Development of tensile cracks from a horizontal narrow flaw in gypsum. Length of the pre-existing flaw is 0.5". (i) view just after the initiation of the TWC pair, (ii) development of multiple tensile cracks, far from flaw tips after peak load (same image as picture A in figure 5.3).

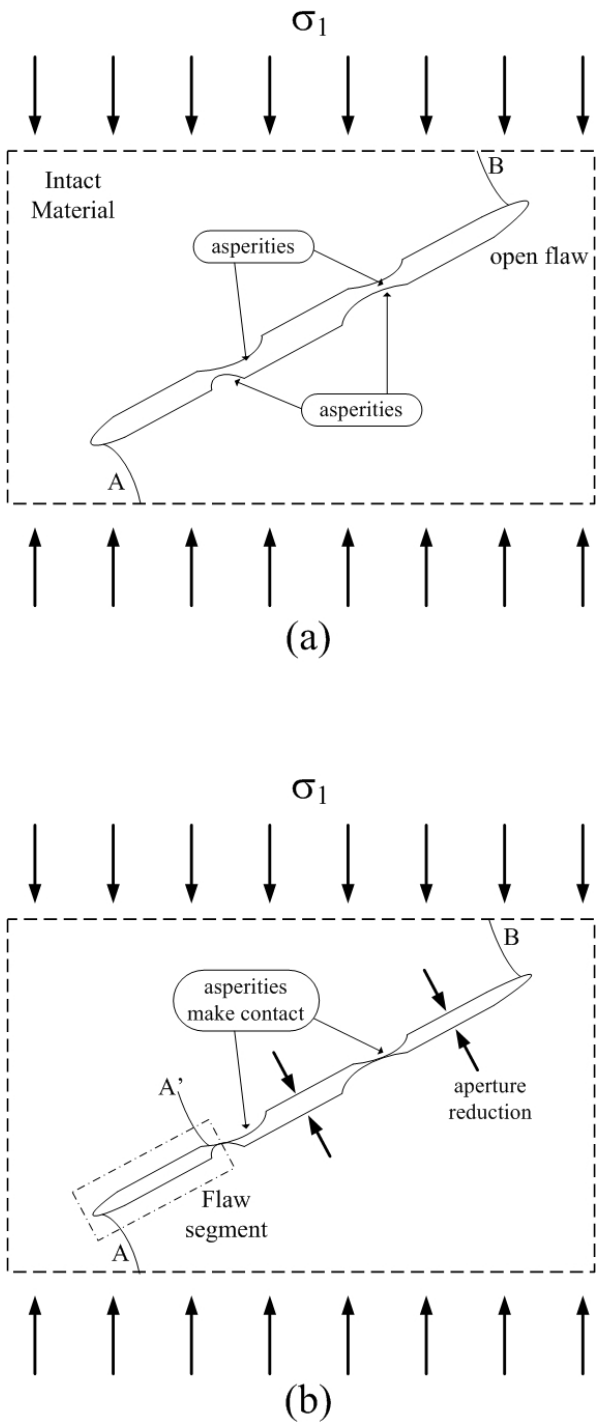

Figure 5.16 – Schematic illustration (not to scale) of an inclined narrow flaw under uniaxial compression. (a) The flaw faces are not completely smooth and consist of multiple asperities. Tensile wing cracks initiate from the two flaw tip regions. (b) Further applied loading reduces the flaw aperture and leads to the formation of contacts between flaw faces. The flaw segment on the left of the main flaw behaves as an independent flaw with the initiation of a new tensile crack A' from its right tip.

5.4.2 Influence of material type on fracturing behavior

The similarities of the fracturing behavior observed in gypsum and marble specimens containing flaws of the same aperture size (0.05") are:

- Tensile cracks, either type 1 or type 2, originating from the flaw tip regions are always the first cracks to initiate in both types of specimens (except horizontal flaws in marble).

- In both material types in specimens containing steeply-inclined ($\beta = 60^o, 75^o$) flaws, the initiation of tensile cracks is concurrent with specimen failure. However, in specimens containing shallowly-inclined flaws ($\beta = 0^o, 30^o, 45^o$), the initiation of first cracks usually does not lead to immediate specimen failure. Specimen failures are due to initiation of other cracks (tables 5.3 & 5.4).

Some distinct differences noticed in the formation of cracks in gypsum and marble are:

- In marble specimens containing horizontal ($\beta = 0^o$) flaws (table 5.4), the first cracks to initiate are tip cracks of a mixed mode I and mode II character, which are oriented almost parallel with the loading direction. In gypsum specimens containing horizontal flaws (table 5.3), the first cracks initiated are TWCs instead.

- Even though tensile cracks are often the first cracks to initiate, they can be of two types. As described earlier in section 5.3.2, in geometries with large flaw inclination angles ($60^o, 75^o$), the first cracks to initiate in marble are type 2 tensile cracks (images L & O in figure 5.3), as compared to type 1 tensile cracks (TWCs) in gypsum (images K & N in figure 5.3). In geometries with smaller flaw inclination angles ($30^o, 45^o$), both type 1 and type 2 tensile cracks are observed to initiate as first cracks in marble, while only type 1 tensile cracks (TWCs) in gypsum.

- Development of a process zone (distinctive white patch) before the initiation of actual cracks is observed in most marble experiments. This phenomenon is not observed in gypsum, which may be due to its fine-grained nature.

- The initiation of TWCs in gypsum is usually accompanied by a distinct cracking sound and a rapid crack propagation taking place across the specimens. The fracturing behavior in marble is different, in that individual tensile segments usually first initiate along some previously-developed white patches (figure 5.17(i)). The cracks then progressively and individually propagate until coalescence occurs as the stress is continuously increased (figure 5.17(ii)).

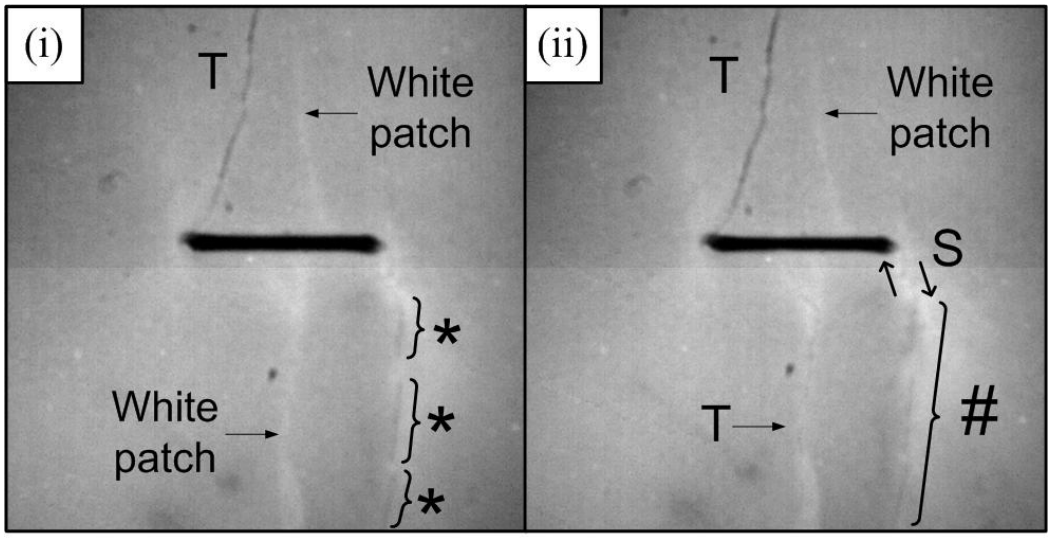

Figure 5.17 – (i) Individual tensile crack segments (darker traces indicated by *) develop along a white patch initiated from the right flaw tip in marble. (ii) The tensile segments coalesce to form a longer crack (long dark trace indicated by #). Note also the development of another tensile crack along the central bottom white patch and the occurrence of shearing movement (arrows indicate sense of shearing) at the crack adjacent to the right flaw tip. T indicates tensile crack. Length of the pre-existing flaw is 0.5".

5.5 Conclusions

This experimental study has confirmed that tensile cracks (type 1 tensile cracks, i.e. tensile wing cracks, and type 2 tensile cracks) are in most cases the first cracks to appear in fracture propagation from existing flaws independent of *aperture* and *material* (one exception is for horizontal flaw in marble). In specimens containing steeply-inclined flaws, the initiation of tensile cracks is concurrent with specimen failure (figure 5.9). However, in specimens containing more flatly-inclined flaws, the initiation of first cracks usually does not lead to immediate specimen failure. The study, in addition, has shown that complex additional cracking occurs which depends on the flaw inclination angle, flaw aperture and material (figure 5.3).

Tests in gypsum specimens containing two different flaw *aperture* sizes revealed that the fracturing behavior and types of new cracks are in general very similar. One distinct difference was the preferential initiation of tensile cracks in the middle portions of the thin flaws (figure 5.15), which is rare in specimens containing wide flaws. A postulation based on the possible partial closure of flaw aperture has been put forward to explain the phenomenon (figure 5.16).

Tests in gypsum and marble specimens containing flaws of the same aperture size reveal the influence of *material* type on crack initiation and propagation. Formation of a process zone prior to the development of actual cracks could be visually observed in most marble experiments containing flaws at varying inclination angles (figure 5.10), but not in gypsum experiments. In geometries with large flaw inclination angles (60^o, 75^o), the first cracks initiated from the flaw tip regions are all type 2 tensile cracks in marble (images L and O in figure 5.3) as compared to type 1 tensile cracks (TWCs) initiated in gypsum of the same flaw geometries (figure 5.11). Besides, the first cracks to develop in marble with horizontal flaws are neither type 1 tensile cracks (TWCs) nor type 2 tensile cracks, but are cracks of a mixed mode I and mode II character trending along the loading direction. The high speed video system reveals in marble, but not in gypsum, that some

tensile cracks formed from coalescence of multiple individual tensile segments which have initiated along the previously-developed white patches (figure 5.17).

To conclude, the present systematic experimental study reveals that fracturing behavior in specimens containing single pre-existing flaws is far more complicated than what has been reported before. Besides, the study is important for two additional reasons. First, it forms the basis for further experimental work in which propagation and coalescence of cracks initiated from two or more flaws is investigated, which will be discussed in next chapter. Second, it forms the basis for analytical models in which the crack initiation, propagation and coalescence process is described.

CHAPTER 6 - Uniaxial Compression Tests in Specimens Containing Double Flaws

6.1 Introduction

In chapter 3, the high speed videos recording the fracturing and coalescence behavior in White Vermont Marble were reviewed. From this review, a number of crack types were identified. Besides, flaw inclination angle, bridging angle and ligament length were found to have different influences on the fracturing and coalescence behavior of pre-existing flaw pairs. In this chapter, the results obtained in the present experimental study on molded gypsum and Carrara Marble tested under uniaxial loading are described and discussed. The main objective of the tests is to study the fracturing and coalescence behavior in these two materials, in particular the influences of material type, flaw inclination angle, bridging angle and ligament length on the coalescence patterns.

6.2 Experimental Details

A total of eight series of uniaxial compression tests were conducted on molded gypsum specimens and Carrara Marble specimens containing double flaws (four series for gypsum and four series for marble). The specimens were prepared according to the procedures described in chapter 4. Recall that the geometry of a flaw pair is defined by three geometrical parameters – flaw inclination angle β, bridging angle α and ligament length L as shown in the figure below.

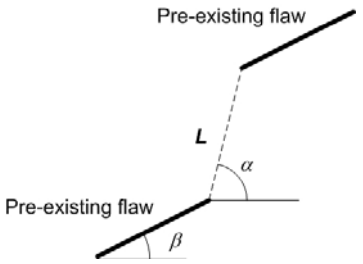

For example, a specimen of geometry **2a-30-(-60)** indicates that ***L*** is equal to **2a** (**a** is half flaw length), β is equal to 30^o and α is equal to -60^o. Experimental parametric studies are conducted by varying one of the three parameters in any particular series. In the present study, ***L*** ranges between 2a and 4a, β varies between 30^o and 75^o, and α between -60^o and 120^o.

The geometries of the four series, which were tested in both materials, are listed below and summarized in table 6.1:

1) Coplanar flaw pairs (i.e. bridging angle = 0^o) with ligament length equal to "2a" and varying flaw inclination angles (figure 6.1),
2) Stepped flaw pairs with flaw inclination angle equal to 30^o, ligament length equal to "2a" and varying flaw inclination angles (figure 6.2),
3) Coplanar flaw pairs (i.e. bridging angle = 0^o) with ligament length equal to "4a" and varying flaw inclination angles (figure 6.3),
4) Stepped flaw pairs with flaw inclination angle equal to 30^o, ligament length equal to "4a" and varying flaw inclination angles (figure 6.4).

Series	**General flaw pair relationship**	**Bridging angle α (^{o})**	**Ligament length**	**Flaw inclination β (^{o})**
1	Coplanar	0	2a	0, 30, 45, 60, 75
2	Stepped	-60, -30, 0, 30, 60, 90, 120	2a	30
3	Coplanar	0	4a	0, 30, 45, 60, 75
4	Stepped	-60, -30, 0, 30, 60, 90, 120	4a	30

Table 6.1 – Flaw geometries tested in gypsum and marble.

β	Sketch	β	Sketch
0°		60°	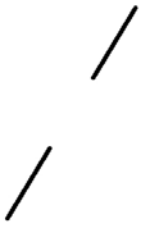
30°	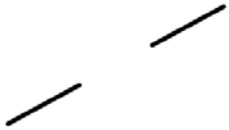		
45°	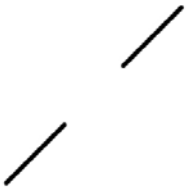	75°	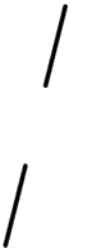

Figure 6.1 – Coplanar flaw pair geometry with ligament length 2a and varying flaw inclination angle.

α	Sketch	Stepping Relationship	Overlapping Condition
-60°		Right-stepping	Non-overlapping
-30°	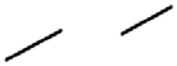	Right-stepping	Non-overlapping
0°	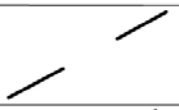	Coplanar	Non-overlapping
30°	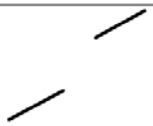	Left-stepping	Non-overlapping
60°		Left-stepping	Non-overlapping
90°	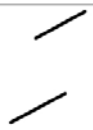	Left-stepping	Partial Overlapping
120°		Left-stepping	Complete Overlapping

Figure 6.2 – Stepped flaw pair geometry with flaw inclination angle 30°, ligament length 2a and varying bridging angle.

β	Sketch	β	Sketch
0°		60°	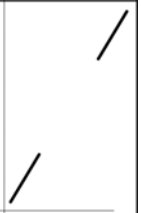
30°	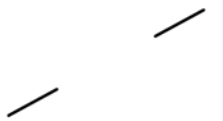		
45°	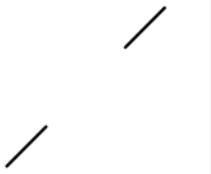	75°	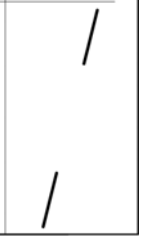

Figure 6.3 – Coplanar flaw pair geometry with ligament length 4a and varying flaw inclination angle.

α	Sketch	Stepping Relationship	Overlapping Condition
-60°		Right-stepping	Non-overlapping
-30°		Right-stepping	Non-overlapping
0°	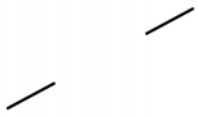	Coplanar	Non-overlapping
30°	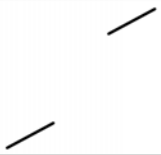	Left-stepping	Non-overlapping
60°		Left-stepping	Non-overlapping
90°		Left-stepping	Complete Overlapping
120°	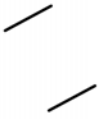	Left-stepping	Partial Overlapping

Figure 6.4 – Flaw pair geometry with flaw inclination angle 30°, ligament length 4a and varying bridging angle.

As noted in figures 6.1 to 6.4, the flaw pair geometries are further classified according to the stepping relationship (right-stepping, left-stepping, coplanar) and overlapping condition (non-overlapping, partial overlapping, complete overlapping).

In the following sections, the coalescence behavior observed in all tested specimens is described according to series, first on gypsum and subsequently on marble. See the table below for the relevant sections of different gypsum and marble series. The last column of the same table shows the appendix number of the corresponding section in which the fracturing and coalescence behavior of the tested specimens are described in detail.

Series	**Section**	**Appendix**
Gypsum – Coplanar – "2a"	6.3.1	H
Gypsum – Stepped – "2a"	6.3.2	I
Marble – Coplanar – "2a"	6.3.3	J
Marble – Stepped – "2a"	6.3.4	K
Gypsum – Coplanar – "4a"	6.4.1	L
Gypsum – Stepped – "4a"	6.4.2	M
Marble – Coplanar – "4a"	6.4.3	N
Marble – Stepped – "4a"	6.4.4	O

Each appendix first begins with a table summarizing the specimen geometries and specimen numbers tested within that particular series. It is then followed by summaries of the fracturing and coalescence pattern for individual specimens. The nature of all new cracks developed from the pre-existing flaws and the crack development sequence are shown in the sketches in accordance with the system described earlier in section 4.5. Additional information which includes the time of crack initiation relative to the occurrence of specimen maximum stress, and whether the cracking events are observed

by camcorder or high speed camera are shown below the sketch of each specimen (see below).

The cracks developed in the specimens are classified into one of the three classes: those developed before the maximum stress are classified as **pre-max**; those developed after that are classified as **post-max**; and those which initiated concurrently with the occurrence of specimen maximum stress are classified as **max**. In the example shown in the box below, crack 1 initiates before maximum stress (Pre-max), crack 2 initiates at the maximum stress (Max), and cracks 3, 4, 5 and 6 initiate after the occurrence of maximum stress (Post-max).

Pre-max : 1	
Max : 2	CAM : 1-2
Post-max : 3-6	HS : 3-6

The right column in the same box above indicates whether the initiation of cracks is recorded by the **camcorder** (CAM) or the **high speed camera** (HS). The initiation of cracks 1 and 2 is recorded by the camcorder (CAM), and the initiation of cracks 3, 4, 5 and 6 is recorded by the high speed camera (HS). Notice that since the resolution of the HS video is higher than that of the CAM, finer details can be observed in the former than in the latter.

It is also necessary to mention that throughout this chapter, all new cracks identified in the tested specimens are classified and named according to the scheme presented in figure 3.15 (reproduced below) and the relevant section in chapter 3.

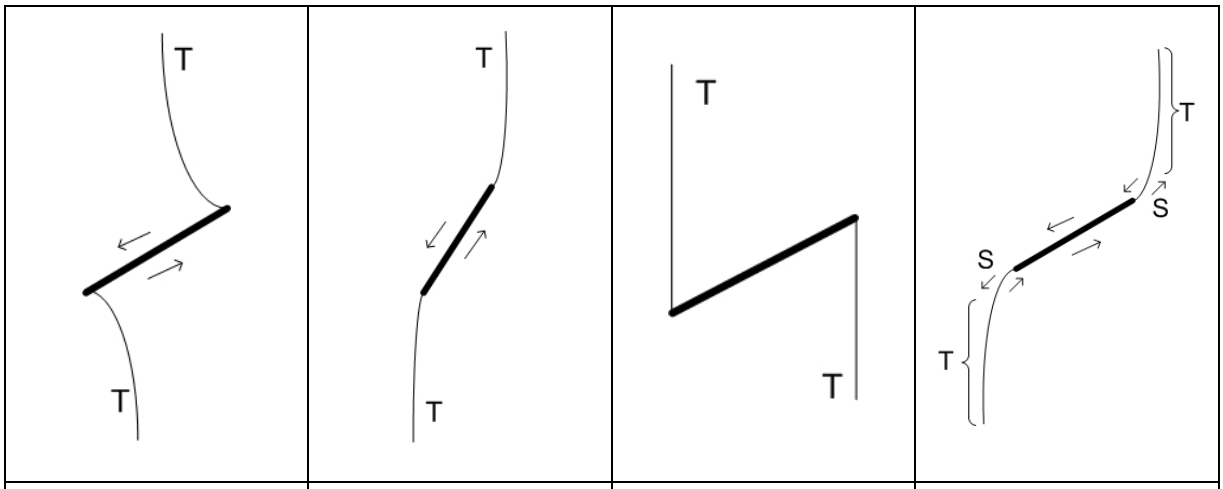

(a) Type 1 tensile crack (tensile wing crack)	(b) Type 2 tensile crack	(c) Type 3 tensile crack	(d) Mixed tensile-shear crack

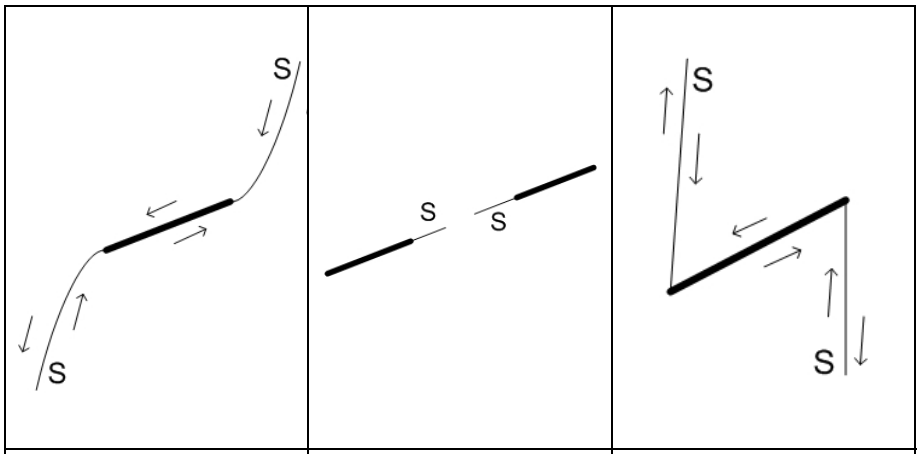

(e) Type 1 shear crack	(f) Type 2 shear crack	(g) Type 3 shear crack

Figure 3.15 – Types of cracks observed in gypsum and marble.

The coalescence crack types to be described and discussed within this chapter will be classified according to the categories shown in figure 6.5. The newly proposed classification scheme contains nine categories. The flaw pairs, which are represented by thicker lines in figure 6.5, are for illustrative purposes only. There is no implication that the crack coalescence defined for a particular category is only restricted to the illustrated flaw pair geometry. Coalescence of other flaw pair geometries can still be included in the same category provided that the nature of the associated coalescence cracks meets the description for that particular category. For example, only a coplanar flaw pair is illustrated in category 3, but stepped flaw pairs, which coalesce also by type 2 shear cracks, can fall into category 3.

Notice that the underlying idea of this classification scheme is similar to that proposed by the MIT-Purdue group (see section 2.7.2 for relevant discussion), i.e. the nature of the coalescence cracks were first identified and the coalescence types were then classified accordingly. Bobet and Einstein (1998a) classified crack types into either tensile crack or shear crack, and five coalescence types were classified based on the different combinations of these cracks. Sagong and Bobet (2002) classified crack types into tensile crack, quasi-coplanar shear crack and oblique shear crack, and nine different coalescence types were classified based on the different combinations of these cracks.

With the use of the high speed camera, many new fracturing and coalescence features have been identified in the present study. The existing MIT-Purdue crack coalescence classification scheme is found to be inadequate to describe all the newly identified features, particularly the seven crack types that have now been systematically recognized (figure 3.15). Since coalescence is often due to the initiation, propagation and linkage of one or more of these fundamental crack types, it makes sense to relate these mechanisms to the coalescence categories. This has the additional advantage that it will be easier and more systematic to expand the classification scheme to include additional crack coalescence categories identified in the future.

Category	Coalescence patterns	Crack types involved
1	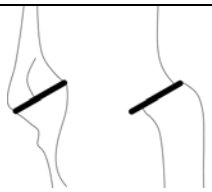	**No** coalescence
2	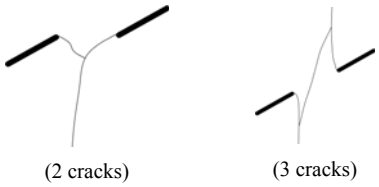	**Indirect** coalescence by two or multiple cracks (crack types vary)
3	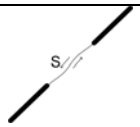	Type 2 **S** crack(s)
4	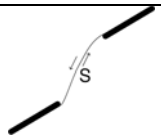	Type 1 **S** crack(s)
5	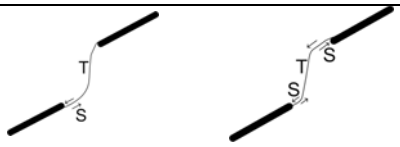	One or more type 2 **S** crack(s) and type 2 **T** crack segments between inner flaw tips
6	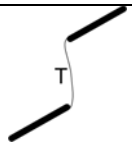	Type 2 **T** crack(s). There may be occasional short **S** segments present along the coalescence crack.
7		Type 1 **T** crack(s)
8		Flaw tips of the same side linked up by **T** crack(s) not displaying wing appearance (crack type not classified). There may be occasional short **S** segments present along the coalescence crack.
9	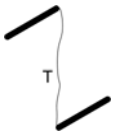	Type 3 **T** crack(s) linking right tip of the top flaw and left tip of the bottom flaw. There may be occasional short **S** segments present along the coalescence crack.

Figure 6.5 – Crack coalescence types. S = shear, T = tensile.

Here is a brief description of the characteristics of the coalescence types shown in figure 6.5.

Category 1

This category consists of flaw pairs without coalescence. Cracks of various types (mostly vertical or steeply-inclined) initiate from the flaw tips, but no coalescence occurs between them.

Category 2

This category refers to coalescence processes which occur in an indirect manner. Indirect coalescence usually occurs at or after the specimen maximum stress is reached in the loading tests. In contrast, the coalescence processes in all the remaining categories belong to direct manner. Indirect and direct coalescence processes are characterized by the following properties.

	Indirect coalescence	**Direct coalescence**
Crack coalescence category	2	3 to 9
Number of coalescence cracks involved	Must be two or more	Can be one or more
Nature of coalescence cracks	Always inclined, steeply inclined or vertical	Cracks of various orientations are possible
Location of coalescence (figure 6.6)	Slightly outside the central bridging region (at a significant distance from the reference line which links up the inner flaw tips). See figure 6.6.	Within the central bridging region (close to the reference line which links up the inner flaw tips). See figure 6.6.
Time of coalescence	At or after the specimen maximum stress is reached	Before or at the specimen maximum stress is reached

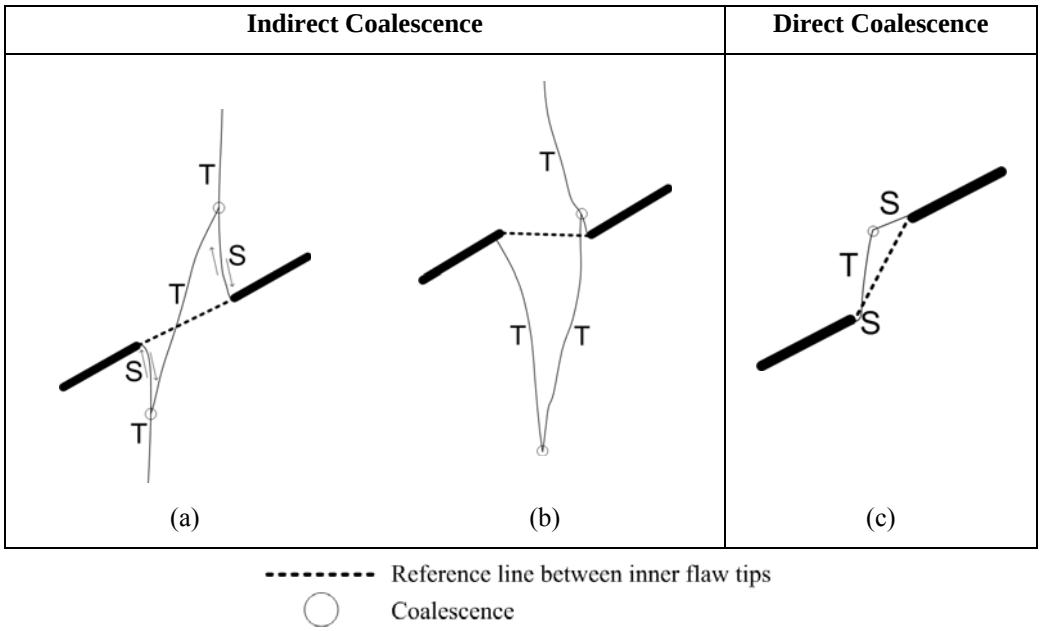

Figure 6.6 – (a, b) Coalescence points far away from the reference line for indirect coalescence, (c) coalescence point close to reference line for direct coalescence.

Category 3

In this category, the inner flaw tips are linked up either by **one type 2 shear crack** or **two type 2 shear cracks** which have independently initiated from the flaw tips earlier. These coalescence cracks are coplanar with the pre-existing flaws.

Category 4

In this category, the inner flaw tips are linked up either by **one type 1 shear crack** or **two type 1 shear cracks** which have independently initiated from the flaw tips earlier. These coalescence cracks are usually inclined at an angle with the pre-existing flaws.

Category 5

In this category, the inner flaw tips are linked up by a generally 'S' shaped crack consisting of one continuous crack or multiple individual crack segments. The crack segments adjacent to the flaw tips are usually shear crack which are coplanar with the pre-existing flaws (**type 2 shear cracks**), while the segments in the central bridging region are usually steeply-inclined **type 2 tensile cracks**.

Category 6

In this category, the inner flaw tips are linked up by either **one type 2 tensile crack** or **two type 2 tensile cracks** which have independently initiated from the flaw tips earlier.

Category 7

In this category, the two pre-existing flaws are linked up by a **type 1 tensile crack** (tensile wing crack). Depending on the flaw pair geometry, the coalescence crack can initiate from the tip of one flaw and propagate towards the face of the other flaw at a distance from the flaw tip, or it can initiate from the face of one flaw at a distance from the flaw tip and propagate towards the tip of the other flaw.

Category 8

In this category, flaw tips of the same side of the two pre-existing flaws are linked up by a curvilinear crack dominantly of **tensile** nature. Occasional short shear segments could be observed along this coalescence crack. Note that this crack curves in an opposite direction to that of the conventional wing crack, and is thus not regarded as a type 1 tensile crack (tensile wing crack).

Category 9

In this category, the right tip of the top flaw and the left tip of the bottom flaw are linked up by a **type 3 tensile crack**. This crack either initiates as a single continuous crack or forms due to the linkage of multiple short crack segments initiated earlier. Occasional short shear segments are present along this coalescence crack.

6.3 Coalescence behavior in gypsum

In this section, the coalescence behavior of flaw pairs in gypsum with ligament length "2a" is first described, and is then followed by those with longer ligament length "4a".

6.3.1 Coplanar flaws separated by '2a'

Details of the fracturing and coalescence behavior of the coplanar flaws with ligament length "2a" are presented in Appendix H and summarized in table 6.2 according to flaw geometries. In all specimens, tensile wing cracks (TWCs, type 1 tensile cracks) were always the first cracks to initiate, but they were not the coalescence cracks.

Flaw inclination angle β (^{o})	**First cracks appeared**	**Coalescence cracks**
0	Tensile wing cracks **(type 1 T cracks)**	- in 2/3 specimens, **no** coalescence - in 1/3 specimen, a **type 1 S crack** coalesced with another **inner tip crack** which consisted of **T** and **S** segments
30		**Type 2 S crack** linking up the inner flaw tips
45		Stepwise crack which consisted of multiple **S** and **T** segments linking up inner flaw tips (S-T, S-T-S or S-T-S-T-S)
60		"S" shaped crack which consisted of **S** segments adjacent to flaw tips and central vertical **T** segment linking up inner flaw tips (S-T-S)
75		

Table 6.2 – Summary of coalescence behavior of coplanar flaws in gypsum with '2a' bridging length. S = shear, T = tensile.

The coalescence behavior varies with the flaw inclination angle β (figure 6.7). For horizontal flaw pairs), coalescence was absent in two out of the three tested specimens. In these two specimens, multiple steep **type 2 tensile cracks** and **mixed tensile-shear cracks** developed from the flaw tips and did not coalesce. In the remaining one specimen with $\beta = 0^o$ where coalescence occurred, it was achieved in an **indirect** manner – linkage of two steep cracks independently initiated from the inner flaw tips.

In contrast, coalescence occurred in all specimens with larger flaw inclination angles (30^o, 45^o, 60^o, 75^o) and it was achieved in a **direct** manner – linkage of the inner flaw tips by a continuous generally S-shaped single crack in the central bridging region. See further discussion below.

The coalescence crack for $\beta = 30^o$ was dominantly of a shear nature, while that for larger flaw inclination angles (45^o, 60^o, 75^o) typically consisted of a central vertical or steeply-inclined tensile segment and shear segments adjacent to the two inner flaw tips. Notice also that in one specimen (2a-45-0-B), a shear segment was only observed adjacent to one of the two inner flaw tips, but absent at the other tip.

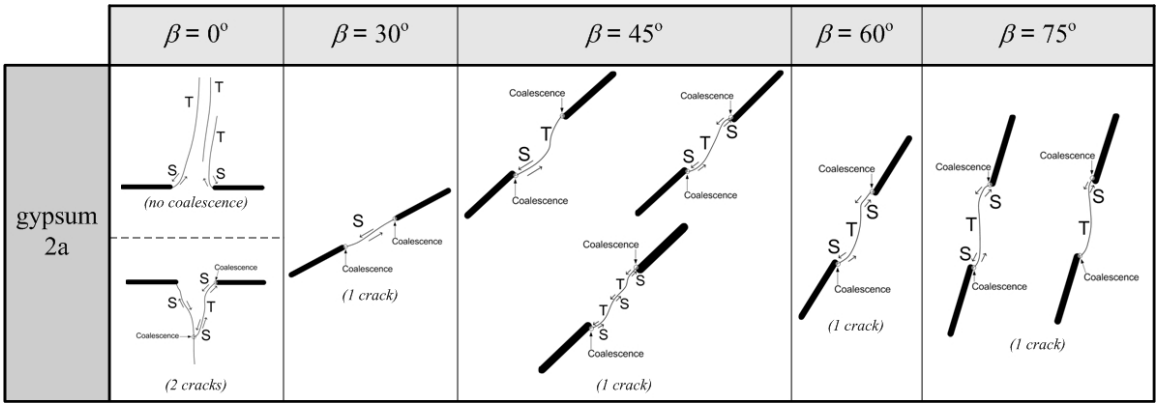

Figure 6.7 – Schematic illustration of the coalescence behavior of coplanar flaws in gypsum with '2a' ligament length.

6.3.2 Stepped flaws separated by '2a'

Details of the fracturing and coalescence behavior of the stepped flaws with ligament length "2a" and flaw inclination angle 30^o are presented in Appendix I and summarized in table 6.3 according to flaw geometries. In all specimens, tensile wing cracks (TWCs, **type 1 tensile cracks)** were always the first cracks to initiate.

Bridging angle α (°)	First cracks appeared	Coalescence cracks
-60	Tensile wing cracks (**type 1 tensile cracks**)	- In 1/4 specimens, **no coalescence** - In 3/4 specimens, a coalescence crack linked up one inner flaw tip and a crack initiated from another flaw tip (**indirect coalescence**)
-30		- In 1/4 specimens, **no coalescence** - In 2/4 specimens, two inner inclined tip cracks coalesced - In 1/4 specimens, a third crack (**S**) linked up two inner tips cracks
0		- **Type 2 S crack** linking up the inner flaw tips

30		- Coalescence occurred to link up the two inner flaw tips
		- In 3/5 specimens, the coalescence crack was a single coalescence crack consisting of multiple crack segments (**S-T** or **S-T-S**).
		- In 2/5 specimens, 2 cracks took part in coalescence :
		  - Specimen 2a-30-30-C: The tip of a new crack initiating from an inner flaw tip coalesced with the tip of another new crack initiating independently from the other inner flaw tip
		  - Specimen 2a-30-30-F: Two **mixed T-S cracks** (E & E') initiated independently from the two inner flaw tips. Coalescence occurred between the tip of crack E and the middle segment of crack E', and between the tip of crack E' and the middle segment of crack E.

60		- Coalescence occurred to link up the inner flaw tips - In 4/6 specimens, the coalescence crack was a single coalescence crack consisting of multiple crack segments (**S-T** or **S-T-S**). - In 1/6 specimens, a **type 2 T crack** coalesced with a **type 2 S crack**. - In 1/6 specimens, 3 cracks were involved: two cracks (**mixed T-S crack** & **type 2 T crack**) initiated independently from the two inner flaw tips. Coalescence occurred between these cracks by a third crack (an inclined **S** crack).
90		- A tensile wing crack (**type 1 T crack**) linked up the inner flaw tips
120		- Tensile wing cracks (**type 1 T cracks**) linked up the inner tip of one flaw and the middle section of the other flaw

Table 6.3 – Summary of coalescence behavior of stepped flaws in gypsum with flaw inclination angle 30° and '2a' bridging length. S = shear, T = tensile.

The coalescence behavior varies with the bridging angle α in this series (figure 6.8). The coalescence behavior for multiple specimens with the same flaw geometry with negative bridging angles (figure 6.8 a) was observed to be far less consistent than those with positive bridging angles (figures 6.8 b & c).

(a)

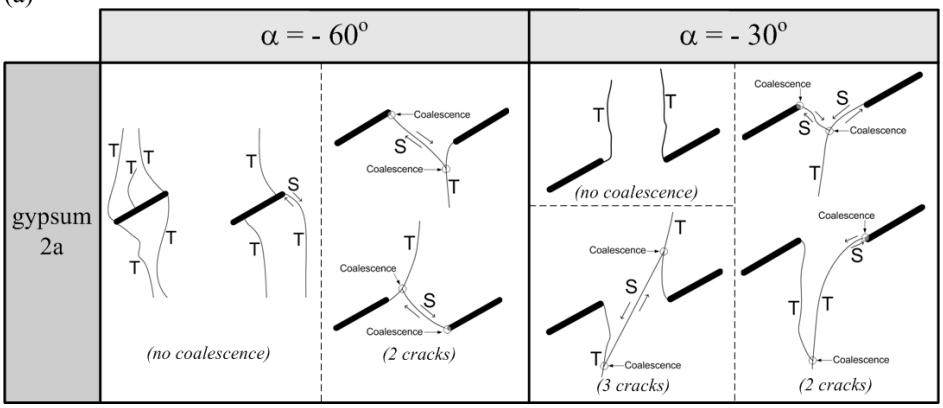

(b)

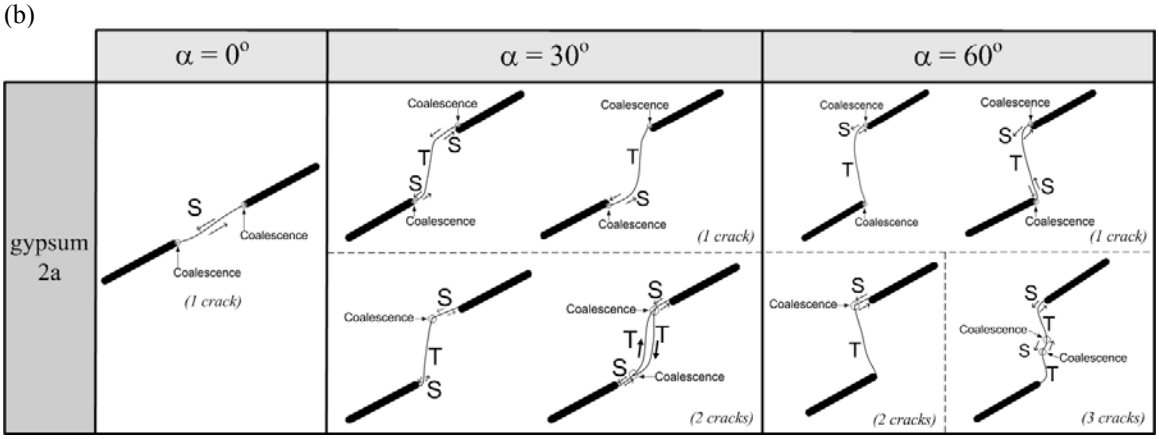

(c)

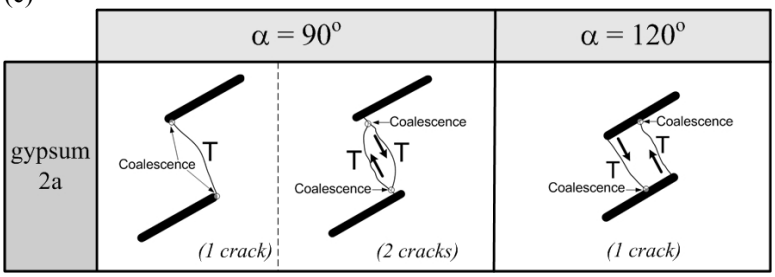

Figure 6.8 – Schematic illustration of the coalescence behavior of stepped flaws in gypsum with flaw inclination angle 30° and '2a' bridging length.

As shown in the sketches (figure 6.8 a), no coalescence occurred in certain specimens with negative bridging angles (α = -60°, -30°). In these specimens, multiple tensile wing cracks and/or steeply-inclined cracks simply initiated from the flaw tips but did not coalesce. In other specimens with negative bridging angles (α = -60°, -30°) where coalescence occurred, coalescence was observed to be achieved in an **indirect** manner – linkage of two (figure 6.9A) or three cracks (figure 6.9B) which had independently initiated from the inner flaw tips. In figure 6.9A, the **tip** of a new crack (**S**) coalesced with the **face** of the other new crack (**T**). In figure 6.9B, a shear crack linked up two previously initiated tensile cracks from flaw tips.

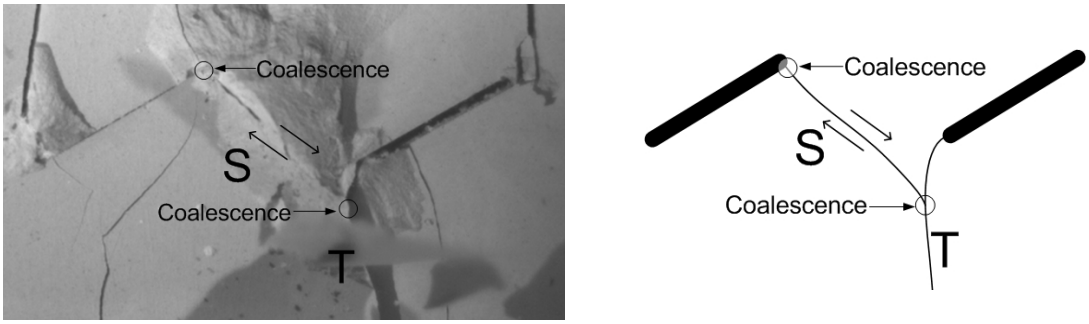

(a) (b)

Figure 6.9A – A new shear crack (S) links up one inner flaw tip and the face of the other new tensile crack (T). (a) high speed image, (b) sketch of the pre-existing flaws and coalescence cracks.

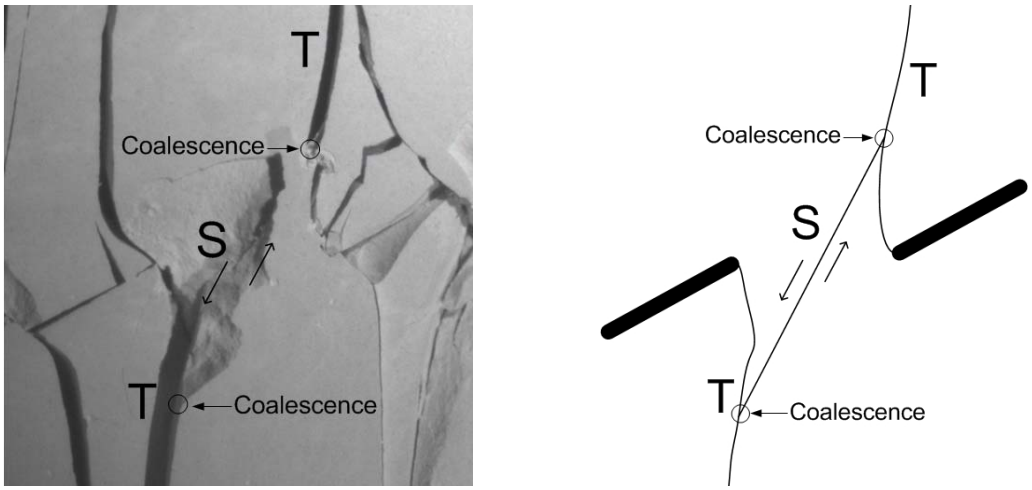

(a) (b)

Figure 6.9B – A new shear crack (S) links up two tensile cracks (T) independently initiated from the inner flaw tips. (a) high speed image, (b) sketch of the pre-existing flaws and coalescence cracks.

In contrast to the negative bridging angles, for positive bridging angles (α = 0°, 30°, 60°, 90° and 120°), coalescence was achieved in a **direct** manner – the two pre-existing flaws were linked up directly by a continuous crack which consisted of either one or multiple crack segments in the **central bridging region** (figures 6.8 b and c). For coalescence involving multiple cracks, the **tip** of an individual new crack coalesced with the **tip** of the other new crack, in contrast to negative bridging angles in which the **tip** of a new crack linked up the **face** of another new crack.

The sketches shown in figures 6.8 b and c also demonstrate a clear trend of variation of coalescence behavior with bridging angle. In general, small bridging angle (α = 0°) favored the formation of **shear** coalescence cracks, while large bridging angles (α = 90° & 120°) favored the formation of **tensile** coalescence cracks. For intermediate bridging angles (α = 30° & 60°), coalescence cracks of both **tensile** and **shear** segments were observed. See further description below.

For **coplanar flaws (α = 0°)**, a coalescence shear crack (**type 2 shear crack**) linked up the two inner flaw tips in the central bridging region. The sense of shearing is sinistral as observed from the front face of the specimen.

For **intermediate bridging angles (α = 30°, 60°)**, coalescence between the two inner flaw tips in the central bridging region was achieved by one, two or even three multiple crack segments. In all cases, the central crack segments were usually vertical or steeply-inclined **tensile** cracks, while the segments adjacent to inner flaw tips were usually **shear** cracks.

For **large bridging angles (α = 90°, 120°)**, coalescence was achieved by tensile wing cracks (TWCs, **type 1 tensile cracks**). For α = 90°, the coalescence crack linked up the inner flaw tips, while for α = 120°, the coalescence crack linked up the tip of one flaw and the face of the other flaw.

6.3.3 Coplanar flaws separated by 4a

Details of the fracturing and coalescence behavior of the coplanar flaws with ligament length "4a" are presented in Appendix J and summarized in table 6.4 according to flaw geometries. In all specimens, tensile wing cracks (TWCs, type 1 tensile cracks) were always the first cracks to initiate, but they were not the coalescence cracks.

Flaw inclination angle β (^{o})	**First cracks appeared**	**Coalescence cracks**
0	Tensile wing cracks **(type 1 T cracks)**	- In 2/4 specimens, **no coalescence** - In 2/4 specimen, two inclined cracks initiated from the inner flaw tips coalesced.
30		- In 2/5 specimens, **no coalescence** - In 3/5 specimen, two cracks (**type 1 S cracks** & **mixed T-S cracks**) initiated independently from the inner flaw tips coalesced
45		**Type 2 S crack** coplanar with the pre-existing flaw linked up the inner flaw tips
60		
75		"S" shaped crack which consisted of **S** segments adjacent to flaw tips and central vertical **T** segment linking up inner flaw tips (S-T-S)

Table 6.4 – Summary of coalescence behavior of coplanar flaws in gypsum with '4a' bridging length. S = shear, T = tensile.

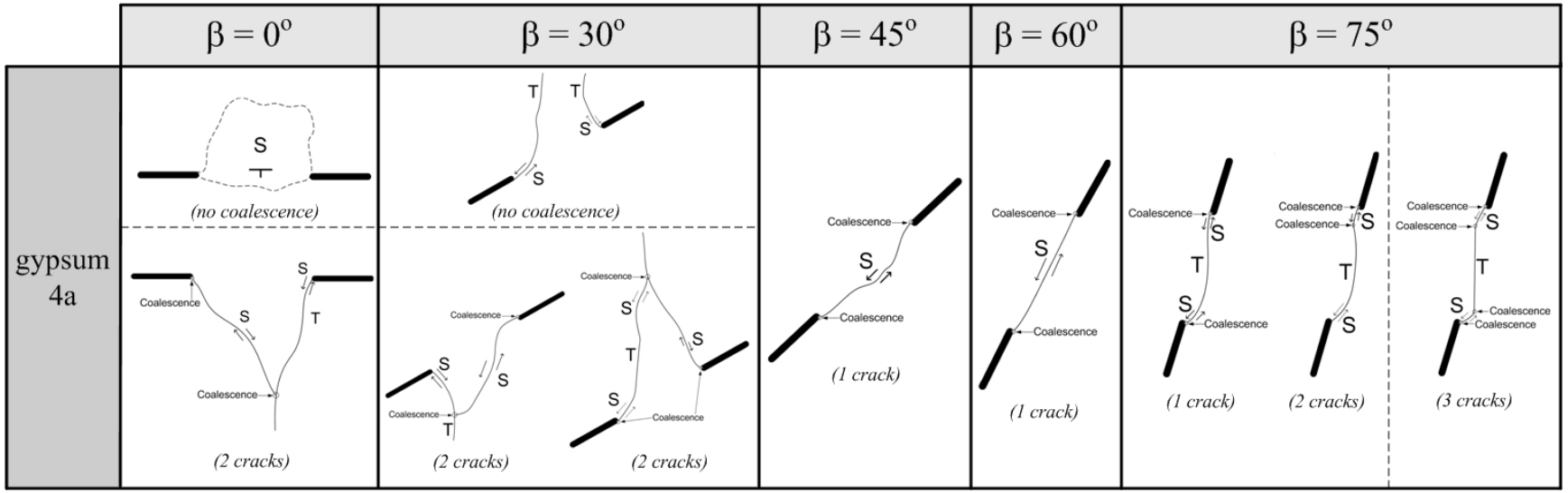

Figure 6.10 – Schematic illustration of the coalescence behavior of coplanar flaws in gypsum with '4a' ligament length.

The coalescence behavior varies with the flaw inclination angle β (figure 6.10). For small inclination angles β, coalescence only occurred in two out of the four tested specimens with $\beta = 0^o$ and three out of the five specimens with $\beta = 30^o$. The coalescence occurred in these two geometries was similarly achieved in an **indirect** manner – linkage of two inclined to steeply-inclined cracks independently initiated from the inner flaw tips. One of the cracks was usually a **shear crack** and the other was usually of mixed **tensile-shear** nature.

In contrast, the coalescence occurring for larger flaw inclination angles ($\beta = 45^o$, 60^o, 75^o) was achieved in a **direct** manner in the central bridging region.

The coalescence crack for $\beta = 45^o$ and 60^o was dominantly of a **shear** nature. The initiation of the coalescence shear was often associated with overlying localized surface spalling.

The coalescence crack for $\beta = 75^o$ was generally of a **shear-tensile-shear (S-T-S)** pattern. Variation occurred among the tested specimens with regard to the number of distinguishable individual crack segments involved in the coalescence:

One crack - In specimen 4a-75-0-C, the coalescence crack was a 'S' shaped single crack consisting of **S-T-S** segments.

Two cracks – In specimens 4a-75-0-D and 4a-75-0-F, a **type 2 shear crack** (coplanar) coalesced with a **mixed tensile-shear** crack.

Three cracks – In specimen 4a-75-0-A, two **type 2 shear cracks** (coplanar) initiated independently from the two inner flaw tips linked up a vertical tensile crack in the central bridging region.

6.3.4 Stepped flaws separated by 4a

Details of the fracturing and coalescence behavior of the stepped flaws with ligament length "4a" and flaw inclination angle 30^{o} are presented in Appendix K and summarized in table 6.5 according to flaw geometries. In all specimens, tensile wing cracks (TWCs, type 1 tensile cracks) were always the first cracks to initiate.

Bridging angle α (°)	First cracks appeared	Coalescence cracks
-60	Tensile wing cracks (**type 1 T cracks**)	- **No coalescence** in 1/3 specimens - Coalescence in 2/3 specimens : an inclined **type 1 S crack** linked up one inner flaw tip and the face of a steeply-inclined **type 2 T crack** or **mixed T-S crack** initiated earlier from the other inner flaw tip
-30		- **No coalescence**
0		- In 2/4 specimens, **no coalescence** - In 2/4 specimen, two inclined cracks initiated from the inner flaw tips coalesced
30		- The two inner flaw tips were linked up by a continuous 'S' shaped crack consisting of single or multiple crack segments. - In 1/4 specimens, a single crack consisting of **S-T-S** segments linked up the inner flaw tips. - In 3/4 specimens, two or three cracks linked up to form the coalescence crack. The segments adjacent to flaw tips were **S** and the vertical segment in the central bridging region was **T**
60		- The two inner flaw tips were linked up by a continuous 'S' shaped crack consisting of **S** segments adjacent to inner flaw tips and vertical **T** segment in the middle - In 1/3 specimens, the coalescence crack was a single crack consisting of **S-T-S** segments - In 1/3 specimens, two cracks were involved in which a **coplanar S crack** (**type 2 S crack**) linked up a **type 2 T crack** initiated earlier from the other inner flaw tip - In 1/3 specimens, four crack segments were linked up for coalescence
90		- Single **type 1 T crack** linked up the tips of the same side (left or right) of the two pre-existing flaws
120		- In 1/4 specimens, a **type 1 T crack** propagated from right tip of the bottom flaw upwards to link up the right tip of the top flaw. Similarly, another **type 1 T crack** propagated from the left tip of the top flaw downwards to link up the left tip of the bottom flaw - In 3/4 specimens, a single coalescence crack consisting of **S-T-S** crack segments linked up the right tip of the top flaw and the left tip of the bottom flaw

Table 6.5 – Summary of coalescence behavior of stepped flaws in gypsum with flaw inclination angle 30° and '4a' bridging length. S = shear, T = tensile.

The coalescence behavior varies with the bridging angle α in this series (figure 6.11). The coalescence behavior for multiple specimens with the same flaw geometry with negative and zero bridging angles was observed to be far less consistent than those for positive bridging angles.

(a)

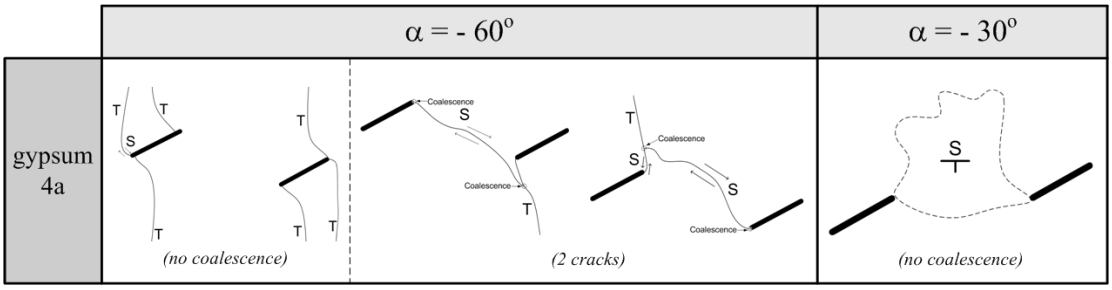

(b)

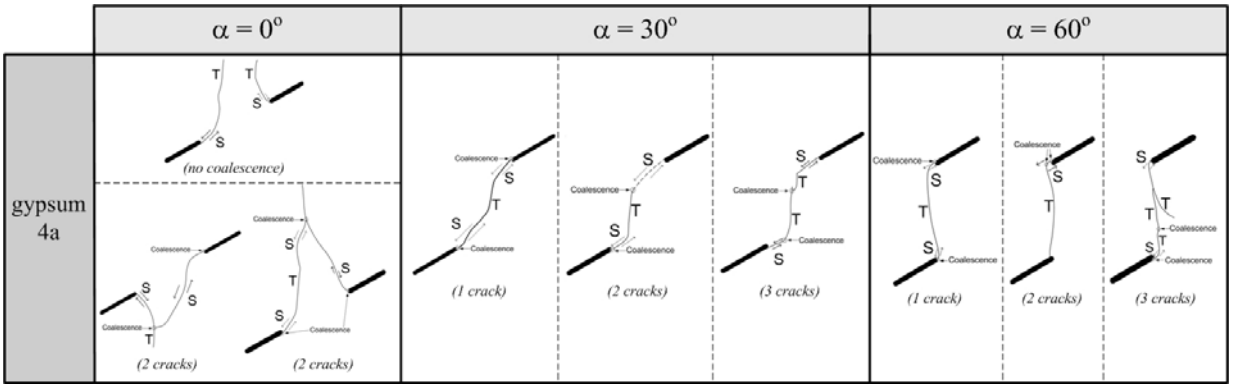

(c)

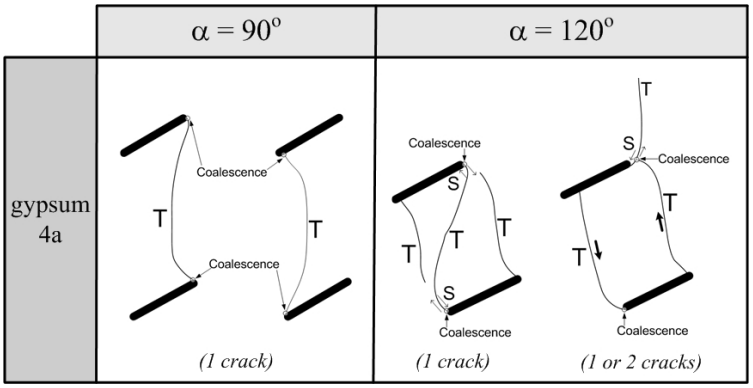

Figure 6.11 – Schematic illustration of the coalescence behavior of stepped flaws in gypsum with flaw inclination angle 30° and '4a' bridging length.

As observed in the sketches presented in figure 6.11a, no coalescence occurred in specimens with bridging angles α = -30^o and certain specimens with bridging angles α = -60^o and 0^o.

In all the tested specimens with α = -30^o, at the end of the loading process, an inclined shear crack which dipped out of the specimen front face in the central bridging region was observed to have developed (figure 6.12). The development of these shear cracks in this group of specimens took place well after the maximum stress was reached.

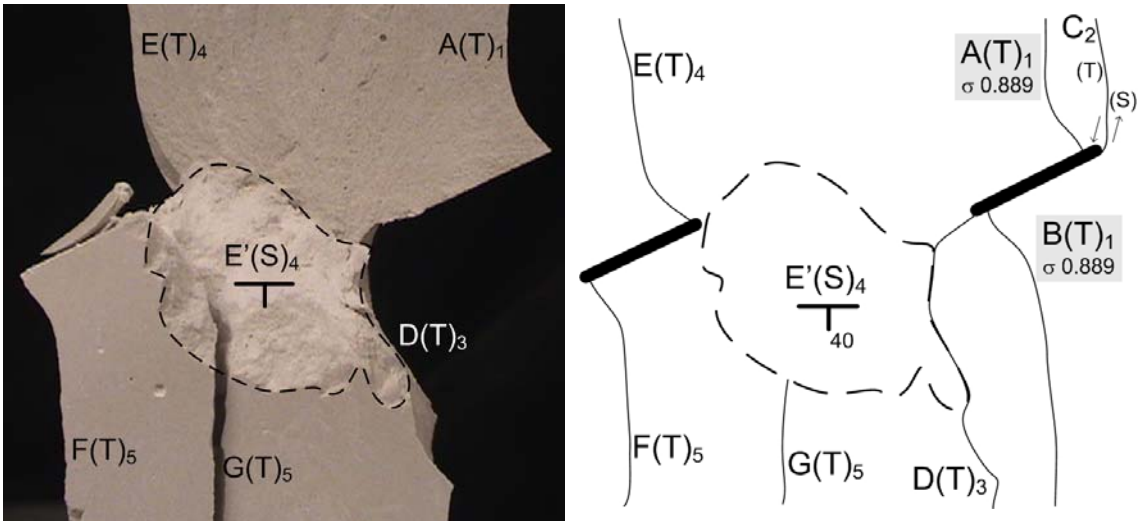

(a) (b)

Figure 6.12 – A shear crack E' dipped out at the specimen front face (a) digital camera image, (b) sketch of the pre-existing flaws and other cracks. Note that the traces of cracks B and C are not observable in figure (a) because of the right edge of the specimen had collapsed and detached from the main part of the specimen. The specimen number is 4a-30-(-30)-C.

In those specimens with bridging angles α = -60^o and 0^o where coalescence did not occur, multiple tensile wing cracks and/or steeply-inclined cracks simply initiated from the flaw tips but did not coalesce (figures 6.11 a & b).

In other specimens with bridging angles α = -60^o and 0^o where coalescence occurred, coalescence was observed to be achieved in an **indirect** manner – linkage of two cracks which independently initiated from the inner flaw tips. In one typical example as shown in figure 6.13, the **tip** of a new crack **S** coalesced with the **face** of the other new crack **S-T**.

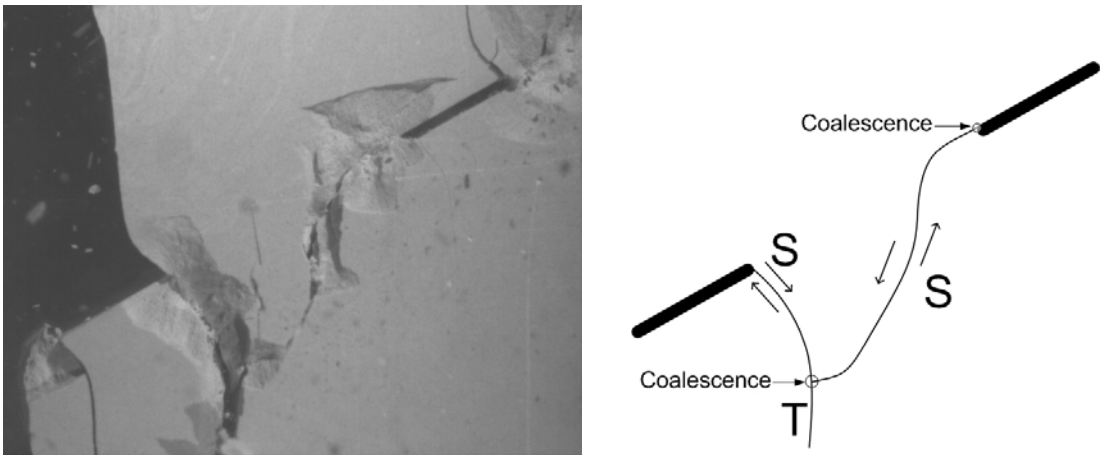

(a) (b)

Figure 6.13 – A new shear crack (S) links up the right inner flaw tip and the face of the other new mixed tensile-shear crack (T-S). (a) high speed image, (b) sketch of the pre-existing flaws and coalescence cracks.

In contrast to the negative bridging angles, for positive bridging angles (α = 30^o, 60^o, 90^o and 120^o), coalescence was achieved in a **direct** manner – the two pre-existing flaws were linked up directly by a continuous crack which consisted of either one or multiple crack segments in the **central bridging region** (figures 6.11 b and c). For coalescence involving multiple cracks, the **tip** of an individual new crack coalesced with the **tip** of the other new crack, in contrast to negative bridging angles in which the **tip** of a new crack linked up the **face** of another new crack. See further description below.

For **intermediate bridging angles (α = 30^o, 60^o)**, coalescence between the two inner flaw tips in the central bridging region was achieved by one, two or even three multiple crack segments. In all cases, the central crack segments were usually vertical or steeply-

inclined **tensile cracks**, while the segments adjacent to inner flaw tips were usually **shear cracks**.

For **large bridging angles (α = 90°, 120°)**, coalescence was achieved by tensile wing cracks (TWCs, type 1 tensile cracks) which usually linked up the tips of the same side of the two pre-existing flaws (figure 6.11 c). A completely different coalescence pattern was also observed for $\alpha = 120^{o}$, in which a single coalescence crack consisting of **shear-tensile-shear (S-T-S)** crack segments linked up the right tip of the top flaw and the left tip of the bottom flaw (figure 6.14).

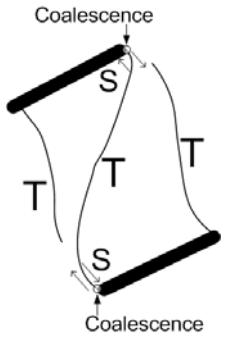

Figure 6.14 – Crack coalescence achieved by a S-T-S crack..

6.3.5 Influence of ligament length on coalescence in gypsum

In the previous sections, the fracturing and coalescence behavior of each series in gypsum has been individually discussed. In this section, discussion is focused on the influence of ligament length on coalescence patterns in gypsum.

6.3.5.1 Coplanar flaws

The coalescence patterns observed for coplanar flaws with ligament length '2a' and '4a' previously shown in figures 6.7 and 6.10 are summarized in figure 6.15 below. In both series (ligament lengths '2a' and '4a'), the coalescence behavior also varies with the flaw inclination angle β. The general trend is summarized in table 6.6.

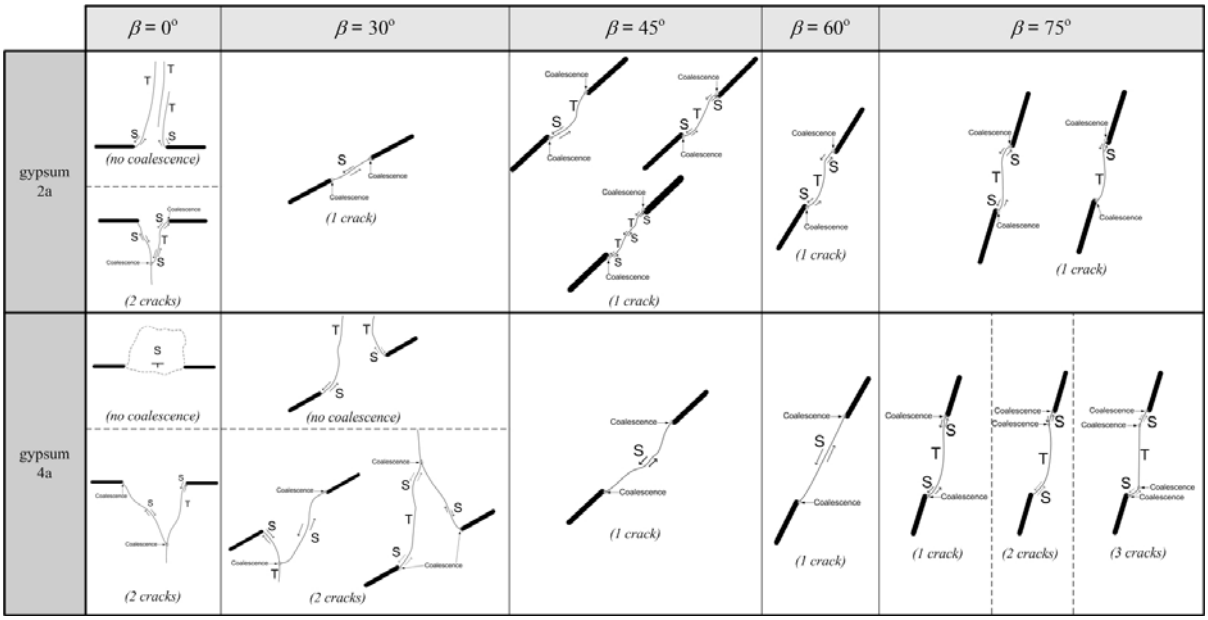

Figure 6.15 – Schematic illustration of the coalescence behavior of coplanar flaws in gypsum with '2a' and '4a' ligament length.

Category	**Flaw inclination angles β (°)**		**Coalescence Behavior**
	Ligament length 2a	Ligament length 4a	
1	0	0, 30	**No** coalescence
2	0	0, 30	**Indirect** coalescence
3	30	45, 60	Direct coalescence by **type 2 S cracks** between inner flaw tips
5	45, 60, 75	75	Direct coalescence by a generally **S-T-S** 'S' shaped crack consisting of only one or more crack segments

Table 6.6 – Generalized coalescence behavior of coplanar flaws in gypsum with '2a' and '4a' ligament length. S = shear, T = tensile.

Coalescence behavior of both **category 1** (no coalescence) and **category 2** (indirect coalescence) were observed in specimens of small flaw inclination angles ($\beta = 0^o$ for 2a, $\beta = 0^o$, 30^o for 4a). For the **indirect** coalescence, one of the coalescence cracks was usually a shear crack and the other was usually of mixed tensile-shear nature.

In contrast, the coalescence occurring in **categories 3 and 5** was achieved in a **direct** manner. The two inner flaw tips were linked up directly by a continuous crack which consisted of either one or more crack segments in the central bridging region.

In **category 3** of intermediate flaw inclination angles ($\beta = 30^o$ for 2a, $\beta = 45^o$, 60^o for 4a), the coalescence crack was dominantly a shear crack which linked up the two inner flaw tips. The initiation of the coalescence shear was often associated with overlying localized surface spalling.

In **category 5** of large flaw inclination angles ($\beta = 45^o$, 60^o, 75^o for 2a, $\beta = 75^o$ for 4a), the coalescence crack was generally of a shear-tensile-shear (S-T-S) pattern which linked up the inner flaw tips. The central crack segments were usually vertical or steeply-inclined **tensile cracks**, while the segments adjacent to inner flaw tips were usually **shear cracks**. Variation occurred among the tested specimens with regard to the number of distinguishable individual crack segments involved in the coalescence.

Notice that even though both series (ligament lengths '2a' and '4a') displayed a similar trend of variation of coalescence behavior with the flaw inclination angle β, the influence of ligament length on coalescence behavior is significant as reflected by the different boundaries between adjacent categories in the two series (table 6.6). For example, $\beta = 30^o$ belonged to **category 3** for ligament length **2a**, while it belonged to either **category 1 and category 2** for ligament length **4a** (figure 6.15). Physically speaking, wider separation between the inner flaw tips reduces the mutual influence/interaction between the flaws. It is thus not surprising to observe that coalescence always occurred in specimens with geometry 2a-30-0, but it was absent in some tested specimens with geometry 4a-30-0.

6.3.5.2 Stepped flaws

The coalescence patterns observed for stepped flaws with flaw inclination angle $\beta = 30^o$ and ligament length '2a' and '4a' previously shown in figures 6.8 and 6.11 are summarized in figure 6.16 below. In both series (ligament lengths '2a' and '4a'), the coalescence behavior also varies with the bridging angle α. The general trend is summarized in table 6.7.

(a)

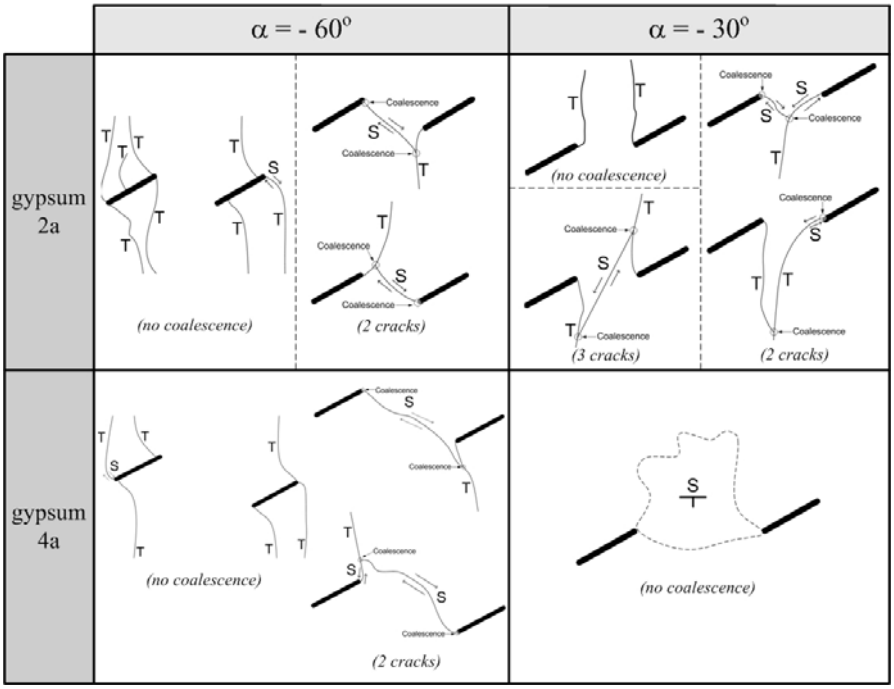

Figure 6.16 – Schematic illustration of the coalescence behavior of stepped flaws in gypsum with flaw inclination angle 30° and '2a' and '4a' ligament length.

(b)

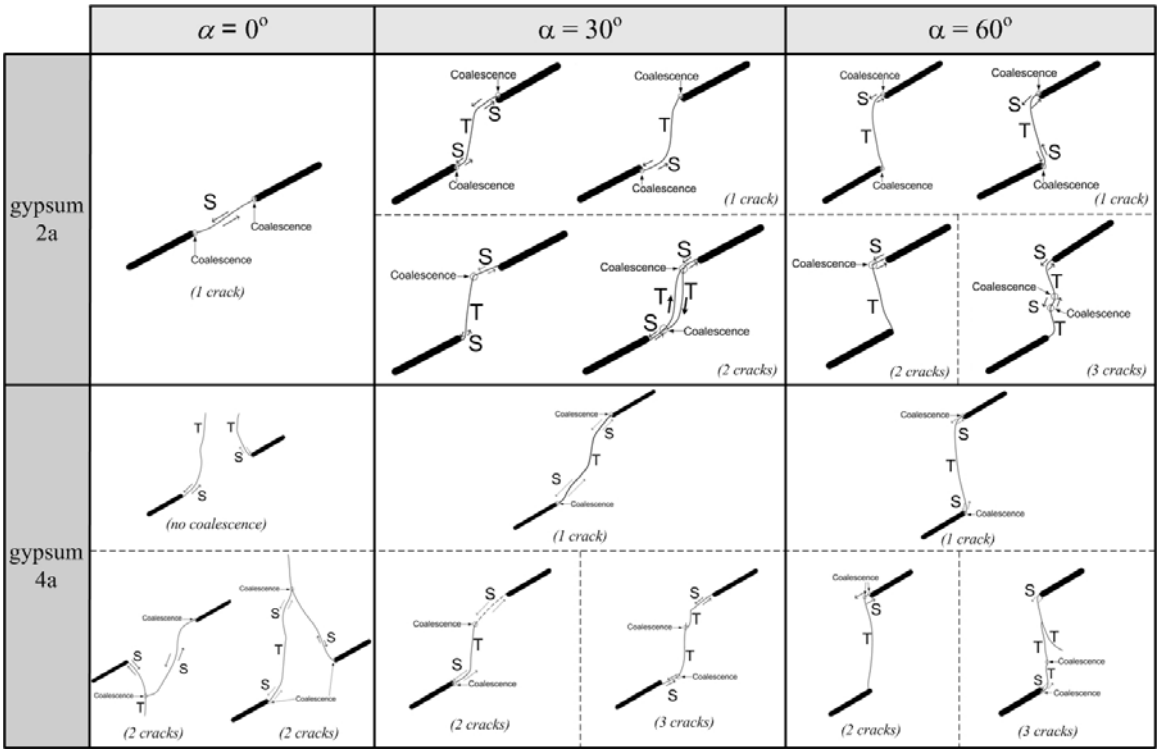

(c)

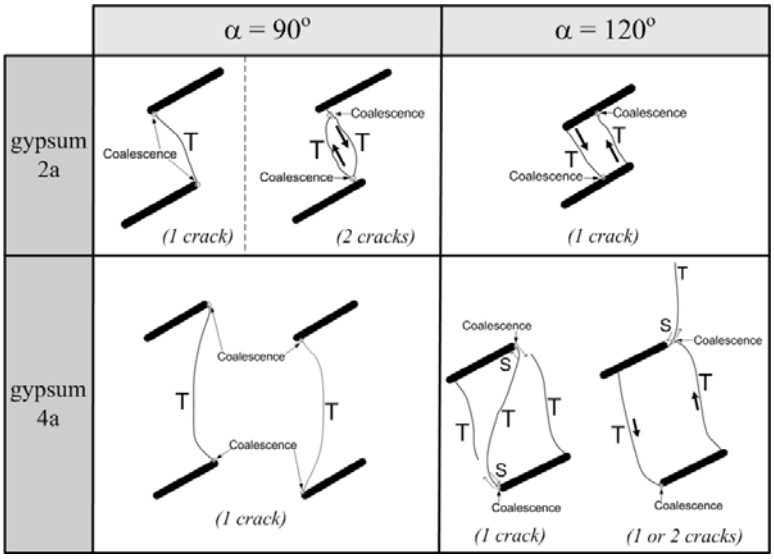

Figure 6.16 – Schematic illustration of the coalescence behavior of stepped flaws in gypsum with flaw inclination angle 30° and '2a' and '4a' ligament length (continued).

Category	Bridging angles α (^{o})		Coalescence Behavior
	Ligament length 2a	Ligament length 4a	
1	-60, -30	-60, -30, 0	**No** coalescence
2	-60, -30	-60, 0	**Indirect** coalescence
3	0	-	Direct coalescence by **type 2 S cracks** between inner flaw tips
5	30, 60	30, 60	Direct coalescence by a generally **S-T-S** 'S' shaped crack consisting of only one or more crack segments
7	90, 120	90, 120	Direct coalescence by **T** wing cracks

Table 6.7 – Generalized coalescence behavior of stepped flaws in gypsum with '2a' and '4a' ligament length. S = shear, T = tensile.

Coalescence behavior of **category 1** (no coalescence) was observed in specimens of negative and zero flaw inclination angles (α = -60^o, -30^o for 2a, α = -60^o, -30^o, 0^o for 4a). Coalescence behavior of **category 2** (indirect coalescence) was similarly observed in specimens with the same bridging angles, except for α = -30^o (table 6.7). For the **indirect** coalescence, one of the coalescence cracks was usually a **shear** crack and the other crack was usually of **mixed tensile-shear** nature. Note also that the coalescence patterns are more varied for the specimens with α = -30^o for 2a. In one particular specimen, three cracks were involved (figure 6.9B which is reproduced below again). In this specimen, a shear crack initiated to link up two previously developed tensile cracks initiated individually from the inner flaw tips.

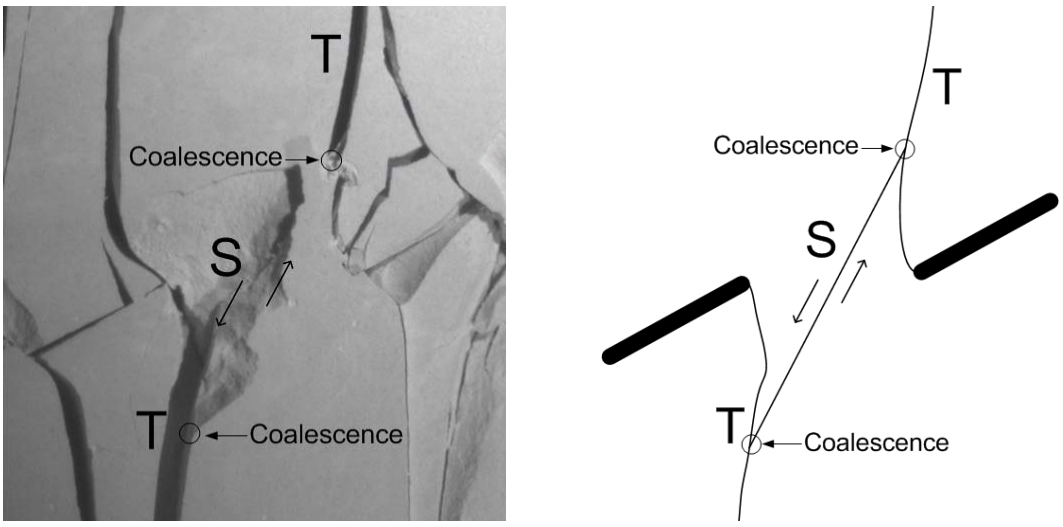

(a) (b)

Figure 6.9B – A new shear crack (S) links up two tensile cracks (T) independently initiated from the inner flaw tips. (a) high speed image, (b) sketch of the pre-existing flaws and coalescence cracks.

In contrast, the coalescence occurring in categories 2, 3 and 4 was achieved by a **direct** manner. The two inner flaw tips were linked up directly by a continuous crack which consisted of either one or multipe crack segments in the central bridging region.

In **category 3** ($\alpha = 0^o$ for 2a, but not for 4a), the coalescence crack which linked up the two inner flaw tips was dominantly of **shear** nature (table 6.7). The initiation of the coalescence shear crack was often associated with the overlying localized surface spalling.

In **category 5** ($\alpha = 30^o$, 60^o for both 2a and 4a), the coalescence crack which linked up the inner flaw tips was generally of a **shear-tensile-shear (S-T-S)** pattern (table 6.7). The central crack segments were usually vertical or steeply-inclined **tensile cracks**, while the segments adjacent to inner flaw tips were usually **shear cracks**. Differences occurred among the tested specimens with regard to the number of distinguishable individual crack segments involved in the coalescence.

In **category 7** (α = 90^o, 120^o for both 2a and 4a), coalescence between the two pre-existing flaws was mainly achieved by **tensile wing cracks** (TWCs, type 1 tensile cracks). See table 6.7. In this category, depending on the relative position between the two pre-existing flaws, the location of crack initiation and location of crack coalescence varied. In some specimens, the high speed camera was able to capture the propagation direction of the newly initiated cracks. Some of the determined propagation directions are indicated in figure 6.16c. It is interesting to note that a completely different coalescence pattern was also observed for α = 120^o with ligament length '4a', in which a single coalescence crack consisting of **shear-tensile-shear (S-T-S)** crack segments linked up the right tip of the top flaw and the left tip of the bottom flaw.

Notice that even though both series (ligament lengths '2a' and '4a') displayed a similar trend of variation of coalescence behavior with the flaw inclination angle β, the influence of the ligament length is significant as reflected from specimens with β = -30^o and 0^o. For example, coalescence was observed in some specimens with flaw geometry **2a**-30-(-30), but it was absent in those specimens with flaw geometry **4a**-30-(-30). Similarly, coalescence was observed in all specimens with flaw geometry **2a**-30-0, but it was absent in some specimens with flaw geometry **4a**-30-0. A wider separation between the inner flaw tips obviously reduces the mutual influence/interaction between the flaws for these geometries.

6.4 Coalescence behavior in Carrara Marble

Similar to gypsum in the previous section, coalescence behavior of flaw pairs in marble with ligament length "2a" is first described in this section, which is then followed by flaw pairs with ligament length "4a".

Before describing in detail the fracturing and coalescence behavior, it is noteworthy to mention that in all marble specimens, there was usually a development of white (very distinctive white color) patches, indicating the presence of process zones, prior to the

initiation of cracks. Some of these white patches developed early in the loading process, and later propagated (increased in length), widened and intensified in color with increased loading; while some of them appeared and propagated just before the specimen strength was reached. Although many of the white patches later developed into either shear cracks or tensile cracks in response to loading (white patches A and B in figure 6.9C), some of them still remained intact with no observable cracking (white patch C in figure 6.9C).

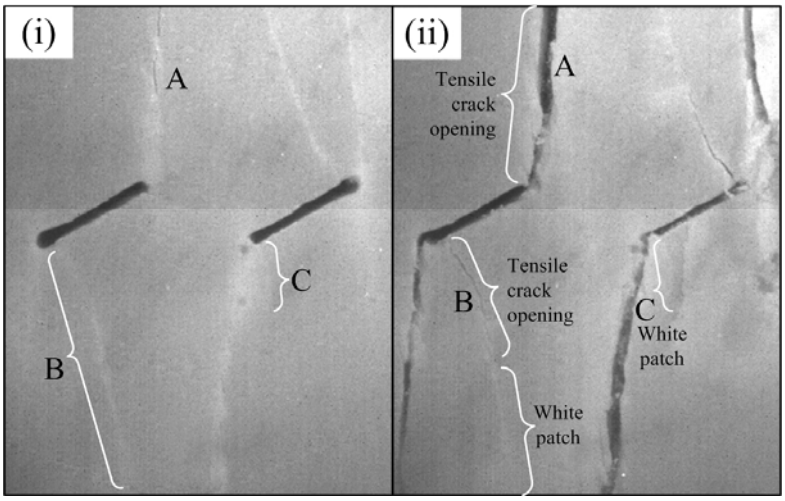

Figure 6.9C. (i) View of white patches in marble with incipient localized tensile cracking at the top segment of white patch A. (ii) As loading increased, complete tensile crack opening occurred along white patch A. Cracking occurred at the top segment of white patch B, but not at its bottom segment. No observable crack opening along white patch C. Specimen number is 2a-30-(-60)-A.

6.4.1 Coplanar flaws separated by 2a

Details of the fracturing and coalescence behavior of the coplanar flaws with ligament length "2a" are presented in Appendix L and summarized in table 6.8 according to flaw geometries.

Flaw inclination angle β (°)	First cracks appeared	Coalescence cracks
0	Inner tip **type 2 T cracks**	**No coalescence**
30	**Mixed T-S cracks**	An **inclined T crack** linking up the earlier developed inner tip **mixed T-S** cracks
45	**Type 2 T** and **mixed T-S cracks**	- In 1/3 specimens, no coalescence - In 1/3 specimens, a **type 2 S crack** linked up the inner flaw tips - In 1/3 specimens, a **mixed T-S crack** linked up a **type 2 T crack**
60	Inner tip **T** cracks almost coplanar with pre-existing flaws AND outer tip **type 2 T** cracks	**Inner tip T** cracks coplanar with pre-existing flaws coalesced
75		Multiple **inner tip T cracks** almost coplanar with pre-existing flaws coalesced

Table 6.8 – Summary of coalescence behavior of coplanar flaws in marble with '2a' ligament length.
S = shear, T = tensile.

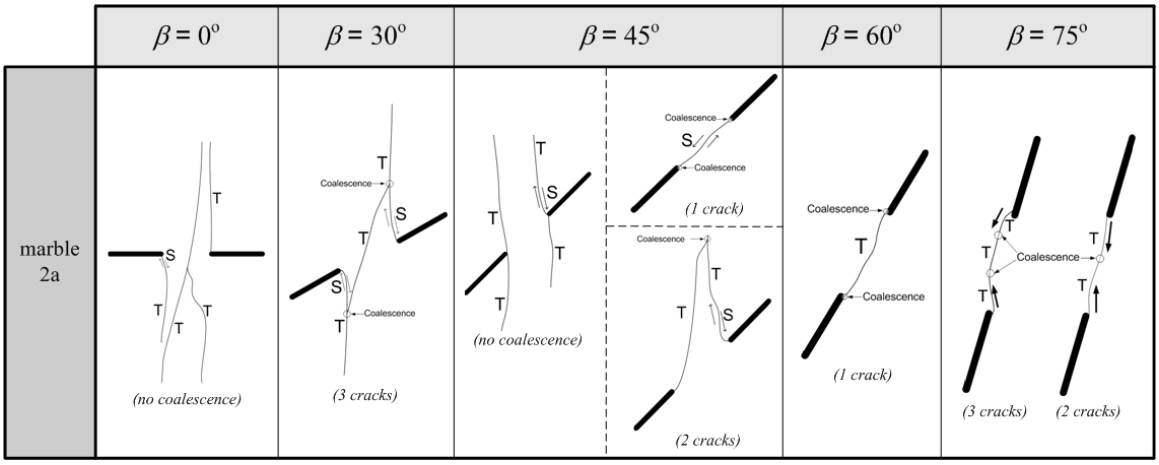

Figure 6.17 – Schematic illustration of the coalescence behavior of coplanar flaws in marble with '2a' ligament length.

In contrast to gypsum specimens in which tensile wing cracks (TWCs, type 1 tensile cracks) were always the first cracks to initiate in response to the uniaxial loading, TWCs were **NEVER** the first cracks to initiate in this series of marble specimens (table 6.8). The first cracks in marble were always **type 2 tensile cracks** and/or **mixed tensile-shear cracks** initiated from the flaw tips.

The coalescence behavior varies with the flaw inclination angle β (figure 6.17). See the description below.

For $\beta = 0^o$, no coalescence occurred. In these specimens, steeply-inclined to vertical cracks initiated from the flaw tips and additional steeply-inclined cracks initiated in the central bridging region, but no coalescence occurred between them.

For $\beta = 30^o$, coalescence occurred and was achieved in an **indirect** manner – linkage of two steeply-inclined mixed tensile-shear cracks which independently initiated earlier from the inner flaw tips by a **inclined tensile crack** (see figure 6.18).

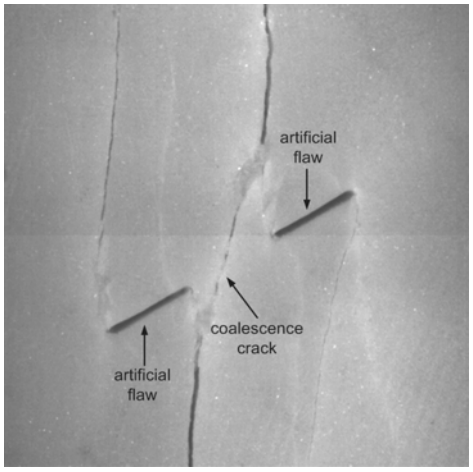

Figure 6.18– High speed image showing the development of an inclined coalescence crack in marble specimen with flaw geometry 2a-30-0.

The coalescence patterns were more varied for $\beta = 45^o$. In one specimen, no coalescence occurred. In one specimen, direct coalescence occurred by a **type 2 shear crack** which linked up the two inner flaw tips. In one specimen, indirect coalescence occurred by linkage of a **type 2 tensile crack** and a **mixed tensile-shear crack**.

For $\beta = 60^o$ and 75^o, coalescence was achieved in a **direct** manner – the two pre-existing flaws were linked up directly by a continuous crack which consisted of either one or multiple tensile cracks in the **central bridging region** (figure 6.19).

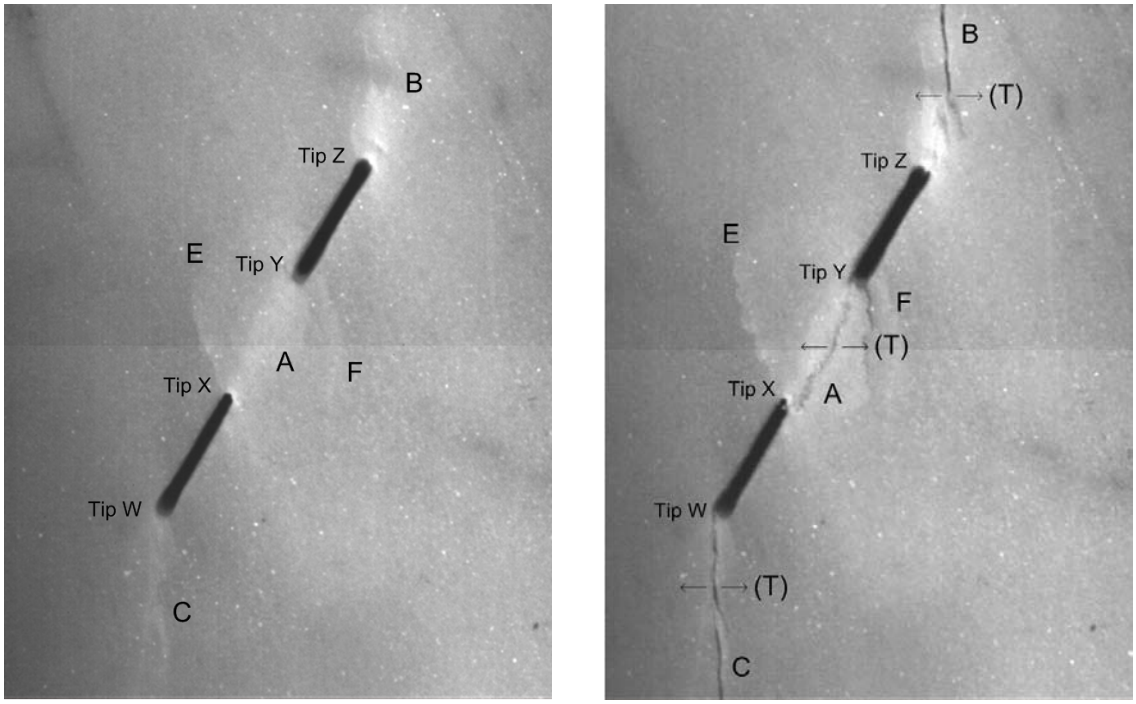

(a) High Speed Image # - 1482

(b) High Speed Image # - 1481

Figure 6.19– High speed images (a) before and (b) after the initiation of coalescence crack A in marble specimen 2a-60-0-A. The high speed camera frame rate is 2,000 pps. The time difference between this pair of consecutive images is thus 0.0005 seconds.

6.4.2 Stepped flaws separated by 2a

Details of the fracturing and coalescence behavior of the stepped flaws with ligament length "2a" and flaw inclination angle 30^o are presented in Appendix M and summarized in table 6.9 according to flaw geometries.

Bridging angle α (^{o})	**First cracks appeared**	**Coalescence cracks**
-60	**Type 2 T cracks** initiated from **inner flaw tips**	- In 1/2 specimens, **no coalescence** - In 1/2 specimens, an inclined **T crack** linking up two **type 2 T cracks** initiated independently from the two inner flaw tips
-30		- In 1/2 specimens, **no coalescence** - In 1/2 specimens, a steeply-inclined **T** inner tip crack coalesced with another steeply-inclined **T** inner tip crack
0	**Mixed T-S cracks**	An **inclined T crack** linking up the earlier developed inner tip **mixed T-S** cracks
30	**Outer tip** TWCs (in 1/2 specimens, the **coalescence S cracks** was also the first crack)	An inclined **S crack** (**type 1 S crack**) linking up the inner flaw tips
60	**Outer tip** TWCs (in 1/3 specimens, the **coalescence T crack** between the inner flaw tips was also the first crack)	A vertical **T crack** (**type 2 T crack**) linking up the inner flaw tips
90	- In 2/3 specimens, outer tip **TWCs** - In 1/3 specimens**,** steeply inclined **type 2 T cracks** initiated from outer flaw tips	Two symmetrical **TWCs** propagated independently from the face of one flaw to the tip of another flaw
120	- in 1/2 specimens, **TWCs** & **coalescence T crack** not displaying wing appearance - in 1/2 specimens, **TWC** which was also the coalescence crack	- In 1/2 specimens, a **TWC** propagated from the tip of one flaw to the face of the other flaw - In 1/2 specimens, a **T crack** curving in a different direction as compared to the TWC linked up the right tips of the top flaw and the bottom flaw

Table 6.9 – Summary of coalescence behavior of stepped flaws in marble with flaw inclination angle 30^o and '2a' bridging length. S = shear, T = tensile.

(a)

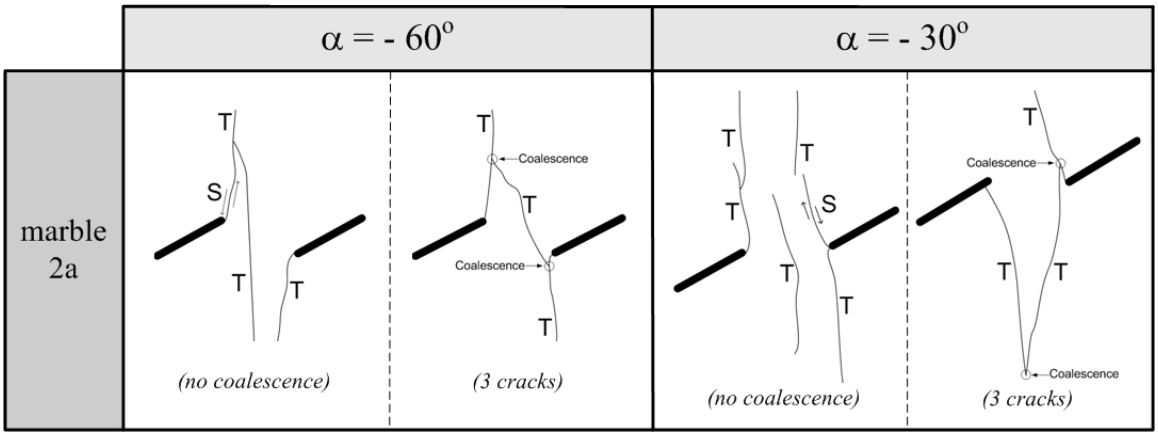

(b)

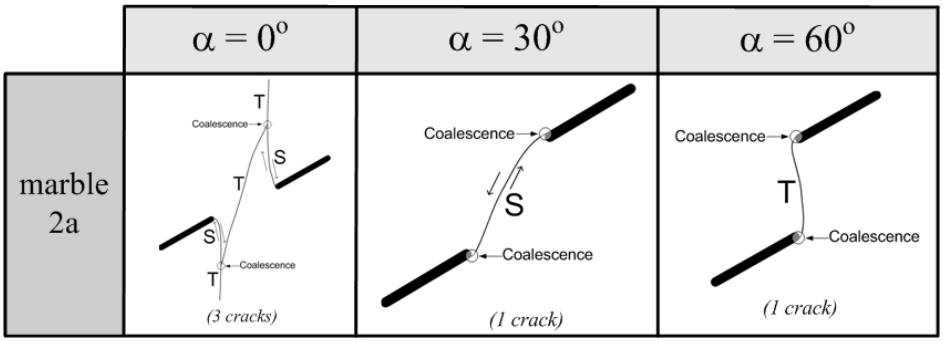

(c)

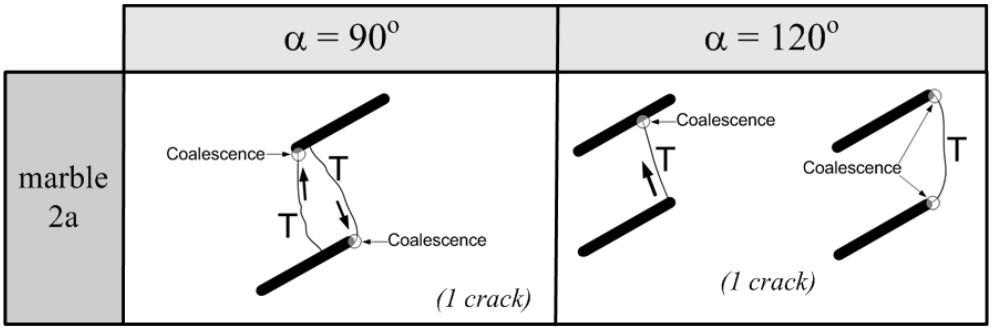

Figure 6.20 – Schematic illustration of the coalescence behavior of stepped flaws in marble with flaw inclination angle 30° and '2a' ligament length.

The coalescence behavior varies with the bridging angle α in this series (figure 6.20). See the description below.

In those specimens with bridging angles α = -60° and -30° where coalescence was absent in certain specimens, multiple **steeply-inclined cracks** and/or **tensile wing cracks** simply initiated from the flaw tips but did not coalesce.

In other specimens with bridging angles α = -60°, -30° and also 0° where coalescence occurred, coalescence was observed to be achieved in an **indirect** manner – linkage of two cracks (figure 6.20 a & b) which had initiated independently from the inner flaw tips by a third cracks. In the example shown in figure 6.21, a new inclined tensile crack linked up two vertical type 2 tensile cracks which had initiated earlier from the inner flaw tips.

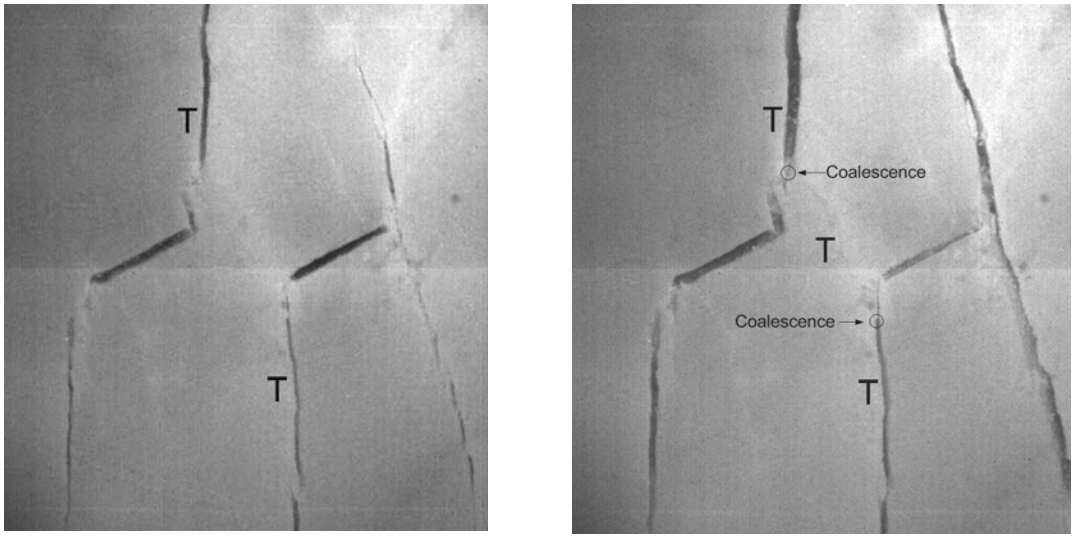

(a) (b)

Figure 6.21 – A new inclined tensile crack links up two vertical type 2 T cracks which had initiated earlier independently from the two inner flaw tips. (a) Before the initiation of the coalescence crack, (b) Just after the initiation of the coalescence crack. The high speed images were captured at a frame rate of 3,800 pps.

In contrast to the negative bridging angles, for positive bridging angles ($\alpha = 30^o$, 60^o, 90^o and 120^o), coalescence was achieved in a **direct** manner – the two pre-existing flaws were linked up directly by a single crack in the **central bridging region** (figures 6.20 b and c).

The sketches shown in figures 6.20 b and c however also demonstrate a clear trend of variation of coalescence behavior with different positive bridging angles. In general, a small bridging angle ($\alpha = 30^o$) favored the formation of **shear** coalescence cracks and large bridging angles ($\alpha = 60^o$, 90^o & 120^o) favored the formation of **tensile** coalescence cracks.

For $\alpha = 60^o$, the coalescence tensile crack was a single **type 2 tensile crack** which linked up the two inner flaw tips. For $\alpha = 90^o$ and 120^o, the coalescence tensile crack was generally a **tensile wing crack** (**TWC, type 1 tensile crack**) which linked up the two inner flaw tips. However, there was one exception for $\alpha = 120^o$. In specimen CM 2a-30-120-B (figure 6.22 b), the coalescence crack was a **tensile crack (crack C)** curving in a different direction as compared to the **TWC (crack A)** in specimen CM 2a-30-120-A which linked up the right tips of the top flaw and the bottom flaw (figure 6.22 a). Also refer to the sketches presented in figure 6.23 for the trajectories of the cracks (a detailed description is contained in Appendix M). Note also that coalescence cracks following a similar trajectory as of crack C in CM 2a-30-120-B were observed in specimen CM 2a-30-120-A (cracks D and E). However, since their initiation was later than the initiation of tensile wing crack A which was the **first** coalescence crack, trajectory of crack A, but not that of crack D or crack, was shown in figure 6.20 c.

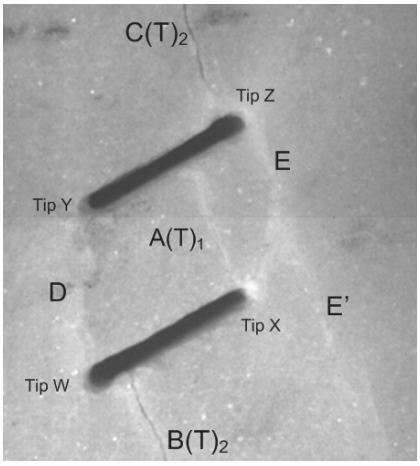

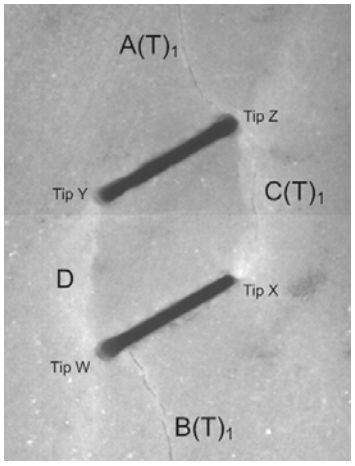

(a) CM 2a-30-120-A (b) CM 2a-30-120-B

Figure 6.22 – High speed images of specimens (a) CM 2a-30-120-A with coalescence crack A, and (b) CM 2a-30-120-B with coalescence crack C.

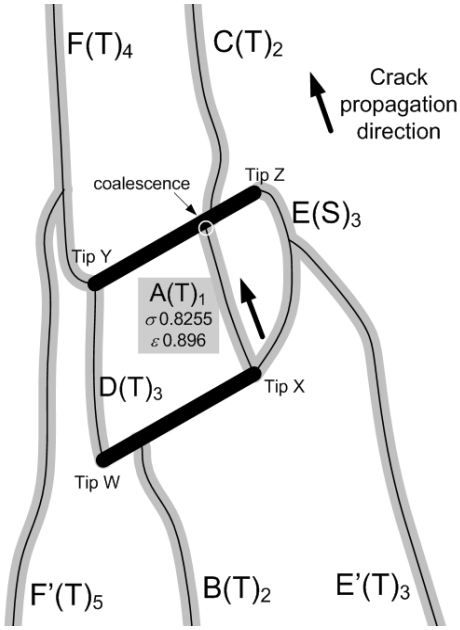

Pre-max : 1-2 CAM : 1-2
Post-max : 3-5 HS : 3-5

(a) CM 2a-30-120-A

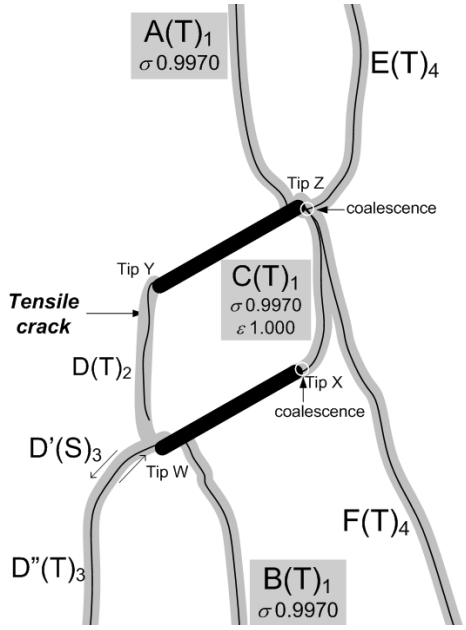

Pre-max : 1 CAM : 1
Post-max : 2-4 HS : 2-4

(b) CM 2a-30-120-B

Figure 6.23 – Sketches of fracturing and coalescence patterns for marble 2a-30-120.

6.4.3 Coplanar flaws separated by 4a

Details of the fracturing and coalescence behavior of the coplanar flaws with ligament length "4a" are presented in Appendix N according to flaw geometries and summarized in table 6.10.

Flaw inclination angle β (^{o})	**First cracks appeared**	**Coalescence cracks**
0	**Type 2 T cracks** from flaw tips	- In 1/3 specimens (C), **no coalescence** - In 2/3 specimens (A & B), a **mixed T-S crack** linked up a **type 1 S crack**
30	Tensile wing cracks (**type 1 T cracks**)	**No coalescence**
45	**Type 3 T cracks** from flaw tips	
60	**Type 2 T cracks** along white patches initiated from outer flaw tips	Two **type 2 S cracks** coplanar with the pre-existing flaws initiated independently from the inner flaw tips coalesced
75	Short **T cracks** along the previously developed white patches in the central bridging region which had already linked up the two inner flaw tips	- In 2/3 specimens (A & C), a short **S crack** developed to link up cracks which had initiated earlier in the central bridging region - In 1/3 specimen (B), a **type 2 S crack** coplanar with the pre-existing flaw developed from one inner flaw tip coalesced with a **T crack** initiated independently from another flaw tip

Table 6.10 – Summary of coalescence behavior of coplanar flaws in marble with '4a' bridging length.
S = shear, T = tensile.

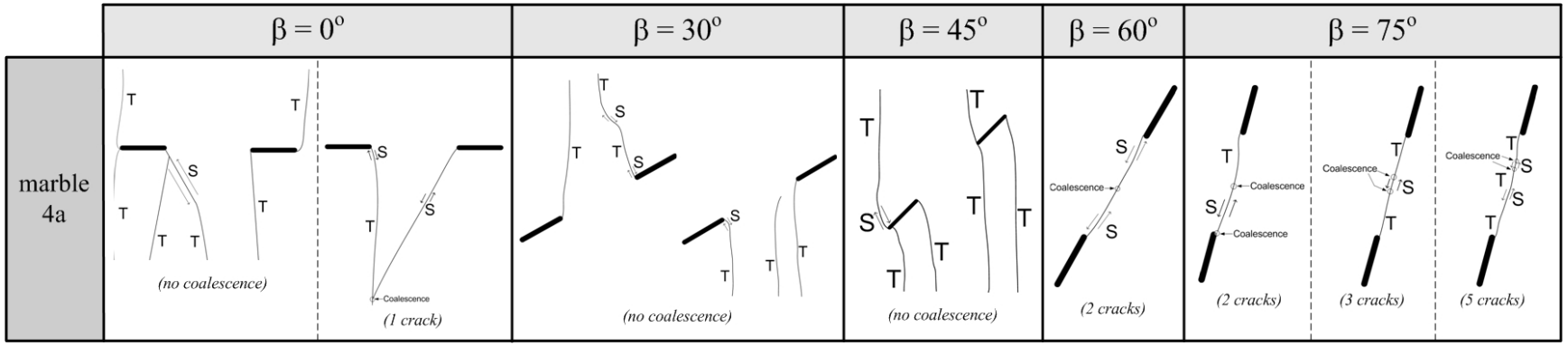

Figure 6.24 – Schematic illustration of the coalescence behavior of coplanar flaws in marble with '4a' ligament length.

The coalescence behavior varies with the flaw inclination angle β (figure 6.24). See description below.

For small inclination angles (β = **0°, 30°, 45°**), no coalescence occurred in most of the tested specimens. Coalescence only occurred in two out of the three tested specimens with $\beta = 0^{o}$ in which the coalescence was achieved in an **indirect** manner – linkage of two inclined to steeply-inclined cracks independently initiated from the inner flaw tips. One of the cracks was a **shear crack** and the other was of **mixed tensile-shear nature**.

In contrast, the coalescence occurring in specimens with larger flaw inclination angles (β = **60°, 75°**) was achieved in a **direct** manner in the central bridging region in which the two inner flaw tips were linked up by a continuous crack which consisted of either one or more crack segments. Variation occurred among the tested specimens with regard to the number of distinguishable individual crack segments involved in the coalescence and the initiation mode (tensile/shear) of these cracks:

Two cracks – In specimens 4a-60-0-A, 4a-60-0-B and 4a-75-0-B, crack segments coplanar with the pre-existing flaws initiated independently from the inner flaw tips and coalesced. In specimens with $\beta = 60^{o}$ (4a-60-0-A, 4a-60-0-B), the above-mentioned crack segments were **type 2 shear cracks**. In specimen 4a-75-0-B, one of the coalescence crack segments was **tensile** and the other coalescence crack segments was **shear (type 2 shear crack)**.

Three cracks – In specimen 4a-75-0-A, **two type 2 shear cracks** first initiated independently from the two inner flaw tips and were later linked up to form a continuous crack by a **third** crack which was **shear** in nature.

Five cracks – In specimen 4a-75-0-C, three individual **tensile** crack segments first initiated in the central bridging region and were later linked up to form a

continuous crack by two late-stage **shear** crack segments (refer to figure 6.25 for further details).

The above detailed observation regarding the formation of multiple individual short crack segments and their subsequent coalescence was made possible by the use of the high speed camera. These crack coalescence events were not differentiable in the camcorder video recordings.

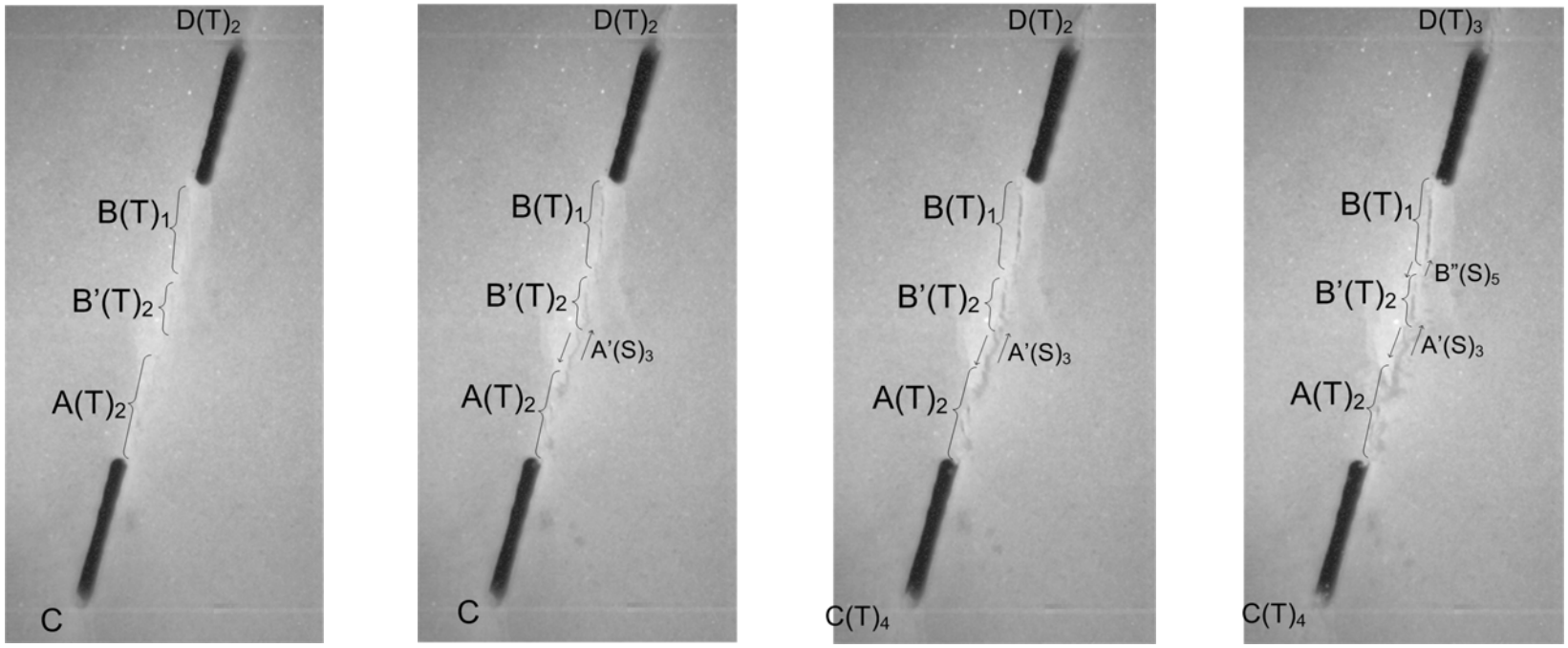

(a) HS image # - 11883 (73.26 MPa)

(b) HS image # - 9635 (73.06 MPa)

(c) HS image # - 9611 (73.05 MPa)

(d) HS image # - 9564 (73.05 MPa)

(a) Individual tensile crack opening (crack B first, which was followed by cracks A and B') occurred along the white patch in the central bridging region between the two inner flaw tips. Tensile crack D has also developed from the right tip of the top flaw.

(b) The aperture of cracks B, B' and A along the central white patch increased. Shearing (A') occurred to link up tensile crack segments A and B'.

(c) Tensile crack opening commenced along the white patch C adjacent to the left tip of the bottom flaw.

(d) Shearing (B") occurred to link up tensile crack segments B and B', leading to complete coalescence between the two internal tips of the two flaws.

Figure 6.25 – Fracturing and coalescence behavior in marble specimen 4a-75-0-C. High speed camera frame rate was 19,047 pps.

6.4.4 Stepped flaws separated by 4a

Details of the fracturing and coalescence behavior of the stepped flaws with ligament length "4a" and flaw inclination angle 30^o are presented in Appendix O and summarized in table 6.11 according to flaw geometries.

Bridging angle α (^{o})	**First cracks appeared**	**Coalescence cracks**
-60	**Type 2 T cracks**	- In 2/3 specimens, no coalescence - In 1/3 specimens, two inclined **S cracks** (**type 1 S crack, type 3 S crack**) individually initiated from the two inner flaw tips and coalesced
-30	In 1/2 specimens, **type 1 S crack** In 1/2 specimens, **type 2 T crack**	- In 1/2 specimens, no coalescence - In 1/2 specimens, an inclined crack consisting of **T** and **S** segments linked up two steeply-inclined cracks independently initiated from the two inner flaw tips
0	Tensile wing cracks (**type 1 T cracks**)	No coalescence
30	**Type 2 T cracks** and **type 1 T cracks**	An **inclined S crack** in the central bridging region linked up some previously developed cracks in the bridging region and/or some steeply-inclined tip cracks
60	Tensile wing cracks (**type 1 T cracks**)	An almost vertical **type 2 T crack** linked up the inner flaw tips
90	**Type 2 T cracks**	Two coalescence cracks (almost symmetrical) developed independently - a **type 2 T crack** propagated downwards from the left tip of the top flaw, and was later linked up to the left tip of the bottom flaw by a **S** crack - a **type 2 T crack** propagated upwards from the right tip of the bottom flaw, and was later linked up to the right tip of the top flaw by a **S** crack
120	Multiple short **T** cracks along the white patch in the bridging region	Coalescence was achieved by the propagation and subsequent linkage of short **T** cracks along the central white patch in the bridging region

Table 6.11 – Summary of coalescence behavior of stepped flaws in marble with flaw inclination angle 30^o and '4a' bridging length. S = shear, T = tensile.

(a)

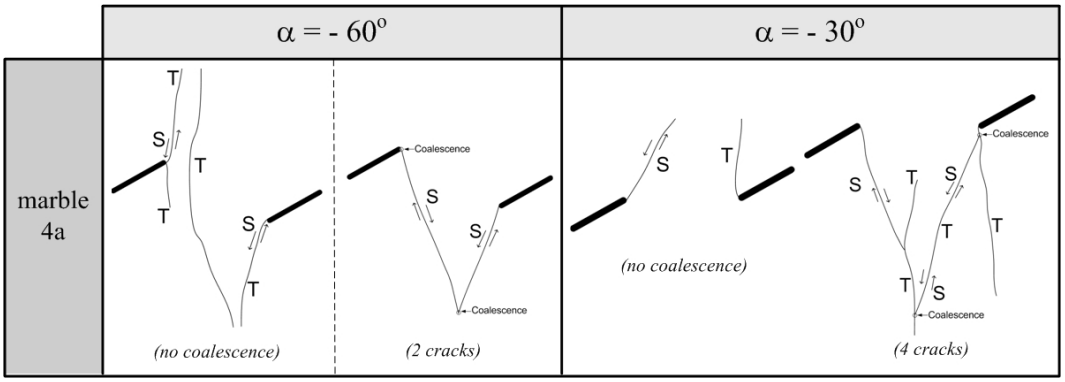

(b)

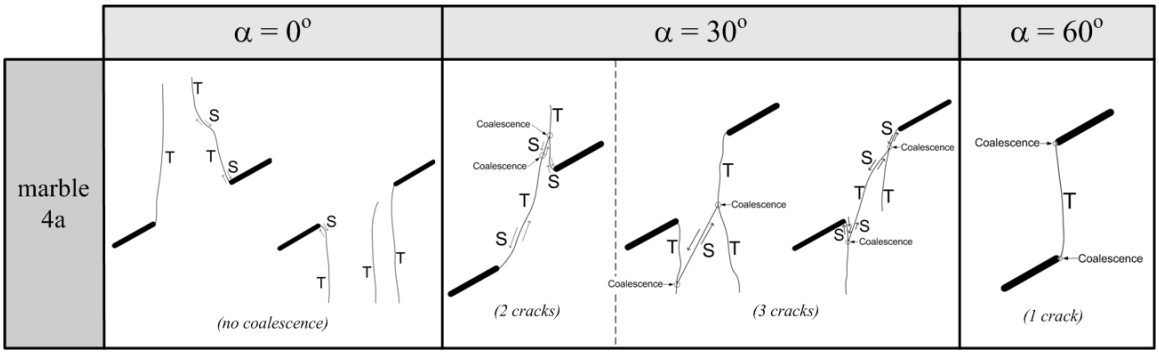

(c)

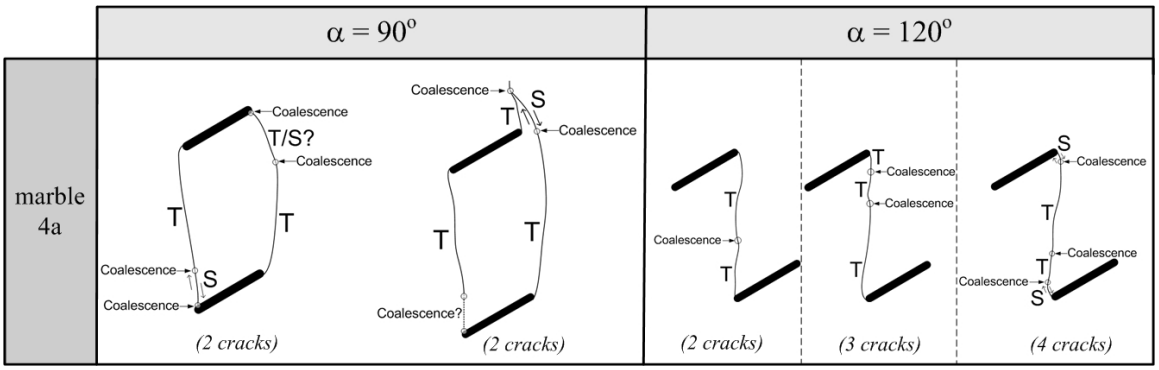

Figure 6.26 – Schematic illustration of the coalescence behavior of stepped flaws in marble with flaw inclination angle 30° and '4a' ligament length.

The coalescence behavior varies with the bridging angle α in this series (figure 6.26). See further description below.

Coalescence was either absent or only present in certain specimens for bridging angles α = -60°, -30° and 0° (absent in 2 out of 3 specimens for α = -60°, 1 out of 2 specimens for α = -30° and 2 out of 2 specimens for α = 0°). In those specimens where coalescence was absent, multiple steeply-inclined **type 2 tensile cracks** and **type 3 tensile cracks** simply initiated from the flaw tips but did not coalesce.

In other specimens with bridging angles α = -60°, -30° and also 30°, where coalescence occurred, coalescence was observed to be achieved in an **indirect** manner – coalescence of **two** inclined cracks (figure 6.26 a & b) which had initiated independently from the inner flaw tips or linkage of **two** steeply-inclined cracks, which had initiated independently from the inner flaw tips by a **third crack**. For example, as shown in figure 6.27, multiple crack segments **G**, **F** and **F**' which developed along the central inclined white patch linked up the two cracks **K** and **L** which had already initiated independently from the two inner flaw tips. As indicated by the cracking sequence shown in figure 6.27b, shear crack **F**' was the last crack segment to initiate to complete the whole coalescence process.

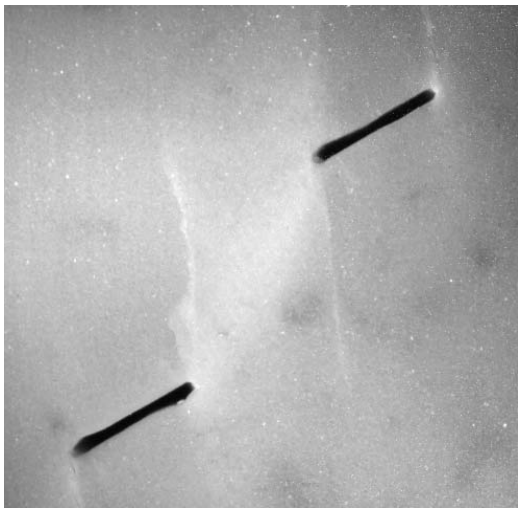

(a)

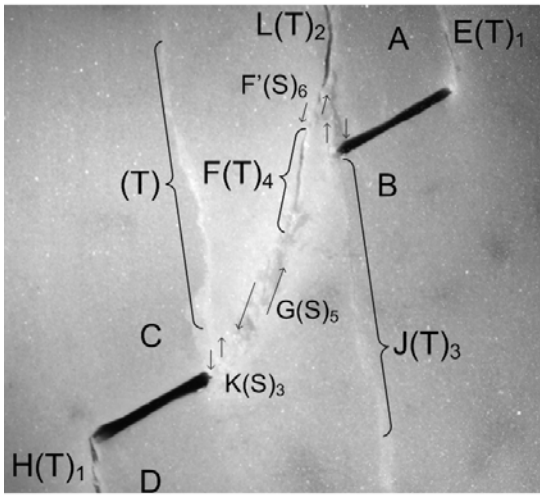

(b)

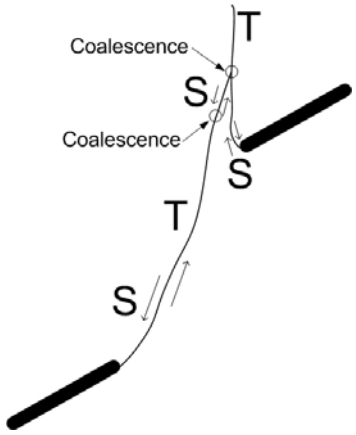

(c)

Figure 6.27 – (a) Development of white patches in marble before any observable cracking, (b) Under further loading, multiple cracks developed in the central bridging region which led to coalescence, (c) Sketch of the cracks involved in coalescence. The specimen number is 4a-30-30-D and the high speed images were captured at a frame rate of 10,000 pps.

In contrast to the negative bridging angles and small positive bridging angles, for larger bridging angles (α = 60°, 90° and 120°), coalescence was achieved in a **direct** manner – the two pre-existing flaws were linked up directly by a continuous crack which consisted of either a single crack or multiple crack segments in the **central bridging region** (figures 6.26 b and c).

For α **= 60°**, the coalescence crack was a single, almost vertical **type 2 tensile crack** which linked up the two inner flaw tips in the central bridging region.

For α = **90^o**, the tips of the same side of the two pre-existing flaws were linked up. Specifically, **type 2 tensile cracks** first initiated respectively from the left tip of the top flaw and the right tip of the bottom flaw. After the crack on each side had propagated for a certain length, another short crack then initiated from the tip (of the same side) of the other flaw to link up the **type 2 tensile crack**. This later **short crack** was observed to be either **type 3 shear crack or type 3 tensile crack**. Due to the presence of overlying rock fragments, the identity (shear/tensile?) of some of these short cracks was sometimes impossible to determine.

For α = **120^o**, the eventual coalescence pattern was due to the linkage of the right tip of the top flaw with the left tip of the bottom flaw by a **type 3 tensile crack**. With the use of the high speed camera, it was possible to observe the coalescence process in detail as shown in figure 6.28 for specimen 4a-30-120-A. Multiple short vertical **tensile cracks** first initiated along the white patch which had previously developed in the central bridging region already linking up the two inner flaw tips (figures 6.28 a & b). Note also that the initiation of these short cracks was **slightly earlier** than the occurrence of specimen maximum stress. These short tensile crack segments subsequently lengthened (figure 6.28 c) and **coalesced** to form a continuous tensile crack which eventually linked up the two inner flaw tips (figure 6.28 d). The formation of such a continuous crack occurred **slightly after** the specimen maximum stress was reached.

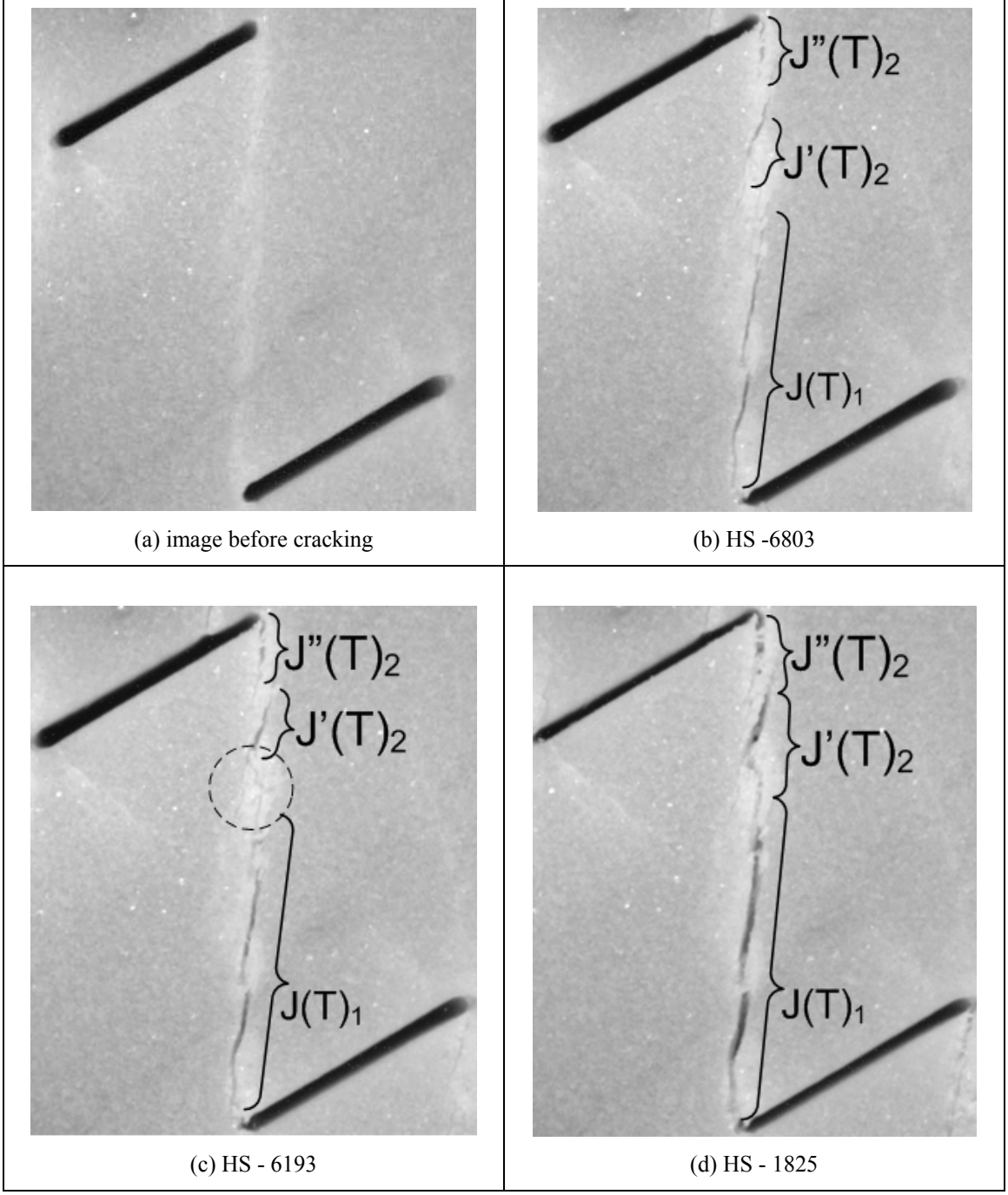

(a) image before cracking

(b) HS -6803

(c) HS - 6193

(d) HS - 1825

Figure 6.28 – Development of coalescence cracks in specimen 4a-30-120-A. (a) A white patch developed early during the uniaxial loading test in the central bridging region to link up the inner flaw tips. (b) Individual short tensile crack segments J, J', J" developed along the central white patch. (c) Minute local shearing (enclosed region) occurred to link up crack segments J and J'. (d) Formation of a continuous coalescence crack due to the linkage of the multiple short tensile crack segments. The high speed images were recorded at a frame rate of 6,600 pps.

6.4.5 Influence of ligament length on coalescence in marble

In the previous sections, the fracturing and coalescence behavior of each series in marble has been individually discussed. In this section, discussion is focused on the influence of ligament length on coalescence patterns in marble.

6.4.5.1 Coplanar flaws

The coalescence patterns observed for coplanar flaws with ligament length '2a' and '4a' previously shown in figures 6.17 and 6.24 are summarized in figure 6.29 below. In both series (ligament lengths '2a' and '4a'), the coalescence behavior also varies with the flaw inclination angle β. The general trend is summarized in table 6.12.

Category	**Flaw inclination angles β (°)**		**Coalescence Behavior**
	Ligament length 2a	Ligament length 4a	
1	0, 45	0, 30, 45	**No coalescence**
2	30, 45	0	**Indirect coalescence**
3	45	60	Direct coalescence by type 2 **S** cracks between inner flaw tips
6	60, 75	75	Direct coalescence by dominantly **T** crack segments between inner flaw tips. There may be occasional short **S** segments present along the coalescence crack.

Table 6.12 – Generalized coalescence behavior of coplanar flaws in marble with '2a' and '4a' ligament length. S = shear, T = tensile.

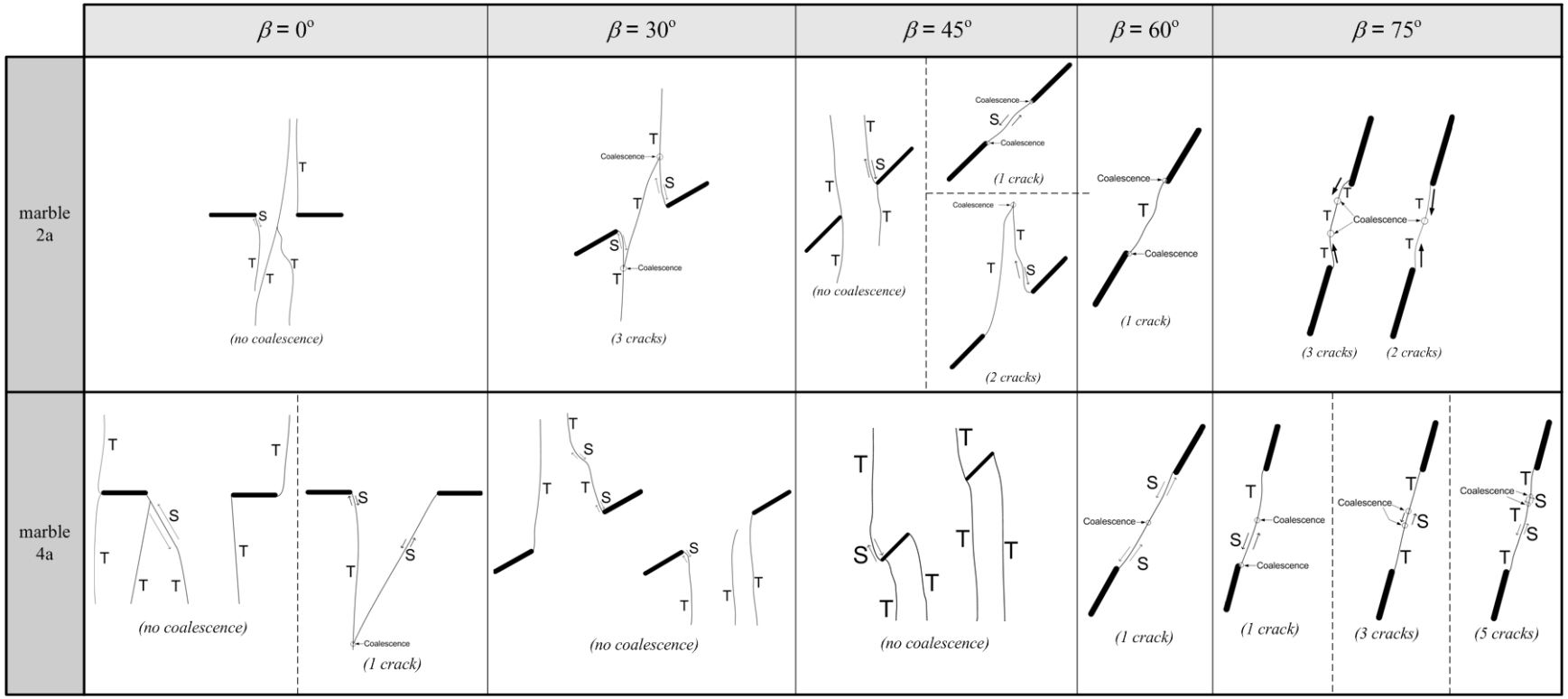

Figure 6.29 – Schematic illustration of the coalescence behavior of coplanar flaws in marble with ‘2a’ and ‘4a’ ligament length.

For specimens with small flaw inclination angles (β = 0°, 30°, 45° for both 2a and 4a), coalescence was either absent (**category 1**) in some tested specimens or occurred in some specimens in an **indirect** manner (**category 2**) – linkage of **two** inclined to steeply-inclined cracks independently initiated from the inner flaw tips **or** linkage of **two** inclined to steeply-inclined cracks independently initiated from the inner flaw tips by a **third crack**.

In contrast, the coalescence occurring in **categories 3 and 6** was achieved in a **direct** manner. The two inner flaw tips were linked up directly by a continuous crack which consisted of either one or multiple crack segments in the central bridging region.

In **category 3** with intermediate flaw inclination angles (1 out of 3 specimens with β = 45° for 2a, 2 out of 2 specimens with β = 60° for 4a), the coalescence crack was dominantly a shear crack which linked up the two inner flaw tips. The initiation of the coalescence shear crack was often associated with the occurrence of overlying localized surface spalling. In **category 6** with large flaw inclination angles (β = 60°, 75° for 2a, β = 75° for 4a), the eventual coalescence crack was a continuous crack which linked up the inner flaw tips. Some of these coalescence cracks consisted entirely of **tensile crack** segments as for ligament length '2a'. Some of them consisted of mainly **tensile crack** segments with occasional short **shear crack** segments between them as for ligament length '4a'. Variation also occurred among the tested specimens with regard to the number of distinguishable individual crack segments involved in the coalescence.

Notice that even though both series (ligament lengths '2a' and '4a') displayed a similar trend of variation of coalescence behavior with the flaw inclination angle β, the influence of ligament length is significant as reflected by the different boundaries between adjacent categories within the two series. For example, the boundary between **categories 3 and 6** is located between 45° and 60° for ligament length '2a' and is located between 60° and 75° for ligament length '4a'. As shown in table 5.12, for β = 60°, the coalescence crack for ligament length **2a** was **tensile** (category 6), while that for ligament length **4a** was **shear** (category 3).

Physically speaking, wider separation between the inner flaw tips reduces the mutual influence/interaction between the flaws. It is thus not surprising to observe that coalescence was always absent in specimens with geometry **4a-30-0** and **4a-45-0**, but it was observed in certain specimens with geometry **2a-30-0** and **2a-45-0**. However, the occurrence of coalescence in geometry 4a-0-0 (1 out of 2 tested specimens), but not in specimens with geometry 2a-0-0 is an unexpected phenomenon.

6.4.5.2 Stepped flaws

The coalescence patterns observed for stepped flaws with flaw inclination angle $\beta = 30^o$ and ligament length '2a' and '4a' previously shown in figures 6.20 and 6.26 are summarized in figure 6.30 below. In both series (ligament lengths '2a' and '4a'), the coalescence behavior varies with the bridging angle α. The general trend is summarized in table 6.13.

(a)

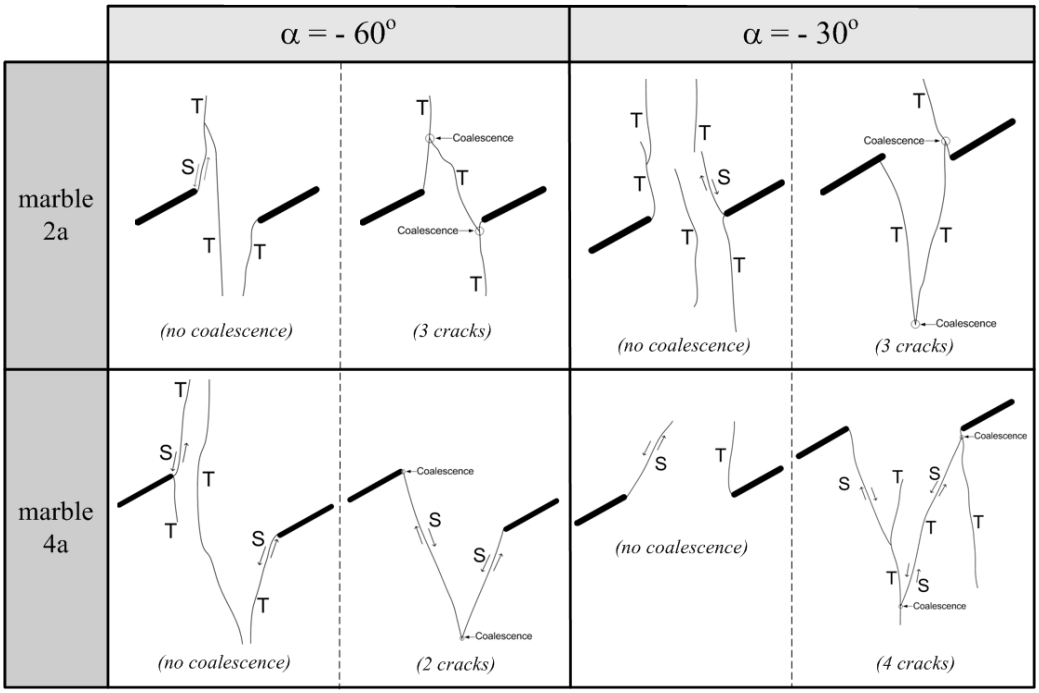

Figure 6.30 – Schematic illustration of the coalescence behavior of stepped flaws in marble with flaw inclination angle 30^o and '2a' and '4a' ligament length.

(b)

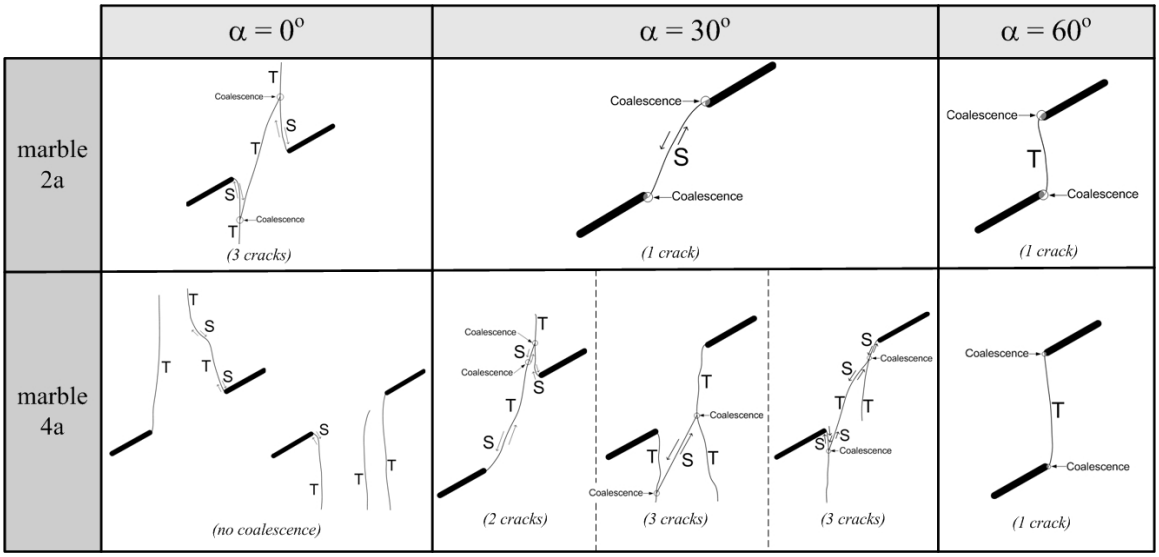

(c)

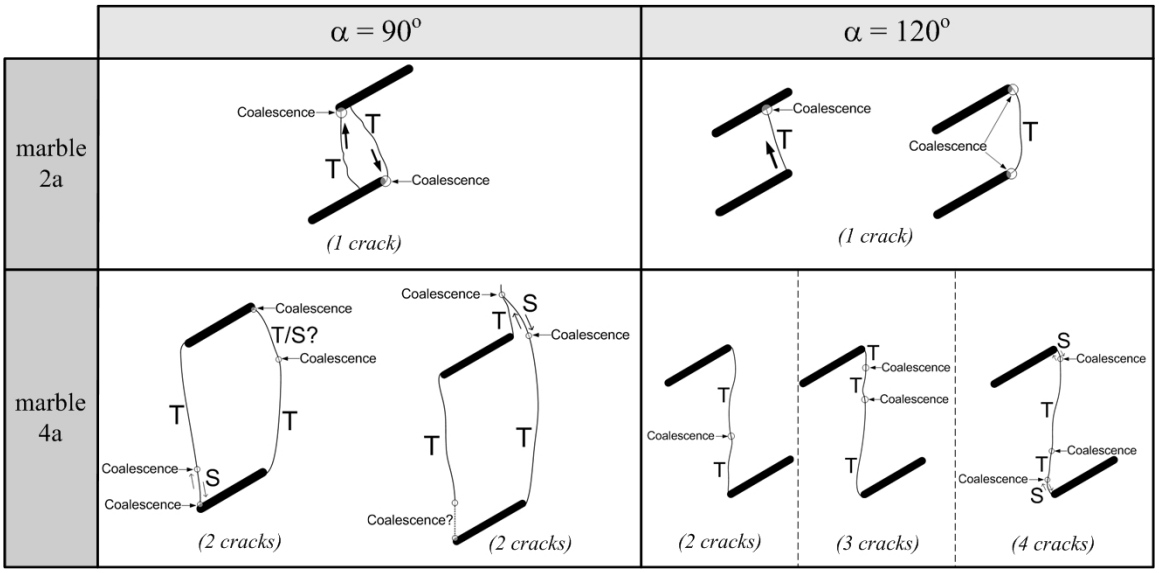

Figure 6.30 – Schematic illustration of the coalescence behavior of stepped flaws in marble with flaw inclination angle 30° and '2a' and '4a' ligament length (continued).

Category	Bridging angles α (^{o})		Coalescence Behavior
	Ligament length 2a	Ligament length 4a	
1	-60, -30	-60, -30, 0	**No coalescence**
2	-60, -30, 0	-60, -30, 30	**Indirect coalescence**
4	30	-	Direct coalescence by a **type 1 S crack** between inner flaw tips
6	60	60	Direct coalescence by a **type 2 T crack** between inner flaw tips
7	90, 120	-	Direct coalescence by a **type 1 T crack** (tensile wing crack)
8	120	90	Direct coalescence of the flaw tips of the same side by **tensile cracks** and/or short **shear cracks**
9	-	120	Direct coalescence of the right tip of top flaw and the left tip of bottom flaw by a continuous crack which consisted of multiple **type 3 tensile crack segments**

Table 6.13 – Generalized coalescence behavior of stepped flaws in marble with '2a' and '4a' ligament length. S = shear, T = tensile.

Coalescence **category 1 (no coalescence) and category 2 (indirect coalescence)** were observed in specimens with negative flaw inclination angles (β = -60^o, -30^o for both 2a and 4a). **Category 1** also includes β = 0^o for 4a, while **category 2** also includes β = 0^o for 2a. In other words, there was a significant influence of ligament length on coalescence patterns for coplanar flaw geometries 2a-30-0 and 4a-30-0 (figures 6.30 b, 6.31), in which coalescence occurred in the former but not the latter.

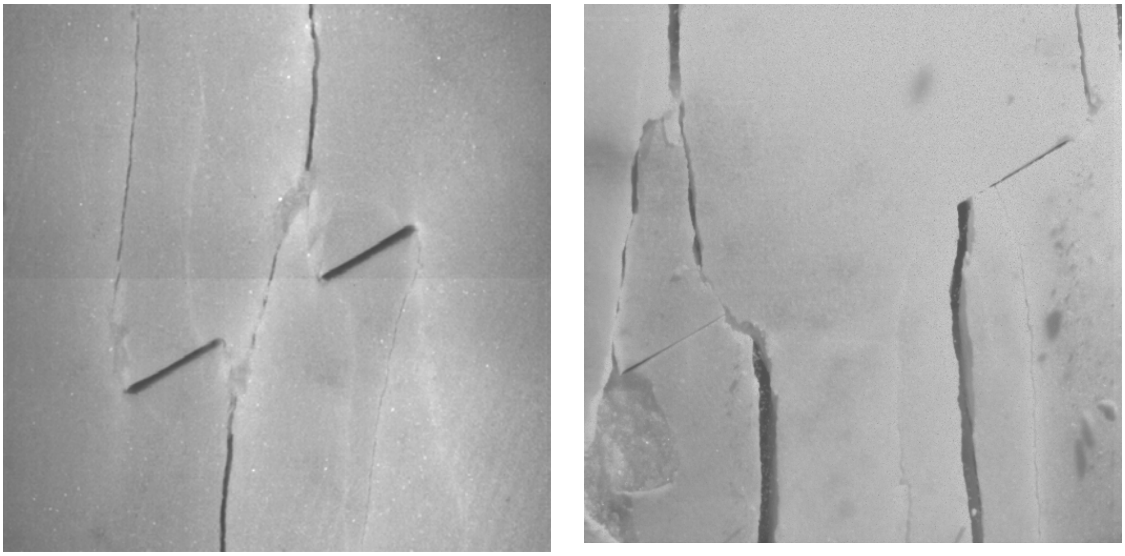

(a) 2a-30-0-A (b) 4a-30-0-B

Figure 6.31 – Coalescence occurred in marble specimen with flaw geometry (a) 2a-30-0, but not in specimen with flaw geometry (b) 4a-30-0. Note that both specimens have the same bridging angle but different ligament lengths

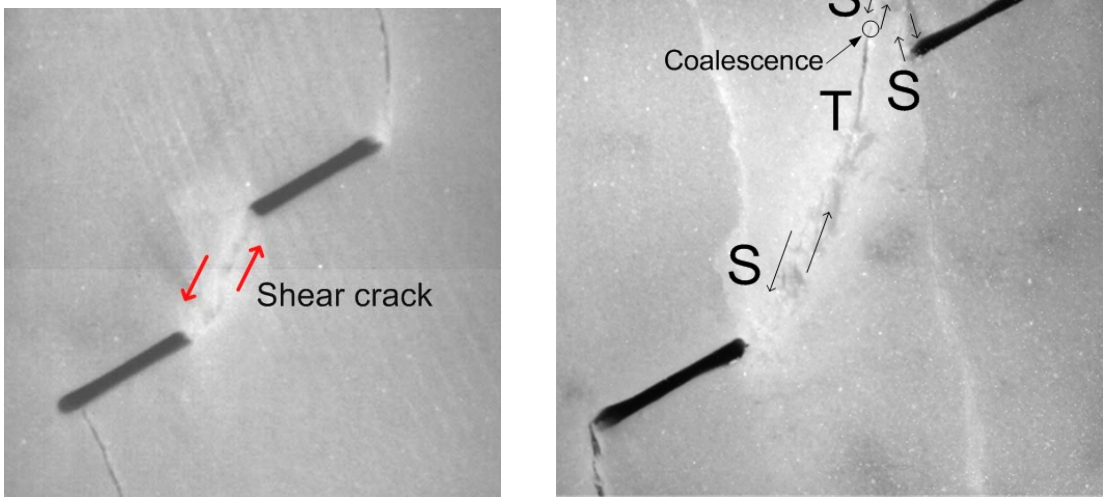

(a) 2a-30-30-A (b) 4a-30-30-D

Figure 6.32 – Different coalescence patterns in marble specimens with the same bridging angle but different ligament lengths (a) 2a-30-30 and (b) 4a-30-30.

In **category 4** ($\alpha = 30^o$ for 2a, not for 4a), the coalescence crack which was dominantly of a **shear** nature linked up the two inner flaw tips. The initiation of the coalescence shear crack was often associated with the overlying localized surface spalling (figure 6.32a). Although the coalescence behavior of $\alpha = 30^o$ for 4a (**category 2**) was similar to that of $\alpha = 30^o$ for 2a, in the way that dominantly shear cracks developed along the white patch which had already developed in the central bridging region between the inner flaw tips, the coalescence of $\alpha = 30^o$ for 4a was achieved in an indirect manner (thus it is the reason of belonging to **category 7**). Instead of a continuous single crack, multiple crack segments were involved for coalescence. As shown in figure 6.32 b earlier, a crack consisting of multiple **shear** and **tensile** segments initiated in the central inclined white patch to link up the **right tip of the bottom flaw** and a **mixed tensile-shear crack** previously initiated from the **left tip of the top flaw**.

In **category 6** ($\alpha = 60^o$ for both 2a and 4a), the coalescence crack was a single, almost vertical **type 2 tensile crack** which linked up the two inner flaw tips in the central bridging region (figure 6.33).

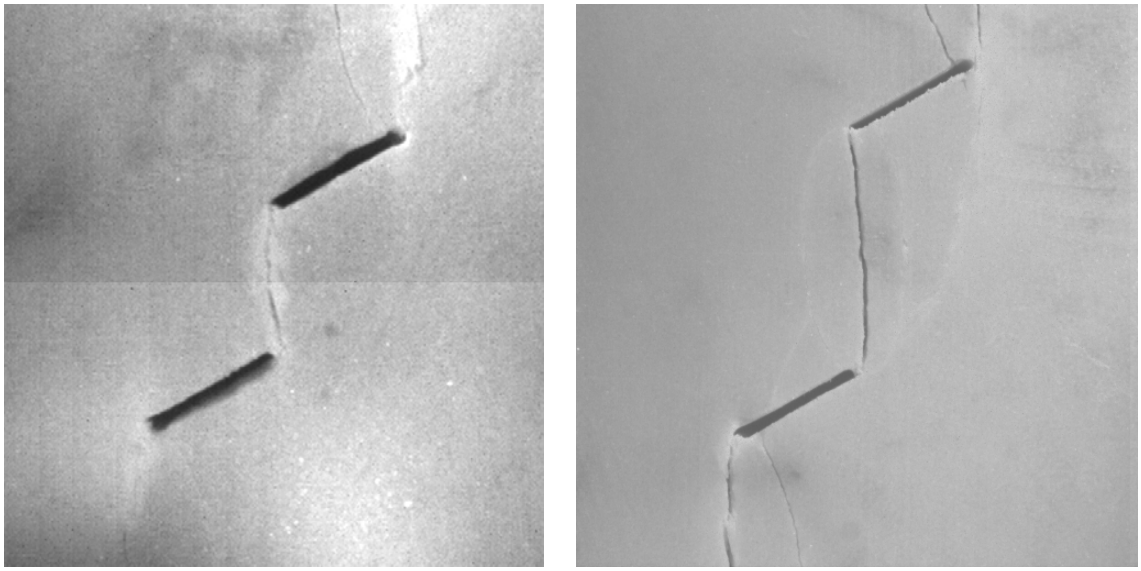

(a) 2a-30-60-C (b) 4a-60-0-B

Figure 6.33 – Coalescence similarly achieved by a type 2 tensile crack in marble specimen with the same bridging angle and different ligament lengths (a) 2a-30-60, and (b) 4a-30-60.

In **category 7** (α = 90°, 120° for 2a, but not for 4a), coalescence between the two pre-existing flaws was mainly achieved by **tensile wing cracks** (TWCs, type 1 tensile cracks) – specimens CM 2a-30-90-A, B, C and CM 2a-30-120-A (figure 6.34a). Depending on the relative position between the two pre-existing flaws, the location of crack initiation and location of crack coalescence varied.

Marble 2a-30-120		**Marble 4a-30-90**
Category 7	**Category 8**	
CM 2a-30-120-A (2,000pps)	CM 2a-30-120-B (2,000pps)	4a-30-90-C (6,600 pps)
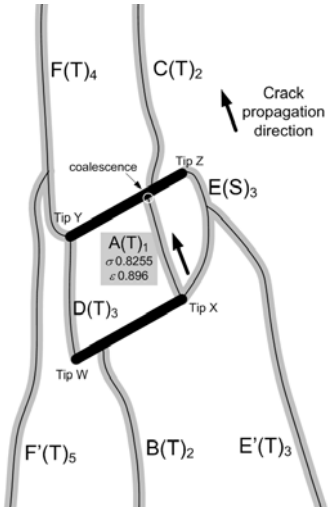	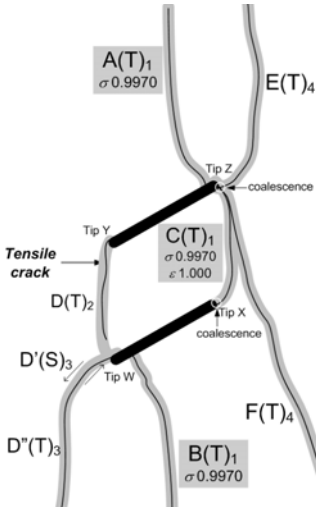	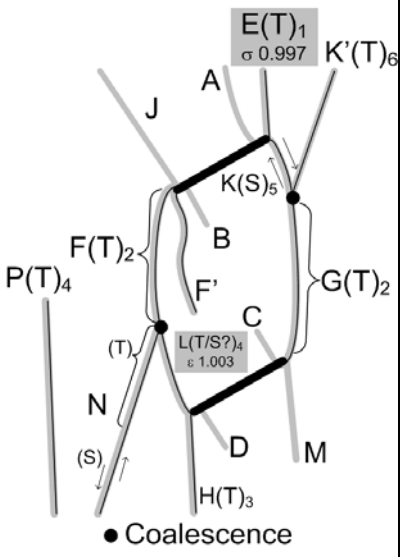
Pre-max : 1-2 CAM : 1-2 Post-max : 3-5 HS : 3-5	Pre-max : 1 CAM : 1 Post-max : 2-4 HS : 2-4	Pre-max : 1-2 CAM : 1-2 Post-max : 3-6 HS : 3-6
(a)	(b)	(c)

Figure 6.34 – Sketches of fracturing and coalescence patterns for marble (a) 2a-30-120-A (category 7), (b) 2a-30-120-B (category 8), (c) 4a-30-90-C (category 8).

The coalescence patterns observed in marble specimens CM 2a-30-120B, CM 4a-30-90-A, B, C belong to **category 8** (figures 6.34 b, c). Although the bridging angles for these two flaw geometries were different (90^o vs 120^o), the overall flaw geometries are very similar in a way that one flaw is arranged directly above (below) the other flaw. Under **category 8**, tips of the same side of the two pre-existing flaws were linked up. Variation occurred among the specimens regarding the number of cracks involved in the coalescence process (one tensile crack in specimen CM 2a-30-120-B, two cracks in specimens CM 4a-30-90-A, B, C).

It is interesting to note in specimen CM 2a-30-120A (figure 6.34a) that although coalescence cracks **D and E** also developed in the specimen to link up the flaw tips of the same side the two pre-existing flaws, CM 2a-30-120A was not classified as **category 8.** It is because the classification is based on the nature of the **first** coalescence crack, which was tensile wing crack **A** in CM 2a-30-120A (**category 7**).

Category 9 only consisted of specimens with $\alpha = 120^o$ for ligament length '4a' but not for '2a'. The coalescence processes have been described in detail in section 6.4.4 and illustrated in figure 6.28. The eventual coalescence pattern was the linkage of the right tip of the top flaw with the left tip of the bottom flaw by a **type 3 tensile crack**. Analysis of high speed images revealed that multiple short vertical **tensile cracks** first initiated along the white patch which had previously developed in the central bridging region linking up the two inner flaw tips. These short tensile crack segments subsequently lengthened and **coalesced** to form a continuous tensile crack which eventually linked up the two inner flaw tips.

6.5 Influence of material type on coalescence behavior

In previous sections, the fracturing and coalescence behavior observed in all tested specimens have been described according to series, first on gypsum (sections 6.3.1 – 6.3.4) and subsequently on marble (sections 6.4.1 – 6.4.4). The influences of ligament

length on coalescence behavior respectively in gypsum (section 6.3.5) and marble (section 6.4.5) have also been discussed.

In this section, the influence of material type (gypsum *vs* marble) on coalescence behavior are described and discussed, first on coplanar flaws (sections 6.5.1 – 6.5.2) and subsequently on stepped flaws (sections 6.5.3 – 6.5.4). Coalescence patterns will again be classified into different categories according to the scheme shown in figure 6.5.

6.5.1 Coplanar flaws with ligament length "2a"

The coalescence patterns observed for coplanar flaws with ligament length '2a' in gypsum and marble previously shown in figures 6.5 and 6.15 are summarized in figure 6.35 and table 6.14.

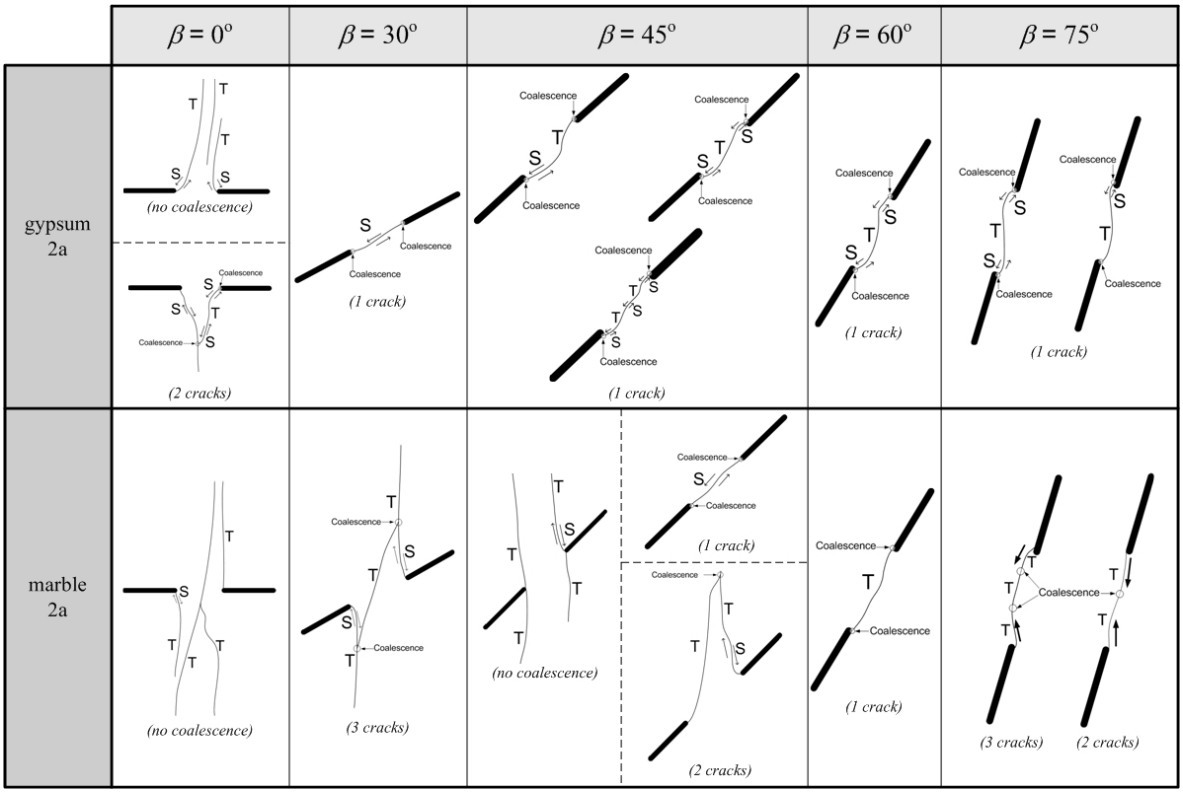

Figure 6.35 – Schematic illustration of the coalescence behavior of coplanar flaws in gypsum and marble with '2a' ligament length.

Category	Flaw inclination angles β (^{o})		Coalescence Behavior
	Gypsum	Marble	
1	0	0, 45	**No coalescence**
2	0	30, 45	**Indirect coalescence**
3	30	45	Direct coalescence by **type 2 S cracks** between inner flaw tips
5	45, 60, 75	-	Direct coalescence by multiple **S** and **T** crack segments between inner flaw tips (dominantly tensile)
6	-	60, 75	Direct coalescence by one or multiple **type 2 T** crack segments between inner flaw tips

Table 6.14 – Generalized coalescence behavior of coplanar flaws in gypsum and marble with '2a' ligament length.

In **category 1** with small flaw inclination angles (0^o for gypsum, 0^o, 30^o, 45^o for marble), coalescence was **absent** in the tested specimens (gypsum 2a-0-0-A, B, marble 2a-0-0-A, B, 2a-45-0-D). A number of steeply-inclined and/or vertical cracks initiated from the flaw tips but did not coalesce.

In **category 2** with also small flaw inclination angles (0^o for gypsum, 30^o, 45^o for marble), coalescence was achieved in an **indirect** manner in the other tested specimens (gypsum 2a-0-0-C, marble 2a-30-0-A, B, 2a-45-0-A) – linkage of **two** inclined to steeply-inclined cracks independently initiated from the inner flaw tips or linkage of **two** inclined to steeply-inclined cracks independently initiated from the inner flaw tips by an inclined **third** crack.

In contrast, the coalescence occurred in **categories 3, 5 and 6** was achieved in a **direct** manner in the central bridging region. See further description below.

In **category 3,** which consisted of all four tested specimens with flaw inclination angle β = 30^o for gypsum, and only one out of the three tested specimens with β = 45^o for marble (specimen 2a-45-0-C), the coalescence crack was dominantly a **type 2 shear crack** which linked up the two inner flaw tips. The initiation of the coalescence **shear crack** was often associated with the occurrence of overlying localized surface spalling.

In **category 5** (45^o, 60^o, 75^o for gypsum, but not for marble), the eventual coalescence crack which linked up the two inner flaw tips was a continuous crack of a shear-tensile-shear (S-T-S) pattern. The central crack segments were usually vertical or steeply-inclined **tensile cracks**, while the segments adjacent to inner flaw tips were usually **type 2 shear cracks**. Differences occurred among the tested specimens with regard to the number of distinguishable individual crack segments involved in the coalescence.

In **category 6** (60^o, 75^o for marble, but not for gypsum), the eventual coalescence crack which linked up the two inner flaw tips was a continuous **tensile** crack consisting of **one** or **multiple** tensile crack segments.

From the above description, the influence of material type on coalescence patterns can be summarized as follow:

1) Coalescence occurred less frequently (category 1) in **marble** than in **gypsum** with the same small flaw inclination angles (β = 0^o, 30^o, 45^o for ligament length 2a, β = 30^o, 45^o for ligament length 4a). This phenomenon appears to be related to the fact that in the marble specimens, the initiation of **vertical** and/or **steeply-inclined cracks** from the inner flaw tips occurred more frequently than the initiation of **coplanar cracks** from the inner flaw tips, compared to the fracturing behavior in gypsum specimens. Due to the geometrical configuration of the pre-existing **coplanar** flaws, direct linkage of **vertical** and/or **steeply-inclined cracks** newly

initiated from one pre-existing flaw with the other flaw was physically infeasible (figure 6.36 a). Coalescence (indirect) thus could only occur in the following two special cases (figures 6.36 b & c):

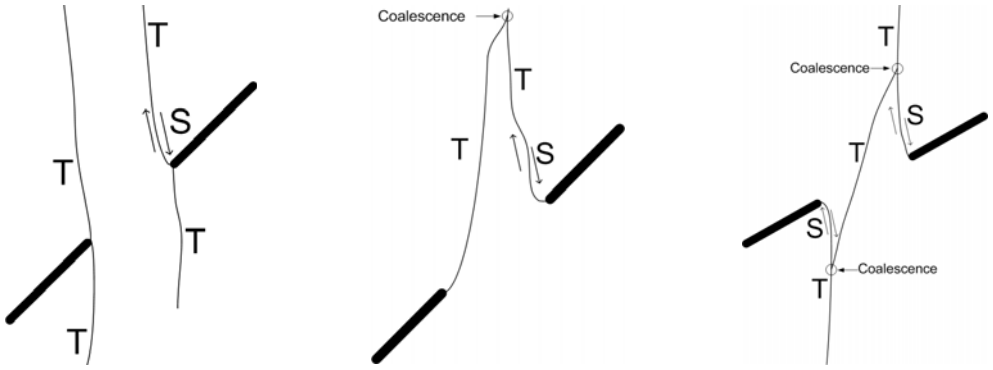

(a) (b) (c)

Figure 6.36 – (a) Coalescence did not occur due to the initiation of steep cracks from the inner flaw tips, (b) Coalescence occurred due to linkage of shallowly-inclined cracks initiated from the inner flaw tips, (c) Coalescence which involved the initiation of three new cracks.

a) When the newly initiated tip cracks (mentioned above) were not oriented vertically or at a very steep inclination, but of a shallower inclination, they would then have chance to connect with the other crack initiated and propagated from the other flaw tip (figure 6.36 b)

b) There was a development of a third crack oriented in such a way that it could link up the two vertical and/or steeply-inclined cracks initiated from the inner flaw tips (figure 6.36 c).

2) It is interesting to note that for large flaw inclination angles, although coalescence in gypsum ($\beta = 45^o, 60^o, 75^o$) and marble ($\beta = 60^o, 75^o$) was similarly achieved in a **direct** manner, in which the inner flaw tips were linked up by a continuous crack consisting of one of multiple individual crack segments, the crack segments adjacent to inner flaw tips in gypsum were mainly **shear**, while those in marble were mainly **tensile**.

6.5.2 Coplanar flaws with ligament length "4a"

The coalescence patterns observed for coplanar flaws with ligament length '4a' in gypsum and marble previously shown in figures 6.10 and 6.24 are summarized in figure 6.37 and table 6.15.

Category	**Flaw inclination angles β (°)**		**Coalescence Behavior**
	Gypsum	Marble	
1	0, 30	0, 30, 45	**No coalescence**
2	0, 30	0	**Indirect coalescence**
3	45, 60	60	Direct coalescence by **type 2 S cracks** between inner flaw tips
5	75	-	Direct coalescence by multiple **S** and **T** crack segments between inner flaw tips
6	-	75	Direct coalescence by one or multiple **type 2 T crack** segments between inner flaw tips

Table 6.15 – Generalized coalescence behavior of coplanar flaws in gypsum and marble with '4a' ligament length. S = shear, T = tensile.

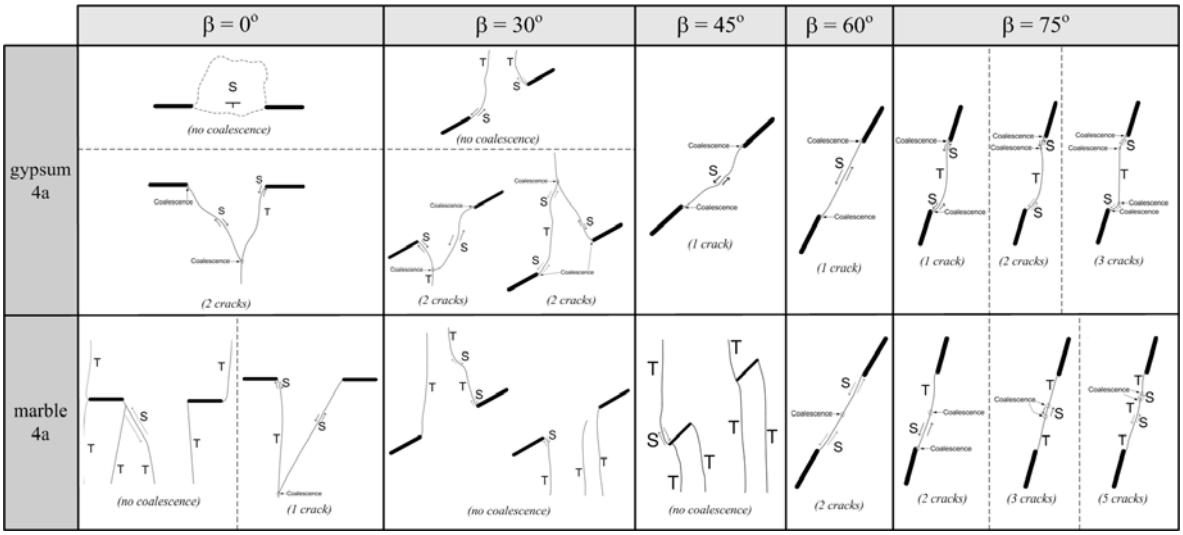

Figure 6.37 – Schematic illustration of the coalescence behavior of coplanar flaws in gypsum and marble with '4a' ligament length.

In **category 1** of small flaw inclination angles ($\beta = 0^o$, 30^o for gypsum, $\beta = 0^o$, 30^o, 45^o for marble), coalescence was **absent** in some tested specimens (gypsum 4a-0-0-C, F, 4a-30-0-A1, B1, marble 4a-0-0-C, 4a-30-0-B, C, 4a-45-0-A, B, C)

In **category 2** again of small flaw inclination angles ($\beta = 0^o$, 30^o for gypsum, $\beta = 0^o$ for marble), coalescence was achieved in an **indirect** manner (gypsum 4a-0-0-A, E, 4a-30-0-C1, D1, marble 4a-0-0-A, B) – linkage of **two** inclined to steeply-inclined cracks independently initiated from the inner flaw tips. In contrast, the coalescence occurring in **categories 3, 5 and 6** was achieved in a **direct** manner in the central bridging region. See further description below.

In **category 3** ($\beta = 45^o$, 60^o for gypsum, $\beta = 60^o$ for marble), the coalescence between the two inner flaw tips was achieved by the initiation of one **type 2 shear crack** (gypsum) or two **type 2 shear cracks** which had initiated independently from the flaw tips earlier. The initiation of the coalescence **shear cracks** was often associated with the occurrence of overlying localized surface spalling.

In **category 5** (75^o for both gypsum), the eventual coalescence crack which linked up the two inner flaw tips was a continuous crack of a shear-tensile-shear (S-T-S) pattern. The central crack segments were usually vertical or steeply-inclined **tensile cracks**, while the segments adjacent to inner flaw tips were usually **type 2 shear cracks**. Differences occurred among the tested specimens with regard to the number of distinguishable individual crack segments involved in the coalescence.

In **category 6** (75^o for marble), the eventual coalescence crack, which linked up the two inner flaw tips was a continuous crack, generally consisting of **tensile crack segments**, with some relatively short shear segments between them. Notice also that most the crack segments adjacent to the flaw tips were of tensile nature. Again, differences occurred among the tested specimens with regard to the number of distinguishable individual crack segments involved in the coalescence.

The influence of **material type** on coalescence patterns was significant for flaw inclination angles $\beta = 45^{o}$, in which coalescence was completely **absent** in marble, but occurred in gypsum. This phenomenon was again appears to be related to the fact that in the marble specimens, the initiation of **vertical** and/or **steeply-inclined cracks** from the inner flaw tips was favored compared to the initiation of **coplanar cracks** from the inner flaw tips, which was different from the fracturing behavior in gypsum specimens (similar observation reported for ligament '2a' in the previous section). Due to the geometrical configuration of the pre-existing **coplanar** flaws, direct linkage of **vertical** and/or **steeply-inclined cracks** newly initiated from one pre-existing flaw with the other flaw was physically infeasible (figure 6.38).

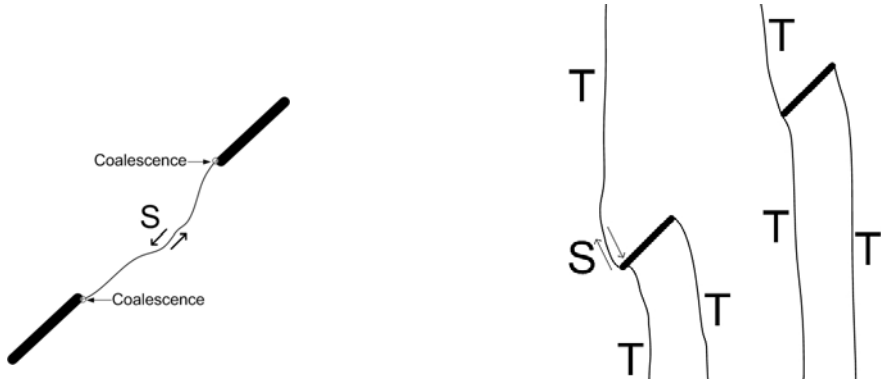

(a) (b)

Figure 6.38 – Coalescence occurred in (a) gypsum, but not in (b) marble with the same flaw pair geometry of 4a-45-0.

A similar interesting phenomenon as noted in the previous section on large flaw inclinations ($\beta = 75^{o}$) for ligament length '2a' was also observed for ligament length '4a'. For the particular flaw inclination $\beta = 75^{o}$, although coalescence in gypsum and marble was similarly achieved in a direct manner in which the inner flaw tips were linked up by a continuous crack consisting of one or multiple individual crack segments, the crack segments adjacent to inner flaw tips in gypsum were mainly **shear**, while those in marble were mainly **tensile**.

6.5.3 Stepped flaws with ligament length "2a"

The coalescence patterns observed for stepped flaws with ligament length '2a' in gypsum and marble previously shown in figures 6.8 and 6.20 are summarized in figure 6.39 and table 6.16.

Category	**Bridging angles α (°)**		**Coalescence Behavior**
	gypsum	marble	
1	-60, -30	-60, -30	**No coalescence**
2	-60, -30	-60, -30, 0	**Indirect coalescence**
3	0	-	Direct coalescence by a **type 2 S crack** between inner flaw tips
4	-	30	Direct coalescence by a **type 1 S crack** between inner flaw tips
5	30, 60	-	Direct coalescence by a generally **S-T-S** 'S' shaped crack consisting of only one or more crack segments
6	-	60	Direct coalescence by a **type 2 T crack** between inner flaw tips
7	90, 120	90, 120	Direct coalescence by **type 1 T cracks**
8	-	120	Direct coalescence of the flaw tips of the same side by **T cracks**

Table 6.16 – Generalized coalescence behavior of stepped flaws with 30° flaw inclination angle and ligament length "2a" in gypsum and marble. S = shear, T = tensile.

(a)

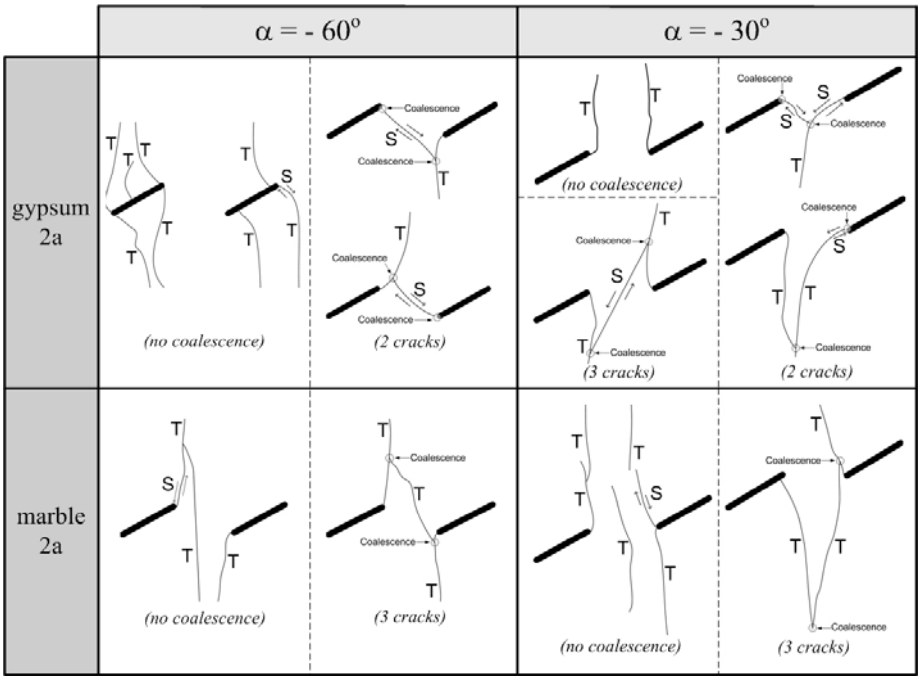

(b)

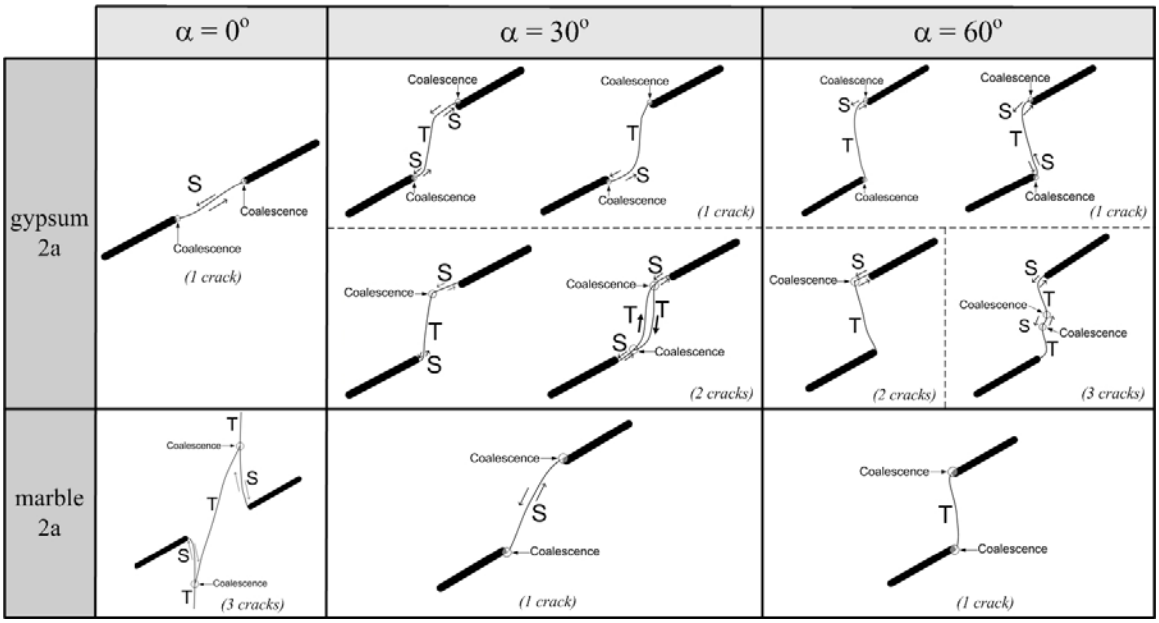

Figure 6.39 – Schematic illustration of the coalescence behavior of stepped flaws in gypsum and marble with flaw inclination angle 30° and '2a' ligament length.

(c)

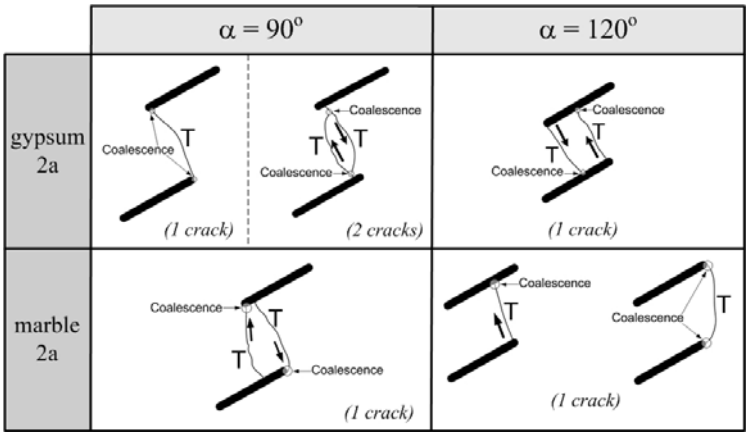

Figure 6.39 – Schematic illustration of the coalescence behavior of stepped flaws in gypsum and marble with flaw inclination angle 30° and '2a' ligament length (continued).

In **category 1** (α = -60°, -30° for gypsum, α = -60°, -30° for marble), coalescence was **absent** in some tested specimens with negative bridging angles (gypsum: 2a-30-(-60)-A, F, 2a-30-(-30)-A, marble: 2a-30-(-60)-A, 2a-30-(-30)-B)

In **category 2** (α = -60°, -30° for gypsum, α = -60°, -30°, 0° for marble), coalescence was achieved in some tested specimens with negative or zero bridging angles in an **indirect** manner (gypsum: 2a-30-(-60)-B, E, F, 2a-30-(-30)-B, D, F, marble: 2a-30-(-60)-B, 2a-30-(-30)-A) – linkage of **two** inclined to steeply-inclined cracks independently initiated from the inner flaw tips. In contrast, the coalescence occurring in **categories 3 to 8** was achieved in a **direct** manner in the central bridging region. See further description below.

In **category 3** (α = 0° for gypsum, not for marble), the coalescence crack which linked up the two inner flaw tips was a **type 2 shear crack** which was coplanar with the pre-existing flaws. The initiation of the coalescence shear crack was often associated with the occurrence of the overlying localized surface spalling.

In **category 4** (α = 30° for marble, not for gypsum), the coalescence crack which linked up the two inner flaw tips was a **type 1 shear crack** which was at an inclination with the

pre-existing flaws. The initiation of the coalescence shear crack was also often associated with the occurrence of the overlying localized surface spalling.

In **category 5** (α = 30°, 60° for gypsum, but not for marble), the coalescence crack which linked up the inner flaw tips was generally of a **shear-tensile-shear (S-T-S)** pattern. The central crack segments were usually vertical or steeply-inclined **tensile cracks**, while the segments adjacent to inner flaw tips were usually **shear cracks**. Variation occurred among the tested specimens with regard to the number of distinguishable individual crack segments involved in the coalescence.

In **category 6** (α = 60° for marble, but not for gypsum), the coalescence crack was a single, almost vertical **type 2 tensile crack** which linked up the two inner flaw tips in the central bridging region.

In **category 7** (α = 90°, 120° for both gypsum and marble), coalescence between the two pre-existing flaws was mainly achieved by **tensile wing cracks** (TWCs, type 1 tensile cracks). Depending on the relative position between the two pre-existing flaws, the location of crack initiation and location of crack coalescence varied. In some specimens, the high speed camera was able to capture the propagation direction of the newly initiated cracks.

In **category 8** (α = 120° for marble, but not for gypsum), the eventual coalescence pattern was the linkage of the tips of the same side of the two pre-existing flaws by a curvilinear **tensile crack**. This crack curved in a different direction as compared to the conventional direction of tensile wing crack.

From the above analysis, material type (gypsum *vs* marble) has demonstrated to have a strong influence on crack coalescence behavior for specific stepped flaw pair geometries with ligament length "2a". Coalescence pattern of **category 5** was unique to gypsum, while those of **categories 6 and 8** were unique to marble (table 6.16). More specifically, for **α = 30° and 60°**, the coalescence crack in **gypsum** which linked up the inner flaw tips

was a generally 'S'- shaped crack consisting of **shear-tensile-shear** crack segments. In contrast, the coalescence crack in marble was an inclined **type 1 shear crack** linking up the inner flaw tips for $\alpha = 30^o$, and it was a **type 2 tensile crack** linking up the inner flaw tips with no observable shear segments adjacent to the flaw tips for $\alpha = 60^o$.

6.5.4 Stepped flaws with ligament length "4a"

The coalescence patterns observed for stepped flaws with ligament length '4a' in gypsum and marble previously shown in figures 6.11 and 6.26 are summarized in figure 6.40 and table 6.17.

Category	**Bridging angles α (^{o})**		**Coalescence Behavior**
	gypsum	marble	
1	-60, -30, 0	-60, -30, 0	**No coalescence**
2	-60, 0	-60, -30, 30	**Indirect coalescence**
5	30, 60	-	Direct coalescence by a generally **S-T-S** 'S' shaped crack consisting of only one or more crack segments
6	-	60	Direct coalescence by a **type 2 T crack** between inner flaw tips
7	90, 120	-	Direct coalescence by **type 1 T cracks**
8	-	90	Direct coalescence of the flaw tips of the same side by **T** cracks and/or short **S** cracks
9	120	120	Direct coalescence of the right tip of top flaw and the left tip of bottom flaw by a continuous crack which consisted of multiple **T** crack segments and occasionally short shear segments adjacent to flaw tips

Table 6.17 – Generalized coalescence behavior of stepped flaws with 30^o flaw inclination angle and ligament length "4a" in gypsum and marble. S = shear, T = tensile.

(a)

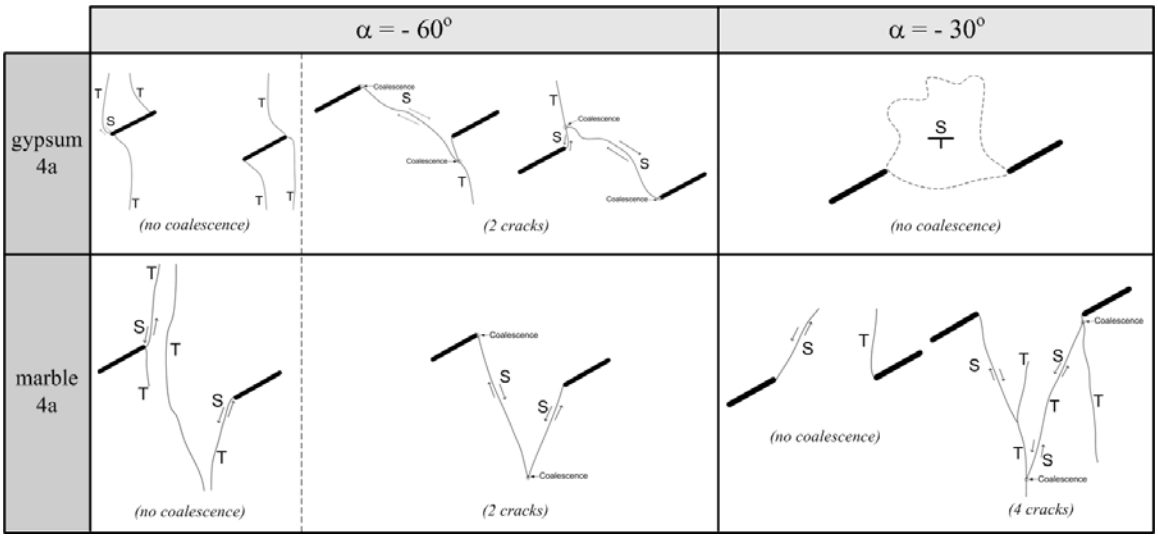

(b)

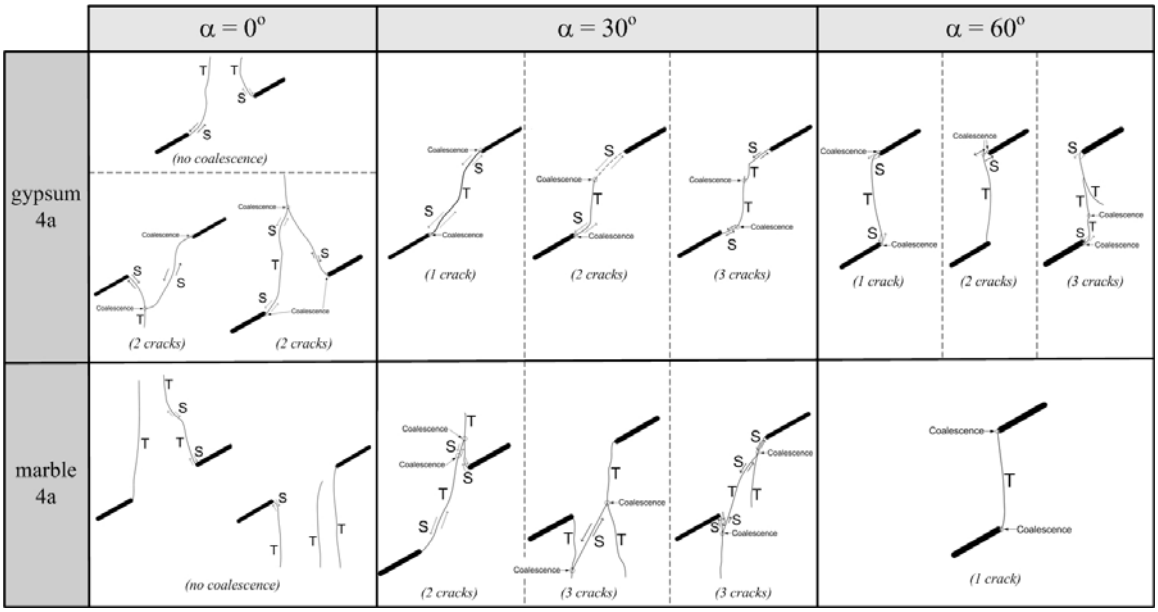

Figure 6.40 – Schematic illustration of the coalescence behavior of stepped flaws in gypsum and marble with flaw inclination angle 30° and '4a' ligament length.

(c)

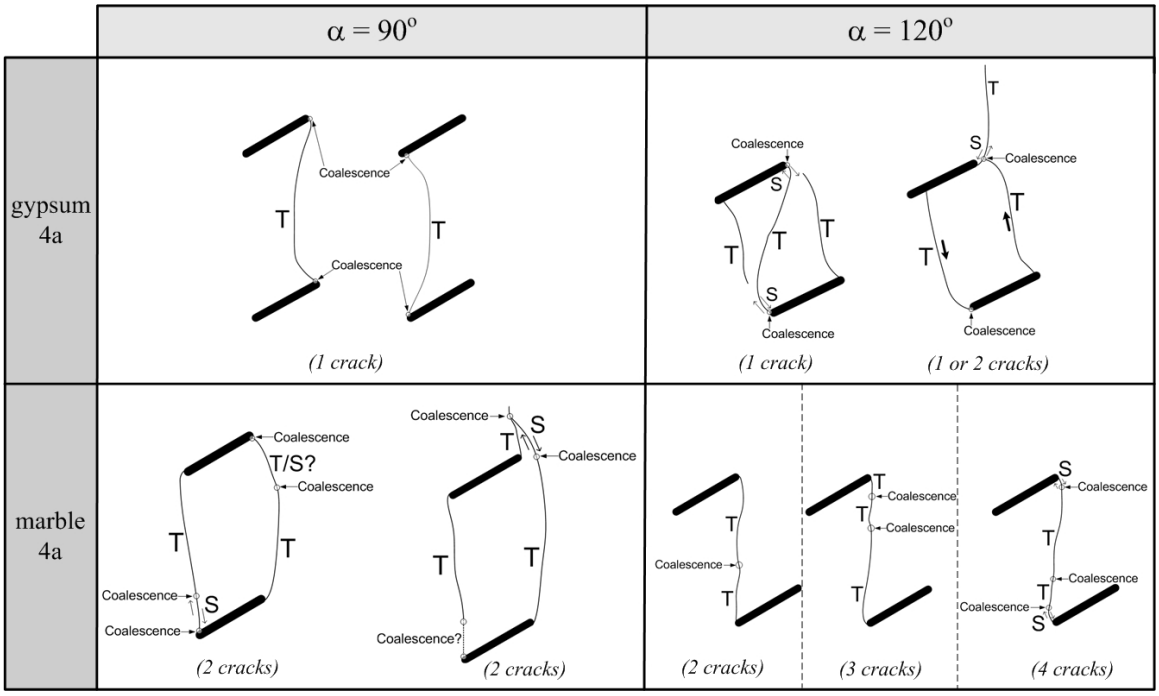

Figure 6.40 – Schematic illustration of the coalescence behavior of stepped flaws in gypsum and marble with flaw inclination angle 30° and '4a' ligament length (continued).

In **category 1** (α = -60°, -30°, 0° for gypsum and marble), coalescence was **absent** in some tested specimens with negative and zero bridging angles (gypsum: 4a-30-(-60)-D, 4a-30-(-30)-A, B, C, D, 4a-30-0-A1, B1, marble: 4a-30-(-60)-A, 4a-30-(-30)-A, C, 4a-30-0-B, C)

In **category 2**, coalescence was achieved in some specimens with negative or zero bridging angles (α = -60°, 0° for gypsum, α = -60°, -30°, 30° for marble) in an **indirect** manner (gypsum: 4a-30-(-60)-B, C, 4a-30-0-C1, D1, E1, marble: 4a-30-(-60)-B, 4a-30-(-30)-C, 4a-30-30-B, C, D). **Two** inclined to steeply-inclined cracks independently initiated from the inner flaw tips coalesced. In contrast, the coalescence occurring in **categories 5 to 9** was achieved in a **direct** manner in the central bridging region. See further description below.

In **category 5** (α = 30°, 60° for gypsum, not for marble), the coalescence crack which linked up the inner flaw tips was generally of a **shear-tensile-shear (S-T-S)** pattern. The central crack segments were usually vertical or steeply-inclined **tensile cracks**, while the segments adjacent to inner flaw tips were usually **shear cracks**. Differences occurred among the tested specimens with regard to the number of distinguishable individual crack segments involved in the coalescence. Note that although similar mixed shear-tensile cracks were also involved in coalescence for marble with α = 30°, they did not link up the flaw tips directly. They linked up some steep cracks, which had initiated earlier from the inner flaw tips (**category 2**). Refer to the previous paragraph for relevant description.

In **category 6** (α = 60° for marble, but not for gypsum), the coalescence crack was a single, almost vertical **type 2 tensile crack** which linked up the two inner flaw tips in the central bridging region.

In **category 7** (α = 90°, 120° for gypsum), coalescence between the two pre-existing flaws was mainly achieved by **tensile wing cracks** (TWCs, type 1 tensile cracks). In some specimens, the high speed camera was able to capture the propagation direction of the newly initiated cracks.

In **category 8** (α = 90° for marble, but not for gypsum), the eventual coalescence pattern was the linkage of the tips of the same side of the two pre-existing flaws by a curvilinear **tensile crack** and a short **shear crack**.

In **category 9** (α = 120° for both gypsum and marble), the eventual coalescence pattern was due to the linkage of the right tip of the top flaw with the left tip of the bottom flaw. With the use of the high speed camera, it was possible to observe the coalescence process in detail. In some specimens (both gypsum and marble), **shearing** was observed to be present along the end segments of the coalescence crack.

A main difference between gypsum and marble in **category 9** is that a coalescence crack in marble usually formed from the linkage of multiple short vertical **tensile cracks** which

had developed earlier along a white patch. Most of these white patches developed around the flaw tips during the early loading process. They lengthened and/or enlarged in size with an intensification of white color as loading increased. Upon reaching a particular load, which was dependent on flaw geometries, observable minute cracks then initiated along the white patches. Further loading led to a lengthening of these minute cracks till they coalesced to form a continuous crack (refer to figure 6.28 for details). In gypsum, however, such a development and evolution of white patches was not observed. There were usually no signs preceding the development of the coalescence crack, which usually appeared as a continuous crack abruptly within a very short time.

From the above analysis of stepped flaws with ligament length "4a", material type (gypsum *vs* marble) was again demonstrated to have a strong influence on crack coalescence behavior. Coalescence patterns of **categories 5 and 7** were unique to gypsum, while those of **categories 6 and 8** were unique to marble (table 6.17).

More specifically, distinct differences were identified for $\alpha = 30^o, 60^o$ and 90^o:

For $\alpha = 30^o$, the coalescence crack in **gypsum** which linked up the inner flaw tips was a generally 'S'- shaped crack consisting of **shear-tensile-shear** crack segments. In contrast, the coalescence in marble was achieved in an indirect manner which was due to the linkage of multiple shear and tensile cracks.

For $\alpha = 60^o$, the coalescence crack in **gypsum** which linked up the inner flaw tips was a generally 'S'- shaped crack consisting of **shear-tensile-shear** crack segments. In contrast, the coalescence in marble was achieved by a vertical **type 2 tensile crack**.

For $\alpha = 90^o$, the coalescence crack in **gypsum** which linked up the inner flaw tips was a **type 1 tensile crack** (tensile wing crack). In contrast, the coalescence in marble was due to the linkage of the tips of the same side of the two pre-existing flaws by a curvilinear **type 2 tensile crack** and a short **shear crack**.

For α **= 120^{o}**, one out of the four tested gypsum specimens coalesced by a **type 1 tensile crack,** i.e. **category 7** (table 6.17), while none of the marble specimens displayed that kind of coalescence pattern. However, it is worthwhile to mention that although coalescence in marble was not achieved by the tensile wing cracks in a similar way as in gypsum. White patches displaying wing appearance actually developed in marble during the early stage of the loading process. In some specimens (e.g. white patches B and C in 4a-30-120-A as shown in figure 6.40A b), the white patches remained intact and did not develop into cracks, while in some other specimens (e.g. white patches B and C in 4a-30-120-B as shown in figure 6.40A c), the white patches developed into tensile wing cracks, but did not propagate far enough to reach the tips of the other flaw to cause coalescence.

Gypsum	**Marble**	
4a-30-120-E (14,035 pps)	4a-30-120-A (6,600 pps)	4a-30-120-B (6,600 pps)
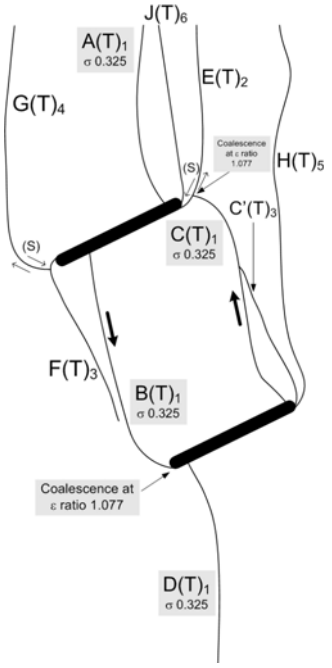	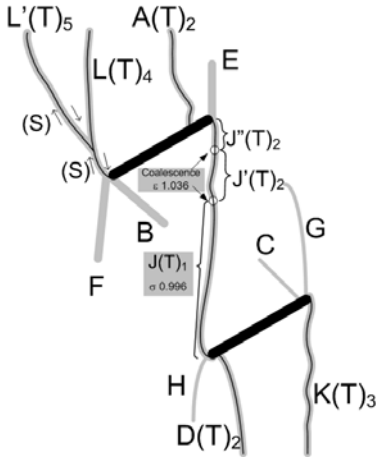 Coalescence was achieved by the propagation and subsequent linkage of individual tensile crack segments J, J' and J".	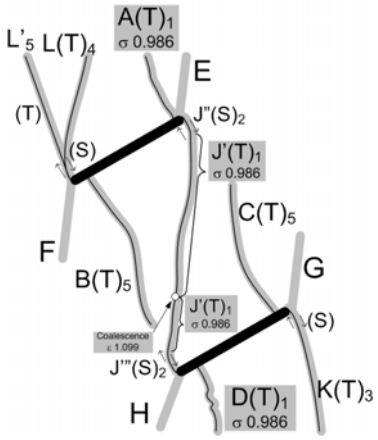
(a)	(b)	(c)

Figure 6.40A – (a) Crack coalescence category 7 in gypsum 4a-30-120-E, (b, c) Crack coalescence category 9 in marble 4a-30-120-A and 4a-30-120-B.

6.6 Stress Analysis

In the previous sections within this chapter, the focus has been placed on the fracturing processes and the coalescence patterns. In this section, some of the stress data also obtained from the uniaxial compression loading tests are analyzed and discussed.

6.6.1 Specimen maximum stresses

The prismatic specimens in the present experimental study were all loaded until failure occurred. The peak stresses corresponding to specimen failure (specimen maximum stress) for all the gypsum and marble specimens are shown in figures 6.41 to 6.44. All the stresses are normalized by the uniaxial compressive strength (UCS) of the respective material – 33.85 MPa for gypsum, 84.63 MPa for Carrara Marble. The data show that the strength of specimens containing a flaw pair is always lower than that of the intact specimens without the artificial flaws. The general trends of variation of normalized specimen maximum stress with bridging angles α (for stepped flaws) and flaw inclination angles β (for coplanar flaws) are also quite similar between gypsum and marble. The bridging angles α (for stepped flaws) and flaw inclination angles β (for coplanar flaws) corresponding to the maximum and minimum specimen failure stresses of the eight series shown in the four figures are summarized in table 6.18 and described below.

For stepped flaw pairs, the bridging angles α corresponding to the maximum specimen failure stress vary among the four series, while the bridging angles α corresponding to the minimum specimen failure stress are either $\alpha = 30^{o}$ or $\alpha = 60^{o}$, which are the intermediate positive bridging angles.

For coplanar flaw pairs, the flaw inclination angles β corresponding to the minimum specimen failure stress are $\beta = 30^{o}$ for marble and $\beta = 45^{o}$ for gypsum. For the maximum

specimen failure stress, except for gypsum with ligament length 2a where it occurs at $\beta = 0^{o}$ [1], it occurs at $\beta = 75^{o}$ for the other three series.

	Material	Ligament length	α (°) corresponding to ***minimum*** specimen maximum σ	α (°) corresponding to ***maximum*** specimen maximum σ
Stepped	Gypsum	2a	30	120
	Marble	2a	30	-60
	Gypsum	4a	30	0
	Marble	4a	60	-30

	Material	Ligament length	β (°) corresponding to ***minimum*** specimen maximum σ	β (°) corresponding to ***maximum*** specimen maximum σ
Coplanar	Gypsum	2a	45	0
	Marble	2a	30	75
	Gypsum	4a	45	75
	Marble	4a	30	75

Table 6.18 – Summary of values of bridging angle (α) and flaw inclination angle (β) corresponding to minimum and maximum "specimen maximum stresses" for gypsum and marble.

[1] The second highest value occurs at $\beta = 75^{o}$.

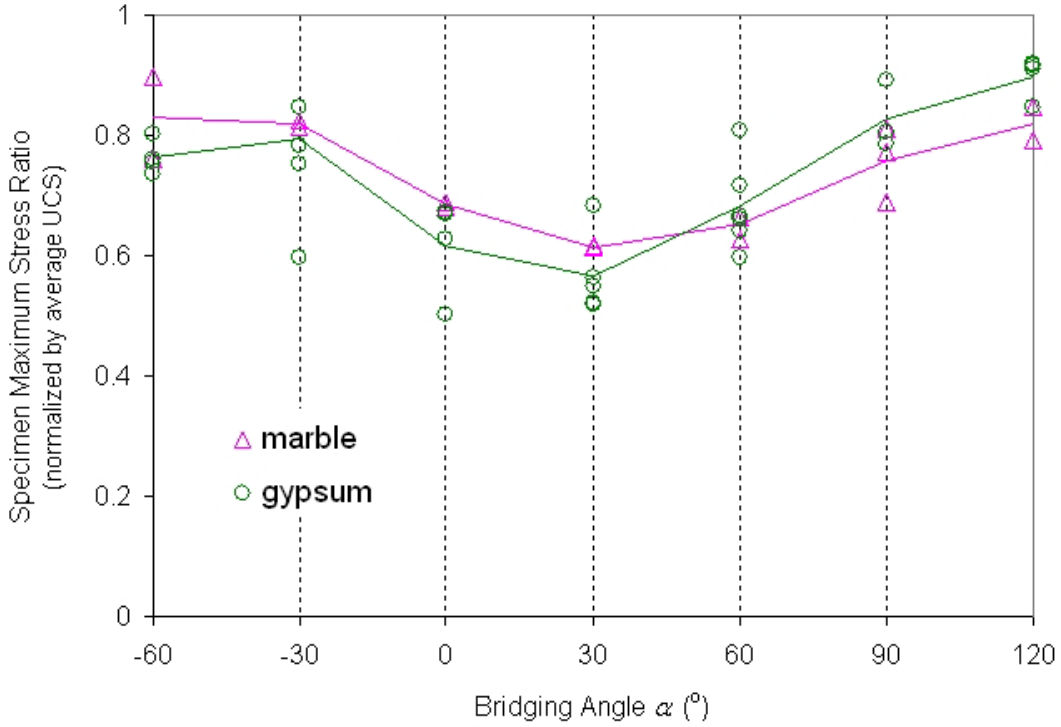

Figure 6.41 – Normalized specimen maximum stress versus bridging angle $\boldsymbol{\alpha}$ in gypsum and marble for stepped flaw pairs of 30° flaw inclination angle with ligament length **2a**.

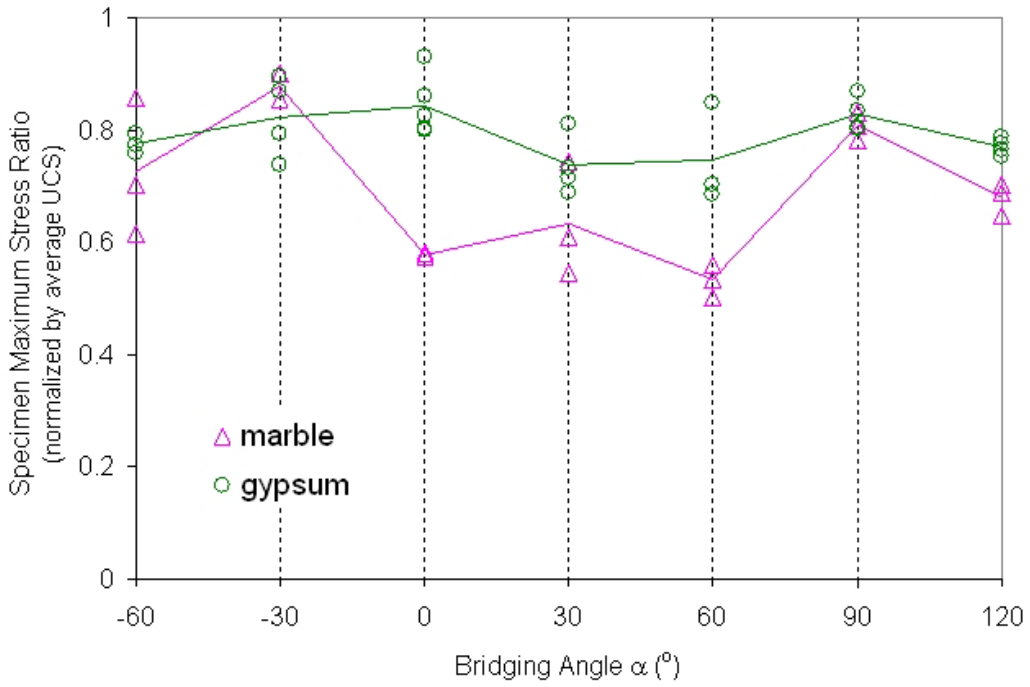

Figure 6.42 – Normalized specimen maximum stress versus bridging angle $\boldsymbol{\alpha}$ in gypsum and marble for stepped flaw pairs of 30° flaw inclination angle with ligament length **4a**.

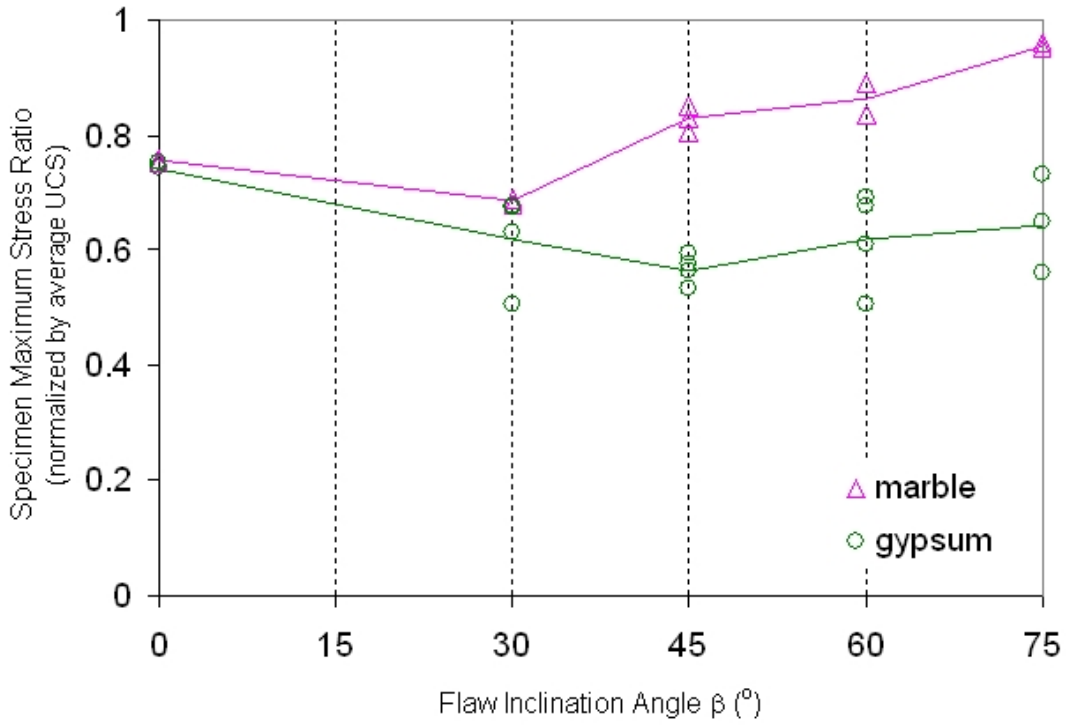

Figure 6.43 – Normalized specimen maximum stress versus flaw inclination angle β in gypsum and marble for coplanar flaw pairs with ligament length **2a**.

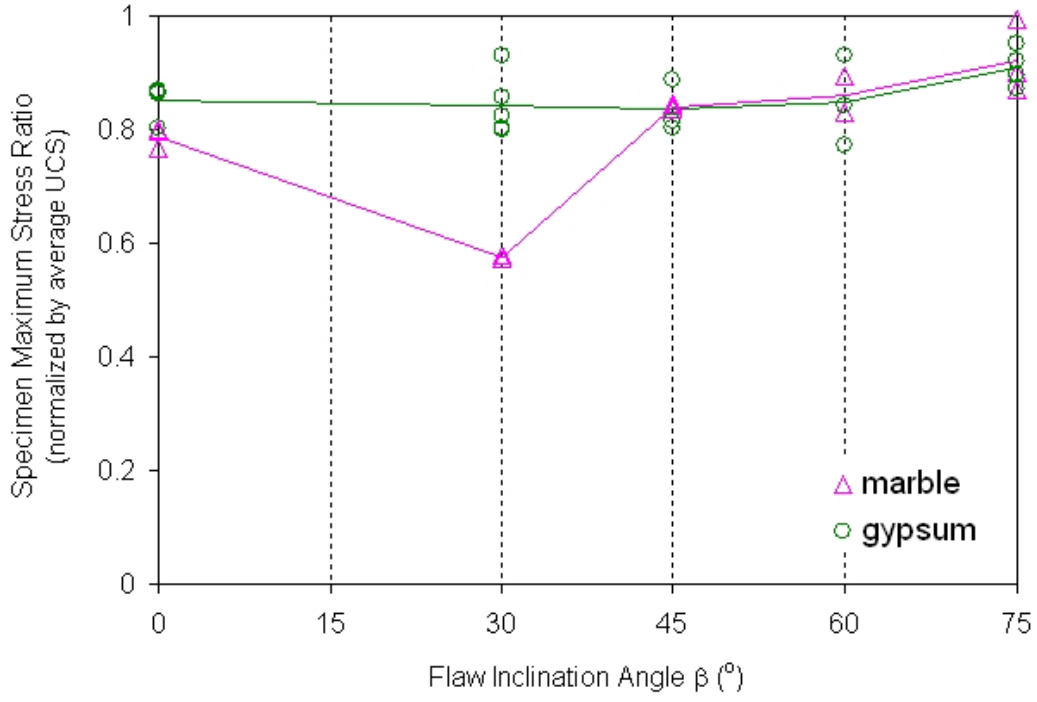

Figure 6.44 – Normalized specimen maximum stress versus flaw inclination angle β in gypsum and marble for coplanar flaw pairs with ligament length **4a**.

6.6.2 Stresses associated with crack initiation

The stresses (normalized by the respective UCS to become σ_{R1}) at which the first cracks initiated in all the gypsum and marble specimens are shown in figures 6.45 to 6.48.

The crack initiation stress ratio σ_{R1} is defined as

$$\sigma_{R1} = \frac{\text{first crack initiation stress}}{\text{average material uniaxial compressive strength}} \qquad (6.1)$$

The bridging angles α (for stepped flaws) and flaw inclination angles β (for coplanar flaws) corresponding to the maximum and minimum crack initiation stresses of the eight series shown in the four figures are summarized in table 6.19 and described below. The crack initiation stress ratio for gypsum is represented by $\sigma_{R1\text{-gypsum-pair}}$ and that for marble is represented by $\sigma_{R1\text{-marble-pair}}$.

For stepped flaw pairs, the bridging angles α corresponding to the maximum crack initiation stress vary among the four series, but are mainly of negative and zero angles. For the minimum crack initiation stress, except for gypsum with ligament length 4a where it occurs at $\beta = 120^o$, it occurs at $\beta = 60^o$ for the other three series.

For coplanar flaw pairs, the flaw inclination angles β corresponding to the minimum crack initiation stress are $\beta = 30^o$ for marble and $\beta = 45^o$ for gypsum. For the maximum crack initiation stress, it occurs at $\beta = 75^o$ for all the four series.

Note also that $\sigma_{R1\text{-marble-pair}}$ is always higher than $\sigma_{R1\text{-gypsum-pair}}$ for the same flaw pair geometry, with only one exception at $\alpha = 0$ for ligament length 4a (figure 6.46). This flaw pair geometry corresponds to the same flaw pair geometry with $\beta = 0$ in figure 6.48.

	Material	Ligament length	α (°) corresponding to ***minimum*** crack initiation σ	α (°) corresponding to ***maximum*** crack initiation σ
Stepped	Gypsum	2a	60	-30
	Marble	2a	60	-60
	Gypsum	4a	120	0
	Marble	4a	60	-30

	Material	Ligament length	β (°) corresponding to ***minimum*** crack initiation σ	β (°) corresponding to ***maximum*** crack initiation σ
Coplanar	Gypsum	2a	45	75
	Marble	2a	30	75
	Gypsum	4a	45	75
	Marble	4a	30	75

Table 6.19 – Summary of values of bridging angle (α) and flaw inclination angle (β) corresponding to the minimum and the maximum first crack initiation stresses for gypsum and marble.

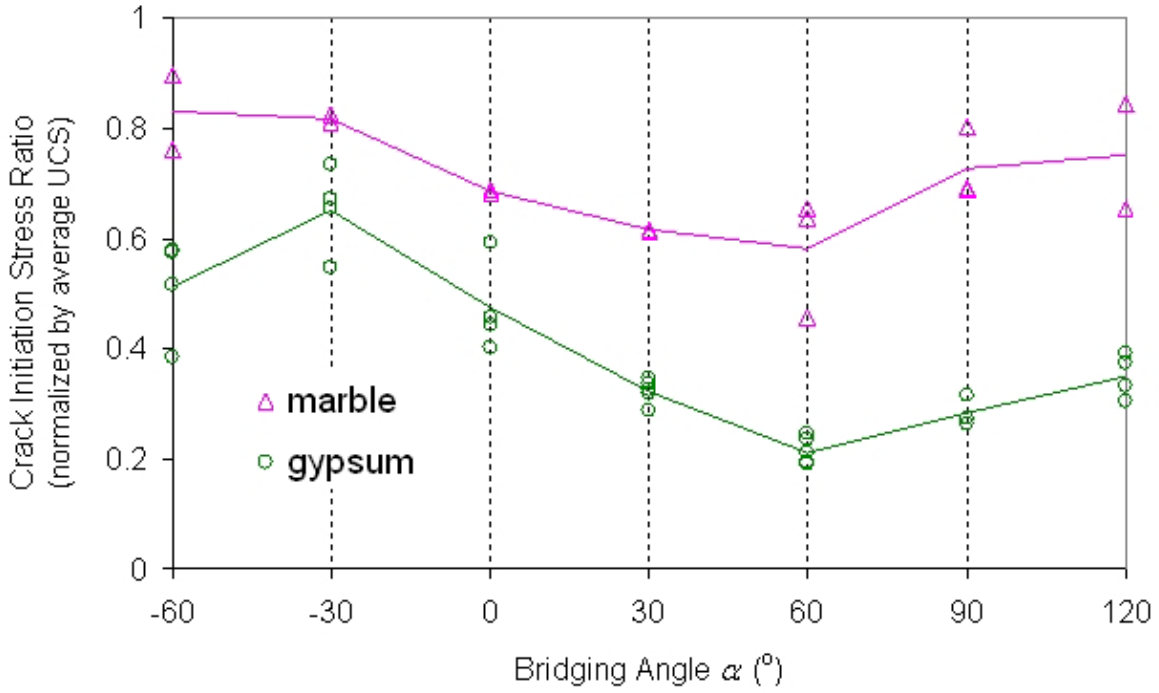

Figure 6.45 – Normalized crack initiation stress versus bridging angle α in gypsum and marble for stepped flaw pairs of 30° flaw inclination angle with ligament length **2a**.

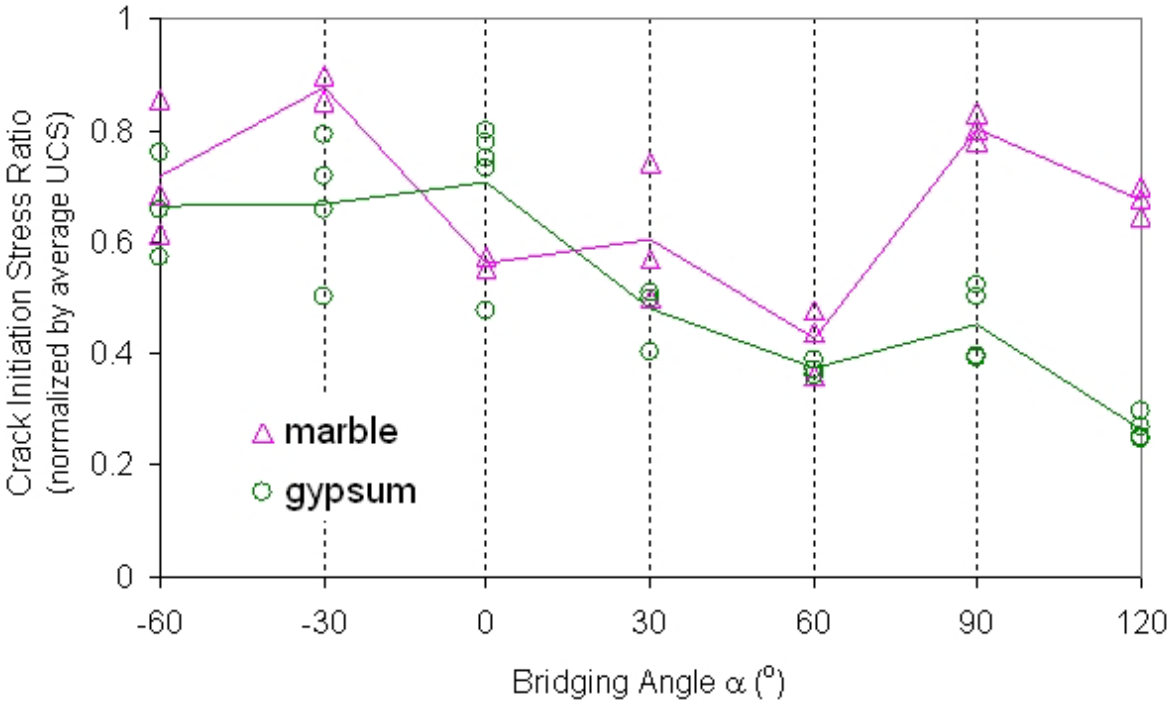

Figure 6.46 – Normalized crack initiation stress versus bridging angle α in gypsum and marble for stepped flaw pairs of 30° flaw inclination angle with ligament length **4a**.

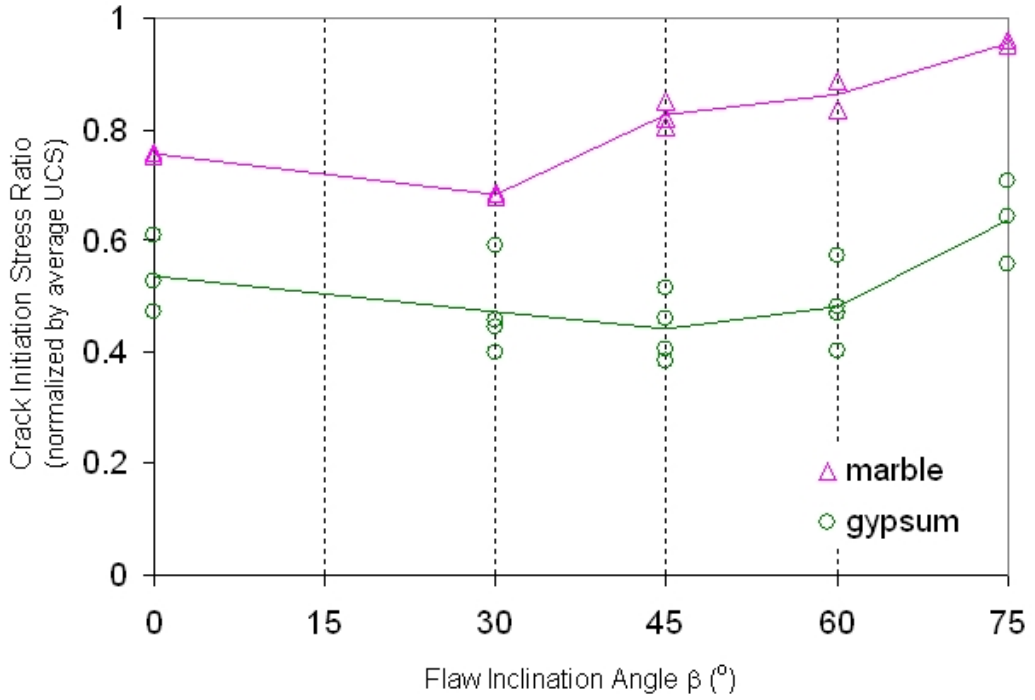

Figure 6.47 – Normalized crack initiation stress versus flaw inclination angle β in gypsum and marble for stepped flaw pairs of 30° flaw inclination angle with ligament length **2a**.

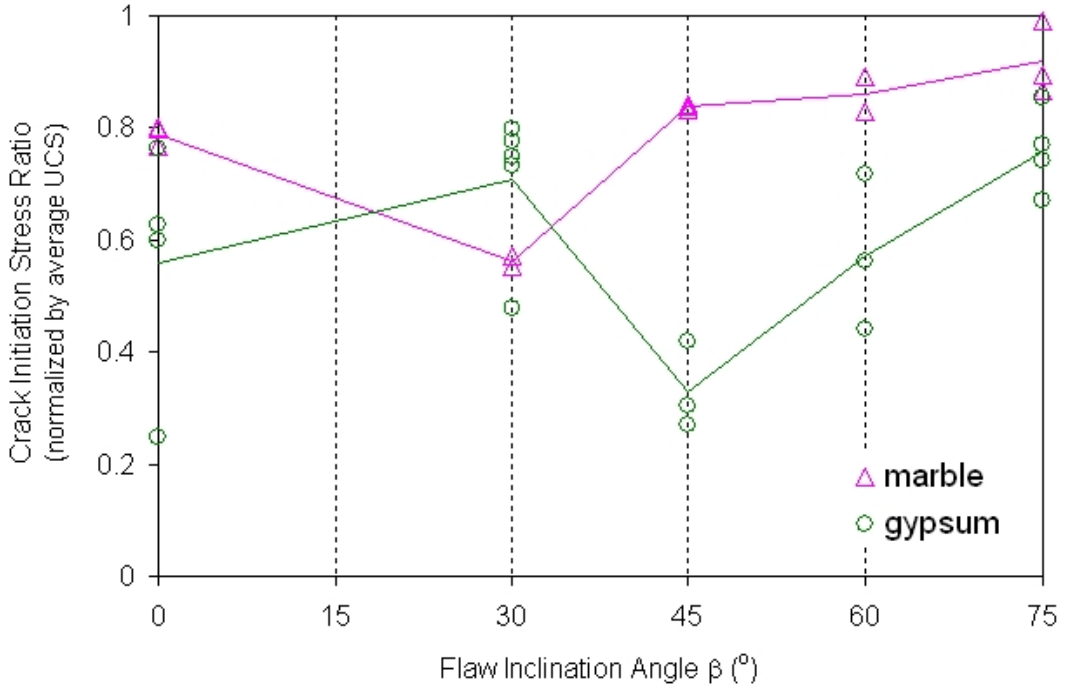

Figure 6.48 – Normalized crack initiation stress versus flaw inclination angle β in gypsum and marble for stepped flaw pairs of 30° flaw inclination angle with ligament length **4a**.

In the plots shown in figures 6.45 to 6.48, the crack initiation stresses are normalized by the respective UCS (see equation 6.1). In the plots shown in figures 6.49 to 6.52, the crack initiation stress obtained from each specimen is normalized by the respective specimen failure stress (specimen failure stress) instead to obtain a different crack initiation stress ratio σ_{R2} :

$$\sigma_{R2} = \frac{\text{first crack initiation stress}}{\text{respective specimen maximum stress}} \tag{6.2}$$

It is important to emphasize that both the first crack initiation stress and the specimen maximum stress used for the computation of each σ_{R2} are obtained from the same specimen in one loading test. The crack initiation stress ratio for gypsum is represented by $\sigma_{R2\text{-gypsum-pair}}$ and that for marble is represented by $\sigma_{R2\text{-marble-pair}}$. An interesting feature revealed from these plots is that $\sigma_{R2\text{-marble-pair}}$ is always greater than $\sigma_{R2\text{-gypsum-pair}}$ for the same flaw pair geometry. Besides, most $\sigma_{R2\text{-marble-pair}}$ values are very close to 1. A σ_{R2} value equal to one indicates that the initiation of the first cracks is concurrent with the specimen maximum stress. A σ_{R2} value close to one indicates that the initiation of first cracks was immediately followed by the occurrence of specimen maximum stress. On the other hand, most $\sigma_{R2\text{-gypsum-pair}}$ values are lower than one, i.e. gypsum specimens had to be loaded further to reach the specimen maximum stress. In addition, $\sigma_{R2\text{-gypsum-pair}}$ values vary with the flaw pair geometry, in a way quite similar to that for $\sigma_{R1\text{-gypsum-pair}}$ as shown in figures 6.45 to 6.48.

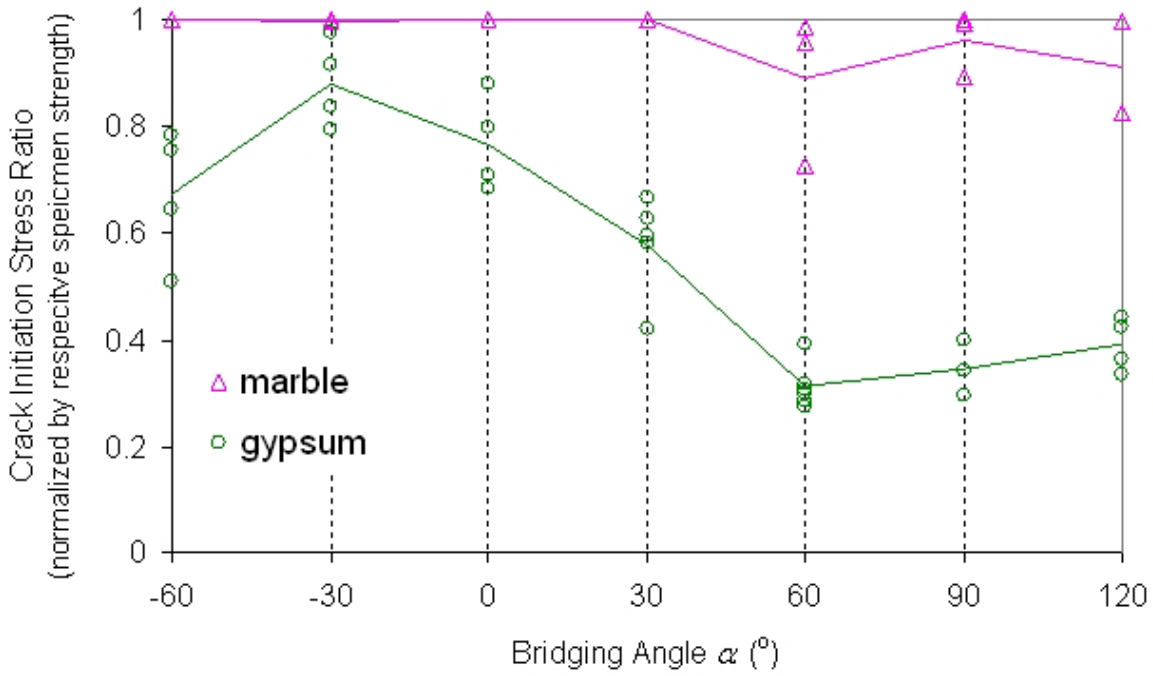

Figure 6.49 – Crack initiation stress normalized by the respective specimen failure stress versus bridging angle α in gypsum and marble for stepped flaw pairs of 30° flaw inclination angle with ligament length **2a**.

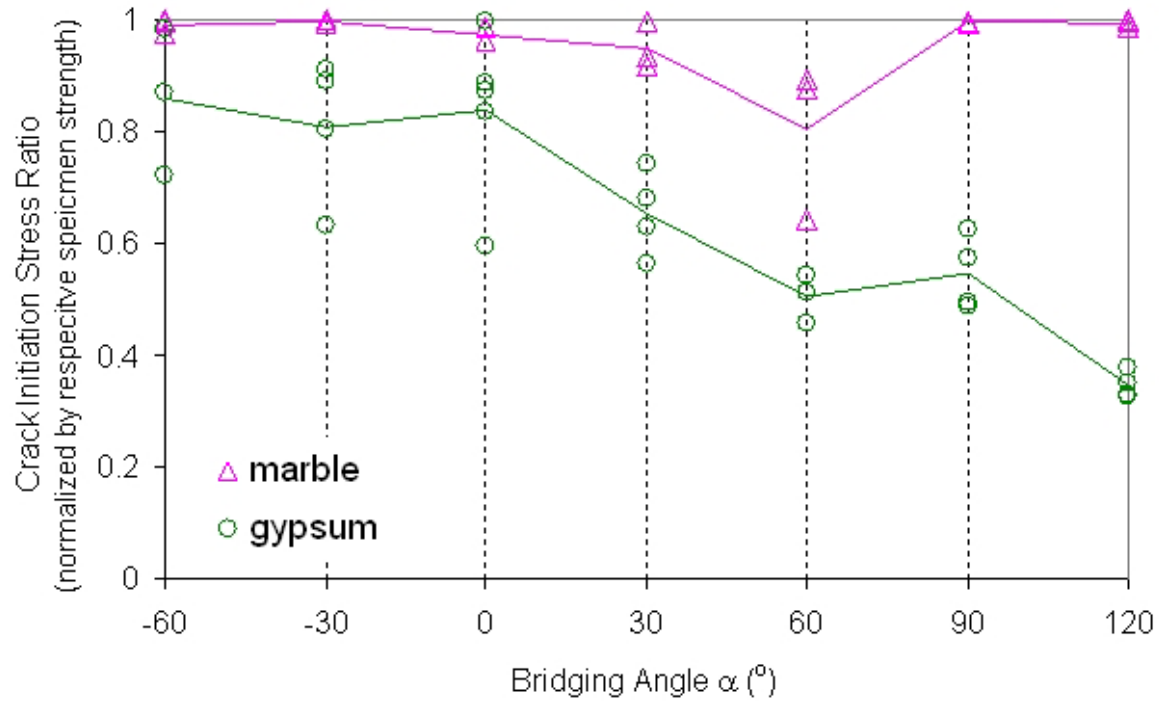

Figure 6.50 – Crack initiation stress normalized by the respective specimen failure stress versus bridging angle α in gypsum and marble for stepped flaw pairs of 30° flaw inclination angle with ligament length **4a**.

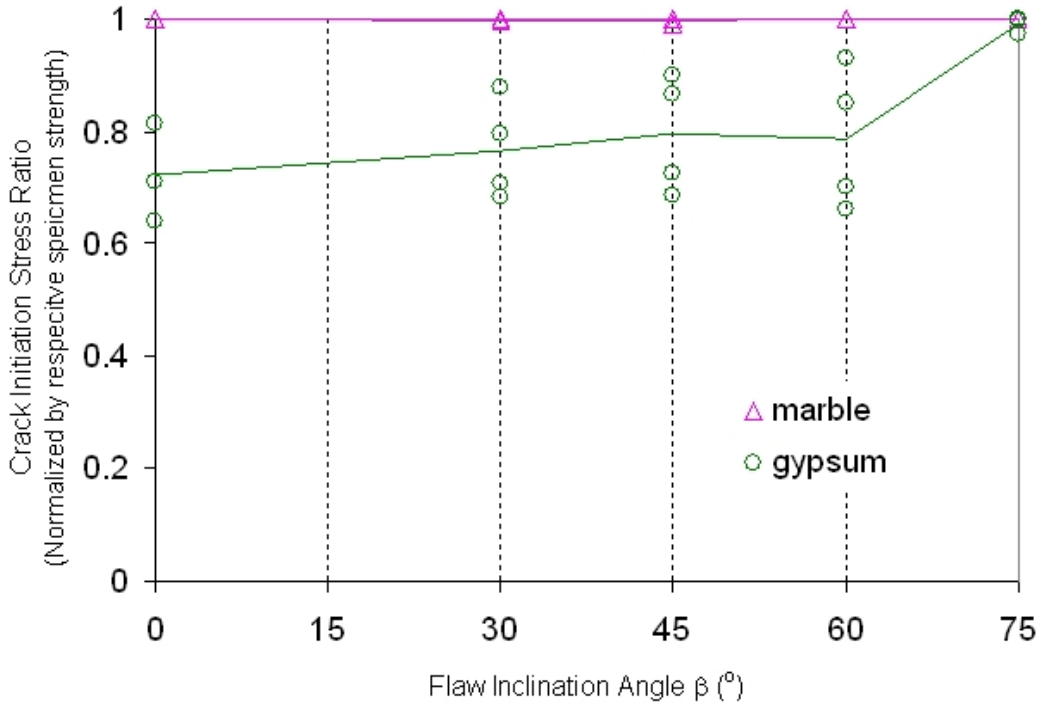

Figure 6.51 – Crack initiation stress normalized by the respective specimen failure stress versus flaw inclination β in gypsum and marble for coplanar flaw pairs with ligament length **2a**.

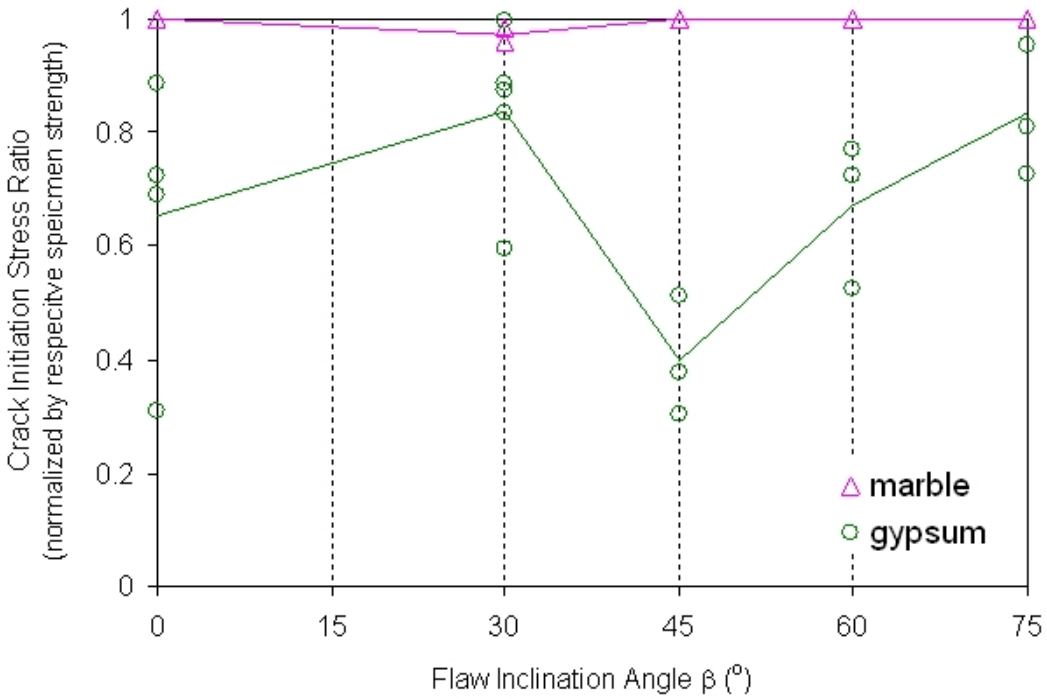

Figure 6.52 – Crack initiation stress normalized by the respective specimen failure stress versus flaw inclination β in gypsum and marble for coplanar flaw pairs with ligament length **4a**.

6.6.3 First cracks in gypsum vs white patches in marble

In response to loading, the first observable changes in gypsum and marble specimens were respectively the initiation of cracks and the development of white patches without observable cracking (as observed in the video recordings). Such a development of white patches was not observed in gypsum. It thus may not be informative enough to simply compare the first crack initiation stresses in gypsum and marble as was done above. It appears to be more appropriate to compare the stresses corresponding to the development of the first observable white patches from the pre-existing flaws in marble with the first crack initiation stress in gypsum.

Two ratios similar to the crack initiation stress ratio σ_{R1} of equation (6.1) and σ_{R2} of equation (6.2) are defined for the white patch initiation :

$$\sigma_{\text{R1-white patch}} = \frac{\text{stress corresponding to the initiaiton of first observable white patch}}{\text{average material uniaxial compressive strength}} \tag{6.3}$$

$$\sigma_{\text{R2-white patch}} = \frac{\text{stress corresponding to the initiaiton of first observable white patch}}{\text{respective specimen maximum stress}} \tag{6.4}$$

In figures 6.53 to 6.56, the first plot in each figure shows the variation of $\sigma_{\text{R1-white patch}}$ and $\sigma_{\text{R1-gypsum-pair}}$ with the bridging angles α (for stepped flaws) and flaw inclination angles β (for coplanar flaws), i.e. the stresses are normalized by the average material UCS; the second plot shows the variation of $\sigma_{\text{R2-white patch}}$ and $\sigma_{\text{R2-gypsum-pair}}$ with the bridging angles α (for stepped flaws) and flaw inclination angles β (for coplanar flaws), i.e. the stresses are normalized by the specimen maximum stress.

The bridging angles α (for stepped flaws) and flaw inclination angles β (for coplanar flaws) corresponding to the maximum and minimum crack initiation stresses (gypsum) or

white patch initiation stresses (marble) of the eight series are summarized in tables 6.20 a and b.

It is interesting to note that the stress ratios for marble are generally **higher** than those for gypsum for ligament length ***2a*** (figures 6.53 & 6.55), while the stress ratios for marble are **lower** than those for gypsum for ligament length ***4a*** (figures 6.54 & 6.56). Nonetheless, the two materials not only show a similar trend of variation of stress ratio (crack initiation in gypsum and white patch initiation in marble) with bridging angle (stepped flaws) and flaw inclination angle (coplanar flaws), but also have close stress ratios for certain angle ranges:

- negative bridging angles and small positive bridging angles for stepped flaws with ligament length **2a (**figure 6.53),
- large positive bridging angles for stepped flaws with ligament length **4a (**figure 6.54),
- whole range of flaw inclination angles for coplanar flaws with ligament length **2a** (figure 6.55),
- flaw inclination angle $\beta = 45^{o}$ for coplanar flaws with ligament length **4a** in (figure 6.56).

There thus appears to be an analogy between the white patch in marble and the first crack occurrence in gypsum. The production of white patches is speculated to indicate the presence of microcracks associated with the process zone. The microstructural nature of the white patches in marble will be studied in detail in the following chapter.

	Material	Ligament length	α (^{o}) corresponding to ***minimum*** crack initiation σ (gypsum) OR white patch initiation σ (marble)	α (^{o}) corresponding to ***maximum*** crack initiation σ (gypsum) OR white patch initiation σ (marble)
Stepped	Gypsum	2a	60	-30
	Marble	2a	30	-30
	Gypsum	4a	120	0
	Marble	4a	-60	0

	Material	Ligament length	β (^{o}) corresponding to ***minimum*** crack initiation σ (gypsum) OR white patch initiation σ (marble)	β (^{o}) corresponding to ***maximum*** crack initiation σ (gypsum) OR white patch initiation σ (marble)
Coplanar	Gypsum	2a	45	75
	Marble	2a	60	75
	Gypsum	4a	45	75
	Marble	4a	0	75

Table 6.20a – Summary of values of bridging angle (α) and flaw inclination angle (β) corresponding to the minimum and the maximum first crack initiation stresses for gypsum and white patch initiation stresses for marble. **The stresses are normalized by the average UCS.**

	Material	Ligament length	α (°) corresponding to ***minimum*** crack initiation σ (gypsum) OR white patch initiation σ (marble)	α (°) corresponding to ***maximum*** crack initiation σ (gypsum) OR white patch initiation σ (marble)
Stepped	Gypsum	2a	60	-30
	Marble	2a	90	0
	Gypsum	4a	120	-60
	Marble	4a	-60	0

	Material	Ligament length	β (°) corresponding to ***minimum*** crack initiation σ (gypsum) OR white patch initiation σ (marble)	β (°) corresponding to ***maximum*** crack initiation σ (gypsum) OR white patch initiation σ (marble)
Coplanar	Gypsum	2a	0	75
	Marble	2a	60	30
	Gypsum	4a	45	30
	Marble	4a	0	30

Table 6.20b – Summary of values of bridging angle (α) and flaw inclination angle (β) corresponding to the minimum and the maximum first crack initiation stresses for gypsum and white patch initiation stresses for marble. **The stresses are normalized by the respective specimen failure stress.**

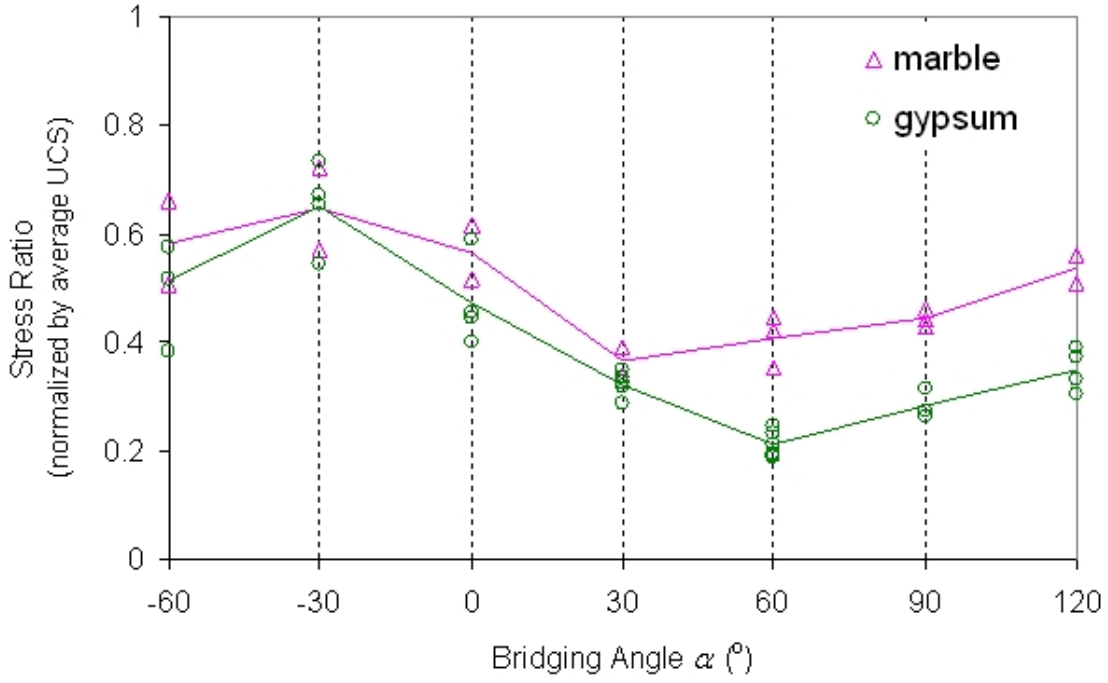

(a)

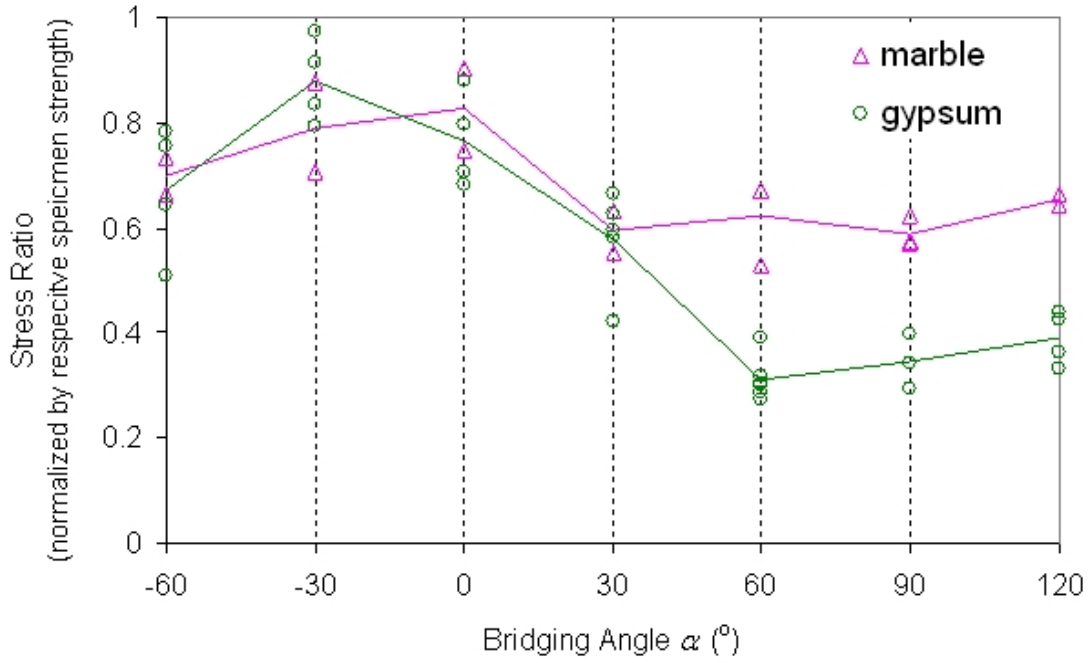

(b)

Figure 6.53 – Comparison of first crack initiation stress in gypsum with the stress corresponding to the first white patch initiation in marble, (a) normalized by the average UCS, (b) normalized by the respective specimen strength. All stepped flaw pairs were oriented at flaw inclination angle (β) 30° with ligament length **2a**.

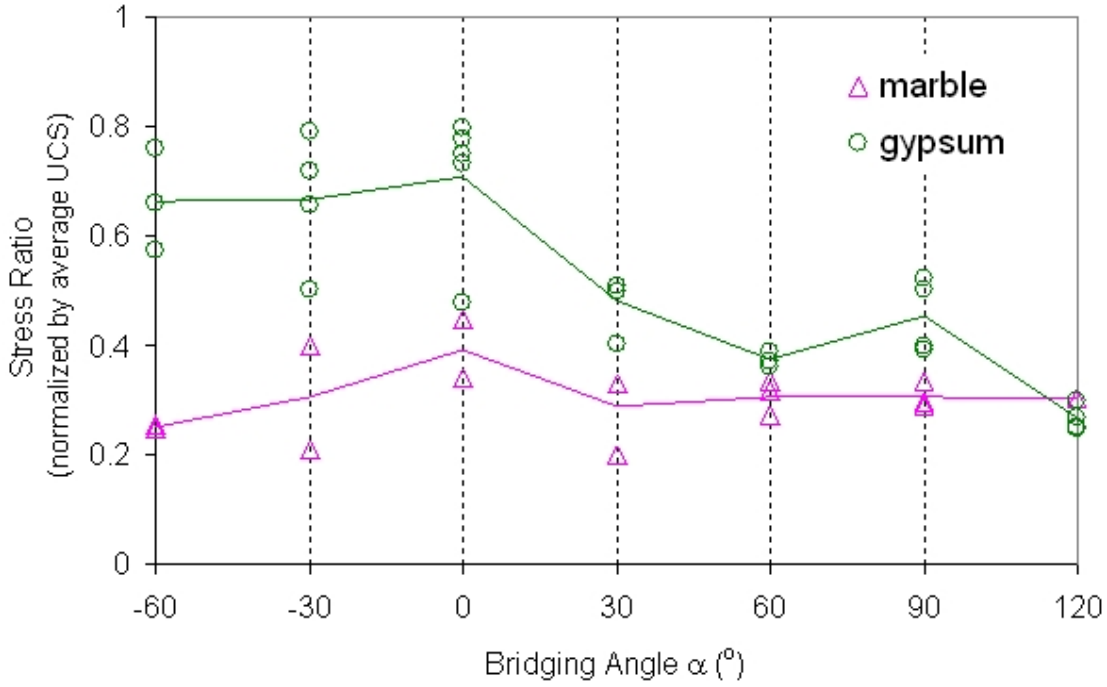

(a)

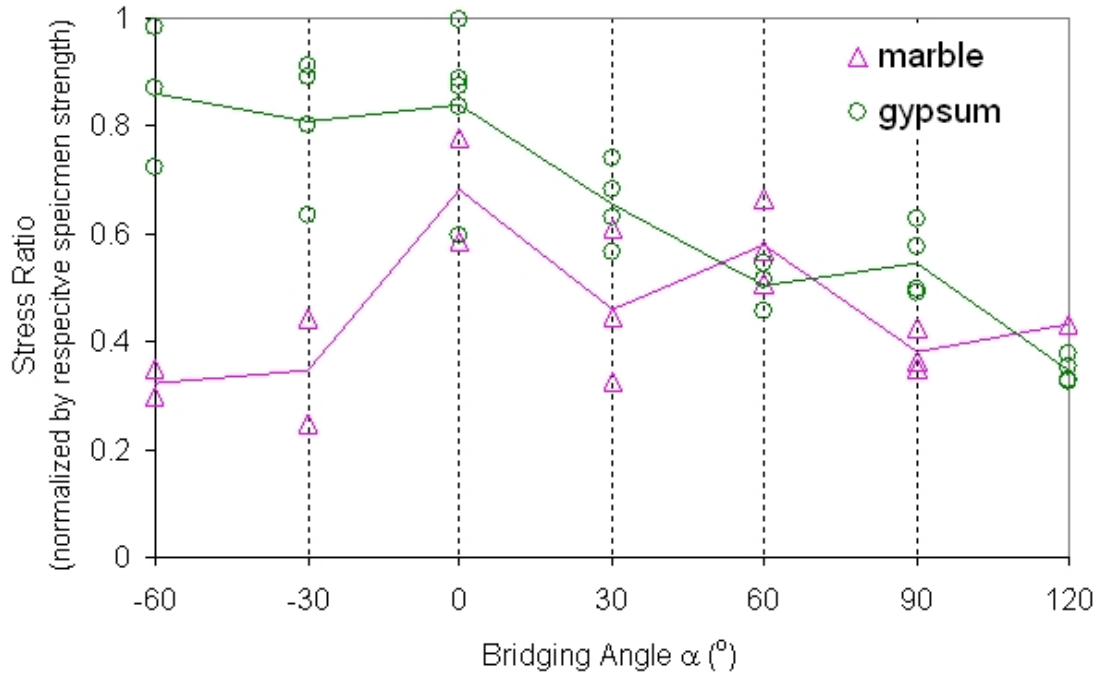

(b)

Figure 6.54 – Comparison of first crack initiation stress in gypsum with the stress corresponding to the first white patch initiation in marble, (a) normalized by the average UCS, (b) normalized by the respective specimen strength. All stepped flaw pairs were oriented at flaw inclination angle (β) 30° with ligament length **4a**.

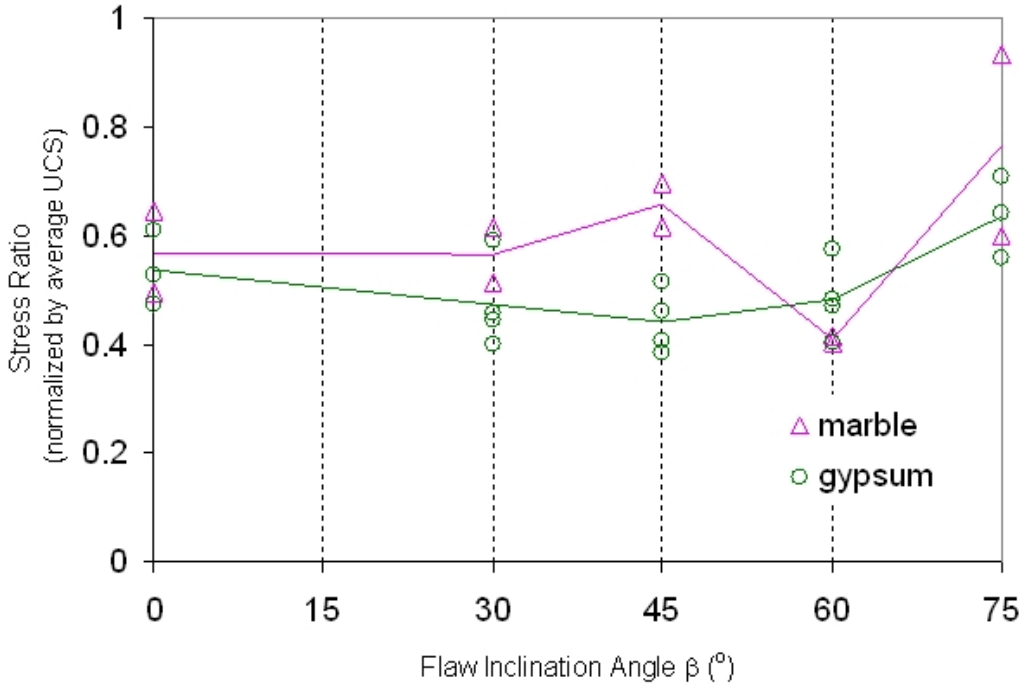

(a)

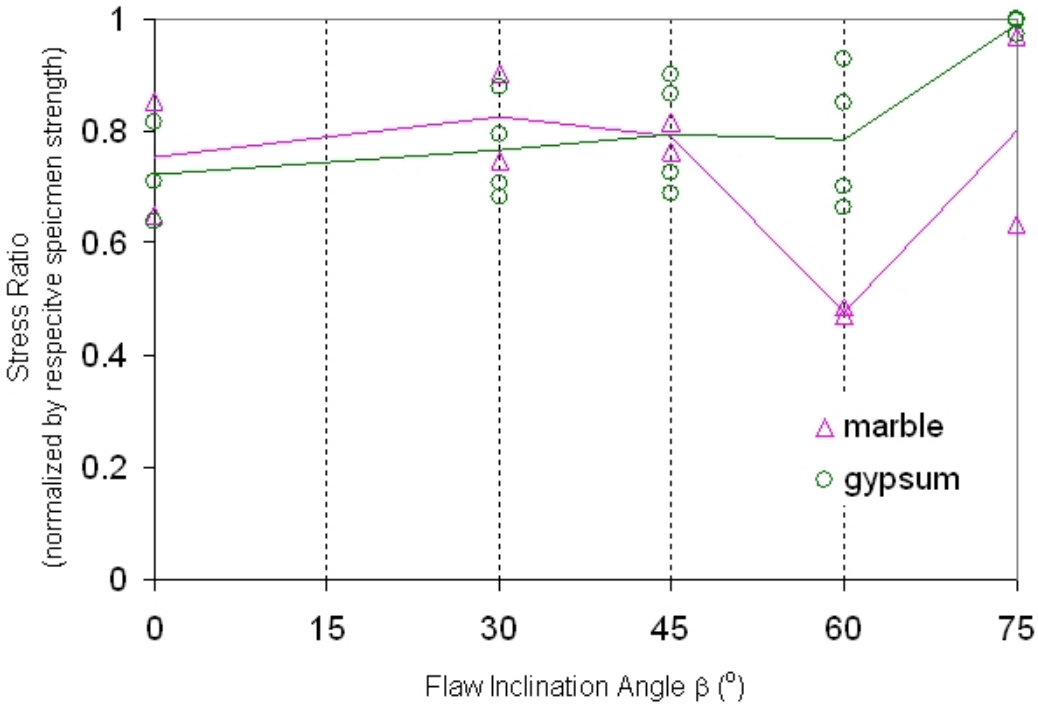

(b)

Figure 6.55 – Comparison of first crack initiation stress in gypsum with the stress corresponding to the first white patch initiation in marble, (a) normalized by the average UCS, (b) normalized by the respective specimen strength. All coplanar flaw pairs were with ligament length **2a**.

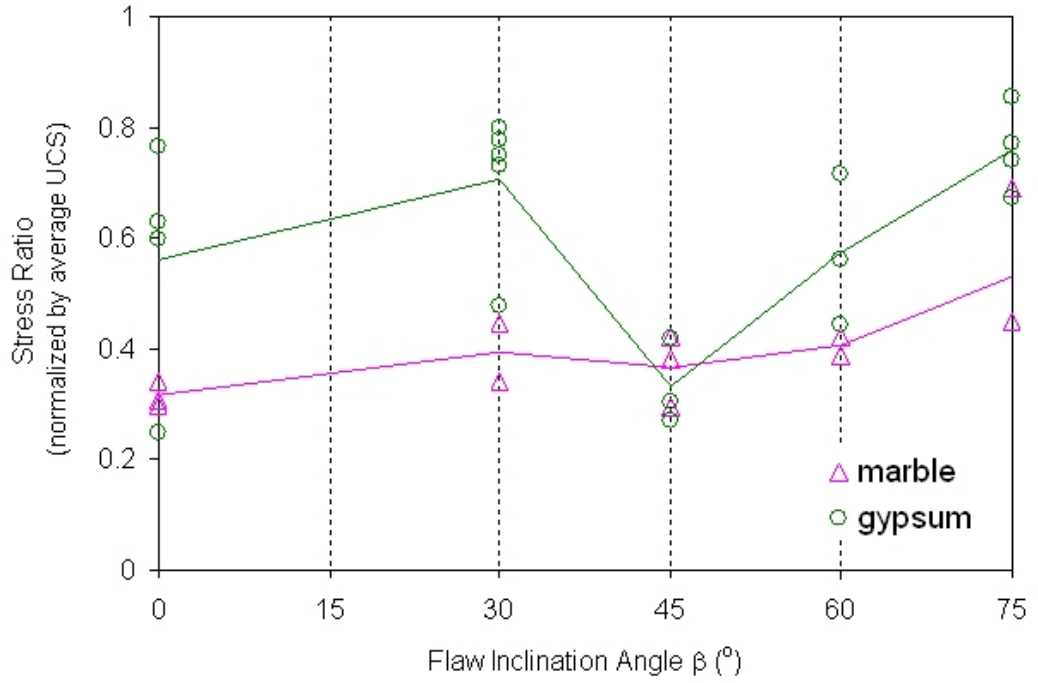

(a)

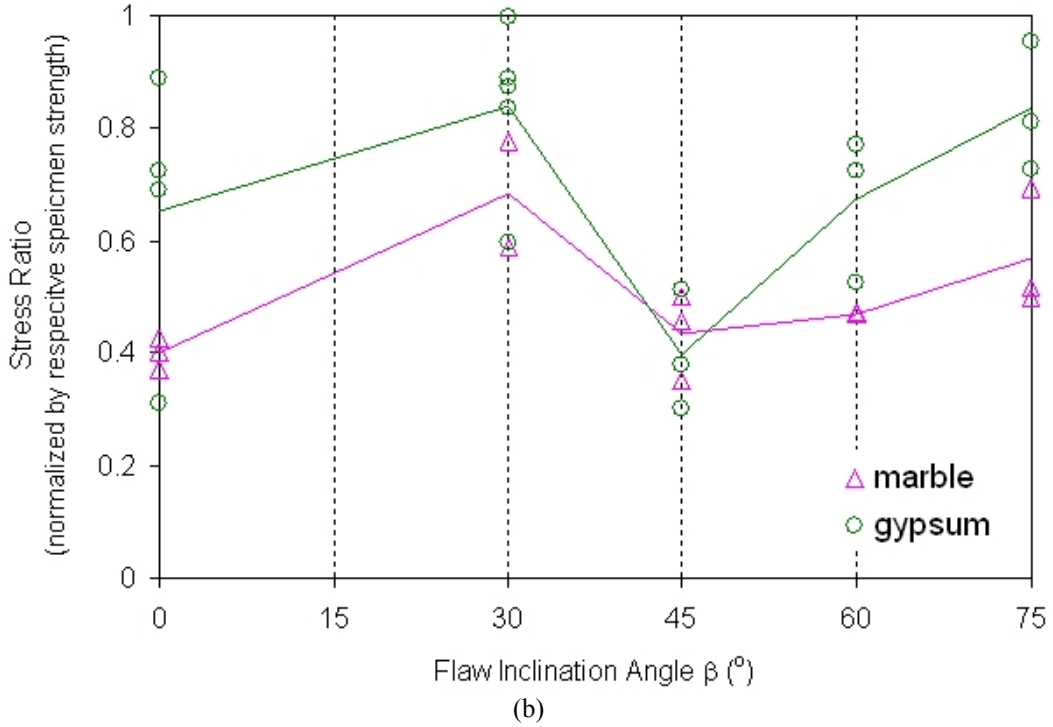

(b)

Figure 6.56 – Comparison of first crack initiation stress in gypsum with the stress corresponding to the first white patch initiation in marble, (a) normalized by the average UCS, (b) normalized by the respective specimen strength. All coplanar flaw pairs were with ligament length **4a**.

6.7 Summary

The results obtained from uniaxial compression tests conducted on molded gypsum and Carrara Marble specimens with different flaw pair geometries (eight series) are reviewed in this chapter (see table below). This section summarizes the results, particularly the influence of material type, flaw inclination angle β, bridging angle α and ligament length L on the crack coalescence patterns obtained from the parametric studies.

Series	Section	Appendix
Gypsum – Coplanar – "2a"	6.3.1	H
Gypsum – Stepped – "2a"	6.3.2	I
Marble – Coplanar – "2a"	6.3.3	J
Marble – Stepped – "2a"	6.3.4	K
Gypsum – Coplanar – "4a"	6.4.1	L
Gypsum – Stepped – "4a"	6.4.2	M
Marble – Coplanar – "4a"	6.4.3	N
Marble – Stepped – "4a"	6.4.4	O

Table 6.21 – Eight experimental series tested in gypsum and marble.

6.7.1 Coalescence categories

The newly proposed crack coalescence classification scheme contains nine categories. Refer to figure 6.5 which is reproduced below. The principle is to classify crack coalescence patterns according to the type of the coalescence cracks involved. Figure 6.5 is tabulated in such a way that that the **categories 1 and 2** are no coalescence and indirect coalescence respectively. Higher category numbers are arranged with a general trend of variation of coalescence types from shear (**categories 3, 4**) to mixed shear-tensile (**category 5**) to tensile (**categories 6, 7, 8, 9**). See table 6.22 below.

Category	1	2	3 - 4	5	6 - 9
Nature of coalescence	no coalescence	indirect coalescence	direct shear coalescence	direct mixed shear-tensile coalescence	direct tensile coalescence

Table 6.22 – Nature of different coalescence categories.

Except **categories 1, 2 and 8**, the coalescence processes of the other coalescence categories are due to the initiation and propagation of one or more cracks with types shown in figure 3.15 (reproduced on a subsequent page). For example, coalescence of **category 3** is achieved by one type 2 shear crack or two type 2 shear cracks, while that of **category 4** is achieved by one type 1 shear crack or two type 1 shear cracks.

The crack coalescence classification scheme shown in figure 6.5 forms the basis of the discussion in the remaining part of this summary section. Notice that this classification scheme is different from the one previously proposed by the MIT-Purdue group.

Category	Coalescence patterns	Crack types involved
1	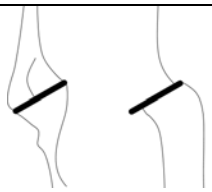	**No** coalescence
2	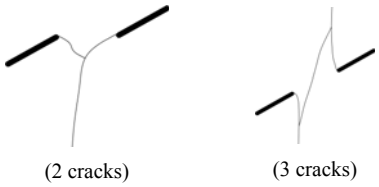	**Indirect** coalescence by two or multiple cracks (crack types vary)
3	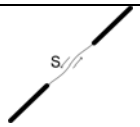	Type 2 **S** crack(s)
4	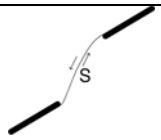	Type 1 **S** crack(s)
5	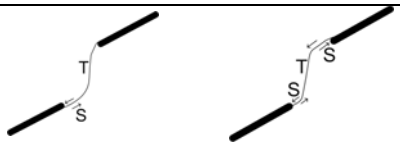	One or more type 2 **S** crack(s) and type 2 **T** crack segments between inner flaw tips
6	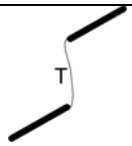	Type 2 **T** crack(s). There may be occasional short **S** segments present along the coalescence crack.
7		Type 1 **T** crack(s)
8		Flaw tips of the same side linked up by **T** crack(s) not displaying wing appearance (crack type not classified). There may be occasional short **S** segments present along the coalescence crack.
9	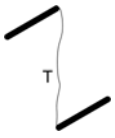	Type 3 **T** crack(s) linking right tip of the top flaw and left tip of the bottom flaw. There may be occasional short **S** segments present along the coalescence crack.

Figure 6.5 – Crack coalescence types.

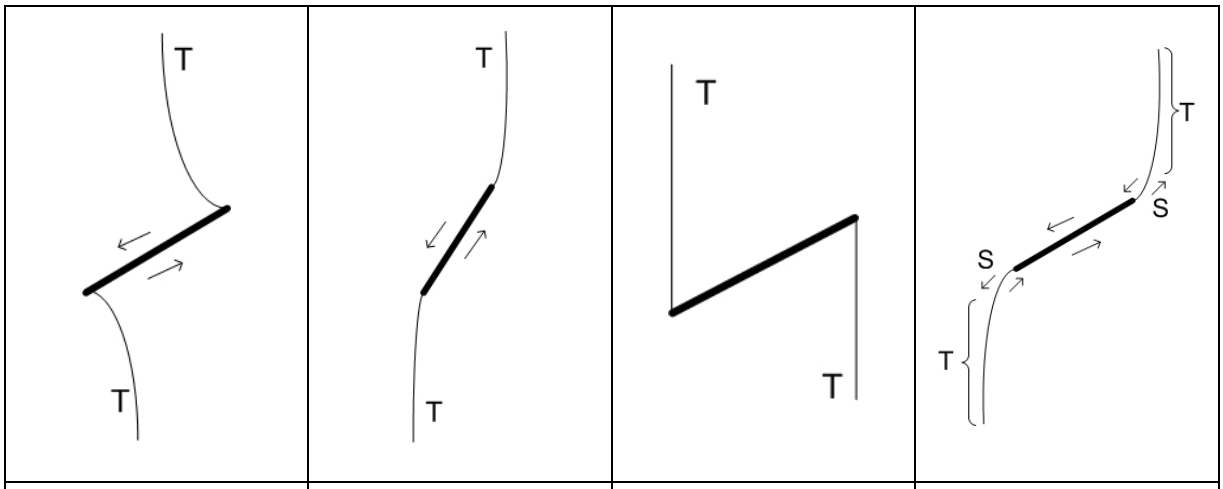

(a) Type 1 tensile crack (tensile wing crack)	(b) Type 2 tensile crack	(c) Type 3 tensile crack	(d) Mixed tensile-shear crack

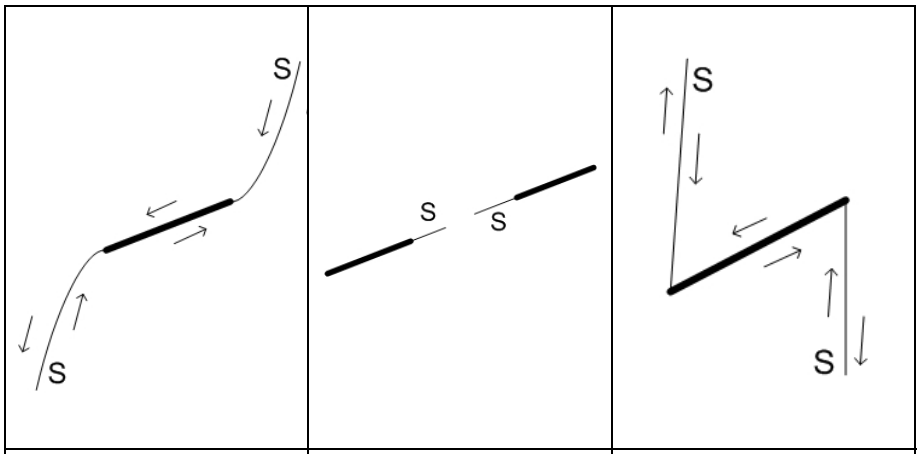

(e) Type 1 shear crack	(f) Type 2 shear crack	(g) Type 3 shear crack

Figure 3.15 – Types of cracks observed in gypsum and marble.

6.7.2 Influence of flaw inclination angle

Flaw inclination angle was observed to have a strong influence on the fracturing and crack coalescence patterns in the four series of experimental tests on gypsum and marble with **coplanar** flaw pair geometries (bridging angle $\alpha = 0^o$). See table 6.23 below.

Category		**Gypsum (table 6.6)**		**Marble (table 6.12)**	
		Ligament length 2a	Ligament length 4a	Ligament length 2a	Ligament length 4a
1	No coalescence	0	0, 30	0, 45	0, 30, 45
2	Indirect coalescence	0	0, 30	30, 45	0
3	Shear	30	45, 60	45	60
5	Mixed shear-tensile	45, 60, 75	75	-	-
6	Tensile	-	-	60, 75	75

Table 6.23 – Coalescence behavior of coplanar flaws in gypsum and marble with '2a' and '4a' ligament length. The numbers indicated are the flaw inclination angles β (^{o})

The overall trend of coalescence behavior variation with flaw inclination angle in gypsum and marble specimens with ligament length '**2a**' and '**4a**' were similar, i.e. the coalescence patterns of flaw pairs with small flaw inclination angles belong to low category numbers, while those flaw pairs with large flaw inclination angles belong to high category numbers. Note that since the coalescence cracks involved in coalescence

categories 4, 7, 8 and 9 were all out-of-plane cracks (i.e. not parallel with the pre-existing flaws), these four coalescence categories thus only developed in stepped flaw pairs, but not in coplanar flaw pairs. The influence of material is revealed by the unique occurrence of **category 5** in gypsum (but not in marble), and unique occurrence of **category 6** in marble (but not in gypsum). Specific flaw inclination angles at which there were transitions of crack coalescence categories were found to depend on the ligament length (e.g. in gypsum $\beta = 45^o$, 60^o belong to **category 5** for ligament length 2a, while they belong to **category 3** for ligament length 4a). The influence of material type and ligament length on coalescence will be summarized later.

6.7.3 Influence of bridging angle

Bridging angle was observed to have a strong influence on the fracturing and crack coalescence in the four series of experimental tests on gypsum and marble with **stepped** flaw pair geometries (flaw inclination angle $\beta = 30^o$). See table 6.24 below.

The overall trend of coalescence behavior variation with bridging angle α in gypsum and marble specimens with ligament length '**2a**' and '**4a**' were quite similar, i.e. the coalescence patterns of flaw pairs with negative and small positive α belonged to low category numbers, while those flaw pairs with large α belonged to high category numbers. More specifically, $\alpha = -60^o$, -30^o, and occasionally 0^o favored no coalescence (**category 1**) or indirect coalescence (**category 2**). As α increased, direct coalescence became achieved by shear crack(s), i.e. **categories 3 and 4**. As shown in table 6.24, these categories were however absent in some series, which indicated the significant influence of other parameters, i.e. material type and ligament length. The influence of these two parameters persisted as α increased to intermediate values – **category 5** was present in both series in gypsum, but absent in marble. As α further increased to large values, "tensile" coalescence became dominant (**categories 6 to 9**). The occurrence of particular coalescence categories was again dependent on the material type and ligament length.

Category		Gypsum (table 6.7)		Marble (table 6.13)	
		Ligament length 2a	Ligament length 4a	Ligament length 2a	Ligament length 4a
1	No coalescence	-60, -30	-60, -30, 0	-60, -30	-60, -30, 0
2	Indirect coalescence	-60, -30	-60, 0	-60, -30, 0	-60, -30, 30
3	Shear	0	-	-	-
4		-	-	30	-
5	Mixed shear-tensile	30, 60	30, 60	-	-
6	Tensile	-	-	60	60
7		90, 120	90, 120	90, 120	-
8		-	-	120	90
9		-	-	-	120

Table 6.24 – Coalescence behavior of stepped flaws in gypsum and marble with '2a' and '4a' ligament length. The numbers indicated in the tables are bridging angles α (^{o})

To summarize, the whole spectrum of crack coalescence categories (from 1 to 9) was observed from the four stepped flaw pair series – generally from no coalescence, indirect coalescence to direct coalescence. Due to the influence of two other parameters, i.e. material type and ligament length, the occurrence of particular coalescence categories varied among the tested series.

6.7.4 Influence of ligament length

The influence of ligament length on coalescence patterns was discussed in sections 6.3.5 (gypsum) and 6.4.5 (marble). Physically speaking, wider separation between the inner flaw tips reduces the mutual influence/interaction between the flaws, and hence the less chance of coalescence. To better reveal the influence of ligament length, tables 6.23 and 6.24 are reorganized to tables 6.25 and 6.26.

<table>
<tr><th rowspan="2">Flaw inclination angles β (^{o})</th><th colspan="2">Gypsum</th><th colspan="2">Marble</th></tr>
<tr><td>Ligament length 2a</td><td>Ligament length 4a</td><td>Ligament length 2a</td><td>Ligament length 4a</td></tr>
<tr><td>0</td><td>Category 1, 2</td><td>Category 1, 2</td><td>Category 1</td><td>Category 1, 2</td></tr>
<tr><td rowspan="2">30</td><td>Category 3</td><td>Category 1, 2</td><td>Category 2</td><td>Category 1</td></tr>
<tr><td colspan="2">(figure 6.57)
Note in figure 6.57b for L = 4a, only image corresponding to category 2 (but not category 1) is shown.</td><td colspan="2">(figure 6.58)</td></tr>
<tr><td rowspan="2">45</td><td rowspan="2">Category 5</td><td rowspan="2">Category 3</td><td>Category 1, 2, 3</td><td>Category 1</td></tr>
<tr><td colspan="2">(figure 6.59)
Note in figure 6.59a for L = 2a, only image corresponding to category 2 (but not categories 1 & 3) is shown.</td></tr>
<tr><td rowspan="2">60</td><td rowspan="2">Category 5</td><td rowspan="2">Category 5</td><td>Category 6</td><td>Category 3</td></tr>
<tr><td colspan="2">(figure 6.60)</td></tr>
<tr><td>75</td><td>Category 5</td><td>Category 5</td><td>Category 6</td><td>Category 6</td></tr>
</table>

Table 6.25 – Coalescence categories of coplanar flaws in gypsum and marble with ‘2a’ and ‘4a’ ligament length.

<table>
<tr><th rowspan="2">Bridging angles α (^{o})</th><th colspan="2">Gypsum</th><th colspan="2">Marble</th></tr>
<tr><td>Ligament length 2a</td><td>Ligament length 4a</td><td>Ligament length 2a</td><td>Ligament length 4a</td></tr>
<tr><td>-60</td><td>Category 1, 2</td><td>Category 1, 2</td><td>Category 1, 2</td><td>Category 1, 2</td></tr>
<tr><td>-30</td><td>Category 1, 2</td><td>Category 1</td><td>Category 1, 2</td><td>Category 1, 2</td></tr>
<tr><td rowspan="2">0</td><td>Category 3</td><td>Category 1, 2</td><td>Category 2</td><td>Category 1</td></tr>
<tr><td colspan="2">(figure 6.57)
Note in figure 6.57b for L = 4a, only image corresponding to category 2 (but not category 1) is shown.</td><td colspan="2">(figure 6.58)</td></tr>
<tr><td rowspan="2">30</td><td rowspan="2">Category 5</td><td rowspan="2">Category 5</td><td>Category 4</td><td>Category 2</td></tr>
<tr><td colspan="2">(figure 6.61)</td></tr>
<tr><td>60</td><td>Category 5</td><td>Category 5</td><td>Category 6</td><td>Category 6</td></tr>
<tr><td rowspan="2">90</td><td rowspan="2">Category 7</td><td rowspan="2">Category 7</td><td>Category 7</td><td>Category 8</td></tr>
<tr><td colspan="2">(figure 6.62)</td></tr>
<tr><td rowspan="2">120</td><td rowspan="2">Category 7</td><td rowspan="2">Category 7</td><td>Category 7, 8</td><td>Category 9</td></tr>
<tr><td colspan="2">(figure 6.63)
Note in figure 6.63a for L = 2a, only image corresponding to category 8 (but not category 7) is shown.</td></tr>
</table>

Table 6.26 – Coalescence categories of stepped flaws in gypsum and marble with ‘2a’ and ‘4a’ ligament length.

The influence of ligament length (***L***) on coalescence patterns was revealed in two different ways. First, for certain geometries with the same flaw inclination angle and bridging angle, coalescence occurred for ***L*** = 2a, but not for ***L*** = 4a. Second, coalescence occurred for both ***L*** = 2a and ***L*** = 4a in certain geometries with the same flaw inclination angle and bridging angle, but with different coalescence categories. See below for further information.

As shown in table 6.27, coalescence occurred for a number of coplanar flaw pairs with ***L*** = 2a, but not for some tested specimen with ***L*** = 4a.

Flaw geometries	**Particulars**
Gypsum with $\beta = 30^o$, and $\alpha = 0^o$ (figure 6.57)	coalescence category 3 for ligament length 2a, but no coalescence (category 1) in some specimens for ligament length 4a
Marble with $\beta = 30^o$, and $\alpha = 0^o$ (figure 6.58)	coalescence category 2 for ligament length 2a, but no coalescence (category 1) for ligament length 4a
Marble with $\beta = 45^o$, and $\alpha = 0^o$ (figure 6.59)	coalescence categories 3 for ligament length 2a, but no coalescence (category 1) for ligament length 4a

Table 6.27 – Summary of flaw geometries with ligament length **4a** in which no coalescence occurred.

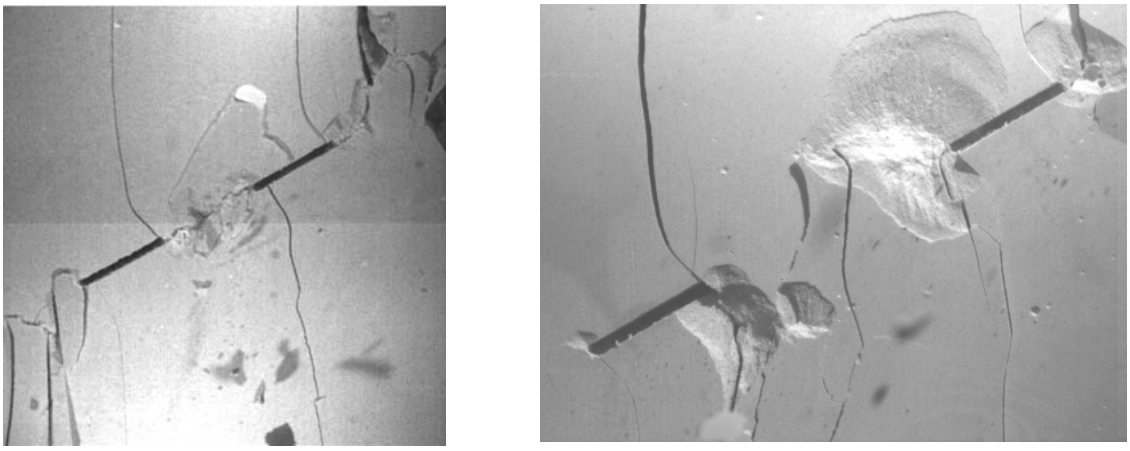

(a) (b)

Figure 6.57 – (a) direct shear coalescence (category 3) for gypsum 2a-30-0, (b) no coalescence (category 1) for gypsum 4a-30-0.

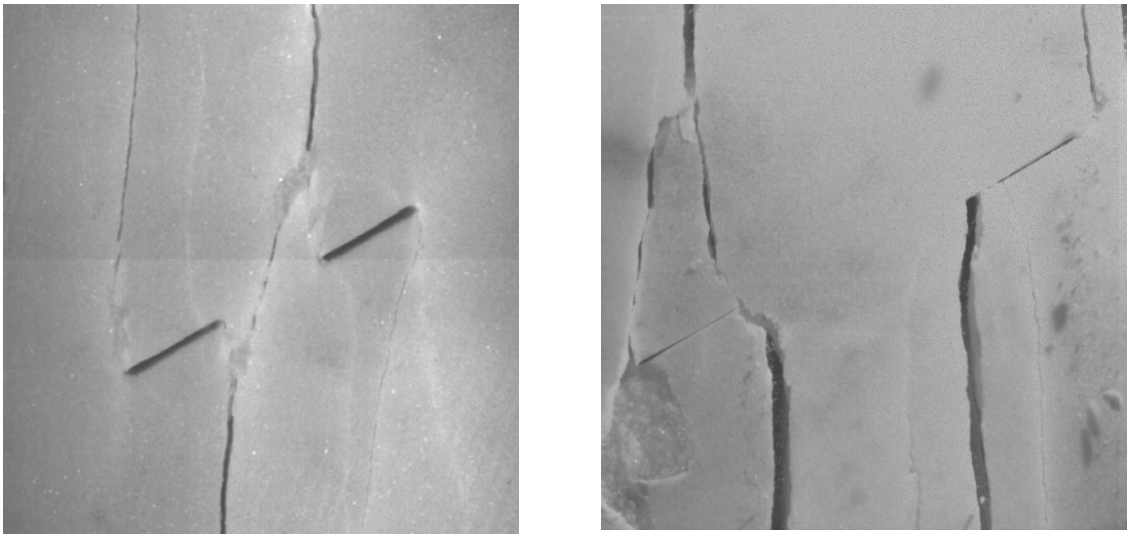

(a) (b)

Figure 6.58 – (a) indirect coalescence (category 2) for marble 2a-30-0, (b) no coalescence (category 1) for marble 4a-30-0.

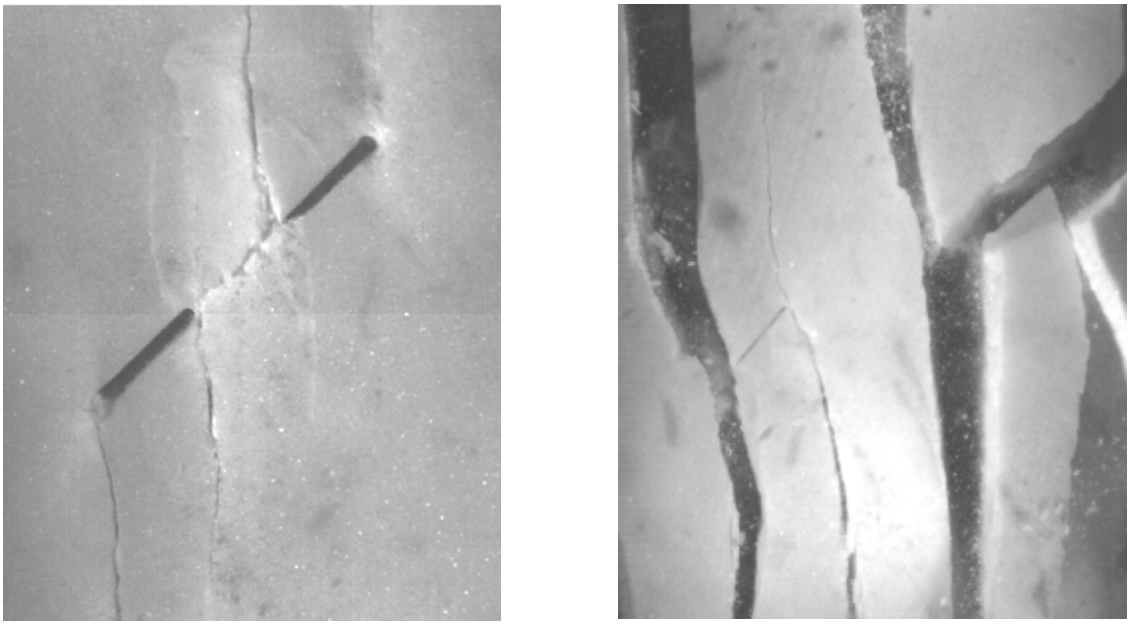

(a) (b)

Figure 6.59 – (a) direct coalescence (category 3) for marble 2a-45-0, (b) no coalescence (category 1) for marble 4a-45-0.

Wider flaw separation not only suppressed the occurrence of coalescence in certain flaw geometries as discussed above, but also led to different coalescence categories for a number of flaw geometries as shown in tables 6.25 and 6.26. Some of these examples are illustrated in figures 6.60 to 6.63 below.

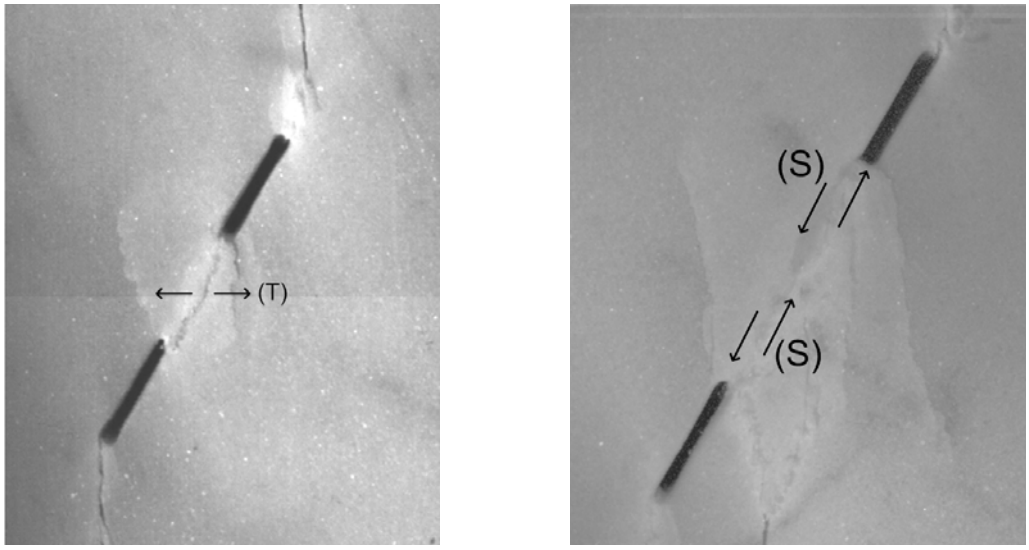

(a) (b)

Figure 6.60 – (a) Tensile coalescence (category 6) for marble 2a-60-0, (b) Shear coalescence (category 3) for marble 4a-60-0.

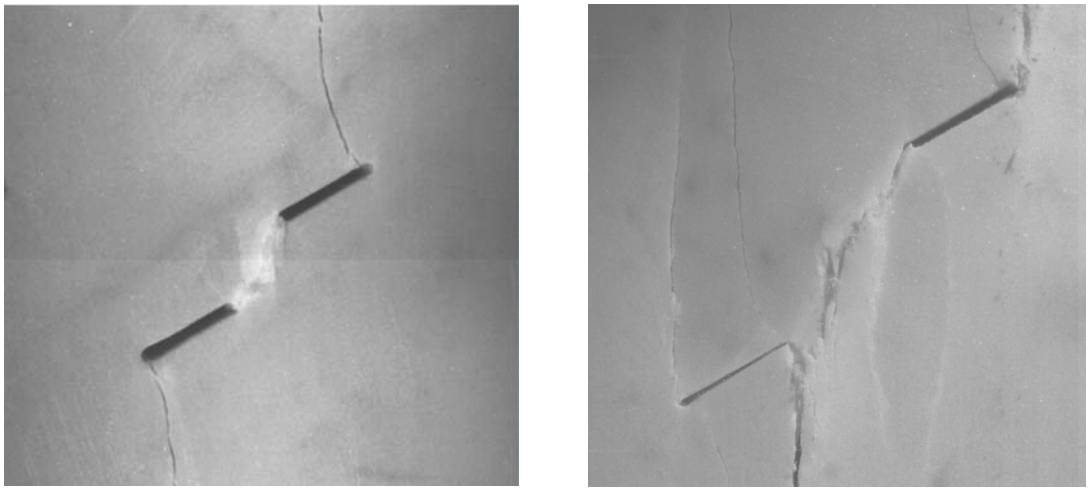

(a) (b)

Figure 6.61 – (a) Direct coalescence (category 4) for marble 2a-30-30, (b) indirect coalescence (category 2) for marble 4a-30-30.

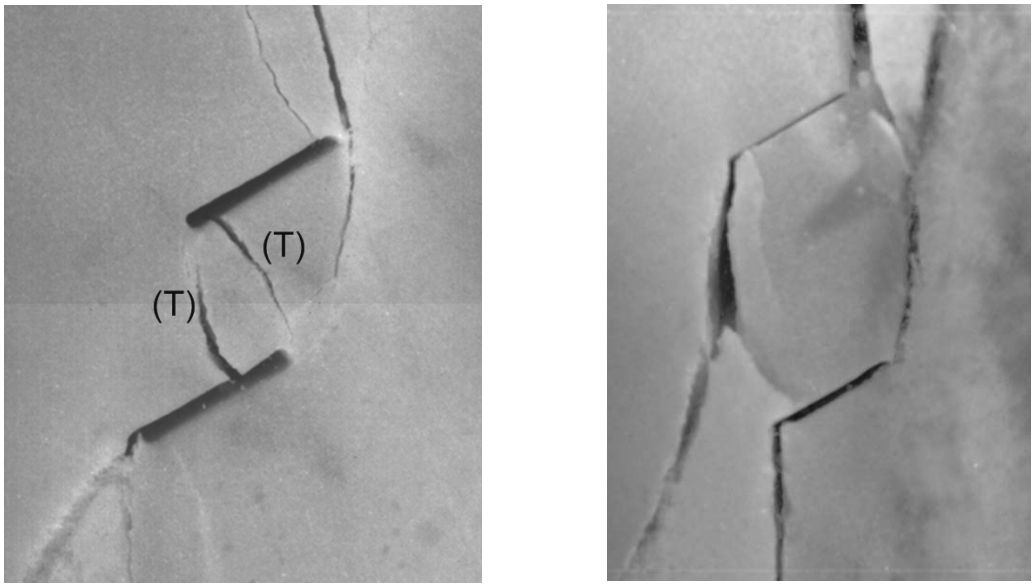

(a) (b)

Figure 6.62 – (a) Coalescence category 7 for marble 2a-30-90, (b) Coalescence category 8 for marble 4a-30-90.

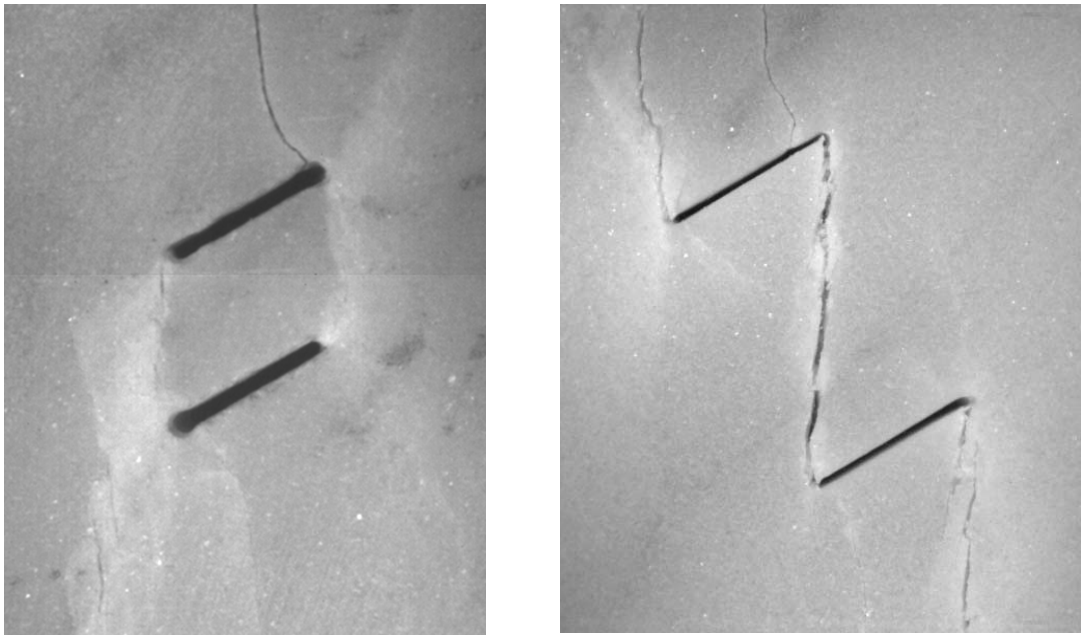

(a) (b)

Figure 6.63 – (a) Coalescence category 8 for marble 2a-30-120, (b) Coalescence category 9 for marble 4a-30-120.

6.7.5 Influence of material

The influence of material type on crack coalescence was discussed in section 6.5. The coalescence cracks in marble usually formed from the linkage of multiple short vertical **tensile cracks** which had developed earlier along white patches. Most of these white patches developed around the flaw tips early during the loading process, which lengthened and/or enlarged in size with an intensification of white color as loading increased. Upon reaching a particular load, which was dependent on flaw geometries, observable minute cracks initiated along the white patches. Further loading led to a lengthening of these minute cracks till they coalesced to form a continuous crack (refer to figure 6.28 for details). In gypsum, however, such a development and evolution of white patches was not observed in the camcorder recordings and high speed camera images. There were usually no observable signs preceding the development of the coalescence crack, which usually appeared as a continuous crack abruptly within a very short time.

Other key points about the influence of material with regard to coplanar flaws and stepped flaws respectively are summarized below.

Coplanar flaws

Coalescence was less favored (category 1) in **marble** than in **gypsum** with the same small flaw inclination angles (β = 0°, 30°, 45° for ligament length 2a, β = 30°, 45° for ligament length 4a). This phenomenon appears to be related to the fact that in the marble specimens, the initiation of **vertical** and/or **steeply-inclined cracks** from the inner flaw tips occurred more frequently than the initiation of **coplanar cracks** from the inner flaw tips, compared to the fracturing behavior in gypsum specimens. Due to the geometrical configuration, direct linkage of **vertical** and/or **steeply-inclined tip cracks** was physically infeasible (figure 6.64 a). Coalescence (indirect) could only occur when the new cracks were shallower (figure 6.64 b) or a third crack was also involved (figure 6.64 c).

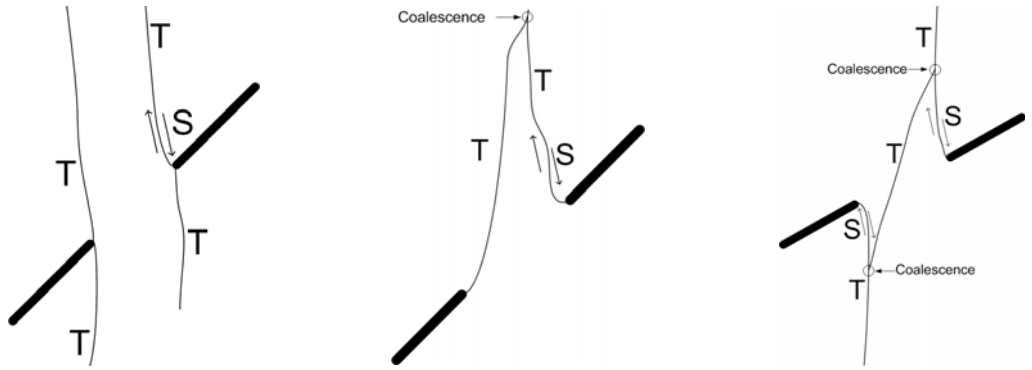

(a) (b) (c)

Figure 6.64 – (a) Coalescence did not occur due to the initiation of steep cracks from the inner flaw tips, (b) Coalescence occurred due to linkage of shallowly-inclined cracks initiated from the inner flaw tips, (c) Coalescence which involved the initiation of three new cracks.

Another distinct difference regarding coalescence was observed for large flaw inclination angles β. For large flaw inclination angles, coalescence in gypsum ($\beta = 45^o$, 60^o, 75^o for ligament length 2a, $\beta = 75^o$ for ligament length 4a) and marble ($\beta = 60^o$, 75^o for ligament length 2a, $\beta = 75^o$ for ligament length 4a) were similarly achieved in a **direct** manner in which the inner flaw tips were linked up by a continuous crack consisting of one or multiple individual crack segments. However, the crack segments adjacent to inner flaw tips in gypsum were mainly **shear**, while those in marble were mainly **tensile**.

Stepped flaws

For stepped flaw pairs, some coalescence categories were unique to gypsum with specific flaw geometries, while some coalescence categories were unique to marble with specific flaw geometries.

For ligament length "2a", coalescence pattern of **category 5** was unique to gypsum, while those of **categories 4, 6 and 8** were unique to marble (tables 6.24 & 6.26). More specifically, for α **= 30^o and 60^o**, the coalescence crack in **gypsum** which linked up the inner flaw tips was a generally 'S'- shaped crack consisting of **shear-tensile-shear** crack

segments. In contrast, the coalescence crack in marble was an inclined **type 1 shear crack** linking up the inner flaw tips for α **= 30°**, a **type 2 tensile crack** linking up the inner flaw tips with no observable shear segments adjacent to the flaw tips for α **= 60°**, and a tensile crack (not displaying wing appearance) linking up the tips of the same side of the pre-existing flaws for α **= 120°**.

For stepped flaw pair geometries with ligament length "4a", coalescence patterns of **categories 5 and 7** were unique to gypsum, while those of **categories 6 and 8** were unique to marble (table 6.26). More specifically, distinct differences were identified for α **= 30°, 60°** and **90°**:

For α **= 30°**, the coalescence crack in **gypsum** which linked up the inner flaw tips was a generally 'S'- shaped crack consisting of **shear-tensile-shear** crack segments. In contrast, the coalescence in marble was achieved in an indirect manner which was due to the linkage of multiple shear and tensile cracks.

For α **= 60°**, the coalescence crack in **gypsum** which linked up the inner flaw tips was a generally 'S'- shaped crack consisting of **shear-tensile-shear** crack segments. In contrast, the coalescence in marble was achieved by a vertical **type 2 tensile crack**.

For α **= 90°**, the coalescence crack in **gypsum** which linked up the inner flaw tips was a **type 1 tensile crack** (tensile wing crack). In contrast, the coalescence in marble was due to the linkage of the tips of the same side of the two pre-existing flaws by a curvilinear **type 2 tensile crack** and a short **shear crack**.

The second part of this chapter studies the stress values associated with crack initiation in gypsum and marble specimens and white patch initiation especially in marble specimens. The stress level at which the first observable cracks initiated in a marble specimen was usually very close to the respective specimen failure stress. In contrast, after the initiation of the first cracks in gypsum, the specimens often had to be loaded further in order to reach failure. Comparing the stress ratios for the initiation of the first white patch in marble with the stress ratios for the initiation of the first crack in gypsum (figures 6.53 to 6.56), one can state that both materials not only show a similar trend of variation of stress ratio with bridging angle, but also have close values for certain ranges of bridging angles (stepped flaws) and flaw inclination angles (coplanar flaws). There is thus an analogy between the white patch in marble and the first crack occurrence in gypsum. The production of white patches is speculated to indicate the presence of microcracks associated with the process zone. The microstructural nature of the white patches in marble will be studied in detail in the following chapter.

CHAPTER 7 – Microscopic Investigations of Cracking Processes in Marble and Gypsum

7.1 Introduction

As shown in chapters 5 and 6, in marble under uniaxial compression loading, there was usually a development of white (very distinctive white color) patches prior to the initiation of cracks. Some of these white patches developed early in the loading process, and later propagated (increased in length), widened and intensified in color with increased loading; while some of them appeared and propagated just before the specimen strength was reached. Although many of the white patches later developed into either shear cracks or tensile cracks in response to loading, some of them still remained intact with no observable cracking.

In the present study, the scanning electron microscope (SEM) imaging technique with a magnification power of up to 1,000 times was used to observe the underlying microscropic characteristics of these white patches. The SEM imaging technique has been successfully used to observe the details of cracks in rocks (Sprunt & Brace, 1974, Tapponnier & Brace, 1976, Kranz, 1979). A number of marble specimens of selected flaw geometries with pre-existing open flaws (single or double) were uniaxially loaded up to varying stress levels to produce white patches and were then studied by the SEM. In the first half of this chapter, details of the loading scheme used to produce the white patches, some technical aspects of the SEM imaging technique and the microscopic nature of the white patches are discussed. Results of the SEM images revealed that the white patches can be correlated with the underlying microcracking and the extent of microcracking generally increases with the applied load. The microcracking zone can thus be regarded as a process zone which developed prior to the subsequent initiation of visible cracks in marble.

In contrast, no observable white patches developed in gypsum as revealed from the video recordings. Under loading, the development of observable tensile cracks was preceded

by the development of hair-line cracks (invisible to unaided eyes, but discernable with 10x hand lens). The second half of this chapter describes the results obtained from an environmental scanning electron microscope (ESEM) study in gypsum. The ESEM study was conducted in the region in the vicinity of a fine hair-line tensile crack to reveal if process zones (microcracking processes) similar to that associated with white patches in marble also developed in gypsum. The study revealed that hair-line cracks were associated only with a very narrow microcracking zone, consisting of multiple central dominant microcracks and a limited number of microcracks flanking it.

7.2 Experimental Details

The objective of the experimental study is to observe and identify the microstructures underlying the white patches in marble using the SEM imaging technique. The extent of white patch and its white color increases with loading as shown in previous experimental studies (chapters 5 & 6). It is thus instructive to load the pre-cracked marble specimens to different stress levels before the development of any observable cracking events, and observe the microstructural characteristics of the white patches at those particular stress levels. The three specific tasks involved in this experimental study are:

Task 1 – Cutting flaws into marble specimens using the water abrasive jet
Task 2 – Producing white patches in marble by uniaxially loading the specimens up to varying load levels
Task 3 – Studying the white patches with the SEM imaging technique

Task 1 – Cutting flaws into marble specimens using the water abrasive jet

Multiple Carrara Marble specimens of three different representative flaw geometries were prepared – (A) Single flaw inclined at 30^o (figure 7.2a). (B) Stepped flaws inclined at 30^o with bridging angle 30^o and ligament length 2a (figure 7.2b). (C) Coplanar flaws inclined at 60^o with ligament length 4a (figure 7.2c). '**a**' represents half of the flaw length. Refer to figure 3.18 for the definition of flaw geometry and associated flaw parameters.

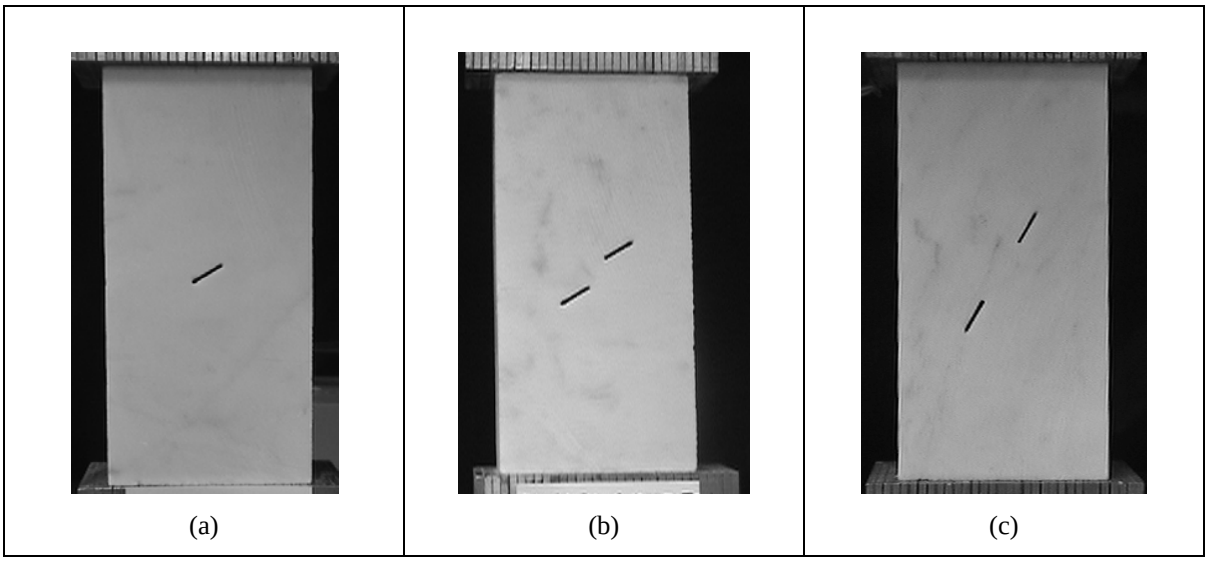

Figure 7.2 – The three flaw geometries prepared for the white patch study in marble specimens (a) single flaw, (b) stepped double flaws, (c) coplanar double flaws. Each flaw is 13 mm long and 1.3 mm wide.

These specific geometries were chosen due to their unique shear and tensile fracturing and coalescence behavior where applicable. Initiation and subsequent propagation of conventional tensile wing cracks from the flaw tip regions of pre-existing flaws were observed in geometry (A) as shown in figure 7.3. In geometry (B), apart from the development of conventional tensile wing cracks, there was also a substantial white patch development between the inner flaw tips in the bridging region with a subsequent initiation of a coalescence shear crack along it (figure 7.4). Similar to geometry (B), there is also a substantial white patch development in the bridging region in geometry (C). Additional white patches also developed around the outer flaw tips along which observable cracks later developed (figure 7.47).

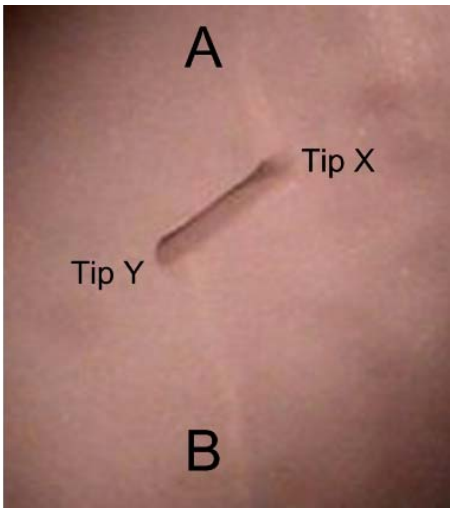

(a)

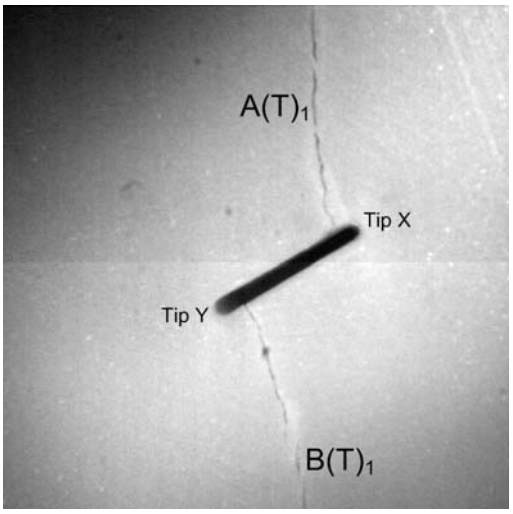

(b)

Figure 7.3 – Development of white patches and cracks in marble (single flaw at 30^{o} inclination angle). (a) White patches A and B developed from the flaw tips (recorded by camcorder), (b) As loading increased, tensile crack opening occurred along the white patches A and B (recorded by high speed camera). The central inclined pre-existing flaw is 0.5" (13mm) long and the loading direction is vertical.

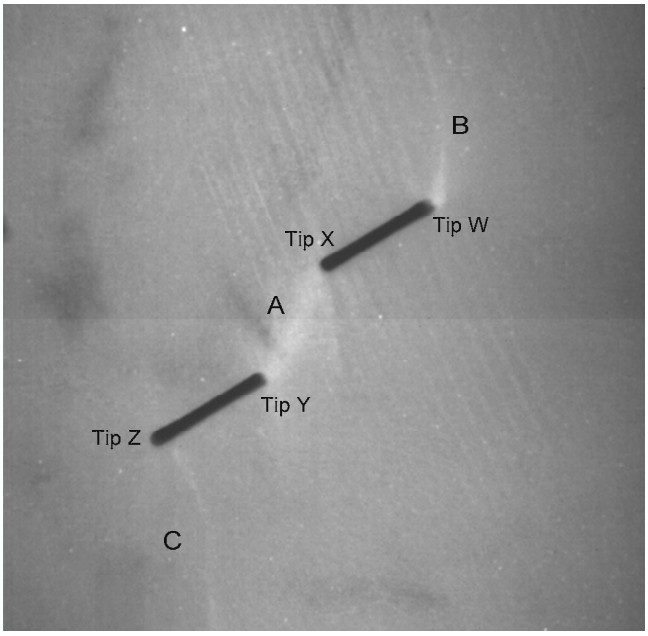	(52.05 MPa) {HS image # -3576} View of the white patches after substantial loading had been applied. This was the first image recorded by the high speed video system under
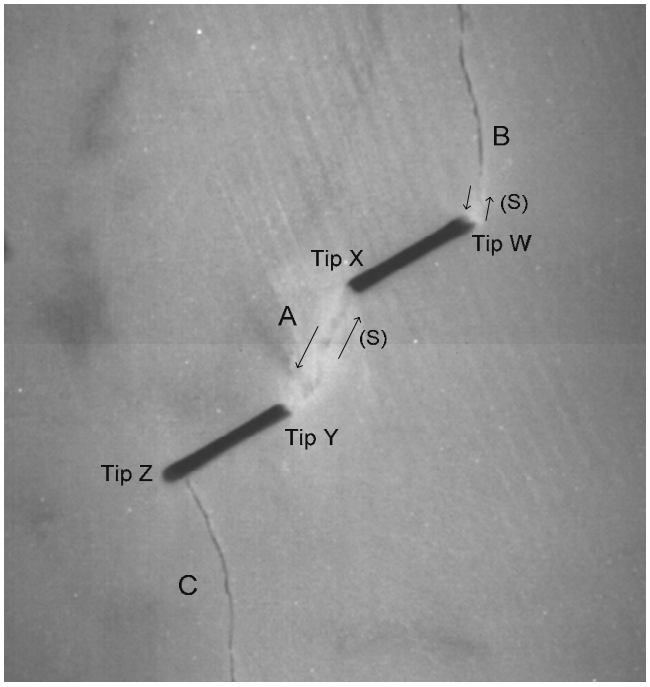	(52.06 MPa – Coalescence and tensile wing crack initiation) {HS image # -2914} Shearing occurred along the whole length of white patch A to form shear crack A. Tensile wing crack C formed. Crack B also formed. Its lower segment was shear in nature, while its upper segment was tensile in nature. The indented tooth shape of tips W and X indicated the occurrence of the relative sliding between the upper face and the lower face of the top pre-existing flaw.

Figure 7.4 – Development of white patches which later led to the formation of a coalescence shear crack between inner flaw tips and tensile wing cracks close to outer flaw tips. Images were recorded using the High Speed Video System. (Specimen : CM 2a-30-30-A and the high speed camera frame rate is 2,000 pps)

Task 2 – Producing white patches in marble by uniaxially loading the specimens up to varying load levels

White patches were obtained by loading the marble specimens uniaxially in a way similar to that for other specimens as discussed earlier in chapter 3, but terminated before the development of any observable cracks. The specimens were loaded to different stress levels (with the exception of geometry C for which only one specimen was prepared) according to the following scheme (table 7.1).

Table 7.1 – Loading details for the creation of white patches in marble specimens.

Geometry	Specimen No.(1)	Percentage of specimen failure stress to be applied (2)	Stress level to be applied (MPa)	Actual load to be applied (Lb)
(A) single flaw inclined at 30^o with horizontal (figure 6.2a)	SA	50%	30	15767
	SB	70%	42	23552
	SD	95%	57	32408
(B) double stepped flaws 2a-30-30 (figure 6.2b)	DA	50%	26	12848
	DB	70%	36	18483
	DC	90%	47	27322
(C) double flaws 4a-60-0 (figure 6.2c)	DD	94%	69	36310

Notes:

(1) The average specimen failure stresses determined from previous tests (chapters 5 & 6) are **59.9 MPa** for geometry (A), **52.0 MPa** for geometry (B), and **72.3 MPa** for geometry (C). These stresses are used for the computation of percentage of failure stress to be applied onto marble specimens.

(2) A specimen of geometry (A) and a specimen of geometry (B) were subjected to 90% and 95% of their respective failure stresses. However, both specimens failed pre-maturely during the uniaxial loading process and could not be used in the subsequent SEM study.

Task 3 – Studying the white patches with the SEM imaging technique

The loaded marble specimens were then trimmed down to appropriate sizes and polished to obtain flat and smooth surfaces before being placed in the scanning electron microprobe (SEM) for studying the underlying microstructural characteristics. Details of specimen polishing involved and some fundamentals of the SEM for qualitative imaging are described in Appendix I.

7.3 Microstructural characteristics of white patches in marble

In this section, the microstructural characteristics of white patches are examined. It will begin by showing SEM images of an unloaded intact marble specimen and an unloaded marble specimen containing a pre-existing flaw which was cut by the water abrasive jet. SEM images for the loaded specimens can then be compared against them to identify the development of microstructures in the marble specimens due to uniaxial loading.

7.3.1 Intact unloaded specimen

Figure 7.5a shows a SEM image of a piece of intact marble specimen (free of observable surface cracks) without undergoing the uniaxial loading test. The constituent marble grains are mostly equigranular in shape and displaying an interlocking texture. The grain size is within a general range of 50 to 200 μm. Careful inspection reveals that most of the grains are crack-free, and intra-granular micro-cracks are only present in a small population of marble grains, and inter-granular cracking along grain boundaries is less than 20%.

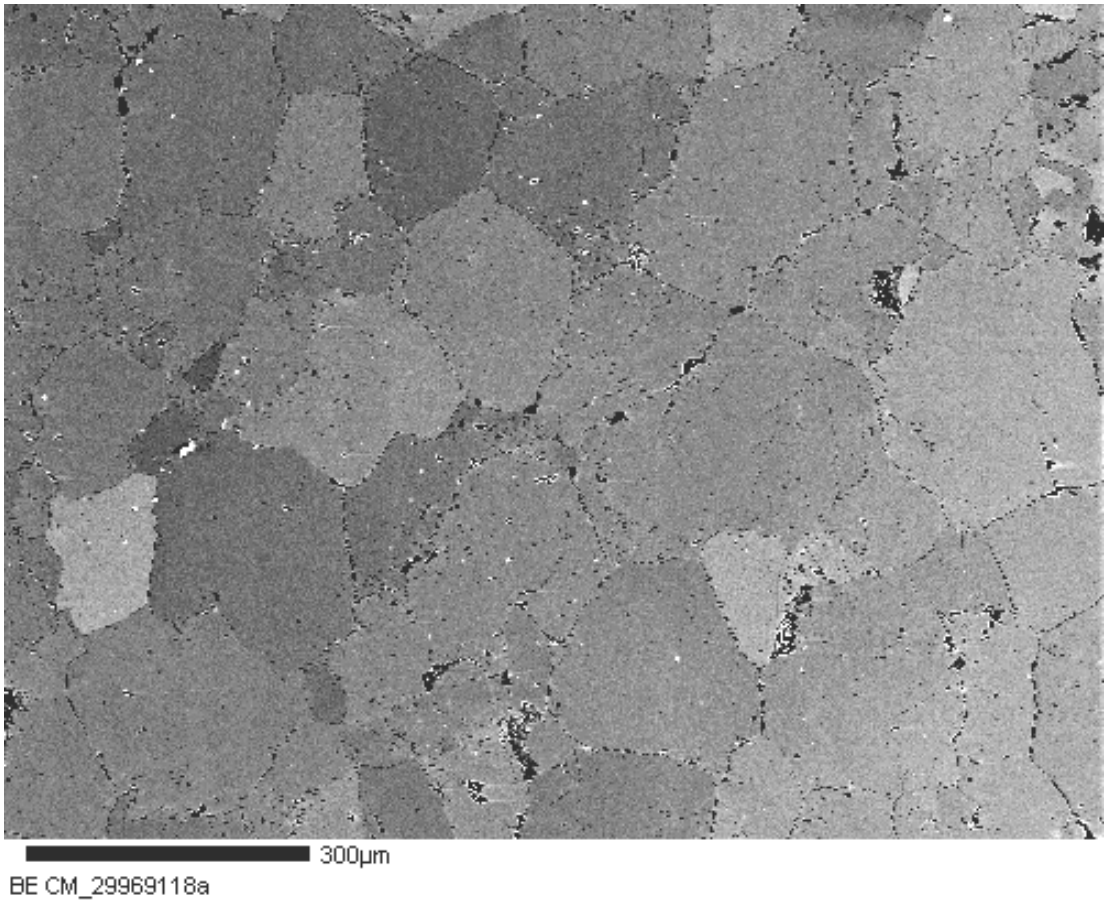

Figure 7.5a – A SEM image of intact marble specimen (magnification power = 100 X)

Figure 7.5b illustrates schematically the relationship between grain boundaries (grey line), intra-granular cracks (short thin lines) and inter-granular cracks (thicker black lines along grain boundaries). It is very common that the boundary of an individual grain is not rimmed completely, but partially by inter-granular cracks. Various cross-cutting relationships between intra-granular cracks (labeled in figure 7.5b) and grain boundaries are also shown. As will be discussed in later sections, inter-granular cracks along grain boundaries are of two main types – tensile and shear. Shear cracks are usually associated with black spalling features, while tensile cracks simply express as thick black lines along grain boundaries without the spalling features.

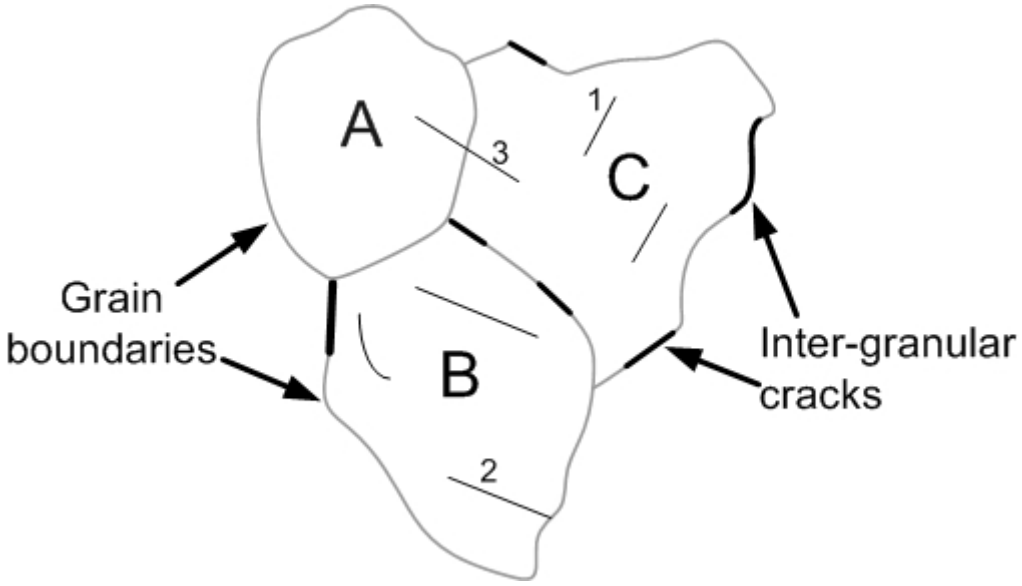

Figure 7.5b – Schematic illustration of the relationship between grain boundaries, inter-granular cracks and intra-granular cracks in marble grains. Intra-granular crack 1 is completely within grain C. Intra-granular crack 2 terminates at the grain boundary of grain B. Intra-granular crack 3 cuts through grains A and C.

7.3.2 Unloaded specimen containing a pre-existing flaw

A marble specimen containing a half an inch-long pre-existing flaw (cut by the water abrasive jet), which was not subject to the uniaxial loading test is shown in figure 7.6. An assemblage of multiple SEM images around the right tip on the bottom flaw face is shown in figure 7.7. Damage in the region around the flaw due to the cutting action by the water abrasive jet is considered to be very limited as suggested by the presence of a very high proportion of crack-free marble grains around the flaw perimeter. Although intra-granular microcracks could occasionally be found, they are very short (about 20 μm long) and only present in those grains close to the flaw face within one to two grain-sized distance (figures 7.8a & b).

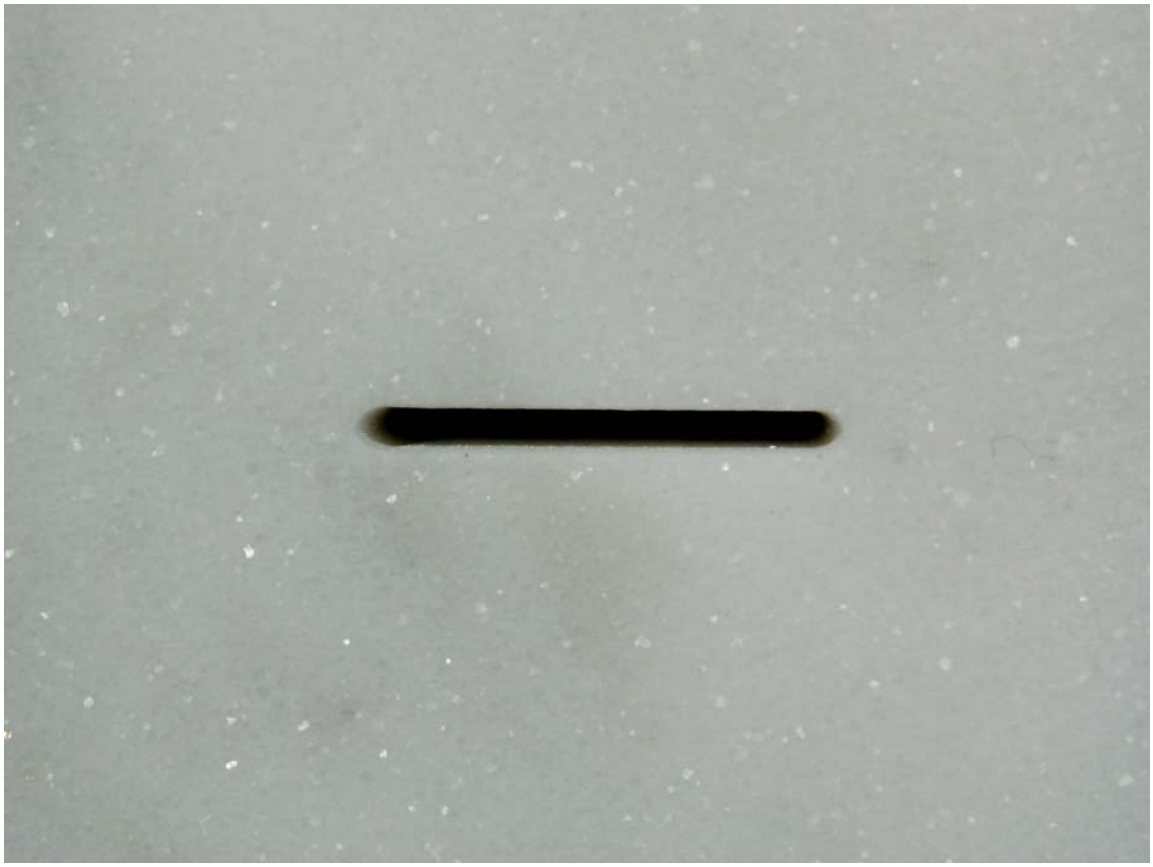

Figure 7.6 – A straight open flaw created by water abrasive jet in marble. Length of the flaw is 0.5" (13mm). The bright white spots are muscovite flakes. Image was taken by a digital camera.

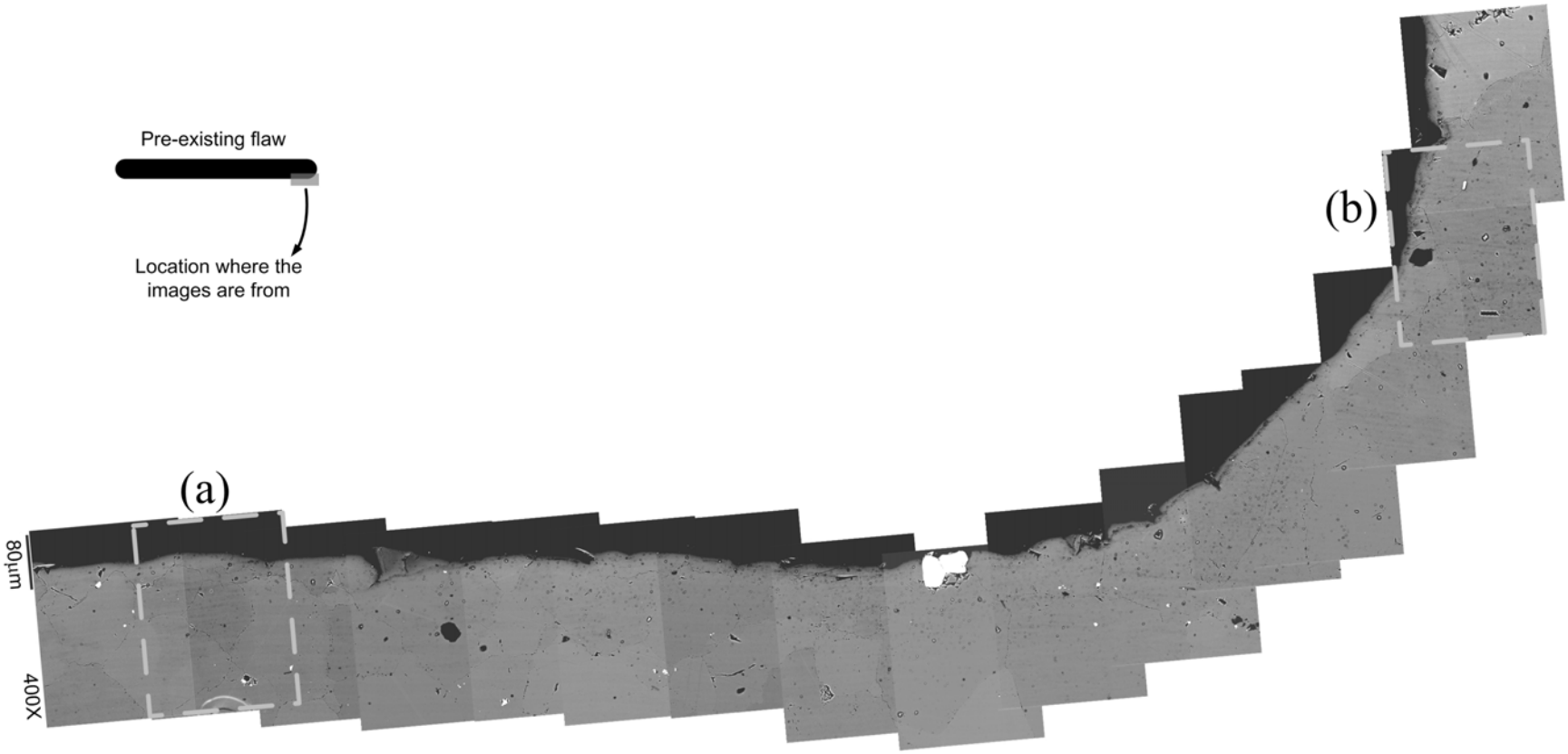

Figure 7.7 – An assemblage of SEM images of the bottom face close to the right tip of the same specimen as shown in figure 7.6. The length of the scale bar on the left edge is 80 μm. Magnified views of the two areas (a) and (b) enclosed by dashed-lined rectangles are shown in figure 7.8. (magnification power = 400 X)

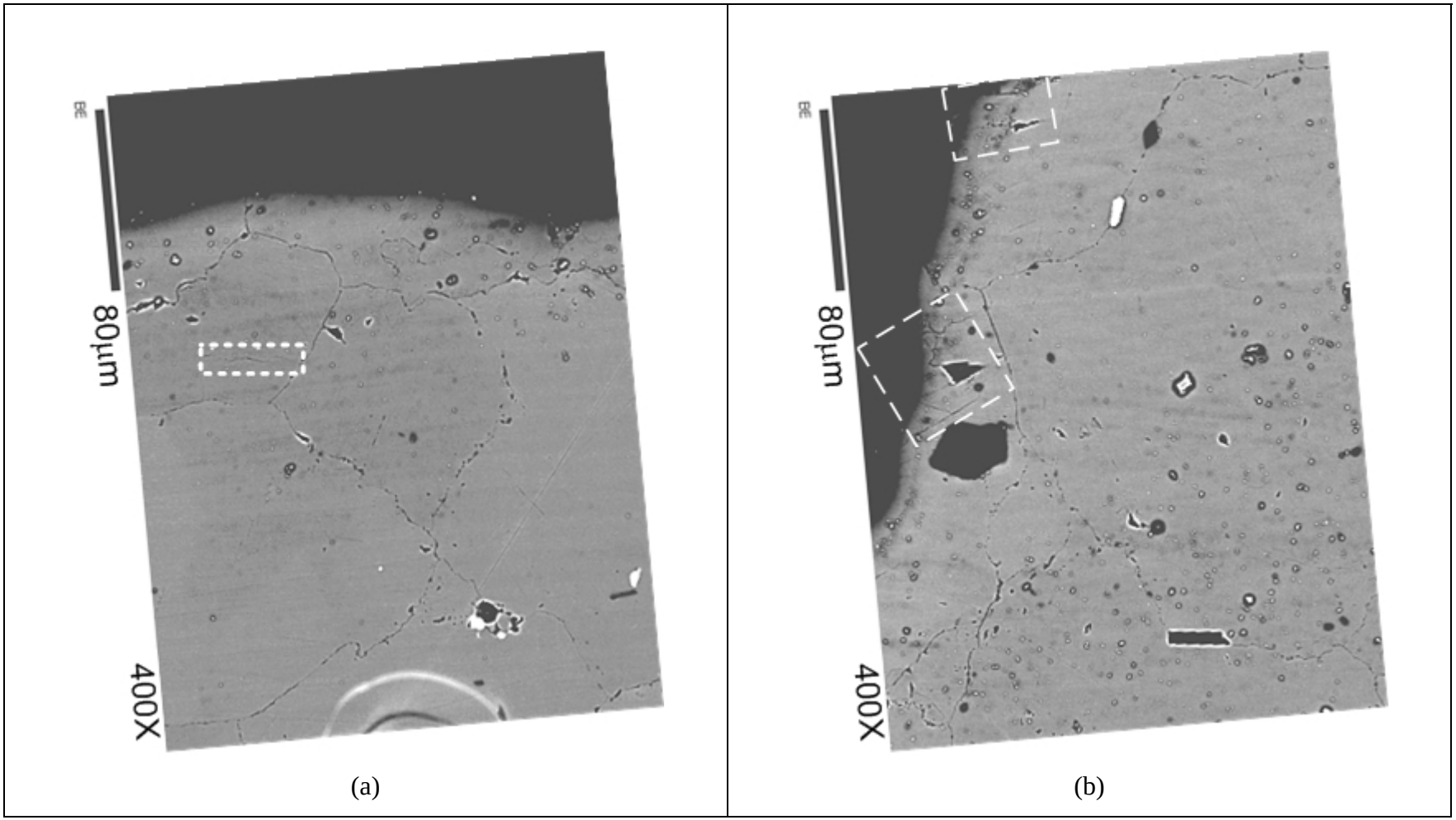

Figure 7.8 – Magnified images of the enclosed dashed-lined rectangles shown in figure 7.7 (a) away from the flaw tip, and (b) at the flaw tip. Identifiable microcracks are enclosed within dashed-lined rectangles in these images. Most of the marble grains are crack-free. (magnification power = 400 X)

A number of magnified images around the left flaw tip are shown in figure 7.9 to illustrate the variation of the degree of inter-granular microcracking with distance away from the flaw face. Both inter-granular tensile cracks and shear cracks are identified. Inter-granular tensile cracks appear as thick black lines (as compared with intact grain boundaries which have a low relief and a tight appearance separating well-fused neighboring grains) and follow the existing grain boundaries (figure 7.9a). Inter-granular shear cracks, which are usually associated with the occurrence of localized surface spalling along grain boundaries, are of a usual triangular or polygonal shape (figure 7.9b). Most of the grains shown in figures 7.9a and b, which are within the 1 mm annular zone around the flaw boundary, are rimmed by inter-granular microcracks of a relatively dark and thick appearance. The degree of inter-granular microcracking decreases with distance away from the flaw face. As shown in figures 7.9c and d, about half of the grain boundaries are rimmed by inter-granular cracks (some of them are indicated by dashed-lined brackets) and about half of them are rimmed by “intact” grain boundaries (some of them are indicated by solid brackets).

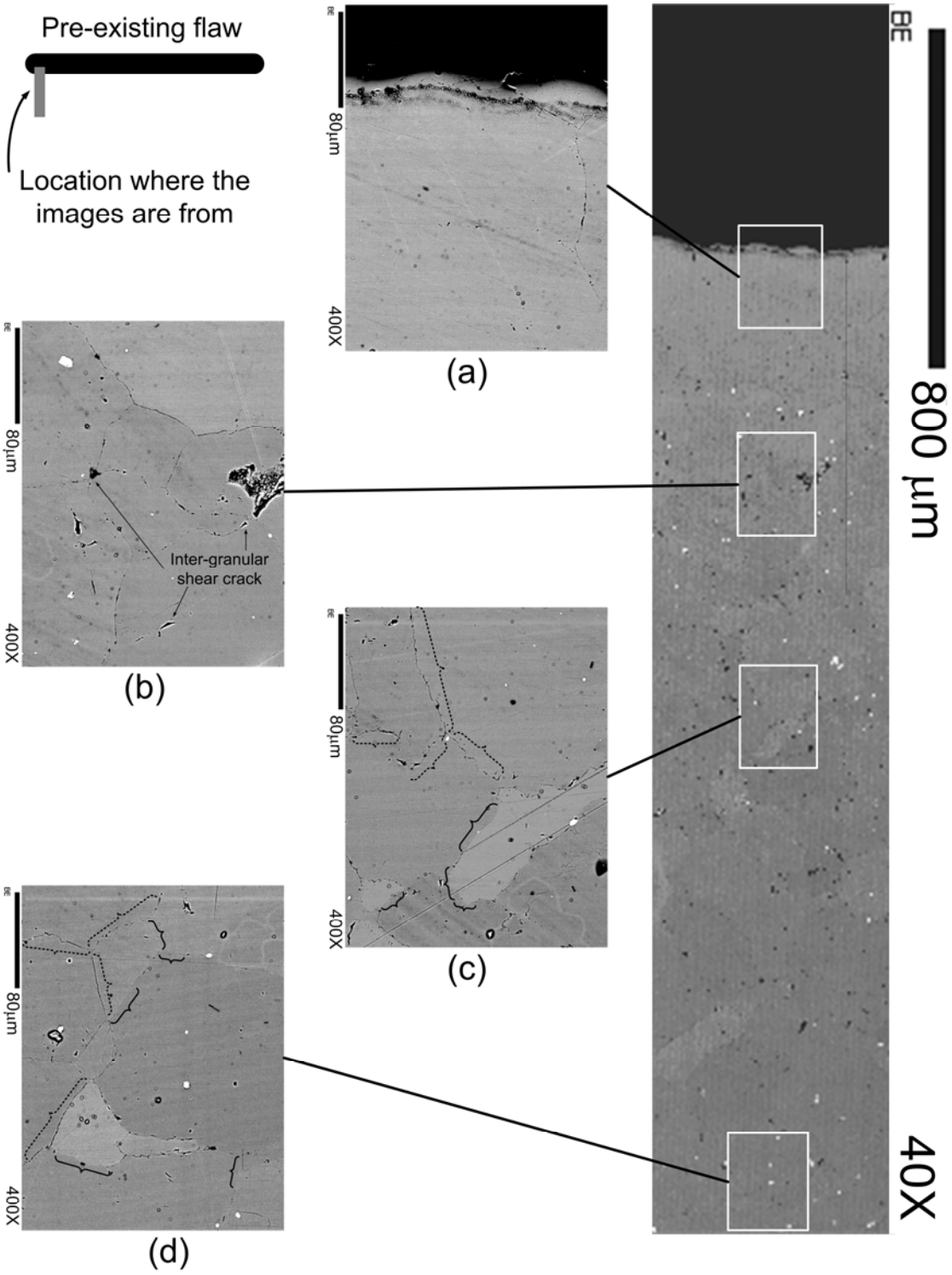

Figure 7.9 – Selected magnified images in a zone close to the left tip of the pre-existing flaw (see the sketch on the top left part). Some of the inter-granular microcracks are indicated by dotted brackets and some of the intact grain boundaries are indicated by solid brackets. The length of the scale bars of the four magnified images are 80 μm (magnification power = 400 X). The vertical strip on the right was taken at a magnification power of 40X.

7.3.3 Single flaw subject to 50% failure stress

A view of specimen SA which was loaded uniaxially up to 50% of the failure stress (table 7.1) is shown in figure 7.10. A white patch is observed to have developed rimming the flaw perimeter, which is especially most prominent around the left tip region on the bottom flaw face.

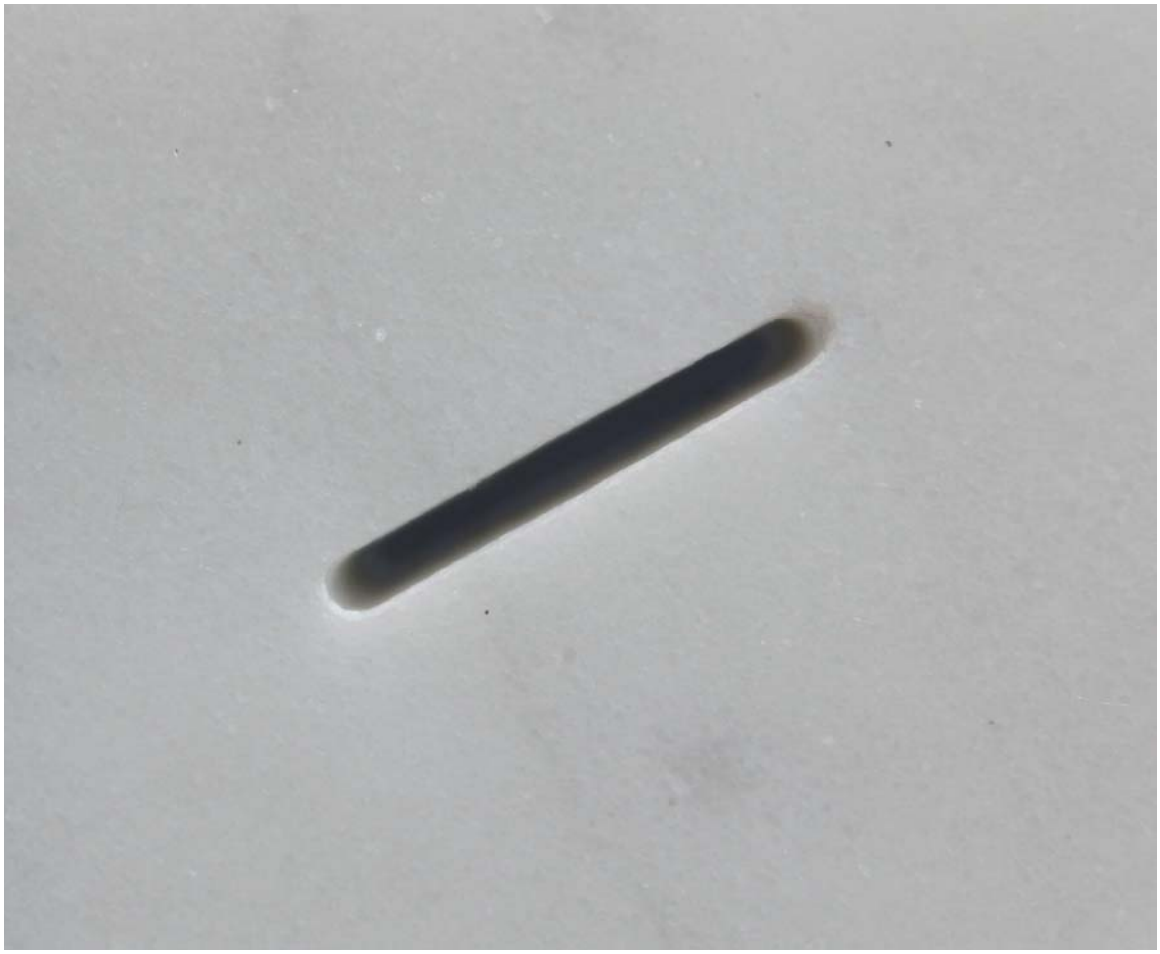

Figure 7.10 – Marble specimen SA containing a straight open flaw which has been uniaxially loaded up to 50% of the failure stress. Length of the flaw is 0.5" (13mm). Image was taken by a digital camera. Note the development of a prominent white patch rimming the bottom left part of the flaw.

An assemblage of SEM images of the whole flaw and its surrounding area is shown in figure 7.11. The bright white spots close to the flaw are due to imperfect carbon coating. Under that magnification power, many of the fine details concerning grain boundaries and microcracking cannot be observed clearly. Magnified images of selected regions around the flaw are shown in figures 7.12 to 7.16. These images and the subsequent images shown in the remaining part of this chapter will be oriented in such a way that the uniaxial loading direction is vertical.

An assemblage of magnified images of the bottom face of flaw SA close to the left tip is shown in figure 7.12. The boundaries of marble grains could be clearly seen in the figure, which is very likely due to occurrence of inter-granular tensile cracking. Some spalling features (black in color) of sizes varying between 10 and 50 μm are indicated by arrows in the same figure. Some are found within grains, but most of them are located along grain boundaries or at junctions of multiple grain boundaries. They are thus likely to be associated with the development of inter-granular shear cracks. A magnified image of a center region of figure 7.12 is shown in figure 7.13. In figure 7.13, some of the intra-granular microcracks are marked by white arrows. They are very short (< 20 μm) and appear as very thin traces. Inter-granular spalling features as discussed above are also indicated in the bottom part of figure 7.13, which are enclosed in two rectangles.

Figure 7.14 shows an assemblage of SEM images along a strip extending from the left flaw tip to illustrate the variation of microcracking behavior with distance from the flaw face. Close to the flaw face, most of the grain boundaries are opened up as inter-granular cracks (black traces). As the distance from the flaw face increases, the amount of inter-granular cracking decreases. Close to the bottom end of the strip (see a further magnified image on the left of the strip), at a distance of about 7-10 mm away from the flaw face, grains (indicated in the grain center by * in figure 7.14) which are relatively free of inter-granular cracking can be found. Most of the grain boundaries found at or beyond that distance are of low relief and appear as thin lines separating grains of a subtle color difference.

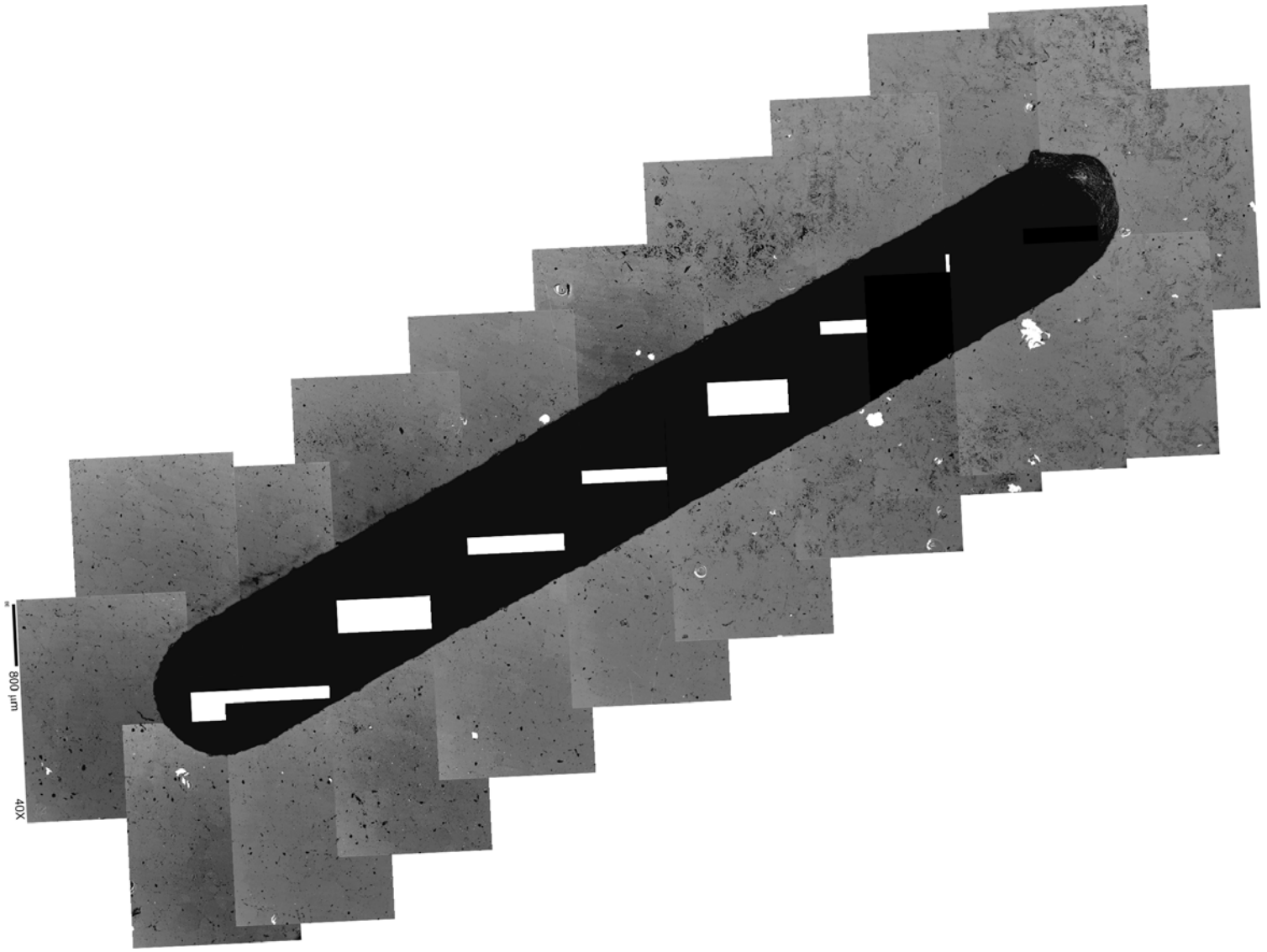

Figure 7.11 – An assemblage of SEM images of single flaw SA and its surrounding area. The length of the scale bar on the left edge is 800 µm. (magnification power = 40 X)

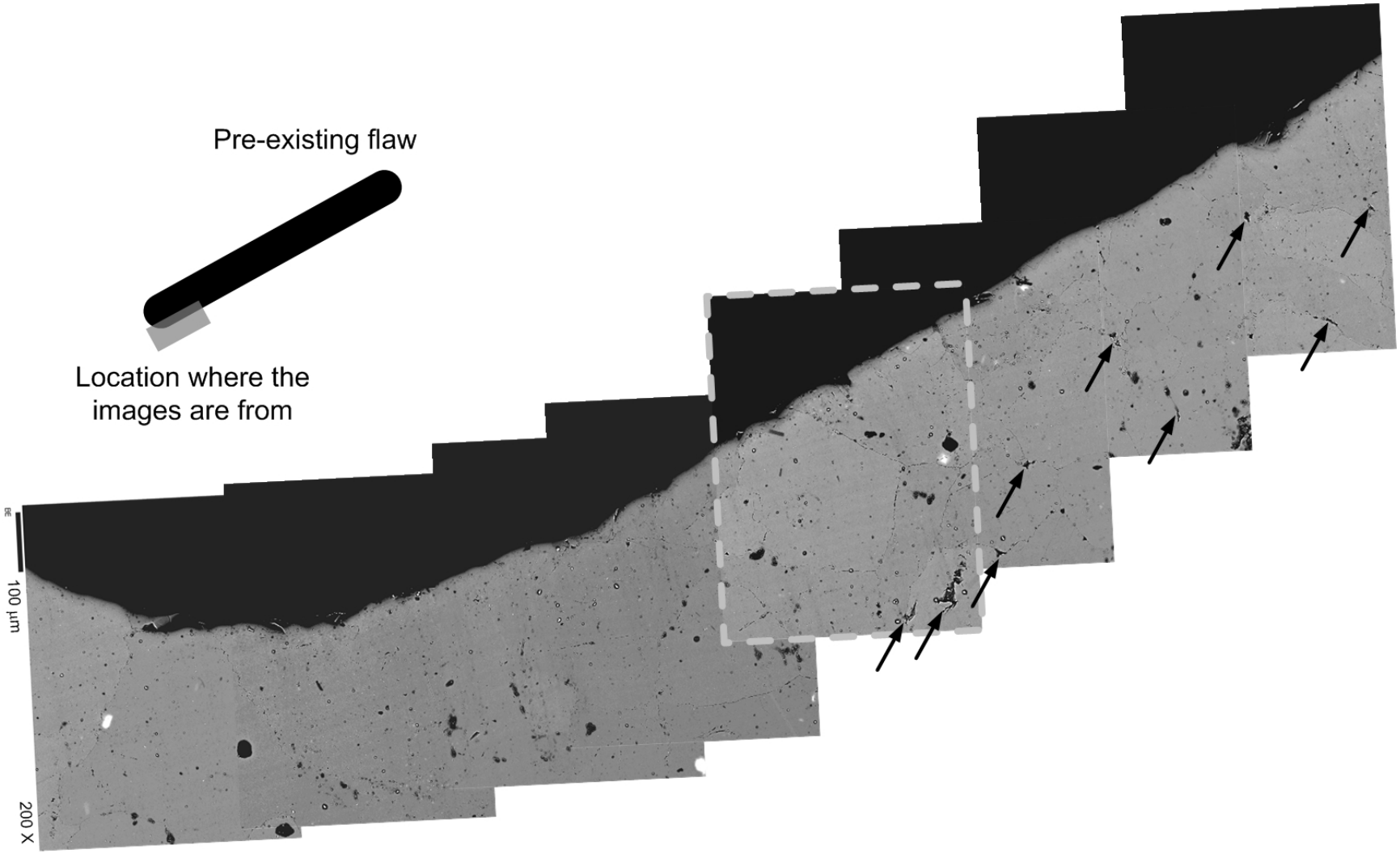

Figure 7.12 – An assemblage of SEM images of the bottom face of flaw SA close to the left tip. Some spalling features are indicated by arrows. The length of the scale bar on the left edge is 100 µm (magnification power = 200 X). A magnified image of the enclosed dashed-lined rectangle in the middle is shown in figure 7.13.

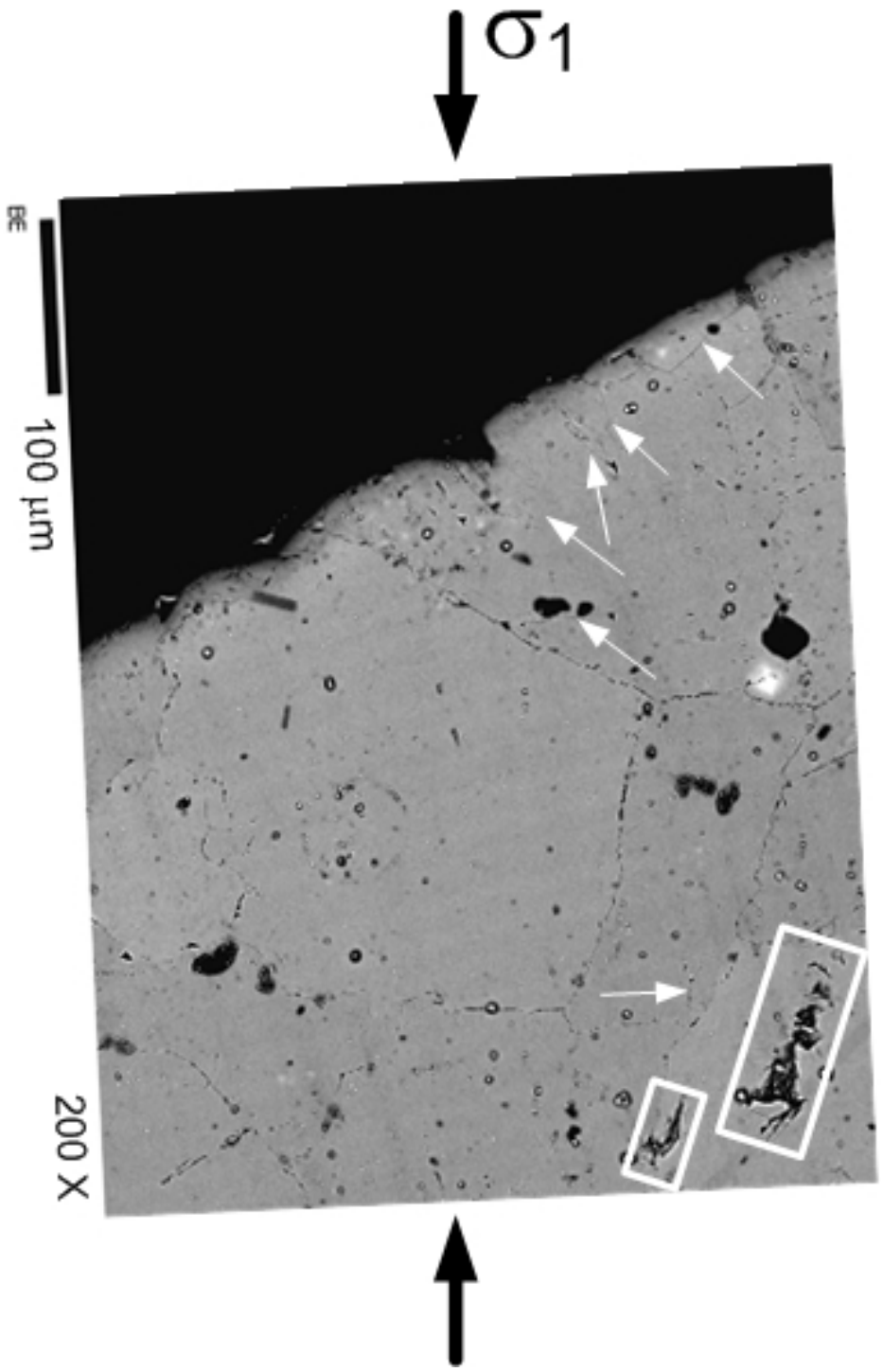

Figure 7.13 – Some of the intra-granular cracks are indicated by arrows. The rectangles enclose two local spalling zones. (magnification power = 200 X)

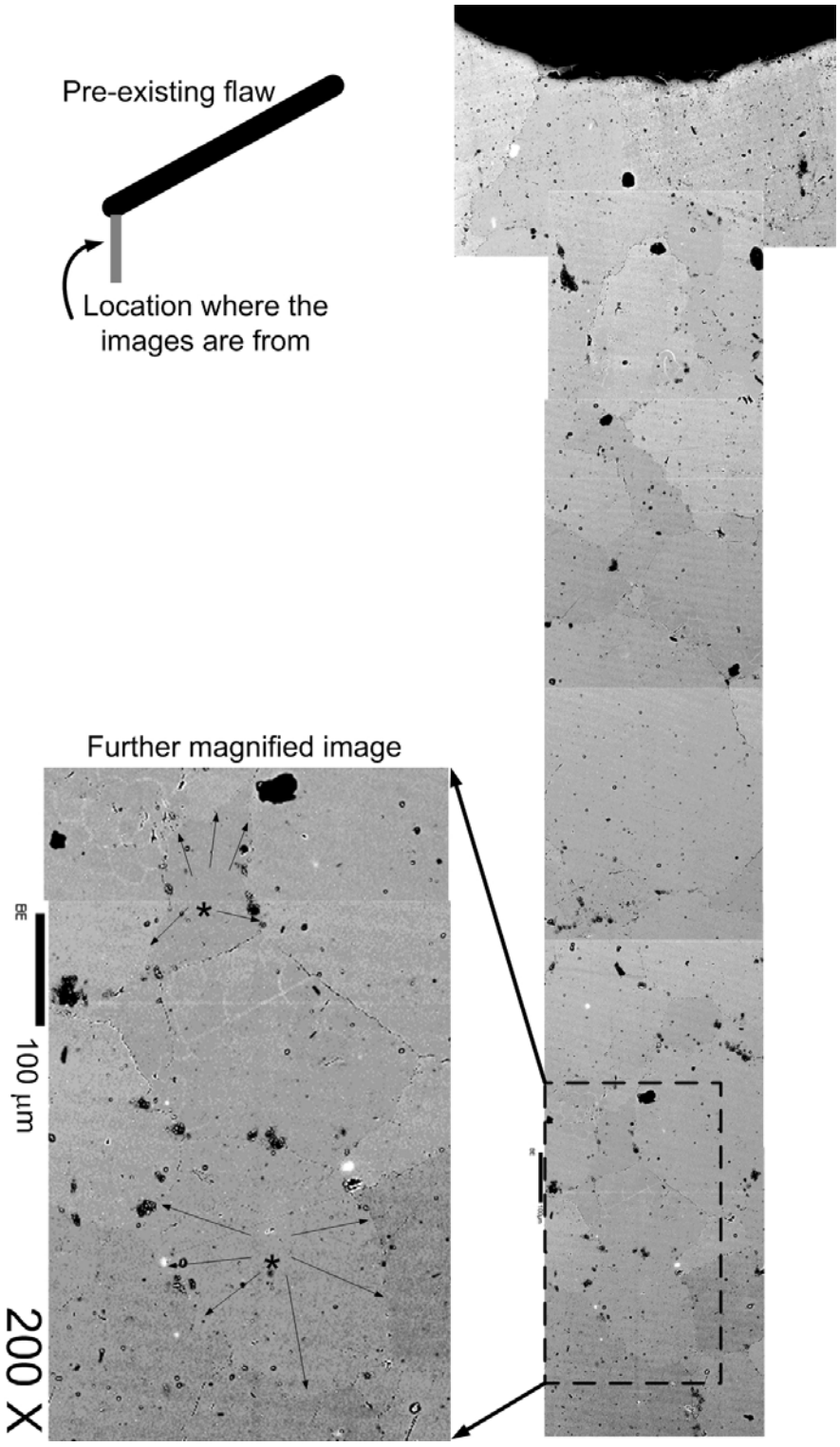

Figure 7.14 – An assemblage of images along a strip extending from the bottom flaw face close to the left flaw tip. A magnified image of the bottom part of the strip is shown on the left. Two grains which are relatively free of inter-granular cracking are indicated by * and they are rimmed by crack-free grain boundaries (pointed by arrows). (magnification power = 200 X)

The discussion above is mainly about the microcracking characteristics around the left flaw tip. In the following section the right tip will be examined (figure 7.15). Similar to the left tip region, marble grains of clear boundaries which are likely associated with inter-granular cracking can be seen in figure 7.15. Besides, spalling features are also very common, especially in the right part of the figure very close to the flaw tip. Intra-granular cracks are also observed. Similar to those observed in figures 7.7 and 7.8, intra-granular cracks are mostly observed in those grains adjacent to the flaw face (figure 7.15). However, the crack density in specimen SA is higher than that in the specimens without undergoing uniaxial loading. Shear related inter-granular spalling features are also found close to the flaw face (figure 7.15). See also figure 7.16 for a magnified view of these features.

To summarize, the white patch developed around the flaw perimeter as observed in figure 7.10 is found to be associated with underlying inter-granular and intra-granular microcracking among the marble grains. Intra-granular cracking is restricted to an annular zone around the flaw perimeter with a width of 1 to 2 grain sizes. Inter-granular tensile and shear cracking can be observed in a wider zone around the flaw. However, the degree of inter-granular cracking decreases with distance away from the flaw face. At a distance of about 7 to 10 mm away from the flaw face, individual grains completely free of inter-granular cracks are found.

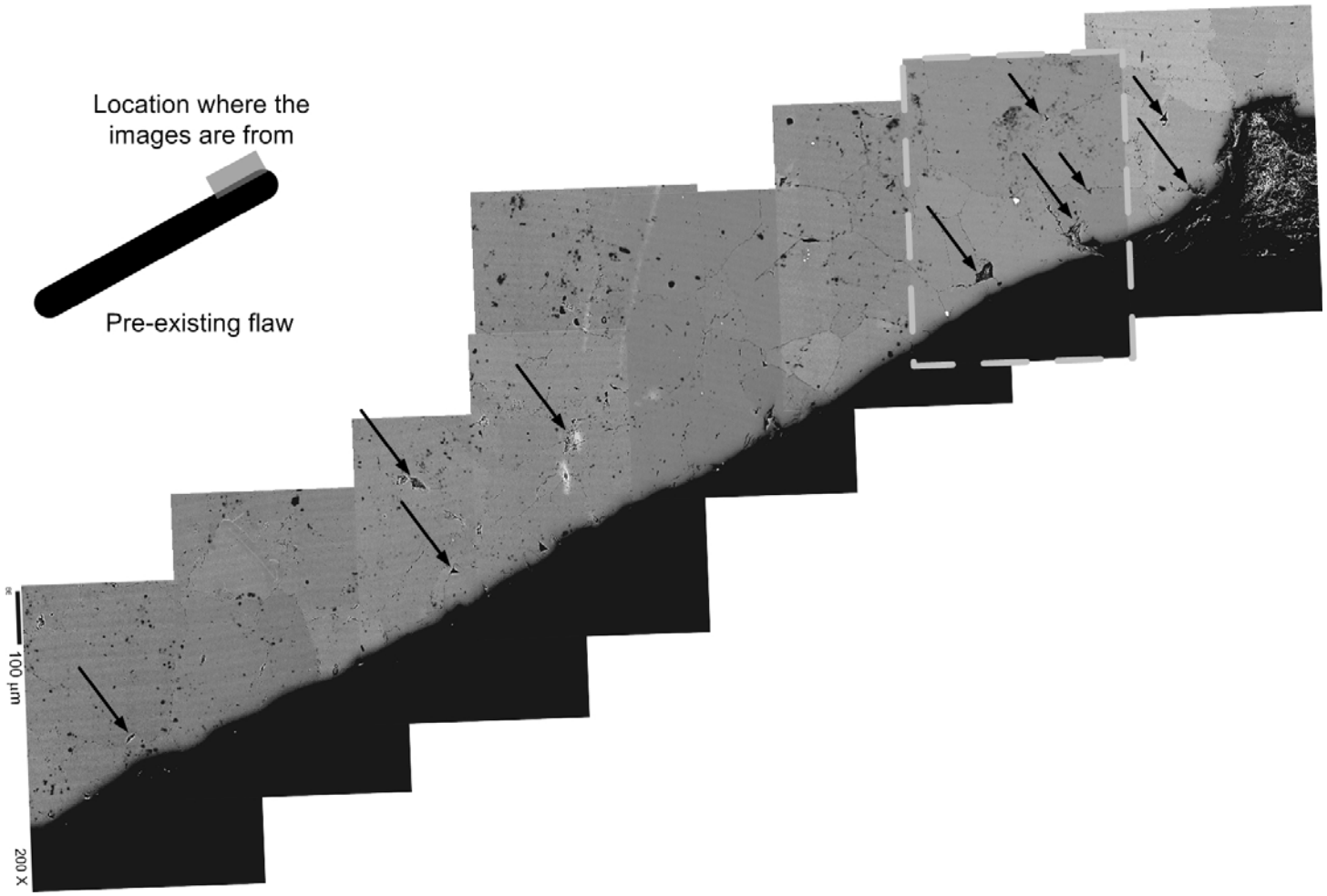

Figure 7.15 – An assemblage of SEM images of on the top face of flaw SA close to the right tip. The length of the scale bar on the left edge is 100 µm. A magnified image of the enclosed dashed rectangle in the middle is shown in figure 7.16. Some spalling features are indicated by arrows. (magnification power = 200 X)

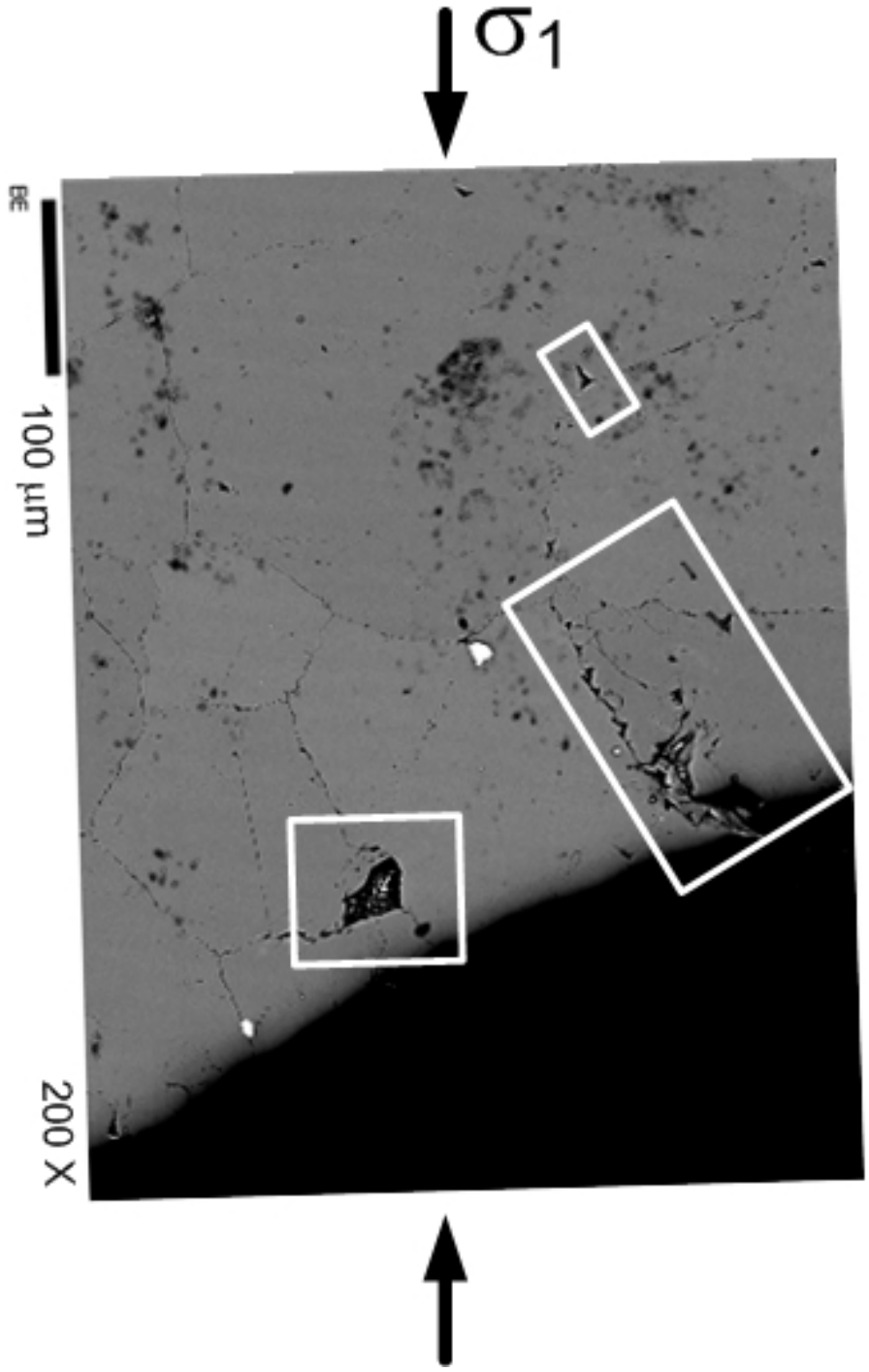

Figure 7.16 - Magnified image of the enclosed dashed rectangle shown in figure 7.15. Shear-related spalling features which are commonly found along grain boundaries are marked in this figure. (magnification power = 200 X)

7.3.4 Single flaw subject to 70% failure stress

A view of specimen SB which was loaded uniaxially up to 70% of the failure stress (table 7.1) is shown in figure 7.17. A short white patch is observed to have developed from the upper face of the flaw close to the right tip. There is also a similar white patch developed from the bottom flaw face. However, the bottom part of the specimen was damaged during the trimming process and could not be further examined by the SEM.

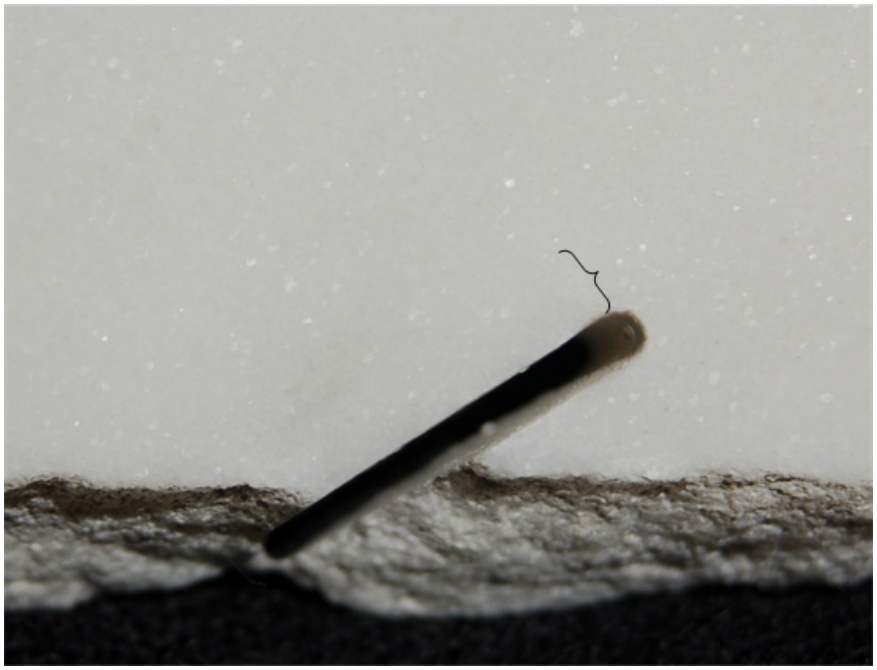

(a)

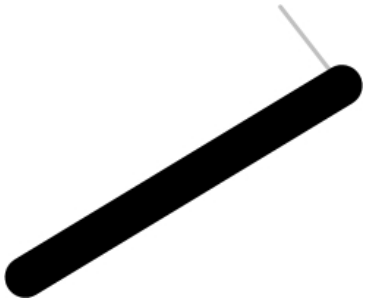

(b)

Figure 7.17 – (a) Marble specimen SB containing a straight open flaw which has been uniaxially loaded up to 70% of the failure stress. Length of the flaw is 0.5" (13mm). Image was taken by a digital camera. Note the development of a short white patch from the top face close to the right tip. (b) sketch of the flaw and the white patch.

An assemblage of SEM images of the flaw and its surrounding area is shown in figure 7.18. Under that magnification power, many of the fine details concerning grain boundaries and microcracking cannot be observed clearly. The region around the flaw perimeter was examined comprehensively at a higher magnification (400 to 1000 times) to identify any microscopic features which may be associated with the white patch observed in the hand specimen. Magnified images of the regions enclosed in figure 7.18 are shown in figures 7.19 and 7.20.

In a region close to the right tip corresponding to the white patch trajectory as shown in figure 7.17, a relatively continuous dark undulating feature which extends from the flaw face for about 1mm is observed (figure 7.19). It trace is indicated by multiple black arrows in the figure, but it is very difficult to determine with confidence which part is due to inter-granular cracking and which part is due to intra-granular cracking because of the poor color contrast between neighboring grains. At the top part of figure 7.19, a relatively wide crack (compared with neighboring intact grain boundaries), which is indicated by a white bracket, can be identified with confidence to be an intra-granular crack due to its strikingly straight appearance.

Close to the crack which extends for about 1mm from the flaw face as mentioned above, there exist multiple short (50 – 150 μm) parallel intra-granular tensile cracks. Examples of such details are revealed in a magnified image as shown in figure 7.20.

To summarize, the white patch developed from the flaw face close to the tip regions observed in the hand specimen which has been loaded up to 70% of the failure stress can be correlated with a microcracking zone. This microcracking zone consists of a central dominant undulating crack generally following grain boundaries and multiple other much shorter intra-granular cracks flanking the dominant crack. The latter trend more or less parallel with the dominant crack.

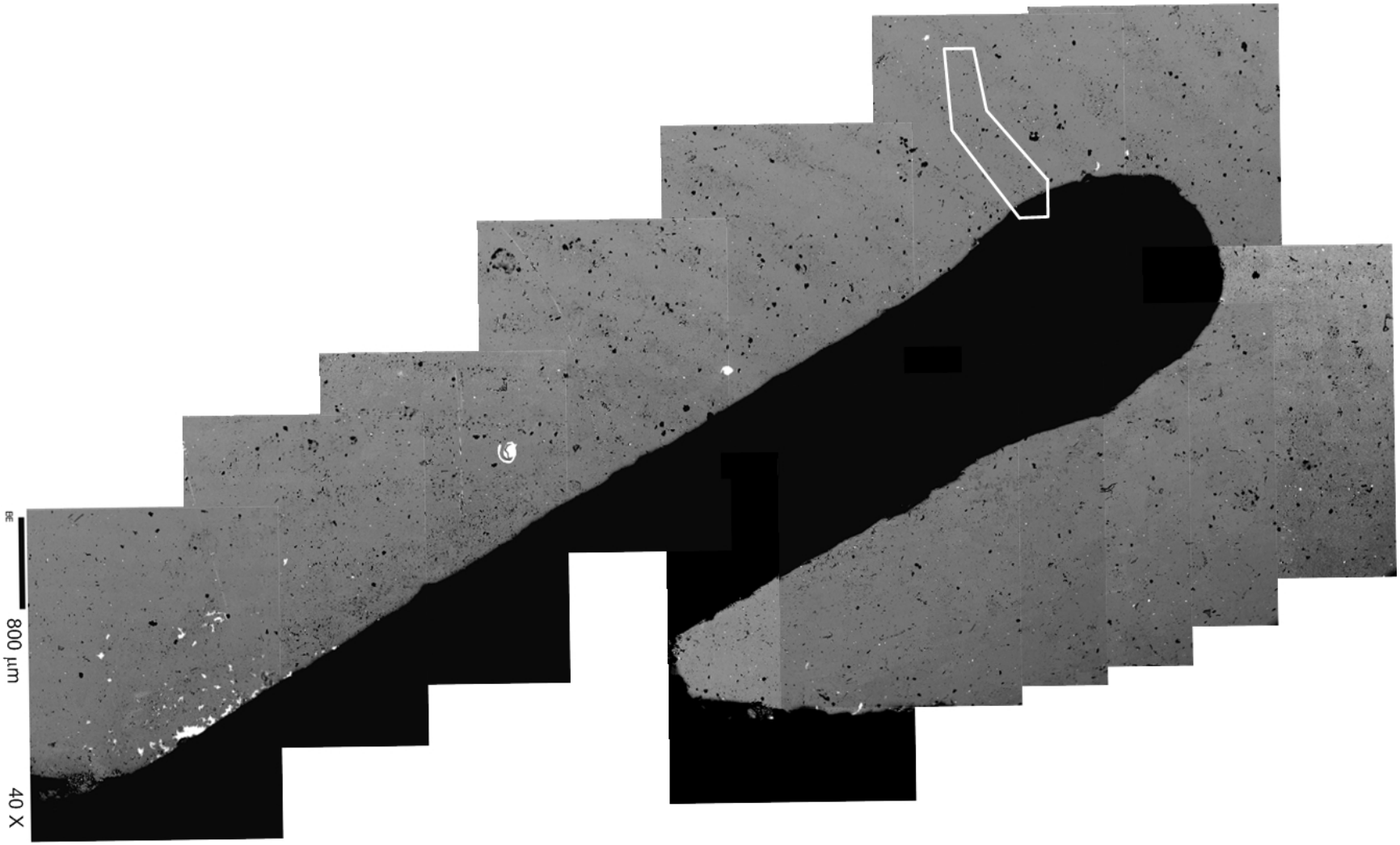

Figure 7.18 – An assemblage of SEM images of single flaw SB and its surrounding area. The length of the scale bar on the left edge is 800 µm. (magnification power = 40X)

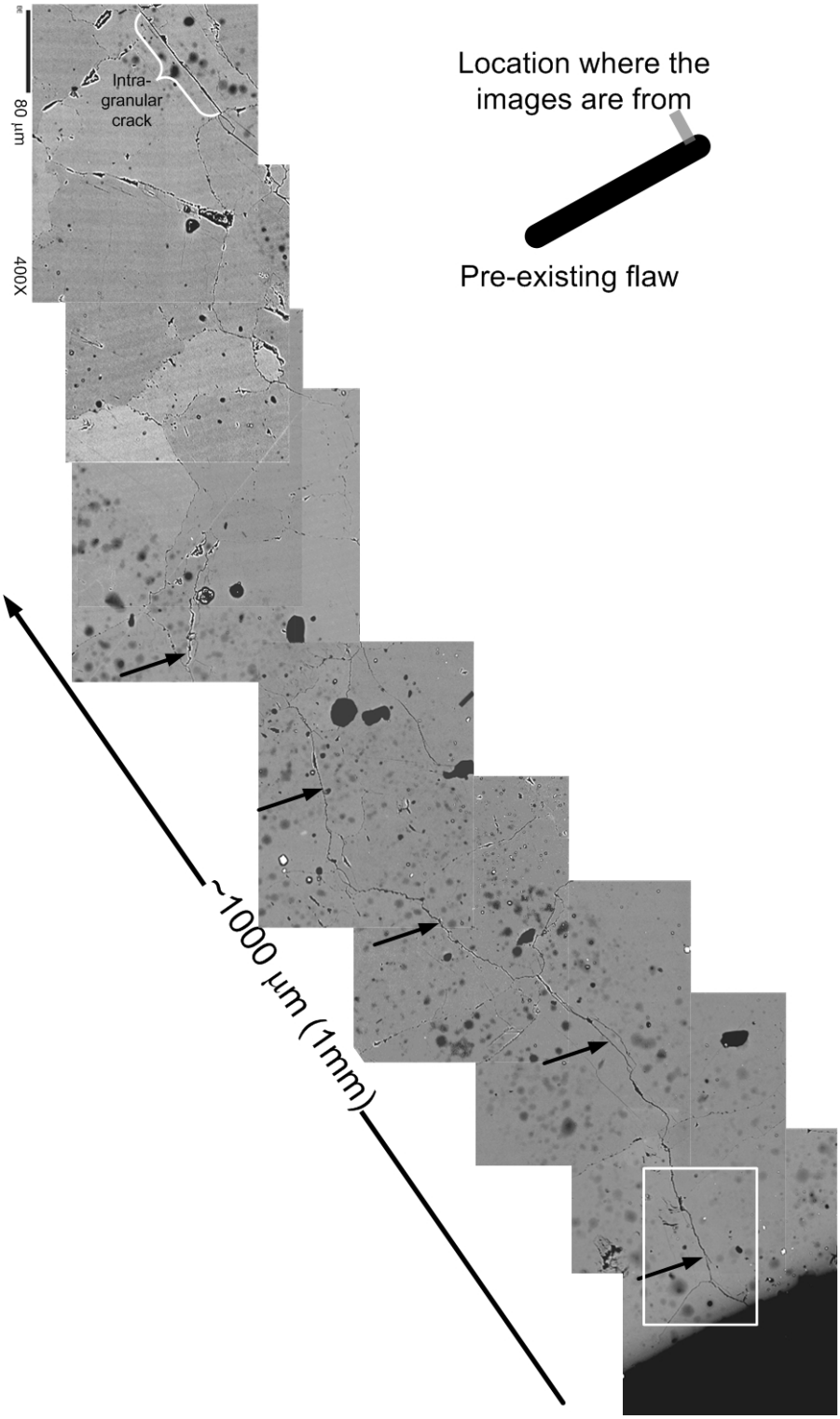

Figure 7.19 – An assemblage of magnified images of the area at the top face of the flaw close to the right tip, which is enclosed in figure 7.18. The length of the scale bar shown on the top left edge is 80 μm. The trace of a dominant crack is marked by black arrows. A further magnified image of the area enclosed by a white rectangle close to the flaw face is shown in figure 7.20. (magnification power = 400X)

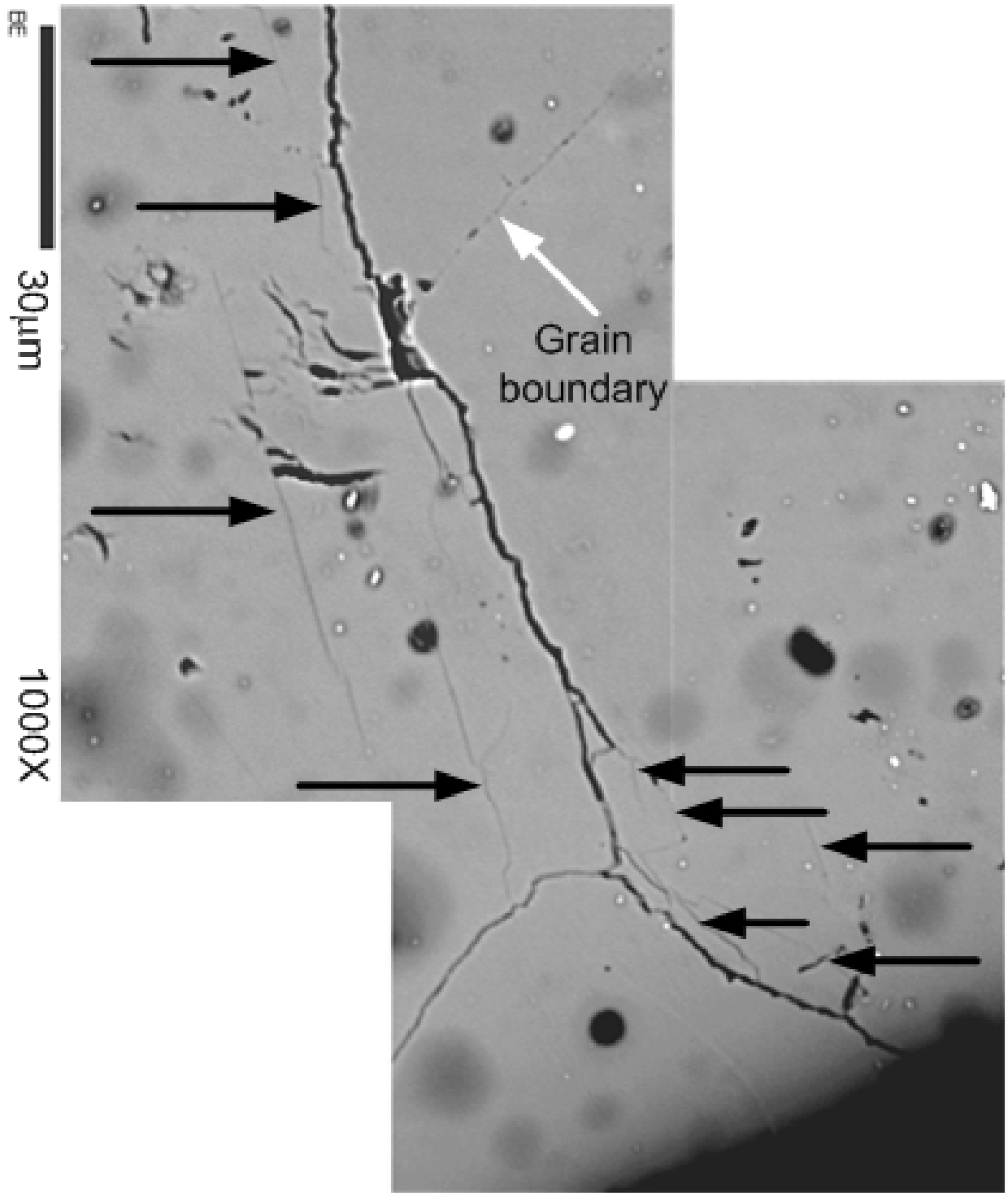

Figure 7.20 – Intra-granular cracks (indicated by horizontal arrows) developed beside the central dominant crack (thicker trace) close to the flaw face. This image is a magnified view of the enclosed region shown in figure 7.19. (magnification power = 1000X)

7.3.5 Single flaw subject to 95% failure stress

A view of specimen SD which was loaded uniaxially up to 95% of the failure stress (table 7.1) is shown in figure 7.21. Short white patches (without observable cracks) are observed to have developed from the upper face of the flaw close to the right tip and lower face of the flaw close to the left tip. These white patches are longer than those developed in specimen SB (70 % loading).

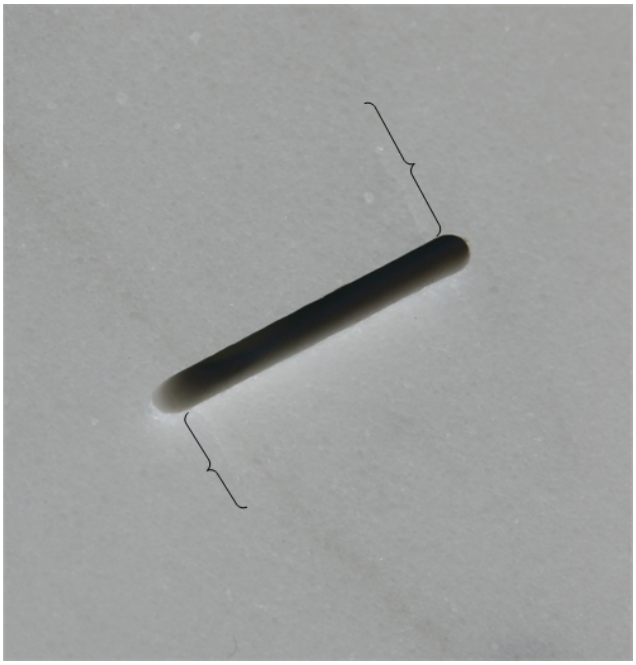

(a)

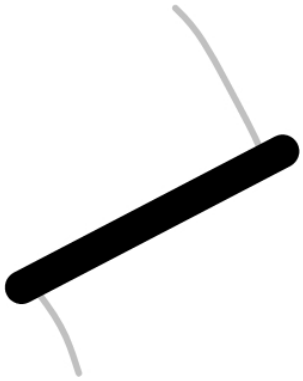

(b)

Figure 7.21 – (a) Marble specimen SD containing a straight open flaw which has been uniaxially loaded up to 95% of the failure stress. Length of the flaw is 0.5" (13mm). Image was taken by a digital camera. Note the development of white patches close to the two flaw tips. (b) sketch of the flaw and the white patches.

An assemblage of SEM images of the flaw and its surrounding area is shown in figure 7.22. Under that magnification power, even though many of the fine details concerning grain boundaries and microcracking cannot be observed clearly, two black traces of microcracks are identified close to the two flaw tip regions which correspond to the white patch trajectories as shown in figure 7.21. Magnified images of these two regions are shown in figures 7.23 and 7.24 and further discussed below.

Figure 7.23 shows a microcracking zone developed from the top face of SD close to the right flaw tip. This zone consists of a central undulating crack which generally follows grain boundaries and multiple intra-granular cracks flanking its two sides (indicated by arrows). These intra-granular cracks are of a typical length between 20 and 50 μm (some may reach 80 μm) and generally trend parallel with the central crack. However, shorter intra-granular cracks orthogonal to them could also sometimes be observed. A typical marble grain which consists of these features is shown in the further magnified image (a) in the same figure. As shown in this image, multiple intra-granular cracks are embedded within a marble grain (about 200 μm long), which is rimmed by thicker inter-granular cracks along its grain boundary. Another interesting feature contained in figure 7.23 is the development of spalling features along the microcracking zone. Most of these spalling zones are of a triangular shape of a length between 5 and 60 μm. They are generally scattered as black patches along grain boundaries. Two of such spalling patches are shown in the magnified image (b). Also observe in figure 7.23 that intra-granular crack density is highest beside the central undulating crack (within three grain sized-distance) and it drops off rapidly with distance from this central crack. This is well-illustrated in the top right corner of figure 7.23, where marble grains almost completely free of intra-granular cracks are found.

Similar to the white patch developed on the top face of SD close to the right flaw tip, the white patch developed from the bottom face of SD close to the left flaw tip is also underlain by a similar microcracking zone (figure 7.24), which again consists of a central undulating crack generally following grain boundaries and multiple intra-granular cracks flanking its two sides. Shear-related spalling zones are also scatted beside the central crack (figure 7.24).

Magnified images of some typical microstructural features observed within the microcracking zone in figure 7.24 are shown in figures 7.24a and b. In figure 7.24a, a spalling zone developed along the trajectory of the central main crack as shown previously in figure 7.24. Note also the development of multiple orthogonal intra-granular cracks. In figure 7.24b, the main crack cuts across a marble grain (enclosed by a dashed line) on its course of propagation. Multiple intra-granular cracks also develop in a neighboring grain to the right of it with its boundary rimmed by inter-granular cracks and localized triangular spalling zones.

To summarize, the white patches developed from the flaw face close to the tip regions observed in the hand specimen which has been loaded up to 95% of the failure stress can be correlated with zones of microcracks. Each of these microcracking zones consists of a central dominant undulating crack generally following grain boundaries and multiple much shorter orthogonal intra-granular cracks flanking the dominant crack. The density of intra-granular and inter-granular microcracks, which is highest beside the dominant crack, drops off rapidly with distance from this central crack. Shear-related spalling zones are also found to be scatted close to the central crack.

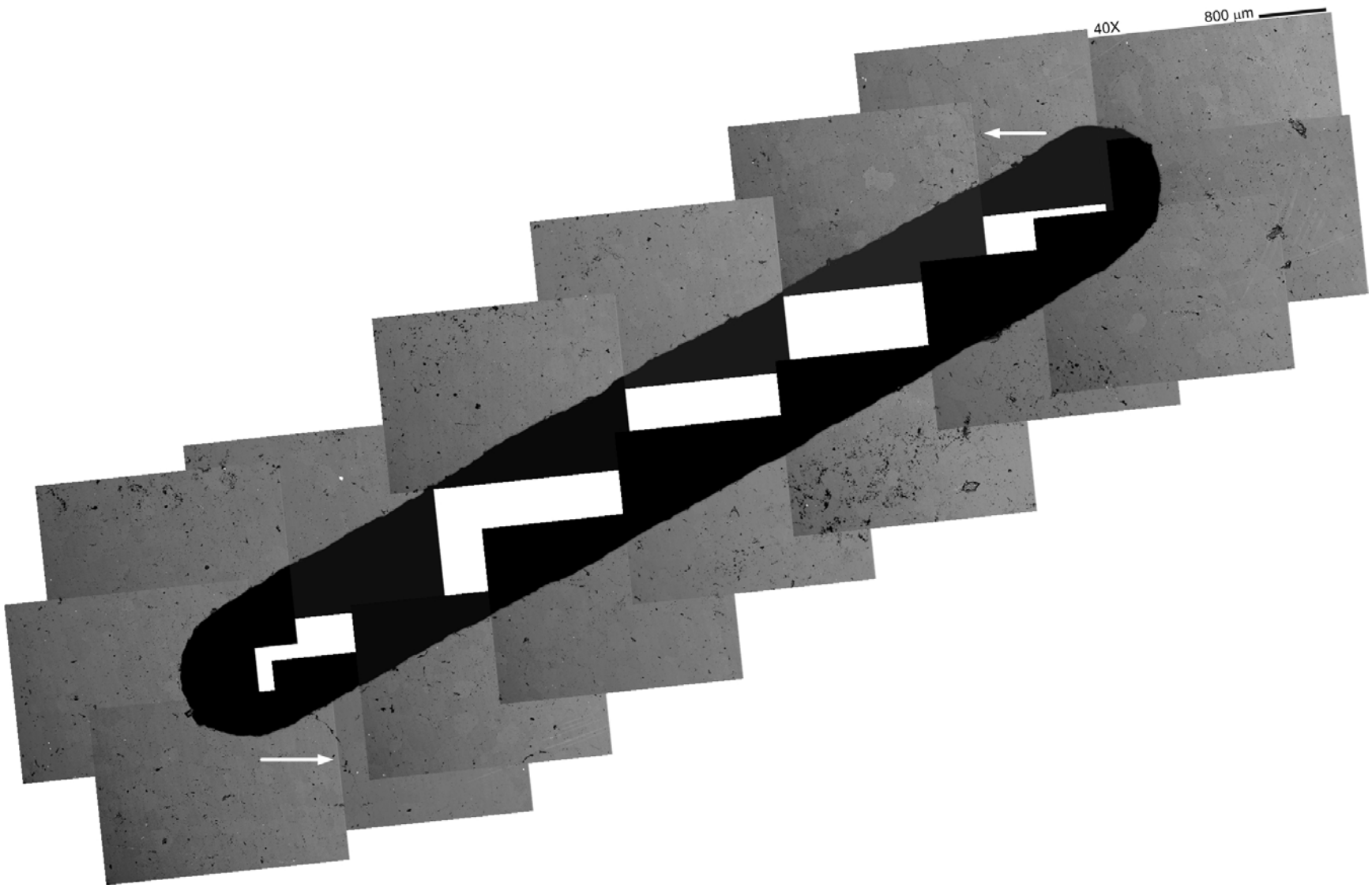

Figure 7.22 – An assemblage of SEM images of single flaw SD and its surrounding area. The length of the scale bar on the top right edge is 800 µm. Zones of microcracks corresponding to white patches observed in hand specimen are indicated by two white arrows. (magnification power = 40X)

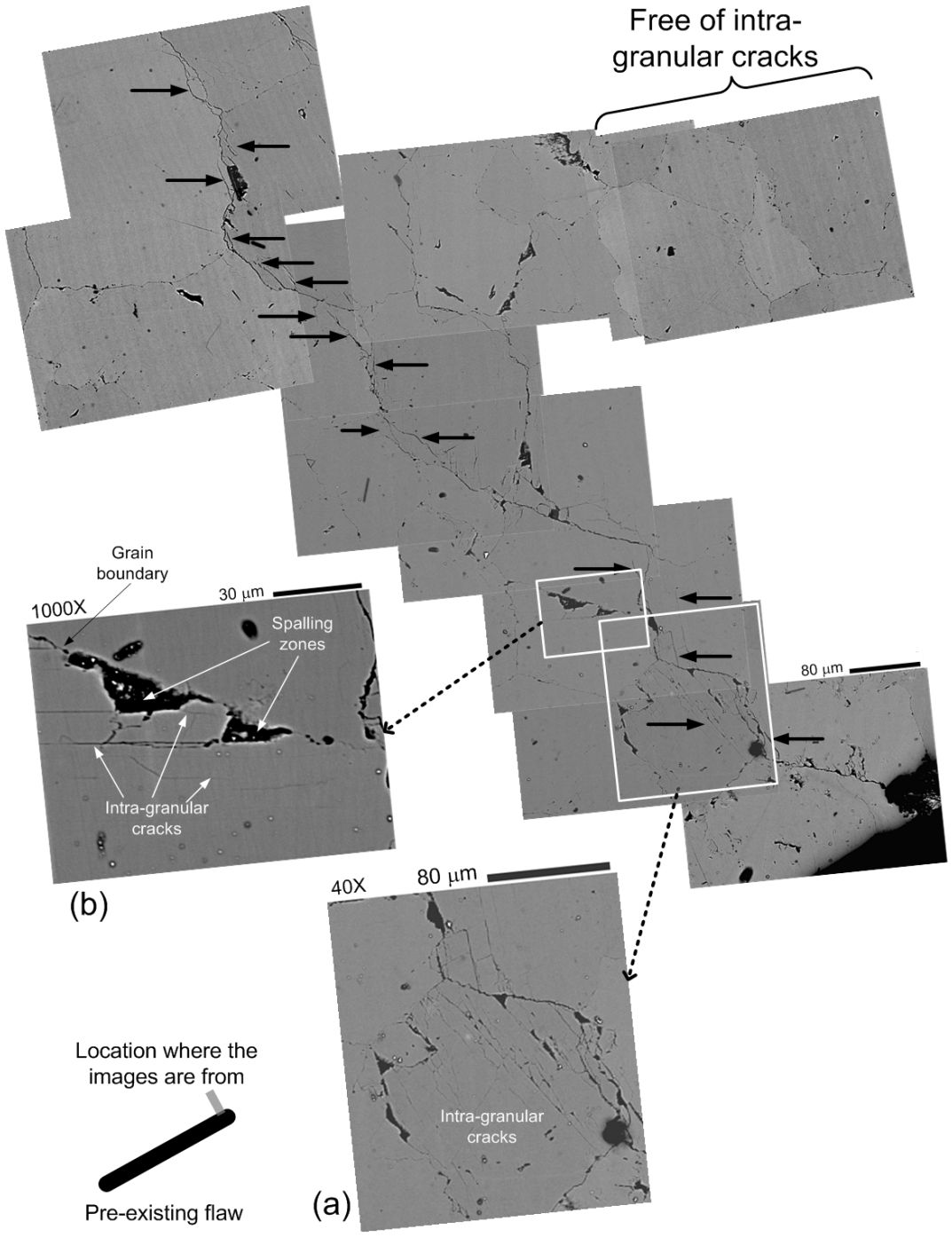

Figure 7.23 – A microcracking zone developed from the top face of SD close to the right flaw tip. The zone consists of a central undulating crack generally following grain boundaries and multiple intra-granular cracks flanking its two sides (indicated by horizontal arrows). In magnified image (a), a marble grain is rimmed by inter-granular cracks along its grain boundary. Multiple intra-granular cracks form within the grain. In magnified image (b), triangular spalling zones form along a grain boundary. Individual images within the assemblage and figure (a) are taken at a magnification power of 400X, while figure (b) is taken at 1000X.

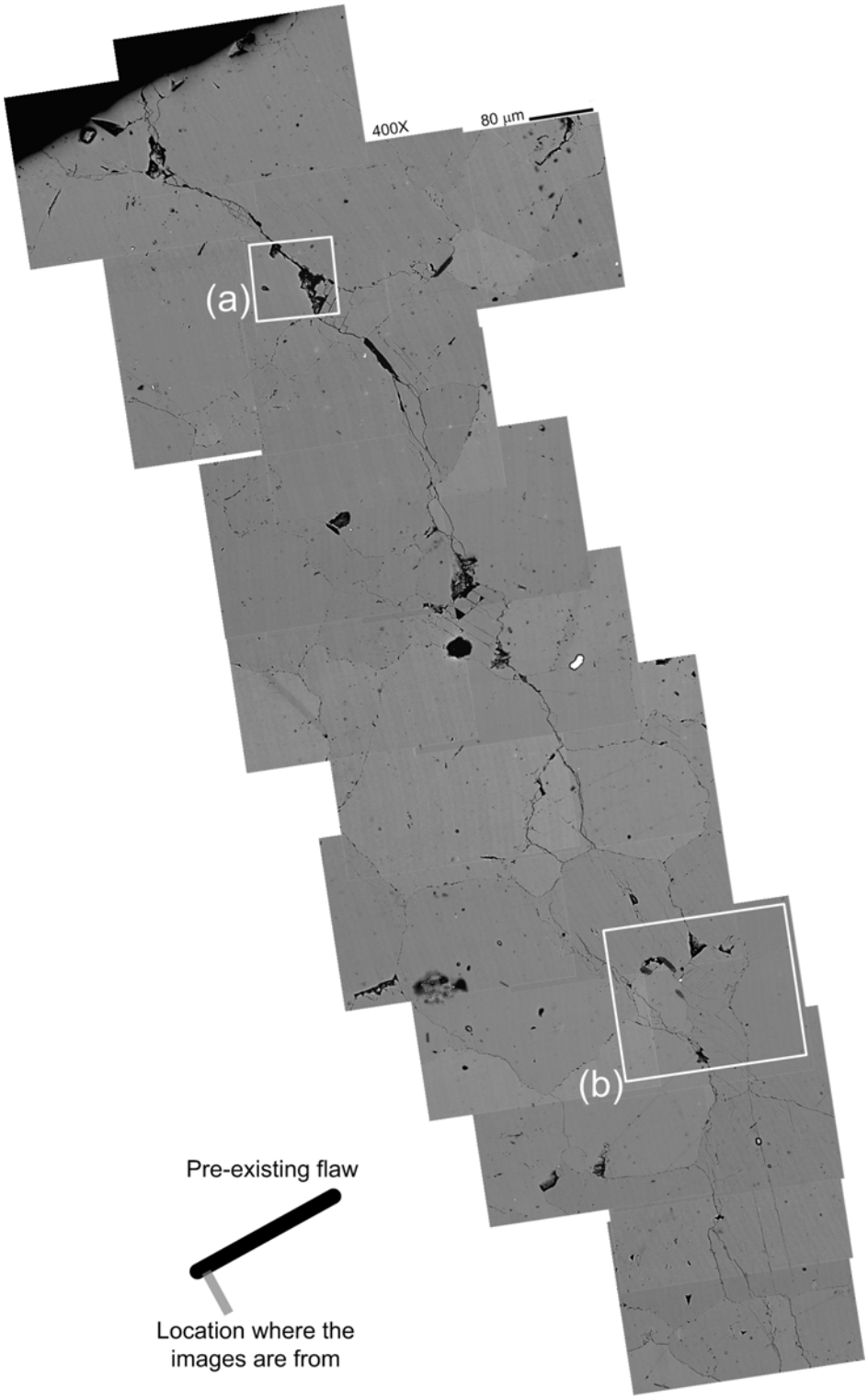

Figure 7.24 – A microcracking zone developed from the bottom face of SD close to the left flaw tip. The zone consists of a central undulating crack generally following grain boundaries and multiple intra-granular cracks flanking its two sides (indicated by horizontal arrows). This assemblage of images was captured at a magnification power = 400X. See figures 7.24 (a) and (b) for the magnified views of the enclosed regions.

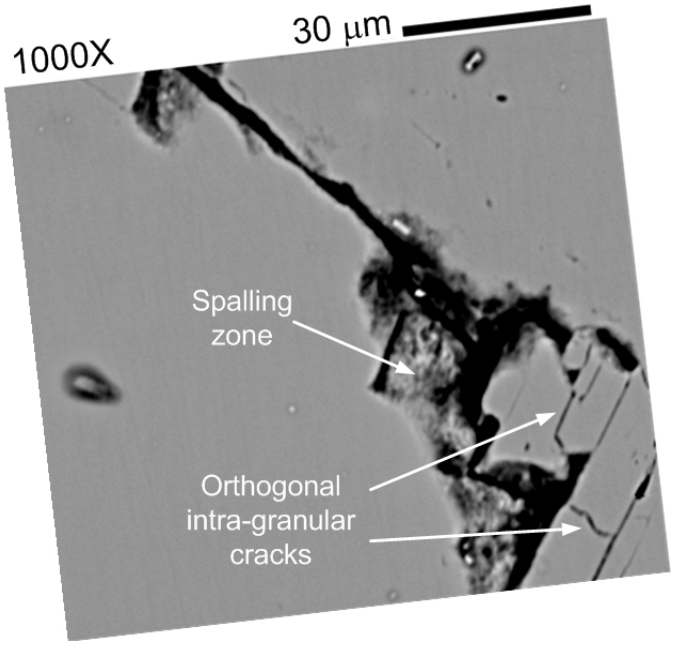

Figure 7.24 (a) – A spalling zone developed along the trajectory of the central main crack as shown in figure 7.24. Note also the development of multiple orthogonal intra-granular cracks at the bottom right corner. (magnification power = 1000X)

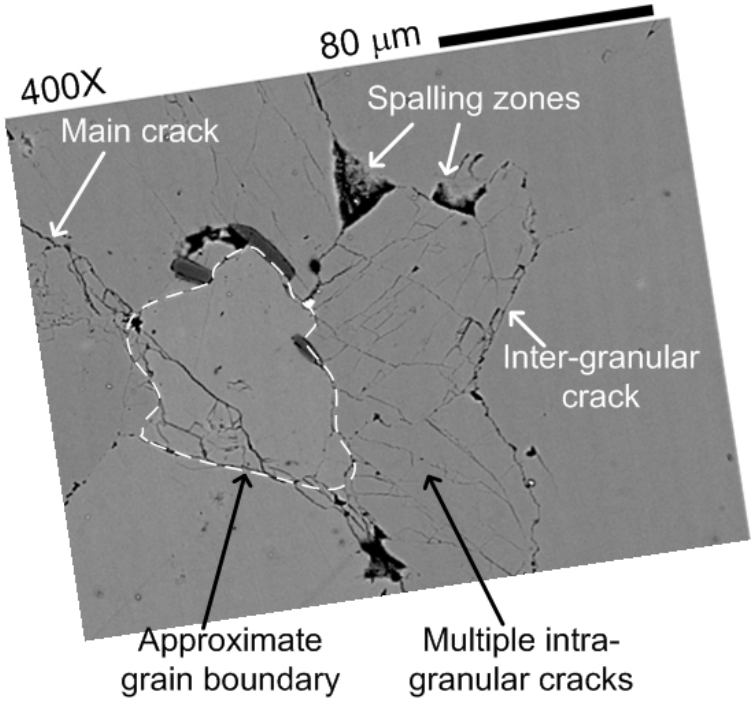

Figure 7.24 (b) – Different microscopic features along the microcracking zone corresponding to the white patch observed in the hand specimen. A main crack cuts through a marble grain (enclosed by a dashed line) on its course of propagation. Multiple intra-granular cracks develop in a neighboring grain to the right of it with its boundary rimmed by inter-granular cracks and localized triangular spalling zones. (magnification power = 400X)

7.3.6 Double flaws subject to 50% failure stress

A view of specimen DA which was loaded uniaxially up to 50% of the failure stress (table 7.1) is shown in figure 7.25. Short thin white patches are again observed to have developed close to the four flaw tips.

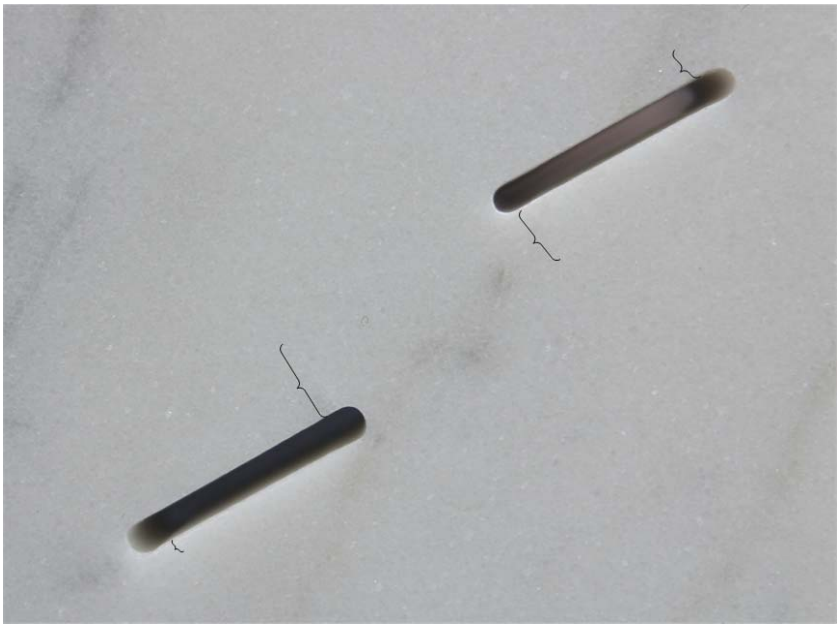

(a)

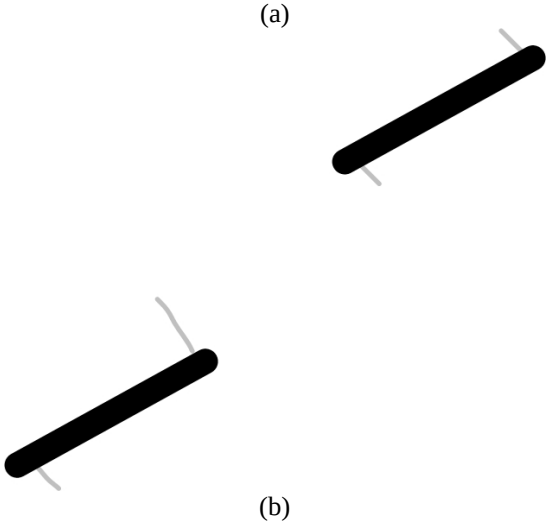

(b)

Figure 7.25 – (a) Marble specimen DA containing a pair of straight open flaws which has been uniaxially loaded up to 50% of the failure stress. Length of the flaw is 0.5" (13mm). Image was taken by a digital camera. Note the development of white patches from the flaws close to the tips. (b) sketch of the flaws and the white patches.

Assemblages of SEM images of the two flaws (top and bottom) and their surrounding areas are shown in figures 7.26 and 7.27. Under that magnification power, however, many of the fine details concerning grain boundaries and microcracking cannot be observed clearly. A positive correlation cannot be made between the white patches observed in the hand specimen (figure 7.25) and any microstructural features in SEM images (figures 7.26 & 7.27).

The flaw faces and its surrounding areas are then comprehensively examined with higher magnification powers (200 to 400 times). Magnified images of the flaw tip regions corresponding to the same locations where the white patches are observed in the hand specimen are shown in figures 7.28 to 7.32.

The upper face of the top flaw close to the right tip is observed to be scattered with a number of very short (20 – 50 μm) intra-granular cracks and black spalling features (figure 7.28). The latter are commonly located along grain boundaries. About half of the grain boundaries are found to be opened up as cracks (darker and thicker traces) and about half of them remain intact. Similar microcracking behavior is also observed on the lower face of the same flaw close to the left tip (figure 7.29). In both locations, however, there is not an observable dominant microstructure similar to those in specimens DB and DC (to be shown in later sections) which can be identified to correlate with the white patch trajectories observed in the hand specimens.

An assemblage of SEM images close to the right tip at the upper face of the bottom flaw is shown in figure 7.30. Most of the marble grains shown in this image are generally free of intra-granular cracks, except the occurrence of scattered spalling features along some grain boundaries and junctions of grain boundaries. Due to an adequate color contrast between neighboring grains, the presence of intra-granular cracks can thus be easily identified. Magnified images of some of the most conspicuous ones marked by white brackets in figure 7.30 are shown in figure 7.31. Based on the trending direction of these intra-granular cracks and the inter-granular cracks in the neighboring grains, it is reasonable to correlate their presence with the white patch which follows a similar trajectory in the hand specimen (figure 7.25).

An assemblage of SEM images close to the left tip at the lower face of the bottom flaw is shown in figure 7.32. Similar to the two tip regions of the top flaw, there is not an observable dominant microstructure which can be easily correlated with the white patch trajectories observed in the hand specimen. This region is scattered with a number of very short (10 – 50 μm) intra-granular cracks and black spalling features (figure 7.28). Inter-granular cracking also occur along many of the grain boundaries. However, most of them are relatively short and disconnected.

To summarize, the white patches observed in the hand specimen which was loaded uniaxially up to 50% of the failure stress can be correlated with zones of short microcracks. In one of the four tip regions being examined (figure 7.30), the intra-granular and inter-granular cracks within the microcracking zone generally trend in an orientation similar to the white patch. However, this feature is not observed in three other flaw tip regions.

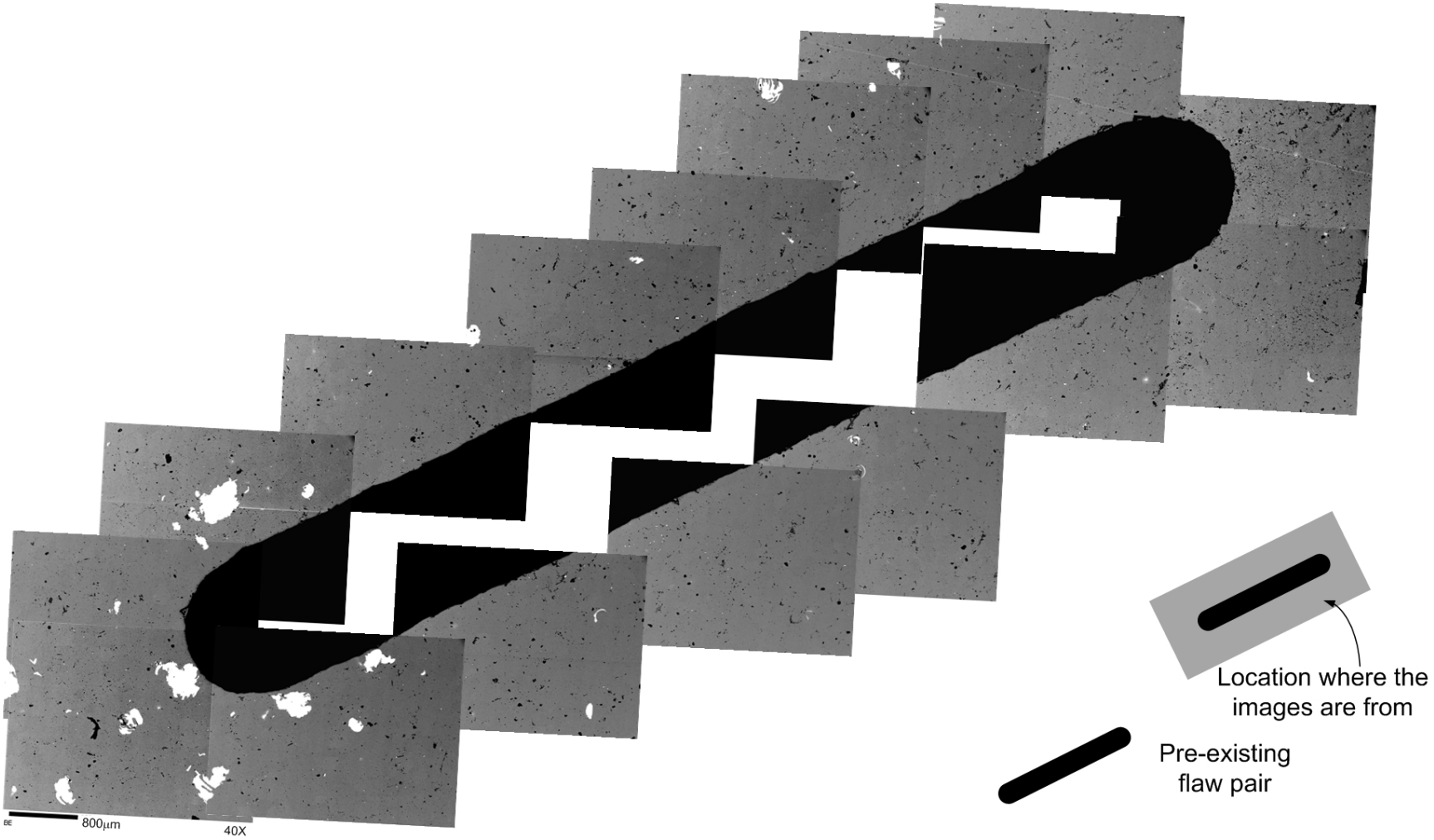

Figure 7.26 – An assemblage of SEM images of the top flaw of flaw pair DA and its surrounding area. The length of the scale bar on the bottom left edge is 800 μm. (magnification power = 40X)

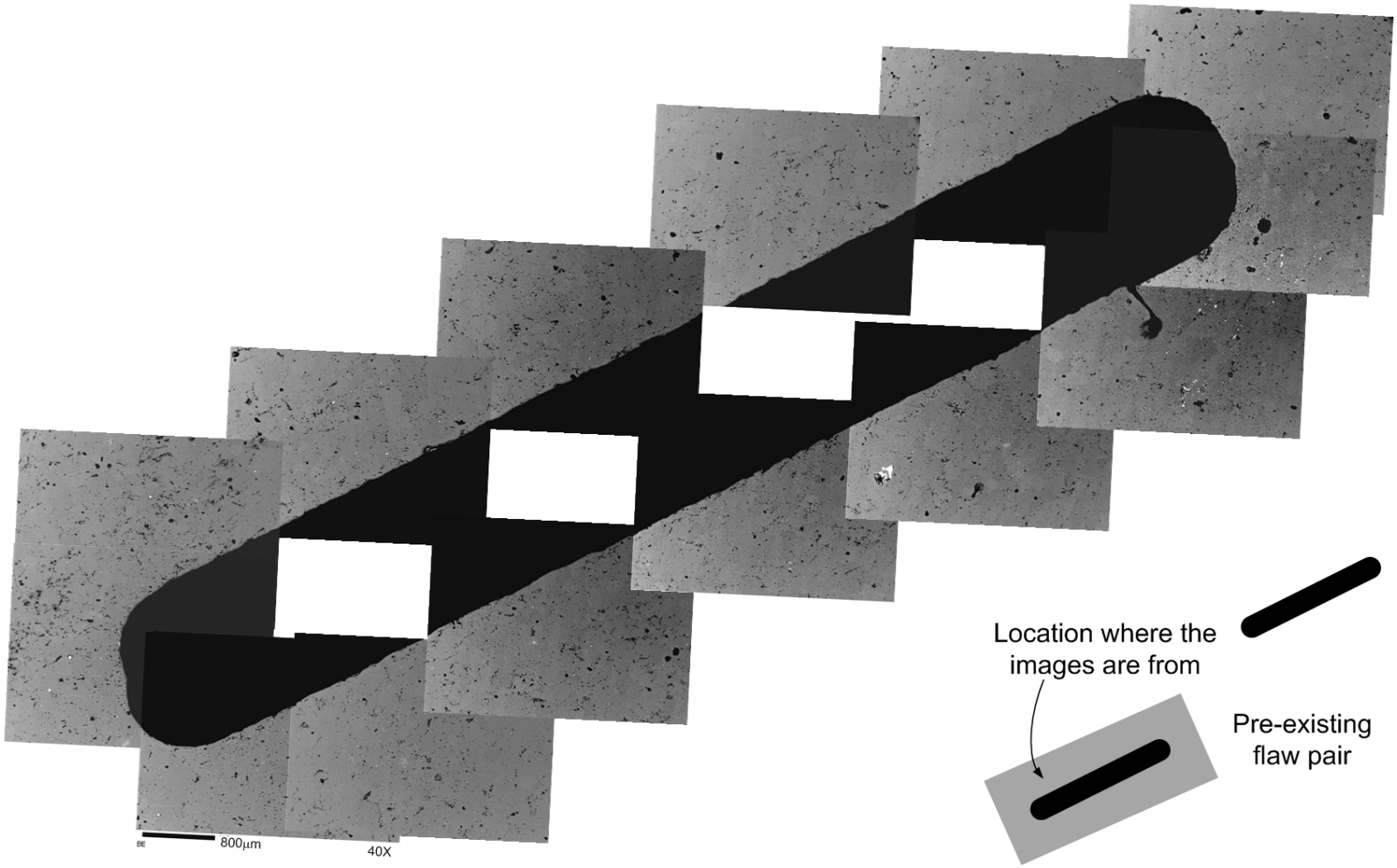

Figure 7.27 – An assemblage of SEM images of the bottom flaw of flaw pair DA and its surrounding area. The length of the scale bar on the bottom left edge is 800 μm. (magnification power = 40X)

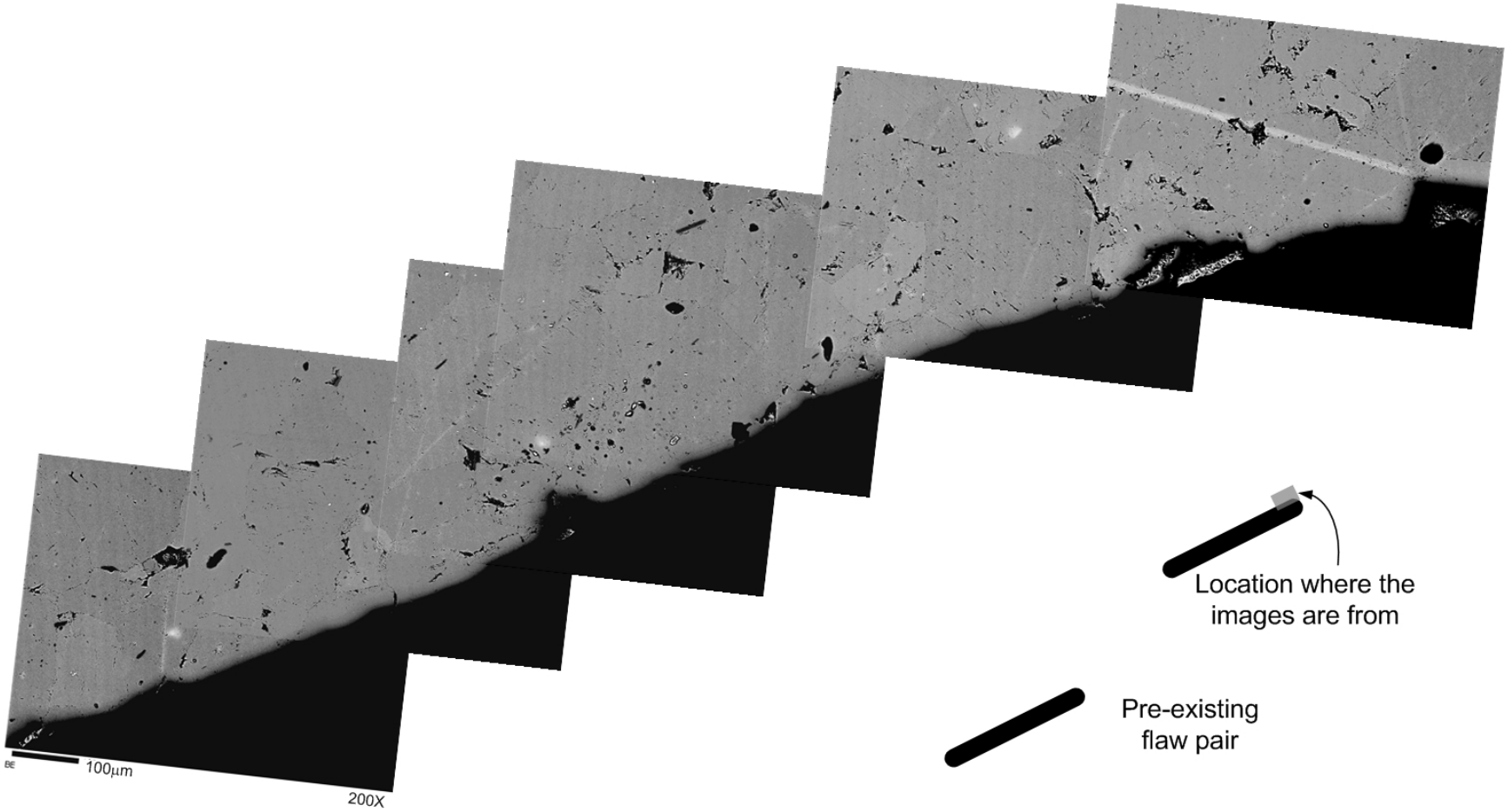

Figure 7.28 – An assemblage of magnified images of an area close to the right tip of the top flaw. (magnification power = 200X)

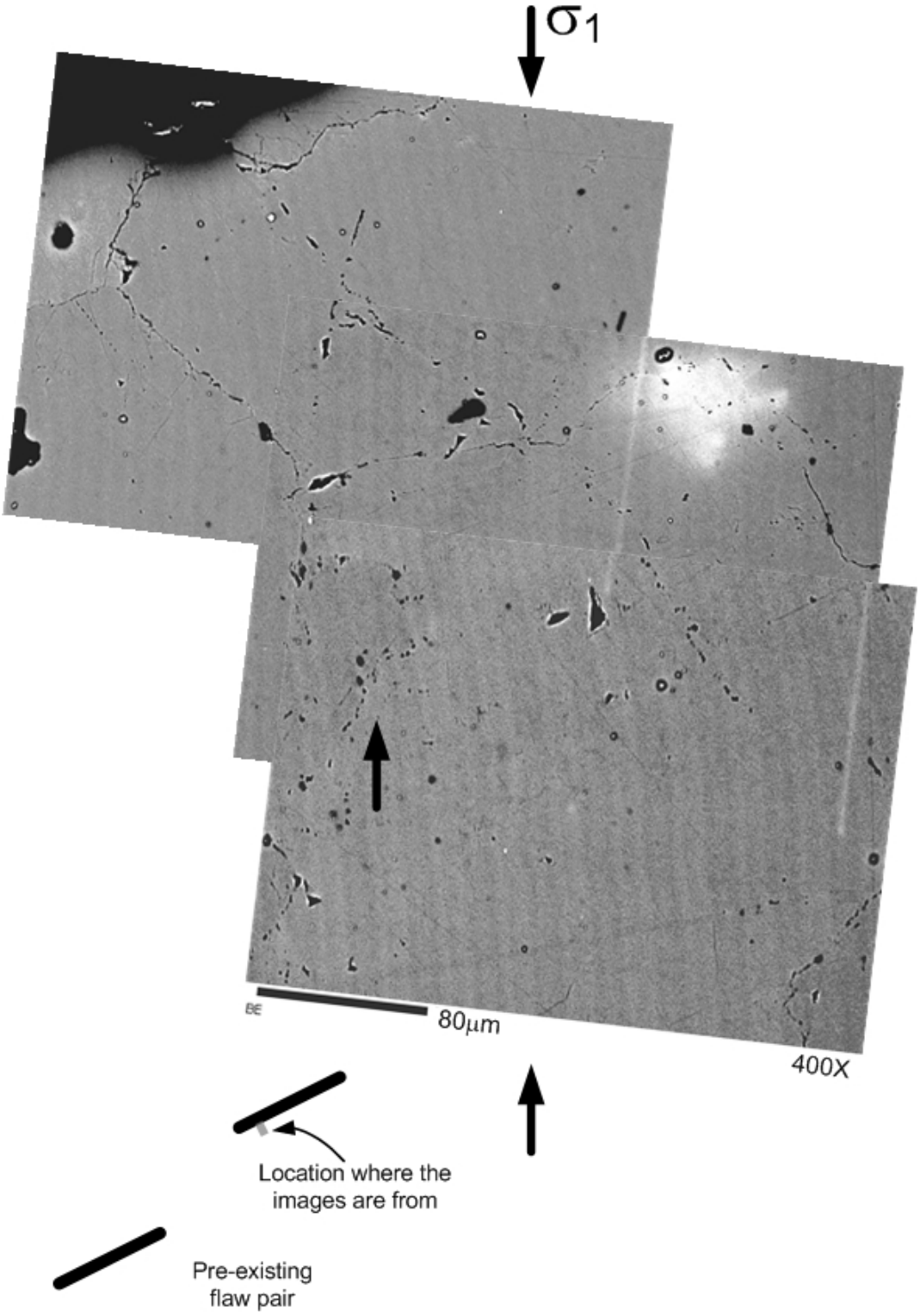

Figure 7.29 – An assemblage of magnified images of an area close to the left tip of the top flaw. (magnification power = 400X)

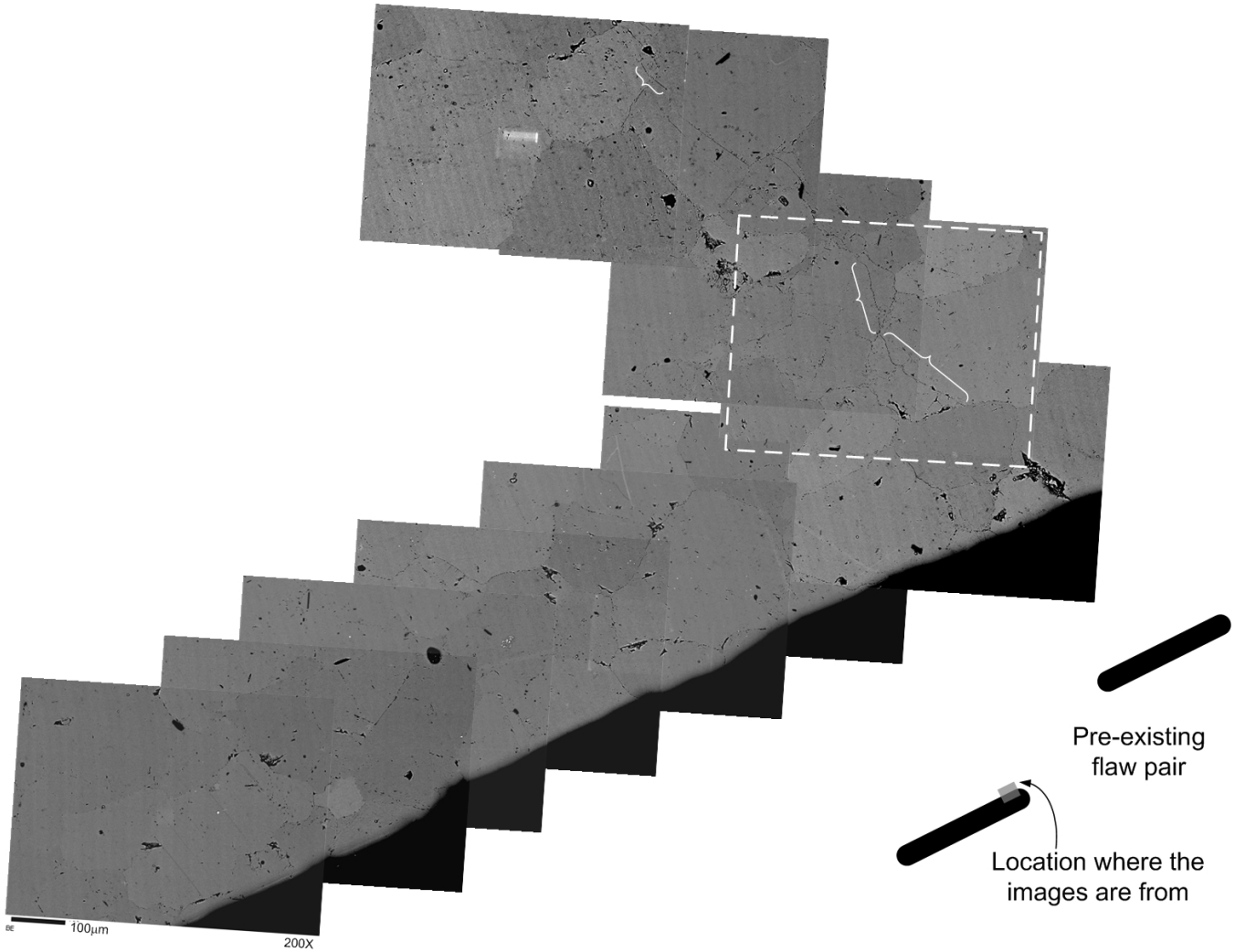

Figure 7.30 – An assemblage of magnified images of an area close to the right tip of the bottom flaw. Two conspicuous intra-granular cracks are indicated by white brackets and shown in figure 7.31. (magnification power = 200X)

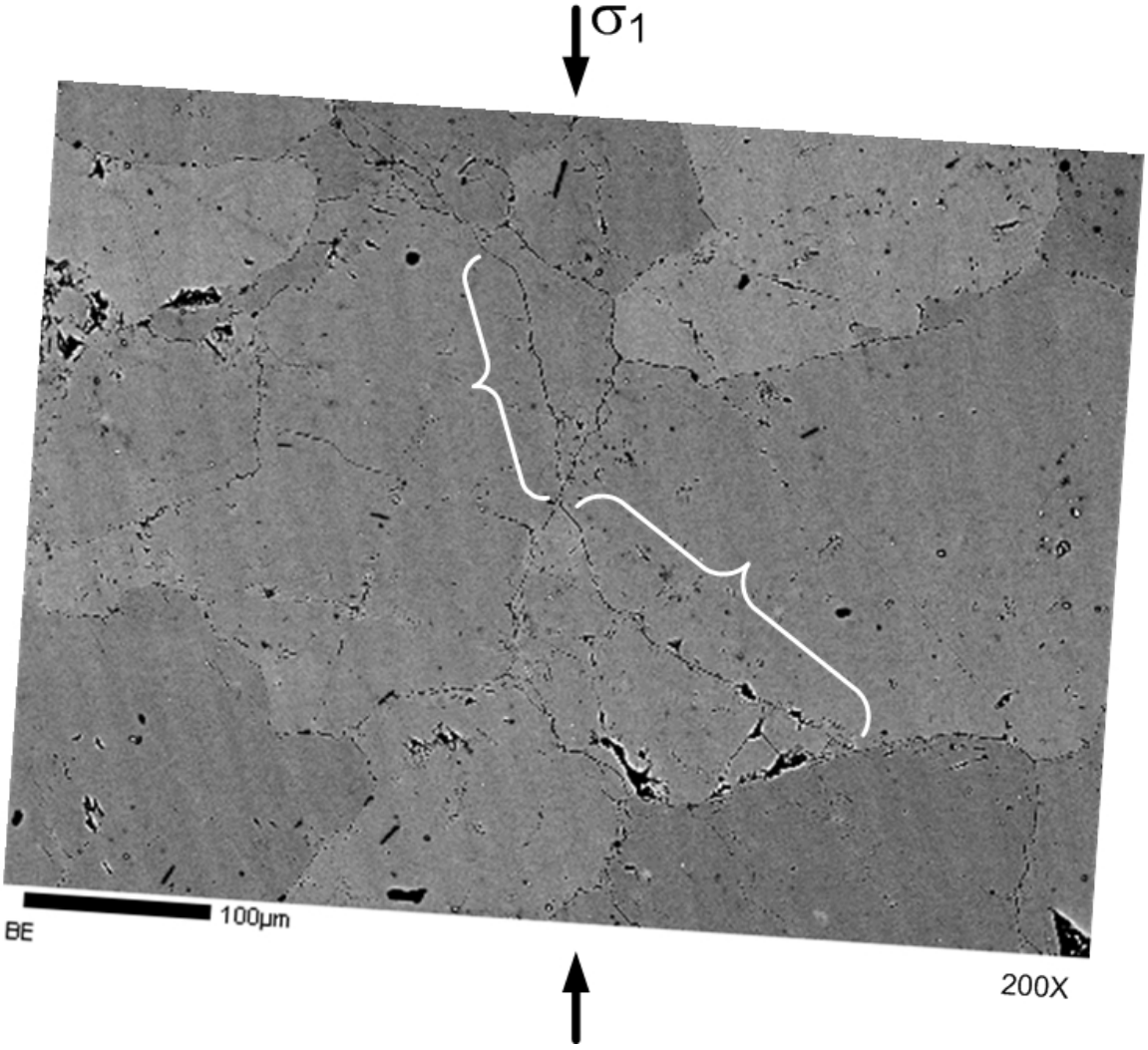

Figure 7.31 – Magnified image of an area enclosed in figure 6.30 which contains two intra-granular cracks. (magnification power = 200X)

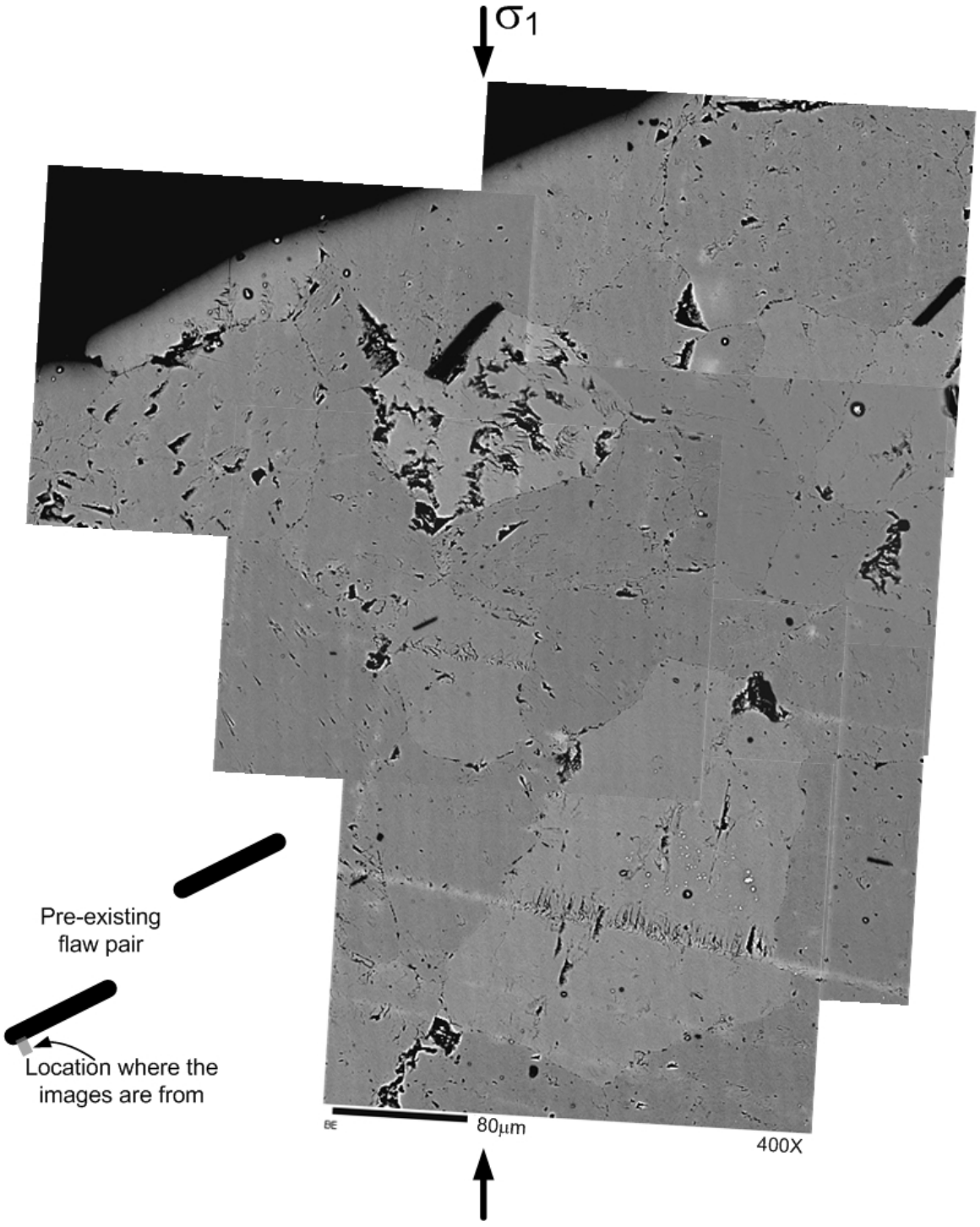

Figure 7.32 – An assemblage of magnified images of an area close to the left tip of the bottom flaw. (magnification power = 400X)

7.3.7 Double flaws subject to 70% failure stress

A view of specimen DB which was loaded uniaxially up to 70% of the failure stress (table 7.1) is shown in figure 7.33. Short thin white patches, which are longer than those observed in specimen DA (50% loading) are again observed to have developed close to the four flaw tips.

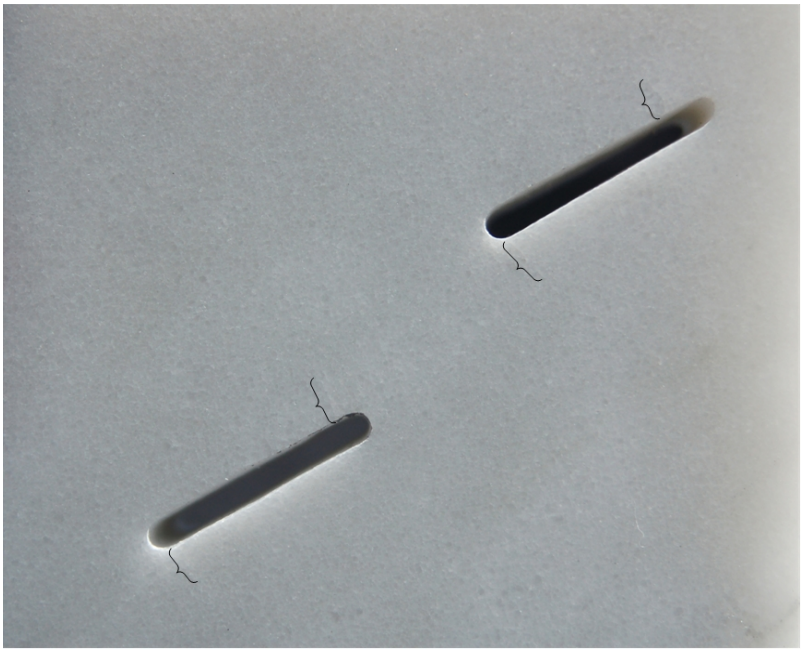

(a)

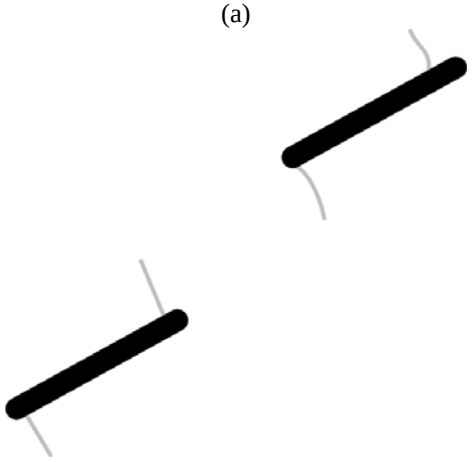

(b)

Figure 7.33 – (a) Marble specimen DB containing a pair of straight open flaws which has been uniaxially loaded up to 70% of the failure stress. Length of the flaw is 0.5" (13mm). Image was taken by a digital camera. Note the development of white patches from the flaws close to the tips. (b) sketch of the flaws and the white patches.

Assemblages of SEM images of the two flaws (top and bottom) and their surrounding areas are shown in figures 7.34 and 7.35. Under that magnification power, although many of the fine details concerning grain boundaries and microcracking cannot be observed, it is still possible to identify zones of mircocracking enclosed in figures 7.34 and 7.35 which may be correlated with the white patches observed in the hand specimen (figure 7.33).

Areas around the flaw faces are comprehensively examined with higher magnification powers (200 to 400 times). Magnified images of the flaw tip regions corresponding to the same locations where the white patches are observed in the hand specimen are shown in figures 7.36 to 7.40 [1].

The area around the left tip of the top flaw is scattered with multiple black spalling features which are indicated by white arrows in figure 7.36. Most of them are located along grain boundaries or at junctions of grain boundaries. Microcracking (inter-granular and intra-granular) is commonly observed for those grains close to the flaw face. However, individual grains completely free of intra-granular cracks can also sometimes be found adjacent to the flaw face. The white curvilinear lines observed in the left part of the image is probably not associated with any microcracking events due to loading, but incomplete polishing before carbon coating is carried out. On the lower face of the flaw, a relatively more fractured zone is identified (enclosed by a dashed-lined rectangle). An assemblage of magnified images of this zone is shown in figure 7.37.

In figure 7.37, a crack extends from the top left corner (flaw face) to the bottom right corner. However, it is difficult to determine which part of the crack is along grain boundaries (inter-granular) and which part is though the grain (intra-granular) due to a poor color contrast of marble grains. Nonetheless, it is very clear that the density of intra-granular cracks and spalling features is the highest adjacent to the flaw face, and decreases away from the flaw face.

[1] Due to the presence of multiple shiny white zones because of imperfect carbon coating, magnified images could not be obtained from the right tip region of the upper face of the top flaw.

Magnified images of the two microcracking zones identified for the bottom flaw (figure 7.35) are shown in figures 7.38 and 7.40. In figure 7.38, the microcracking zone which generally trends vertically, consists mainly of a central undulating crack and multiple intra-granular cracks on its two sides. The cross-cutting intra-granular cracks often form a rectangular grid pattern. In the region close to the flaw face, closer examination reveals that the micocracking zone consists of several dominant thick cracks instead of a single dominant crack. See figure 7.39 for details. Those intra-granular cracks are of a length typically between 5 and 50 μm (some may reach 80 μm). Most of them trend parallel with the dominant crack, but shorter intra-granular cracks orthogonal to them are also very common (see a further magnified view in figure 7.39). It is again often difficult to determine which part of the crack is along grain boundaries and which part is though the grain (intra-granular) due to a poor color contrast of marble grains, especially at the region close to the flaw face. However, in certain parts, based on the cutting relationship between microcracks and marble grains, it is possible to identify that the dominant crack does not propagate through grain A, but bisects grain B into two halves (top part of figure 7.38). Many spalling features are found along the dominant crack and its vicinity, which are especially abundant close to the flaw face. They are indicated by white arrows in figures 7.38 and 7.39. Most of them are of triangular shape and a size between 5 and 50 μm. The density of micro-cracks and spalling features is the highest adjacent to the flaw face, which decreases with distance from the flaw face. This density is similarly the highest along and adjacent to the dominant crack, but deceases away from the dominant crack.

The microstructural features associated with the white patch observed in the hand specimen at the left tip of the bottom flaw (figure 7.40) are very similar to those observed at the right tip of the bottom flaw (figure 7.38), i.e. there is a dominant crack initiating form the flaw face and extending outward. The density of microcracks and spalling features is the highest close to the flaw face and the central dominant crack, and decreases with distance outwards. Figure 7.41 contains a marble grain being cut through by the dominant crack. It is however, impossible to determine if the trace of the dominant crack (marked as A) at the top of it is also an intra-granular feature due to a

poor color contrast of marble grains. Note also the generally parallel traces of intra-granular cracks developed in vicinity of crack A.

To summarize, the white patches developed close to the flaw tips observed in the hand specimen which has been loaded up to 70% of the failure stress can be correlated with zones of microcracks. Each microcracking zone consists of a central dominant undulating crack and multiple much shorter intra-granular cracks flanking the dominant crack. In the region close to the flaw face, the micocracking zone consists of several dominant thick cracks instead of a single dominant crack. The density of intra-granular microcracks and spalling features, which is highest near the dominant crack and adjacent to the flaw face, drops off rapidly with distance from this dominant crack and the flaw face.

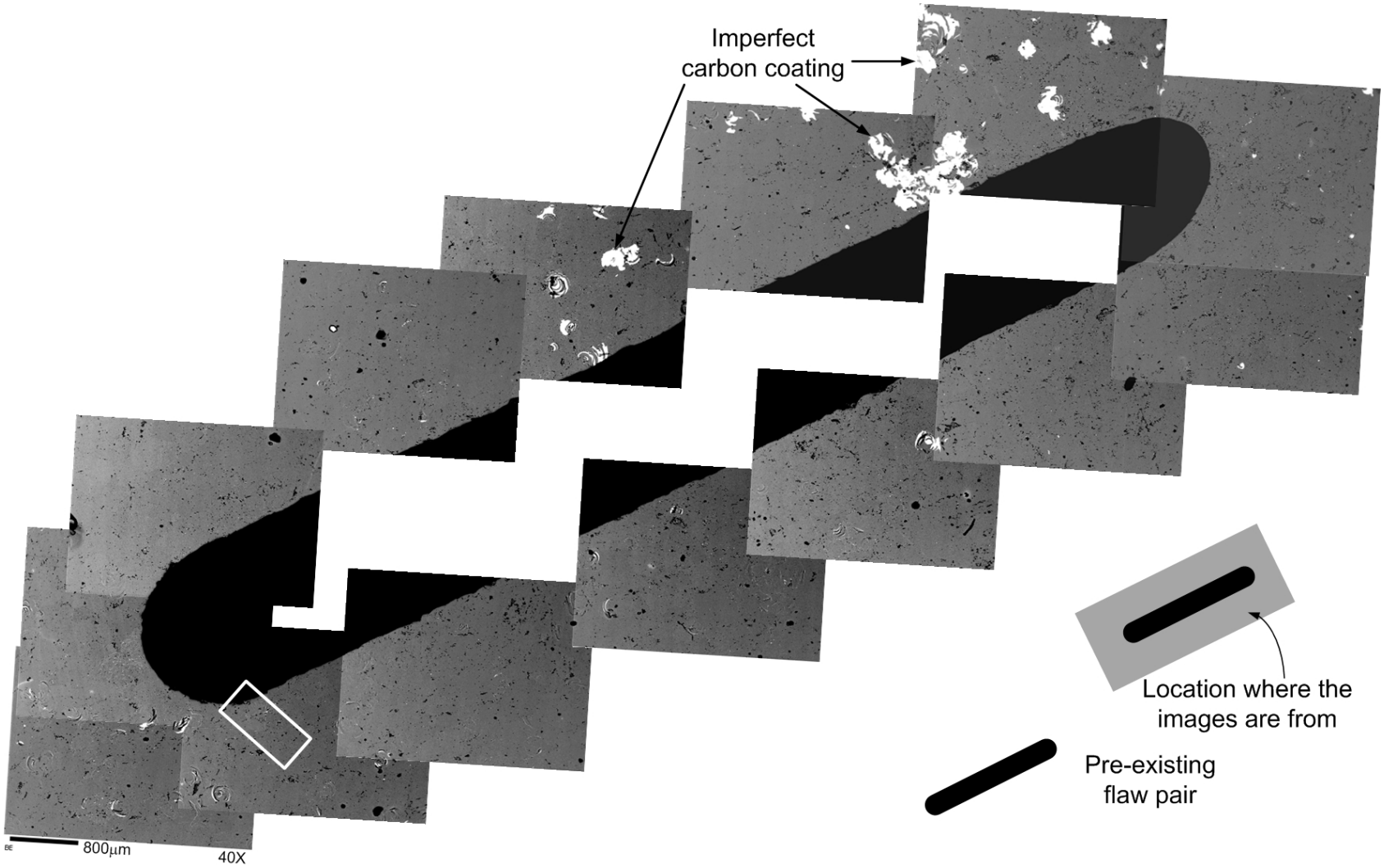

Figure 7.34 – An assemblage of SEM images of the top flaw of flaw pair DB and its surrounding area. The length of the scale bar on the bottom left edge is 800 µm. The region enclosed by a white rectangle close to the left tip corresponds to the white patch observed in the hand specimen. (magnification power = 40X)

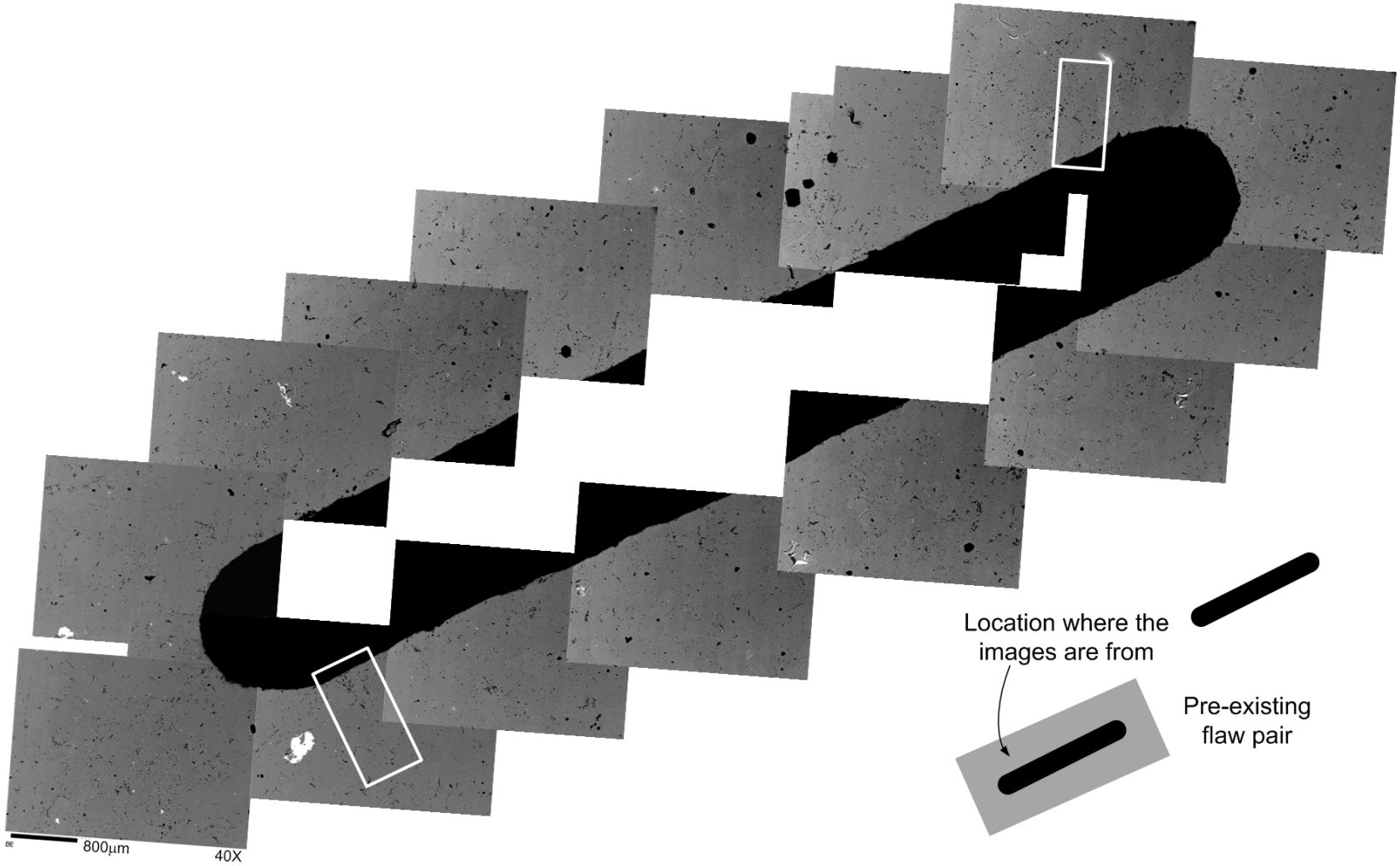

Figure 7.35 – An assemblage of SEM images of the bottom flaw of flaw pair DB and its surrounding area. The length of the scale bar on the bottom left edge is 800 µm. The two regions enclosed by white rectangles close to the tips correspond to the two white patches observed in the hand specimen. (magnification power = 40X)

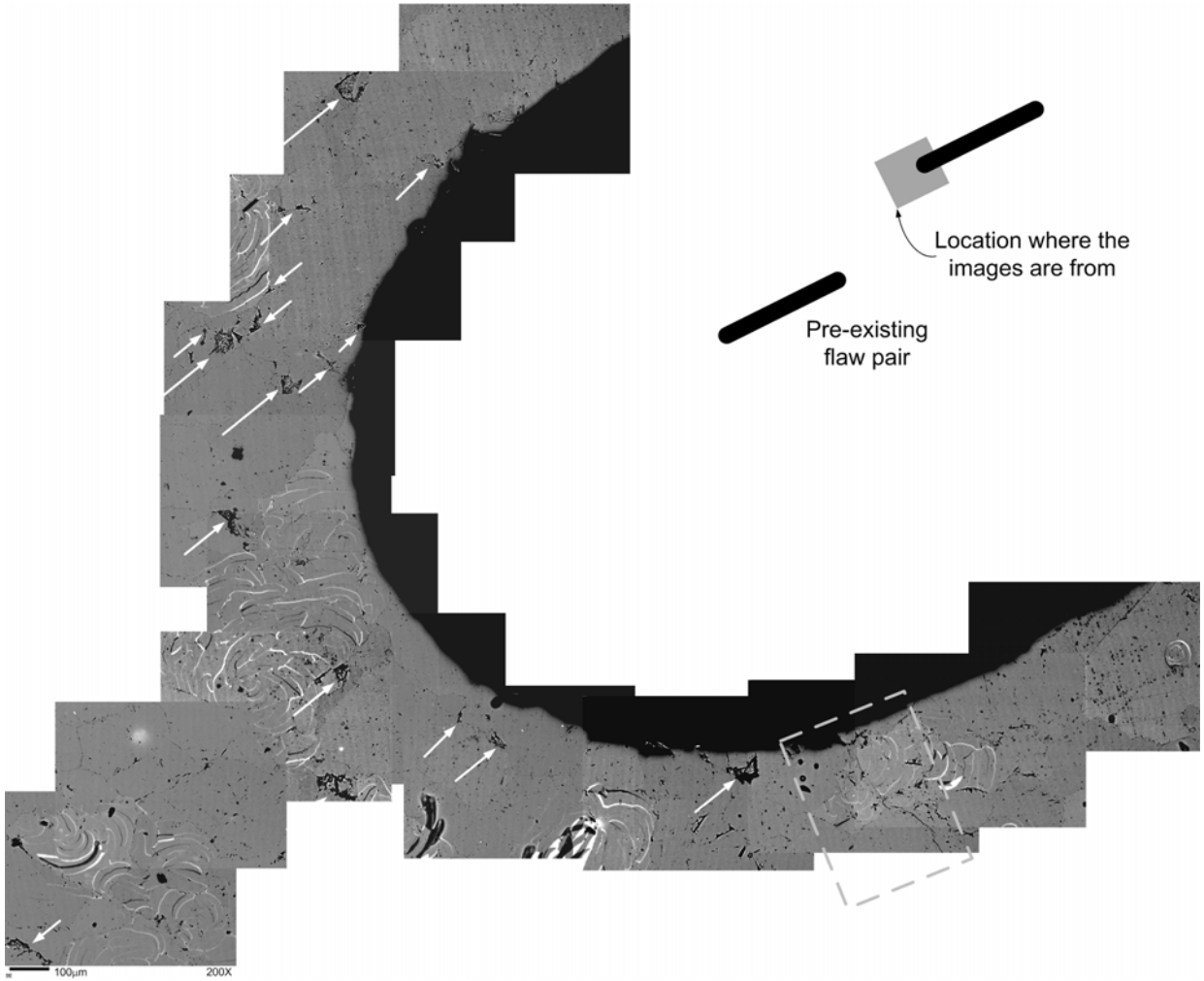

Figure 7.36 – An assemblage of SEM images of the left tip of top flaw of flaw pair DB. (magnification power = 200X) The white arrows indicated spalling features. The dashed-lined rectangle encloses a microcracking zone which may be associated with the white patch observed in the hand specimen. A magnified image of this zone is shown in figure 7.37.

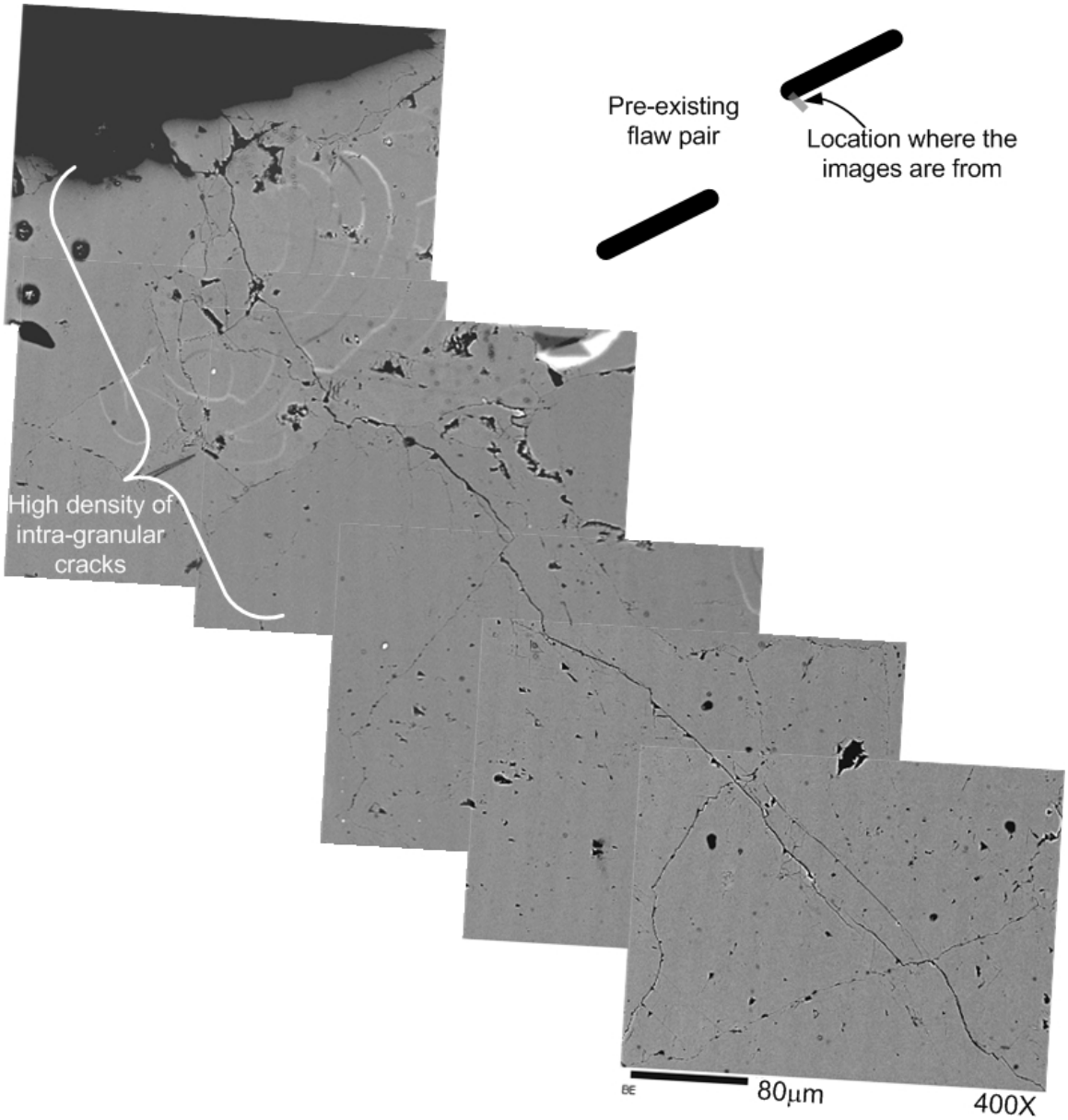

Figure 7.37 – An assemblage of SEM images of the lower face of top flaw of flaw pair DB close to the left flaw tip. A continuous thick line (crack) extends from the flaw face and propagates to the bottom right. (magnification power = 400X)

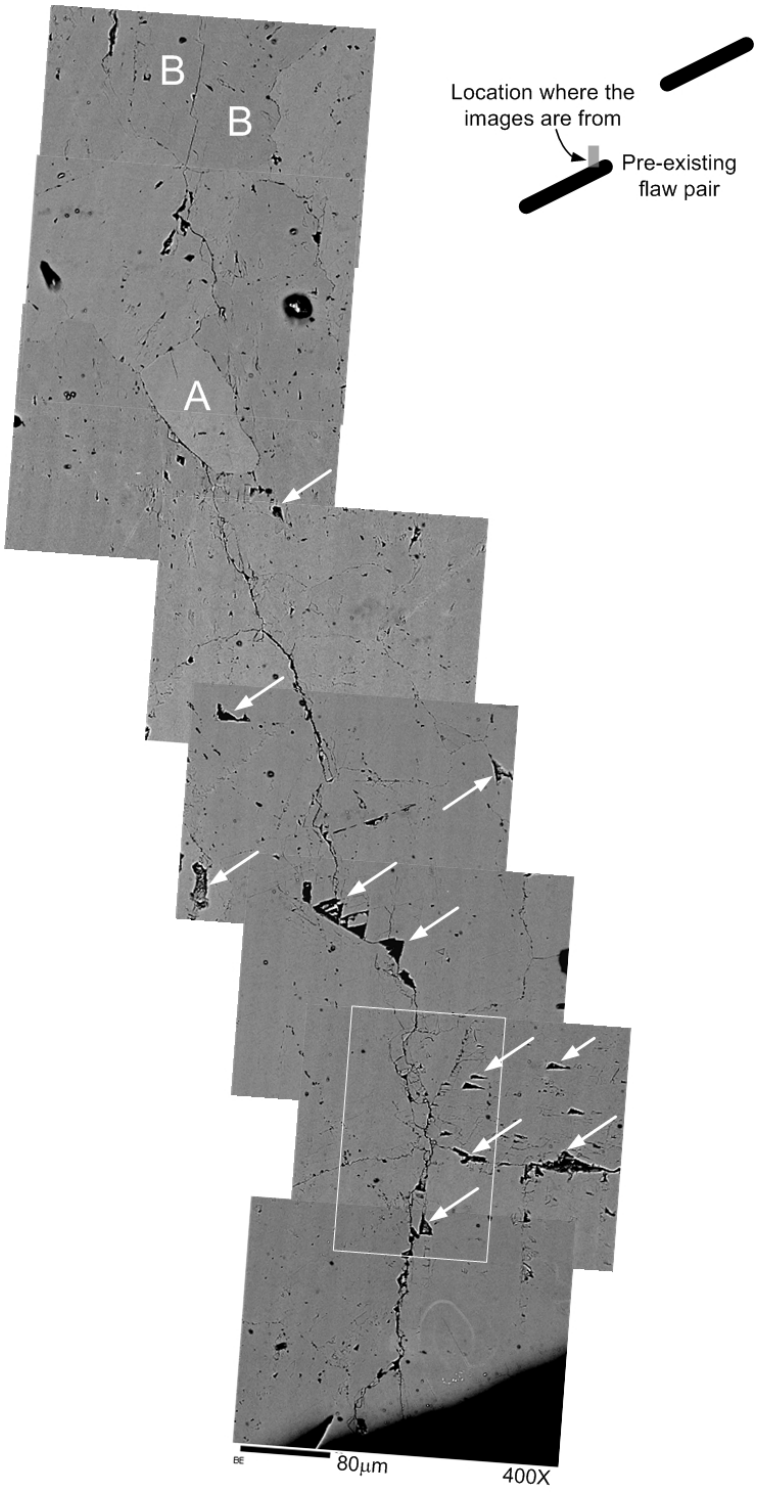

Figure 7.38 – An assemblage of SEM images of the upper face of bottom flaw of DB close to the right tip. (magnification power = 400X) An undulating thick line (crack) extends from the flaw face and propagates to the top. This crack does not propagate through grain A, but bisects grain B into two halves. Some of the spalling features are indicated by arrows. A magnified image of a region enclosed by a rectangle is shown in figure 7.39.

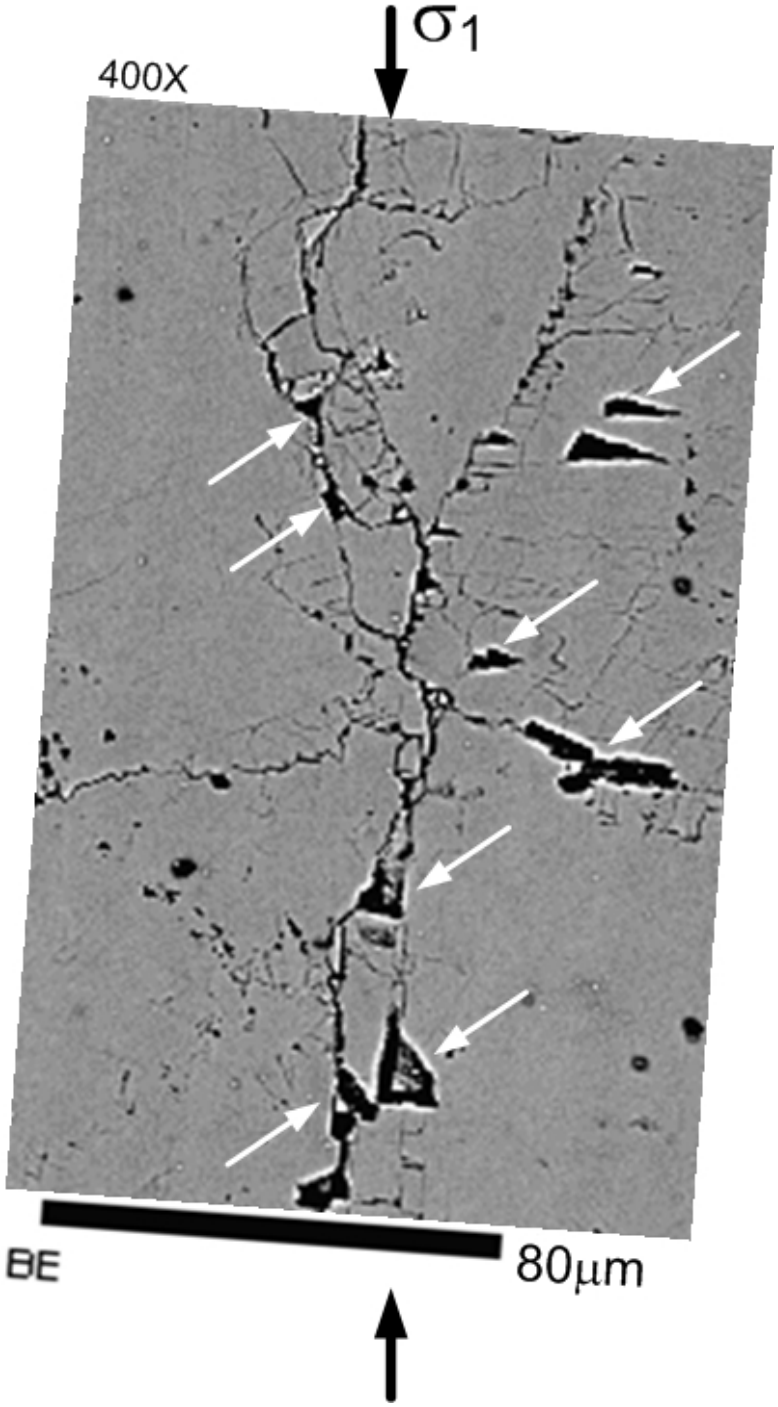

Figure 7.39 – Magnified view of the enclosed region shown in figure 7.38. (magnification power = 400X) The microcracking zone shown here consists of multiple almost vertical thick lines instead of one single dominant crack. In the vicinity of the central fracture zone, the intra-granular cracks which are oriented generally orthogonal to each other form a rectangular grid pattern. Spalling features are indicated by arrows.

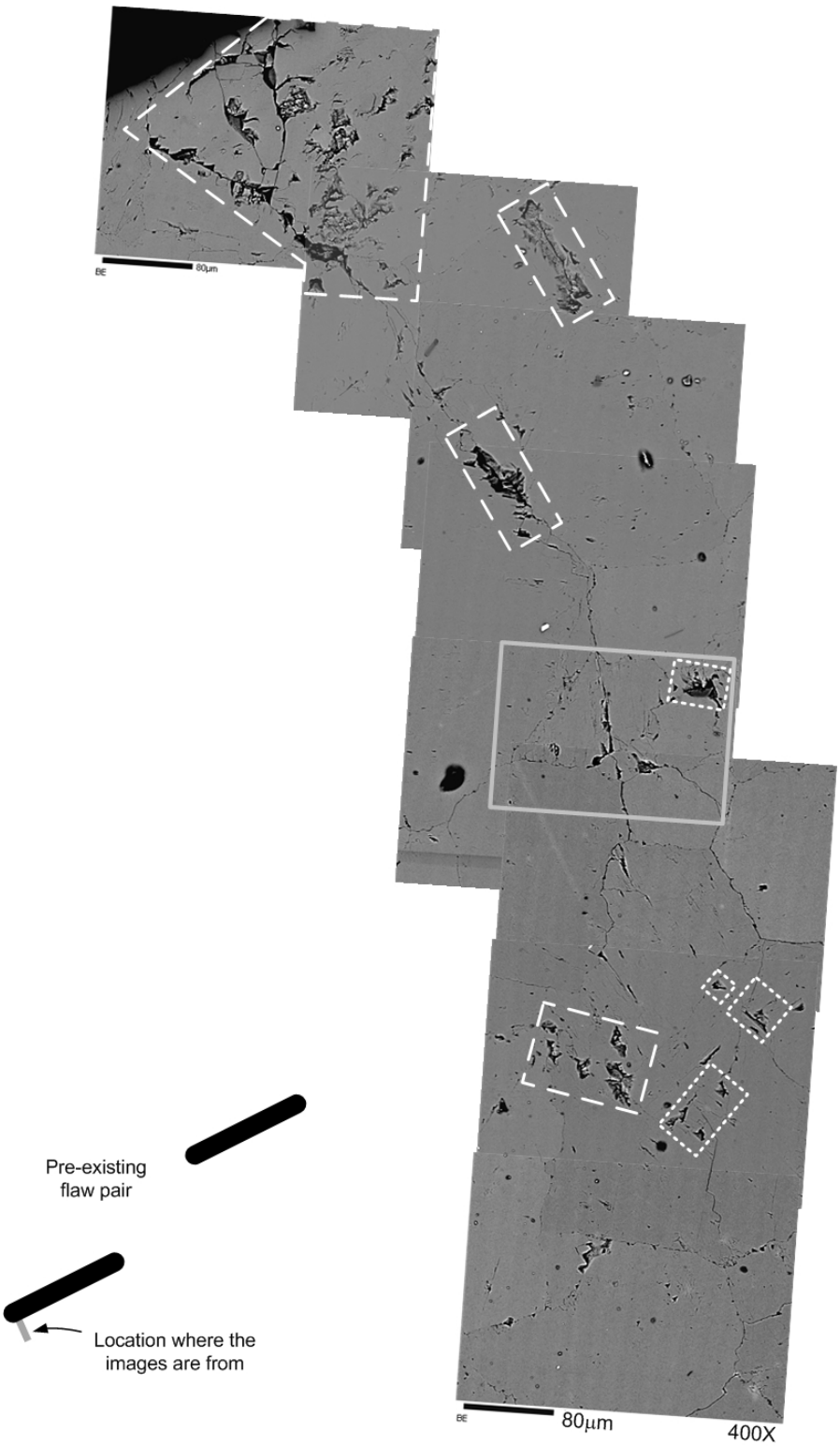

Figure 7.40 – An assemblage of SEM images of the lower face of bottom flaw of flaw pair DB close to the left flaw tip. (magnification power = 400X) A continuous thick line (crack) extends from the flaw face and propagates to the bottom right. Some of the spalling zones are enclosed by dashed-lined rectangles. The magnified view of the region enclosed by a solid-lined rectangle is shown in figure 7.41.

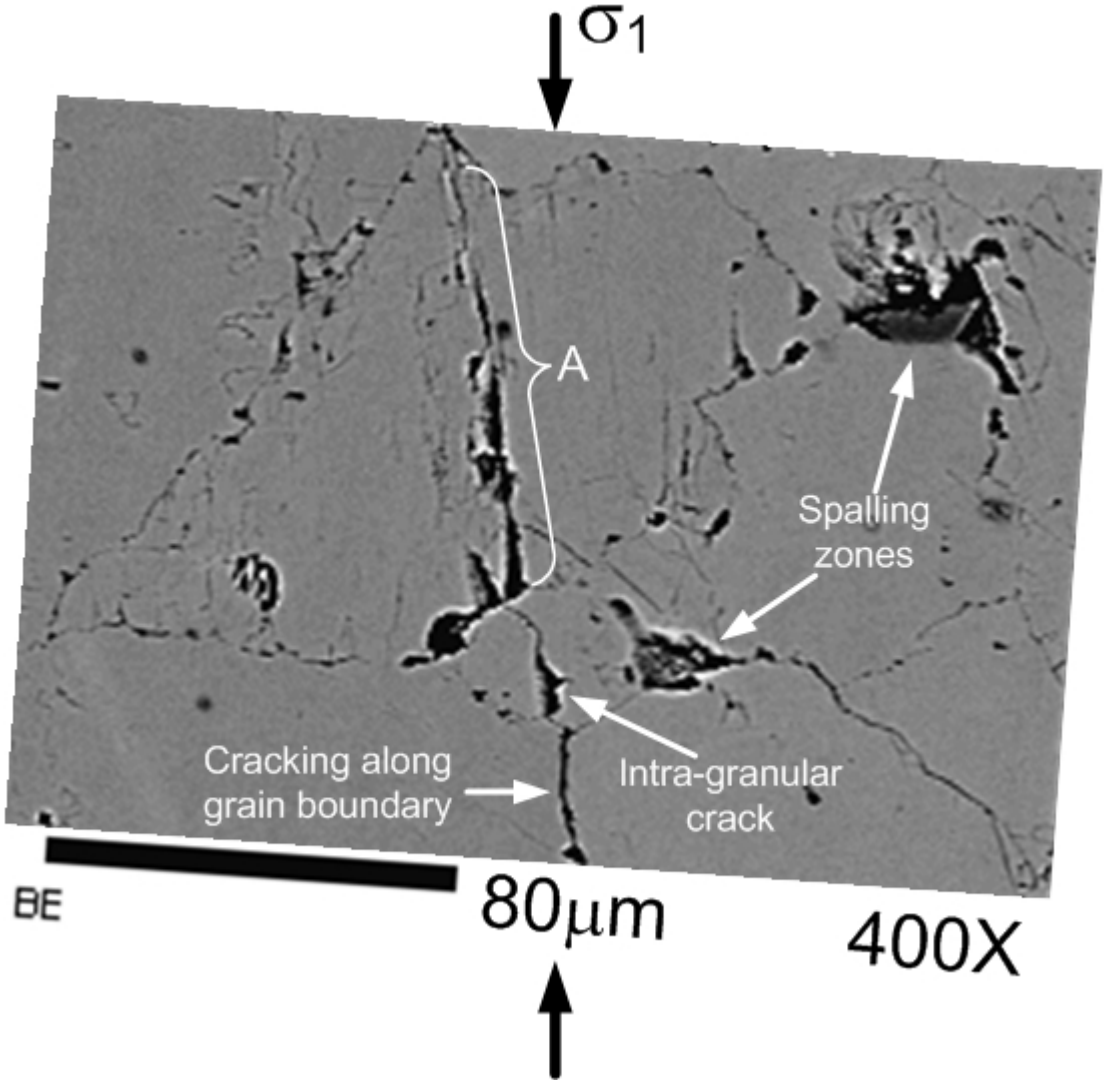

Figure 7.41 – Magnified image of the area enclosed by the solid-lined rectangle shown in figure 7.40. (magnification power = 400X) In the lower half of the figure center, an intra-granular crack propagates through an ellipsoid marble grain. The crack then follows the grain boundary below and propagates downwards. The nature (inter-granular or intra-granular) of the crack marked by 'A' at the top of the previously-mentioned intra-granular crack cannot be determined. Note also the development of multiple parallel short intra-granular cracks beside crack A.

7.3.8 Double flaws subject to 90% failure stress

A view of specimen DC which was loaded uniaxially up to 90% of the failure stress (table 7.1) is shown in figure 7.42. Short thin white patches, which are longer than those observed in specimens DA (50% loading) and DB (70%) are again observed to have developed close to the four flaw tips. Note that the color contrast of the **white** patch developed from the right tip of the bottom flaw against with the background (**pale grey**) is less pronounced than the white patches developed from the other three tips.

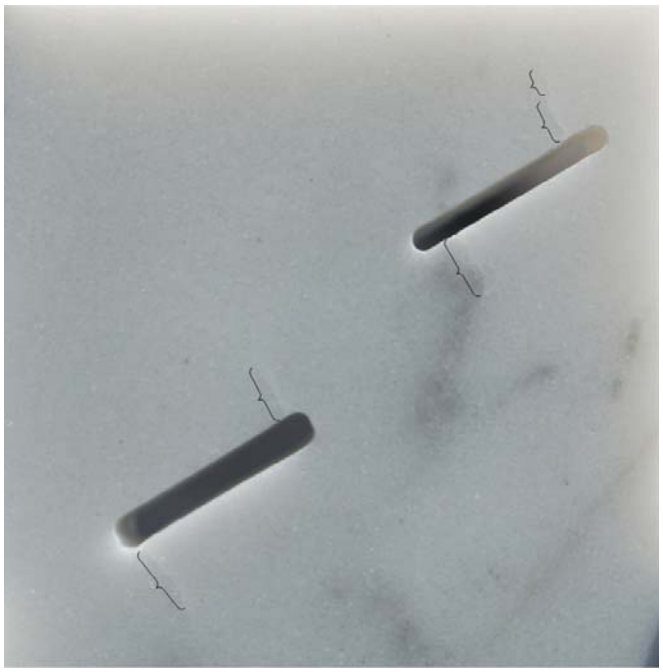

(a)

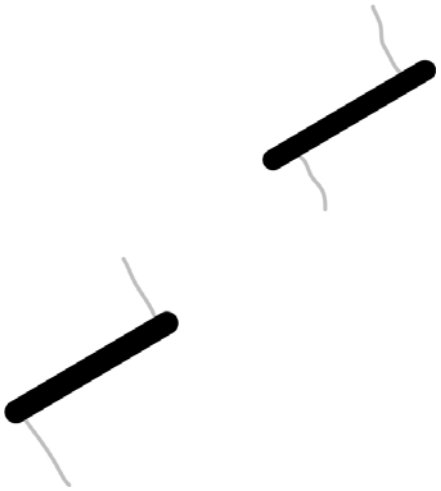

(b)

Figure 7.42 – (a) Marble specimen DC containing a pair of straight open flaws which has been uniaxially loaded up to 90% of the failure stress. Length of the flaw is 0.5" (13mm). Image was taken by a digital camera. Note the development of white patches from the flaws close to the tips. (b) sketch of the flaws and the white patches.

Annular zones around the two flaws are scanned comprehensively for microstructural features (with magnification powers of 100 times and 400 times) which can be associated with the white patches. Along the corresponding trajectories of the white patches, the cracking phenomena observed at the right tip of the bottom flaw are found to be different from those at the other three tips. As will be described in detail below, the microcracking zone at the right tip of the bottom flaw is of a smaller extent than those at the other three tips.

Assemblages of SEM images of the regions around flaw tips are shown in figures 7.43 to 7.46. Due to the difference in the extent of microcracking mentioned above, images around the right tip of the bottom flaw are captured with a magnification power of 400 times (figure 7.43), while the other tip regions are captured with a lower magnification power of 100 times (figures 7.44, 7.45 & 7.46) in order to cover a larger area which is associated with wider microcracking zones. Images captured with these two magnification powers are discussed below separately.

An assemblage of images of the upper face of the bottom flaw close to the right tip is shown in figure 7.43 (magnification power of 400 times). A microcracking zone which consists of a central dominant crack is observed to extend from the flaw face to the top part of the image. Both inter-granular and intra-granular crack segments can be identified along this crack. Some of the grains which are cut through by the central dominant crack are labeled with letters A, B and C in figure 7.43. Grain A is cut into two halves by a curvilinear intra-granular crack which is part of the central dominant crack, while grains B and C are cut into three parts by two almost parallel intra-granular cracks. However, it is not difficult to differentiate that one of the intra-granular cracks (thicker trace) is a segment of the central dominant crack and the other is not. Short intra-granular cracks are commonly found in vicinity of the central crack, especially in the lower part of the microcracking zone adjacent to the flaw face. In addition to the above features, spalling features of length between 20 and 50 μm are commonly found close to the central dominant crack (indicated by arrows).

Since the microcracking characteristics shown in figures 7.44 to 7.46 (magnification power of 100 times) for the other three flaw tip regions is similar, they are collectively discussed below. It is common for all three of them that a relatively wide microcracking zone (high microcrack density) is present close to the flaw face. As the distance from the flaw face increases, the microcrack density decreases and a narrower microcracking zone is observed. In this narrow microcracking zone, an undulating black feature (crack) which consists of both intra-granular and inter-granular crack segments can usually be clearly identified. At an even farther distance away from the flaw, the microcrack density further decreases. Also, the microcracks are no longer clustered together, but are scattered randomly. It is no longer possible to locate a dominant crack. The extents of these zones are marked in figures 7.44 to 7.46 and rough estimates of the lengths of the 'wide' and 'narrow' microcracking zones present along the three white patches are summarized in the following table. Note that placing a boundary between two adjacent zones is very subjective process and the numbers listed below are corrected to the nearest 100 μm.

		Length (μm)	
Location	Figure	Wide microcracking zone	Narrow microcracking zone
Left tip of bottom flaw	7.44	1100	2900
Left tip of top flaw	7.45	900	2900
Right tip of top flaw	7.46	1200	2200

Note : The above lengths are measured normal to the flaw face.

As mentioned at the beginning of this section, the color contrast of the **white** patch developed from the right tip of the bottom flaw against the background (**pale grey**) is less pronounced than the white patches developed from the other three tips. This may be explained by the different extent of the underlying mircocracking zones.

To summarize, the white patches developed close to the flaw tips observed in hand specimen DC which has been loaded up to 90% of the failure stress can be correlated with zones of microcracks. The general microcracking features are similar to those observed in specimen DB (70% loading), i.e., each microcracking zone consists of a central dominant undulating crack and multiple much shorter orthogonal intra-granular cracks beside the dominant crack. The density of intra-granular microcracks and spalling features, which is highest beside the dominant crack and adjacent to the flaw face, drops off rapidly with distance from this central crack and the flaw face.

However, in the region close to the flaw face in specimen DC, the microcracking zone is wider and it consists of several thick cracks instead of a single dominant crack (observed in three out of four white patches in DC). The overall microcrack density in the microcracking zones in DC is also higher than that in DB. In addition, the white patches (hand specimen) and microcracking zone (SEM images) in DC are longer than those in DB.

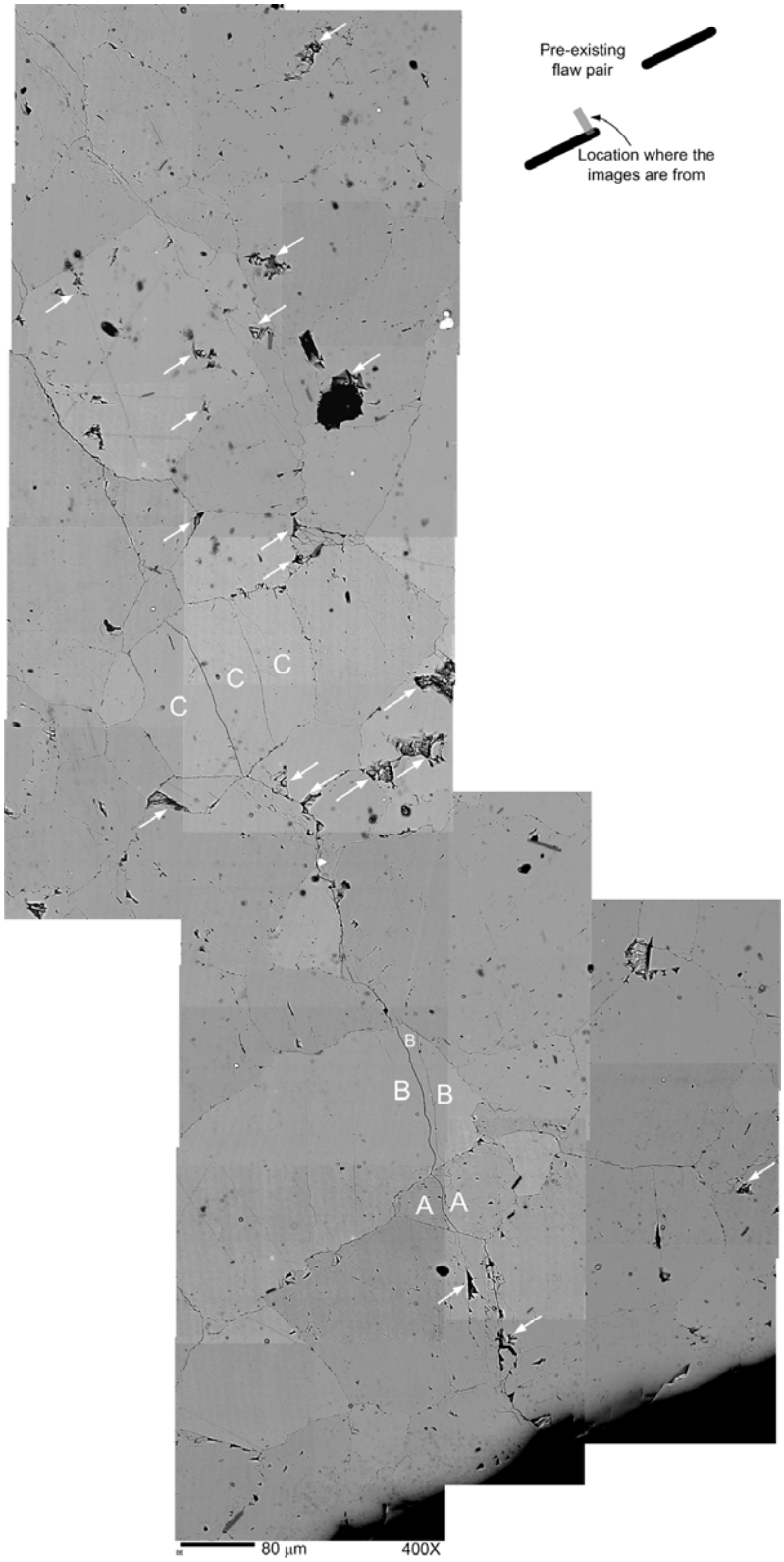

Figure 7.43 – An assemblage of SEM images of the upper face of bottom flaw of flaw pair DC close to the right flaw tip. Spalling features are indicated by white arrows. Some of the marble grains (A, B & C) are cut through by intra-granular cracks. (magnification power = 400 X)

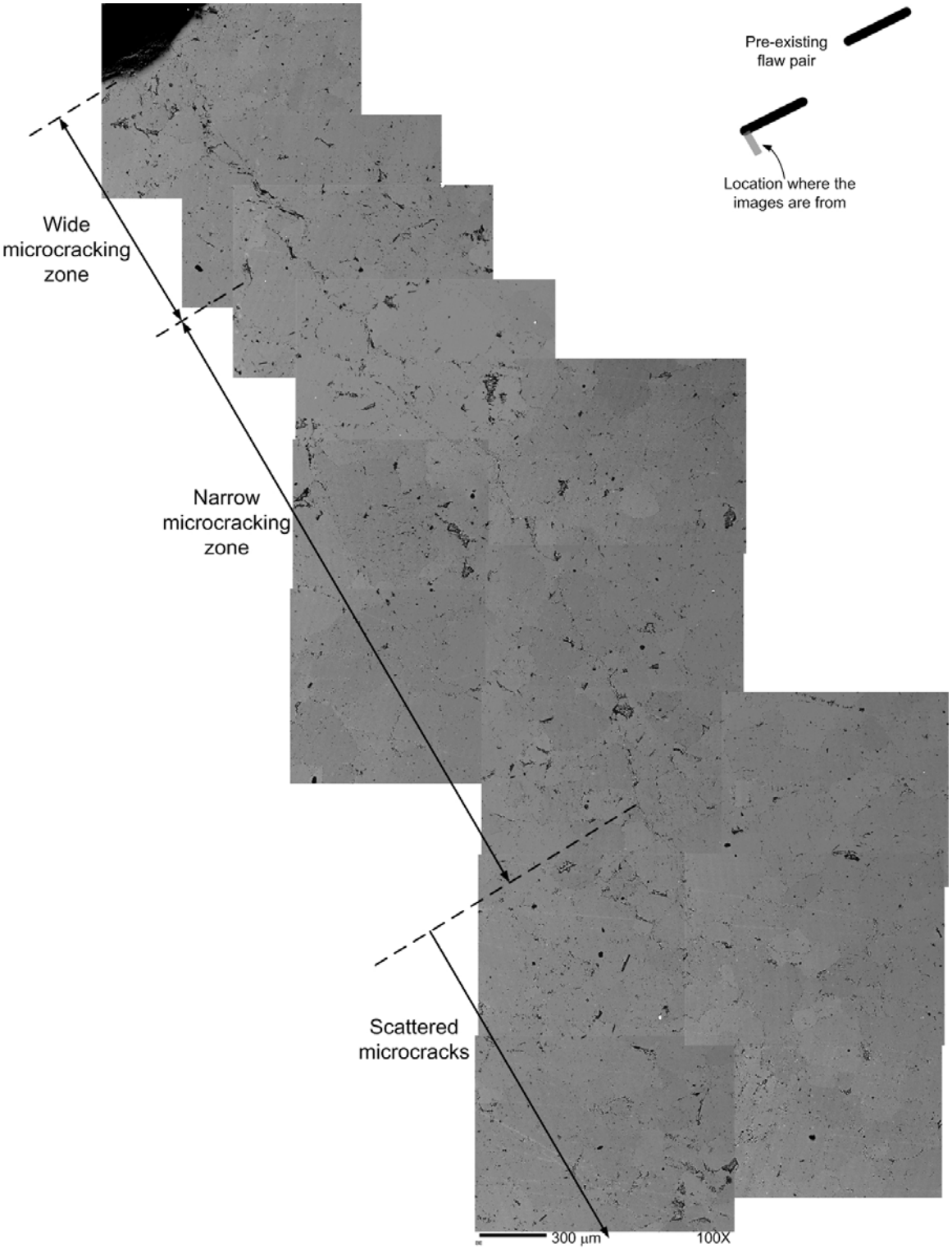

Figure 7.44 – An assemblage of SEM images of the lower face of bottom flaw of flaw pair DC close to the left flaw tip. A wider microcracking zone is located close to the flaw face. A narrower microcracking zone is located below it. At a farther distance away from the flaw, microcracks are scattered randomly. (magnification power = 100 X)

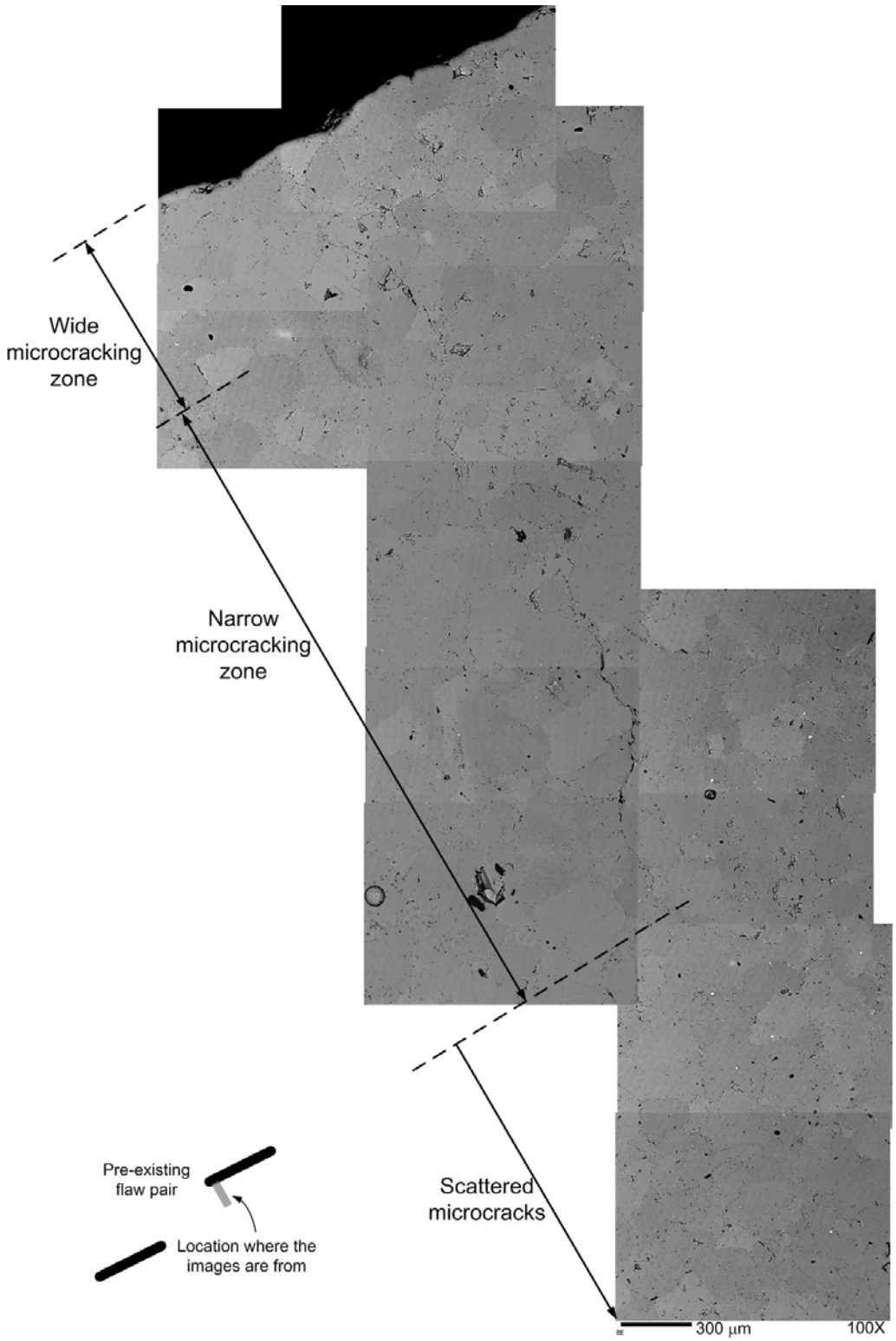

Figure 7.45 – An assemblage of SEM images of the lower face of top flaw of flaw pair DC close to the left flaw tip. A wider microcracking zone is located close to the flaw face. A narrower microcracking zone is located below it. At a farther distance away from the flaw, microcracks are scattered randomly. (magnification power = 100 X)

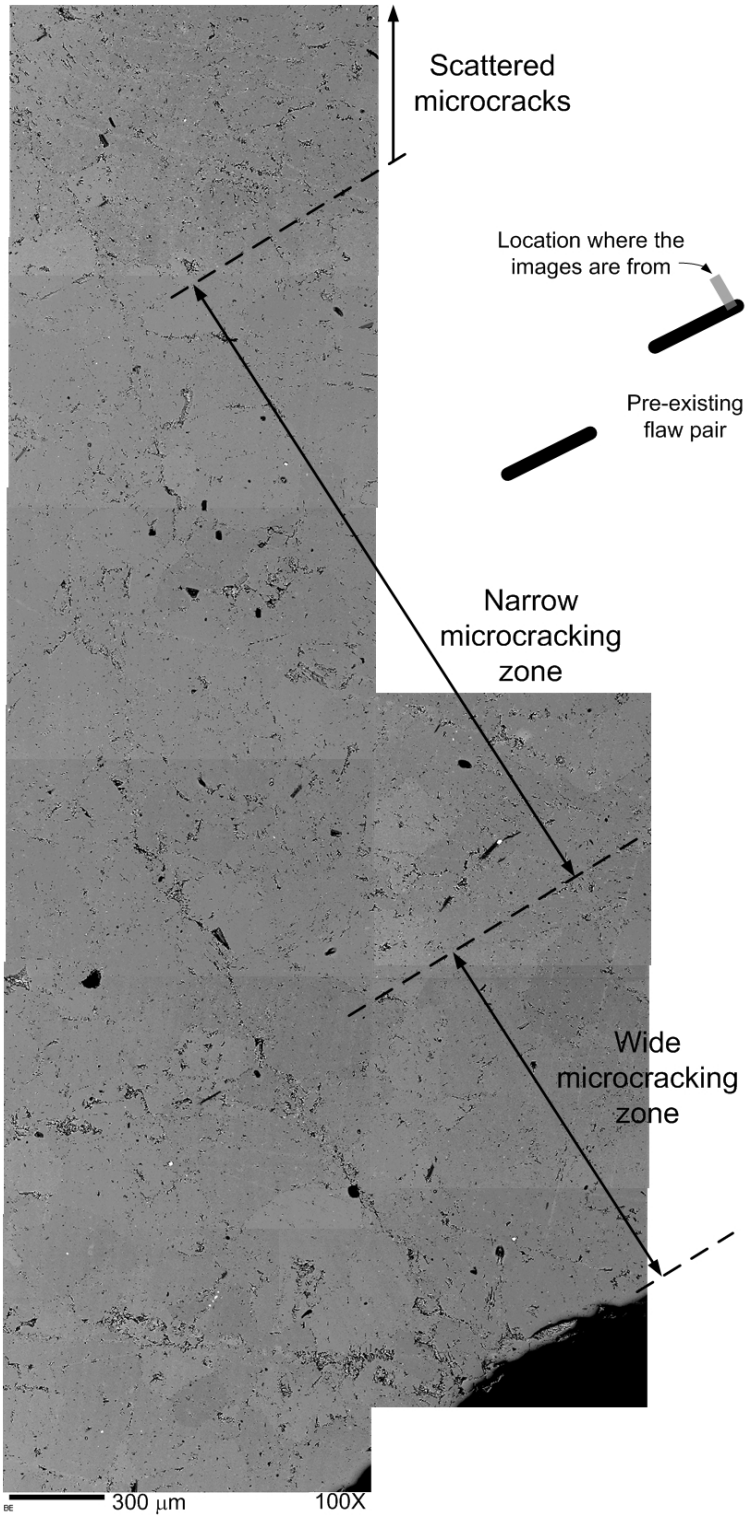

Figure 7.46 – An assemblage of SEM images of the upper face of top flaw of flaw pair DC close to the right flaw tip. A wider microcracking zone is located close to the flaw face. A narrower microcracking zone is located above it. At a farther distance away from the flaw, microcracks are scattered randomly. (magnification power = 100 X)

7.3.9 Coplanar flaws subject to 94% failure stress

A view of specimen DD of coplanar flaw geometry 4a-60-0 which was loaded uniaxially up to 94% of the failure stress (table 7.1) is shown in figure 7.47. Multiple white patches are observed to have developed close to the flaw tips and in the central bridging region. Note that the flaw geometry of DD is different from DA, DB and DC.

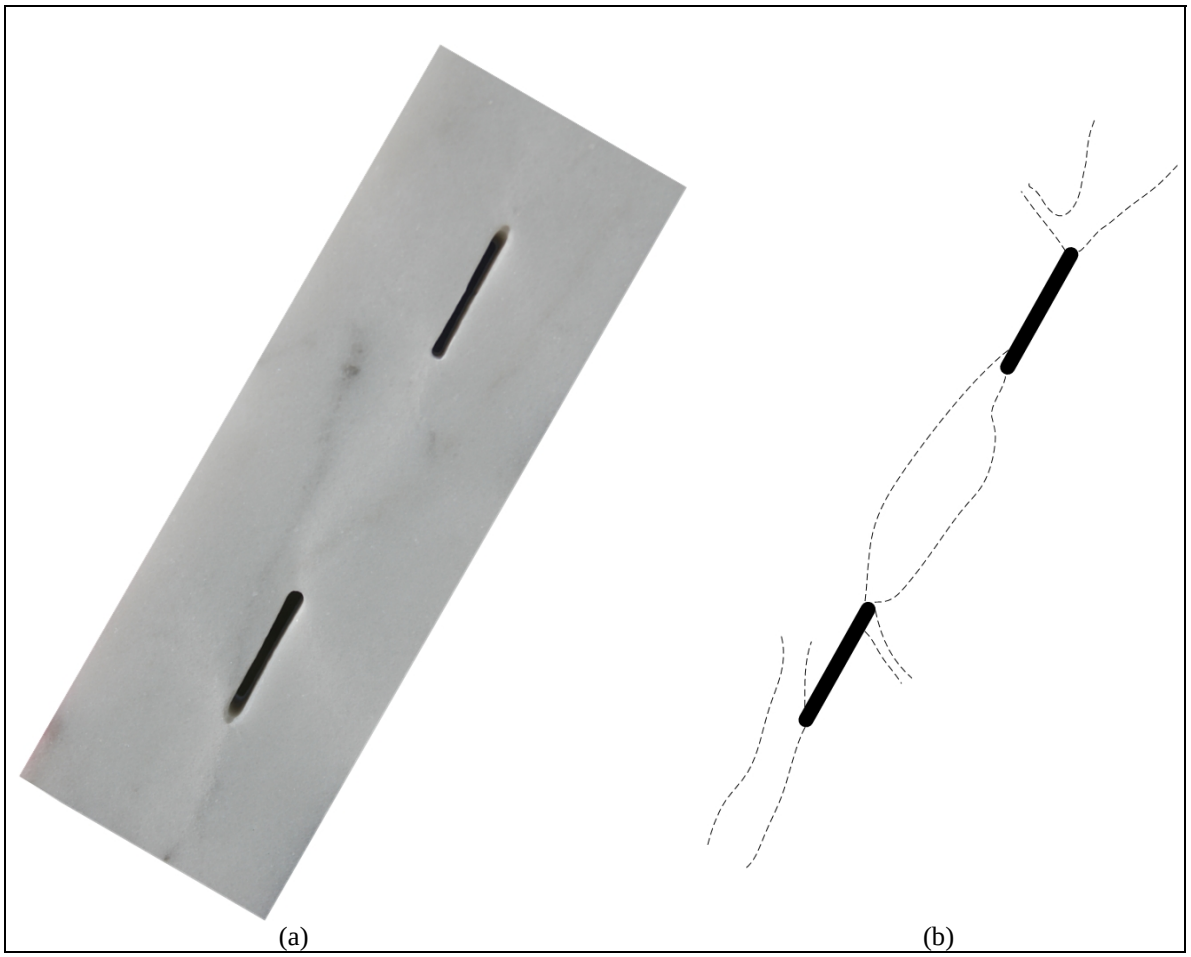

Figure 7.47 – (a) Marble specimen DD containing a pair of coplanar straight open flaws which has been uniaxially loaded up to 94% of the failure stress. Length of the flaw is 0.5" (13mm). Image was taken by a digital camera. Note the extensive development of white patches from the flaws. (b) Sketch of the flaws and the white patches. The extent of white patches is delineated by dotted lines.

Assemblages of SEM images of the regions around the flaw tips and the bridging region between the two inner flaw tips are shown in figures 7.48 to 7.50. Although the images are captured with a low magnification power (40 times) and fine details of grain boundaries could not be observed, it is still possible to identify several intensely fractured zones which are around 600 to 1000 μm long (indicated by white arrows in figures 7.48 – 7.50) developed close to the inner flaw tips. These fractured zones are however not found in the middle part of the bridging region (figure 7.50). Microscopic details of these fractured zones are examined and discussed below based on other SEM images captured with a higher magnification power.

Magnified images of these intensely fractured zones are shown in figures 7.51 and 7.53, respectively corresponding to the right tip of the bottom flaw and the left tip of the top flaw. These zones form a right-stepping en echelon pattern and trend almost parallel to the vertical loading direction. Careful examination reveals that each of these microcracking zones consists of a central dominant crack. Some segments of this crack are observed to preferentially follow grain boundaries (inter-granular cracks) and some segments cut through grains (intra-granular cracks). The presence of individual black patches along this central dominant crack makes these microcracking zones conspicuous. From their morphology, these black patches are found to be depressions/pits probably formed by local spalling events. With the detachment of the surface spalling materials, the underlying pits are then exposed. Refer to figures 7.52a and b for further details of these spalling features. Although some of these black patches are found within the marble grains (intra-granular), most of them follow existing grain boundaries or junctions of grain boundaries. The density of microcracks (both inter-granular and intra-granular) is very high in the vicinity of the central dominant cracks and it drops down rapidly as the distance from the central cracks decreases.

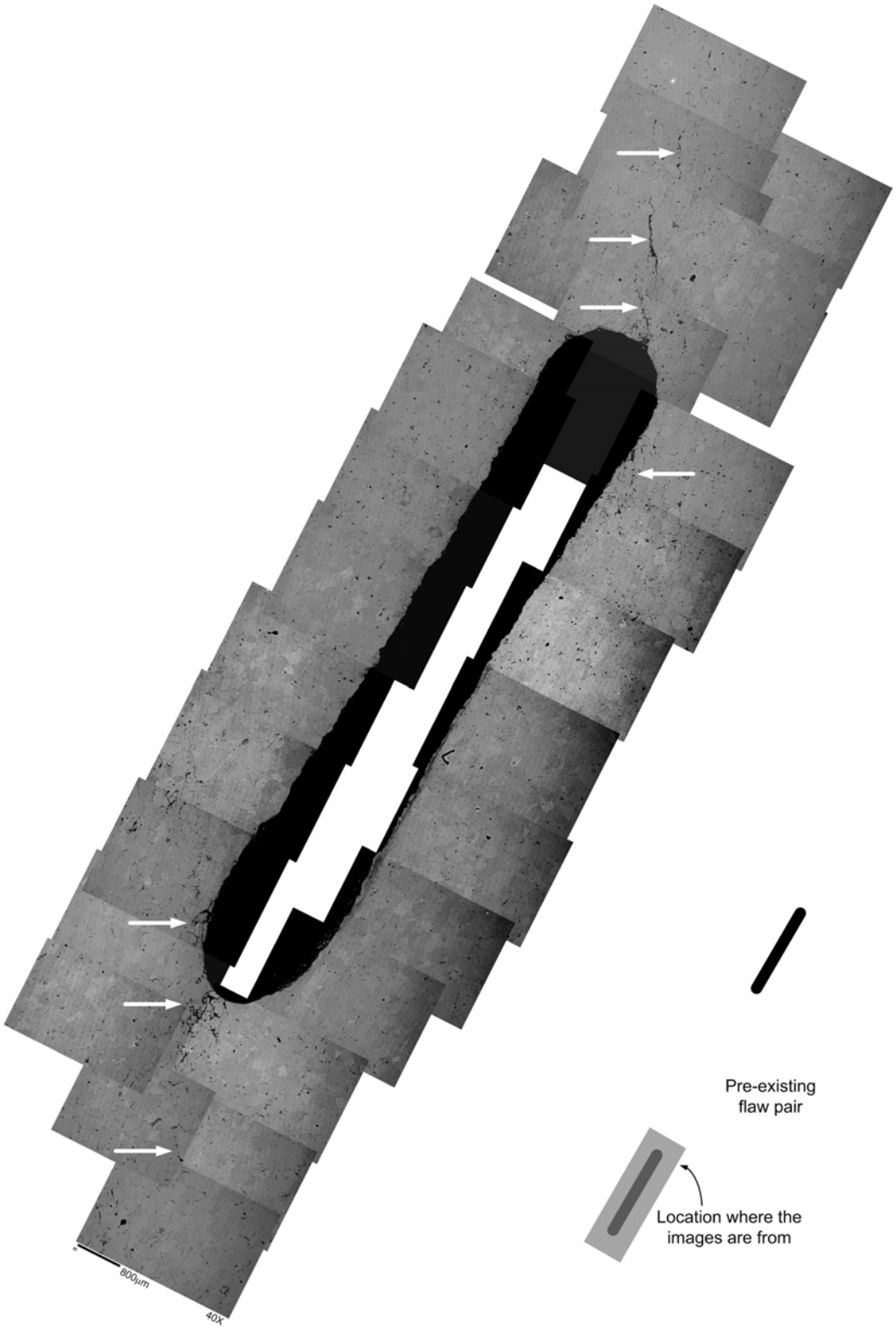

Figure 7.48 – An assemblage of SEM images of the bottom flaw of flaw pair DD. Microcracking zones are indicated by white arrows. The length of the scale bar at the bottom of the image is 800 μm. (magnification power = 40 X)

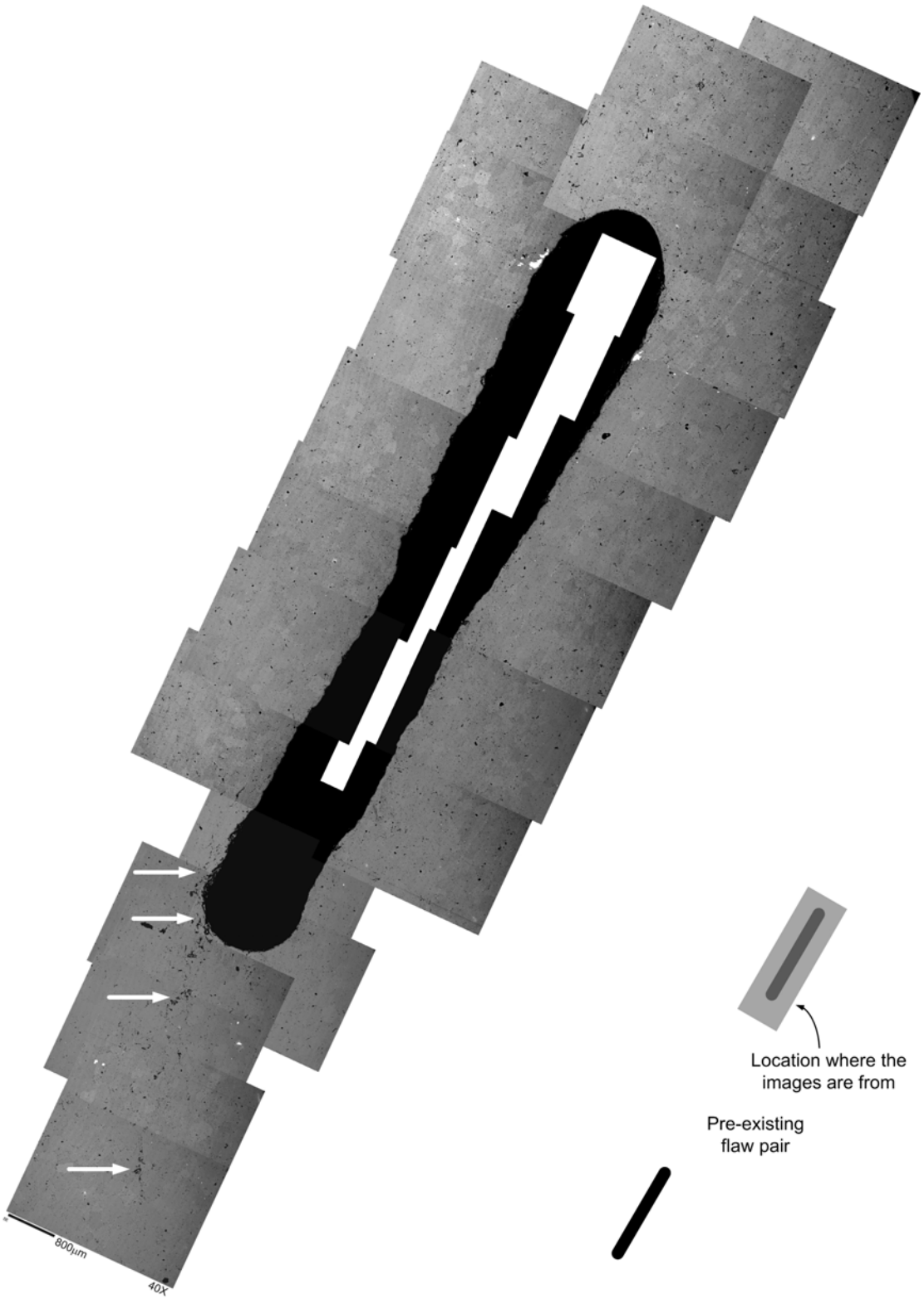

Figure 7.49 – An assemblage of SEM images of the top flaw of flaw pair DD. Microcracking zones are indicated by white arrows. The length of the scale bar at the bottom of the image is 800 μm. (magnification power = 40 X)

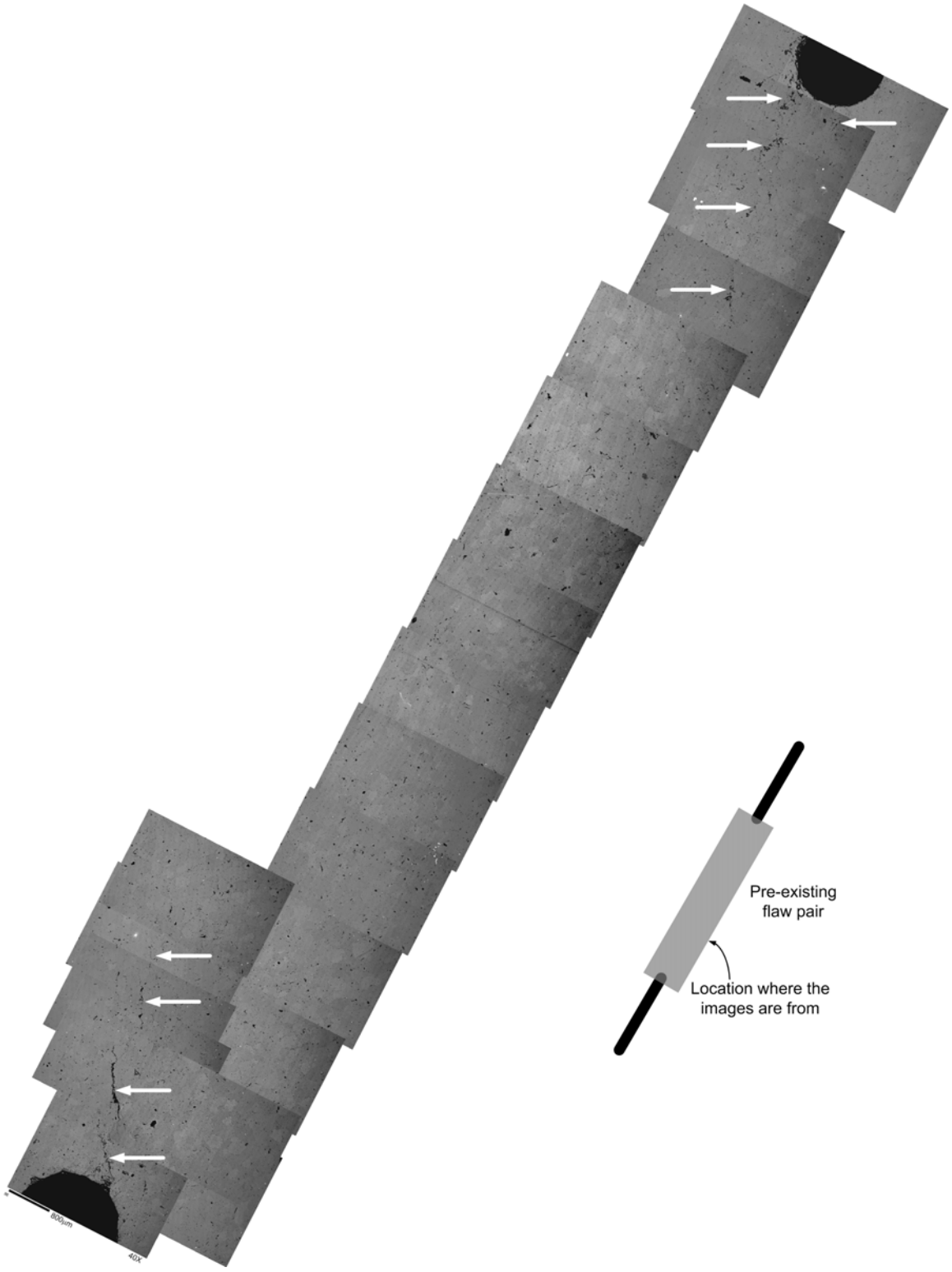

Figure 7.50 – An assemblage of SEM images of the bridging region between inner flaw tips of flaw pair DD. Microcracking zones are indicated by white arrows. The length of the scale bar at the bottom of the image is 800 μm. (magnification power = 40 X)

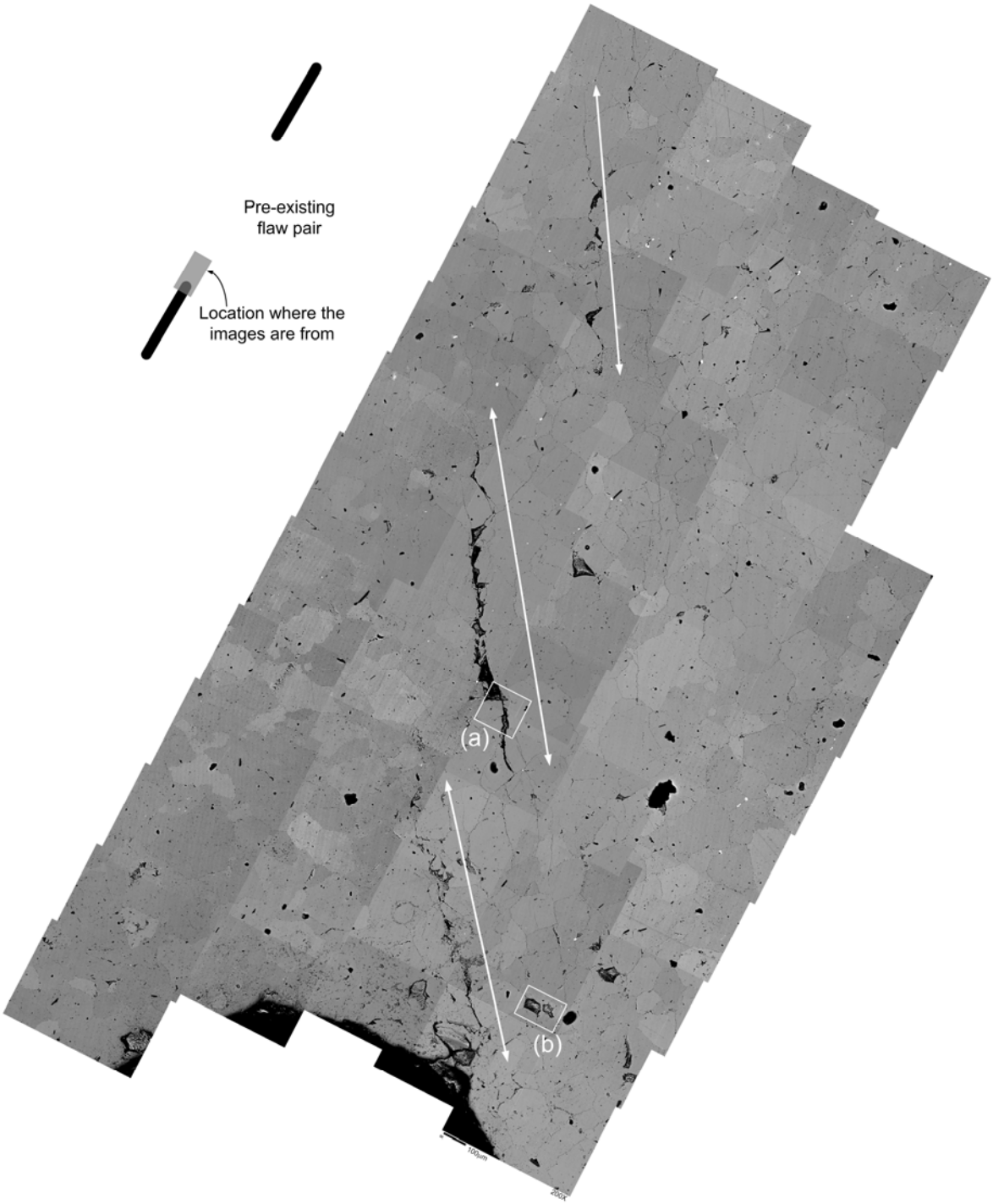

Figure 7.51 – An assemblage of SEM images of the area around the right flaw tip of the bottom flaw. Magnified images of the two enclosed areas are shown in figure 7.52. The intensely fractured zones, whose traces are indicated by arrows, trend almost parallel to the loading direction. The length of the scale bar at the bottom of the image is 100 μm. Note that the loading direction is vertical. (magnification power = 200 X)

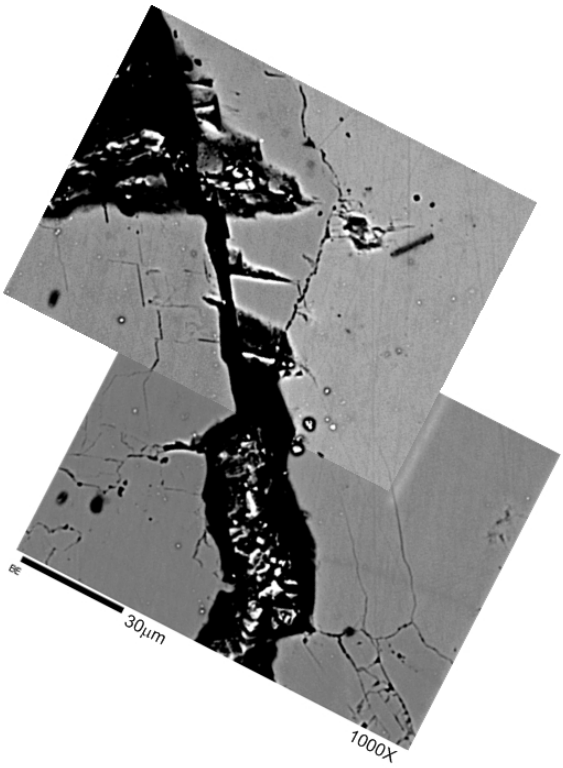

(a)

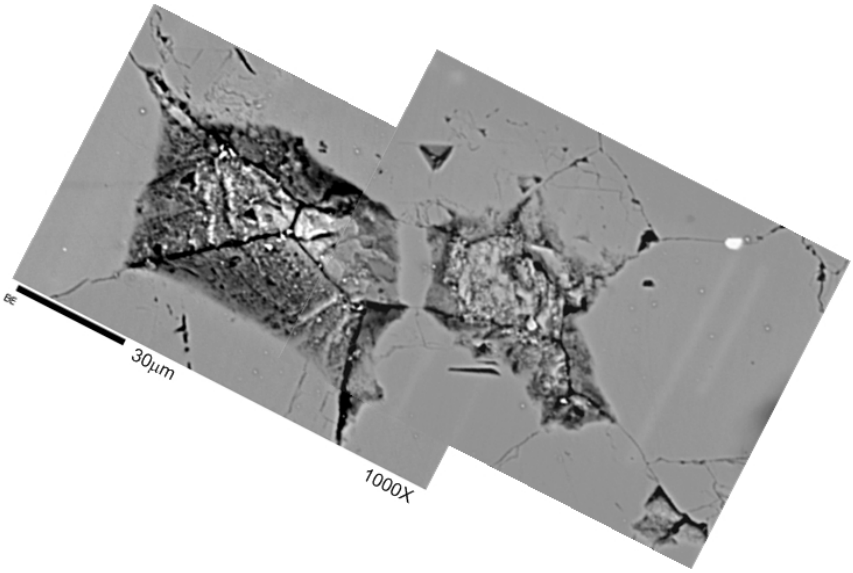

(b)

Figure 7.52 – Magnified images corresponding to the two enclosed areas (a) and (b) shown in figure 7.51. In image (a), spalling occurs along the central dominant crack. Note also the development of multiple short intra-granular cracks in the surrounding area. Image (b) shows a magnified image of two adjacent spalling zones, which contain multiple Y-junctions formed by intersection of neighboring grains boundaries. (magnification power = 1000 X)

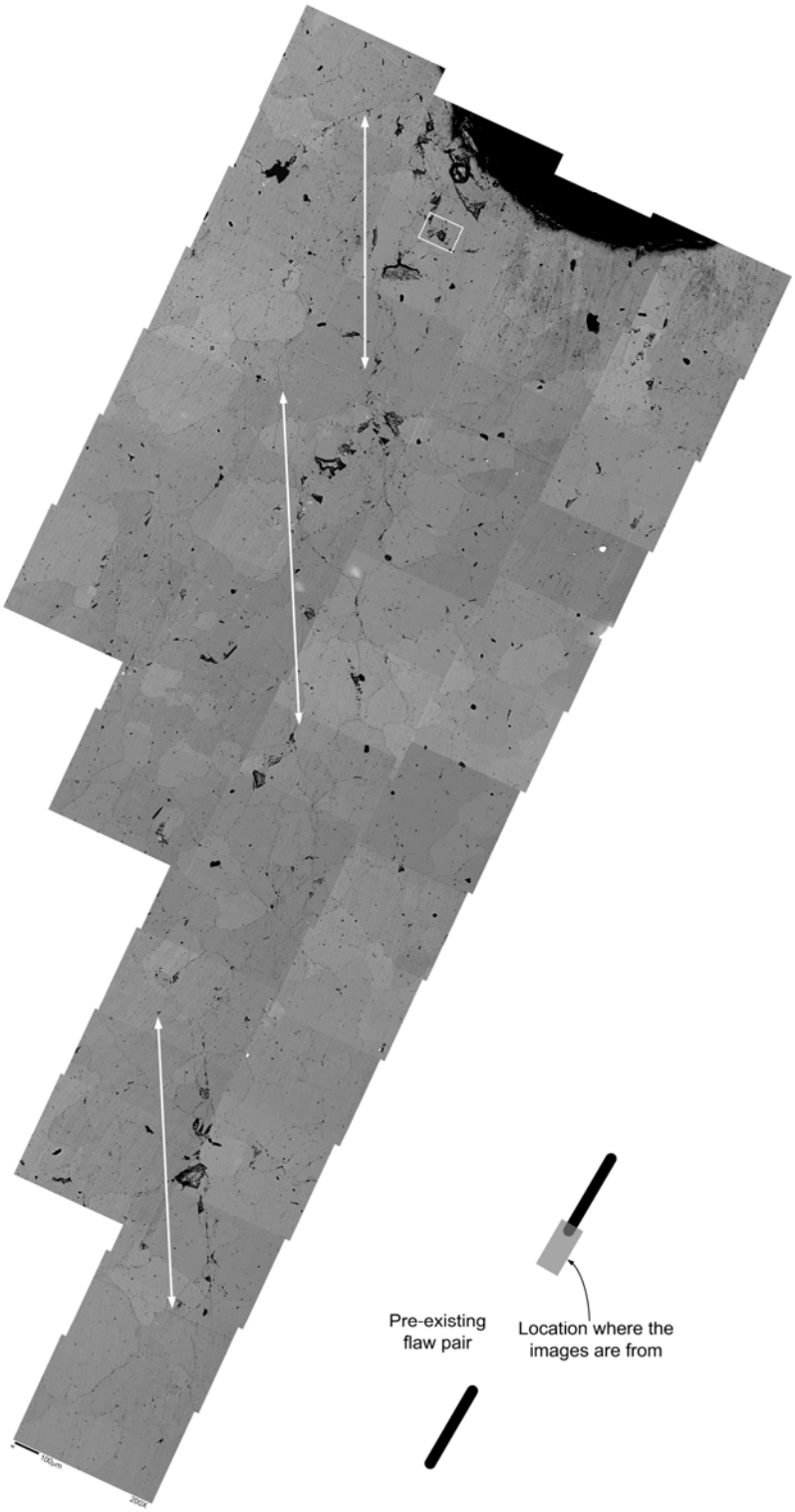

Figure 7.53 – An assemblage of SEM images of the area around the left flaw tip of the top flaw. The intensely fractured zones, whose traces are indicated by arrows, trend almost parallel to the loading direction. The length of the scale bar at the bottom of the image is 100 μm. Note that the loading direction is vertical. (magnification power = 200 X)

As shown in figure 7.47a, white patches are not only found close to the two inner flaw tips in the bridging region, but also around the outer flaw tips. Magnified images around these two regions are shown in figure 7.54 to 7.56.

Close to the left tip of the bottom flaw, an intensely fractured zone, which consists of abundant cracks (intra-granular and inter-granular) and wide spalling zones, is identified to be present within 300 μm measured normal to the flaw face (figure 7.54). Outside this zone, spalling features of size between 10 and 100 μm are scattered randomly along grain boundaries or at junctions of grain boundaries (indicated by white arrows). A small number of the spalling features are also found within the marble grains (intra-granular). Most of the traces of intra-granular and inter-granular cracks are differentiable due to a relatively good color contrast among the marble grains. They are illustrated in the magnified images of two marble grains shown in figures 7.55a and b. Grain A is rimmed by inter-granular cracks along its grain boundary and it is free of any observable intra-granular cracks. Observe also that intra-granular cracks develop in all grains adjacent to grain A. In figure 7.55b, grain B is cut into five parts by multiple vertical intra-granular cracks which are almost vertical parallel to each other.

Figure 7.56 shows an assemblage of SEM images around the right tip of the top flaw. The amount of microcracking in vicinity of the flaw tip shown here is much less than that for the left tip of the bottom flaw as shown in figure 7.54. Similarly, spalling features of size between 10 and 100 μm are scattered randomly (indicated by white arrows in figure 7.56). As shown in the further magnified images on the left in figure 7.56, the spalling features can be found along the grain boundaries (inter-granular) and within the grains (intra-granular). Development of intra-granular and inter-granular cracks is also common within that tip region.

To summarize, white patches are observed in the hand specimen, but these white patches are correlated with different microcracking patters around the inner flaw tips as compared to the outer flaw tips. In the bridging region close to the inner flaw tips, multiple right-stepping en echelon microcracking zones trending almost parallel to the vertical loading

direction are observed. Each of them consists of a central dominant crack with widespread development of spalling along it. Microcracks (both inter-granular and intra-granular) are also found within the bridging region, but the density the microcrack density drops down rapidly as the distance from the microcracking zone decreases. Around the outer flaw tips, there is not a dominant microcracking feature similar to those found close to the inner flaw tips. The region is simply scattered with microcracks (both inter-granular and intra-granular) and spalling features.

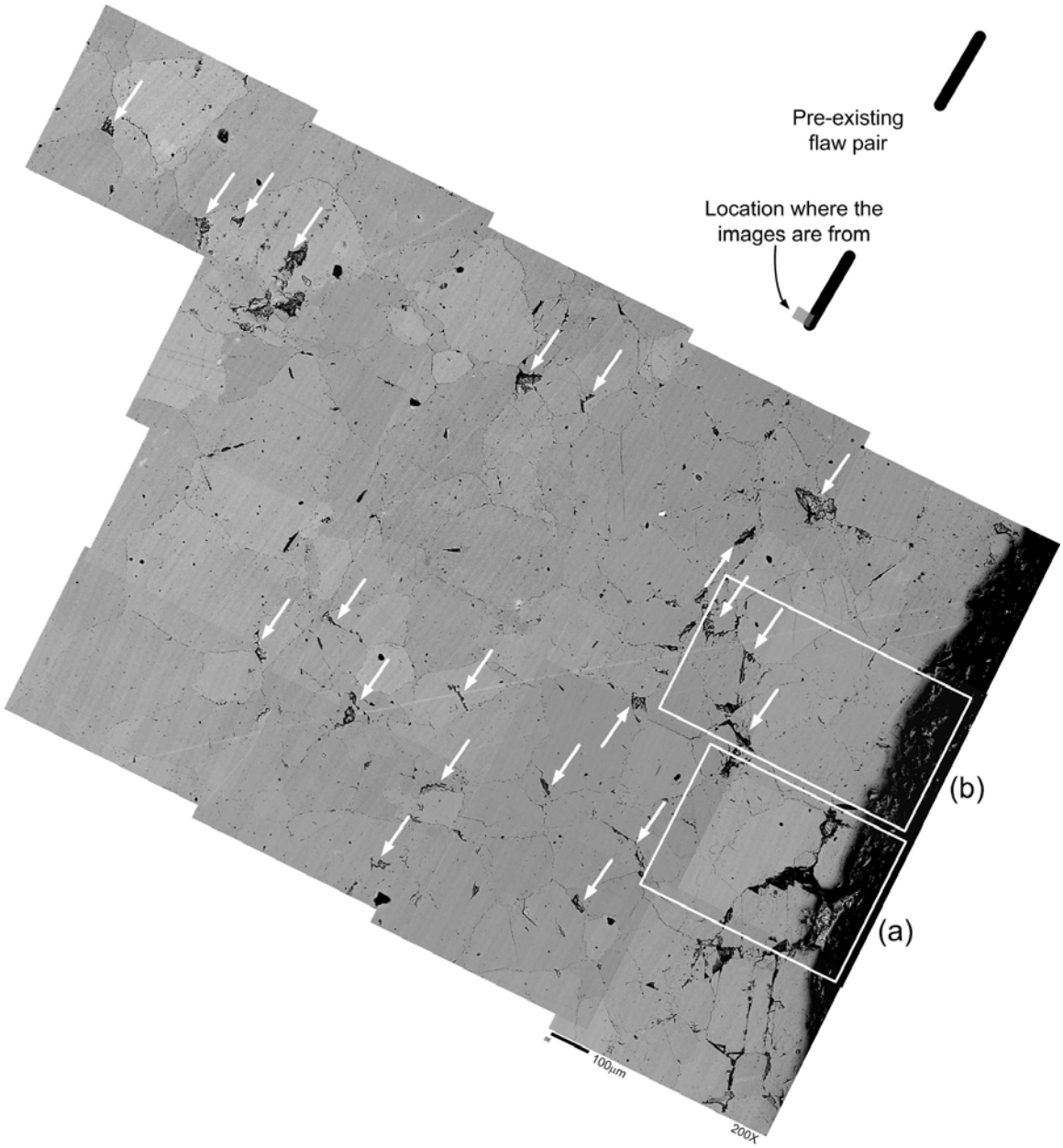

Figure 7.54 – An assemblage of SEM images of the area around the left flaw tip of the bottom flaw. (magnification power = 200 X) Spalling features are indicated by white arrows. Note the intensely fractured zone close to the flaw face (bottom right corner). Magnified images of the two enclosed areas are shown in figure 7.55.

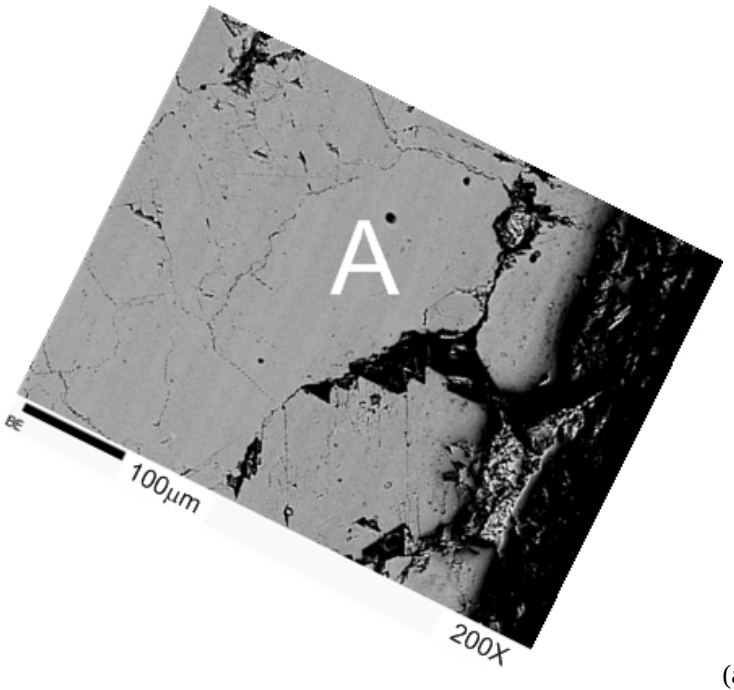

(a)

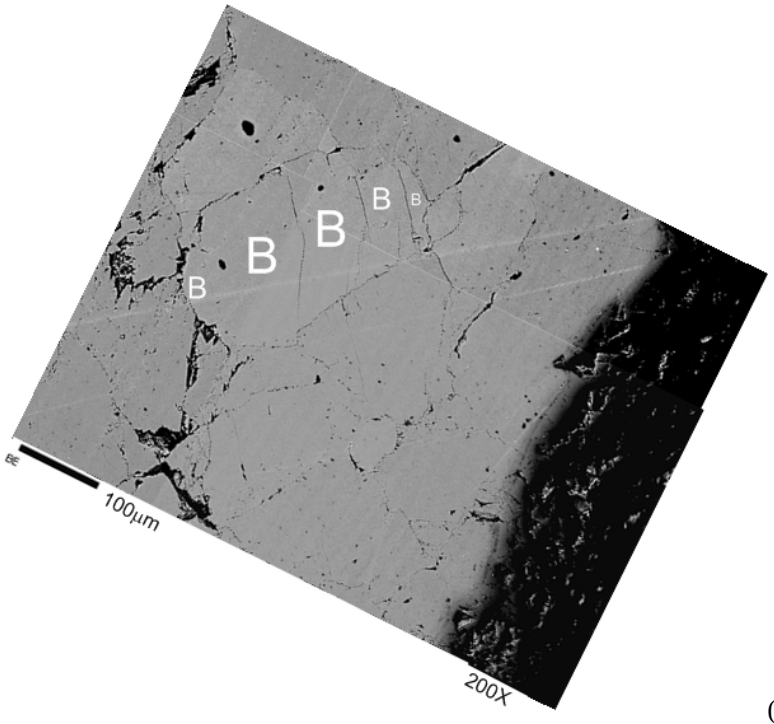

(b)

Figure 7.55 (a) – Magnified image of the enclosed region (a) shown in figure 7.54. (magnification power = 200 X) Dark spalling features are abundant adjacent to the flaw face. Grain A is free of any observable intra-granular cracks, while intra-granular cracks develop in all grains adjacent to grain A. (b) – Magnified image of the enclosed region (b) shown in figure 7.54. Grain B is cut into five parts by almost vertical intra-granular cracks which are parallel to each other.

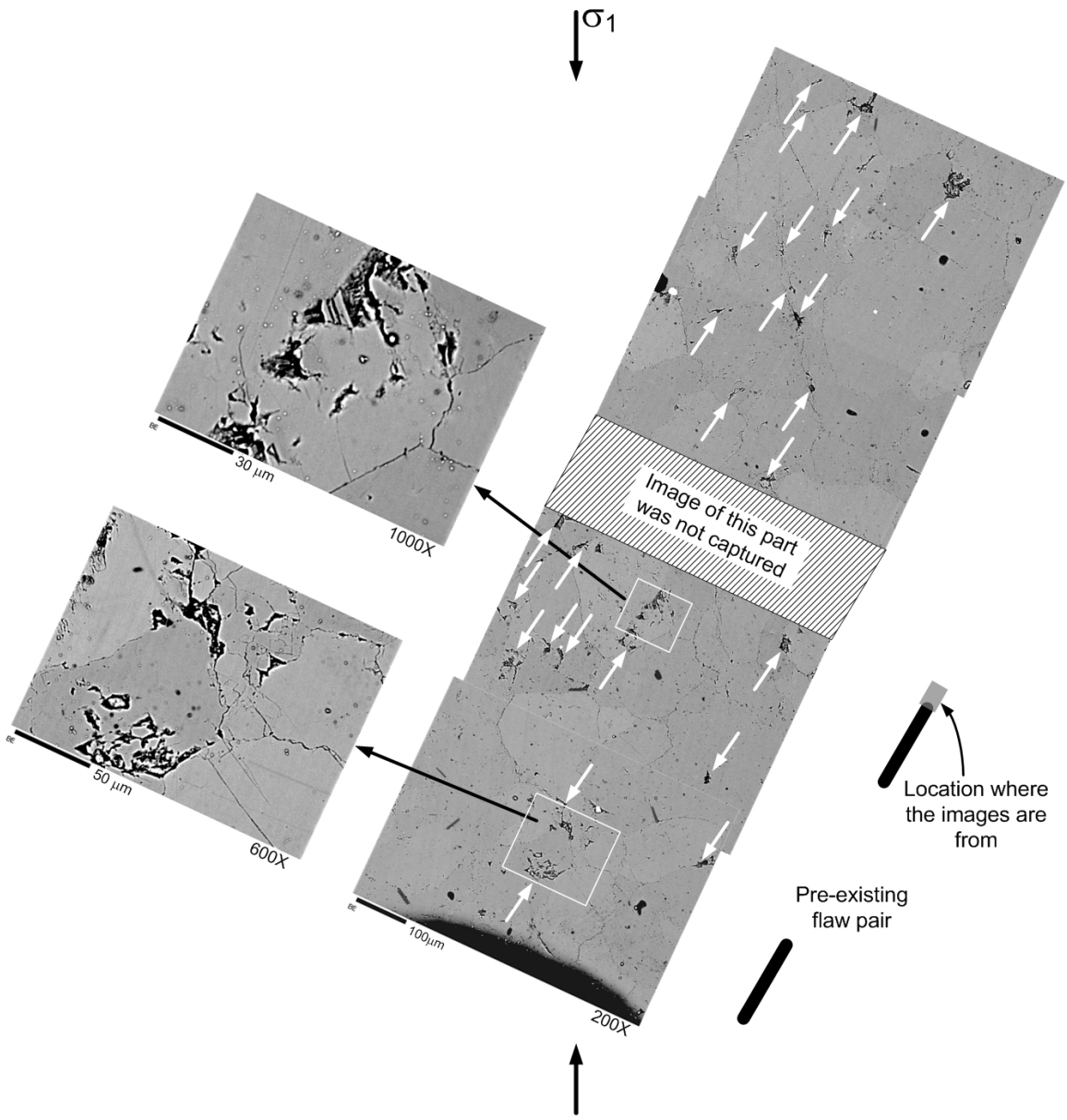

Figure 7.56 – An assemblage of SEM images of the area around the right flaw tip of the top flaw. Spalling features are indicated by white arrows. In the magnified images on the left, the spalling features are found to be located along the grain boundaries (inter-granular) and within the grains (intra-granular). Scale bars and magnification powers are labeled at the bottom edges of individual images.

7.4 Discussion

7.4.1 Introduction

In the previous sections, the microstructural characteristics of different flaw geometries subject to varying load levels are systematically analyzed based on study of SEM images. Recall that the objective of the SEM imaging study is to correlate the white patches observed in the hand specimens (laboratory-tested specimens) with the underlying microstructural features. More specifically, the objective is the identification and generalization of the progressive microstructural changes during the evolution of white patches prior to the occurrence of any cracking events observable in the high speed camera and camcorder recordings along these white patches. The present SEM study reveals that regions of increased microcrack density, which can be regarded as processes zones, develop prior to the subsequent formation of macroscopic cracks. This section begins by summarizing the different microstructural features of the white patches identified with the SEM imaging technique. It is then followed by a discussion of the microstructural evolution of white patches which leads to the eventual formation of tensile wing cracks and coalescence shear cracks.

7.4.2 General microcracking features

White patches, which are free of any observable cracks observed in the high speed camera and camcorder recordings, are examined by the SEM imaging technique. Analysis of the SEM images suggests that microcracks of different types (inter-granular cracks, intra-granular cracks and spalling features) and amount are present within the white patches (see the schematic sketch in figure 7.5b). SEM images of some typical examples are reproduced in figure 7.57 and summarized below.

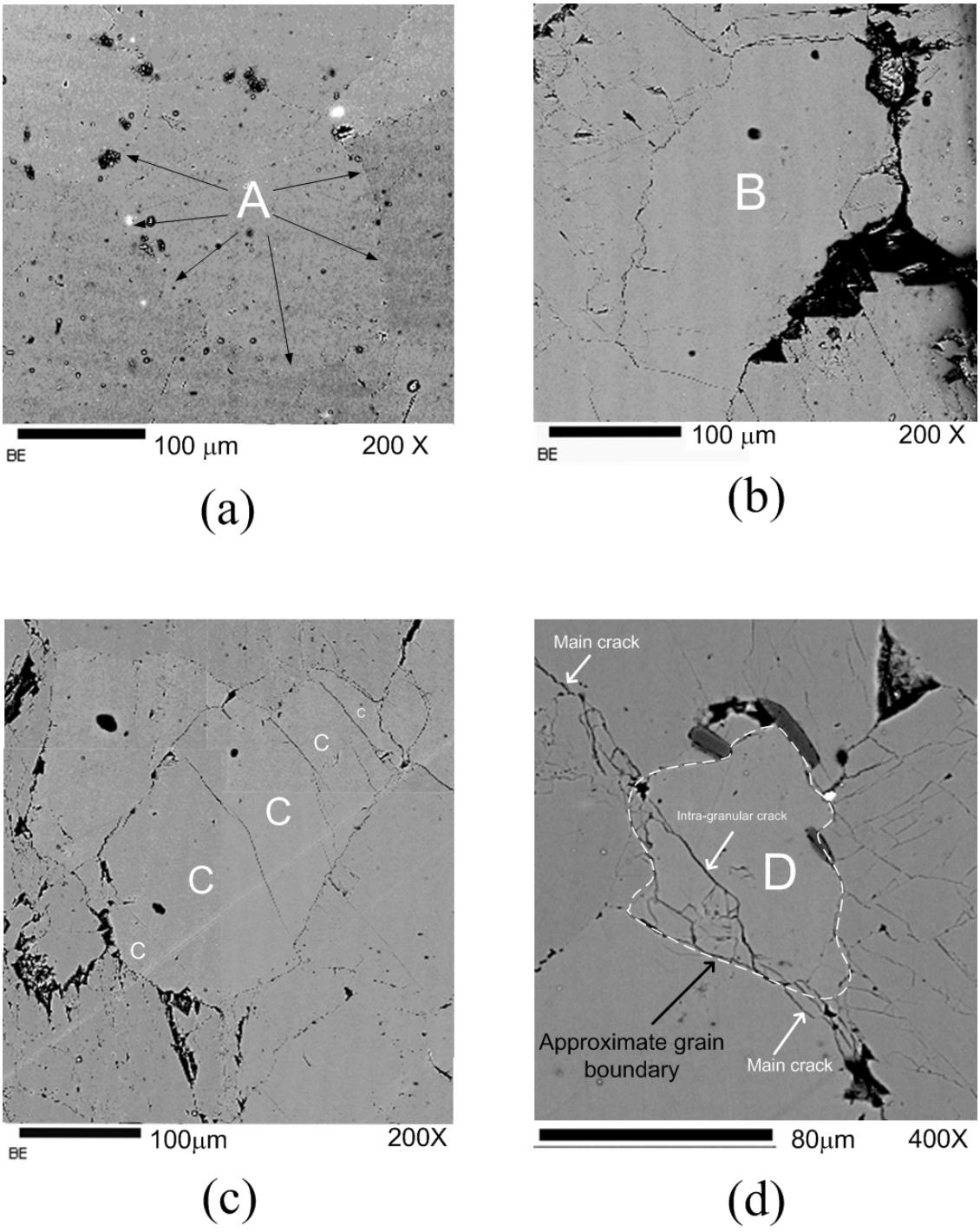

Figure 7.57 – (a) a large portion of grain boundary of grain A is crack-free, (b) grain boundary cracking (inter-granular crack) occurred around grain B, (c) grain C is cut into five parts by multiple almost parallel intra-granular cracks which terminate at the boundary of grain C, (d) an intra-granular crack (main crack) cuts through grain D and its boundary. Note that in all the images shown here, the σ_1 direction is not marked and is not necessarily vertical.

Grain boundaries without any crack opening generally have a low relief and are identifiable where there is an adequate color contrast between adjacent grains (see grain A in figure 7.57a). Occurrence of **inter-granular cracking** along grain boundaries makes them appear black in color in the SEM images (see grain B in figure 7.57b) and thus distinguishable from the intact grain boundaries. **Intra-granular cracks** refer to those cracks present within mineral grains, but not along grain boundaries. These cracks can be terminated at grain boundaries (see grain C in figure 7.57c) or cut across grain boundaries (see grain D in figures 7.57d).

It has been extensively shown in chapters 5 and 6 that the macroscopic tensile and shear cracks observed in the video recordings are significantly different – the traces of newly developed tensile cracks are usually relatively thin (narrow aperture), while those of shear cracks are usually more conspicuous as their initiation is usually associated with the occurrence of localized surface spalling. Microstructural observation with the SEM reveals a similar fracturing phenomenon at grain-scale. As discussed earlier, most of the microcracks created in response to artificial loading are distinguishable from intact grain boundaries due to their darker traces. Based on some displacement markers such as slightly displaced grain boundaries, the identity of shear cracks and the sense of shearing can be inferred. Close examination reveals that shear cracks are often accompanied by **spalling features** scattered along grain boundaries (see example in figure 7.58a) and at junctions of grain boundaries (see example in figure 7.58b). The spalling features are usually of a triangular or polygonal shape and appear black in color with distinguishable relief. Additional examples are shown in figures 7.16 and 7.24a.

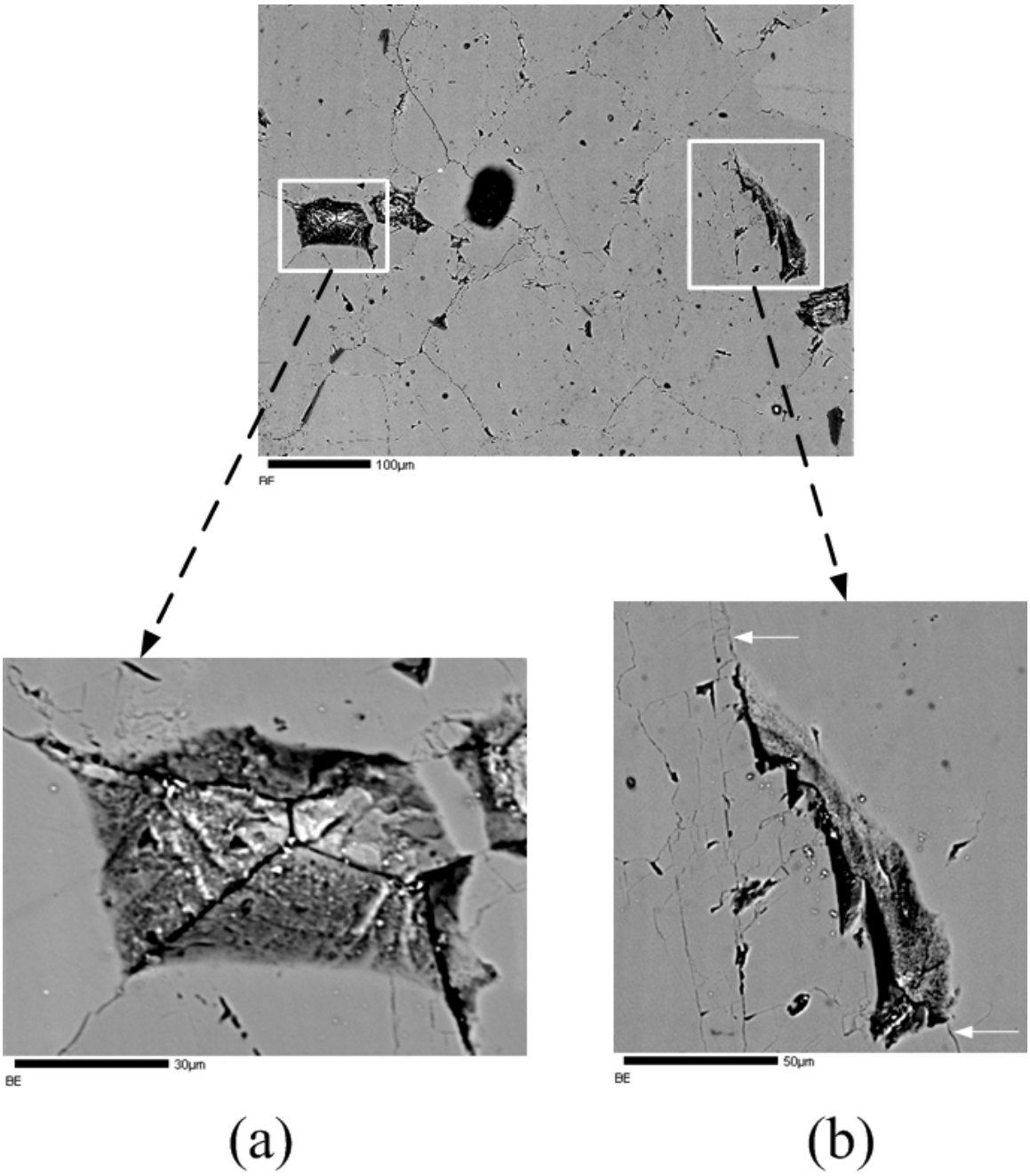

Figure 7.58 – scattered spalling zones with different morphological features (a) a spalling zone around a junction of grain boundaries, (b) an elongated spalling zone along a grain boundary. The upper portion and the lower portion of the grain boundary are marked by horizontal white arrows. Note that the σ_1 direction, which is not marked in the figure, is not necessarily vertical.

7.4.3 Evolution of white patches

The purpose of this section is to summarize the key characteristics of the microstructural evolution of the white patches, which are observed in the prismatic marble specimens that have been loaded to varying levels. The summary consists of two parts. The first part focuses on the white patches, which will lead to the eventual formation of **tensile wing cracks** and the second part focuses on the white patches, which will lead to the eventual formation of **shear cracks**. Representative SEM images shown earlier within this chapter will be reproduced in the summary below.

7.4.3.1 White patches leading to formation of tensile wing cracks

In both types of specimens containing single flaws (geometry A) or stepped double flaws (geometry B) tested for the present SEM study, white patches of conventional wing appearance are observed to develop close to the flaw tips in response to the applied uniaxial loading. They are easily identifiable even with unaided eyes. The higher the loading is, the longer the white patches are and the more intense the white color is. Examination of the SEM images captured along the trajectories of the white patches reveals the changes of microstructural features associated with the progressive evolution of white patches. At a sufficiently high loading, the population and density microcracks (as viewed with the SEM) developed along the white patches become observable and a **microcracking zone** is formed. This zone consists of a **dominant crack** and **multiple microcracks** flanking its two sides. Outside this zone, the microcrack density is much lower than that within the microcracking zone (see the schematic illustration in figure 7.59).

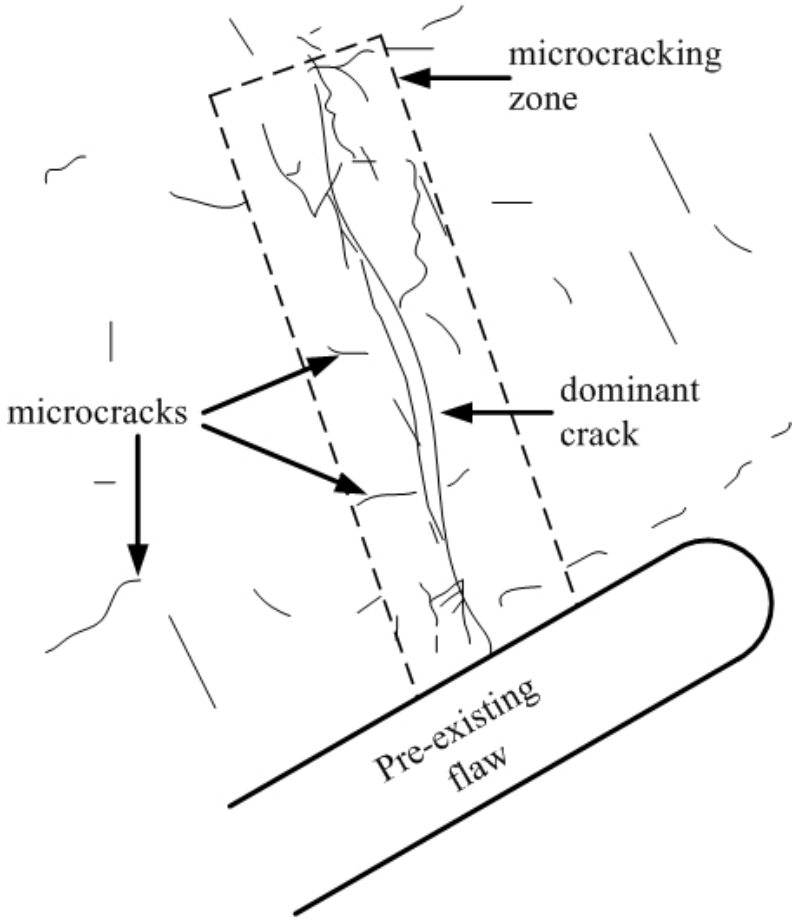

Figure 7.59 – Schematic illustration of a microcracking zone initiated from a pre-existing flaw. This zone consists of a dominant crack and multiple microcracks of a relatively high density. Outside this zone, the crack density is much lower.

Representative SEM images of the corresponding white patches in specimens DA, DB and DC are reproduced in figure 7.60A (original images), 7.60B (crack traces) and 7.60C (overlay of crack density distributions on crack traces). Note that in figure 7.60C, the crack density distribution is based on a qualitative assessment and the crack density is classified into one of the four classes – **background (B), low (L), medium (M) and high (H)**. The crack densities contained within the four grids shown in the top left portion of figure 7.60C serve as a reference for the qualitative assessment. Note that the background crack density (B) is due to two sources – inherent micocracks and microcracks due to the cutting action of water abrasive jet. A microcracking zone is hereby defined as containing regions with crack densities of classes **L**, **M** and **H**.

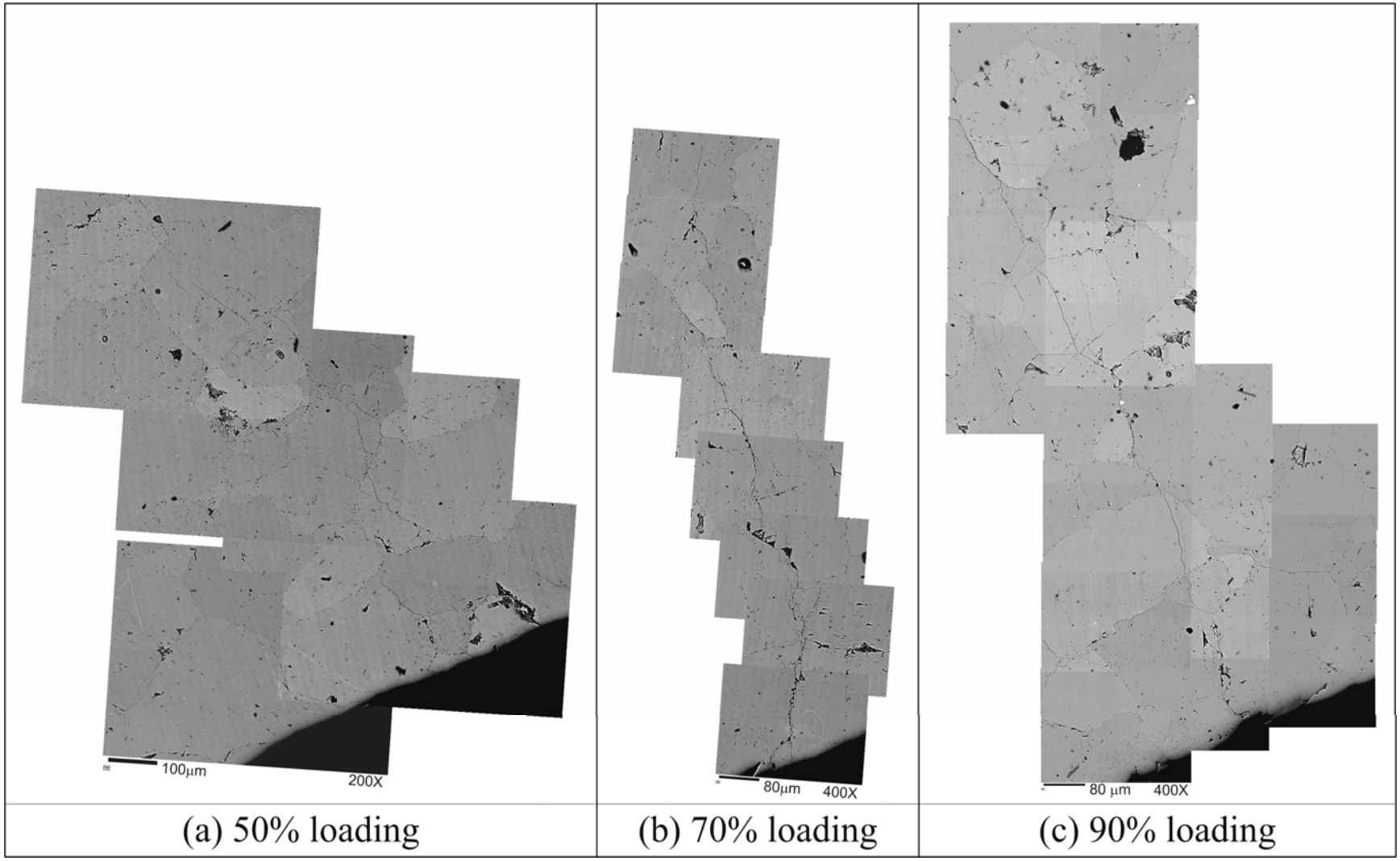

Figure 7.60A – Assemblages of SEM images for individual white patches observed in (a) specimen DA, (b) specimen DB, and (c) specimen DC.

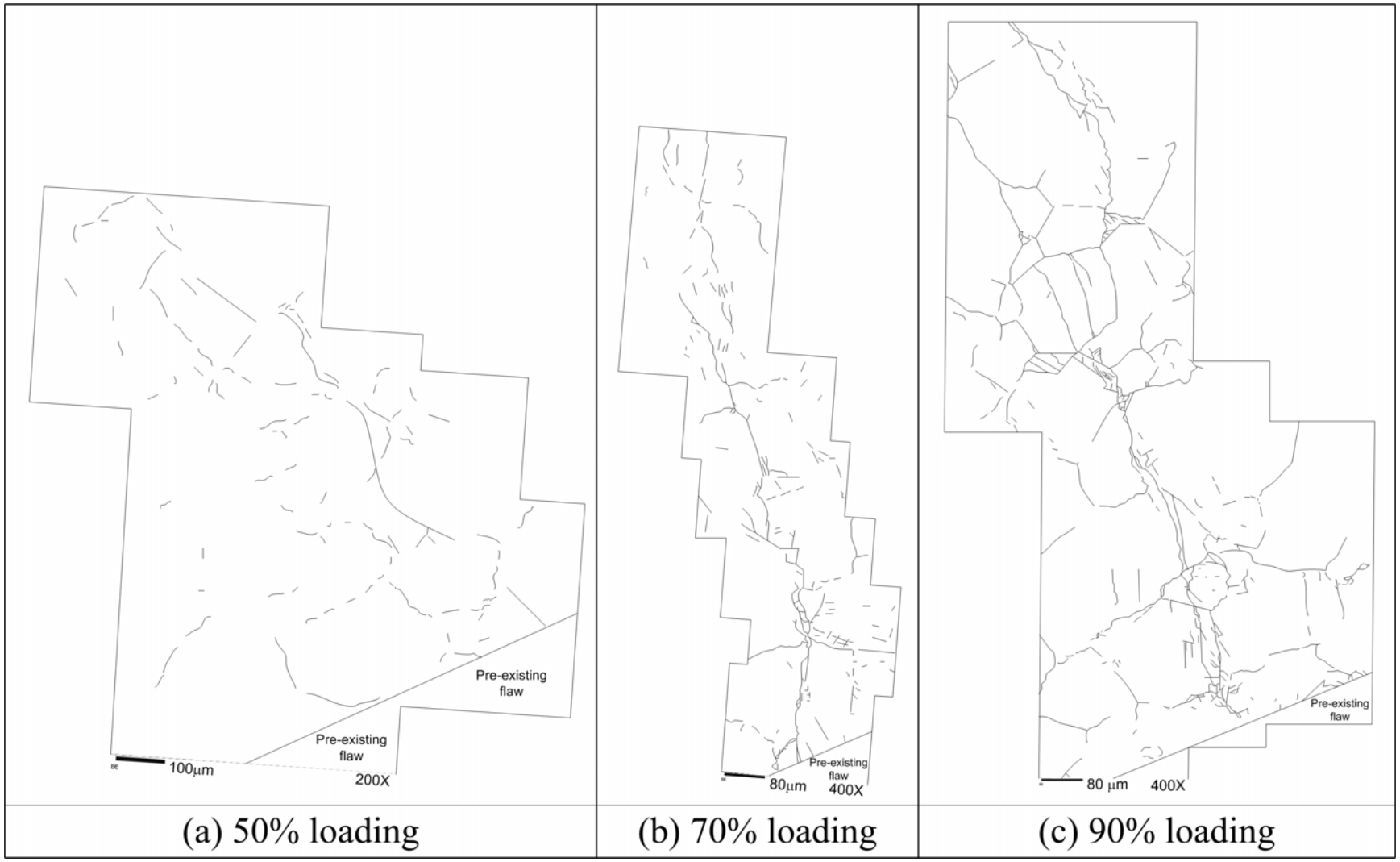

Figure 7.60B – Sketches of crack traces of the images shown in figure 7.59 for (a) specimen DA, (b) specimen DB, and (c) specimen DC.

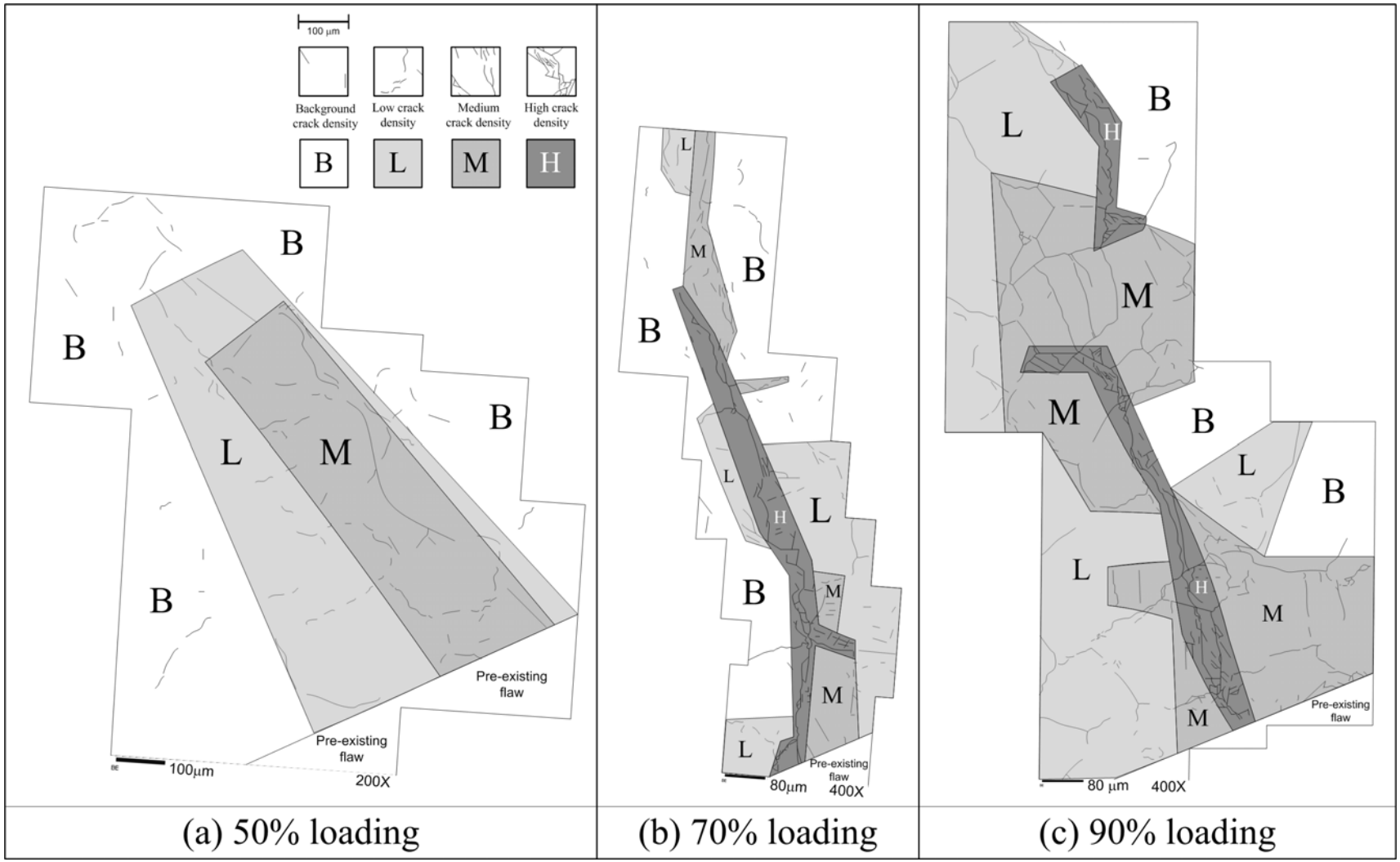

Figure 7.60C – Overlays of crack density distribution over the sketches of crack traces shown in figure 6.60A for (a) specimen DA, (b) specimen DB, and (c) specimen DC. The keys of the different classes of crack density (qualitative) – background, low, medium and high are shown in the top left region of the figure.

(1) **At 50% loading** (figures 7.60Aa, Ba & Ca) **–** An individual white patch observed to have developed close to the flaws can be correlated with an underlying zone consisting of multiple short microcracks (inter-granular and intra-granular), but not with any observable dominant cracks [2]. As shown in figure 7.60Ca, the crack density inside the core of the microcracking zone belongs to **class M** and its vicinity belongs to **class L**. Note that crack density of **class H** has not developed up to this level of loading. Outside the microcracking zone, the crack density falls back to **class B**. Figure 7.60Ca also clearly illustrates that the amount of microcracking also decreases with distance away from the flaw face. At a sufficiently remote distance (not shown in figure 7.60), individual grains completely free of inter-granular cracks can be found (see figure 7.14).

(2) **At 70% (intermediate) loading** (figures 7.60Ab, Bb & Cb) – An individual white patch developed close to the flaw tips can be correlated with an underlying zone of microcracks. The microcracking zone consists of a central dominant undulating generally continuous crack (**class H**), which usually following grain boundaries. This central dominant crack is also flanked by multiple much shorter intra-granular cracks (**classes L and M**). The density of these intra-granular cracks, which usually trend more or less parallel to the dominant crack, is highest next to the central dominant crack (**class H**). It drops off rapidly with distance from this central crack (note that many parts of the central region of **class H** is flanked by regions of relatively low crack density **class L & class B**). The crack density also drops as it traverses orthogonally from the flaw face outwards. See further examples of similar microcracking zones in figures 7.19, 7.37 and 7.40.

[2] The cracks observed in all uniaxially loaded specimens are of two origins – background (inherent microcracks and those due to the cutting action of water abrasive jet) and loading. By comparing the crack nature and density observed in loaded specimens with the intact specimen (figure 7.5) and the specimen with a pre-existing flaw without undergoing the unaxial loading (figures 7.7 – 7.9), it is possible to identify whether uniaxial loading induces additional cracks in the specimens.

(3) **At very high loading** (figures 7.60Ac, Bc & Cc). Similar to those specimens subject to intermediate loading, an individual white patch developed close to the flaw tips in specimen SD (95% loading) and specimen DC (90% loading) can also be correlated with a microcracking zone which extends from the flaw face. The microcracking zone similarly consists of a central dominant undulating crack (**class H**) and multiple much shorter orthogonal intra-granular cracks flanking the dominant crack (**classes M and L**). The density of the microcracks, is highest next to the central dominant crack (**class H**) and it drops off with distance from this central crack. The crack density also drops as it traverses orthogonally from the flaw face outwards. This phenomenon is much better illustrated in figure 7.44, 7.45 and 7.46. As shown in figure 7.45 which is reproduced on the following page, as the distance from the flaw face increases, the microcrack density decreases (a gradually narrowing microcracking zone is observed). At an even greater distance from the flaw, the microcrack density further reduces and it is no longer possible to identify a single dominant microcrack feature.

As defined earlier, a microcracking zone consists of regions with crack densities of **classes L**, **M** and **H**. Comparing figure 7.60Cb with figure 7.60Cc, it can be noted that the extent of regions of **class M** and **class L** which flank the central **class H** region in figure 7.60Cc is larger than that in figure 7.60Cb. Therefore, it can be concluded that the microcracking zone produced by the very high loading (specimen DC) are **longer** and **wider** than the microcracking zone produced by the intermediate loading (specimen DB). See further examples in figures 7.24 for specimen SD, and figures 7.44, 7.45 and 7.46 for other white patches for specimen DC.

Apart from the difference of the overall size of the microcracking zones as discussed above, the microstructural nature of the regions of **class H** belonging respectively to “intermediate loading” and “very high loading” are also different. The region of **class H** inside the microcracking zones corresponding to white patches in specimens DC (very high loading) are characterized by the presence of multiple long cracks (figure 7.60Cc) which trend along with the general orientation of the white patch. In contrast, there is

only one single dominant crack in the region of class H in specimens DB (intermediate loading) as shown in figure 7.60Cb.

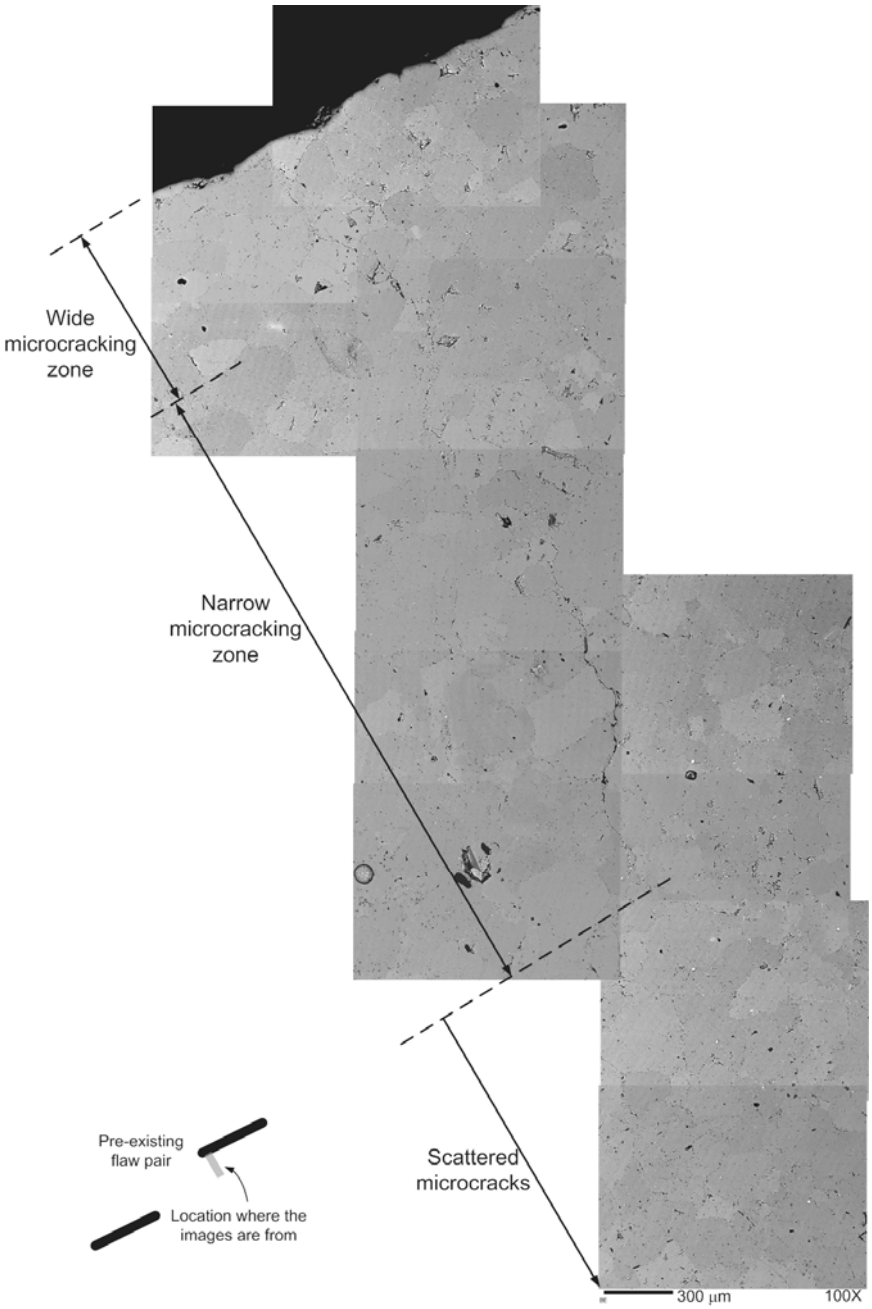

Figure 7.45 – An assemblage of SEM images of the lower face of top flaw of flaw pair DC close to the left flaw tip. A wider microcracking zone is located close to the flaw face. A narrower microcracking zone is located below it. At a farther distance away from the flaw, microcracks are scattered randomly. (magnification power = 100 X)

To summarize, along the white patch of a future tensile wing crack, an elongated zone scattered with microcracks (**classes M and L**) first form adjacent to the flaw face around the tip regions in response to the initially low applied loading. As the applied loading progressively increases, a microcracking zone consisting of a dominant continuous crack becomes identifiable. This dominant crack (**class H**) is flanked by multiple microcracks with a density decreasing away from the dominant feature and the flaw face (**classes M and L**). As the applied loading increases further, the microcracking zone lengthens and becomes wider (larger extent of regions of **classes M and L**). The density of microcracks next to the central dominant crack also becomes higher.

7.4.3.2 White patches leading to the formation of shear cracks

The flaw pair geometry 2a-30-30 is particularly chosen in the present SEM study because a distinct white patch which eventually leads to the formation of a coalescence shear crack has been observed in earlier tests (figure 7.61a). However, the expected development of the coalescence white patches is not observed for specimens DA, DB and DC which have been loaded to varying stress levels (figure 7.61b). It is thus impossible to study the microscopic nature of a white patch which will lead to the formation of shear cracks based on this group of specimens.

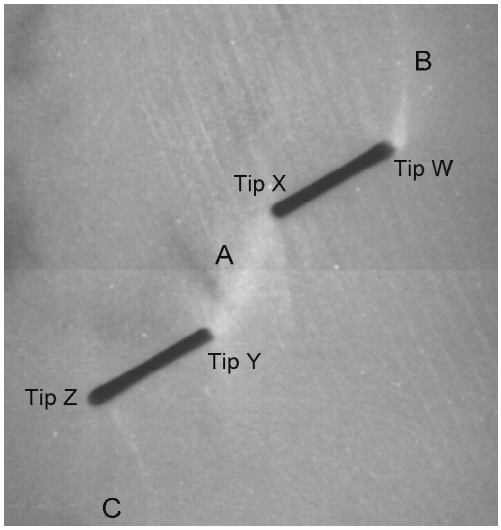

(a)

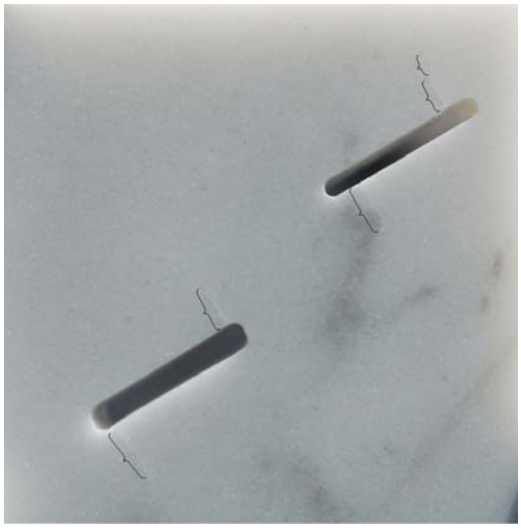

(b)

Figure 7.61 – (a) development of white patch between inner flaw tips in specimen CM 2a-30-30-A, (b) only tensile wing white patches develop from the flaw tips in specimen DC which has been subject to 90% of failure stress.

In specimen DD (loaded up to 94% of the failure stress), which contains a pair of coplanar flaws of geometry 4a-60-0, an extensive white patch develops in the central bridging region between the two inner flaw tips (figure 7.62a). In other uniaxial loading tests on specimens with the same flaw geometry, the appearance of the central white patch is followed by an initiation of shear coalescence cracks which link up the two inner flaw tips. The sketches contained in figures 7.62b and 7.62c show the traces of the coalescence shear cracks and the other cracks developed from the pre-existing flaw pairs for two other similar specimens uniaxially loaded till failure. The SEM study focusing on the white patch in the bridging region in specimen DD can thus reveal the underlying microstructural features prior to the development of the coalescence shear crack.

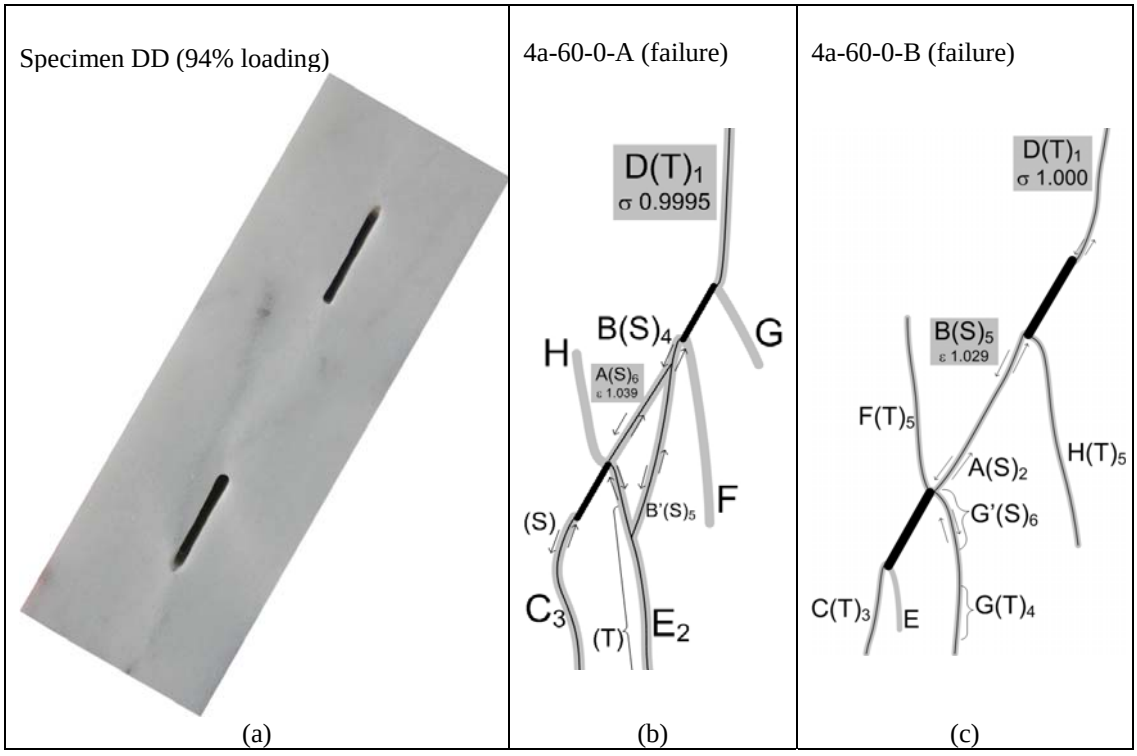

Figure 7.62 – (a) Specimen DD with developed white patches. (b, c) Development of coalescence cracks and other cracks from the pre-existing flaw pairs of geometry 4a-60-0. Refer to chapter 6 for explanation of symbols. In both specimens, coalescence is achieved by linkage of shear cracks A and B, which initiated from the inner flaw tips separately. The step-by-step analyses of cracking events of these two specimens are contained in Appendix N.

Examination of the high speed videos of specimens 4a-60-0-A and 4a-60-0-B as shown in figures 7.62b and 7.62c reveals that **two short** shear cracks, which are generally coplanar with the pre-existing flaws, first initiate separately from the inner flaw tips. Coalescence occurs between these two shear cracks as they propagate towards each other (refer to Appendix N and section 6.4.3 for the details of the fracturing processes involved). In other words, the coalescence is not achieved by the initiation of a **single** coalescence crack, which initiates from one of the inner flaw tips and propagates towards the other inner flaw tip, but by linkage of two cracks.

As revealed from the SEM study for specimen DD, the central white patch is underlain by multiple vertically oriented microcracking zones which are parallel with the uniaxial direction. Refer to figures 7.50, 7.51 and 7.52 (reproduced on the following pages) for the location and size of these zones. Instead of being evenly distributed themselves throughout the bridging region, these microcracking zones preferentially develop close to the inner flaw tips. Although observable cracks have not yet developed in the specimen as observed by unaided eyes, it is reasonable to speculate that regions containing these micorcracking zones are very likely to be where subsequent observable cracks will develop. This speculation agrees well with the high speed camera observation described above that individual cracks first initiate from the two inner flaw tips and later coalesce.

Combining the above observations, it is reasonable to conclude that the microcracking zones underlying the white patches, which develop prior to the initiation of observable cracks (viewed with the high speed camera) can be regarded as the associated **process zones**.

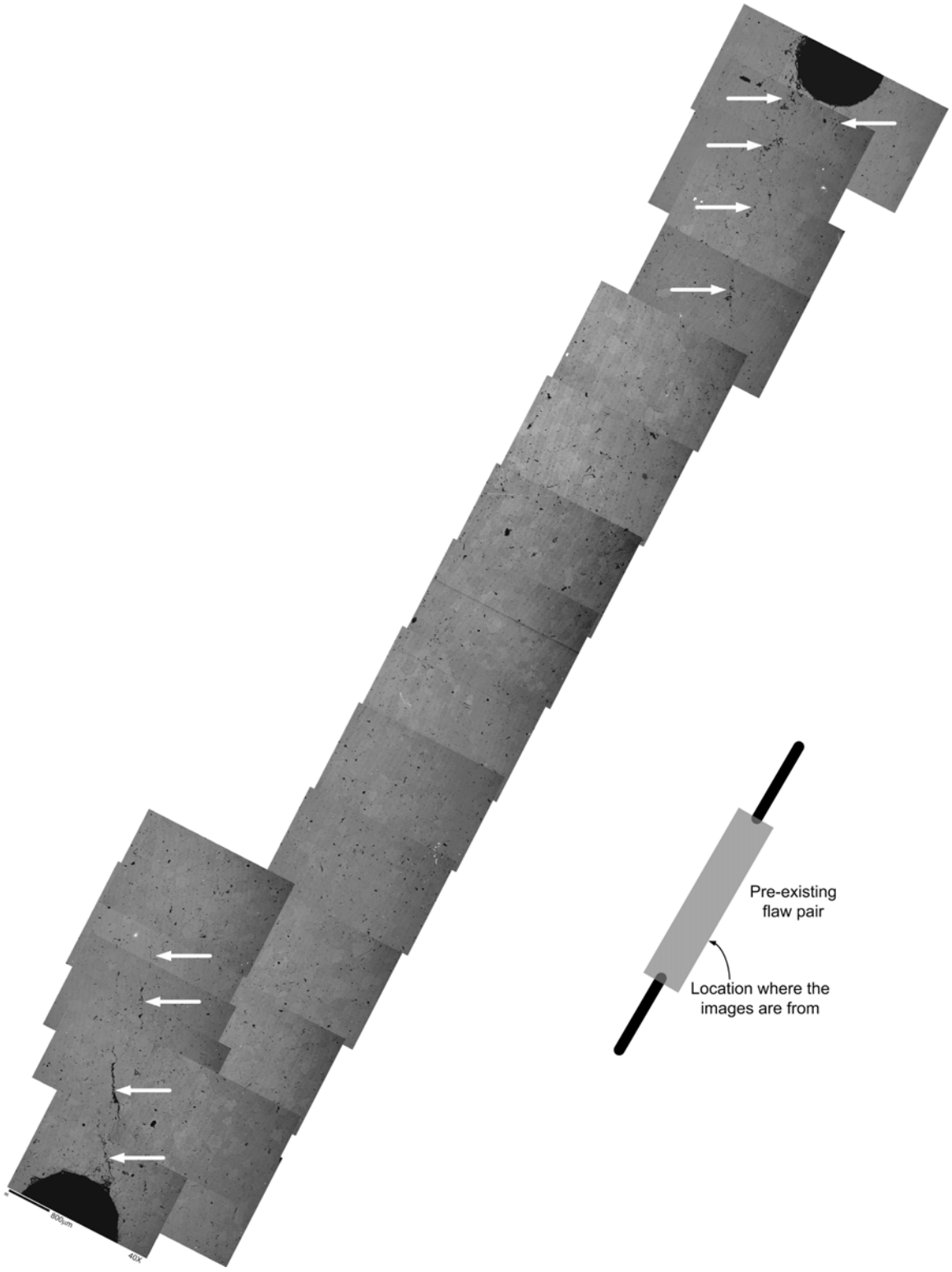

Figure 7.50 – An assemblage of SEM images of the bridging region between inner flaw tips of flaw pair DD. Microcracking zones are indicated by white arrows. The length of the scale bar at the bottom of the image is 800 μm. (magnification power = 40 X)

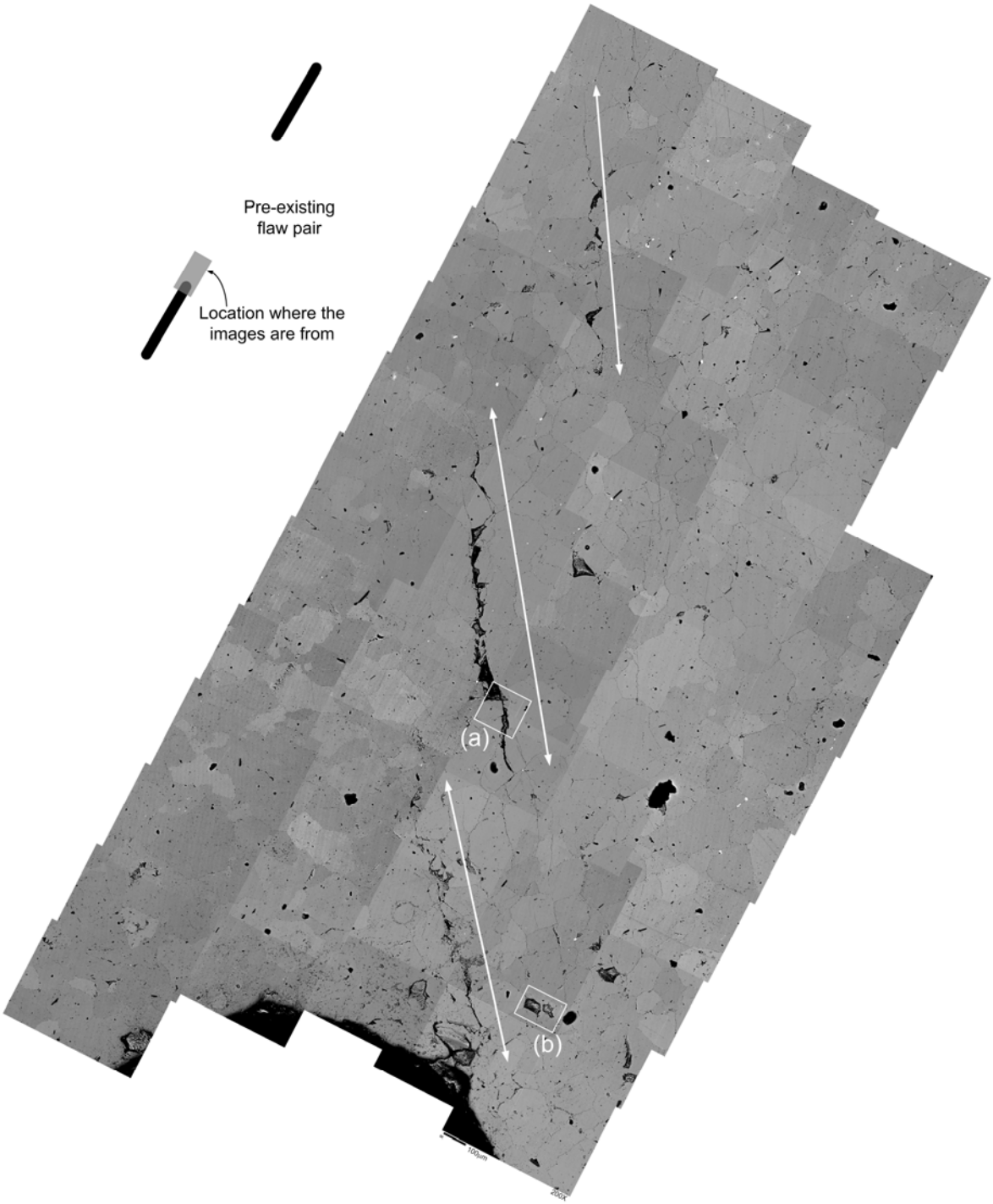

Figure 7.51 – An assemblage of SEM images of the area around the right flaw tip of the bottom flaw. Magnified images of the two enclosed areas are shown in figure 7.52. The intensely fractured zones, whose traces are indicated by arrows, trend almost parallel to the loading direction. The length of the scale bar at the bottom of the image is 100 μm. Note that the loading direction is vertical. (magnification power = 200 X)

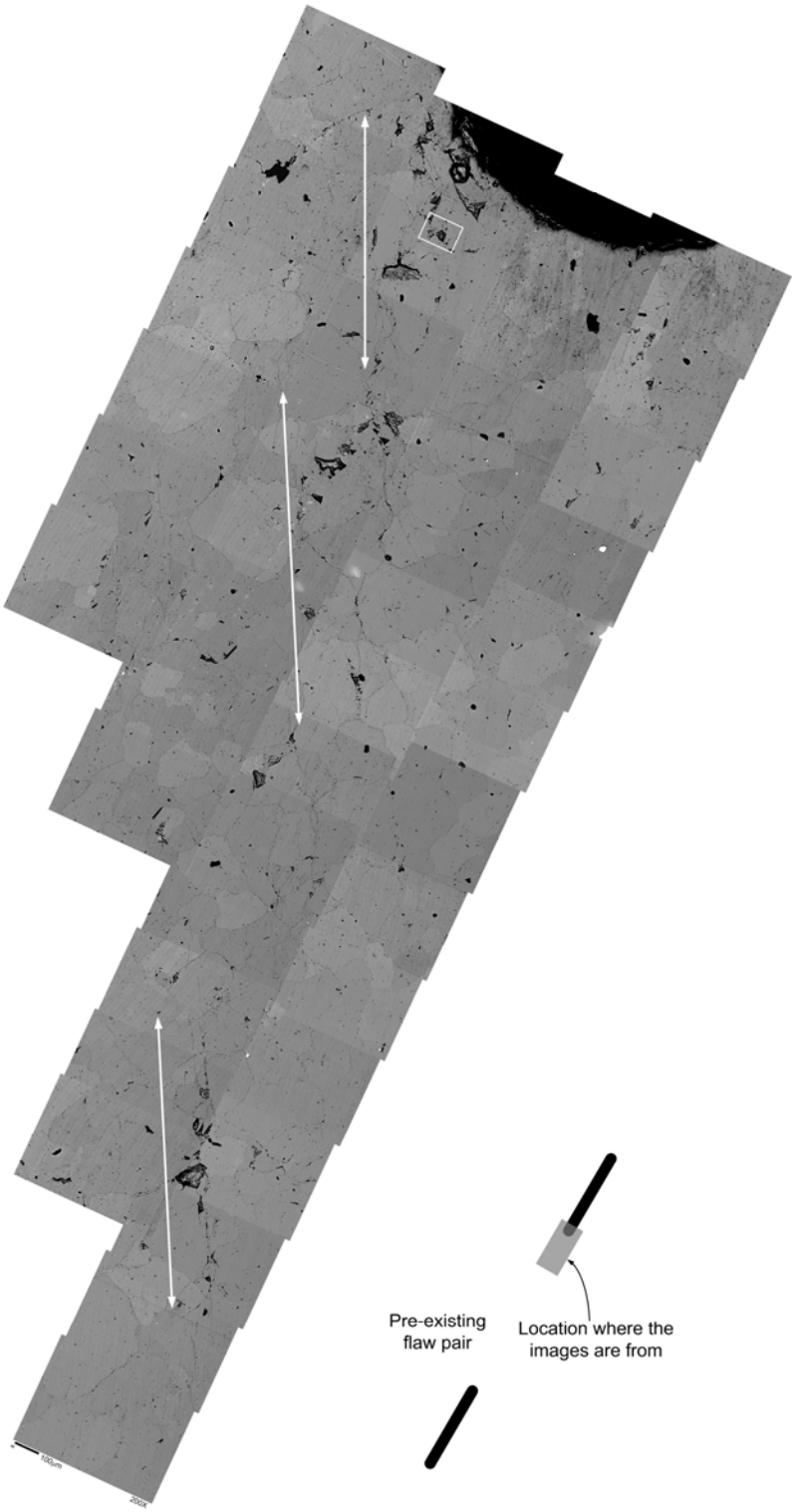

Figure 7.53 – An assemblage of SEM images of the area around the left flaw tip of the top flaw. The intensely fractured zones, whose traces are indicated by arrows, trend almost parallel to the loading direction. The length of the scale bar at the bottom of the image is 100 μm. Note that the loading direction is vertical. (magnification power = 200 X)

Apart from confirming the role of microcracking zones as process zones prior to any observable cracking as discussed above, the SEM images offer additional information regarding the formation of coalescence cracks. The en echelon arrays of microcracking zones developed close to the flaw tips are oriented almost parallel with the uniaxial loading direction (which is vertical in figure 7.50). However, the macroscopic coalescence shear cracks subsequently initiated from the inner flaw tips (observed with high speed camera) are oriented almost coplanar with the pre-existing flaws, i.e. inclined at approximately 30^o with the loading direction. These observations suggest that the development of the observable shear cracks from the inner flaw tips is very likely due to a late-stage linkage of the previously developed vertically oriented microcracking zones. Additional experimental studies are however required to verify this postulation.

7.4.4 Conclusions

Prior to the initiation of cracks in marble, there is usually a development of white (very distinctive white color) patches in the rock. The microstructural properties of a number of white patches which are observed to be crack-free by unaided eyes are examined by the scanning electron microprobe (SEM) imaging technique in the present study. Comparing the SEM images (with magnification powers ranging between 40X and 1000X) obtained for unloaded specimens and artificially loaded specimens, white patches are found to be underlain by multiple loading-induced microcracks. These microcracks, which appear before the initiation of the macroscopic cracks, can be regarded as process zones.

In the present study, multiple specimens of the same flaw geometry are loaded to varying stress levels. As the applied loading increases, the area of the white patches increases and their white color becomes more intense. The SEM imaging technique reveals that the amount of microcracking also increases with applied loading. In addition, the microstructural characteristics of these microcracking zones corresponding to the

respective eventual formation of tensile cracks and shear cracks are observed to be very different:

Tensile crack

Along the white patch of a future tensile wing crack, an elongated microcracking zone scattered with microcracks first forms adjacent to the flaw face around the tip regions in response to the initially low applied loading. As the applied loading progressively increases, the microcracking zone evolves to consist of a dominant continuous crack and multiple microcracks. This density of the microcracks, which flank the central dominant crack, decreases as the distance from the dominant crack increases. In addition, the microcrack density decreases as the distance from the pre-existing flaw increases. As the applied loading increases further, the microcracking zone lengthens and becomes wider. The density of microcracks beside the central dominant feature also becomes higher.

Shear crack

Along the white patch of a future coalescence shear crack, which links up the two inner flaw tips of coplanar flaws inclined at 60^{o}, en echelon arrays of microcracking zones are observed to have developed in response to the applied loading. These microcracking zones are oriented almost parallel with the uniaxial loading direction and develop preferentially close to the flaw tips. On the other hand, the macroscopic coalescence shear cracks subsequently initiated from the inner flaw tips (observed with the high speed camera) are trending in a direction coplanar with the pre-existing flaws, which are different from that of the en echelon arrays. It is thus postulated that the development of the observable shear cracks is due to a late-stage linkage of these previously developed vertically oriented microcracking zones.

7.5 Microstructural characteristics of tensile cracks in molded gypsum

The microstructural characteristics of molded gypsum were examined under the environmental scanning electron microscope (FEI/Philips XL30 FEG ESEM, ESEM in short for the subsequent discussion), which is housed at the MIT Center for Materials Science and Engineering. In contrast to the JEOL JXA-733 SEM (SEM in short) housed in the Department of Earth, Atmospheric and Planetary Science which was used for studying Carrara Marble, the samples to be examined by the ESEM need not be carbon coated prior to the imaging work. In addition, the ESEM can operate at a lower vacuum condition than the SEM, which is more suitable to gypsum with its relatively higher porosity.

The tensile cracks developed from a flaw pair of geometry 4a-30-120 in a molded gypsum specimen as shown in figure 7.63 were examined by the ESEM. This specimen was uniaxially loaded up to a level such that tensile wing cracks (visible to unaided eyes) and very fine hair-line tensile cracks (barely visible to unaided eyes and visible with a 10x hand lens) had just developed in the specimen. The microscopic imaging work on this specimen containing these two types of tensile cracks can thus provide information about the tensile crack development.

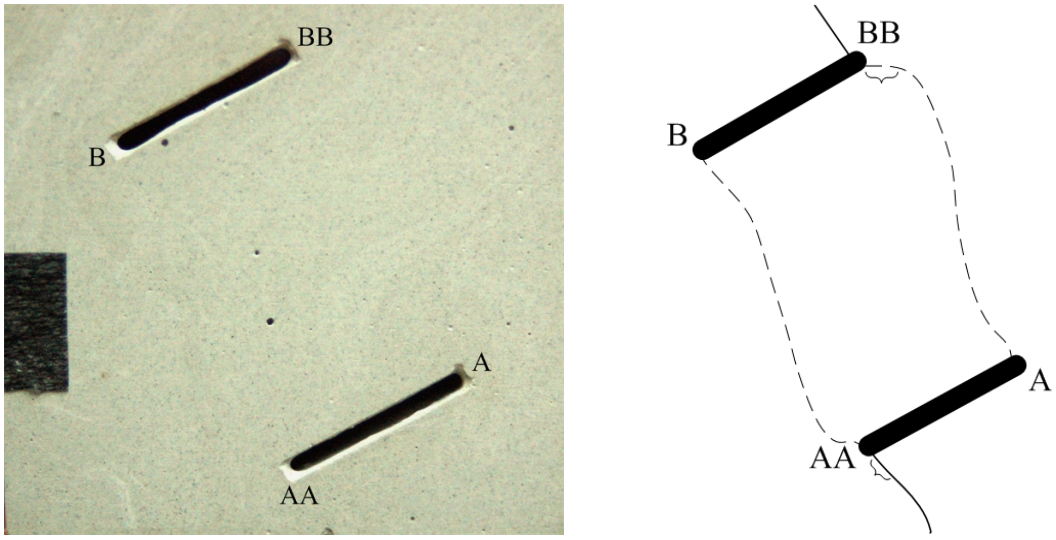

(a) (b)

Figure 7.63 – (a) View and (b) sketch of a gypsum specimen with flaw pair geometry 4a-30-120. The tensile wing cracks initiating from tips AA and BB, which are visible to unaided eyes are represented by solid lines. The hair-line cracks (which are not visible to unaided eyes, but become visible with a 10x hand lens) are represented by dashed line. The two regions examined by ESEM are indicated by brackets. The loading direction is vertical and the length of the pre-existing flaw is 0.5" (12.7 mm).

7.5.1 Hair-line tensile crack

ESEM images of the region adjacent to tip BB of the top flaw as indicated in figure 7.63 are shown in figures 7.64 (650x magnification) and 7.65 (2000x magnification). The ESEM images reveal that the very fine hair-line tensile crack actually consists of multiple crack segments (central cracks), with a decreasing aperture size as it progresses away from the flaw tip (figure 7.64) – 20 μm next to the pre-existing flaw, and becomes constantly narrow of ~ 1 to 2 μm beyond a distance of around 250 μm from the flaw tip. Multiple much shorter microcracks, which appear as much narrower shallow black depressions are also found next to the central crack segments. See figure 7.65 which corresponds to the enclosed region in figure 7.64. Detailed examination of the region in the microcracking zone (central cracks + surrounding microcracks) and its vicinity over a much larger area (out of the field of view of figure 7.64) reveals that the microcrack density is high in the close vicinity of the central dominant microcracks, and decreases as the distance from the central dominant microcracks increases.

In contrast to the Carrara Marble, which is made up of well-fused interlocking grains, the individual platy grains in molded gypsum are more loosely-packed. The irregularly stacked platy gypsum grains leads to the formation of numerous fine pores among grains, in addition to the trapped air bubbles created during the specimen casting process. Since the pores are of a size (1 – 5 μm) comparable to that of individual mineral grains, it is thus very difficult to distinguish intergranular cracks of very small aperture from the inherent pores. Due to this constraint, only cracks of wide enough aperture and considerable length (approximately > 5 grain sizes) can be identified.

A very large proportion of the observable cracks on these figures are *intergranular* as indicated by the presence of abundant individual intact gypsum plates/needles beside the crack segments (figure 7.65). A small proportion is *intragranular* cracks, which appear as straight fractures within individual grains (figure 7.66).

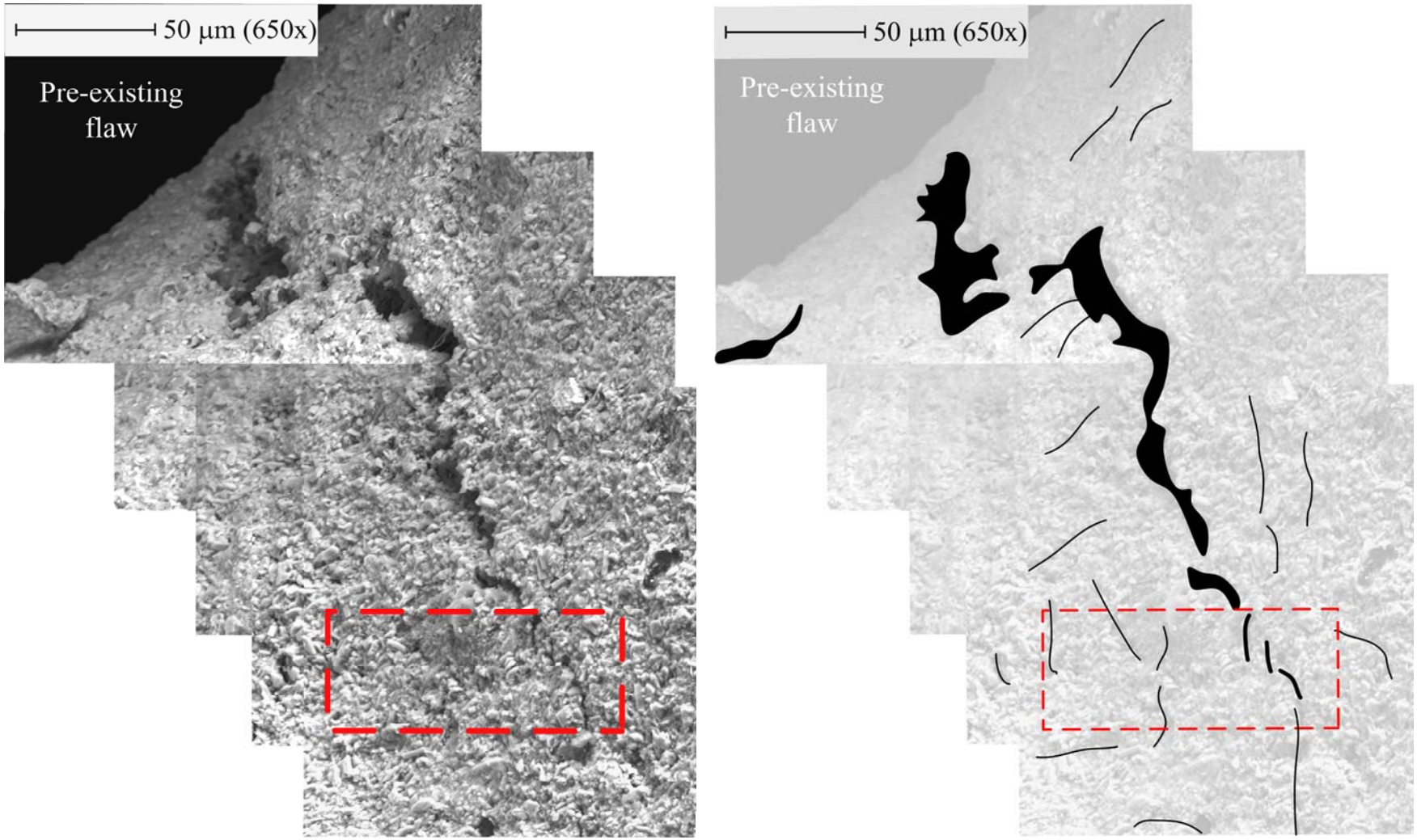

(a) (b)

Figure 7.64 – View of a hair-like tensile crack initiating from top right flaw tip BB. (a) original ESEM image, (b) overlay of traces of identified microcracks onto the ESEM image. The top left region is the pre-existing flaw. A magnified view of the enclosed region is shown in the next figure.

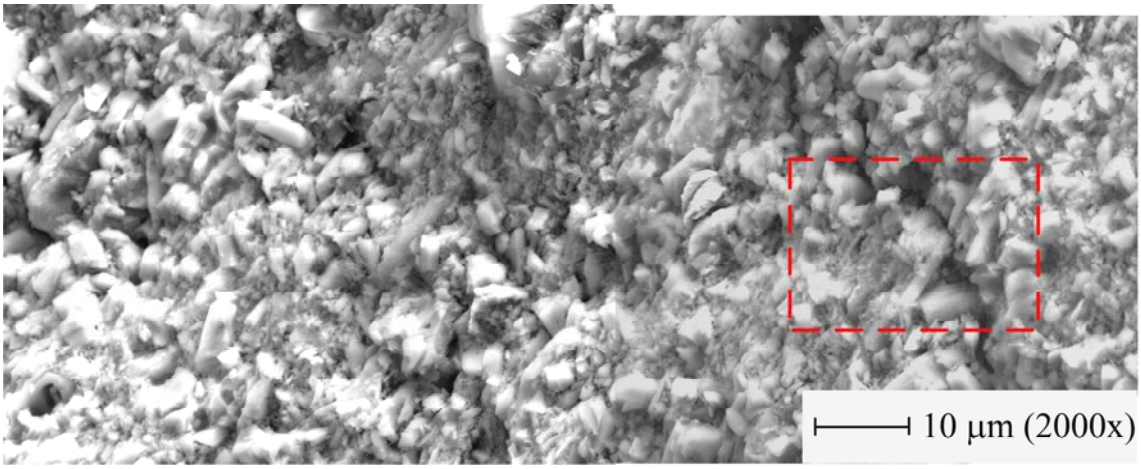

(a)

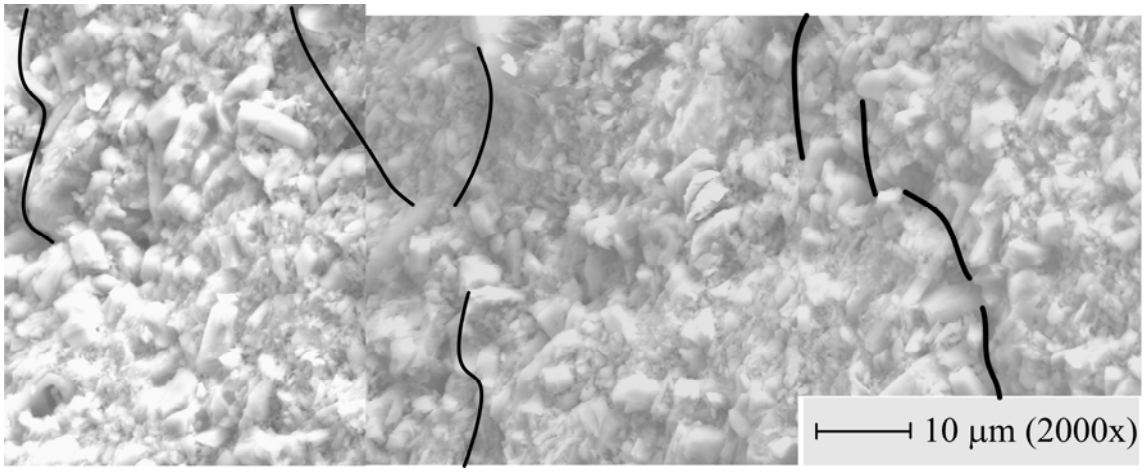

(b)

Figure 7.65 – Magnified ESEM image of the enclosed area as shown in figure 7.64. (a) original ESEM image, (b) overlay of traces of identified cracks onto the ESEM image. The thicker traces on the right are the extension of the dominant microcracks identified in figure 7.64. A magnified view of the enclosed region in (a) is shown in the next figure.

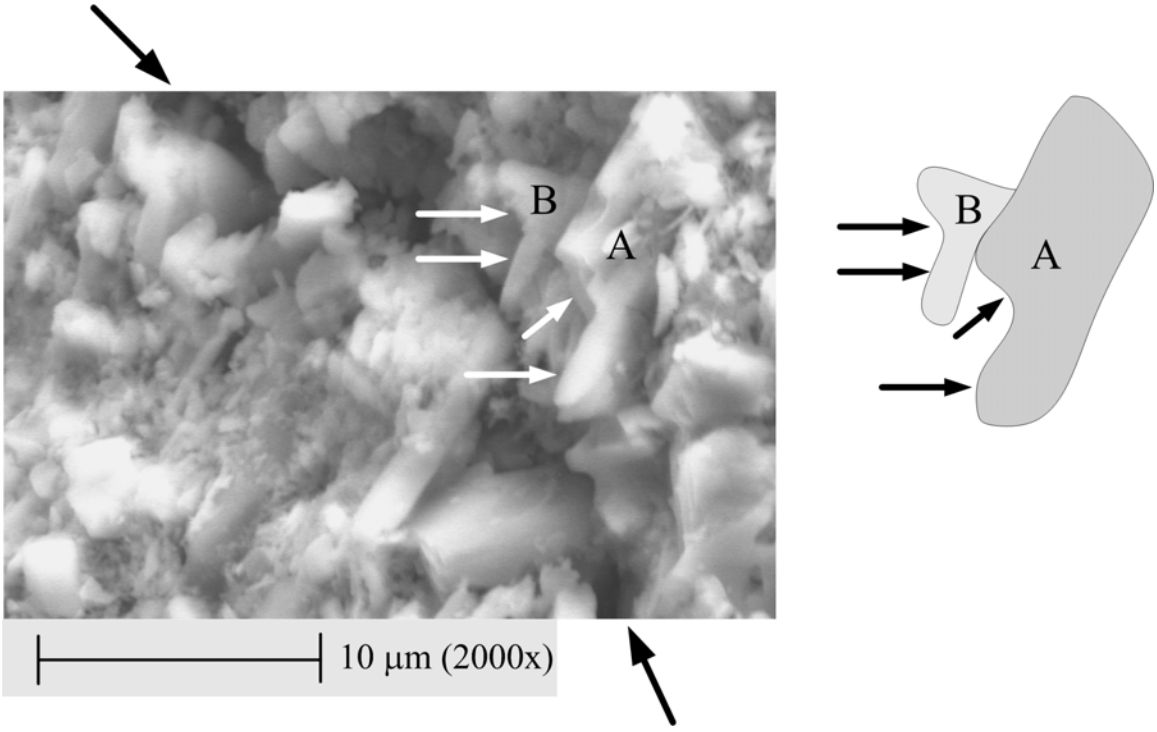

Figure 7.66 – ESEM image of the magnified region of the enclosed rectangular region shown in figure 7.65. Two gypsum grains A and B of indented shape due to intragranular cracks are labeled in the ESEM image and sketched on the right. The two black arrows to the top and bottom of the image indicate the trace of the trajectory of the dominant microcrack.

7.5.2 Well-developed tensile wing crack

Figures 7.67 to 7.69 show the ESEM images taken in the vicinity of a well-developed continuous tensile wing crack (TWC) initiating from the left tip AA of the bottom flaw as indicated in figure 7.63. Note the uniaxial loading direction in figure 7.67. Comparing figures 7.64 (hair-like crack) and 7.68 (well-developed tensile crack), which are both taken at 650X magnification, the aperture of this tensile wing crack is obviously much wider than that of the hair-line crack.

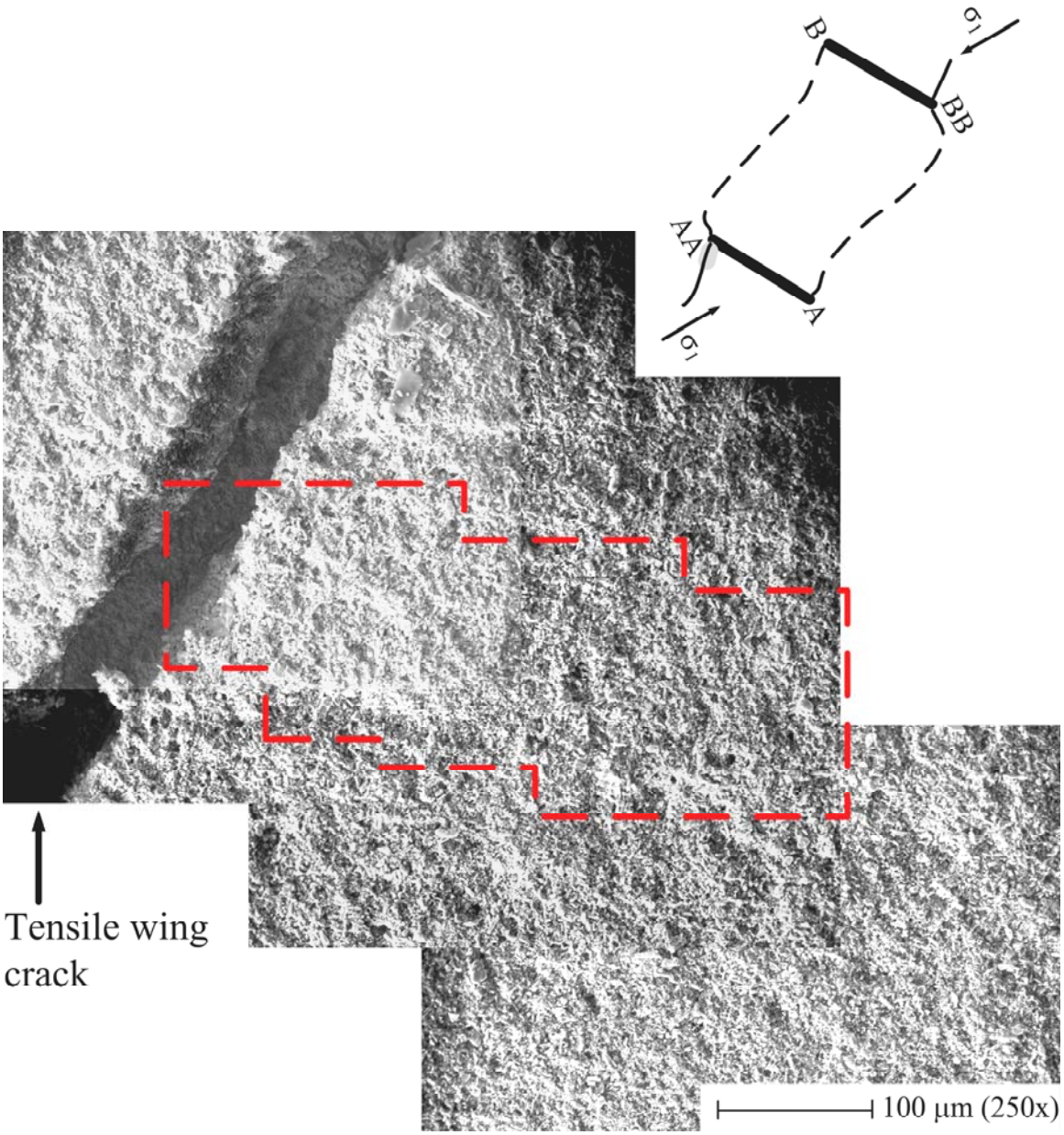

Figure 7.67 – A magnified (250X) ESEM image of the region in vicinity of the well-developed tensile wing crack as indicated in figure 7.63. The location of this image is also marked as a grey region in the top sketch. Traces of microcracks are of a too small aperture to be discernable in this image. A magnified (650X) view of the central enclosed region is shown in figure 7.68.

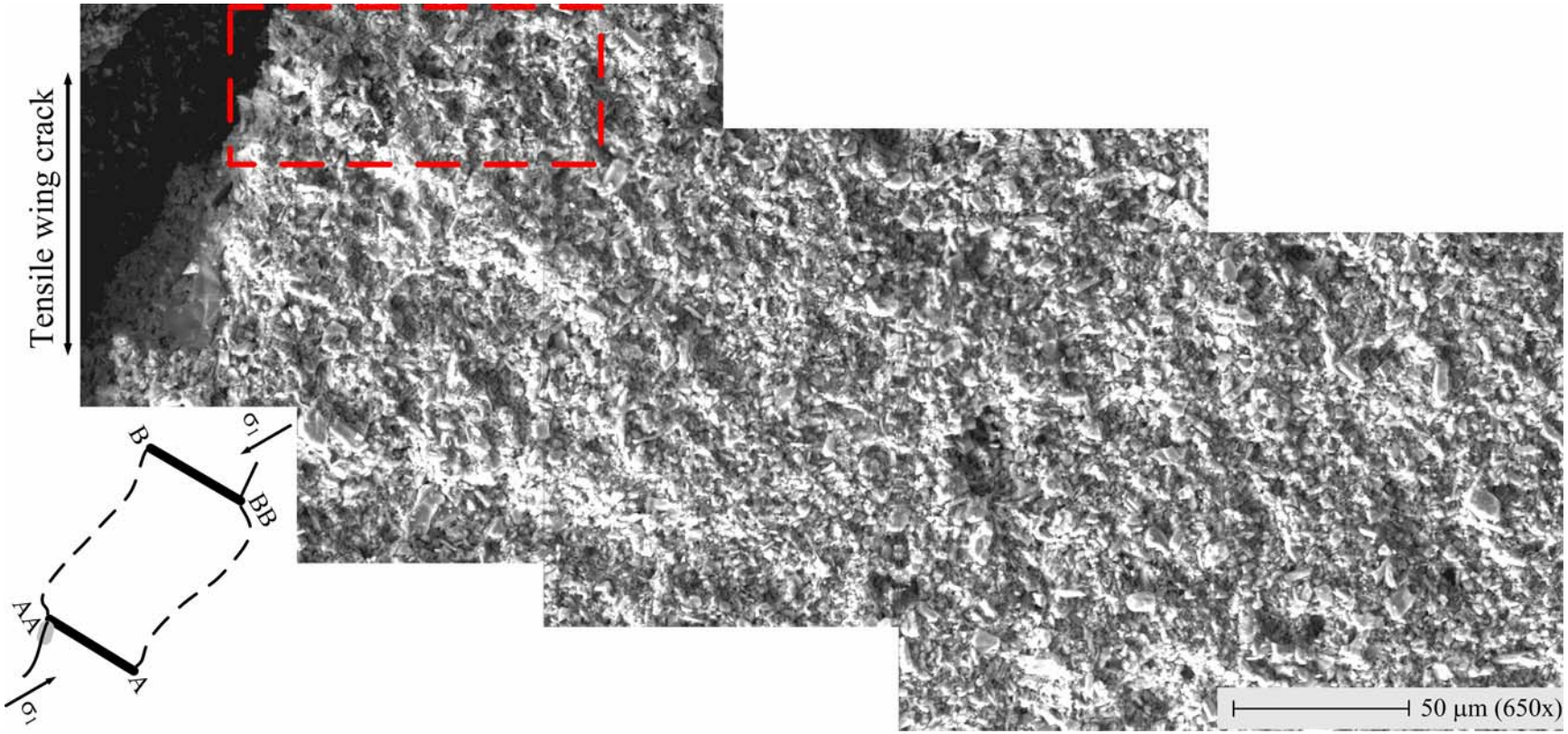

Figure 7.68 – Magnified (650X) ESEM image of the region enclosed in figure 7.67. Traces of microcracks are of too small aperture to be discernable. A further magnified (2000X) view of the central enclosed region is shown in figure 7.69. Refer to figure 7.67 the uniaxial loading direction.

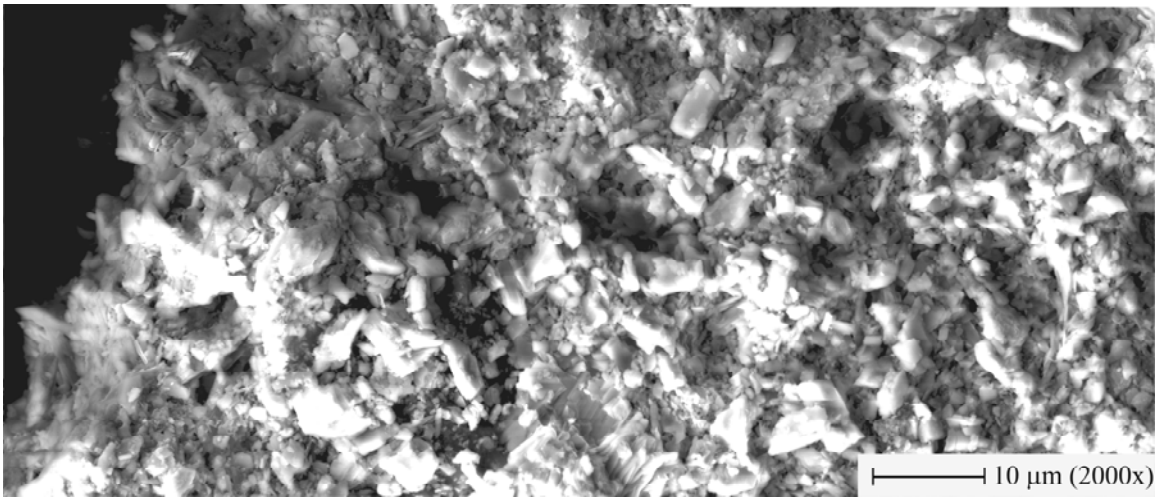

(a)

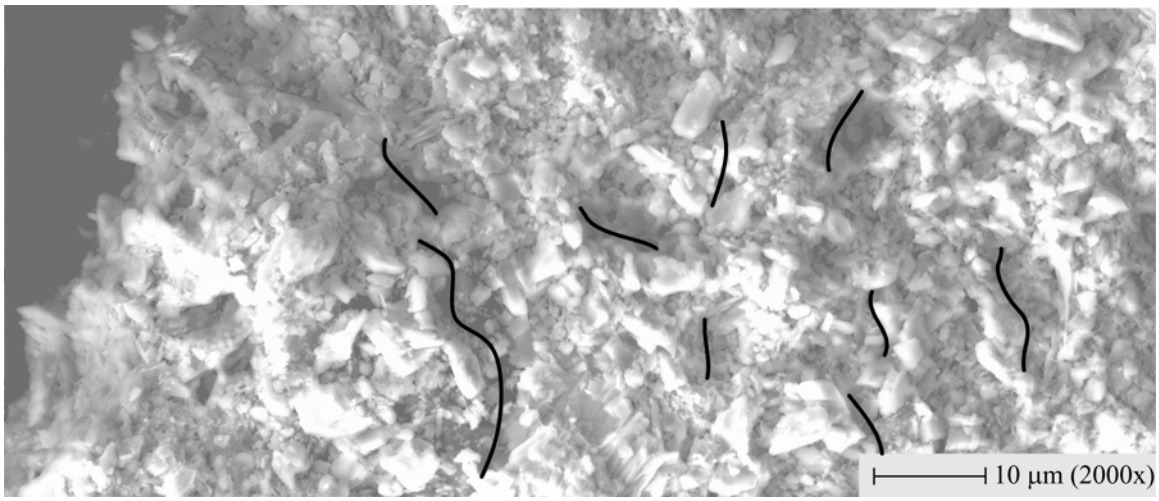

(b)

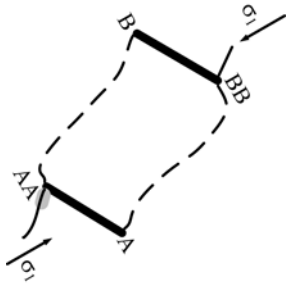

Figure 7.69 – Magnified ESEM image of the enclosed area as shown in figure 7.68. (a) original ESEM image, (b) overlay of traces of identified crack segments onto the ESEM image. Refer to figure 7.67 the uniaxial loading direction.

Similar to the hair-line cracks, the regions flanking the **wide** TWC do not display signs of intense microcrack development (figure 7.67 to 7.69). In figures 7.65 (hair-line crack) and 7.69 (well-developed TWC), which are both taken at 2000X magnification, multiple scattered short microcracks are identified. In addition, the density and nature of the microcracks observed next to a hair-like tensile crack and a well-developed TWC is quite similar. It implies that the eventual development of a tensile wing crack which becomes visible to unaided eyes (figure 7.68) is not accompanied by a substantial initiation of microcracks in the vicinity. The overall process is very likely due to the lengthening (propagation) and linkage of the already developed much shorter hair-line tensile crack segments (figure 7.64). See the schematic sketches shown in figure 7.70.

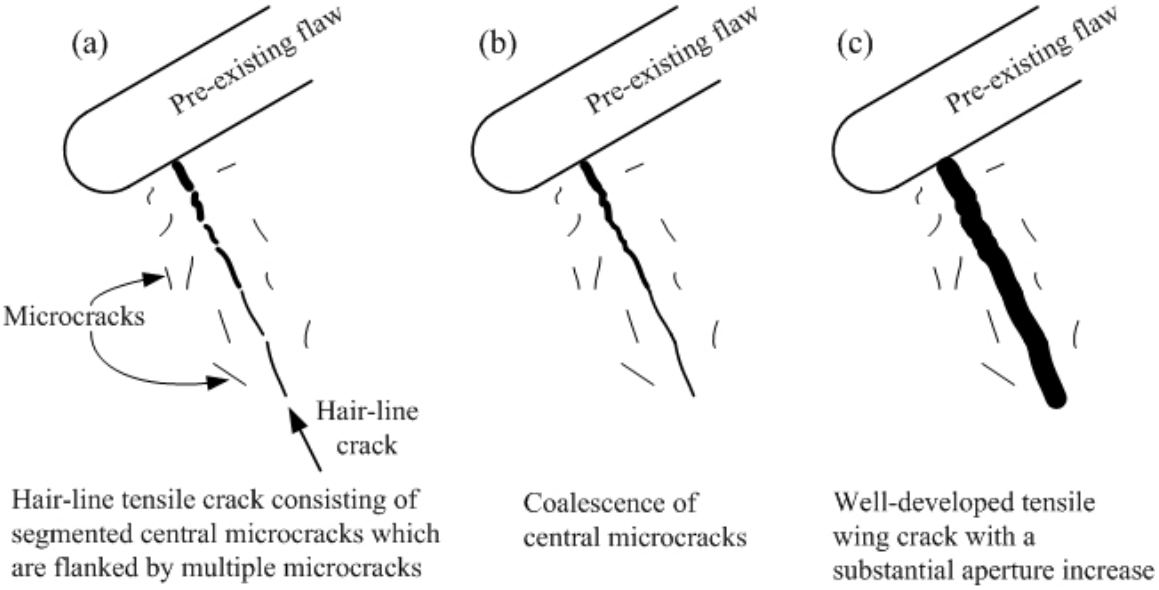

Figure 7.70 – Schematic illustration of a probable mechanism of the evolution of a hair-line tensile crack to a well-developed tensile wing crack

7.6 Comparison between Carrara Marble and molded gypsum

The scanning electron microscope studies provide a powerful tool in revealing how the microstructural material characteristics and their evolution influence the eventual macroscopic fracturing behavior as observed in experiments. The microscope imaging work conducted on hair-line cracks in molded gypsum and white patches in Carrara Marble, both of which develop prior to the development of observable cracks (visible to unaided eyes) reveal a number of similarities and differences with regard to their formation and evolution. The key results are summarized in table 7.2, which will form the basis for discussing the observed fracturing and coalescence behavior later in chapter 9.

		Hair-line crack in molded gypsum	White patch in Carrara Marble
Similarities	Time of occurrence	The respective development is the first sign observed in the specimen in response to the applied loading.	
	Structure	Dominant individual crack segments flanked by multiple microcracks	
	Microcrack distribution density	Microcrack density is high in the close vicinity of the central dominant microcracks, and decreases as the distance from the central dominant microcracks increases.	
Differences	Crack types	Mostly intergranular cracks, few intragranular cracks.	Both intergranular and intragranular cracks are common
	Width of microcracking zone	Relatively narrower – less than 100 μm wide	Relatively wider – around 500 μm wide
	Overall microcrack density	Lower	Higher
	Applied stress required	The development from a hair-like tensile crack to an observable tensile crack takes place over a very small applied stress increment (<1 MPa).	The difference of the applied stresses between the initiation of white patch and the eventual formation of macroscopic observable cracks is larger (20 to 50 MPa).
	Microscopic evolution to become observable cracks	Increased loading leads to lengthening and coalescence of the central dominant microcrack segments and increase of the crack aperture. The microcrack density does not increase significantly.	Increased loading lengthens the central dominant cracks and increases the microcrack density beside it (intensification of the white color macroscopically), which are then followed by an increase of crack aperture.

Table 7.2 – Summary of similarities and differences in the development of hair-line cracks in molded gypsum and white patches in Carrara Marble.

CHAPTER 8 – Numerical Modeling

8.1 Introduction

This chapter is divided into two parts. The first part describes the strain-based crack initiation criterion and the stress-based crack initiation criterion proposed previously by the MIT rock mechanics group. The second part shows some modeling results obtained by using the in-house numerical code FROCK to model fracturing and coalescence behavior.

8.2 Crack initiation criteria proposed by the MIT rock mechanics

8.2.1 Strain-based crack initiation criterion by Reyes

The model formulated by Reyes combines a smeared crack/damage mechanics approach with a strain based failure criterion (Reyes, 1991, Reyes & Einstein, 1991). New cracks are assumed to initiate at locations of high strain concentration, more specifically the maximum tensile principal strain.

The stiffness degradation model is the basis of the whole analytical model:

$$\sigma_{ij} = (1 - D) C_{ijkl}\, \varepsilon_{kl} \tag{8.1}$$

where σ_{ij}, ε_{kl}, C_{ijkl} are components of the stress, strain and elastic constitutive tensors respectively. D is an internal state variable (damage variable) used to quantify the damage in the material and is dependent on the equivalent strain ε_{eq}:

$$D = \begin{cases} 0 & for \;\; \varepsilon_o \le \varepsilon_{eq} \le \dfrac{\varepsilon_o}{A} \\ H(\varepsilon_{eq}) & for \;\; \varepsilon_o \le \varepsilon_{eq} \le \dfrac{\varepsilon_o}{A} \\ H(\dfrac{\varepsilon_o}{A}) & for \;\; \dfrac{\varepsilon_o}{A} \le \varepsilon_{eq} \end{cases} \tag{8.2}$$

where

$$H(\varepsilon_{eq}) = 1 - \exp\left[A\left(1 - \frac{\varepsilon}{\varepsilon_o} \right) \right] \tag{8.3}$$

and the equivalent strain (ε_{eq}) is defined as:

$$\begin{aligned} \varepsilon_{eq} &= \varepsilon_1 \qquad for \quad \varepsilon_{eq} > 0 \\ \varepsilon_{eq} &= 0 \qquad for \quad \varepsilon_{eq} \le 0 \end{aligned} \tag{8.4}$$

where ε_1 is the maximum principal tensile strain, ε_o is a damage threshold value, and the parameter A controls the rate at which D varies with strain. The authors assumed that a saturation value of D less than **1** exists, which corresponds to the damage at the peak of the stress-strain curve. This saturation value, D_{sat} is given by:

$$D_{sat} = \frac{E\varepsilon_o}{A} \frac{1}{\exp(1 - A)} \tag{8.5}$$

For the molded gypsum material tested, the authors calibrated the model to obtain ε_o = 0.0024, A = 0.785 and D_{sat} = 0.19. This set of parameters was then used to simulate damage evolution for different flaw pair geometries. For each geometry, they obtained a series of damage contour plots at different load levels (e.g. figures 8.1 & 8.2), and the stress value associated with the occurrence of coalescence. The latter was defined at the stress level when the value of the damage variable D in the region between the flaw tips reached the saturation value D_{sat} (Note the distribution of contour level 8 corresponding to D = 0.190 in figure 8.2).

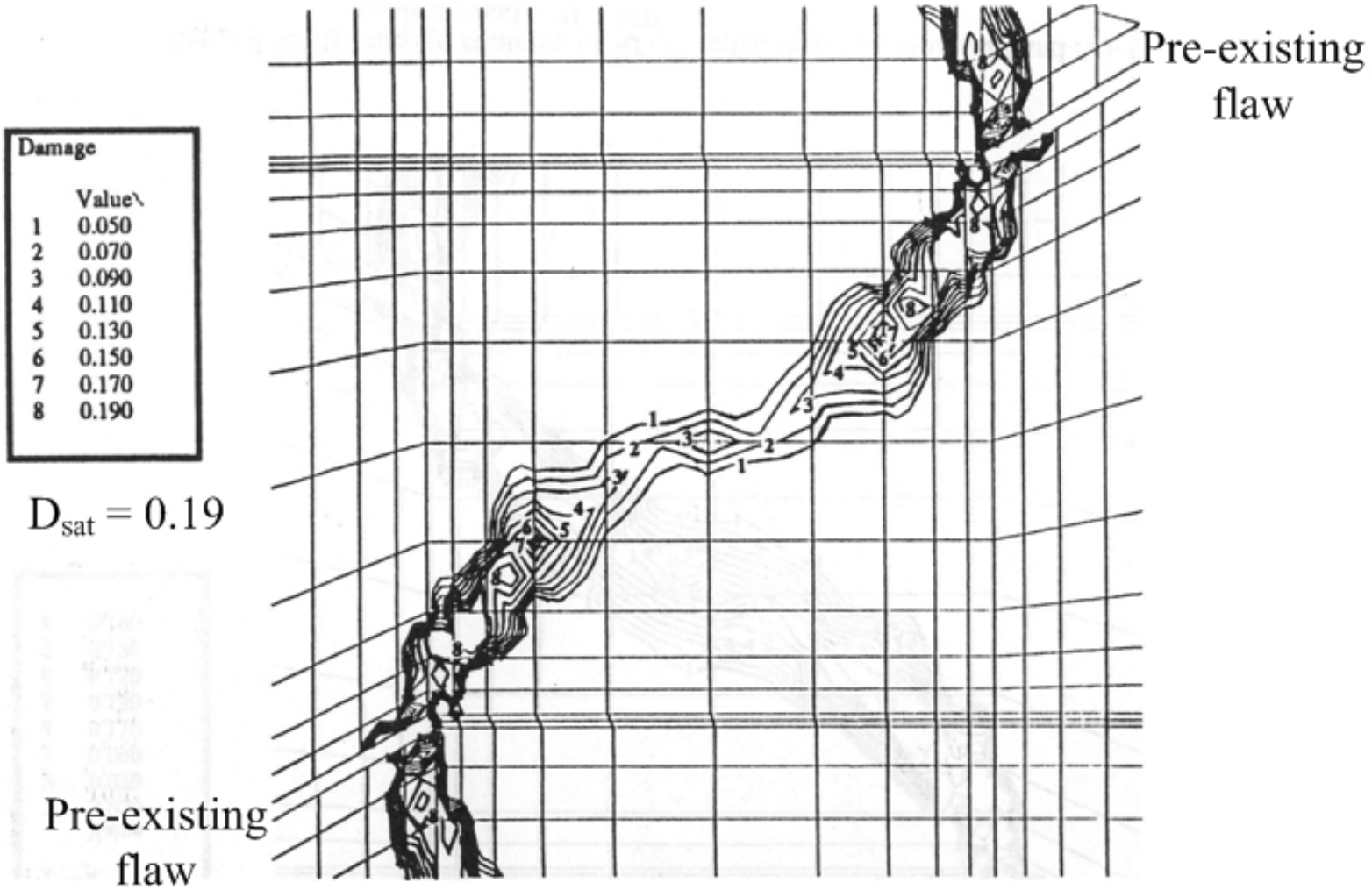

Figure 8.1 – Damage contours for flaw pair 2a-30-15 at applied uniaxial stress level of 20.8MPa.

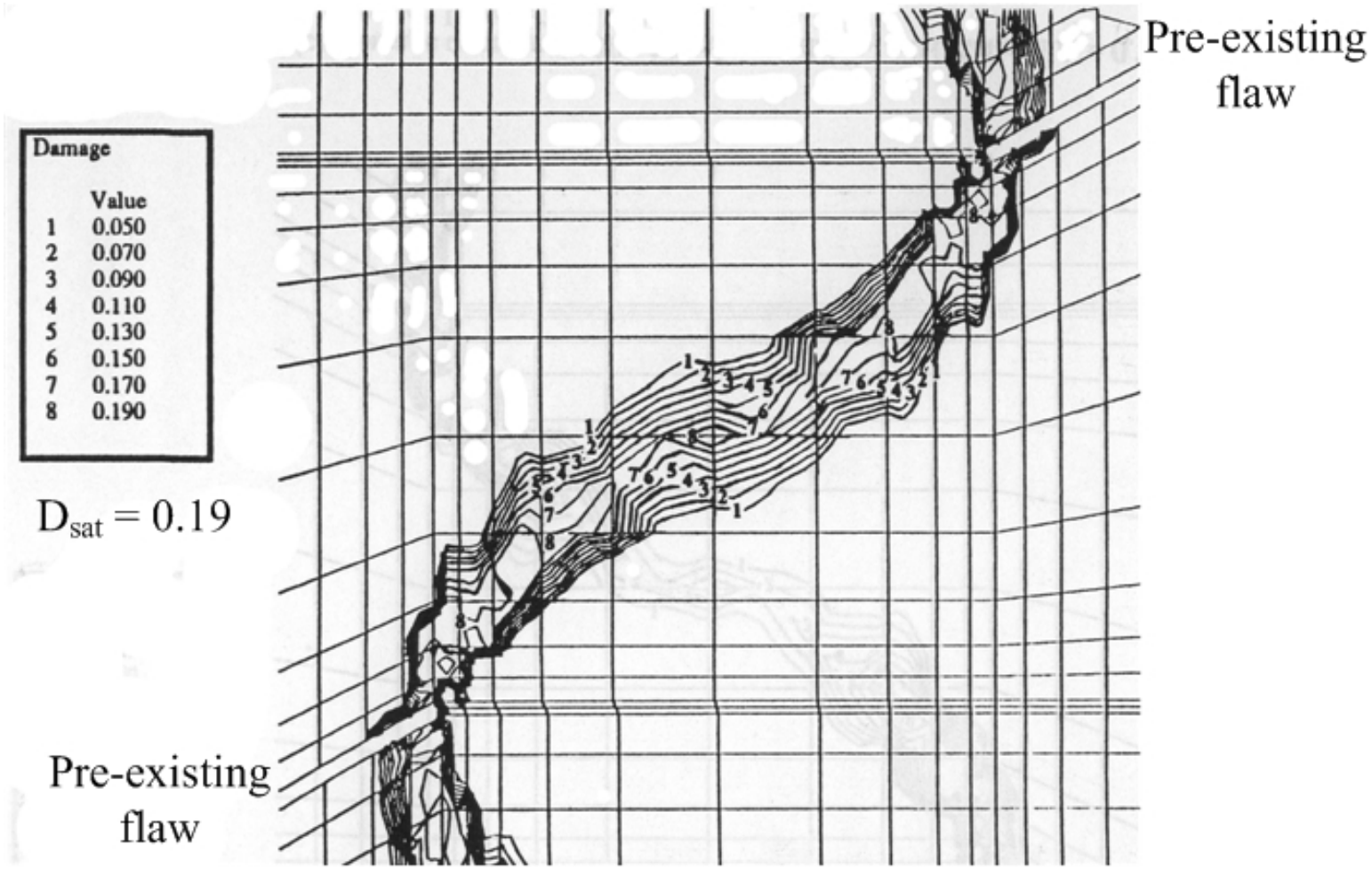

Figure 8.2 – Damage contours for flaw pair 2a-30-15 at applied uniaxial stress level of 21.4MPa. The inner flaw tips have been linked up by a continuous region of damage level $D = D_{sat} = 0.19$.

8.2.2 Stress-based crack initiation criterion by Bobet

The underlying principle of this stress-based crack initiation criterion proposed by Bobet is a comparison of the local stress state with the strength of the material, rather than the consideration of the stress intensity factors (SIFs)[1]. More specifically, the tangential and shear stresses at the boundary of a core region centered around a flaw tip are first computed (Bobet & Einstein, 1998b, Bobet, 2000). The radius r_0 of the core region or plastic zone is considered to be of cylindrical shape (figure 8.4 a). The **shape** of the core region is taken "*as independent of the magnitude and type of external loading, and of the geometry of the problem.*" The size r_0 however "*will depend on the local stress conditions around the tip of the flaw, but for simplicity it is made dependent on the exterior mode of loading; that is, the core radius will be different in uniaxial compression compared to biaxial compression, or to tension.*" In addition, the size r_0 is also material-dependent.

[1] The stress field in any linear elastic cracked body can be given by the expression below (Anderson, 2005).

$$\sigma_{ij} = \left(\frac{k}{\sqrt{r}} \right) f_{ij}(\theta) + \sum_{m=0}^{\infty} A_m r^{\frac{m}{2}} g_{ij}^{(m)}(\theta)$$

where

σ_{ij} = stress tensor
r and θ are defined in figure on the right
k = constant
f_{ij} = dimensionless function of θ in the leading term

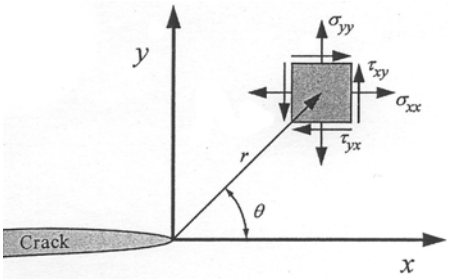

Figure 8.3 – Region around a flaw tip.

The three modes of loading as shown in figure 2.3 produce the $1/\sqrt{r}$ singularity at the flaw tip and the proportionality constants k and f_{ij} depend on the mode. It has been a common practice to replace k by the stress intensity factor (SIF) K, where $K = k\sqrt{2\pi}$. The SIFs for the three modes of loading as shown in figure 2.3 are denoted by K_I, K_{II}, K_{III} respectively.

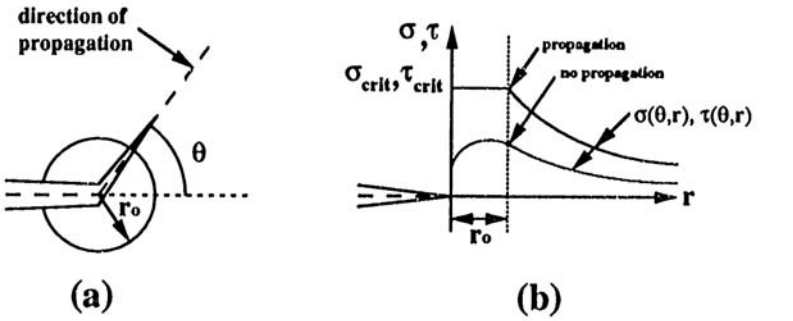

propagation criterion

tensile	shear
$\frac{\delta \sigma_\theta}{\delta \theta}\Big\|_{r=r_o} = 0$	$\frac{\delta \tau}{\delta \theta}\Big\|_{r=r_o} = 0$
$\frac{\delta^2 \sigma_\theta}{\delta \theta^2}\Big\|_{r=r_o} > 0$	$\frac{\delta^2 \tau}{\delta \theta^2}\Big\|_{r=r_o} < 0$
$\sigma = \sigma_{crit}$	$\tau = \tau_{crit}$

(c)

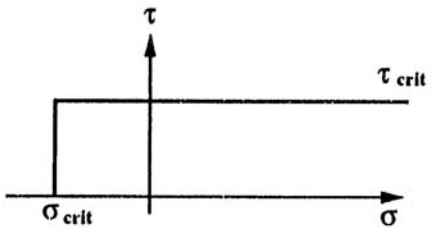

(d)

Figure 8.4 – Crack initiation and propagation criterion. (a) core region, (b) crack propagation criteria, (c) mathematical formulation, (d) failure envelope (Bobet & Einstein, 1998b).

The computed tangential and shear stresses are then compared with the material strengths. The comparison can lead to two possibilities as shown in figure 8.4 b:

(1) No crack propagation case – stresses are below the critical values at the boundary of the core region,

(2) Crack propagation case – stresses at the boundary are equal to the critical values. The core region is fully plastified and crack propagation occurs.

The above statements are represented in mathematical form shown in figure 8.4 c.

- A tensile crack will initiate in the direction perpendicular to the direction in which the tangential stress reaches a minimum (most negative). This direction gives the initiation angle θ. Hence,

$$\left.\frac{\partial \sigma_\theta}{\partial \theta}\right|_{r=r_0} = 0 \qquad \text{and} \qquad \left.\frac{\partial^2 \sigma_\theta}{\partial \theta^2}\right|_{r=r_0} > 0 \tag{8.6}$$

- A tensile crack will initiate when the tangential tensile stress reaches a critical value ($\boldsymbol{\sigma_{crit}}$) which is material dependent:

$$\left(\sigma_\theta\right)_{\text{minimum}}\Big|_{r=r_0} = \sigma_{\text{crit}} \tag{8.7}$$

- A shear crack will initiate in a direction (given by the angle θ) in which the absolute value of the shear stress attains a maximum; then,

$$\left.\frac{\partial \tau}{\partial \theta}\right|_{r=r_0} = 0 \qquad \text{and} \qquad \left.\frac{\partial^2 |\tau|}{\partial \theta^2}\right|_{r=r_0} > 0 \tag{8.8}$$

- A shear crack will initiate when the maximum shear stress reaches a critical value ($\boldsymbol{\tau_{crit}}$) which is material dependent:

$$\left(\tau\right)_{\text{maximum}}\Big|_{r=r_0} = \tau_{\text{crit}} \tag{8.9}$$

As noted above, three material parameters are needed: the critical tensile strength $\boldsymbol{\sigma_{crit}}$, the critical shear strength $\boldsymbol{\tau_{crit}}$, and the core radius $\boldsymbol{r_0}$. Figure 8.4 d shows the corresponding failure envelope of the material showing the relationship of $\boldsymbol{\sigma_{crit}}$ and $\boldsymbol{\tau_{crit}}$.

As noted in many other stress-based crack initiation criteria contained in Appendix Q, stress-dependent strength parameters are often considered instead. The authors, however, concluded from their experience that the relations proposed in figure 8.4 are sufficient as a first approximation (Bobet & Einstein, 1998b, Bobet, 2000).

8.3 Fundamentals of FROCK

The crack initiation criterion proposed by Bobet as described above was incorporated into the code FROCK (Fractured Rock), which was developed by Chan et al. (1990) and extensively revised by Bobet and Einstein (1998b). FROCK is a two-dimensional Hybridized Indirect Boundary Element Method, which is a class of the Displacement Discontinuity Method (DDM), first introduced by Crouch (1976).

Details of FROCK are contained in the thesis by Bobet (1997). See also reviews by Bobet and Einstein (1998b), and Vásárhelyi and Bobet (2000). The purpose of this section is to provide the basics about the principle and the modeling procedures of FROCK. The internal and external boundaries of the medium are first divided into 'N' straight elements (figure 8.5 a). Depending on the element type, each element has one or more collocation points (reference points). Each collocation point can have two movements – sliding and opening. Figure 8.5 b shows the two fundamental variables, V_1 and V_2 which represent the sliding and opening movements respectively of a collocation point. Compression and tension stresses are taken as positive and negative respectively (figure 8.5 c).

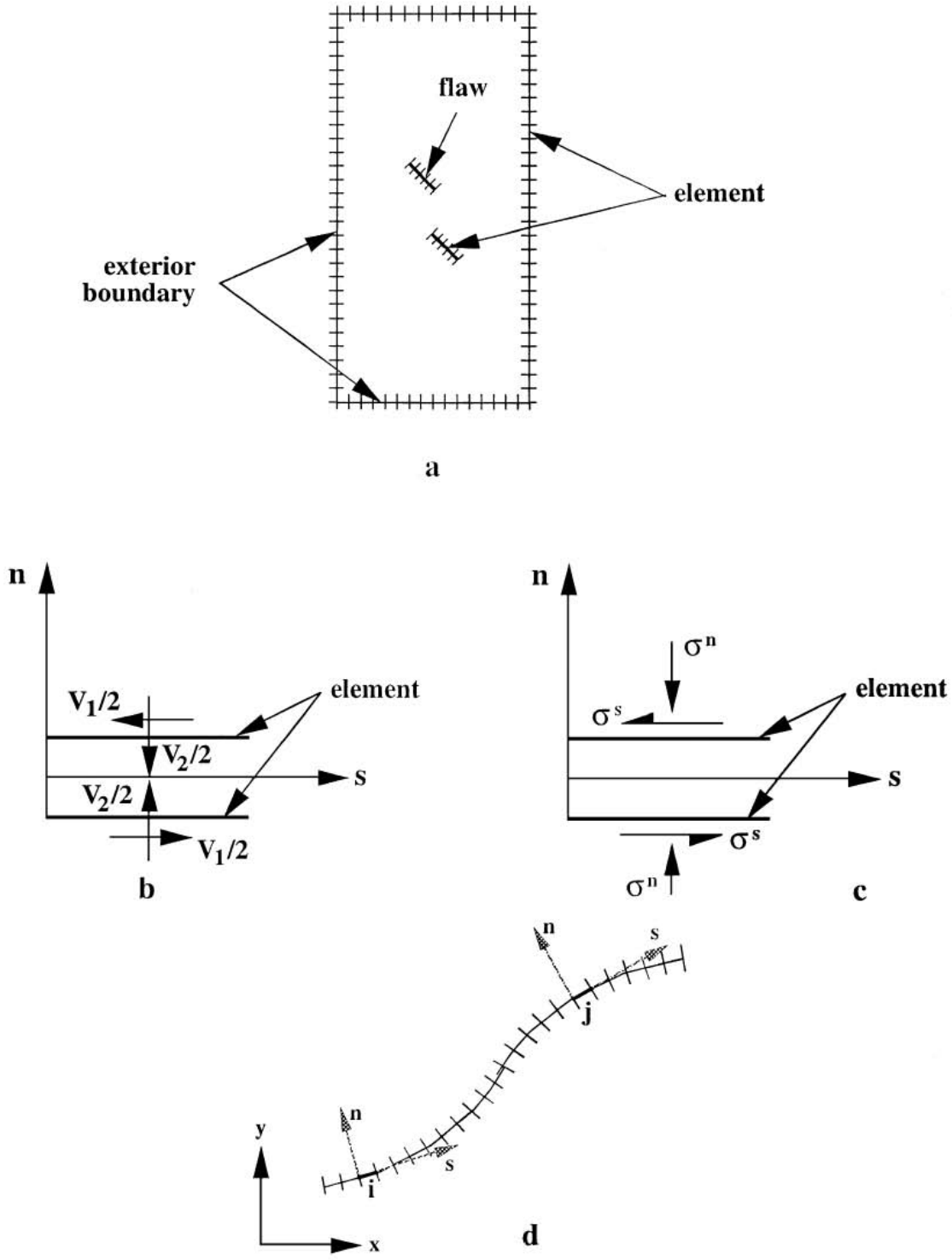

Figure 8.5 – DDM discretization and element definition. (a) discretization of a specimen with boundary elements, (b) fundamental variables, (c) stresses, (d) discretization with boundary elements (Vásárhelyi & Bobet, 2000).

If the solid is divided into 'N' elements, and each element has one or more collocation points arranged from 1 to M, the stresses and displacements at a particular collocation point 'm' in the local coordinate system (w.r.t. the element) are given by:

$$\sigma_{m,k} = \left\{ \sigma_{m,s}, \sigma_{m,n}, u_{m,s}, u_{m,n} \right\} \text{ for } m = 1 \text{ to } M, \text{ and } k = 1 \text{ to } 4 \tag{8.10}$$

Because of the assumption of elasticity in the model, the stresses or displacements at any given point in the body are obtained by linear superposition of the contributions of all the elements (figure 8.5 d), i.e.

$$\sigma_{m,k} = A_{m,k,j} \, V_j \tag{8.11}$$

where Vj is a vector with the opening and sliding magnitudes of all the collocation points ranging from 1 to $2M$. $A_{m,k,j}$ is the influence function of the fundamental variable 'j', of the stress 'k' of the collocation point 'm'.

The above is based on the assumption that any analytical solution is known for the stresses and/or displacements at any point in the solid due to a unit change of the fundamental variables of a given collocation point and element. Equation (8.11) can be written in incremental form:

$$\sigma_{m,k}^{\Delta t} = A_{m,k,j} \, V_j^{\Delta t} \tag{8.12}$$

As noted by the authors, equation (8.12) represents a linear system of '$4M$' equations. By definition, displacements and/or stresses at each collocation point at the boundaries of the medium are known, which provide '$2M$' known values. Since each collocation point has only two movements, the number of unknown variables $V_j^{\Delta t}$ is '$2M$'. A system of '$2M$' linear equations with '$2M$' unknowns can be extracted from equation (8.12) and solved for $V_j^{\Delta t}$. Once $V_j^{\Delta t}$ is known, the remaining '$2M$' equations will give the rest of the undefined boundary conditions. The stresses and displacements at any other point in the continuum can also be obtained from equation (8.11).

8.4 Numerical results

The scope of the present numerical study is to model the crack coalescence processes for flaw pairs with FROCK. The objectives are to verify the modeling results against the present experimental study, and to identify the probable areas where the code can be modified. With regard to these objectives, the modeling work at present is limited to molded gypsum. The Carrara Marble experiments are not included. The main reason is that the result database that exists is for tests with gypsum, which allows for the sensitivity analysis carried out in this study.

8.4.1 Input parameters

Plain strain conditions are assumed in FROCK, but plane stress conditions can be easily assessed by modifying the material elastic constants:

$$E(\textit{plane stress}) = \frac{(1+2\nu)}{(1+\nu)^2} E \quad ; \quad \nu(\textit{plane stress}) = \frac{\nu}{(1+\nu)}$$

where E and ν are the Young's modulus and the Poisson's ratio respectively (to use without modification for plane strain) (Bobet, 1997). The medium in which the flaws are embedded is assumed to be homogeneous, isotropic and linear elastic. The values of the input parameters for molded gypsum are summarized in table 8.2.

Input parameters	Values	Input parameters	Values
Young's modulus $\boldsymbol{E}$	5960 MPa	Radius of core region $\mathbf{r_0}$	0.23 mm
Poisson's ratio $\boldsymbol{\nu}$	0.15	Critical tensile strength $\boldsymbol{\sigma_{crit}}$	-18.1 MPa
Friction coefficient of newly initiated cracks $\boldsymbol{\mu}$	0.7	Critical shear strength $\boldsymbol{\tau_{crit}}$	29.5 MPa

Table 8.2 – Input parameters used for modeling fracturing and crack coalescence processes in gypsum with FROCK (Bobet, 1997, Bobet & Einstein, 1998b).

In table 8.2, the values of E, ν and μ on the left are measurable material properties, while the values of σ_{crit}, τ_{crit} and r_0 on the right are obtained by Bobet based on a back-fitting analysis which compared his own experimental results with the numerical results. These three particular parameters are not directly related to any measurable macroscopic strength parameters.

8.4.2 Modeling results

The modeling results obtained in the present FROCK study, along with the present experimental results and the previous FROCK results obtained by Bobet are shown in figures 8.7 to 8.24. The results shown in the figures include the crack initiation stresses σ_c and coalescence patterns. Table 8.3 summarizes the flaw pair geometries that are tested.

Flaw pair geometry [1]		**Modeling result in the present study**	**Modeling result by Bobet**	**Experimental result obtained from the present study**
$\beta - s - c$	$L - \beta - \alpha$			
45-0-2a	2a-45-0	fig. 8.7	fig. 8.8	fig. 8.9
45-a-2a	2a-45-27	fig. 8.10	fig. 8.11	N.A. [4]
45-2a-2a	2a-45-45	fig. 8.12	fig. 8.13	N.A. [4]
30-a-2a	2a-30-27	fig. 8.14	fig. 8.15	fig. 8.16 [2]
30-0-2a	2a-30-0	fig. 8.17	N.A. [3]	fig. 8.18
30-0-a	a-30-0	fig. 8.19	N.A. [3]	fig. 8.20
60-0-2a	2a-60-0	fig. 8.21	N.A. [3]	fig. 8.22
75-0-2a	2a-75-0	fig. 8.23	N.A. [3]	fig. 8.24

[1] Flaw pair geometries are represented by both conventions as shown in figure 8.6.

[2] Experimental result corresponding to the closest flaw pair geometry is shown instead.

[3] Corresponding coalescence figures are not available (N.A.) in Bobet's thesis

[4] Corresponding flaw pair geometries are not tested in the present experimental study

Table 8.3 – Summary of flaw pair geometries modeled by FROCK.

Note that the present experimental studies on crack coalescence were conducted on wide flaws (aperture size 0.05”), while those studied by Bobet were conducted on narrow flaws (aperture size 0.004”). Also, in describing the flaw pair geometries, Bobet adopted the β–s–c convention (figure 8.6 a) and the present study adopted the L–β –α convention (figure 8.6 b). In the subsequent discussion on the following pages, flaw pair geometries will be represented by both conventions where appropriate.

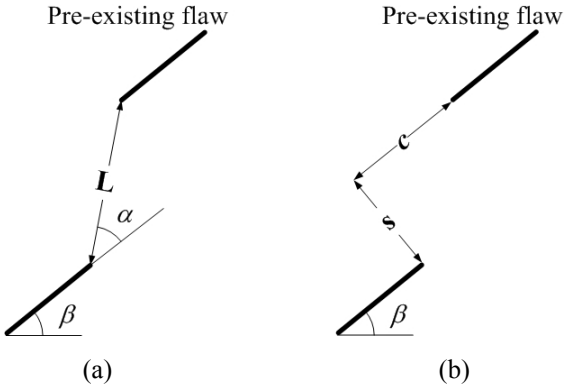

Figure 8.6 – Flaw pair geometry defined by (a) flaw inclination angle $\boldsymbol{\beta}$, bridging angle $\boldsymbol{\alpha}$ and ligament length $\boldsymbol{L}$, or (b) flaw inclination angle $\boldsymbol{\beta}$, spacing $\boldsymbol{s}$ and continuity $\boldsymbol{c}$.

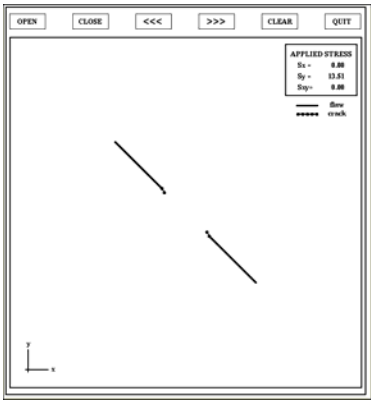 **(a) σ_c = 13.51 MPa**	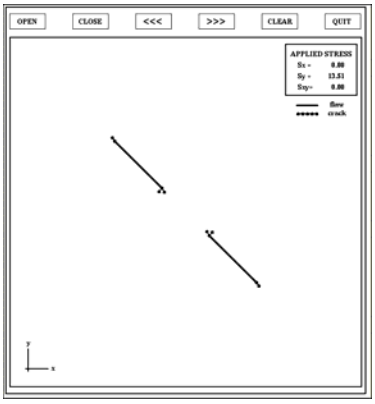 (b) σ = 13.51 MPa	(a) shear crack initiated (b) internal tensile wing cracks initiated
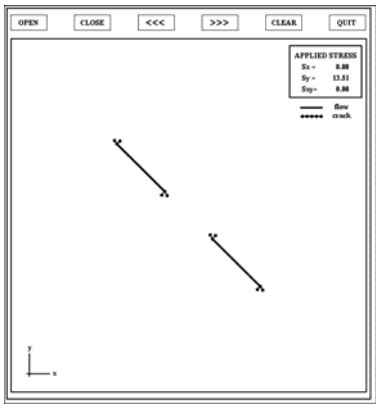 (c) σ = 13.51 MPa	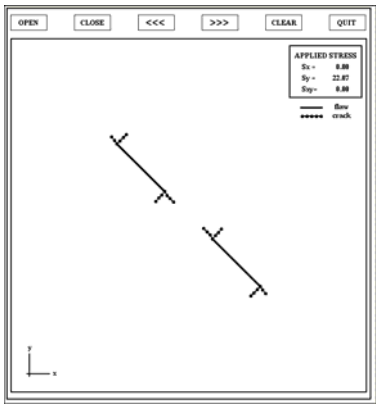 (d) σ = 22.07 MPa	(c) external tensile wing cracks initiated (d) internal shear cracks propagated
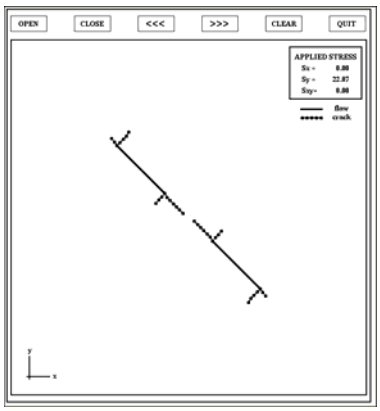 (e) σ = 22.07 MPa	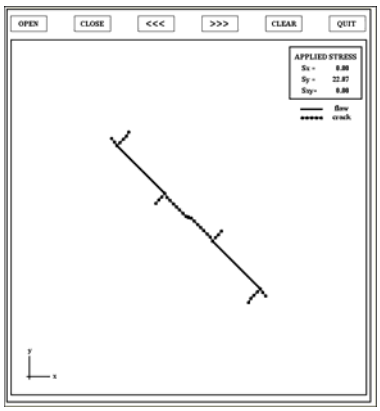 (f) σ = 22.07 MPa	(e) internal shear cracks propagated (f) coalescence

Figure 8.7 – Modeling of crack initiation, propagation and coalescence in gypsum for flaw pair geometry 45-0-2a ($\beta - s - c$) or 2a-45-0 ($L - \beta - \alpha$) obtained in the present study.

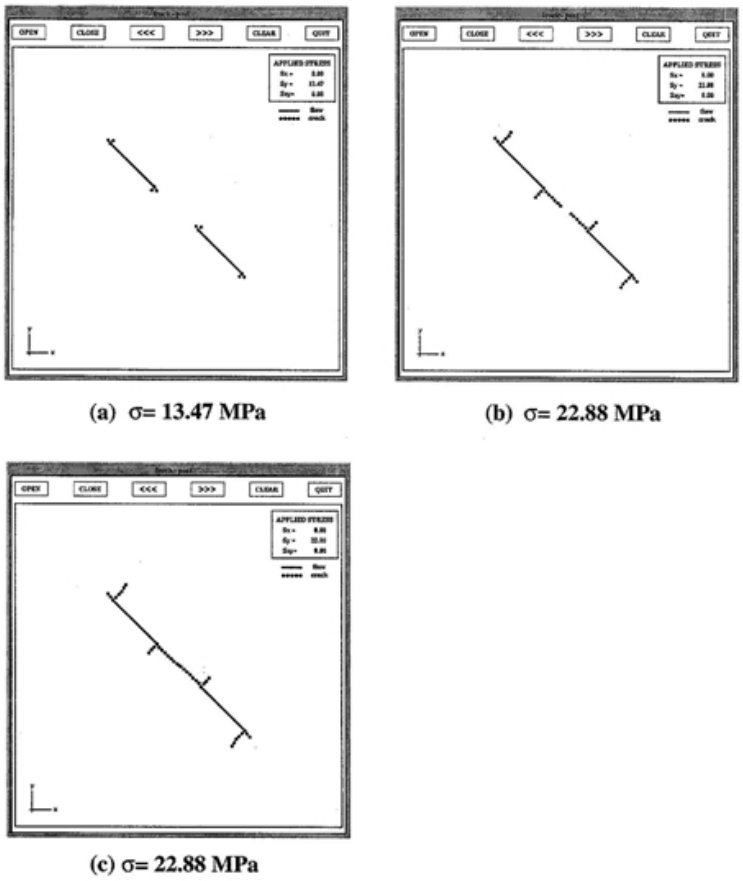

Figure 8.8 – Modeling of crack initiation, propagation and coalescence in gypsum for flaw pair geometry 45-0-2a ($\beta - s - c$) or 2a-45-0 ($L - \beta - \alpha$) by Bobet and Einstein (1998b).

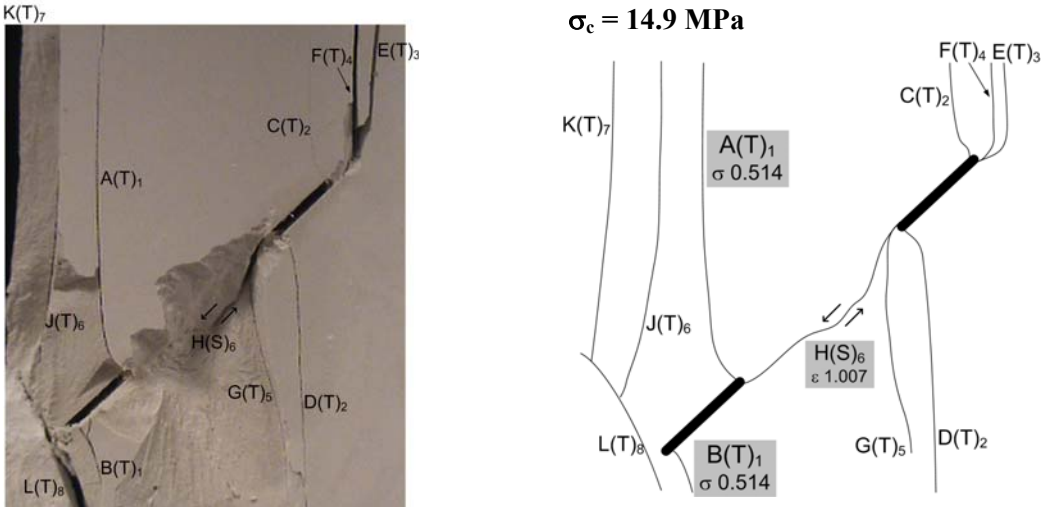

(a) actual specimen (b) sketch

Figure 8.9 – Fracturing and coalescence patterns in gypsum for flaw pair geometry 45-0-2a ($\beta - s - c$) or 2a-45-0 ($L - \beta - \alpha$).

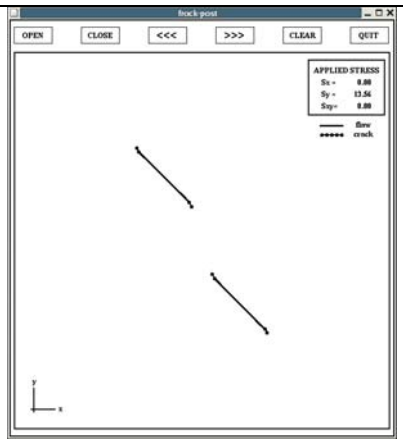 **(a) σ_c = 13.56 MPa**	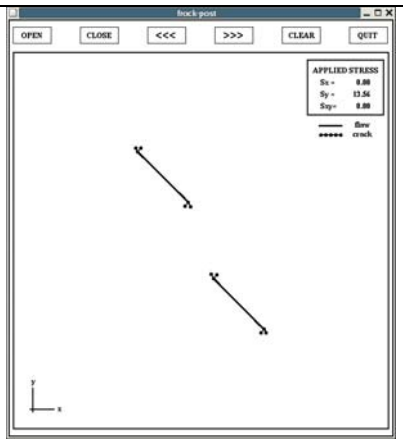 (b) σ = 13.56 MPa	(a) shear crack initiated (b) tensile wing cracks initiated
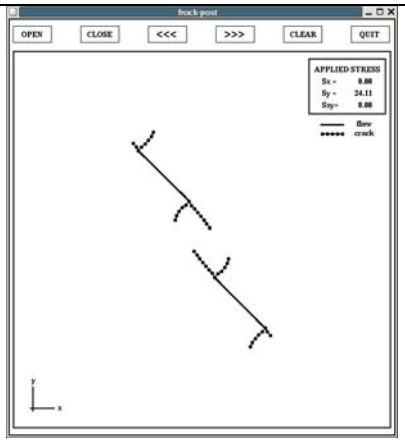 (c) σ = 24.11 MPa	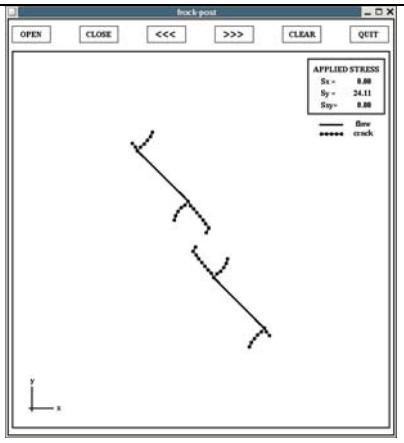 (d) σ = 24.11 MPa	(c) cracks propagated (d) tensile cracks initiated from the internal shear cracks
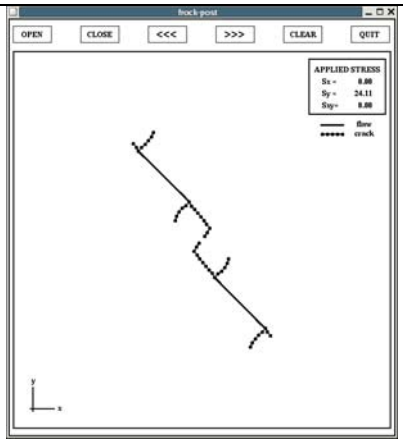 (e) σ = 24.11 MPa	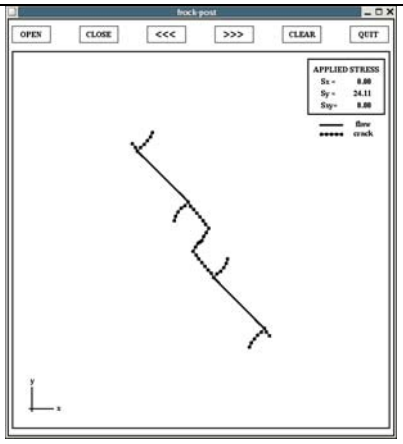 (f) σ = 24.11 MPa	(e) the tensile cracks just initiated from the internal shear cracks propagated (f) coalescence

Figure 8.10 – Modeling of crack initiation, propagation and coalescence in gypsum for flaw pair geometry 45-a-2a ($\beta - s - c$) or 2a-45-27 ($L - \beta - \alpha$) obtained in the present study.

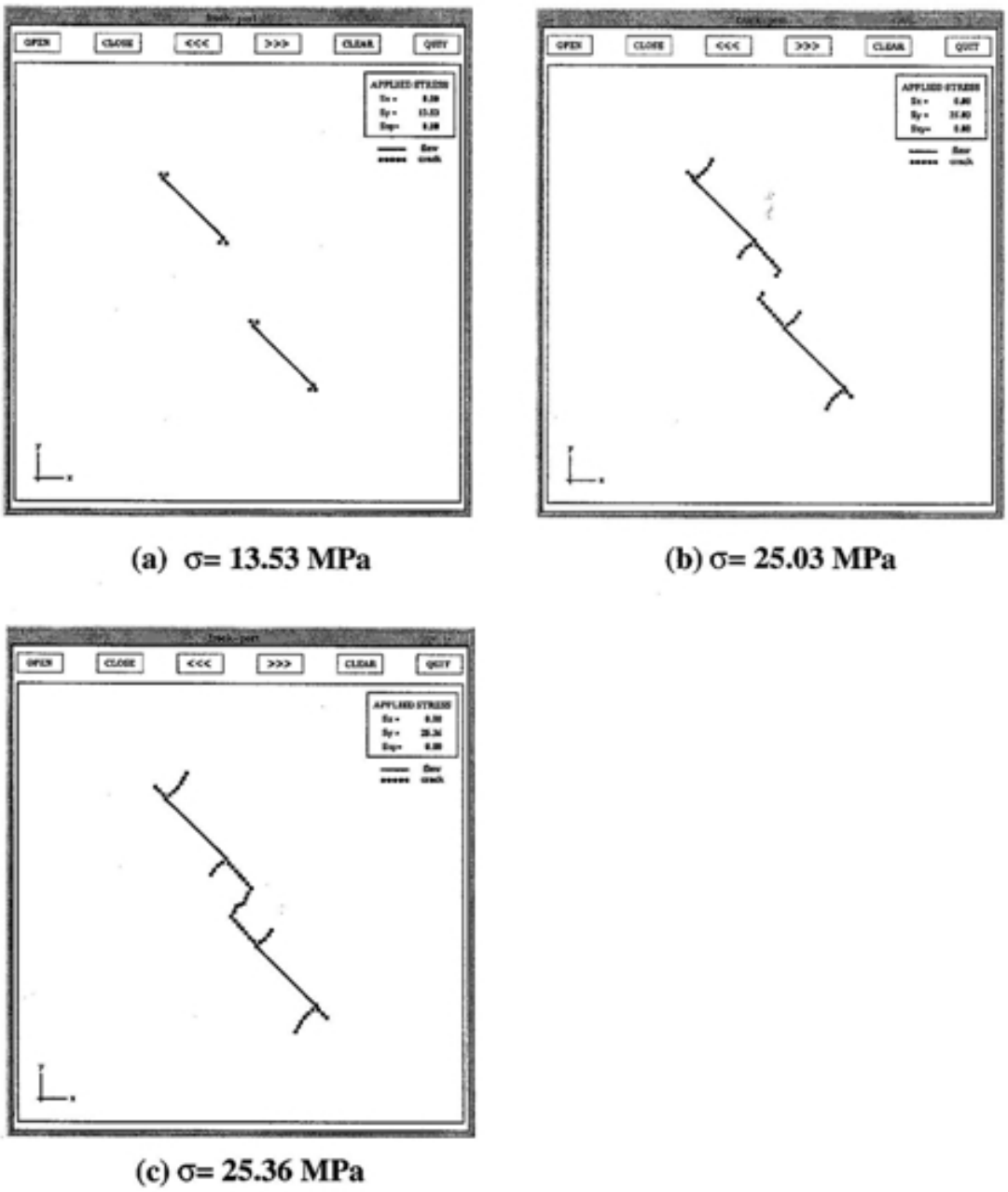

Figure 8.11 – Modeling of crack initiation, propagation and coalescence in gypsum for flaw pair geometry 45-a-2a ($\beta - s - c$) or 2a-45-27 ($L - \beta - \alpha$) by Bobet and Einstein (1998b).

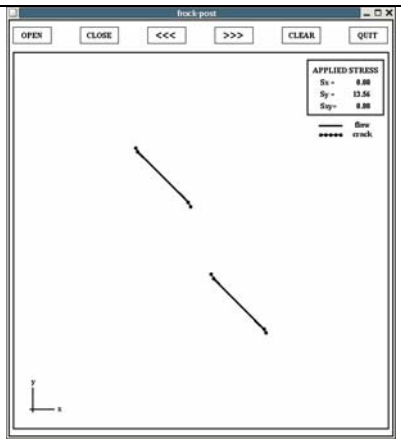 **(a) σ_c = 14.08 MPa**	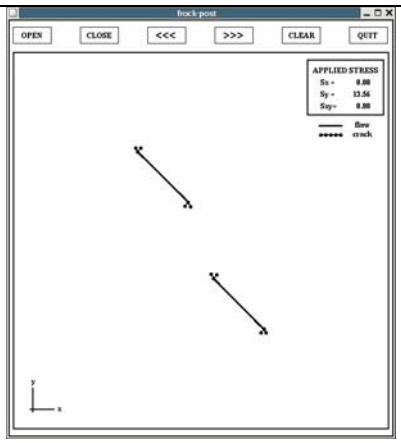 (b) σ = 14.08 MPa	(a) shear crack initiated (b) tensile wing cracks initiated
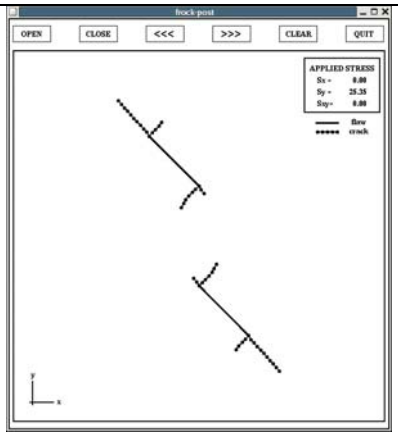 (c) σ = 25.35 MPa	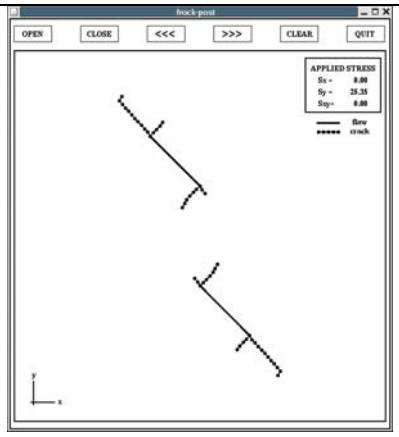 (d) σ = 25.35 MPa	(c) cracks propagated (d) tensile cracks initiated from the outer shear cracks
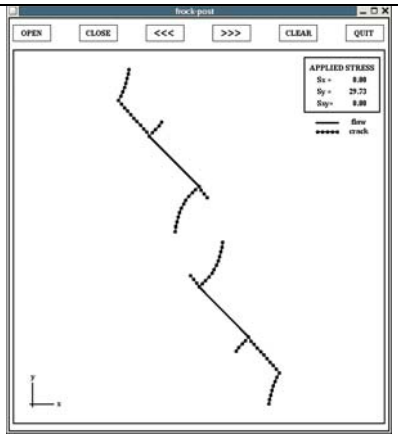 (e) σ = 29.73 MPa	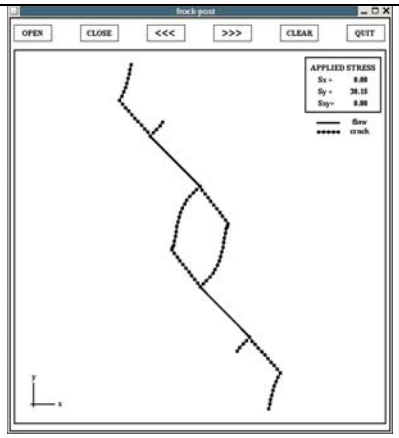 (f) σ = 30.15 MPa	(e) cracks propagated (f) coalescence

Figure 8.12 – Modeling of crack initiation, propagation and coalescence in gypsum for flaw pair geometry 45-2a-2a ($\beta - s - c$) or 2a-45-45 ($L - \beta - \alpha$) obtained in the present study.

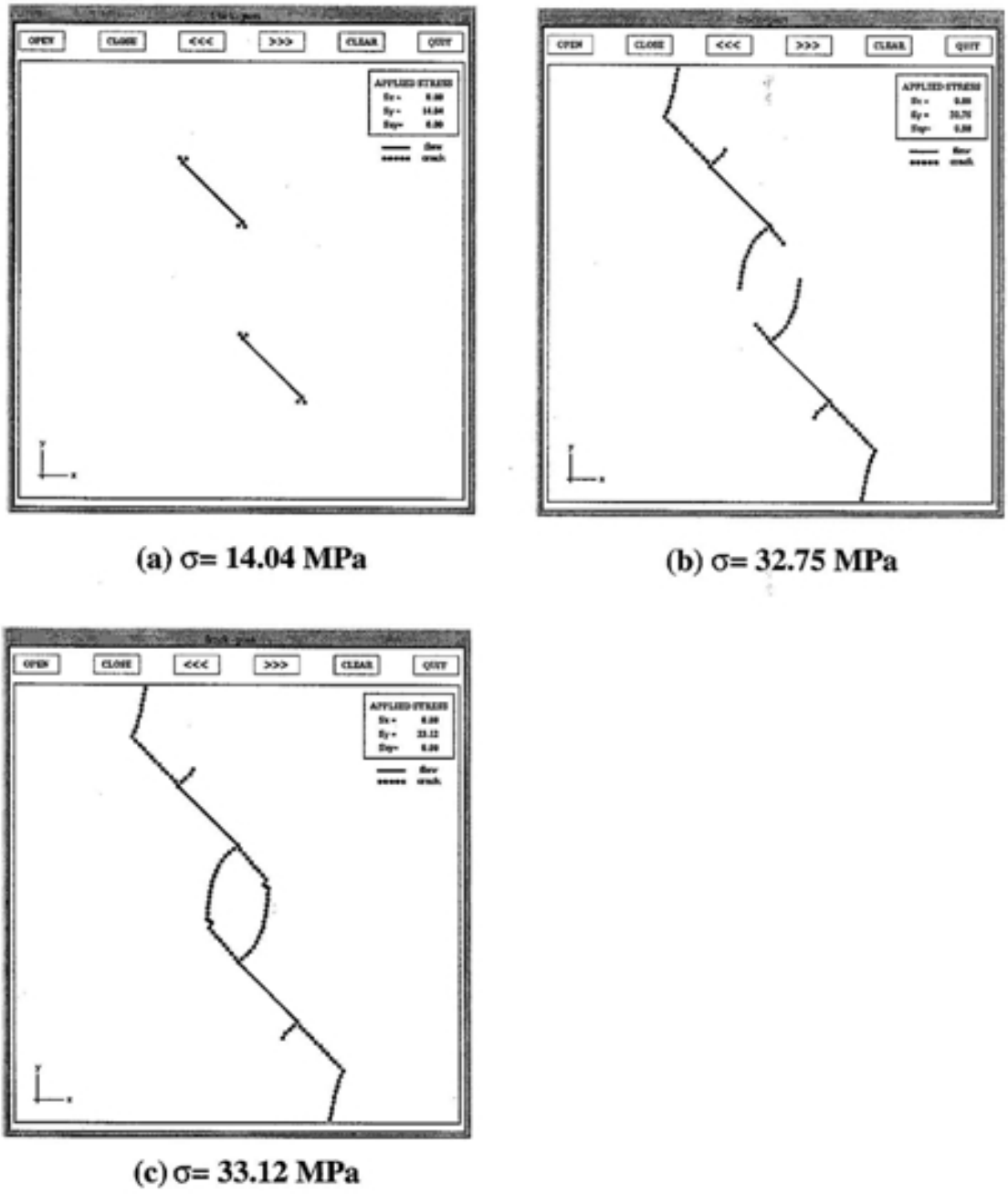

Figure 8.13 – Modeling of crack initiation, propagation and coalescence in gypsum for flaw pair geometry 45-2a-2a ($\beta - s - c$) or 2a-45-45 ($L - \beta - \alpha$) by Bobet and Einstein (1998b).

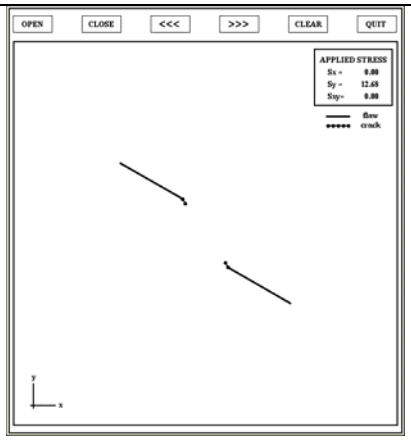 **(a) σ_c = 12.68 MPa**	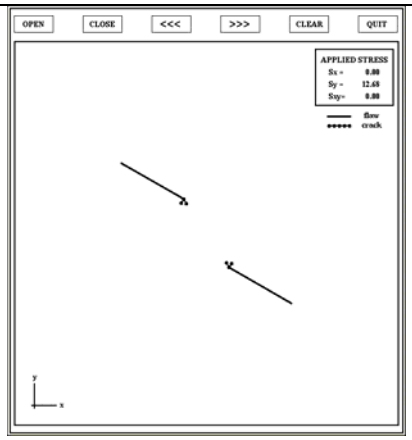 (b) σ = 12.68 MPa	(a) internal shear crack initiated (b) internal tensile wing cracks initiated
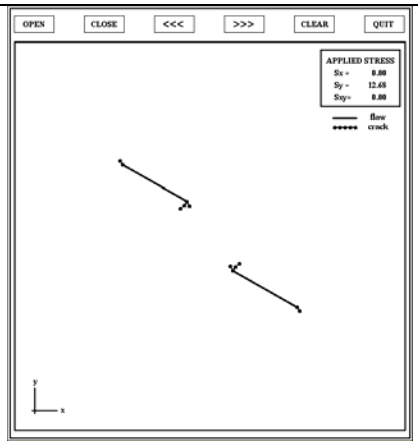 (c) σ = 12.68 MPa	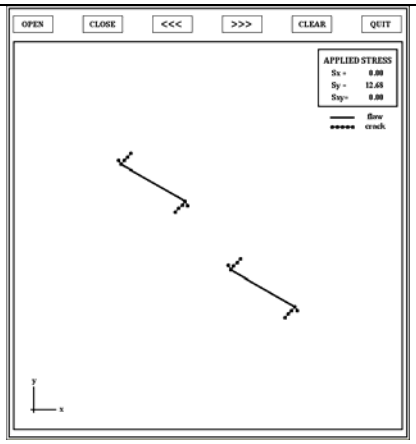 (d) σ = 12.68 MPa	(c) outer shear cracks initiated (d) outer tensile wing cracks initiated
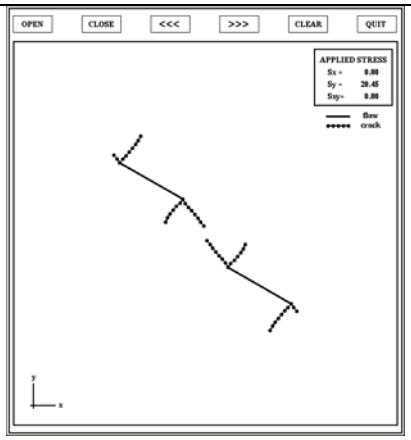 (e) σ = 20.45 MPa	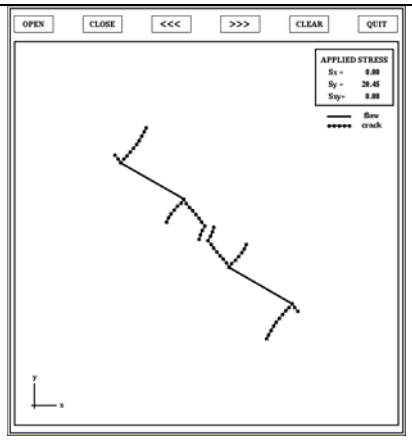 (f) σ = 20.45 MPa	(e) cracks propagated (f) no coalescence

Figure 8.14 – Modeling of crack initiation, propagation and coalescence in gypsum for flaw pair geometry 30-a-2a ($\beta - s - c$) or 2a-30-27 ($L - \beta - \alpha$) obtained in the present study.

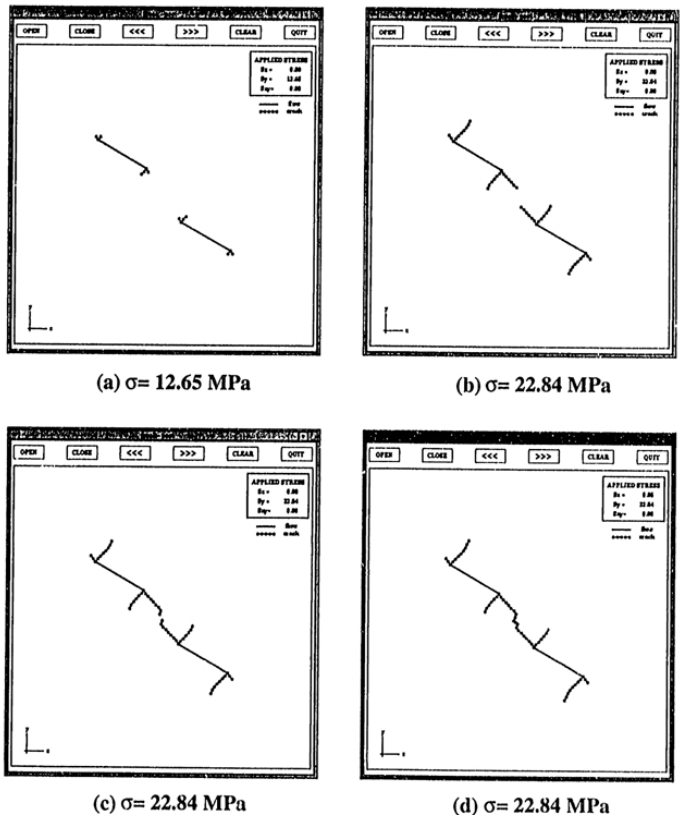

Figure 8.15 – Modeling of crack initiation, propagation and coalescence in gypsum for flaw pair geometry 30-a-2a ($\beta - s - c$) or 2a-30-27 ($L - \beta - \alpha$) by Bobet (1997).

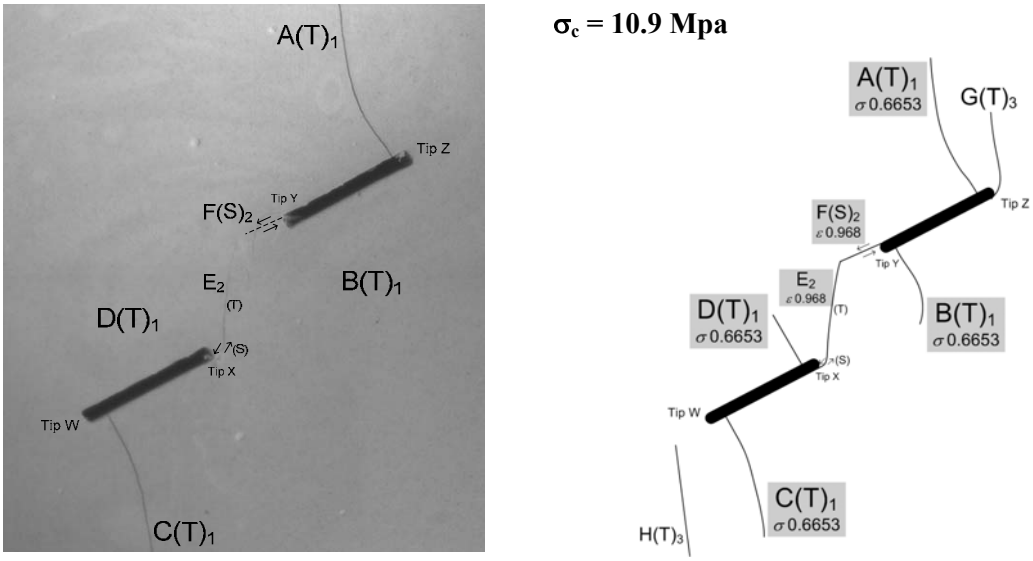

(a) actual specimen (b) sketch

Figure 8.16 – Fracturing and coalescence patterns in gypsum for flaw pair geometry 30-a-1.7a ($\beta - s - c$) or 2a-30-30 ($L - \beta - \alpha$). Note that cracks G and H which appeared later are not shown in figure (a).

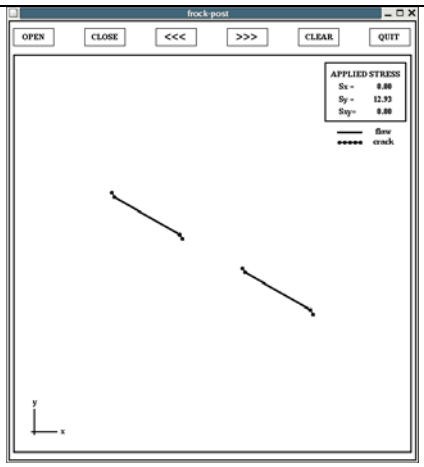 **(a) σ = 12.93 MPa**	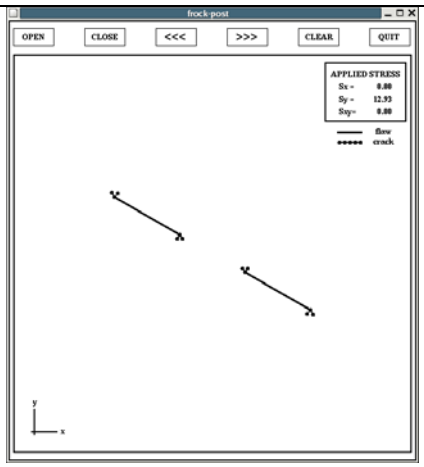 (b) σ = 12.93 MPa	(a) shear cracks initiated (b) tensile wing cracks initiated
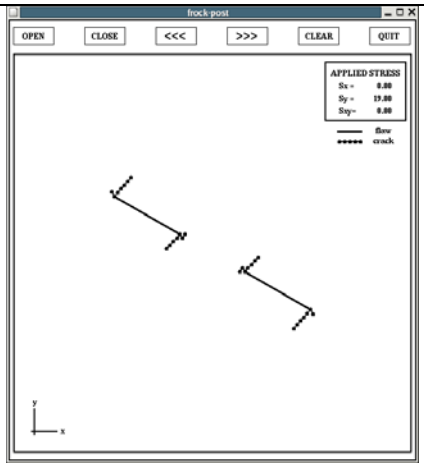 (c) σ = 19.00 MPa	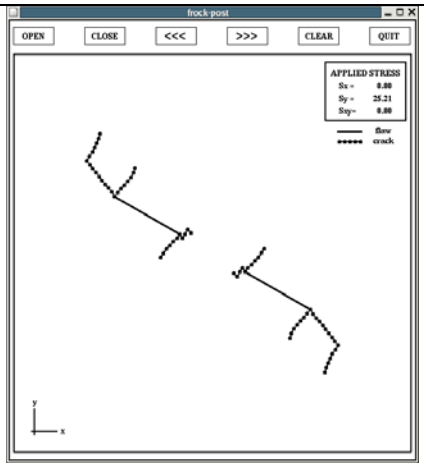 (d) σ = 25.21 MPa	(c) cracks (tensile/shear ?) initiated from the inner shear cracks (d) cracks propagated
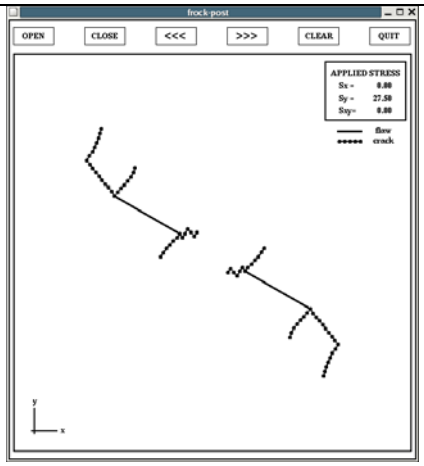 (e) σ = 27.50 MPa	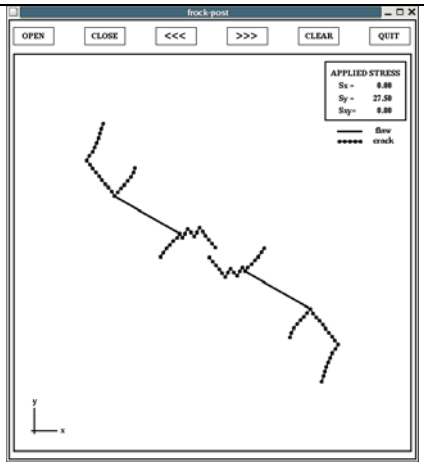 (f) σ = 27.50 MPa	(e) cracks propagated (f) no coalescence

Figure 8.17 – Modeling of crack initiation, propagation and coalescence in gypsum for flaw pair geometry 30-0-2a ($\beta - s - c$) or 2a-30-0 ($L - \beta - \alpha$) obtained in the present study.

σ_c = 16.0 Mpa

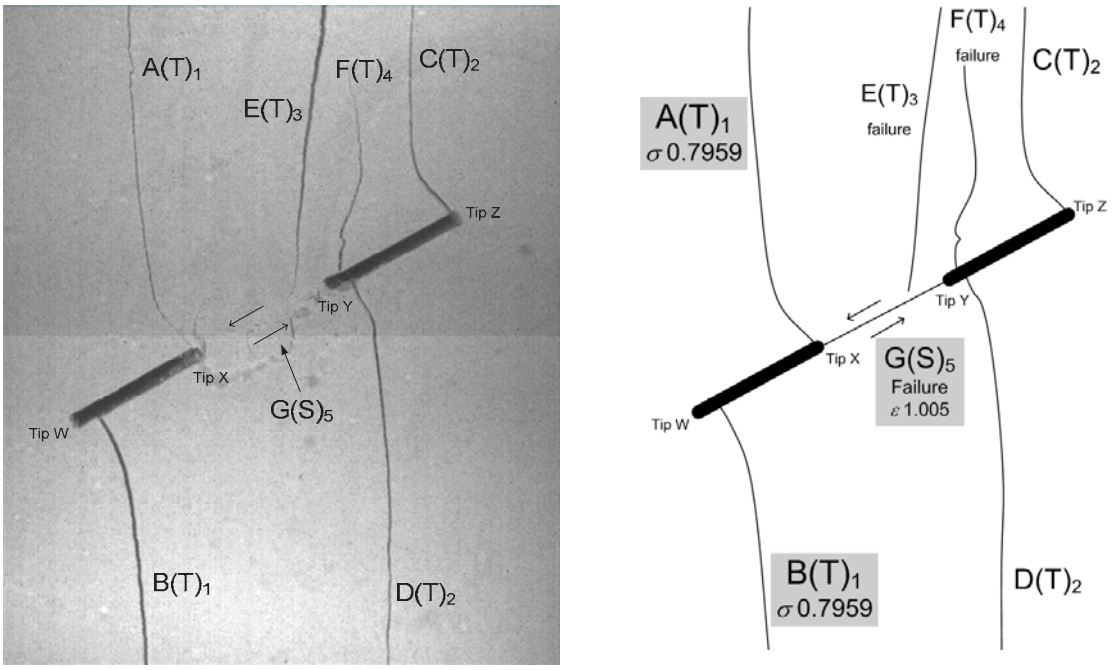

(a) actual specimen (b) sketch

Figure 8.18 – Fracturing and coalescence patterns in gypsum for flaw pair geometry30-0-2a ($\beta - s - c$) or 2a-30-0 ($L - \beta - \alpha$).

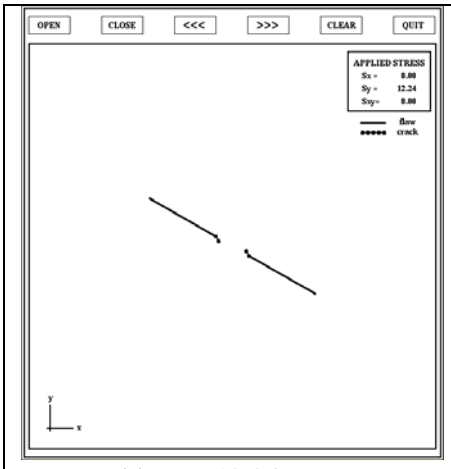

(a) σ_c = **12.24 MPa**

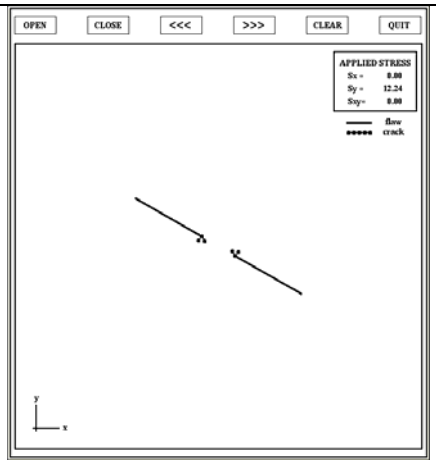

(b) σ = 12.24 MPa

(a) internal shear cracks initiated

(b) internal tensile wing cracks initiated

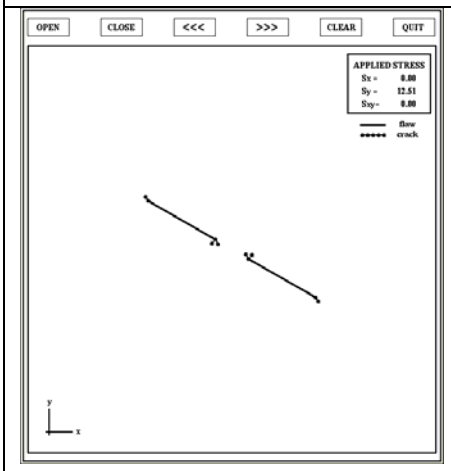

(c) σ = 12.51 MPa

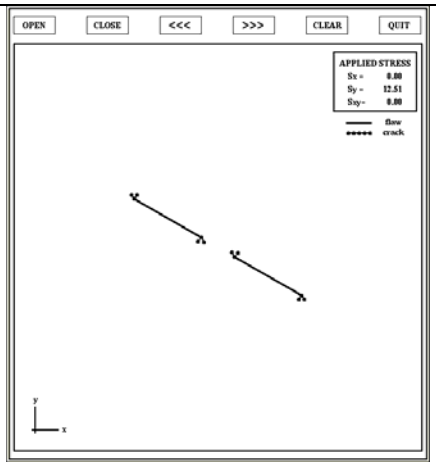

(d) σ = 12.51 MPa

(c) external shear cracks initiated

(d) external tensile wing cracks initiated

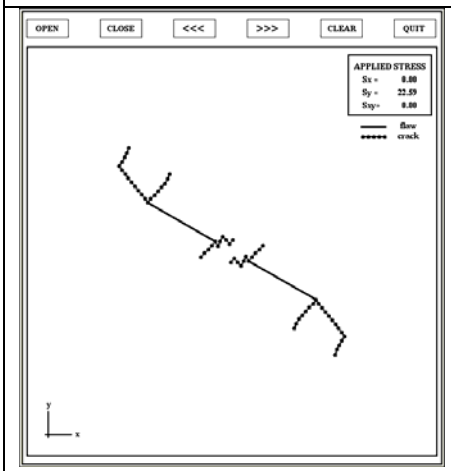

(e) σ = 22.59 MPa

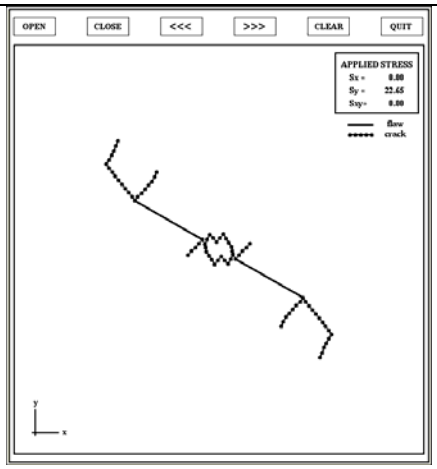

(f) σ = 22.65 MPa

(e) cracks propagated

(f) coalescence

Figure 8.19 – Modeling of crack initiation, propagation and coalescence in gypsum for flaw pair geometry 30-0-a ($\beta - s - c$) or a-30-0 ($L - \beta - \alpha$) obtained in the present study.

σ_c = 19.7 MPa

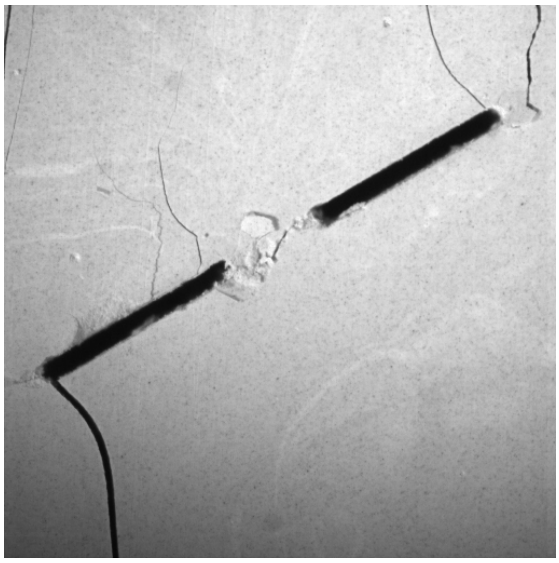

Figure 8.20 – Fracturing and coalescence patterns in gypsum for flaw pair geometry 30-0-a ($\beta - s - c$) or a-30-0 ($L - \beta - \alpha$). Note the development of a shear crack between the inner flaw tips.

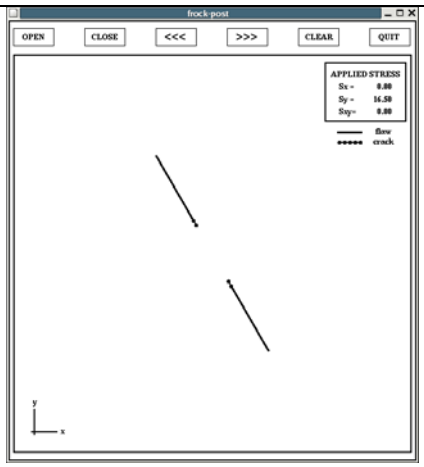 (a) σ_c = **16.50 MPa**	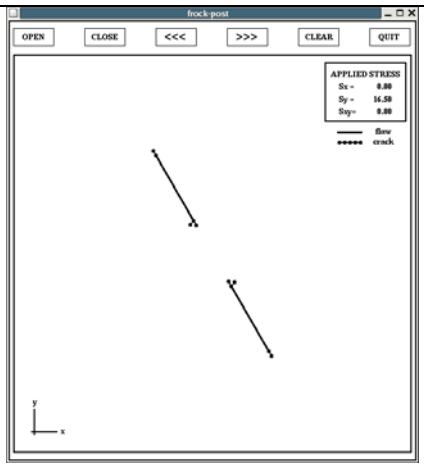 (b) σ = 16.50 MPa	(a) internal shear cracks initiated (b) internal tensile wing cracks and external shear cracks initiated
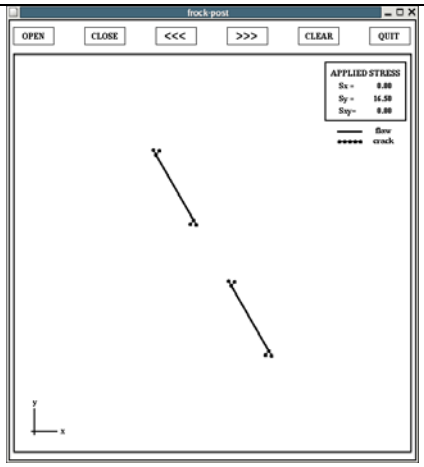 (c) σ = 16.50 MPa	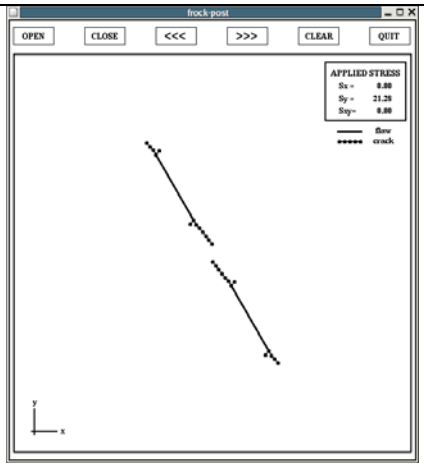 (d) σ = 21.28 MPa	(c) external tensile wing cracks initiated (d) shear cracks (internal & external) propagated
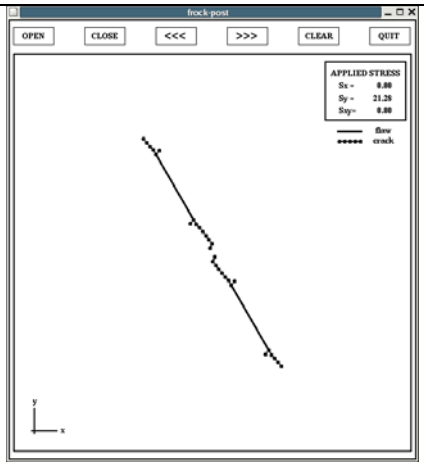 (e) σ = 21.28 MPa	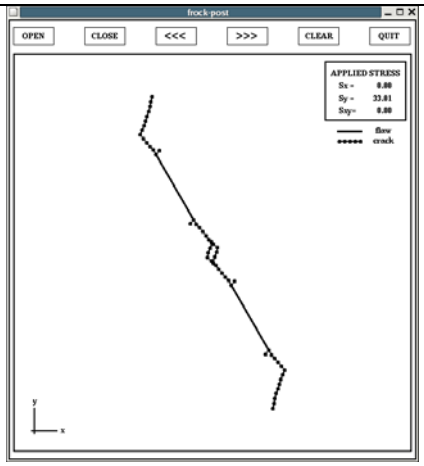 (f) σ = 33.01 MPa	(e) tensile cracks initiated from the tips of the internal shear cracks (f) coalescence by new shear crack segments

Figure 8.21 – Modeling of crack initiation, propagation and coalescence in gypsum for flaw pair geometry 60-0-2a ($\beta - s - c$) or 2a-60-0 ($L - \beta - \alpha$) obtained in the present study.

σ_c = 16.30 MPa

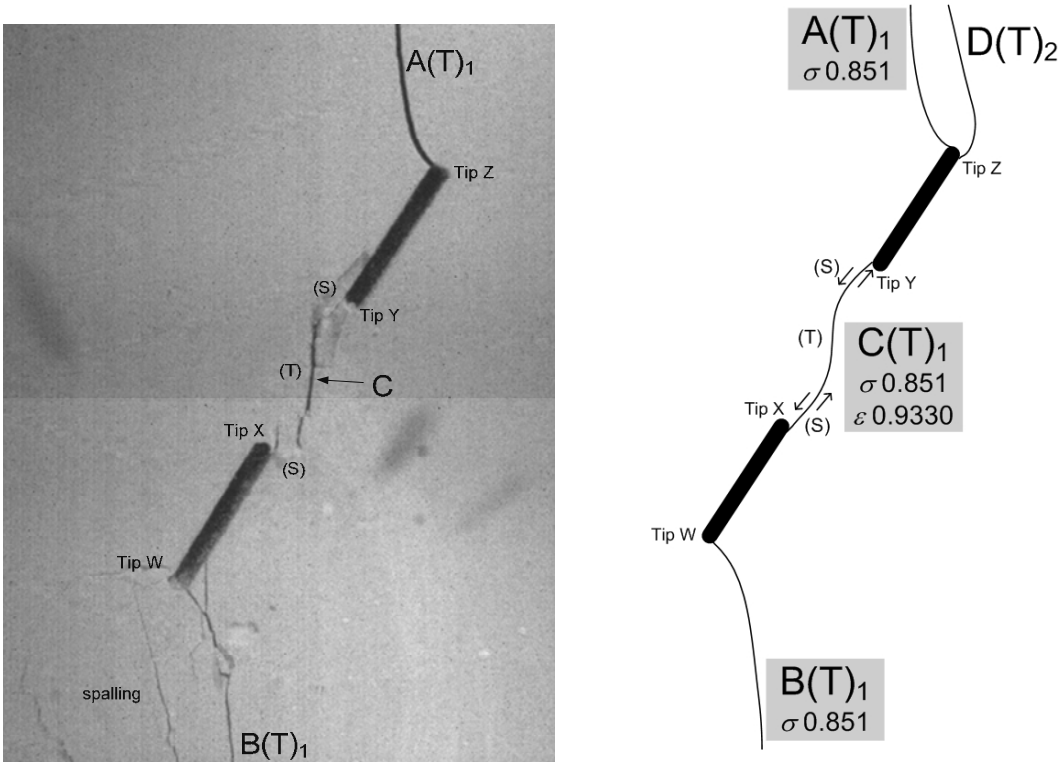

(a) actual specimen (b) sketch

Figure 8.22 – Fracturing and coalescence patterns in gypsum for flaw pair geometry 60-0-2a ($\beta - s - c$) or 2a-60-0 ($L - \beta - \alpha$).

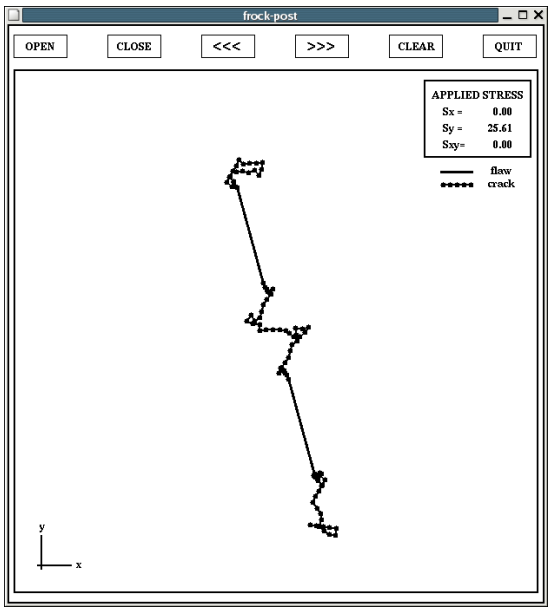

Figure 8.23 – Coalescence in gypsum for flaw pair geometry 75-0-2a ($\beta - s - c$) or 2a-75-0 ($L - \beta - \alpha$) obtained in the present study.

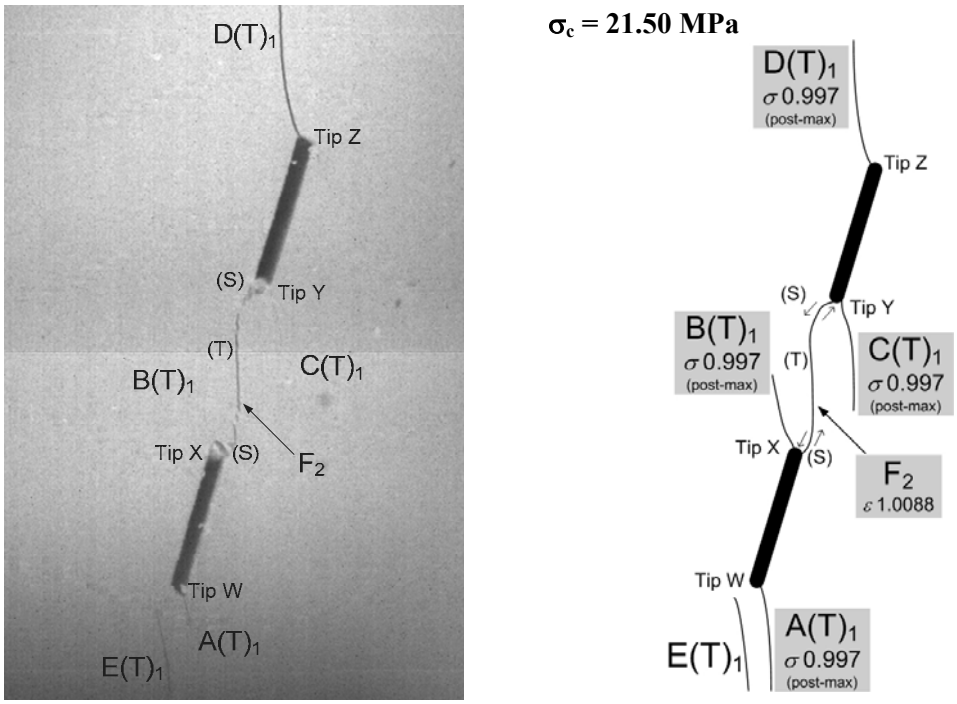

(a) actual specimen (b) sketch

Figure 8.24 – Fracturing and coalescence patterns in gypsum for flaw pair geometry 75-0-2a ($\beta - s - c$) or 2a-75-0 ($L - \beta - \alpha$).

Flaw pair geometry [1]		Coalescence pattern [2]				
$\beta - s - c$	$L - \beta - \alpha$	**Present FROCK result**	**Bobet's FROCK result**	**Present experimental result**	**Present FROCK result matches Bobet's FROCK result?**	**Present FROCK result matches present experimental result?**
45-0-2a	2a-45-0	Type 1 S- Type 1 S	Type 1 S- Type 1 S	Type 1 S- Type 1 S or Type 1 S	Yes	Yes
45-a-2a	2a-45-27	Type 1 S + Type 2 T + Type 2 T + Type 1 S	Type 1 S + Type 2 T + Type 2 T + Type 1 S	N.A.	Yes	N.A. [4]
45-2a-2a	2a-45-45	Type 1 S- Type 1 T	Type 1 S- Type 1 T	N.A.	Yes	N.A. [4]
30-a-2a	2a-30-27	No coalescence	Type 1 S + Type 2 T + Type 2 T + Type 1 S	Type 1 S + Type 2 T + Type 1 S	No	No
30-0-2a	2a-30-0	No coalescence	N.A. [3]	Type 1 S- Type 1 S or Type 1 S	N.A. [3]	No
30-0-a	a-30-0	Odd coalescence	N.A. [3]	Type 1 S- Type 1 S or Type 1 S	N.A. [3]	No
60-0-2a	2a-60-0	Type 1 S + Type 2 T + Type 2 T + Type 1 S	N.A. [3]	Type 1 S + Type 2 T + Type 1 S	N.A. [3]	Yes
75-0-2a	2a-75-0	Odd coalescence	N.A. [3]	Type 1 S + Type 2 T + Type 1 S	N.A. [3]	No

[1] Flaw pair geometries are represented by both conventions as shown in figure 8.6.
[2] Refer to figure 3.15 for crack type classification.
[3] Corresponding coalescence figures are not available (N.A.) in Bobet's thesis
[4] Corresponding flaw pair geometries are not tested in the present experimental study

Table 8.4 – Comparison of crack coalescence patterns.

Flaw pair geometry [1]		Crack initiation stress σ_c (MPa)		
$\beta - s - c$	$L - \beta - \alpha$	**Bobet's FROCK result**	**Present FROCK result**	**Present experimental result**
45-0-2a	2a-45-0	13.5	13.5	14.9
45-a-2a	2a-45-27	13.5	13.7	N.A.
45-2a-2a	2a-45-45	14.0	14.1	N.A.
30-a-2a	2a-30-27	12.7	12.7	10.9
30-0-2a	2a-30-0	12.3	12.9	16.0
30-0-a	a-30-0	N.A.	12.2	19.7
60-0-2a	2a-60-0	21.5	16.5	16.3
75-0-2a	2a-75-0	N.A.	25.6	21.5

N.A. = results not available

[1] Flaw pair geometries are represented by both conventions as shown in figure 8.6.

Table 8.5 – Comparison of crack initiation stress.

It is shown in table 8.4 that the coalescence patterns of flaw pairs with flaw inclination 45^o, i.e. 2a-45-0, 2a-45-27 and 2a-45-45, obtained in the present FROCK study agree well with those obtained in the FROCK study by Bobet. In addition, the present FROCK results agree with the experimental results in the present study for the coplanar flaw geometries 2a-45-0 and 2a-60-0. The coalescence patterns obtained from FROCK for other flaw inclination angles, however were less satisfactory (2a-30-27, 2a-30-0, a-30-0, 2a-75-0) as compared to the present experimental study.

Regarding crack initiation stress ($\boldsymbol{\sigma_c}$), there is a general good agreement between the present FROCK study and the FROCK study by Bobet, particularly for flaw pairs with flaw inclination angles 30^o and 45^o (table 8.5). The slight discrepancy between the Bobet's and present $\boldsymbol{\sigma_c}$ values may be attributed to the different levels of precision associated with the computing facilities over different times. However, for geometry 2a-60-0, there is a significant difference (21.5 MPa from Bobet's FROCK study *vs* 16.5 MPa from present FROCK study). Table 8.5 also contains $\boldsymbol{\sigma_c}$ values obtained from the present

experimental studies, which generally show a good agreement with the prediction obtained from the present FROCK study, except 30-0-a.

8.4.3 Variation of input parameters

Recall in table 8.2 that there are two types of input parameters required in FROCK. The first type, which includes Young's modulus, Poisson's ratio and friction coefficient, are measurable material quantities. The other type, which includes critical tensile strength, critical shear strength and radius of core region are obtained from a back-fitting process based on experimental results. Refer to Bobet (1997) for details of the back-fitting process. With regard to the unsatisfactory modeling results (i.e. modeling results different from experimental results) for some of the flaw pair geometries (2a-30-27, 2a-30-0, a-30-0 and 2a-75-0 as shown in tables 8.4 & 8.5), one of the four input parameters (table 8.2) – radius of core region (r_0), critical shear strength (τ_{crit}), critical tensile strength (σ_{crit}) or friction coefficient (μ) [2], is varied progressively each time below to observe the change of fracturing and coalescence patterns (figures 8.25 to 8.28). The objectives are twofold – to observe the degree of dependence of crack initiation stresses and coalescence patterns on these parameters, and when possible to obtain modeling results that can match the experimental results by varying the input parameters.

As stated by Bobet (1997), the magnitudes of σ_{crit} and τ_{crit} determine the stress at which cracks initiate, and the ratio σ_{crit} / τ_{crit} establishes what type of crack initiates first. For example, when the critical shear strength (τ_{crit}) is decreased, the initiation and propagation of shear cracks should be more favorable, while that of tensile cracks should be less favorable or suppressed, and it is vice versa for the critical tensile strength (σ_{crit}). In figures 8.25 to 8.28, comments of **bolded** fonts are included to indicate whether the

[2] Only a single μ value of 0.7 is used in FROCK for all newly created cracks. From the experimental studies, tensile cracks and shear cracks in gypsum are found to have different degrees of surface roughness. μ is thus also included in the parametric study to observe the sensitivity of fracturing and coalescence patterns towards μ.

expected (reasonable) effect due to the change of the critical strength parameters is obtained or not.

The effects of varying the friction coefficient (μ) and the radius of core region (r_0) are less intuitive. The SIFs associated with an open crack and a closed crack are given by (Maugis, 1982):

Open crack :
$$K_I = \sigma_1 \frac{\sqrt{\pi a}}{2}(1+\cos 2\beta)$$
$$K_{II} = -\sigma_1 \frac{\sqrt{\pi a}}{2}\sin 2\beta$$

Closed crack :
$$K_I = 0$$
$$K_{II} = -\sigma_1 \frac{\sqrt{\pi a}}{2}(\sin 2\beta - \mu \cos 2\beta)$$

where β = the crack inclination angle, a = half the crack length. In the present modeling study, since the pre-existing flaws are open and the associated SIFs are free of μ, μ will not influence the crack initiation stress and the crack type initiating from the pre-existing flaws. However, along the newly created crack segments, increasing the value of μ will lead to a decrease of K_{II} (see equation above). The effect is then to decrease the driving force for both subsequent *shear crack* and *tensile crack* initiation from the tips of these closed crack segments. Hence, it is impossible to state if a change of μ will favor the initiation of either one crack type.

Recall that along the boundary of the core region (r_0), the tangential and shear stresses are computed and compared against the shear and tensile crack initiation criteria respectively. Since both the tangential and shear stresses decrease with distance away from the flaw tip, higher crack initiation stresses are thus expected when a larger core radius is used. However, the rate at which these two stresses decrease away from the flaw tip depends on the overall flaw pair geometry. Thus it is expected that by increasing r_0, the far-field

stress at which crack initiation occurs will decrease. Also, the direction of initiation will change.

The modeling results obtained by varying one of the four parameters as suggested above for four flaw pair geometries (30-a-2a, 30-0-2a, 30-0-a, 75-0-2a) are shown in figures 8.25 to 8.28. General comments are made in these figures to indicate whether the coalescence patterns obtained from FROCK resemble those obtained form the present experimental study.

As illustrated in figures 8.25 – 8.28 and summarized in table 8.6, except for 30-0-2a, a slight variation of a particular parameter can successfully lead to satisfactory coalescence patterns for other flaw pairs (30-a-2a, 30-0-a, 75-0-2a). For 30-0-2a, no satisfactory coalescence patterns can be obtained no matter how the four input parameters are varied.

Flaw pair geometry [1]		**Vary critical shear strength (τ_{crit})**	**Vary critical tensile strength (σ_{crit})**	**Vary core radius (r_0)**	**Vary friction coefficient (μ)**	**Crack initiation stress σ_c**	
β - s- c	L-β-α					Bobet's FROCK result	Present experimental result
30-a-2a	2a-30-27	Satisfactory coalescence by decreasing τ_{crit} (11.7 – 12.1 MPa)	Satisfactory coalescence by increasing σ_{crit} (12.7 MPa)	Satisfactory coalescence by increasing r_0 (≥13.4 MPa)	Satisfactory coalescence by increasing μ (12.7 MPa)	12.7 MPa	10.9 MPa
30-0-2a	2a-30-0	Odd coalescence by increasing τ_{crit} (≥13.5 MPa)	Odd coalescence by increasing σ_{crit} (12.9 MPa)	Odd coalescence by increasing r_0 (13.4 – 14.6 MPa)	No coalescence	12.3 MPa	16.0 MPa
30-0-a	a-30-0	Odd coalescence by decreasing τ_{crit} (≥11.8 MPa)	Odd coalescence by increasing σ_{crit} (12.2 MPa)	Satisfactory coalescence by increasing r_0 (12.0 – 14.8 MPa)	Odd coalescence by decreasing μ (12.2 MPa)	N.A.	19.7 MPa
75-0-2a	2a-75-0	Satisfactory coalescence by increasing τ_{crit} (31.9 MPa)	Satisfactory coalescence by decreasing σ_{crit} (25.6 MPa)	Odd coalescence by increasing r_0 (26.8 – 31.1 MPa)	Odd coalescence by decreasing μ (25.6 MPa)	N.A.	21.5 MPa

[1] Flaw pair geometries are represented by both conventions as shown in figure 8.6.

- The left part of the table contains flaw pair geometries.
- In the center part of the table, the coalescence patterns obtained by FROCK are compared with those observed in the present experimental study. If similar coalescence patterns are obtained, they are stated as *satisfactory*; otherwise, they are stated as *odd*. The stress values in parentheses specify the range of crack initiation stress values associated with the occurrence of either the satisfactory or odd coalescence patterns.
- The right part of the table contains crack initiation stresses obtained from Bobet's FROCK study and the present experimental study.

Table 8.6 – Effect on coalescence patterns by varying one input parameter at a time.

Coalescence patterns

As indicated in table 8.6, for the three input parameters τ_{crit}, σ_{crit} and μ, there is no definite trend of whether increasing or decreasing of the relevant parameter can lead to coalescence (either satisfactory or odd type, see caption of table 8.6). For example, τ_{crit} has to *decrease* for geometry 30-a-2a in order to get a satisfactory coalescence, while τ_{crit} has to *increase* for geometry 75-0-2a in order to get a satisfactory coalescence. For $\mathbf{r_0}$, however, decreasing its value does not lead to coalescence. Coalescence (either satisfactory or odd type) can only be achieved by increasing $\mathbf{r_0}$.

For flaw pair **30-a-2a** (or 2a-30-27), the coalescence patterns obtained by varying the input parameters (figures 8.25 a, b, c, d) are similar to those obtained by Bobet (figure 8.15) and in the present experimental study (figure 8.16), i.e. coplanar shear cracks initiated from the inner flaw tips, which were later linked up by one tensile crack / two tensile cracks.

For flaw pair **30-0-a** (or a-30-0), the coalescence patterns obtained by varying the input parameters (figure 8.27 c) are similar to those obtained in the present experimental study (figure 8.20), i.e. the inner flaw tips are linked up by shear cracks.

For flaw pair **75-0-2a** (or 2a-75-0), the coalescence patterns obtained by varying the input parameters (figure 8.28 a, b) are similar to those obtained in the present experimental study (figure 8.24), i.e. coplanar shear cracks initiated from the inner flaw tips, which were linked up by one tensile crack / two tensile cracks.

Crack initiation stresses

For flaw pairs **30-a-2a** and **30-0-2a**, the *new* crack initiation stresses associated with the change of individual input parameters are in a general good agreement with the Bobet's FROCK values and the present experimental values.

Since flaw pairs **30-0-a** and **75-0-2a** were not studied by Bobet's FROCK values, comparison can only be made with the present experimental values for these two flaw

pair geometries. For 30-0-a, the *new* crack initiation stresses are always lower than experimental values, while for 75-0-2a, the *new* crack initiation stresses are always higher than experimental values.

(a) Vary critical shear strength (τ_{crit}) only (Bobet's τ_{crit} = 29.5 MPa)

<table>
<tr><td>$\tau_{crit} \leq 27.1$</td><td>$\tau_{crit} = 27.2 – 28.2$</td><td>$\tau_{crit} = 28.3 – \mathbf{29.5}$</td><td>$\tau_{crit} = 29.6 – 33.7$</td><td>$\tau_{crit} \geq 33.8$</td></tr>
<tr><td> 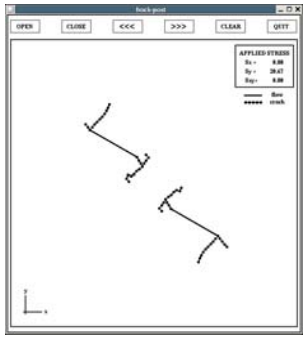
$\sigma_c \leq 11.7$ MPa</td><td> 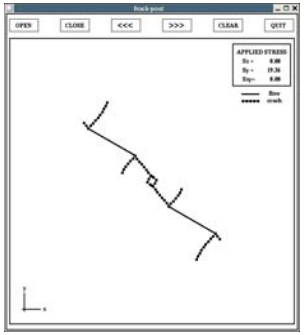
$\sigma_c = 11.7 – 12.1$ MPa</td><td> 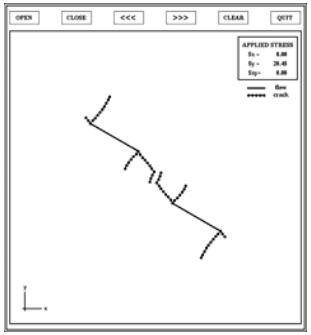
$\sigma_c = 12.2 – 12.7$ MPa</td><td> 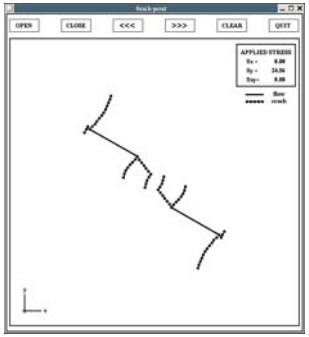
$\sigma_c = 12.7 – 14.5$ MPa</td><td> 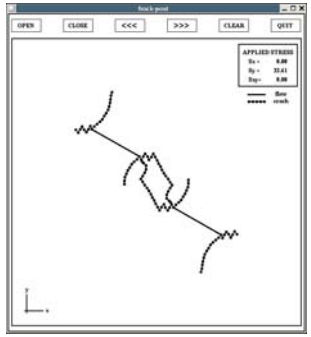
$\sigma_c = 14.5$ MPa</td></tr>
<tr><td>No Coalescence</td><td>Coalescence similar to experiment (figure 8.16)</td><td>No coalescence</td><td>No coalescence</td><td>Odd Coalescence</td></tr>
<tr><td colspan="2" rowspan="2">Decrease τ_{crit} → should favor shear crack, suppress tensile crack

(reasonable effect due to the change of input parameter)</td><td rowspan="2">-</td><td colspan="2">Increase τ_{crit} → should favor tensile crack, suppress shear crack</td></tr>
<tr><td>The shear cracks initiated from the inner flaw tips were shorter than those for τ_{crit} = 28.3 – 29.5 (the left column)

(reasonable effect due to the change of input parameter)</td><td>(unreasonable effect due to the change of input parameter)</td></tr>
</table>

Figure 8.25 – Variation of input parameters for flaw pair geometry 30-a-2a (2a-30-27).

(b) Vary critical tensile strength (σ_{crit}) only (Bobet's σ_{crit} = 18.1 MPa)

$\sigma_{crit} \leq 3.2$	σ_{crit} = 3.3 – 18.0	σ_{crit} = **18.1** – 19.7	σ_{crit} = 19.8 – 20.2	$\sigma_{crit} \geq 20.3$
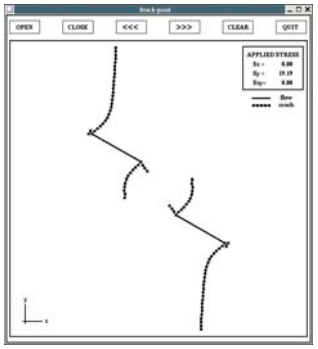	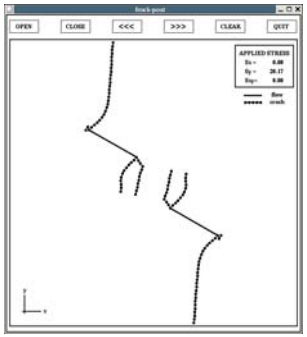	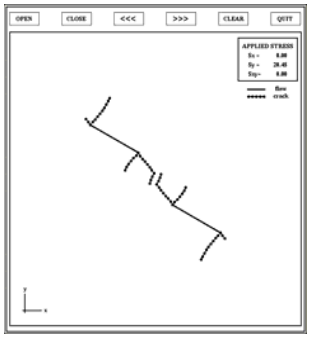	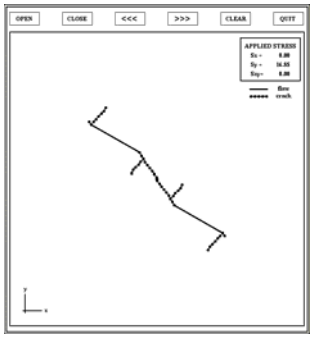	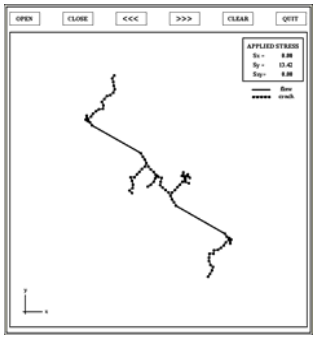
$\sigma_c \leq 2.6$ MPa	σ_c = 2.6 – 12.7 MPa	σ_c = 12.7 MPa (constant over whole range)	σ_c = 12.7 MPa (constant over whole range)	σ_c = 12.7 MPa
No coalescence	No coalescence	No coalescence	Coalescence similar to experiment (figure 8.16)	Odd coalescence
Decrease σ_{crit} → should favor tensile crack, suppress shear crack **(reasonable effect due to the change of input parameter)**		-	Increase σ_{crit} → should favor shear crack, suppress tensile crack **(reasonable effect due to the change of input parameter, also coalescence pattern resembles the experimental result)**	**(unreasonable effect due to the change of input parameter)**

Figure 8.25 – Variation of input parameters for flaw pair geometry 30-a-2a (2a-30-27) (continued).

(c) Vary core radius (r_0) on new cracks only (Bobet's $\mathbf{r_0}$ = 0.023 cm)

$r_0 \leq 0.019$	$r_0 =$ **0.020 – 0.025**	$r_0 = 0.026 – 0.028$	$r_0 \geq 0.029$
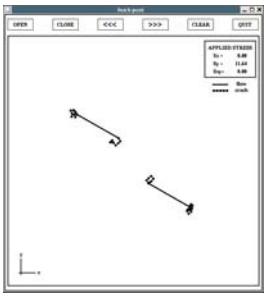	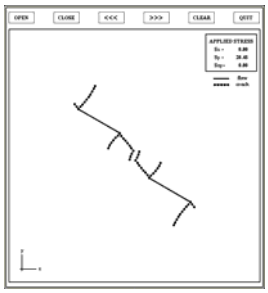	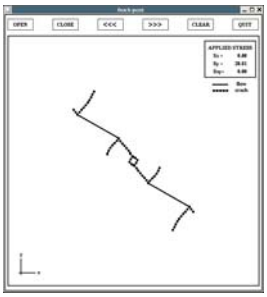	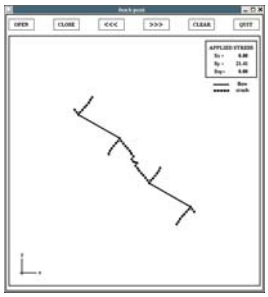
$\sigma_c \leq 11.6$ MPa	$\sigma_c = 11.9 – 13.2$ MPa	$\sigma_c = 13.4 – 13.8$ MPa	$\sigma_c \geq 14.1$
No coalescence	No coalescence	Coalescence similar to experiment (figure 8.16)	
-	-	Increasing r_0 favors the initiation of *shear* crack more than the *tensile* crack as indicated by the longer *shear cracks* initiating from the inner flaw tips.	

Figure 8.25 – Variation of input parameters for flaw pair geometry 30-a-2a (2a-30-27) (continued).

(d) Vary friction coefficient (μ) on new cracks only (Bobet's **μ** = 0.70)

μ ≤ 0.69	μ = **0.70**-0.73	μ = 0.74-0.78	μ ≥ 0.79
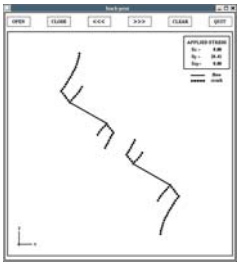	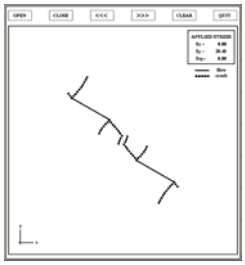	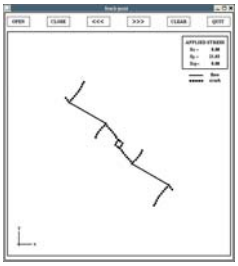	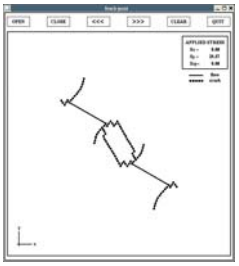
σ_c = 12.7 MPa (constant over whole range)	σ_c = 12.7 MPa (constant over whole range)	σ_c = 12.7 MPa (constant over whole range)	σ_c = 12.7 MPa (constant over whole range)
No coalescence	No coalescence	Coalescence similar to experiment (figure 8.16)	Odd Coalescence
Decreasing μ favors the initiation of *tensile* crack more than the *shear* crack	-	Increasing μ favors the initiation of *shear* crack more than the *tensile* crack	

Figure 8.25 – Variation of input parameters for flaw pair geometry 30-a-2a (2a-30-27) (continued).

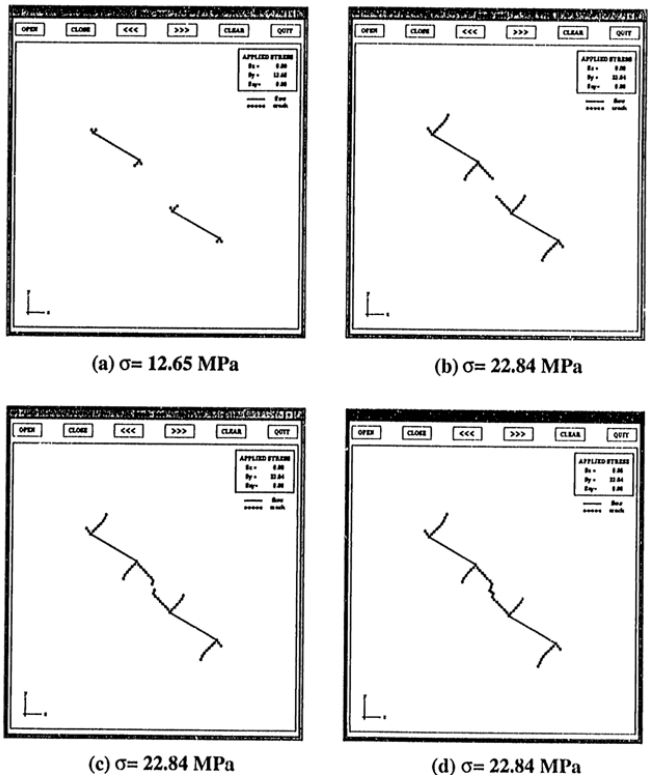

Figure 8.15 – Modeling of crack initiation, propagation and coalescence in gypsum for flaw pair geometry 30-a-2a ($\beta - s - c$) or 2a-30-27 ($L - \beta - \alpha$) by Bobet (1997).

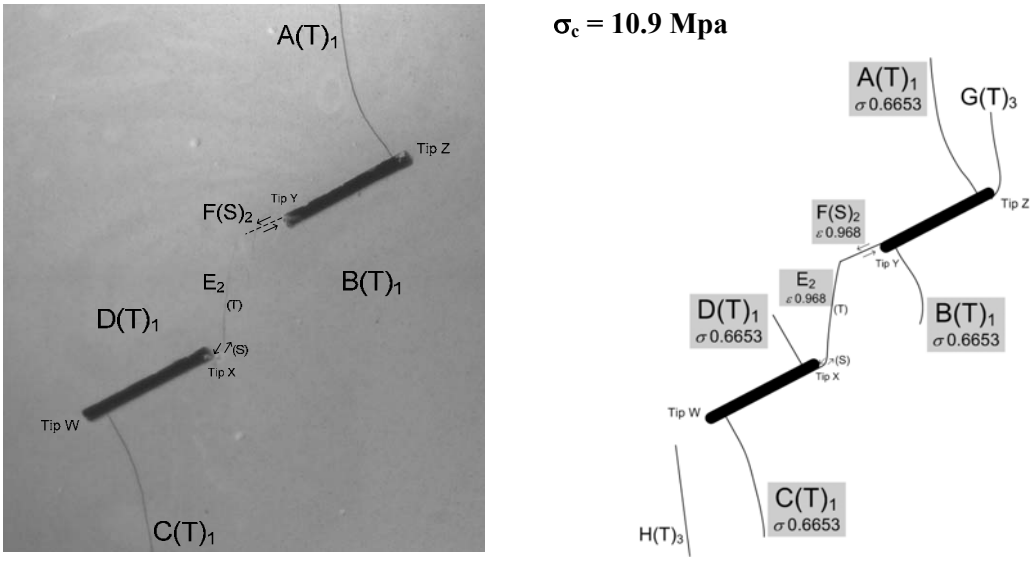

(a) actual specimen (b) sketch

Figure 8.16 – Fracturing and coalescence patterns in gypsum for flaw pair geometry 30-a-1.7a ($\beta - s - c$) or 2a-30-30 ($L - \beta - \alpha$). Note that cracks G and H which appeared later are not shown in figure (a).

(a) Vary critical shear strength ($\boldsymbol{\tau_{crit}}$) only (Bobet's $\boldsymbol{\tau_{crit}}$ = 29.5 MPa)

$\tau_{crit} \leq 29.1$	τ_{crit} = 29.15 – **29.5**	τ_{crit} = 29.6 – 30.8	$\tau_{crit} \geq 30.9$
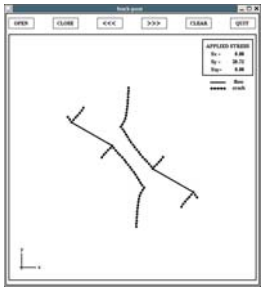	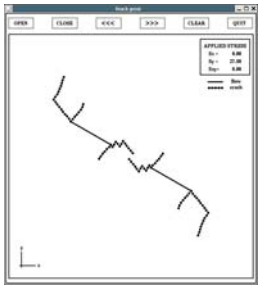	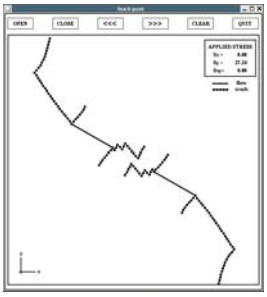	 
$\sigma_c \leq 12.8$ MPa	σ_c = 12.8 – 12.9 MPa	σ_c = 13.0 – 13.5 MPa	$\sigma_c \geq 13.5$ MPa
No Coalescence	No coalescence	No coalescence	Odd coalescence compared to experiment (figure 8.18)
Decrease τ_{crit} → should favor shear crack, suppress tensile crack **(reasonable effect due to the change of input parameter)**	-	Increase τ_{crit} → should favor tensile crack, suppress shear crack **(unreasonable effect due to the change of input parameter as indicated by longer shear cracks initiating from the outer flaw tips compared to the image on the left)**	Increase τ_{crit} → should favor tensile crack, suppress shear crack. Note the coalescence in the center of the bridging region was achieved by a tensile crack segment. **(reasonable effect due to the change of input parameter)**

Figure 8.26 – Variation of input parameters for flaw pair geometry 30-0-2a (2a-30-0).

(b) Vary critical tensile strength (σ_{crit}) only (Bobet's $\boldsymbol{\sigma_{crit}}$ = 18.1 MPa)

$\sigma_{crit} \leq$ 18.0	σ_{crit} = **18.1**-18.4	$\sigma_{crit} \geq$18.5
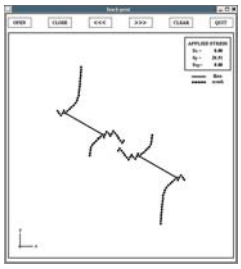 σ_c = 12.9 MPa	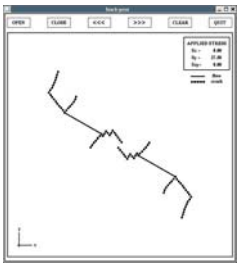 σ_c = 12.9 MPa (constant over whole range)	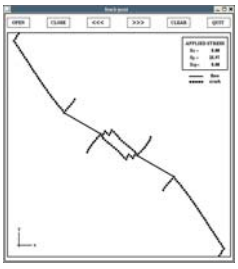 σ_c = 12.9 MPa
No coalescence	No coalescence	Odd coalescence compared to experiment (figure 8.18)
Decrease σ_{crit} → should favor tensile crack, suppress shear crack. Note the preferential propagation of tensile wing crack from outer flaw tips **(reasonable effect due to the change of input parameter)**	-	Increase σ_{crit} → should favor shear crack, suppress tensile crack **(reasonable effect due to the change of input parameter; however, coalescence pattern is different from the experimental result)**

Figure 8.26 – Variation of input parameters for flaw pair geometry 30-0-2a (2a-30-0) (continued).

(c) Vary core radius (r_0) on new cracks only (Bobet's $\mathbf{r_0}$ = 0.023 cm)

$r_0 \leq 0.020$	$r_0 = 0.021$	$r_0 = 0.022 – 0.024$	$r_0 = 0.025 – 0.030$	$r_0 \geq 0.031$
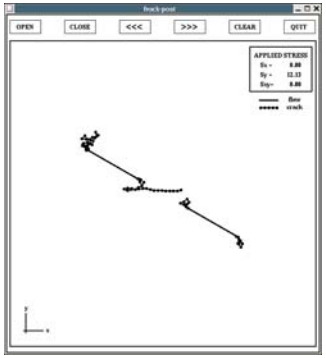	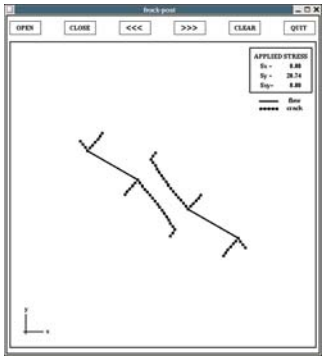	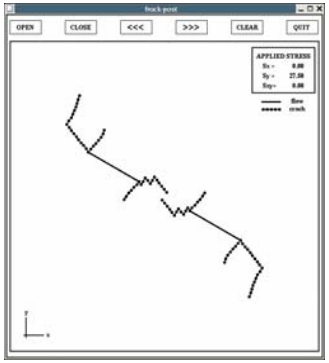	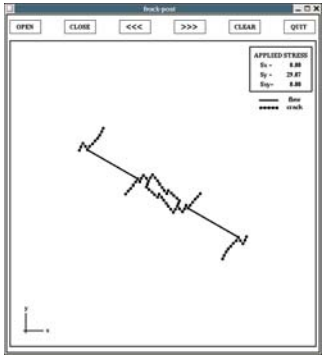	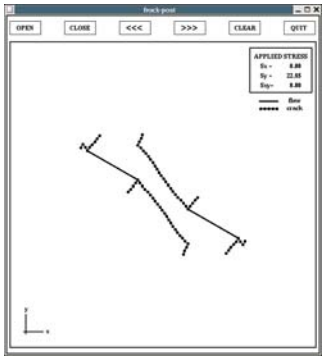
$\sigma_c \leq 12.1$ MPa	$\sigma_c = 12.4$ MPa	$\sigma_c = 12.7 – 13.2$ MPa	$\sigma_c = 13.4 – 14.6$ MPa	$\sigma_c \geq 14.8$ MPa
No coalescence	No coalescence	No coalescence	Odd coalescence compared to experiment (figure 8.18)	No coalescence

Figure 8.26 – Variation of input parameters for flaw pair geometry 30-0-2a (2a-30-0) (continued).

(d) Vary friction coefficient (μ) on new cracks only (Bobet's **μ** = 0.70)

μ ≤ 0.69	μ = **0.70**	μ ≥ 0.71
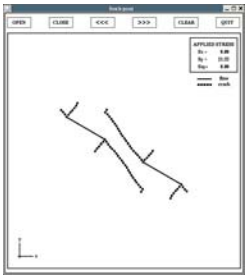	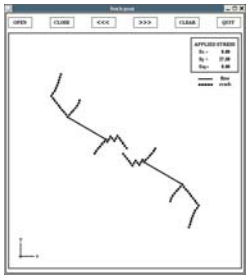	
σ_c = 12.9 MPa	σ_c = 12.9 MPa	σ_c = 12.9 MPa
No coalescence	No coalescence	No coalescence
Decreasing μ favors the initiation of *shear* crack more than the *tensile* crack	-	Increasing μ favors the initiation of *tensile* crack (compared with μ = **0.70)**

Figure 8.26 – Variation of input parameters for flaw pair geometry 30-0-2a (2a-30-0) (continued).

σ_c = 16.0 Mpa

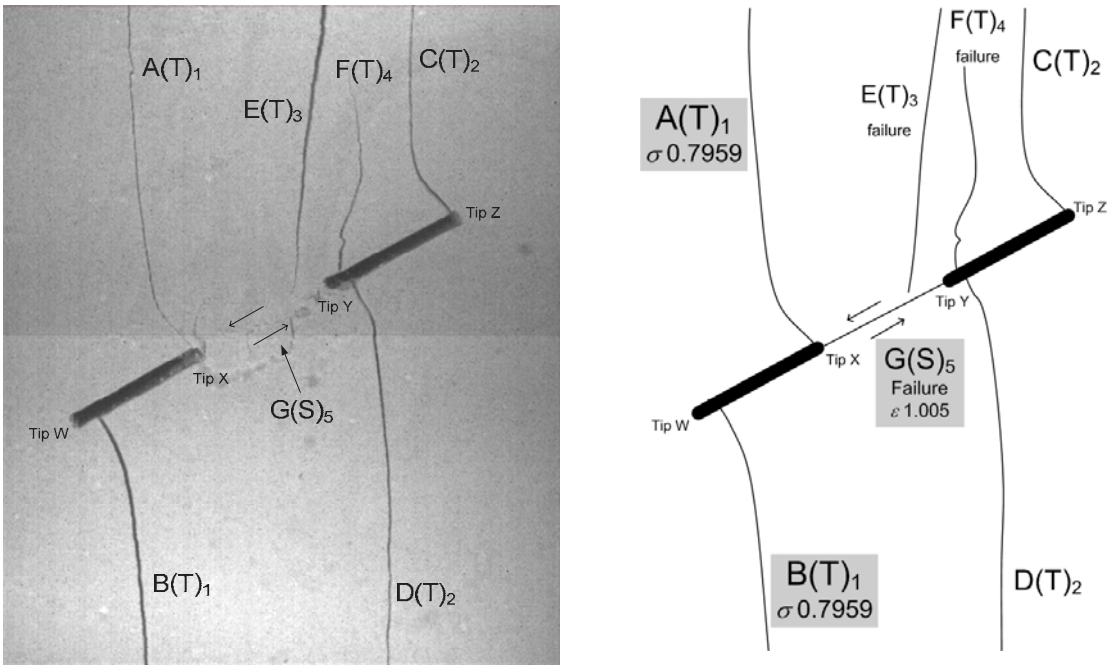

(a) actual specimen (b) sketch

Figure 8.18 – Fracturing and coalescence patterns in gypsum for flaw pair geometry30-0-2a ($\beta - s - c$) or 2a-30-0 ($L - \beta - \alpha$).

(a) Vary critical shear strength ($\boldsymbol{\tau_{crit}}$) only (Bobet's $\boldsymbol{\tau_{crit}}$ = 29.5 MPa)

$\tau_{crit} \leq 28.2$	$\tau_{crit} = 28.3 – 28.4$	$\tau_{crit} = 28.5 –$ **29.5**	$\tau_{crit} = 29.6 – 31.8$	$\tau_{crit} \geq 31.9$
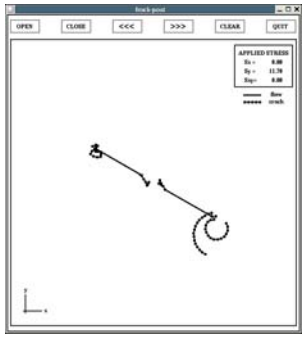	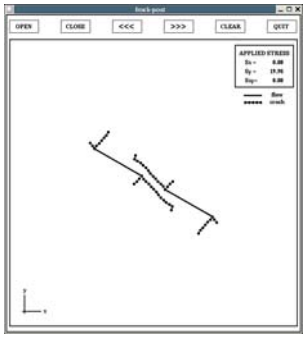	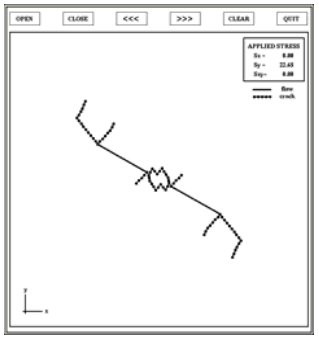	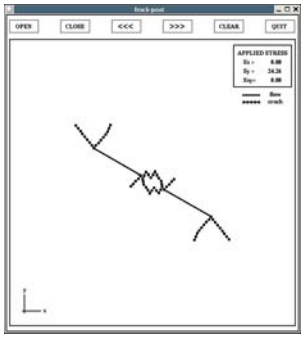	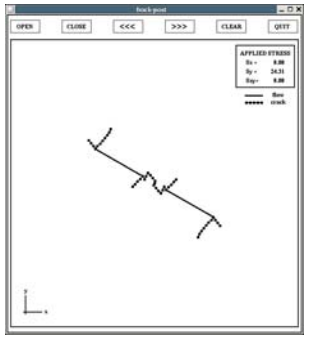
$\sigma_c \leq 11.7$ MPa	$\sigma_c = 11.7 – 11.8$ MPa	$\sigma_c = 11.8 – 12.2$ MPa	$\sigma_c = 12.3 – 13.2$ MPa	$\sigma_c \geq 13.2$ MPa
No coalescence	No coalescence	Odd coalescence compared to experiment (figure 8.20)	Odd coalescence compared to experiment (figure 8.20)	Odd coalescence compared to experiment (figure 8.20)
Decrease τ_{crit} → should favor shear crack, suppress tensile crack **(reasonable effect due to the change of input parameter for τ_{crit} = 28.3 – 28.4)** **(unreasonable effect due to the change of input parameter for $\tau_{crit} \leq 28.2$)**		-	Increase τ_{crit} → should favor tensile crack, suppress shear crack **(the effect due to the change of input parameter could not be determined)**	Increase τ_{crit} → should favor tensile crack, suppress shear crack **(reasonable effect due to the change of input parameter; however, coalescence pattern is different from the experimental result)**

Figure 8.27 – Variation of input parameters for flaw pair geometry 30-0-a (a-30-0).

(b) Vary critical tensile strength (σ_{crit}) only (Bobet's $\boldsymbol{\sigma_{crit}}$ = 18.1 MPa)

$\sigma_{crit} \leq 18.0$	σ_{crit} = **18.1**-18.8	$\sigma_{crit} \geq 18.9$
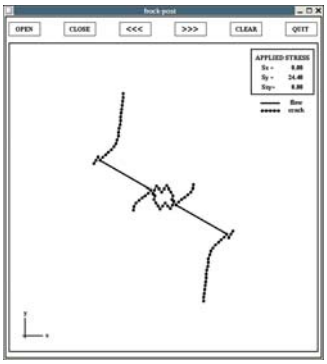 σ_c = 12.2 MPa	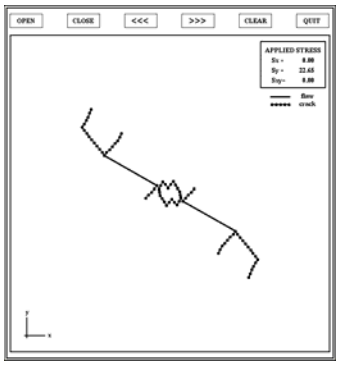 σ_c = 12.2 MPa	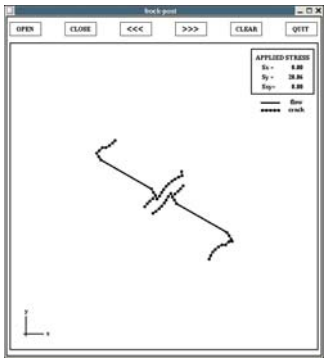 σ_c = 12.2 MPa
Odd coalescence compared to experiment (figure 8.20)	Odd coalescence compared to experiment (figure 8.20)	No coalescence
Decrease σ_{crit} → should favor tensile crack, suppress shear crack **(reasonable effect due to the change of input parameter as indicated by the cracks initiating from the outer flaw tips; however, coalescence pattern is still different from the experimental result)**	-	Increase σ_{crit} → should favor shear crack, suppress tensile crack **(unreasonable effect due to the change of input parameter as indicated by the prefential propagation of tensile cracks in the bridging region)**

Figure 8.27 – Variation of input parameters for flaw pair geometry 30-0-a (a-30-0) (continued).

.

(c) Vary core radius (r_0) on new cracks only (Bobet's $\mathbf{r_0}$ = 0.023 cm)

$r_0 \leq 0.021$	$r_0 =$ **0.022 – 0.026**	$r_0 = 0.027 – 0.035$	$r_0 \geq 0.036$
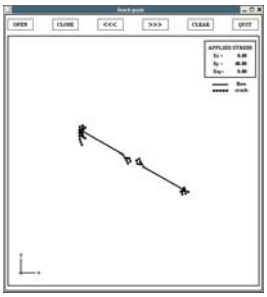	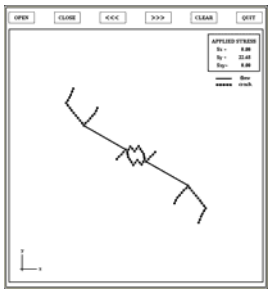	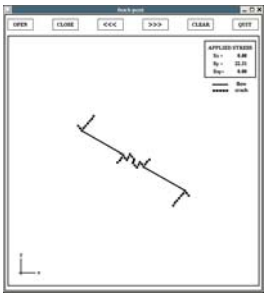	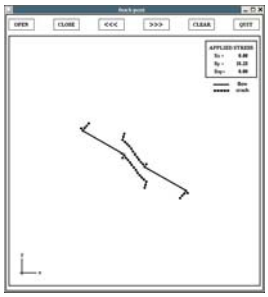
$\sigma_c \leq 11.7$ MPa	$\sigma_c = 12.0 – 12.9$ MPa	$\sigma_c = 13.2 – 14.8$ MPa	$\sigma_c \geq 15.0$
No coalescence	Odd coalescence compared to experiment (figure 8.20)	Coalescence similar to experiment (figure 8.20)	No coalescence
-	-	-	Increasing r_0 favors the initiation of *shear* crack more than the *tensile* crack as indicated by the longer *shear cracks* initiating from the inner flaw tips.

Figure 8.27 – Variation of input parameters for flaw pair geometry 30-0-a (a-30-0) (continued).

(d) Vary friction coefficient (μ) on new cracks only (Bobet's $\boldsymbol{\mu} = 0.70$)

$\mu \leq 0.67$	$\mu = 0.68 - \mathbf{0.70}$	$\mu \geq 0.71$
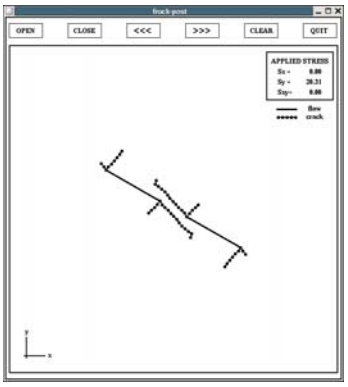	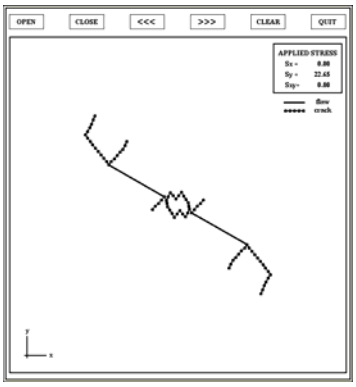	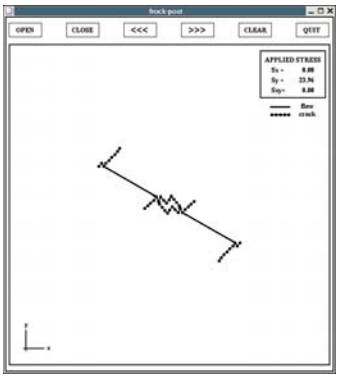
$\sigma_c = 12.2$ MPa	$\sigma_c = 12.2$ MPa	$\sigma_c = 12.2$ MPa
No coalescence	Odd coalescence compared to experiment (figure 8.20)	Odd coalescence compared to experiment (figure 8.20)
Decreasing μ favors the initiation of *shear* crack more than the *tensile* crack	-	Decreasing μ favors the initiation of *tensile* crack more than the *shear* crack

Figure 8.27 – Variation of input parameters for flaw pair geometry 30-0-a (a-30-0) (continued).

$\sigma_c = 19.7$ MPa

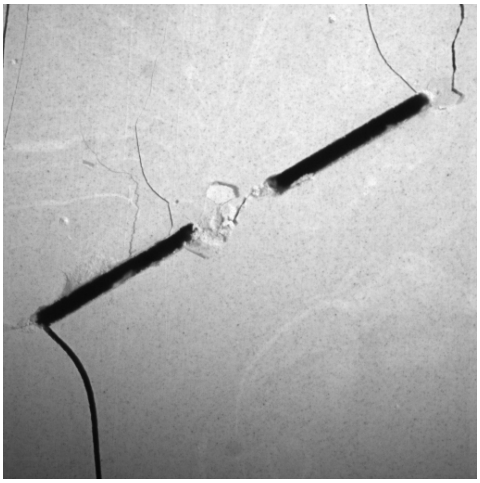

Figure 8.20 – Fracturing and coalescence patterns in gypsum for flaw pair geometry 30-0-a ($\beta - s - c$) or a-30-0 ($L - \beta - \alpha$). Note the development of a shear crack between the inner flaw tips.

(a) Vary critical shear strength (τ_{crit}) only (Bobet's τ_{crit} = 29.5 MPa)

$\tau_{crit} \leq 29.5$	τ_{crit} = 29.6 - 35.0	τ_{crit} = 35.1 - 36.7	τ_{crit} = 36.8 - 37.4	$\tau_{crit} \geq 37.5$
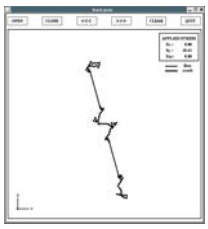	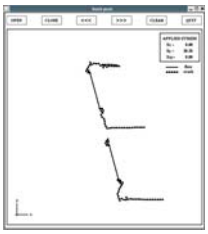	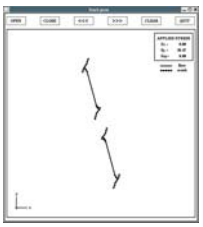	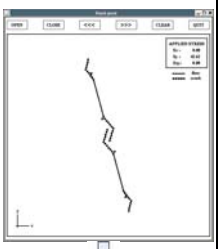 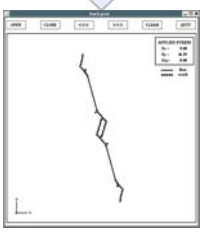	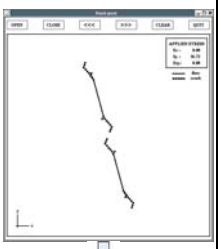 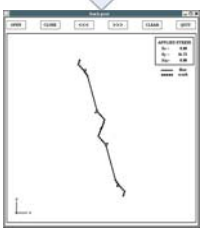
σ_c = 25.6 MPa	σ_c = 25.7 – 30.4 MPa	σ_c = 30.5 – 31.9 MPa	σ_c = 31.9 – 32.5 MPa	σ_c = 32.6 MPa
Odd coalescence compared to experiment (figure 8.24)	No coalescence	No coalescence	Coalescence similar to experiment (figure 8.24)	Coalescence similar to experiment (figure 8.24)
Decrease τ_{crit} → should favor shear crack, suppress tensile crack **(unreasonable effect due to the change of input parameter)**	Increase τ_{crit} → should favor tensile crack, suppress shear crack			
	(unreasonable effect due to the change of input parameter)		**(reasonable effect due to the change of input parameter; and coalescence pattern is similar to the experimental result)**	

Figure 8.28 – Variation of input parameters for flaw pair geometry 75-0-2a (2a-75-0).

.

(b) Vary critical tensile strength (σ_{crit}) only (Bobet's $\boldsymbol{\sigma_{crit}}$ = 18.1 MPa)

$\sigma_{crit} \leq 10.1$	σ_{crit} = 10.2-11.6	σ_{crit} = 11.7-14.2	σ_{crit} = 14.3-14.5	σ_{crit} = 14.6-18.0	σ_{crit} = **18.1**-20.0	$\sigma_{crit} \geq$ 20.1
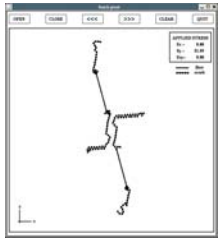 σ_c = 25.6 MPa	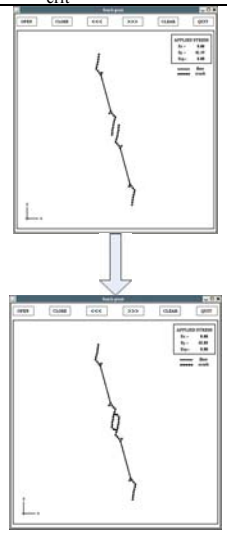 σ_c = 25.6 MPa	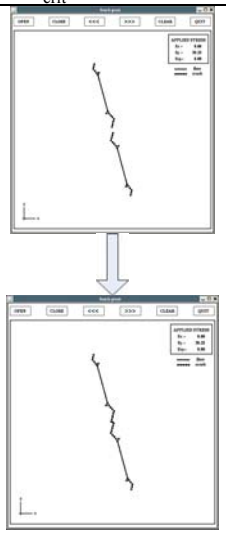 σ_c = 25.6 MPa	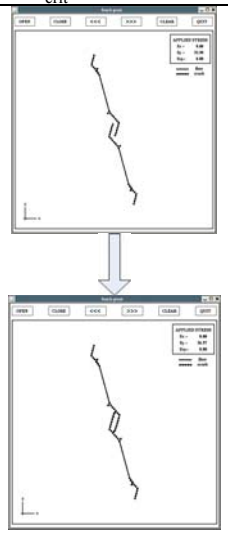 σ_c = 25.6 MPa	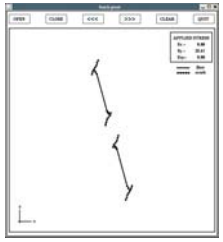 σ_c = 25.6 MPa	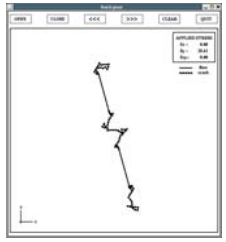 σ_c = 25.6 MPa	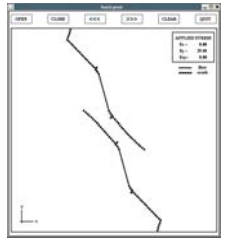 σ_c = 25.6 MPa
No coalescence	Coalescence similar to experiment (figure 8.24)	Coalescence similar to experiment (figure 8.24)	Coalescence similar to experiment (figure 8.24)	No coalescence	Odd coalescence compared to experiment (figure 8.24)	No coalescence
unreasonable effect due to the change of input parameter	Decrease σ_{crit} → should favor tensile crack, suppress shear crack					
	reasonable effect due to the change of input parameter; and coalescence pattern is similar to the experimental result			**reasonable effect due to the change of input parameter**	**unreasonable effect due to the change of input parameter**	**reasonable effect due to the change of input parameter**

Figure 8.28 – Variation of input parameters for flaw pair geometry 75-0-2a (2a-75-0) (continued).

(c) Vary core radius (r_0) on new cracks only (Bobet's $\mathbf{r_0}$ = 0.023 cm)

$r_0 \leq 0.022$	$r_0 = 0.023$	$r_0 = 0.024 – 0.025$	$r_0 = 0.026 – 0.040$	$r_0 \geq 0.041$
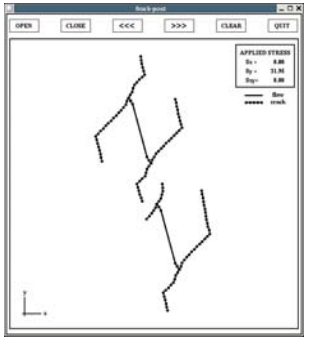	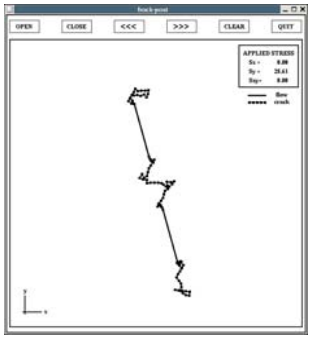	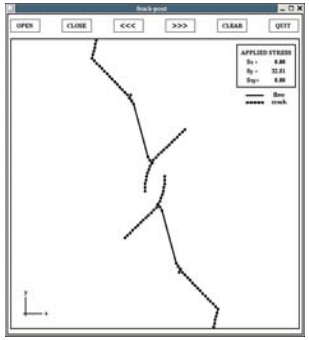	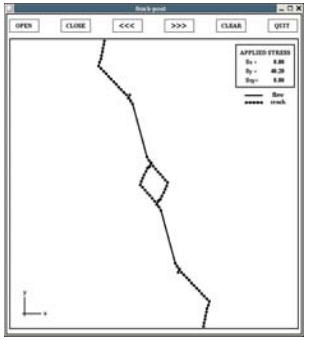	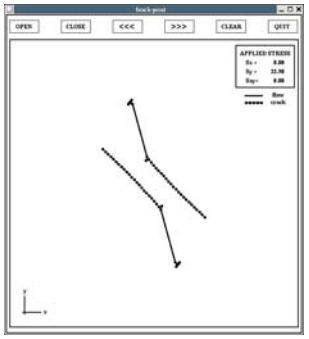
$\sigma_c \leq 25.2$ MPa	$\sigma_c = 25.6$ MPa	$\sigma_c = 26.0 – 26.4$ MPa	$\sigma_c = 26.8 – 31.1$ MPa	$\sigma_c \geq 31.3$ MPa
No coalescence	Odd coalescence compared to experiment (figure 8.24)	No coalescence	Odd coalescence compared to experiment (figure 8.24)	No coalescence

Figure 8.28 – Variation of input parameters for flaw pair geometry 75-0-2a (2a-75-0) (continued).

(d) Vary friction coefficient (μ) on new cracks only (Bobet's $\mu = 0.70$)

$\mu \leq 0.27$	$\mu = 0.28 - 0.49$	$\mu = 0.5 - 0.98$	$\mu \geq 0.99$
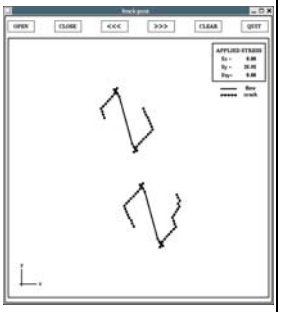 $\sigma_c = 25.6$ MPa	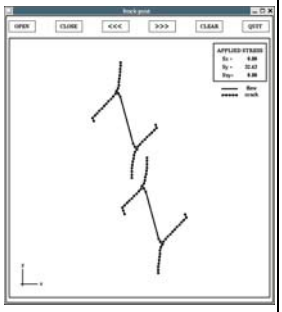 $\sigma_c = 25.6$ MPa	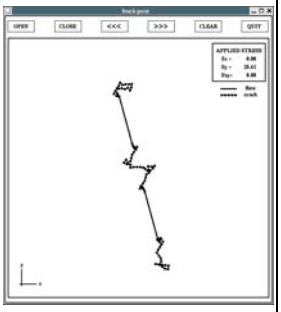 $\sigma_c = 25.6$ MPa	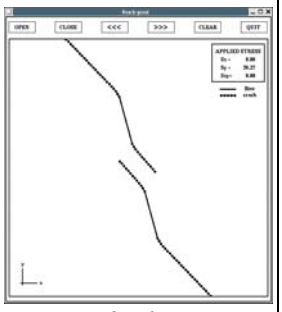 $\sigma_c = 25.6$ MPa
No Coalescence	No Coalescence	Odd coalescence compared to experiment (figure 8.24)	No Coalescence
Decreasing μ favors the initiation of *tensile* crack more than the *shear* crack		-	Decreasing μ favors the initiation of *shear* crack more than the *tensile* crack

Figure 8.28 – Variation of input parameters for flaw pair geometry 75-0-2a (2a-75-0) (continued).

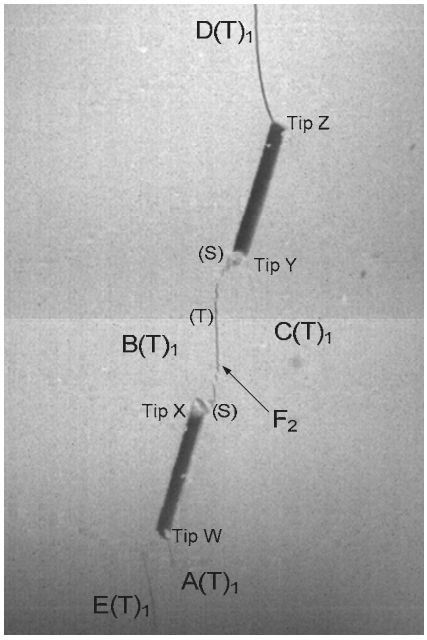

(a) actual specimen

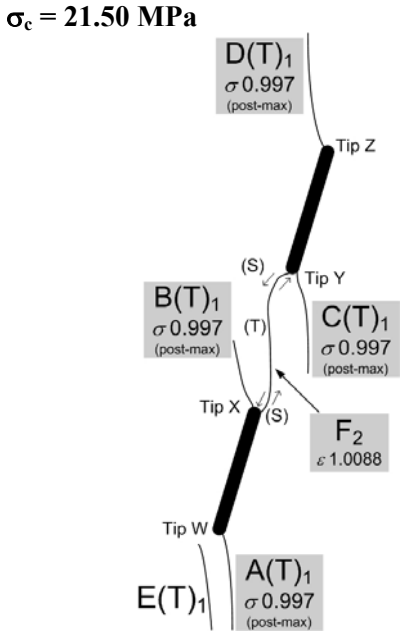

(b) sketch

Figure 8.24 – Fracturing and coalescence patterns in gypsum for flaw pair geometry 75-0-2a ($\beta - s - c$) or 2a-75-0 ($L - \beta - \alpha$).

8.4.4 Simultaneous variation of two input parameters

The results in previous sections show that for certain flaw pairs which could not be modeled satisfactorily by FROCK by the original set of Bobet's parameters, varying one of the four input parameters, namely critical shear strength (τ_{crit}), critical tensile strength (σ_{crit}), radius of core region (r_0) or friction coefficient (μ) can lead to satisfactory modeling results.

It makes sense to take one step further by varying two of the above-mentioned input parameters to observe how sensitive the coalescence behavior of a flaw pair towards the input parameters is. Note that the purpose however is not to obtain another set of best-fit input parameters, which is out of the scope of the present study.

Out of the four flaw pair geometries shown in table 8.6, two flaw pair geometries are chosen for this purpose – **30-0-2a** and **30-a-2a**[3]. As shown in table 8.6, satisfactory coalescence pattern could not be obtained by varying one of the four input parameters for **30-0-2a.** It would thus be useful to observe if satisfactory coalescence pattern could be obtained by simultaneously varying two input parameters. On the other hand, although satisfactory coalescence pattern could be obtained by varying one of the four input parameters for **30-a-2a,** it would still be worthwhile to observe if a similar satisfactory coalescence pattern could be obtained by simultaneously varying two input parameters, but to different extents[4]. See further details below.

---

[3] These two flaw geometries (**30-0-2a** and **30-a-2a**) instead of the other two (**30-0-a** and **75-0-2a**) are chosen because the former two geometries were also studied by Bobet. His results can be used for comparison in subsequent discussion.

[4] To limit the scope of the study, only three parameters, namely critical shear strength (τ_{crit}), critical tensile strength (σ_{crit}) and friction coefficient (μ) are chosen to vary in this section. The radius of core region (r_0) is not varied and the original Bobet's value of 0.23 mm is used throughout the remaining modeling study.

Geometry 30-a-2a

No coalescence occurs when the three input parameters are kept at the original Bobet's values (τ_{crit} = 29.5, σ_{crit} = 18.1, μ = 0.7). See 8.29a below, which is reproduced from figure 8.25a. The overall fracturing remains similar (still no coalescence) when τ_{crit} is deceased from 29.5 to 28.3. Coalescence first occurs when τ_{crit} is deceased down to 28.2. The objective below is to apply slight changes to the other two parameters σ_{crit} and μ individually, while keeping τ_{crit} at 28.3 and observe if coalescence can occur or not.

Slight changes are applied separately onto σ_{crit} (increment of 0.1) and μ (increment of 0.01). As shown in figure 8.29 below, the above individual changes can lead to coalescence. It means that a simultaneous change of τ_{crit} and σ_{crit} (figure 8.29b) or simultaneous change of τ_{crit} and μ (figure 8.29c) can also lead to satisfactory coalescence patterns similar to the coalescence pattern obtained by only varying τ_{cri} (figure 8.29a). The crack initiation stresses due to these two changes (12.2 MPa in figure 8.29b & c) are still in good agreement with that obtained from FROCK by Bobet (12.7 MPa).

τ_{crit} = 28.2 (decreased from 29.5) μ = 0.7 (Bobet's value) σ_{crit} =18.1 (Bobet's value)	τ_{crit} = 28.3 (decreased from 29.5) μ = 0.7 (Bobet's value) **σ_{crit} =18.2 (increased from 18.1)**	τ_{crit} = 28.3 (decreased from 29.5) σ_{crit} = 18.1 (Bobet's value) **μ = 0.71 (increased from 0.70)**
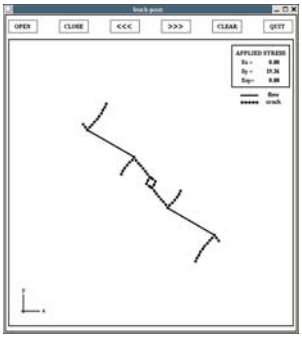 σ_c = 12.1 MPa	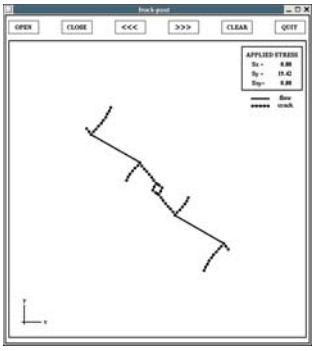 σ_c = 12.2 MPa	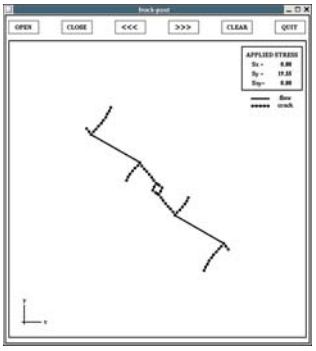 σ_c = 12.2 MPa
(a)	(b)	(c)

Figure 8.29 – Effect on coalescence pattern by (a) only decreasing τ_{crit}, (b) decreasing τ_{crit} and increasing σ_{crit}, (c) decreasing τ_{crit} and increasing μ . Flaw geometry is 30-a-2a. σ_c obtained from FROCK by Bobet is 12.7 MPa.

Similarly, no coalescence occurs when σ_{crit} is equal to 18.1 (original Bobet's value). As shown in figure 8.30a (reproduced from figure 8.25b), when σ_{crit} is increased to 19.8 from the original Bobet's value of 18.1, coalescence can occur. Note that no coalescence occurs in the range between 18.1 and 19.7 inclusively (figure 8.25b). The objective below is to apply slight changes to τ_{crit} and μ individually while keeping σ_{crit} at 19.7 and observe if coalescence can occur or not.

μ = 0.7 (Bobet's value)	
σ_{crit} =19.8 (increased from 18.1) τ_{crit} =29.5(Bobet's value)	σ_{crit} =19.7 (increased from 18.1) **τ_{crit} =29.4 (decreased from 29.5)**
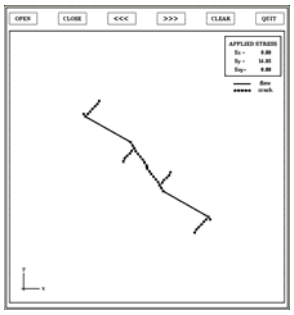	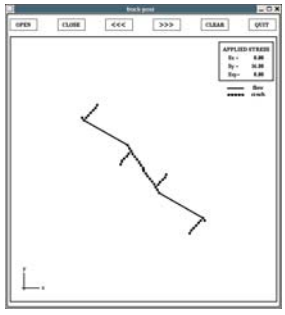
σ_c = 12.7 MPa	σ_c = 12.6 MPa
(a)	(b)

Figure 8.30 – Effect on coalescence pattern by (a) only increasing σ_{crit}, (b) by increasing σ_{crit} and decreasing τ_{crit}. Flaw geometry is 30-a-2a. σ_c obtained from FROCK by Bobet is 12.7 MPa.

Slight changes are applied separately onto τ_{crit} (decrement of 0.1 in figurer 8.30) and μ (incremental changes of 0.01 in figure 8.31) while keeping σ_{crit} at 19.7. As shown in figure 8.30 above, a slight change made to τ_{crit} (decrement of 0.1 from the original Bobet's value of 29.5 to new value of 29.4) can lead to coalescence. In other words, the effect of increasing σ_{crit} from 18.1 to19.8 is equivalent to the combined effect of increasing σ_{crit} from 18.1 to19.7 and decreasing τ_{crit} from 29.5 to 29.4. Also, the *new* crack initiation stress associated with the change of parameters (12.6 MPa) is still in good agreement with that obtained from FROCK by Bobet (12.7 MPa).

τ_{crit} =29.5 (Bobet's value)				
σ_{crit} =19.8 (increased from 18.1)	σ_{crit} =19.7 (increased from 18.1)			
μ = 0.7 (Bobet's value)	**μ = 0.71-0.75**	**μ = 0.76-0.78**	**μ = 0.79**	**$\mu \geq$ 0.80**
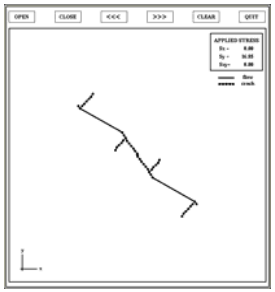 σ_c = 12.7 MPa	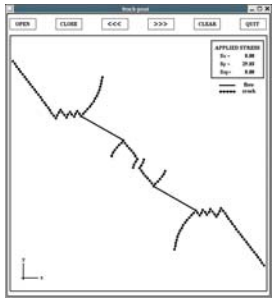 σ_c = 12.7 MPa	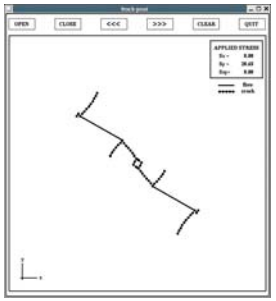 σ_c = 12.7 MPa	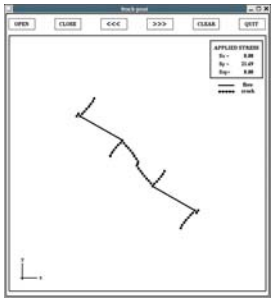 σ_c = 12.7 MPa	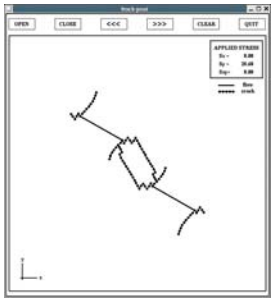 σ_c = 12.7 MPa
	No coalescence	Coalescence	Coalescence	Coalescence
(a)	(b)	(c)	(d)	(e)

Figure 8.31 – Effect on coalescence pattern by increasing μ from its original value of 0.70. Flaw geometry is 30-a-2a. σ_c obtained from FROCK by Bobet is 12.7 MPa.

On the other hand, while keeping σ_{crit} at 19.7, a slight increase of μ up to the range of 0.71 – 0.75 cannot immediately lead to coalescence (figure 8.31). Coalescence can however be obtained when μ is increased to a high enough value ($\geq$ 0.76). As shown in figure 8.31, the effect of solely increasing σ_{crit} from 18.1 to19.8 is thus equivalent to the combined effect of increasing σ_{crit} from 18.1 to19.7 and increasing μ from 0.70 to the range 0.76 – 0.79. Note that various coalescence patterns are obtained for different μ values. Also, changing the value of μ does not affect the crack initiation stress values, which still remains at 12.68 MPa.

Geometry 30-0-2a

Coalescence is not achieved in the FROCK model for flaw pair geometry 30-0-2a. Besides, as shown in figure 8.26, the effect on coalescence patterns due to the change of one of the three input parameters varies – coalescence can be obtained by separately increasing τ_{crit} (figure 8.32a) or σ_{crit} (figure 8.32b), but no coalescence can be obtained no matter how μ is varied. However, the coalescence patterns obtained from the change of one parameter are very different from that observed in the present experimental study (figure 8.18), which is achieved by linking up the inner flaw tips by coplanar shear cracks. See figure 8.32d below.

(a)	(b)	(c)
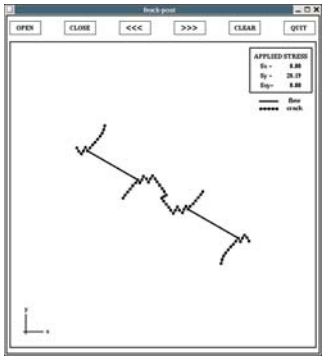	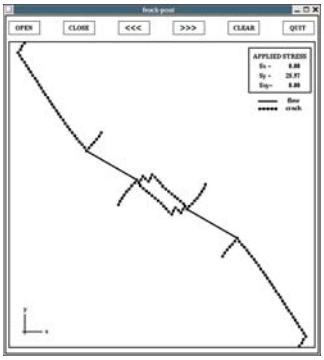	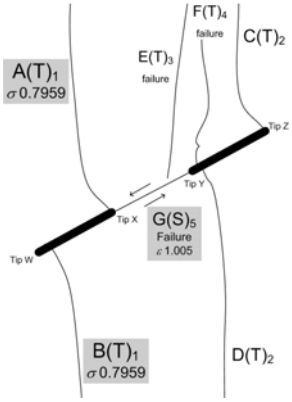
$\sigma_c \geq 13.5$ MPa	$\sigma_c \geq 12.9$ MPa	$\sigma_c = 16.0$ MPa
Keep σ_{crit} and μ at original values; vary $\tau_{crit} \geq 30.9$	Keep τ_{crit} and μ at original values; vary $\sigma_{crit} \geq 18.5$	Present experimental study

Figure 8.32 – Coalescence patterns obtained (a) by varying τ_{crit} only, (b) by varying σ_{crit} only, (c) from the present experimental study. Flaw geometry is 30-0-2a.

As shown in figure 8.26a (reproduced in figure 8.33a below), when τ_{crit} is increased to equal to or larger than 30.9 from the original Bobet's value of 29.5 (σ_{crit} remains at 18.1 and μ remains at 0.7), coalescence can occur. Note that no coalescence occurs in the range between 29.6 and 30.8 inclusively. The objective below is to apply slight changes to σ_{crit} and μ individually while keeping τ_{crit} at 30.8 and observe if coalescence can occur or not.

Slight changes are applied onto σ_{crit} as shown in figure 8.33. Coalescence can occur when σ_{crit} is increased to a value higher than or equal to 18.3 (figure 8.33d) or decreased to a value lower or equal to 17.9 (figure 8.33b); and the pattern is similar to that due to the change of τ_{crit} only (figure 8.33a). In other words, the effect of increasing τ_{crit} from 29.1 to 30.9 is equivalent to the combined effect of increasing τ_{crit} from 29.1 to 30.8 and increasing σ_{crit} from 18.1 to $\geq$18.3 or the combined effect of increasing τ_{crit} from 29.1 to 30.8 and decreasing σ_{crit} from 18.1 to $\leq$17.9.

Changing the critical tensile strength σ_{crit} does not change the crack initiation stresses (σ_c = **13.5**). It is reasonable since the first cracks initiating from the pre-existing flaws as modeled by FROCK are shear cracks, which are unaffected by the value of σ_{crit}. This value (σ_c = **13.5**) is also in good agreement with that obtained from FROCK by Bobet (12.3 MPa). Note that in the experimental observation, the first cracks initiating from the pre-existing flaws are however tensile wing cracks (figure 8.32c).

μ =0.7 (Bobet's value)			
τ_{crit} =30.9 (increased from 29.1)	τ_{crit} =30.8 (increased from 29.1)		
σ_{crit} =18.1 (Bobet's value)	$\sigma_{crit} \leq 17.9$	**σ_{crit} = 18.0 – 18.2**	$\sigma_{crit} \geq 18.3$
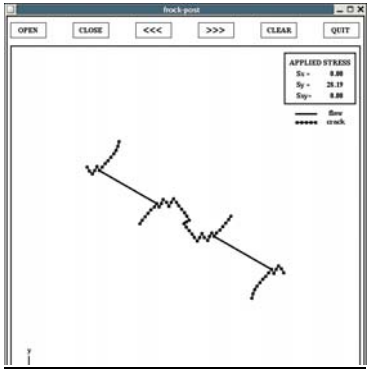	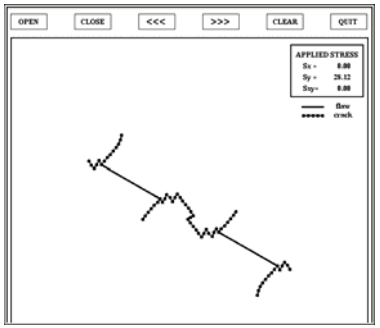	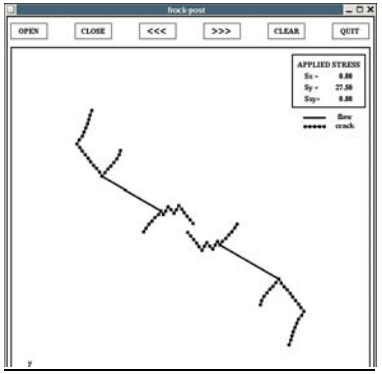	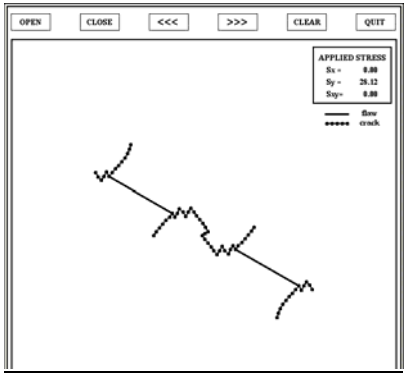
σ_c = 13.5 MPa	σ_c = 13.5 MPa	σ_c = 13.5 MPa	σ_c = 13.5 MPa
	Coalescence	No coalescence	Coalescence
(a)	(b)	(c)	(d)

Figure 8.33 – Effect on coalescence pattern by (a) varying $\boldsymbol{\tau_{crit}}$ only, (b, c, d) varying $\boldsymbol{\tau_{crit}}$ and $\boldsymbol{\sigma_{crit}}$. Flaw geometry is 30-0-2a. σ_c obtained from FROCK by Bobet is 12.3 MPa.

As shown in figure 8.26b (reproduced in figure 8.34a below), when σ_{crit} is increased to 18.5 from the original Bobet's value of 18.1 (τ_{crit} remains at 29.5 and μ remains at 0.7), coalescence can occur. Note that no coalescence occurs in the range between 18.1 and 18.4 inclusively. The objective below is to apply slight changes to τ_{crit} and μ individually while keeping σ_{crit} at 18.4 and observe if coalescence can occur or not.

As shown in figure 8.34, changes are made continually to τ_{crit}, around its original value of 29.5, while keeping σ_{crit} (18.4) and μ (0.7) constant. For τ_{crit} = **29.2 – 30.6** (figure 8.34c), multiple segments of tensile and shear cracks develop from the internal flaw tips and propagate away from each other, which leads to no coalescence. For $\tau_{crit} \leq$ **29.1** (figure 8.34b), the development of shear cracks from internal flaw tips is more favored. It is logical due to the change of the input parameter. However, these two internal shear cracks do not coalesce. For $\tau_{crit} \geq$ **30.7** (figure 8.34d), the development of shear cracks is less favored as indicated from the cracks initiating from the outer flaw tips. It is logical due to the change of the input parameter. A short tensile segment links up the multiple crack segments initiating independently from the inner flaw tips. However, the resultant coalescence pattern is different from the one due to the change of one input parameter (increasing σ_{crit} from 18.1 to 18.5) as shown in figure 8.34a.

Increasing the critical shear strength τ_{crit} increases the crack initiation stresses (σ_c). This is reasonable since the first cracks initiating from the pre-existing flaws as modeled by FROCK are shear cracks. When τ_{crit} = 30.7 at which coalescence occurs, σ_c = 13.45 MPa, which is still in good agreement with that obtained from FROCK by Bobet (12.3 MPa).

$\mu = 0.7$ (Bobet's value)			
σ_{crit} =18.5 (increased from 18.1)	σ_{crit} =18.4 (increased from 18.1)		
τ_{crit} =29.5 (Bobet's value)	$\tau_{crit} \leq 29.1$	**τ_{crit} = 29.2 – 30.6**	$\tau_{crit} \geq 30.7$
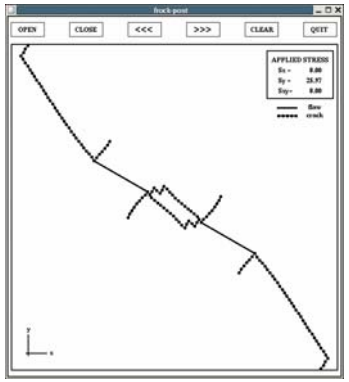 σ_c = 12.9 MPa	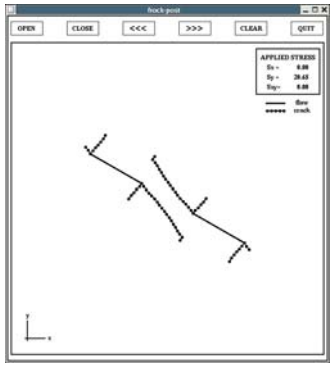 $\sigma_c \leq 12.8$ MPa	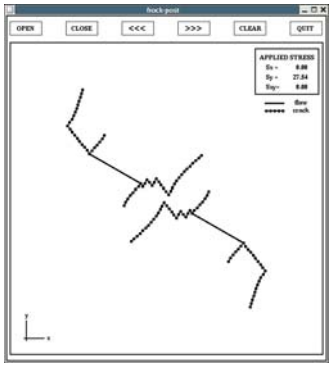 σ_c = 12.8 – 13.4 MPa	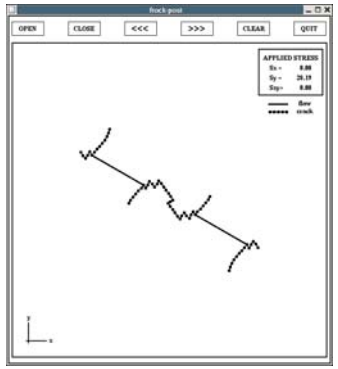 $\sigma_c \geq 13.5$ MPa
	No coalescence	No coalescence	Coalescence
(a)	(b)	(c)	(d)

Figure 8.34 – Effect on coalescence pattern by (a) varying $\boldsymbol{\sigma_{crit}}$ only, (b, c, d) varying $\boldsymbol{\sigma_{crit}}$ and $\boldsymbol{\tau_{crit}}$. Flaw geometry is 30-0-2a. σ_c obtained from FROCK by Bobet is 12.3 MPa.

<table>
<tr><td colspan="3">τ_{crit} =29.5 (Bobet's value)</td></tr>
<tr><td>σ_{crit} =18.5 (increased from 18.1)</td><td colspan="2">σ_{crit} =18.4 (increased from 18.1)</td></tr>
<tr><td>μ = 0.7 (Bobet's value)</td><td>$\mu \leq 0.69$</td><td>$\mu \geq 0.70$</td></tr>
<tr><td> 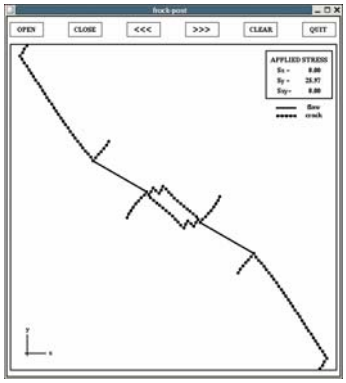
σ_c = 12.9 MPa</td><td> 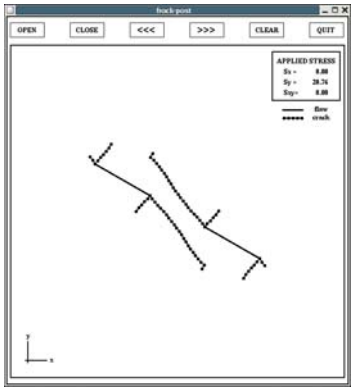
σ_c = 12.9 MPa</td><td> 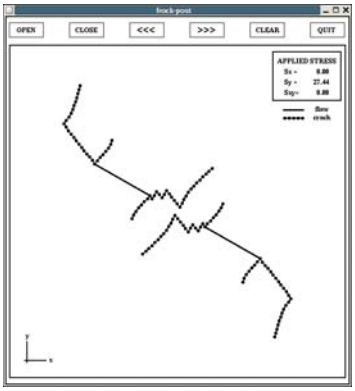
σ_c = 12.9 MPa</td></tr>
<tr><td></td><td>No coalescence</td><td>No coalescence</td></tr>
<tr><td>(a)</td><td>(b)</td><td>(c)</td></tr>
</table>

Figure 8.35 – Effect on coalescence pattern by (a) varying σ_{crit} only, (b, c) varying σ_{crit} and μ . Flaw geometry is 30-0-2a. σ_c obtained from FROCK by Bobet is 12.3 MPa.

As shown in figure 8.35 above, changes are made continually to μ, while keeping τ_{crit} (29.5) and σ_{crit} (18.4) constant. Decreasing μ to values equal to or less than 0.69 favors the propagation of shear cracks from the inner flaw tips (it is logical due to the change of input parameter), which however does not lead to coalescence (figure 8.35b). The coalescence patterns due to the increase of μ are similar to that obtained from the original value of μ = 0.70, in which multiple shear and tensile segments initiated from the inner flaw tips, but do no coalesce (figure 8.35c). It means that by keeping σ_{crit} at 18.4, it is impossible to obtain the same coalescence pattern as of σ_{crit} equal to 18.5 (figure 8.35a) no matter how μ is varied. Note also that changing the value of μ does not affect the crack initiation stress values, which still remains at 12.9 MPa.

To conclude, this section studies the effect on coalescence behavior by varying two of the input parameters. The method is: One of the three parameters is first chosen at a marginal value, along with two other parameters at original values, at which no coalescence occurs. A second parameter is then varied (the third one is still kept at its original value) to observe the change of coalescence pattern, specifically if coalescence can be obtained.

For flaw geometries **30-a-2a** and **30-0-2a**, coalescence is not achieved in FROCK by using the original Bobet's parameter values, while the effect on coalescence in these two flaw geometries varies by varying one of the three input parameters.

For **30-a-2a**, in which a satisfactory coalescence pattern is obtained by varying one of the three input parameters in FROCK, similar satisfactory coalescence patterns could again be obtained by varying two of the three input parameters simultaneously (figure 8.29 – 8.31).

For **30-0-2a**, as noted earlier in section 8.4.3 (table 8.6), although coalescence could be obtained by varying one of the three input parameters in FROCK, the coalescence patterns obtained are different from those observed in the present experimental study (figure 8.32) and are unsatisfactory. By varying two of the three input parameters simultaneously, similar unsatisfactory coalescence patterns are again obtained.

In all of the above changes, however, the crack initiation stresses are still in agreement with those obtained from the FROCK study by Bobet.

The above results for the two flaw geometries tested (30-a-3a and 30-0-2a) thus suggest that the coalescence patterns are very sensitive to the simultaneous changes of two input parameters, while the crack initiation stresses are not. The same coalescence pattern can be obtained by different sets of input parameters. Notice that the values of σ_{crit} and τ_{crit} obtained by Bobet were based on a back-fitting analysis which compared his own experimental results and numerical results. They were not directly related to any

measurable macroscopic specimen strength parameters. The availability of more experimental data thus implies that there is room for improving the back-fitting analysis.

8.5 Summary and discussion

Two crack initiation criteria have been reviewed in the first part of this chapter – strain-based and stress-based proposed by Reyes (1991) and Bobet (1997), respectively, at the MIT rock mechanics group. The second part shows some fracturing and coalescence modeling results obtained by using the in-house numerical code FROCK, in which the crack-based crack initiation criterion was incorporated (Bobet & Einstein, 1998b). The modeling work was mainly based on the parameters obtained previously by the authors, Variations of some input parameters (one or two at a time) were made to observe the sensitivity of the fracturing and coalescence patterns towards those input parameters. The results are compared with the previous modeling results (Bobet, 1997, Bobet & Einstein, 1998b) and the present experimental results, when available.

In the comparison of the present modeling results obtained from FROCK (6 flaw pair geometries) with the present experimental results, agreement is found for only two flaw pair geometries (2a-45-0, 2a-60-0). For the remaining four geometries in which coalescence is observed to occur in experiments, no coalescence is obtained from FROCK modeling.

The coalescence patterns of flaw pairs with flaw inclination 45^o obtained in the present FROCK study generally agree well with those obtained in the FROCK study by Bobet. Slight discrepancies are however observed for the crack initiation stress values. Since all the input parameters are the same as those used before, it thus appears that the discrepancies may arise from the different degrees of precision associated with the computing facilities used over different times.

For geometries with flaw inclination angles other than 45°, the present FROCK results are less consistent with the Bobet's FROCK results and/or present experimental study (see table 8.4 for details). Note also that in FROCK all new cracks initiating from the pre-existing flaws are assumed to originate from the flaw tips. In the present experimental studies, some new tensile wing cracks (TWCs) were found to initiate from the pre-existing flaws at a distance slightly away from the flaw tips (e.g. figure 8.16 for flaw inclination angle 30°). As discussed earlier in chapter 5, this phenomenon is related to the flaw inclination angle (β) of the pre-existing flaws. As β decreases, the position where TWCs initiate shifts from a position close to/at the flaw tips towards the flaw centers. This phenomenon may have a significant influence in the comparison, but it has not been investigated further as it is outside the capability of FROCK.

With regard to those flaw geometries with unsatisfactory modeling results, FROCK was run again by either varying one parameter of a set of four at a time or two parameters at a time of a set of three parameters. The four input parameters are critical shear strength (τ_{crit}), critical tensile strength (σ_{crit}), core radius (r_0) and friction coefficient (μ). For some flaw pair geometries (30-a-2a, 30-0-a, 75-0-2a), a slight variation of **one** particular parameter(s) can successfully lead to coalescence patterns (table 8.6). However, the crack initiation stresses (σ_c) associated with the change of parameters for the three flaw pair geometries are not always in good agreement with the Bobet's FROCK values or the present experimental values. For the flaw pair geometry 30-0-2a, no satisfactory coalescence patterns can be obtained no matter how the four input parameters are varied individually.

A preliminary attempt was also carried out to observe the effect on crack initiation stresses and coalescence patterns by varying **two** input parameters simultaneously. It can again be concluded from the modeling results that the coalescence patterns are very sensitive to slight variations of the input parameters. The same coalescence pattern sometimes can be obtained by different sets of input parameters with no significant effects on the crack initiation stresses (σ_c).

The values of the input parameters σ_{crit}, τ_{crit} and r_0 provided by Bobet were obtained from a back-fitting analysis, by comparing his own experimental results with numerical results. The present numerical and experimental studies suggest that with the availability of more experimental data, there is still room for improving the back-fitting analysis to obtain the input values σ_{crit}, τ_{crit} and r_0. Although the friction coefficient of the newly generated cracks (μ) does not affect the crack initiation stress and the crack type, it influences the subsequent crack propagation and hence coalescence patterns. Improvements through better characterization of the surface roughness of the newly produced *tensile cracks* and *shear cracks* by different values of μ are certainly desirable.

CHAPTER 9 – Discussion

9.1 Introduction

Based on the results presented in previous chapters, this chapter focuses on discussing the results with the following emphases:

- the influence of material on deformation and fracturing behavior
- the different crack types observed in the experiments
- the different crack coalescence patterns observed in the experiments

This chapter is divided into four main parts reflecting these emphases.

The first part is a summary of the key findings, which form the foundation for subsequent discussion (Section 9.2).

The second part discusses the influence of material type on some of the macroscopically observed fracturing behavior. It begins with comparing the macroscopic deformation and fracturing behavior in gypsum and marble during the loading test observed in the video recordings. These macroscopic phenomena are then correlated with the microscopic deformation phenomena. The differences in the microscopic deformation phenomena observed in the two materials are then further investigated by relating them to the inherent material properties and textural characteristics (Sections 9.3 & 9.4).

The third part discusses the seven crack types identified in the present study. As a corollary, the inconsistent use of terminologies in the past studies is also discussed and rectified (Section 9.5).

Eventually, in the fourth part, the nine coalescence categories generalized in the present study are discussed regarding the controlling parameters. Attempts are also made to

explain some of the different coalescence patterns observed in gypsum and marble based on the correlation previously made in the second and the third parts (Sections 9.6 – 9.8).

9.2 Key findings

1) In the present study, a **high speed camera** has been successfully incorporated into the uniaxial loading experimental set-up to study the dynamic fracturing and crack coalescence events in molded gypsum and Carrara marble. Although the set-up was similar to that previously used by Martinez (1999), the frame rate used in the present study was much higher within the range of 1,000 to 24,000 pps (pictures per second), compared to 250 pps by Martinez (1999). In addition, the digital format of the videos allowed a much easier image manipulation with an improved image resolution. In earlier studies without the use of the high speed camera (e.g. Wong & Chau, 1998, Bobet & Einstein, 1998a), the determination of crack initiation mode relied mostly on the fractographical features left on the crack surfaces, which was less accurate. With the use of the high speed camera, it became possible to make detailed observations of the crack initiation mode (shear/tensile) and hence coalescence types – a total of *seven* crack types and *nine* coalescence categories have been systematically identified in the present study. See sections 9.5 and 9.6.

2) At a **macroscopic** scale as observed in the video recordings, the **tensile crack** development in gypsum and marble was quite different. The tensile crack in **gypsum** initiated as a hair-line crack, which was not discernable to unaided eyes, but observable with a 10x hand lens. It appeared to be *continuous* (see further comments in key findings point 3) and propagated from the pre-existing flaws in response to the compressive loading. Continued loading increased the aperture of the tensile crack to make it discernable to unaided eyes. In **marble**, the first observable change in response to loading was the development of multiple white patches from the pre-existing flaws. These white patches, which were oriented in different directions, lengthened and propagated away from the flaws as loading increased. As loading

further increased, tensile cracks began to initiate along the white patches, preferentially along the vertical white patches and those white patches displaying conventional wing appearance. Instead of initiating and propagating from the pre-existing flaw as a macroscopic continuous crack, multiple individual tensile cracks usually developed as short en echelon crack segments. These en echelon cracks lengthened, which eventually linked up to form a continuous crack as loading further increased. It has to be emphasized that the above observations are based on video recordings at a macroscopic scale. See section 9.3.1.

3) In **marble**, at a **microscopic** scale based on SEM study, macroscopic **white patches** (free of observable cracks to unaided eyes) associated with **tensile** crack development were found to be underlain by microcracking zones (process zones). The microcrack density in the process zones, which consisted of central dominant cracks and flanking microcracks, increased with the applied loading. In **gypsum**, on the other hand, the **macroscopic** hair-line tensile crack was found to consist of segmented tensile cracks on a **microscopic** scale in the ESEM study. Since they were very short and in very close proximity, they can not be differentiated macroscopically and appeared to be continuous with a 10x hand lens. Although microcracking zones (process zones) associated with crack development were also identified in gypsum, their extent was much more limited as seen in an ESEM study, and they did not appear as white patches at a macroscopic scale. See section 9.3.2.

4) At a **macroscopic** scale as observed in the video recordings, the **shear crack** development in gypsum and marble was quite different. The initiation of shear cracks in **gypsum** was not preceded by any observable signs and it was due to the shear movement in the intact material. In **marble**, however, the initiation of shear cracks in was preceded by a development of white patches. The white patches lengthened and widened in response to the applied loading, until a load level at which shear cracks initiated along them. In both materials, the shear crack initiation was often accompanied by an occurrence of local surface spalling, indicating the presence of a

local compressive stress field. The extent of spalling in gypsum was however often greater than that in marble. See section 9.4.

5) At a **microscropic** scale, the white patch in **marble** preceding the initiation of a coplanar shear crack from a pre-existing flaw tip was found to be underlain by multiple en echelon microcracking zones close to the flaw tips. However, since a similar study was not conducted in **gypsum**, the microscopic features associated with the subsequent macroscopic shear cracks are not known at the present stage. See section 9.4.

6) Pre-existing flaw pair geometries (flaw inclination angle, bridging angle, ligament length) have a strong influence on crack coalescence processes and eventual patters. In addition, the nature and extent to which the **flaw pair geometries** influence the coalescence behavior is different between molded gypsum and Carrara Marble. A total of nine coalescence categories were identified and generalized in the present study. See section 9.6.

Note that the list above is only a brief summary of the key observations. Further discussion will continue in the subsequent sections and will be supplemented by additional details. See the relevant section numbers stated at the end of each point above.

9.3 Influence of material type

In this section, the similarities and differences of the *macroscopic* deformations observed in gypsum and marble in response to uniaxial compression loading are first discussed. They are then correlated with the microscopic deformations observed from the SEM and ESEM studies where appropriate. The differences of the microscopic deformation mechanisms are then explained at the end based on the inherent material properties (texture). The above scheme for discussion is summarized in table 9.1. The eventual goal is to conclude how the material properties and inherent texture influence the macroscopic deformation and fracturing processes.

Macroscopic deformation observed during loading test	←*correlation*→	*Microscopic* deformation observed during loading test	←*correlation*→	*Microscopic* material texture and material properties
o types of cracks initiating from pre-existing flaws o crack development sequence o coalescence category o stress-strain behavior o other features, e.g. development of hair-line cracks, white patches		o types of microcracks (intergranular, intragranular) o density and distribution of microcracks		o grain size o grain shape o arrangement relationship between grains o uniaxial compressive strength

Table 9.1 – Correlation of macroscopic observations and microscopic observations.

9.3.1 Macroscopic observations

In earlier experimental studies, identification of **shear cracks** relied mainly on indicators such as striations, slickensides, shear fragments and pulverized powder, while the absence of the above-mentioned features and the presence of plumose features and/or arrest rings served as indicators of **tensile cracks**. However, the main limitation of associating crack surface features (fractography) with crack type is that "*there may be initial tensile fractures followed by shearing, and the latter then obfuscate the pre-existing tensile fractures*" (Einstein & Meyer, 1999). In the present study, the determination of the type (shear/tensile) of the newly-formed cracks did not solely rely on the fractographical features. With the use of the high speed camera operating up to the frame rate of 24,000 frames/second, signs of incipient tensile crack opening and shear displacement can be identified and used to determine the crack nature.

In response to applied uniaxial compression, the tested Carrara Marble and molded gypsum prismatic specimens behaved differently. Cracks always developed in gypsum in a brittle manner without any preceding signs. Their initiation was often accompanied by a distinct cracking sound and a pronounced stress drop on the stress-strain curve. In marble, individual white patches first developed in response to loading. Minute cracks later initiated and lengthened along the white patches. The initiation of the white patches and the overlying minute cracks was often not accompanied by any distinct cracking sound. Stress drops on the stress-strain curve were sometimes observed, but not as pronounced as in gypsum. As observed in the video recordings, some of the white patches in marble developed very early[1] in the loading process. They propagated (increased in length), widened and intensified in color as applied loading further increased. Very often, additional white patches also developed just before the specimen strength was reached. Such a development of white patches was however not observed in gypsum in the video recordings.

[1] White patch initiation can be represented by the white patch initiation stress ratio, which is the stress corresponding to the first appearance of white patch normalized by the respective specimen strength. Further discussion follows later in this section.

Another pronounced difference between gypsum and marble in response to the uniaxial loading was with respect to the initiation of **tensile cracks**. The initiation of some tensile cracks in Carrara Marble was found to be due to the initiation, propagation and coalescence of multiple much shorter crack segments along some earlier developed white patches. One typical example in **marble** is shown in figure 9.1 which captures the deformation observed on the front face of the specimen. The general trending orientation of the short en echelon crack segments often deviates slightly from that of the underlying white patch In the examples shown in figures 9.1 b & c, the white patch was inclined at 10^o with the vertically applied σ_1, while the individual tensile crack segments inclined at 5^o with the vertically applied σ_1. In contrast, such a development and evolution of white patches was not observed in **gypsum** in both the camcorder recordings and high speed camera images. Without being preceded by any observable signs, the tensile cracks usually appeared abruptly as continuous hair-line cracks as in response to loading at this *macroscopic* scale. Note however that at a *microscopic* scale, the hair-line tensile cracks in gypsum were found to consist of segmented tensile cracks.

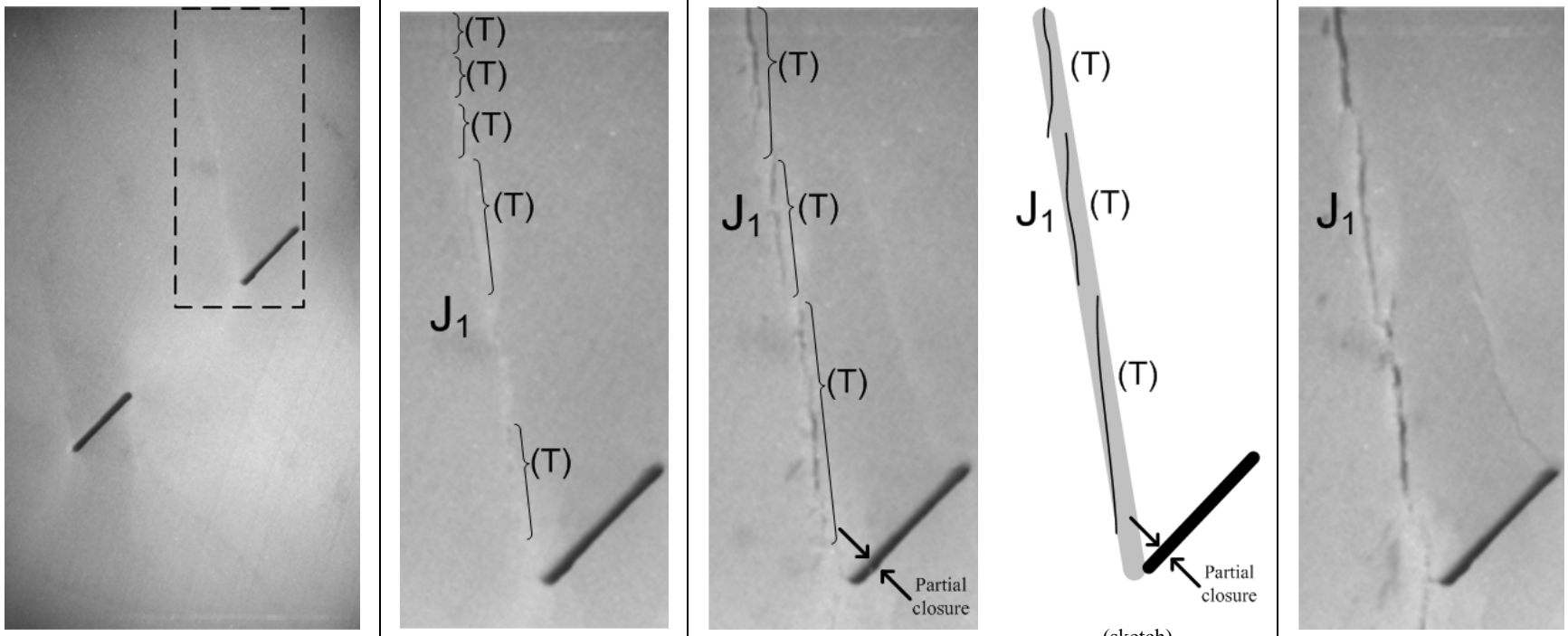

(a) 70.54 MPa

(b) 70.49 MPa
HS Image # - 5425

(c) 70.40 MPa
HS Image # - 5067

(d) 66.71 MPa
HS Image # - 4182

Figure 9.1 – Development of a type 3 tensile crack (J) along a white patch which had initiated from the left tip of the right flaw. The region shown in figures (b), (c) and (d) is enclosed in figure (a). In the sketch shown in (c), the grey patch represents the white patch observed in the high speed video image. The traces of the echelon cracks are represented by black lines. The high speed images were recorded at a frame rate of 11,019 pps. The length of the pre-existing flaw is 0.5" (12.7 mm).

The initiation of shear cracks in gypsum and marble was generally similar, which was due to the occurrence of shear displacement in intact material. The high speed videos revealed that their initiation was often accompanied by the occurrence of local surface spalling, indicating the presence of a local compressive stress field. The extent of spalling in gypsum (figure 9.2) was however often larger than in marble (figure 9.3).

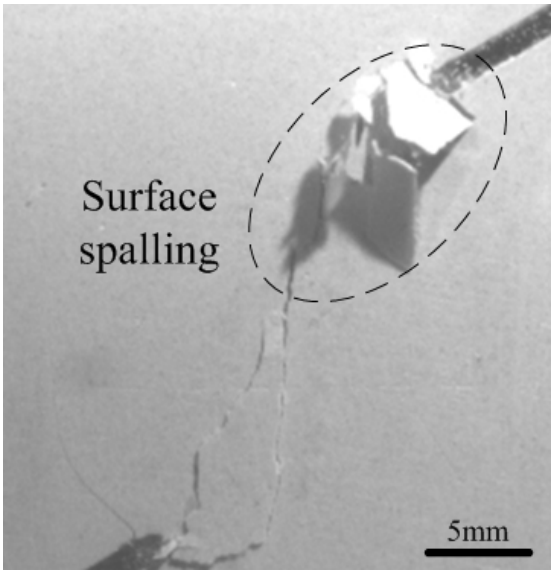

Stress level – 22.36 MPa
High speed image number : -4600

(a) Spalling occurs in a region adjacent to the left tip of the top flaw.

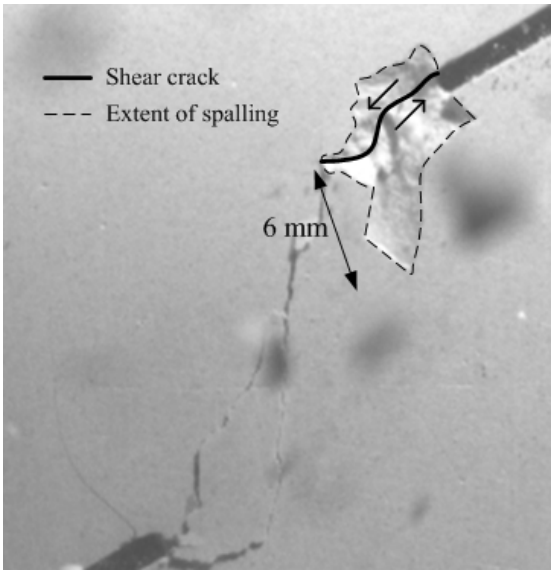

Stress level – 21.86 MPa
High speed image number : - 4458

(b) After the surface spalling detaches from the specimen front face, the trace of the underlying shear crack is exposed.

Figure 9.2 – Development of surface spalling zone overlying a shear crack in gypsum (specimen 4a-30-30-A1). The trace of the shear crack and the extent of the associated spalling zone are traced in the figure on the right. High speed camera frame rate is 10,000 frames per second.

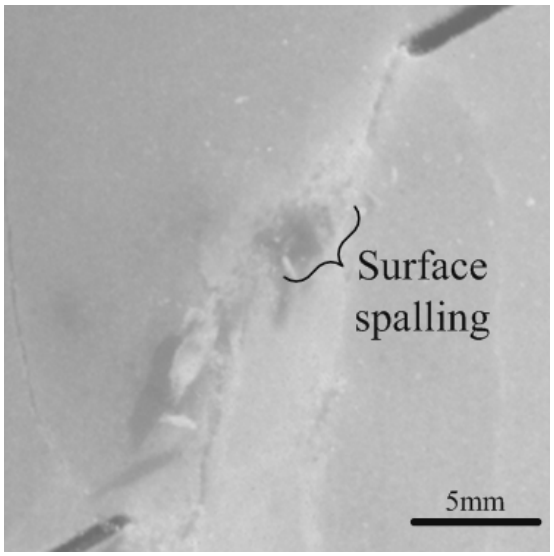

Stress level – 50.54 MPa
High speed image number : -4399

(a) Spalling occurs in the center of the bridging region.

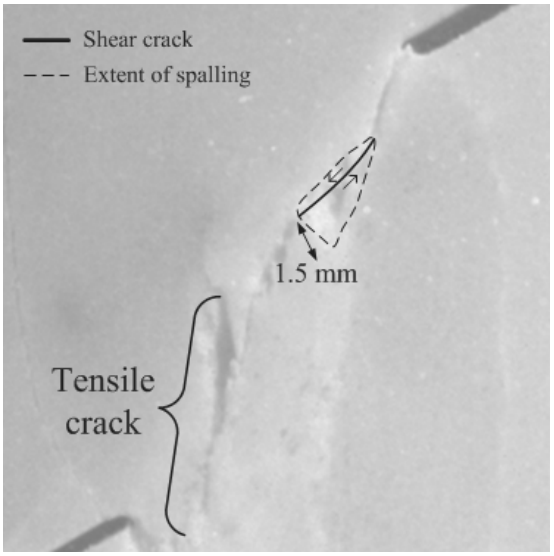

Stress level – 48.36 MPa
High speed image number : -4014

(b) After the surface spalling detaches from the specimen front face, the trace of the underlying shear crack is exposed. The trace of a nearby steeply inclined tensile crack is also marked.

Figure 9.3 – Development of surface spalling zone overlying a shear crack in marble (specimen CM 4a-30-30-C). The trace of the shear crack and the extent of the associated spalling zone are traced in the figure on the right. High speed camera frame rate is 8,213 frames per second.

Typical stress-strain curves corresponding to uniaxial compression tests on gypsum and marble specimens containing a flaw pair are shown together in figure 9.4. Different macroscopic deformation events observed from the video recordings can be correlated with stress-strain curves. In gypsum, the first observable change in response to the applied loading was the macroscopic crack initiation (indicated by an open square in figure 9.4). For the particular specimen shown here, this crack was also the coalescence crack which linked up the two pre-existing flaws. However, the first cracks were not necessarily the coalescence cracks as observed in the experiments, which was dependent on the flaw pair geometry (see chapter 6). The specimen which has the first crack as the coalescence crack as shown in figure 9.4 is thus only one possibility. Further loading

induced additional cracks in the specimen (not shown in figure 9.4). High speed videos revealed that the sudden strength loss (maximum stress indicated by an open circle in figure 9.4) in gypsum was due to the initiation and propagation of one or multiple unstable cracks.

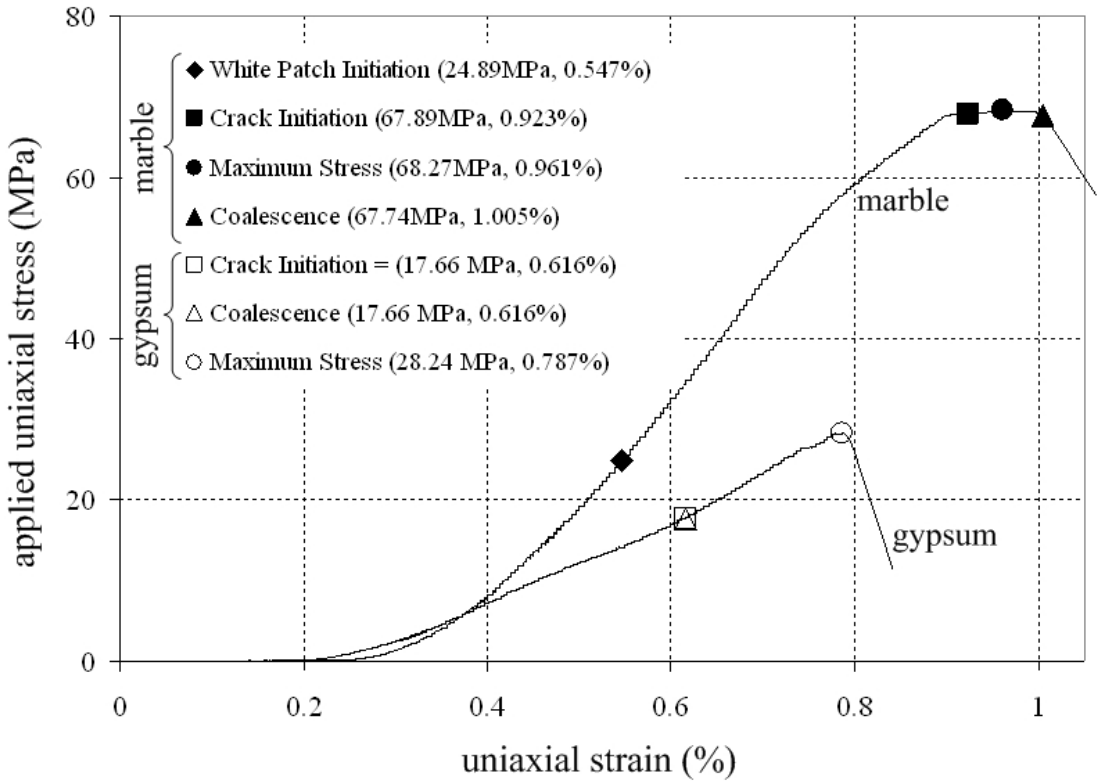

Figure 9.4 – Stress-strain curves of obtained from uniaxial compression tests on a gypsum specimen and a marble specimen, both with flaw geometry 4a-30-90. The numbers in parentheses are the stress and strain value corresponding to the indicated events identified from the video recordings.

In marble, the first observable macroscopic change in response to the applied loading was the development of white patches from the pre-existing flaws (indicated by a solid diamond in figure 9.4). As loading increased, additional white patches developed and they continually lengthened and widened. Up to a particular load level, observable cracks began to initiate along the white patches (indicated by a solid square). Around the maximum stress level (indicated by a solid circle), there was usually a plateau on the stress-strain curve. In this region, the specimen continued to sustain the applied loading

by developing new or enlarging the pre-existing white patches, in addition to some new macroscopic crack initiation in the specimen as observed in the high speed videos. A majority of these new cracks developed in a stable manner until the development of one or multiple unstable new cracks which led to an immediate loss of specimen strength. In the case shown in figure 9.4, it was the initiation of coalescence crack (indicated by a triangle) that marked the abrupt of specimen strength. Again, the load level associated with the occurrence of the coalescence cracks in marble varied among the flaw geometries (see chapter 6), but not necessarily after the maximum stress.

To summarize, the stress-strain curve of gypsum suggests a **brittle** deformation behavior, while that of marble suggests a **semi-brittle** deformation behavior. With reference to the high speed video recordings, the unique behavior of marble is probably due to the development of white patches (associated with inelastic deformation due to development of process zones – discussed further in next section) during a large portion of the loading history, and its ability to sustain the applied stress around the maximum stress level by an extensive development of white patches and multiple stable cracks.

From the stress-strain curves similar to those shown in figure 9.4, the specimen failure stress, first crack initiation stress (stress corresponding to the initiation of first observable cracks) and coalescence stress corresponding to each uniaxial compression test in both gypsum and marble was obtained. The first crack initiation stresses (normalized by the respective specimen failure stresses) are plotted against the flaw pair bridging angle α (figure 6.49 which is reproduced below). Note that the plot only shows the values for stepped flaw pairs with flaw inclination angle 30^o and ligament length **2a**. Refer to figures 6.50 to 6.52 for plots of the other three series of flaw pair geometries. Figure 6.49 is replotted in figure 6.45 with crack initiation stresses normalized by the average uniaxial compressive stress of the respective material instead.

An interesting feature revealed from figure 6.49 is that the crack initiation stress ratio (normalized by respective specimen strength) in marble is always greater than that in gypsum for the same flaw pair geometry. Besides, the normalized ratios in marble are

equal to or very close to 1, indicating that the initiation of the first cracks is concurrent with or immediately followed by the occurrence of specimen maximum stress. The relatively lower ratios in gypsum indicate that gypsum specimens have to be loaded further to reach the specimen maximum stress.

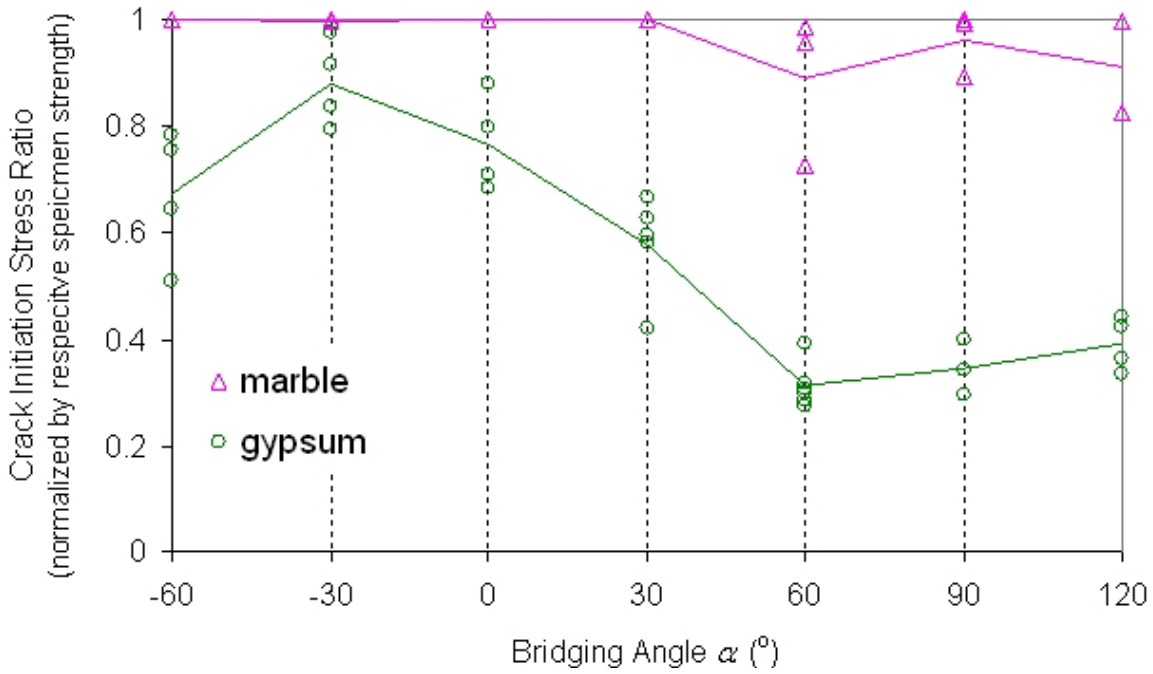

Figure 6.49 – Crack initiation stress normalized by the respective specimen failure stress versus bridging angle α in gypsum and marble for stepped flaw pairs of 30° flaw inclination angle with ligament length **2a**.

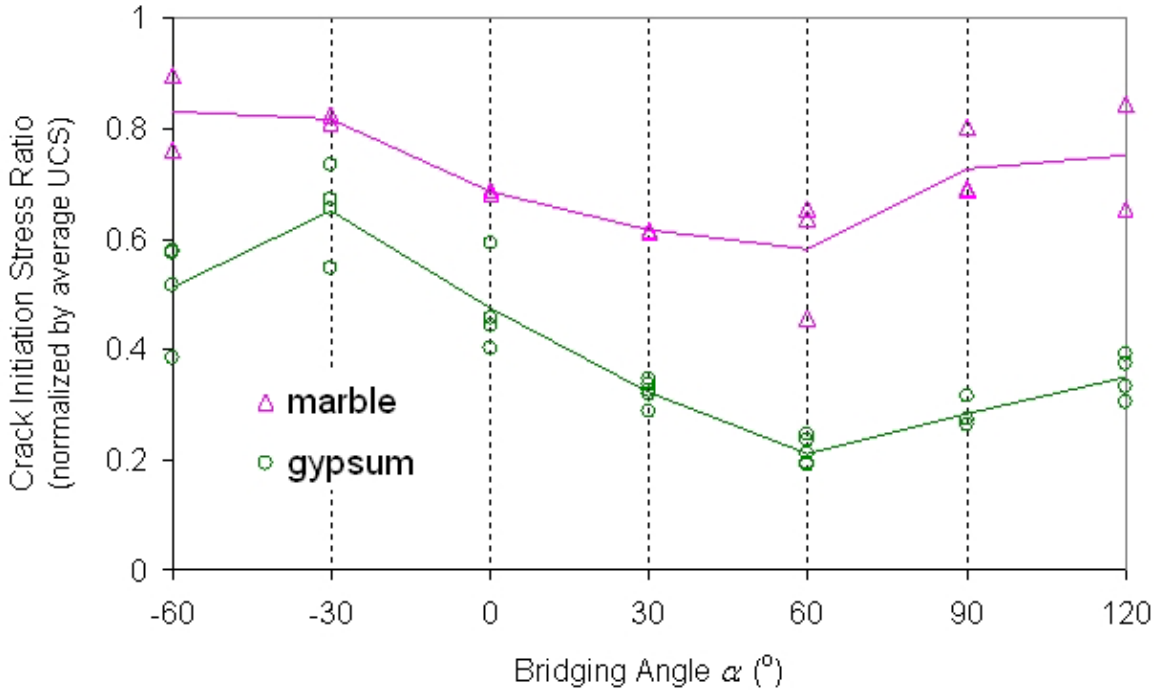

Figure 6.45 – Crack initiation stress normalized by the average USC versus bridging angle α in gypsum and marble for stepped flaw pairs of 30° flaw inclination angle with ligament length **2a**.

In figure 6.45, the crack initiation stress is normalized by the average uniaxial compressive stress (UCS) of the respective material instead. A ratio always lower than 1 is expectable in both marble and gypsum for all flaw pair geometries since flaws in a specimen should lower the overall strength compared to the intact specimen. The higher stress ratio in marble than in gypsum for the same flaw pair geometry indicates a difference in the fundamental crack initiation mechanisms in both materials, which will be discussed further in later sections.

It is also possible to plot the stresses corresponding to the development of the first observable white patches in marble along with the first crack initiation stress in gypsum (figures 6.53 a & b). The two materials not only show a similar trend of variation of the stress ratios (crack initiation in gypsum and white patch initiation in marble) with bridging angle, but also have close stress ratios for the negative bridging angles and small positive bridging angles in both plots (figures 6.53 a & b). There thus appears to be an analogy between the formation of white patch in marble and the first crack occurrence in gypsum. The production of white patches is speculated to indicate the presence of microcracks associated with the process zone.

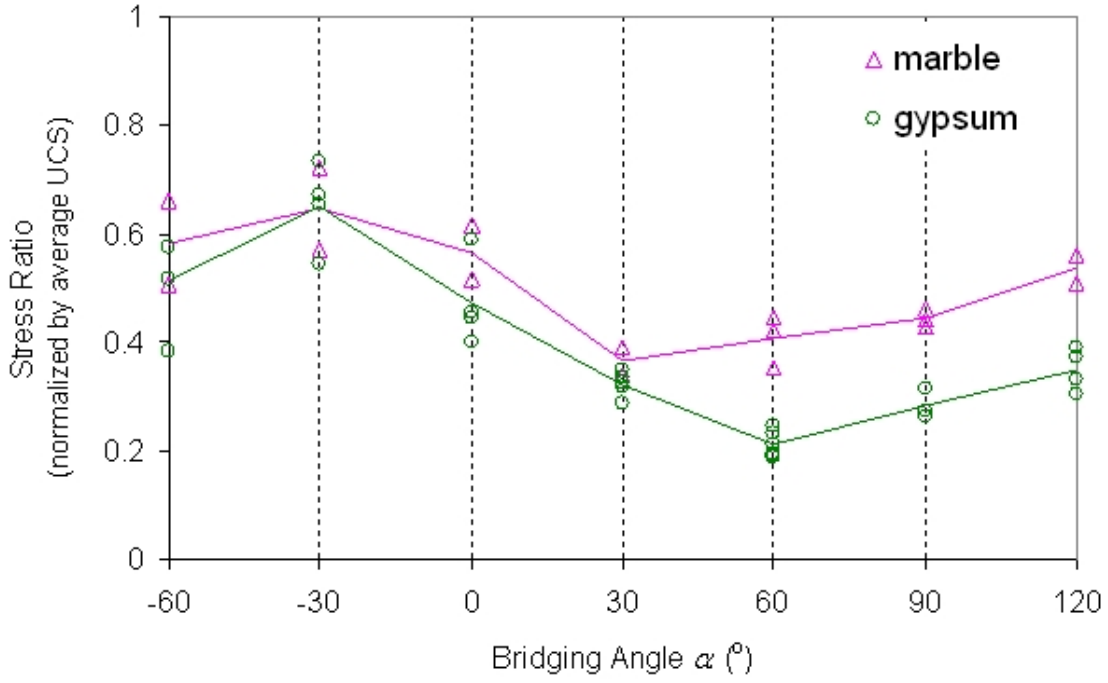

(a)

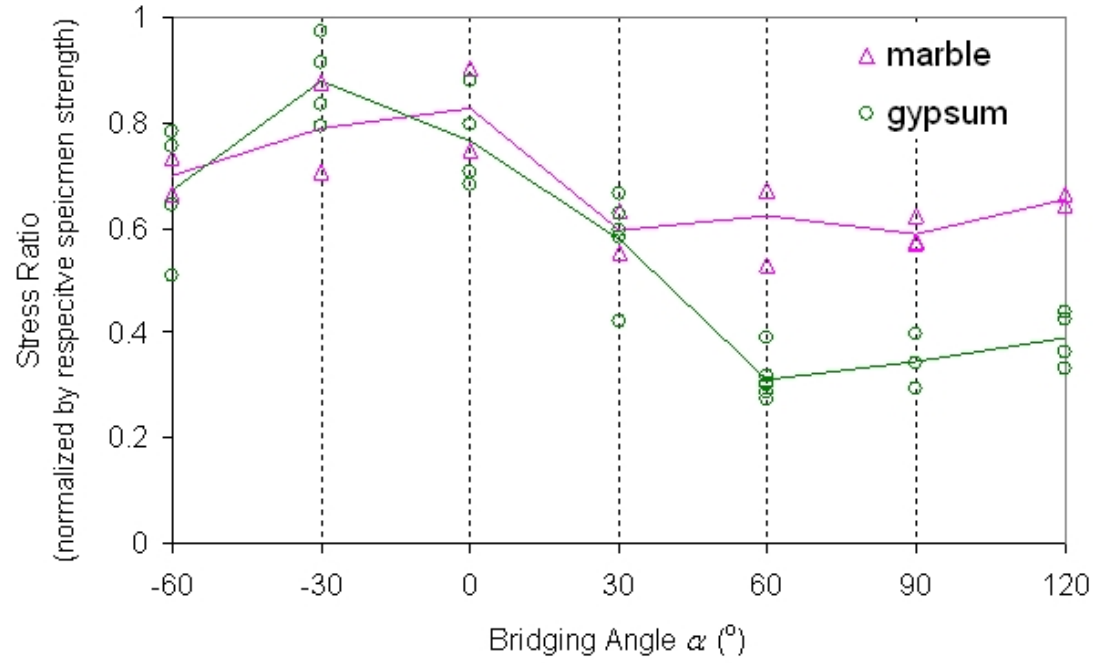

(b)

Figure 6.53 – Comparison of first crack initiation stress in gypsum with the stress corresponding to the first white patch initiation in marble, (a) normalized by the average UCS, (b) normalized by the respective specimen strength. All stepped flaw pairs were oriented at flaw inclination angle (β) 30° with ligament length **2a**.

A similar white patch development was also observed by Chen et al. (1995), Martinez (1999) and Li et al. (2005) in their tested marble specimens. These regions of color change were suspected to be due to the presence of induced microcracks (Chen et al., 1995) or deviation and failure of crystalline grains (Li et al., 2005). However, no experimental attempts (e.g. microscopic imaging) were made by these authors to confirm their hypotheses.

To summarize this section, the differences mentioned above regarding the *macroscopic* fracturing behavior observed in gypsum and marble are listed in table 9.2.

	Molded gypsum	**Carrara Marble**
General deformation behavior	Brittle *(figure 9.4)*	Semi-brittle *(figure 9.4)*
Sign preceding crack initiation	No observable signs	Development of white patches along future crack trajectories
Crack initiation stress ratio	Lower *(figures 6.49, 6.45, 6.53)*	Higher *(figures 6.49, 6.45, 6.53)*
Tensile crack initiation	Initiated and appeared as a continuous hair-line crack (1), which was followed by an aperture increase	Multiple short cracks usually first developed and coalesced to form a continuous crack *(figures 9.1)*
Shear crack initiation	Shear displacement in intact material usually accompanied by a *larger* spalling zone *(figures 9.2)*	Shear displacement in intact material usually accompanied by a *smaller* spalling zone *(figures 9.3)*

(1) hair-line crack observed to consist of segmented tensile cracks at a microscopic scale (ESEM study)

Table 9.2 – Key differences of **macroscopic** deformations observed in molded gypsum and Carrara Marble.

9.3.2 Microscopic observation

The preceding discussion focuses on the macroscopic observations and measurable physical quantities obtained from the loading tests. It is very useful to examine if a correlation can be made between these macroscopic observations with the underlying microscopic changes in both materials (table 9.1). As mentioned earlier, a SEM (scanning electron microscope) study and an ESEM (environmental scanning electron microscope) study were conducted to review the microstructural characteristics of marble and gypsum[2] respectively. The objective of the SEM/ESEM study is to answer the following two important questions:

What is the nature of white patches in marble?
Why are white patches observed in marble, but not in gypsum?

From the SEM study, along the white patch of a future tensile wing crack, an elongated microcracking zone scattered with microcracks first formed adjacent to the flaw face around the tip regions in response to the initially low applied loading (figures 7.60Aa & 7.60Ca). As the applied loading progressively increased, the microcracking zone evolved to consist of a dominant continuous crack and multiple microcracks (figures 7.60Ab & 7.60Cb). The density of the microcracks, which flanked the central dominant crack, decreased as the distance from the dominant crack increased. This type of microcrack distribution was also reported by Kranz (1983). As the applied loading increased further, the microcracking zone lengthened and became wider. The density of microcracks next to the central dominant feature also became higher (figures 7.60Ac & 7.60Cc). These also corresponded to a lengthening and widening of the macroscopic white patches. Note that both intergranular and intragranular cracks were identified for both the central microcracks and the mircrocracks on their flanks.

[2] The environmental scanning electron microscope (ESEM) was used instead of the scanning electron microscope (SEM) since the relatively high porosity in gypsum makes the carbon coating process of the specimen surface impractical, which is necessary prior to the SEM study. The ESEM however does not require such a carbon coating process.

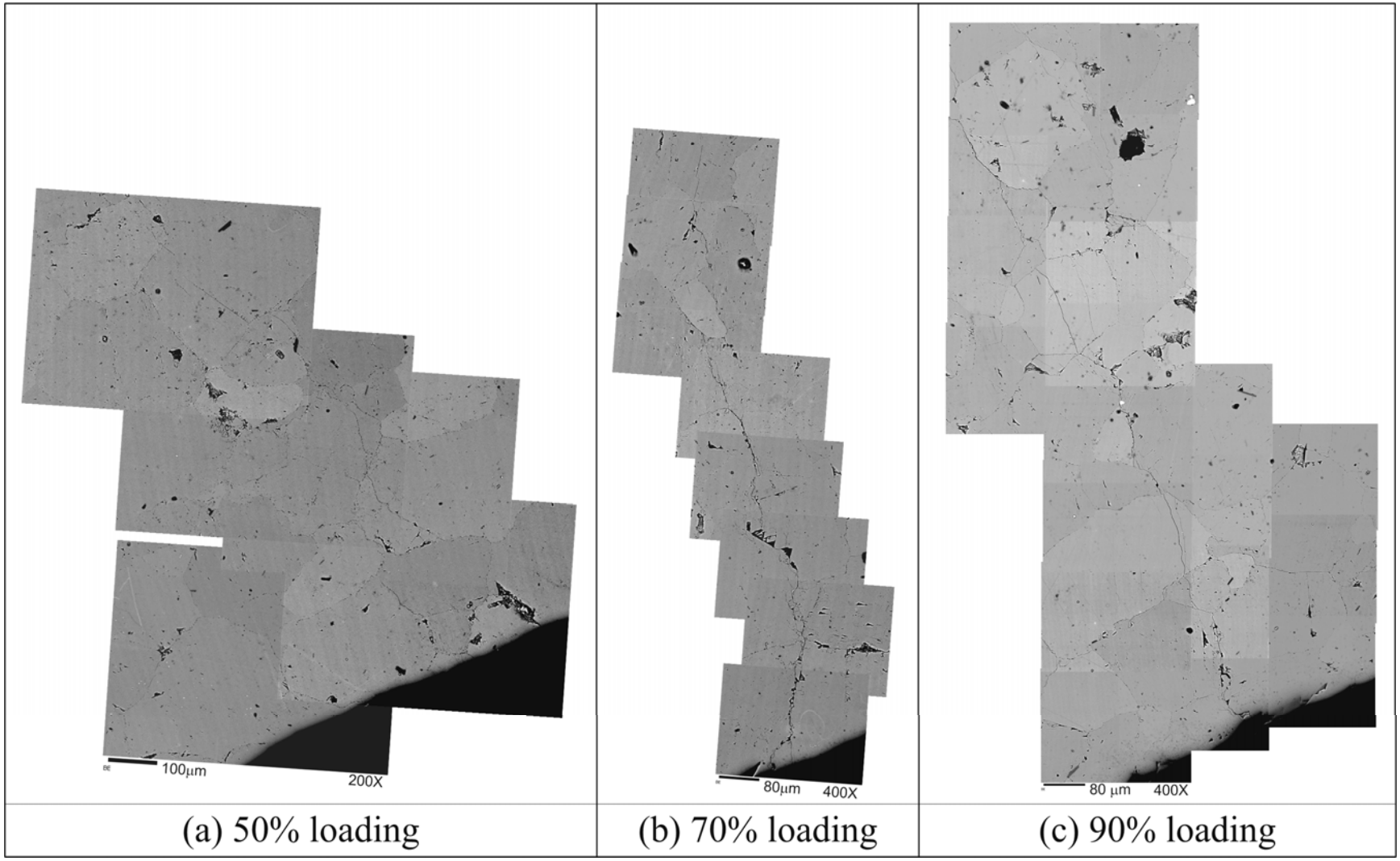

Figure 7.60A – Assemblages of SEM images for individual white patches observed in (a) specimen DA, (b) specimen DB, and (c) specimen DC.

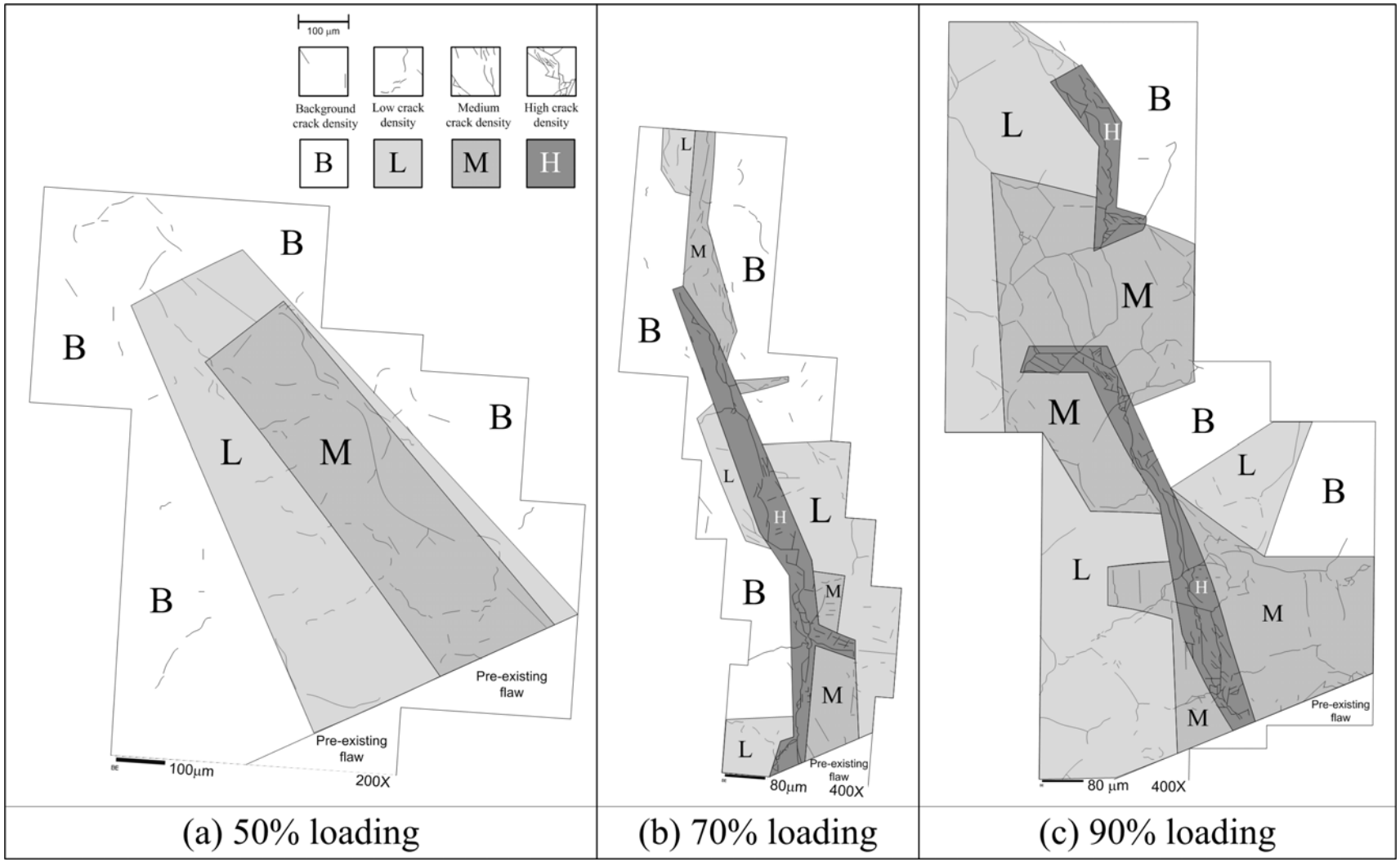

Figure 7.60C – Overlays of crack density distribution over the sketches of crack traces shown in figure 6.60A for (a) specimen DA, (b) specimen DB, and (c) specimen DC. The keys of the different classes of crack density (qualitative) – background, low, medium and high are shown in the top left region of the figure.

In contrast, no observable white patches developed in gypsum as revealed from the video recordings. Under loading, the development of observable tensile cracks was preceded by the development of hair-line cracks (invisible to unaided eyes, but discernable with a 10x hand lens). An ESEM study was conducted to study the **hair-line cracks** and their vicinity, to reveal if process zones (microcracking processes) similar to that associated with white patches in marble also developed in gypsum. The ESEM study revealed two key features. *First*, the hair-line tensile crack which was observed to be continuous with a 10x hand lens actually consisted of multiple discontinuous crack segments at a microscopic scale. *Second*, the hair-line cracks were associated only with a very narrow microcracking zone, consisting of multiple central dominant microcracks and a limited number of microcracks flanking it (figure 9.5).

As noted in other gypsum specimens, when similar hair-line tensile cracks were further loaded, tensile cracks with an opened observable (macroscpopic) aperture then developed. The ESEM study was thus also conducted in the region in the vicinity of a well-developed **tensile wing crack** (observable to the unaided eyes). The ESEM study revealed that the extent of microcracking beside a well-developed tensile crack (figure 9.6) was very similar to that next to a hair-line tensile crack (figure 9.5). These observations indicate that once the incipient hair-line microcracks formed, additional loading (1) led to the coalescence of the segmented hair-line microcracks formed earlier, resulting in an eventual crack aperture increase, (2) but with a very limited damage to the area nearby. Most of the observable cracks were of intergranular nature as indicated by the perseverance of intact gypsum grains beside the cracks. However, it was very difficult to observe and determine the extent of intragranular crack development.

Comparing the coalescence of the *microscopic* segmented hair-line tensile cracks in gypsum (figure 9.5 and discussion above) with the coalescence of the *macroscopic* en echelon tensile crack segments in marble (figure 9.1 and relevant discussion in section 9.3.1), it is interesting to notice the similarities between them – individual short tensile crack segments oriented almost parallel to the applied σ_1 first initiate in response to loading, which then coalesce to form a continuous crack. The above phenomenon thus

appears to operate at two different scales in these two different materials. Recall that as noted in earlier sections, the hair-line cracks, which were found to consist of multiple crack segments at a microscopic scale, appeared to be continuous as observed with a 10x hand lens.

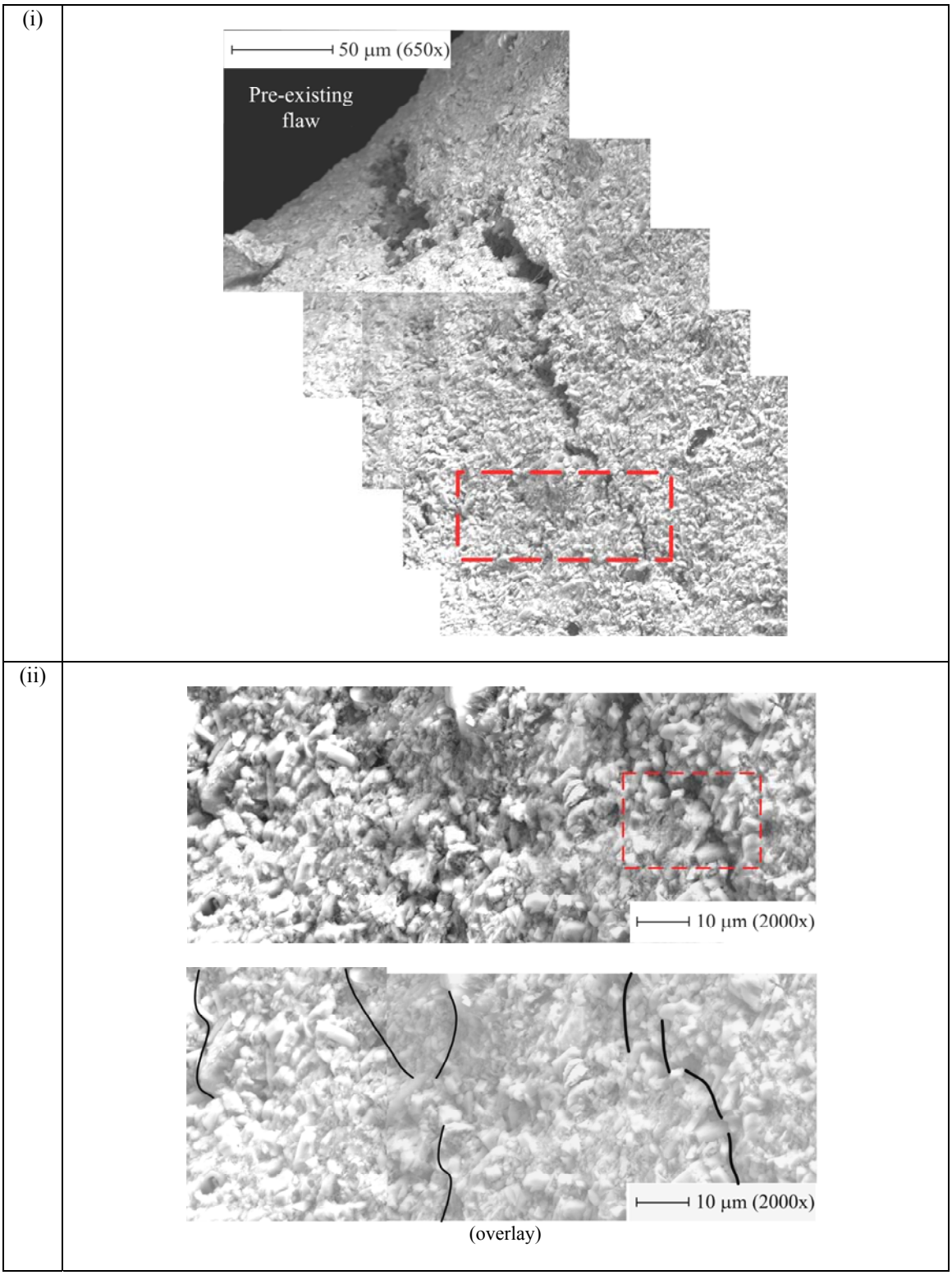

Figure 9.5 – Magnified ESEM images (i) 650x, (ii) 2000x of the region in vicinity of a hair-line tensile crack. Image (ii) is a magnified image of the enclosed region marked in image (i). As shown in image (ii), the hair-line crack actually consists of multiple shorter segments. Their traces are marked by thick lines in the right part of the overlay. The locations of other microcracks are traced by thin black lines.

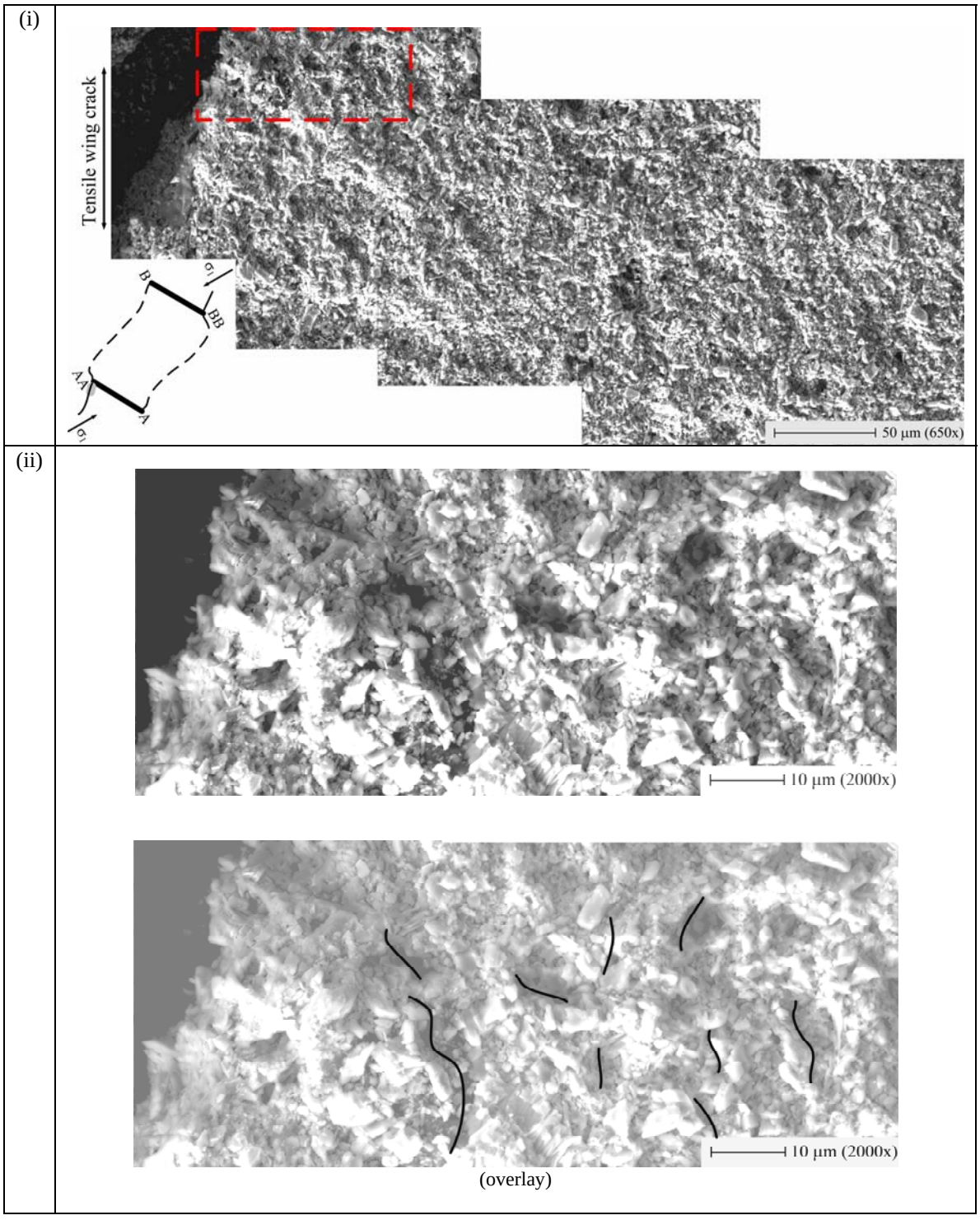

Figure 9.6 – Magnified ESEM images (i) 650x, (ii) 2000x of the region in vicinity of a well-developed tensile wing crack. Image (ii) is a magnified image of the enclosed region marked in image (i). The black region on the left in all images is the opening of the tensile wing crack. The locations of microcracks are traced in the overlay of image (ii) by thin black lines.

		Hair-line crack in molded gypsum	White patch in Carrara Marble
Similarities	Time of occurrence	The respective development is the first sign observed in the specimen in response to the applied loading.	
	Structure	Dominant individual microcrack segments flanked by multiple microcracks	
	Microcrack distribution density	Microcrack density is high in the close vicinity of the central dominant microcracks, and decreases as the distance from the central dominant microcracks increases. However, the width of the microcracking zone and the crack density differs in the two material (see below).	
Differences	Crack types	Mostly intergranular cracks, difficult to determine the extent of intragranular cracks development	Both intergranular and intragranular cracks are common
	Width of microcracking zone	Relatively narrow – less than 100 μm wide, which is equal to 5 to 20 times the grain size	Relatively wide – around 500 μm wide, which is equal to 2 to 10 times the grain size
	Overall microcrack density	Lower *	Higher*
	Applied stress required	The development from a hair-line tensile crack to an observable tensile crack takes place over a very small applied stress increment (<1 MPa).	The difference of the applied stresses between the initiation of white patch and the eventual formation of macroscopic observable cracks is larger (20 to 50 MPa).
	Microscopic evolution to become observable cracks	Increased loading leads to lengthening and coalescence of the central dominant microcrack segments. Further loading leads to the increase of crack aperture. The microcrack density does not increase significantly.	Increased loading leads to lengthening and coalescence of the central dominant microcrack segments and increase of microcrack density beside it (intensification of the white color macroscopically). Further loading leads to the increase of crack aperture.

* The crack density is assessed based on a qualitative basis (e.g. figure 7.60C), instead of detailed frequency counting.

Table 7.2 – Summary of similarities and differences in the development of hair-line cracks in molded gypsum and white patches in Carrara Marble associated with the development of macroscopic tensile cracks.

The similarities and differences regarding the microscopic characteristics revealed from the SEM and ESEM studies in marble and gypsum are summarized in table 7.2. These results thus establish a correlation between the macroscopic and microscopic observations in the two materials regarding the changes preceding the formation of observable (macroscopic) tensile cracks, and provide answers to the two questions stated earlier in this section.

Q: *What* is the nature of white patches in marble?

A: White patches in marble are associated with the underlying development of *microcracks* (process zone) in response to loading.

Q: *Why* are white patches observed in marble, but not in gypsum?

A: Macroscopic white patches are not observed in gypsum because the initiation of a hair-line crack and its later evolution into a well-developed tensile crack is associated with a *process zone only of limited size*. Note that this conclusion is based on the ESEM study in gypsum with a similar magnification as that used to study the microcracking zone in marble.

9.3.3 Material properties

The previous two sections summarize the macroscopic and microscopic deformation behavior in gypsum and marble and try to relate the observations obtained from these two scales to each other. This section summarizes the inherent material properties and texture, based on which future discussion of deformation mechanisms can be made (table 9.3).

	Molded gypsum	**Carrara Marble**
Grain shape	Plate to needle	Equigranular
Typical grain size	5 μm long and 2 μm wide	50 to 200 μm
Arrangement relationship between grains	Individual platy mineral grains stacking randomly together	Well-fused, interlocking structure
Porosity	High (0.3) (estimated based on specific gravity 2.2)	Low (0.004) (Alber & Hauptfleisch, 1999)
Existing sites of weakness	Mainly pores between mineral grains	Grain boundaries, cleavage planes
Specimen density (measured in present study)	1.54 g/cm^3	2.7 g/cm^3

Table 9.3 – Microscopic characteristics and texture of molded gypsum and Carrara Marble.

Carrara Marble has a well-fused interlocking crystalloblastic fabric (Best, 2001), which is characterized by a mutually interfering growth pattern in which the constituent polygonal equigranular grains meet at approximately 120^o triple junctions (figure 9.7 a). The grain size varies within a range of 50 to 200 μm. The overall porosity of the rock is very low at a value of 0.4%. As observed in the marble specimens before being subjected to loading tests, intergranular cracking occurs along less than 20% of the grain boundaries. Careful inspection reveals that most grains are crack-free. Intragranular microcracks are present in only a small population of marble grains and their development is in part controlled by the mineral cleavage planes. There are three directions of cleavages (trigonal) associated with calcite. On a two-dimensional plane as examined under the SEM, usually only two directions can be recognized. The traces of the cleavage planes become more pronounced once cracking occurred along them. See the example shown in figure 9.8, which illustrates a SEM image of a marble specimen that has been subjected to loading tests.

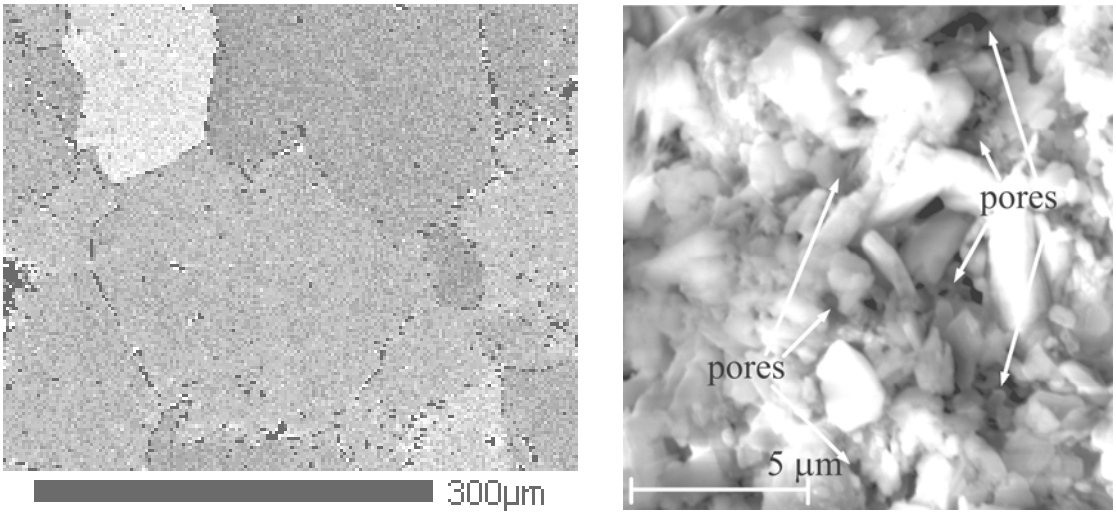

(a) (b)

Figure 9.7 (a) SEM image showing the interlocking calcite grains in Carrara Marble. (b) ESEM image showing the presence of numerous minute pores in molded gypsum.

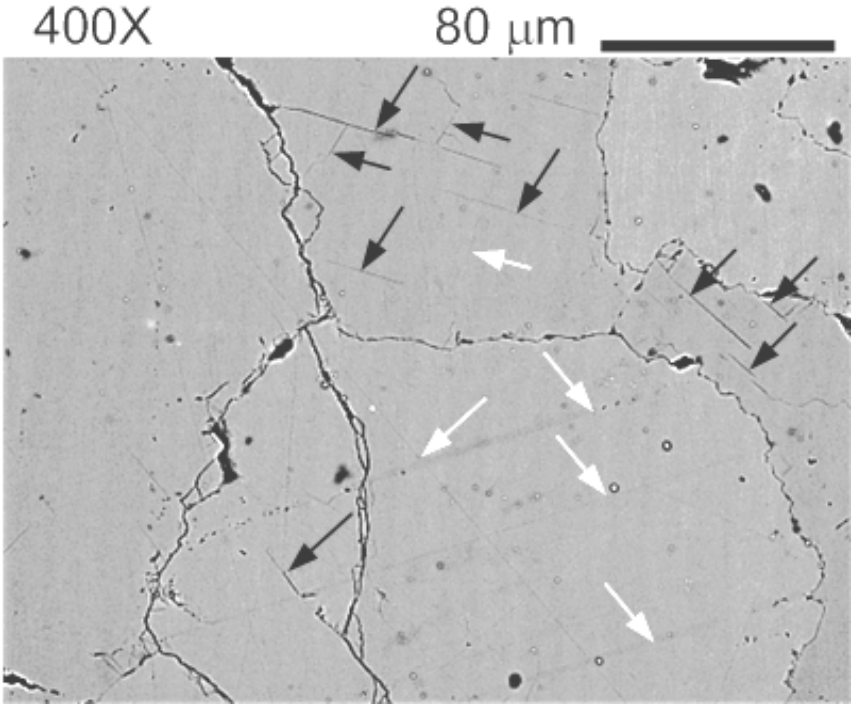

Figure 9.8 – Cleavage planes in Carrara Marble. The very thin black straight lines indicated by white arrows are very likely to be crack-free cleavage planes, while the thicker black straight lines indicated by black arrows are opened-up cracks. Note the cleavage orientations vary among grains and the termination of these cleavage planes at the calcite grain boundaries.

In contrast, the molded gypsum is made up of numerous much smaller plate to needle shaped gypsum grains (5 μm long and 2 μm wide) and characterized by a very porous texture (9.7 b). In-between the plates, small inter-connected pores with approximately 1 to 5 μm size are present due to the quite open structure related to the inherent stacking arrangement of gypsum plates, and the entrapped air bubbles during the specimen preparation. The estimated porosity based on the specific gravity (~2.2) and specimen density (1.54 g/cm^3) is around 0.3, which is of three orders of magnitude larger than that of marble.

9.3.4 Deformation mechanisms

The previous section summarizes the different **microscopic** characteristics of the two materials in section 9.3.3. This section attempts to account for the differences of the fracturing behavior in gypsum and marble. Three specific questions to address are:

(1) *Why* is the crack initiation in marble associated with an observable white patch, but in gypsum it is not (at a macroscopic scale)?
(2) *Why* is the crack initiation in marble associated with a wider process zone and higher microcrack density that that in gypsum (at a microscopic scale)?
(3) *Why* does marble behave in a more ductile manner than gypsum?

Here are some remarks about the three questions. Since it has been established in section 9.3.2 that the development of white patches (macroscopic) in marble is related to the underlying microcrack development (process zone), questions *(1)* and *(2)* above thus basically refer to the same phenomenon, but at different scales of observation. The contrast in ductility (or brittleness) in question (3) is based on the characterizing shapes of the stress-strain loading curves obtained respectively for marble and gypsum (see figure 9.4 and relevant discussion in section 9.3.1). As shown in the typical curves for gypsum and marble contained in figure 9.4, the slope of the marble stress-strain curve generally increases in the initial half of loading and decreases slightly in the final half of

loading. The curve later levels off around the specimen maximum stress, which is then followed by failure. In contrast, the slope of the gypsum stress-strain curve remains more or less the same throughout the whole loading process. It is also characterized by an abrupt stress drop after the specimen maximum stress has reached.

When mechanisms answering the above questions are satisfactorily established, they can be used to account for other different macroscopic deformation/fracturing behavior observed in gypsum and marble. The **microstructural** evolution leading to the formation a **macroscopic tensile wing crack** is first discussed below.

(1) Microcrack initiation

(i) Gypsum & (ii) Marble

Microscopic events/observations: The stress distribution around a single open flaw embedded in an infinite medium subjected to a remote stress field can be theoretically predicted by the Griffith's stress theory (1924) as outlined in appendix R. Regions of local compression and local extension stress fields develop around the pre-existing flaw in response to the applied loading. As the applied load continuously increases, microcracks first initiate close to the pre-existing flaw and along the locus where the maximum local tensile stress (sketch *a* on the left in figure 9.9) is large enough to overcome the local tensile strength. Since heterogeneities are inherently present on a microscopic grain scale in rocks (Friedman et al., 1972, Hoagland et al., 1973, Peck et al., 1985, Labuz et al., 1987), there are localities which are *stronger* and *weaker* due to the absence and presence of sites of micro-defects. Instead of initiating as a continuous crack extending from the pre-existing flaw face and propagating outwards, formation of discontinuous segmented microcracks at local sites of weakness is more favored instead at this incipient loading stage.

Macroscopic events/observations: The microcracks in gypsum are too fine to be discernable in the video recordings (sketch *a* for gypsum in figure 9.10), but can be identified with the ESEM imaging technique. The microcracks in marble are also too fine to be observed in the video recordings, but they are associated with the very short

white patches (1 – 2 mm) initiating from the pre-existing flaws (sketch *a* for marble in figure 9.10).

(2) Growth of microcracks

(i) Gypsum & (ii) Marble

Microscopic events/observations: As loading increases, the trajectory along which the local tensile stress large enough to overcome the local tensile strength lengthens. Additional microcracks thus initiate at farther distance away from the pre-existing flaw along this trajectory. At the same time, the already developed microcracks close to the pre-existing flaw also become preferential sites for further crack lengthening and coalescence in response to loading (sketch *b* in figure 9.9).

Macroscopic events/observations: The microcracks in gypsum are still too fine to be discernable to unaided eyes or 10x hand lens (sketch *b* for gypsum in figure 9.10), while they appear as lengthened white patches in marble (sketch *b* for marble in figure 9.10).

(3) Development into a microcracking zone

(i) Gypsum

Microscopic events/observations: The microcracks developed in previous stages in gypsum now have a length (5 – 10 grain sizes, see figure 9.5(ii)) generally larger than the constituent grain size and pores. These already developed microcracks thus become the more preferential sites, which can then lead to further local stress concentration and lengthening of the microcracks dominantly in response to further applied loading (sketch *c* for gypsum in figure 9.9). Note also that there is also a development of multiple microcracks flanking the central dominant microcracks, but their density is very low.

Macroscopic events/observations: The traces of these microcracks are now so pronounced that they become observable as a hair-line crack with a 10x hand lens (sketch *c* for gypsum in figure 9.10).

(ii) Marble

Microscopic events/observations: The development of microcracks in marble is observed to be controlled by the grain boundaries (inter-granular grain boundary cracks), the favorably oriented cleavage planes (intra-granular cracks) and other sites of defects such as pre-existing microcracks. In response to the further loading, there is not only a lengthening and coalescence of the already developed microcracks, but also microcrack initiation form the nearby sites of weakness (sketch *c* for marble in figure 9.9). This leads to the formation of the central dominant microcracks and the microcracks on the flanks which both constitute the microcracking zone.

Macroscopic events/observations: The above microscopic evolution associated with the formation of the microcracking zone including the central dominant microcracks and the microcracks on the flanks leads to the widening, lengthening and color intensification of the white patches (sketch *c* for marble in figure 9.10).

To summarize this stage of "*development into a microcracking zone*", in response to loading, microcracks in both materials lengthen and coalesce to form a central dominant more or less continuous microcrack. In addition in marble, but to a lesser extent in gypsum, additional microcracks also develop next to this central dominant microcrack. The central dominant microcrack and the microcracks on its flanks make up the microcracking zone.

(4) Development into macroscopic cracks

(i) Gypsum

Microscopic events/observations: Further loading leads to different responses in gypsum and marble. A very slight increase in applied loading (<1 MPa) rapidly leads to an abrupt aperture increase of the central microcracks in gypsum to form a through-going tensile crack (without crack face contact). The density and distribution of microcracks next to the well-developed crack remains more or less the same as revealed from the ESEM study (sketch *d* for gypsum in figure 9.9).

Macroscopic events/observations: A macroscopic through-going tensile wing crack forms (sketch *d* for gypsum in figure 9.10).

(ii) Marble

Microscopic events/observations: Continued loading not only leads to lengthening and coalescence of the central dominant micorcracks, but also induces extensive microcracking beside the central microcracks (sketch *d* for marble in figure 9.9). The above changes take place over a wide range of applied stress, which spans from 20 MPa to 50 MPa. Although the crack density generally decreases away from the pre-existing flaw, there can be zones of variations, i.e., regions of different microcrack densities consisting of microcracks with different lengths and types (intergranular, intragranular) could be traced along and away from the white patch. As shown in figure 7.60Cc, for example, two regions of high crack density (**H**) are separated by a region of medium crack density (**M**). It is reasonable to expect that macroscopic tensile cracks will first form around the **H** regions, hence leading to separate initiation of tensile cracks (en echelon cracks) within the white patch in marble (sketch *e* for marble in figure 9.9) before the initiation of a continuous observable macroscopic crack (sketch *f* for marble in figure 9.9).

Macroscopic events/observations:

Multiple macroscopic en echelon cracks initiate within the white patch (sketch *e* for marble in figure 9.10), which then coalesce to form a continuous through-going crack with opened aperture (sketch *f* for marble in figure 9.10).

The above deformation stages associated the development of white patches and their evolution into macroscopic tensile cracks in marble, and the initiation of hair-line tensile cracks and their evolution into macroscopic cracks in gypsum are summarized in table 9.4 below.

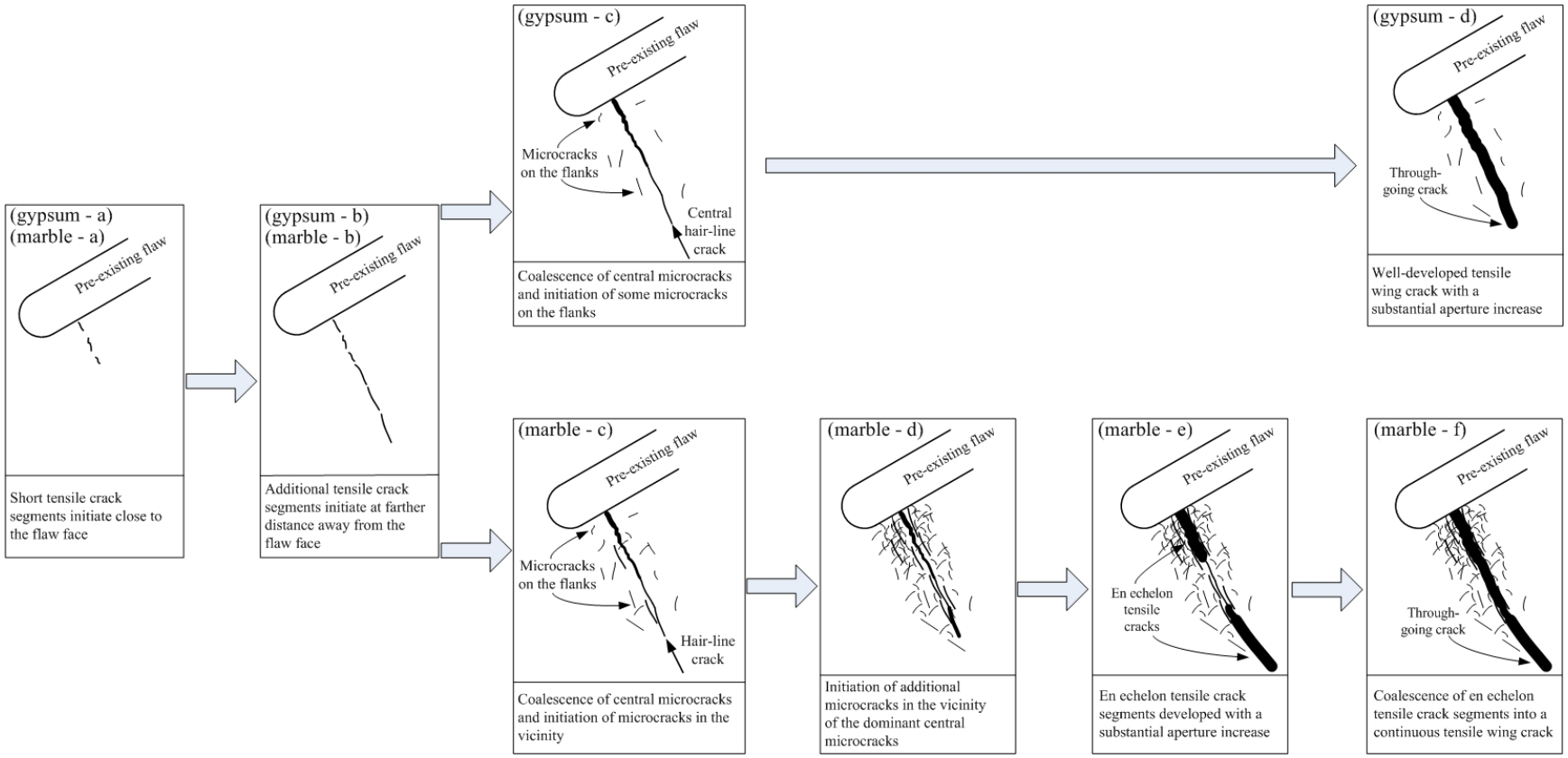

Figure 9.9 – Schematic illustration of the *microscopic* tensile wing crack development in marble and gypsum. Both gypsum and marble share the same figure on the left.

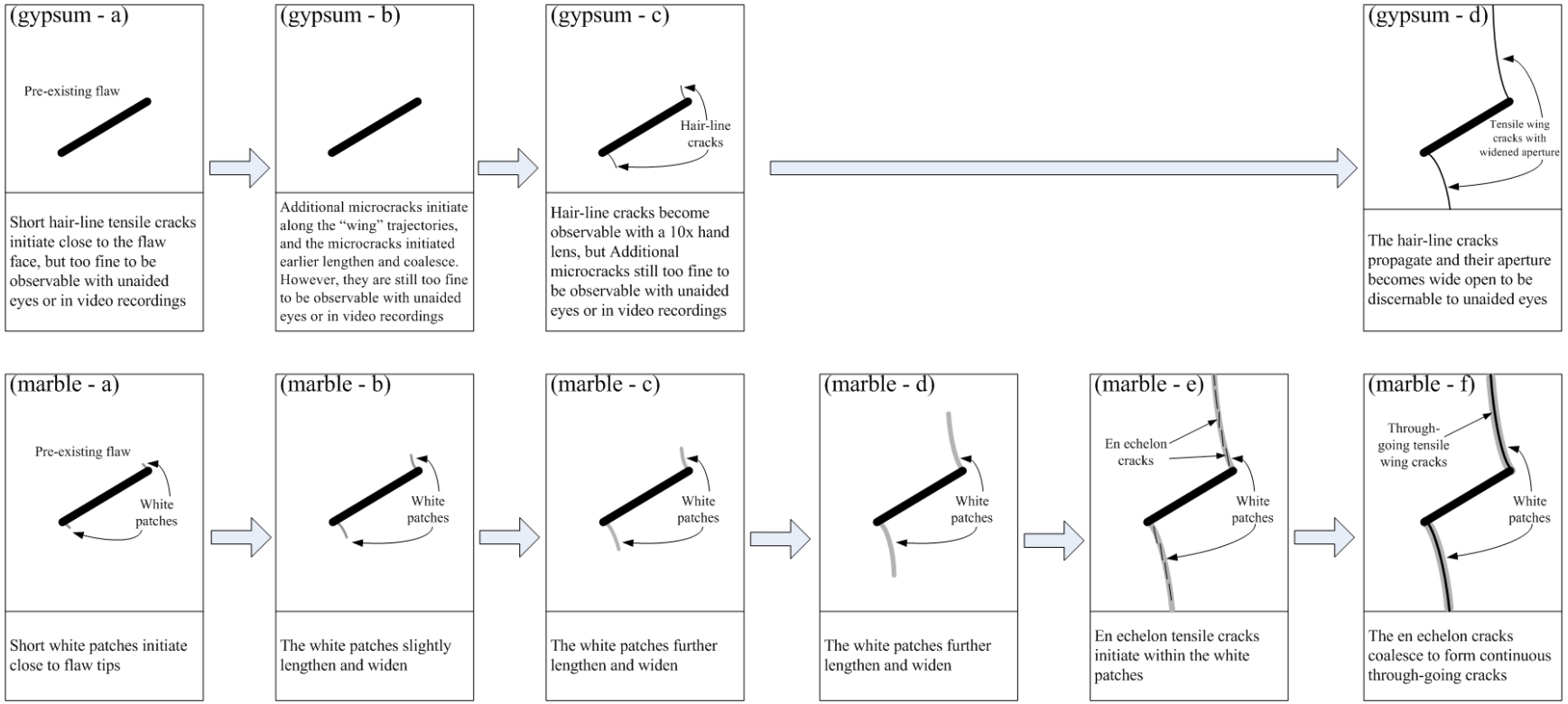

Figure 9.10 – Schematic illustration of the *macroscopic* tensile wing crack development in marble and gypsum. The top row is for gypsum and the bottom row is for marble.

	Gypsum (typical grain size = 5μm long and 2μm wide)	Marble (typical grain size = 50 to 200 μm)
(1) Microcrack initiation	**Microscopic events/observations:** *(figure 9.9 gypsum – a)* Discontinuous segmented microcracks (~5 μm long) initiate at local sites of weakness along the "*wing*" trajectory where the local tensile stress is large enough to overcome the local tensile strength in response to the early loading. **Macroscopic events/observations:** *(figure 9.10 gypsum – a)* Microcracks are too fine to be discernable in the video recordings.	**Microscopic events/observations:** *(figure 9.9 marble – a)* Discontinuous segmented microcracks (~10-20 μm long) initiate at local sites of weakness close to the flaw in response to the early loading. **Macroscopic events/observations:** *(figure 9.10 marble – a)* The microcracks are associated with very short white patches (~2 mm long) initiating from the pre-existing flaws.
(2) Growth of microcracks	**Microscopic events/observations:** *(figure 9.9 gypsum – b)* The microcracks lengthen (~10 μm long) and coalesce in response to increased loading. The microcracks generally follow the "*wing*" trajectory as observed at 650x magnification, but appear to be parallel to the applied σ_1 direction as observed at 2000x magnification. **Macroscopic events/observations:** *(figure 9.10 gypsum – b)* The microcracks in gypsum are still too fine to be discernable.	**Microscopic events/observations:** *(figure 9.9 marble – b)* The microcracks lengthen (~50-100 μm long) and coalesce in response to increased loading. The microcracks generally follow the "*wing*" trajectory as observed at 200x magnification, but appear to follow the local grain boundaries inclined at 10-20^o with the applied σ_1 direction as observed at 1000x magnification. **Macroscopic events/observations:** *(figure 9.10 marble – b)* The white patches lengthen, widen (1-2 mm) and intensify in color.
(3) Development into a micro-cracking zone	**Microscopic events/observations:** *(figure 9.9 gypsum – c)* The microcracks developed in previous stages in gypsum now have a length (5-10 grain sizes, 25-50μm long) and become the preferential sites for further crack lengthening in response to applied loading. There is also a development of multiple microcracks (5-10 μm long) flanking the central dominant microcracks, but their density is very low. The central dominant microcracks and the flanking microcracks collectively form a microcracking zone of a width less than 100 μm, which is equal to 5 to 20 times the grain size.	**Microscopic events/observations:** *(figure 9.9 marble – c)* Further loading leads to (1) lengthening and coalescence of the already developed microcracks reaching an average continuous length of 200 μm, and (2) microcrack initiation (~10-20 μm long) at nearby sites of weakness. The central dominant microcracks and the microcracks on the flanks collectively form a pronounced microcracking zone. *(figure 9.9 marble – d)* Further loading increases the overall crack density of both the central dominant cracks and the flanking microcracks in the microcracking zone, which has a width of around 500 μm (2 to 10 times the grain size).

Table 9.4 – Comparison of microscopic and macroscopic changes associated with the tensile crack development in gypsum and marble.

	Gypsum	Marble
(3) Development into a micro-cracking zone (continued)	**Macroscopic events/observations:** *(figure 9.10 gypsum – c)* The traces of microcracks become observable as hair-line cracks with a 10x hand lens, but not unaided eyes.	**Macroscopic events/observations:** *(figure 9.10 marble – c & d)* The white patches progressively widen (2-3 mm), lengthen towards the direction of the applied load until they reach the top and bottom specimen edges, and intensify in color.
(4a) Development of macroscopic en echelon cracks	**No corresponding observations**	**Microscopic events/observations:** *(figure 9.9 marble – e)* Further loading continues to increase the overall crack density of both the central dominant cracks and the flanking microcracks in the microcracking zone. However, local regions of higher microcrack densities develop along the microcrack zone. **Macroscopic events/observations:** *(figure 9.10 marble – e)* Individual short tensile cracks (en echelon cracks) of length 2-5 mm initiate along the white patch where local crack density is higher. They are inclined at ~5^{o} with the underlying white patch.
(4b) Development of macroscopic through-going cracks	**Microscopic events/observations:** *(figure 9.9 gypsum – d)* A very slight increase in applied loading (<1 MPa) rapidly leads to an abrupt aperture increase of the central microcracks to form a single through-going tensile crack. The density and distribution of microcracks next to the well-developed crack remains more or less the same. **Macroscopic events/observations:** *(figure 9.10 gypsum – d)* A through-going tensile wing crack extending from the pre-existing flaw to the top/bottom specimen edges develops and is discernable with unaided eyes.	**Microscopic events/observations:** *(figure 9.9 marble – f)* Further loading continues to increase the overall crack density in the microcracking zone, including the regions between the en echelon cracks. **Macroscopic events/observations:** *(figure 9.10 marble – f)* The individual en echelon tensile cracks lengthen (10-20 mm long) and coalesce within the white patch to form a through-going tensile wing crack, which extends from the pre-existing flaw to the top/bottom specimen edges.

Table 9.4 – Comparison of microscopic and macroscopic changes associated with the tensile crack development in gypsum and marble (continued).

Further remarks

Another remark concerns the **orientation of the microcracks** within the microcracking zone (i.e. central dominant microcracks + microcracks on the flanks). The **central dominant microcracks** are observed to follow the general orientation of the macroscopic wing feature in both materials at medium magnifications of 400x for marble (1000-1500 μm in figure 7.60C) and 650x for gypsum (50-150 μm figure 9.5). At a higher magnification, the orientation of the central dominant microcracks in both **marble** (50-100 μm long) and **gypsum** (10-20 μm long) is found to vary within a range of 10-20^{o} with the general wing direction. Due to a much larger grain size in marble, the influence of grain boundaries and cleavage planes on the orientation of individual microcracks in marble is observed be more pronounced.

On the other hand, although the **flanking microcracks** in **marble** generally follow the grain boundaries and cleavage planes, they are more randomly oriented compared to the central dominant microcracks, i.e. less parallel to the general wing direction. In contrast, the flanking microcracks in **gypsum** are still more or less aligned parallel to the central dominant microcracks.

Conclusions

The explanations and interpretations offered in this section to account for the different deformation behavior in marble and gypsum are based on the microscopic features of these two materials obtained at a similar magnification. Note that since the grain size of gypsum is almost one order of magnitude smaller than that of marble, there may be a limitation in discerning the presence of intragranular cracks in gypsum. Based on the above discussion, the following answers are offered to the three questions stated earlier in this section. Due to the same fundamental nature of questions (1) and (2), they are answered as a whole.

Q. *Why* is the crack initiation in marble associated with an observable white patch, while gypsum is not (at a macroscopic scale)? *Why* is the crack initiation in marble associated with a wider process zone and higher microcrack density that that in gypsum (at a microscopic scale)?

A. White patches are associated with the underlying microcracking zone consisting of central dominant microcracks and microcracks scattered on the flanks. In **marble**, the length of microcracks is mostly equal to or less than 1 to 2 grain sizes (50 – 400 μm), i.e. the microcracks are of similar size to other pre-existing sites of weakness (including weakened/partially opened grain boundaries, inherent microcracks and favorably oriented cleavage planes). Therefore, apart from lengthening and coalescence of the already developed microcracks in the central region, there is also a similar microcrack development in the vicinity where sites of weakness are located. It thus leads to a more extensive development of white patches (wider microcracking zone). In contrast, the microcracks in **gypsum** developed in the early loading stages readily reach a length of 5 – 10 grain sizes. Crack lengthening and coalescence are thus more preferential at these central dominant microcracks rather than the new microcrack initiation in the vicinity. This thus leads to a much smaller microcracking zone development in gypsum.

Q. *Why* does marble behave in a more ductile manner than gypsum (at a microscopic scale)?

A. Following the same line of reasoning, the differences of brittleness/ductility displayed in the two materials can possibly be explained. The much larger process zone developed in marble than in gypsum means that the amount of inelastic deformation associated with crack propagation in marble is also larger than that in gypsum. One probable explanation is based on the concept of energy balance. The creation of each branched microcrack involves the dissipation of surface crack energy. Therefore, more energy is dissipated in creating a much larger *total* crack surface area in marble. It thus displays a higher degree of ductility than gypsum.

9.4 Shear cracks

The preceding sections focused mainly on *tensile* crack development in both materials. This section focuses on *shear* crack development.

9.4.1 Macroscopic observations

The macroscopic changes associated with the initiation of shear cracks in gypsum and marble are schematically illustrated in figure 9.11. Although the following macroscopic description is based on one coplanar flaw geometry of 4a-60-0, the discussion on shear crack initiation mechanism can reasonably be generalized to most other geometries in which shear cracks coplanar with the pre-existing flaws also initiate. However, the discussion of coalescence should be regarded as restricted to this flaw pair geometry only.

In **gypsum**, the initiation of shear cracks as observed in the video recordings is not accompanied by any prior observable changes (sketch *a* for gypsum in figure 9.11). Shear crack initiation, which occurs as a relative shear displacement in the intact material, is often accompanied by a simultaneous occurrence of local surface spalling (sketch *b* for gypsum in figure 9.11). The extent of spalling as measured from the trace of shear crack is about 3 to 6 mm. In the specific flaw geometry illustrated in figure 9.11, coalescence occurs by the propagation and linkage of the two coplanar shear cracks initiated from the inner flaw tips (sketch *c* for gypsum in figure 9.11).

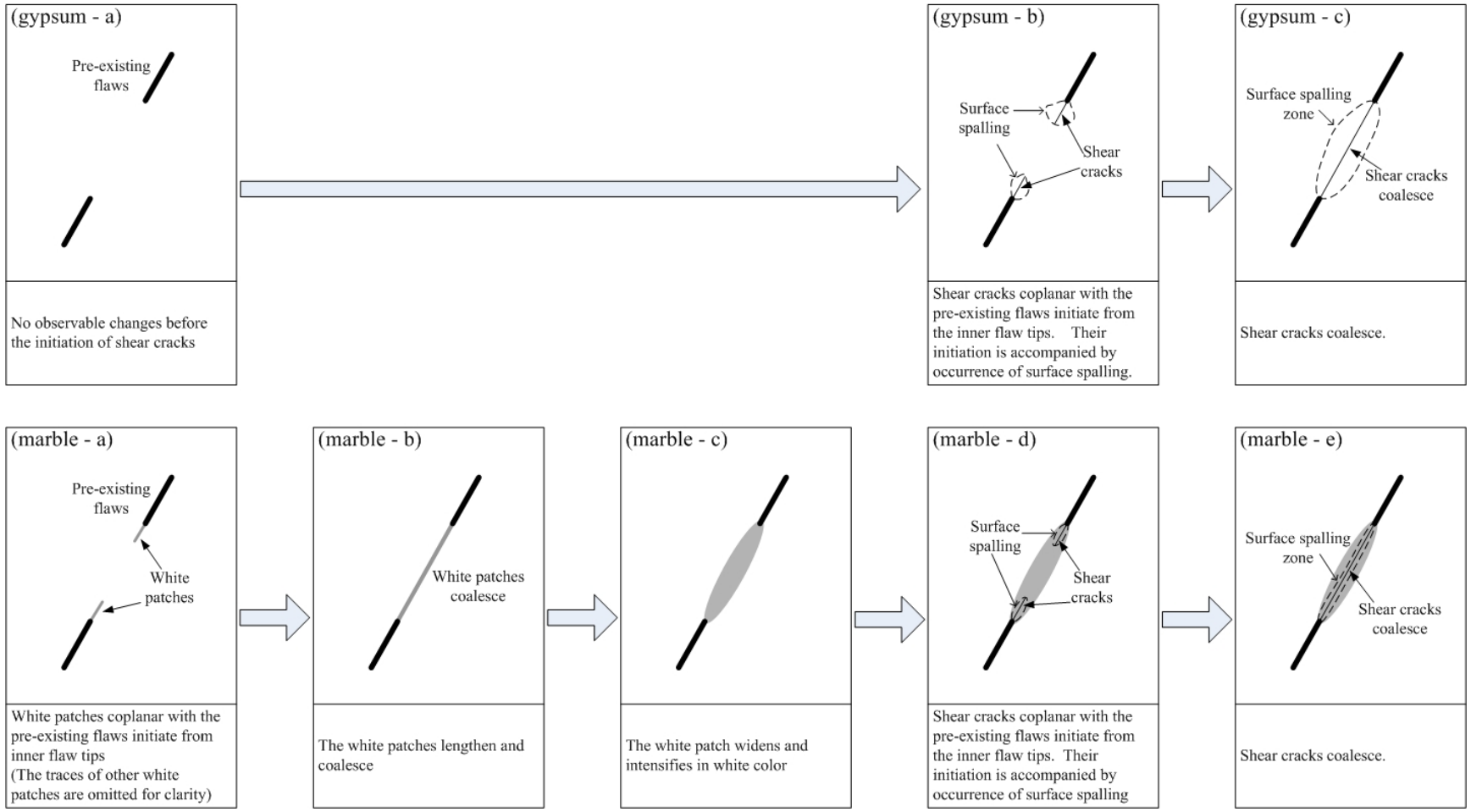

Figure 9.11 – Schematic illustration of the *macroscopic* shear crack development in marble and gypsum. The top row is for gypsum and the bottom row is for marble.

In **marble**, the initiation of shear cracks as observed in the video recordings is preceded by an initiation of white patches. In the sketch *a* for marble in figure 9.11, only two white patches which lead to the eventual formation of shear cracks are shown, white patches at other locations are not shown. The white patches lengthen and widen as the applied loading increases. Generally, for coplanar flaw geometries, including the one illustrated here, the individual coplanar white patches lengthen and coalesce in response to the further applied loading (sketch *b* marble in figure 9.11), which is then followed by a further widening and color intensification of the white patch in the bridging region (sketch *c* marble in figure 9.11). Further loading later leads to crack initiation, which is a relative shear displacement in the intact material adjacent to and coplanar with the flaw tips (sketch *d* for marble in figure 9.11). The shear crack initiation is often accompanied by a simultaneous occurrence of local surface spalling. The extent of spalling as measured from the trace of shear crack is about 1 to 3 mm. Eventually, the coplanar shear cracks propagate towards each other and coalesce (sketch *e* for marble in figure 9.11).

9.4.2 Microscopic observations

A detailed SEM study was conducted in a marble specimen, which had been loaded to 94% of the failure stress. A white patch, which was free of any macroscopic observable cracks, with a trace similar to the one shown in sketch *b* for marble in figure 9.11 was examined. The SEM images revealed that the white patch consisted of multiple en echelon arrays of microcracking zones close to the pre-existing flaw tips (figure 7.51). The properties of these microcracking zones are summarized as:

- They were dominantly of tensile origin with localized spalling features formed along them.
- They were oriented almost parallel (or with ~5^{o} inclination) with the uniaxial loading direction (σ_1), i.e. inclined at ~30^{o} with the future shear crack.
- They developed preferentially close to the flaw tips, and absent in the middle bridging region far away from flaw tips.

- The length of each individual microcracking zone is around 10 grain sizes (1 to1.5 mm long), and the horizontal spacing between them is 5 to 10 grain sizes (observed at this particular stress level).

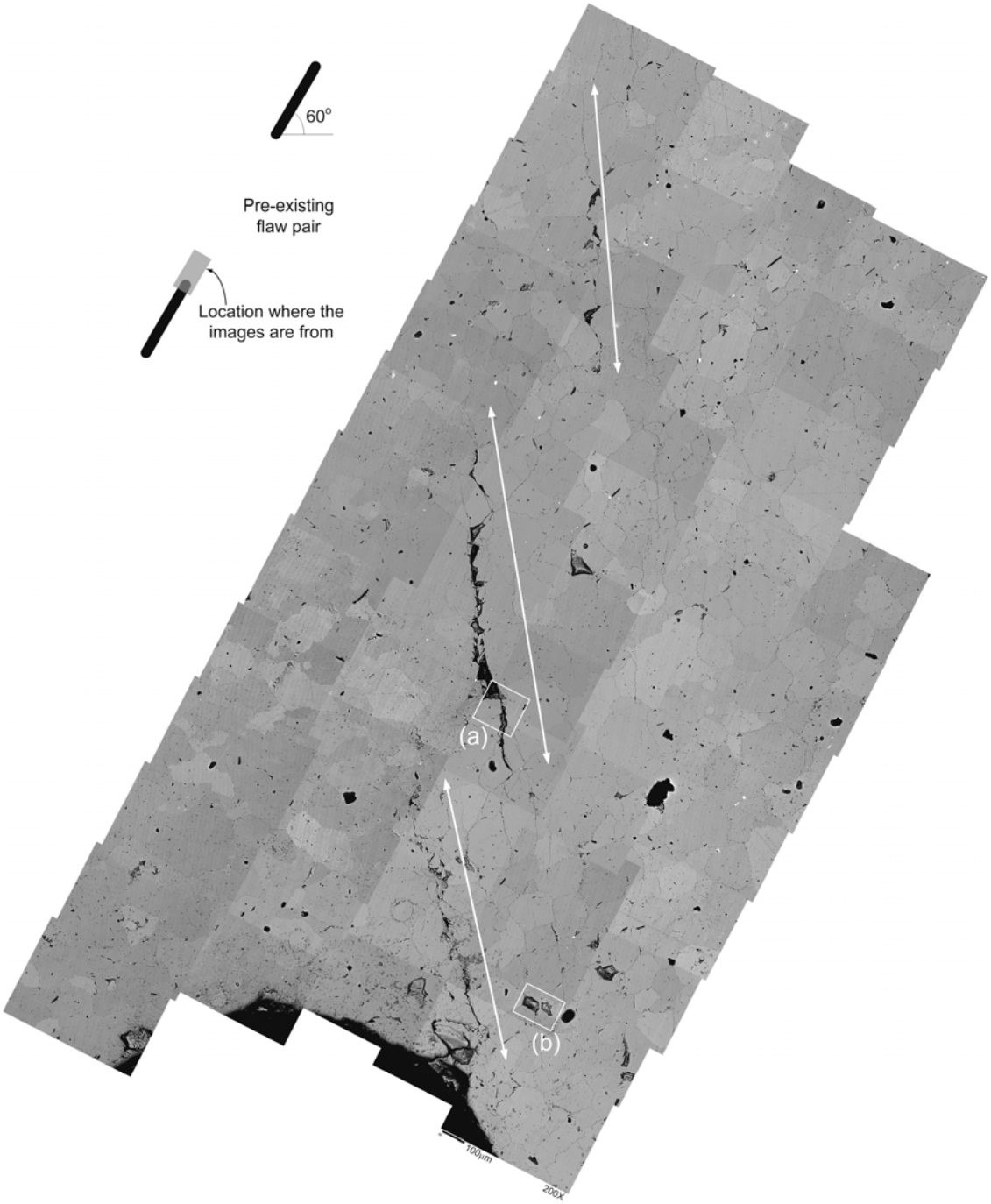

Figure 7.51 – An assemblage of SEM images of the area around the right flaw tip of the bottom flaw. Refer to figure 7.52 in chapter 7 for magnified images of the two enclosed areas. The intensely fractured zones, whose traces are indicated by arrows, trend almost parallel to the vertical loading direction. The length of the bottom scale bar is 100 μm. (magnification power = 200 X)

The micoscropic and macroscopic associated with the shear crack initiation in gypsum and marble are summarized in table 9.5. Note that no SEM/ESEM study was conducted in gypsum and the SEM study was only conducted on one specimen in marble.

	Gypsum	Marble
(1)	**Microscopic events/observations:** Microscopic imaging work was not conducted. **Macroscopic events/observations:** *(figure 9.11 gypsum – a)* No observable change was observed in video recordings.	**Microscopic events/observations:** Microscopic imaging work was not conducted. **Macroscopic events/observations:** *(figure 9.11 marble – a)* Short white patches (~2 mm long) coplanar with the pre-existing flaws initiating from the inner flaw tips.
(2)	**Microscopic events/observations:** Microscopic imaging work was not conducted. **Macroscopic events/observations:** *(figure 9.11 gypsum – a)* No observable change was observed in video recordings.	**Microscopic events/observations:** Microscopic imaging work was not conducted. **Macroscopic events/observations:** *(figure 9.11 marble – b)* The coplanar white patches, which have initiated earlier from the inner flaw tips, propagate towards each other and coalesce.
(3)	**Microscopic events/observations:** Microscopic imaging work was not conducted. **Macroscopic events/observations:** *(figure 9.11 gypsum – a)* No observable change was observed in video recordings.	**Microscopic events/observations:** *(figure 7.51)* En echelon microcracking zones (~1000 to 1500 μm long) trending almost parallel to the loading direction initiate close to the pre-existing flaw tips. **Macroscopic events/observations:** *(figure 9.11marble – c)* The white patches widen and intensify in color.

Table 9.5 – Comparison of microscopic and macroscopic changes associated with the shear crack development in gypsum and marble.

	Gypsum	Marble
(4)	**Microscopic events/observations:** Microscopic imaging work was not conducted. **Macroscopic events/observations:** *(figure 9.11 gypsum – b)* Shear displacement occurs in the intact material from the two inner flaw tips individually as recorded by the high speed camera. Its initiation is often associated with the development of a local surface spalling zone, which is about 3 to 6 mm wide as measured from the crack trace.	**Microscopic events/observations:** Microscopic imaging work was not conducted. **Macroscopic events/observations:** *(figure 9.11 marble – d)* Shear displacement occurs in the intact material from the two inner flaw tips individually and along the white patch as recorded by the high speed camera. Its initiation is often associated with the development of a local surface spalling zone, which is about 1 to 3 mm wide as measured from the crack trace.
(5)	**Microscopic events/observations:** Microscopic imaging work was not conducted. **Macroscopic events/observations:** *(figure 9.11 gypsum – c)* Coplanar shear cracks propagate and coalesce.	**Microscopic events/observations:** Microscopic imaging work was not conducted. **Macroscopic events/observations:** *(figure 9.11 marble – e)* Coplanar shear cracks propagate and coalesce.

Table 9.5 – Comparison of microscopic and macroscopic changes associated with the shear crack development in gypsum and marble (continued).

9.4.3 Discussion

Note that the above observations were generalized from the SEM study of only one marble specimen loaded to 94% of the failure stress. Although the way how the microcracking zones evolved with continually increasing load is unknown, some clues can be obtained from two other marble specimens with the same pre-existing flaw geometry which were loaded to higher stress level until macroscopic coalescence cracks developed (no SEM study was conducted on these specimens). In these two specimens, macroscopic shear cracks coplanar with the pre-existing flaws were observed to initiate from the two inner flaw tips in the bridging region (observed with the high speed camera) and then propagated towards each other until coalescence. Since the en echelon

microcracking zones were only observed close to the flaw tips in the SEM study, but not in the center of the bridging region, the initiation of shear cracks should be closely related to the development of en echelon microcracking zones. However, the exact mechanism of how the micro- en echelon microcracking zones evolve to macroscopic shear cracks is not known at this stage. Further experimental studies on additional specimens loaded to varying stress levels are then necessary to establish the relationship between the microscopic and macroscopic observations.

9.4.4 Comparison of en echelon cracks at different scales

The **macroscopic** tensile wing crack development in gypsum was observed not to be associated with any **macroscopic** en echelon crack development, but was found to be preceded by a development of **microscopic** en echelon cracks. Refer to figure 9.5(ii) again. Similarly, the **macroscopic** shear crack development in gypsum was observed not to be associated with any **macroscopic** en echelon crack development. However, no conclusion can be drawn at a **microscopic** scale since imaging studies at that scale were not done.

In marble, microscopic en echelon cracks associated with shear crack initiation (figure 7.51) and macroscopic en echelon cracks associated with the tensile crack initiation (see figure 9.1 which is reproduced below) were observed.

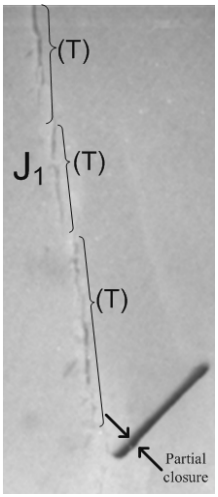

Figure 9.1 (c) – En echelon tensile crack segments developed along a white patch. The length of the pre-existing flaw is 0.5" (12.7 mm).

The above two types of en echelon features in marble are both oriented almost parallel (with a ~5^{o} inclination) to the applied loading axis. Some of the differences between them are listed in table 9.6 below. Note that the comparison is far from ideal due to the different scales (means) adopted for observations.

	Macro- en echelon tensile crack segments leading to formation of macroscopic *tensile crack*	**Micro-** en echelon microcracking zones leading to formation of macroscopic *shear crack*
Scale and means of observation	Macroscopic – high speed videos	Microscopic – SEM study
Length and shape of individual segments	2 to 5 mm long and straight (first observable traces in the high speed videos)	1 to 1.5 mm long and wiggly (in a specimen loaded up to 94% of the failure stress), but the aperture is too fine to be visible to unaided eyes
Subsequent Evolution	Individual macro- en echelon tensile cracks lengthened and coalesced as loading continued	Evolution of the micro- en echelon cracks at a microscopic scale is not known due to the availability of only one specimen for SEM study.

Table 9.6 – Differences of en echelon features leading to eventual formation of tensile cracks and shear cracks in marble.

With regard to the development of macroscopic en echelon tensile cracks in marble, an attempted explanation was offered earlier in the section "*Development into a macroscopic crack*" (under section 9.3.4). The locations where the macroscopic en echelon tensile cracks initiate are possibly associated with local microcracking zones of high crack densities. However, from the geometry of the macroscopic en echelon cracks (i.e. small inclination angle between the trending direction of the echelon cracks and that of the underlying white patch) observed on the specimen front face, it is also possible that the development of the macro- en echelon cracks was due to a combined mode I – mode III or mode I – mode II loading condition. A similar argument may also be applicable to the micro- en echelon microcracking zones since they are also inclined at an angle with

general direction of the underlying white patch. See an analogy shown in figure 2.42 below. However, since only the front face of the specimen was monitored during the loading tests, further experimental studies are thus required to validate this postulation (see the relevant recommendation in chapter 10).

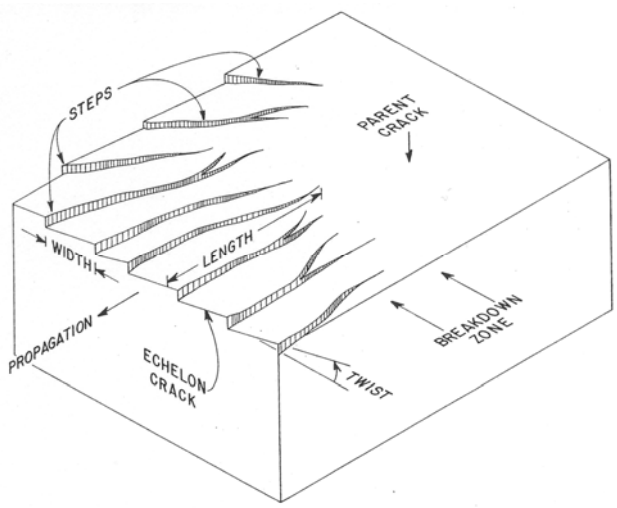

Figure 2.42 – Schematic illustration of multiple echelon cracks initiating from a parent crack. The breakdown zone is located between the echelon cracks and the parent crack (Pollard et al., 1982).

A similar development of echelon tensile cracks, but of a macroscopic scale, was observed by Petit and Barquins (1988). In their experiments, 1.5 mm diameter hole was first drilled in a PMMA plate (5mm thick, 50 mm long, 32 mm wide), which was followed by sawing to both sides to obtain a 8 mm long and 0.3 mm wide slot on each side. The slot had an inclination angle of 60^{o}. Under uniaxial compression loading, echelon tensile cracks progressively developed from the two pre-existing flaw tips (figure 9.12 b). Note also the closely spaced *maximum shear stress isochromes* around the tip regions (figure 9.12 a). The authors stated that

> *"In PMMA the formation of tensile cracks within the shear zone suggests that mode I fracturing is possibly a precursive mechanism of the loss of cohesion at the tip of the shear zone."*

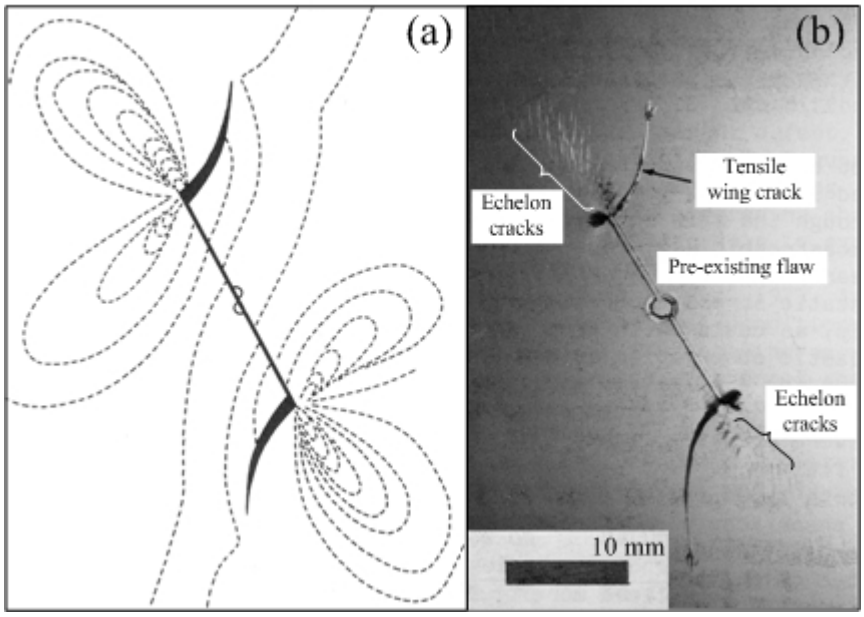

Figure 9.12 – (a) Maximum shear stress isochromes around a pre-existing flaw inclined at 30^{o} with the vertical uniaxial compression. (b) Tensile wing cracks and echelon arrays of much shorter tensile cracks developed from flaw tip regions (Petit & Barquins, 1988).

Based on their experimental observations, Petit and Barquins (1988) held the view that mode II is not an elementary fracture mechanism, but can only be a macroscopic phenomenon which must involve tensile (mode I) microfractures. This view has also been held by part of the geologist community for years (e.g. Peng & Johnson, 1972, Engelder, 1987, Reches & Lockner, 1994, Healy et al., 2006).

9.5 Generalization of crack types

The present experimental study showed that a variety of tensile and shear cracks initiated from the pre-existing flaws in response to the applied loading. *Seven* crack types with different trajectories and nature (tensile/shear) were classified (figure 9.13). Three of them are tensile and three of them are shear. The remaining one is of mixed tensile-shear nature, with shearing occurring adjacent to the flaw tips and simultaneous tensile opening occurring at farther segments.

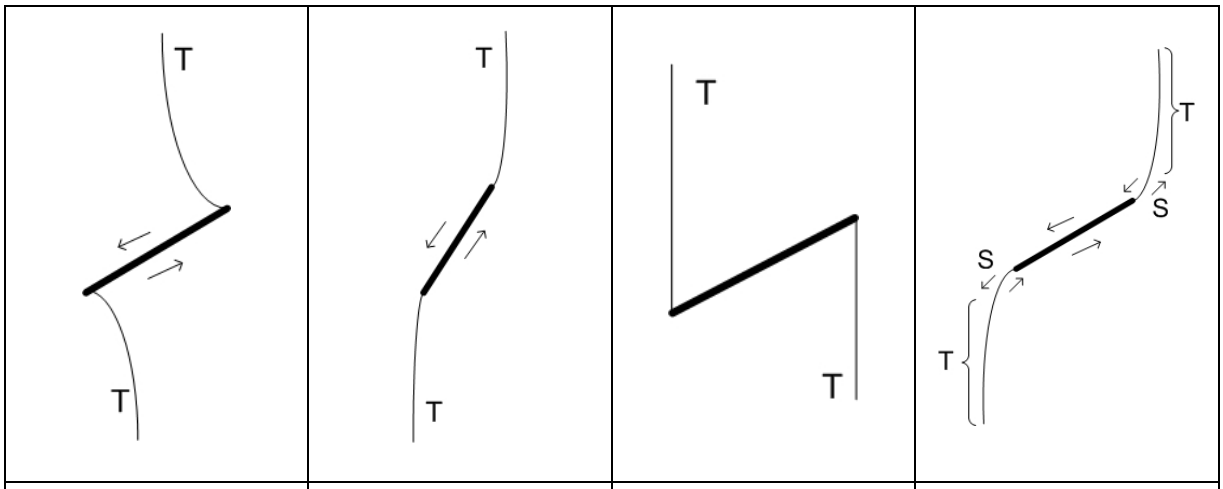

(a) Type 1 tensile crack (tensile wing crack)	(b) Type 2 tensile crack	(c) Type 3 tensile crack	(d) Mixed tensile-shear crack

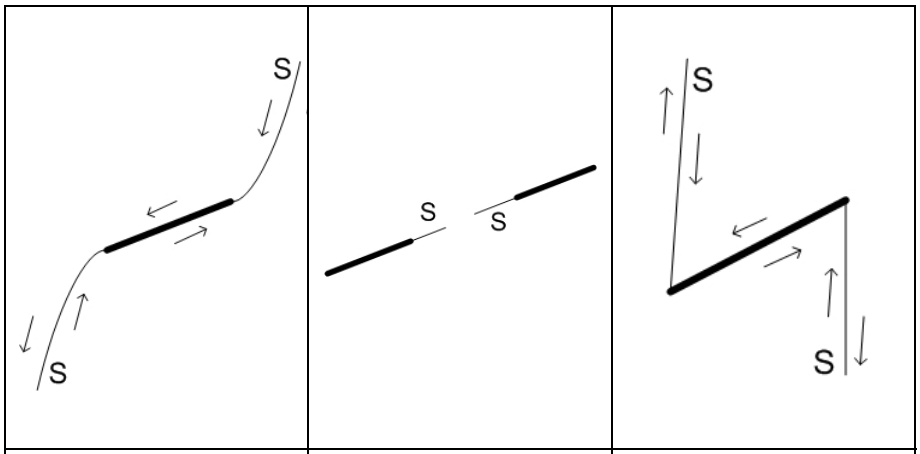

(e) Type 1 shear crack	(f) Type 2 shear crack	(g) Type 3 shear crack

Figure 9.13 – Various crack types initiated from the pre-existing flaws identified in the present study.

It has to be emphasized that a proper identification of the crack types relies on the capabilities of the high speed camera used. The significance of its use is illustrated in figure 9.14. The idealized sketches shown in this figure correspond to the fracturing and deformation events observed on a series of high speed images. In image number 1, no observable cracking has yet occurred. In image number 2, a **tensile** crack initiates. In image number 3, **shearing** immediately follows to take place along the crack faces. If the nature of crack is determined solely by the examination of fractographical features

without the use of the high speed camera, the tensile crack initiation mode probably will be removed and only signs of shearing are left on the crack surfaces after the loading test. Even if a high speed camera is used, but not of a high enough frame rate, it is possible that only images 1 and 3 are identified. The tensile opening event, which indicates the crack initiation mode, may not be captured by the camera.

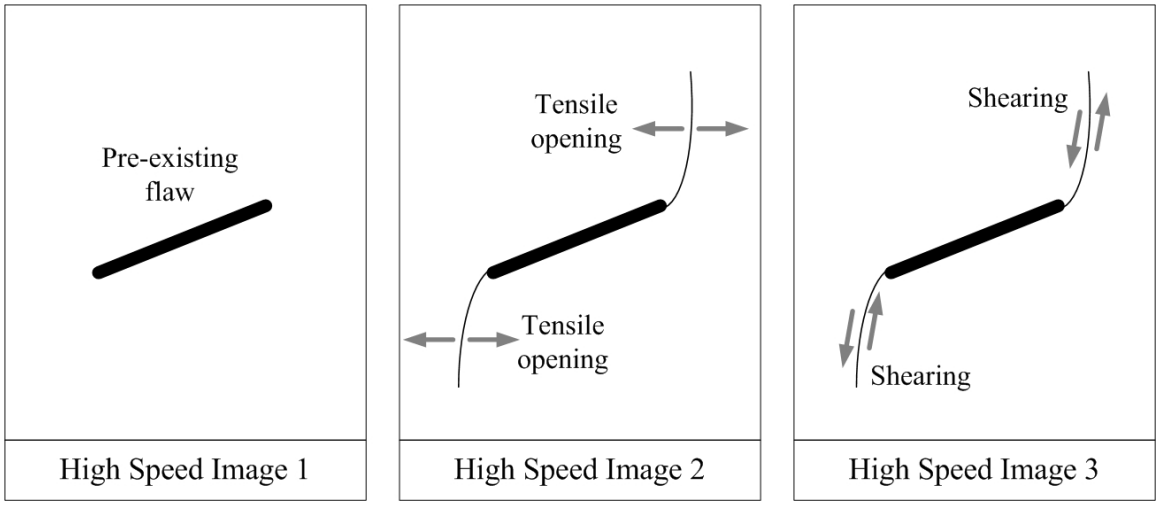

Figure 9.14 – Schematic illustration of the occurrence of shearing on newly initiated tensile cracks.

Experiments were conducted on prismatic specimens containing single flaws and double flaws. Results from single flaw experiments with regard to the type of first cracks initiated from the pre-existing flaws are summarized in table 9.7.

Series (*)	Flaw inclination angle β (°)	Type 1 Tensile	Type 2 Tensile	Type 3 Tensile	Mixed Tensile-Shear	Type 1 Shear	Type 2 Shear	Type 3 Shear
Gypsum narrow flaws	0	√						
	15	√						
	30	√						
	35	√						
	40	√						
	45	√						
	50	√						
	55	√						
	60	√						
	70	√						
	75	√						
Gypsum wide flaws	0	√						
	30	√						
	45	√						
	60	√						
	75	√						
Marble wide flaws	0		√					
	30 (#)	√	√					
	45 (#)	√	√					
	60 (#)	√	√					
	75 (#)	√	√					

(*) The aperture of narrow flaws is 0.004" and that of wide flaws is 0.05".

(#) In some specimens, either one of the two indicated crack types appears as the first crack; while in some specimens, both indicated crack types appear as the first cracks. Refer to appendix G for details.

Table 9.7 – Summary of the type of first cracks observed in gypsum and marble specimens containing single flaws.

As indicated in table 9.7, **type 1 tensile cracks** are the first cracks to develop in almost all single flaw geometries in gypsum and marble. However, horizontal flaws ($\beta = 0^o$) in marble are an exception, in which **type 2 tensile cracks**[3] initiate as the first cracks instead (figure 9.15).

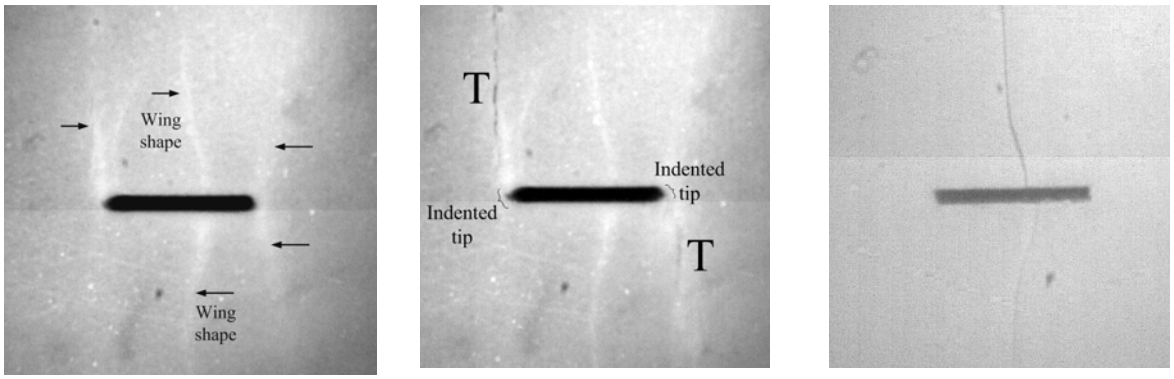

(a) (b) (c)

Figure 9.15 – (a) In uniaxial (vertical) compression test on Carrara Marble, multiple white patches first develop from the horizontal pre-existing flaw, which are then followed by (b) tensile crack opening (T) along the two almost vertical white patches at the two flaw tips (type 2 tensile cracks). (c) In gypsum containing a single horizontal flaw, tensile wing cracks initiate in response to uniaxial loading far away from the flaw tips. The length of the pre-existing flaws is 0.5" (12.7mm).

As shown in figure 9.15 c, the first observable change in gypsum in response to the uniaxial compression was the initiation of tensile wing cracks from the middle portion of the pre-existing flaw. Their initiation positions indicated that the locus of maximum tangential stresses. Once the cracks initiated, which were accompanied by a distinct cracking sound, they immediately propagated towards the edges of the specimen. The overall fracturing process was thus very brittle.

In contrast, white patches first develop in response to the applied loading in marble. As shown in figure 9.15 a, apart from the wing-shaped white patches which developed at the flaw center similar to those in gypsum (figure 9.15 c) , straight and steeply-inclined white patches also developed from the flaw tips. When the applied loading further increased

[3] The trajectory of type 2 tensile crack is equivalent to type 3 tensile crack for horizontal flaws. For simplicity, only type 2 tensile crack is mentioned for the relevant discussion.

(figure 9.15 b), the white patches lengthened, widened and intensified in color, indicating the increased amount of inelastic deformation along them. Further loading eventually led to an observable tensile crack opening, which was more favored at the tip regions. Comparing figures 9.15 a and b reveals that right after the initiation of the white patches, the initiation of the cracks from flaw tips was enhanced (or accompanied) by a minute deformation of the pre-existing flaw as indicated by the slightly deformed/ indented tips (figure 9.15 b). Once these steeply-inclined cracks initiated from the flaw tips, the initiation of tensile wing cracks in the center of the flaw then followed (not shown in figure 9.15).

Referring again to table 9.7, it is very common in marble specimens containing inclined flaws that in addition to the **type 1 tensile cracks**, **type 2 tensile cracks** are also the first cracks to initiate. Similar to the horizontal flaws, white patches associated with microfracturing zones, which delineate the future trajectories of **type 1 and type 2 tensile cracks** first develop. The degree of microcracking then increases and reaches a level that observable **type 1 and type 2 tensile cracks** appear simultaneously or almost simultaneously as recorded by the high speed camera.

Recall that all the tested specimens are loaded until specimen failure occurred. After the initiation of the first cracks, additional crack types usually also develop in the specimens. Table 9.8 summarizes all the crack types (including the first cracks shown previously in table 9.7) which initiate in the specimens throughout the whole loading process.

The following features can be generalized from table 9.8:

1) **Type 1 tensile cracks**, either initiating as first cracks or later cracks, develop in all single flaw geometries throughout the whole loading process.

2) **Type 2 tensile cracks** develop in almost all single flaw geometries, except $\beta = 70^o$ **and** 75^o for single narrow flaws in gypsum, and $\beta = 75^o$ for singles wide flaws in gypsum. For these flaw geometries, the initiation of **type 1 tensile cracks**, which are the first cracks, is concurrent with the specimen maximum stress (specimen failure). Other crack types thus have no chance to develop afterwards.

Series (*)	Flaw inclination angle β (°)	Type 1 Tensile	Type 2 Tensile	Type 3 Tensile	Mixed Tensile-Shear	Type 1 Shear	Type 2 Shear	Type 3 Shear
Gypsum narrow flaws	0	√ [1]	√	√	√			
	15	√ [1]	√	√				
	30	√ [1]	√	√	√			
	35	√ [1]	√	√	√			
	40	√ [1]	√	√	√			
	45	√ [1]	√	√	√			
	50	√ [1]	√	√	√			
	55	√ [1]	√	√	√			
	60	√ [1]	√	√	√			
	70	√ [1]						
	75	√ [1]						
Gypsum wide flaws	0	√ [1]	√	√	√			
	30	√ [1]	√	√	√			
	45	√ [1]	√	√	√			
	60	√ [1]	√		√			
	75	√ [1]						
Marble wide flaws	0	√	√ [1]	√	√	√		
	30	√ [1]	√ [1]	√	√	√		
	45	√ [1]	√ [1]	√	√	√		√
	60	√ [1]	√ [1]				√	
	75	√ [1]	√ [1]				√	

(*) The aperture of narrow flaws is 0.004" and that of wide flaws is 0.05".

Table 9.8 – Summary of all crack types observed in gypsum and marble specimens containing single flaws. √ [1] indicates that the crack is the first crack to initiate (see table 9.1).

3) **Type 3 tensile cracks** and **mixed tensile-shear cracks** are very common among the specimens, except for large flaw inclination angles (β **= 70° & 75°** for single narrow flaws in gypsum, β **= 75°** for single wide flaws in gypsum, and β **= 60° & 75°** for single wide flaws in marble). For these large flaw inclination angles, due to the

similar reason stated in point (2) above, the initiation of **type 1 and/or type 2 tensile cracks** is concurrent with the specimen maximum stress. Other crack types thus have no chance to develop afterwards.

4) Shear cracks commonly develop in marble specimens during late stages of loading and the initiation of them often leads to specimen failure. These shear cracks, which initiate from the flaw tips, are generally inclined at an angle of about 55^o to 65^o with the horizontal regardless of the orientation of the pre-existing flaw. It means that these shear cracks make a varying inclination angle with the shallowly inclined flaws ($\beta = 0^o, 30^o$ & 45^o), and trend almost coplanar with the more steeply inclined flaws ($\beta = 60^o$ & 75^o). The shear cracks in the former group are thus mostly of **type 1** (figure 9.16 a), while those in the latter group are mostly of **type 2** (figure 9.16 b), based on the consideration of crack geometry. The consistent angle of shear cracks (with the horizontal) initiating from flaw tips is compared with the θ_c (the angle between the failure plane and the minimum principal stress) predicted by the Coulomb failure criterion for an originally intact specimen:

$$\theta_c = 45^o + \phi / 2$$

where ϕ is the angle of internal friction of the rock. Substituting a value of $\phi = 28^o$ (Pollard & Fletcher, 2005) will yield $\theta_c = 59^o$, which is close to the observed inclination angle of these shear cracks (figure 9.16). It thus suggests a similarity in the fundamental cracking processes occurring in intact specimens and specimens with a pre-existing artificial flaw. One of the postulations is that prior to the development of the eventual failure plane in an intact specimen, a number of microcracks would have developed in the specimen already. They then become sources of stress concentrations and preferential sites for further crack development. The role of these newly developed cracks is then very similar to that of the flaws artificially created in the specimens shown in figure 9.16. Further new cracks then developing from these early cracks lead to specimen failure. Considered within the context of the Coulomb

failure, it is the orientation at which the shear stress component due to the applied loading is maximum.

In contrast, such an initiation and propagation of shear cracks are less common in gypsum. Although most of the failure cracks in gypsum also originate from the flaw tips, they are mainly of tensile origin (type 2 or type 3 tensile cracks) or mixed shear-tensile cracks. Their initiation easily leads to a tensile splitting of the specimen and an abrupt drop of specimen strength.

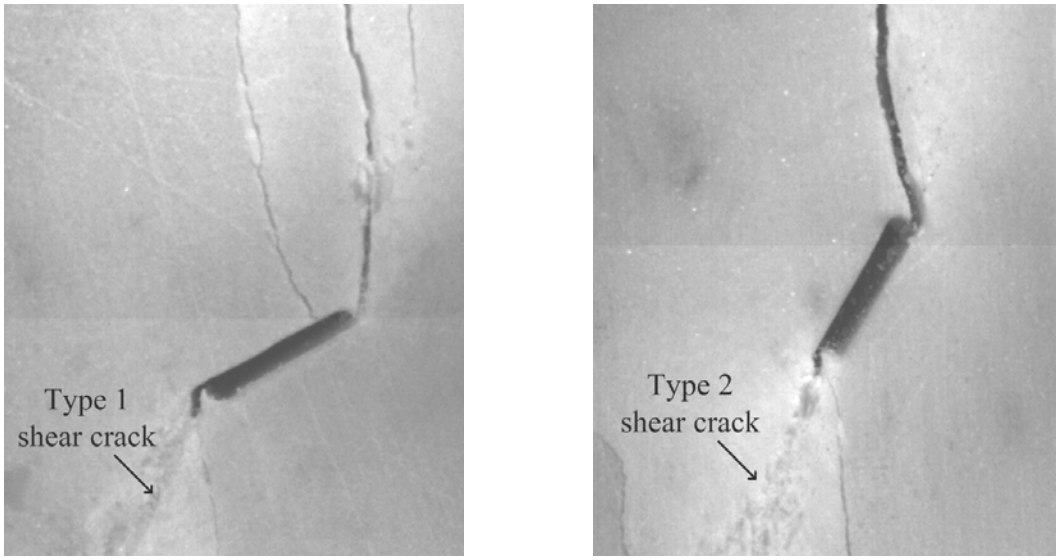

(a) CM 30-D (b) CM 60-C

Figure 9.16 – Shear crack initiation in marble. (a) Type 1 shear crack initiated from a pre-existing flaw with inclination angle 30^o. (b) Type 2 shear crack initiated from a pre-existing flaw with inclination angle 60^o.

5) The initiation of **type 3 shear cracks** is rare in the tested specimens, and is only observed in marble specimens with flaw inclination angle $\beta = 45^o$, but not in any gypsum specimens.

Generally speaking, the fracturing behavior and the types of new cracks produced in gypsum specimens containing *narrow* and *wide* flaws are very similar[4]. However, due to a smaller aperture size, partial or complete closure occurs more frequently for narrow flaws. This in turn leads to the more favorable initiation of additional tensile cracks in the middle portions of the flaws, especially those which are shallowly inclined (figure 5.15). Figure 5.16 explains schematically how such a crack closure creates contacts along the flaw face from which additional tensile wing cracks subsequently initiate.

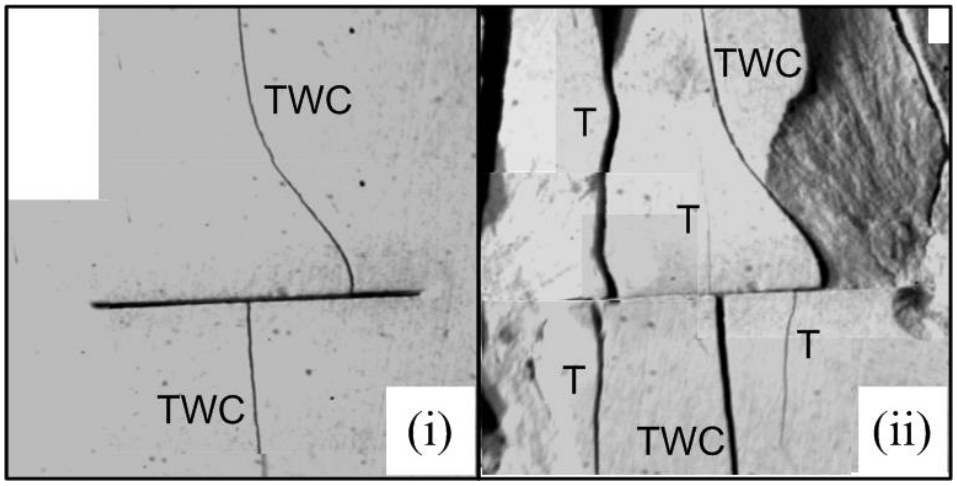

Figure 5.15 – Development of tensile cracks from a horizontal narrow flaw in gypsum. Length of the pre-existing flaw is 0.5". (i) view just after the initiation of the TWC pair, (ii) development of multiple tensile cracks, far from flaw tips after peak load.

[4] This is based on the observations of uniaxial loading compression tests conducted on specimens containing *single* flaws. For tests in gypsum and marble specimens containing *double* flaws, only wide flaws (0.05" aperture) were tested.

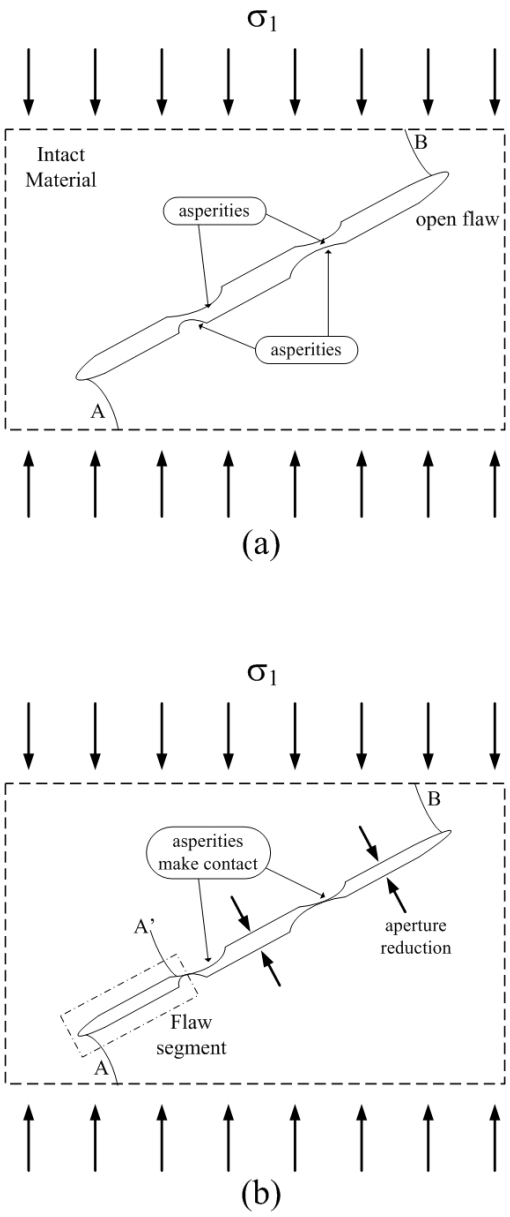

Figure 5.16 – Schematic illustration (not to scale) of an inclined narrow flaw under uniaxial compression. (a) The flaw faces are not completely smooth and consist of multiple asperities. Tensile wing cracks initiate from the two flaw tip regions. (b) Further applied loading reduces the flaw aperture and leads to the formation of contacts between flaw faces. The flaw segment on the left of the main flaw behaves as an independent flaw with the initiation of a new tensile crack A' from its right tip.

As a corollary, the present thesis also reviews the types of cracks identified and the relevant terminologies used in the past studies (see chapter 2). It is noted that, the terms **primary cracks**, **tensile cracks** and **wing cracks** were often used interchangeably; while the terms **secondary cracks** and **shear cracks** were similarly used interchangeably. The present study however finds that such a usage of terms is sometimes confusing and thus very undesirable in describing the fracturing behavior for the reasons below.

In agreement with previous experiments by others (see references in figure 9.18), **shear cracks** are not the first cracks to initiate from the prismatic specimens containing single flaws as observed in the present experimental studies in gypsum and marble. Tensile cracks are always the first cracks. However, as shown in table 9.5 and discussed above, **type 1 tensile cracks** (tensile wing cracks) are not the only first cracks to initiate in marble. **Type 2 tensile cracks** which do not display the conventional wing appearance also initiate as the first cracks. Therefore, using the terms **primary cracks** interchangeably with **wing cracks** is inappropriate. It is hereby suggested that the term **primary** should only be used to indicate a temporal relationship which refers to all cracks initiating as the first cracks. In addition, **tensile cracks** should only describe cracks that initiate in a tensile mode, without any implication of the shape of crack trajectory. On the other hand, **wing cracks** should only imply the shape of crack trajectory and be restricted to describe type 1 tensile cracks only.

As shown in table 9.6 and discussed above, various types of cracks initiated after the initiation of the first cracks. Most importantly, these later cracks were not only restricted to shear cracks, but also include tensile cracks (e.g. type 2 tensile cracks, type 3 tensile cracks for a majority of gypsum specimens). It implies that using the terms **secondary cracks** and **shear cracks** interchangeably is inappropriate. It is hereby suggested that the term **secondary** should only be used for indicating a temporal relationship to describe those cracks initiated later than the first cracks. **Shear cracks** should solely be used to refer the shearing crack initiation mode, without implying any temporal relationship.

The crack types observed and generalized in earlier studies are hereby reviewed, with the objective to unify the terminology. The crack types are reclassified according to the scheme shown in figure 9.13. See summary shown in figure 9.18. In cases where the nature of new cracks was not clearly stated, several possible crack types are then assigned based on the shape of the crack trajectories. Note also that the terms **primary** and **secondary** have been omitted unless there is a strong indication that such a usage is necessary and does not cause confusion (e.g. figure 9.18 d).

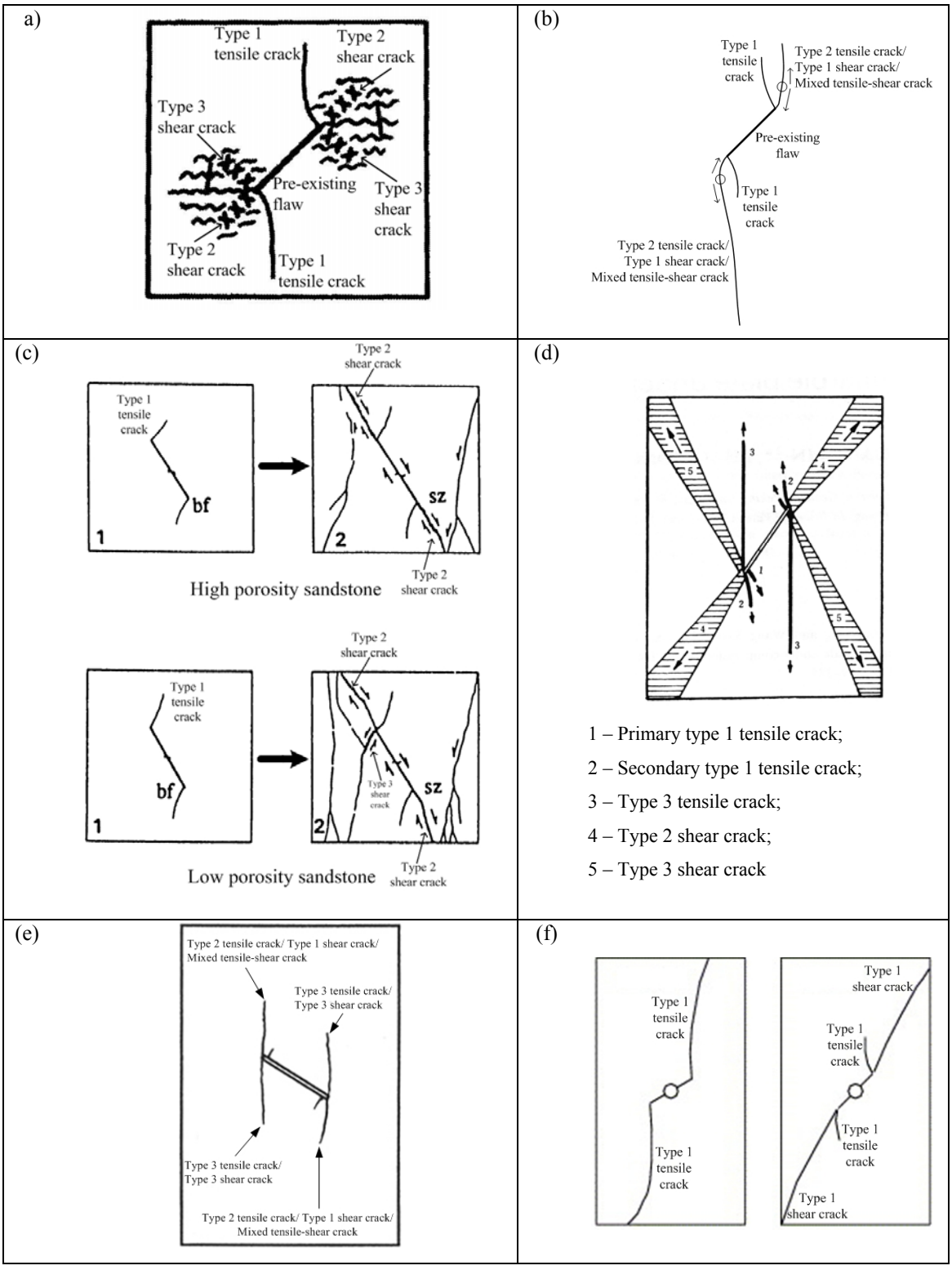

Figure 9.18 – Fracturing patterns in specimens containing single pre-existing flaws (a) Lajtai (1974), (b) Ingraffea and Heuze, 1980), (c) Petit and Barquins (1988), (d) Huang et al. (1990), (e) Chen et al. (1995), (f) Li et al. (2005).

9.6 Coalescence categories

Crack coalescence has been extensively studied experimentally in different man-made and natural rocks by different groups. However, comparing their results to reach conclusions is sometimes challenging. *First*, the studied specimen material, specimen dimensions and flaw sizes varied among research groups. *Second*, the quality of crack observation varied due to differences in experimental set-ups, including the means of crack development observation. The question of whether the same coalescence patterns can be observed in artificial material and natural rock with the same flaw geometries and loading conditions is thus still unanswered. The objective of this thesis is thus not only to study the influence of individual *geometrical* factors on the eventual fracturing processes and coalescence patterns as discussed in section 9.3, but also the dependence of fundamental fracturing behavior and coalescence patterns on *material* type.

Nine coalescence categories with different crack types and trajectories were observed in the present experimental study in gypsum and marble and they are schematically summarized in figure 9.19. Most of them are achieved by the various combinations of the crack types shown in figure 9.13. **Category 1** refers to fracturing patterns *without* the occurrence of coalescence. **Category 2** refers to *indirect* coalescence patterns which involve two or more inclined, steeply inclined or vertical coalescence cracks. The coalescence usually occurs at or after the specimen maximum stress is reached and the location of coalescence is far away from the central bridging region. In contrast, **categories 3 to 9** are *direct* coalescence, which are organized with a general trend of variation of coalescence crack types from shear (**categories 3, 4**) to mixed shear-tensile (**category 5**) to tensile (**categories 6, 7, 8, 9**).

As reviewed in chapter 2, most of the cracks leading to coalescence in the field were identified to be of *tensile* origin. From the present experimental study, in addition to some recent ones (Bobet & Einstein, 1998a, Wong & Chau, 1998, Sagong & Bobet, 2002, Mughieda & Alzo'ubi, 2004, Li et al., 2005), *shear* cracks are also known to be coalescence cracks (**categories 2, 3, 4, 5**) at least at the laboratory scale being studied.

Category	Coalescence patterns	Crack types involved
1	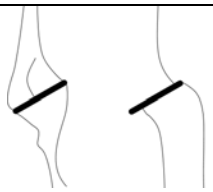	**No** coalescence
2	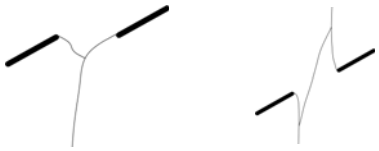	**Indirect** coalescence by two or multiple cracks (crack types vary)
3	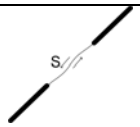	Type 2 **S** crack(s)
4	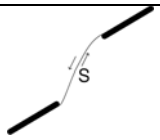	Type 1 **S** crack(s)
5	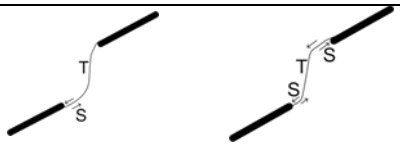	One or more type 2 **S** crack(s) and type 2 **T** crack segments between inner flaw tips
6	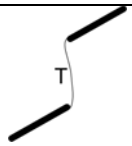	Type 2 **T** crack(s). There may be occasional short **S** segments present along the coalescence crack.
7		Type 1 **T** crack(s)
8		Flaw tips of the same side linked up by **T** crack(s) not displaying wing appearance (crack type not classified). There may be occasional short **S** segments present along the coalescence crack.
9	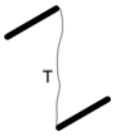	Type 3 **T** crack(s) linking right tip of the top flaw and left tip of the bottom flaw. There may be occasional short **S** segments present along the coalescence crack.

Figure 9.19 – Crack coalescence types. S = shear, T = tensile.

The coalescence between pre-existing **coplanar** flaws in both molded gypsum (figure 6.15) and Carrara Marble (figure 6.29) is achieved by a linkage of the inner flaw tips according to any one of the coalescence categories from 1 to 6 (except 4). In general, small flaw inclination angles (β) favor low number categories, while large flaw inclination angles favor high number categories. In other words, there is a general trend of variation from no coalescence, shear coalescence to tensile coalescence as β increases (table 6.23). Since there exists a competition of initiation between **tensile** crack and **shear** crack from the inner flaw tips, such experimental results suggest that **tangential stress** increases and **shear stress** decreases at the inner flaw tips as β increases.

Physically speaking, wider separation between the inner flaw tips reduces the mutual influence/interaction between the flaws, and hence the less chance of coalescence in certain flaw geometries. For example, for geometries 2a-30-0 vs 4a-30-0 (both in gypsum and marble) and 2a-45-0 vs 4a-45-0 (only in marble), some or all of the tested specimens show **coalescence** (either indirect or direct) for ligament length 2a, but **no coalescence** occurs for ligament length 4a (figures 6.15 & 6.19). For those flaw geometries with no coalescence, various types of cracks (except type 2 shear cracks) similar to those observed in the specimens containing single pre-existing flaws initiate from the inner flaw tips. Since most of the newly initiated cracks from flaw tips are steeply inclined to vertical and hence parallel to each other, it is impossible for such an individual tip crack to intersect the tip crack initiating from the other flaw or the neighboring pre-existing flaw. See sketch below.

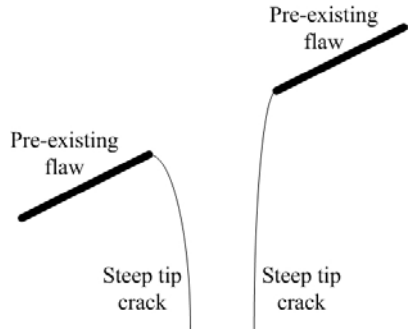

Figure 9.20 – Non-intersecting tip cracks initiating from coplanar flaws.

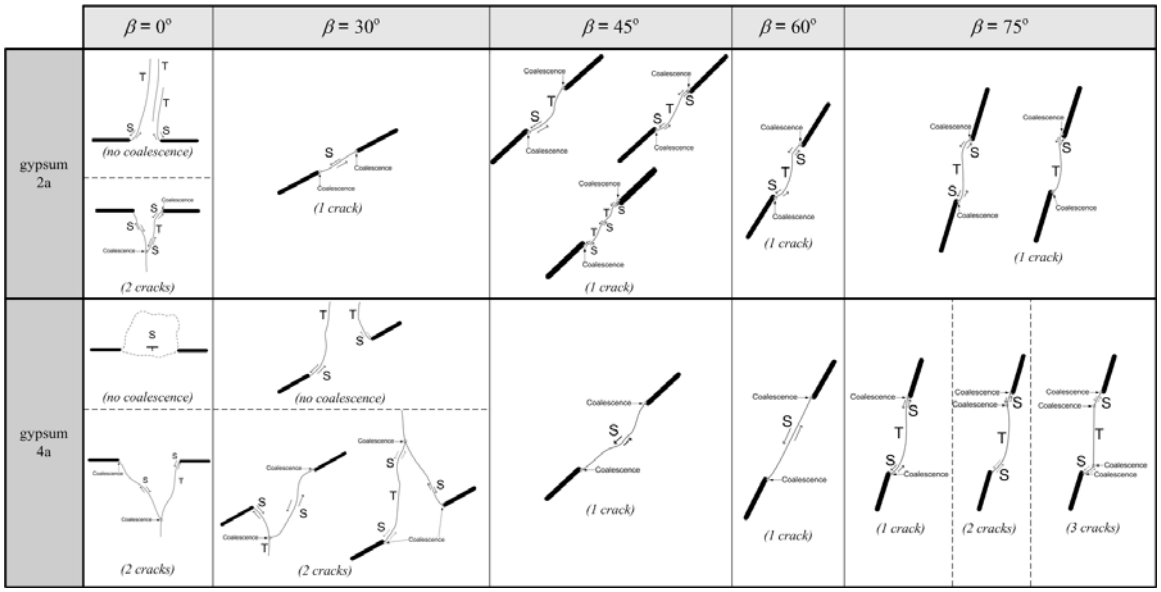

Figure 6.15 – Schematic illustration of the coalescence behavior of coplanar flaws in gypsum with '2a' and '4a' ligament length.

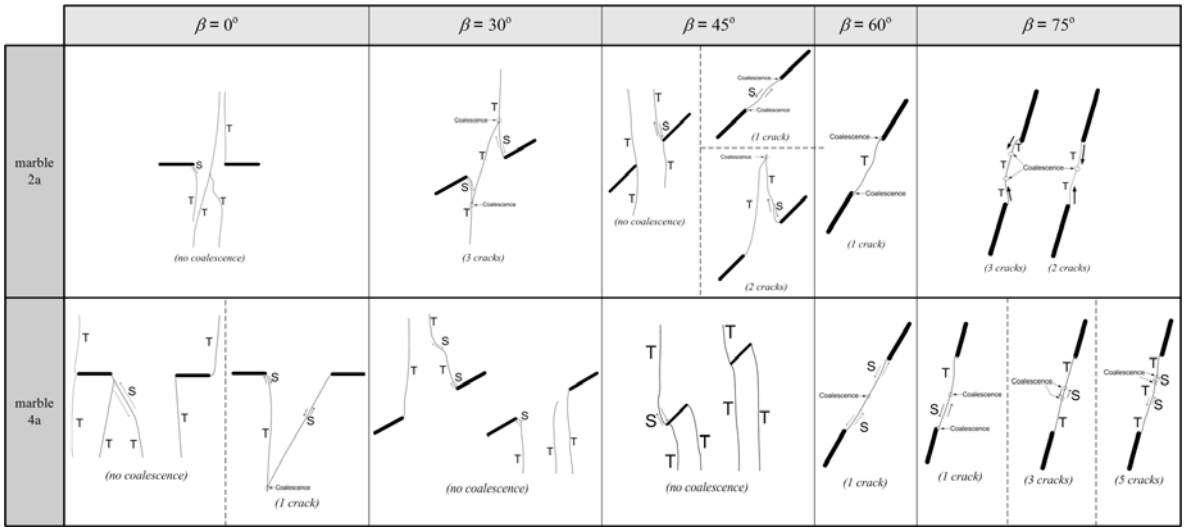

Figure 6.29 – Schematic illustration of the coalescence behavior of coplanar flaws in marble with '2a' and '4a' ligament length.

Category		Gypsum		Marble	
		Ligament length 2a	Ligament length 4a	Ligament length 2a	Ligament length 4a
1	No coalescence	0	0, 30	0, 45	0, 30, 45
2	Indirect coalescence	0	0, 30	30, 45	0
3	Shear	30	45, 60	45	60
5	Mixed shear-tensile	45, 60, 75	75	-	-
6	Tensile	-	-	60, 75	75

Table 6.23 – Coalescence behavior of coplanar flaws in gypsum and marble with '2a' and '4a' ligament length. The numbers indicated are the flaw inclination angles β (^{o})

The whole spectrum of crack coalescence categories (from 1 to 9) is observed in the **stepped** flaw pair series in molded gypsum (figure 6.16) and Carrara Marble (figure 6.30) – generally from low number categories to high number categories, i.e. from no coalescence, indirect coalescence to direct coalescence as bridging angles (α) increase from negative values to small positive values, and further up to large positive values (table 6.24). Regarding direct coalescence, the coalescence categories generally progresses from shear, to mixed shear-tensile and to tensile as bridging angles (α) increase. Such experimental results hence suggest that **tangential stress** and **shear stress** at the inner flaw tip regions increases and decreases respectively as α increases from 0^o to 120^o.

(a)

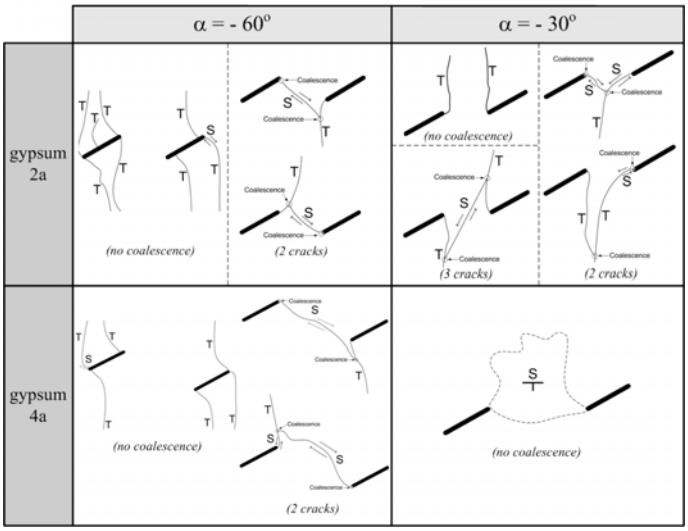

(b)

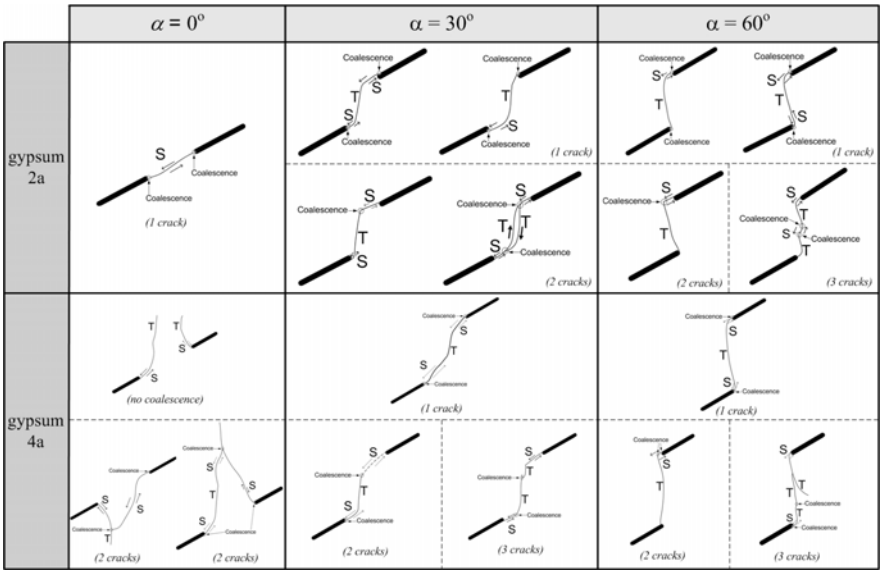

(c)

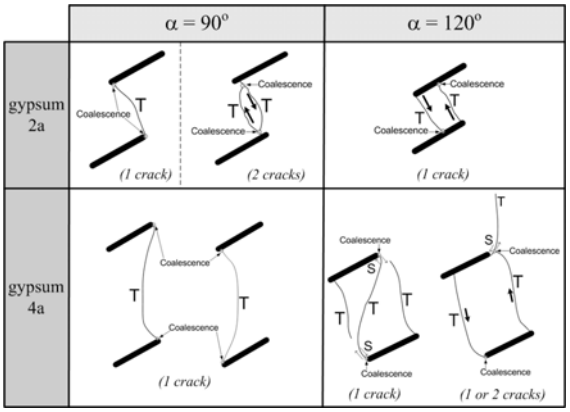

Figure 6.16 – Schematic illustration of the coalescence behavior of stepped flaws in gypsum with flaw inclination angle 30° and '2a' and '4a' ligament length.

(a)

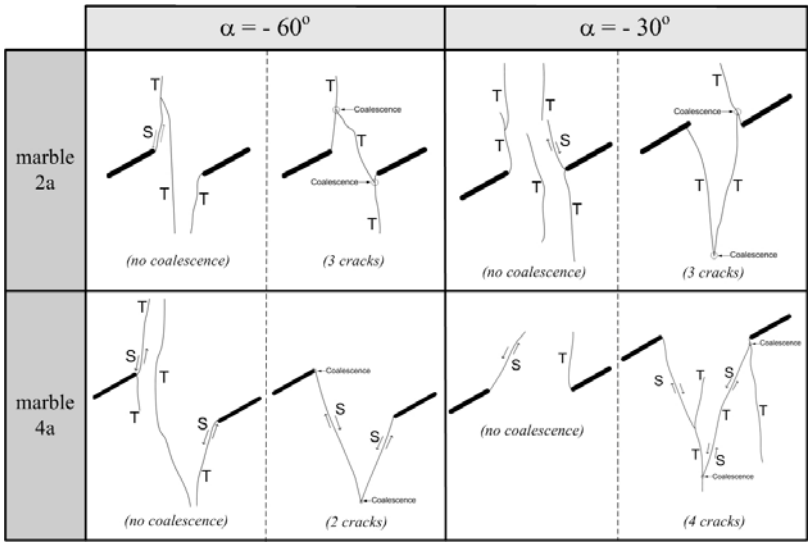

(b)

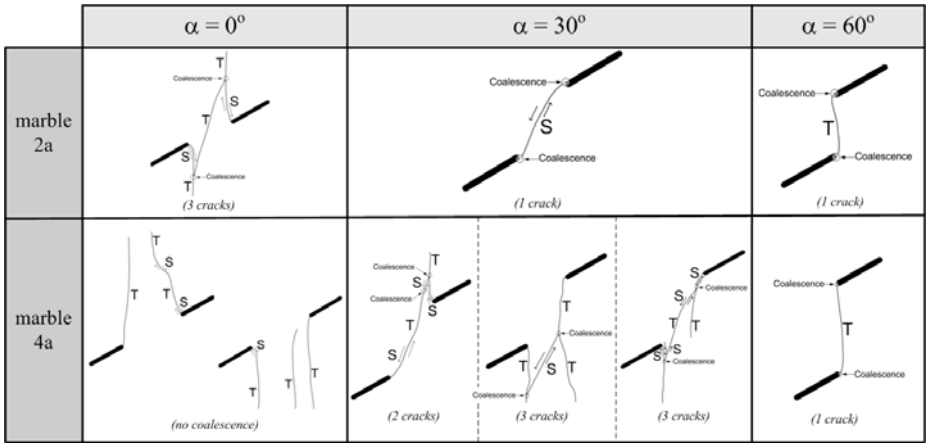

(c)

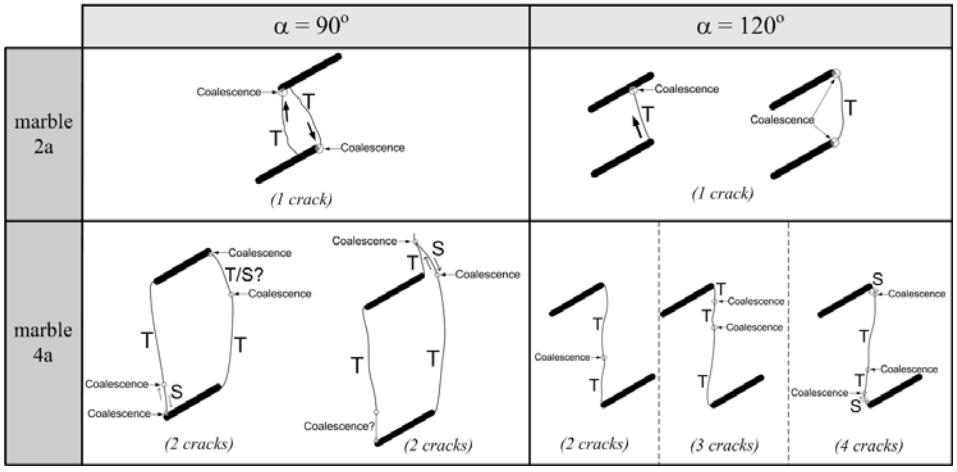

Figure 6.30 – Schematic illustration of the coalescence behavior of stepped flaws in marble with flaw inclination angle 30° and '2a' and '4a' ligament length.

Category		Gypsum		Marble	
		Ligament length 2a	Ligament length 4a	Ligament length 2a	Ligament length 4a
1	No coalescence	-60, -30	-60, -30, 0	-60, -30	-60, -30, 0
2	Indirect coalescence	-60, -30	-60, 0	-60, -30, 0	-60, -30, 30
3	Shear	0	-	-	-
4		-	-	30	-
5	Mixed shear-tensile	30, 60	30, 60	-	-
6	Tensile	-	-	60	60
7		90, 120	90, 120	90, 120	-
8		-	-	120	90
9		-	-	-	120

Table 6.24 – Coalescence behavior of stepped flaws in gypsum and marble with '2a' and '4a' ligament length. The numbers indicated in the tables are bridging angles α (^{o})

The stress distribution around a single open flaw embedded in an infinite medium subjected to a remote stress field can be theoretically predicted by the Griffith's stress theory. Regions of local compression and local extension stress fields are present around the pre-existing flaws. However, when two or more such flaws are located close to each other, the overall stress field will then be quite different from that due to only one flaw.

Depending on the relative position of the pre-existing flaws, the local compression (or local extension) stress fields induced by individual flaws can be superimposed to various extents assuming elastic conditions. The stress fields can be either reinforced or counter-balanced by the stress field associated with a neighboring stress field. If the stress field is reinforced, a lower applied load level is thus required to initiate the new crack. On the other hand, if the stress field is partially or completely counter-balanced, the location from which a crack previously initiates may no longer be favorable for crack initiation. The crack initiation location will then be shifted to another position. It is also possible that due to the perturbation of the stress field by a neighboring flaw, a specific crack type can initiate which is infeasible from a single flaw. Refer to the sketches (figure 9.21) which depict the crack development from the *wide* (0.5" aperture size) flaws inclined at 30^{o} as an example. A shear crack coplanar with the pre-existing flaw, which does not develop from the single flaw, develops in double flaws to achieve coalescence.

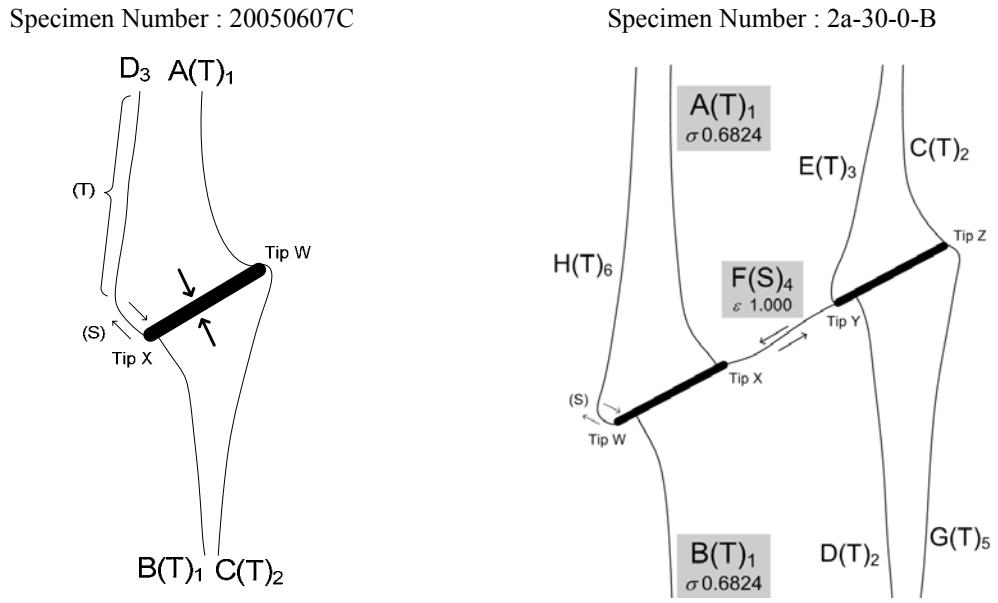

(a) single flaw (b) double flaws

Figure 9.21 – Comparison of fracturing processes in single flaw and double flaws in gypsum. (a) Absence of coplanar shear crack in single flaw; (b) Development of coplanar shear crack in double flaw.

Further complication arises as new cracks initiate and propagate from the pre-existing flaws, since their presence further perturbs the previously existing stress field. No simple analytical solution is available to compute the stress distribution around the flaws due to this type of complexity. To obtain the stress distribution around the multiple flaws and to determine the nature of new cracks and their propagating direction, numerical computational tools thus have to be used. By assuming that there is a *competition* between *tensile* crack initiation and *shear* crack initiation at the pre-existing flaw tips and the tips of the newly developed cracks, FROCK has been demonstrated successfully in capturing some of the fundamental crack growth and coalescence mechanisms in gypsum. It has also been shown in chapter 8 that the key in obtaining satisfactory coalescence patterns depends on a proper choice of the material strength parameters, namely the critical shear strength and the critical tensile strength.

As discussed in previous sections, gypsum is more brittle, while marble is more ductile due to the development of white patches (process zones) before the initiation of macroscopic observable cracks. This difference should be a key reason in leading to different fracturing and hence coalescence behavior in these two materials. The influence of **material type** will be further discussed below under the following two headings – coplanar flaws and stepped flaws.

Coplanar flaws

As discussed in the previous section, there is a general trend of variation from shear coalescence to tensile coalescence as β increases (table 6.23). However, in the small flaw inclination angle range, coalescence is less favored (category 1) in **marble** than in **gypsum** ($\beta = 0^o$, 30^o, 45^o for ligament length 2a, $\beta = 30^o$, 45^o for ligament length 4a). This phenomenon appears to be related to the fact that in the marble specimens, the initiation of **vertical** and/or **steeply-inclined cracks** (dominantly tensile) from the inner flaw tips occurs more frequently than the initiation of **coplanar cracks** from the inner

flaw tips (figure 9.22 a), compared to the fracturing behavior in gypsum specimens (figure 9.22 d).

Due to the geometrical configuration, direct linkage of pre-existing flaws by the **vertical** and/or **steeply-inclined tip cracks** is often physically impossible (figure 9.22 a). Crack coalescence (indirect) can occasionally occur when the new cracks are shallower (figure 9.22 b) or a third crack is also involved to link up the individual tip cracks (figure 9.22 c).

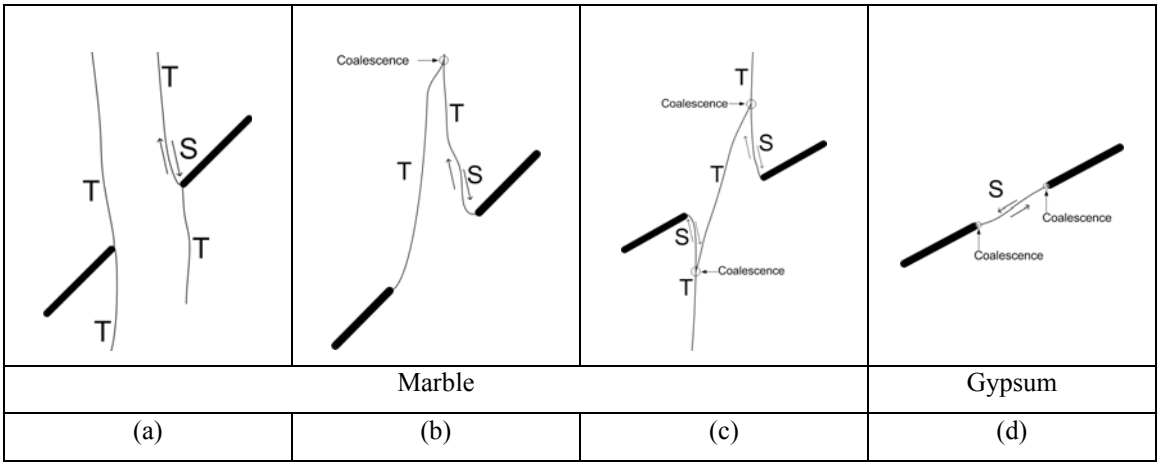

Figure 9.22 – (a) Coalescence did not occur due to the initiation of steep cracks from the inner flaw tips, (b) Coalescence occurred due to linkage of shallowly-inclined cracks initiated from the inner flaw tips, (c) Coalescence which involved the initiation of three new cracks, (d) direct coalescence involving a coplanar shear crack in gypsum.

Another distinct difference of coalescence in coplanar flaws is observed for large flaw inclination angles β. For large flaw inclination angles, coalescence in gypsum ($\beta = 45^o$, 60^o, 75^o for ligament length 2a, $\beta = 75^o$ for ligament length 4a) and marble ($\beta = 60^o$, 75^o for ligament length 2a, $\beta = 75^o$ for ligament length 4a) are similarly achieved in a **direct** manner in which the inner flaw tips are linked up by a continuous crack consisting of one or multiple individual crack segments. However, the crack segments adjacent to inner flaw tips in gypsum are mainly **shear** (figure 6.15), while those in marble are mainly **tensile** (figure 6.29).

It is thus clear that over the whole range of flaw inclination angles β, the initiation of *tensile cracks* is more preferable to *shear cracks* in marble than in gypsum. As assumed in FROCK, crack propagation occurs when the stress at the boundary of the core region around the flaw tip is equal to the critical value. To determine the specific crack type initiating from flaw tip, the computed stresses are compared against two material strength parameters – the critical tensile strength σ_{crit} and the critical shear strength τ_{crit}. The above observed fracturing differences (the more preferential tensile crack initiation in marble than in gypsum for the same flaw geometry) indicates that the criterion of *tensile* crack initiation, instead of the criterion of *shear* crack initiation is easier to meet at the flaw tip in marble. It is possible if the ratio of $\sigma_{crit}/\tau_{crit}$ in marble is lower than that in gypsum. Note that the magnitudes of σ_{crit} and τ_{crit} in marble should both be higher than the corresponding values in gypsum due to a higher overall strength of marble.

In gypsum, multiple tensile cracks first initiate from the pre-existing flaws (figure 9.23 a). A shear crack later develops to link up the two inner flaw tips (figures 9.23 b & c). In marble, however, white patches develop early in response to the applied loading, including a white patch linking up the two flaw tips (figure 9.24 a & b). Crack initiation, instead of taking place along this coalescing white patch, first occurs along a vertical white patch from an inner flaw tip (figure 9.24 c). Comparing figures 9.23 b and 9.24b, it is interesting to note that most white patches developed in marble have corresponding crack counterparts in gypsum which follow a similar trajectory, except for white patches C, E, F and G. It is thus hypothesized that the development of white patches prior to cracking leads to a stress perturbation, which favors the initiation of vertical and steep tip cracks (dominantly tensile) instead of the shear cracks from the flaw tips (figure 9.22).

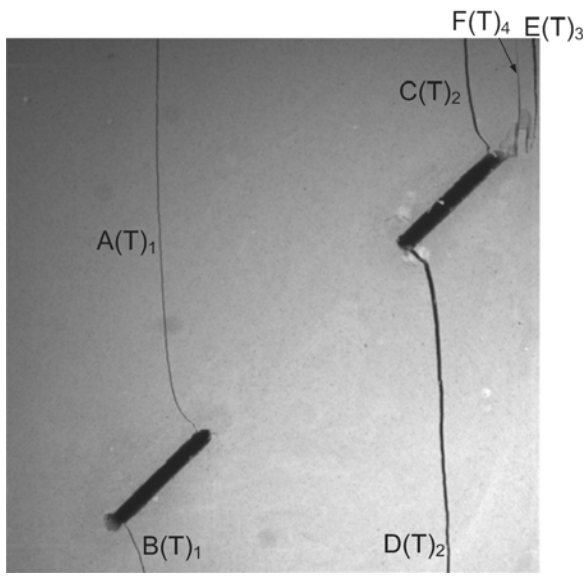

(Recorded by High Speed Video System)

(27.54 MPa)

HS Image # - 5420

(a)

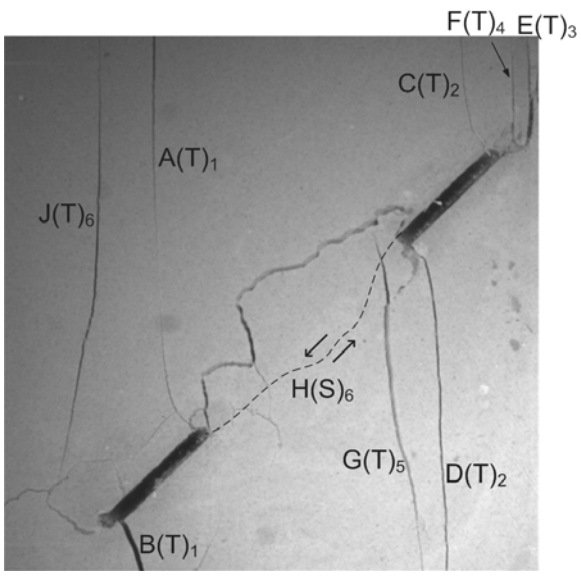

(Recorded by High Speed Video System)

(25.28 MPa – coalescence)

HS Image # - 3970

(b)

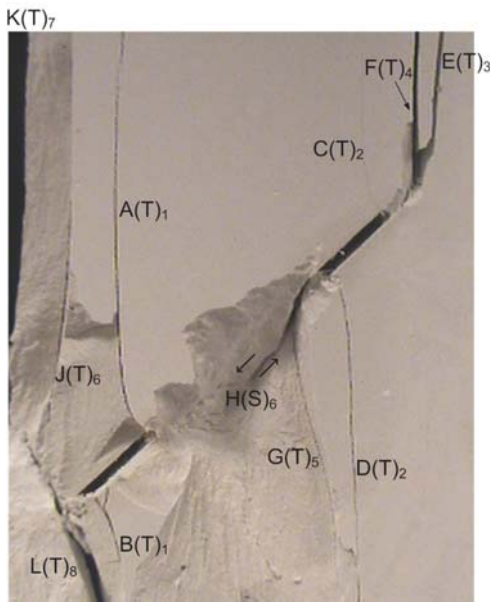

(Recorded by camcorder)

(c)

Figure 9.23 – (a) Tensile cracks initiate from the two pre-existing flaws. (b) A shear crack H (with dotted trace) initiates to link up the two flaw tips. Its initiation is associated with the overlying local surface spalling. (c)The trace of the coalescence shear crack (H) is exposed after the detachment of the surface spalling fragments.

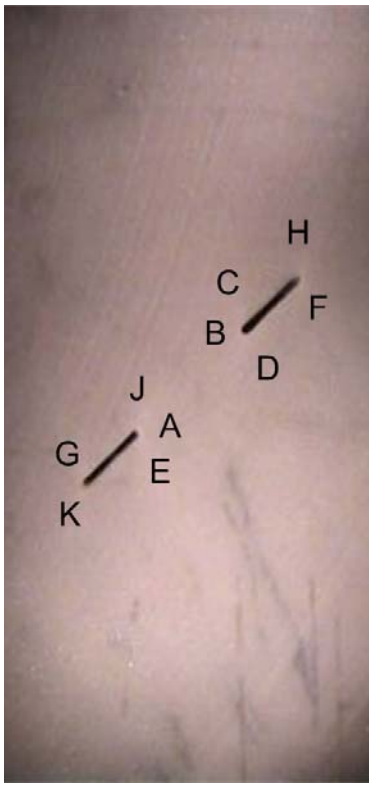

(Recorded by camcorder)

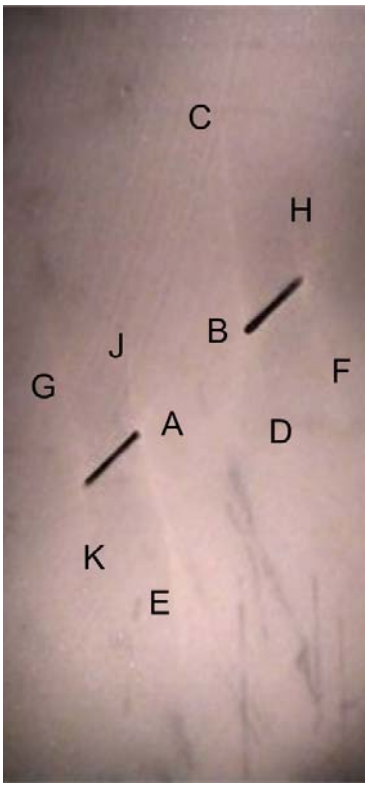

(Recorded by camcorder)

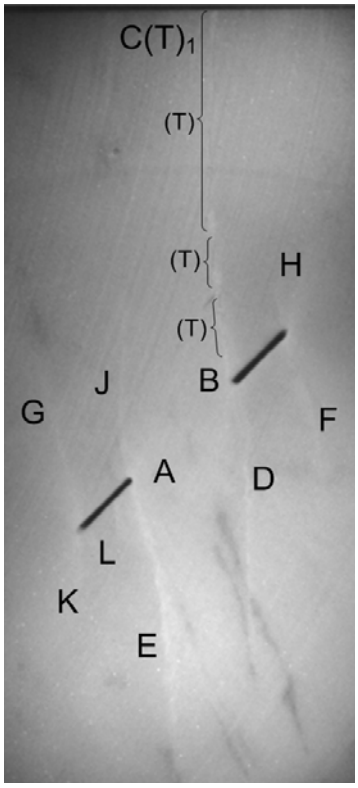

(Recorded by High Speed Video System)

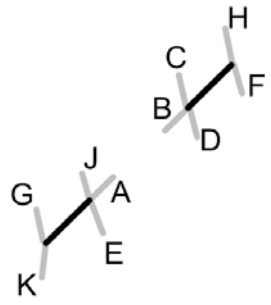

(sketch)

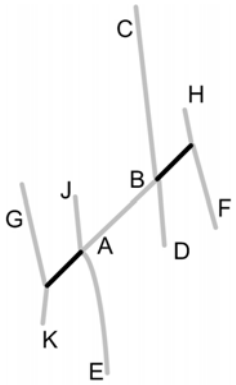

(sketch)

(61.46 MPa)
v10m3.27s
(a)

(71.46 MPa)
v12m21.47s
(b)

(71.31 MPa – crack initiation)
HS Image # - 6505
(c)

Figure 9.24 – (a) White patches initiate from the flaw tips, (b) The white patches extend in response to loading. White patches A and B coalesce, (c) En echelon tensile cracks initiate along white patch C.

Stepped flaws

As discussed earlier, as bridging angles (α) increase from negative values to small positive values, and further up to large positive values, the coalescence categories progress from low number categories to high number categories, i.e. from no coalescence, indirect coalescence to direct coalescence. For the direct coalescence (high number categories), another trend is also observed, which varies from shear, mixed shear-tensile to tensile as α increases. Observe also in table 6.24 that some coalescence categories are unique to gypsum with specific flaw geometries, while some coalescence categories are unique to marble with specific flaw geometries. These unique coalescence categories are described below, first for ligament length "2a", and then ligament length "4a".

Ligament length "2a"

For ligament length "2a", coalescence pattern of **category 5** is unique to gypsum, while those of **categories 4, 6 and 8** are unique to marble (see an excerpt of table 6.24 below).

Category		**Gypsum**	**Marble**
4	Shear	-	$\alpha = 30$
5	Mixed shear-tensile	$\alpha = 30, 60$	-
6	Tensile	-	$\alpha = 60$
8		-	$\alpha = 120$

In **gypsum** for α **= 30^o and 60^o**, the coalescence crack which links up the inner flaw tips is a generally 'S'- shaped crack consisting of **shear-tensile-shear** crack segments (category 5).

In **marble** for α **= 30^o**, the coalescence crack is an inclined **type 1 shear crack** linking up the inner flaw tips (category 4). For α **= 60^o**, the coalescence crack is a **type 2 tensile**

crack which links up the inner flaw tips with no observable shear segments adjacent to the flaw tips (category 6). For α **= 120^o**, the coalescence crack is a tensile crack (not displaying wing appearance) which links up the tips of the same side of the pre-existing flaws (category 8).

Ligament length "4a"

For ligament length "4a", coalescence patterns of **categories 5 and 7** are unique to gypsum, while those of **categories 6, 8 and 9** are unique to marble (see an excerpt of table 6.24 below).

Category		**Gypsum**	**Marble**
5	Mixed shear-tensile	α = 30, 60	-
6	Tensile	-	α = 60
7		α = 90, 120	-
8		-	α = 90
9		-	α = 120

In **gypsum** for α **= 30^o** and **60^o**, the coalescence crack is a generally 'S'- shaped crack consisting of **shear-tensile-shear** crack segments (category 5). For α **= 90^o** and **120^o**, the coalescence crack is a **type 1 tensile crack** which links up the inner flaw tips is (category 7).

In **marble** for α **= 60^o**, the coalescence crack is a vertical **type 2 tensile crack** (category 6). For α **= 90^o**, the coalescence is due to the linkage of the tips of the same side of the two pre-existing flaws by a curvilinear **type 2 tensile crack** and a short **shear crack** (category 8). For α **= 120^o**, the coalescence crack is a **type 3 tensile crack** which links up the right tip of the top flaw and the left tip of the bottom flaw.

Observe also in table 6.24 that for the same flaw pair geometry (positive α), marble generally tends to have a higher coalescence category. In other words, tensile crack initiation is more favored in marble than in gypsum. This is similar to the general observation obtained from *coplanar flaws*. Therefore, the difference between gypsum and marble could again be in part explained by the reasons put forward for *coplanar flaws* previously – stress field perturbation due to the development of white patches, and a probable lower ratio of $\sigma_{crit}/\tau_{crit}$ in marble than in gypsum.

9.7 Revision of coalescence patterns in Vermont White Marble

The coalescence patterns observed in the Vermont White Marble tested by Martinez (chapter 3) were reviewed and classified according to coalescence categories shown in figure 9.19. Recall that three inclinations of 30^o, 45^o, 60^o were tested, and the flaw geometry is represented as *flaw inclination angle – spacing – continuity*, where the length measurements are stated in terms of the half flaw length *a*.

Coplanar flaws

For coplanar flaws, **small flaw inclination angles** of 30^o and 45^o generally do not favor coalescence (category 1, with occasional categories 2 & 3), while **large flaw inclination angle** of 60^o favors direct coalescence of category 3, which is achieved by a coplanar shear crack (table 9.7). As shown in the same table for β **= 30^o and 45^o**, the influence of ligament length is revealed from the absence of coalescence for ligament length **2a**, but presence in some of the tested specimens for ligament length **a.**

Geometries	Coalescence category	Geometries	Coalescence category
30-0-a	1 or 2	30-0-2a	1 (2)
45-0-a	1 or 3	45-0-2a	1 (1, 2 or 3)
60-0-a	3	60-0-2a	3 (6)

Table 9.7 – Crack coalescence categories observed for coplanar flaws in Martinez's tests. The bracketed numbers indicate the crack coalescence categories obtained for Carrara Marble in the present study.

The category numbers for coplanar flaw pairs with ligament length 2a observed in Carrara Marble (present study) are also included in table 9.7 for comparison. The main differences are:

- Coalescence occurs in Carrara Marble for β **= 30° and 45°** [5], but not in Vermont White Marble.
- Coalescence is achieved by a tensile crack (category 6) in Carrara Marble for β **= 60°**, but by a shear crack (category 3) in Vermont White Marble.

Stepped flaws

The coalescence categories corresponding to the stepped flaw pair geometries in Vermont White Marble are summarized in table 9.8a. Within each flaw inclination series (β = 30, 45, 60), the flaw pair geometries differ from each other by a simultaneous change of **ligament length** and **bridging angle**. Thus it is difficult to investigate the effect on the crack coalescence patterns solely due to one of these two parameters, as what has been done in the present thesis. Nonetheless, a general trend of coalescence categories can still be concluded as both **ligament length** and **bridging angle** increase – the coalescence pattern changes from *low* numbered categories to *high* numbered categories, i.e. from no coalescence, indirect coalescence to direct coalescence. Also for all these non-overlapping flaw pair geometries, the highest category achieved is **category 6**.

[5] Except for one specimen.

Flaw inclination angle β (^{o})	Geometries	Bridging angle α (^{o})	Ligament length	Coalescence category
30	30-0-a	0	a	1 or 2
	30-0-2a	0	2a	1
	30-a-2a	26.5	2.24a	1 or 4
	30-a-a	45	1.41a	4
	30-2a-2a	45	2.83a	4 or 5 or 6
45	45-0-a	0	a	1 or 3
	45-0-2a	0	2a	1
	45-a-2a	26.5	2.24a	4 or 5 or 6
	45-a-a	45	1.41a	5 or 6
	45-2a-2a	45	2.83a	5 or 6
60	60-0-a	0	a	3
	60-0-2a	0	2a	3
	60-a-2a	26.5	2.24a	5 or 6

Table 9.8a – Crack coalescence categories observed for stepped flaws in Martinez's tests. The highlighted geometries are also studied in Carrara Marble in the present experimental study.

Although a direct comparison of crack coalescence categories for the same flaw geometries between Vermont White Marble and Carrara Marble for the stepped flaw pair geometries is impossible, an attempt is still made below for stepped flaw pairs with flaw inclination angle 30^o. In table 9.8b, the coalescence categories of some selected flaw geometries for Vermont White Marble are shown on the left and Carrara Marble on the right. The variation of the coalescence categories with respect to the bridging angles α appears to fit into a common trend, i.e. the crack coalescence category numbers increase with the α values, although the ligament lengths are different in all geometries in the two materials.

Vermont White Marble

Geometries	Bridging angle (Ligament length)	Coalescence categories
30-a-2a	**26.5** (2.24a)	1 or 4
30-a-a	**45** (1.41a)	4
30-2a-2a	**45** (2.83a)	4 or 5 or 6

Carrara Marble

Geometries	Bridging angle (Ligament length)	Coalescence categories
2a-30-30	**30** (2a)	4
4a-30-30	**30** (4a)	2

Carrara Marble

Geometries	Bridging angle (Ligament length)	Coalescence categories
2a-30-60	**60** (2a)	6
4a-30-60	**60** (4a)	6

Table 9.8b – Comparison of crack coalescence categories for stepped flaws in Vermont White Marble and Carrara Marble. The stepped flaw pairs listed here all have flaw inclination angle 30^{o}.

9.8 Revision of other coalescence patterns

Similar to the single flaws above (figure 9.18), the crack types observed in specimens containing double or multiple flaws studied by other authors shown in chapter 2 are also reviewed. The crack types are again classified according to the crack type classification scheme proposed in the present study (figure 9.12). Based on that, the coalescence patterns are then classified according to the category classification scheme shown in figure 9.19. The new information is shown from figures 9.25 to 9.33.

The crack type classification and crack coalescence classification schemes generalized from **earlier** experimental studies were based on normal speed video recordings (less than 100 frames per second) and/or the examination of features left on crack surfaces (fractography) after the loading tests. These old schemes are now found to be inadequate in describing all the newly identified fracturing and crack coalescence processes in rocks satisfactory, which are based on a high speed imaging technology with a capability of up to 24,000 frames per second. New classification schemes are hence proposed to facilitate the description of the seven crack types and the nine coalescence patterns generalized from the present study.

Almost all of the previously-observed coalescence patterns can be classified into the corresponding crack coalescence categories. In cases where the crack nature (shear/tensile) of some coalescence cracks was not identified by the authors, more than one possible crack coalescence category is then assigned where appropriate, e.g. category 4/category 6 is assigned for the coalescence pattern shown in figure 9.26 b.

It is interesting to note that some coalescence types previously identified by others are not observed in the present study, e.g. crack coalescence **type V** and **type VIII** shown in figure 9.24 by Sagong and Bobet (2002). Their **type V** coalescence pattern is similar to **category 8** of the present study (figure 9.19), but the former was reported to be achieved by shear cracks, while the latter was achieved mainly by tensile cracks. The discrepancy may be due to the inherent material behavior, or the means of observing crack initiation with a high speed camera in the present study but not by Sagong & Bobet (2002). **Type VIII** coalescence pattern, which involves a *type 3 shear crack* linking up the two inner flaw tips, was observed by Sagong and Bobet in flaw pairs with negative bridging angle. In the present study, *type 3 shear cracks* are observed to take part in indirect coalescence (**category 2**) instead – two cracks, one as a *type 3 shear crack*, and the other as a steeply-inclined crack, initiate individually from the inner flaw tips and coalesce.

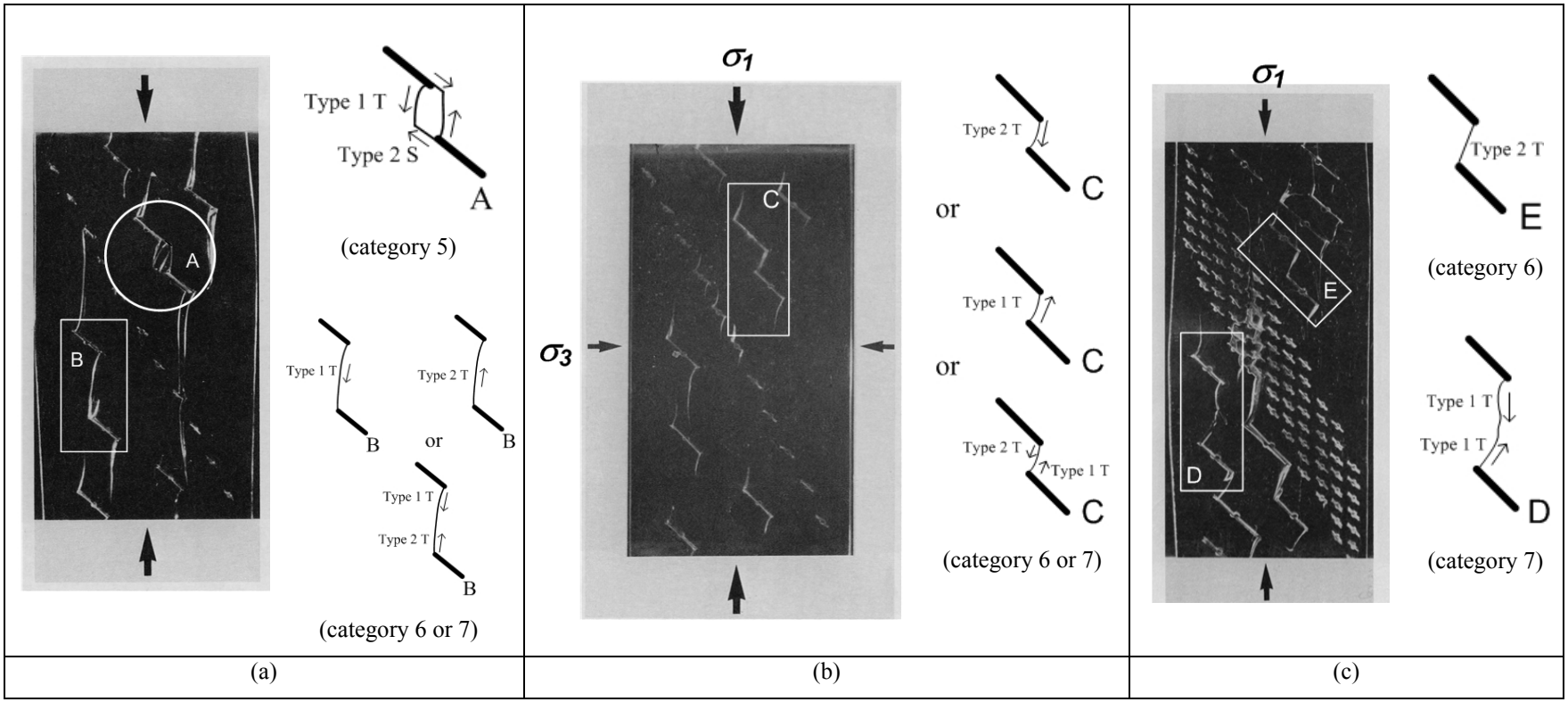

Figure 9.25 – Crack coalescence observed by Horii and Nemat-Naser (1985) classified according the coalescence category classification scheme presented in this study.

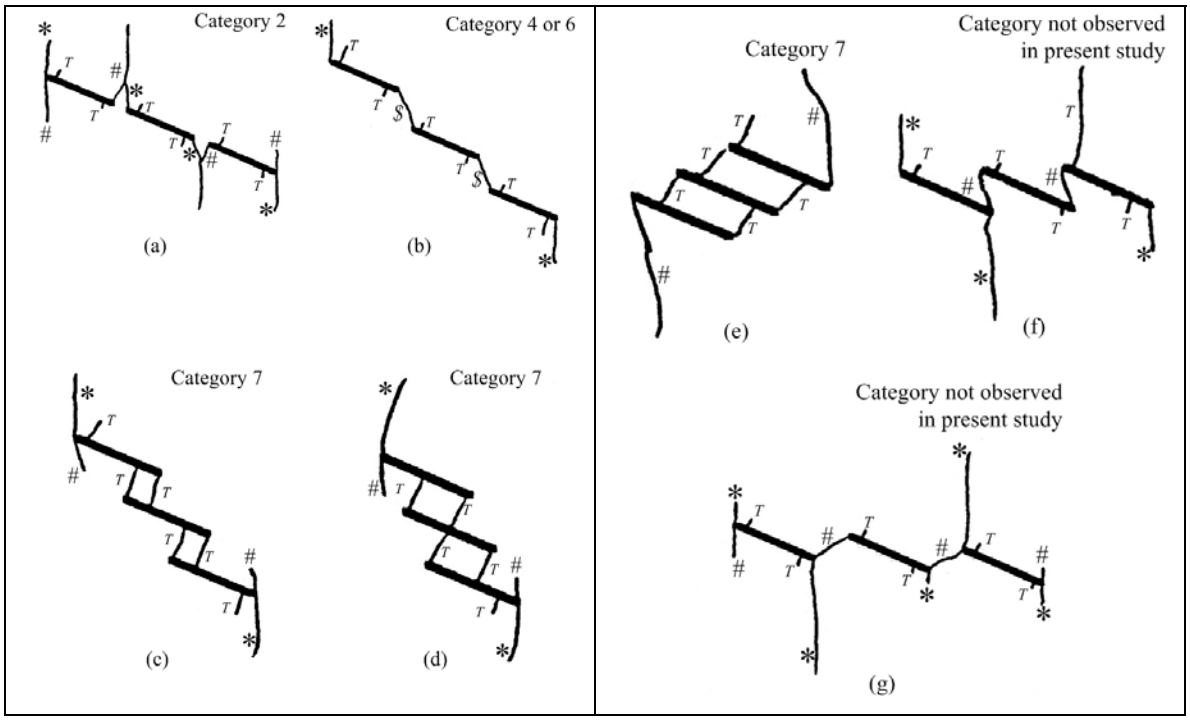

Key

T = type 1 tensile crack

* = type 2 tensile crack/ type 1 shear crack/ mixed tensile-shear crack

$ = type 2 tensile crack/ type 1 shear crack

= type 3 tensile crack/ type 3 shear crack

Figure 9.26 – Crack coalescence observed by Chen et al. (1995) classified according the coalescence category classification scheme presented in this study.

Number	Specimen	Critical Load at Coalescence, MPa	Schematic Path of Coalescence (a) frictional (b) nonfrictional	Description of Coalescence	Coalescence cracks (Coalescence categories)
1	30°/15° (2 specimens with friction fractures + 1 specimen with nonfrictional fractures)	No coalescence (frictional fractures) 17.2 MPa (nonfrictional fractures)	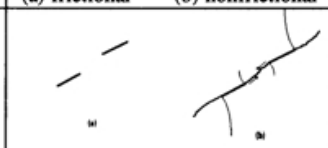	Type of coalescing fracture: secondary fracture. Initiation position: preexisting fracture tips. Surface characterization: rough, with many small kink steps; containing crushed gypsum.	Type 2 S + Type 2 S (Category 3)
2	45°/0° (2 + 2)	21.9, 22.2 MPa (frictional fractures) 19.4, 17.9 MPa (nonfrictional fractures)	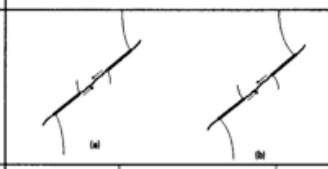	Type of coalescing fracture: secondary fracture. Initiation position: preexisting fracture tips. Surface characterization: rough, with many small kink steps; containing crushed gypsum.	Type 2 S + Type 2 S (Category 3)
3	45°/15° (1 + 1)§	17.8 MPa (frictional fractures) 14.1 MPa (nonfrictional fractures)	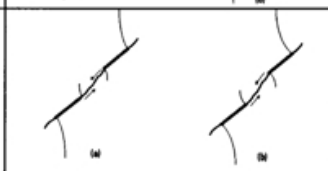	Type of coalescing fracture: secondary fracture. Initiation position: preexisting fracture tips. Surface characterization: rough, with several large kink steps. Noticeable crushed gypsum presented.	Type 2 S + Type 2 S (Category 3)
4	45°/30° (1 + 1)§	19.2 MPa (frictional fractures) 14.1 MPa (nonfrictional fractures)	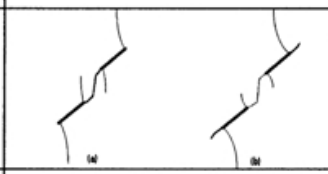	Type of coalescing fracture: secondary fracture. Initiation position: unclear. Surface characterization: rough, with two big kink steps. No noticeable crushed gypsum.	Type 2 S + T+ Type 2 S (Category 5)
5	45°/45° (2 + 1)	(a) 17.8, MPa (a') 16.8* MPa (frictional fractures) (b) 16.4 MPa (nonfrictional fractures)	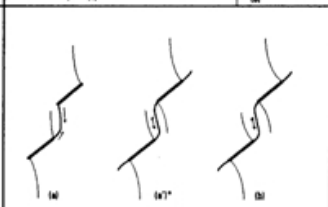	Type of coalescing fracture: (a) wing fracture + secondary fracture; (a') and (b) secondary fracture. Initiation position: (a) preexisting fracture tips; (a') and (b) intact material. Surface characterization: some parts are clean and smooth while other parts are rough with crushed gypsum.	(a) Type 1 T + Type 1 S (Category 5) (a') (b) Type 1 S + Type 1 S (Category 4)
6	45°/60° (2 + 1)	17.8, 16.8 MPa (frictional fractures) 16.4 MPa (nonfrictional fractures)		Type of coalescing fracture: wing fracture. Initiation position: preexisting fracture tips. Surface characterization: smooth and clean. Note: additional secondary fractures occur from the outer tips in case (b).	Type 1 T (Category 7)
7	45°/75° (2 + 1)	(a) 21.0 MPa (a') 23.1 MPa (frictional fractures) (b) 17.6 MPa (nonfrictional fractures)	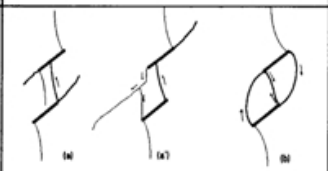	Type of coalescing fracture: wing fracture. Initiation position: preexisting fracture tips. Surface characterization: smooth and clean. Note additional coalescence by secondary fractures occurs in case (b).	(a) (a') Type 1 T (Category 7) (b) Type 1 T + Type 1 T (Category 7)

Figure 9.27 – Crack coalescence observed by Shen et al. (1995) classified according the coalescence category classification scheme presented in this study.

Number	Specimen	Critical Load at Coalescence MPa	Schematic Path of Coalescence (a) frictional (b) nonfrictional	Description of Coalescence	Coalescence cracks (Coalescence categories)
8	60°/-15° (2 + 1)	22.4, 21.4 MPa (frictional fractures) 17.8 MPa (nonfrictional fractures)	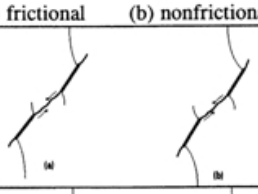	Type of coalescing fracture: secondary fracture. Initiation position: preexisting fracture tips. Surface characterization: rough, with many small kink steps; containing crushed gypsum.	Type 2 S + Type 2 S (Category 3)
9	60°/0° (4+ 1)	20.5, 17.8, 20.3, 20.9 MPa (frictional fractures) 15.2 MPa (nonfrictional fractures)	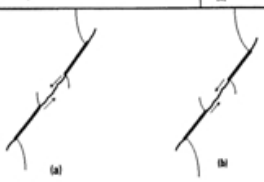	Type of coalescing fracture: secondary fracture. Initiation position: preexisting fracture tips. Surface characterization: rough, with several large kink steps. Noticeable crushed gypsum presented.	Type 2 S + Type 2 S (Category 3)
10	60°/15° (1 + 1)§	18.5 MPa (frictional fractures) 13.7 MPa (nonfrictional fractures)	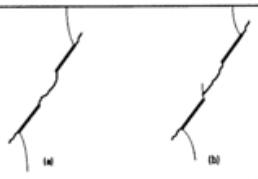	Type of coalescing fracture: (a) secondary fracture ; (b) secondary fracture + wing fracture. Initiation position: pre-existing fracture tips. Surface characterization: rough, with a few kink steps. No noticeable crushed gypsum.	(a) Type 2 S (Category 3) (b) Type 1 T + Type 2 S (Category 5)
11	60°/30° (1 + 1)§	19.2 MPa (frictional fractures) 14.2 MPa (nonfrictional fractures)	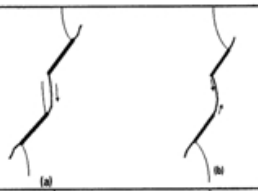	Type of coalescing fracture: (a) wing fracture ; (b) wing fracture + secondary fracture. Initiation position: preexisting fracture tips; Surface characterization: most parts are clean and smooth.	(a) Type 1 T (Category 7) (b) Type 1 T + Type 1 S (Category 5)
12	60°/45° (2 + 1)	19.9, 22.2 MPa (frictional fractures) 18.0 MPa (nonfrictional fractures)	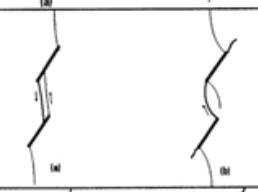	Type of coalescing fracture: wing fracture. Initiation position: preexisting fracture tips. Surface characterization: smooth and clean.	Type 1 T (Category 7)
13	60°/60° (1 + 1)§	23.5 MPa (frictional fractures) 21.0 MPa (nonfrictional fractures)		Type of coalescing fracture: secondary fracture. Initiation position: preexisting fracture tips. Surface characterization: very rough, coated with a lot of crushed gypsum.	Type 1 S + Type 2 S (similar coalescence pattern not observed in the present study)

§ Only two of the three specimens produced useful results, the other specimen failed due to mismanipulation of the loading machine.

* The frictional fractures in this specimen have weaker contact than other frictional fractures. The polyethylene sheets were left longer (45 min) by mistake before they were pulled out. As a result, the created fractures did not close firmly.

Figure 9.27 – Crack coalescence observed by Shen et al. (1995) classified according the coalescence category classification scheme presented in this study (continued).

Type	Schematic path of Coalescence	Description of Coalescence	Coalescence cracks (Coalescence categories)
I	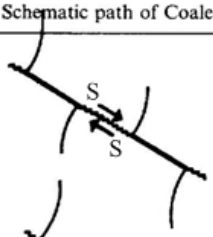	Type of coalescing fracture: secondary shear crack. Initiation position: preexisting flaw tips. Crack surface characterization: rough, with many small kink steps; contains crushed gypsum	Type 2 S + Type 2 S (Category 3)
II	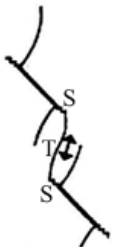	Type of coalescing fracture: secondary shear and tensile cracks. Initiation position: preexisting flaw tips. Crack surface characterization: some parts are clean and smooth while other parts are rough with crushed gypsum	Type 2 S + T + Type 2 S (Category 5)
III	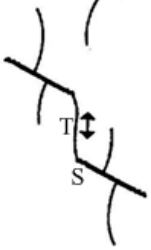	Type of coalescing fracture: secondary shear crack and wing crack. Initiation position: preexisting flaw tips. Crack surface characterization: some parts are clean and smooth while other parts are rough with crushed gypsum	Type 2 T + Type 2 S (Category 5)
IV	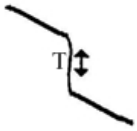	Type of coalescing fracture: wing crack. Initiation position: preexisting flaw tips. Crack surface characterization: smooth and clean.	Type 2 T (Category 6)
V	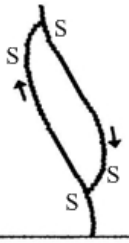	Type of coalescing fracture: secondary crack. Initiation position: preexisting flaw tips. Crack surface characterization: very rough, coated with a lot of crushed gypsum	Type 2 S + Type 1 S (similar coalescence pattern not observed in the present study)

Figure 9.28 – Crack coalescence observed by Bobet and Einstein (1998) classified according the coalescence category classification scheme presented in this study. The coalescence type numbers originally given by the authors are retained.

Type	Left Stepping	Type	Right Stepping	Coalescence cracks (Coalescence categories)
I	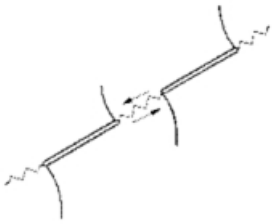	VI	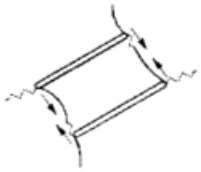	Type I: Type 2 S (Category 3) Type IV: Type 1 T + Type 3 S (Category 8)
II	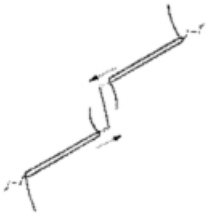	VII		Type II: Type 2 S + T + Type 2 S (Category 5) Type VII: Type 3 S + T + Type 3 S (Category 9)
III	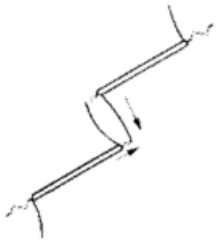	VIII		Type III: Type 2 S + Type 1 T (Category 5) Type VIII: Type 3 S (-)
IV	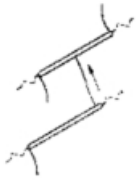	IX	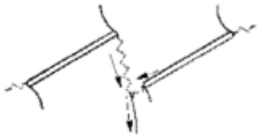	Type IV: Type 1 T (Category 7) Type IX: Type 2 S + Type 3 S (Category 2)
V	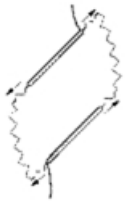			Type V: Type 2 S + S (type not classified) + Type 2 S (-)

Figure 9.29 – Crack coalescence observed by Sagong and Bobet (2002) classified according the coalescence category classification scheme presented in this study. The coalescence type numbers originally given by the authors are retained. Coalescence type which has no corresponding coalescence category is assigned with (-) in the right column.

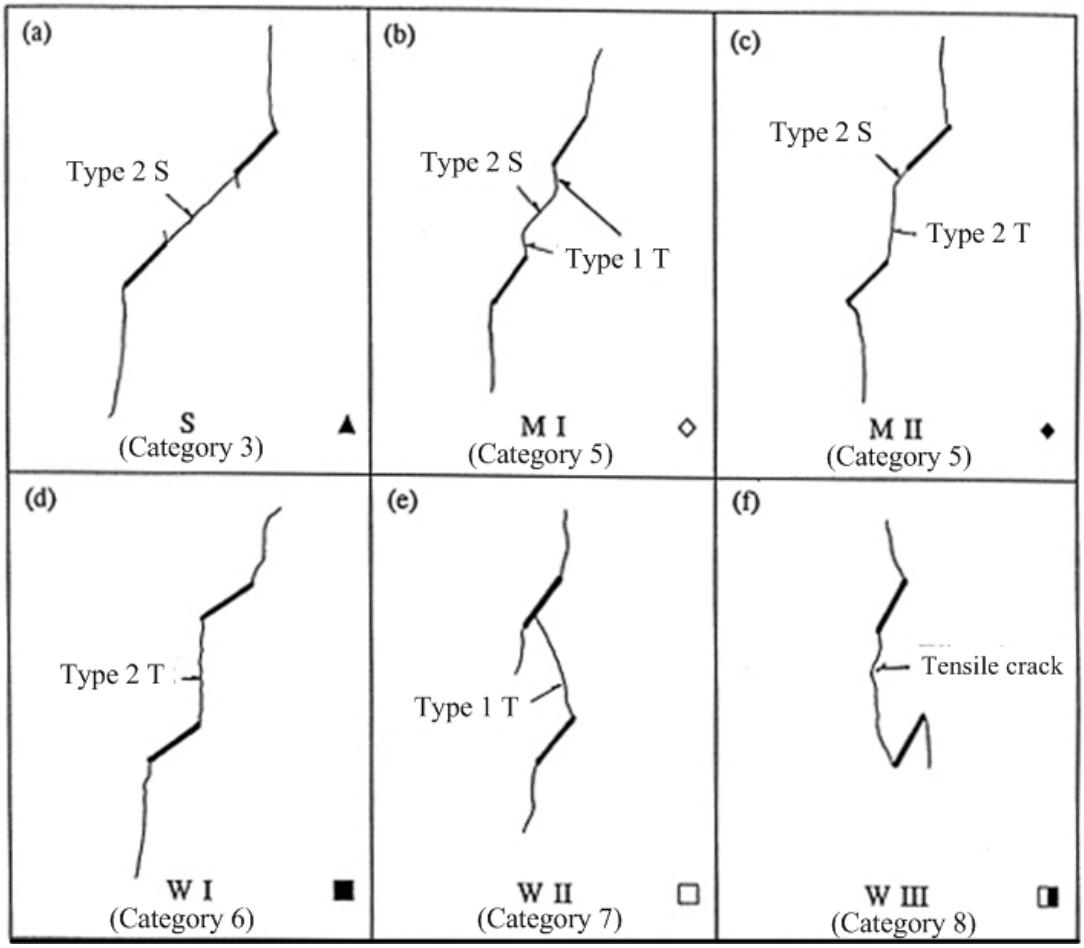

Figure 9.30 – Crack coalescence observed by Wong and Chau (1998) classified according the coalescence category classification scheme presented in this study.

Bridging angle (^{o})	Fracturing and coalescence patterns	Coalescence crack types (Coalescence category)
0	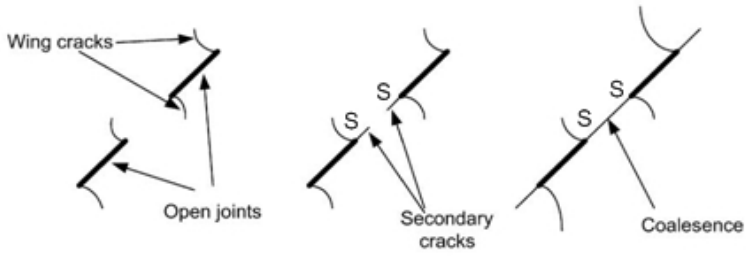	Type 2 S (Category 3)
30	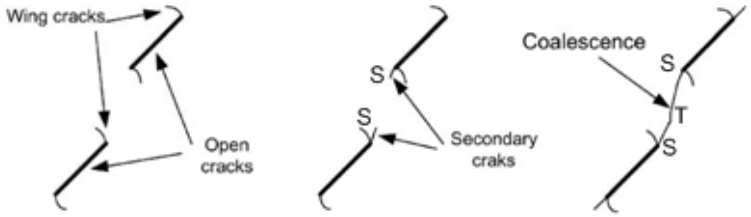	Type 2 S + T + Type 2 S (Category 5)
45	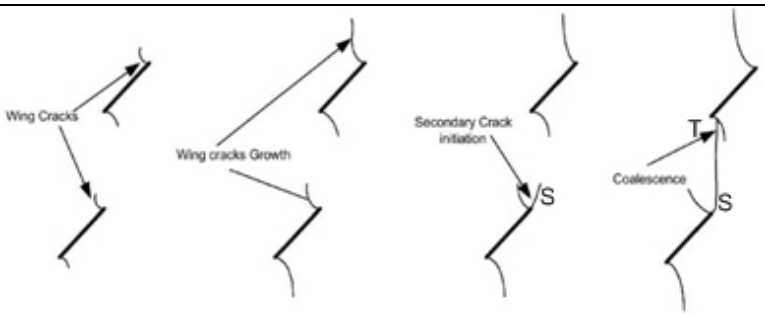	Type 1 S + Type 1 T (Category 5)
60	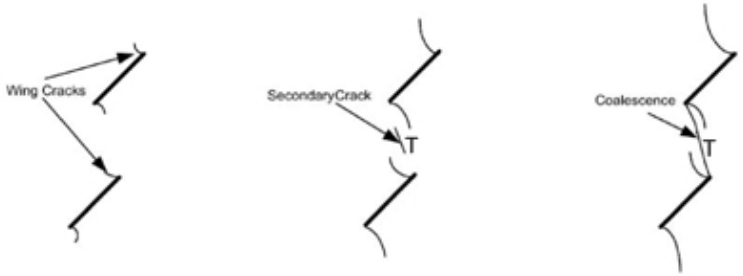	Type 2 T (Category 6)

Figure 9.31 – Fracturing and coalescence patterns in man-made sandstone specimens observed by Mughieda and Alzo'ubi (2004). S = shear crack. T = tensile crack.

Bridging angle (^{o})	Fracturing and coalescence patterns	Coalescence cracks
75	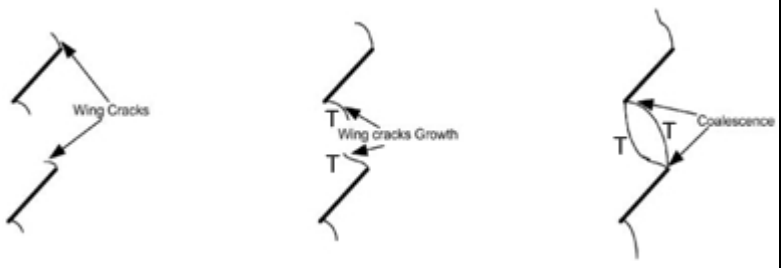	Type 1 T (Category 7)
105	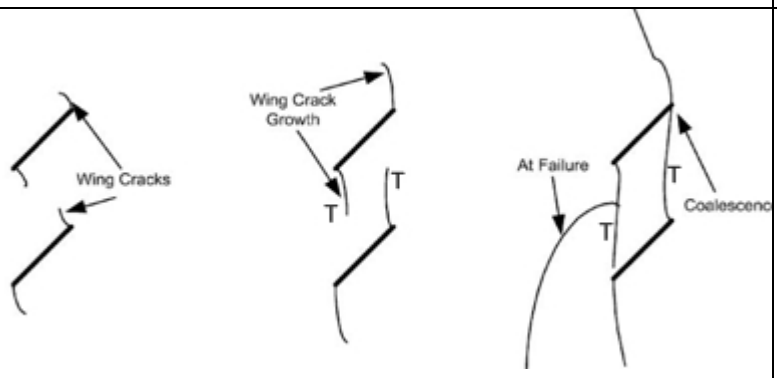	Type 1 T (Category 7)
120	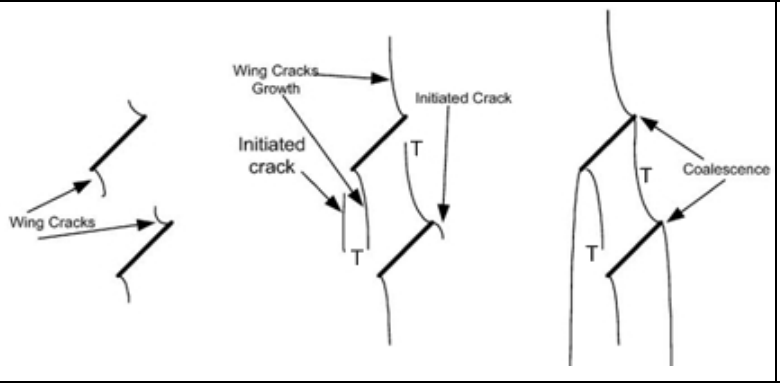	Type 1 T (Category 7)

Figure 9.31 – Fracturing and coalescence patterns in man-made sandstone specimens observed by Mughieda and Alzo'ubi (2004) S = shear crack. T = tensile crack. (continued).

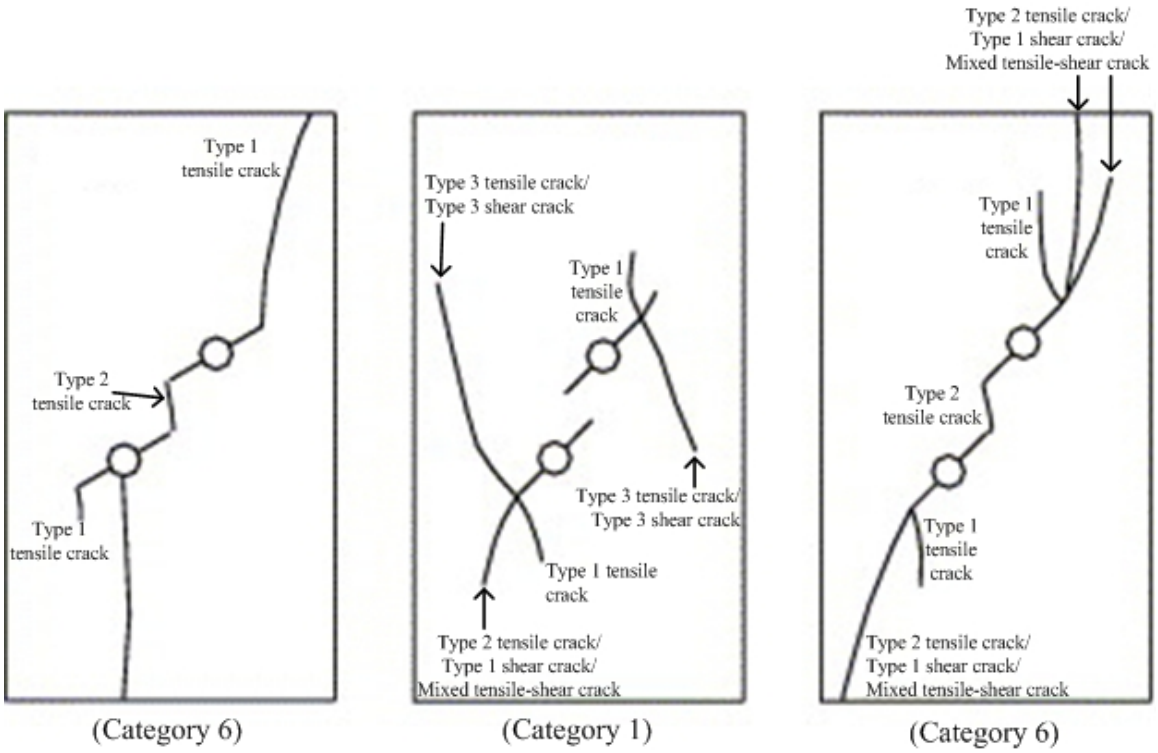

Figure 9.32 – Crack coalescence observed by Li et al (2005) classified according the coalescence category classification scheme presented in this study.

9.9 Scale of crack coalescence

As discussed above, different crack types and coalescence categories are identified in the present study at a laboratory scale. As illustrated in the Müller Lecture by Einstein and Meyer (1999) and in the literature review contained in chapter 2, crack coalescence also occurs at a much larger scale in nature. See the analogy in figure 9.33, which compares the occurrence of coalescence in a laboratory tested Carrara Marble specimen containing a pair of stepped flaws and the development of a pull-apart zone, which links up two sinistral faults (F) in limestone. Although scaling is not the research focus in the present study, the above information indicates that scaling might be possible and further study is warranted.

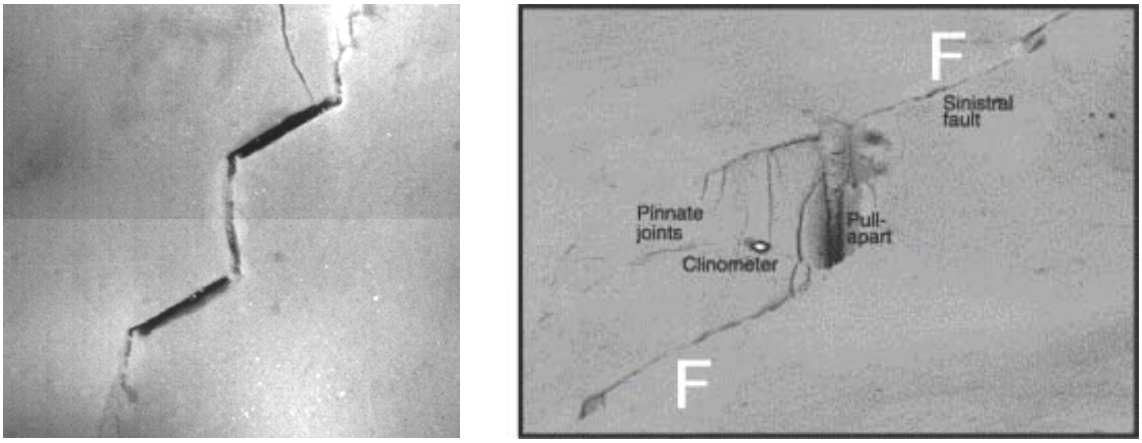

(a) (b)

Figure 9.33 – (a) A coalescence crack (center of the image) linking up two parallel pre-existing flaws (wider aperture size) each of length 12.7 mm observed in Carrara Marble in the present study. (b) A pull-apart zone linking up two sinistral faults (F) in limestone. Note the clinometer for scale (after Peacock, 2001, Crider & Peacock, 2004).

CHAPTER 10 – Conclusions and Recommendations

10.1 Introduction

Crack coalescence in brittle materials, especially rock, involves many complicated fracturing processes. It has been shown in the present and previous similar studies that the overall fracturing and crack coalescence behavior in man-made rocks and natural rocks depends on the geometry of the pre-existing flaws. Although parallel straight double flaws (open or closed) were the most common flaw geometry being tested, differences occurred among different research groups with respect to specimen dimensions, flaw dimensions, loading conditions, experimental set-up (e.g. means of observing crack propagation and coalescence) and most importantly material type. These differences make the direct comparison of results obtained from different research groups challenging.

The present research focuses on enhancing the understanding of the fundamental fracturing processes which lead to crack coalescence in rocks. A comprehensive laboratory study was conduced in molded gypsum and Carrara Marble to observe the fundamental fracturing mechanisms in prismatic specimens containing single or double pre-existing flaws. For the double flaws, the influence of three geometrical parameters, namely flaw inclination angle, bridging angle and ligament length, associated with the presence of a neighboring flaw on the fracturing and coalescence behavior was studied parametrically. The cracking processes were recorded and observed with a high speed camera. This allowed one to observe many fracturing details and crack development sequences, which was not possible before. A parallel microscopic study with SEM and ESEM was also carried out to relate the macroscopic deformation to the underlying microscopic deformation. Hypotheses were proposed based on the inherent textural and strength differences between the two materials to account for the different styles of process zone development and fracturing behavior in the two materials. The following sections summarize the most important results obtained in this research.

10.2 New experimental procedures

The present experimental study has incorporated a number of different techniques to facilitate the specimen preparation, loading test and crack observation procedures at both the macro- and micro-scales. See table 10.1 below.

Equipment	Purpose	Comparison with similar previous techniques
Water abrasive jet	To create open flaws in marble	The undesirable tapping effect at the flaw tips is reduced as compared to that by Martinez (1999).
High speed camera	To monitor and record the fracturing processes in rocks during loading test	The present camera offers a higher frame rate than the one used by Martinez (1999). (24,000 pps vs 250 pps) *pps = picture per second*. The recorded videos are now of digital format for easy manipulation. The videos were recorded on VHS tapes by Martinez (1999).
Scanning electron microscope (SEM)	To study the microcracking processes associated with white patch development in marble	White patches were similarly observed by Chen et al. (1995), Martinez (1999), Li et al. (2005), but their composition was not microscopically investigated in previous studies.
Environmental scanning electron microscope (ESEM)	To study the microcracking processes associated with tensile crack development in gypsum	A similar study was conducted by Sagong and Bobet (2001), but on well-developed tensile cracks and shear cracks. The present study focuses on the microscopic changes when a hair-line tensile crack evolves to become a well-developed tensile crack.

Table 10.1 – Summary of experimental techniques.

10.3 Crack type classification

Based on the crack nature (tensile/shear) and the trajectories, *seven* crack types (figure 10.1) are identified to have initiated from the pre-existing flaws in the present experimental studies with the use of the high speed camera. Of the seven crack types, three are tensile, three are shear and one is mixed tensile-shear.

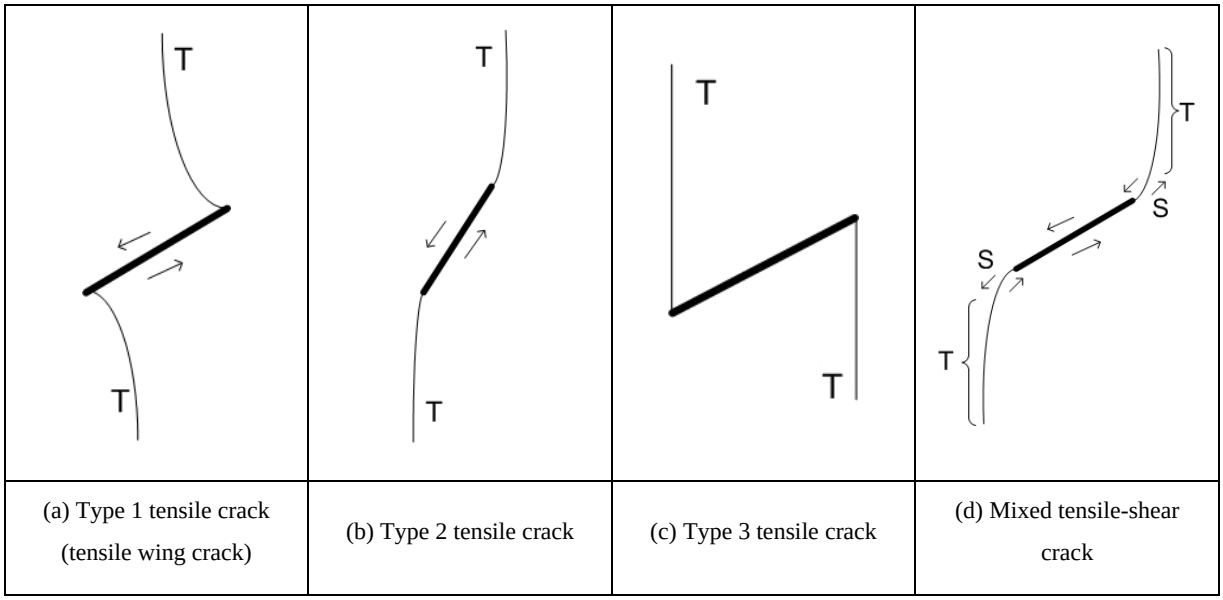

(a) Type 1 tensile crack (tensile wing crack)	(b) Type 2 tensile crack	(c) Type 3 tensile crack	(d) Mixed tensile-shear crack
(e) Type 1 shear crack	(f) Type 2 shear crack	(g) Type 3 shear crack	

Figure 10.1 – Types of cracks observed in gypsum and marble.

10.4 Experimental study in specimens containing single flaws

Uniaxial compression loading tests were conducted in prismatic gypsum and marble specimens containing single flaws. Two different flaw aperture sizes and various flaw inclination angles were tested (Table 5.1).

Series	Material	Flaw Aperture	Flaw Inclination β (^{o})
1	Gypsum	0.004”	0, 15, 30, 35, 40, 45, 50, 55, 60, 70, 75
2	Gypsum	0.05”	0, 30, 45, 60, 75
3	Marble	0.05”	0, 30, 45, 60, 75

Table 10.2 – Single flaw geometries tested in gypsum and marble specimens.

From the analysis of the camcorder videos and high speed videos, the type of newly initiated cracks was determined and the crack development sequence was established.

In both gypsum and marble, **Type 1 tensile cracks** (tensile wing cracks, TWCs) are the first cracks to develop in almost all single flaw geometries. However, horizontal flaws (β = 0^o) in marble are an exception, in which **type 2 tensile cracks**[1] initiate as the first cracks instead (figure 9.14). It is very common in marble specimens containing inclined flaws that in addition to the **type 1 tensile cracks**, **type 2 tensile cracks** are also the first cracks to initiate.

In both gypsum and marble specimens with $\beta \geq 60^o$, the initiation of first cracks is often concurrent with the specimen maximum stress (specimen failure). Other crack types thus have no chance to develop afterwards. On the other hand, for $\beta < 60^o$, after the initiation of the first cracks, additional crack types, including **type 3 tensile cracks** and **mixed tensile-shear cracks,** can also develop in the specimens.

[1] The trajectory of type 2 tensile crack is equivalent to type 3 tensile crack for horizontal flaws. For simplicity, only type 2 tensile crack is mentioned for the relevant discussion.

For both narrow and wide flaws in gypsum, as β increases, the initiation position of TWCs is closer to the flaw tips. Also, the stress required to initiate the TWCs generally increases with β. However, as β reaches 60^o or above, the TWC initiation stress appears to approach a constant value of 40 MPa.

The fracturing behavior and the types of new cracks produced in gypsum specimens containing *narrow* and *wide* flaws are very similar[2]. However, due to a smaller aperture size, partial or complete closure occurs more frequently for narrow flaws. This in turn leads to the more favorable initiation of additional tensile cracks in the middle portions of the flaws, especially those which are shallowly inclined

Shear cracks commonly develop in marble specimens during late stages of loading and the initiation of them often leads to specimen failure. These shear cracks, which initiate from the flaw tips, generally inclined at an angle of about 55^o to 65^o with the horizontal regardless of the orientation of the pre-existing flaw (figures 10.2 a & b). In contrast, such an initiation and propagation of shear cracks are less common in gypsum. The failure in gypsum is usually associated with the initiation of tensile cracks (type 2 or type 3) or mixed shear-tensile cracks, which then leads to a tensile splitting of the specimen and an abrupt drop of specimen strength. See the mixed shear-tensile crack example in figure 10.2 c.

[2] This is based on the observations of uniaxial loading compression tests conducted on specimens containing *single* flaws. For tests in gypsum and marble specimens containing *double* flaws, only wide flaws (0.05" aperture) were tested.

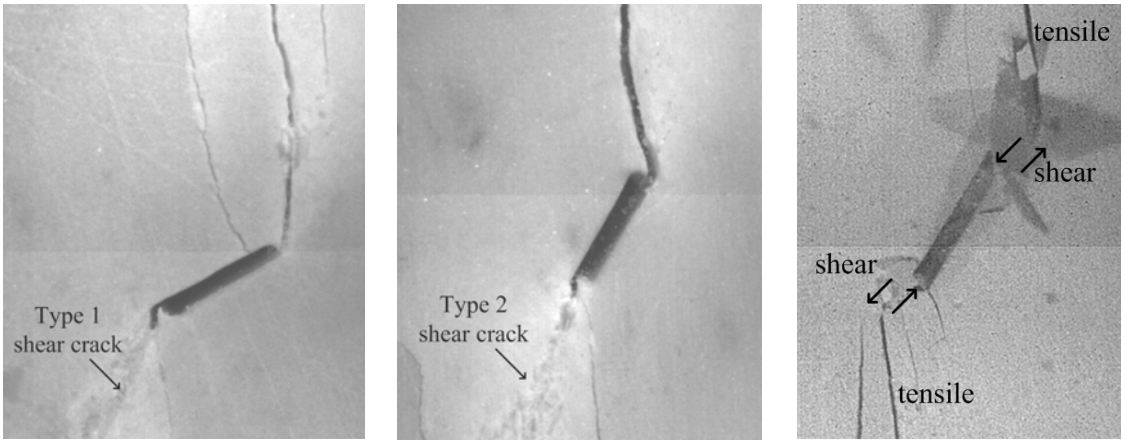

(a) (b) (c)

Figure 10.2 – (a) Type 1 shear crack initiated from a pre-existing flaw with inclination angle 30^o in marble (b) Type 2 shear crack initiated from a pre-existing flaw with inclination angle 60^o in marble. (c) Mixed shear-tensile crack initiated from a pre-existing flaw with inclination angle 60^o in gypsum.

10.5 Experimental study in specimens containing double flaws

A total of *eight* series of uniaxial compression tests were conducted on molded gypsum specimens and Carrara Marble specimens containing coplanar or stepped double flaws (four series for gypsum and four series for marble). See table 10.3 below.

Series	**General flaw pair relationship**	**Bridging angle α (^{o})**	**Ligament length *L***	**Flaw inclination β (^{o})**
1	Coplanar	0	2a	0, 30, 45, 60, 75
2	Stepped	-60, -30, 0, 30, 60, 90, 120	2a	30
3	Coplanar	0	4a	0, 30, 45, 60, 75
4	Stepped	-60, -30, 0, 30, 60, 90, 120	4a	30

Note : β is the inclination of the pre-existing flaw with the horizontal

α is the inclination of a line linking up the two flaw tips

L is the intact rock length between the flaw tips

Table 10.3 – Double flaw geometries tested in gypsum and marble.

Nine coalescence categories with different crack types and trajectories were observed in the present experimental study in gypsum and marble and they are schematically summarized in figure 10.3. Most of them are achieved by the various combinations of the crack types shown in figure 10.1.

- **Category 1** refers to fracturing patterns *without* the occurrence of coalescence.
- **Category 2** refers to *indirect* coalescence patterns which involve two or more inclined, steeply inclined or vertical coalescence cracks. The coalescence usually occurs at or after the specimen maximum stress is reached and the location of coalescence is far away from the central bridging region.
- **Categories 3 to 9** are *direct* coalescence, which are organized with a general trend of variation of coalescence crack types from shear (**categories 3, 4**) to mixed shear-tensile (**category 5**) to tensile (**categories 6, 7, 8, 9**).

Category	Coalescence patterns	Crack types involved
1	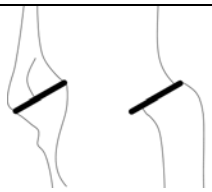	**No** coalescence
2	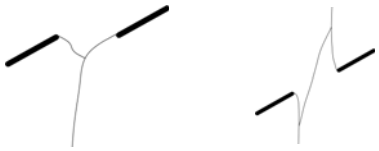 (2 cracks) (3 cracks)	**Indirect** coalescence by two or multiple cracks (crack types vary)
3	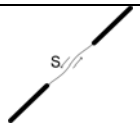	Type 2 **S** crack(s)
4	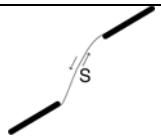	Type 1 **S** crack(s)
5	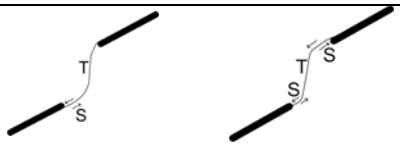	One or more type 2 **S** crack(s) and type 2 **T** crack segments between inner flaw tips
6	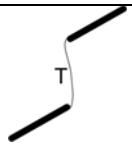	Type 2 **T** crack(s). There may be occasional short **S** segments present along the coalescence crack.
7		Type 1 **T** crack(s)
8		Flaw tips of the same side linked up by **T** crack(s) not displaying wing appearance (crack type not classified). There may be occasional short **S** segments present along the coalescence crack.
9	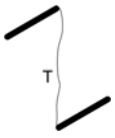	Type 3 **T** crack(s) linking right tip of the top flaw and left tip of the bottom flaw. There may be occasional short **S** segments present along the coalescence crack.

Figure 10.3 – Crack coalescence types. S = shear, T = tensile.

Influence of ligament length

Physically speaking, wider separation between the inner flaw tips reduces the mutual influence/interaction between the flaws, and hence reduces the chance of coalescence in certain flaw geometries. The influence of ligament length (*L = 2a vs L = 4a*) is observed to be more pronounced in coplanar flaws than in stepped flaws. For example, for geometries 2a-30-0 vs 4a-30-0 (both in gypsum and marble) and 2a-45-0 vs 4a-45-0 (only in marble), some or all of the tested specimens show **coalescence** (either indirect or direct) for ligament length 2a, but **no coalescence** occurs for ligament length 4a.

Influence of flaw inclination angle (coplanar flaws)

The coalescence between pre-existing **coplanar** flaws in both molded gypsum and Carrara Marble is achieved by a linkage of the inner flaw tips according to any one of the coalescence categories from 1 to 6 (except 4). There is a general trend of variation from no coalescence, to shear coalescence to tensile coalescence (from low number categories to high number categories) as flaw inclination angles β increase.

Influence of bridging angle (stepped flaws)

The whole spectrum of crack coalescence categories (from 1 to 9) is observed in the **stepped** flaw pair series in molded gypsum and Carrara Marble – generally from low number categories to high number categories, i.e. from no coalescence, indirect coalescence to direct coalescence as bridging angles (α) increase from negative values to small positive values, and further up to large positive values. Regarding direct coalescence, the coalescence categories generally progress from shear, to mixed shear-tensile to tensile as bridging angles (α) increase.

Influence of material

Coplanar flaws

In the small flaw inclination angle range, coalescence is less favored (category 1) in **marble** than in **gypsum** ($\beta = 0^o, 30^o, 45^o$ for ligament length 2a, $\beta = 30^o, 45^o$ for ligament length 4a). This phenomenon appears to be related to the fact that in the marble specimens, the initiation of **vertical** and/or **steeply-inclined cracks**

(dominantly tensile) from the inner flaw tips occurs more frequently than the initiation of **coplanar cracks** from the inner flaw tips, compared to the fracturing behavior in gypsum specimens.

In the large flaw inclination angle range, coalescence in gypsum (β = 45°, 60°, 75° for ligament length 2a, β = 75° for ligament length 4a) and marble (β = 60°, 75° for ligament length 2a, β = 75° for ligament length 4a) are also achieved in a **direct** manner in which the inner flaw tips are linked up by a continuous crack consisting of one or multiple individual crack segments. However, the crack segments adjacent to inner flaw tips in gypsum are mainly **shear**, while those in marble are mainly **tensile**. Note that the above observation is obtained from the video recordings at a macroscopic scale.

It is thus clear that over the whole range of flaw inclination angles β, the initiation of *tensile cracks* is more preferable to *shear cracks* in marble than in gypsum.

Stepped flaws

Some coalescence categories are unique to gypsum with specific flaw geometries, while some coalescence categories are unique to marble with specific flaw geometries (see below).

(a)

Ligament length 2a			
Category		**Gypsum**	**Marble**
4	Shear	-	α = 30
5	Mixed shear-tensile	α = 30, 60	-
6	Tensile	-	α = 60
8		-	α = 120

(b)

Ligament length 4a			
Category		**Gypsum**	**Marble**
5	Mixed shear-tensile	α = 30, 60	-
6	Tensile	-	α = 60
7		α = 90, 120	-
8		-	α = 90
9		-	α = 120

Table 10.4 – Summary of the coalescence categories unique to gypsum or marble.

Note from above that for the same flaw pair geometry (positive α), marble generally tends to have a higher coalescence category. In other words, tensile crack initiation is more favored in marble than in gypsum.

As revealed from both coplanar and stepped flaw geometries, tensile crack initiation is generally more favored in marble than in gypsum, hence leading to different coalescence patterns. An explanation based on the premises of FROCK (further details of the numerical work associated with FROCK are provided in section 10.6) is given below. As assumed in FROCK, crack propagation occurs when the stress at the boundary of the core region around the flaw tip is equal to the critical value. To determine the specific crack type initiating from the flaw tip, the computed stresses are compared against two material strength parameters – the critical tensile strength σ_{crit} and the critical shear strength τ_{crit}. The above observed fracturing differences indicate that the criterion for *tensile* crack initiation, instead of *shear* crack initiation is easier to meet at the flaw tip in marble. This is possible if the ratio of $\sigma_{crit}/\tau_{crit}$ in marble is lower than that in gypsum.

10.6 Microscopic study in gypsum and marble

A pronounced difference associated with the fracturing and coalescence processes in the two tested materials is the development of white patches in marble, but not in gypsum. SEM and ESEM imaging studies have also been conducted in the present study and identified that the macroscopic cracking in marble is associated with an extensive development of mircocracking zones or process zones, which appear as macroscopic white patches. However, the process zone development in gypsum is less compared to that in marble. Correlations between the *macroscopic* deformation and *microscopic* deformation in both gypsum and marble, regarding the formation of tensile cracks (figures 10.4 & 10.5) and shear cracks (figures 10.6 & 10.7), have been established in the present study.

- At a **macroscopic** scale as observed in the video recordings, the **tensile crack** development in gypsum and marble was quite different (figure 10.4). The tensile crack in **gypsum** initiated as a hair-line crack, which was not discernable to unaided eyes, but observable with a 10x hand lens. It appeared to be *continuous* (see further comments in the subsequent point at a microscopic scale) and propagated from the pre-existing flaws in response to the compressive loading. Continued loading increased the aperture of the tensile crack to make it discernable to unaided eyes. In **marble**, the first observable change in response to loading was the development of multiple white patches from the pre-existing flaws. These white patches, which were oriented in different directions, lengthened and propagated away from the flaws as loading increased. As loading further increased, tensile cracks began to initiate along the white patches, preferentially along the vertical white patches and those white patches displaying conventional wing appearance. Instead of initiating and propagating from the pre-existing flaw as a macroscopic continuous crack, multiple individual tensile cracks usually developed as short en echelon crack segments. These en echelon cracks lengthened, which eventually linked up to form a continuous crack as loading further increased. It has to be emphasized that the above observations are based on video recordings at a macroscopic scale.

- In **marble**, at a **microscopic** scale based on SEM study, macroscopic **white patches** (free of observable cracks to unaided eyes) associated with **tensile** crack development were found to be underlain by microcracking zones (process zones). The microcrack density in the process zones, which consisted of central dominant cracks and flanking microcracks, increased with the applied loading. In **gypsum**, on the other hand, the **macroscopic** hair-line tensile crack was found to consist of segmented tensile cracks on a **microscopic** scale in the ESEM study. Since they were very short and in very close proximity, they can not be differentiated macroscopically and appeared to be continuous with a 10x hand lens. Although microcracking zones (process zones) associated with crack development were also identified in gypsum, their extent was much more limited as seen in an ESEM study, and they did not appear as white patches at a macroscopic scale. See figure 10.5.

- At a **macroscopic** scale as observed in the video recordings, the **shear crack** development in gypsum and marble was quite different (figure 10.6). The initiation of shear cracks in **gypsum** was not preceded by any observable signs and it was due to the shear movement in the intact material. In **marble**, however, the initiation of shear cracks in was preceded by a development of white patches. The white patches lengthen and widen in response to the applied loading, until a load level at which shear cracks initiated along them. In both materials, the shear crack initiation was often accompanied by an occurrence of local surface spalling, indicating the presence of a local compressive stress field. The extent of spalling in gypsum was however often greater than that in marble.

- At a **microscropic** scale, the white patch in **marble** preceding the initiation of a coplanar shear crack from a pre-existing flaw tip was found to be underlain by multiple en echelon microcracking zones close to the flaw tips (figure 10.7). However, since a similar study was not conducted in **gypsum**, the microscopic features associated with the subsequent macroscopic shear cracks are not known at the present stage.

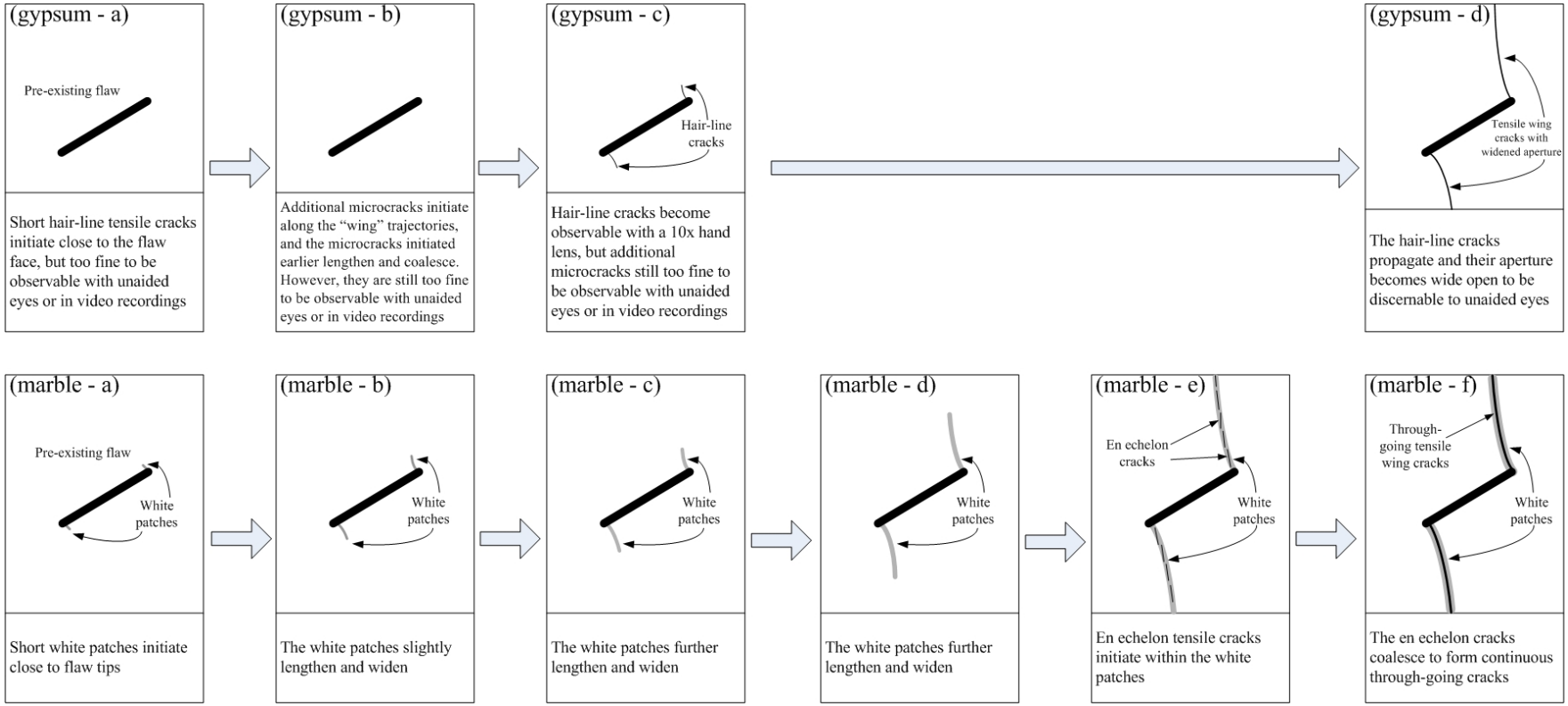

Figure 10.4 – Schematic illustration of the *macroscopic* development of white patch and hair-line crack in marble and gypsum. The top row is for gypsum and the bottom row is for marble.

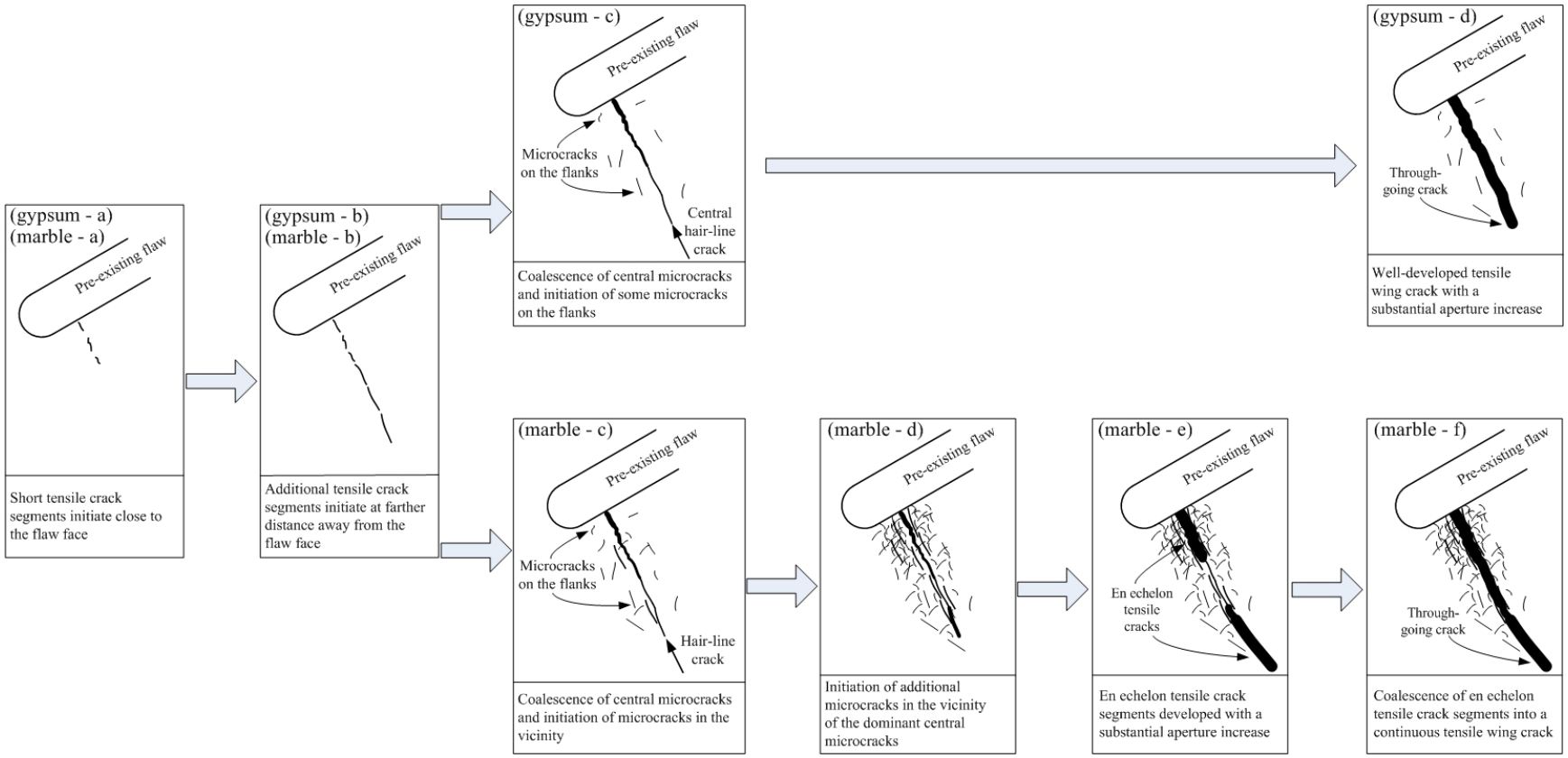

Figure 10.5 – Schematic illustration of the *microscopic* development of white patch and hair-line crack in marble and gypsum. Both gypsum and marble share the same figure on the left.

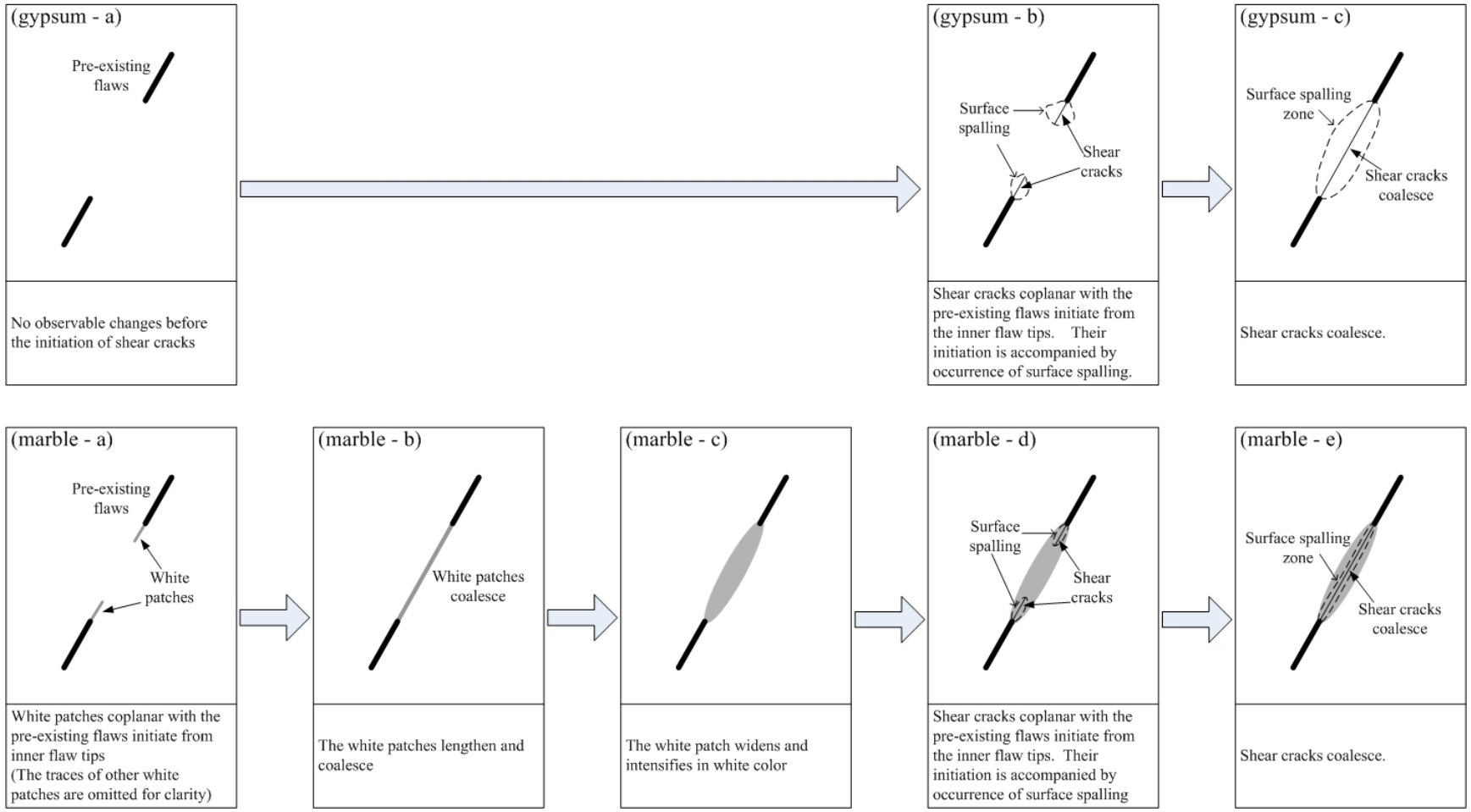

Figure 10.6 – Schematic illustration of the *macroscopic* development of white patch and hair-line crack in marble and gypsum. The top row is for gypsum and the bottom row is for marble.

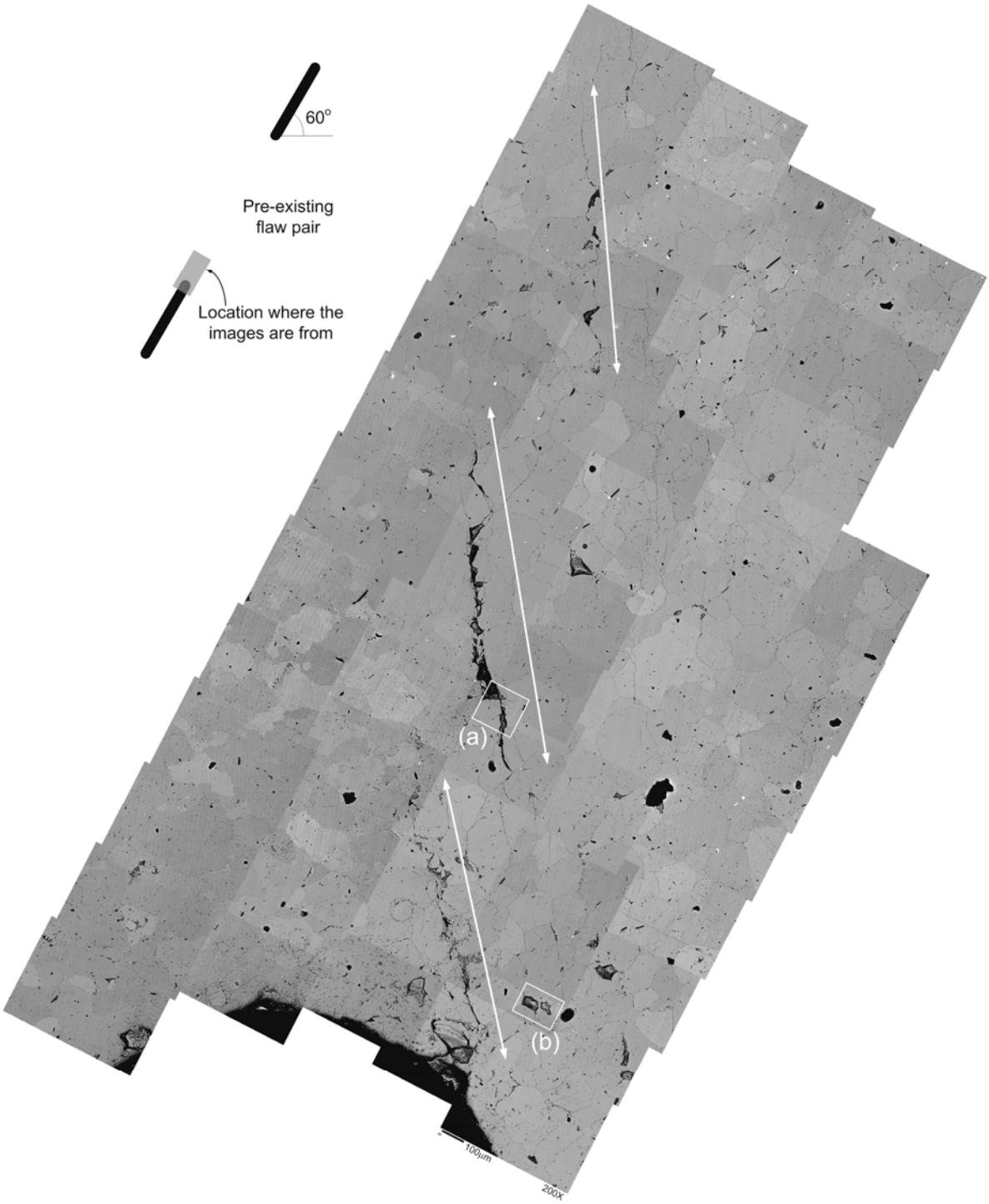

Figure 10.7 – An assemblage of SEM images of the area around the right flaw tip of the bottom flaw. Refer to figure 7.52 in chapter 7 for magnified images of the two enclosed areas. The intensely fractured zones, whose traces are indicated by arrows, trend almost parallel to the vertical loading direction. The length of the bottom scale bar is 100 μm. (magnification power = 200 X)

10.7 Numerical modeling

The numerical code FROCK, which is based on the Displacement Discontinuity Method and was extensively modified by Bobet (1997) was used to model the crack coalescence processes observed in gypsum in the present experiments. The input parameters originally provided by Bobet were used. The coalescence patterns of flaw pairs with flaw inclination 45^o obtained in the present FROCK study generally agree well with those obtained in the FROCK study by Bobet. However, discrepancies were observed for other flaw pair geometries.

With regard to those flaw geometries with unsatisfactory modeling results, FROCK was run again by either varying one parameter of a set of four at a time or two parameters at a time of a set of three parameters. The four input parameters are critical shear strength (τ_{crit}), critical tensile strength (σ_{crit}), core radius (r_0) and friction coefficient (μ). For some flaw pair geometries (30-a-2a, 30-0-a, 75-0-2a), a slight variation of the particular parameter(s) can successfully lead to coalescence. However, the crack initiation stresses (σ_c) associated with the varied parameters for the three flaw pair geometries are not always in good agreement with the Bobet's FROCK values or the present experimental values. For another flaw pair geometry 30-0-2a, no satisfactory coalescence patterns can be obtained no matter how the four input parameters are varied individually. The present study indicates that with the availability of more experimental data, there is room for improving the back-fitting to obtain the input parameters.

As observed in the present experimental study for marble, the *tensile* crack initiation occurs more frequently than the *shear* crack initiation as compared to gypsum. As stipulated in FROCK, crack propagation occurs when the stress at the boundary of the core region around the flaw tip is equal to the critical value. To determine the specific crack type initiating from the flaw tip, the computed stresses are compared against two material strength parameters – the critical tensile strength σ_{crit} and the critical shear strength τ_{crit}. Since the present modeling study demonstrates that the crack type initiated from the pre-existing flaws is sensitive to the ratio of the critical strength values (also

reported by Bobet (1997)), the different fracturing behavior observed in marble and gypsum can possibly be due to a lower critical strength ratio $\sigma_{crit}/\tau_{crit}$ in marble than in gypsum.

10.8 Recommendations for future research

Experimental techniques

- In the present study, pre-existing flaws in marble were created by using the water abrasive jet, which was able to cut a minimum flaw aperture size of 0.05" in the intact Carrara Marble. It is foreseen that with the advance of technology, narrower flaws can be cut by the next generation of water abrasive jet.

- Another improvement is foreseen in the high speed video system. With the enhanced capability to capture the video at a higher frame rate and the availability of a larger internal memory storage in the future, it will then be possible to monitor and record the whole loading process instead of the crack coalescence events. They will allow one to better establish the crack initiation sequence, i.e. which crack is the first crack, second crack, etc. and the observation of the relevant cracks which are directly associated with specimen failure.

Additional tests

The effects of four key parameters on cracking and coalescence behavior have been studied in this thesis, namely flaw inclination angle, bridging angle, ligament length and material. Specific recommendations regarding these parameters are made below:

- Coplanar flaw pair geometries were tested for a range of flaw inclination angles in the present study. However, only flaw inclination angle of 30^o was tested for stepped flaws to study the influence of bridging angle and ligament length on the coalescence behavior. More experimental work on stepped flaws with other flaw inclination

angles, e.g. 45^o, 60^o is required to comprehensively understand the effects of bridging angle and ligament length.

- The present study has established the correlations between the macroscopic changes and the microscopic changes associated with tensile crack initiation in the two materials, and similarly for shear crack. However, they were limited to only one type of tensile crack (type 1 tensile crack) or only one shear crack (type 2 shear crack). As identified in the present study, seven crack types with different nature and trajectories have been identified. Similar correlation studies on the remaining five crack types are thus recommended to generalize the relationship between microscopic and macroscopic observations observed in the present study.

- *Macroscopic* en echelon cracks associated with a *macroscopic* tensile crack development and *microscopic* en echelon cracks associated with a *microscopic* shear crack development were observed in marble specimens. As discussed in chapter 9, the macro- and micro- en echelon cracks can also possibly be due to a combined mode I – mode III or mode I – mode II loading condition, and be linked to a continuous parent crack in the specimen center. However, since only the front face of the specimen was monitored during the loading tests, it seems necessary to conduct additional uniaxial compression loading tests on the same flaw geometries in marble. The specimens, which have been loaded to generate the white patch, shall be sliced at multiple depths beneath the specimen front face for examining the 3-dimensional crack development inside.

- The two rock types Carrara Marble and molded gypsum tested in the present study are isotropic and homogeneous. The SEM study on Carrara Marble reveals that the microscopic material features such as grain boundaries and cleavage planes have a significant influence on the fracturing behavior. Experiments analogous to those conducted in the present study can be extended to other rock types, which are more heterogeneous. Being aided by the SEM imaging study, the differences in

macroscopic fracturing and/or coalescence behavior can possibly be related to the underlying microstructural properties.

Numerical work

- Adjustments were made in the present FROCK study to the input parameters which were originally provided by Bobet in order to improve the modeling results. With the availability of more experimental data, the present study indicates that there is room for improving the back-fitting to obtain the input parameters.

- The present numerical work is conducted for gypsum only, but can also be extended to marble. The present experimental study observes that tensile fracturing generally occurs more often in marble than in gypsum for the same flaw pair geometries. It implies that a variation of the input strength parameters, particularly decreasing the ratio of the critical tensile strength/critical shear strength will likely be the first step in the back-fitting process in obtaining the corresponding input parameters for marble.

REFERENCES

Alber, M. and Hauptfleisch, U. (1999) Generation and visualization of microfractures in Carrara Marble for estimating fracture toughness, fracture shear and fracture normal stiffness. *Int. J Rock Mech Min Sci*, 36: 8, pp. 1065-1071.

An, L.J. and Sammis, C.G. (1996) A cellular automation for the development of crustal shear zones, *Tectonophysics*, 253, pp. 247-270.

Anderson, T.L. (2005) *Fracture Mechanics: Fundamentals and Applications*, Edition 3, CRC Press, Boca Raton, FL.

Ashby, M. F. and Hallam, S.D. (1986) the failure of brittle solids containing small cracks under compressive stress states. *Acta Metall*., 34, pp. 497-510.

Atkinson, B.K. (1979) Fracture toughness of Tennessee sandstone and Carrara marble using the double torsion testing method. *Int. J. Rock Mech. Min. Sc*., 16, pp. 49-53.

Aydin, A., 2000, Fractures, Faults, and Hydrocarbon Migration and Flow. *Marine and Petroleum Geology*, 17, pp. 797-814.

Aydin, A., 2006, Failure modes of the lineaments on Jupiter's moon, Europa: Implications for the evolution of its icy crust. *Journal of Structural Geology*, 28(12), pp. 2222-2236.

Barenblatt, G.I. (1962) The mathematical theory of equilibrium cracks in brittle fracture. *Advances in Applied Mechanic*s, Vol. VII, Academic Press, NY, pp. 55-109.

Barlett, W.L., Friedman, M. and Logan, J.M. (1981) Experimental folding and faulting of rocks under confining pressure. *Tectonophysics*, 79, pp. 255-277.

Best, M.G. and Christiansen, E.H. (2001) *Igneous Petrology*. Madlen, Mass.: Blackwell Science.

Bieniawski, Z.T. (1967) Mechanism of brittle fracture of rock, Part II – experimental studies, *Int. J. Rock. Mech. Min. Sci.*, Vol. 4, pp. 407-423.

Bobet, A. (1997) *Fracture Coalescence in Rock Materials: Experimental Observations and Numerical Predictions*, Sc.D. Thesis, Massachusetts Institute of Technology.

Bobet, A. (2000) The initiation of secondary cracks in compression. *Engineering Fracture Mechanics*, 66, pp. 187-219.

Bobet, A. and Einstein, H.H. (1998a) Fracture coalescence in rock-type materials under uniaxial and biaxial compression. *Int. J Rock Mech Min Sci*, 35: 7, pp. 863-88.

Bobet, A. and Einstein, H.H. (1998b) Numerical modeling of fracture coalescence in a model rock material. *Int. J. Fracture*, 92, pp. 221-252.

Bombolakis, E.G. (1963) Photoelastic stress analysis of crack propagation within a compressive stress field, *Ph.D. Thesis*, Massachusetts Institute of Technology, Cambridge, 38p.

Brace, W. F. (1961) Dependence of fracture strength of rocks on grain size. *Bulletin of the Mineral Industries Experiment Station, Mining Engineering Series. Rock Mech.* 76, 99-103.

Brace, W.F. and Bombolakis, E.G. (1963) A note on brittle crack growth in compression, *J. Geophys Res*, 68(12), pp. 3709-3713.

Cai, M., Kaiser, P.K., Tasaka, Y., Maejima, T., Morioka, H. and Minami, M. (2004) Generalized crack initiation and crack damage stress thresholds of brittle rock masses near underground excavations. *Int. J Rock Mech Min Sci*, 41, pp. 833-847.

Cakir, M., Aydin, A. and Campagna, D. J. (1998) Deformation pattern around conjoining strike-slip faults systems in the Basin and Range, southeast Nevada: The role of strike-slip faulting in basin formation and inversion. *Tectonics*, 17(3), p. 344-359.

Cardani, G. and Meda A. (1999) Flexural strength and notch sensitivity in natural building stones: Carrara and Dionysos marble. *Construction and Building Materials*, 13(7), pp. 393-403.

Chaker, C. and Barquins, M. (1996) Sliding effect on branch crack. *Phys. Chem. Earth*, Vol.21, No.4, pp.319-323.

Chen, G., Kemeny, J.M. and Harpalani, S. (1995) Fracture propagation and coalescence in marble plates with pre-cut notches under compression, In L.R. Myer, N.G.W. Cook, R.E. Goodman & C.F. Tsang (Eds). *Symposium on Fractured and Jointed Rock Mass*, Lake Tahoe, CA, pp. 435-439.

Childs, C., Nicol, A., Walsh, J.J. and Watterson, J. (1996) Growth of vertically segmented normal faults. *Journal of Structural Geology*, 18(12), pp. 1389–1397.

Chinnery, M.A. (1966) Secondary faulting. *Canadian Journal of Earth Sciences*, 3, pp. 163-174.

Cooke, M.L. (1997) Fracture localization along faults with spatially varying friction. *Journal of Geophysical Research*, 102, pp. 22425-22434.

Cooke, M.L. and Pollard, D.D. (1996) Fracture propagation paths under mixed mode loading within rectangular blocks of polymethyl methacrylate, *Journal of Geophysical Research*, 101, B2, pp. 3387-3400.

Costamagna, R., Renner, J and Bruhns, O.T. (2007) Relationship between fracture and friction for brittle rocks. *Mechanics of Materials*, 39(4), pp. 291-301.

Costin, L.S. (1985) Damage mechanics in the post-failure region. *Mech. Mat.* 4, pp. 149-160.

Cox, K.G., Price, N.B. and Harte, B. (1988) *An Introduction to the Practical Study of Crystals, Minerals, and Rocks*. Revised First Edition, McGraw-Hill Book Company (UK) Limited.

Crider, J.G. and Pollard, D.D. (1998) Fault linkage: Three-dimensional mechanical interaction between echelon normal faults. *Journal of Geophysical Research*, 103, B10, pp. 24373-24391.

Crider, J.G. and Peacock, D.C.P. (2004) Initiation of brittle faults in the upper crust: a review of field observations. *Journal of Structural Geology*, 26, pp. 691–707.

Cruikshank, K. M., Zhao, G. H. and Johnson, A. M. 1991. Analysis of Minor Fracture Associated with Joints and Faulted Joints. *Journal of Structural Geology* 13(8), 865-886.

Cruikshank, K.M. and Aydin, A. (1994) Role of fracture localization in arch formation, Arches National Park, Utah. *Geological Society of America Bulletin*, 106, pp. 879-891.

Dugdale, D.S. (1960) Yielding in steel sheets containing slits. *Journal of the Mechanics and Physics of Solids*, 8, pp. 100-104.

Dyskin, A.V., Jewell, R.J., Joer, H., Sahouryeh, E. and Ustinov, K.B. (1994) Experiments on 3-D crack growth in uniaxial compression, International Journal of Fracture, 65(4), pp. 77-83.

Dyskin, A.V., Sahouryeh, E., Jewell, R.J., Joer, H., and Ustinov, K.B. (2003) Influence of shape and locations of initial 3-D cracks on their growth in uniaxial compression, Engineering Fracture Mechanics, 70(15), pp. 2115-2136.

Eberhardt, E., Stimpson, B. and Stead, D. (1999) Effects of grain size on the initiation and propagation thresholds of stress-induced brittle fractures. *Rock Mech Rock Engng*, 32(2), pp.81-99.

Einstein, H.H. and Hirschfeld R.C. (1973) Model studies on mechanics of jointed rocks, *ASCE Journal of the Geotechnical Division*, Vol. 99, SM3.

Einstein, H.H., Nelson, R.A., Bruhn, R.W. and Hirschfeld, R.C. (1969) Model studies of jointed rock behavior, *Proc. 11th Symposium on Rock Mechanics*, pp. 83-103.

Einstein, H.H. and Meyer, T. (1999) Müller lecture: puzzles in rock. *Proc. Int'l. Congress of the ISRM*, Vol. 3, Paris, pp. 1707-1740.

Elkadi, A.S.K. (2005) *Fracture scaling of concrete under multiaxial compression*. DUP Science.

Engelder, T. (1987) Joints and shear fractures in rock. In B.K. Atkinson (ed) *Fracture Mechanics of Rock* , Academic Press, pp. 27-69.

Erdogan, F. and Sih, G.C. (1963) on the crack extension in plates under plane loading and transverse shear. *Journal of Basic Engineering*, 85, pp.305-321.

Fredrich, J.T., Evans, B. and Wong, T.F. (1990) Effect of grain size on brittle and semibrittle strength: implications for micromechanical modelling of failure in compression, *Journal of Geophysical Research*, 95, pp. 10907–10920.

Friedman, M., Handin, J. and Alani, G. (1972) Fracture energy of rocks. *Int. J. Rock. Mech. Min. Sci.*, 9, pp. 757-766.

Gdoutos, E.E. (1990) *Fracture Mechanics Criteria and Applications*, Kluwer Academic Publishers, 1990.

Germanovich, L.N., Salganik, R.L., Dyskin, A.V. and Lee, K.K (1994) Mechanisms of brittle fracture of rock with multiple pre-existing cracks in compression. *Pure and Applied Geophysics (PAGEOPH)* 143(13), pp. 117–149.

Germanovich, L.N. and Dyskin, A.V. (2000) Fracture mechanisms and instability of openings in compression. *Int. J. Rock. Mech. Min. Sci.*, 37, pp. 263-284.

Gramberg, J. (1965) Axial cleavage fracturing, a significant process in mining and geology, *Engineering Geology*, 1(1), pp. 31-72.

Griffith, A.A. (1920) The phenomenon of rupture and flow in solids. *Philosophical Transactions*, Series A, 221, pp. 163-198.

Griffith, A.A. (1924) The theory of rupture. *International Congress of Applied Mechanics, 1st*, Delft, pp. 55-63.

Gueguen, Y., Reuschlé, T. and Darot, M. (1990) Single-crack behavior and crack statistics. In D.J. Barber and Meredith, P.G. (eds) Deformation Processes in Minerals, Ceramics and Rocks. London: unwin Hyman, pp. 48-71.

Guo, Y.S.H., Wong, R.H.C., Chau, K.T., Zhu, W.S. and Li, S.C. (2006) Crack growth mechanisms from 3-D surface flaw with varied dipping angle under uniaxial compression. In *Asian Pacific Conference on Fracture and Strength*, Sanya, Hainan Island, China, p. 335.

Hallam, S.D. and Ashby, M.F. (1990) Compressive brittle fracture and the construction of multi-axial failure maps. In D.J. Barber and Meredith, P.G. (eds) *Deformation Processes in Minerals, Ceramics and Rocks*. London: Unwin Hyman, pp. 84-108.

Hatzor, Y. H., Palchik, V. (1997) The influence of grain size and porosity on crack initiation stress and critical flaw length in dolomites. *Int. J. Rock Mech. Min. Sci.* 34 (5), pp. 805 – 816.

Healy, D., Jones, R.R. and Holdsworth, R.E. (2006) Three-dimensional brittle shear fracturing by tensile crack interaction, Nature, pp. 64 – 67.

Hillerborg, A., Modeer, M., and Petersson, P.E. (1976) Analysis of crack formation and crack growth in concrete by means of fracture mechanics and finite elements. *Cement and Concrete Research*, 6, pp. 773-782.

Hillerborg, A. (1991) Application of the fictitious crack model to different materials. *International Journal of Fractur*e, 51, pp. 95-102.

Hoagland, R. G., Hahn, G.T. and Rosenfield, A.R. (1973) Influence of microstructure on fracture propagation in rock. *Rock Mechanics*, 5, pp. 77-106.

Hoek, E. and Bieniawski, Z.T. (1965) Brittle fracture propagation in rock under compression, *Int. J of Fracture Mechanics*, Vol.1, pp. 137-155.

Horii, H. & Nemat-Nasser, S. (1985) Compression-induced microcrack growth in brittle solids: Axial splitting and shear failure. *Journal of Geophysical Research*, 90 (B4), pp.3105-3125.

Huang J.F., Chen G.L., Zhao Y.H. and Wang R. (1990) An experimental study of the strain field development prior to failure of a marble plate under compression. *Tectonophysics*, Vol. 175, pp. 283-290.

Hussain, M.A., Pu, S.L. and Underwood, J. (1974) Strain energy release rate for a crack under combined mode I and mode II. *Fract Anal ASTM STP* 560, pp. 2–28.

Inglis, C.E. (1913) Stresses in a plate due to the presence of cracks and sharp corners. *Inst. Naval Architecture, London*, 55, pp. 219-230.

Ingraffea, A.R. and F.E. Heuze. (1980) Finite element models for rock fracture mechanics, *Int. J. Num. Anal. Meths. in Geomechs*., 4, pp.25.

Ingraffea, A. and Wawrzynek, P.A. (2001) Encyclopedia of Materials: Science and Technology, pp. 1745-1750.

Irwin, G.R. (1956) Onset of fast crack propagation in high strength steel and aluminum alloys. *Sagamore Research Conference Proceedings*, 2, pp. 289-305.

Irwin, G.R. (1957) Analysis of stresses and strains near the end of a crack traversing a plate. *Journal of Applied Mechanics*, 24, pp. 361-364.

Isaksson, P. and Ståhle, P. (2002) Prediction of shear crack growth direction under compressive loading and plane strain conditions. *International Journal of Fracture*, 113, pp. 175-194.

Kemeny, J.M. and Cook, N.G.W. (1987) Crack models for the failure of rocks in compression. In *Proc. 2nd Int. Conf. on Constitutive Laws for Engineering Materials*, Tucson, Arizona.

Kim, Y.S., Peacock, D.C.P. and Sanderson, D.J. (2003) Strike–slip faults and damage zones at Marsalforn, Gozo Island, Malta. *Journal of Structural Geology*, 25, pp. 793–812.

Ko, T.Y. (2005) Crack coalescence in rock-like material under cyclic loading, *Civ. Eng. Thesis*, Massachusetts Institute of Technology, 184p.

Ko, T.Y., Einstein, H.H. and Kemeny, J. (2006) Crack coalescence in brittle material under cyclic loading. Golden Rocks 2006, *Proc. of the 41st U.S. Symposium on Rock Mechanics (USRMS): "50 Years of Rock Mechanics - Landmarks and Future Challenges."*, Golden, Colorado, June 17-21, ARMA/USRMS 06-930.

Kranz, R.L. (1979) Crack growth and development during creep of Barre Granite, *Int. J. Rock. Mech. Min. Sci.& Geomech. Abstr*., 16, pp. 23-35.

Kranz, R.L. (1983) Microcracks in rocks: a review. *Tectonophysics*, 100, pp. 449-480.

Labuz, J.F., Shah, S.P. and Dowding, C.H. (1987) The fracture process zone in granite: evidence and effect. *Int. J. Rock Mech. Min. Sci.*,24, pp. 235-246.

Lajtai, E.Z. (1971) A theoretical and experimental evaluation of the Griffith theory of brittle fracture, *Tectonophysics*, 11, pp.129-156.

Lajtai, E.Z. (1974) Brittle fracture in compression. *Int. J. Fract.*, 10, pp. 525-536.

Lee, M. and Haimson, B. (1993) Laboratory study of borehole breakouts in Lac du Bonnet granite: a case of extensile failure mechanism, *Int. J. Rock Mech. Min. Sci. Geomech. Abstr.* 30, pp. 1039–1045.

Li, Y.P., Chen, L.Z. and Wang, Y.H. (2005) Experimental research on pre-cracked marble under compression, *International Journal of Solids and Structures*, 42, pp. 2505-2516.

Maji, A.K. and Wang, J. (1992) Fracture mechanics of a tension-shear macrocrack in rocks. *Experimental Mechanics*, 32(2), pp. 190-196.

Mansfield, C. and Cartwright, J. (2001) Fault growth by linkage: observations and implications from analogue models. *Journal of Structural Geology*, 23, pp. 745–763.

Martel, S.J. (1990) Formation of compound strike-slip fault zones, Mount Abbot quadrangle, California. *Journal of Structural Geology*, 12(7), pp. 869-882.

Martel, S.J. (1997) Effects of cohesive zones on small faults and implications of secondary fracturing and fault trace geometry. *Journal of Structural Geology*, 19, pp. 835-847.

Martel, S.J. and Boger, W.A. (1998) Geometry and mechanics of secondary fracturing around small three-dimensional faults in granitic rock. *Journal of Geophysical Research*, 103, pp. 21299-21314.

Martinez, A.R. (1999) *Fracture coalescence in natural rock*, MSc Thesis, Massachusetts Institute of Technology, 341p.

Maso, J.C. (1994) *Interfacial Transition Zone in Concrete*. RILEM. Technical Committee 108-ICC Interfaces in Cementitious Composites.

Maugis, D. (1982) Stresses and displacements around cracks and elliptical cavities: exact solutions. *Engineering Fracture Mechanics*, 43(2), pp. 217-255.

McClintock, and Walsh, J.B. (1962) Friction on Griffith cracks in rocks under pressure. *Proc. 4th U.S. National Congr. Appl. Mech.*

McGrath, A.G. and Davison, I. (1995) Damage zone geometry around fault tips. *Journal of Structural Geology*, 17(7), pp. 1011-1024.

Melin, S. (1986) When does a crack grow under mode II conditions? *International Journal of Fracture*, 30, pp. 103-114.

Melin, S. (1987) Fracture from a straight crack subjected to mixed-mode loading. *International Journal of Fracture*, 32, pp. 257-263.

Mitaim, S. and Detournay, E. (2004) Damage around a cylindrical opening in a brittle rock mass. *Int. J. Rock. Mech. Min. Sci.*, 41, pp. 1447-1457.

Mollema, P.N. and Antonellini, M. (1999) Development of strike-slip faults in the dolomites of the Sella Group, Northern Italy. *Journal of Structural Geology*, 21, pp. 273-292.

Moore, D.E. and Lockner, D.A. the role of microcracking in shear-fracture propagation in granite, *Journal of Structural Geology*, 17, pp. 95-114.

Moss, W.C. and Gupta, Y.M. (1982) A constitutive model describing dilatancy and cracking in brittle rocks. *Journal of Geophysical Research*, 87 (B4), pp. 2985-2998.

Motoyama, H. and Hirschfeld, R.C. (1971) The effect of joint configurations on the strength and deformability of model rock masses, Final Report, Federal Railroad Administration, Department of Transportation, Washington, D.C. 20591., 183 p.

Mughieda, O. and Alzo'ubi, A.K. (2004) Fracture mechanics of offset rock joints – a laboratory investigation, *Geotechnical and Geological Engineering*, 22, pp. 545-562.

Muller, J.R. and Aydin, A. (2005) Using mechanical modeling to constrain fault geometries proposed for the northern Marmara Sea. *Journal of Geophysical Research*, 110, B03407.

Myers, R. and Aydin, A. (2004) The evolution of faults formed by shearing across joint zones in sandstone. *Journal of Structural Geology*, 26, pp. 947-966.

Nelson, R.A. (1968) Modelling a Jointed Rock Mass, MSc Thesis, Massachusetts Institute of Technology, 218p.

Nemat-Nasser, S. and Horii, H. (1982) Compression-induced nonplanar crack extension with application to splitting, exfoliation, and rockburst, *Journal of Geophysical Research*, 87 (8), pp. 6805-6821.

Nesetova V. and Lajtai, E.Z. (1973) Fracture from compressive stress concentrations around elastic flaws. *Int. J. Rock Mech. Min. Sci. & Geomech. Abstr*. 10, pp. 265-284.

Olson, J.E. and Pollard, D.D. (1991) The initiation and growth of en echelon veins. *Journal of Structural Geology*, 13, pp. 595-608.

Olsson, W.A. (1974) Grain size dependence of yield stress in marble, *Journal of Geophysical Research* 79, pp. 4859–4862.

Peacock, D.C.P. (2001) The temporal relationship between joints and faults. *Journal of Structural Geology*, 23, pp. 329-341.

Peacock, D.C.P., Knipe, R.J. and Sanderson, D.J. (2000) Glossary of normal faults. *Journal of Structural Geology*, 22, pp. 291-305.

Peck, L., Barton, C.C. and Gordon, R.B. (1985) Microstructure and the resistance of rock to tensile fracture. *Journal of Geophysical Research*, 90, pp. 111533-11546.

Peng, S. and Johnson, A.M. (1972) Crack growth and faulting in cylindrical specimens of Chelmsford granite, *Int. J. Rock. Mech. Min. Sci.*, 9, pp. 37-86.

Petit, J. and Barquins, M. (1988) Can natural faults propagate under Mode II conditions? *Tectonics*, 7(6), pp. 1246-1265.

Pollard, D.D. and Fletcher, R.C. (2005) Fundamentals of structural geology. Cambridge University Press.

Pollard, D.D. and Segall, P. (1987) Theoretical displacements and stresses near fractures in rock: with applications to faults, joints, veins, dikes, and pressure solution surfaces. In: Atkinson, B.K. (Eds.), *Fracture Mechanics of Rock*. Academic Press, London, pp. 277-349.

Pollard, D.D. and Aydin, A.A. (1988) Progress in understanding jointing over the past century: *Geological Society of America Bulletin*, v. 100, pp. 1181-1204.

Pollard, D.D., Segall, P. and Delaney, P.T. (1982) Formation and interpretation of dilatant echelon cracks, *Geological Society of America Bulletin*, 93, pp.1291-1303.

Qian, J. and Fatemi, A. (1996) Mixed mode fatigue crack growth: a literature survey. *Engineering Fracture Mechanics*, 55(6), pp. 969-990.

Rapp, G. (2002) *Archaeomineralogy*. Verlag Berlin Heidelberg New York: Springer, 326p.

Rawnsley, K.D. Rives, T., Petit, J.P., Hencher, S.R. and Lumsden, A.C. (1992) Joint development in perturbed stress fields near faults. *Journal of Structural Geology*, 14(8/9), pp. 939-951.

Raynaud, S. and Delair, J. (1978) Genèse et mechanisms de la rupture fragile dans un calcaire et un granite soumis à un champ naturel de contrainte en compression. *Bull. Bur. Rech. Géol. Minières* (in French), Sect. 2., IV.

Reches, Z. and Lockner, D.A. (1994) Nucleation and growth of faults in brittle rocks. *Journal of Geophysical Research*, 99(B9), pp. 18159-18173.

Renshaw, C.E. and Schulson, E. (2001) universal behavior in compressive failure of brittle materials. *Nature*, 412 (30), pp.897-900.

Reyes, O. (1987) Numerical modelling of fracture propagation in tension softening materials, *S.M. Thesis*, Massachusetts Institute of Technology, Cambridge.

Reyes, O. (1991) Experimental study and analytic modeling of compressive fracture in brittle materials, *Ph.D. Thesis*, Massachusetts Institute of Technology, Cambridge.

Reyes, O. and Einstein, H.H. (1991) Failure mechanism of fractured rock – a fracture coalescence model. In W. Wittke (ed) *Proceedings of the 7th International Congress of Rock Mechanics 1991*, Aachen, Germany, 1, pp. 333-340. Rotterdam: Balkema.

Rispoli, R. (1981) Stress fields about strike-slop faults inferred from stylolites and tension gashes. *Tectonophysics*, 75, pp. T29-T36.

Roering, C. (1968) The geometrical significance of natural en-echelon crack arrays, *Tectonophysics*, 5(2), pp. 107-123.

Sagong, M. (2001) The study of the fracture of multiple flaw specimens, *Ph.D. Thesis*, Purdue University, Indiana.

Sagong, M. and Bobet, A. (2002) Coalescence of multiple flaws in a rock-model material in uniaxial compression. *Int. J. Rock. Mech. Min. Sci.*, 39, pp. 229-241.

Scholz, C.H. (2002) *The Mechanics of Earthquakes and Faulting*. Second Edition, Cambridge University Press.

Scholz, C.H., Dawers, N.H., Yu, J.Z., Anders, M.H. and Cowie, P.A. (1993) Fault growth and fault scaling laws – preliminary results. *J. Geophys Res*, 98, pp. 21951-21961.

Segall, P. and Pollard, D.D. (1983) Nucleation and growth of strike slip faults in granite. *J. Geophys Res*, 88, pp. 555-568.

Shen, B. and Stephansson, O. (1993) Numerical analysis of mixed mode I and mode II fracture propagation. *Int. J. Rock. Mech. Min. Sci. & Geomech. Abstr,* 30(7), pp. 861-867.

Shen, B., Stephansson, O., Einstein, H.H. and Ghahreman, B. (1995) Coalescence of fractures under shear stress experiments. *J. Geophys Res*, 100(6), pp. 5975-90.

Siegesmund, S., Ullemeyer, K., Weiss, T. and Tschegg, E.K. (2000) Physical weathering of marbles caused by anisotropic thermal expansion. *International Journal of Earth Sciences*, 89(1), pp. 170-182.

Sih, G.C. (1973) Some basic problems in fracture mechanics and new concepts. *Engineering Fracture Mechanics,* 5, pp. 365–377.

Sih, G.C. (1974) Strain-energy-density factor applied to mixed mode crack problems. *International Journal of Fracture*, 10(3), pp. 305-321.

Sprunt, E.S. and Brace, W.F. (1974) Direct observation of microcavities in crystalline rocks. *Int. J. Rock. Mech. Min. Sci. & Geomech. Abstr*, 11, pp. 139-150.

Sternlof, K.R., Rudnicki, J.W., Pollard, D.D. (2005) Anticrack-inclusion model for compaction bands in sandstone. *Journal of Geophysical Research*, 110, B11403.

Tapponnier, P. and Brace, W.F. (1976) Development of stress-induced microcracks in Westerly granite. *Int. J. Rock. Mech. Min. Sci. & Geomech. Abstr*, 13, pp. 103-112.

Thomas, A.L. and Pollard, D.D. (1993) The geometry of echelon fractures in rock: implications from laboratory and numerical experiments. *Journal of Structural Geology*, 15(3-5), pp. 323-334.

Tikoff, B. and Teyssier, C. (1992) Crustal-scale, en echelon “P-shear” tensional bridges: a possible solution to the batholithic room problem. *Geology*, 20, pp. 927-930.

van der Zee, W. and Urai, J.L. 2005. Processes of normal fault evolution in a siliciclastic sequence: a case study from Miri, Sarawak, Malaysia. *Journal of Structural Geology*, 27(12), pp. 2281-2300.

Vita-Finzi, C. and King, G.C.P. (1985) The seismicity, geomorphology and structural evolution of the Corinth area of Greece, *Philos. Trans. R. Soc.* London, Ser. A, 314, pp. 379-407.

Vsrhelyi, B. and Bobet, A. (2000) Modeling of crack initiation, propagation and coalescence in uniaxial compression. *Rock Mech. Rock Engng*, 33(2), pp. 119-139.

Veremilye, J.M. and Scholz, C.H. (1998) The process zone: A microstructural view of fault growth. *Journal of Geophysical Research*, 103, 12223-12237.

Veremilye, J.M. and Scholz, C.H. (1999) Fault propagation and segmentation insight from the microstructural examination of a small fault. *Journal of Structural Geology,* 21, pp. 1623-1636.

Wang, E.Z. and Shrive, N.G. (1995) Brittle fracture in compression: mechanics, models and criteria. *Engineering Fracture Mechanics*, 52(6), pp. 1107 – 1126.

Wang, R.Q. and Kemeny, J.M. (1992) Fracturing mechanisms in Apache Leap tuff under compressive stress, In L.R. Myer, N.G.W. Cook, R.E. Goodman & C.F. Tsang (Eds). *Symposium on Fractured and Jointed Rock Mass*, Lake Tahoe, CA, pp. 407-414.

Willemse, E.J.M., Peacock, D.C. and Aydin, A. (1997) Nucleation and growth of strike-slip faults in limestones from Somerset, U.K. *Journal of Structural Geology*, 19(12), pp. 1461-1477.

Willemse, E.J.M. and Pollard, D.D. (1998) On the orientation and patterns of wing cracks and solution surfaces at the tips of a sliding flaw or fault. *Journal of Geophysical Research*, 103, 2427-2438.

Wong, L.N.Y. and Einstein, H.H. (2006) Fracturing Behavior of Prismatic Specimens Containing Single Flaws. *Golden Rocks 2006, The 41st U.S. Symposium on Rock Mechanics (USRMS): "50 Years of Rock Mechanics - Landmarks and Future Challenges."*, Golden, Colorado, June 17-21, 2006, ARMA/USRMS 06-899.

Wong, L.N.Y. and Einstein, H.H. (2007) Coalescence behavior in Carrara marble and molded gypsum containing artificial flaw pairs under uniaxial compression. In E. Eberhardt, D. Stead, T. Morrison (eds) *Proceedings of the 1st Canada-US Rock Mechanics Symposium, Vancouver, Canada, 27-31 May 2007*, p.581-589.

Wong, R.H.C. and Chau, K.T. (1998) Crack coalescence in a rock-like material containing two cracks. *Int. J. Rock. Mech. Min. Sci.*, 35(2), pp. 147-164.

Wong, R.H.C., K.T. Chau, C.A. Tang and P. Lin. (2001) Analysis of crack coalescence in rock-like materials containing three flaws – Part I: experimental approach. *Int. J. Rock. Mech. Min. Sci.*, 38, pp. 909-924.

Wong, R.H.C., Guo, Y.S.H., Li, L.Y., Chau, K.T., Zhu, W.S. and Li, S.C. (2006) Anti-wing crack growth from surface flaw in real rock under uniaxial compression. In *16th European Conference of Fracture (EFC16)*. Alexandroupolis, Greece, p.825.

Wong, R.H.C., Li, T.C., Chau, K.T., Li, S.C. and Zhu, W.S. (2007) Crack growth study of a 3-D surface fracture under compression using strain and acoustic emission measurements. In E. Eberhardt, D. Stead, T. Morrison (eds) *Proceedings of the 1st Canada-US Rock Mechanics Symposium, Vancouver, Canada, 27-31 May 2007*, p.565-573.

APPENDIX A – High Speed Video Images of Selective Vermont White Marble Specimens

A.1 Introduction

High speed videos of the uniaxial compression tests conducted on forty two marble specimens by Martinez (1999) were reviewed in the present study. This appendix contains the analyses of three of the marble specimens – MA43 of flaw geometry 45-a-a, MA45 of flaw geometry 45-0-a, and MA47 of flaw geometry 45-2a-2a.

Specimen : MA43 (45-a-a)

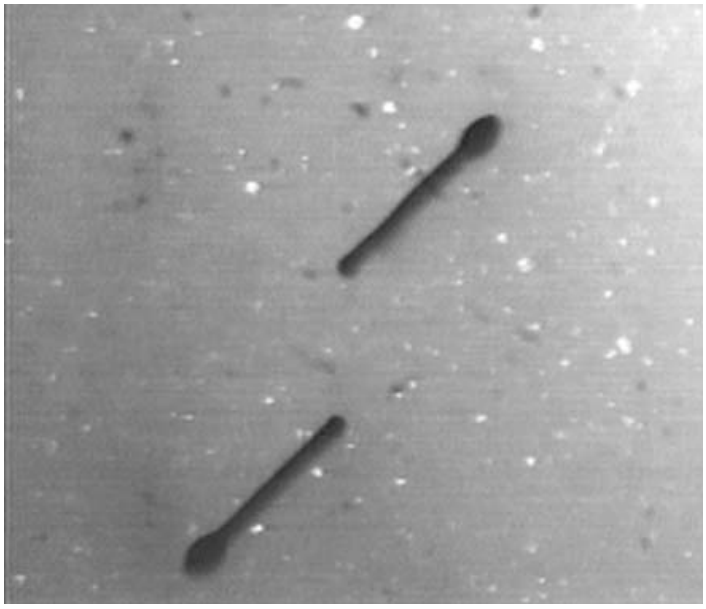	Initial flaw geometry.
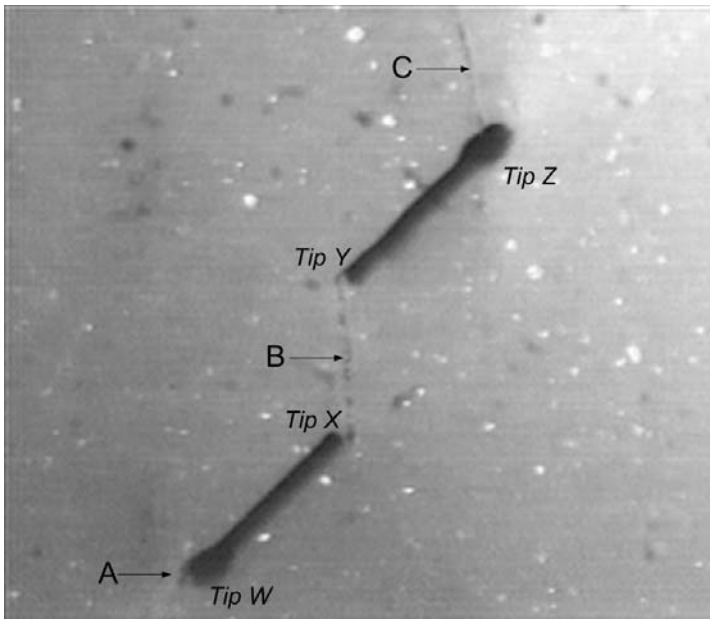	Image # - 594 Crack A initiated from the outer tip W of the lower flaw and propagated downwards. Crack B (coalescence crack) developed to link up the two inner flaw tips X and Y. The top and bottom segments of crack B were shear in origin as indicated by the local generation of shear fragments. Tensile crack C initiated close to the tip Z of the upper flaw.

Specimen : MA43 (45-a-a) (continued)

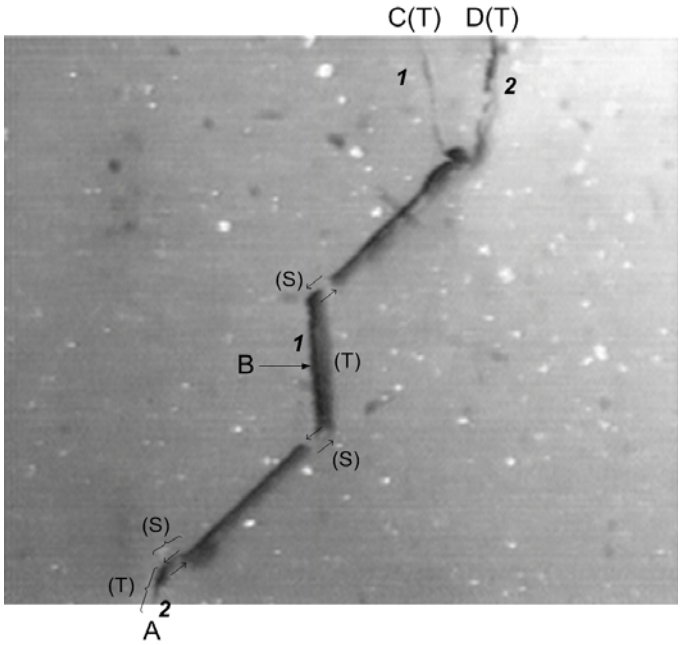

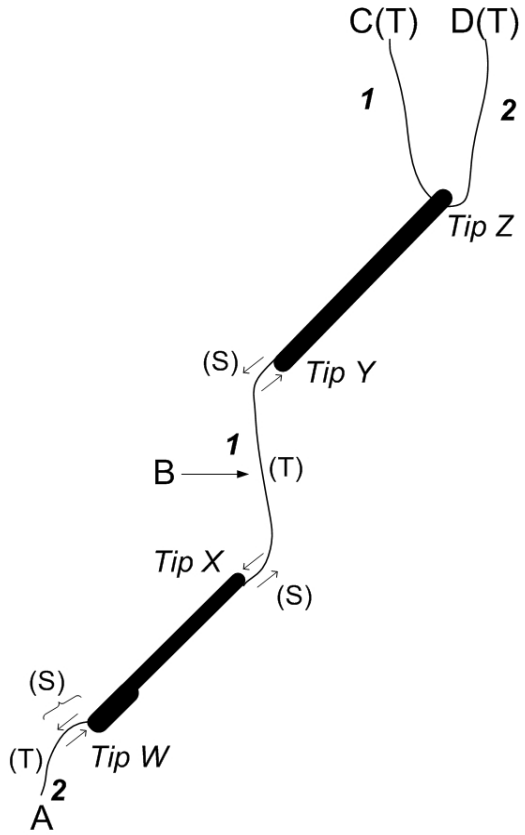

(sketch)

Image # - 554

The aperture of the two pre-existing flaws reduced. There was also a relative displacement between the upper face and lower face of the flaws. Note also the fractured tip where crack C initiated.

The aperture of cracks A and B increased.

Another new crack D (tensile) initiated at tip Z of the upper flaw.

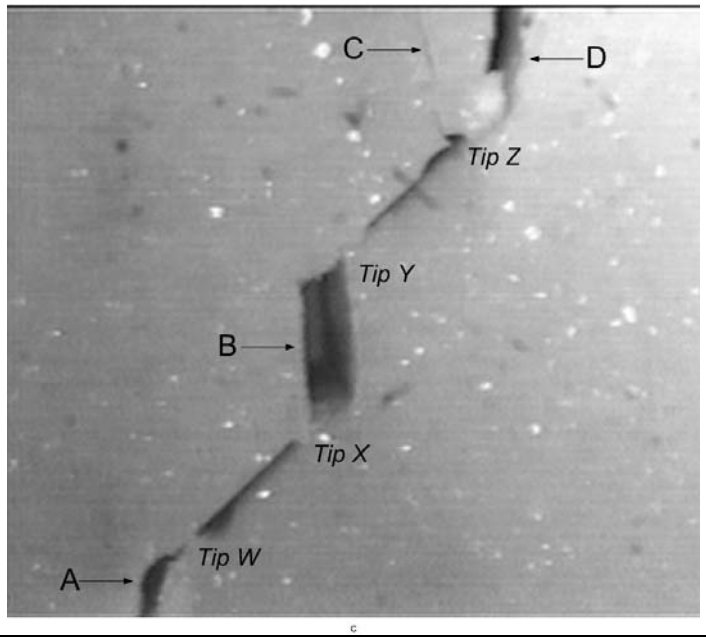	Image # - 389 Final crack configuration after substantial sliding had occurred on the two flaws.

Specimen : MA45 (45-0-a)

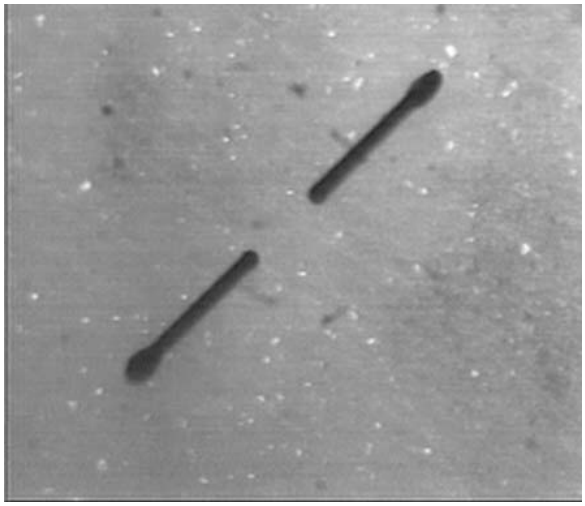	Initial flaw geometry.
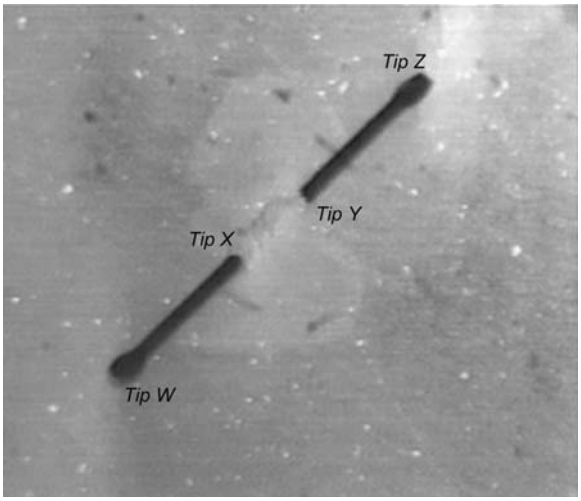 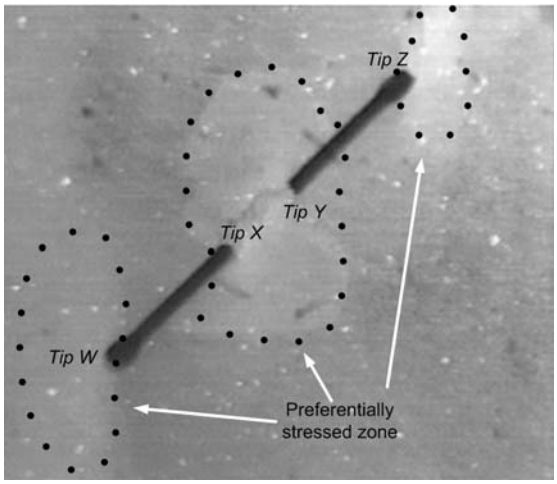	Image # - 661 A gradual whitening color change (became more light reflective) appeared between the two inner flaw tips in the central bridging region and to the surrounding of the two outer flaw tips W and Z.

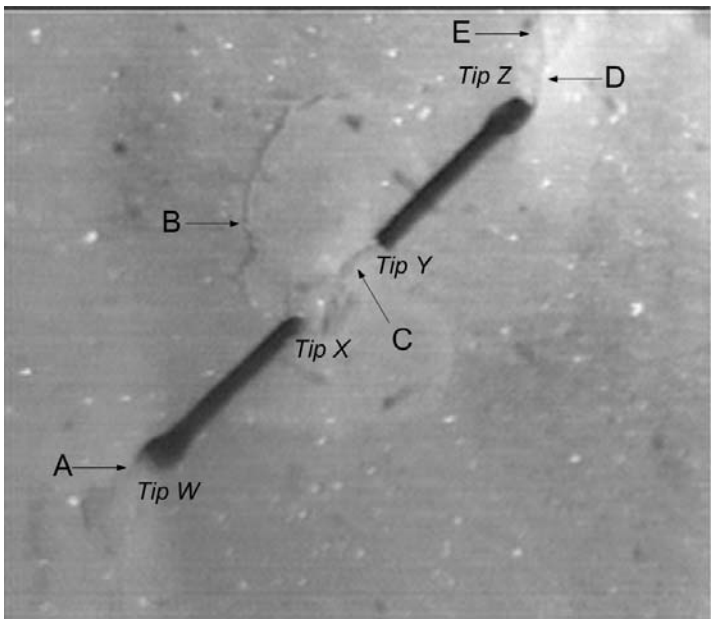

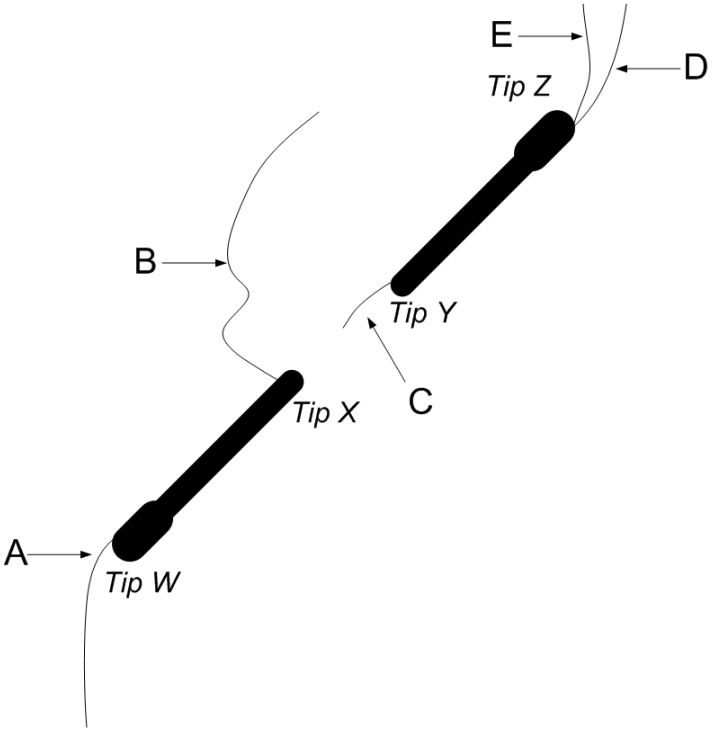

Image # - 625

Crack A (tensile) initiated from the outer tip W of the lower flaw and propagated downwards.

Crack B, which rimmed the central surface spalling, initiated near tip X of the lower flaw and propagated upwards.

Shear crack C initiated from the inner tip Y of the upper flaw and propagated into the central white zone in the bridging region.

Two cracks initiated from the outer tip Z of the upper flaw and propagated upwards – shear crack D and tensile crack E.

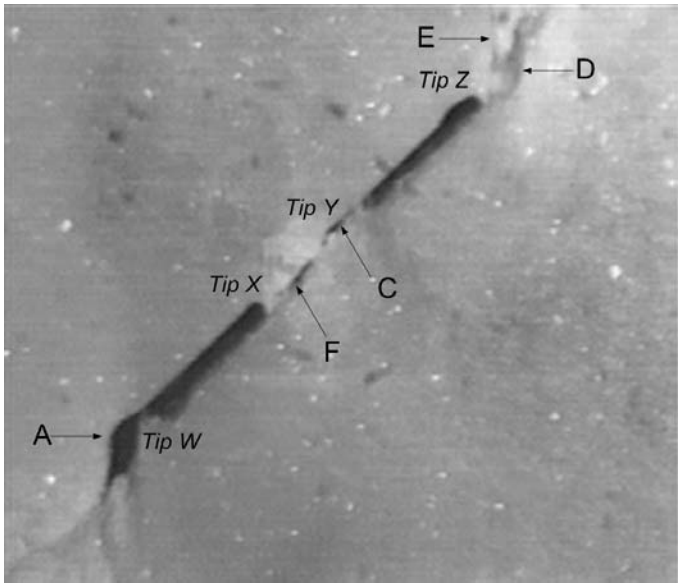

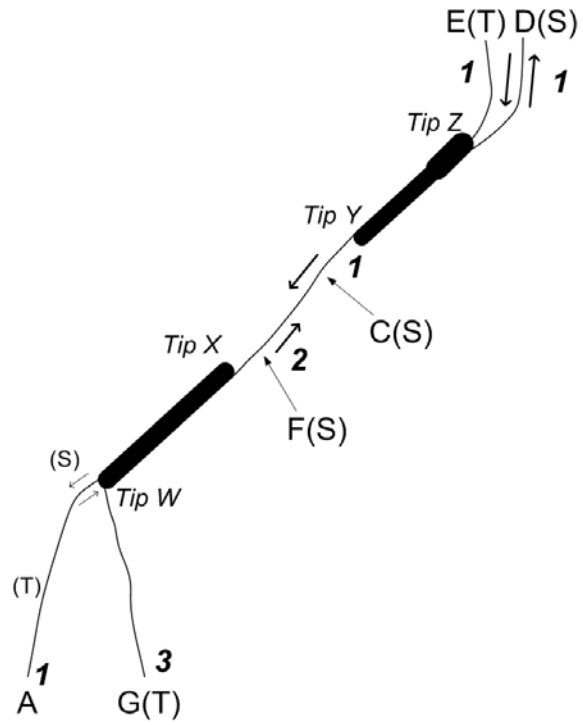

(sketch)

Image # - 595

The aperture of crack A increased and it was associated with a relative displacement between the upper face and lower face of the lower flaw.

The trace of crack B disappeared. This suggested that crack B was associated with the surface spalling of the specimen, but not through the whole specimen thickness.

A new shear crack F initiated from the inner tip X of the lower flaw and coalesced with crack C.

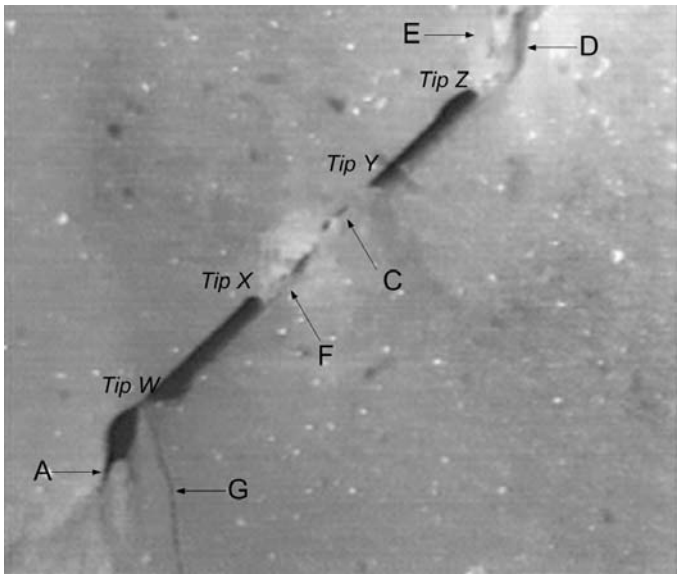

Image # - 565

Further sliding and aperture compression occurred on the two pre-existing flaws.

Another new crack G (tensile) initiated near the outer tip W of the lower flaw and propagated downwards.

Specimen : MA47 (45-2a-2a)

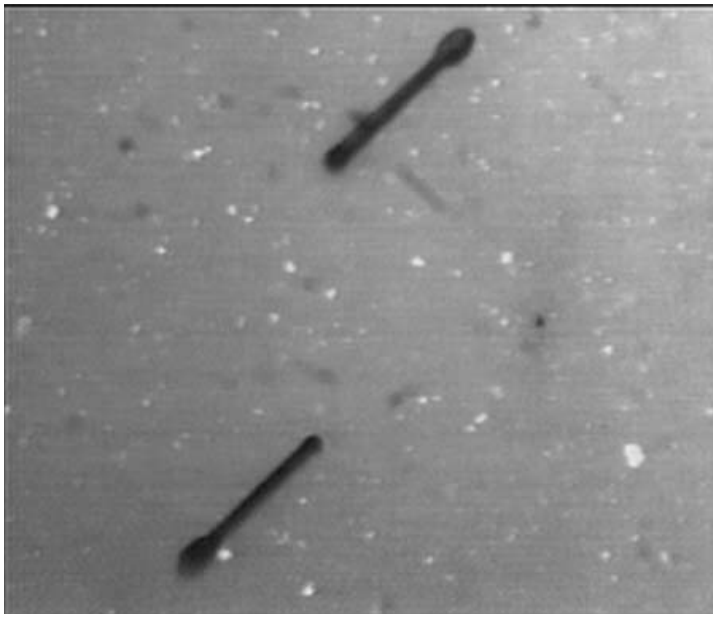	Initial flaw geometry.
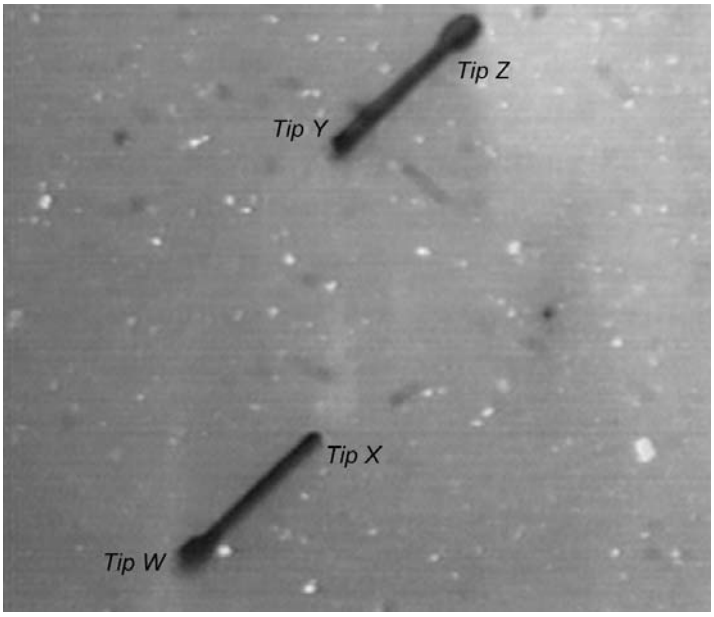	A gradual whitening color change (became more light reflective) appeared between the two inner flaw tips in the central bridging region and to the regions around the two outer flaw tips W and Z.

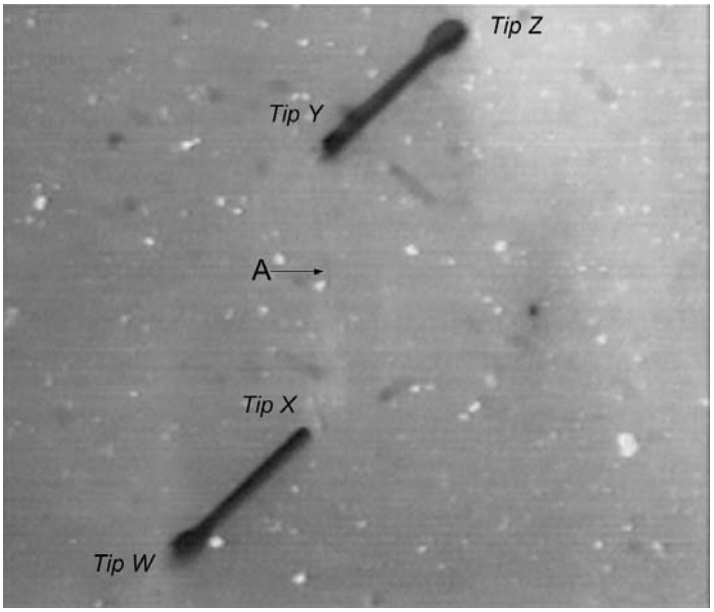

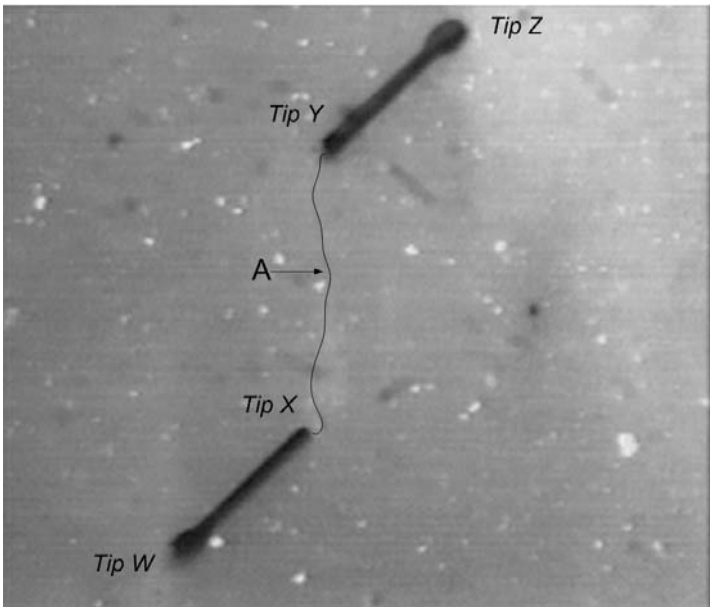

Image # - 1251

Tensile crack A (coalescence crack) initiated to link up the two inner flaw tips X and Y.

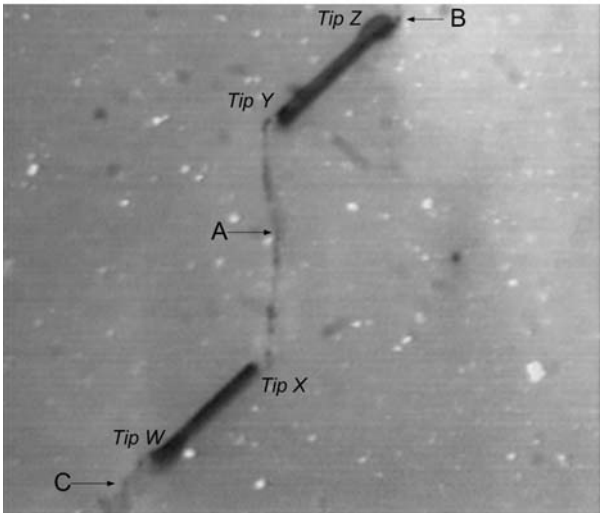	Image # - 475 Tensile crack B initiated from the outer tip of the upper flaw. Shear crack C initiated from the outer tip of the lower flaw.
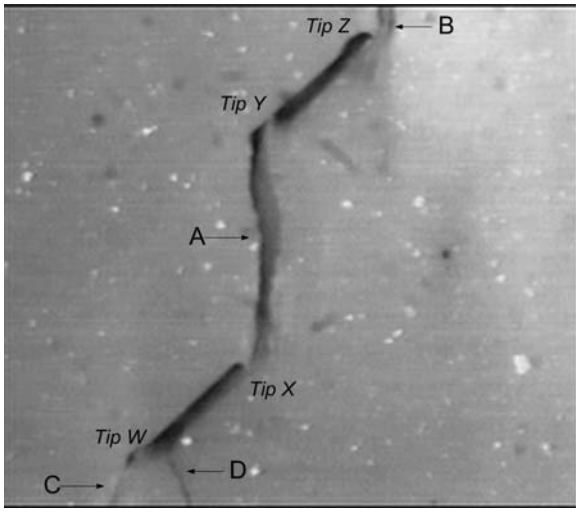 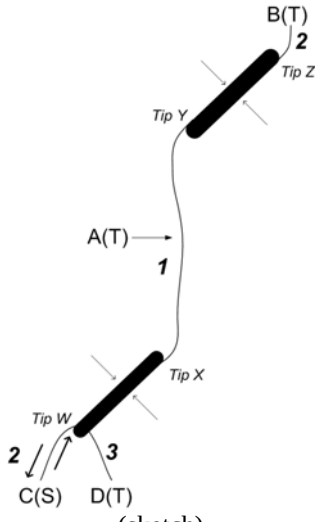 (sketch)	Image # - 464 Further relative displacement occurred between the upper face and lower face of the two pre-existing flaws and it led to substantial aperture opening of the crack A. A new tensile crack D initiated near the outer tip W of the lower flaw.

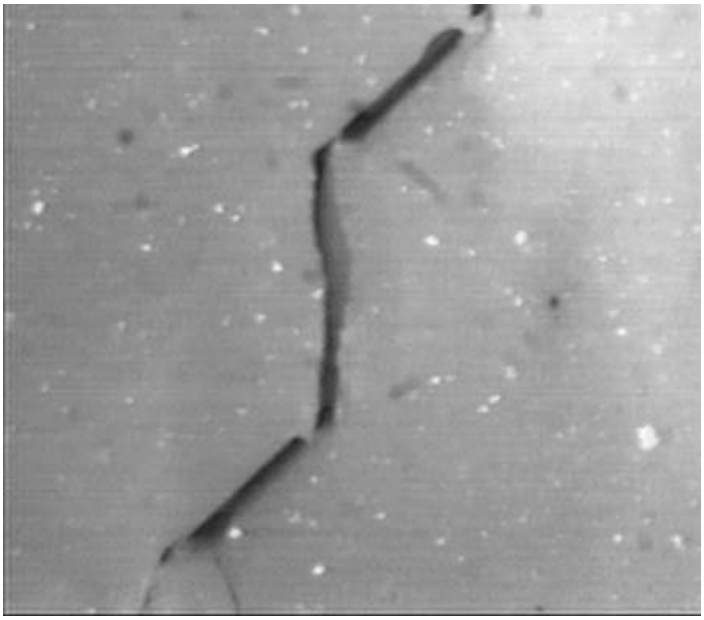	Final crack configuration.

APPENDIX B – Uniaxial Compression Tests in Uncracked Specimens

B.1 Introduction

In the previous studies conducted at MIT by Bobet (1997) and Ko (2004), compression tests on gypsum specimens were conducted four days after they were fabricated and stored in the 40^{o}C oven. In the present study, uniaxial compression tests were conducted on gypsum specimens which had been stored in the 40^{o}C oven for different lengths of time (from four days up to 76 days) since fabrication. From the pioneering study conducted by Nelson (1968) and a series of uniaxial compression tests undertaken in the present study, the length of oven storage time appears not to have a significant influence on the specimen uniaxial compressive strength (UCS) values.

B.2. Previous study

On pages 99 and 104 of his thesis, Nelson (1968) stated that.

> "*Some samples were kept in the oven for three days and some for three weeks. No definite trend of strength values as a function of length of time in the oven was noted ……If the oven temperature is kept at 105^{o}F (~40^{o}C) and a constant weight (zero excess free moisture) has been attained, additional storage time in the oven has no observable effect on strength values.*"

Nelson (1968) observed that once the mass of the oven-stored gypsum specimens reach a constant value, oven storage time would then have no significant influence on the gypsum UCS values.

B.3 Present Study

The purpose of the present study is to investigate if the strength of the prismatic gypsum specimens is sensitive to the length of oven storage time. A total number of 73 intact (with no fabricated flaws) prismatic gypsum specimens were prepared. After the specimen was left to set for about one hour after mixing, the mold was dismantled and the specimen was weighed. The time at which that first mass measurement was made was assigned as time zero. The weighed specimen was then immediately placed in the 40^{o}C oven for drying. Since then, the specimens were further weighed periodically. It was more frequent on its first half day (~1 hr interval) and less frequent in subsequent days (~1 day interval).

A series of uniaxial compression tests were then conducted on gypsum specimens which had been stored in the 40^{o}C oven for different lengths of time (from four days up to 76 days) since fabrication to determine the uniaxial compressive strength (UCS) values.

B.4 Results and Conclusions

Almost all specimens reached a constant mass after being stored for 4 days (96 hrs) to 5 days (120 hrs) in the 40^{o}C oven (figure B.1). The average percentage mass decrease (loss of water content) for all the 73 specimens was 15.4% (standard deviation of 0.36%).

The variation of specimen UCS with oven storage time is shown in figure B.2. The length of 40^{o}C oven storage time (four days or longer) appears not to have a significant influence on the uniaxial compressive strength of gypsum specimens. The average UCS value is 33.85 MPa with a standard deviation of 2.85 MPa.

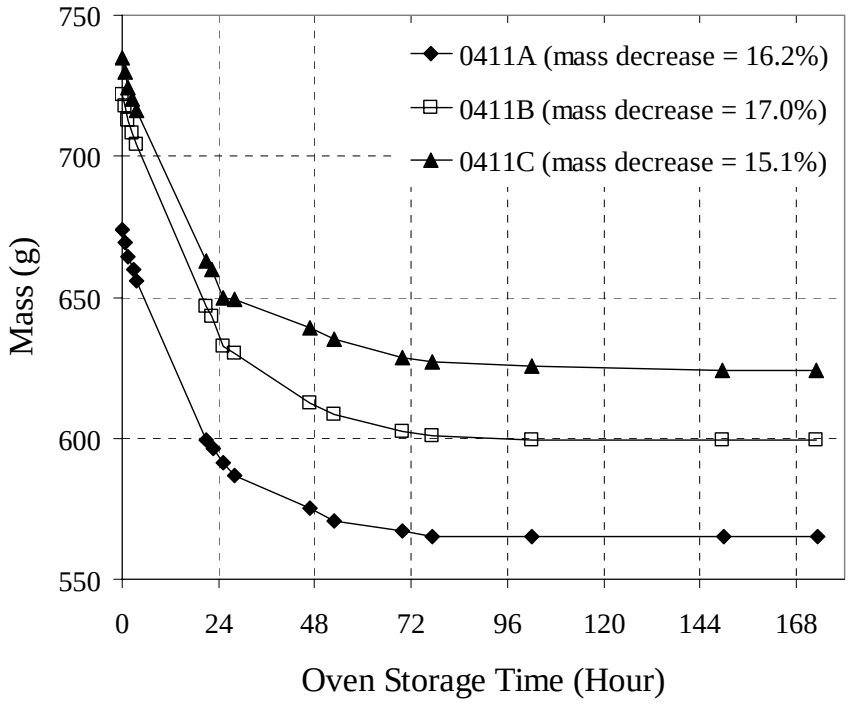

Figure B.1 – Mass variation of three gypsum specimens (0411A, 0411B & 0411C) with 40^{o}C oven storage time.

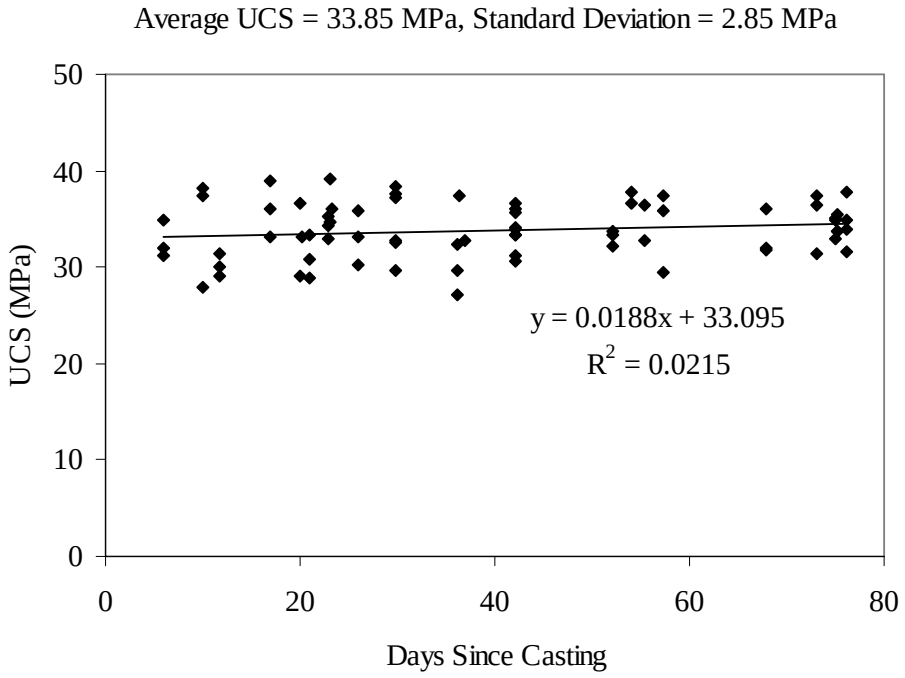

Figure B2 – Uniaxial compressive strength (UCS) of gypsum specimens versus number of days since casting.

APPENDIX C – OMAX Abrasive Jet

C.1 Introduction

The two OMAX abrasive jet machines housed in the Department of Aeronautics and Astronautics and the Hobby Shop, both at MIT, were used to create straight open flaws in marble specimens in the present study. The operation of the abrasive jet is highly computerized (figure C.1). Cutting action is achieved by ejecting a high-speed stream of garnet abrasive-laden water at a speed of about 100 feet per second from a jet nozzle onto the material (marble specimens) to be cut[1] (figure C.2). The garnet grains have a size of 75 μm. The extremely high erosive power of water stream is able to create straight flaws of rounded tips within tens of seconds.

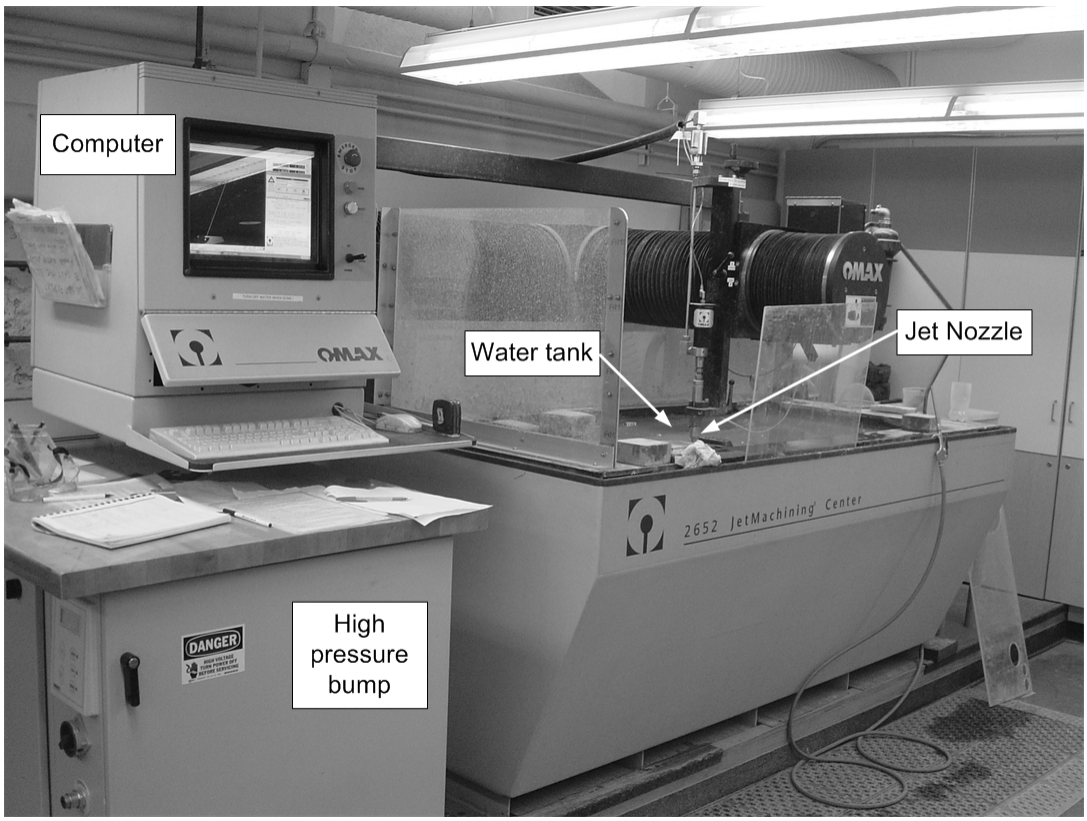

Figure C.1 – OMAX abrasive jet housed in the Department of Aeronautics and Astronautics.

[1] If only water without abrasive is used, the ejecting stream can reach a speed of 2500 ft/s (760 m/s).

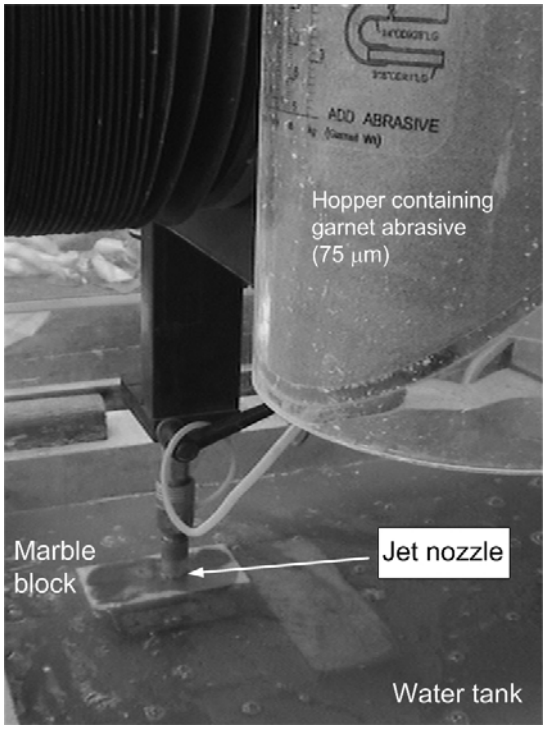

Figure C.2 – Close-up view of the jet nozzle.

C.2 Flaw-cutting procedures

The movement of the jet nozzle, hence the geometries of the lines to be cut, is pre-defined by the user. A drawing file is first created by using the drawing program called OMAX Layout (figure C.3) by the user. In this drawing file, the lines to be cut are drawn and the quality of cutting of individual lines is specified (from class 1 to class 5). The larger the number, the longer will be the cutting time and hence quality. The beginning position of the jet is defined as at the origin and multiple traverse lines are drawn to instruct the movement of the jet nozzle between the origin and the flaws, along the flaws and also between the two flaws. No cutting will be carried out along the traverse lines. Martinez (1999) noticed that bulging is more significant in the regions where the water jet first hits the specimens than in the regions where the cut ends. Since coalescence, if it occurred, is commonly achieved by cracks initiated from the inner flaw tips, cutting paths are thus all designed in a way that the cutting direction is from the outer tip towards the inner tip (see figure C.3 again).

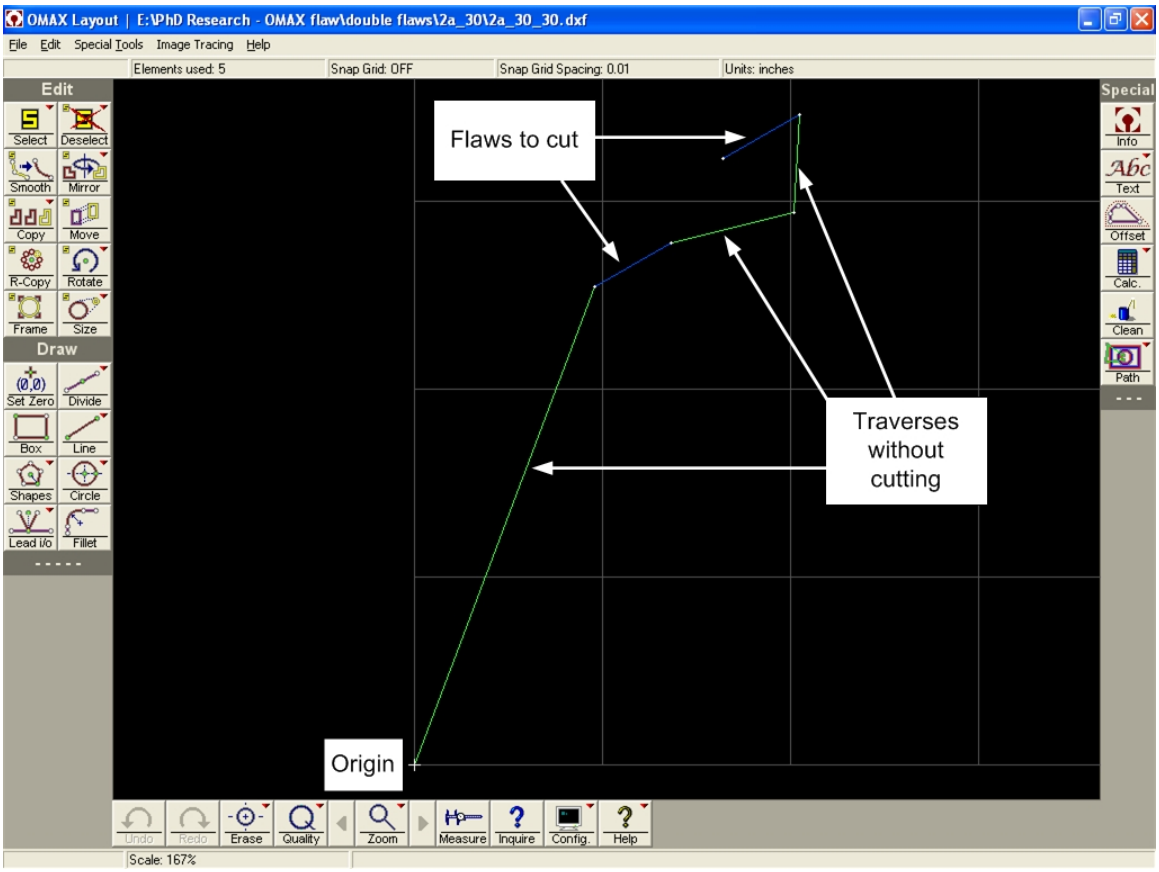

Figure C.3 – View of OMAX layout program in which the flaw geometry (2a-30-30) to be cut and the traverse paths are defined.

OMAX Make is the program to carry out the actual cutting process (figure C.4). Upon feeding the OMAX Layout drawing file into OMAX Make, the user is then asked to enter the machineability index (MI) of the material to be cut and the material thickness within the "Change Path Setup" window (figure C.5). Based on these two indexes, the jet will adjust the stream-ejecting speed and the speed of jet transverse, which both in turn control the overall erosive power and cut quality. The rules are (1) the higher the MI specified, the weaker is the erosive power, (2) the smaller the material thickness specified, the weaker is the erosive power. The OMAX Make program has a list of recommended MIs for a number of common materials. The suggested value for "Stone: White Marble" is 425.5. After these two parameters are set, the "Begin Machining" icon (enclosed by a dotted-lined rectangle in figure C.4) can be hit to start the cutting process.

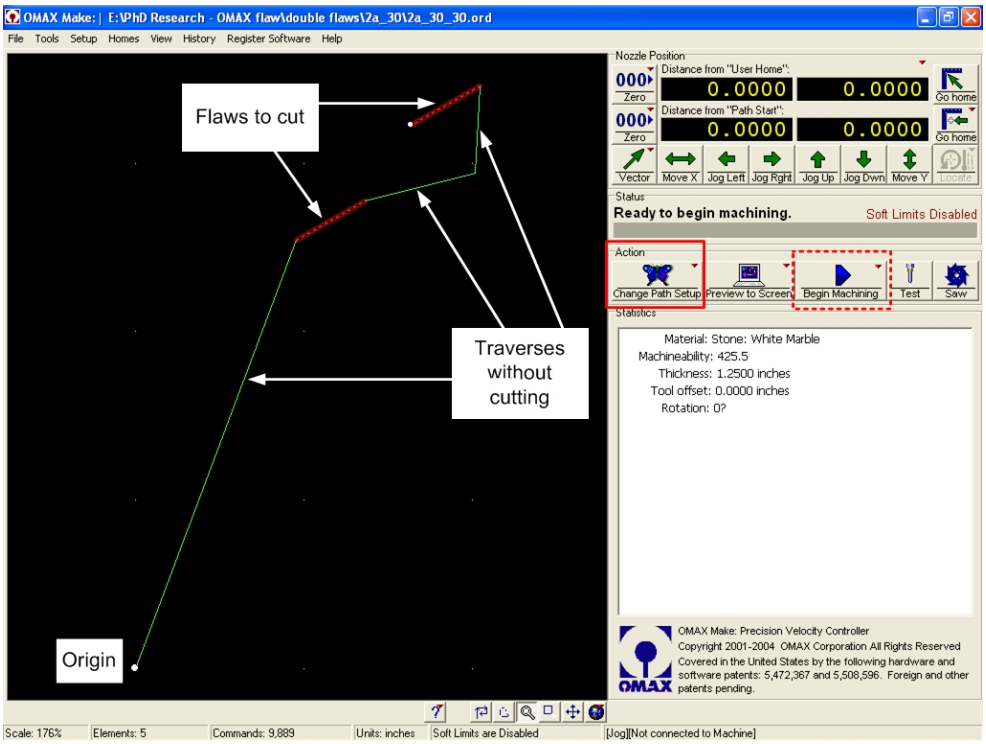

Figure C.4 – View of the OMAX Make program which carries out the cutting work of the same flaw geometry as shown in figure C.5.

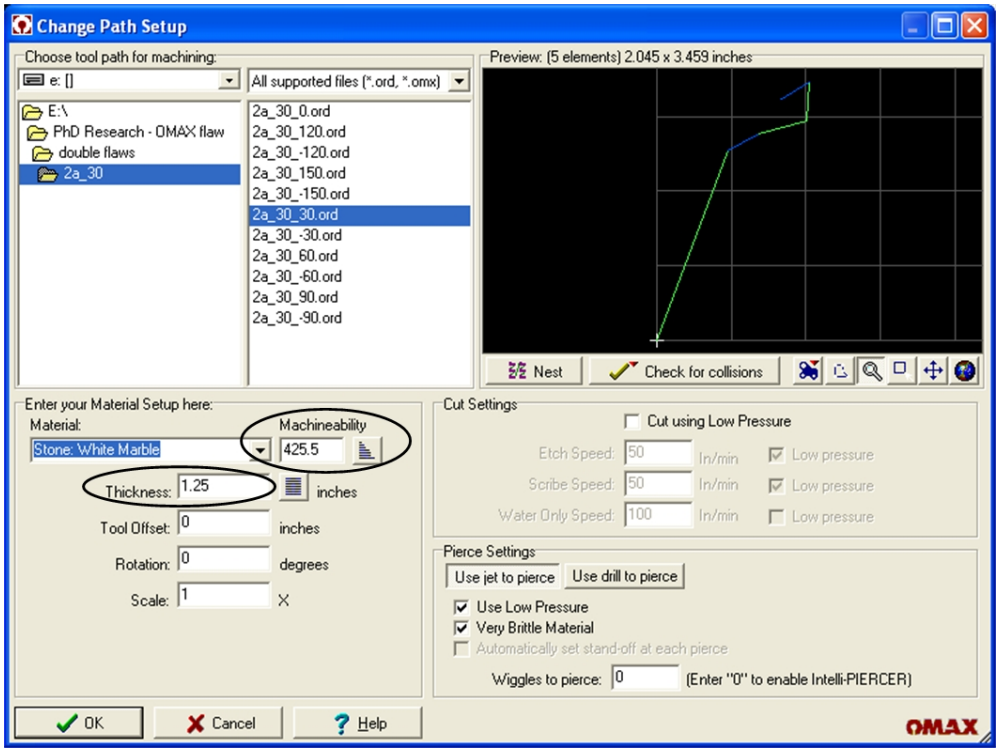

Figure C.5 – View of the “Change Path Setup” window.

A tapering effect (figure C.6) frequently occurs in abrasive jet cutting, especially when cutting thick specimens. It refers to the undesirable outcome that the flaw is wider at the top part of the specimen and narrower at the bottom part of the specimen (figure C.6). One way to overcome this undesirable effect is to run repeated cuts along the same flaw trace by traversing the jet nozzle along it multiple times.

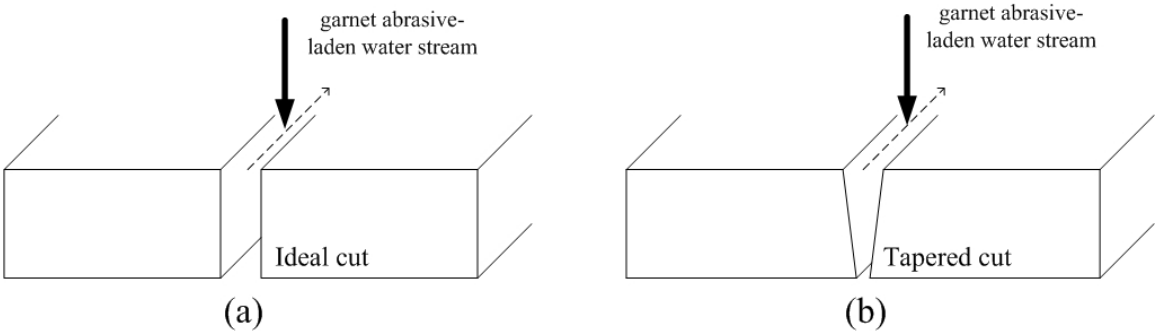

Figure C.6 – (a) Ideal situation when the two faces of the flaw cut by the abrasive jet are vertically straight and parallel to each other. (b) Usual situation where a tapered flaw is obtained. The dotted arrows indicate the moving direction of the jet nozzle.

Appendix D – Phantom High Speed Video System

D.1 Introduction

High speed video systems (or also known as high speed camera) are widely employed in various fields of research concerning motion, e.g. biomedical science, material science, chemical engineering and applied physics. In these studies, a high speed camera is used to capture images of fast moving objects or dynamic events for subsequent analysis. In the present study, a high speed camera was used to study the dynamic fracturing and crack coalescence events in brittle geo-materials (molded gypsum and Carrara marble).

D.2 Fundamentals of Phantom high speed

The V-series of high speed digital cameras manufactured by the Vision Research, Inc, were used in the present study. The operation of the high-speed cameras is controlled by a laptop computer with a pre-installed controlling software. Three different camera models have been used – Phantom V5.0, Phantom V7.1 and Phantom V9.0. The first two were on loan from the Edgerton Center of MIT, and the third one was rented from the Vision Research, Inc. Each camera essentially contains a compact unit housing a CMOS (complimentary metal-oxide semiconductor) sensor, a processor with internal operating system, and an internal memory. Specifications vary among different models, but two of the most important features affecting the present use are the maximum allowable image resolution and the size of the internal memory within the camera. The former affects the overall quality of the image, and the latter determines the length of the videos that can be captured. These two aspects are further addressed below.

The high speed cameras used in the present study, which have a limited internal memory size (1 GMb in Phantom 5.0, 2GMb in Phantom 7.1, 10 GMb in Phantom 9.0), can only hold a few seconds to tens of seconds of images. The larger the internal memory, the higher the number of images can be captured and stored. The exact number of images

can be captured also depends on the resolution of the image and the recording frame rate (e.g. 500 frames/sec vs 3000 frames/sec), which are keyed in by the user before the start of the experiment (figure D.1).

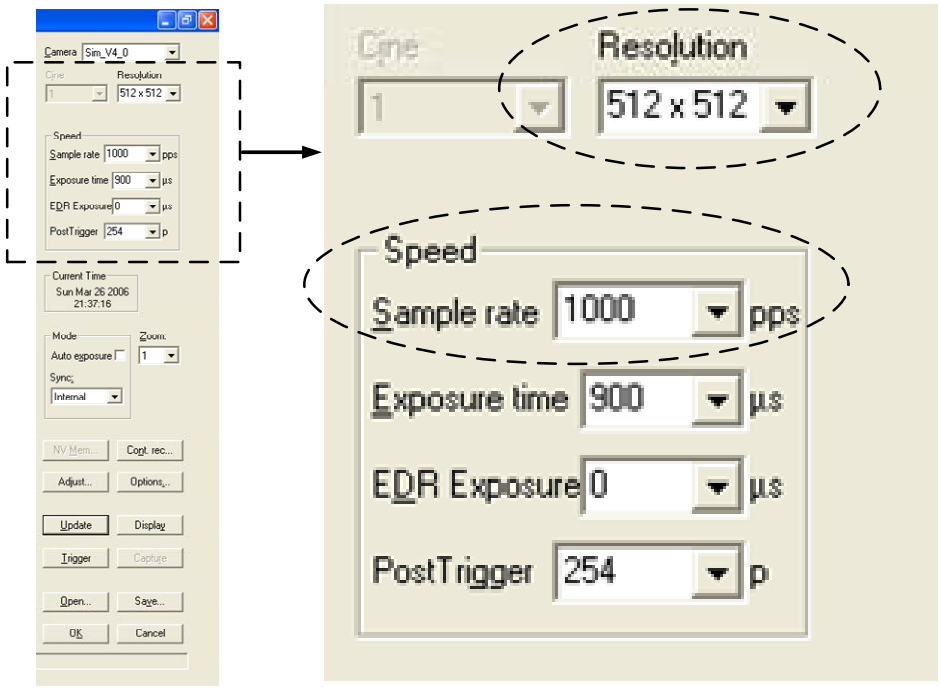

Figure D.1 – The user needs to pre-set the image resolution and the image sample rate before recording.

The lower the resolution, the higher will be the number of images allowed to be captured. Similarly, the lower the recording frame rate, the higher will also be the number of images allowed to be captured, which means that events happening over a longer period of time can be monitored. Some of the settings for Phantom V5.0 are illustrated in the table D.1. For instance, a combination of a 1024 x 1024 pixels resolution at a frame rate of 1000 pictures per second (pps) can only capture images spanning over one second. By adopting an appropriate sample rate and an image resolution, it is thus possible to view the cracking mechanisms precisely and with sufficient details, in particular to determine if shear or tensile fracturing takes place.

Pre-set image resolution (pixels)	Pre-set frame rate (pictures per second)	Duration of videos to be captured (seconds)
1024 x 1024	1000	1
512 x 512	4000	1
512 x 512	1000	4

Table D.1 – Relationship between image resolution, frame rate and duration of videos.

D.3 Video capturing mechanism

When the image resolution, frame rate and other image quality settings have been entered by the user, the camera can be set to the recording mode by hitting the **Cont. Rec.** (representing continuous recording) icon on the controlling laptop computer. After that, images are continuously fed into the camera and stored in its internal memory. Due to the limited internal memory size as discussed above, only a finite number of images can be stored in the camera. The earliest-captured images would thus be continuously discarded and replaced by the most recent images, i.e. the images stored in the camera are in a volatile state. In order to store the images permanently in a non-volatile state, the user needs to hit the **Trigger** icon on the controlling laptop computer. After that, the captured images are securely saved in the camera and no longer volatile, which can then be exported to an external storage medium, e.g. a DVD burner.

Apart from the human trigger, the high speed camera has also an automatic trigger based on specific detectable physical changes such as sudden increase of sound level or change of light intensity. Although the initiation of coalescence cracks is accompanied by these physical changes, the adoption of an automatic trigger is found unsuitable in the present study. It is due to the fact that coalescence crack, which is the research objective, is not the only crack to develop in rock specimens during the loading process. Other cracking events, such as local surface spalling or initiation of cracks other than coalescence cracks, usually occur prior to the crack coalescence. The camera will then be triggered too early to capture these cracking events and fails to capture the coalescence crack.

There is always an inevitable reaction time lag between the recognition of coalescence and the human trigger on laptop computer. There is however a built-in feature of the camera which can handle the time lag. Before the start of the experiment, in addition to the resolution and frame rate, the user is also asked to specify the **Post Trigger** value, which is also under the speed category (figure D.2). As shown in the bottom part of figure D.2, 509 images which span over 0.5 seconds can be captured. By setting the **Post Trigger** value to 1, one image after the moment of trigger and 508 (= 509 - 1) images acquired at and before the moment of trigger can be saved (figure D.3). By setting it to different values, the proportion of the number of images captured after and before the trigger can vary (see the example (b) in figure D.3). To best accommodate the human reaction time, the **Post Trigger** value is usually set to 1.

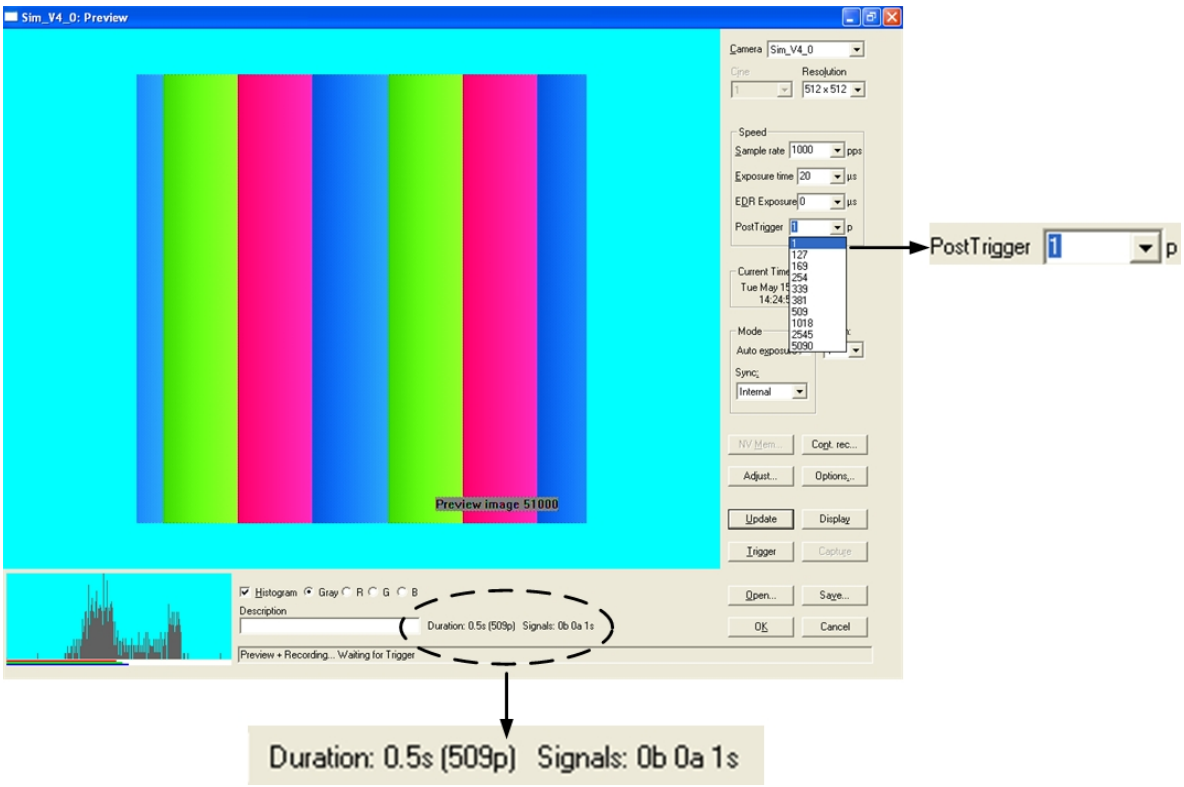

Figure D.2 – The user needs to specify the number of post trigger images to be captured.

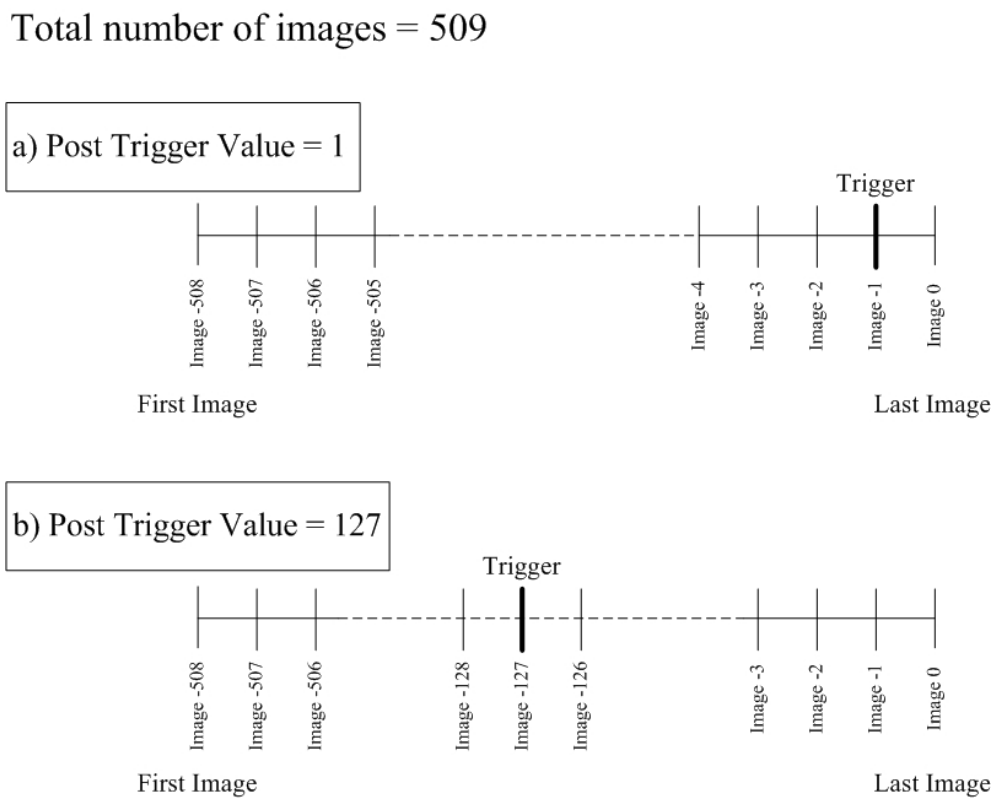

Figure D.3 – Setting different post-trigger values (1 *vs* 127) lead to different number of images acquired before and after the time of trigger. The total number of images of 509 remains the same in both cases.

The above details about the triggering and image capturing mechanism of the Phantom high speed cameras are schematically illustrated in figure D.4. At time ***t = 0***, which is shown on the left of the time line, vertical uniaxial loading begins to be applied to a prismatic rock specimen. When a certain amount of load has been applied, some cracks, but usually not the coalescence cracks (tensile wing cracks as shown in this example) initiate. Further loading subsequently leads to the initiation of a coalescence crack. In this example, it is a crack which links up the two inner flaw tips. This coalescence event is observed and recognized by the experimenter who then hits the **Trigger** icon on the laptop computer in order to permanently save the images in the camera. Since the total span of the final video recording (2.0375 seconds) is much longer than the human reaction time, the time lag between the occurrence of coalescence event and the human

trigger can be accommodated. Images containing the coalescence event can thus be captured.

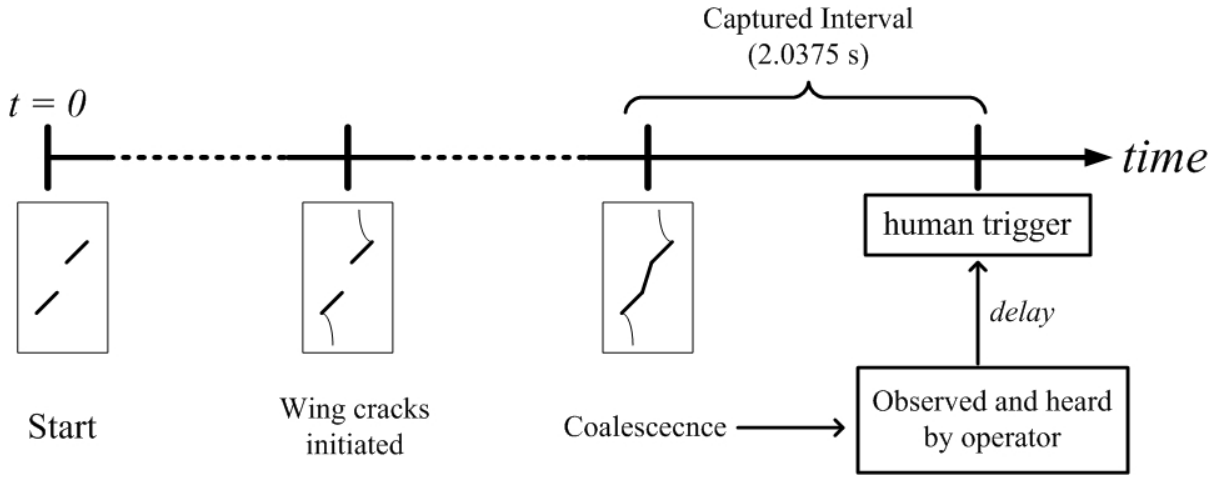

Figure D.4 – High speed video system is triggered after the occurrence of coalescence. In this example, the following high speed camera settings are used – 2000 frames per second, 512 x 512 pixels. 4075 images which span over 2.0375 seconds can eventually be captured.

APPENDIX E – Test Results of Gypsum Specimens Containing Narrow Single Flaws

In this appendix, sketches of cracking patterns observed in all gypsum specimens containing narrow single flaws (0.004" aperture) are illustrated. Refer to section 3.5 for the meaning of the symbols used in the sketches. In some specimens where the initiation of certain crack(s) is identified with confidence to be concurrent with specimen failure, these cracks are also labeled as **"failure"** in the sketches. The cracking phenomena for each flaw inclination group are also generalized below the sketches.

The total number of specimens successfully tested for each flaw inclination is summarized below.

Flaw inclination angle (^{o})	Number
0	4
15	6
30	6
35	2
40	5
45	2
50	7
55	3
60	7
70	3
75	3
	48 (total)

Flaw Inclination – 0°	
20050401A 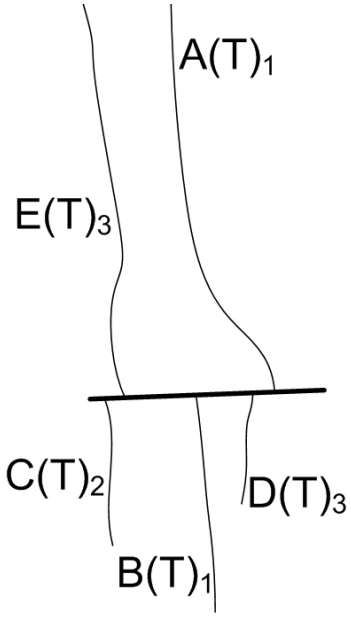 camcorder	20050405A 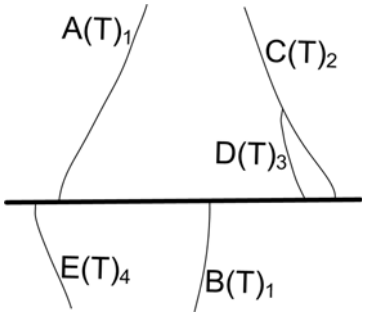 camcorder
20050405D 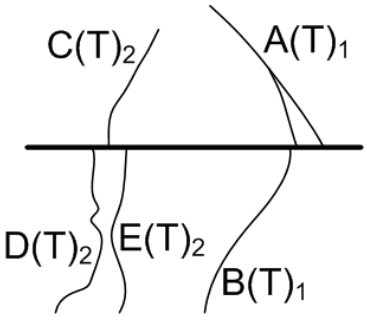 camcorder	20050531B 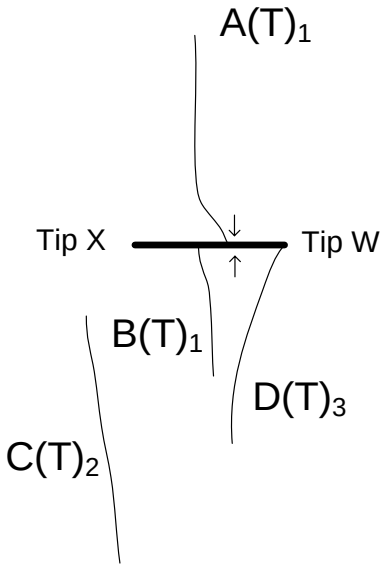

Flaw Inclination – 0^o (continued)

Notes:

- Curvilinear tensile wing cracks A and B were always the first cracks to initiate from the pre-existing flaws at a distance away from the flaw tips. These tensile wing cracks developed as a pair, one from the upper face of the pre-existing flaw and one from the lower face of the pre-existing flaw. These two cracks initiated simultaneously well before the specimen failure.

- Additional cracks initiated when the maximum strength of the specimen was reached or overcome. Some of these cracks initiated from the tips of the pre-existing flaws, and some initiated on the pre-existing flaw faces at a distance away from the tips.

- The aperture of the pre-existing flaw was almost completely closed at the end of the loading process.

Flaw Inclination – 15°	
20050317F 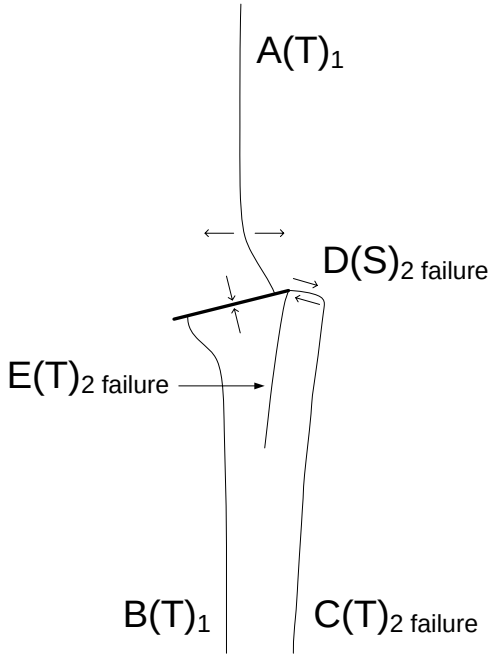 	20050317I 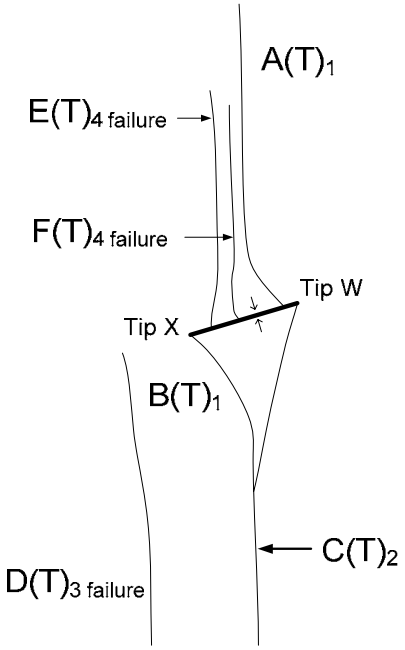
20050318A 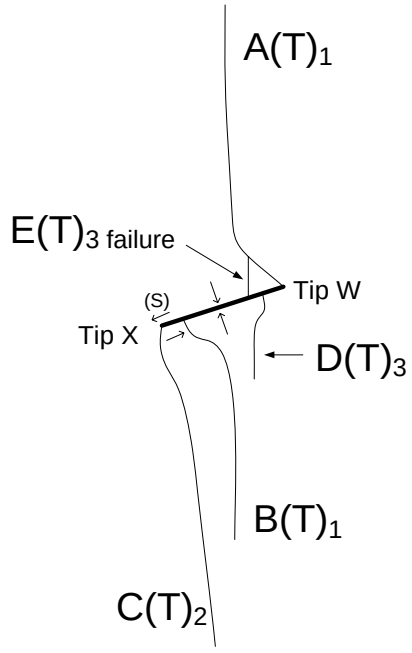 Additional cracks developed in other parts of the specimen when the specimen strength was reached or overcome are not shown.	20050318F 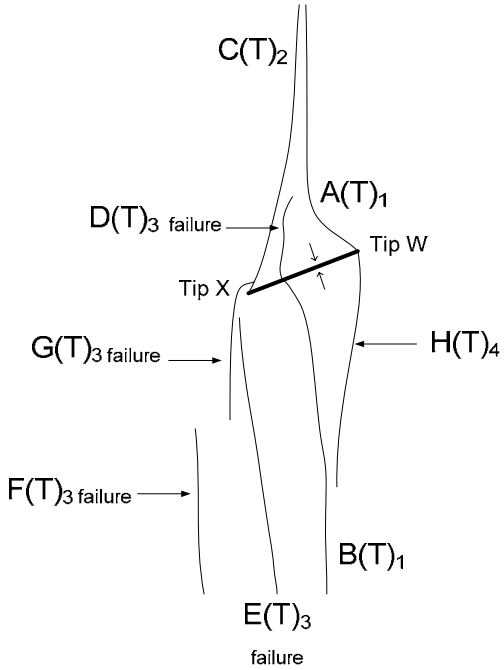 Additional cracks developed in other parts of the specimen when the specimen strength was reached or overcome are not shown.

Flaw Inclination – 15^{o} (continued)

20050318G

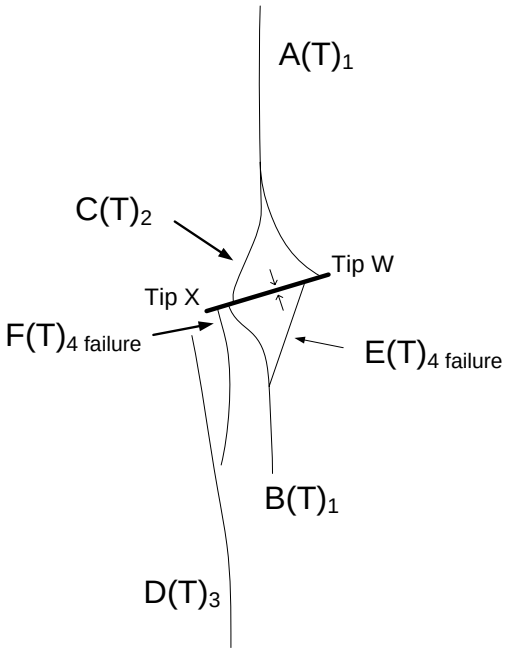

Additional cracks developed in other parts of the specimen when the specimen strength was reached or overcome are not shown.

20050318I

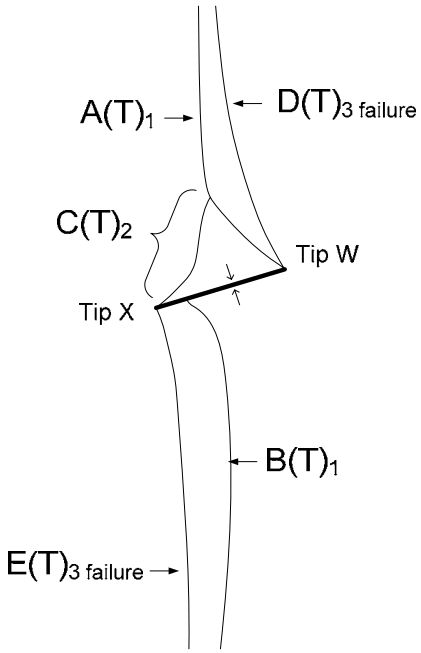

Additional cracks developed in other parts of the specimen when the specimen strength was reached or overcome are not shown.

Notes:

- Curvilinear tensile wing cracks A and B were always the first cracks to initiate from the pre-existing flaws – some at the tips and some at a distance away from the end tips. These tensile wing cracks developed as a pair, one from the upper face of the pre-existing flaw and one from the lower face of the pre-existing flaw. These two cracks initiated simultaneously well before the specimen failure.

- Additional cracks initiated when the maximum strength of the specimen was reached or overcome. Some of these cracks initiated from the tips of the pre-existing flaws and some at a distance away from the flaw tips.

- The aperture of the pre-existing flaw was almost completely closed at the end of the loading process.

Flaw Inclination – 30°

20050317G

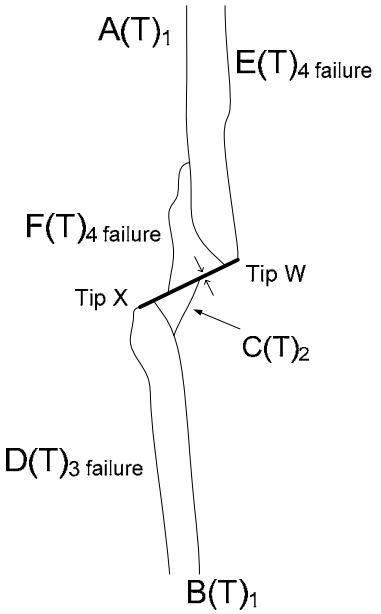

Additional cracks developed in other parts of the specimen when the specimen strength was reached or overcome are not shown.

20050317J

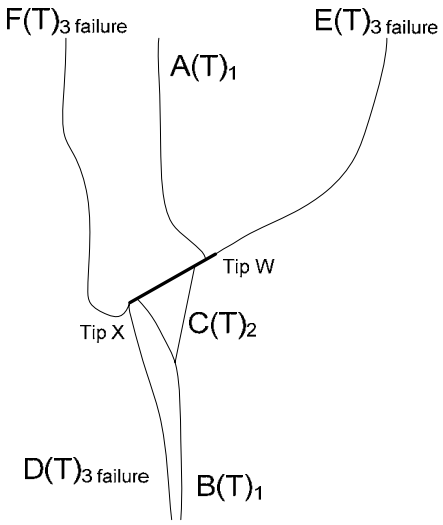

The aperture of the pre-existing flaw **was not closed** at the end of the loading test.

20050318B

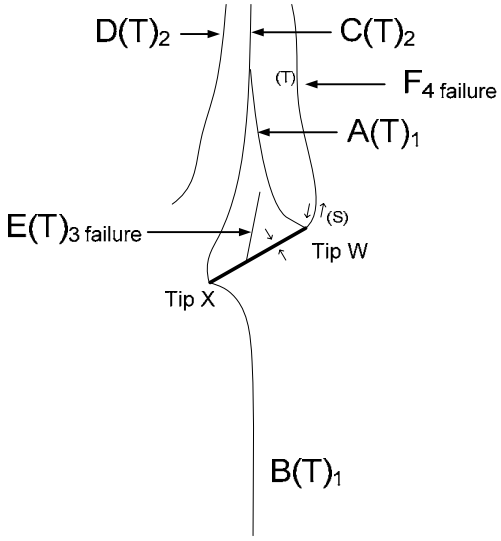

Additional cracks developed in other parts of the specimen when the specimen strength was reached or overcome are not shown.

20050318D

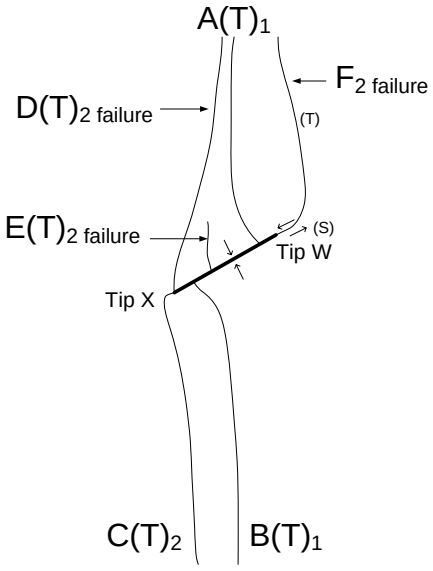

Additional cracks developed in other parts of the specimen when the specimen strength was reached or overcome are not shown.

Flaw Inclination – 30^{o} (continued)

20050318H

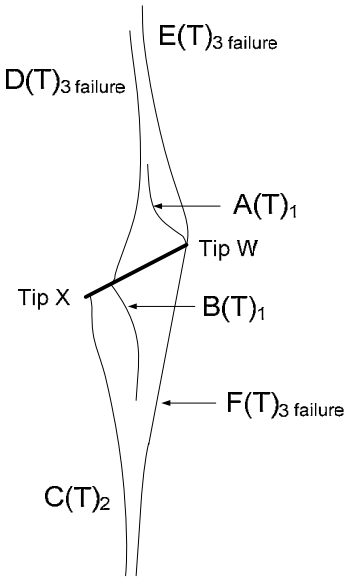

The aperture of the pre-existing flaw was slightly reduced at the end of the loading test.

20050318J

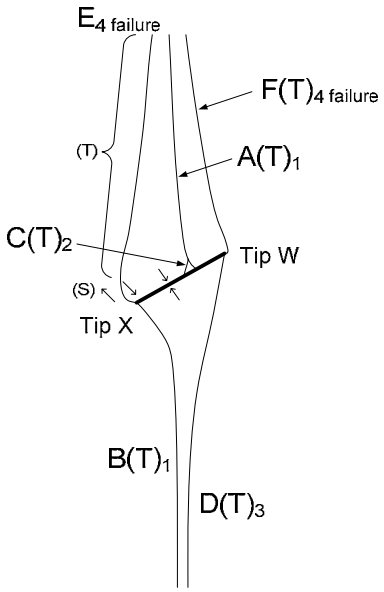

The aperture of the pre-existing flaw was slightly reduced at the end of the loading test.

Notes:

- Curvilinear tensile wing cracks A and B were always the first cracks to initiate from the pre-existing flaws – some at the tips and some at a distance away from the end tips. These tensile wing cracks developed as a pair, one from the upper face of the pre-existing flaw and one from the lower face of the pre-existing flaw. These two cracks initiated simultaneously well before the specimen failure.

- Additional cracks initiated when the maximum strength of the specimen was reached or overcome. Many of these cracks initiated from the tips of the pre-existing flaws, while only few initiated in the middle portions of the pre-existing flaws (cracks E in 20050318B & 20050318D). These cracks initiated from the tips were generally oriented coplanar with the loading direction. They were type 2 tensile cracks (cracks E in 20050317G, 20050317J, 20050318H, crack F in 20050318J), and mixed tensile-shear crack (cracks F in 20050318B, 20050318D, crack E in 20050318J) according to the crack type classification scheme in figure 2.15.

- At the end of the loading process, some flaws were partially closed, and some were completely closed.

Flaw Inclination – 35°	
20050118C 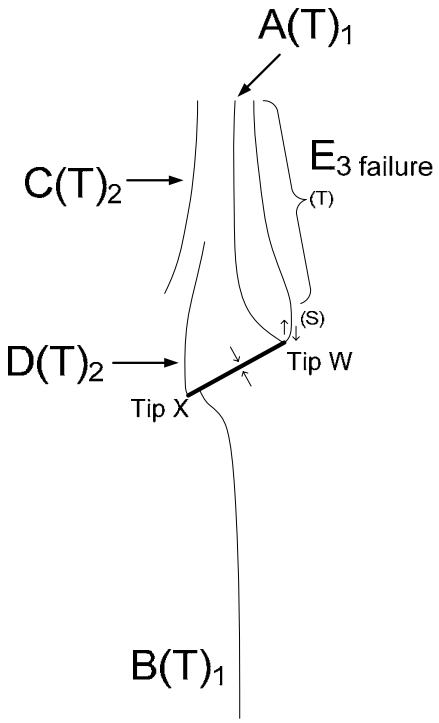 	20050317C 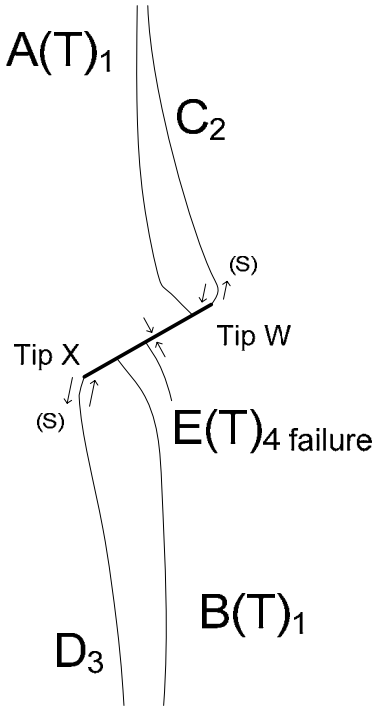

Notes:

- Curvilinear tensile wing cracks A and B were always the first cracks to initiate from the pre-existing flaws close to the end tips and at the tips. These tensile wing cracks developed as a pair, one from the upper face of the pre-existing flaw and one from the lower face of the pre-existing flaw. These two cracks initiated simultaneously well before the specimen failure.

- Additional cracks initiated when the maximum strength of the specimen was reached or overcome. These cracks generally initiated from the tips of the pre-existing flaws and they displayed a shear-tensile (S-T) character, i.e. the segments closer to the flaw tips were shear and the segments closer to the steel brush were tensile. They were mixed tensile-shear according to the crack type classification scheme in figure 2.15.

- The aperture of the pre-existing flaw was partially closed at the end of the loading process.

Flaw Inclination – 40°

20050327A

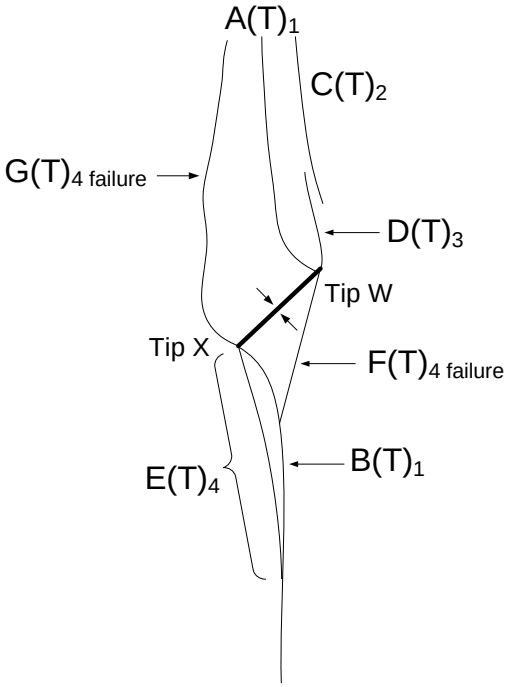

20050729L

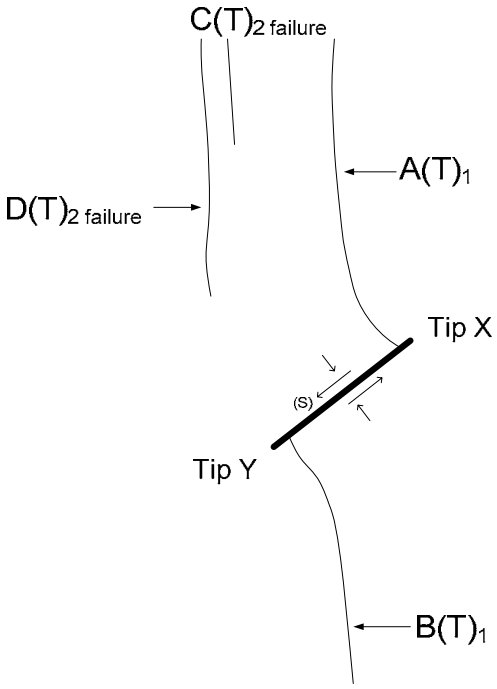

20050729M

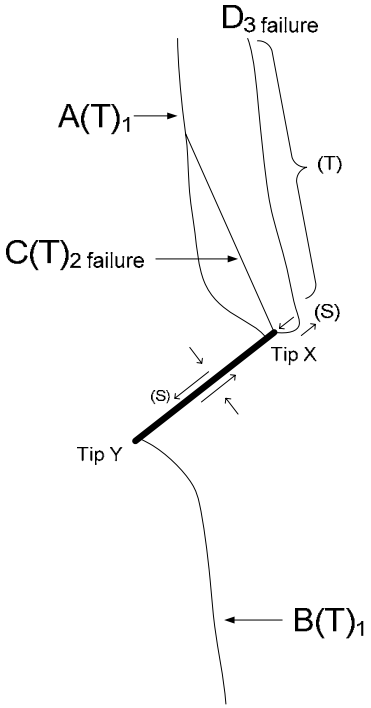

20050729P

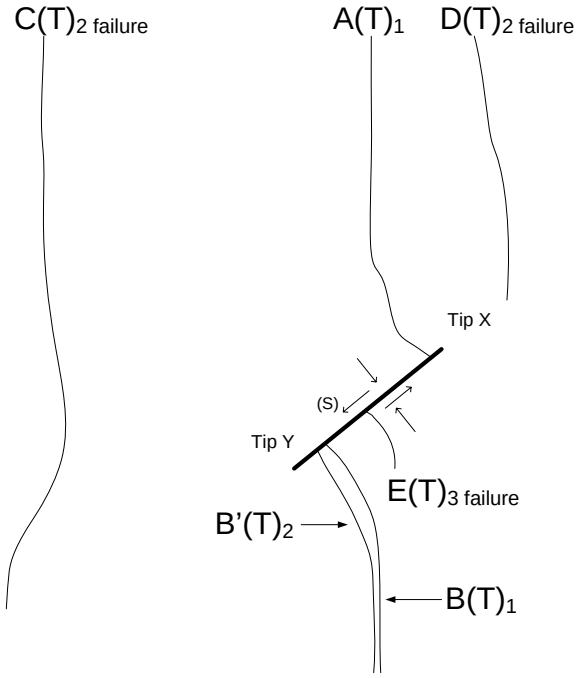

Flaw Inclination – 40^{o} (continued)

20050729Q

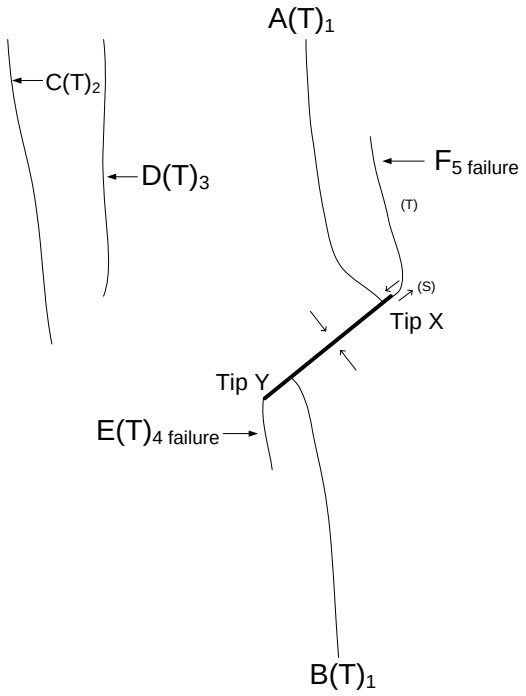

Notes:

- Curvilinear tensile wing cracks A and B were always the first cracks to initiate from the pre-existing flaws close to and at the flaw tips. These tensile wing cracks developed as a pair, one from the upper face of the pre-existing flaw and one from the lower face of the pre-existing flaw. These two cracks initiated simultaneously just before the specimen failure.

- Additional cracks initiated when the maximum strength of the specimen was reached or overcome. Some of these cracks – type 2 tensile crack (crack E in 20050729Q) and mixed tensile-shear cracks (crack D in 20050729M & crack F in 20050729Q) initiated from the tips of the pre-existing flaws, while some initiated at a distance from the end tips (e.g. crack E in 20050729P).

- The aperture of the pre-existing flaw was reduced at the end of the loading process, and there was an observable relative shear displacement between the upper half and lower half of the pre-existing flaw.

Flaw Inclination – 45^{o}	
20050327B 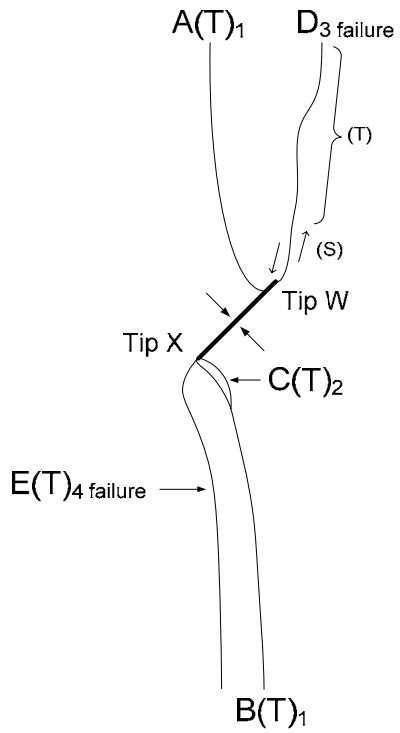	20050328A 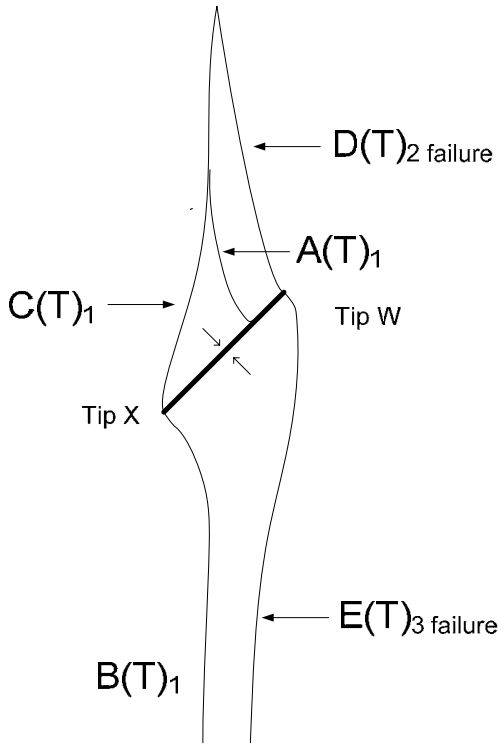

Notes:

- Curvilinear tensile wing cracks A and B, which were always the first cracks to initiate from the pre-existing flaws, initiated at the tips and at a short distance away from the tips of the pre-existing flaws.

- These tensile wing cracks developed as a pair, one from the upper face of the pre-existing flaw and one from the lower face of the pre-existing flaw. These two cracks initiated simultaneously.

- Additional cracks initiated when the maximum strength of the specimen was reached or overcome. These cracks were type 1 tensile crack (crack D in 20050328A), type 2 tensile cracks (cracks E in 20050327B & 20050328A) or mixed tensile-shear crack (crack D in 20050327A) according to the classification scheme shown in figure 2.15.

- The aperture of the pre-existing flaws was substantially reduced at the end of the loading processes.

Flaw Inclination – 50°

20050328B

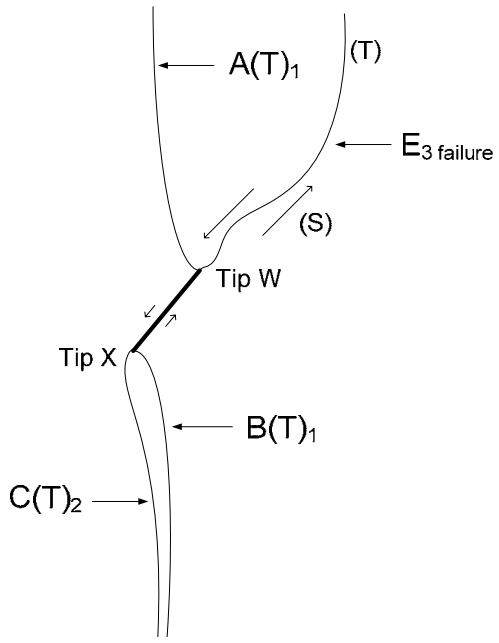

Aperture of the pre-existing flaw was not closed.

20050705I

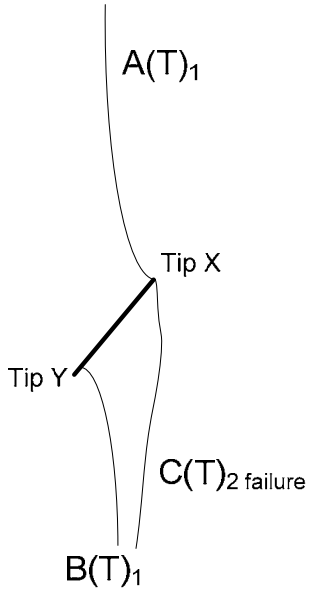

Aperture of the pre-existing flaw was not closed. Additional cracks developed in other parts of the specimen when the specimen strength was reached or overcome.

20050705L

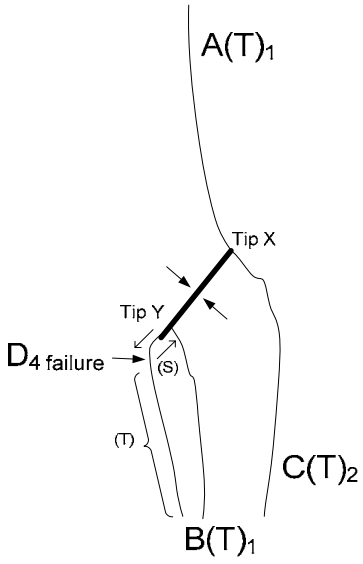

Aperture of the pre-existing flaw was closed. Sliding occurred along the pre-existing flaw.

20050712A

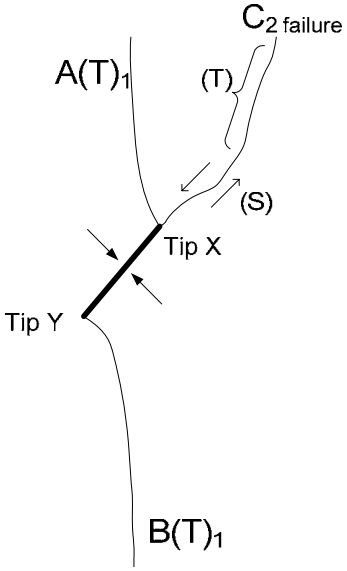

Aperture of the pre-existing flaw was closed.

Flaw Inclination – 50^{o} (continued)

20050712D

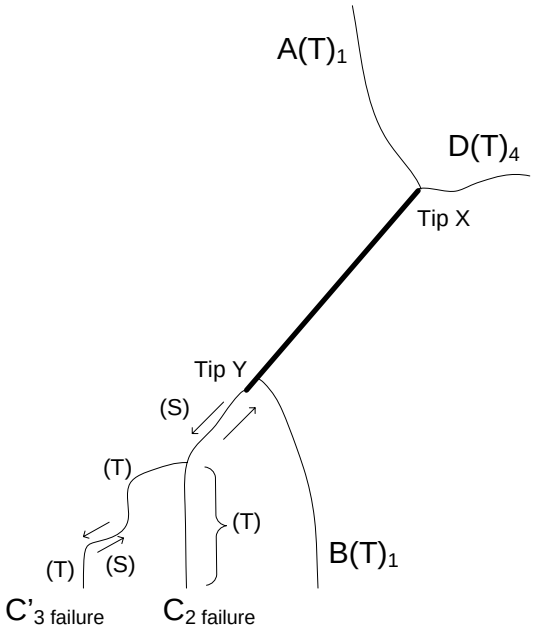

20050712F

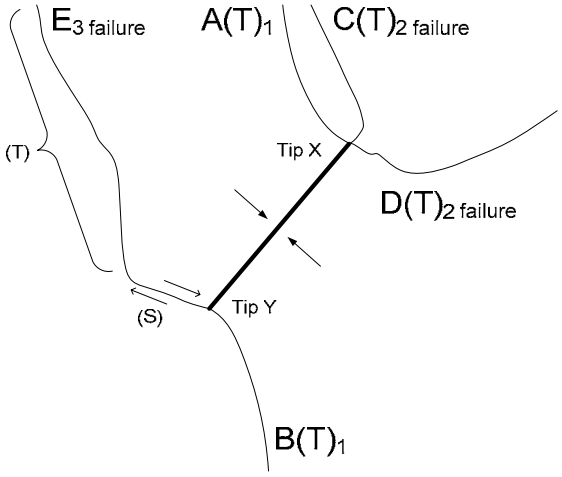

20050729R

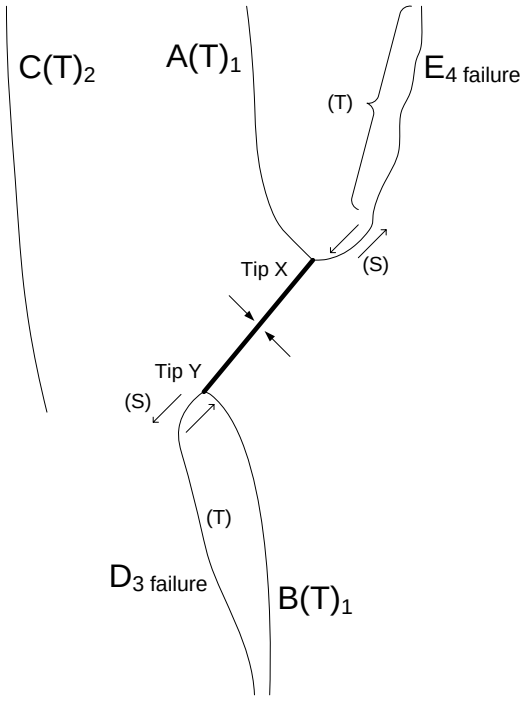

Flaw Inclination – 50^{o} (continued)

Notes:

- Curvilinear tensile wing cracks A and B were the first cracks to initiate and most of them initiated from the tips of the pre-existing flaws.

- Other than the pair of tensile wing cracks, few other cracks initiated from the pre-existing flaws during the whole course of loading process before specimen failure

- Additional cracks initiated when the maximum strength of the specimen was reached or overcome. These cracks were type 2 tensile cracks (cracks C in 20050328B & 20050712F), and mixed tensile-shear crack in all specimens according to the classification scheme shown in figure 2.15.

Flaw Inclination – 55^{o}		
20050118A	20050118D	20050317D
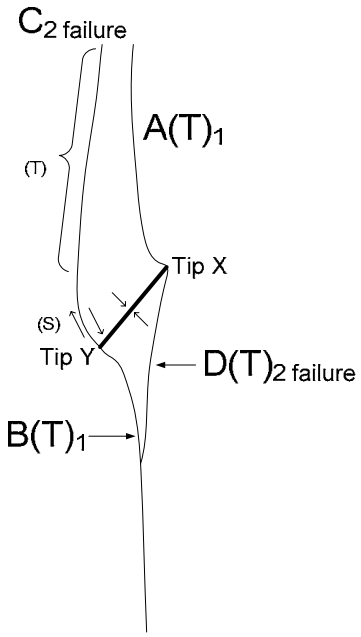	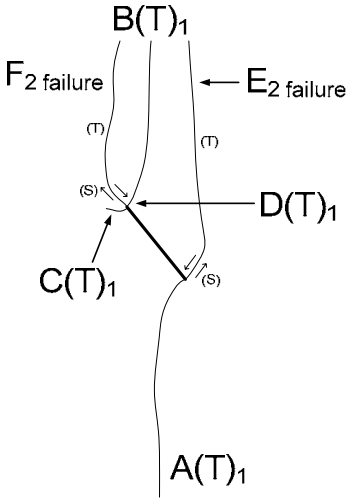	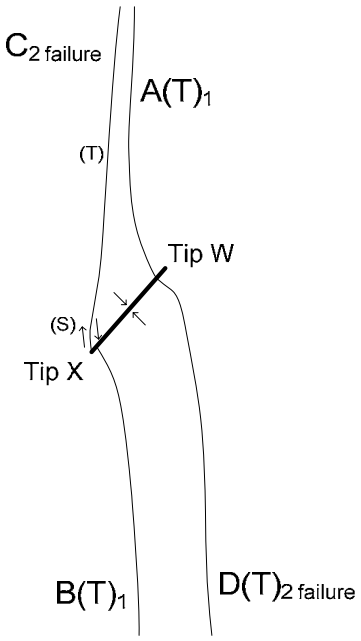
The aperture of the pre-existing flaw was partially closed.	The aperture of the pre-existing flaw was partially closed.	The aperture of the pre-existing flaw was partially closed.

Notes:

- Curvilinear tensile wing cracks A and B were the first cracks to initiate, and they initiated from the tips of the pre-existing flaws simultaneously.

- Other than the pair of tensile wing cracks, few other cracks initiated from the pre-existing flaws during the whole course of loading process before specimen failure.

- Additional cracks initiated when the maximum strength of the specimen was reached or overcome. These cracks were type 2 tensile cracks (cracks D in 20050118A & 20050317D), and mixed tensile-shear crack in three specimens according to the classification scheme shown in figure 2.15.

Flaw Inclination – 60^{o}	
20050118B 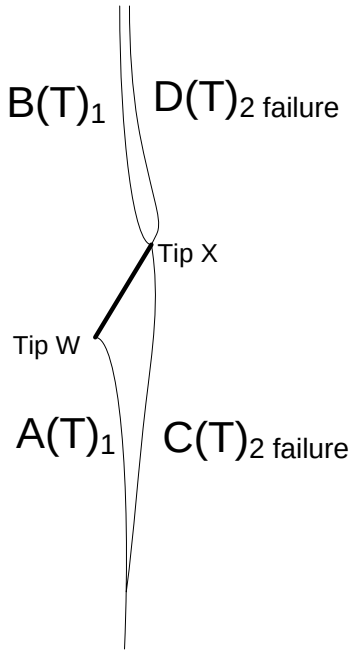 The aperture of the pre-existing flaw increased.	20050317B 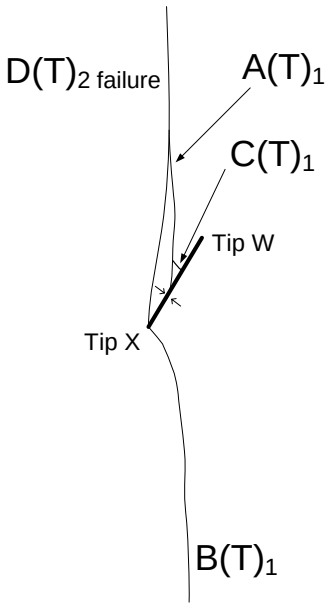
20050317E 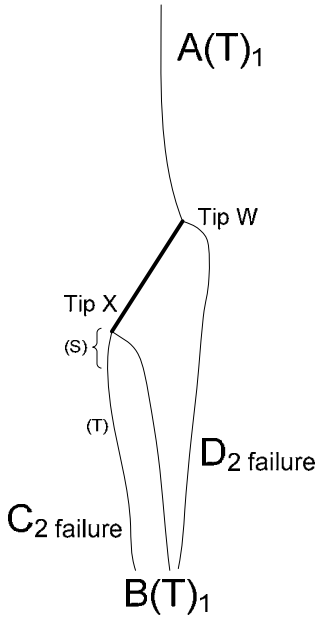 The aperture of the pre-existing flaw increased slightly.	20050401B 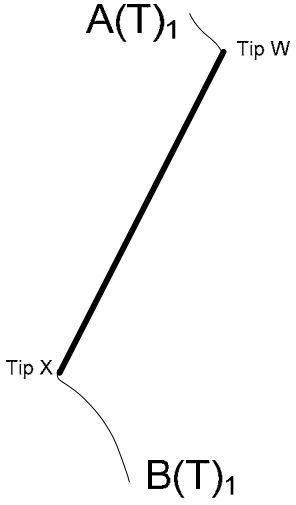 The pictures showing the failure processes were not captured.

Flaw Inclination – 60^{o} (continued)		
20050405E	20050522B	20050522C
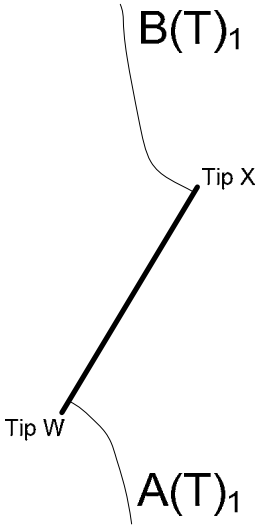	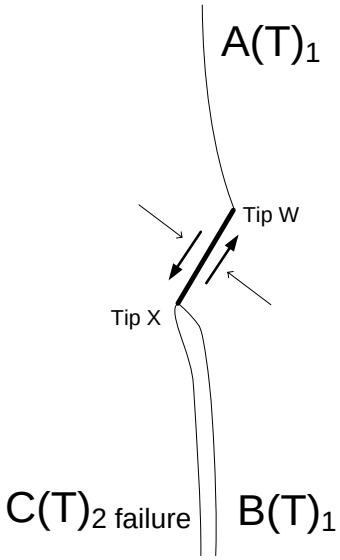	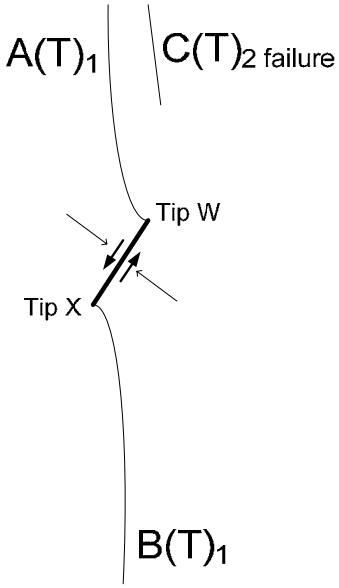
Additional cracks developed in other parts of the specimen when the specimen strength was reached or overcome.	The aperture of the pre-existing flaw was partially closed.	The aperture of the pre-existing flaw was partially closed.

Notes:

- Curvilinear tensile wing cracks A and B, which were the first cracks to initiate, initiated from the tips of the pre-existing flaw and immediately led to specimen failure.

- Other than the pair of tensile wing cracks, few other cracks initiated from the pre-existing flaws during the whole course of loading process before specimen failure.

- Additional type 2 tensile cracks (figure 2.15) initiated from the tips of the pre-existing flaws when the maximum strength of the specimen was reached or overcome.

- At the end of the loading process, the aperture of some pre-existing flaws was slightly reduced, while that of some flaws slightly increased. Also, a small amount of relative shear displacement occurred between the upper face and lower face of the pre-existing flaw.

Flaw Inclination – 70^{o}	
20050522A 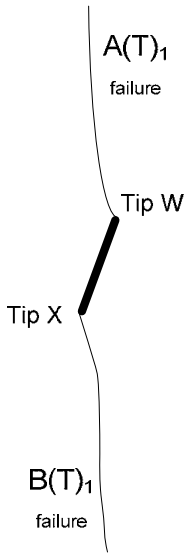 Additional cracks developed in other parts of the specimen when the specimen strength was reached or overcome are not shown. The aperture of the pre-existing flaw increased.	20050522E 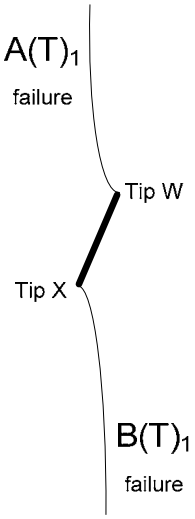 Additional cracks developed in other parts of the specimen when the specimen strength was reached or overcome are not shown. The aperture of the pre-existing flaw increased.
20050531A 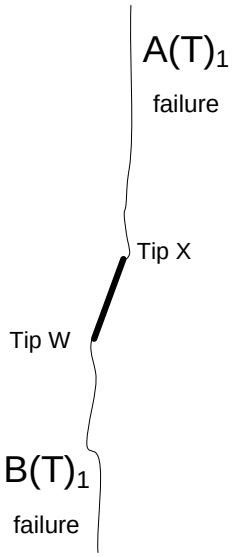 Additional cracks developed in other parts of the specimen when the specimen strength was reached or overcome are not shown. The aperture of the pre-existing flaw increased.	20050531C No cracks initiated from the pre-existing flaw. Failure occurred in other parts of the specimen.

Flaw Inclination – 70^{o} (continued)

Notes:

- Curvilinear tensile wing cracks A and B, which were the first cracks to initiate, initiated from the tips of the pre-existing flaw and immediately led to specimen failure.

- Other than the pair of tensile wing cracks, few other cracks initiated from the pre-existing flaws during the whole course of loading process before specimen failure.

- Additional cracks developed in other parts of the specimen far away from the flaw when the specimen strength was reached or overcome.

- At the end of the loading process, the aperture of the pre-existing flaw increased slightly. Also, a small amount of relative shear displacement occurred between the upper face and lower face of the pre-existing flaw.

Flaw Inclination – 75^{o}	
20050317H 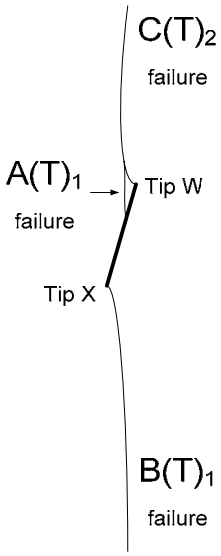 Additional cracks developed in other parts of the specimen when the specimen strength was reached or overcome are not shown. The aperture of the pre-existing flaw increased.	20050318C 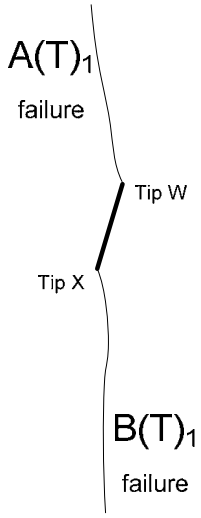 Additional cracks developed in other parts of the specimen when the specimen strength was reached or overcome are not shown. The aperture of the pre-existing flaw increased.
20050318E 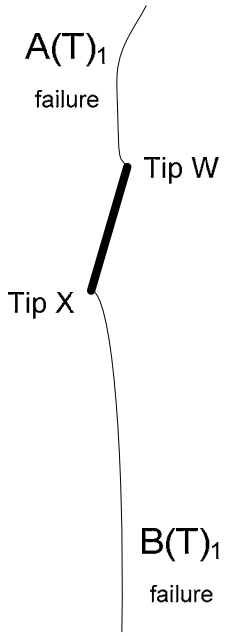 Additional cracks developed in other parts of the specimen when the specimen strength was reached or overcome are not shown. The aperture of the pre-existing flaw increased.	

Flaw Inclination – 75^{o} (continued)

Notes:

- Curvilinear tensile wing cracks A and B, which were the first cracks to initiate, initiated from the tips of the pre-existing flaw and immediately led to specimen failure.

- Other than the pair of tensile wing cracks, few other cracks initiated **from** the pre-existing flaws during the whole course of loading process before specimen failure.

- Additional cracks developed in **other parts of the intact specimen** far away from the flaw when the specimen strength was reached or overcome (not shown in the sketches).

- At the end of the loading process, the aperture of the pre-existing flaw increased slightly. Also, a small amount of relative displacement occurred between the upper face and lower face of the pre-existing flaw.

APPENDIX F – Test Results of Gypsum Specimens Containing Wide Single Flaws

In this appendix, sketches of cracking patterns observed in all gypsum specimens containing wide single flaws (0.05" aperture) are illustrated. Refer to section 3.5 for the meaning of the symbols used in the sketches. The cracking phenomena for each flaw inclination group are also generalized below the sketches.

The total number of specimens successfully tested for each flaw inclination is summarized below.

Flaw inclination angle (^{o})	Number
0	8
30	8
45	6
60	4
75	7
	33 (total)

Flaw Inclination – 0°	
20050705G 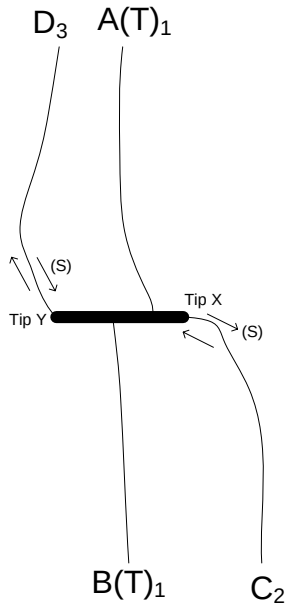 	20050705M 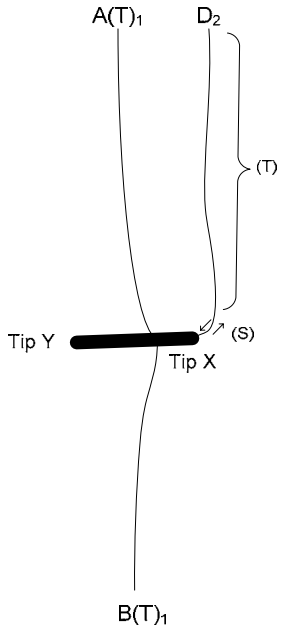
20050712G 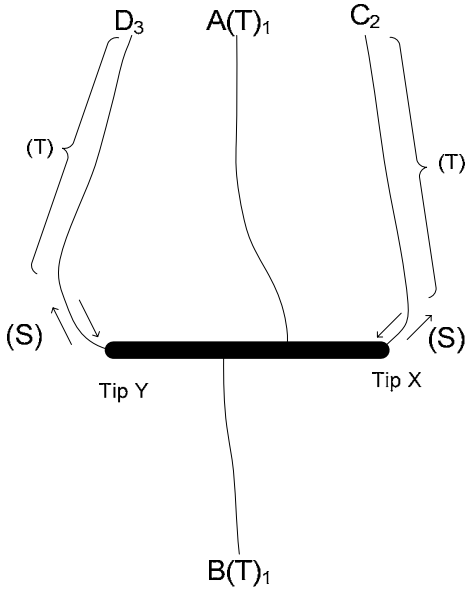 	20050729A 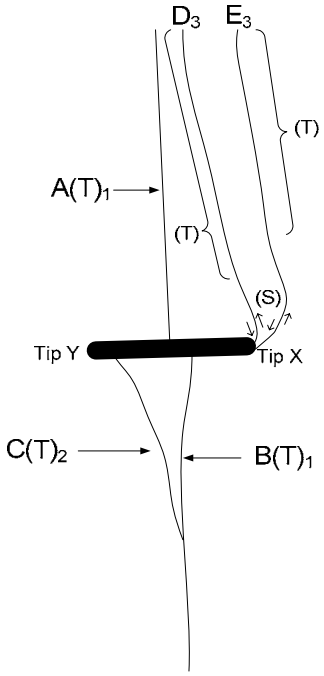

Flaw Inclination – 0° (continued)

20050729B

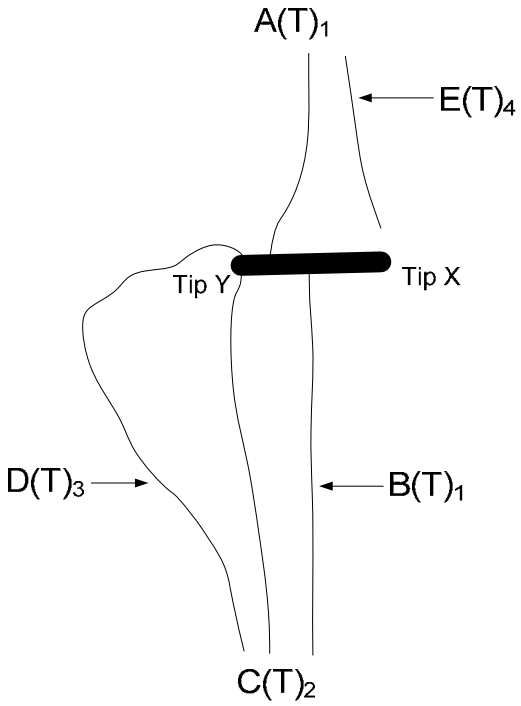

20050729C

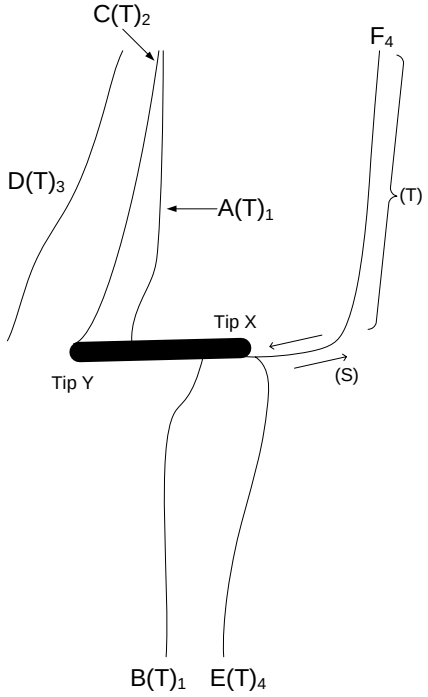

20050729D

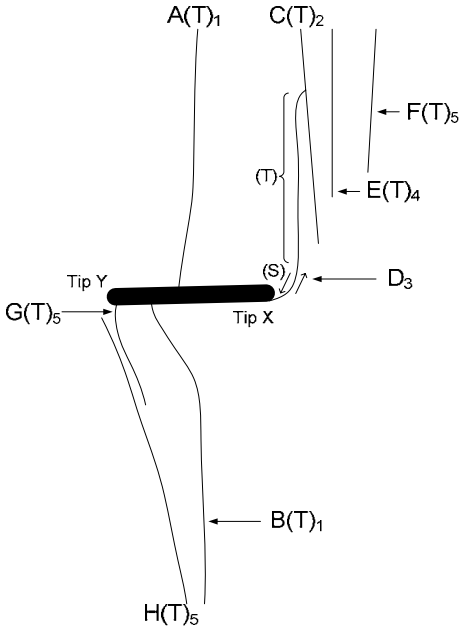

20050729E

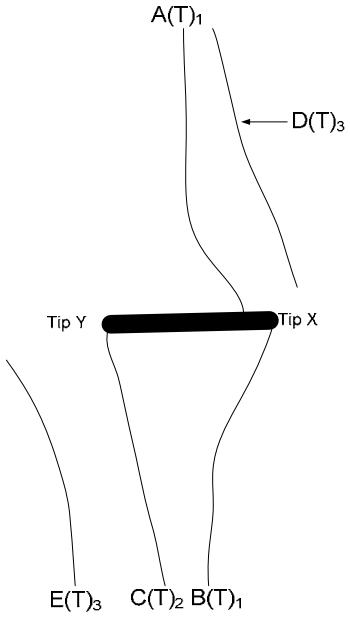

Flaw Inclination – 0^o (continued)

Notes:

- Curvilinear tensile wing cracks were always the first cracks to initiate from the pre-existing flaws at a distance away from the flaw tips. These tensile wing cracks developed as a pair, one from the upper face of the pre-existing flaw and one from the lower face of the pre-existing flaw. These two cracks initiated simultaneously well before the specimen failure.

- Additional cracks initiated when the maximum strength of the specimen was reached. These cracks were mixed tensile-shear cracks according to the classification scheme shown in figure 2.15.

- The aperture of the pre-existing flaw was almost completely closed at the end of the loading process.

Flaw Inclination – 30°	
20050531D 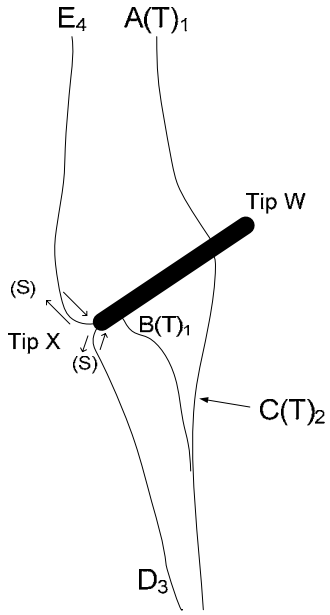	20050531E 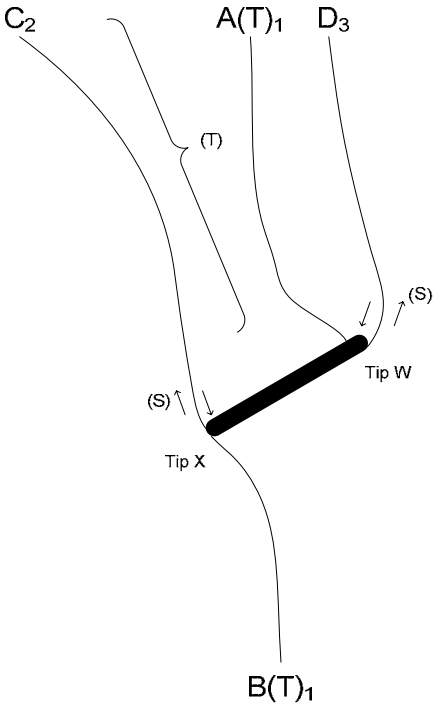
20050531F 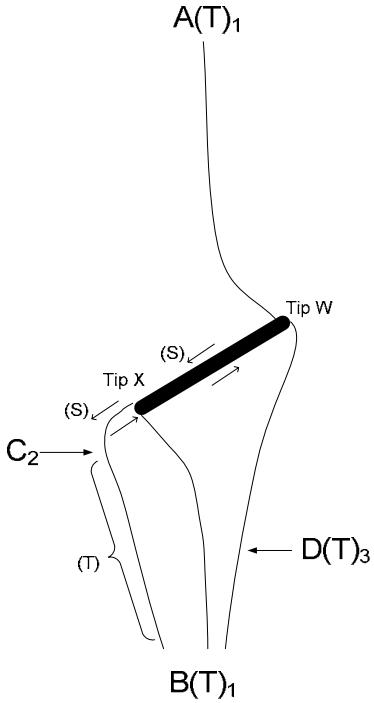	20050607A 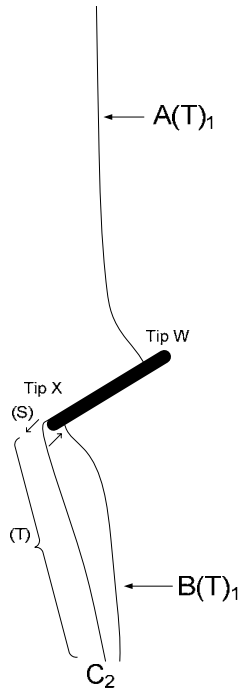

Flaw Inclination – 30° (continued)

20050607C

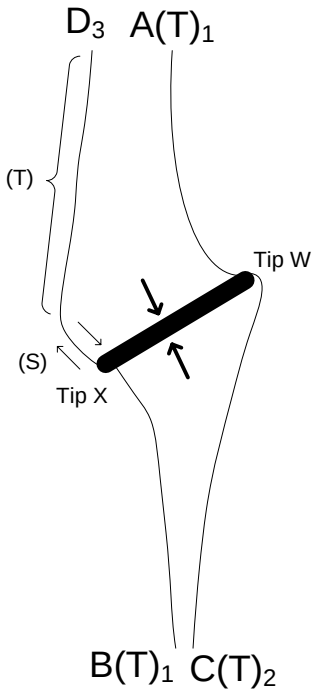

20050607E

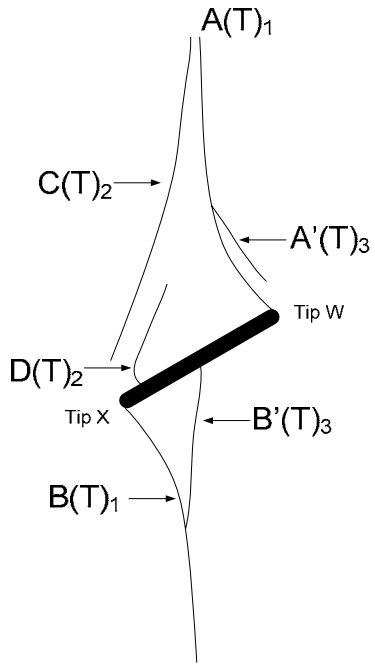

20050705A

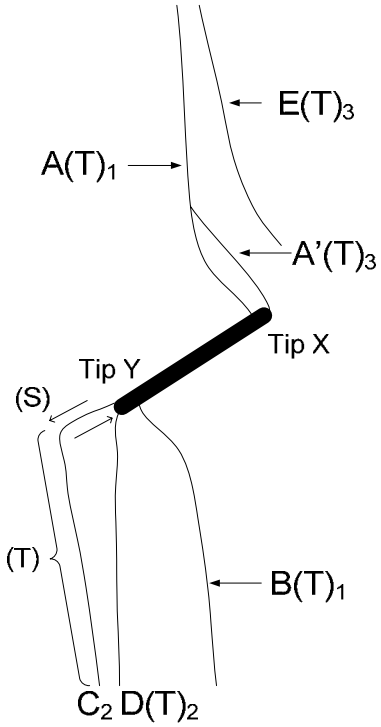

20050705C

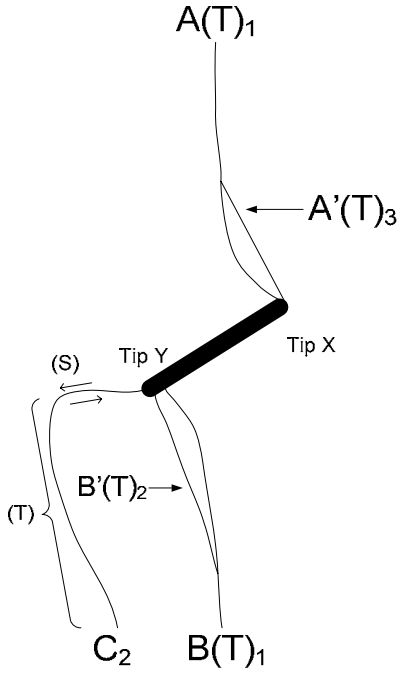

Flaw Inclination – 30^{o} (continued)

Notes:

- Curvilinear tensile wing cracks were always the first cracks to initiate from the pre-existing flaws close to the flaw tips. These tensile wing cracks developed as a pair, one from the upper face of the pre-existing flaw and one from the lower face of the pre-existing flaw. These two cracks initiated simultaneously well before the specimen failure.

- Additional cracks initiated when the maximum strength of the specimen was reached. These cracks always initiated from the tips of the pre-existing flaws, and were mixed tensile-shear cracks according to the classification scheme shown in figure 2.15.

- The aperture of the pre-existing flaw was almost completely closed at the end of the loading process.

Flaw Inclination – 45°	
20050607B 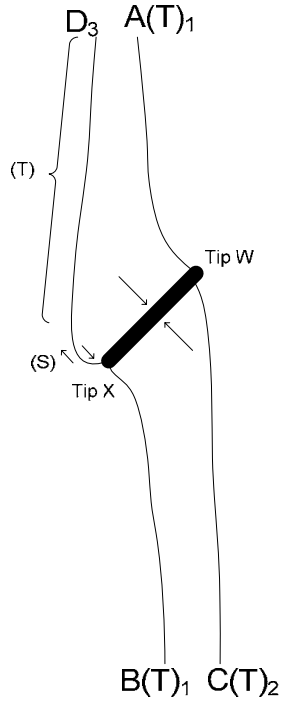	20050607D 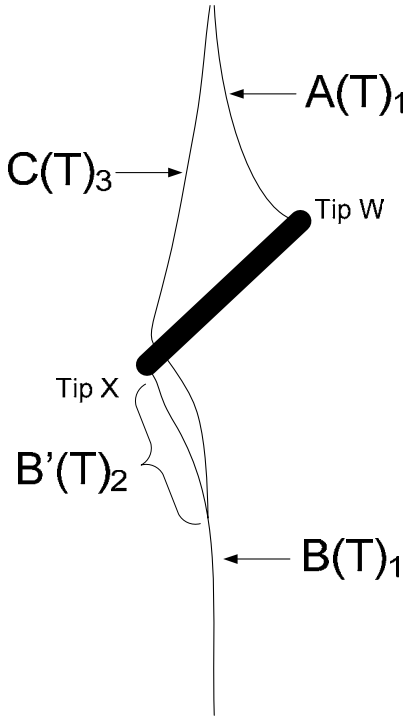
20050607F 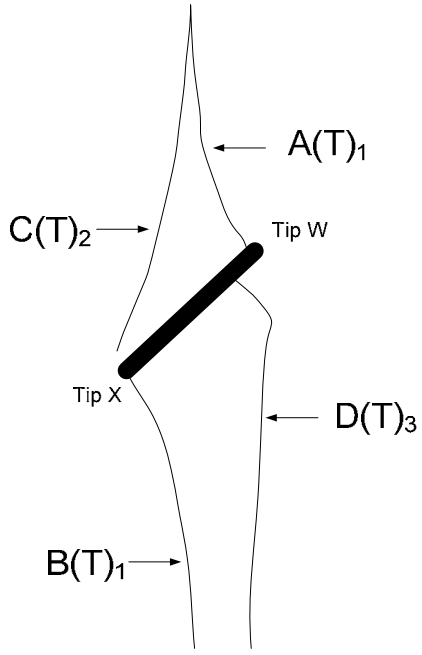	20050705B 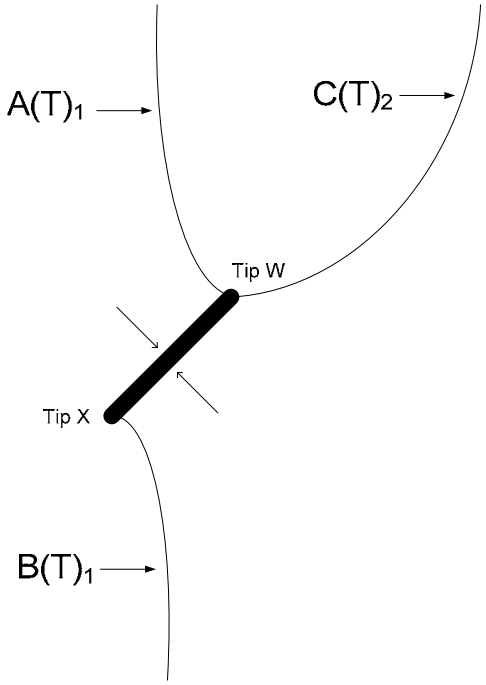

Flaw Inclination – 45^o (continued)

20050705D

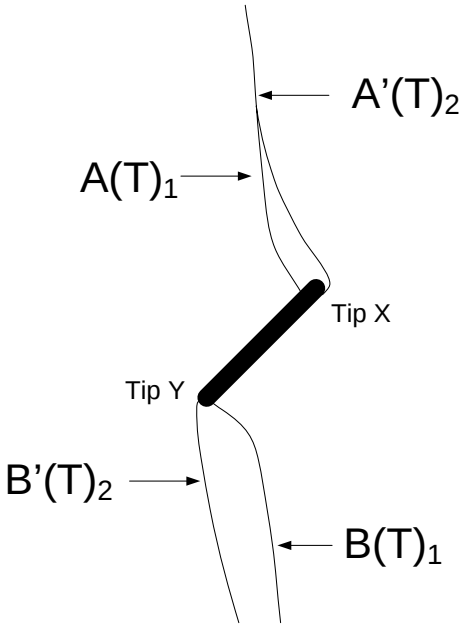

20050705K

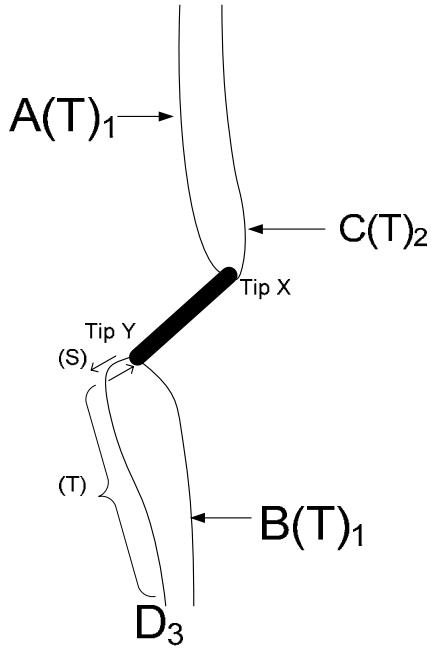

Notes:

- Curvilinear tensile wing cracks were always the first cracks to initiate from the pre-existing flaws close to the flaw tips. These tensile wing cracks developed as a pair, one from the upper face of the pre-existing flaw and one from the lower face of the pre-existing flaw. These two cracks initiated simultaneously just before the specimen failure.

- Additional cracks initiated when the maximum strength of the specimen was reached. These cracks often initiated from the tips of the pre-existing flaws. Most of these cracks were type 2 tensile cracks (cracks A' & B' in 20050705D), and mixed tensile-shear cracks (cracks D in 20050607B & 20050705K) according to the classification scheme shown in figure 2.15.

- The aperture of the pre-existing flaw was partially reduced at the end of the loading process, and there was a small, yet observable, amount of relative shear displacement between the upper face and lower face of the pre-existing flaw.

Flaw Inclination – 60°	
20050729F 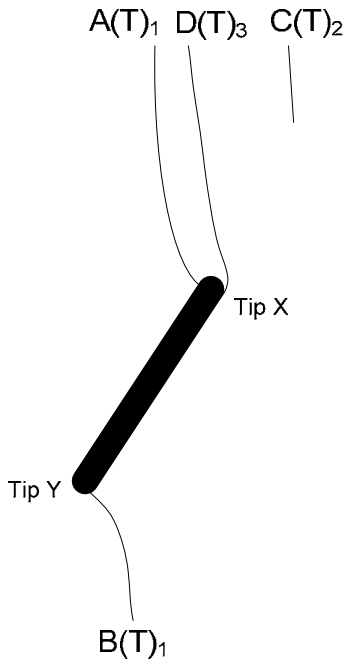 	20050729G 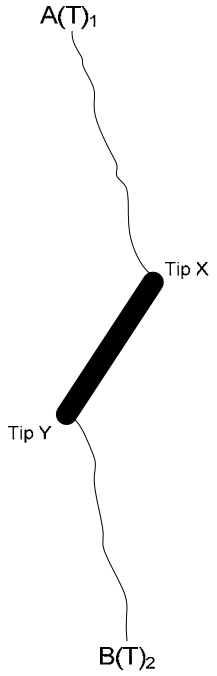
20050812C 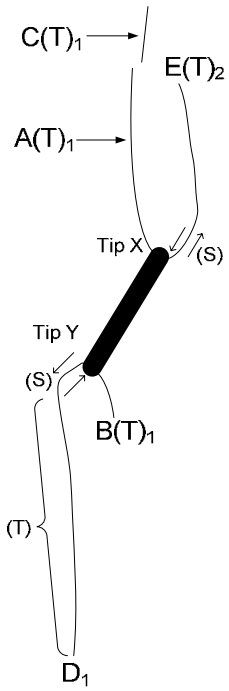 	20050812D 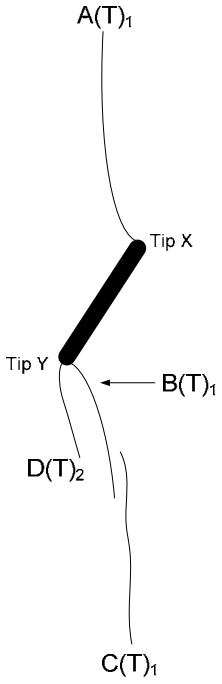

Flaw Inclination – 60^{o} (continued)

Notes:

- Tensile wing cracks initiated from the tips of the pre-existing flaw and immediately led to specimen failure.

- These tensile wing cracks developed as a pair, one from the upper face of the pre-existing flaw and one from the lower face of the pre-existing flaw. These two cracks initiated simultaneously.

- Additional cracks sometimes initiated. These cracks often initiated from the tips of the pre-existing flaws. Most of these cracks were type 2 tensile cracks (cracks D in 20050729F & 20050812D), and mixed tensile-shear crack (crack E in 20050812C) according to the classification scheme shown in figure 2.15.

- At the end of the loading process, the aperture of the pre-existing flaws remained more or less the same. Also, a substantial relative shear displacement occurred between the upper face and lower face of the pre-existing flaw.

Flaw Inclination – 75°	
20050705N 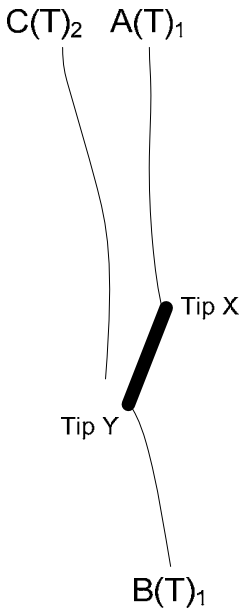 	20050712E 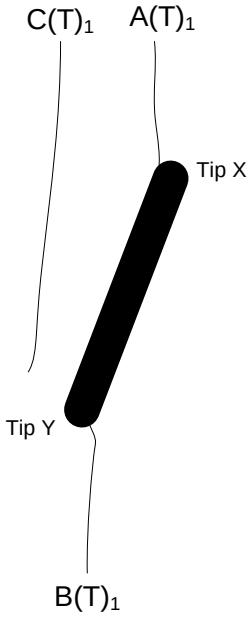
20050712H 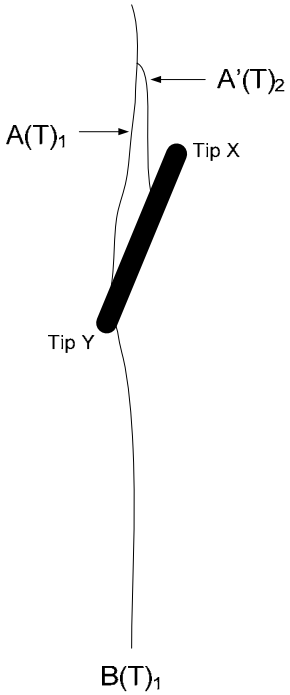 	20050712I 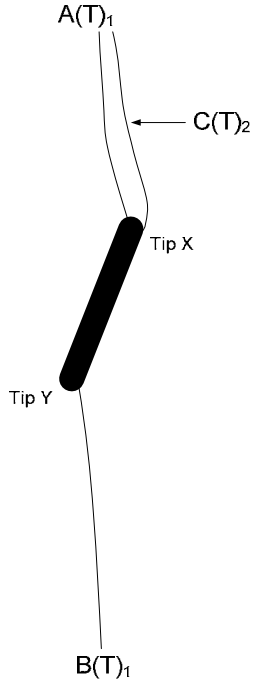

Flaw Inclination – 75^{o} (continued)

20050729H

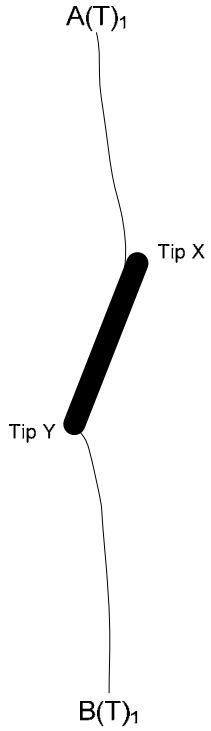

20050729I

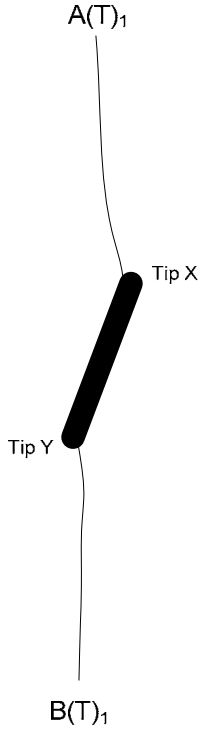

20050729J

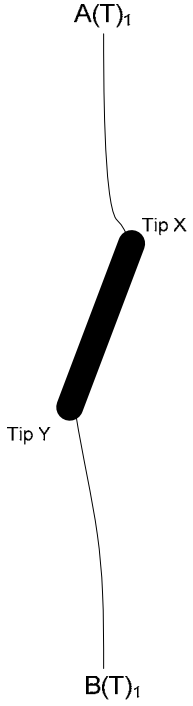

Notes:

- Tensile wing cracks initiated from the tips of the pre-existing flaw and immediately led to specimen failure.

- The tensile wing cracks A, which propagated upwards from the right tips, initiated from the top face of the pre-existing flaw, while the tensile wing cracks B, which propagated upwards from the left tips, initiated from the bottom face of the pre-existing flaw. These two cracks initiated simultaneously.

- Other than the pair of tensile wing cracks, few other cracks initiated from the pre-existing flaws during the whole course of loading process.

- At the end of the loading process, the aperture of the pre-existing flaw increased slightly. Also, a small amount of relative shear displacement occurred between the upper face and lower face of the pre-existing flaw.

APPENDIX G – Test Results of Marble Specimens Containing Single Flaws

In this appendix, sketches of cracking patterns observed in all marble specimens containing single flaws (0.05" aperture) are illustrated. Refer to section 3.5 for the meaning of symbols used in the sketches. The cracking phenomena for each flaw inclination group are also generalized below the sketches.

The total number of specimens successfully tested for each flaw inclination is summarized below.

Flaw inclination angle (^{o})	Number
0	3
30	3
45	3
60	3
75	3
	15 (total)

Flaw Inclination – 0^o	
CM0-A 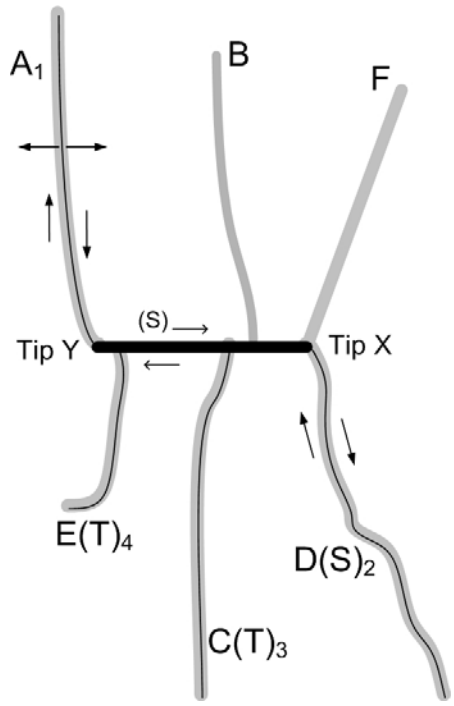 	CM0-B 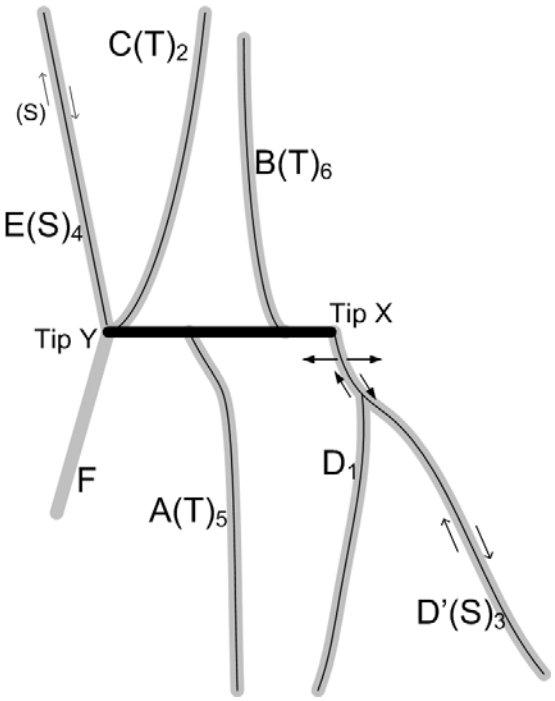
CM0-C 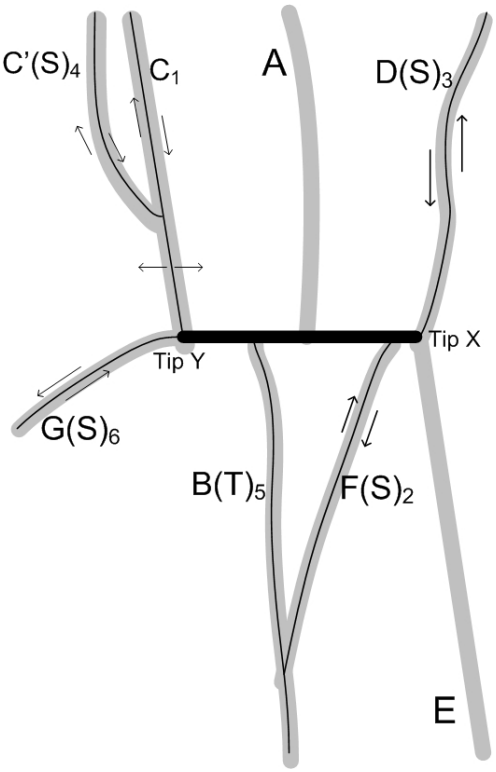 	

Flaw Inclination – 0^o (continued)

Notes:

- Curvilinear white patches, which displayed the shape of conventional wing appearance, developed in all specimens close to the middle of the pre-existing flaw, well before the initiation of other cracks. Some of the white patches developed into cracks, and some of them remained intact and unopened.

- Shear cracks, whose shearing sense was almost coaxial with the loading direction (σ_1), were usually the first cracks to initiate from the end tips. In all cases, tensile wing cracks were not the first cracks to initiate.

- The aperture of the pre-existing flaw was almost completely closed as shearing occurred along the almost vertical shear cracks originating from the flaw tips till the end of the loading process.

Flaw Inclination – 30°

CM30-A

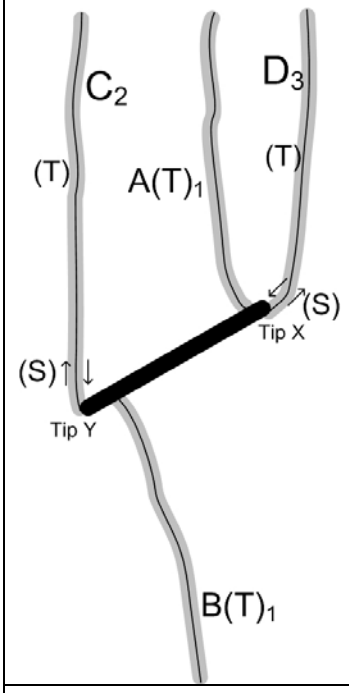

CM30-B

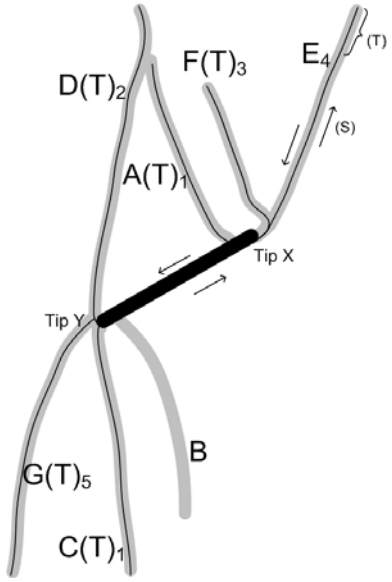

CM30-D

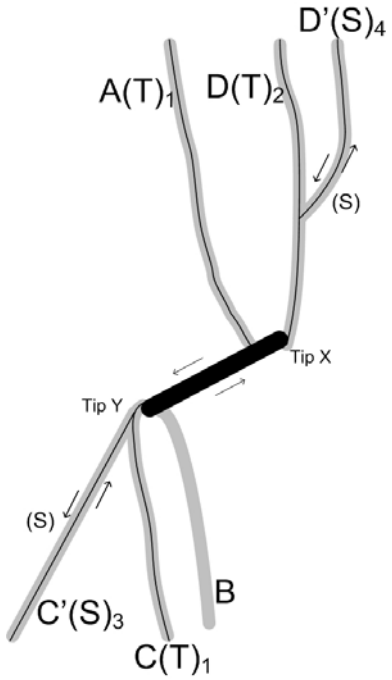

Notes:

- Tensile wing cracks, which first developed as white patches, were always the first cracks to initiate. The tensile wing cracks usually initiated at a distance away from the flaw tips and the initiation of these cracks did not lead to immediate specimen failure.

- In CM30-B and CM30-D, tensile wing cracks did not develop from the lower flaw face. Tensile cracks C, which were almost parallel to the loading direction, initiated from the left flaw tips instead in these two specimens. They were type 2 tensile cracks according to the classification scheme shown in figure 2.15.

- Relative shear displacement between the upper face and the lower face of the pre-existing flaw occurred once the first cracks initiated, leading to the subsequent development of cracks (cracks E & G in CM30-B, cracks C & D in CM30-D) which were generally trending from the top right to the bottom left of the specimen.

- The aperture of the pre-existing flaw substantially decreased at the end of the loading processes.

Flaw Inclination – 45^o		
CM45-A	CM45-B	CM45-C
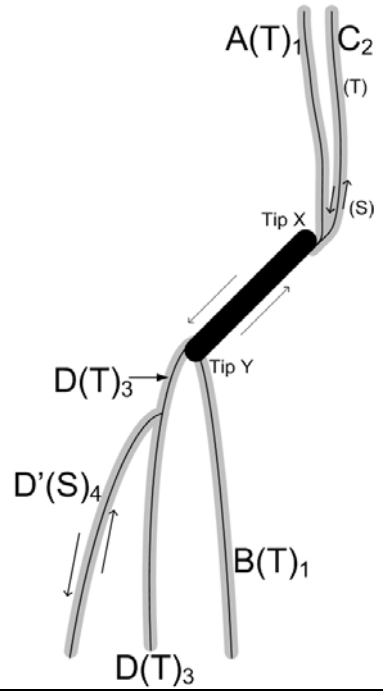	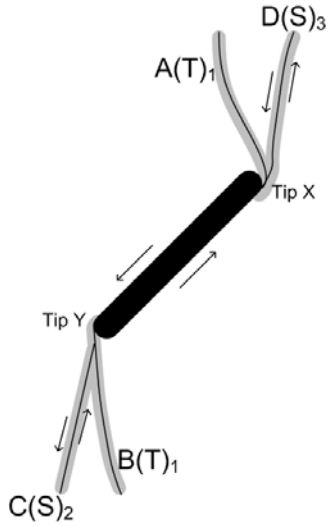	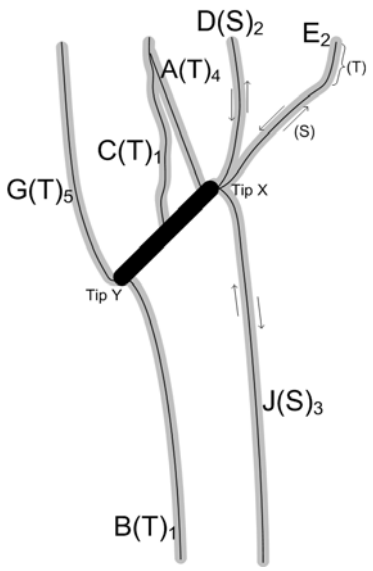

Notes:

- Tensile wing cracks, which first developed as white patches close to the flaw tips, were always the first cracks to initiate. The initiation of these cracks did not lead to immediate specimen failure.

- The other tensile cracks which were also the first cracks to initiate (crack A in CM45-A, cracks A & B in CM45-B), were distinctly different from the conventional tensile wing cracks. They were type 2 tensile cracks according to the classification scheme shown in figure 2.15.

- The next cracks developed were usually shear cracks originating from the flaw tips, which were associated with the relative displacement between the upper face and the lower face of the pre-existing flaw.

- The aperture of the pre-existing flaw substantially decreased at the end of the loading processes.

Flaw Inclination – 60°		
CM60-A	CM60-B	CM60-C
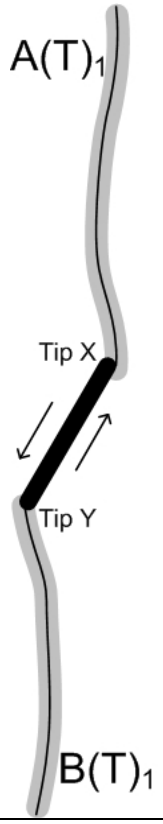	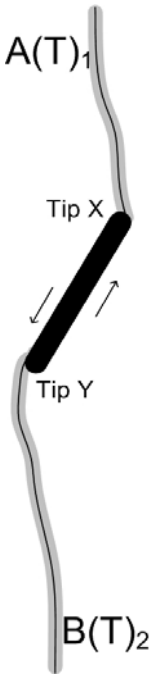	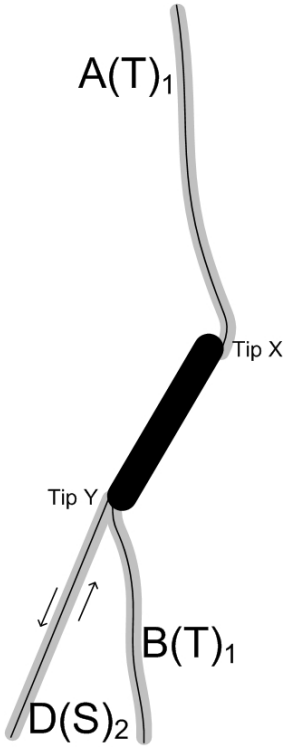

Notes:

- Type 2 tensile cracks (according to the classification scheme in figure 2.15) initiated from the tips of the pre-existing flaw and immediately led to specimen failure.

- The tensile cracks A, which propagated upwards from the right tips, initiated from the bottom face of the pre-existing flaw, while the tensile cracks B, which propagated upwards from the left tips, initiated from the top face of the pre-existing flaw.

- At the end of the loading process, the aperture of the pre-existing flaw increased slightly.

Flaw Inclination – 75°

CM75-A

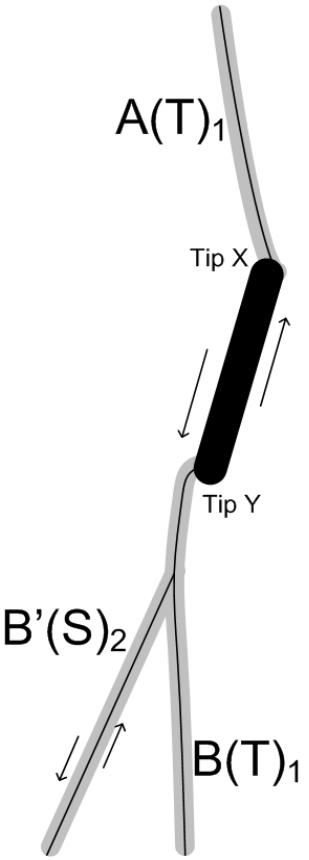

CM75-B

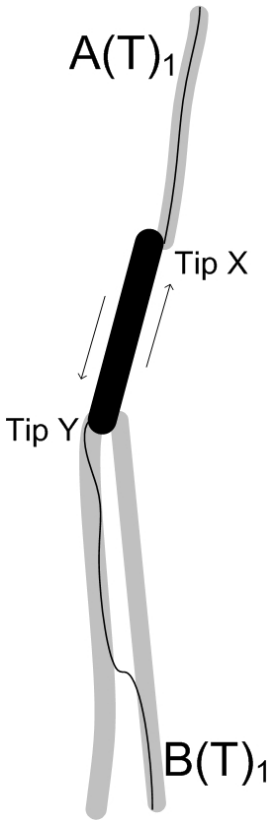

CM75-C

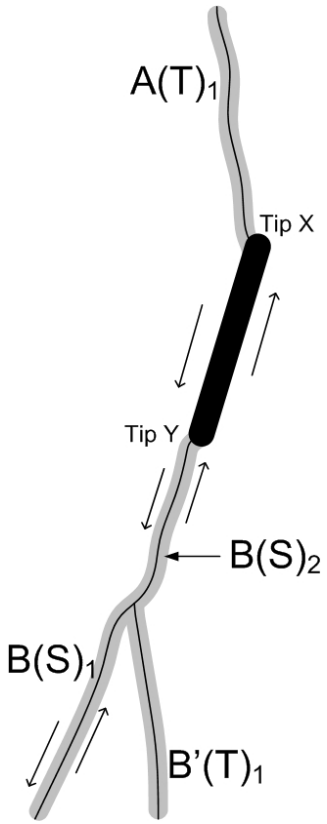

Notes:

- Type 2 tensile cracks (according to the classification scheme in figure 2.15) initiated from the tips of the pre-existing flaw and immediately led to specimen failure.

- Except in specimen CM75-C, the type 2 tensile cracks A, which propagated upwards from the right flaw tips, initiated from the bottom face of the pre-existing flaw.

- In all three specimens, the type 2 tensile cracks B, which propagated downwards from the left tips, initiated from the top face of the pre-existing flaw.

- At the end of the loading process, the aperture of the pre-existing flaw increased substantially.

APPENDIX H – Test Results of Gypsum Specimens Containing Coplanar Double Flaws of Ligament Length '2a'

In this appendix, the cracking phenomena of gypsum specimens containing coplanar double flaws (0.05" aperture) of ligament "2a" are described. Sketches of cracking patterns observed in all specimens are also illustrated. Refer to section 3.5 and section 5.2 for the meaning of symbols used in the sketches.

Nineteen gypsum specimens were tested in this series (see table below). Three or more specimens were tested for each geometry in order to obtain consistent coalescence behavior.

Flaw inclination (^{o})	**Specimens**	**Total**
0	2a-0-0-A 2a-0-0-B 2a-0-0-C	3
30	2a-30-0-A 2a-30-0-B 2a-30-0-D 2a-30-0-E	4
45	2a-45-0-A 2a-45-0-B 2a-45-0-C 2a-45-0-D 2a-45-0-E	5
60	2a-60-0-B 2a-60-0-C 2a-60-0-D 2a-60-0-E	4
75	2a-75-0-B 2a-75-0-C 2a-75-0-D	3
		19 (Total)

Gypsum 2a-0-0 (figure H.1)

Tensile wing cracks (TWCs, type 1 tensile cracks) were always the first cracks to initiate in the specimen. Additional TWCs initiated as loading continued. Some of them initiated at a short distance away from the flaw tips (cracks A, B, C & D in specimen B; cracks C & J in specimen C), while some initiated at the middle of the flaws (cracks A, B, C & D in specimen A; cracks A & B in specimen C). Steep **type 2 tensile cracks** and **mixed tensile-shear cracks** always developed from the flaw tips during the later stages of loading.

Coalescence was achieved only in one out of three of the specimens. In specimen C where coalescence occurred, a steeply inclined **type 1 shear crack** first initiated from the inner tip of the left flaw. After 1/1000 seconds (resolution of the high speed video set of this specimen), another crack initiated from the inner tip of the right flaw. This later crack, which consisted of **tensile and shear segments**, coalesced with the earlier developed inner tip **type 1 shear crack**.

Surface spalling frequently occurred around flaw tips, where shearing occurred along the underlying segments of curvilinear tip cracks.

The crack initiation stress ratio and coalescence strain ratio (refer to section 3.5 for definitions) are summarized below.

Crack Initiation Stress Ratio *Average value (min – max)*	0.722 (0.639 – 0.815)
Coalescence Strain Ratio *Average value (min – max)*	1.000 (coalescence in 1 our of 3 specimens only)

Gypsum 2a-0-0

2a-0-0-A (1,000pps) – no coalescence

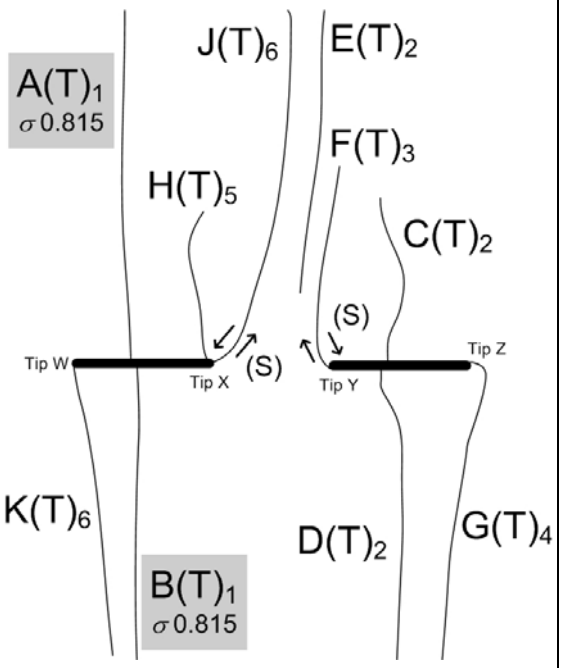

Pre-max : 1
Max : 2
Post-max : 3-6

CAM : 1
HS : 2-6

2a-0-0-B (1,000pps) – no coalescence

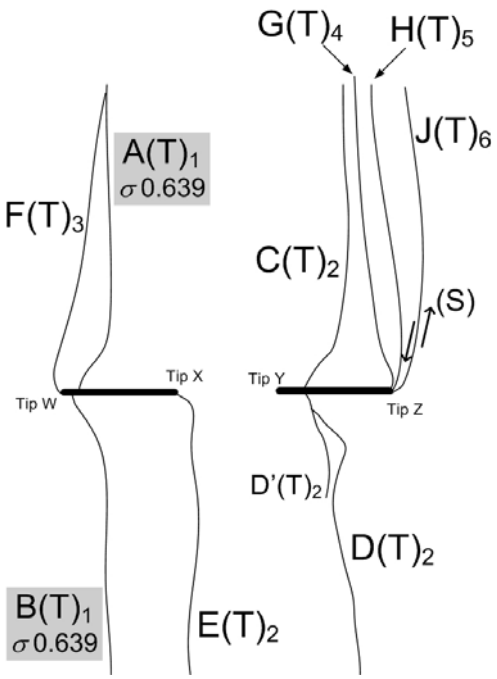

Pre-max : 1
Max : 2
Post-max : 3-6

CAM : 1
HS : 2-6

Figure H.1 – Fracturing and coalescence patterns for gypsum 2a-0-0.

2a-0-0-C (1,000pps) – coalescence

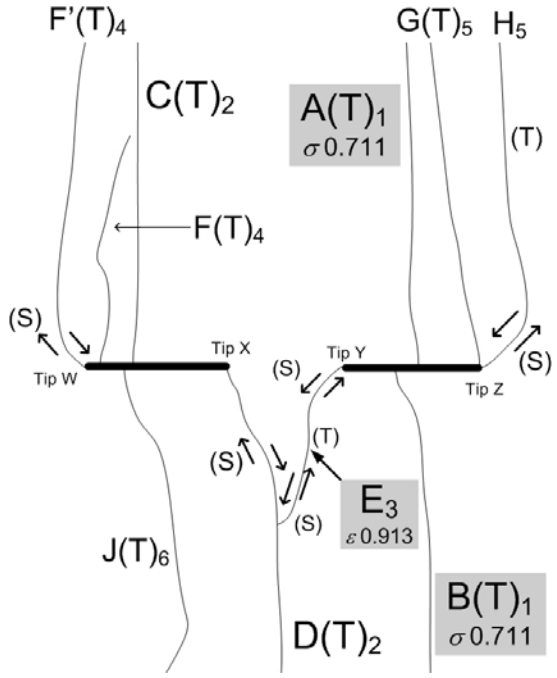

Pre-max : 1
Max : 2
Post-max : 3-6

CAM : 1
HS : 2-6

Figure H.1 – Fracturing and coalescence patterns for gypsum 2a-0-0 (continued).

Gypsum 2a-30-0 (figure H.2)

Tensile wing cracks (TWCs, type 1 tensile cracks) were always the first cracks to initiate from the pre-existing flaws in the specimen. Most of them initiated at a **short distance away** from the flaw tips. **Type 2 tensile cracks** and **mixed tensile-shear cracks**, developed from the flaw tips during the later stages of loading.

Coalescence was achieved in all specimens by sinistral **type 2 shear cracks** developed between the inner flaw tips. Observation with the high speed camera at 2,000 pps and 2,800 pps suggested that the crack initiation was an instantaneous event during which a single crack developed between the two inner flaw tips.

Localized surface spalling was frequently associated with the formation of the coalescence crack between the inner flaw tips. Once the spalling fragments fell off from the front face of the specimen, the true traces of the underlying shear cracks were revealed.

The crack initiation stress ratio and coalescence strain ratio (refer to section 3.5 for definitions) are summarized below.

Crack Initiation Stress Ratio *Average value (min – max)*	0.766 (0.682 – 0.879)
Coalescence Strain Ratio *Average value (min – max)*	1.001 (1.000 - 1.005) 3/4 coalesced at maximum stress 1/4 coalesced after maximum stress

Gypsum 2a-30-0

2a-30-0-A (2,000pps) – coalescence

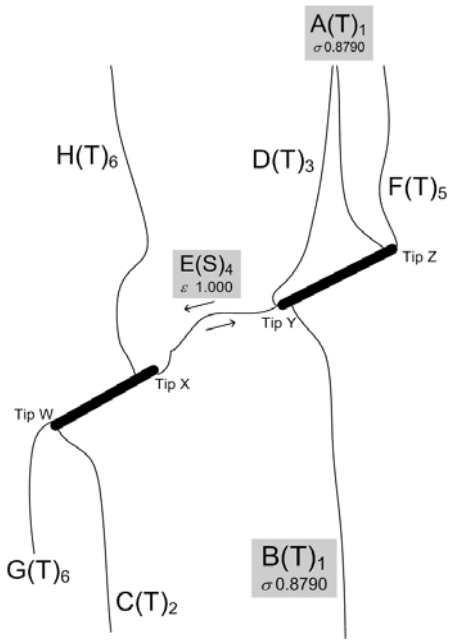

Pre-max : 1-4 CAM : 1-2
Post-max : 5-6 HS : 3-6

2a-30-0-B (2,000pps) – coalescence

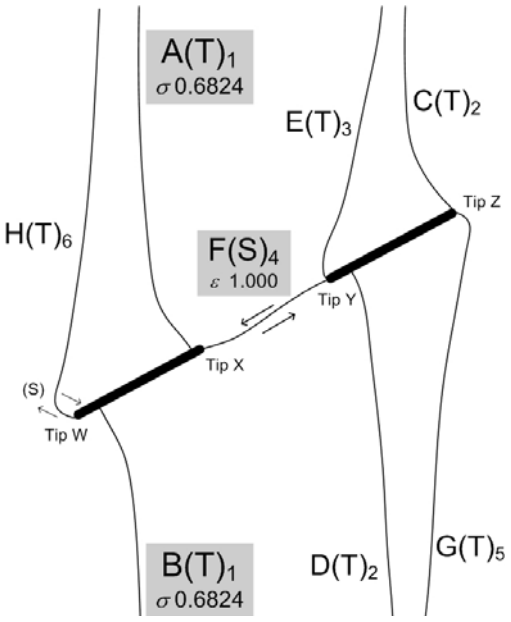

Pre-max : 1-2
Max : 3 CAM : 1
Post-max : 4-6 HS : 2-6

2a-30-0-D (2,800pps) – coalescence

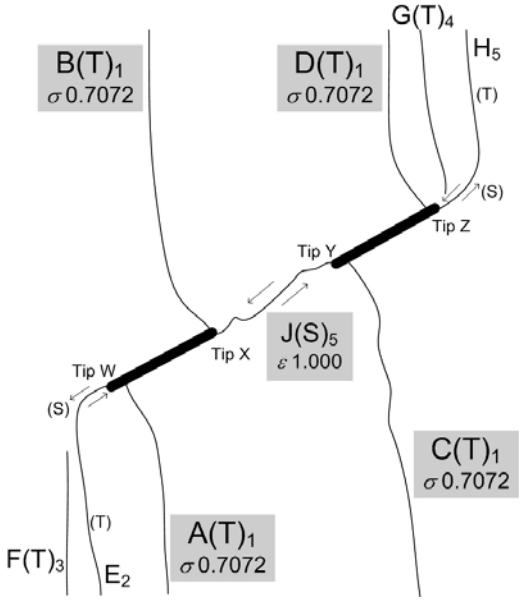

Pre-max : 1-4 CAM : 1
Max : 5 HS : 2-5

2a-30-0-E (2,800pps) – coalescence

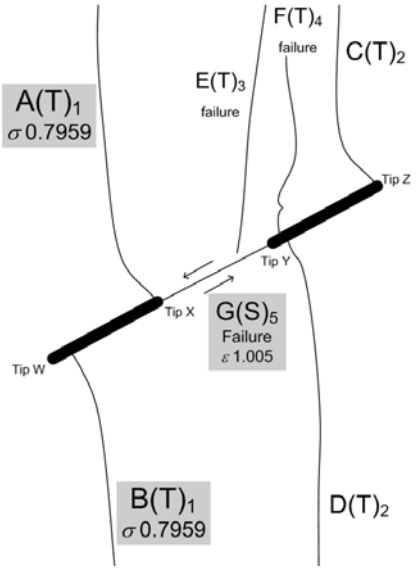

Pre-max : 1-2
Max : 3 CAM : 1-2
Post-max : 4-6 HS : 3-6

Figure H.2 – Fracturing and coalescence patterns for gypsum 2a-30-0.

Gypsum 2a-45-0 (figure H.3)

Tensile wing cracks (TWCs, type 1 tensile cracks) were always the first cracks to initiate in the specimen. Most of them initiated **close to** or **at** the flaw tips. **Type 2 tensile cracks** and **mixed tensile-shear cracks**, developed from the flaw tips during the later stages of loading.

Coalescence was achieved in all specimens by a crack developed between the two inner tips. The crack linked up the bottom right part of the inner tip X of the lower pre-existing flaw and the top left part of the inner tip Y of the upper pre-existing flaw.

The coalescence crack usually displayed a **stepwise** appearance, consisting of a number of kinked segments – tensile **(T)** opening preferentially occurred along those steeply inclined vertical segments, while shearing **(S)** occurred along those segments which were coplanar/almost coplanar with the pre-existing flaws. The coalescence crack segments adjacent to the inner tips were **coplanar** with the pre-existing flaws and were **shear** in origin (specimen B: S-T, specimens C, D & E: S-T-S, specimen A: S-T-S-T-S). Coalescence events in specimens B, C and E were recorded by **camcorder**; while those in specimens A and D were recorded by **high speed camera**. In those cases recorded by the camcorder, it was **unable** to determine if the multiple segments along the coalescence cracks initiated at **different times separately** or if they initiated as **segments of a continuous crack**.

Localized surface spalling was frequently associated with the formation of the coalescence crack between the inner flaw tips. Once the spalling fragments fell off from the front face of the specimen, the true traces of the underlying shear cracks were revealed.

The crack initiation stress ratio and coalescence strain ratio (refer to section 3.5 for definitions) are summarized below. Coalescence in specimens A and E occurred **before** the occurrence of specimen maximum stress, while that in specimens B, C and D occurred **after** the maximum stress.

Crack Initiation Stress Ratio *Average value (min – max)*	0.794 (0.687 – 0.899)
Coalescence Strain Ratio *Average value (min – max)*	0.984 (0.946 – 1.019) 3 specimens coalesced before maximum stress 2 specimens coalesced before maximum stress

Gypsum 2a-45-0

2a-45-0-A (2,000pps) – coalescence

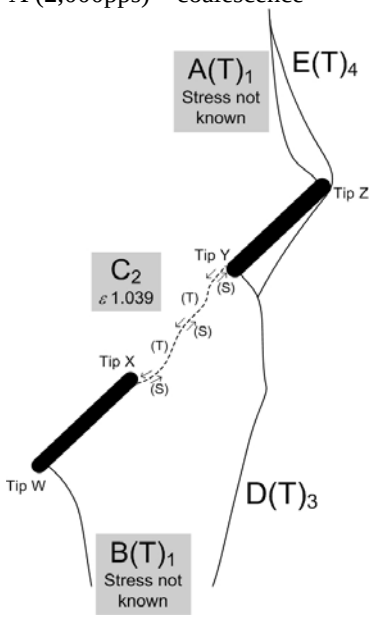

Pre-max : 1
Post-max : 2-4

CAM : no recording
HS : 2-4

2a-45-0-B (2,000pps) – coalescence

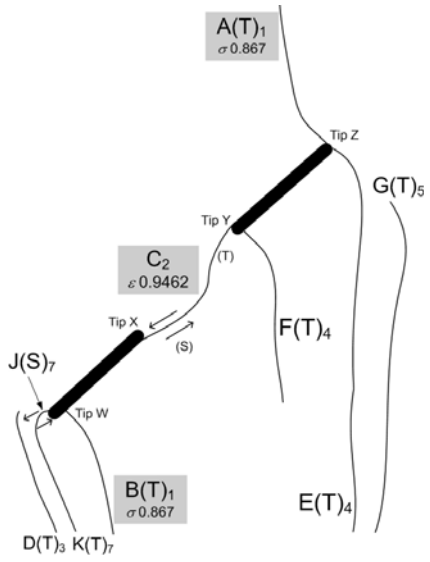

Pre-max : 1-2
Max : 2-4
Post-max : 4-7

CAM : 1-2
HS : 3-7

Figure H.3 – Fracturing and coalescence patterns for gypsum 2a-45-0.

Gypsum 2a-45-0	
2a-45-0-C (2,000pps) – coalescence 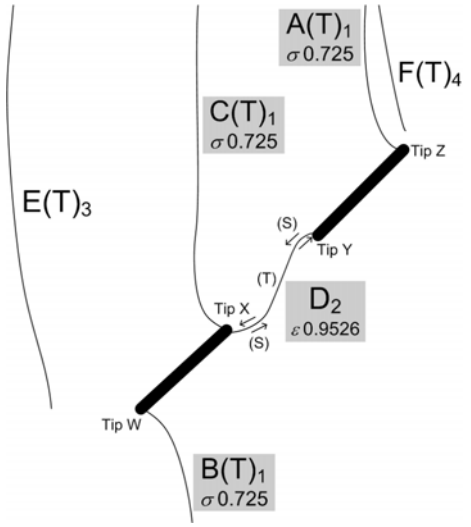 Pre-max : 1-2 CAM : 1-2 Max : 3 HS : 3-4 Post-max : 4	2a-45-0-D (2,000pps) – coalescence 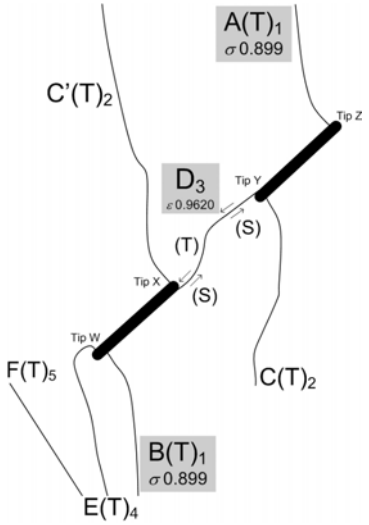 Pre-max : 1-4 CAM : 1-2 Post-max : 5 HS : 3-5
2a-45-0-E (2,000pps) – coalescence 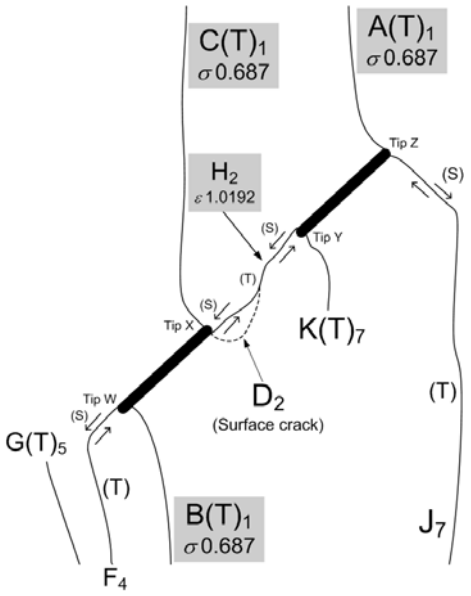 Pre-max : 1-2 CAM : 1-3 Max : 5 HS : 4-6 Post-max : 4-6	

Figure H.3 – Fracturing and coalescence patterns for gypsum 2a-45-0 (continued).

Gypsum 2a-60-0 (figure H.4)

Tensile wing cracks (TWCs, type 1 tensile cracks) were always the first cracks to initiate in the specimen. Most of them initiated **at** the flaw tips (cracks A & B in all specimens, also crack C in specimen D). **Inner tip TWCs** did not develop in specimens B and E. In specimens C and D, the **inner tip TWCs** propagated almost vertically for a length roughly equal to the flaw length (2a). **Type 2 tensile cracks** and **mixed tensile-shear cracks**, developed from the flaw tips during the later stages of loading.

Coalescence was achieved in all specimens by a crack developed between the two inner tips. The crack linked up the bottom right part of the inner tip X of the lower pre-existing flaw and the top left part of the inner tip Y of the upper pre-existing flaw. The coalescence in all specimens was all recorded by the **lower resolution camcorder**. The coalescence crack usually displayed a "S" shape appearance consisting of S-T-S segments. Its segments adjacent to the inner tips were **coplanar** with the pre-existing flaws and were **shear (S)** in origin, while the central segment was oriented almost vertically and was **tensile (T)** in origin.

The extent of surface spalling within the bridging region between the two inner flaw tips was much less than those specimens containing coplanar flaw pairs inclined at 30^{o} and 45^{o}.

The crack initiation stress ratio and coalescence strain ratio (refer to section 3.5 for definitions) are summarized below. Coalescence in all specimens occurred **before** the specimen maximum stress.

Crack Initiation Stress Ratio *Average value (min – max)*	0.786 (0.663 – 0.929)
Coalescence Strain Ratio *Average value (min – max)*	0.895 (0.799 – 0.960) All coalesced before maximum stress

Gypsum 2a-60-0

2a-60-0-B (2,800pps) – coalescence

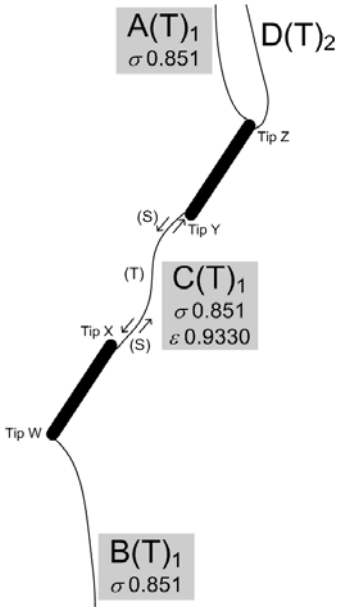

Pre-max : 1
Post-max : 2

CAM : 1
HS : 2

2a-60-0-C (2,800pps) – coalescence

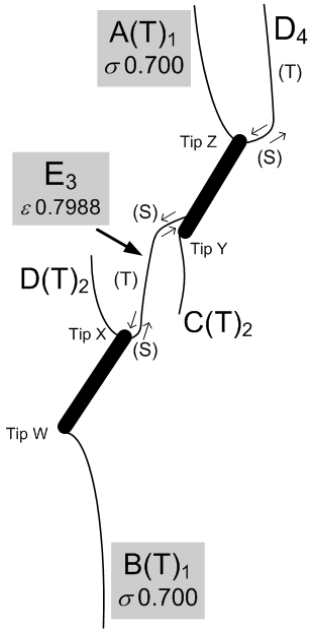

Pre-max : 1-4

CAM : 1-3
HS : 4

2a-60-0-D (2,800pps) – coalescence

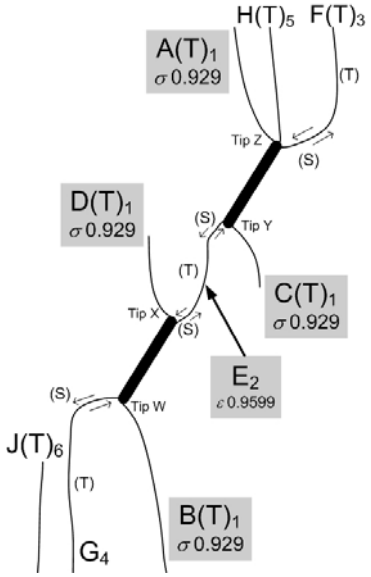

Pre-max : 1-2
Post-max : 3-5

CAM : 1-2
HS : 3-5

2a-60-0-E (3,000pps) – coalescence

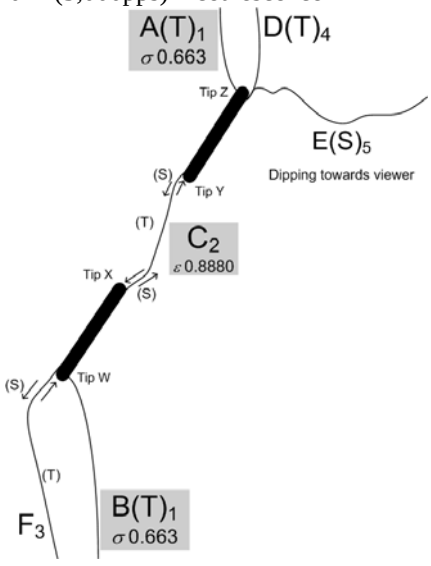

Pre-max : 1-2
Max : 3
Post-max : 4-5

CAM : 1-2
HS : 3-5

Figure H.4 – Fracturing and coalescence patterns for gypsum 2a-60-0.

Gypsum 2a-75-0 (figure H.5)

Tensile wing cracks (TWCs, type 1 tensile cracks) were always the first cracks to initiate in the specimen. Most of them initiated **at** the flaw tips. The **outer** tip tensile wing cracks propagated toward the upper and lower edges of the specimens, while the **inner** tip tensile wing cracks only propagated for a distance roughly equal to half to full flaw length of the pre-existing flaw.

Coalescence occurred in all specimens and the coalescence cracks developed after the first cracks had initiated (see above). **Coalescence** was achieved in all specimens by a crack developed between the two inner tips. The crack linked up the bottom right part of the inner tip X of the lower pre-existing flaw and the top left part of the inner tip Y of the upper pre-existing flaw. The coalescence crack usually displayed a "S" shape appearance consisting of shear (S) and tensile (T) segments. Its segments adjacent to the inner tips were **shear** in origin, while the central segment was oriented almost vertically and was **tensile** in origin. Since the initiation of the coalescence cracks was recorded by the high speed camera, one is confident that a single continuous coalescing crack developed, instead of multiple cracks developed first which later coalesced.

The extent of **surface spalling** within the bridging region between the two inner tips were much less than those specimens containing coplanar flaw pairs inclined at 30^{o} and 45^{o}.

The crack initiation stress ratio and coalescence strain ratio (refer to section 3.5 for definitions) are summarized below. The coalescence occurred **after the specimen maximum stress** was reached.

Crack Initiation Stress Ratio *Average value (min – max)*	0.990 (0.912 – 1.000)
Coalescence Strain Ratio *Average value (min – max)*	1.022 (1.009 – 1.035) All coalesced after maximum stress

Gypsum 2a-75-0	
2a-75-0-B (3,000pps) – coalescence 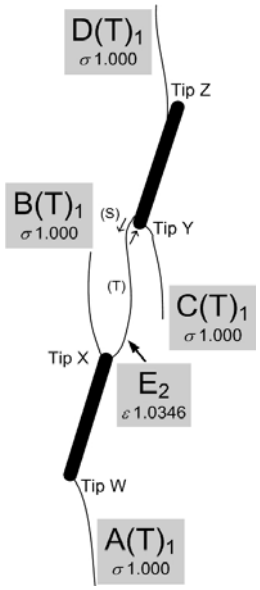 Pre-max : 1 CAM : no cracking Post-max : 2 HS : 1-2	2a-75-0-C (3,800pps) – coalescence 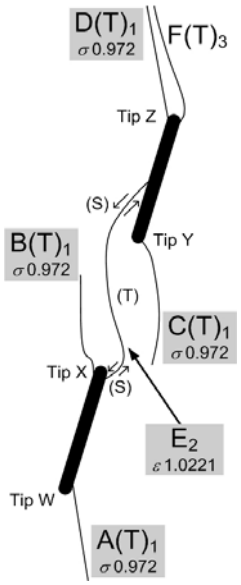 Pre-max : 1 CAM : 1 Post-max : 2-4 HS : 2-4
2a-75-0-D (3,800pps) – coalescence 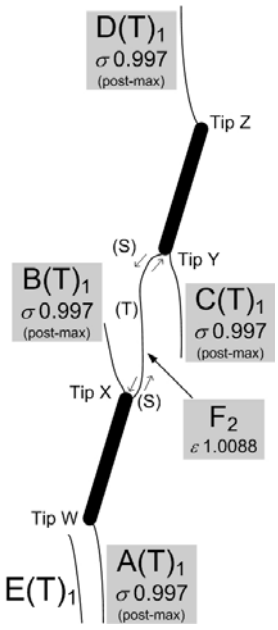 CAM : 1 Post-max : 1-2 HS : 2	

Figure H.5 – Fracturing and coalescence patterns for gypsum 2a-75-0.

APPENDIX I – Test Results of Gypsum Specimens Containing Stepped Double Flaws of Ligament Length '2a'

In this appendix, the cracking phenomena of gypsum specimens containing stepped double flaws (0.05" aperture) of ligament "2a" are described. Sketches of cracking patterns observed in all specimens are also illustrated. Refer to section 3.5 and section 5.2 for the meaning of symbols used in the sketches.

Thirty gypsum specimens with flaw inclination angle 30^o were tested in this series (see below). Three or more specimens were tested for each geometry in order to obtain consistent coalescence behavior.

Bridging angles α (^{o})	**Specimens**	**Total**
-60	2a-30-(-60)-A, 2a-30-(-60)-B 2a-30-(-60)-E, 2a-30-(-60)-F	4
-30	2a-30-(-30)-A, 2a-30-(-30)-B 2a-30-(-30)-D, 2a-30-(-30)-F	4
0	2a-30-0-A, 2a-30-0-B 2a-30-0-D, 2a-30-0-E	4
30	2a-30-30-A, 2a-30-30-B 2a-30-30-C, 2a-30-30-E 2a-30-30-F	5
60	2a-30-60-A, 2a-30-60-B 2a-30-60-C, 2a-30-60-D 2a-30-60-E, 2a-30-60-F	6
90	2a-30-90-A, 2a-30-90-B 2a-30-90-C	3
120	2a-30-120-A, 2a-30-120-C 2a-30-120-D, 2a-30-120-E	4
		30 (Total)

Gypsum 2a-30-(-60) (figure I.1)

The first cracks to initiate were **tensile wing crack** (TWC, type 1 tensile crack) pairs from the upper face and lower face of the right flaw, which were close to or at the flaw tips. TWCs also developed on the upper face and lower face of the left flaw, but at a later time. It is at present not certain if the difference in the time of initiation of the TWCs between the left and right flaws was due to experimental errors (e.g. imperfect specimen dimensions, roughness of the top and bottom specimen faces) or truly inherent material behavior under compression. Additional curvilinear **mixed tensile-shear cracks** sometimes initiated from the flaw tips during the later stage of loading.

Coalescence was achieved in three out of the four specimens by a dextral **type 2 shear crack** linking up the inner tip of one flaw and a new crack initiated earlier from the other flaw (specimens B, E, F). In specimen B, the coalescence crack linked up the inner tip (tip Y) of the right flaw and a new crack initiated earlier from the left flaw. In specimens E and F, the coalescence crack linked up the inner tip (tip X) of the left flaw and a new crack initiated earlier from the right flaw.

Localized surface spalling was frequently associated with the formation of the coalescence crack between the inner flaw tips. Once the spalling fragments fell off from the front face of the specimen, the true traces of the underlying shear cracks were revealed. These were observed for crack E in specimen B, crack K in specimen E, crack G and top segment of crack F in specimen G.

The crack initiation stress ratio and coalescence strain ratio (refer to section 3.5 for definitions) are summarized below. In specimens B and E, coalescence occurred after the maximum stress was surpassed. In specimen F, coalescence occurred when the maximum stress was reached.

Crack Initiation Stress Ratio *Average value (min – max)*	0.672 (0.508 – 0.783)
Coalescence Strain Ratio *Average value (min – max)*	1.013 (1.000 – 1.048) 1 specimen coalesced at maximum stress 2 specimens coalesced after maximum stress

Gypsum 2a-30-(-60)

2a-30-(-60)-A (1,000pps) – no coalescence

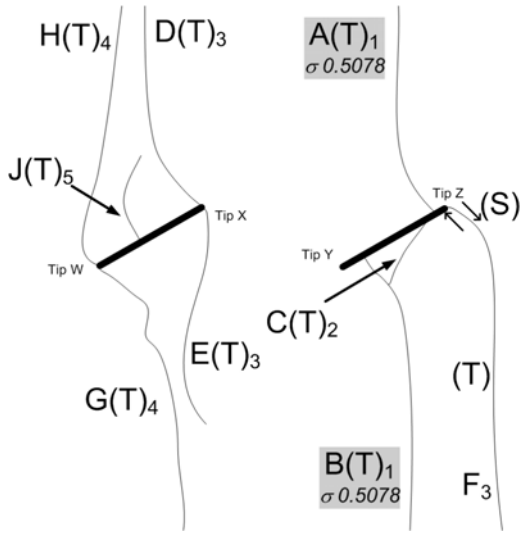

Pre-max : 1-2 CAM : 1-2
Post-max : 3-5 HS : 3-5

2a-30-(-60)-B (1,000pps) – coalescence

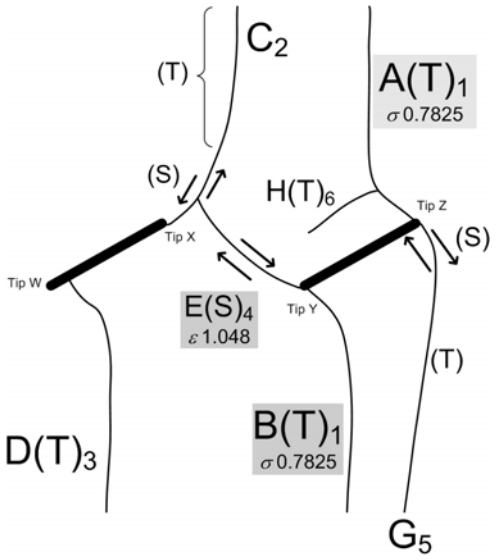

Pre-max : 1
Max : 2 CAM : 1-2
Post-max : 3-6 HS : 3-6

2a-30-(-60)-E (1,000pps) – coalescence

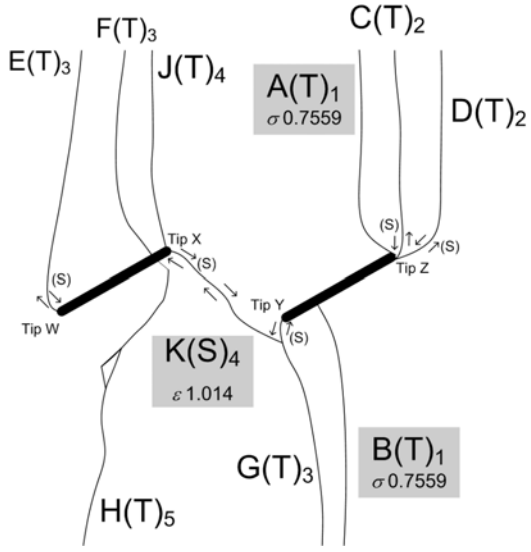

Pre-max : 1-2 CAM : 1-2
Post-max : 3-4 HS : 3-4

2a-30-(-60)-F (1,000pps) – coalescence

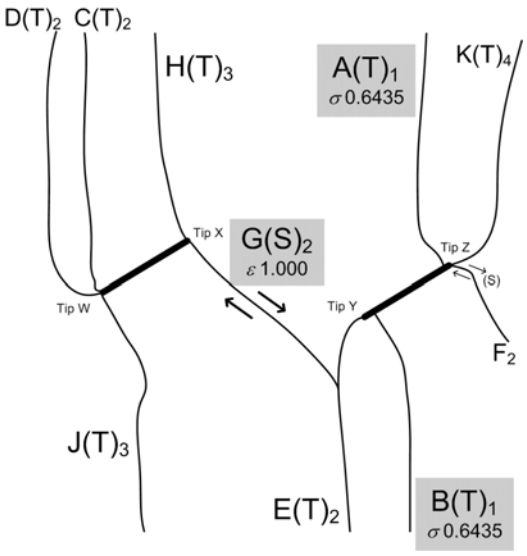

Pre-max : 1
Max : 2 CAM : 1-4
Post-max : 3-4 HS : none

Figure I.1 – Fracturing and coalescence patterns for gypsum 2a-30-(-60).

Gypsum 2a-30-(-30) (figure I.2)

The **first cracks** to initiate were **tensile wing crack** (TWC, type 1 tensile crack) pairs from the upper face and lower face of one of the two flaws (2 of the 4 specimens on the left flaw, 2 of the 4 specimens on the right flaw), which were close to or at the flaw tips. TWCs also developed on the upper face and lower face of the other flaw, but at a later time. The development of **type 2 tensile** (T) and **mixed tensile-shear** (T-S) outer tip cracks was common during later stage of loading.

Coalescence was achieved in three out of the four specimens (no coalescence in specimen A), but the coalescence patterns were different among them. Generally, there were two coalescence modes.

- specimens B and D – coalescence was achieved by **two inner tip cracks**, i.e. one crack initiated from the inner tip of the left flaw coalesced with another crack initiated from the inner tip of the right flaw.

- Specimen F – An inclined coalescence **shear crack** developed to link up the earlier developed **inner tip cracks**.

Localized surface spalling was frequently associated with the formation of the coalescence crack between the inner flaw tips. Once the spalling fragments fell off from the front face of the specimen, the true traces of the underlying shear cracks were revealed. These were observed for top segment of crack F in specimen A, top segment of crack D in specimen B, crack F and top segment of crack E in specimen D, crack K and bottom segment of crack J in specimen F.

The crack initiation stress ratio and coalescence strain ratio (refer to section 3.5 for definitions) are summarized below. In specimens B and D, coalescence occurred at the maximum stress. In specimen F, coalescence occurred after the maximum stress was reached.

Crack Initiation Stress Ratio *Average value (min – max)*	0.879 (0.794 – 0.974)
Coalescence Strain Ratio *Average value (min – max)*	1.005 (1.000 – 1.015) 2 specimens coalesced at maximum stress 1 specimen coalesced after maximum stress

Gypsum 2a-30-(-30)

2a-30-(-30)-A (1,000pps) – no coalescence

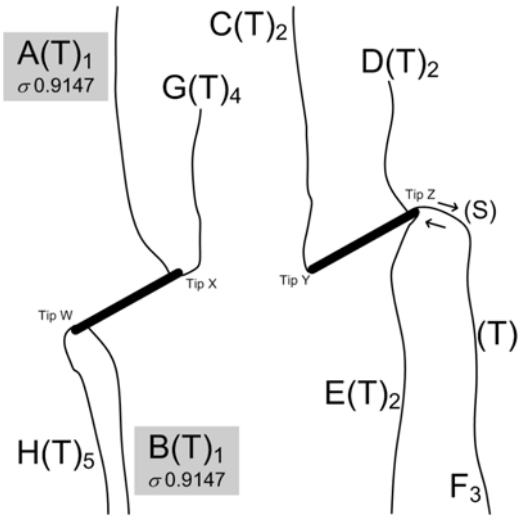

Pre-max : 1
Post-max : 2-5
CAM : 1
HS : 2-5

2a-30-(-30)-B (1,000pps) – coalescence

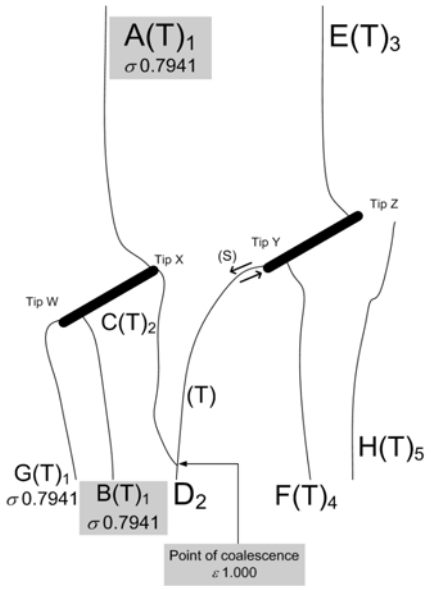

Pre-max : 1-3
Max : 4
Post-max : 5
CAM : 1
HS : 2-5

2a-30-(-30)-D (1,000pps) – coalescence

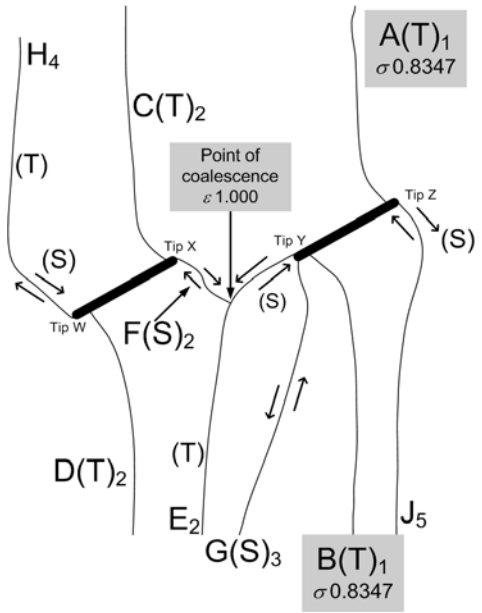

Pre-max : 1-4
Post-max : 5
CAM : 1
HS : 2-5

2a-30-(-30)-F (1,000pps) – coalescence

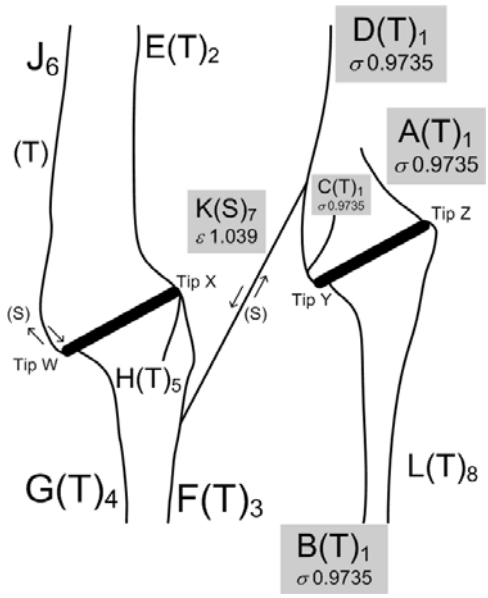

Pre-max : 1-4
Max : 5
Post-max : 6-7
CAM : 1-4
HS : 5-7

Figure I.2 – Fracturing and coalescence patterns for gypsum 2a-30-(-60).

Gypsum 2a-30-0

Refer to the corresponding description in Appendix H.

Gypsum 2a-30-30 (figure I.3)

Tensile wing cracks (TWCs, type 1 tensile cracks) were always the first cracks to initiate in the specimens (one pair on each flaw). These cracks initiated close to or at the flaw tips. The development of **type 2 tensile cracks** and **mixed tensile-shear cracks** from outer tip cracks was common during later stage of loading.

Coalescence occurred in all specimens in the region between the two inner flaw tips. Three coalescence types were recognized.

- Specimens A, B, E – A coalescence crack developed to link up the **two inner flaw tips. In specim**ens A and E, the coalescence cracks is **S-T-S**, which means the segments close to flaw tips are **shear** in origin, while the central segment is **tensile** in origin. In specimen B, the coalescence crack is **S-T**, which means that one segment of the coalescence crack adjacent to flaw tip is **shear** in origin, while the remaining segment is **tensile** in origin. With the frame rate of 1,000 pps used by the high speed camera, all segments were observed to initiate at the same time.

- Specimen C – **Two new cracks initiated independently.** The tip of a new crack which initiated from an inner flaw tip coalesced with the tip of another new crack which initiated from the other inner flaw tip. The two cracks were respectively **mixed tensile-shear crack** and **type 2 shear crack**.

- Specimen F – Two **mixed tensile-shear cracks** (E & E') initiated independently from the two inner flaw tips. Coalescence occurred between the tip of crack E and the middle segment of crack E', and between the tip of crack E' and the middle segment of crack E. The initiation of these cracks and the coalescence

processes were recorded by the camcorder, which had a poorer resolution than the high speed camera.

Localized surface spalling was frequently associated with the formation of the coalescence crack between the inner flaw tips. Once the spalling fragments fell off from the front face of the specimen, the true traces of the underlying shear cracks were revealed. These cases were observed for the ***shear segments*** of the coalescence cracks and also the shear segments of the outer tip mixed tensile-shear cracks (crack F in specimen A, crack H in specimen B, crack G in specimen E, crack F in specimen F).

The crack initiation stress ratio and coalescence strain ratio (refer to section 3.5 for definitions) are summarized below.

Crack Initiation Stress Ratio *Average value (min – max)*	0.578 (0.421 – 0.626)
Coalescence Strain Ratio *Average value (min – max)*	0.902 (0.811 – 0.968) All coalesced before maximum stress

Gypsum 2a-30-30

2a-30-30-A (1,000pps) – coalescence

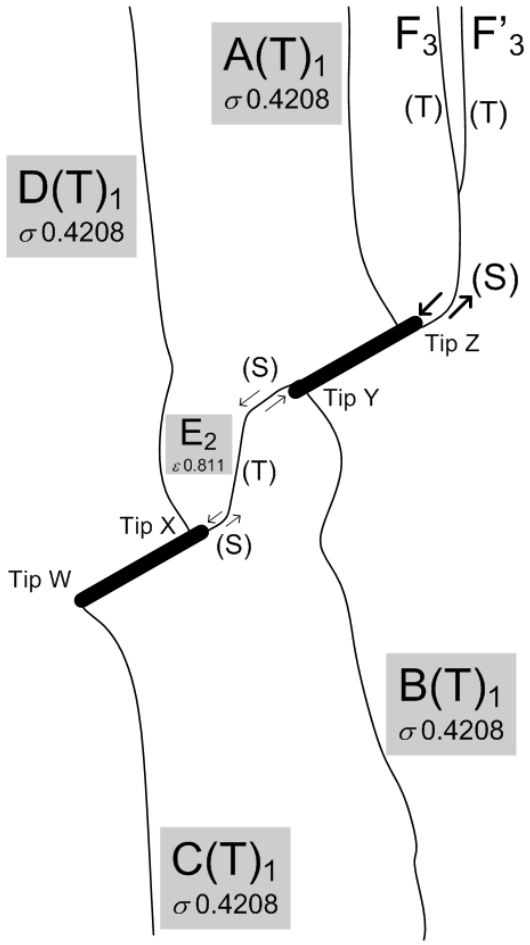

Pre-max : 1-2
Post-max : 3

CAM : 1-2
HS : 3

2a-30-30-B (1,000pps) – coalescence

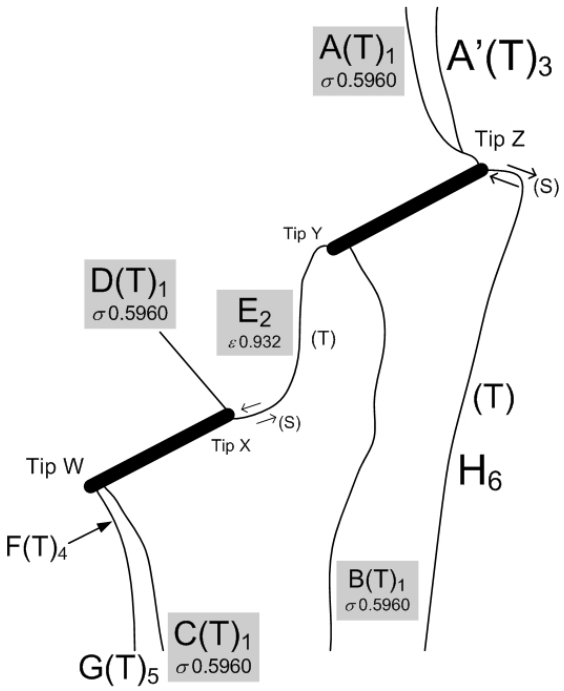

Pre-max : 1-5
Post-max : 6

CAM : 1-5
HS : 6

Figure I.3 – Fracturing and coalescence patterns for gypsum 2a-30-30.

Gypsum 2a-30-30 (continued)

2a-30-30-C (1,000pps) – coalescence

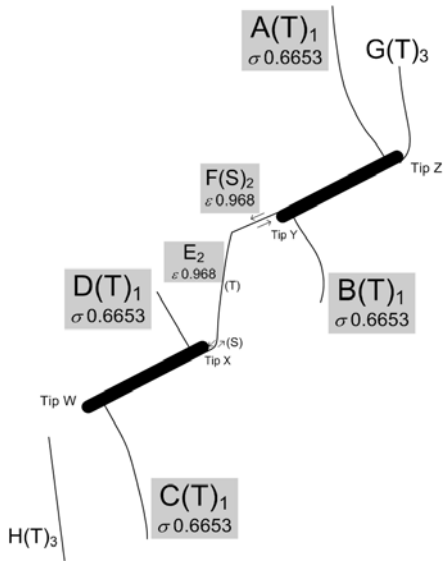

Pre-max : 1-2
Post-max : 3

CAM : 1
HS : 2-3

2a-30-30-E (1,000pps) – coalescence

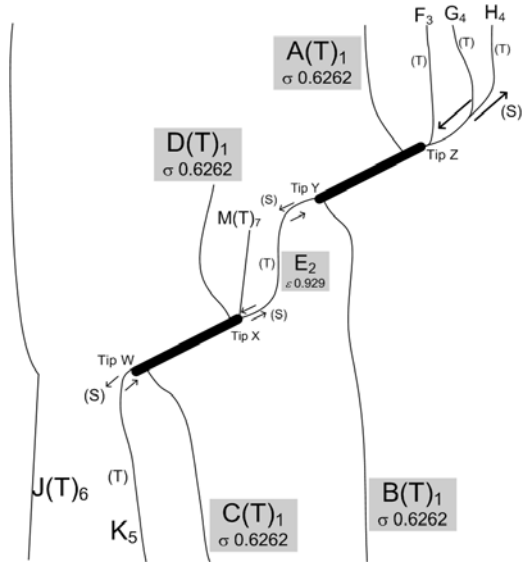

Pre-max : 1-3
Max : 4
Post-max : 5-7

CAM : 1-5
HS : 6-7

2a-30-30-F (1,000pps) – coalescence

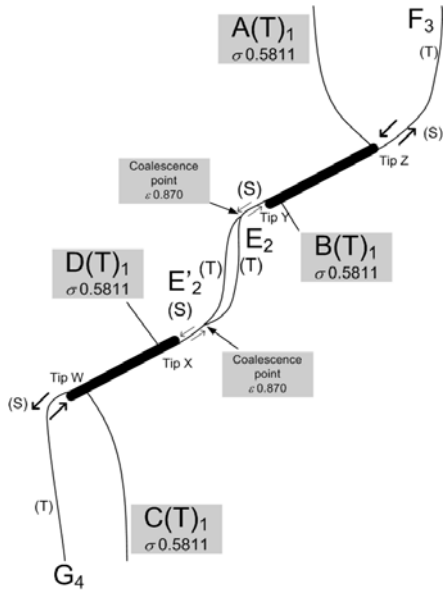

Pre-max : 1-3
Post-max : 4

CAM : 1-4
HS : no recording

Figure I.3 – Fracturing and coalescence patterns for gypsum 2a-30-30 (continued).

Gypsum 2a-30-60 (figure I.4)

Tensile wing cracks (TWCs, type 1 tensile cracks) were always the first cracks to initiate in the specimens (one pair on each flaw). These cracks initiated close to or at the flaw tips. For those wing cracks closer to the outer flaw tips (cracks A and C in all specimens), they tended to align with the loading axis after propagating for a short initial segment. For those wing cracks closer to the inner flaw tips (cracks B and D in all specimens), they tended to **curve** towards the other inner flaw tips. The development of **type 2 tensile** cracks and **mixed tensile-shear** outer tip cracks was common during later stage of loading.

Coalescence occurred in the central bridging region between the two inner flaw tips. Three coalescence types were recognized.

- Specimens A, B, C, D – A **coalescence crack** developed to link up the two inner flaw tips. In specimens A and D, the single coalescence cracks is **S-T-S**, which means the segments close to flaw tips are shear in origin, while the central segment is tensile in origin. In specimens B and C, the coalescence crack is **S-T**, which means that one segment of the coalescence crack adjacent to flaw tip is shear in origin, while the remaining segment is tensile in origin. With the frame rate of 1,000 pps used by the high speed camera, all segments were observed to initiate as a continuous crack at the same time.

- Specimen E – The tip of a new crack which initiated from an inner flaw tip coalesced with the tip of another new crack which initiated from the other inner flaw tip. In that particular case, a **type 2 tensile** crack (crack K) coalesced with a **type 2 shear** crack (crack J).

- Specimen F – Three cracks were involved. Two cracks (K & K') initiated independently from the two inner flaw tips. Coalescence occurred between cracks K and K' by the development of a third crack, which was an inclined shear crack. Crack K was a **type 2 tensile crack**. Crack K' was a **mixed tensile-shear crack**.

Localized surface spalling frequently occurred at the shear segments of the outer tip cracks and the shear segments of the coalescence cracks adjacent to the inner flaw tips.

The crack initiation stress ratio and coalescence strain ratio (refer to section 3.5 for definitions) are summarized below. In specimen C, coalescence occurred at the maximum stress. In other specimens (A, B, D, E, F), coalescence occurred after the maximum stress was reached.

Crack Initiation Stress Ratio *Average value (min – max)*	0.312 (0.273 – 0.391)
Coalescence Strain Ratio *Average value (min – max)*	1.125 (1.000 – 1.297) 1 specimen coalesced at maximum stress 4 specimens coalesced after maximum stress

Gypsum 2a-30-60

2a-30-60-A (1,000pps) – coalescence

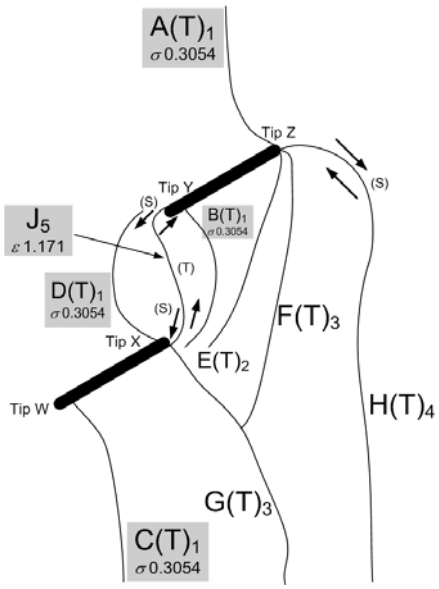

Pre-max : 1-2 CAM : 1-2
Post-max : 3-5 HS : 3-5

2a-30-60-B (1,000pps) – coalescence

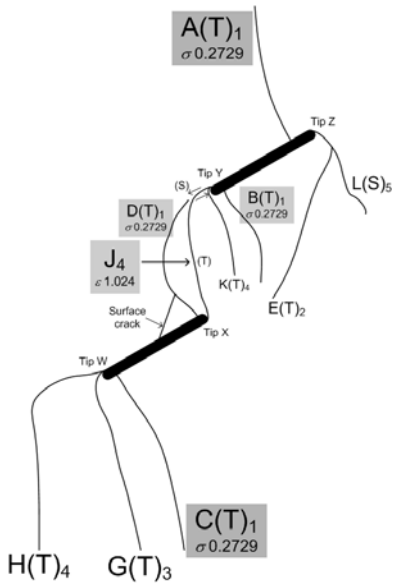

Pre-max : 1-2 CAM : 1-3
Post-max : 3-5 HS : 4-5

2a-30-60-C (1,000pps) – coalescence

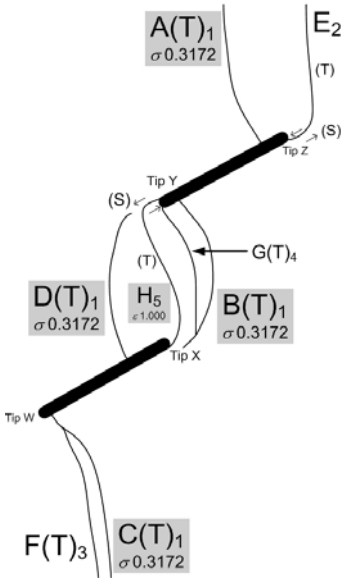

Pre-max : 1-5 CAM : 1-2
Post-max : None HS : 3-5

2a-30-60-D (1,000pps) – coalescence

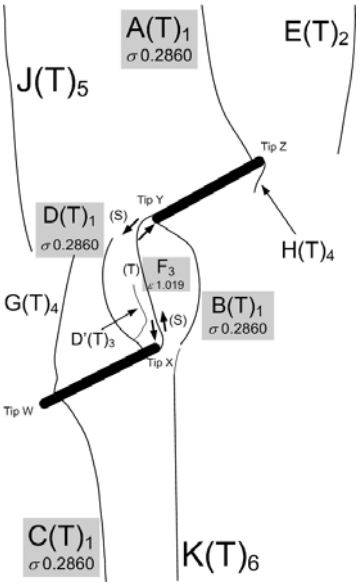

Pre-max : 1-2 CAM : 1-2
Post-max : 3-6 HS : 3-6

Figure I.4 – Fracturing and coalescence patterns for gypsum 2a-30-60.

Gypsum 2a-30-60 (continued)

2a-30-60-E (1,000pps) – coalescence

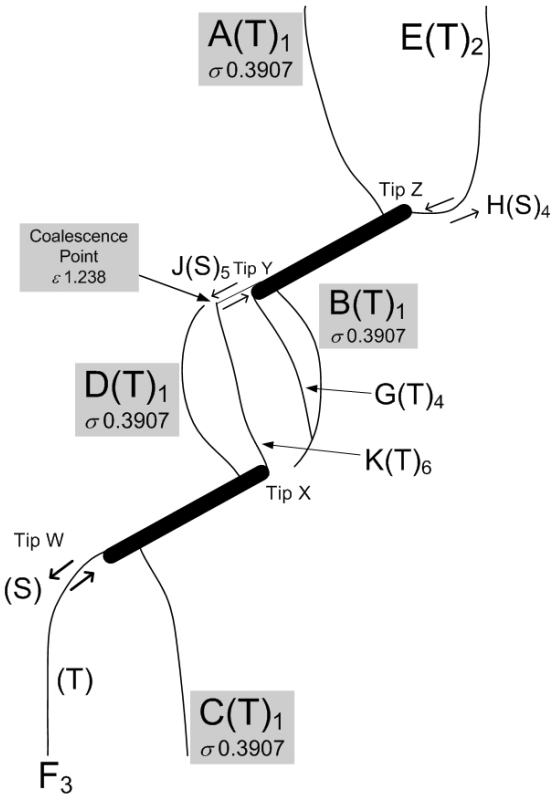

Pre-max : 1-2
Post-max : 3-6

CAM : 1-2
HS : 3-6

2a-30-60-F (1,000pps) – coalescence

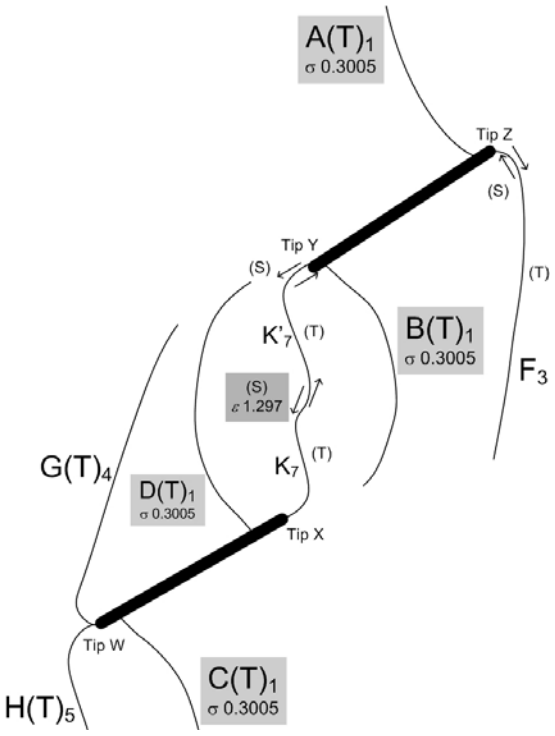

Pre-max : 1-5
Max : 6 (out of field of view)
Post-max : 7

CAM : 1-5
HS : 6-7

Figure I.4 – Fracturing and coalescence patterns for gypsum 2a-30-60 (continued).

Gypsum 2a-30-90 (figure I.5)

The first cracks to initiate in the specimens were **tensile wing cracks** (TWCs, type 1 tensile cracks). The **TWCs** (cracks A and B in all specimens) initiated close to/at the outer tips of the pre-existing flaws were not coalescence cracks, while some of the others were also the **coalescence cracks** – In the bridging region, the **TWCs** initiated to link up the inner flaw tips close to/at the flaw tips. The coalescence was from tip to tip in specimen A, and it was from tip to the other TWC in specimens B and C.

Additional coalescence cracks developed with increased loading which linked up the **left** tip (inner tip) of the top flaw and the **left** tip (outer tip) of the bottom flaw (crack D in specimen A, crack H in specimen B, crack F in specimen C) and/or the **right** tip (outer tip) of the top flaw and the **right** tip (inner tip) of the bottom flaw (crack D in specimen B, crack E in specimen C). Most of these cracks were **tensile** in origin, with some having **shear** segments adjacent to flaw tips (lower segment of crack D in specimen A, lower segment of crack H in specimen B, upper segment of crack E). The sense of **shearing** along those crack segments was physically compatible with the deformation/fracturing at the flaw tips which was associated with a reduction of the flaw aperture.

Localized surface spalling frequently occurred along the shear segments of the tip cracks.

The crack initiation stress ratio and coalescence strain ratio (refer to section 3.5 for definitions) are summarized below.

Crack Initiation Stress Ratio *Average value (min – max)*	0.345 (0.294 – 0.399)
Coalescence Strain Ratio *Average value (min – max)*	0.611 (0.521 – 0.704) All coalesced before maximum stress

Gypsum 2a-30-90 (continued)

2a-30-90-A (1,000pps) – coalescence

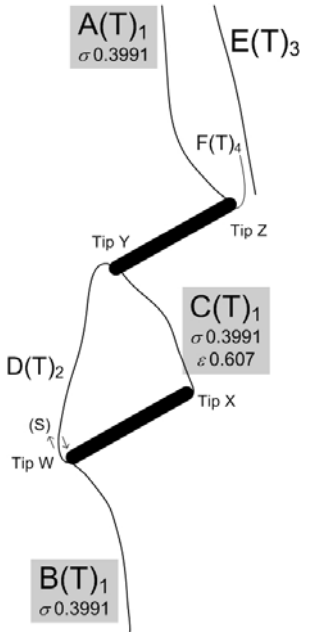

Pre-max : 1-2 CAM : 1-2
Post-max : 3 HS : 3

2a-30-90-B (1,000pps) – coalescence

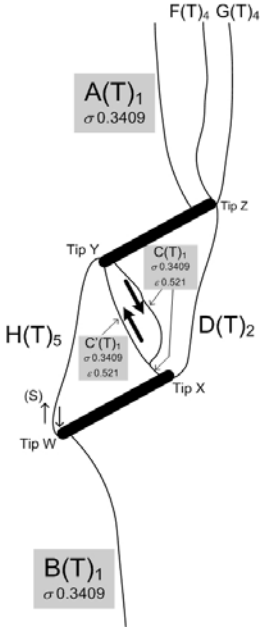

Pre-max : 1-4 CAM : 1-4
Post-max : 5-6 HS : 5-6

2a-30-90-C (1,000pps) – coalescence

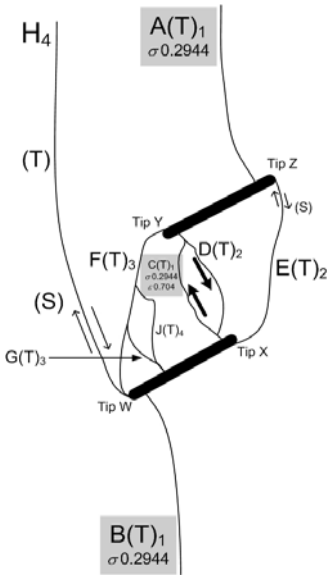

Pre-max : 1 CAM : 1-2
Post-max : 2-4 HS : 3-4

Figure I.5 – Fracturing and coalescence patterns for gypsum 2a-30-90.

Gypsum 2a-30-120 (figure I.6)

The first cracks to initiate in the specimens were **tensile wing cracks** (TWCs, type 1 tensile cracks). The **TWCs** A and B in all specimens initiated close to/at the outer tips of the pre-existing flaws. They initiated respectively from the upper face of the top flaw and the lower face of the bottom flaw.

The first coalescence cracks, which were found in the bridging region, were also TWCs. All of these coalescence cracks linked up the inner tip of one flaw and the middle section of the other flaw.

Similar to the flaw geometry of 2a-30-90, **additional coalescence cracks** developed with increased loading which linked up the **left** tip of the top flaw and the **left** tip of the bottom flaw (crack G in specimen A, crack E in specimen E) and/or the **right** tip of the top flaw and the **right** tip of the bottom flaw (crack E in specimen A, crack D in specimen C). Most of these cracks were **tensile** in origin, with some having **shear** segments adjacent to flaw tips. The **sense of shearing** along those crack segments was physically compatible with the deformation/fracturing at the flaw tips which was associated with a reduction of the flaw aperture.

It was also common that **type 2 tensile cracks** and **mixed tensile-shear cracks** developed from the pre-existing flaw tips with increased loading, but they did not coalescence with the other flaw (crack H in specimen C, cracks D & G in specimen D, crack G in specimen E).

Localized surface spalling frequently occurred at the shear segments of the tip cracks.

The crack initiation stress ratio and coalescence strain ratio (refer to section 3.5 for definitions) are summarized below.

Crack Initiation Stress Ratio *Average value (min – max)*	0.390 (0.334 – 0.440)
Coalescence Strain Ratio *Average value (min – max)*	0.821 (0.737 – 0.992) All coalesced before maximum stress

Gypsum 2a-30-120

2a-30-120-A (1,000pps) – coalescence

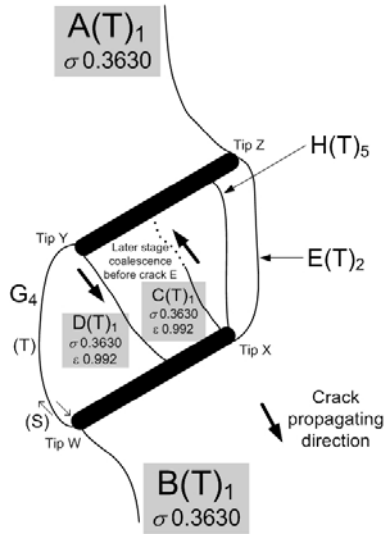

Pre-max : 1-2 CAM : 1
Post-max : 3-5 HS : 2-5

2a-30-120-C (1,000pps) – coalescence

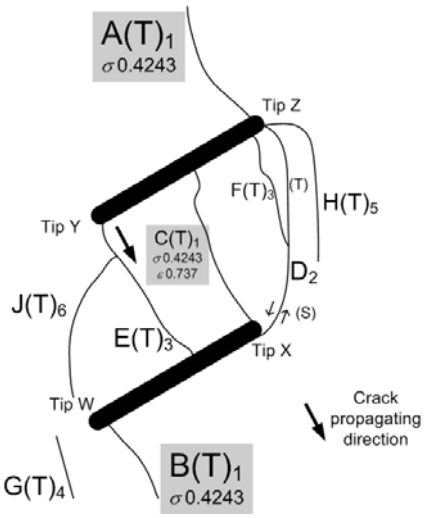

Pre-max : 1-4 CAM : 1-4
Post-max : 5-6 HS : 5-6

2a-30-120-D (1,000pps) – coalescence

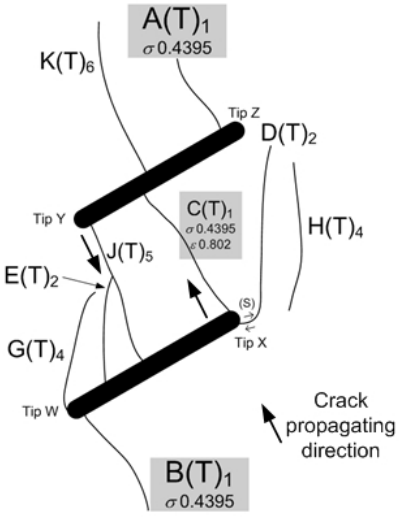

Pre-max : 1-2
Max : 3 (out of field of view) CAM : 1
Post-max : 4-6 HS : 3-6

2a-30-120-E (1,000pps) – coalescence

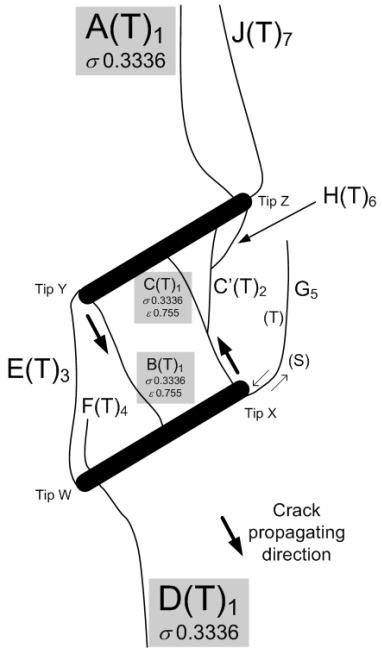

Pre-max : 1-2 CAM : 1-2
Post-max : 3-7 HS : 3-7

Figure I.6 – Fracturing and coalescence patterns for gypsum 2a-30-120.

APPENDIX J – Test Results of Gypsum Specimens Containing Coplanar Double Flaws of Ligament Length '4a'

In this appendix, the cracking phenomena of gypsum specimens containing coplanar double flaws (0.05" aperture) of ligament "4a" are described. Sketches of cracking patterns observed in all specimens are also illustrated. Refer to section 3.5 and section 5.2 for the meaning of symbols used in the sketches.

Nineteen gypsum specimens were tested in this series (see table below). Three or more specimens were tested for each geometry in order to obtain consistent coalescence behavior.

Flaw inclination (^{o})	**Specimens**	**Total**
0	4a-0-0-A, 4a-0-0-C, 4a-0-0-E, 4a-0-0-F	4
30	4a-30-0-A1, 4a-30-0-B1 4a-30-0-C1, 4a-30-0-D1 4a-30-0-E1	5
45	4a-45-0-B 4a-45-0-E 4a-45-0-F	3
60	4a-60-0-C 4a-60-0-D 4a-60-0-E	3
75	4a-75-0-A, 4a-75-0-C 4a-75-0-D, 4a-75-0-F	4
		19 (Total)

Gypsum 4a-0-0 (figure J.1)

Tensile wing cracks (TWCs, type 1 tensile cracks) were always the first cracks to initiate in the specimen. Most of them initiated far from the flaw tips on the flaw faces.

Coalescence occurred in half (two out of four) of the specimens tested, while it was absent in the other half of the specimens. In specimens C and F where no coalescence occurred, an inclined shear crack dipping out of the specimen front face in the central bridging region formed instead. In specimens A and E, coalescence was achieved by a linkage of two inclined cracks from the inner flaw tips. In both specimens, coalescence occurred after maximum stress was reached.

In all specimens, there was also a development of multiple **type 2 tensile cracks** and/or **mixed tensile-shear cracks** from flaw tips after the initiation of the tensile wing cracks. In addition, the aperture of the two pre-existing flaws was completely closed at the end of the loading test.

The crack initiation stress ratio and coalescence strain ratio (refer to section 3.5 for definitions) are summarized below.

Crack Initiation Stress Ratio *Average value (min – max)*	0.653 (0.310 – 0.887)
Coalescence Strain Ratio *Average value (min – max)*	1.103 (1.056 - 1.149)

Gypsum 4a-0-0

4a-0-0-A (10,000 pps) – coalescence

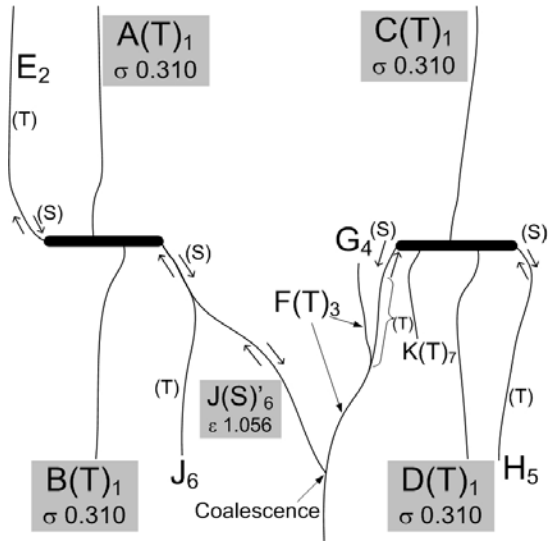

Pre-max : 1
Post-max : 2-7

CAM : 1-2
HS : 3-7

4a-0-0-C (12,000 pps) – no coalescence

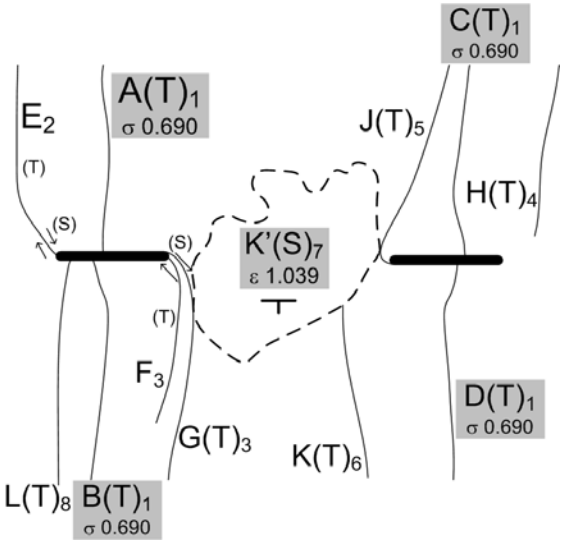

Pre-max : 1-2
Max : 2
Post-max : 3-8

CAM : 1
HS : 2-8

4a-0-0-E (10,000 pps) – coalescence

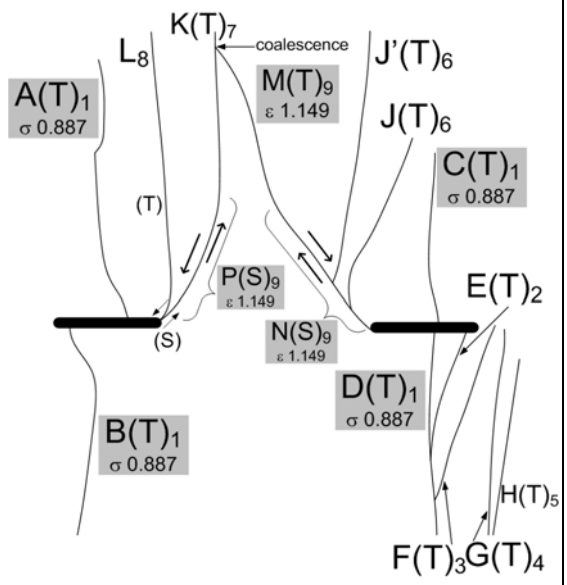

Pre-max : 1
Max : 2
Post-max : 3-9

CAM : 1-3
HS : 4-9

4a-0-0-F (10,000 pps) – no coalescence

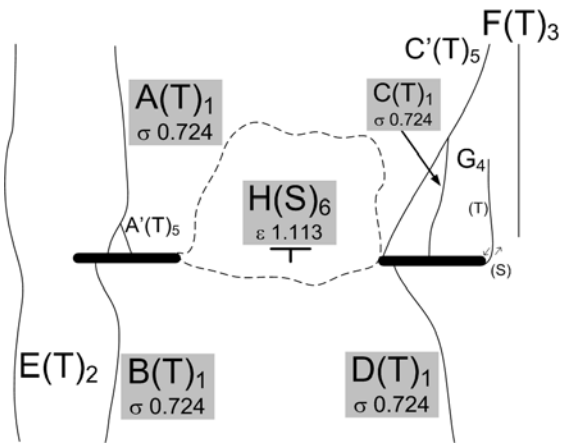

Pre-max : 1-2
Post-max : 3-6

CAM : 1-2
HS : 3-6

Figure J.1 – Fracturing and coalescence patterns for gypsum 4a-0-0.

Gypsum 4a-30-0 (figure J.2)

Tensile wing cracks (TWCs, type 1 tensile cracks) were always the first cracks to initiate in the specimen. Most of them initiated close to or at the flaw tips.

Coalescence was present in three out of five tested specimens, but absent in the remaining two. In the specimens where coalescence occurred, two cracks (type 1 shear cracks & mixed tensile-shear cracks) independently initiated from the inner flaw tips and coalesced. The coalescence was achieved by linking the **tip** of one crack and the **face** of the other crack. Note also that coalescence always occurred after maximum stress was reached.

Development of ***steep mixed tensile-shear cracks*** from outer flaw tips was common and these cracks often initiated before the occurrence of coalescence (if it occurred).

The crack initiation stress ratio and coalescence strain ratio (refer to section 3.5 for definitions) are summarized below.

Crack Initiation Stress Ratio *Average value (min – max)*	0838 (0.596 – 0.998)
Coalescence Strain Ratio *Average value (min – max)*	1.040 (1.029 - 1.062)

Gypsum 4a-30-0

4a-30-0-A1 (10,000 pps) – no coalescence

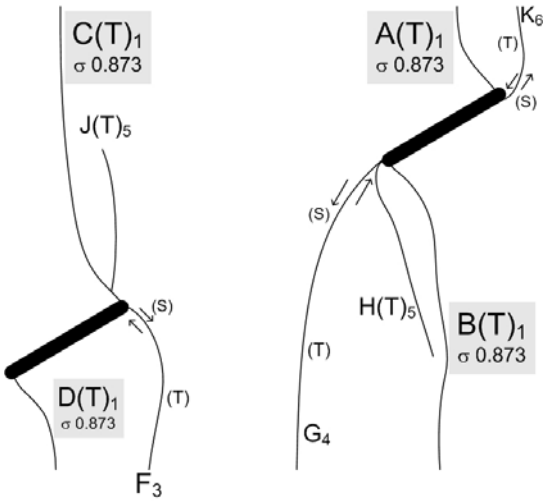

Pre-max : 1 CAM : 1-2
Post-max : 2-6 HS : 3-6

4a-30-0-B1 (10,000 pps) – no coalescence

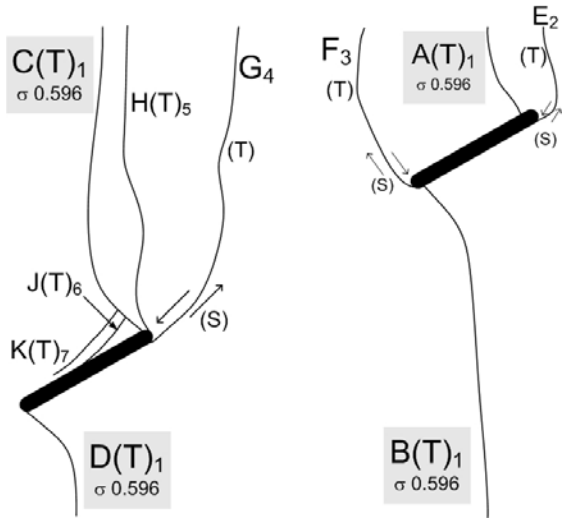

Pre-max : 1 CAM : 1
Post-max : 2-7 HS : 2-7

4a-30-0-C1 (10,000 pps) – coalescence

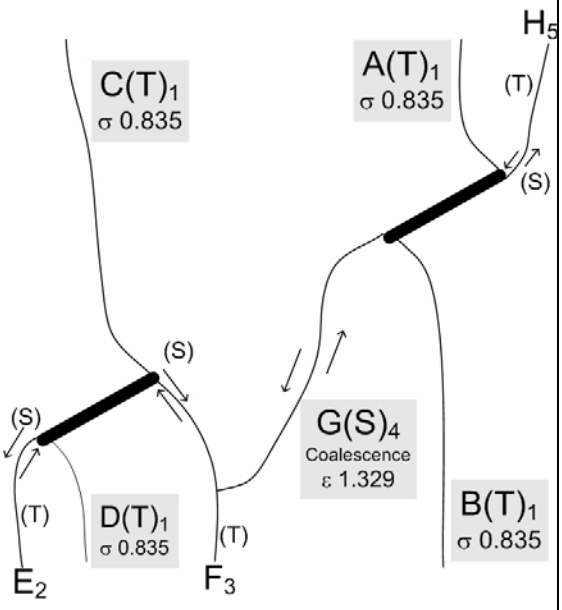

Pre-max : 1 CAM : 1
Post-max : 2-5 HS : 2-5

4a-30-0-D1 (7,207 pps) – coalescence

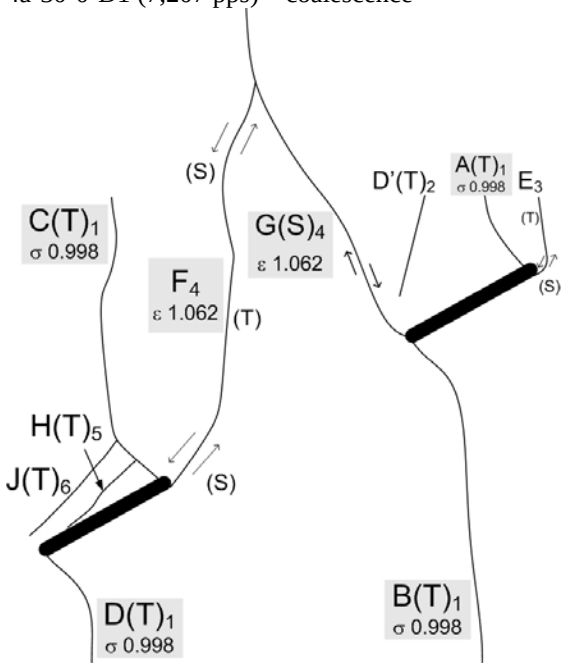

Pre-max : 1 CAM : 1
Post-max : 2-6 HS : 2-6

Figure J.2 – Fracturing and coalescence patterns for gypsum 4a-30-0.

Gypsum 4a-30-0 (continued)

4a-30-0-E1 (24,096 pps) – coalescence

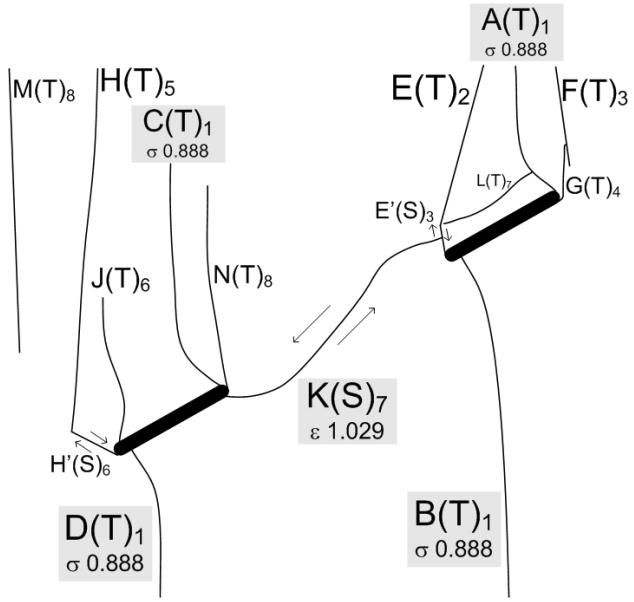

Pre-max : 1 CAM : 1
Post-max : 2-8 HS : 2-8

Figure J.2 – Fracturing and coalescence patterns for gypsum 4a-30-0 (continued).

Gypsum 4a-45-0 (figure J.4)

Tensile wing cracks (TWCs, type 1 tensile cracks) were always the first cracks to initiate in the specimen. All of them initiated close to or at the flaw tips.

Coalescence occurred in all three specimens by a coplanar shear cracks (type 2 shear cracks) linking up the two inner flaw tips. The initiation of such shear cracks in specimens B and F was recorded by the camcorder, while that in specimen E was recorded by the high speed camera. Although the trace of the coalescence crack was not directly exposed in specimen E, the time when the coalescence crack H initiated could be inferred from the occurrence of extensive surface spalling in the central bridging region[1]. The trace of the coalescence crack was exposed when the overlying surface spalling fragments fell off from the specimen front face.

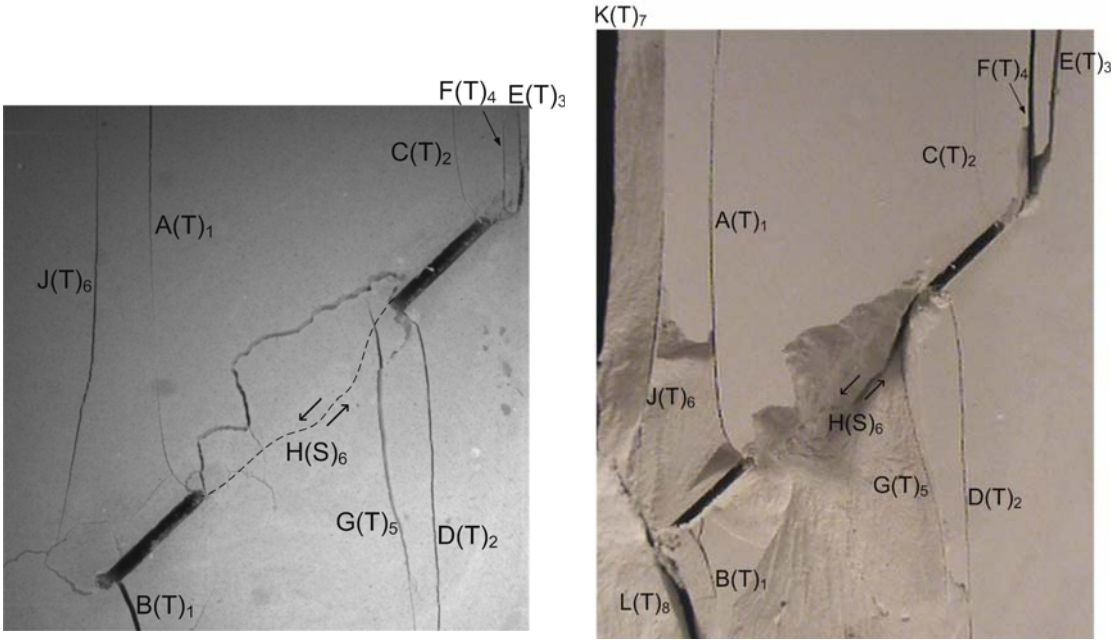

(a) (b)

Figure J.3 – (a) High speed image of specimen 4a-45-0-E. The occurrence of extensive surface spalling was used as an indicator when the underlying shear crack initiated. (b) Camcorder image at the end of the loading test.

[1] The close association of surface spalling and the development of underlying shear cracks is extensively observed in various specimens in the present experimental study.

Additional **type 2 tensile cracks** initiated from the flaw tips well after the initiation of tensile wing cracks.

The crack initiation stress ratio and coalescence strain ratio (refer to section 3.5 for definitions) are summarized below.

Crack Initiation Stress Ratio *Average value (min – max)*	0.398 (0.303 – 0.514)
Coalescence Strain Ratio *Average value (min – max)*	1.044 (1.007 – 1.097)

Gypsum 4a-45-0

4a-45-0-B (8,213 pps) – coalescence

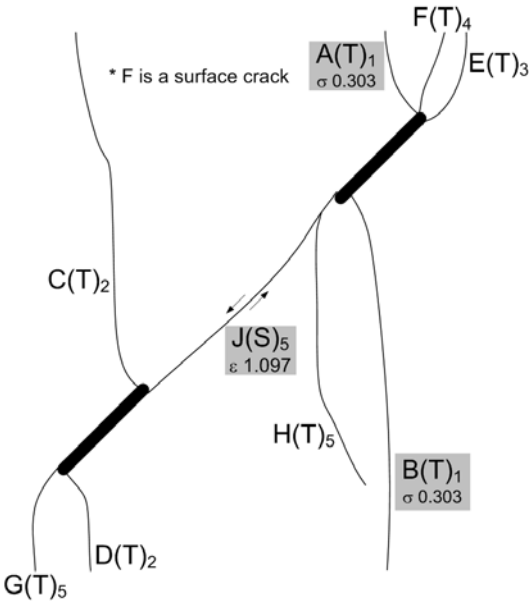

Pre-max : 1-4
Post-max : 5

CAM : 1-5
HS : nil

4a-45-0-E (8,213 pps) – coalescence

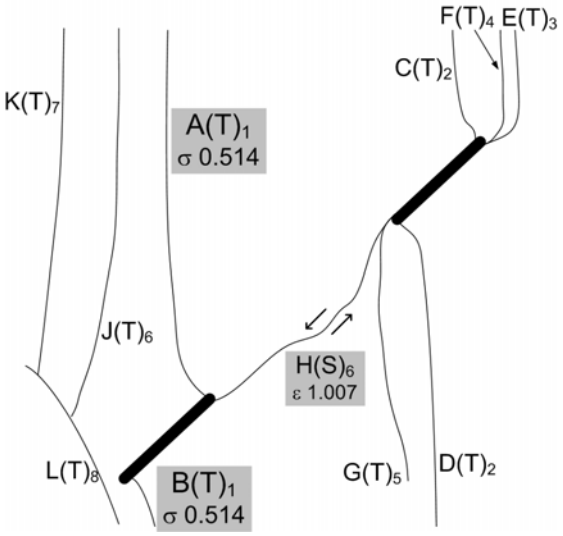

Pre-max : 1-4
Max : 5
Post-max : 6-8

CAM : 1-4
HS : 5-8

4a-45-0-F (8,213 pps) – coalescence

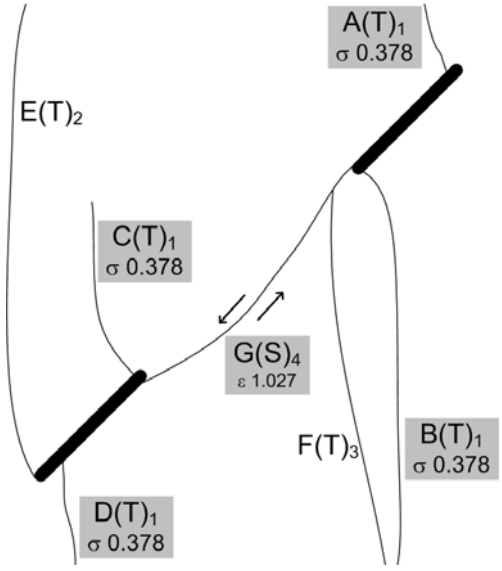

Pre-max : 1-3
Post-max : 4

CAM : 1, 3,4
HS : 2

Figure J.4 – Fracturing and coalescence patterns for gypsum 4a-45-0 (continued).

Gypsum 4a-60-0 (figure J.5)

Tensile wing cracks (TWCs, type 1 tensile cracks) were always the first cracks to initiate in the specimen. All of them initiated at the flaw tips.

Coalescence which occurred after the maximum stress was reached was achieved by a single shear crack (type 2 shear crack) linking up the inner flaw tips. Surface spalling was very common in the central bridging region before and/or during the occurrence of coalescence.

Apart from the coalescence shear cracks, additional **type 2 tensile cracks** and **mixed tensile-shear cracks** initiated from flaw tips, especially at the outer flaw tips.

The crack initiation stress ratio and coalescence strain ratio (refer to section 3.5 for definitions) are summarized below.

Crack Initiation Stress Ratio *Average value (min – max)*	0.673 (0.525 – 0.770)
Coalescence Strain Ratio *Average value (min – max)*	1.037 (1.004 – 1.056)

Gypsum 4a-60-0

4a-60-0-C (10,000 pps) – coalescence

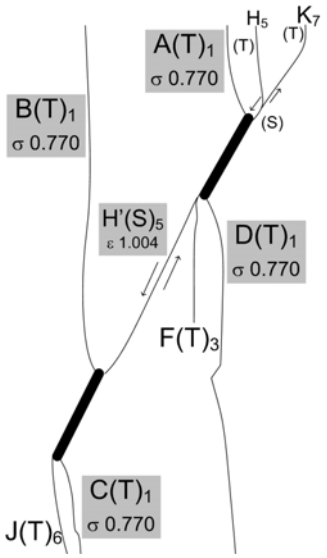

Surface cracks $E(T)_2$ and $G(T)_4$ are not show in the sketch.

Pre-max : 1-2 CAM : 1-2
Post-max : 3-7 HS : 3-7

4a-60-0-D (12,000 pps) – coalescence

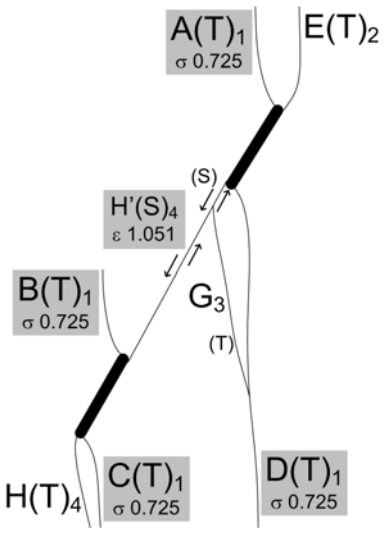

Pre-max : 1-2 CAM : 1-2
Post-max : 3-4 HS : 3-4

4a-60-0-E (12,000 pps) – coalescence

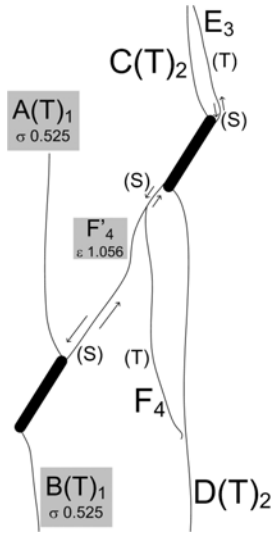

Pre-max : 1-2 CAM : 1-2
Post-max : 3-4 HS : 3-4

Figure J.5 – Fracturing and coalescence patterns for gypsum 4a-60-0.

Gypsum 4a-75-0 (figure J.6)

Tensile wing cracks (TWCs, type 1 tensile cracks) were always the first cracks to initiate in the specimen. All of them initiated at the flaw tips. Note however that the propagating length of the steeply inclined inner tip tensile wing cracks were short, only about the length of the pre-existing flaw. In contrast, the TWCs initiated from the outer tips propagated to reach the top and bottom edges of the specimens.

Coalescence which occurred after the maximum stress was reached was generally of a shear-tensile-shear (S-T-S) pattern. Variation occurred among the tested specimens with regard to the number of distinguishable individual crack segments involved in the coalescence:

One crack - In specimen C, the coalescence crack was a 'S' shaped single crack consisting of S-T-S segments.

Two cracks – In specimens D and F, a type 1 shear crack (coplanar) coalesced with a mixed tensile-shear crack.

Three cracks – In specimen A, two type 1 shear cracks (coplanar) initiated independently from the two inner flaw tips linked up a vertical tensile crack in the central bridging region.

Apart from the coalescence shear cracks, additional **type 2 tensile cracks** and **mixed tensile-shear cracks** initiated from flaw tips, especially at the outer flaw tips.

The crack initiation stress ratio and coalescence strain ratio (refer to section 3.5 for definitions) are summarized below.

Crack Initiation Stress Ratio *Average value (min – max)*	0.835 (0.728 – 0.954)
Coalescence Strain Ratio *Average value (min – max)*	1.050 (1.0001 – 1.179)

Gypsum 4a-75-0

4a-75-0-A (10,000 pps) – coalescence

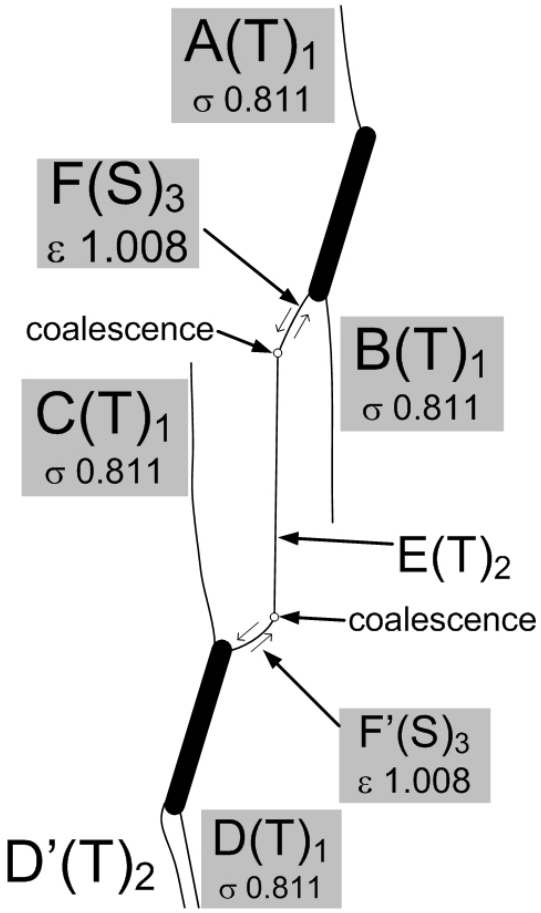

Pre-max : 1-2
Post-max : 3

CAM : 1-2
HS : 3

4a-75-0-C (14,035 pps) – coalescence

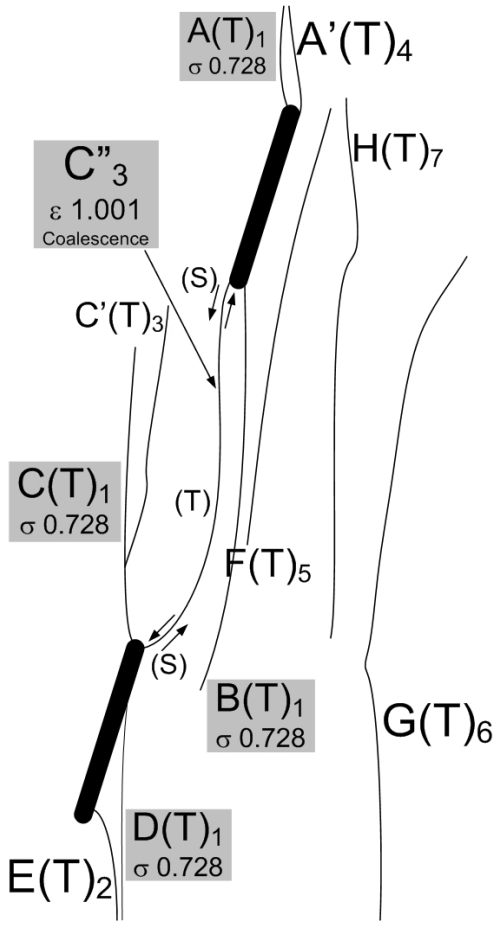

Pre-max : 1-2
Post-max : 3-7

CAM : 1-2
HS : 3-7

Figure J.6 – Fracturing and coalescence patterns for gypsum 4a-75-0.

Gypsum 4a-75-0 (continued)

4a-75-0-D (14,035 pps) – coalescence

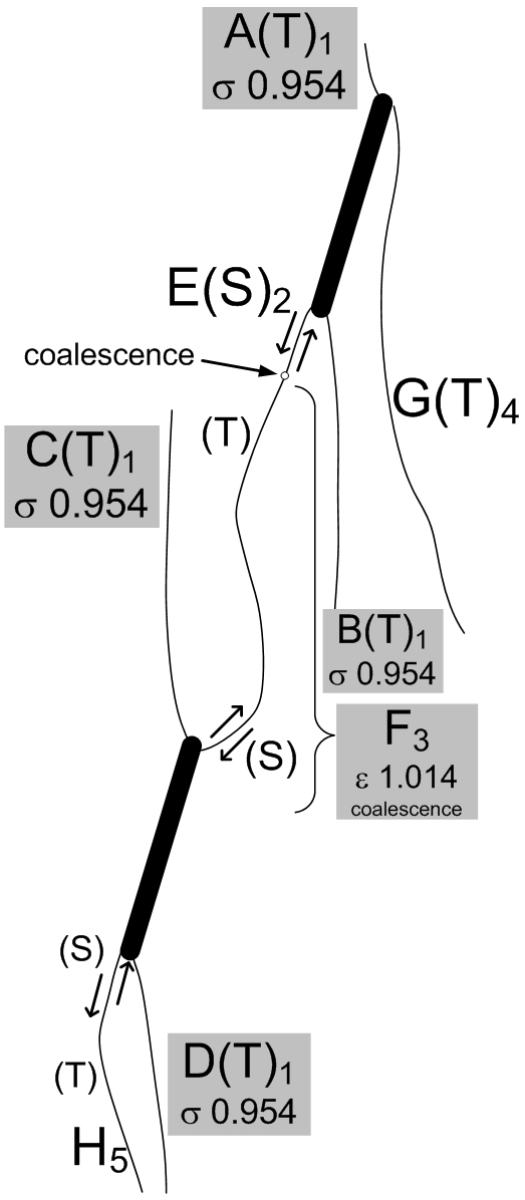

Pre-max : 1-2 CAM : 1-3
Post-max : 3-5 HS : 4-5

4a-75-0-F (11,019 pps) – coalescence

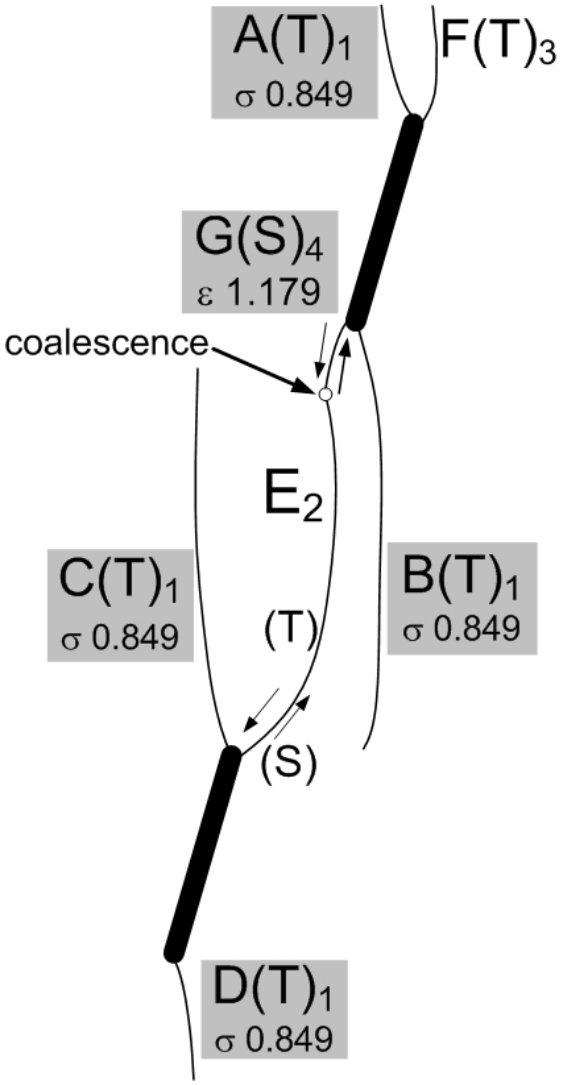

Pre-max : 1-2 CAM : 1-2
Post-max : 3-4 HS : 3-4

Figure J.6 – Fracturing and coalescence patterns for gypsum 4a-75-0 (continued).

APPENDIX K – Test Results of Gypsum Specimens Containing Stepped Double Flaws of Ligament Length '4a'

In this appendix, the cracking phenomena of gypsum specimens containing stepped double flaws (0.05" aperture) of ligament "4a" are described. Sketches of cracking patterns observed in all specimens are also illustrated. Refer to section 3.5 and section 5.2 for the meaning of symbols used in the sketches.

Twenty-seven gypsum specimens with flaw inclination angle 30^o were tested in this series (see below). Three or more specimens were tested for each geometry in order to obtain consistent coalescence behavior.

Bridging Angles α (^{o})	**Specimens**	**Number of specimens**
-60	4a-30-(-60)-B, 4a-30-(-60)-C 4a-30-(-60)-D	3
-30	4a-30-(-30)-A, 4a-30-(-30)-B 4a-30-(-30)-C, 4a-30-(-30)-D	4
0	4a-30-0-A1, 4a-30-0-B1 4a-30-0-C1, 4a-30-0-D1 4a-30-0-E1	5
30	4a-30-30-A1, 4a-30-30-B1 4a-30-30-C1, 4a-30-30-D1	4
60	4a-30-60-B1, 4a-30-30-C1 4a-30-30-E1	3
90	4a-30-90-B, 4a-30-90-C 4a-30-90-D, 4a-30-90-F	4
120	4a-30-120-A, 4a-30-120-C 4a-30-120-E, 4a-30-120-F	4
		27 (Total)

Gypsum 4a-30-(-60) (figure K.1)

The first cracks to initiate were **tensile wing crack** (TWC, type 1 tensile crack) pairs from the upper face and lower face of the right flaw, which were close to or at the flaw tips (see below).

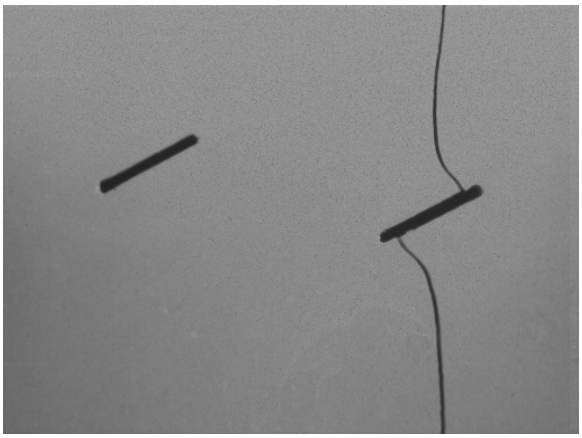

Coalescence was absent in one out of the three tested specimens (specimen D), while it occurred in the other two specimens. In these specimens (specimens B & C), coalescence in the specimens was achieved by an inclined **type 1 shear crack** which linked up one internal flaw tip and the face of a **steeply-inclined tensile crack** initiated earlier from the other internal flaw tip.

Additional curvilinear **type 2 tensile cracks and mixed tensile-shear cracks** initiated from the flaw tips during the later stage of loading.

The crack initiation stress ratio and coalescence strain ratio (refer to section 3.5 for definitions) are summarized below.

Crack Initiation Stress Ratio *Average value (min – max)*	0.858 (0.722 – 0.983)
Coalescence Strain Ratio *Average value (min – max)*	1.078 (1.036 – 1.121)

Gypsum 4a-30-(-60)

4a-30-(-60)-B (10,000 pps) – coalescence

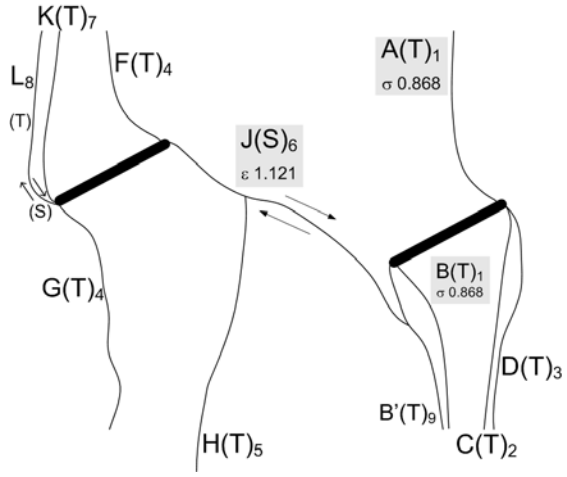

Pre-max : 1 CAM : 1
Post-max : 2-9 HS : 2-9

4a-30-(-60)-C (10,000 pps) – coalescence

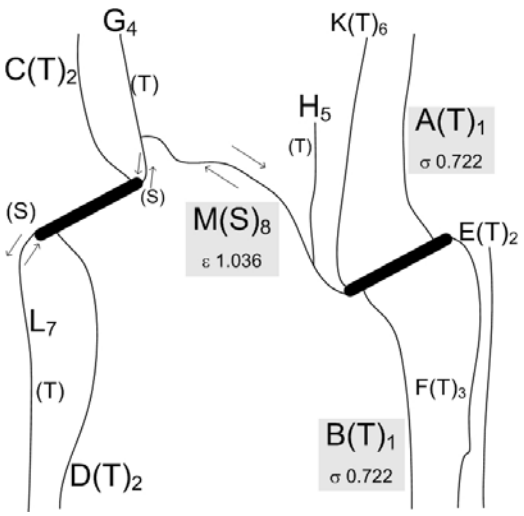

Pre-max : 1 CAM : 1
Post-max : 2-8 HS : 2-8

4a-30-(-60)-D (10,000 pps) – no coalescence

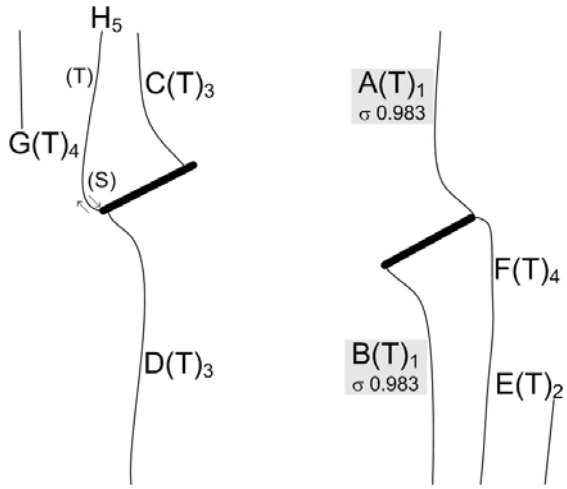

Pre-max : 1-3 CAM : 1-3
Post-max : 4-5 HS : 4-5

Figure K.1 – Fracturing and coalescence patterns for gypsum 4a-30-(-60).

Gypsum 4a-30-(-30) (figure K.2)

The first cracks to initiate were **tensile wing crack** (TWC, type 1 tensile crack) pairs close to or at the flaw tips. Additional curvilinear **mixed tensile-shear cracks** initiated from the flaw tips during the later stage of loading.

Coalescence was absent in all the four tested specimens, instead an inclined shear crack which dipped out of the specimen front face in the central bridging region was observed to have developed. The development of these shear cracks took place well after the maximum stress was reached.

The crack initiation stress ratio and coalescence strain ratio (refer to section 3.5 for definitions) are summarized below.

Crack Initiation Stress Ratio *Average value (min – max)*	0.808 (0.632 – 0.910)
Coalescence Strain Ratio *Average value (min – max)*	No coalescence

Gypsum 4a-30-(-30)

4a-30-(-30)-A (10,000 pps) – no coalescence

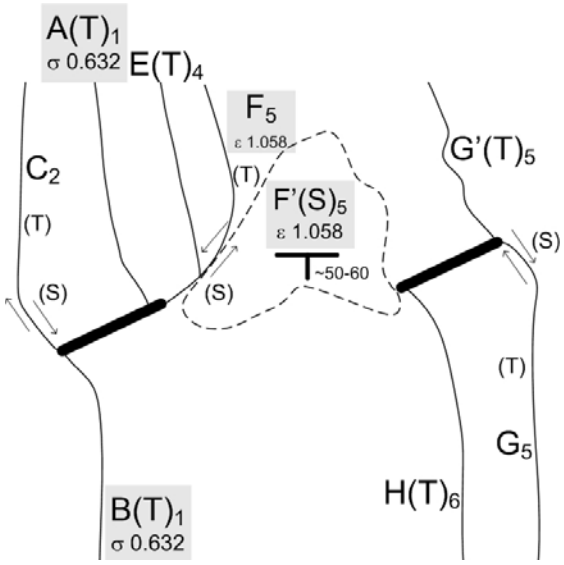

Crack F' was a shear crack dipping out on the front face of the specimen.

Pre-max : 1 CAM : 1
Post-max : 2-6 HS : 2-6

4a-30-(-30)-B (10,000 pps) – no coalescence

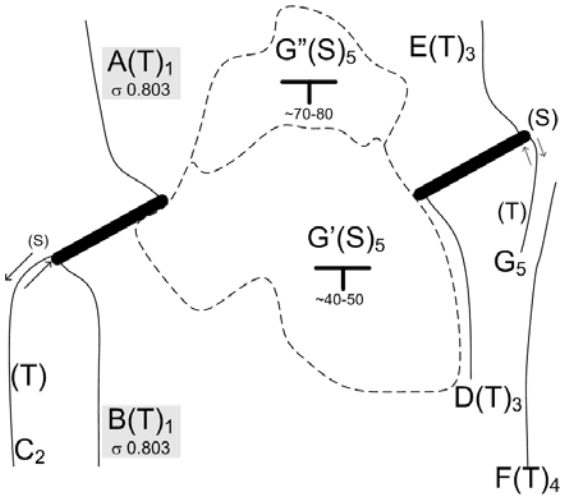

Cracks G' and G" were shear cracks dipping out on the front face of the specimen.

Pre-max : 1 CAM : 1
Post-max : 2-5 HS : 2-5

4a-30-(-30)-C (10,000 pps) – no coalescence

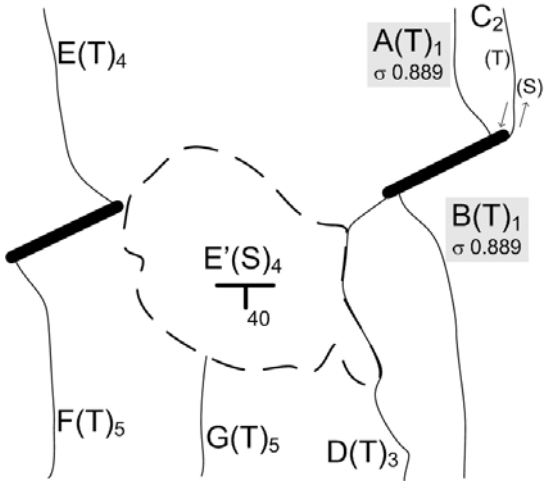

Crack E' was a shear crack dipping out on the front face of the specimen.

Pre-max : 1 CAM : 1
Post-max : 2-5 HS : 2-5

4a-30-(-30)-D (7,207 pps) – no coalescence

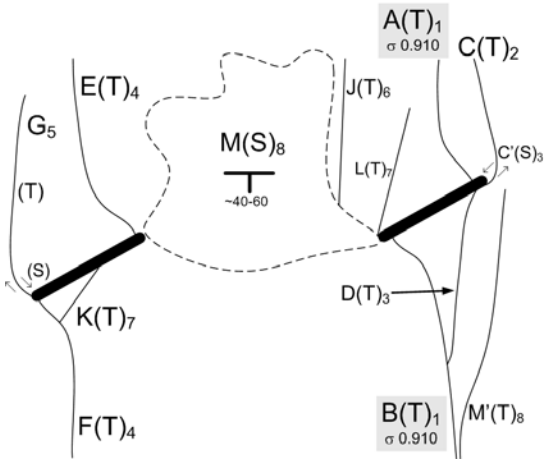

Crack M was a shear crack dipping out on the front face of the specimen.

Pre-max : 1 CAM : 1
Post-max : 2-8 HS : 2-8

Figure K.2– Fracturing and coalescence patterns for gypsum 4a-30-(-30).

Gypsum 4a-30-0

Refer to the corresponding description in Appendix J.

Gypsum 4a-30-30 (figure K3)

The first cracks to initiate were **tensile wing crack** (TWC, type 1 tensile crack) pairs close to or at the flaw tips (see figure below). Additional curvilinear **mixed tensile-shear cracks** initiated from the flaw tips during the later stages of loading.

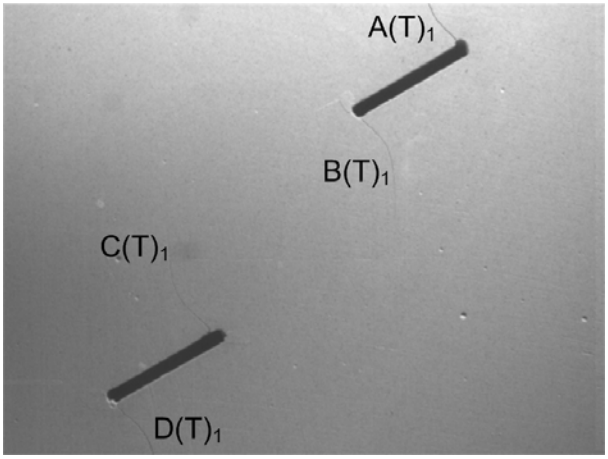

Coalescence occurred in all specimens after passing the maximum stress – the two inner flaw tips were linked up by a single or multiple cracks which generally displayed a 'S' shaped appearance. In one out of four specimens (specimen B), a **single crack** consisting of shear-tensile-shear segments linked up the inner flaw tips. In three out of four specimens (specimens A, C, D), **two or three cracks** linked up to form the coalescence crack. The segments close to flaw tips were shear and the vertical segment in the central bridging region was tensile.

Surface spalling often occurred around inner flaw tips and was associated with the underlying development of shear crack segments.

The crack initiation stress ratio and coalescence strain ratio (refer to section 3.5 for definitions) are summarized below.

Crack Initiation Stress Ratio *Average value (min – max)*	0654 (0.565 – 0.741)
Coalescence Strain Ratio *Average value (min – max)*	1.037 (1.005 – 1.128)

Gypsum 4a-30-30

4a-30-30-A1 (10,000 pps) – coalescence

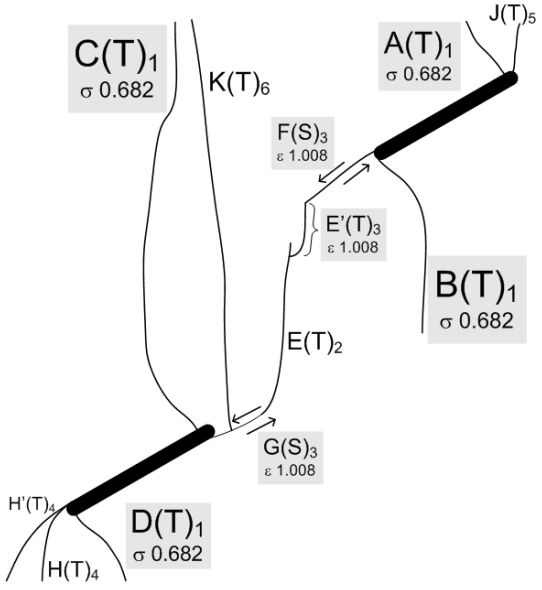

Pre-max : 1 CAM : 1
Post-max : 2-6 HS : 2-6

4a-30-30-B1 (10,000 pps) – coalescence

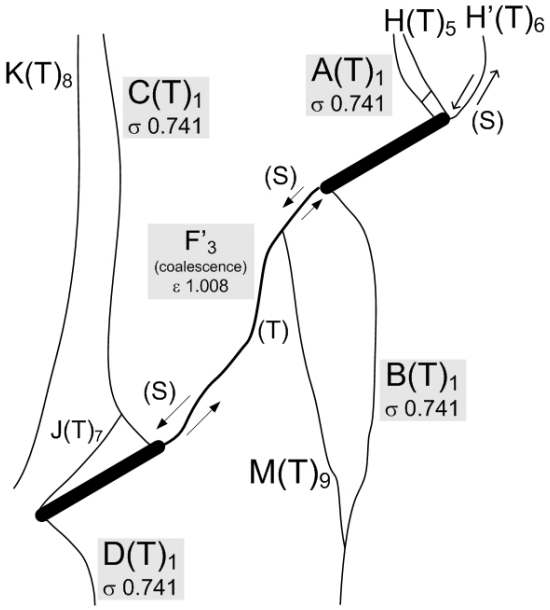

Pre-max : 1 CAM : 1
Post-max : 2-8 HS : 2-7

4a-30-30-C1 (24,096 pps) – coalescence

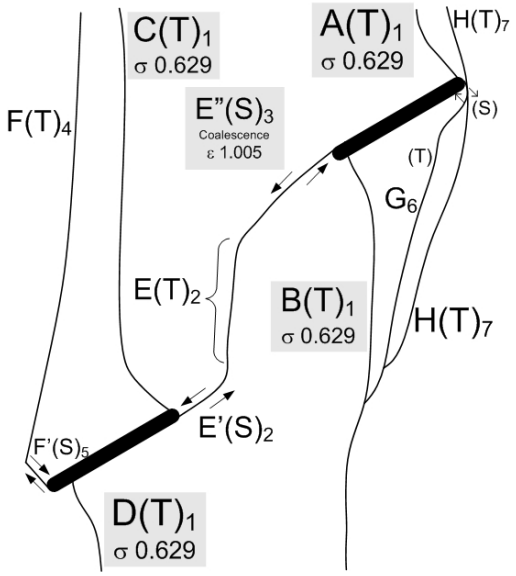

Pre-max : 1 CAM : 1
Post-max : 2-7 HS : 2-7

4a-30-30-D1 (no high speed recording) – coalescence

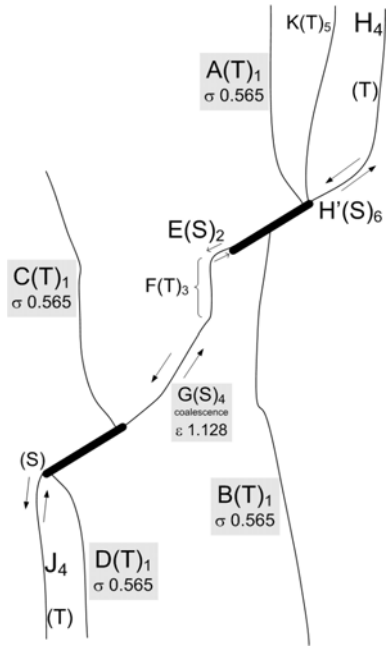

Pre-max : 1 CAM : 1-6
Post-max : 2-6

Figure K.3– Fracturing and coalescence patterns for gypsum 4a-30-30.

Gypsum 4a-30-60 (figure K.4)

The first cracks to initiate were **tensile wing crack** (TWC, type 1 tensile crack) pairs close to or at the flaw tips. **Outer tip tensile wing cracks** (cracks A & D in figure K.5) tended to align with the loading axis after propagating for a short segment. **Inner tip tensile wing cracks** (cracks B & C in figure K.5) tended to curve towards the other inner flaw tips after propagating for about twice the flaw length. Additional curvilinear **mixed tensile-shear cracks** initiated from the flaw tips during the later stages of loading.

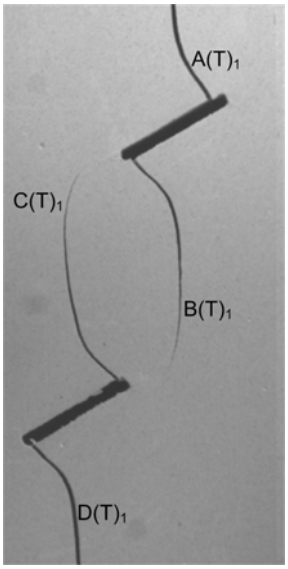

Figure K.5 – Tensile wing cracks initiated from a flaw pair with geometry 4a-30-90.

Coalescence occurred in all specimens between inner flaw tips after occurrence of the maximum stress. The general coalescence patterns were the same for all three specimens, i.e. shear segments adjacent to inner flaw tips and vertical tensile segment in the middle, but the type and number of cracks involved were different. In specimen B1, **one coalescence crack** consisting of shear-tensile-shear segments inked up the inner flaw tips. In specimen E1, **two cracks** were involved in which a coplanar shear crack (type 2 shear crack) developed to link up a type 2 tensile crack initiated earlier from the other inner flaw tip. In specimen C1, **four crack segments** were linked up for coalescence.

The crack initiation stress ratio and coalescence strain ratio (refer to section 3.5 for definitions) are summarized below.

Crack Initiation Stress Ratio *Average value (min – max)*	0.505 (0.457 – 0.544)
Coalescence Strain Ratio *Average value (min – max)*	1.064 (1.036 – 1.081)

Gypsum specimens containing the same flaw pair geometry but with narrower pre-existing flaw aperture (0.004”) were also cast and tested (figure K.6). The general fracturing and coalescence of this group of specimens were very similar to those with wide flaw aperture (0.05”) as shown in figure K.4, indicating the flaw aperture appeared not to have a strong influence on the fracturing and coalescence behavior.

Gypsum 4a-30-60

4a-30-60-B1 (14,035 pps) – coalescence

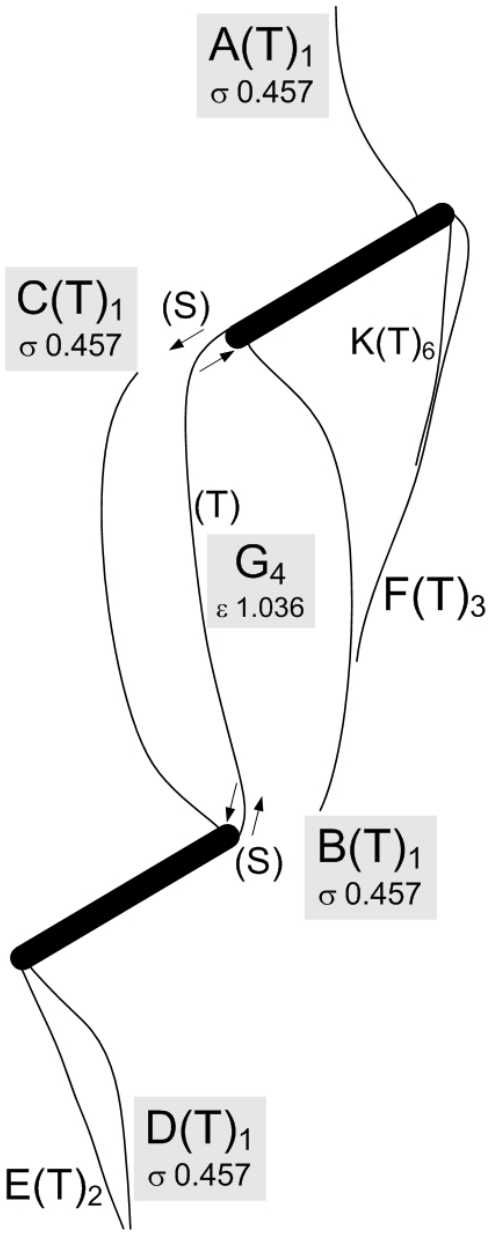

Pre-max : 1
Post-max : 2-6

CAM : 1
HS : 2-6

4a-30-60-C1 (14,035 pps) – coalescence

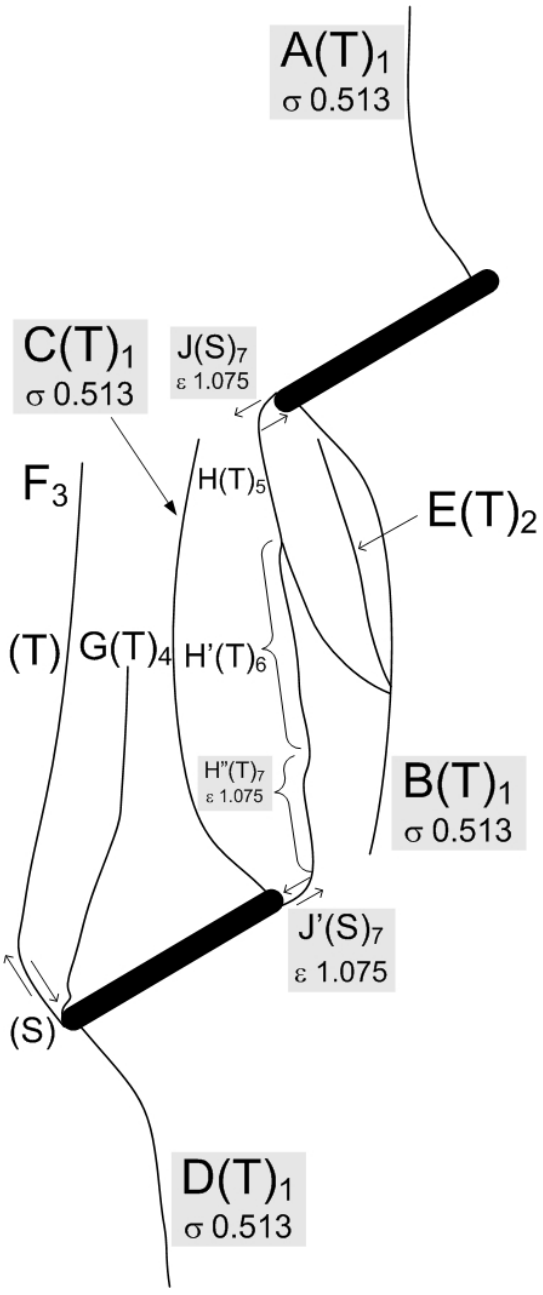

Pre-max : 1-4
Post-max : 5-7

CAM : 1-4
HS : 5-7

Figure K.4 – Fracturing and coalescence patterns for gypsum 4a-30-60

Gypsum 4a-30-60 (continued)

4a-30-60-E1 (14,035 pps) – coalescence

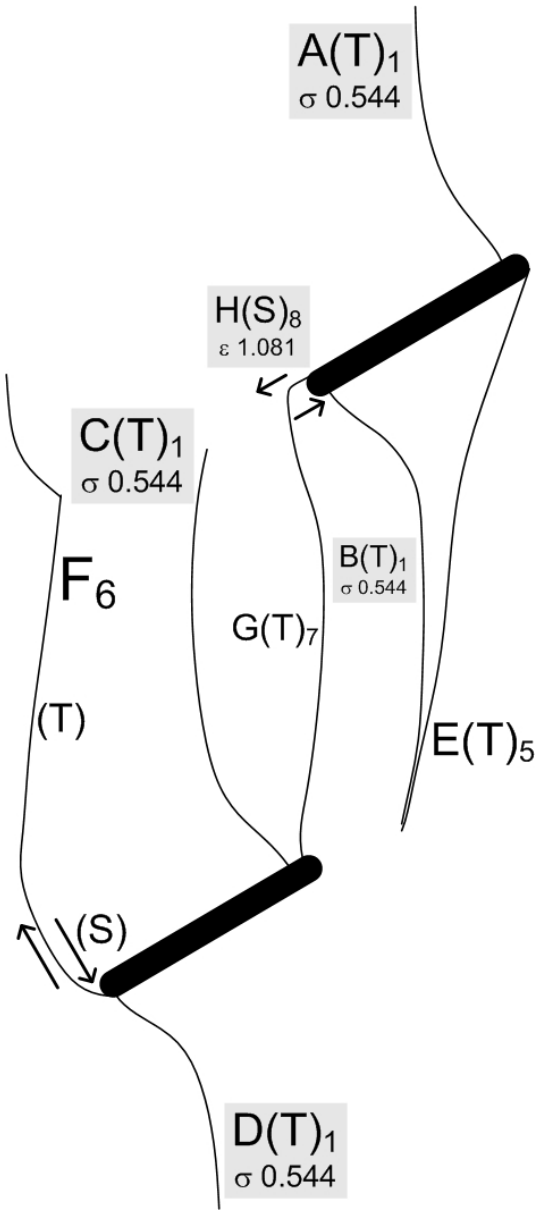

Pre-max : 1-4 CAM : 1-4
Post-max : 5-8 HS : 5-8

Cracks initiating as the 2nd, 3rd, 4th and 5th cracks were located far away from the pre-existing flaws and thus are not represented here.

Figure K.4 – Fracturing and coalescence patterns for gypsum 4a-30-60 (continued)

Gypsum 4a-30-60 (0.004” aperture)

4a-30-60-B (11,019 pps) – coalescence

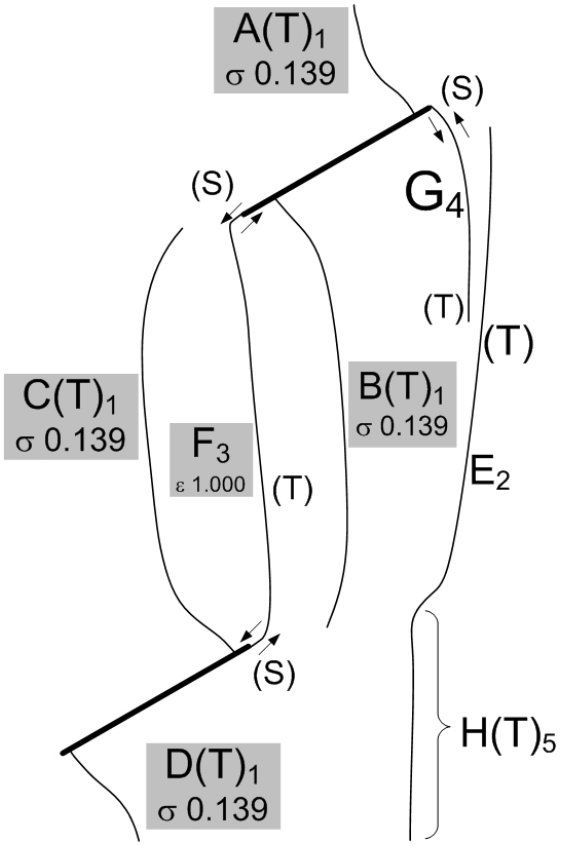

Pre-max : 1-2 CAM : 1-2
Post-max : 3-5 HS : 3-5

4a-30-60-E (11,019 pps) – coalescence

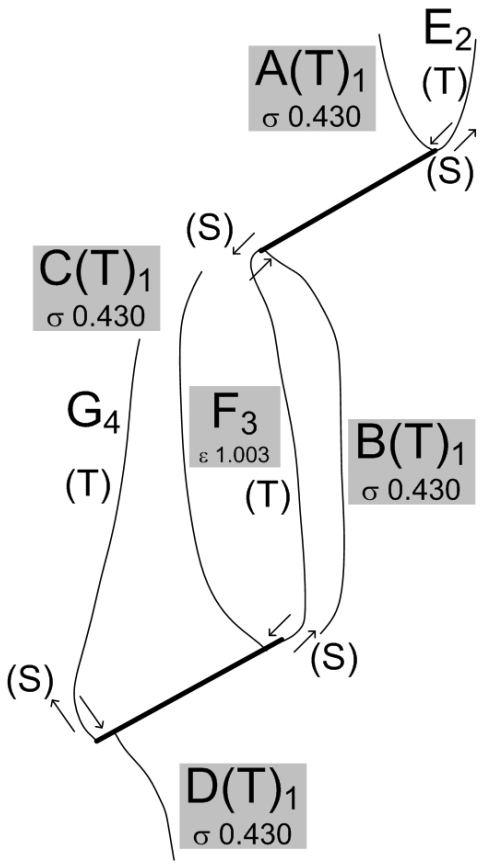

Pre-max : 1-2 CAM : 1-2
Post-max : 3-5 HS : 3-5

Figure K.6 – Fracturing and coalescence patterns for gypsum 4a-30-60 with flaw aperture 0.004”.

Gypsum 4a-30-90 (figure K.8)

The first cracks to initiate were of two main types. (1) coalescence tensile wing crack – crack B as shown in figure K.7, (2) **tensile wing crack** (TWC, type 1 tensile crack) pairs at the flaw tips from the upper face of the top flaw and the lower face of the bottom flaw – cracks A and C as shown in figure K.7. Additional curvilinear **mixed tensile-shear cracks** initiated from the flaw tips during the later stages of loading.

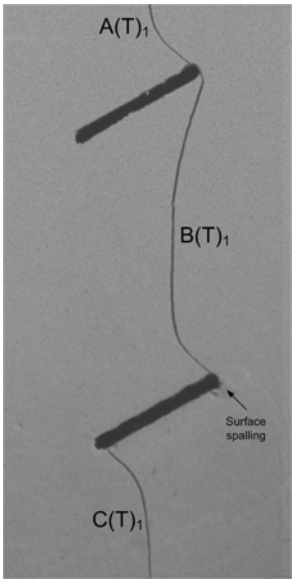

Figure K.7 – Tensile cracks initiated from a flaw pair with geometry 4a-30-90.

The coalescence behavior was very consistent among the different specimens tested in which a **single tensile wing crack** linked up the tips of the same side (left or right) of the two pre-existing flaws. Note also that coalescence always occurred before the occurrence of the maximum stress.

The crack initiation stress ratio and coalescence strain ratio (refer to section 3.5 for definitions) are summarized below.

Crack Initiation Stress Ratio *Average value (min – max)*	0.546 (0.488 – 0.626)
Coalescence Strain Ratio *Average value (min – max)*	0.747 (0.581 – 0.845)

Gypsum 4a-30-90

4a-30-90-B (10,000 pps) – coalescence

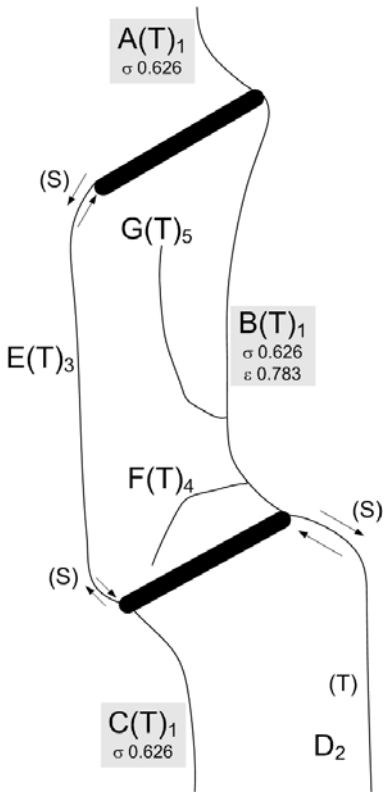

Pre-max : 1 CAM : 1
Post-max : 2-5 HS : 2-5

4a-30-90-C (14,035 pps) – coalescence

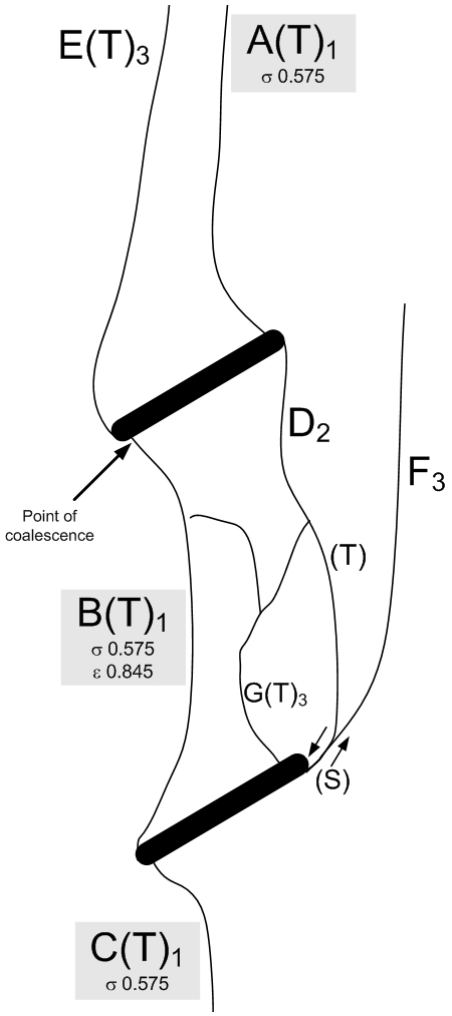

Pre-max : 1 CAM : 2-3
Post-max : 2-3 HS : 1

Figure K.8 – Fracturing and coalescence patterns for gypsum 4a-30-90.

Gypsum 4a-30-90 (continued)

4a-30-90-D (10,000 pps) – coalescence

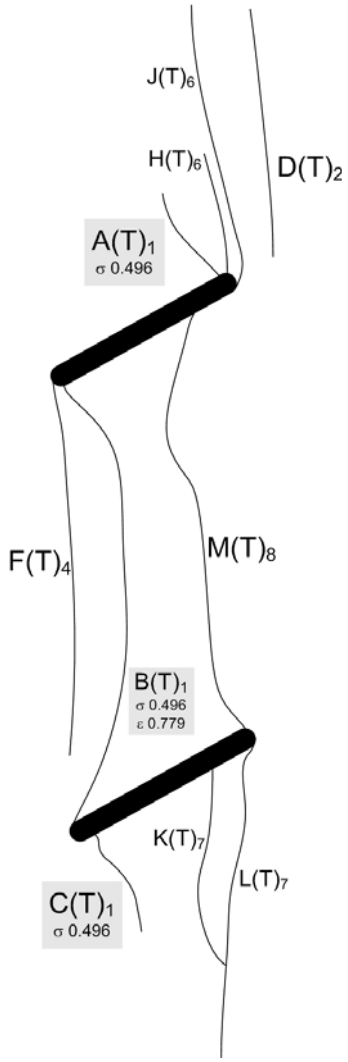

Pre-max : 1-3 CAM : 1
Post-max : 4-8 HS : 2-8

4a-30-90-F (14,035 pps) – coalescence

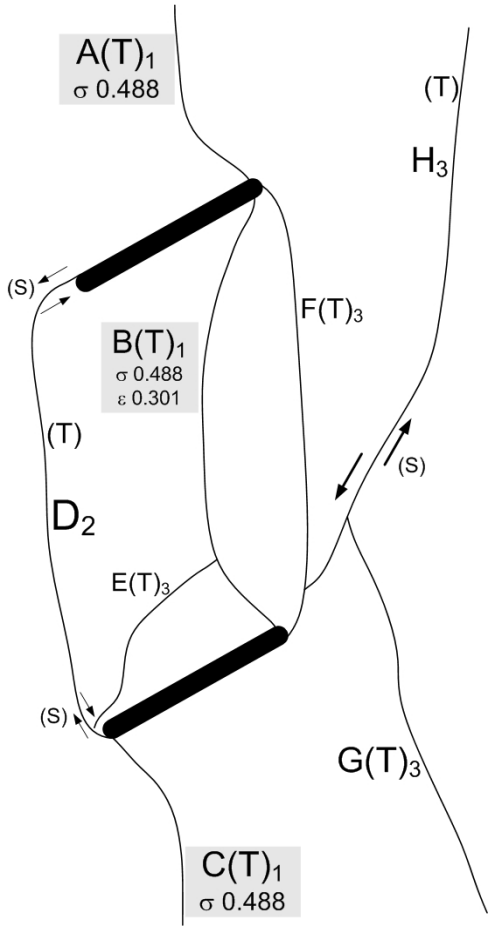

Pre-max : 1 HS : 1
Post-max : 2-3 CAM : 2-3

Figure K.8 – Fracturing and coalescence patterns for gypsum 4a-30-90 (continued)

Gypsum 4a-30-120 (figure K.9)

The first cracks to initiate were **tensile wing crack** (TWC, type 1 tensile crack) pairs close to or at the flaw tips (see the figure below). Additional curvilinear **mixed tensile-shear cracks** initiated from the flaw tips during the later stage of loading.

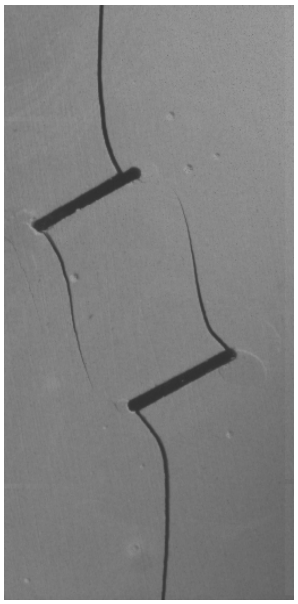

Coalescence occurred in all tested specimens after the maximum stress was reached. Consistent coalescence behavior was observed in three specimens and a completely different coalescence behavior was observed in another specimen:

- In one out of the four tested specimens (E), a tensile wing crack propagated from right tip of the bottom flaw upwards to link up the right tip of the top flaw. Similarly, another tensile wing crack propagated from the left tip of the top flaw downwards to link up the left tip of the bottom flaw.
- In three out of the four tested specimens (A, C, F), a single coalescence crack consisting of shear-tensile-shear (S-T-S) crack segments linked up the right tip of the top flaw and the left tip of the bottom flaw. Tensile cracks similar to those responsible for the coalescence in specimen E were also developed in these three specimens. However, they did not propagate far enough to reach the other flaw for coalescence.

The crack initiation stress ratio and coalescence strain ratio (refer to section 3.5 for definitions) are summarized below.

Crack Initiation Stress Ratio *Average value (min – max)*	0.346 (0.325 – 0.378)
Coalescence Strain Ratio *Average value (min – max)*	1.047 (1.022 – 1.077)

Gypsum 4a-30-120

4a-30-120-A (12,012 pps) – coalescence

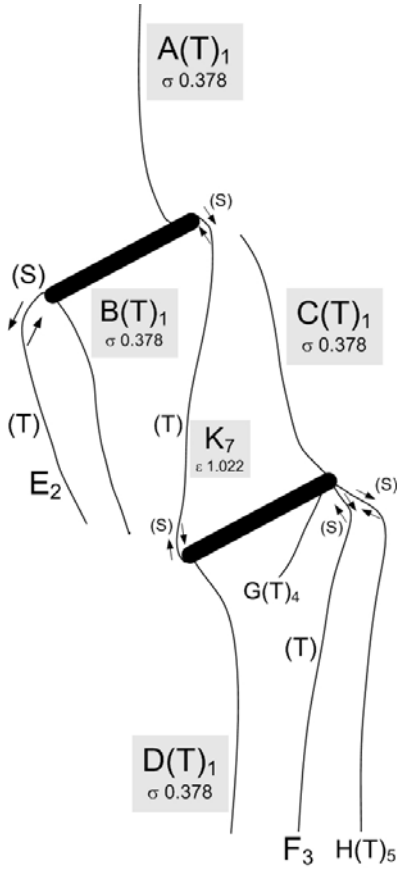

Pre-max : 1 CAM : 1
Post-max : 2-7 HS : 2-7

4a-30-120-C (14,035 pps) – coalescence

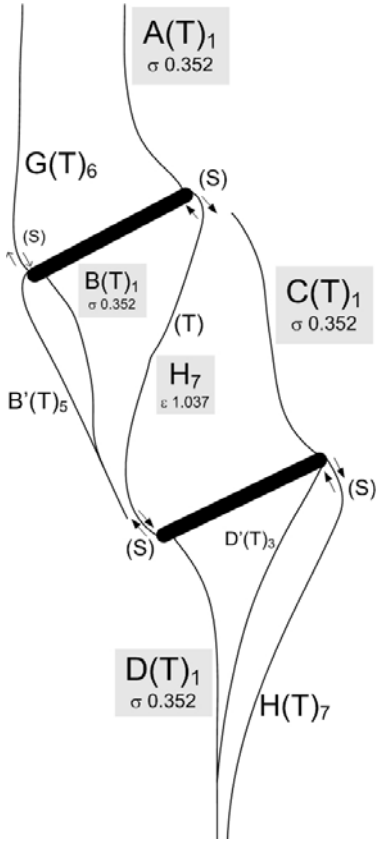

Pre-max : 1-2 CAM : 1
Post-max : 3-7 HS : 3-7

Figure K.9 – Fracturing and coalescence patterns for gypsum 4a-30-120.

Gypsum 4a-30-120 (continued)

4a-30-120-E (14,035 pps) – coalescence

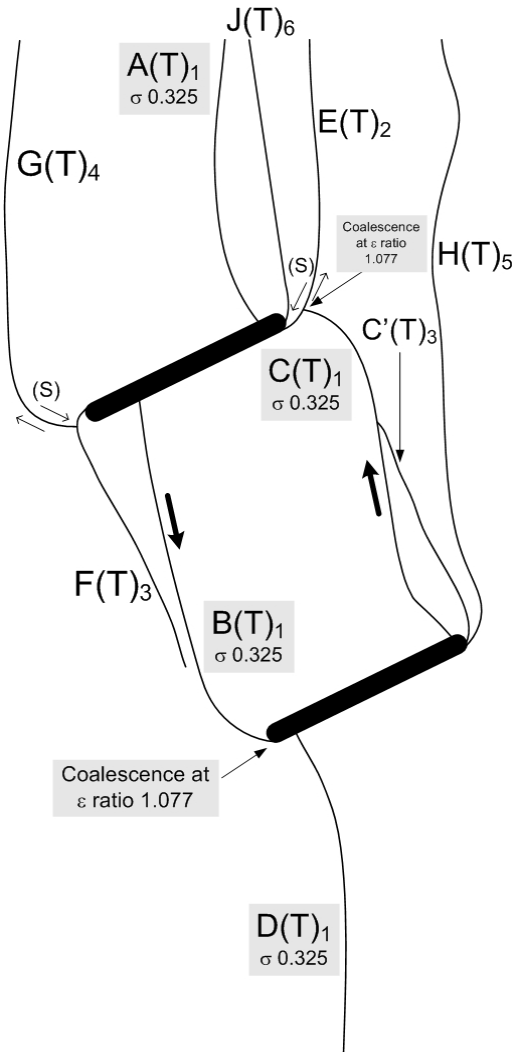

Pre-max : 1-3
Max : 4 CAM : 1-3
Post-max : 5-6 HS : 4-6

4a-30-120-F (14,035 pps) – coalescence

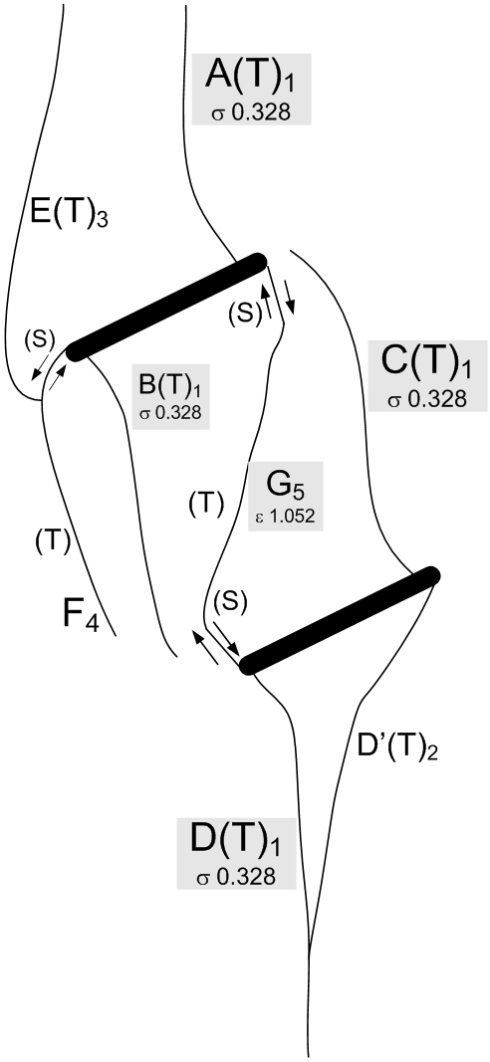

Pre-max : 1-2 CAM : 1-2
Post-max : 3-5 HS : 3-5

Figure K.9 – Fracturing and coalescence patterns for gypsum 4a-30-120 (continued)

APPENDIX L – Test Results of Marble Specimens Containing Coplanar Double Flaws of Ligament Length '2a'

In this appendix, the cracking phenomena of marble specimens containing coplanar double flaws (0.05" aperture) of ligament "2a" are described. Sketches of cracking patterns observed in all specimens are also illustrated. Refer to section 3.5 and section 5.2 for the meaning of symbols used in the sketches.

Eleven marble specimens were tested in this series (see table below). Two or more specimens were tested for each geometry in order to obtain consistent coalescence behavior.

Flaw inclination (^{o})	**Specimens**	**Total**
0	CM 2a-0-0-A CM 2a-0-0-B	2
30	CM 2a-30-0-A CM 2a-30-0-B	2
45	CM 2a-45-0-A CM 2a-45-0-C CM 2a-45-0-D	3
60	CM 2a-60-0-A CM 2a-60-0-B	2
75	CM 2a-75-0-A CM 2a-75-0-B	2
		11 (Total)

Marble 2a-0-0 (figure L.1)

A number of **white patches** developed prior to the initiation of first cracks – white patches A to J developed in specimen A, and white patches A to K developed in specimen B. The **first white patches** to initiate were the curvilinear white patches A, B C and D from in the middle of the pre-existing flaw, which displayed the conventional wing shape. Except patch C in specimen A, which opened up as a tensile crack, all the other curvilinear white patches remained intact. Soon after the development of the central white patches (as mentioned above), the **next white patches** to develop were the inner tip white patches (E, F, G in specimen A; E, F, G in specimen B).

The **first cracks** to initiate in the specimens were steep **type 2 tensile cracks** developed from the **inner** tips of the pre-existing flaws – crack E in specimen A and cracks E and J in specimen B. **Additional cracks** developed at a later stage from both the inner and outer tips of the pre-existing flaws. Most of them were type 2 tensile cracks, type 1 shear cracks, or mixed tensile-shear cracks. Also notice that only **1 of the 8** white patches displaying conventional wing appearance opened up as cracks, the remaining 7 remained intact and did not open up as cracks.

The **aperture** of the pre-existing flaws was closed at the end of the loading processes. **No coalescence** occurred between the two pre-existing flaws in both specimens.

The white patch initiation stress ratio, crack initiation stress ratio and coalescence strain ratio (refer to section 3.5 for definitions) are summarized below.

White patch Initiation Stress Ratio *Average value (min – max)*	0.753 (0.652 – 0.854)
Crack Initiation Stress Ratio *Average value (min – max)*	0.9997 (0.9995 – 0.9998)
Coalescence Strain Ratio *Average value (min – max)*	No coalescence

Marble 2a-0-0

CM 2a-0-0-A (2,000 pps) – no coalescence

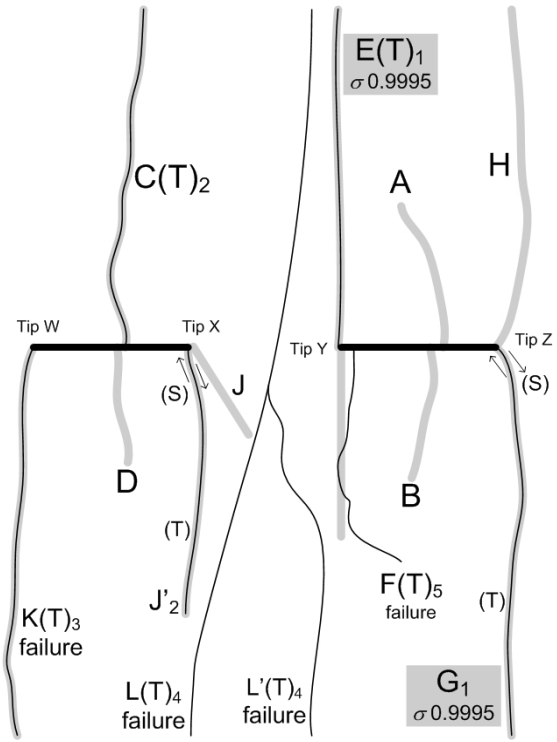

Pre-max : 1-2
Max : 3
Post-max : 4

CAM : white patches
HS : 1-4

CM 2a-0-0-B (2,000 pps) – no coalescence

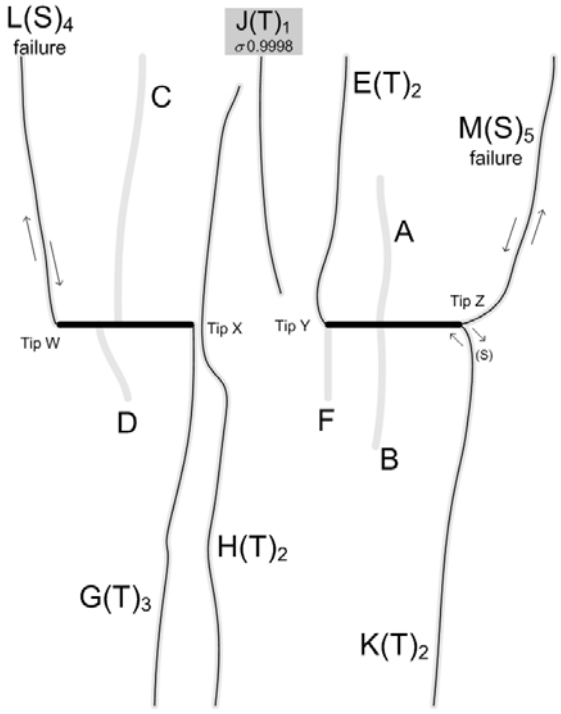

Pre-max : 1-3
Max : 4
Post-max : 5

CAM : white patches
HS : 1-5

Figure L.1 – Fracturing and coalescence patterns for marble 2a-0-0.

Marble 2a-30-0 (figure L.2)

A number of **white patches** initiated early during the loading process. Some patches displayed the **conventional wing appearance** (B, C, D in specimen A; A, B, C in specimen B). These white patches initiated from the tips of the pre-existing flaws. Some patches which **did not** display the conventional wing appearance also developed (A, E, F, G, J in specimen A ; D, E, F, G, J in specimen B).

The **first cracks** to initiate in the specimens were tensile cracks (**not displaying** conventional wing appearance) developed from the inner tips of the pre-existing flaws (crack A in specimen A; cracks D & E in specimen B). Short tensile cracks first initiated along these white patches away from the tip and later lengthened and coalesced to form a long continuous crack. These coalesced tensile segments were eventually linked up to the flaw tips by short shear crack segments.

Some of the white patches displaying **conventional wing** appearance subsequently opened up as tensile wing cracks (cracks B & C in specimen A, crack A in specimen B), while some remained intact without observable cracking (patch D in specimen A; patches B & C in specimen B) even till the end of loading process.

Coalescence was achieved by an **inclined tensile crack** (cracks H in both specimens) linking up the previously developed tensile tip cracks (not displaying a wing appearance). Immediately after its initiation, sinistral shearing occurred along the coalescence crack.

The white patch initiation stress ratio, crack initiation stress ratio and coalescence strain ratio (refer to section 3.5 for definitions) are summarized below.

White patch Initiation Stress Ratio *Average value (min – max)*	0.826 (0.748 – 0.904)
Crack Initiation Stress Ratio	1.0000 (the crack initiation stress of both specimens equal to the specimen maximum stress)
Coalescence Strain Ratio *Average value (min – max)*	1.067 (1.063 – 1.071) 2/2 coalesced after maximum stress

Marble 2a-30-0 (continued)

CM 2a-30-0-A (2,000pps) – coalescence

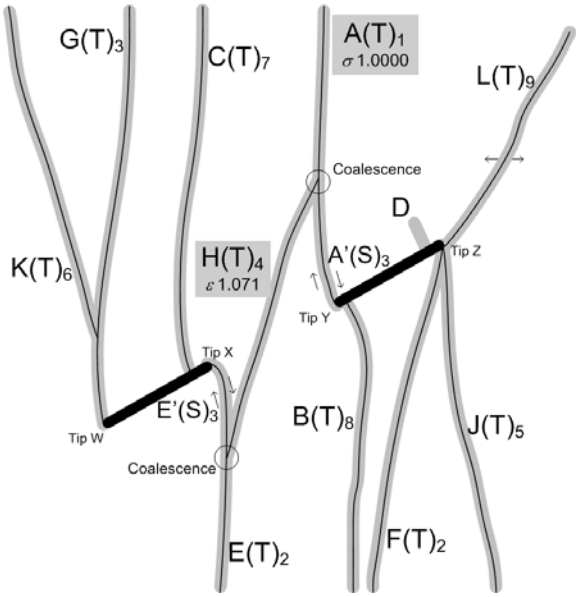

Max : 1
Post-max : 2-9

CAM : white patches
HS : 1-9

CM 2a-30-0-B (2,000pps) – coalescence

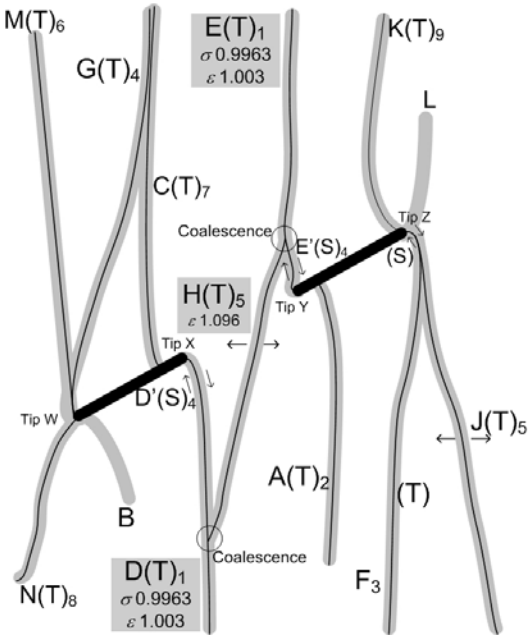

Post-max : 1-9

CAM : white patches
HS : 1-9

Figure L.2 – Fracturing and coalescence patterns for marble 2a-30-0.

Marble 2a-45-0 (figure L.3)

A number of white patches developed early during the loading processes. The following white patches developed before the initiation of first crack – A to H in specimen A, A to G in specimen C, and A to F in specimen D. Some of the white patches displayed conventional wing appearance (C & F in specimen A; G & J in specimen C).

Some of the **white patches** developed into **cracks**, while the others (H in specimen A; F, G & J in specimen C; C & H in specimen D) remained intact with no observable cracking.

The first cracks to initiate were usually steeply inclined/vertical tip cracks. Most of them consisted of a shear segment adjacent to the flaw tips and a vertical tensile segment (crack E in specimen A; crack A in specimen C, crack A in specimen D). **Conventional tensile wing crack** (C) only developed in specimen A. In all the other specimens, they were either absent (specimen D) or only appeared as curvilinear white patches without being opened up (patches F, G & J in specimen C).

Shear cracks, coplanar or almost coplanar with the pre-existing flaws, sometimes developed from the outer flaw tips at a later stage of loading (crack K in specimen C, cracks C & J in specimen D).

Inconsistent coalescence behavior was observed among the four specimens. Coalescence only occurred in two out of three of the specimens, but in different styles.

1. In specimen A, coalescence was achieved by a mixed tensile-shear crack “E” and a type 2 tensile crack “J”.
2. In specimen C, coalescence was achieved by a **type 2 shear** crack which linked up the inner flaw tips.

The white patch initiation stress ratio, crack initiation stress ratio and coalescence strain ratio (refer to section 3.5 for definitions) are summarized below.

White patch Initiation Stress Ratio *Average value (min – max)*	0.815 (0.764 – 0.863)
Crack Initiation Stress Ratio *Average value (min – max)*	09979 (0.9920 – 0.9997)
Coalescence Strain Ratio	1.000 The two specimens coalesced at maximum stress

Marble 2a-45-0

CM 2a-45-0-A (2,000 pps) – coalescence

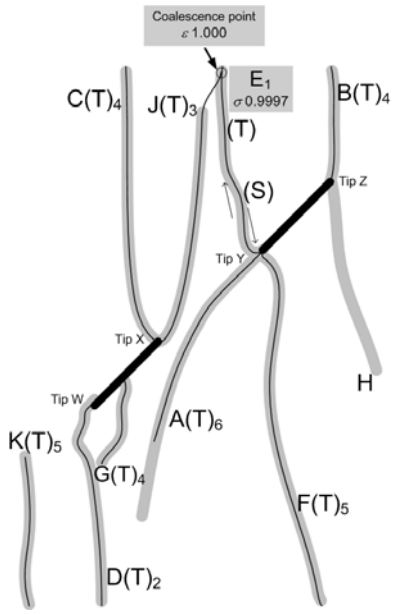

Pre-max : 1-2
Max : 3
Post-max : 4-6

CAM : white patches
HS : 1-6

CM 2a-45-0-C (2,000 pps) – coalescence

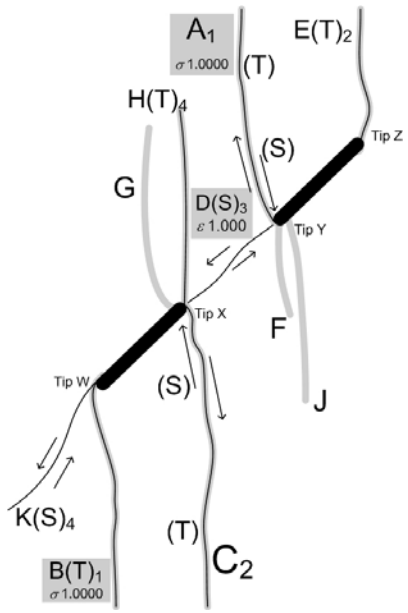

Max : 1
Post-max : 2-4

CAM : white patches
HS : 1-4

CM 2a-45-0-D (2,000 pps) – no coalescence

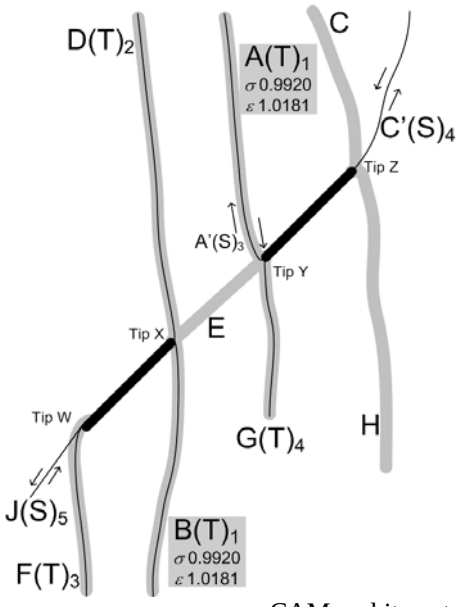

Post-max : 1-5

CAM : white patches
HS : 1-5

Figure L.3 – Fracturing and coalescence patterns for marble 2a-45-0.

Marble 2a-60-0 (figure L.4)

Under loading, **very short white patches** first developed around the inner and outer flaw tips (patch B & C). As loading continued, the white patches around the inner flaw tips lengthened and intensified in color. Eventually, a **long white patch** developed to link up the inner flaw tips (patch A in both specimens). The outer tip white patches also lengthened. Further loading led to the development of steeply inclined white patches (E & F) at or close to the inner flaw tips. These **inner tip white patches** displayed the conventional wing shape appearance. Notice that the development of these white patches occurred before the initiation of first cracks.

The **first cracks** initiated in the specimens were the **coalescence tensile crack** (A) and the **outer tip tensile cracks** (B & C).

Once the **coalescence tensile crack** initiated, shearing immediately occurred on the crack surface. A layer of fine pulverized powder was left on the crack surface. Notice that the crack did not initiate exactly at the tip, but somewhere around the tip. It linked up the point located at the upper face of the top flaw and a point at the lower face of the bottom flaw (see the schematic sketch below).

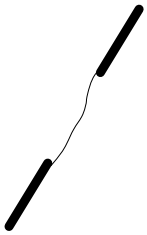

The **outer tip tensile cracks** (type 2 tensile cracks) were steeply inclined to vertical. Again, they did not initiate exactly at the flaw tips, but on the lower face of the top flaw (crack B) and on the upper face of the bottom flaw (crack C) around the tip regions. See the schematic sketch below.

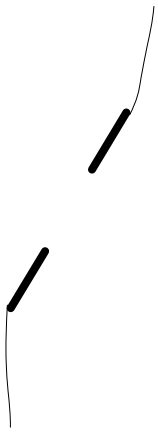

Shear cracks (crack D) which were coplanar with the pre-existing flaw developed during a later stage of loading and their development was concurrent with the specimen maximum stress.

All the white patches displaying conventional wing appearance at **inner flaw tips** remained intact and did not open up as cracks.

The white patch initiation stress ratio, crack initiation stress ratio and coalescence strain ratio (refer to section 3.5 for definitions) are summarized below.

White patch Initiation Stress Ratio *Average value (min – max)*	0.477 (0.469 – 0.484)
Crack Initiation Stress Ratio *Average value (min – max)*	0.9999 (0.7249 – 0.9857)
Coalescence Strain Ratio	1.000 The two specimens coalesced at the maximum stress

Marble 2a-60-0

CM 2a-60-0-A (2,000 pps) – coalescence

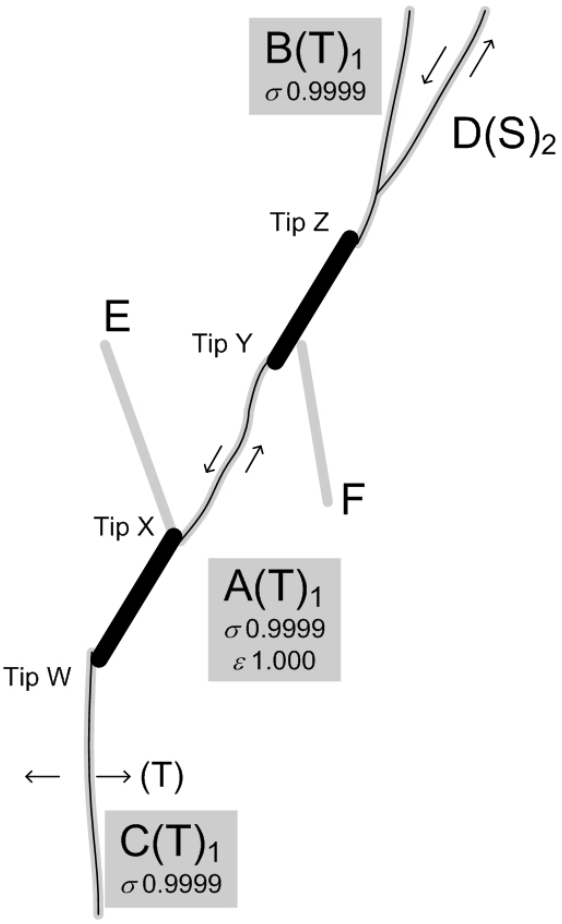

Pre-max : 1 CAM : white patches
Max : 2 HS : 1-2

CM 2a-60-0-B (2,000 pps) – coalescence

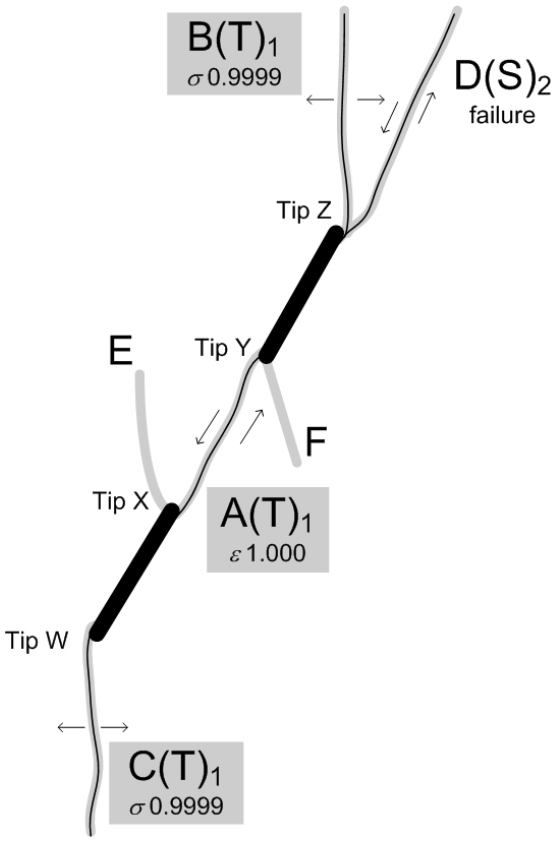

Pre-max : 1 CAM : white patches
Max : 2 HS : 1-2

Figure L.4 – Fracturing and coalescence patterns for marble 2a-60-0.

Marble 2a-75-0 (figure L.5)

Elongated white patches initiated early during the loading processes. Those initiated from the **inner flaw tips** (tip X in both specimens) were generally coplanar with the pre-existing flaws. Those initiated from the **outer flaw tips** were steeply inclined/vertical (patches B & C in both specimens).

Cracking occurred along the earlier developed white patches, which included the **outer tip** cracks (cracks B & C) and the **inner tip** cracks (cracks A1 & A2).

The coalescence behavior was observed in **detail** with the **high speed camera**. In both specimens, the inner tip cracks A1 and A2 initially initiated as **individual short segments** at the flaw tips as the overall first cracks to initiate. Their aperture subsequently increased with loading and the crack length increased till coalescence occurred to form a long continuous crack. In specimen A, the coalescence also involved an additional **central vertical tensile segment** A3, while in specimen B, the coalescence was achieved by linkage of cracks A1 and A2 only.

The **outer tip type 2 tensile cracks** B and C in specimen B were also the first cracks to initiate, and they were concurrent with the initiation of inner tip cracks A1 and A2. In specimen A, they occurred slightly later than those cracks in the bridge region between the inner flaw tips.

After the maximum stress of the specimen was surpassed, **shearing** occurred along the continuous coalescence crack in specimen B, while it only occurred along the segments A1 and A2 in specimen A. Further **tensile opening** occurred along the central segment A3 instead.

The white patch initiation stress ratio, crack initiation stress ratio and coalescence strain ratio (refer to section 3.5 for definitions) are summarized below.

White patch Initiation Stress Ratio *Average value (min – max)*	0.801 (0.632 – 0.970)
Crack Initiation Stress Ratio *Average value (min – max)*	0.9997 (0.9996 – 0.9998)
Coalescence Strain Ratio	1.000 The two specimens coalesced at the maximum stress

Marble 2a-75-0

CM 2a-75-0-A (2,000 pps) – coalescence

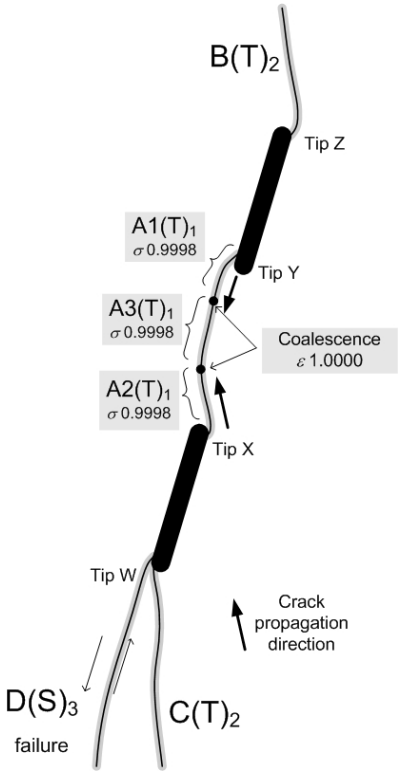

Pre-max : 1-2
Max : 3

CAM : white patches
HS : 1-3

CM 2a-75-0-B (2,000 pps) – coalescence

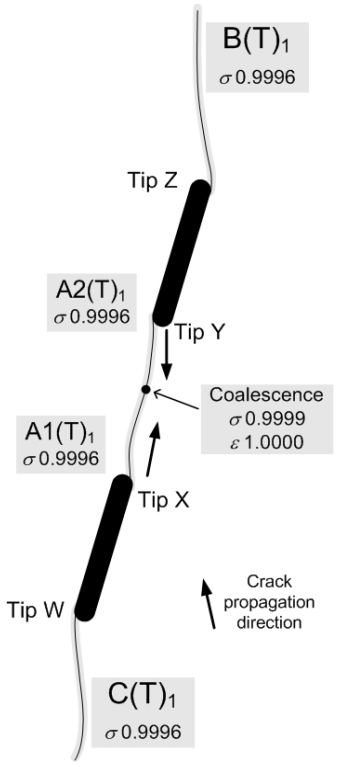

Pre-max : 1

CAM : white patches
HS : 1

Figure L.5 – Fracturing and coalescence patterns for marble 2a-75-0.

APPENDIX M – Test Results of Marble Specimens Containing Stepped Double Flaws of Ligament Length '2a'

In this appendix, the cracking phenomena of marble specimens containing stepped double flaws (0.05" aperture) of ligament "2a" are described. Sketches of cracking patterns observed in all specimens are also illustrated. Refer to section 3.5 and section 5.2 for the meaning of symbols used in the sketches.

Sixteen marble specimens with flaw inclination angle 30^o were tested in this series (see below). Two or more specimens were tested for each geometry in order to obtain consistent coalescence behavior.

Bridging angles α (^{o})	**Specimens**	**Total**
-60	CM 2a-30-(-60)-A, CM 2a-30-(-60)-B	2
-30	CM 2a-30-(-30)-A, CM 2a-30-(-30)-B	2
0	CM 2a-30-0-A, CM 2a-30-0-B	2
30	CM 2a-30-30-A, CM 2a-30-30-B	2
60	CM 2a-30-60-B, CM 2a-30-60-C, CM 2a-30-60-D	3
90	CM 2a-30-90-A, CM 2a-30-90-B CM 2a-30-90-C	3
120	CM 2a-30-120-A, CM 2a-30-120-C	2
		16 (Total)

Marble 2a-30-(-60) (figure M.1)

Curvilinear ***white patches*** (A, B, C, D) displaying a ***wing appearance*** developed close to the tips of the pre-existing flaws at a very early stage. They either remained intact with no observable cracking till the end of loading process (cracks B & C in specimen A, cracks A to D in specimen B) or ***partially opened up*** in a tensile manner (cracks A & D in specimen A).

The ***first cracks*** to initiate in the specimens were **type 2 tensile cracks**. These included cracks E and F in specimen A, and crack F in specimen B. Multiple tensile crack segments developed along white patches which eventually led to the formation of type 2 tensile cracks (see figure M.1 below for two examples in specimen A).

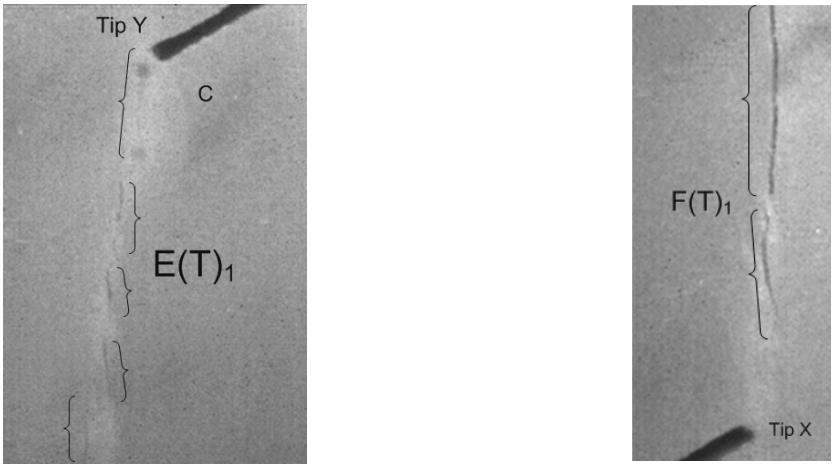

(a) (b)

Figure M.2 – Development of multiple short tensile crack segments along the white patches initiated from flaw tips.

The fracturing behavior in both specimens regarding the types and trajectories of the ***newly initiated cracks*** was very similar, except that ***coalescence*** was absent in specimen A, but present in specimen B. The ***coalescence tensile crack*** L in specimen B initiated ***well after*** the specimen's max stress was reached.

The white patch initiation stress ratio, crack initiation stress ratio and coalescence strain ratio (refer to section 3.5 for definitions) are summarized below.

White patch Initiation Stress Ratio *Average value (min – max)*	0.699 (0.664 – 0.735)
Crack Initiation Stress Ratio *Average value (min – max)*	0.9989 (0.9983 – 0.9996)
Coalescence Strain Ratio	1.170 (coalescence in 1 specimen)

Marble 2a-30-(-60)

CM 2a-30-(-60)-A (3,000pps) – no coalescence

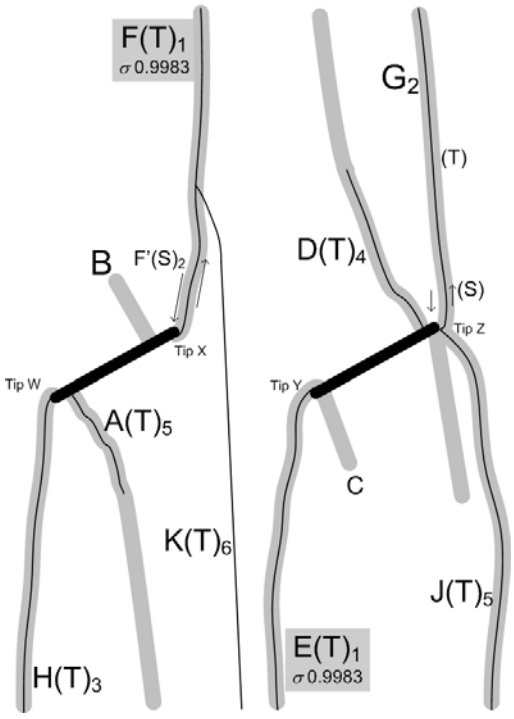

Pre-max : 1 CAM : 1
Post-max : 2-6 HS : 2-6

CM 2a-30-(-60)-B (3,800pps) – coalescence

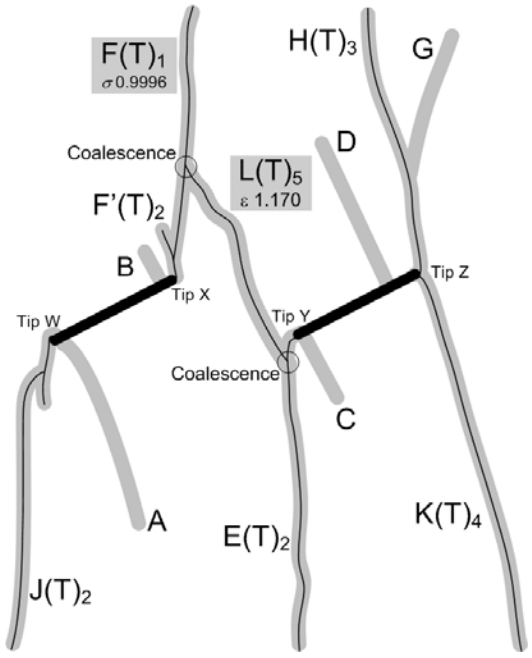

Pre-max : None CAM : white patches
Post-max : 1-5 HS : 1-5

Figure M.1 – Fracturing and coalescence patterns for marble 2a-30-(-60).

Marble 2a-30-(-30) (figure M.3)

A number of **white patches** initiated early during the loading process. Some patches displayed the **conventional wing appearance**, i.e. a curvilinear patch initiated from the upper face of a pre-existing flaw close to the right flaw tip and another curvilinear patch initiated from the lower face of the same pre-existing flaw close to the left flaw tip. Some patches which **did not** display the conventional wing appearance also developed.

Conventional **wing** shaped curvilinear white patches developed close to/at the flaw tips (E, G, K & N in specimen A; B, C, D & E in specimen B) early during the loading process and some of them were subjected to **tensile opening** to become cracks (white patches G & N in specimen A became cracks; white patch B in specimen), while some remained as intact white patches (E & K in specimen A ; C, D & E in specimen B). Similarly, some of those white patches which **did not** display the conventional wing appearance would either remain intact white patches (e.g. patch C in specimen A) or open up as cracks.

Along some white patches, individual tensile crack segments first initiated along them at a location far from the flaw tips. A shear crack later initiated to link up the flaw tip and this tensile crack segment (see example of crack B in specimen A show in figure M.4).

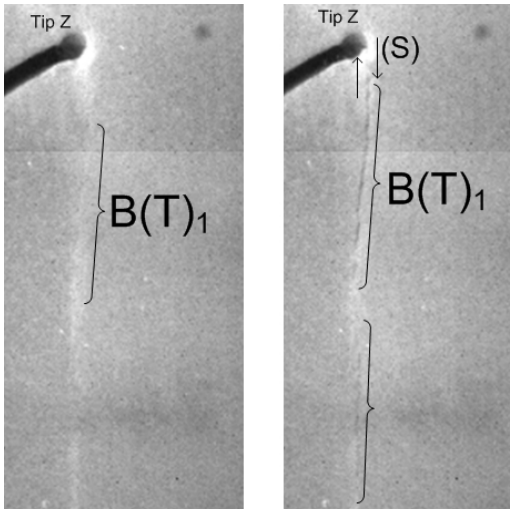

Figure M.4 – Linkage of a tensile crack (B) to the flaw tip by a shear crack segment.

The **first cracks** to initiate in the specimens were those almost vertical tensile cracks (not displaying a wing appearance) developed from the tips of the pre-existing flaws (cracks A & B in specimen A, crack F in specimen B).

Coalescence was absent in specimen B, while the coalescence in specimen A occurred well after the peak stress of the specimen was passed, i.e., during the course of specimen collapse (85% of the peak stress).

The white patch initiation stress ratio, crack initiation stress ratio and coalescence strain ratio (refer to section 3.5 for definitions) are summarized below.

White patch Initiation Stress Ratio *Average value (min – max)*	0.789 (0.704 – 0.874)
Crack Initiation Stress Ratio *Average value (min – max)*	0.9972 (0.9952 – 0.9993)
Coalescence Strain Ratio	1.234 (coalescence in 1 specimen)

Marble 2a-30-(-30)

CM 2a-30-(-30)-A (2,000pps) – coalescence

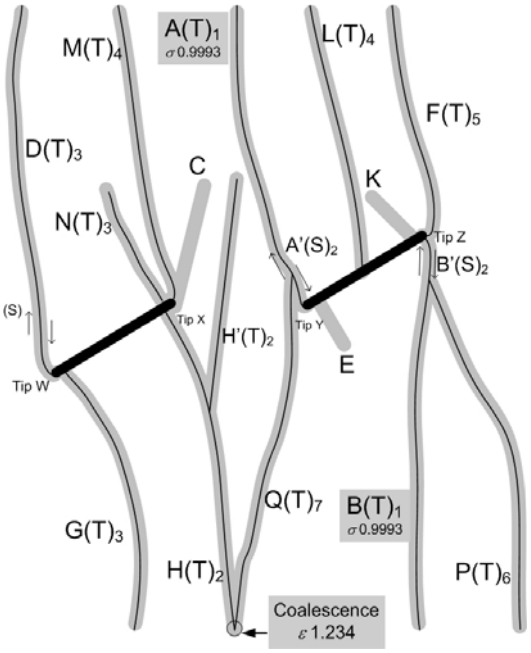

Pre-max : None
Post-max : 1-7

CAM : white patches
HS : 1-7

CM 2a-30-(-30)-B (3,000pps) – no coalescence

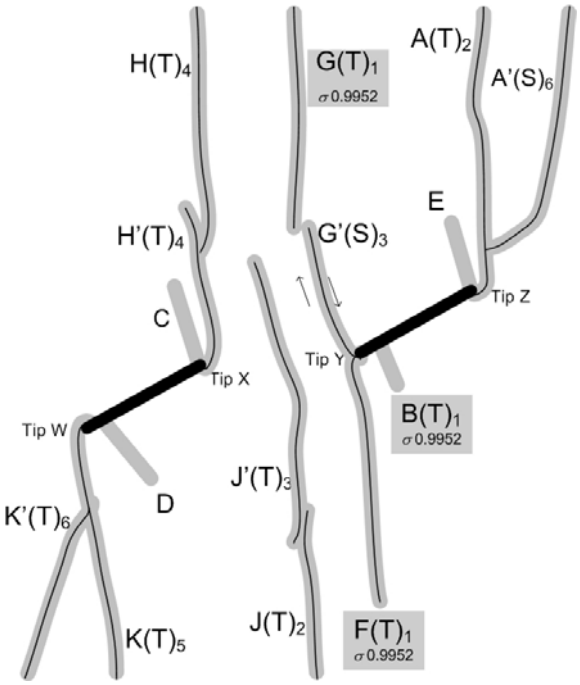

Pre-max : None
Post-max : 1-6

CM : white patches
HS : 1-6

Figure M.3 – Fracturing and coalescence patterns for marble 2a-30-(-30).

Marble 2a-30-0

Refer to the corresponding description in Appendix L.

Marble 2a-30-30 (figure M.5)

A number of **white patches** initiated early during the loading process. Some patches displayed the **conventional wing appearance** (C, H, J, K in specimen A; A, B, C, D in specimen B), i.e. a curvilinear patch initiated from the upper face of a pre-existing flaw close to the right flaw tip and another curvilinear patch initiated from the lower face of the same pre-existing flaw close to the left flaw tip. Some patches which **did not** display the conventional wing appearance also developed (B, D, E in specimen A; F, G in specimen B).

Some of the wing shaped white patches became **tensile cracks**. Generally, those white patches initiating from the **outer tips** tended to develop into **cracks** (crack C in specimen A, cracks A and D in specimen B), while those initiating from **inner tips** remained **intact** with no observable cracking (white patches J & H in specimen A; white patches B & C in specimen B). However, there was one exception (white patch K initiating from the outer tip in specimen A did not develop into a crack).

The **outer tip tensile wing cracks** (discussed above) were always the **first cracks** to develop in the specimen. In specimen A, the initiation of these first cracks was concurrent with the initiation of the **coalescence shear crack** A. In specimen B, the initiation of the coalescence shear crack E was 0.041 seconds after the initiation of those tensile wing cracks.

The coalescence shear crack was observed to develop as a single continuous crack to link up the inner flaw tips with the 2,000pps resolution of the high speed camera (see the figure M.6 below).

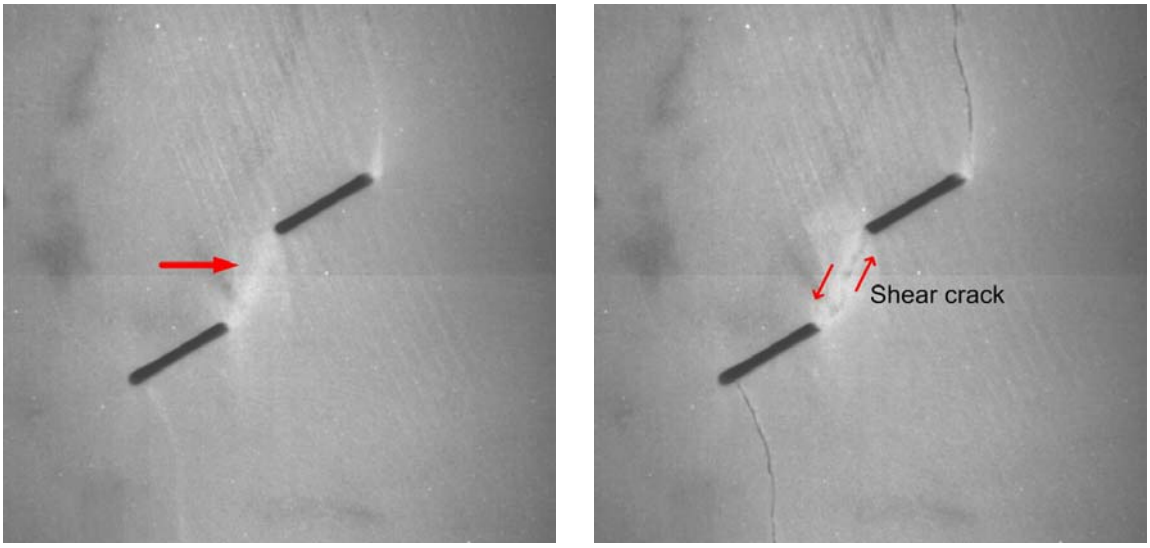

(a) (b)

Figure M.6– Shear crack developed along the white patch in the central bridging region

Substantial sinistral shearing occurred across the two pre-existing flaws and the coalescence cracks, leading to substantial aperture increase of the tensile cracks at the outer flaw tips. Additional type 2 tensile cracks and type 1 shear cracks developed from the flaw tips well after the initiation of the first cracks.

Following the peak on the stress-strain curves, a **trough** (abrupt stress drop and rise) was observed. This was associated with the **shearing** along the coalescence crack (crack A in specimen A; crack E in specimen B). See the graphs below.

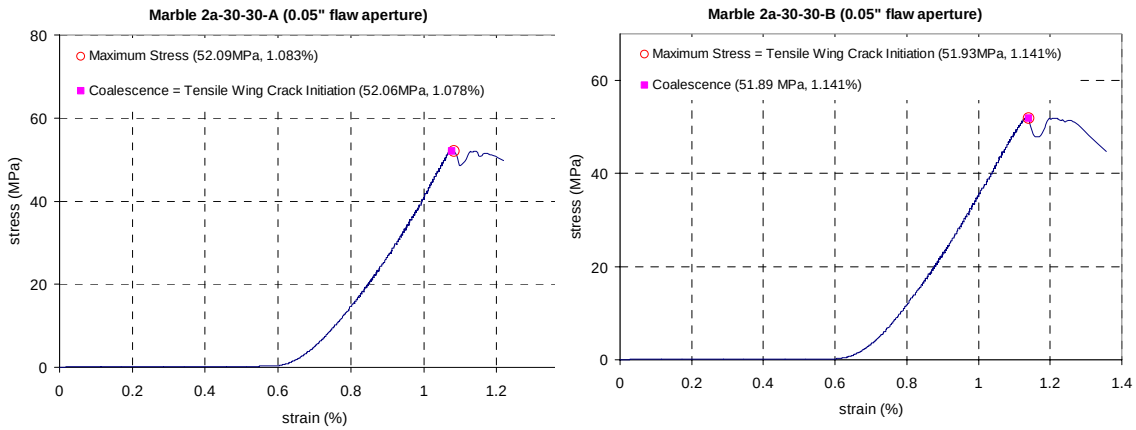

The white patch initiation stress ratio, crack initiation stress ratio and coalescence strain ratio (refer to section 3.5 for definitions) are summarized below.

White patch Initiation Stress Ratio *Average value (min – max)*	0.594 (0.552 – 0.635)
Crack Initiation Stress Ratio *Average value (min – max)*	0.9997 (0.9995 – 1.0000)
Coalescence Strain Ratio *Average value (min – max)*	0.998 (0.995 – 1.000)

Marble 2a-30-30 (continued)

CM 2a-30-30-A (2,000pps) – coalescence

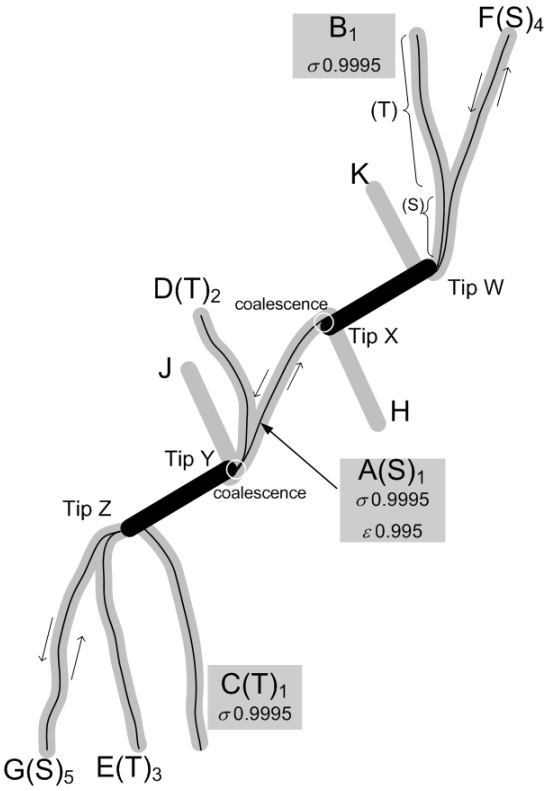

Pre-max : None
Post-max : 1-5

CAM : white patches
HS : 1-5

CM 2a-30-30-B (2,000pps) – coalescence

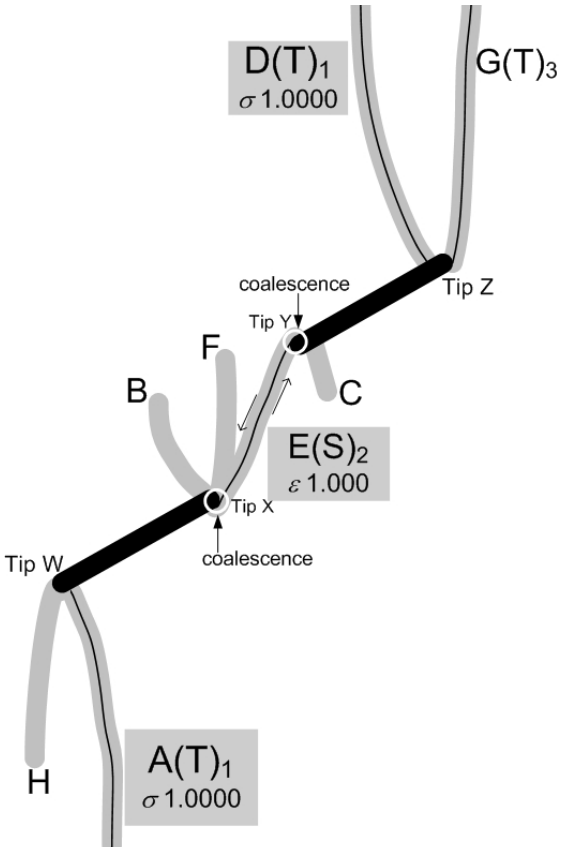

Pre-max : None
Max : 1
Post-max : 2-3

CAM : white patches
HS : 1-3

Figure M.5 – Fracturing and coalescence patterns for marble 2a-30-30.

Marble 2a-30-60 (figure M.6)

A number of **white patches** initiated early during the loading process from the upper and lower face of the flaws (patches A, B, C & D in all specimens). All of these patches displayed the **conventional wing appearance,** which increased in length with increased loading**.**

Only those white patches initiating close to/at the outer tips developed into **tensile wing cracks** (cracks A & D in specimen B, crack D in specimen C, crack B in specimen D). These were also the **first cracks** to initiate in the specimens. Although the outer tip tensile wing cracks were the first cracks to initiate in all specimens, they developed at different times. In specimen B, they appeared early during the loading process (72% of the max stress), while they appeared very late during the loading process just a short while before the max stress in specimen C (98% of the max stress) and specimen D (96% of the max stress). The **inner tip white patches** (also displaying the conventional wing appearance) did not develop into tensile cracks till the end of the loading process.

In specimen B, the **coalescence tensile crack** E between the inner flaw tips was also one of the **first** cracks to initiate, being concurrent with the initiation of **tensile wing cracks** A and D. However, in specimens B and D, they initiated later. Once the **coalescence cracks** formed, its two crack faces then became immediately **separated** and no contact was made to allow for subsequent shearing.

Substantial shearing occurred across the two pre-existing flaws during the late stage of loading, leading to a substantial **aperture increase** of the tensile cracks in all specimens. Additional type 2 tensile cracks and type 1 shear cracks developed from the flaw tips well after the initiation of the first cracks.

The strength of the specimen vanished (an abrupt stress drop on the stress-strain curve) at the time concurrent with the **initiation of oblique type 1 shear cracks** at outer tips (crack H in specimens B, crack F' & H in specimen D) or occurrence of **shearing** along previously initiated outer tip tensile cracks (cracks F' and G' in specimen C).

In specimen B and D, the initiation of coalescence crack in the bridging region was recorded by camcorder and it was observed to initiate as a single continuous crack. As observed with the high speed camera, the coalescence crack E in specimen C was formed from linkage of multiple of steep vertical tensile crack segments in the central bridging region. The first tensile segment initiated at a location far away from the flaw tips. See the figures below.

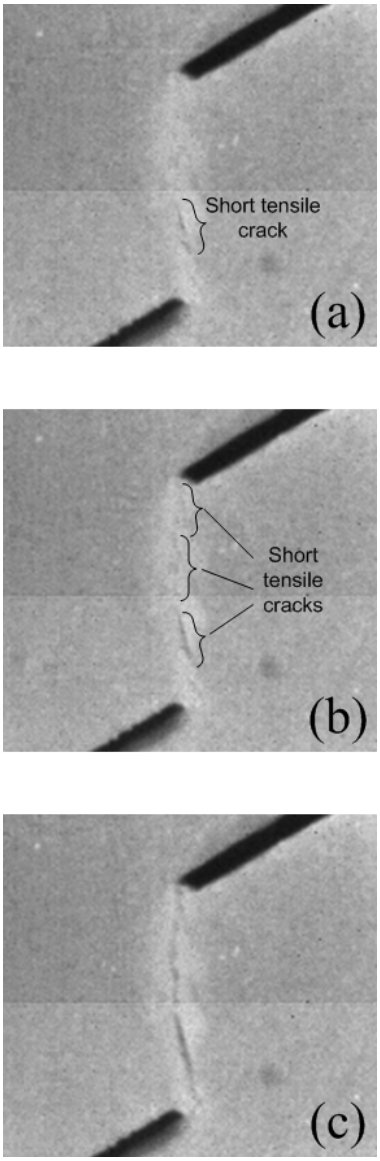

Figure M.7 – Development of tensile crack segments along the white patch in the central bridging region between the inner flaw tips.

The white patch initiation stress ratio, crack initiation stress ratio and coalescence strain ratio (refer to section 3.5 for definitions) are summarized below.

White patch Initiation Stress Ratio *Average value (min – max)*	0.624 (0.529 – 0.672)
Crack Initiation Stress Ratio *Average value (min – max)*	0.889 (0.725 – 0.986)
Coalescence Strain Ratio *Average value (min – max)*	0.938 (0.875 – 0.984)

Marble 2a-30-60

CM 2a-30-60-B (2,000pps) – coalescence

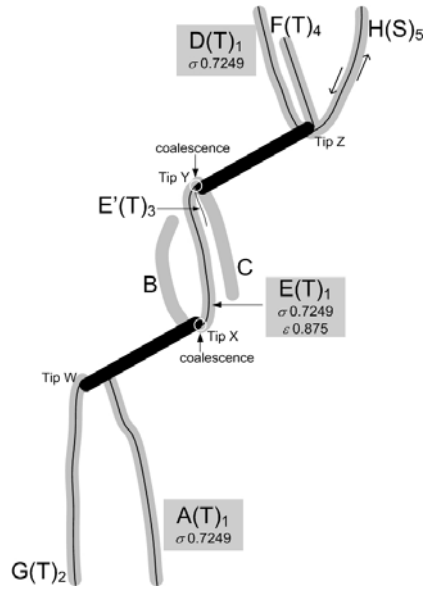

Pre-max : 1-4 CAM : 1-3
Post-max : 5 HS : 4-5

CM 2a-30-60-C (1,000pps) – coalescence

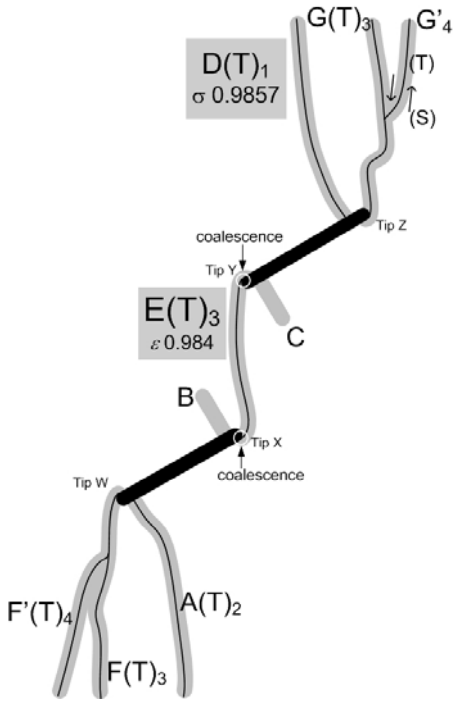

Pre-max : 1-2
Max : 3 CAM : 1-2
Post-max : 4 HS : 3-4

As observed with the high speed camera, the coalescence crack E was formed from linkage of multiple of steep vertical tensile crack segments in the central bridging region. The first tensile segment initiated at a location far away from the flaw tips.

CM 2a-30-60-D (2,000pps) – coalescence

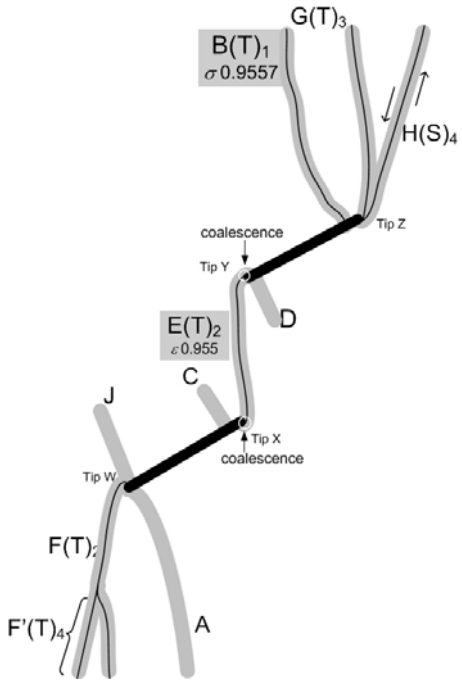

Pre-max : 1-3 CAM : 1-3
Post-max : 4 HS : 4

Figure M.6 – Fracturing and coalescence patterns for marble 2a-30-60.

Marble 2a-30-90 (figure M.8)

A number of **white patches** initiated early during the loading process from the upper and lower face of the flaws (patches A & B initiated close to the outer tips; patches C & D initiated close to the inner tips in all specimens). All of these patches displayed the **conventional wing appearance**, and increased in length with increased loading**.** The **outer tip white patches** A and B increased in length in the direction parallel to the loading axis till they reached the top and bottom edges of the specimens. The **inner tip white patches** C and D increased in length until they coalesced with the other pre-existing flaw. Notice that during the **early course** of white patch lengthening, **no observable cracks** developed along them. Several **white patches** which **did not display the conventional wing appearance** also developed from the flaw tips **after** the initiation of the conventional wing white patches. These white patches included E and F in specimen A, E and G in specimen B, E and F in specimen C.

The **first cracks** to initiate in the specimens included those conventional wing tensile cracks (TWC) and those not displaying tensile wing shape:

- crack B in **specimen A** at 89% peak stress (conventional TWC)
- cracks A and B in **specimen B** at 99% peak stress
- crack F (not displaying conventional TWC shape) in **specimen C** at 99% peak stress

Although the white patches corresponding to the coalescence tensile wing crack pairs developed during the early loading process (patches C & D in specimens A & B, patches B & C in specimen C), cracking did not develop along them immediately, but after some other cracks first developed first (see above). Once the **coalescence cracks developed**, the coalescence crack on the left propagated upwards from the lower pre-existing flaw (crack C in specimens A & B, crack B in specimens C), and the other coalescence crack on the right propagated downwards from the upper pre-existing flaw (crack D in specimens A & B, crack C in specimen C).

The strength of the specimen vanished (an abrupt stress drop on the stress-strain curve) at the time concurrent with the development of **oblique shear cracks** at outer tips (cracks G' & H in specimen A, crack H in specimen B) or occurrence of **substantial aperture increase** on outer tensile tip cracks (cracks E & F in specimen C). Note also the occurrence of shearing along the bottom segment of crack E in specimen C.

At the end of the loading process, the **aperture** of the two pre-existing flaws substantially **decreased**. Additional type 2 tensile cracks and type 1 shear cracks developed from the flaw tips well after the initiation of the first cracks.

The white patch initiation stress ratio, crack initiation stress ratio and coalescence strain ratio (refer to section 3.5 for definitions) are summarized below.

White patch Initiation Stress Ratio *Average value (min – max)*	0.588 (0.571 – 0.621)
Crack Initiation Stress Ratio *Average value (min – max)*	0.9620 (0.8944 – 0.9997)
Coalescence Strain Ratio *Average value (min – max)*	1.032 (1.002 – 1.077)

Marble 2a-30-90 (continued)

CM 2a-30-90-A (2,000pps) – coalescence

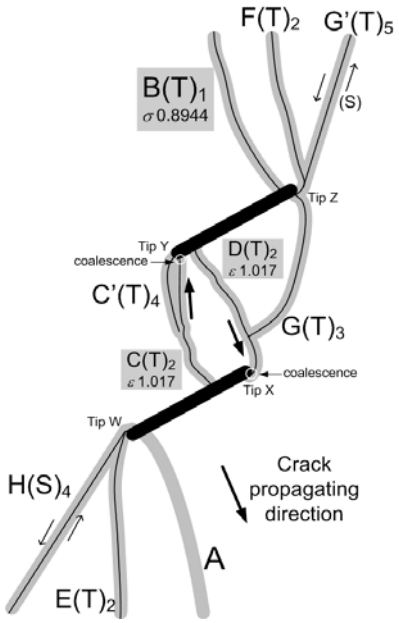

Pre-max : 1-3 CAM : 1-2
Post-max : 4 HS : 3-4

CM 2a-30-90-B (2,000pps) – coalescence

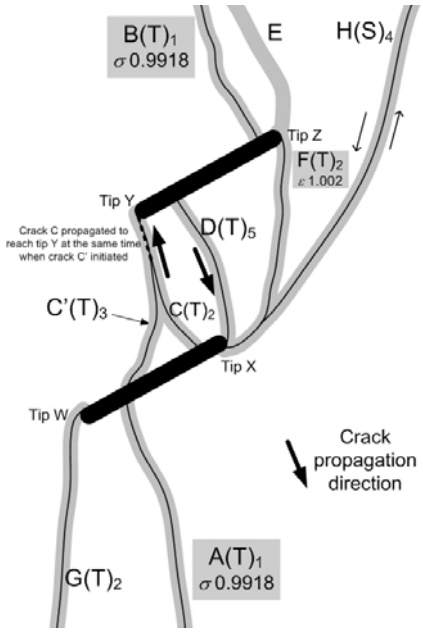

Pre-max : 1-2 CAM : 1
Post-max : 3-4 HS : 2-4

CM 2a-30-90-C (2,000pps) – coalescence

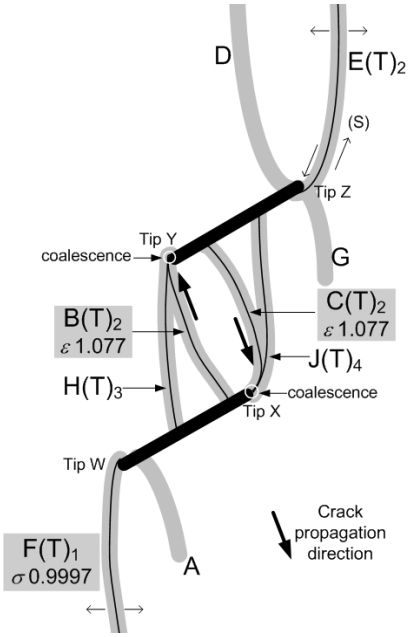

Pre-max : 1-2 CAM : 1-2
Post-max : 3-4 HS : 3-4

Figure M.8 – Fracturing and coalescence patterns for marble 2a-30-90.

Marble 2a-30-120 (figure M.9)

The two pre-existing flaws are arranged vertically, one over each other. Thus, it is inappropriate to use outer tips or inner tips in describing relative position of flaw tips. **Left tips** and **right tips** will be the terms used to refer to the position of the flaw tips.

A number of **white patches** initiated early during the loading process from the upper face of the top flaw and the lower face of the bottom flaw (patches B & C in specimen A; patches A & B in specimen B). All of these patches displayed the **conventional wing appearance,** which increased in length with increased loading, whose subsequent trajectories were parallel to the loading axis. Shortly after the development of those white patches displaying the **conventional wing appearance** (specimen B), another **white patch** also developed from the upper face of the bottom flaw. This white patch also propagated upwards until it reached the lower face of the top flaw. In specimen A, short white patches A, B and C were observed to initiate at the same time. However, it should be cautioned that the above observations were made based on the **camcorder recording** observation, which had a limited resolution regarding the quality of the images.

In specimen A, the **first crack** to initiate was **coalescence crack A** (83% peak stress). This crack coalesced **tip** X of the lower flaw and the **middle portion** of the upper flaw. The next cracks to develop were **tensile wing cracks B and C** (99% peak stress) which propagated towards the bottom and top edges of the specimen respectively.

In specimen B, the **first cracks** to initiate were **coalescence crack C** (99% peak stress) and **tensile wing cracks A and B**. The **coalescence crack** C linked up the right tips X and Z, which was different from that in specimen A.

The strength of the specimen vanished (an abrupt stress drop on the stress-strain curve) at a time which was concurrent with a **substantial reduction of the aperture** of the pre-existing flaws, and the development of steep cracks (crack F' in specimen A, cracks E & F in specimen B).

Development of **steeply inclined tensile tip cracks** from the flaw tips was also very common. Before developing into cracks, they also appeared as white patches. On some of these cracks, **shearing** occurred along segments adjacent to the pre-existing flaw tips.

The white patch initiation stress ratio, crack initiation stress ratio and coalescence strain ratio (refer to section 3.5 for definitions) are summarized below.

White patch Initiation Stress Ratio *Average value (min – max)*	0.654 (0.644 – 0.664)
Crack Initiation Stress Ratio *Average value (min – max)*	0.911 (0.826 – 0.997)
Coalescence Strain Ratio *Average value (min – max)*	0.948 (0.896 – 1.000)

Marble 2a-30-120

CM 2a-30-120-A (2,000pps) – coalescence

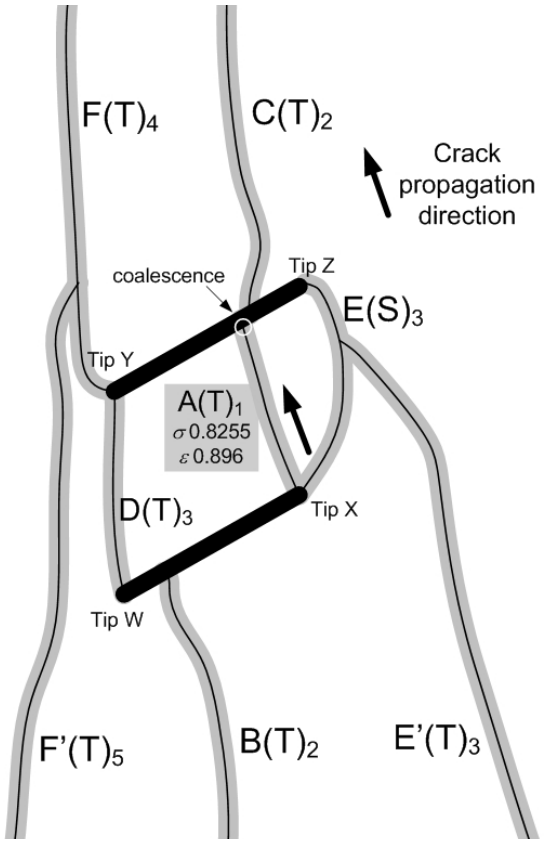

Pre-max : 1-2
Post-max : 3-5

CAM : 1-2
HS : 3-5

CM 2a-30-120-B (2,000pps) – coalescence

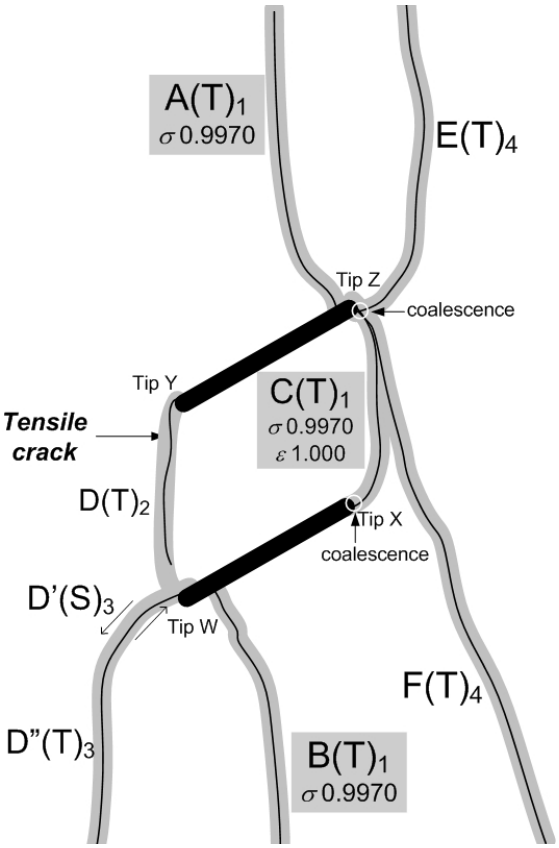

Pre-max : 1
Post-max : 2-4

CAM : 1
HS : 2-4

Figure M.9 – Fracturing and coalescence patterns for marble 2a-30-120.

APPENDIX N – Test Results of Marble Specimens Containing Coplanar Double Flaws of Ligament Length '4a'

In this appendix, the cracking phenomena of marble specimens containing coplanar double flaws (0.05" aperture) of ligament "4a" are described. Sketches of cracking patterns observed in all specimens are also illustrated. Refer to section 3.5 and section 5.2 for the meaning of symbols used in the sketches.

Thirteen marble specimens were tested in this series (see table below). Two or more specimens were tested for each geometry in order to obtain consistent coalescence behavior.

Flaw inclination (^{o})	**Specimens**	**Total**
0	CM 4a-0-0-A CM 4a-0-0-B CM 4a-0-0-C	3
30	CM 4a-30-0-B CM 4a-30-0-C	2
45	CM 4a-45-0-A CM 4a-45-0-B CM 4a-45-0-C	3
60	CM 4a-60-0-A CM 4a-60-0-B	2
75	CM 4a-75-0-A CM 4a-75-0-B CM 4a-75-0-C	3
		13 (Total)

Marble 4a-0-0 (figure N.1)

A number of **white patches** developed prior to the initiation of first cracks – white patches A to M in specimen A, white patches A to J in specimen B, and white patches A to M in specimen C. The **first white patches** to initiate were those displaying wing appearance which initiated from the middle of the pre-existing flaw face (white patches B, C, K in specimen A, white patches C, D, G, H in specimen B, white patches D, E, H, J in specimen C). All of these **first white patches** remained intact and did not develop into cracks. Soon after the development of the central white patches (as mentioned above), the **next white patches** to develop were the vertical white patches initiated from flaw tips.

The **first cracks** to initiate in the specimens were steep **type 2 tensile cracks** developed from the **outer** tips of the pre-existing flaws – crack A in specimen A, cracks A and E in specimen B, and crack A in specimen C. The initiation of first cracks was almost coincident with the specimen maximum stress in all the tested specimens. **Additional cracks** developed at a later stage from both the inner and outer tips of the pre-existing flaws. Most of them were type 2 tensile cracks, type 1 shear cracks, or mixed tensile-shear cracks.

The **aperture** of the pre-existing flaws was closed at the end of the loading processes. **Coalescence** occurred between the two pre-existing flaws in specimens A and B after the specimen maximum stress was reached, but was absent in specimen C. In specimens A and B coalescence occurred as an **inclined shear crack** initiated and propagated from one of the inner flaw tips and coalesced with a steeply-inclined **type 2 tensile crack** which had previously initiated from the other flaw tip.

The white patch initiation stress ratio, crack initiation stress ratio and coalescence strain ratio (refer to section 3.5 for definitions) are summarized below.

White patch Initiation Stress Ratio *Average value (min – max)*	0.399 (0.371 – 0.425)
Crack Initiation Stress Ratio *Average value (min – max)*	0.9997 (0.9993 – 1.0000)
Coalescence Strain Ratio *Average value (min – max)*	1.053 (1.045 – 1.062)

Marble 4a-0-0

4a-0-0-A (6,600 pps) – coalescence

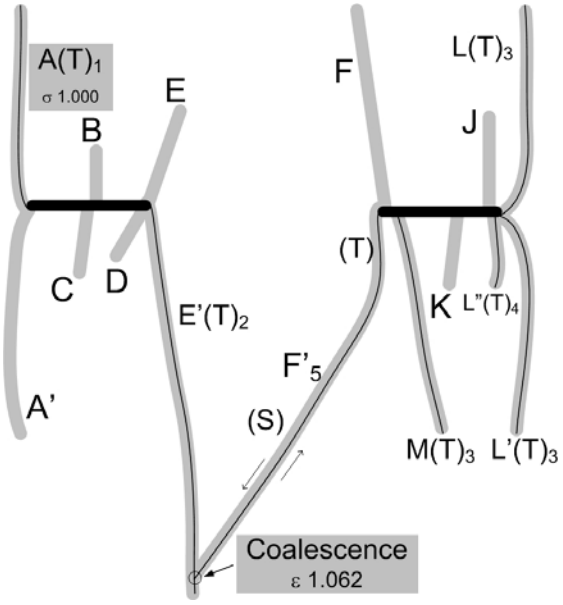

Pre-max : - CAM : -
Post-max : 1-5 HS : 1-5

4a-0-0-B (11,019 pps) – coalescence

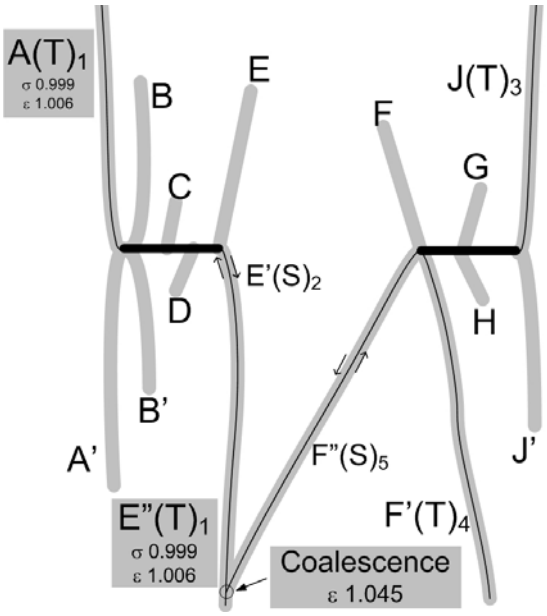

Pre-max : - CAM : -
Post-max : 1-5 HS : 1-5

4a-0-0-C (11,019 pps) – no coalescence

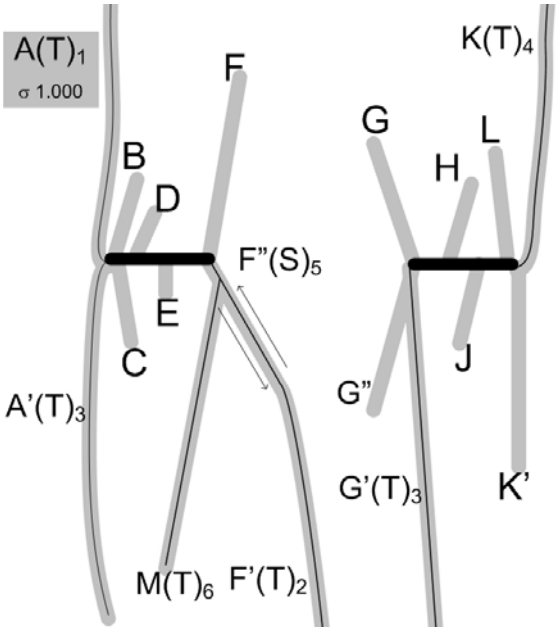

Pre-max : - CAM : -
Post-max : 1-6 HS : 1-6

Figure N.1 – Fracturing and coalescence patterns for marble 4a-0-0.

Marble 4a-30-0 (figure N.2)

A number of **white patches** initiated early during the loading process. Some patches displayed the **conventional wing appearance** (A, B, C, D in specimens A and B). These white patches initiated close to/at the tips of the pre-existing flaws. Some patches which **did not** display the conventional wing appearance also developed.

The **first cracks** to initiate in the specimens were tensile wing cracks (TWCs, type 1 tensile cracks) (crack A in specimen A; crack B in specimen B). In specimen B, type 3 tensile crack E also developed. The initiation of these first cracks occurred slightly earlier than the occurrence of the specimen maximum stress. Except white patch A in specimen B, all the other white patches displaying **conventional wing** appearance subsequently opened up as tensile wing cracks.

Additional cracks developed at a later stage from both the inner and outer tips of the pre-existing flaws. Most of them were type 2 tensile cracks and mixed tensile-shear cracks. However, these cracks did not link up together and **coalescence** was absent in both tested specimens.

The white patch initiation stress ratio, crack initiation stress ratio and coalescence strain ratio (refer to section 3.5 for definitions) are summarized below.

White patch Initiation Stress Ratio *Average value (min – max)*	0.682 (0.586 – 0.778)
Crack Initiation Stress Ratio *Average value (min – max)*	0.973 (0.961-0.985)
Coalescence Strain Ratio *Average value (min – max)*	No Coalescence

Marble 4a-30-0	
4a-30-0-B (7,005 pps) – no coalescence	4a-30-0-C (10,000 pps) – no coalescence
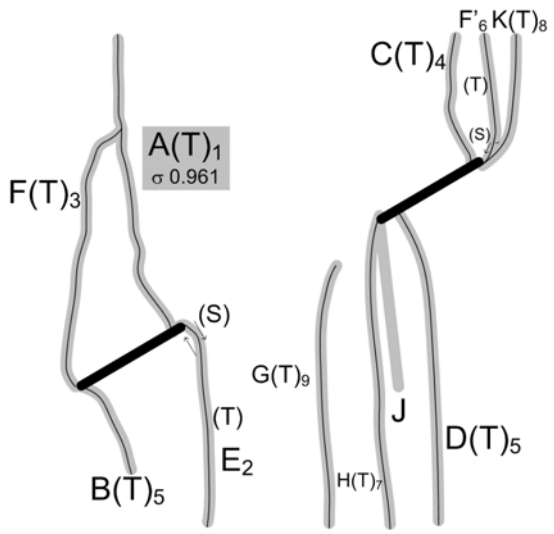	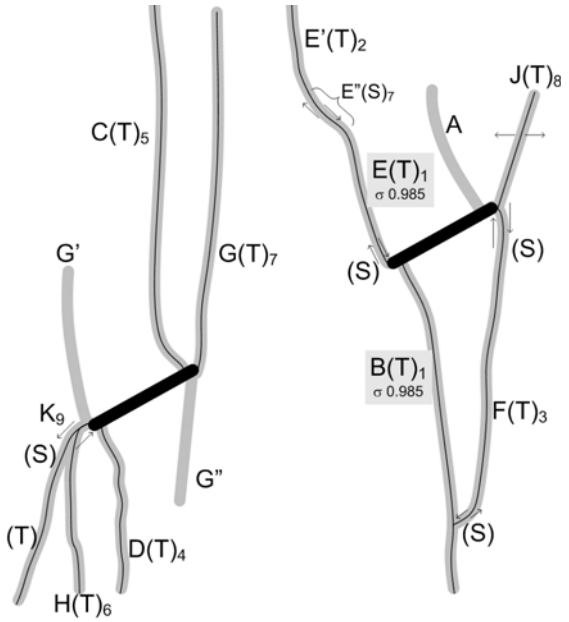
Pre-max : 1-3 Post-max : 4-9 CAM : 1-4 HS : 5-9	Pre-max : 1-6 Post-max : 7-9 CAM : 1-6 HS : 7-9

Figure N.2 – Fracturing and coalescence patterns for marble 4a-30-0.

Marble 4a-45-0 (figure N.3)

A number of **white patches,** which can be generally classified into two main types, initiated early during the loading process. The first type is short white patches coplanar with pre-existing flaws initiated from the inner flaw tips (white patches A & B in specimens A, B & C). The second type is short white patches **displaying conventional wing** appearance initiated close to the tip regions. These white patches lengthened as loading increased. In all specimens, white patches A and B coalesced in the central bridging region.

The **first cracks** to initiate in the specimens were steep **type 3 tensile cracks** developed from the **outer** tips of the pre-existing flaws – cracks J, K, M in specimen A, cracks G, K, M, N in specimen B, and crack C in specimen C. The initiation of first cracks occurred slightly after the specimen maximum stress was reached in all the tested specimens.

Additional cracks developed at a later stage from both the inner and outer tips of the pre-existing flaws. Most of them were tensile wing cracks (type 1 tensile cracks), which included cracks E and F in specimen A, crack D in specimen B, and cracks D and L in specimen C, i.e. **4 of the 12** white patches in the three specimens displaying conventional wing appearance opened up as cracks, the remaining ones remained intact and did not open up as cracks.

Although the two inner flaw tips coalesced by a central white patch which was coplanar with the pre-existing flaw, no cracking occurred along this white patch to cause **actual crack coalescence**. Besides, the additional cracks initiated from the inner flaw tips were mostly steeply-inclined and vertical. They did not link up with each other on their course of propagation.

The high speed camera images revealed that the continuous tensile cracks initiated from the flaw tips were due to the coalescence of multiple much shorter tensile cracks along some previously developed white patches. Their development is illustrated in figure N.4 and summarized below:

1) **Short white patches** initiated from the pre-existing flaw tip regions.
2) White patches **propagated** towards the top/bottom edges of the specimen (figure N.4a).
3) **Tensile crack opening** along individual segments occurred along those white patches. Only the white patch J initiated from the left tip of the right flaw is shown in figure N.4b.
4) Individual tensile crack segments along white patch J lengthened. Some of them linked up the neighboring crack segments (figure N.4c).
5) Further propagation and **linkage** of those tensile crack segments led to the formation of a continuous tensile crack (figure N.4d).

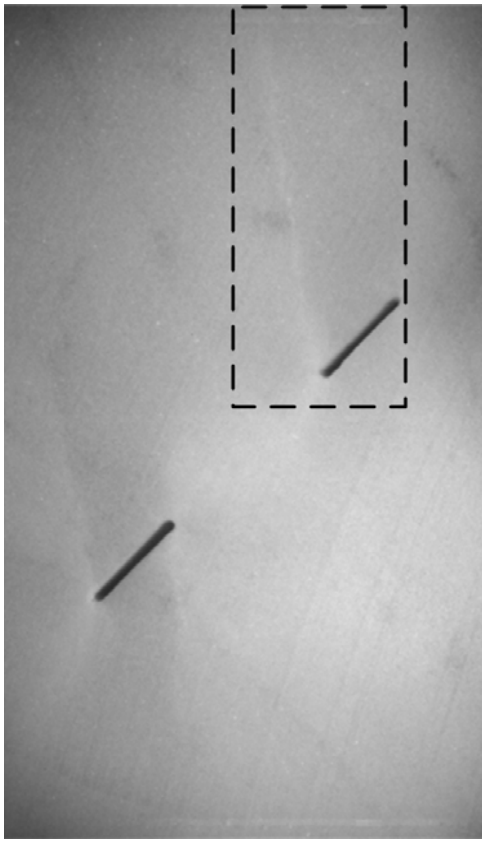

(a) 70.54 MPa

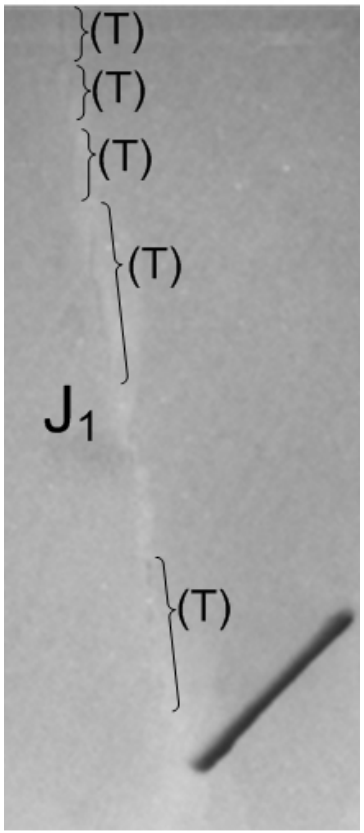

(b) 70.49 MPa

HS Image # - 5425

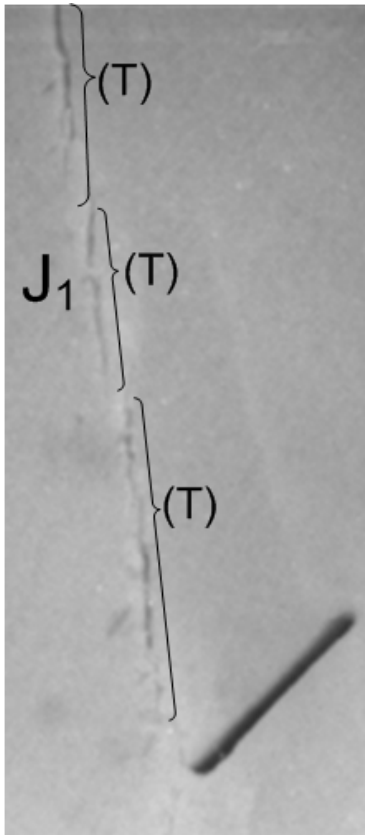

(c) 70.40 MPa

HS Image # - 5067

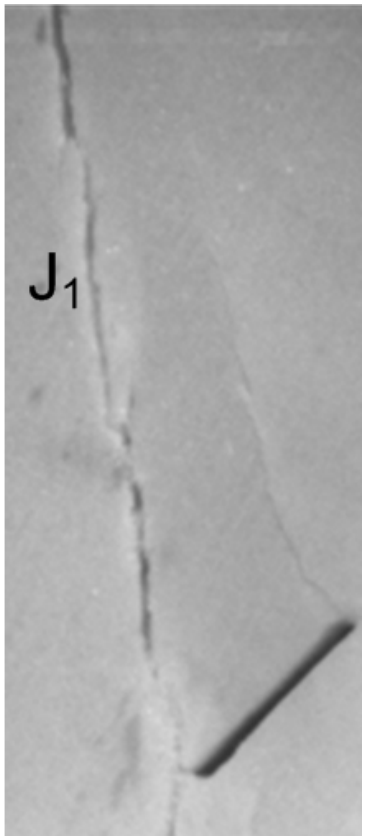

(d) 66.71 MPa

HS Image # - 4182

Figure N.4 – Development of type 3 tensile crack J along a white patch which had initiated from the left tip of the right flaw. The regions shown in figures (b), (c) and (d) is enclosed in figure (a). The high speed images were recorded at a frame rate of 11,019 pps.

The white patch initiation stress ratio, crack initiation stress ratio and coalescence strain ratio (refer to section 3.5 for definitions) are summarized below.

White patch Initiation Stress Ratio *Average value (min – max)*	0.435 (0.350 – 0.499)
Crack Initiation Stress Ratio *Average value (min – max)*	09975 (0.9974 – 0.9996) First cracks in all specimens initiated slightly after max stress at an average strain $\varepsilon = 1.005$ (1.004-1.006)
Coalescence Strain Ratio *Average value (min – max)*	No Coalescence

Marble 4a-45-0

4a-45-0-A (11,019 pps) – no coalescence

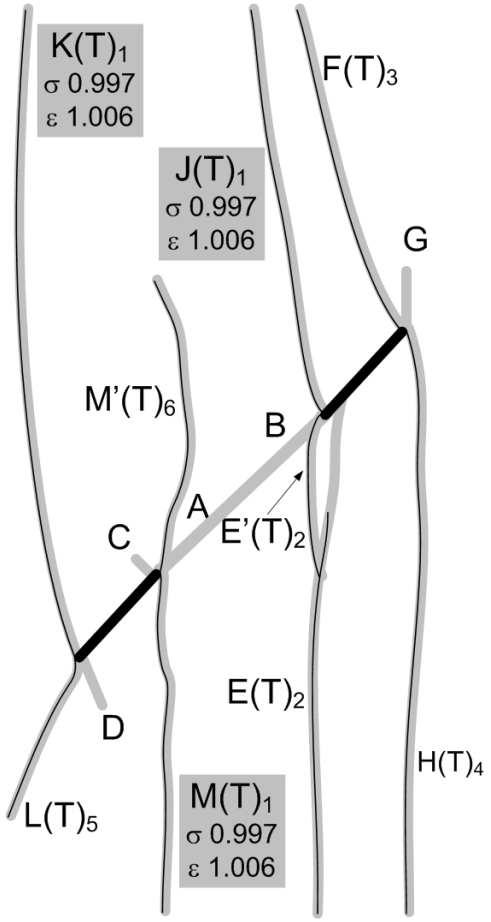

Pre-max : -
Post-max : 1-6

CAM : -
HS : 1-6

4a-45-0-C (14,035 pps) – no coalescence

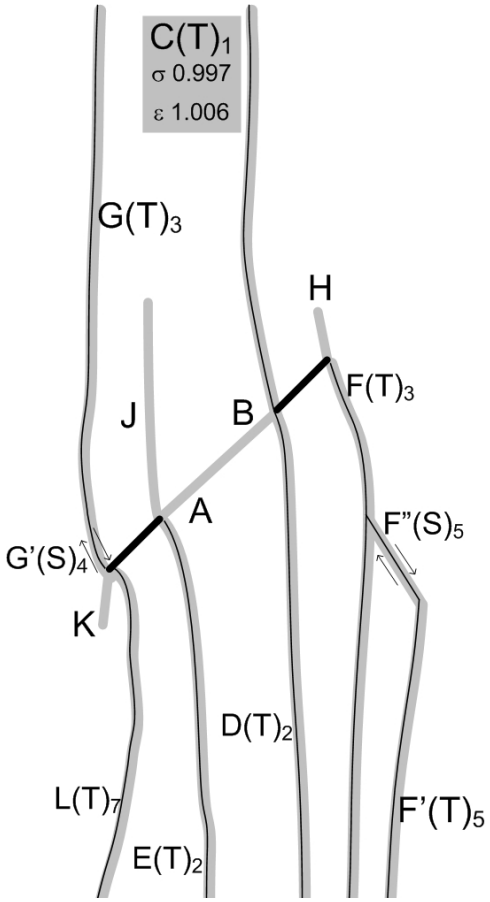

Pre-max : -
Post-max : 1-5

CAM : -
HS : 1-5

Figure N.3 – Fracturing and coalescence patterns for marble 4a-45-0.

Marble 4a-45-0 (continued)

4a-45-0-B (no high speed video) – no coalescence

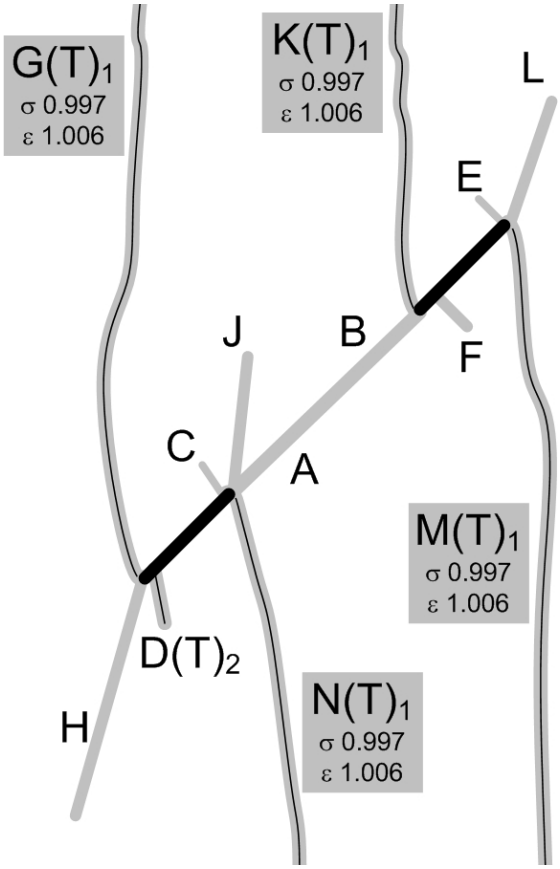

Pre-max : -
Post-max : 1-52

CAM : 1-2
HS : No high speed video

Figure N.3 – Fracturing and coalescence patterns for marble 4a-45-0 (continued).

Marble 4a-60-0 (figure N.5)

A number of **white patches** initiated early during the loading process. The first observable white patches developed are those coplanar with pre-existing flaws initiated from the inner flaw tips (white patches A & B in specimens A & B). These white patches lengthened as loading increased. In both specimens, white patches A and B coalesced in the central bridging region to form a continuous white patch.

The **first cracks** to initiate in the specimens were steep **type 2 tensile cracks** developed from the **outer** flaw tips – cracks D in both specimens. The initiation of first cracks was almost coincident with the occurrence of the specimen maximum stress.

Additional cracks developed at a later stage from both the inner and outer tips of the pre-existing flaws. Most of them were type 2 tensile cracks, type 3 tensile cracks and mixed tensile-shear cracks. It is interesting to note that the white patches displaying wing appearance at the inner flaw tips developed into tensile cracks in specimen B, but not in specimen A.

Coalescence, which occurred after the specimen maximum stress was reached, took place along the central white patch which had developed earlier to link up the two inner flaw tips. Two **type 2 shear cracks** (cracks A & B in both specimens) coplanar with the pre-existing flaws which initiated independently from the inner flaw tips propagated towards each other for coalescence.

The white patch initiation stress ratio, crack initiation stress ratio and coalescence strain ratio (refer to section 3.5 for definitions) are summarized below.

White patch Initiation Stress Ratio *Average value (min – max)*	0.469 (0.468 – 0.471)
Crack Initiation Stress Ratio *Average value (min – max)*	0.998 (0.997 – 1.000)
Coalescence Strain Ratio *Average value (min – max)*	1.034 (1.029 – 1.039)

Marble 4a-60-0

4a-60-0-A (14,035 pps) – coalescence

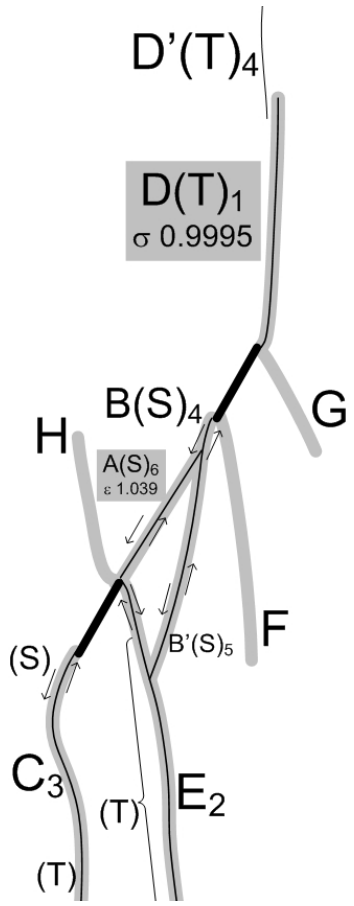

Pre-max : 1
Post-max : 2-6
CAM : -
HS : 1-6

4a-60-0-B (6,006 pps) – coalescence

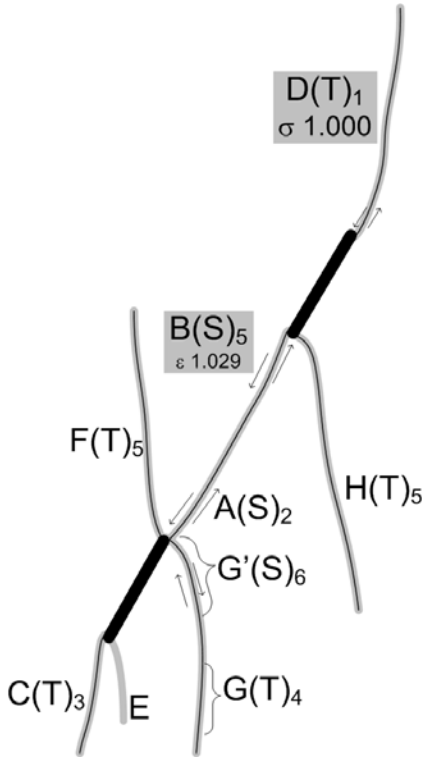

Pre-max : -
Max : 1
Post-max : 2-6
CAM : 1
HS : 2-6

Figure N.5 – Fracturing and coalescence patterns for marble 4a-60-0.

Marble 4a-75-0 (figure N.6)

A number of **white patches** initiated early during the loading process. The first observable white patches developed are those coplanar with pre-existing flaws initiated from the inner and outer flaw tips (white patches A, B, C & D in specimens A & B). These white patches lengthened as loading increased. In both specimens, white patches initiated from the inner flaw tips coalesced in the central bridging region to form a continuous white patch.

The **first cracks** to initiate in the specimens were short **tensile cracks** along the previously developed white patches in the central bridging region which had already linked up the two inner flaw tips. The initiation of first cracks was almost coincident with the occurrence of the specimen maximum stress.

Additional cracks developed at a later stage from both the inner and outer tips of the pre-existing flaws. Most of them were type 2 tensile cracks and mixed tensile-shear cracks.

Coalescence, which occurred after the specimen maximum stress was reached, took place along the central white patch which had developed earlier to link up the two inner flaw tips. In all of the three tested specimens, coalescence was due to the initiation of a new shear crack which linked up the previously initiated tensile crack(s) in the central bridging region. The number of such short tensile crack and shear crack segments varied among the tested specimens. See below.

Two cracks – In specimen 4a-75-0-B, two coplanar crack segments (**tensile crack** and **type 2 shear crack**) initiated independently from the inner flaw tips which later propagated towards each other and coalesced.

Three cracks – In specimen 4a-75-0-A, **two type 2 shear cracks** initiated independently from the two inner flaw tips and were later linked up to form a continuous crack by a third crack which had **shear** nature.

Five cracks – In specimen 4a-75-0-C, three individual **tensile** crack segments first initiated in the central bridging region and were later linked up to form a continuous crack by two late-stage **shear** crack segments.

The white patch initiation stress ratio, crack initiation stress ratio and coalescence strain ratio (refer to section 3.5 for definitions) are summarized below.

White patch Initiation Stress Ratio *Average value (min – max)*	0.569 (0.498 – 0.694)
Crack Initiation Stress Ratio *Average value (min – max)*	0.9967 (0.9955 – 0.9985) First cracks in all three specimens initiated after the max stress at $\varepsilon = 1.011$ (1.004-1.021)
Coalescence Strain Ratio *Average value (min – max)*	1.019 (1.013 – 1.027)

Marble 4a-75-0

4a-75-0-A (11,019 pps) – coalescence

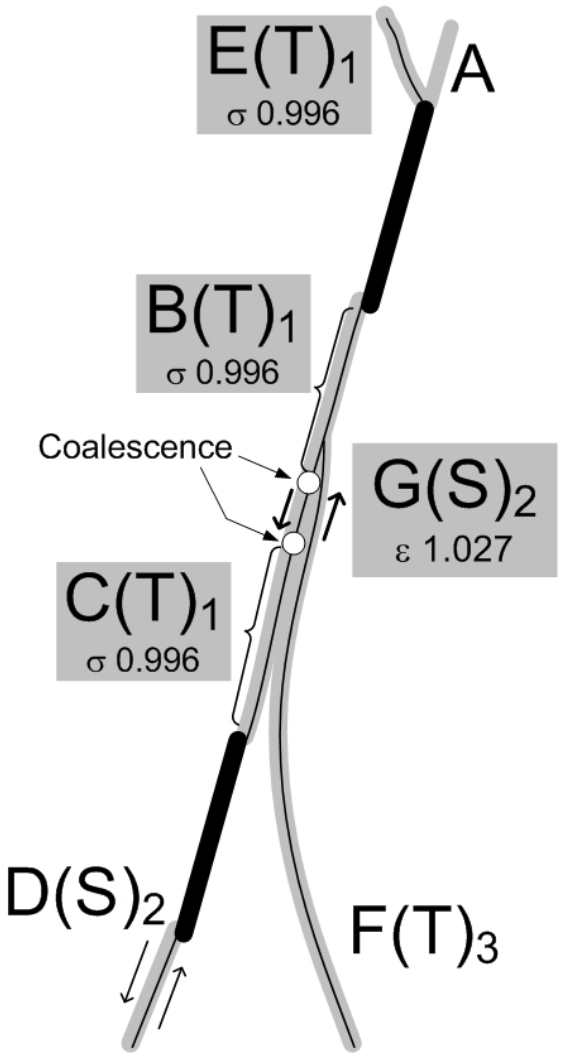

Pre-max : -
Post-max : 1-3

CAM : 1
HS : 2-3

4a-75-0-B (11,019 pps) – coalescence

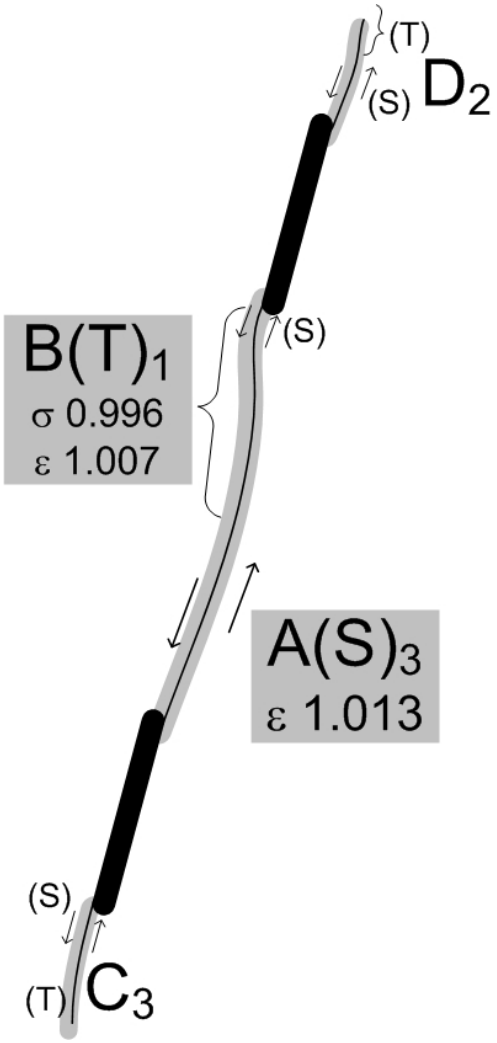

Pre-max : -
Post-max : 1-5

CAM : -
HS : 1-5

Figure N.6 – Fracturing and coalescence patterns for marble 4a-75-0.

Marble 4a-75-0 (continued)	
4a-75-0-C (19,047 pps) – coalescence 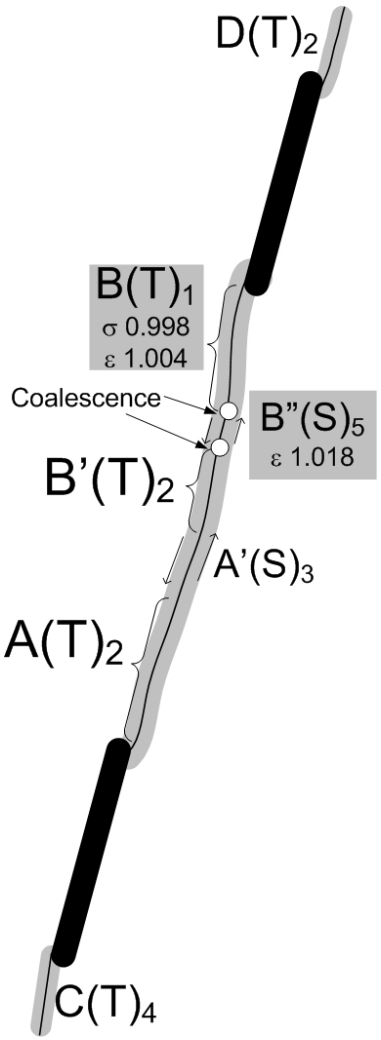 Pre-max : - CAM : - Post-max : 1-5 HS : 1-5	

Figure N.6 – Fracturing and coalescence patterns for marble 4a-75-0 (continued).

APPENDIX O – Test Results of Marble Specimens Containing Stepped Double Flaws of Ligament Length '4a'

In this appendix, the cracking phenomena of marble specimens containing stepped double flaws (0.05" aperture) of ligament "4a" are described. Sketches of cracking patterns observed in all specimens are also illustrated. Refer to section 3.5 and section 5.2 for the meaning of symbols used in the sketches.

Nineteen marble specimens with flaw inclination angle 30^o were tested in this series (see below). Two or more specimens were tested for each geometry in order to obtain consistent coalescence behavior.

Bridging angles α (^{o})	**Specimens**	**Total**
-60	CM 4a-30-(-60)-A, CM 4a-30-(-60)-B, CM 4a-30-(-60)-C	3
-30	CM 4a-30-(-30)-A, CM 4a-30-(-30)-C	2
0	CM 4a-30-0-B, CM 4a-30-0-C	2
30	CM 4a-30-30-B, CM 4a-30-30-C CM 4a-30-30-D	3
60	CM 4a-30-60-A, CM 4a-30-60-B, CM 4a-30-60-C	3
90	CM 4a-30-90-A, CM 4a-30-90-B CM 4a-30-90-C	3
120	CM 4a-30-120-A, CM 4a-30-120-B, CM 4a-30-120-C	3
		19 (Total)

Marble 4a-30-(-60) (figure O.1)

The **first white patches** to initiate were the curvilinear white patches A, B C and D close to or at the flaw tips. Soon after the development of these white patches **additional steeply-inclined white patches** developed from the flaw tips.

The **first cracks** to initiate in the specimens were steep **type 2 tensile cracks** developed from the tips of the pre-existing flaws – cracks G', H in specimen A, cracks B, F* in specimen B, and cracks E, G, J in specimen C. **Additional cracks** developed at a later stage from both the inner and outer tips of the pre-existing flaws – **type 2 tensile cracks** (crack E' in specimen B, crack J', K in specimen C), **type 3 tensile cracks** (crack H' in specimen B, cracks F, M' in specimen C). Also notice that only **2 of the 12** white patches (white patch B in specimen B, white patch C in specimen C) displaying conventional wing appearance opened up as cracks (type 1 tensile cracks), the remaining 10 remained intact and did not open up as cracks.

Coalescence was absent in specimens A and C, and only occurred in specimen B. The coalescence in specimen C which occurred well after the specimen maximum stress was passed, was achieved by the linkage of two inclined **shear cracks** (**type 1 shear crack, type 3 shear crack**) which had individually initiated from the two inner flaw tips.

The white patch initiation stress ratio, crack initiation stress ratio and coalescence strain ratio (refer to section 3.5 for definitions) are summarized below.

White patch Initiation Stress Ratio *Average value (min – max)*	0.323 - average of two values (0.296 – 0.351) only, can not be determined in the remaining one specimen
Crack Initiation Stress Ratio *Average value (min – max)*	0.990 (two crack initiation occur slightly after max stress and one crack initiation occurs slightly earlier than max stress) ε = 0.988, 1.030, 1.013 (average = 1.010)
Coalescence Strain Ratio	1.277 (one specimen)

Marble 4a-30-(-60)

4a-30-(-60)-A (10,000 pps) – no coalescence

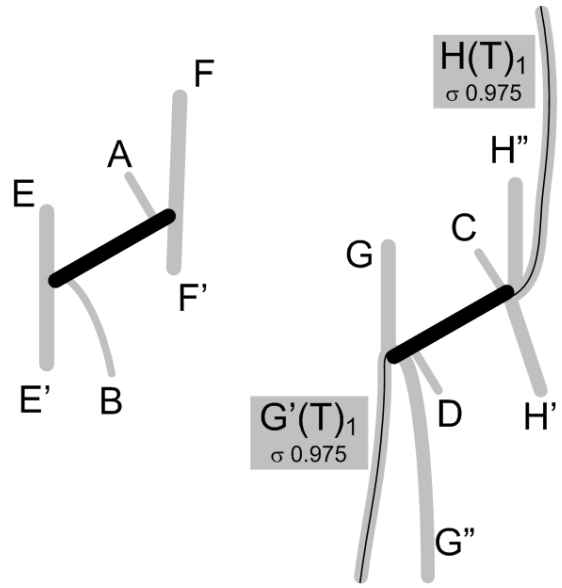

Pre-max : 1 CAM : 1
Post-max : - HS : -

4a-30-(-60)-B (10,000 pps) – coalescence

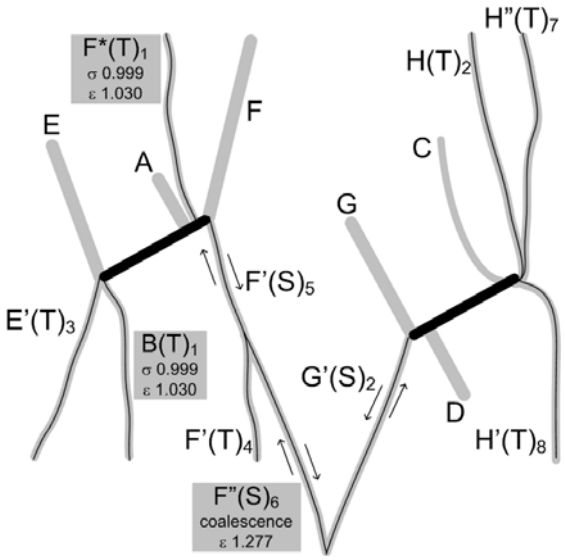

Pre-max : - CAM : 1
Post-max : 1-8 HS : 1-8

4a-30-(-60)-C (6,600 pps) – no coalescence

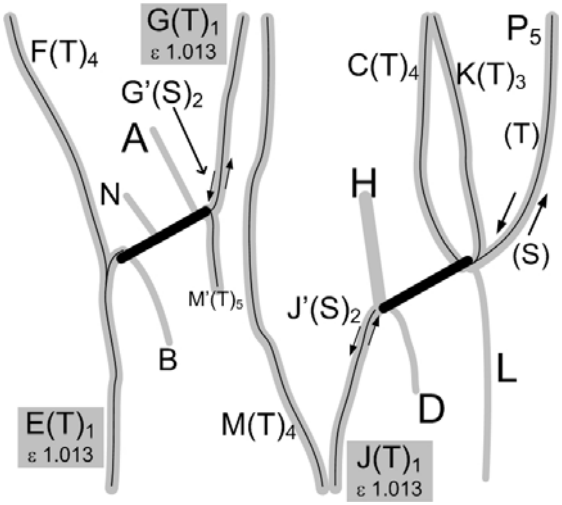

Pre-max : - CAM : -
Post-max : 1-5 HS : 1-5

Figure O.1 – Fracturing and coalescence patterns for marble 4a-30-(-60).

Marble 4a-30-(-30) (figure O.2)

The **first white patches** to initiate were the curvilinear white patches A, B C and D close to or at the flaw tips. Soon after the development of these white patches **additional steeply-inclined white patches** developed from the flaw tips.

The **first cracks** to initiate in the specimens were **type 1 shear crack** (crack F) in specimen A and **type 2 tensile cracks** (cracks H, H") in specimen B. **Additional cracks** developed at a later stage from both the inner and outer tips of the pre-existing flaws – **type 2 tensile cracks** (crack E, H' in specimen A, crack J', K in specimen C), **type 3 tensile cracks** (cracks K, L in specimen A, cracks E in specimen B). Also notice that only **2 of the 8** white patches (white patch C in specimen A, white patch A in specimen B) displaying conventional wing appearance opened up as cracks (type 1 tensile cracks), the remaining 6 remained intact and did not open up as cracks.

Coalescence was absent in specimen A and only occurred in specimen B. The coalescence in specimen B which occurred after the specimen maximum stress was passed, was achieved by an inclined crack L consisting of **tensile** and **shear** segments which linked up two steeply-inclined cracks (G & J) independently originating from the two inner flaw tips

The white patch initiation stress ratio, crack initiation stress ratio and coalescence strain ratio (refer to section 3.5 for definitions) are summarized below.

White patch Initiation Stress Ratio *Average value (min – max)*	0.345 (0.246 – 0.443)
Crack Initiation Stress Ratio *Average value (min – max)*	0.997 (0.995-0.999) crack initiation occurs after max stress at ε = 1.014, 10006, average ε = 1.010
Coalescence Strain Ratio	1.094 (one specimen)

Marble 4a-30-(-30)

4a-30-(-30)-A (6,600 pps) – no coalescence

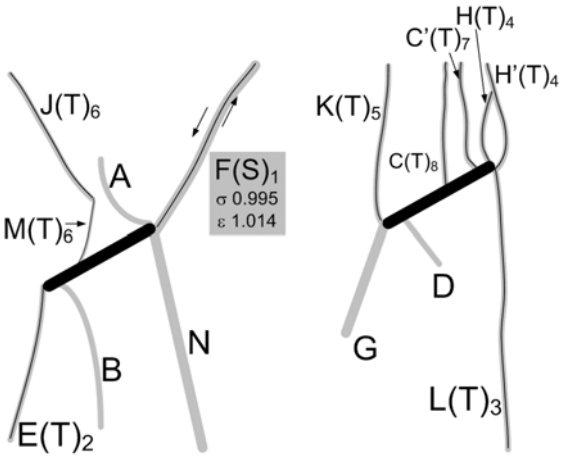

Pre-max : -
Post-max : 1-8

CAM : -
HS : 1-8

4a-30-(-30)-C (6,600 pps) – coalescence

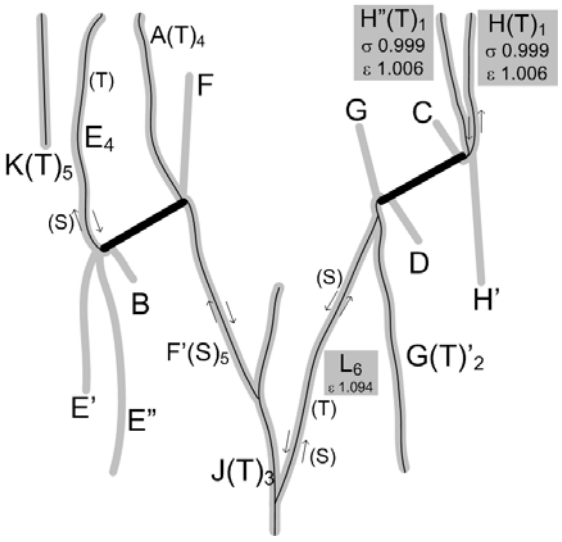

Pre-max : -
Post-max : 1-6

CAM : -
HS : 1-6

Figure O.2 – Fracturing and coalescence patterns for marble 4a-30-(-30).

Marble 4a-30-0

Refer to the corresponding description in Appendix N.

Marble 4a-30-30 (figure O.3)

The **first white patches** to initiate were the curvilinear white patches A, B C and D close to or at the flaw tips. Soon after the development of these white patches **additional steeply-inclined white patches** developed from the flaw tips.

The **first cracks** to initiate in the specimens were **type 2 tensile cracks** (cracks E & H in specimen D) and **TWCs, type 1 tensile cracks** (cracks C, D in specimen B, crack C in specimen C). **Additional type 2 tensile cracks and type 1 tensile cracks** developed at a later stage from both the inner and outer tips of the pre-existing flaws. Also notice that only **8 of the 12** white patches displaying conventional wing appearance eventually opened up as cracks (type 1 tensile cracks), the remaining 3 (white patch B in specimen B, white patches A, C, D in specimen D) remained intact and did not open up as cracks.

Coalescence occurred in all the tested specimens after the specimen maximum stress was passed. The general coalescence behavior was similar among these specimens with the development of an **inclined shear crack** in the central bridging region, which linked up some steep cracks previously initiated from the inner flaw tips.

The white patch initiation stress ratio, crack initiation stress ratio and coalescence strain ratio (refer to section 3.5 for definitions) are summarized below.

White patch Initiation Stress Ratio *Average value (min – max)*	0.460 (0.326 – 0.609)
Crack Initiation Stress Ratio *Average value (min – max)*	0.949 (0.916-0.998)
Coalescence Strain Ratio *Average value (min – max)*	1.067 (1.034 – 1.119)

Marble 4a-30-30

4a-30-30-B (7,005 pps) – coalescence

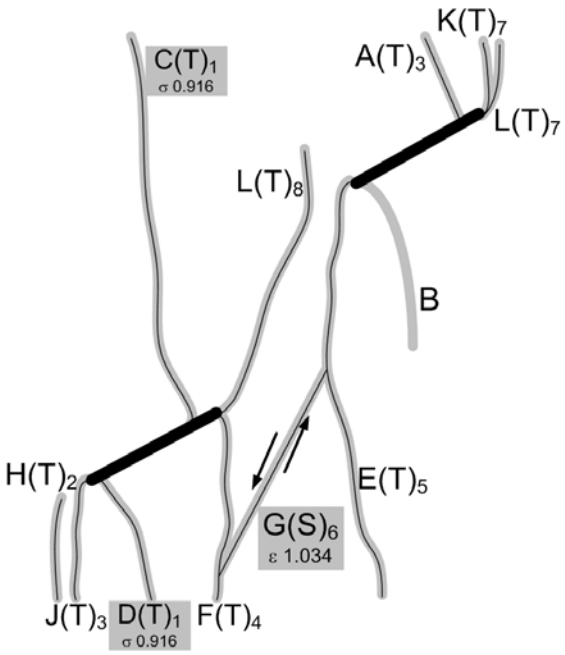

Pre-max : 1 CAM : 1
Post-max : 2-8 HS : 2-8

4a-30-30-C (8,213 pps) – coalescence

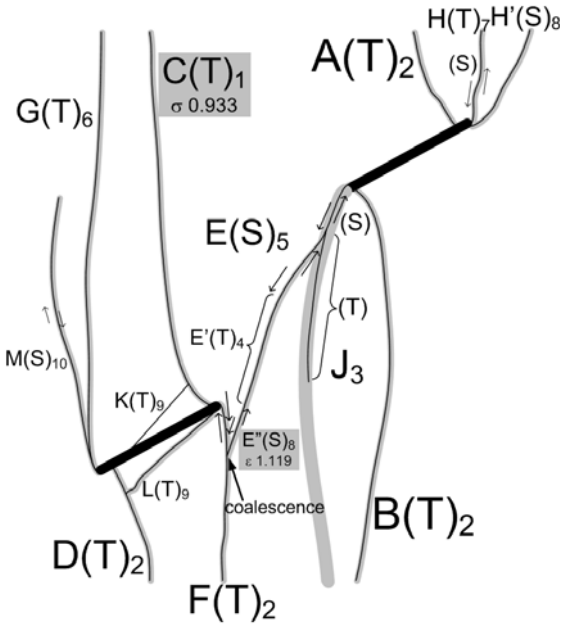

Pre-max : 1-2 CAM : 1-2
Post-max : 3-10 HS : 3-10

4a-30-30-D (10,000 pps) – coalescence

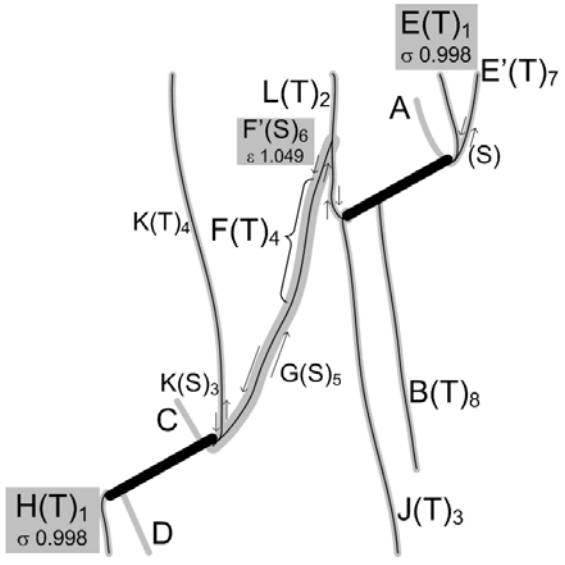

Pre-max : 1 CAM : 1
Post-max : 2-8 HS : 2-8

Figure O.3 – Fracturing and coalescence patterns for marble 4a-30-30.

Marble 4a-30-60 (figure O.4)

The **first white patches** to initiate were the curvilinear white patches A, B C and D close to or at the flaw tips. Soon after the development of these white patches **additional steeply-inclined white patches** developed from the flaw tips.

The **first cracks** to initiate in the specimens were **tensile wing cracks** (TWCs, type 1 tensile cracks). In specimen C, only the tensile wing cracks close to the **outer flaw tips** initiated simultaneously as the first cracks, the tensile wing patches B and C close to the inner flaw tips remained closed throughout the whole course of loading. In specimens A and B, **all** the four TWCs initiated simultaneously as the first cracks. However, notice that even though the white patches underlying TWC B and C in specimens A and B extend from one flaw tip to the other flaw tip, the TWC B and C did not propagate far enough to lead to coalescence.

Additional type 2 tensile cracks (cracks F, G in specimen A, cracks F, K in specimen B, cracks F, G in specimen C) **and type 1 shear cracks** (crack H in specimen C) developed at a later stage from both the inner and outer tips of the pre-existing flaws.

Coalescence occurred in all the tested specimens before the specimen maximum stress was passed. The general coalescence behavior was the same among the three specimens with the development of a vertical **type 2 tensile crack** linking up the inner flaw tips in the central bridging region.

The white patch initiation stress ratio, crack initiation stress ratio and coalescence strain ratio (refer to section 3.5 for definitions) are summarized below.

White patch Initiation Stress Ratio *Average value (min – max)*	0.579 (0.506 – 0.664)
Crack Initiation Stress Ratio *Average value (min – max)*	0.804 (0.644 – 0.894)
Coalescence Strain Ratio *Average value (min – max)*	0.882 (0.768 – 0.946)

Marble 4a-30-60

4a-30-60-A (6,006 pps) – coalescence

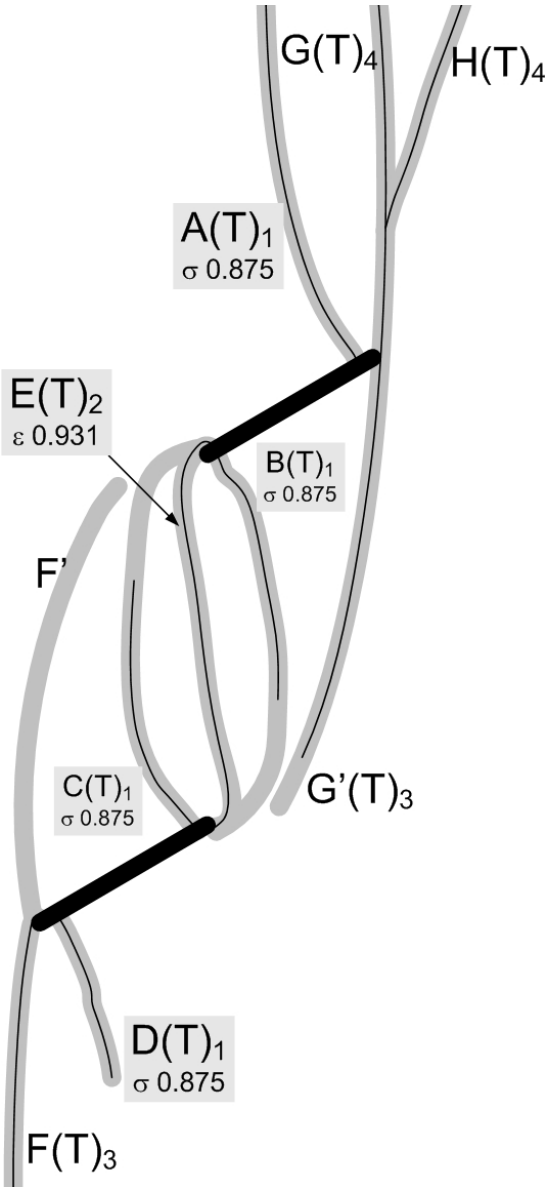

Pre-max : 1-3
Post-max : 4

HS : 1
CAM : 2-6

4a-30-60-B (6,006 pps) – coalescence

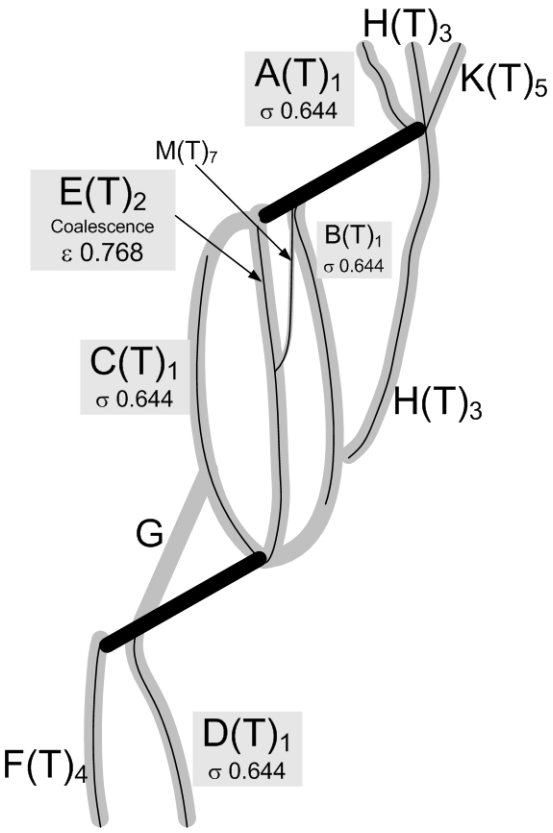

Pre-max : 1-4
Post-max : 5-7

HS : 1-7

Figure O.4 – Fracturing and coalescence patterns for marble 4a-30-60.

Marble 4a-30-60 (continued)	
4a-30-60-C (7,005 pps) – coalescence 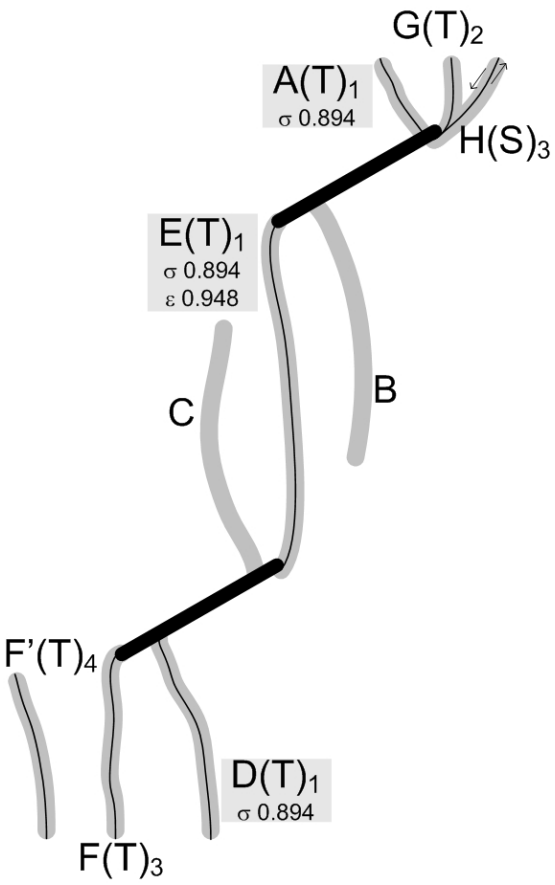 Pre-max : 1 CAM : 1 Post-max : 2-4 HS : 2-4	

Figure O.4 – Fracturing and coalescence patterns for marble 4a-30-60 (continued).

Marble 4a-30-90 (figure O.5)

The **first white patches** to initiate were the curvilinear white patches A, B C and D close to or at the flaw tips. Soon after the development of these white patches **additional steeply-inclined white patches** developed from the flaw tips.

The **first cracks** to initiate in the specimens were **type 2 tensile cracks** from the right tip of the top flaw (cracks E in all three tested specimens). **Additional type 2 tensile cracks** developed at a later stage from both the inner and outer tips of the pre-existing flaws. Some of these cracks took part in coalescence.

In all specimens, the white patches displaying wing appearance remained intact and no cracking developed along them throughout the whole loading process.

Coalescence occurred in all the tested specimens slightly after the specimen maximum stress was passed. The coalescence behavior was very generally similar among the three specimens, in which the flaw tips of the same side of the two pre-existing flaws were first linked up by curvilinear white patches. Cracking then occurred along these white patches to link up the flaw tips.

In all three specimens, **type 2 tensile cracks** first initiated respectively from the left tip of the top flaw and the right tip of the bottom flaw. After the crack on each side had propagated for a certain length, another short crack then initiated from the tip (of the same side) of the other flaw to link up the **type 2 tensile crack**. This later **short crack** was observed to be either **type 3 shear crack or type 3 tensile crack**. Due to the presence of overlying rock fragments, the identity (shear/tensile?) of some of these short cracks was sometimes impossible to determine.

The cracks involved in coalescence in all three specimens were:

Specimen	Type 2 tensile cracks	Type 3 tensile cracks / Type 3 shear cracks
4a-30-90-A	G, F’	F”(S), G’(T/S?)
4a-30-90-B	G, N	K(S)
4a-30-90-C	F, G	L(T/S?), K(S)

The white patch initiation stress ratio, crack initiation stress ratio and coalescence strain ratio (refer to section 3.5 for definitions) are summarized below.

White patch Initiation Stress Ratio *Average value (min – max)*	0.379 (0.349 – 0.424)
Crack Initiation Stress Ratio *Average value (min – max)*	0.9620 (0.8944 – 0.9997)
Coalescence Strain Ratio *Average value (min – max)*	1.042 (1.003 – 1.076)

Marble 4a-30-90

4a-30-90-A (6,600 pps) – coalescence

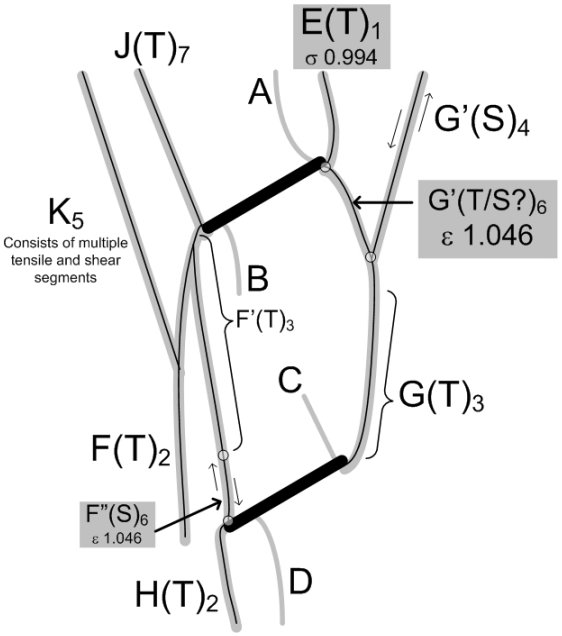

Cracks F" and G' were the coalescence cracks

Pre-max : 1-3 CAM : 1-3
Post-max : 4-7 HS : 4-7

4a-30-90-B (6,600 pps) – coalescence

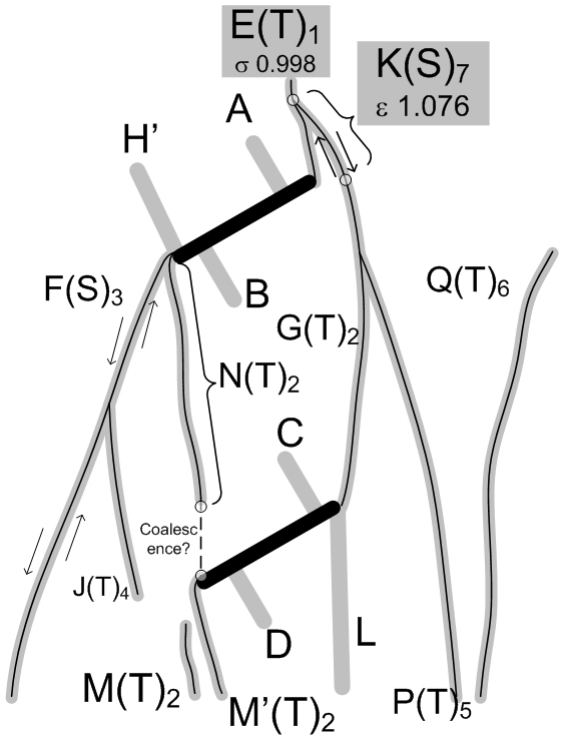

Whether there was coalescence between crack N and the bottom flaw was uncertain.

Pre-max : 1-3 CAM : 1-2
Post-max : 4-7 HS : 3-7

Figure O.5 – Fracturing and coalescence patterns for marble 4a-30-90.

Marble 4a-30-90 (continued)

4a-30-90-C (6,600 pps) – coalescence

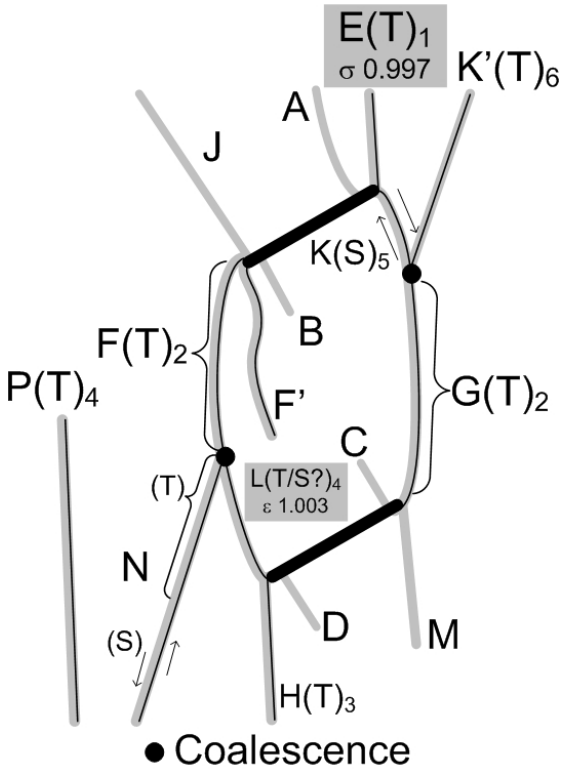

Pre-max : 1-2 CAM : 1-2
Post-max : 3-6 HS : 3-6

Figure O.5 – Fracturing and coalescence patterns for marble 4a-30-90 (continued).

Marble 4a-30-120 (figure O.6)

The **first white patches** to initiate were the curvilinear white patches A, B C and D close to or at the flaw tips. Soon after the development of these white patches **additional steeply-inclined white patches** developed from the flaw tips. Notice also that an almost vertical white patch developed in the central bridging region to link up the right tip of the top flaw and the left tip of the bottom flaw.

The **first cracks** to initiate in the specimens were multiple short vertical **tensile cracks** along the white patch which had previously developed in the central bridging region linking up the two inner flaw tips. The initiation of these short cracks was **slightly earlier** than the occurrence of specimen maximum stress. These short tensile crack segments subsequently lengthened and **coalesced** to form a continuous tensile crack which eventually linked up the two inner flaw tips. The trajectory of this crack is similar to that of **type 3 tensile crack**. The formation of such a continuous crack occurred **slightly after** the specimen maximum stress was reached.

Additional tensile wing cracks (type 1 tensile cracks) (cracks A, B in specimen A, cracks A, B, C, D in specimen B, crack A in specimen C) and **type 3 tensile cracks** (cracks K, L, L' in specimen A, cracks K, L, L' in specimen B, F' in specimen C) developed at a later stage from both the inner and outer tips of the pre-existing flaws.

The white patch initiation stress ratio, crack initiation stress ratio and coalescence strain ratio (refer to section 3.5 for definitions) are summarized below.

White patch Initiation Stress Ratio *Average value (min – max)*	0.432 (can't be determined in two specimens)
Crack Initiation Stress Ratio *Average value (min – max)*	0.994 (0.986 – 0.999)
Coalescence Strain Ratio *Average value (min – max)*	1.050 (1.016 – 1.099)

Marble 4a-30-120

4a-30-120-A (6,600 pps) – coalescence

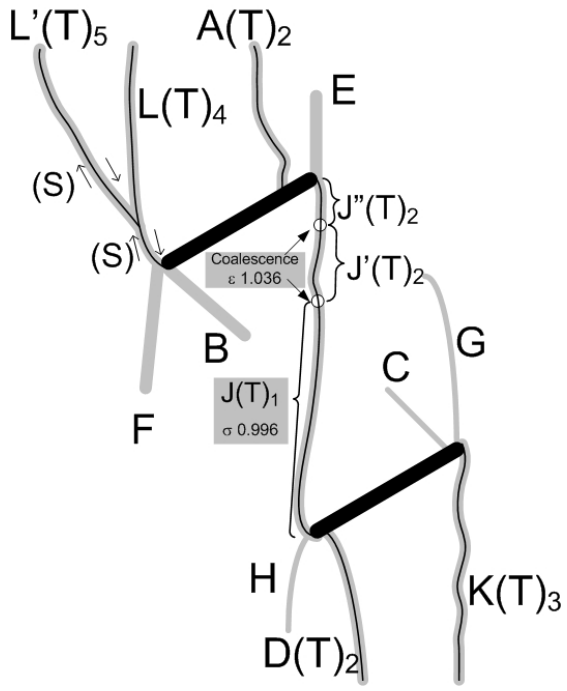

Pre-max : 1-4
Post-max : 5

CAM : 1-2
HS : 3-5

Coalescence was achieved by the propagation and subsequent linkage of individual tensile crack segments J, J' and J".

4a-30-120-B (6,600 pps) – coalescence

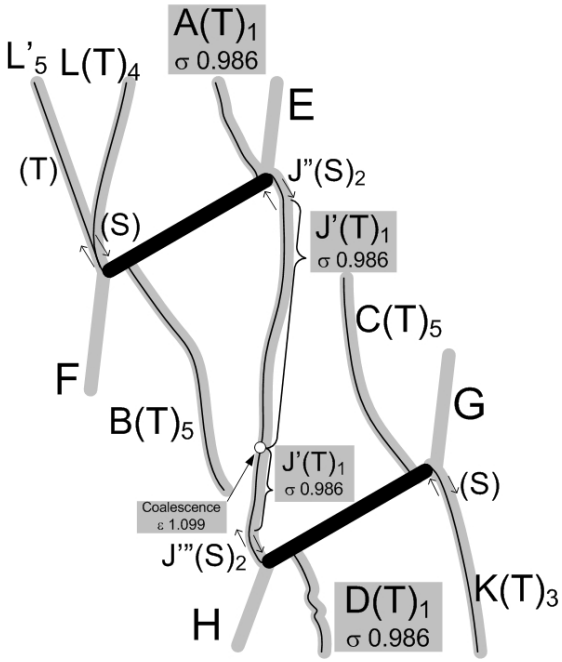

Pre-max : 1-4
Post-max : 5

CAM : 1, 3-5
HS : 2

Figure O.6 – Fracturing and coalescence patterns for marble 4a-30-120.

Marble 4a-30-120 (continued)	
4a-30-120-C (6,600 pps) – coalescence 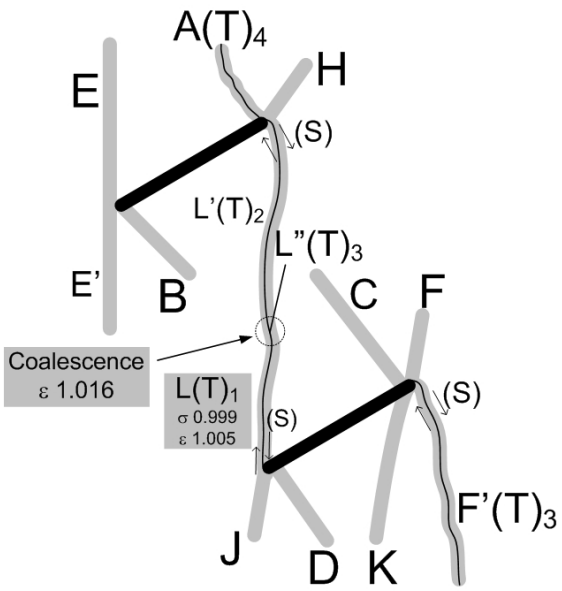 Max : - CAM : no camcorder recording Post-max : 1-4 HS : 1-4 Coalescence was achieved by the propagation and subsequent linkage of individual tensile crack segments L and L'.	

Figure O.6 – Fracturing and coalescence patterns for marble 4a-30-120 (continued).

APPENDIX P – Imaging with Scanning Electron Microprobe

P.1 Introduction

This Appendix consists of two sections. Procedures of preparing the marble specimens prior to scanning electron microprobe (SEM) imaging will first be described. In the subsequent section, the fundamentals of imaging with the scanning electron microprobe are discussed. Refer to Chatterjee (2006) for further details.

P.2 Specimen Preparation

After the loading tests in which the white patches had been produced in the marble specimens, the specimens were first trimmed down to appropriate sizes. The trimming was carried out by water abrasive jet and hand saw. The trimmed marble specimens, which were then of a general thickness of around 10 – 20 mm, would then be wet-polished by hand with a range of polishing grit size, respectively coarse and fine. The specimens first underwent coarse polishing by SiC polishing papers of varying grit size as shown in figure P.1 (began with 240 grit size and finished with 600 grit size).

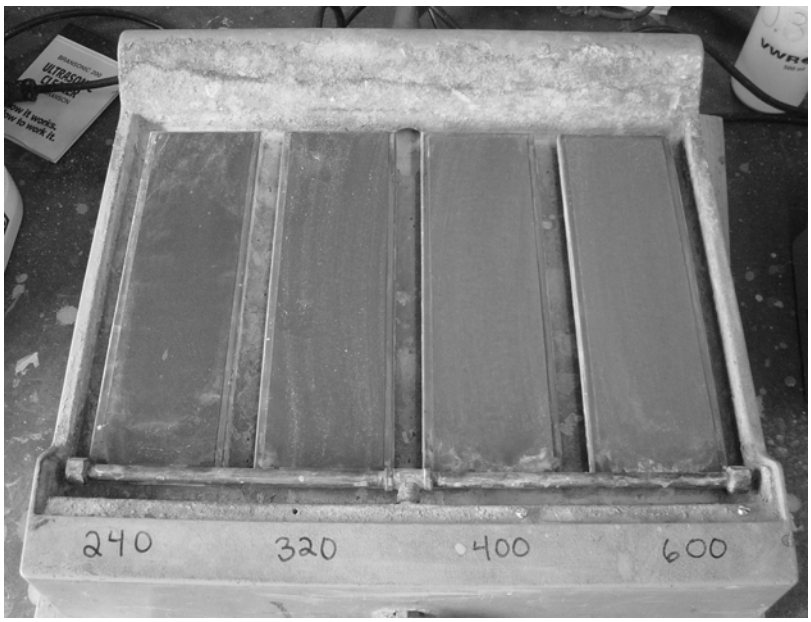

Figure P.1 – SIC polishing papers of varying grit size – 240, 320, 400, 600.

In the subsequent fine polishing stage, the marble specimens were further polished with alumina grit slurry – first with 0.3 μm grit size and then with 0.06 μm grit size.

The polished specimens were then washed with clean water in an ultrasonic cleaner to get rid of the polishing grit and other surface dirt. The specimens were then subsequently dried in air with a blow duster. Completely dried specimens were then carbon coated. Carbon coating refers to the process in which a very thin carbon layer was deposited onto the surfaces of the specimens to be analyzed. It is required for electrically insulating material such as marble for conduction of electron beams during the SEM analysis and imaging process. During the carbon coating process, a graphite rod was locally heated up and became vaporized in a vacuum container, in which marble specimens to be carbon-coated had been placed below the graphite rod (figure P.2). The carbon vapor then adhered to the marble top faces as heating went on. To monitor the coat-thickness, a polished brass block was placed beside the marble specimens and coated at the same time. The continual color change of the brass block due to the carbon coating which could be observed from outside of the container served as a coat-thickness indicator.

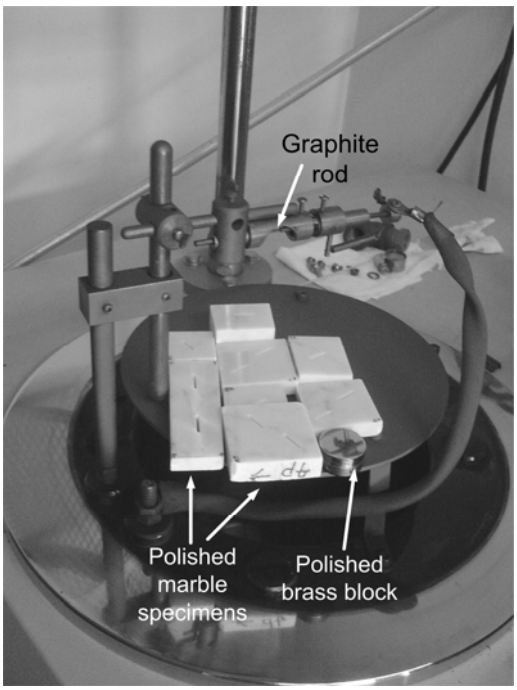

Figure P.2 – carbon coating on marble specimens. Note that the whole facility shown in this picture will be covered by an air-tight container (not shown here) which is to be vacuumed.

P.3 Scanning Electron Microprobe Imaging

The JEOL JXA-733 Superprobe housed in the Department of Earth, Atmospheric and Planetary Science at MIT was used in the present study. This electron microprobe, which is also known as the electron probe micro-analyzer, is usually used for identifying the measuring concentration of chemical composition in a specimen based on the principle of X-ray spectrometry (Chatterjee, 2006). The microprobe, however, is also capable to provide high-resolution scanning back-scattered images.

The technical details and different components of the electron microprobe will not be covered in this section. Only the fundamental concepts related to the imaging technique are briefly discussed here. Refer to Chatterjee (2006) for further details. In the electron microprobe, which is maintained under high vacuum, an electron beam is generated from a heated tungsten filament by thermionic emission with a potential difference in the 10-30 kV range. The beam, which is focused within the facility, is then of a current between 1 pA and 1 μA. When the beam hits the specimens, the incident electrons are scattered (both elastically and inelastically[1]) by the target atoms (figure P.3). High resolution scanned images of the specimen surface are obtained by rastering the electron beam over an area of interest of the specimen surface. The signal is synchronously displayed on an oscilloscope CRT as the beam scans. Scanning electron images can utilize either back-scattered electrons (BE)[2] or secondary electrons (SE)[3] with magnification ranging between 40 and 360,000 times could be obtained. In the present study, the BE technique with a magnification range of 40-1000 times was used. In general, the degree of

[1] When the incident electron undergoes elastic scattering, its kinetic energy is not significantly changed. When the incident electron undergoes inelastic scattering, its kinetic energy is substantially lost. See figure P.3.

[2] Back-scattered electrons are those incident beam electrons which have undergone elastic scattering and have a scattering angle greater than 90^o. They have higher energies between 0 keV and E_0 (energy of the incident electron). See figure P.3.

[3] Secondary electrons originate from the specimens and are produced by inelastic scattering due to the incident beam electrons which involves transfer of energy from the latter to the atoms of the specimens. These secondary electrons overcome the respective energy barrier and escape from the specimen surface. Compared with back-scattered electrons, they have lower energies in the range of 0-50 eV, mostly between 3 and 5 eV.

scattering increases with the atomic number of the target material. It thus allows differentiation of minerals. In addition, when the incident beam electrons hit the specimen surface where cracks or local depressions are present, almost no electrons can be back-scattered and detected. The areas associated with cracks will thus appear black in color on the scanned images.

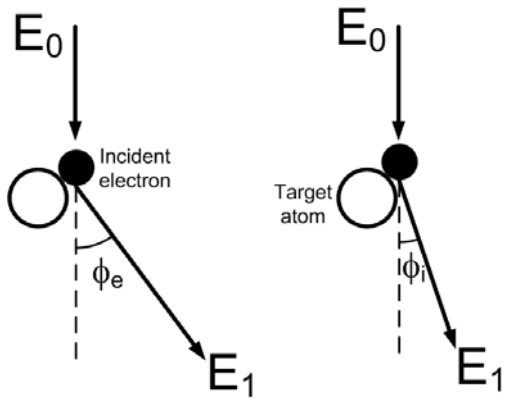

Drawn not to scale

(a) (b)

Figure P.3 – Schematic illustration of consequences of an electron (back circle) after it hits a target atom (open circle) (a) elastic scattering, (b) inelastic scattering. E_0 = energy of the incident electron, E_1 = energy of the electron after scattering, ϕ_e =elastic scattering angle, ϕ_i = inelastic scattering angle (Chatterjee, 2006).

P.4 References

Chatterjee, N. (2006) Electron Microprobe Analysis by Wavelength dispersive X-ray Spectrometry. *Course notes for MIT IAP course 12.141*.

APPENDIX Q – Crack Initiation Criteria

Q.1 Introduction

Different crack initiation criteria are available in the literature to predict the initiation angle of a new crack initiating from a pre-existing flaw and the corresponding required load under a mixed mode I-II loading condition. This appendix will be restricted discussion to two-dimensional cases. Various crack initiation criteria can be generally classified into three main types – ***stress-based***, ***energy-based*** and ***strain-based***. This section provides a general overview of these criteria. Refer to Qian and Fatemi (1996), Khan and Khraisheh (2000, 2004) for a more comprehensive review.

Energy-based	**Stress-based**	**Strain-based**
CR – max energy release rate (G)	CR – max tangential stress (MTS)	max tensile principal strain (MTPSN) [(2)]
CR – min strain energy density (S)	VR – modified max tangential stress (modified MTS)	
VR – max dilatational strain energy (T_v)	CR – zero shear stress ($\tau_{r\theta}$)	
VR – max stress invariant function (I_p)	CR – max stress triaxiality (M)	
J contour integral (J)	CR – critical tensile strength & critical shear strength [(1)]	

Note : [(1)] criterion proposed by MIT rock mechanics group (Bobet, 1997, Bobet & Einstein, 1998b)
[(2)] criterion proposed by MIT rock mechanics group (Reyes, 1991, Reyes & Einstein, 1991)
CR – core region is a circle with a constant radius
VR – core region with a variable radius

Table Q.1 – Summary of crack initiation criteria.

For a flaw of length 2a inclined at an angle β (β = 90-β', where β' is the flaw inclination angle) measured clockwise to the direction of the load (figure Q.1). The *singular elastic stress field* with the omission of higher-order *non-singular* terms (independent of *r* in the denominator) around the flaw tip expressed in Cartesian coordinates (figure Q.2 a) and polar coordinates (figure Q.2 b) is given below. Only 2-D case is considered.

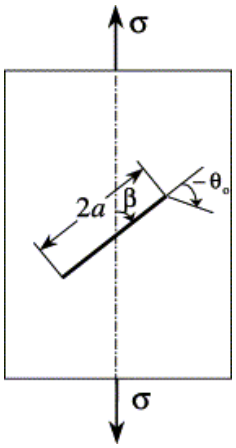

Figure Q.1 – A pre-existing flaw embedded in a prismatic specimen (Khan & Khraisheh, 2000).

Cartesian coordinates (Anderson, 2005) (figure Q.2a)

$$\sigma_x = \frac{1}{\sqrt{2\pi r}}\left\{\left[K_I \cos\frac{\theta}{2}\left(1-\sin\frac{\theta}{2}\sin\frac{3\theta}{2}\right)\right]-\left[K_{II}\sin\frac{\theta}{2}\left(2+\cos\frac{\theta}{2}\cos\frac{3\theta}{2}\right)\right]\right\}$$

$$\sigma_y = \frac{1}{\sqrt{2\pi r}}\left\{\left[K_I \cos\frac{\theta}{2}\left(1+\sin\frac{\theta}{2}\sin\frac{3\theta}{2}\right)\right]+\left[K_{II}\sin\frac{\theta}{2}\cos\frac{\theta}{2}\cos\frac{3\theta}{2}\right]\right\} \qquad (1)$$

$$\tau_{xy} = \frac{1}{\sqrt{2\pi r}}\left\{\left[K_I \cos\frac{\theta}{2}\sin\frac{\theta}{2}\cos\frac{3\theta}{2}\right]+\left[K_{II}\cos\frac{\theta}{2}\left(1-\sin\frac{\theta}{2}\sin\frac{3\theta}{2}\right)\right]\right\}$$

$\sigma_z = \nu(\sigma_x + \sigma_y)$ for plain strain (1a)

$\sigma_z = 0$ for plain stress (1b)

Polar Coordinates (Williams, 1984) (figure Q.2b)

$$\sigma_\theta = \frac{1}{\sqrt{2\pi r}}\left\{\left[\frac{K_I}{2}\cos\frac{\theta}{2}\left(1+\cos\theta\right)\right]-\left[\frac{3K_{II}}{2}\sin\frac{\theta}{2}\left(1+\cos\theta\right)\right]\right\}$$

$$\sigma_r = \frac{1}{\sqrt{2\pi r}}\left\{\left[\frac{K_I}{2}\cos\frac{\theta}{2}\left(3-\cos\theta\right)\right]-\left[\frac{K_{II}}{2}\sin\frac{\theta}{2}\left(1-3\cos\theta\right)\right]\right\} \qquad (2)$$

$$\tau_{r\theta} = \frac{1}{\sqrt{2\pi r}}\left\{\left[\frac{K_I}{2}\sin\frac{\theta}{2}\left(1+\cos\theta\right)\right]-\left[\frac{K_{II}}{2}\cos\frac{\theta}{2}\left(1-3\cos\theta\right)\right]\right\}$$

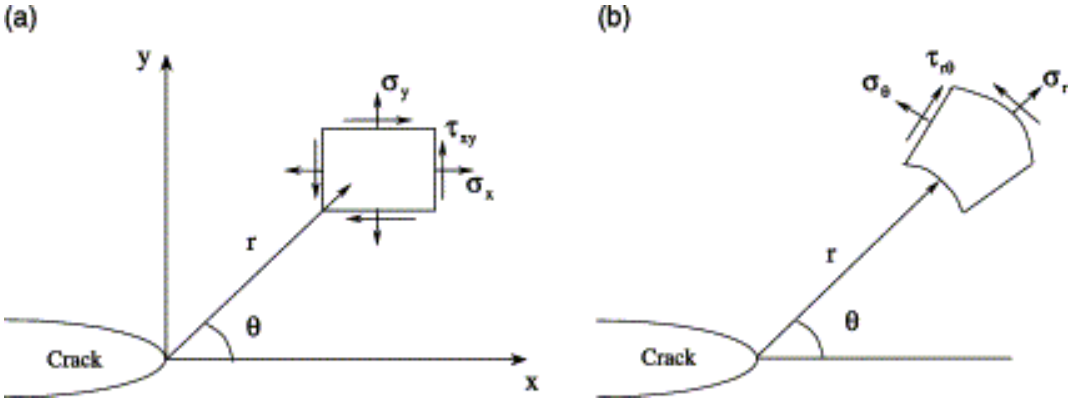

Figure Q.2 – Stress field around a flaw tip in (a) Cartesian coordinates, (b) polar coordinates (Khan & Khraisheh, 2000).

Q.2 Stress-Based Criteria

(1) MTS-criterion (Erdogan & Sih, 1963)

A new crack will initiate from the flaw tip in a direction corresponding to the direction of maximum tangential stress (MTS, σ_θ) along a constant radius around the flaw tip (figure Q.2b). The mathematical formulation is shown below.

$$\frac{\partial \sigma_\theta}{\partial \theta} = 0 \tag{3}$$

$$\frac{\partial^2 \sigma_\theta}{\partial \theta^2} < 0 \tag{4}$$

Substituting the stress field (2) into equations (3) and (4) to obtain equations (5) and (6) which are then solved for θ:

$$\tan^2 \frac{\theta}{2} - \frac{\mu}{2} \tan \frac{\theta}{2} - \frac{1}{2} = 0 \tag{5}$$

$$-\frac{3}{2}\left[\left(\frac{1}{2}\cos^3 \frac{\theta}{2} - \cos \frac{\theta}{2} \sin^2 \frac{\theta}{2}\right) + \frac{1}{\mu}\left(\sin^3 \frac{\theta}{2} - \frac{7}{2} \sin \frac{\theta}{2} \cos^3 \frac{\theta}{2}\right)\right] < 0 \tag{6}$$

where μ is the ratio between the mode I and mode II stress intensity factors

$$\mu = \frac{K_I}{K_{II}} \tag{7}$$

(2) Modified MTS-criterion (Khan & Khraisheh, 2000)

A new crack will initiate from the flaw tip in a direction corresponding to the direction of maximum tangential stress (MTS, σ_θ) along an elastic-plastic boundary at a varying distance from the flaw tip(figure Q.2b). The mathematical formulation is shown below.

Using the stress field in equation (2),

$$\sigma_\theta = \frac{1}{2\sqrt{2\pi r}} f_\theta(\theta)$$
$$\sigma_r = \frac{1}{2\sqrt{2\pi r}} f_r(\theta) \qquad (8)$$
$$\tau_{r\theta} = \frac{1}{2\sqrt{2\pi r}} f_{r\theta}(\theta)$$

where

$$f_\theta(\theta) = \left[K_I \cos\frac{\theta}{2}(1+\cos\theta) \right] - \left[3K_{II} \sin\frac{\theta}{2}(1+\cos\theta) \right]$$
$$f_r(\theta) = \left[K_I \cos\frac{\theta}{2}(3-\cos\theta) \right] - \left[K_{II} \sin\frac{\theta}{2}(1-3\cos\theta) \right] \qquad (9)$$
$$f_{r\theta}(\theta) = \left[K_I \sin\frac{\theta}{2}(1+\cos\theta) \right] - \left[K_{II} \cos\frac{\theta}{2}(1-3\cos\theta) \right]$$

The distortional strain energy (T_D) expressed in terms of (9) is given as

$$T_D = \frac{1+\nu}{24\pi E r}\left(f_r^2 + f_\theta^2 - f_r\, f_\theta + 3 f_{r\theta}^2 \right) \qquad (10a)$$

The radius r corresponding to the constant distortional strain energy ($T_{D,0}$) along the elastic-plastic boundary is found by rearranging the terms in equation (10a).

$$r = \frac{1+\nu}{24\pi E T_{D,0}}\left(f_r^2 + f_\theta^2 - f_r\, f_\theta + 3 f_{r\theta}^2 \right) \qquad (10b)$$

Substituting equation (10b) into the expression of σ_θ in equation (8) to obtain σ_θ,

$$\sigma_\theta = \sqrt{\frac{3ET_{D,0}}{1+\nu}} \frac{f_\theta}{\sqrt{f_r^2 + f_\theta^2 - f_r f_\theta + 3f_{r\theta}^2}} \tag{11}$$

Applying the MTS-criterion given by equations (3) and (4) to equation (11) and using the expressions of $f_\theta(\theta)$, $f_r(\theta)$ *and* $f_{r\theta}(\theta)$ in equation (9), the value of crack initiation angle (θ) can then be solved from:

$$12\tan^6\frac{\theta}{2} - 24\mu\tan^5\frac{\theta}{2} + \left(3+16\mu^2\right)\tan^4\frac{\theta}{2} - \left[\left(5+4\mu^2\right)\mu\right]\tan^3\frac{\theta}{2} + 3\mu^2\tan^2\frac{\theta}{2} - \frac{\left(7+5\mu^2\right)\mu}{2}\tan\frac{\theta}{2} - \frac{\left(9+5\mu^2\right)}{2} = 0 \tag{12}$$

$$\left[177+49\mu^2\right]\sin\frac{\theta}{2} + \left[1269+621\mu^2\right]\sin\frac{3\theta}{2} - \left[255-425\mu^2\right]\sin\frac{5\theta}{2} + \left[189-147\mu^2\right]\sin\frac{7\theta}{2} - \left[\left(305+49\mu^2\right)\mu\right]\cos\frac{\theta}{2} - \left[\left(423+207\mu^2\right)\mu\right]\cos\frac{3\theta}{2} + \left[\left(595-85\mu^2\right)\mu\right]\cos\frac{5\theta}{2} - \left[\left(315-21\mu^2\right)\mu\right]\cos\frac{7\theta}{2} < 0 \tag{13}$$

(3) Zero Shear Stress-criterion (Maiti & Smith, 1983)

A new crack will initiate from the flaw tip in a direction corresponding to the direction of zero shear stress ($\tau_{r\theta}$) along a constant radius around the flaw tip (figure Q.2b). The mathematical formulation is shown below.

Setting the shear stress in equation (2) to zero.

$$\frac{1}{\sqrt{2\pi r}}\left\{\left[\frac{K_I}{2}\sin\frac{\theta}{2}\left(1+\cos\theta\right)\right]-\left[\frac{K_{II}}{2}\cos\frac{\theta}{2}\left(1-3\cos\theta\right)\right]\right\}=0 \qquad (14)$$

Arranging the terms in (14) gives (15) which can be solved for the crack initiation angle (θ) :

$$\mu\sin\frac{\theta}{2}\cos^2\frac{\theta}{2}-2\cos\frac{\theta}{2}+3\cos^3\frac{\theta}{2}=0 \qquad (15)$$

(4) M-criterion (Kong et al., 1995)

A new crack will initiate from the flaw tip in a direction corresponding to the direction of maximum stress triaxiality (M-criterion) along a constant radius around the flaw tip (figure Q.2a). The mathematical formulation is shown below.

$$\frac{\partial M}{\partial \theta} = 0 \tag{16}$$

$$\frac{\partial^2 M}{\partial \theta^2} < 0 \tag{17}$$

where M (maximum stress triaxiality) is the ratio between the hydrostatic stress (σ_H) and the equivalent stress (σ_{eq}).

$$M = \frac{\sigma_H}{\sigma_{eq}} \tag{18}$$

$$\sigma_H = \frac{\sigma_x + \sigma_y + \sigma_z}{3} = \frac{2(1+\nu)}{3\sqrt{2\pi r}}\left[K_I \cos\frac{\theta}{2} - K_{II} \sin\frac{\theta}{2}\right] \tag{19}$$

$$\sigma_{eq} = \left[\frac{(\sigma_x - \sigma_y)^2 + (\sigma_y - \sigma_z)^2 + (\sigma_z - \sigma_x)^2 + 6\tau_{xy}^2}{2}\right]^{1/2} \tag{20a}$$

$$\sigma_{eq}=\frac{1}{\sqrt{2}\sqrt{2\pi r}}\left\{\left(\frac{3}{2}K_I^2-\frac{9}{2}K_{II}^2\right)\sin^2\theta+\left[2(1-2\nu)^2K_I^2+6K_{II}^2\right]\cos^2\frac{\theta}{2}+8\left(1-\nu+\nu^2\right)K_{II}^2\sin^2\frac{\theta}{2}+K_IK_{II}\left[3\sin 2\theta-2(1-2\nu)^2\sin\theta\right]\right\}^{1/2} \quad (20b)$$

Equations (19) and (20b) are obtained by using the stress field (1).

Substituting equation (18) into the criteria equations (16) and (17) to obtain equations (21) and (22) which can be solved for crack initiation angle (θ) :

$$\tan^4\frac{\theta}{2}-3\mu\tan^3\frac{\theta}{2}-\left(1-2\mu^2\right)\tan^2\frac{\theta}{2}+\frac{1}{2}\left(1-\mu^2\right)\mu\tan\frac{\theta}{2}-\frac{1}{2}\left(1+\mu^2\right)=0 \quad (21)$$

$$\left[2\left(\mu^2+5\right)\right]\sin\frac{\theta}{2}+\left[27\left(\mu^2+1\right)\right]\sin\frac{3\theta}{2}+\left[5\left(5\mu^2-3\right)\right]\sin\frac{5\theta}{2} \quad (22)$$
$$-\left[2\left(\mu^2+5\right)\mu\right]\cos\frac{\theta}{2}-\left[9\left(\mu^2+1\right)\mu\right]\cos\frac{3\theta}{2}-\left[5\left(\mu^2-7\right)\mu\right]\cos\frac{5\theta}{2}<0$$

μ is defined in equation (7).

Plane strain and plane stress conditions lead to the same result under the M-criterion.

Q.3 Energy-Based Criteria

(1) G-criterion (Hussain et al., 1974)

A new crack will initiate from the flaw tip in a direction corresponding to the direction of maximum energy release rate (G-criterion) along a constant radius around the flaw tip (figure Q.2a). The mathematical formulation is shown below.

$$\frac{\partial G}{\partial \theta} = 0 \tag{23}$$

$$\frac{\partial^2 G}{\partial \theta^2} < 0 \tag{24}$$

where

$$G = \frac{1}{E'}\left(K_I^2 + K_{II}^2\right) \tag{25}$$

$E' = E$ for plane stress (25a)

$E' = E/(1-\nu^2)$ for plane strain (25b)

In the above derivation, the new crack is assumed to propagate in a direction coplanar with the pre-existing flaw, which is true in mode I compression/tension when the flaw is oriented at 90^o to the loading direction. To account for a new crack initiating under mixed–mode loading conditions when the flaw is oriented inclined to the loading direction, another form of energy release rate, $G(\theta)$ is derived.

$$G(\theta) = \frac{1}{E'}\left(K_I^2(\theta) + K_{II}^2(\theta)\right) \tag{26}$$

where

$$K_I(\theta) = \left(\frac{4}{3+\cos^2\theta}\right)\left(\frac{1-\theta/\pi}{1+\theta/\pi}\right)^{\theta/2\pi}\left(K_I\cos\theta + \frac{3}{2}K_{II}\sin\theta\right) \quad (27)$$

$$K_{II}(\theta) = \left(\frac{4}{3+\cos^2\theta}\right)\left(\frac{1-\theta/\pi}{1+\theta/\pi}\right)^{\theta/2\pi}\left(-\frac{1}{2}K_I\sin\theta + K_{II}\cos\theta\right) \quad (28)$$

Substituting the expressions of $K_I(\theta)$ and $K_{II}(\theta)$ contained in equations (27) and (28) into equation (26) gives,

$$G(\theta) = \frac{4}{E'}\left(\frac{1}{3+\cos^2\theta}\right)^2\left(\frac{1-\theta/\pi}{1+\theta/\pi}\right)^{\theta/\pi}\left[\left(1+3\cos^2\theta\right)K_I^2 + 8\cos\theta\sin\theta K_I K_{II} + \left(9-5\cos^2\theta\right)K_{II}^2\right] \quad (29)$$

Substituting equation (29) into the criteria equations (23) and (24) can then lead to equations from which the crack initiation angle (θ) can be solved.

(2) S-criterion (Sih, 1973, 1974)

A new crack will initiate from the flaw tip in a direction corresponding to the minimum strain energy density (S-criterion) along a constant radius around the flaw tip (figure Q.2a). The mathematical formulation is shown below.

$$\frac{\partial S}{\partial \theta} = 0 \tag{30}$$

$$\frac{\partial^2 S}{\partial \theta^2} > 0 \tag{31}$$

where S is the strain energy density factor

$$S = r\frac{dW}{dV} \tag{32}$$

where r is a finite distance from the point of failure initiation. The strain energy stored in the element $dV = dxdy$ under a general two-dimensional stress system is

$$dW = \left[\frac{1}{2E}\left(\sigma_x^2 + \sigma_y^2\right) - \frac{\nu}{E}\sigma_{xy} + \frac{1}{2\mu}\tau_{xy}^2\right]dV \tag{32a}$$

Substituting the stress field equations contained in (1) into equation (32), the strain energy density function can be rewritten as

$$\frac{dW}{dV} = \frac{1}{r}\left(a_{11}K_I^2 + 2a_{12}K_I K_{II} + a_{22}K_{II}^2\right) + \ldots \tag{32b}$$

The higher order terms in r have been neglected and the strain energy density function near the flaw possesses a *1/r* energy singularity. The strain energy density factor S is thus expressed as

$$S = a_{11}K_I^2 + 2a_{12}K_I K_{II} + a_{22}K_{II}^2 \tag{33}$$

where

$$a_{11} = \frac{1}{16G\pi}\left[(1+\cos\theta)(\kappa-\cos\theta)\right] \tag{33a}$$

$$a_{12} = \frac{1}{16G\pi}\sin\theta\left[2\cos\theta-(\kappa-1)\right] \tag{33b}$$

$$a_{22} = \frac{1}{16G\pi}\left[(\kappa+1)(1-\cos\theta)+(1+\cos\theta)(3\cos\theta-1)\right] \tag{33c}$$

$$\kappa = \frac{3-\nu}{3+\nu} \text{ for plane stress} \tag{33d}$$

$$\kappa = 3-4\nu \text{ for plan strain} \tag{33e}$$

Substituting equation (33) into the criteria equations (30) and (31), equations (34) and (35) are obtained from which θ can be solved:

$$\left[2(1+\kappa)\mu\right]\tan^4\frac{\theta}{2}+\left[2\kappa(1-\mu^2)-2\mu^2+10\right]\tan^3\frac{\theta}{2}-24\mu\tan^2\frac{\theta}{2}$$
$$+\left[2\kappa(1-\mu^2)+6\mu^2-14\right]\tan\frac{\theta}{2}+2(3-\kappa)\mu=0 \tag{34}$$

$$\left[2(\kappa-1)\mu\right]\sin\theta-8\mu\sin2\theta+\left[(\kappa-1)(1-\mu^2)\right]\cos\theta+\left[2(\mu^2-3)\right]\cos2\theta>0 \tag{35}$$

where μ is defined in equation (7).

(3) T-criterion (Theocaris et al., 1982a, b, c)

A new crack will initiate from the flaw tip in a direction corresponding to the maximum dilatational strain energy (T-criterion) along the contour of constant distortional strain energy, which leads to a variable radius for core region (figure Q.2a). The mathematical formulation is shown below.

$$\frac{\partial T_v}{\partial \theta} = 0 \tag{36}$$

$$\frac{\partial^2 T_v}{\partial \theta^2} < 0 \tag{37}$$

Dilatational strain energy (T_v) and distortional strain energy (T_D) are given by the following expressions.

$$T_v = \frac{1-2\nu}{6E}\left(\sigma_x + \sigma_y\right)^2 \tag{38}$$

$$T_D = \frac{1+\nu}{3E}\left(\sigma_x^2 + \sigma_y^2 - \sigma_x\sigma_y + 3\tau_{xy}^2\right) \tag{39}$$

The stress field equations expressed in (1) are rewritten as:

$$\begin{aligned} \sigma_x &= \frac{1}{\sqrt{2\pi r}} f_x(\theta) \\ \sigma_y &= \frac{1}{\sqrt{2\pi r}} f_y(\theta) \\ \sigma_{xy} &= \frac{1}{\sqrt{2\pi r}} f_{xy}(\theta) \end{aligned} \tag{40}$$

where

$$\begin{aligned} f_x(\theta) &= \left[K_I \cos\frac{\theta}{2}\left(1 - \sin\frac{\theta}{2}\sin\frac{3\theta}{2}\right)\right] - \left[K_{II} \sin\frac{\theta}{2}\left(2 + \cos\frac{\theta}{2}\cos\frac{3\theta}{2}\right)\right] \\ f_y(\theta) &= \left[K_I \cos\frac{\theta}{2}\left(1 + \sin\frac{\theta}{2}\sin\frac{3\theta}{2}\right)\right] + \left[K_{II} \sin\frac{\theta}{2}\cos\frac{\theta}{2}\cos\frac{3\theta}{2}\right] \\ f_{xy}(\theta) &= \left[K_I \cos\frac{\theta}{2}\sin\frac{\theta}{2}\cos\frac{3\theta}{2}\right] + \left[K_{II} \cos\frac{\theta}{2}\left(1 - \sin\frac{\theta}{2}\sin\frac{3\theta}{2}\right)\right] \end{aligned} \tag{41}$$

The dilatational strain energy (T_v) and distortional strain energy (T_D) originally given in equations (38) and (39) can be rewritten as:

$$T_v = \frac{1-2\nu}{12\pi E r}\left(f_x + f_y\right)^2 \tag{42}$$

$$T_D = \frac{1+\nu}{6\pi E r}\left(f_x^2 + f_y^2 - f_x\, f_y + 3 f_{xy}^2\right) \tag{43}$$

The radius r corresponding to the constant distortional strain energy ($T_{D,0}$) along the elastic-plastic boundary is found by rearranging the terms in equation (43).

$$r = \frac{1+\nu}{6\pi E T_{D,0}}\left(f_x^2 + f_y^2 - f_x\, f_y + 3 f_{xy}^2\right) \tag{44}$$

The variation of dilatational strain energy (T_v) along the contour of constant distortional strain energy (T_D) is given by substituting equation (44) back to equation (38):

$$T_v = \frac{1-2\nu T_{D,0}}{2(1+\nu)} \frac{\left(f_x + f_y\right)^2}{\left(f_x^2 + f_y^2 - f_x\, f_y + 3 f_{xy}^2\right)} \tag{45}$$

Substituting equation (45) into the criteria equations (36) and (37), equations (46) and (47) are obtained from which θ can be solved

$$\tan^5\frac{\theta}{2} - 4\mu\tan^4\frac{\theta}{2} + \left(5\mu^2 - 1\right)\tan^3\frac{\theta}{2} + \frac{\left(3-5\mu^2\right)}{2}\tan^2\frac{\theta}{2} + \frac{\left(\mu^4 - 2\mu^2 - 1\right)}{2}\tan\frac{\theta}{2} + \frac{\left(1+\mu^2\right)\mu}{2} = 0 \tag{46}$$

$$\left(1-20\mu^2-5\mu^4\right)\cos\theta + 8\left(3+2\mu^2-\mu^4\right)\cos 2\theta - 3\left(3-12\mu^2+\mu^4\right)\cos 3\theta$$
$$+2\left(13+5\mu^2\right)\mu\sin\theta + 32\left(1+\mu^2\right)\mu\sin 2\theta - 6\left(5-3\mu^2\right)\mu\sin 3\theta < 0 \tag{47}$$

where μ is defined in equation (7).

(4) I_p -criterion (Ukadgaonker & Awasare, 1995)

A new crack will initiate from the flaw tip in a direction corresponding to the maximum value of I_p, which is a function of the first invariant and the second invariant (see definition of I_p below) along the elastic-plastic boundary defined by von Mises (figure Q.2a). The mathematical formulation is shown below.

$$\frac{\partial I_p}{\partial \theta} = 0 \tag{48}$$

$$\frac{\partial^2 I_p}{\partial \theta^2} < 0 \tag{49}$$

where I_p is defined below as a function of the first invariant (I_1) and second invariant (I_2):

$$I_p = \left(I_1^2 - 2I_2\right) \tag{50}$$

$$I_1 = \sigma_x + \sigma_y \tag{51}$$

$$I_2 = \sigma_x \sigma_y - \tau_{xy}{}^2 \tag{52}$$

Cartesian stress field equations contained in (1) are substituted into equation (50), which is subsequently substituted into criteria equations (48) and (49). θ can then be solved from them.

Along the elastic-plastic boundary of the core region, the dilatational strain energy (T_v) reaches a maximum (see equation 45) when I_p reaches a maximum also. Therefore, maximizing I_p is equivalent to maximizing T_v. I_p -criterion is thus another equivalent expression of the T-criterion (Khan & Khraisheh, 2000).

(5) *J* contour integral (Rice, 1968)

Using the *J* contour integral to characterize the fracture behavior for nonlinear materials has become a common practice nowadays and there have been many reviews about its principle and applications (e.g. Anderson, 2005). A path-independent contour integral, which was called *J*, is computed to be equal to the energy release rate in a nonlinear elastic body that contains a crack (figure Q.3), i.e.

$$J = -\frac{d\Pi}{dA} \tag{53}$$

where Π is the potential energy and A is the crack area. The potential energy is given by

$$\Pi = U - F \tag{54}$$

where U is the strain energy stored in the body and *F* is the work done by external forces.

Consider an arbitrary counterclockwise path (Γ) around a flaw tip as shown in figure Q.3. The J integral is given by the following expression:

$$J = \int_{\Gamma}\left(w dy - T_i \frac{\partial u_i}{\partial x} ds \right) \tag{55}$$

where

w = strain energy density

T_i = components of the traction vector

u_i = displacement vector components

ds = length increment along the contour Γ.

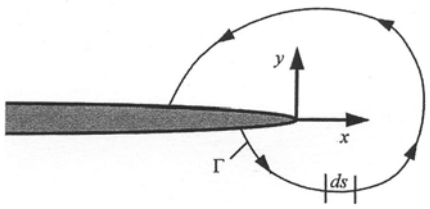

Figure Q.3 – Arbitrary contour around a flaw tip.

The strain energy density w is defined as

$$w = \int_0^{\varepsilon_{ij}} \sigma_{ij} d\varepsilon_{ij} \tag{56}$$

where σ_{ij} and ε_{ij} are the stress and strain tensors, respectively. The traction T is a stress vector at a given point on the contour and its components are given by:

$$T_i = \sigma_{ij} n_j \tag{57}$$

where n_j are the components of the unit vector normal to Γ.

Q.4 References

Anderson, T.L. (2005) *Fracture Mechanics: Fundamentals and Applications*, Edition 3, CRC Press, Boca Raton, FL.

Erdogan, F. and Sih, G.C. (1963) on the crack extension in plates under plane loading and transverse shear. *Journal of Basic Engineering*, 85, pp.305-321.

Hussain, M.A., Pu, S.L. and Underwood, J. (1974) Strain energy release rate for a crack under combined mode I and mode II. *Fract Anal ASTM STP* 560, pp. 2–28.

Khan, S.M.A. and Khraisheh, M.K. (2000) Analysis of mixed mode crack initiation angles under various loading conditions. *Engineering Fracture Mechanics*, 67, pp. 397-419.

Khan, S.M.A. and Khraisheh, M.K. (2004) A new criterion for mixed mode fracture initiation based on the crack tip plastic core region. *International Journal of Plasticity*, 20, pp.55-84.

Kong, X.M., Schluter, N. and Dahl, W. (1995) Effect of triaxial stress on mixed-mode fracture. *Engineering Fracture Mechanics*, 52(2), pp. 379–388.

Maiti, S.K. and Smith, R.A. (1983) Comparison of the criteria for mixed mode brittle fracture based on the preinstability stress–strain field, Part I: Slit and elliptical cracks under uniaxial tensile loading. *International Journal of Fracture*, 23, pp. 281–295.

Qian, J. and Fatemi, A. (1996) Mixed mode fatigue crack growth: a literature survey. *Engineering Fracture Mechanics*, 55(6), pp. 969-990.

Rice, J.R. (1968) a path independent integral and the approximate analysis of strain concentration by notches and cracks, *Journal of Applied Mechanics*, 35, pp. 379-386.

Sih, G.C. (1973) Some basic problems in fracture mechanics and new concepts. *Engineering Fracture Mechanics*, 5, pp. 365–377.

Sih, G.C. (1974) Strain-energy-density factor applied to mixed mode crack problems. *International Journal of Fracture*, 10(3), pp. 305-321.

Theocaris, P.S. and Andrianopoulos, N.P. (1982a) The Mises elastic–plastic boundary as the core region in fracture criteria. *Engineering Fracture Mechanics*, 16(3), pp. 425–432.

Theocaris, P.S., Kardomateas, G.A. and Andrianopoulos, N.P. (1982b) Experimental study of the *T*-criterion in ductile fracture. *Engineering Fracture Mechanics*, 17**(**5), pp. 439–447.

Theocaris, P.S. and Andrianopoulos, N.P. (1982c) The *T*-criterion applied to ductile fracture. *Internal Journal of Fracture* 20, pp. R125–R130.

Ukadgaonker, V.G. and Awasare, P.J. (1995) A new criterion for fracture initiation. *Engineering Fracture Mechanics*, 51(2), pp. 265–274.

Williams., J.G. (1984) *Fracture Mechanics of Polymers*, Wiley, New York.

APPENDIX R – Stress Field around a Rounded Flaw Tip

R.1 Introduction

Most of the fracture mechanics literature deals with flaws with sharp tips under different loading conditions, and new cracks are usually assumed to initiate from the flaw tips. In the present experimental study, pre-existing open flaws with a finite aperture and rounded tips were tested. Under uniaxial compression test, although most of the new cracks were found to initiate from the flaw tips, cracks initiating from different localities around the perimeter of the flaws were also observed. It thus appears that the conventional treatment based on the consideration of sharp flaw tips is not totally applicable. In the literature, three types can be classified according to their flaw tip sharpness (figure R.1).

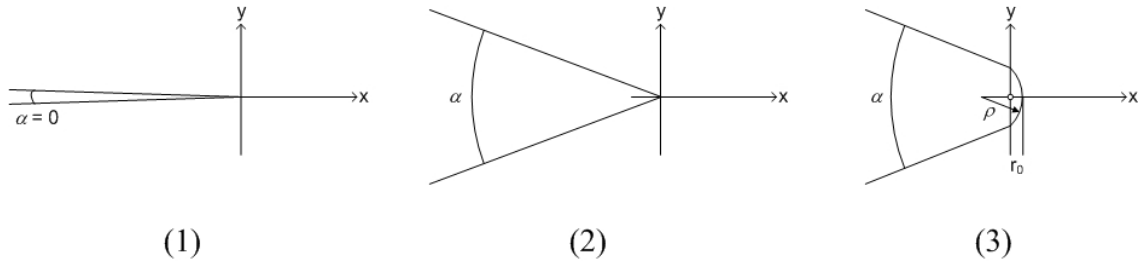

Figure R.1 – Three main type of flaws (1) line crack with an exaggerated scale on α which is equal to 0, (2) infinite sharp V-notch, (3) rounded V-notch.

The present review, which briefly surveys the relevant literature on the mathematical treatment of the third flaw type as shown in figure R.1, identifies that there are two common approaches to deal with this subject. The first approach, which is based on the pioneering work of Inglis (1913) and Griffith (1924), models open flaws as elliptical flaws (Hoek, 1968, Jaeger & Cook, 1969, Lajtai, 1970). It is the ratio between the flaw aperture and the flaw length which determines the stress distribution along the perimeter of the flaw and hence the overall behavior of the flaws. In the second approach, the sharpness of the flaw tip is characterized by the root radius ρ of the flaw tip, based on

which the stress field ahead of flaw tips and the associated notch stress intensity factors (N-SIFs) (Creager & Paris, 1967, Atzori et al., 1999) are computed.

R.2 First approach - Griffith's stress theory

R.2.1 Fundamentals

As discussed in chapter 2, Griffith (1920) first proposed an energy balance concept to account for the relationship between the strength and the flaw size in glass specimens under tension. In predicting crack growth from a flaw under a biaxial remote stress, he later also proposed a stress approach (Griffith, 1924). Griffith's work was based on the solution of Inglis (1913) for an elliptical cavity in an elastic material. Fracture occurs when the most vulnerably oriented flaw in a population of randomly oriented flaws begins to extend under the applied stress. The original formulation by Griffith relating the stress around the boundary of the elliptical flaw was expressed in elliptical coordinates. An excerpt of the original Griffith (1924) paper is reproduced below. Further details are given in subsequent discussion.

Using INGLIS's results, therefore, we form the expression for the stress at all points of the elliptic edge of a small crack in a large plate, to whose outer edges are applied principal tractions Q and P, respectively making angles θ and $\frac{\pi}{2} - \theta$ with the major axis of the crack. These principal stresses may be resolved into two direct stresses and a shear stress, applied in directions parallel and perpendicular to the direction θ, whence the complete stress system may be found by addition of the appropriate solutions given by INGLIS. Using INGLIS's notation, we find that the required stress is:

$$R_{\beta\beta} = \frac{(P+Q)\sinh 2\alpha_0 + (P-Q)(e^{2\alpha_0}\cos 2\beta - 1)\cos 2\theta + (P-Q)e^{2\alpha_0}\sin 2\beta \sin 2\theta}{\cosh 2\alpha_0 - \cos 2\beta}$$

wherein α_0 is the parameter of the ellipse corresponding with the edge of the crack, so that α_0 is nearly equal to zero. β is the coordinate specifying the positions of points on the ellipse. The direction of $R_{\beta\beta}$ is parallel to the edge of the crack. Since we are interested only in tensile stresses, let us postulate that tensile stresses are positive and that P is algebraically greater than Q. An explanatory diagram is given in fig. 2 (for $R_{\alpha\alpha}$ read: $R_{\beta\beta}$).

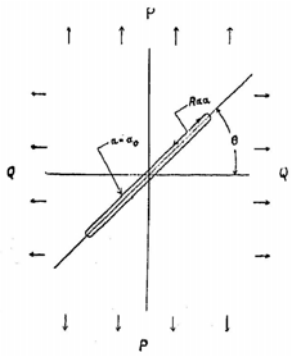

Fig. 2

In the above excerpt, $R_{\beta\beta}$ is the stress computed around the boundary of the elliptical open flaw. As being further explained and illustrated by Hoek (1968) and Paterson (1978), the maximum tensile stress component (σ_b) around an arbitrarily oriented open elliptical flaw with respect to the applied stress is first computed based on the elastic

stress analysis (figure R.2). The critical flaw orientation is then computed for which the maximum local tensile stress is the greatest. Crack initiation is assumed to take place when the maximum local tensile stress at any point around the flaw reaches the critical value necessary to overcome the interatomic cohesion of the material.

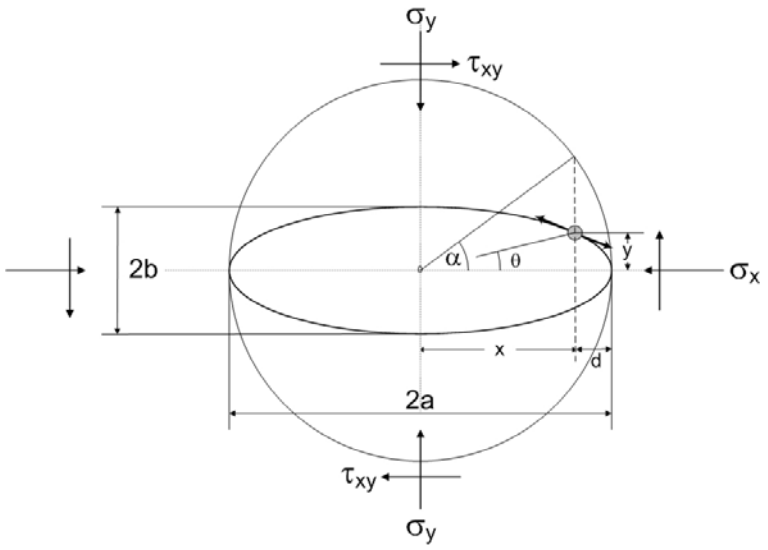

Equation of ellipse:
x = a cos α ; y = b sin α
where α is the eccentric angle

Relationship between θ and α:
tan θ = m tan α
where m = b/a

Figure R.2 – Stresses acting on a two-dimensional elliptical opening (Hoek, 1968).

The original Griffith's formulation is reworked below in Cartesian coordinates based on the work of Hoek (1968). Consider an open flaw which is approximated by an open ellipse as shown in figure R.2. The flaw is oriented at an inclination angle β with σ_3 and subjected to a far-field stress (σ_1 & σ_3), with the resultant stress components of σ_x, σ_y and τ_{xy} acting on the flaw (figure R.2). The tangential stress (σ_b) on the boundary of the elliptical flaw is given by the following equation (Hoek, 1968).

$$\sigma_b = \frac{\sigma_y\left[m(m+2)\cos^2\alpha - \sin^2\alpha\right] + \sigma_x\left[(1+2m)\sin^2\alpha - m^2\cos^2\alpha\right] - \tau_{xy}\left[2(1+m^2)\sin\alpha\cos\alpha\right]}{m^2\cos^2\alpha + \sin^2\alpha} \qquad \text{(R1)}$$

where α is the eccentric angle which defines the position of a point on the boundary of the ellipse (figure R.2) and *m* is the aspect ratio between the minor axis and major axis of the ellipse, i.e. $m = b/a$.

Some of the subsequent mathematical treatments which were skipped by Hoek (1968) are elaborated here. Rewrite equation (R1) as

$$\sigma_b = \frac{\sigma_y A_1 + \sigma_x A_2 - \tau_{xy} A_3}{A_4} \tag{R2}$$

where

$$\begin{aligned} A_1 &= m(m+2)\cos^2\alpha - \sin^2\alpha \\ A_2 &= (1+2m)\sin^2\alpha - m^2\cos^2\alpha \\ A_3 &= 2(1+m^2)\sin\alpha\cos\alpha \\ A_4 &= m^2\cos^2\alpha + \sin^2\alpha \end{aligned} \tag{R2a}$$

Differentiate equation (R2) with respect to α to obtain $\partial\sigma_b / \partial\alpha$ as

$$\frac{\partial\sigma_b}{\partial\alpha} = \frac{\sigma_y\left(A_4A_1' - A_1A_4'\right) + \sigma_x\left(A_4A_2' - A_2A_4'\right) - \tau_{xy}\left(A_4A_3' - A_1A_3'\right)}{\left(A_4\right)^2} \tag{R3}$$

where A_i' represents $\partial A_i / \partial\alpha$ for i = 1 to 4 and

$$\begin{aligned} A_1' &= -2\sin\alpha\cos\alpha(m+1)^2 \\ A_2' &= 4\sin\alpha\cos\alpha(m+1) \\ A_3' &= 2\cos 2\alpha(1+m^2) \\ A_4' &= 2\sin\alpha\cos\alpha(1-m^2) \end{aligned} \tag{R3a}$$

The following key assumption is then invoked for the subsequent computation (Hoek, 1968) – the stress component σ_x has a negligible effect on stress concentration ($\sigma_x = 0$).

A new crack will initiate at a position at the boundary of the flaw (not necessarily at the flaw tip), at which the tensile stress is maximum ($\sigma_{b\text{-}max}$) and this maximum reaches a critical value ($\sigma_{b\text{-}critical}$). Mathematically, $\sigma_{b\text{-}max}$ is obtained from solving (R4a) and (R4b).

$$\frac{\partial \sigma_b}{\partial \alpha} = 0 \qquad \text{(R4a)}$$

$$\frac{\partial^2 \sigma_b}{\partial \alpha^2} < 0 \qquad \text{(R4b)}$$

After $\sigma_{b\text{-}max}$ is solved, the eccentric angle α corresponding to where the maximum local tensile stress occurs, can also be solved from equation (R1). Note that in the above derivation, which simply expands the formula originally given by Griffith (1924) as shown in the excerpt reproduced earlier, the aspect ratio between the minor axis and major axis of the ellipse ($m = b/a$) is retained. In the discussion below, all the equations extended from the original Griffith's stress formulation are collectively called **Griffith's Stress Theory**. In contrast, in the formulation given by Inglis (1913) as shown in equation (2.3) in chapter 2, an approximation was made (a term was dropped) based on the assumption that the *major* flaw axis is much longer than the *minor* flaw axis. In addition, the ratio of the two flaw axis is alternatively expressed in terms of the *major* flaw axis and the radius of curvature at flaw tip[1]. To facilitate the discussion below, the assumption and treatment by Inglis are collectively called **Inglis's assumption**.

Besides, note that the original Griffith's stress theory considered open flaws with no contact during the whole course of loading. McClintock and Walsh (1962) later incorporated friction between the between the two faces of the pre-existing flaw in a theory which has then been commonly referred to as the Modified Griffith Theory.

[1] The stress at the tip of a flaw subjected to an applied stress perpendicular to the major axis is given by $\sigma_A = \sigma\left(1 + 2a/b\right) = \sigma\left(1 + 2\sqrt{a/\rho}\right)$ (equations 2.1 & 2.2), where ρ is the radius of curvature and is equal to b^2/a. Approximation to equation (2.2) is made by dropping the term "1" before the square-root term for a sharp flaw in which the flaw major axis is much longer than its minor axis, i.e. $a >> b$, and hence leads to $\sigma_A = 2\sigma\sqrt{a/\rho}$ (equation 2.3)

R.2.2 Some illustrations of Griffith's stress theory

General

In the present experimental study, 0.5" (12.7 mm) long flaws of two different aperture sizes were studied (0.004 inch for narrow flaw and 0.05 inch for wide flaw). These flaws have straight parallel faces and cylindrical flaw tips at the two ends. By approximating them as elliptical openings as shown in figure R.2 for the flaws, the engineering behavior of the flaws could then be assessed based on the mathematical formulations presented in the previous section.

The value of σ_b around the flaw perimeter is computed for a number of flaw inclination angles ($\beta = 0^o$, 15^o, 30^o, 45^o, 60^o, 75^o) according to the Griffith's stress theory as outlined in the previous section. Both flaw types have a flaw length of 0.5". The aspect ratio *m* of the two flaw types are thus 0.008 (narrow flaw) and 0.1 (wide flaw) respectively. Note that the applied σ_1 is vertical and σ_3 is horizontal. Also, the flaw is oriented at an inclination angle β with σ_3. Compression is taken to be positive and tension is taken to be negative.

In figure R.3a specifically for flaw inclination angle $\beta = 60^o$, the variation of σ_b around the flaw perimeter, normalized by the applied uniaxial stress σ_1 ($\sigma_1 > 0$, σ_2, $\sigma_3 = 0$), is plotted against the eccentric angle α (compressive stress is positive; tensile stress is negative). Refer to figure R.2 for the definition of α. Notice that $\alpha = 0^o$ and 180^o correspond to two flaw tip positions. Figure R.3a shows that close to the tip regions, local stress around the flaw perimeter is greatly amplified. The effect is more pronounced for the narrow flaw (amplification of -31.4 times) than for the wide flaw (amplification of -2.7 times). Besides, the minimum (most negative) occurs closer to the flaw tip for the narrow flaw ($\alpha = 0.8^o$) than for the wide flaw ($\alpha = 10.3^o$), but both of them are not right at the flaw tips. Figure R.3a is re-plotted in figure R.3b which better reveals the stress distribution for the lower range of eccentric angle (α).

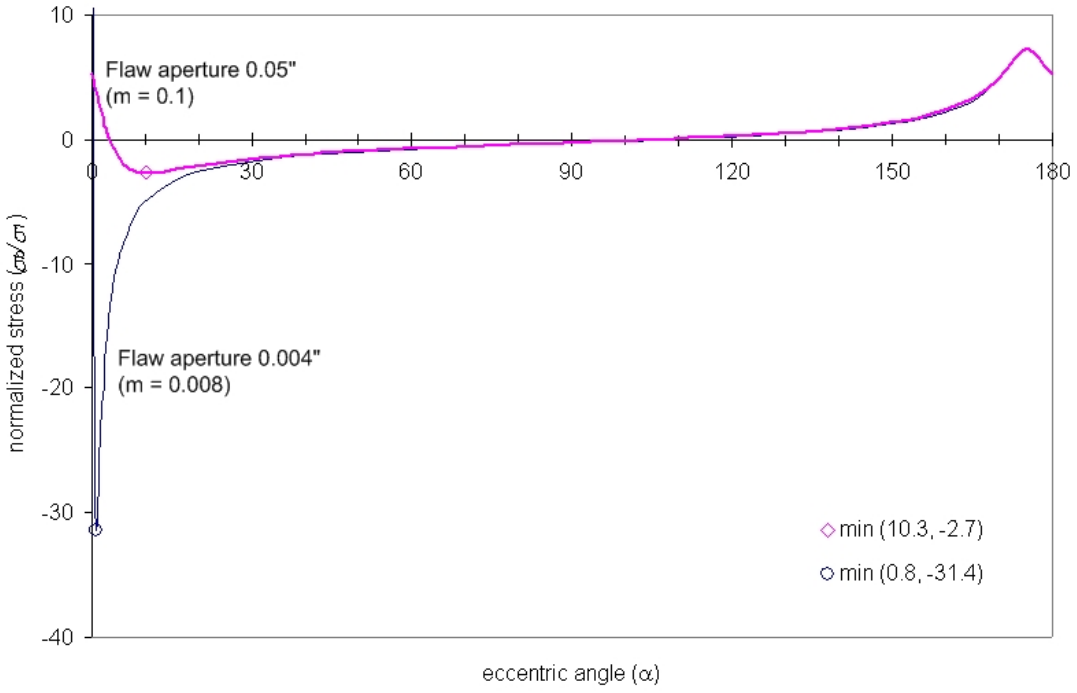

Figure R.3a – Variation of normalized stress with the eccentric angle of flaws oriented at 60° flaw inclination angle.

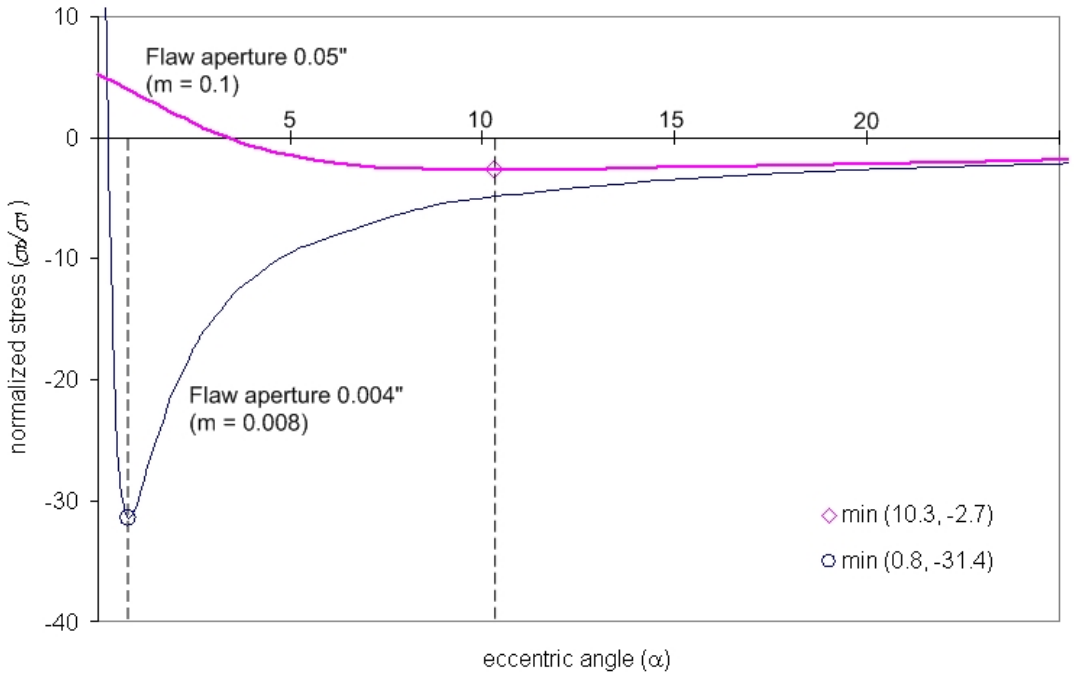

Figure R.3b – Variation of normalized stress with the eccentric angle of flaws oriented at 60° flaw inclination angle (only small range of eccentric angle is shown).

Another interesting feature revealed from figures R.3a and R.3b is the presence of an extensional zone (σ_b/σ_1 <0) and a compressional zone (σ_b/σ_1 >0) around the flaw perimeter. The size of these zones varies with the aspect ratio *m*. For the flaw inclination angle β = 60°, the distribution (in terms of the eccentric angle α, which is defined in figure R.2) of these two zones are summarized in the following table and schematically represented in figure R.4.

	Compression zone	**Extension zone**	**Compression zone**
m = 0.1 (wide flaw)	0 – 3.4°	3.4° – 105.7° (*10.3°*)	105.7° – 180°
m = 0.008 (narrow flaw)	0 – 0.3°	0.3° – 106.1° (*0.8°*)	106.1° – 180°

The angle in parentheses in the column of extension zone indicates where the minimum (most negative) σ_b/σ_1 occurs.

Table R.1 – Extent of compression and extension zones in terms of eccentric angle α along half of the flaw perimeter for β = 60°.

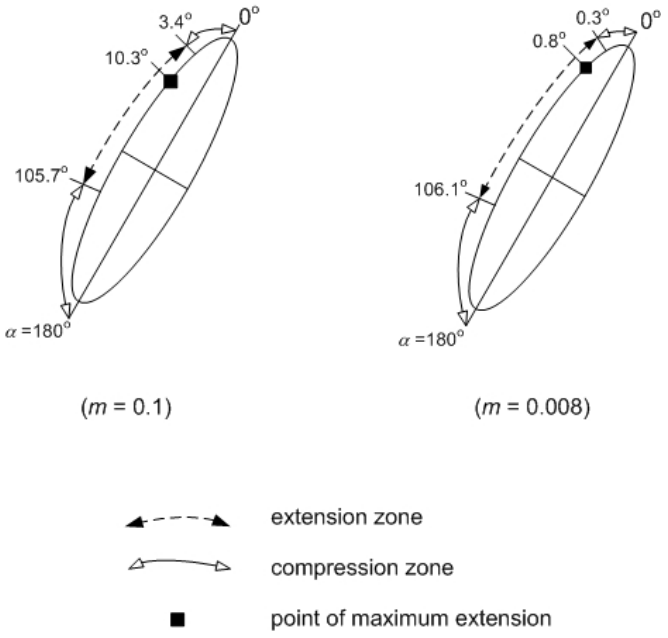

Figure R.4 – Schematic representation of extension and compression zones of wide and narrow flaws inclined at 60°. Note that these sketches are not of the right scale. The upper half of each ellipse is analogous to its lower half, where details are not shown.

The preceding discussion is for a flaw inclined at $\beta = 60^o$. In figures R.5a & b and R.6a & b below, the variation of the normalized stress with the eccentric angle α for a number of flaw inclination angles ($\beta = 0^o$ to 75^o with 15^o increments) are plotted for narrow flaws and wide flaws respectively. The small angle and large angle ranges for narrow flaws are shown in figures R.5a-b. However, only selected β values of 0^o, 30^o, 60^o are plotted for the whole range in figure R.5c for the purpose of clarity. The lines corresponding to m = 0.008 and m = 0.1 for $\beta = 60^o$ previously shown in figures R.3a and R.3b are included in figures R.5a – c and R.6a & b respectively for completeness. Note the symmetry for the plots for $\beta = 0^o$ in both figures R.5c (narrow flaw) and R.6a (wide flaw).

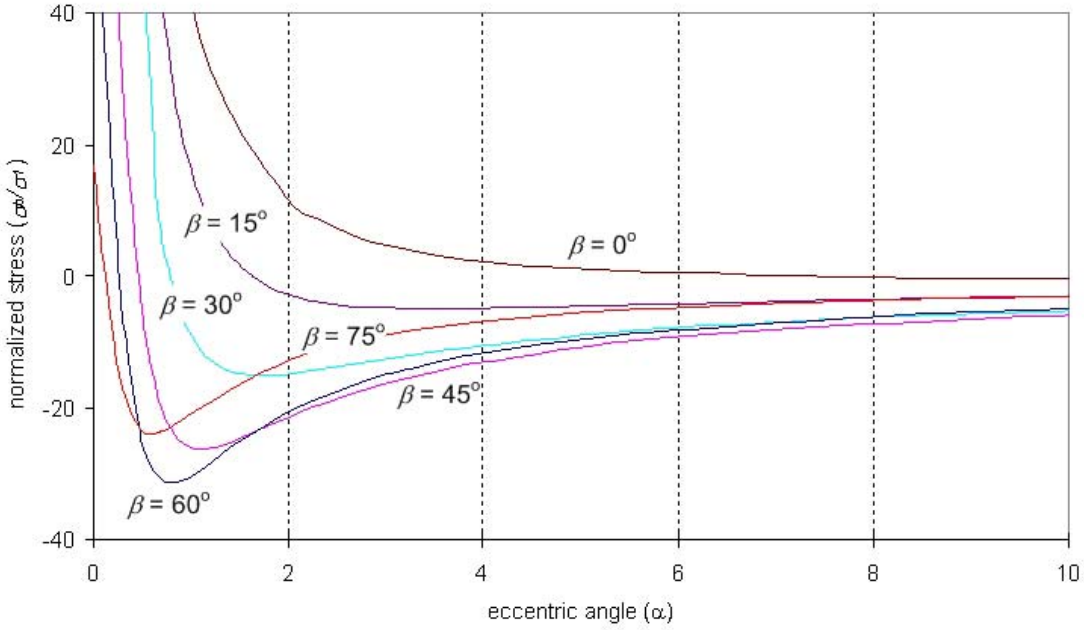

Figure R.5a – Variation of normalized stress against eccentric angle (small angle range) for different flaw inclination angles of small flaw aperture size 0.004".

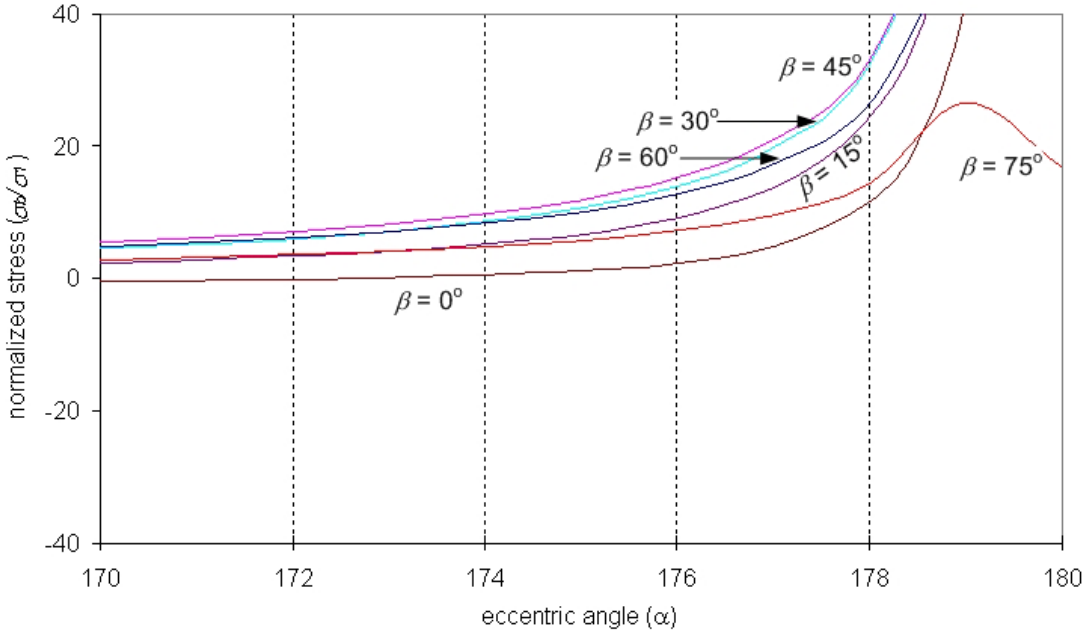

Figure R.5b – Variation of normalized stress against eccentric angle (large angle range) for different flaw inclination angles of small flaw aperture size 0.004".

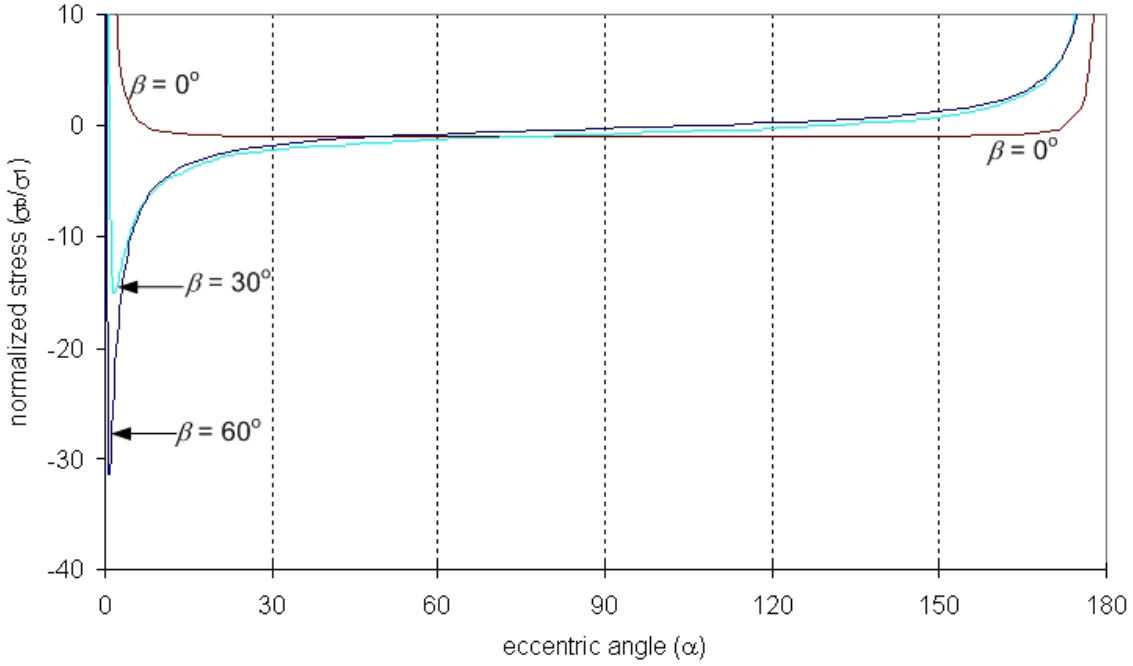

Figure R.5c – Variation of normalized stress against eccentric angle (whole angle range) for different selected flaw inclination angles (0^o, 30^o, 60^o) of small flaw aperture size 0.004".

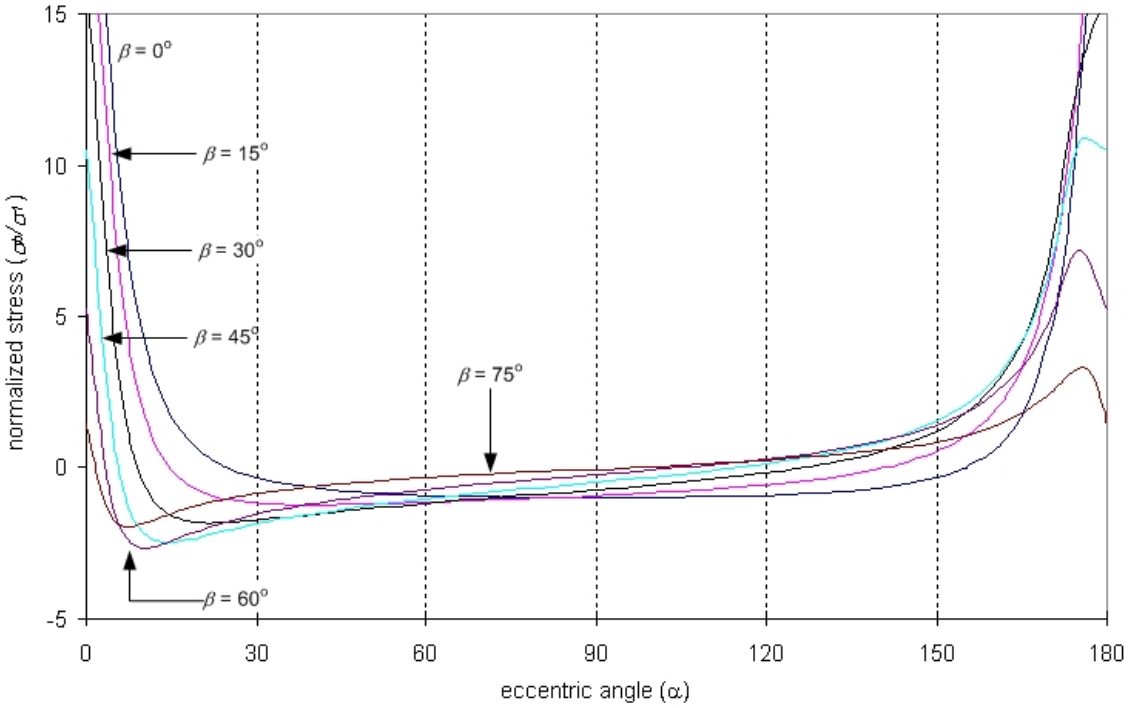

Figure R.6a – Variation of normalized stress against eccentric angle for different flaw inclination angles of large flaw aperture size 0.05".

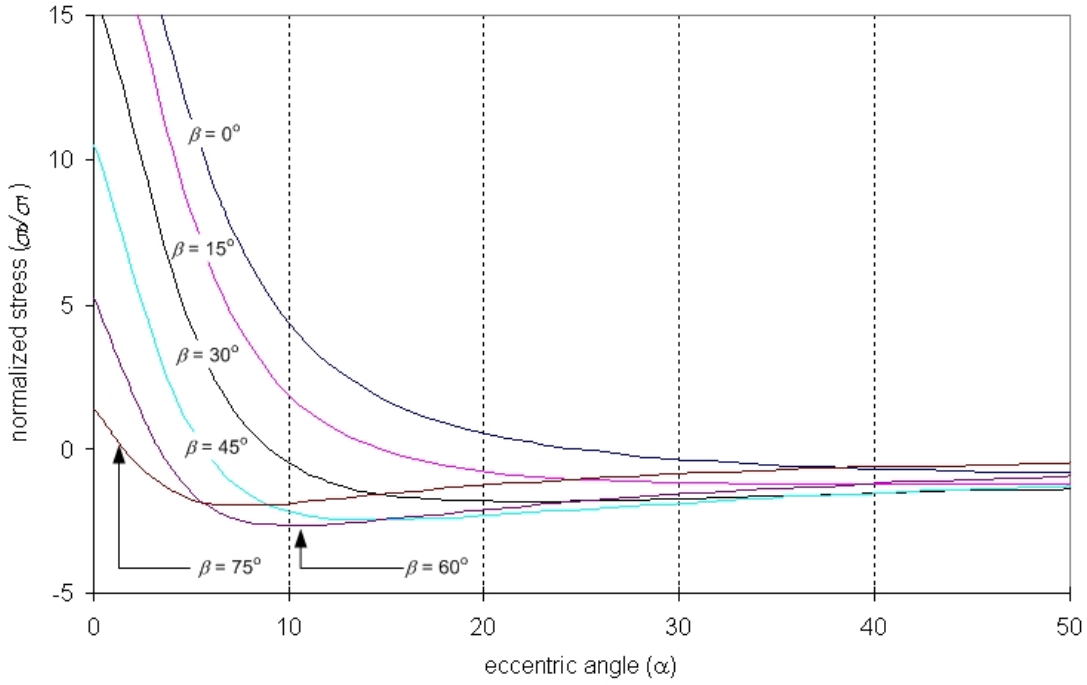

Figure R.6b – Variation of normalized stress against eccentric angle (small angle range) for different flaw inclination angles of large flaw aperture size 0.05".

Narrow Flaw (0.004" flaw aperture, $m = 0.008$)

From the small angle range plot (figure R.5a), minimum stresses are more pronounced for large flaw inclination angles ($\beta = 30^o, 45^o, 60^o, 75^o$) than for small inclination angles ($\beta = 0^o, 15^o$). In addition, the stress gradient around the point of minimum stresses is greater for the large flaw inclination angles than for the small flaw inclination angles.

It is also observed in figure R.5a that as the flaw inclination angle incrementally increases from 0^o to 60^o, the magnitude of the minimum normalized stress also increases. However, as it increases from 60^o to 75^o, the magnitude decreases. These results are also summarized in table R.2.

	m = 0.008		**m = 0.1**	
Flaw inclination angle β (^{o})	α	σ_b/σ_1	α	σ_b/σ_1
0	90.0	-1.00	90.0	-1.00
15	3.5	-5.02	39.5	-1.24
30	1.7	-15.15	21.9	-1.84
45	1.1	-26.17	14.4	-2.47
60	0.8	-31.35	10.3	-2.67
75	0.6	-23.96	7.6	-1.96

Table R.2 – Values of eccentric angles (α) corresponding to the minimum σ_b/σ_1 (most negative) for a number of narrow flaws ($m = 0.008$) and wide flaws ($m = 0.1$) with different flaw inclination angles.

Wide Flaw (0.05" flaw aperture, $m = 0.1$)

The magnitude of the minimum normalized stress for the wide flaw (figures R.6a & R.6b) is less than that for the narrow flaw (figure R.5a). Also see table R.2 for the normalized stress values and the α values at which these minimum values occur. Besides, the figures also show that the stress gradient (magnitude of slope gradient) around the minimum

normalized stress point for a specific flaw inclination for wide flaws is always lower than that for narrow flaws (figures R.5a & R.6b).

The trend suggested in table R.2 is better revealed when the minimum normalized stress (σ_b / σ_1) is plotted against the flaw inclination angle (figure R.7a). Due to the relatively flat shape of the line for wide flaws (m = 0.1), it is replotted in figure R.7b with a different scale. A critical value of flaw inclination $\beta = 59.4^o$ and $\beta = 56.9^o$ are obtained respectively for narrow flaws and wide flaws (figure R.7a). Assuming a specimen contain a population of randomly oriented flaws (either narrow or wide) with equivalent dimensions and there is no mutual influence among them, fracture will first occur from flaws oriented at the critical inclinations ($\beta = 59.4^o$ for narrow flaws and $\beta = 56.9^o$ for wide flaws) according to the above predictions.

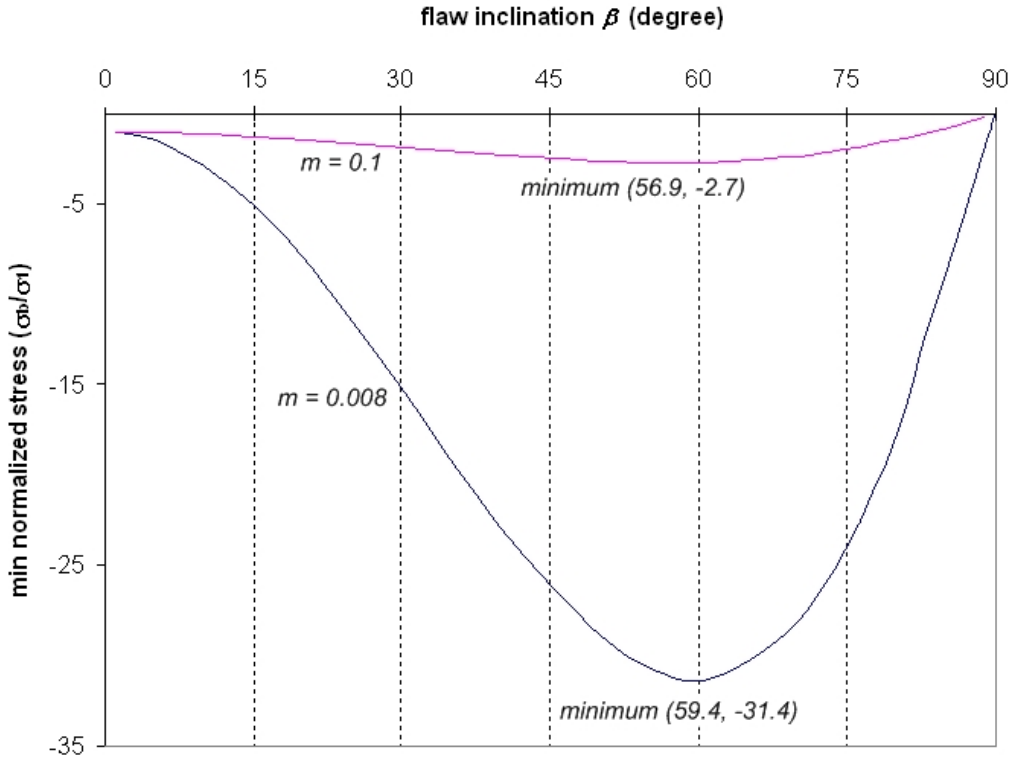

Figure R.7a – Variation of minimum normalized stress with the flaw inclination angle for flaw aperture 0.004" (m = 0.008) and flaw aperture 0.05" (m = 0.1).

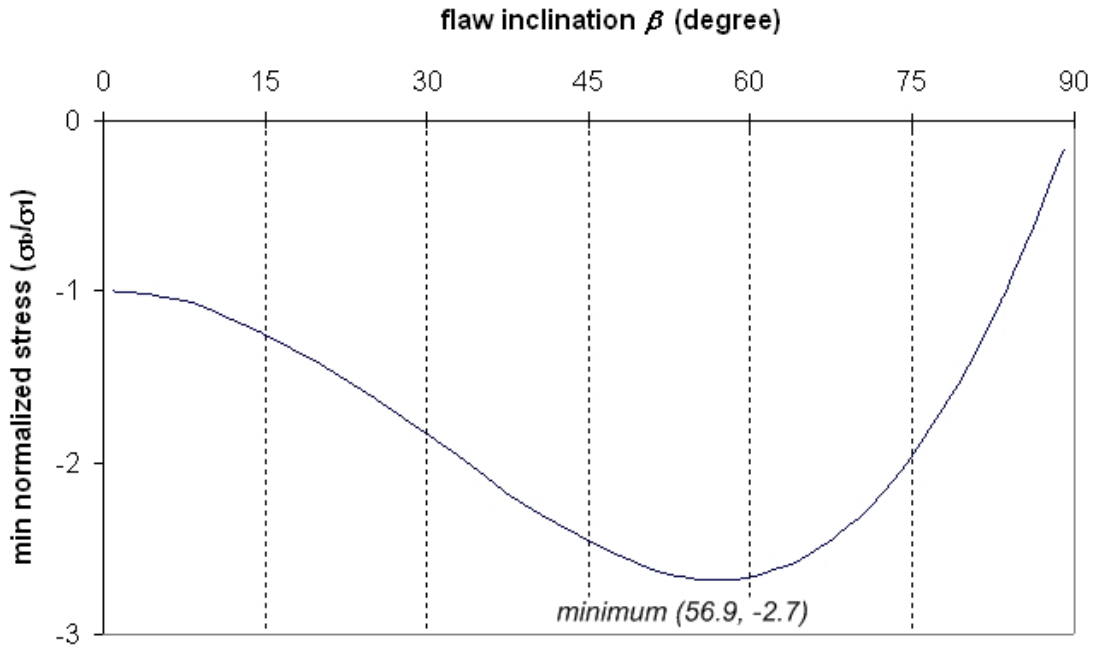

Figure R.7b – Variation of minimum normalized stress with the flaw inclination angle only for flaw aperture 0.05" (m = 0.1).

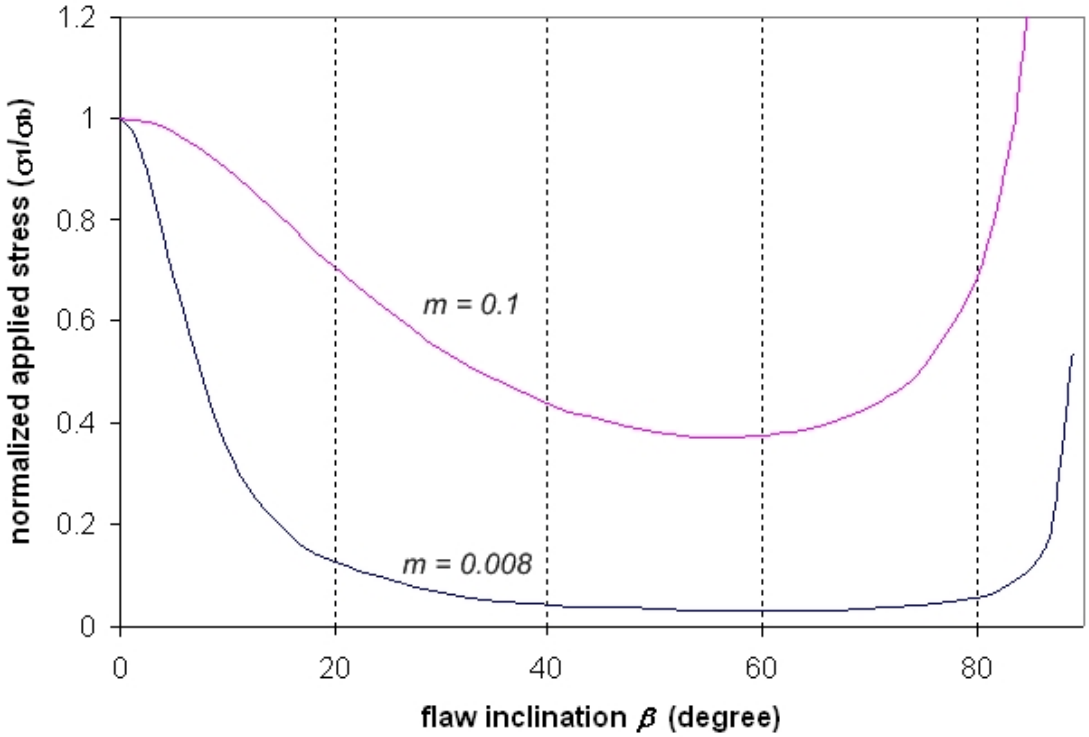

Figure R.8 – Change of applied stress (normalized) required for new crack formation with flaw inclination angle β based on theoretical prediction.

A very negative normalized stress (σ_b / σ_1) implies that a new crack will initiate at a very low applied stress (σ_1). Figure R.7a is replotted with (σ_1 / σ_b) as the vertical axis (figure R.8). When σ_b reaches a critical value, a crack then initiates from the flaw perimeter. Assuming that critical σ_b value is constant for flaws of varying inclination angles, the (σ_1 / σ_b) ratio thus indicates the relative magnitude of applied σ_1 required for crack initiation. Recall that σ_b is the tangential stress on the boundary of the elliptical flaw.

For both narrow and wide flaws, the stress required for the initiation of new cracks is lower in the mid-flaw inclination angle range, and it becomes higher in the low- and high-flaw inclination ranges. Another important conclusion drawn from the theoretical prediction is that except for horizontal flaws (flaw inclination angle $\beta = 0^o$), the stress required for the initiation of new cracks in wide flaws is *higher* than that in narrow flaws, i.e. wide flaws have a higher strength against crack opening than narrow flaws at the same inclination angle. Recall that in the derivation earlier in this appendix, the approximation was not made to assume that the flaw major axis is much longer than its minor axis in a way similar to that by Inglis (1913) as shown in chapter 2. The flaw shape, which is characterized by the flaw aspect ratio *m* is retained throughout the derivation. It is neither the absolute flaw length nor the absolute flaw aperture being assessed in the above discussion.

To sum up, the derivation and discussion above predicts that narrow flaws should have a *lower* crack initiation stress than wide flaws. In addition, the most critical flaw inclination angles are $\beta = 59.4^o$ for narrow flaws and $\beta = 56.9^o$ for wide flaws. Experimental data obtained in the present experimental study however show a completely different behavior in both the stress variation trend and the relative strength against new crack initiation. As illustrated in figure R.9, the applied stress (σ_1) required for crack initiation generally increases with flaw inclination for both narrow and wide flaws, which are different from the trends shown in figure R.8. Although σ_1 is plotted in figure R.9 but σ_1 / σ_b is plotted in figure R.8, logical comparison can still be made if the assumption of constant critical σ_b value for flaw with varying inclination angles holds. Another

difference is that the stress required for the initiation of new cracks in wide flaws is *lower* than that in narrow flaws. It may be related to the validity of assuming an elliptical shape for straight flaws. The differences between the predictions and the experimental results are further discussed in the next section.

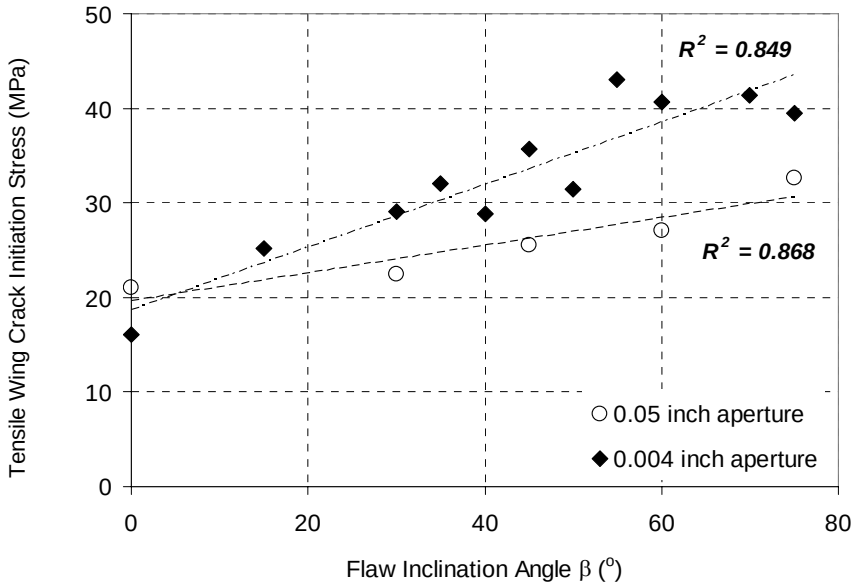

Figure R.9 – Experimental applied σ_1 corresponding to the tensile wing crack initiation (tensile wing crack initiation stress) generally increases with the flaw inclination angle β.

Distance of point of initiation from flaw tips

The mathematics about the computation of the distance (d as shown in figure R.2) between the point of new crack initiation and the flaw tip was skipped by Hoek (1968) in his original work and is again reworked below. Referring to figure R.2 again,

$$\frac{y}{x} = \frac{b}{a}\tan\alpha \qquad \text{(R5)}$$

The equation of ellipse is given by

$$\frac{x^2}{a^2} + \frac{y^2}{b^2} = 1 \qquad \text{(R6)}$$

Substituting equation (R5) to equation (R6) to solve for x (positive value only),

$$x = a\cos\alpha \tag{R7}$$

The distance d is hence given by

$$d = a(1-\cos\alpha) \tag{R8}$$

Equation (R8) is plotted in figure R.10 for a small flaw inclination angle range (β = 0-30^o) and in figure R.11 for a larger range (β = 0-75^o) respectively. The distance d decreases monotonically with flaw inclination (β) and the decrease is more rapid for the narrow flaw (m = 0.008) than for the wide flaw (m = 0.1).

The experimental data obtained in the present study, which are also plotted along with the theoretical predictions in figure R.11, show that as the flaw inclination angle β increases, the distance d between the point of new crack initiation and the flaw tip decreases. This agrees with the theoretical prediction. However, the experimental values are generally higher than the predicted values. Besides, the data of narrow and wide flaws are very close to each other, as opposed to the substantial difference according to the theoretical prediction.

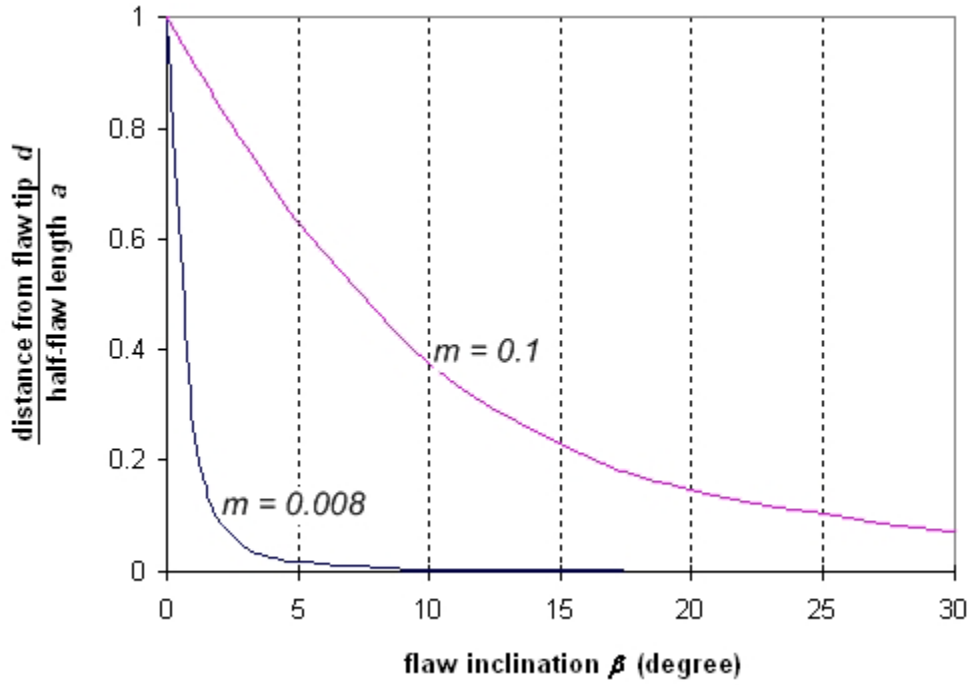

Figure R.10 – Decrease of distance (d) normalized by the half flaw length between the point of new crack initiation and flaw tip with flaw inclination angle (β).

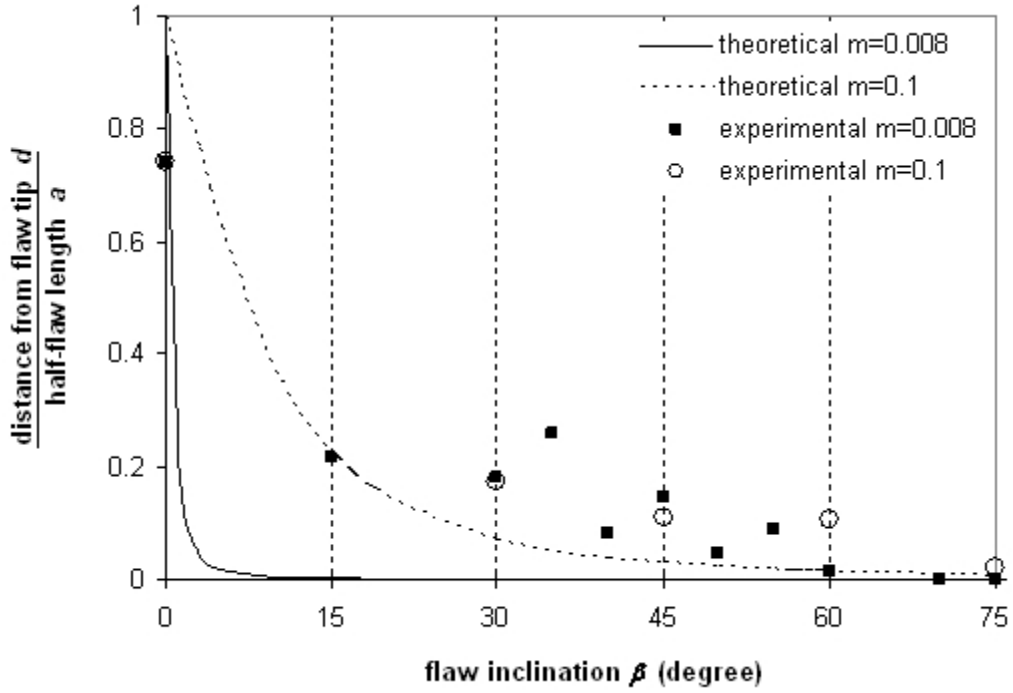

Figure R.11 – Distances (d) (mean values) normalized by the half flaw length between the point of tensile wing crack initiation and flaw tip obtained from experiments plotted along with theoretical predictions.

R.2.3 Discussion of the Griffith's stress theory

As shown in the previous sections on the **Griffith's Stress Theory** (also equation R1) regarding flaws of rounded flaw tips without invoking the **Inglis' assumption**, it is the flaw aspect ratio (*m* value), but neither the absolute flaw length only nor flaw aperture only which determines the crack initiation stress. Both the magnitude of the flaw length and the radius of curvature of flaw tip have to be taken into account. Flaws of the same shape, irrespective of their size, will have the same crack initiation stress according to the derivation. In addition, flaws of a lower *m* value (narrower/sharper flaws) will require a lower crack initiation stress (figure R.8).

In most applications in fracture mechanics, flaws are usually long and sharp. In other words, the major flaw axis *a* is much longer than the minor flaw axis *b*. The ratio of the two flaw axes is alternatively expressed as $a/b = \sqrt{a/\rho}$ where ρ is the radius of curvature and is equal to b^2/a. Since in most applications, ρ is considered more or less constant for **sharp flaws**, it is the flaw length that plays a key role in controlling the crack initiation stress. Therefore, it is very common to state that *longer* flaws have a lower crack initiation stress than a *shorter* flaw.

On the other hand, if the flaws are relatively short with rounded flaw tips, it appears inappropriate to simply assume a constant value of ρ (radius of curvature). The above issue regarding the significance of rounded flaw tips with major flaw axis and minor flaw axis of a comparable order of magnitude can be assessed further under the following three scenarios (figure R.12).

1) Flaws with the same aperture, but with different lengths (longer flaws have lower *m* values).
2) Flaws with the same length, but with different flaw aperture sizes (narrow flaws have lower *m* values).
3) Flaws with different lengths and aperture sizes, but with the same *m* value.

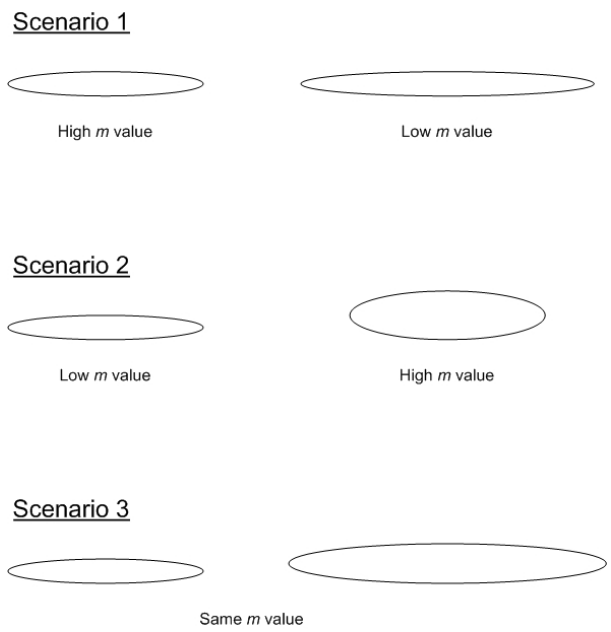

Figure R.12 – Comparison of elliptical flaws under three different three scenarios.

Scenarios 1 and 2 were investigated by Lajtai (1971) experimentally. Regarding scenario 1, flaws of *various lengths* and *constant aperture size* corresponding to *m* values of 0.001, 0.015, 0.02 and 0.04 were tested. His results showed that lower *m* value (sharper flaws) led to lower crack initiation stress, which was in accordance with the Griffith's stress theory (figure 10 of Lajtai, 1971).

Regarding scenario 2, flaws (with inclination angle $\beta = 60^{o}$) of the *same length*, but of *different flaw aperture sizes*, corresponding to *m* ranging between 0.02 and 0.16 were tested. The results showed that lower *m* value (sharper flaws) led to higher crack initiation stress, which is in contrary to that implied by the Griffith's stress theory (figure 11 of Lajtai, 1971). Results similar to that of Lajtai (1971) were also obtained in the present experimental study (figure R.9).

To the author's knowledge, no experimental results exactly corresponding to scenario 3 are available in the literature. However, the tests performed on the cylindrical voids by Lajtai (1971) can offer a good reference. Similar to those tests performed on specimens containing elliptical flaws, the stress corresponding to the first crack initiated from a

cylindrical void was recorded. His results showed that as the void size increased (shape remains the same), the crack initiation stress decreased. This suggested that the absolute size of the pre-existing elliptical flaws may have an influence on the crack initiation stress.

Apart from the above size effect, it is worthwhile to note that the modulus E and Poisson ratio ν of the material do not enter the formulations as shown in equations (R1 to R4).

R.3 Second approach - stress intensity factors (SIFs)

As noted in the introduction, flaw tips can be broadly classified into three main types (figure R.13) - line crack ($\rho = 0$, $\alpha = 0$), infinite sharp V-notch ($\rho = 0$, $\alpha \neq 0$) and rounded V-notch ($\rho \neq 0$, $\alpha \neq 0$). ρ is the notch radius which defines the curvature of the flaw tip and α is the notch angle which defines the angular relationship between the upper and lower flaw faces. The stress distribution and stress intensity factors (SIFs) around the rounded V-notch are described below.

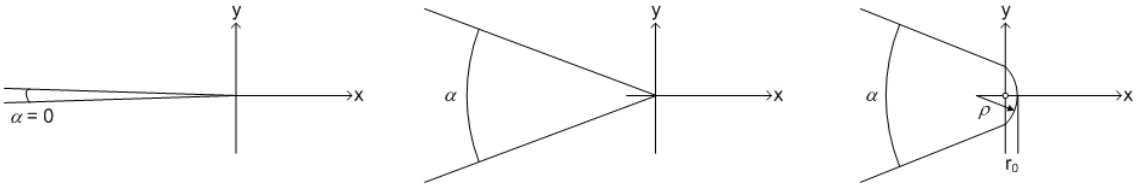

Figure R.13 – Three main type of flaws (1) line crack with an exaggerated scale on α which is equal to 0, (2) infinite sharp V-notch, (3) rounded V-notch.

One significant feature of rounded V-notches is the absence of stress singularity at the flaw tip. In the finite element studies conducted by Pluvinage (1998) in a three point bend specimen containing a rounded V-notch as shown in figure R.14, a maximum stress

($\sigma_{yy\text{-}max}$) occurs at the flaw tip, where stress singularity is absent. The stress σ_{yy}(r) then decreases away from the flaw tip. Note that in figure R.15, the stress σ_{yy}(r) is normalized by the net stress applied at the top of the specimen (σ_N). The distance *r* measured from the flaw tip is normalized by the ligament size *B* as marked in figure R.14. He also concluded that as the notch radius (ρ) increases, the stress σ_{yy}(r) ahead of the flaw tip decreases.

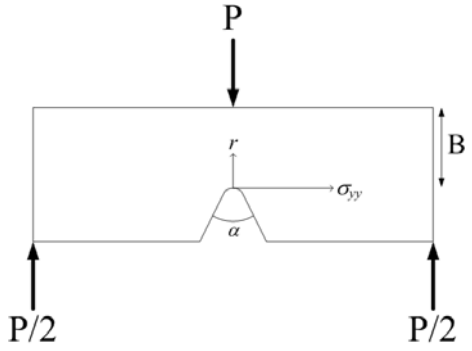

Figure R.14 – Three point bend specimen (after Pluvinage, 1998).

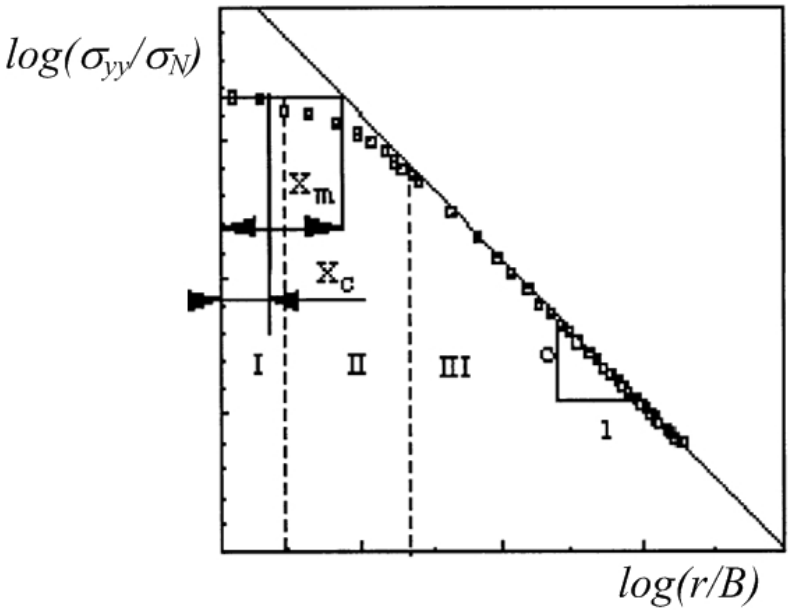

Figure R15 – Schematic illustration (no scale given) of stress distribution (σ_{yy}/σ_N) ahead of a rounded V-notch with normalized distance *r/B* in a three point bend specimen for a particular notch radius. σ_N, which is proportional to the applied load *P*, is the net stress applied at the top of the specimen. Refer to figure R.14 for the testing configuration *r* and *B* (after Pluvinage, 1998).

Figure R.15 illustrates a common stress distribution behavior ahead of a rounded V-notch, from which three stress zones are identified:

1) Zone I– almost constant stress just in front of the flaw tip.
2) Zone II – intermediate between zone I and zone III.
3) Zone III – following a straight line which can be expressed as a power function of the non-dimensional distance:

$$\frac{\sigma_{yy}}{\sigma_N} = C'\left(\frac{r}{B}\right)^{-\beta(\rho)} \qquad \text{(R5)}$$

where *C'* is a constant and $\beta(\rho)$ is another constant function of the notch radius.

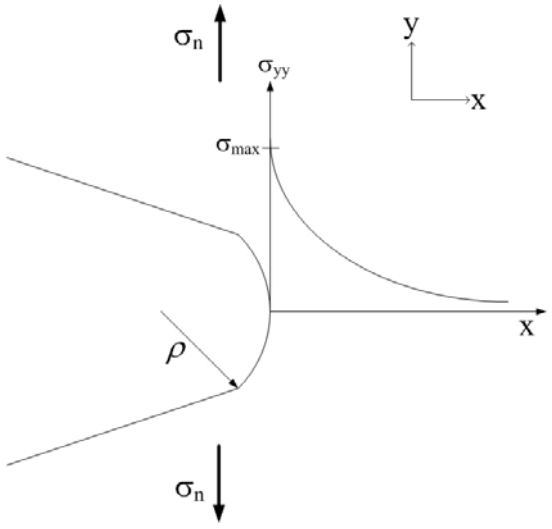

Figure R16 – Schematic representation of the variation of stress σ_{yy} ahead of a rounded V-notch, which is subjected to an applied nominal stress. The stress distribution curve is for illustrative purposes only.

Pluvinage (1998) surveyed the literature about the stress variation with distance along the long axis of the flaw in front of a rounded V-notch tip (Table R.3). σ_{max} is the maximum stress at the flaw tip and σ_n is the applied nominal stress. Refer to figure R.16 for the orientation of *x* and *y* axes.

Authors	Elastic Stress Distribution	Equations
Neuber and Weiss (1962)	$\sigma_{yy} = \sigma_{\max}\sqrt{\dfrac{\rho}{\rho + 4x}}$	(R6)
Chen and Pan (1978)	$\sigma_{yy} = \sigma_{\max}\sqrt{\dfrac{\rho}{\rho + 8x}}$	(R7)
Kujawski (1991)	$\sigma_{yy} = f\,\sigma_{\max}\left[\left(1+\dfrac{2x}{\rho}\right)^{-\frac{1}{2}} + \left(1+\dfrac{2x}{\rho}\right)^{-\frac{3}{2}}\right]$ where $f = 1$ $\quad for \quad \dfrac{x}{\rho} < 0.2$ $f = 1 + \dfrac{\tan\left(\pi/2K_{V,\rho}\right)}{2.8}\left(\dfrac{x}{\rho} - 0.2\right) \quad for \quad \dfrac{x}{\rho} \geq 0.2$	(R8)
Usami (1985)	$\sigma_{yy} = \dfrac{\sigma_{\max}}{3}\left[1 + \dfrac{1}{2}\left(1+\dfrac{x}{\rho}\right)^{-2} + \dfrac{3}{2}\left(1+\dfrac{x}{\rho}\right)^{-4}\right]$	(R9)
Timoshenko and Goodier (1951)	$\sigma_{yy} = \sigma_n\left[1 + \dfrac{1}{2}\left(1+\dfrac{x}{\rho}\right)^{-2} + \dfrac{3}{2}\left(1+\dfrac{x}{\rho}\right)^{-4}\right]$	(R10)
Bhattacharya and Kumar (1995)	$\sigma_1 = \sigma_n K_{V,\rho}\sqrt{\dfrac{\rho}{\rho + 4x}} \quad and \quad 0 \leq x \leq \dfrac{\rho}{4}\left(K_{V,\rho}^2 - 1\right)$	(R11)
Glinka and Newport (1987)	$\sigma_{yy} = \sigma_{\max}\left[1 - 0.235\left(\dfrac{x}{\rho}\right)^{0.5} - 1.33\left(\dfrac{x}{\rho}\right) + 1.28\left(\dfrac{x}{\rho}\right)^{1.5} - 0.037\left(\dfrac{x}{\rho}\right)^{2}\right]$	(R12)

Table R.3 – Stress distribution ahead of a rounded V-notch flaw tip. Refer to figure R.16 for meaning of σ_{yy} and σ_n.

Comparing the expressions by Usami (1985) and Timoshenko and Goodier (1951) in table R.3 (equations R9 & R10) reveals that σ_{max} is three times the magnitude of σ_n. In those equations which contain σ_{max} but not σ_n, the magnitude of σ_{max} relative to the applied stresses has to be computed from some other relations (not shown here).

The stress field ahead of a flaw is commonly expressed in terms of the stress intensity factor. As noted by Pluvinage (1998) also, its definition varies among the three flaw types shown previously in figure R.13. The stress intensity factors associated with mode I loading are illustrated below.

For a line flaw (figure R.13(1)), the stress intensity factor K_I is expressed as

$$K_I = \lim_{r \to 0} \sqrt{2\pi r}\ \sigma_{yy} \tag{R13a}$$

For an infinitely sharp V-notch (figure R.13(2)), the notch stress intensity factor (NSIF) K_I* is expressed as

$$K_I^{\ *} = \lim_{r \to 0} \left(2\pi r\right)^{\psi(\alpha)}\ \sigma_{yy} \tag{R13b}$$

where $\psi(\alpha)$ is a parameter depending on the notch angle α. For a rounded V-notch (figure R.13(3)), the notch stress intensity factor (NSIF) $K^{V,\rho}$ for a blunt notch of radius ρ and notch angle α is expressed as

$$K^{V,\rho} = \left(2\pi r\right)^{\beta(\alpha,\rho)}\ \sigma_{yy} \tag{R13c}$$

where $\beta(\alpha, \rho)$ is a parameter depending on the notch radius (ρ defined in figure R16) and notch angle (α). For an arbitrarily-inclined flaw, the equations shown in table R.3 are inadequate to completely describe the stress field around the flaw. The pioneering work on the complete analytical stress field solution around a rounded flaw tip was provided by Creager (1966). Assuming a very slender elliptical flaw of a small root radius $\rho'/a \approx (b/a)^2 << 1$, Creager and Paris (1967) computed the stresses around rounded flaw tips (figure R.17), with a breakdown into Mode I and Mode II contributions. The main difference of the following equations from those of a sharp flaw tip is the presence of an additional term proportional to ρ' and inversely proportional to the radial distance r from

the focal point. The stresses associated with Mode I and Mode II loading are given below.

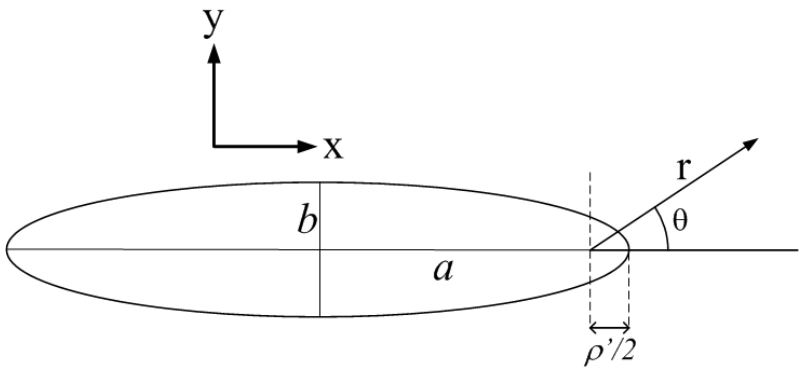

Figure R.17 – Coordinate system for computation of stress field around rounded flaw tip (after Creager & Paris, 1967). ρ' is defined as twice the distance from the nearby flaw tip to the focal point of the ellipse, while ρ shown in figure R.13 corresponds to the notch radius of the flaw.

Mode I (the stresses are denoted by an overhead single bar)

$$\bar{\sigma}_x = \frac{K_I}{\sqrt{2\pi r}}\left[\cos\frac{\theta}{2}\left(1-\sin\frac{\theta}{2}\sin\frac{3\theta}{2}\right)-\frac{\rho'}{2r}\cos\frac{3\theta}{2}\right]$$

$$\bar{\sigma}_y = \frac{K_I}{\sqrt{2\pi r}}\left[\cos\frac{\theta}{2}\left(1+\sin\frac{\theta}{2}\sin\frac{3\theta}{2}\right)+\frac{\rho'}{2r}\cos\frac{3\theta}{2}\right] \qquad \text{(R14)}$$

$$\bar{\tau}_{xy} = \frac{K_I}{\sqrt{2\pi r}}\left[\cos\frac{\theta}{2}\sin\frac{\theta}{2}\cos\frac{3\theta}{2}-\frac{\rho'}{2r}\sin\frac{3\theta}{2}\right]$$

Mode II (the stresses are denoted by an overhead double bar)

$$\bar{\bar{\sigma}}_x = \frac{K_{II}}{\sqrt{2\pi r}}\left[-\sin\frac{\theta}{2}\left(2+\cos\frac{\theta}{2}\cos\frac{3\theta}{2}\right)+\frac{\rho'}{2r}\sin\frac{3\theta}{2}\right]$$

$$\bar{\bar{\sigma}}_y = \frac{K_{II}}{\sqrt{2\pi r}}\left[\sin\frac{\theta}{2}\cos\frac{\theta}{2}\cos\frac{3\theta}{2}-\frac{\rho'}{2r}\sin\frac{3\theta}{2}\right] \qquad \text{(R15)}$$

$$\bar{\bar{\tau}}_{xy} = \frac{K_{II}}{\sqrt{2\pi r}}\left[\cos\frac{\theta}{2}\left(1-\sin\frac{\theta}{2}\sin\frac{3\theta}{2}\right)-\frac{\rho'}{2r}\cos\frac{3\theta}{2}\right]$$

Since the time when the above stress field equations were presented, several more studies have been undertaken to determine the stress field around notches of various geometries. A concise summary of the development is provided by (Atzori et al., 1999). One of such analytical formulations which consider the influence of varying notch radii (ρ) is as follows (Lazzarin & Tovo, 1996, Atzori et al., 1997).

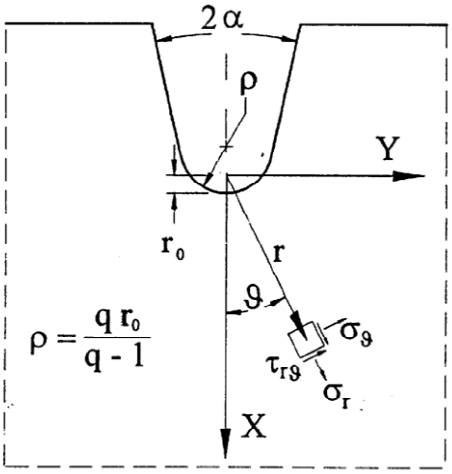

Figure R.18– Coordinate system and symbols used for the stress field components around a notch. Note that the notch angle is denoted as 2α, instead of α as shown in figure R.13.

Mode I (figure R.18)

$$\begin{Bmatrix}\sigma_\theta\\ \sigma_r\\ \tau_{r\theta}\end{Bmatrix}_{\rho\neq 0} = \begin{Bmatrix}\sigma_\theta\\ \sigma_r\\ \tau_{r\theta}\end{Bmatrix}_{\rho=0} + \frac{1}{\sqrt{2\pi}}\frac{K_I}{r_0^{1-\lambda_1}}\left(\frac{r}{r_0}\right)^{\mu_1-1}\left[\frac{(3-\lambda_1)-\chi_1(1-\lambda_1)}{(1+\lambda_1)+\chi_1(1-\lambda_1)}\right]\begin{Bmatrix}\cos(1+\mu_1)\theta\\ -\cos(1+\mu_1)\theta\\ \sin(1+\mu_1)\theta\end{Bmatrix} \qquad \text{(R16)}$$

Mode II (figure R.18)

$$\begin{Bmatrix}\sigma_\theta\\ \sigma_r\\ \tau_{r\theta}\end{Bmatrix}_{\rho\neq 0} = \begin{Bmatrix}\sigma_\theta\\ \sigma_r\\ \tau_{r\theta}\end{Bmatrix}_{\rho=0} + \frac{1}{\sqrt{2\pi}}\frac{K_{II}}{r_0^{1-\lambda_2}}\left(\frac{r}{r_0}\right)^{\mu_2-1}\begin{Bmatrix}\sin(1+\mu_2)\theta\\ -\sin(1+\mu_2)\theta\\ -\cos(1+\mu_2)\theta\end{Bmatrix} \qquad \text{(R17)}$$

where μ_i is a real number which depends on the crack opening angle 2α (see table R.4) and

Mode I

$$\begin{Bmatrix}\sigma_\theta\\ \sigma_r\\ \tau_{r\theta}\end{Bmatrix}_{\rho=0} = \frac{1}{\sqrt{2\pi}}\frac{r^{\lambda_1-1}K_I}{(1+\lambda_1)+\chi_1(1-\lambda_1)}\left[\begin{Bmatrix}(1+\lambda_1)\cos(1-\lambda_1)\theta\\ (3-\lambda_1)\cos(1-\lambda_1)\theta\\ (1-\lambda_1)\sin(1-\lambda_1)\theta\end{Bmatrix}+\chi_1(1-\lambda_1)\begin{Bmatrix}\cos(1+\lambda_1)\theta\\ -\cos(1+\lambda_1)\theta\\ \sin(1+\lambda_1)\theta\end{Bmatrix}\right] \quad \text{(R18)}$$

Mode II

$$\begin{Bmatrix}\sigma_\theta\\ \sigma_r\\ \tau_{r\theta}\end{Bmatrix}_{\rho=0} = \frac{1}{\sqrt{2\pi}}\frac{r^{\lambda_2-1}K_I}{(1-\lambda_2)+\chi_2(1+\lambda_2)}\left[\begin{Bmatrix}-(1+\lambda_2)\sin(1-\lambda_2)\theta\\ -(3-\lambda_2)\sin(1-\lambda_2)\theta\\ (1-\lambda_2)\cos(1-\lambda_2)\theta\end{Bmatrix}+\chi_2(1+\lambda_2)\begin{Bmatrix}-\sin(1+\lambda_2)\theta\\ \sin(1+\lambda_2)\theta\\ \cos(1+\lambda_2)\theta\end{Bmatrix}\right] \quad \text{(R19)}$$

Refer to table R.4 for the values of some constants and exponents required by the above equations.

2α (rad/π)	q	r_0/ρ	Mode I			Mode II		
			λ_1	χ_1	μ_1	λ_2	χ_2	μ_2
0	2.000	0.500	0.500	1.000	−0.500	0.500	1.000	−0.500
$\frac{1}{6}$	1.833	0.455	0.501	1.071	−0.424	0.598	0.921	−0.259
$\frac{1}{4}$	1.750	0.429	0.505	1.166	−0.389	0.660	0.814	−0.145
$\frac{1}{3}$	1.667	0.400	0.512	1.312	−0.354	0.731	0.658	−0.033
$\frac{1}{2}$	1.500	0.333	0.544	1.841	−0.280	0.909	0.219	0.190
$\frac{3}{4}$	1.250	0.200	0.674	4.153	−0.150	1.302	−0.569	0.553

Table R.4 – Constants and exponents as a function of some values of the notch opening angle 2α (Atzori et al., 1999).

R.4 Summary

Stress singularity is present for sharp flaws, while it does not exist for rounded flaw tips. The analytical solution for the stress distribution around the elliptical open flaw tips are commonly found by two approaches.

In the first approach, which is based on the further derivation of the Griffith's stress theory, the initiation of new cracks is not restricted to occur at the flaw tips, but at localities where the highest stress concentration occurs and the material strength is exceeded. The Griffith's stress theory predicts that the crack initiation stress depends on the shape (ratio of the flaw minor axis to the flaw major axis) of the flaw. In common usage for sharp flaws, the minor axis (flaw aperture) is extremely small and is considered constant. Therefore, it is very common simply to consider the effect of flaw length on crack initiation stress. For rounded flaws, however, the minor and major flaw axes have a comparable order of magnitude. Both the magnitude of the flaw length and the radius of curvature of flaw tip have to be taken into account. Note also that the key underlying assumption is the approximation of a straight open flaw as an elliptical opening.

In the second approach, which is based on the conventional treatment of stress fields around sharp flaws, various forms of stress field equations around rounded V-notches are available in the literature. All of them assume that the stress field is dependent on the notch radius ρ and the notch angle α.

R.5 References

Atzori, B., Lazzarin, P. and Tovo, R. (1997) Stress distribution for V-shaped notches under tensile and bending loading. *Fatigue and Fracture Engineering Materials and Structures*, **20**, pp. 1083-1092.

Atzori, B., Lazzarin, P. and Tovo, R. (1999) Stress field parameters to predict the fatigue strength of notched components. *Journal of Strain Analysis*, 34(6), pp. 437-453.

Bhattacharya, S. and kumar, A.N. (1995) Rotational factor using bending moment approach under elasto-plastic situation in 3PB notch geometry. *Engineering Fracture Mechanics*. 50(4), pp.493-505.

Boukharouba, T., Tamine, T., Niu, L., Chehimi, C. and Pluvinage, G. (1995) The use of notch stress intensity factor as a fatigue crack initiation parameter. *Engineering Fracture Mechanics*, 52(3), pp. 503-512.

Chen, C.C. and Pan, H.I. (1978) In: Chen, C. (Ed.) *Collection of Papers on Fracture of Metals* (in Chinese). Metallurgy Industry Press, Beijing, pp. 197-219.

Creager, M. (1966) The elastic stress field near the tip of a blunt crack. *Master Thesis*, Lehigh University.

Creager, M. and Paris, P.C. (1967) Elastic field equations for blunt cracks with reference to stress corrosion cracking. *International Journal of Fracture Mechanics*, **3**, pp. 247-252.

Glinka, G. and Newport, A. (1987) Universal features of elastic notch-tip stress fields. *International Journal of Fatigue*, 9, pp.143-150.

Griffith, A.A. (1924) The theory of rupture. *International Congress of Applied Mechanics, 1st*, Delft, pp. 55-63.

Hoek, E. (1968) Brittle failure of rock. *Rock Mechanics and Engineering Practice*, Wiley & Sons, pp.99-124.

Inglis, C.E. (1913) Stresses in a plate due to the presence of cracks and sharp corners. *Inst. Naval Architecture, London*, 55, pp. 219-230.

Jaeger, J.C. and Cook, N.G.W. (1969) *Fundamentals of Rock Mechanics*. Methuen, London, 513pp.

Kujawski, D. (1991) Estimation of stress intensity factors for small cracks at notches. *Fatigue and Fracture of Engineering Materials and Structures*, 14, pp. 953-065.

Lajtai, E.Z. 1970. A theoretical and experimental evaluation of the Griffith theory of brittle fracture, *Tectonophysics*, 11, pp. 129-156.

Lazzarin, P. and Tovo, R. (1996) A unified approach to the evaluation of linear elastic stress fields in the neighborhood of cracks and notches. *International Journal of Fracture*, 78, pp. 3-19.

Neuber, N. and Weiss, V. (1962). Trans. ASME paper No. 62-WA-270.

Paterson, M.S. (1978) *Experimental Rock Deformation-The Brittle Field*, Springer-Verlag.

Pluvinage G. (1998) Fatigue and fracture emanating from notch; the use of the notch stress intensity factor. *Nuclear Engineering and Design*, 185, pp. 173-184.

Timoshenko, S. and Goodier, J.N. (1951) *Theory of Elasticity*. McGraw-Hill, New York.

Usami, S.I. (1985) In: Tanaka, M., J., Komai, K. (Eds.), Current Research on Fatigue Cracks. The Society of Material Science, Kyoto, Japan, p. 199.

Zhang, S. (1999) Approximate stress intensity factors and notch stresses for common spot-welded specimens. Welding Research Supplement, May, pp.173s-178s.